

REPORT DOCUMENTATION PAGE

*Form Approved
OMB No. 0704-0188*

Public reporting burden for this collection of information is estimated to average 1 hour per response, including the time for reviewing instructions, searching existing data sources, gathering and maintaining the data needed, and completing and reviewing the collection of information. Send comments regarding this burden estimate or any other aspect of this collection of information, including suggestions for reducing this burden, to Washington Headquarters Services, Directorate for Information Operations and Reports, 1215 Jefferson Davis Highway, Suite 1204, Arlington, VA 22202-4302, and to the Office of Management and Budget, Paperwork Reduction Project (0704-0188), Washington, DC 20503.

1. AGENCY USE ONLY (Leave Blank)	2. REPORT DATE May 1998	3. REPORT TYPE AND DATES COVERED Final	
4. TITLE AND SUBTITLE Proceedings of the 1997 IEEE International Symposium on Compound Semiconductors		5. FUNDING NUMBERS G N00014-97-1-0741	
6. AUTHORS Multiple			
7. PERFORMING ORGANIZATION NAME(S) AND ADDRESS(ES) Institute of Electrical and Electronics Engineers, Inc. 445 Hoes Lane, P.O. Box 1331 Piscataway, NJ 08855-1331		8. PERFORMING ORGANIZATION REPORT NUMBER	
9. SPONSORING / MONITORING AGENCY NAME(S) AND ADDRESS(ES) Office of Naval Research Ballston Centre Tower One 800 North Quincy Street Arlington, VA 22217-5660		10. SPONSORING / MONITORING AGENCY REPORT NUMBER	
11. SUPPLEMENTARY NOTES			
12a. DISTRIBUTION / AVAILABILITY STATEMENT APPROVED FOR PUBLIC RELEASE		12b. DISTRIBUTION CODE	
13. ABSTRACT (Maximum 200 words)			
14. SUBJECT TERMS AlAs, AlAs/GaAs, AlGaAs		15. NUMBER OF PAGES 692	
		16. PRICE CODE	
17. SECURITY CLASSIFICATION OF REPORT Unclassified	18. SECURITY CLASSIFICATION OF THIS PAGE Unclassified	19. SECURITY CLASSIFICATION OF ABSTRACT Unclassified	20. LIMITATION OF ABSTRACT UL



Lasers and Electro-Optics Society

12 June 1998

Defense Technical Information Center
8725 John J. Kingman Road
STE 0944
Ft. Belvoir, VA 22060-6218

RE: Grant No. N00014-97-1-0876

Dear Sir/Madam:

In accordance with Grant No. N00014-97-1-0876, Performance Reports and/or Proceedings, Section A and B, Attachment Number 1, please find enclosed one (1) copies of the Proceedings of the 1997 IEEE International Symposium on Compound Semiconductors. A completed "Report Documentation Page" (SF-298) is also included as instructed.

Thank you for your support of this conference.

Sincerely,

A handwritten signature in black ink.

Samantha H. Padilla
IEEE/LEOS Conference Activities Manager

Cc: Grant Administrator, Office of Naval Research
Resident Representative New York
333 Third Avenue, Lower Level
New York, NY 10003-9998

Karen A. Galuchie, IEEE Grants Administrator
IEEE GG232

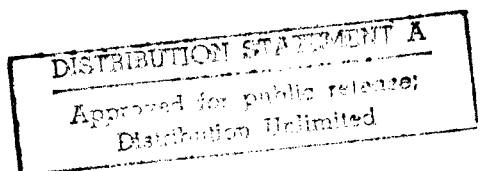


1997 IEEE International Symposium on Compound Semiconductors

Proceedings of the IEEE Twenty-Fourth International Symposium
on Compound Semiconductors held in San Diego, California,
8–11 September 1997

Edited by Mike Melloch and Mark A Reed

*Prior to the 1994 meeting, previous symposia were published as Gallium Arsenide
and Related Compounds in the Institute of Physics Conference Series*



19980619 176



Institute of Physics Publishing, Bristol and Philadelphia

Copyright ©1998 by the Institute of Electrical and Electronics Engineers, Inc.

Copyright and Reprint Permission: Abstracting is permitted with credit to the source. Libraries are permitted to photocopy beyond the limit of U.S. copyright law for private use of patrons those articles in this volume that carry a code at the bottom of the first page, provided the per-copy fee indicated in the code is paid through Copyright Clearance Center, 222 Rosewood Drive, Danvers, MA 01923. For other copying, reprint, or republication permission, write to IEEE Copyrights Manager, IEEE Service Center, 445 Hoes Lane, P.O. Box 1331, Piscataway, NY 08855-1331. All rights reserved.

IEEE Catalog Number: 97TH8272

ISBN 0 7803 3883 9 Hardbound Edition
0 7803 3884 7 Microfiche Edition

Library of Congress Number 97-70758

Published by the Institute of Electrical and Electronics Engineers, 345 East 47th Street, New York, NY 10017, USA, and under licence by Institute of Physics Publishing, wholly owned by The Institute of Physics, London
Institute of Physics Publishing, Dirac House, Temple Back, Bristol BS1 6BE, UK
US Office: Institute of Physics Publishing, The Public Ledger Building, Suite 1035, 150 South Independence Mall West, Philadelphia, PA 19106, USA

Printed in the UK by Galliard (Printers) Ltd, Great Yarmouth, Norfolk

International Symposium on Compound Semiconductors Award and Heinrich Welker Award

The International Symposium on Compound Semiconductors Award was initiated in 1976; the recipients are selected by the International Symposium on Compound Semiconductors Award Committee for outstanding research in the area of III-V compound semiconductors. The Heinrich Welker Award consists of \$5000 and a plaque citing the recipient's contribution to the field. The Award, established by Siemens AG, Munich, honours the foremost pioneer in III-V compound semiconductor development.

The winners of the Symposium Award and the Heinrich Welker Award are:

- | | | |
|------|------------------|--|
| 1977 | Nick Holonyak | for developing the first practical light-emitting diodes |
| 1978 | Cyril Hilsum | for contributions in the fields of transferred electron logic devices (TELDs) and GaAs MESFETs |
| 1980 | Hisayoshi Yanai | for his work on TELDs, GaAs MESFETs and ICs, and laser diode modulation with TELDs |
| 1981 | Gerald L Pearson | for research and teaching in compound semiconductors physics and device technology |
| 1982 | Herbert Kroemer | for his work on hot-electron effects, Gunn oscillators and III-V heterostructure devices |
| 1984 | Izuo Hayashi | for development and understanding of room temperature operation of DH lasers |
| 1985 | Heinz Beneking | for his contributions to III-V semiconductor technology and novel devices |
| 1986 | Alfred Y Cho | for pioneering work on molecular beam epitaxy and his contribution to III-V semiconductor research |
| 1987 | Zhores I Alferov | for outstanding contributions in theory, technology and devices, especially epitaxy and laser diodes |
| 1988 | Jerry Woodall | for introducing the III-V alloy AlGaAs and fundamental contributions to III-V physics |

1989	Don Shaw	for pioneering work on epitaxial crystal growth by chemical vapour deposition
1990	George S Stillmann	for the characterization of high-purity GaAs and developing avalanche photodetectors
1991	Lester F Eastman	in recognition of his dedicated work in the field, especially on ballistic electron transport, δ -doping, buffer layer technique, and AlInAs/GaInAs heterostructures
1992	Harry C Gatos	for his contribution to science and technology of GaAs and related compounds, particularly in relating growth parameters, composition and structure to electronic properties
1993	James A Turner	for pioneering the development of GaAs MESFETs, MMICs, circuit fabrication and analytical techniques
1994	Federico Capasso	for leading work on bandgap engineering of semiconductor devices and discovery of many new phenomena in artificially structured semiconductors
1995	Isamu Akasaki	for his pioneering and outstanding contributions in the field of III-V nitride compound semiconductors
1996	Ben G Streetman	for his seminal contribution to the development of ion implantation techniques for both device fabrication and the study of the properties of nitrogen in ternary alloys, and for pioneering work on microcavity emitters and detectors.

The 1997 Award Committee of the 24th International Symposium on Compound Semiconductors has selected M George Crawford of Hewlett-Packard to receive the award.

M George Crawford was born on 29 December, 1938, in Sioux City, Iowa. He obtained the BA degree in Physics from the University of Iowa in 1961, and the PhD degree in Physics from the University of Illinois in 1967.

Dr Crawford began his professional career in 1967 as a research physicist at Monsanto Chemical Company in St Louis, Missouri. He advanced to the level of Technical Director of the Monsanto Electronics Division in 1974, a position he held until 1979. Initially, his research dealt with the development of optoelectronics materials and devices using a variety of compound semiconductor materials. He later assumed management responsibility of silicon wafer development as well as compound semiconductor materials and device development at Monsanto.



In 1979, Dr Craford joined the Hewlett-Packard Company in Palo Alto, California. He is currently Research and Development Manager in the Optoelectronics Division, responsible for the development of technology and processes for manufacturing visible light emitting diodes (LEDs).

Dr Craford is most well known for his contributions to the development of nitrogen-doped GaAsP technology for yellow and red-orange LEDs developed at Monsanto in the early 1970s. This has become one of the dominant commercial LED technologies. It has for many years been common in products such as digital clocks and radio displays, displays used in electronic measurement devices and test equipment, indoor large area message signs and for a wide variety of other commercial products.

At Hewlett-Packard, Dr Craford and his group have maintained a leadership position in LED performance and production technology with the introduction of AlInGaP devices, which have brighter luminous efficiencies than incandescent lamps.

Dr Craford is a Fellow of the IEEE and a member of the National Academy of Engineering. He has also received the IEEE Morris N Liebmann Award and the Electronics Division Award of the Electrochemical Society. He has published over fifty papers and book chapters, has given invited and plenary talks at a variety of conferences, and holds several commercially important patents. His IEEE activities have included serving on the Program Committee of the IEEE Device Research Conference, as associate editor of the *IEEE Transactions on Electron Devices*, as member and chairman of the IEEE Jack A Morton Technical Field Award Committee, and as a member of the IEEE Electron Devices Society AdCom.

Dr Craford and his wife, Carol, reside in Los Altos Hills, California. They have two children, David and Stephen. His nonprofessional interests include cycling, tennis, hiking, and rock climbing.

Young Scientist Award

The International Advisory Committee of the International Symposium on Compound Semiconductors has established a Young Scientist Award to recognize technical achievements in the field of compound semiconductors by a scientist under the age of forty. The Award consists of a financial reward of \$1000 and a plaque citing the recipient's contribution. This year's Award Fund is provided by EPI.

The Young Scientist Award recipients are:

- | | |
|------------------------|--|
| 1986 Russel D Dupuis | for work in the development of organometallic vapour phase epitaxy of compound semiconductors |
| 1987 Naoki Yokoyama | for contributions to self-aligned gate technology for GaAs MESFETs and ICs and the resonant tunnelling hot-electron transistor |
| 1989 Russel Fischer | for demonstration of state of the art performance, at DC and microwave frequencies, of MESFETs, HEMTs and HBTs using (AlGa)As on Si |
| 1990 Yasuhiko Arakawa | for pioneering work on low-dimensional semiconductor lasers, showing the superior performance of quantum wire and quantum box devices |
| 1992 Umesh K Mishra | for pioneering and outstanding work on AlInAs-GaInAs HEMTs and HBTs |
| 1993 Young-Kai Chen | for significant advancements in the fields of high-speed III-V electronic and optoelectronic devices |
| 1994 Michael A Haase | for contributions on II-VI based blue LEDs and ZnSe-based electro-optic modulators |
| 1995 John D Ralston | for pioneering and outstanding contributions in the field of high-speed high-power semiconductor lasers |
| 1996 Nikolai Ledentsov | for his pioneering and outstanding contribution to the development of physics and MBE growth of InGaAs-GaAs quantum dots and quantum dot lasers. |



The 1997 Award Committee of the 24th International Symposium on Compound Semiconductors has selected Fred Kish, R&D Project Manager, in the Optoelectronics Division of Hewlett-Packard Company, San Jose, CA, for the Young Scientist Award.

Fred A Kish Jr was born in Charlotte, NC, in 1966. He received his BS degree in Electrical Engineering with Highest Honors in 1988, and his MS and PhD degrees in Electrical Engineering in 1989 and 1992, respectively, all from the University of Illinois at Urbana-Champaign. At the University of Illinois, he studied under the direction of Professor Nick Holonyak Jr, performing research on native oxides formed from Al-bearing III-V compound semiconductors with applications to semiconductor laser diodes. This work resulted in the discovery that such native oxides could be employed to form waveguides and index-guided laser diodes.

In 1992, Dr Kish joined the Materials Research and Development Department of Hewlett-Packard Company's Optoelectronics Division. At Hewlett-Packard, he co-invented new techniques for the direct wafer bonding of compound semiconductors which led to the realization and subsequent commercial introduction of high-efficiency wafer-bonded transparent-substrate AlGaInP LEDs (the highest efficiency commercial LEDs in the yellow through red spectral regime). For this work, he was awarded the Adolph Lomb Medal from the Optical Society of America in 1996.

Currently, Dr Kish is project manager of a group focused on developing new compound semiconductor wafer-bonding techniques and high-power, high-efficiency visible-spectrum LEDs. He holds over 10 US patents and has co-authored over 35 peer-reviewed publications.

Preface

The 24th International Symposium on Compound Semiconductors (ISCS) was held 8–11 September 1997 at the Hotel del Coronado in San Diego, California. A total of 160 papers were selected from over 250 submissions from 18 countries for 123 oral and 37 poster presentations. In addition, there were two plenary and 16 invited papers presented. The plenary speakers were Lou Tomasetta of Vitesse Semiconductor who spoke on ‘Commercialization of the Semiconductor of the Future’ and Shuji Nakamura from Nichia Chemical Industries who spoke on ‘III–V Nitride Based Blue/Green LEDs and LDs’.

The chapters are organized by subject. You will find that there are substantial cross-links between them, so we hope you will roam through this digest and utilize the many fine papers for your research.

The 1998 ISCS will be held in Nara, Japan, from 12–16 October 1998, the 1999 ISCS will be held in Berlin, Germany, and then it will return to the United States in 2000.

We would like to thank Herb Goronkin of Motorola who served as the Symposium Chair, the Technical Program Committee for reviewing the abstracts and constructing a high-quality symposium, those who served as session chairs, and we would especially like to thank Melissa Estrin of IEEE/LEOS for her valuable help.

Mark A Reed
Yale University
Technical Program Chair

Mike Melloch
Purdue University
Associate Program Chair

Sponsors

The organizers of the symposium gratefully acknowledge the sponsors for their generous contribution

Motorola
Office of Naval Research
Siemens
Aixtron
EPI

Symposium Committees

Organizing Committee

Herb Goronkin (*Symposium Chair*), Mark Reed (*Program Chair*), Mike Melloch (*Associate Program Chair*), Don Wolford (*Secretary*), Jim Harris (*Treasurer*), Ben Streetman (*Awards Chair*), Marie Meyer (*Publicity Chair*)

International Committee Representatives

L Ralph Dawson, Vassilis Keramidas, Donald Shaw

Committee Members

Alfred Y Cho, Jim Harbison, Michael Spencer, George Crawford, Vassilis G Keramidas, Gerry Stringfellow, Mike Haas, Umesh Mishra, Jerry Woodall

International Advisory Committee

Greg Stillman (*Chair*), Toshiaki Ikoma, Donald Shaw, Zhores Alferov, Vassilis G Keramidas, Takuo Sugano, Aristos Christou, Tsuneo Nakahara, Bryan L H Wilson, L Ralph Dawson, Yoon-Soo Park

Technical Program Sub-Committee Members

Characterization

R Feenstra (*Chair*), T Kuech, M Lagally, D Wolford

Epitaxy and In-Situ Processing

L R Dawson (*Chair*), A Brown, A Cho, R Dupuis, J Harbison, T Mayer, C Palmstrom, J Roth, G Stringfellow, R Tsui, C Tu, J Woodall

Heterostructure Transistors

P Asbeck (*Chair*), J Abrokwah, K Ismail, E Kohn, U Mishra

OEICs and Heterostructure ICs

D Miller (*Chair*), P Bhattacharya, J E Cunningham, T Ishii, Yoon-Soo Park, G Sollner

Processing

Evelyn Hu (*Chair*), A Forchel, K Kavanagh, L Rea, G Traenkle

Quantum Effect Materials and Devices

A Seabaugh (*Chair*), J Allen, S Luryi, G Maracas, L Pfeiffer, L Samuelson, S Tarucha, G Weimann, N Yokoyama

Simulation and Modelling

W Frensliey (*Chair*), K Hess, M Hybertsen, L Sham, J Shen, A Zunger

Visible Emitters

J-M Xu (*Chair*), M G Crawford, S DenBaars, L Guido, M Haas

Wide Bandgap Materials and Devices

J Cooper (*Chair*), H Matsunami, M Spencer and K Moor

Contents

International Symposium On Compound Semiconductors Award and Heinrich Welker Award	v
Young Scientist Award	viii
Preface	xi
Sponsors	xii
Symposium Committees	xiii

Chapter 1: Plenary Paper

III-V nitride-based blue LDs with modulation-doped strained-layer superlattices <i>S Nakamura</i>	1
--	---

Chapter 2: Epitaxy

Growth and doping of β -GaN and β -(In,Ga)N films and heterostructures <i>O Brandt, B Yang, H Yang, J R Müllhäuser and K H Ploog</i>	5
Growth and effects of single-crystalline ZnO buffer layer on GaN epitaxy <i>T F Huang, T Ueda, S Spruytte and J S Harris Jr</i>	11
GaN/GaAs(111)B grown by molecular beam epitaxy using hydrazine <i>V G Antipov, A I Guriev, V A Elyukhin, N N Faleev, Yu A Kudriavtsev, A B Lebedev, T V Shubina, A S Zubrilov, S A Nikishin and H Temkin</i>	15
Demonstration of a GaAs-based compliant substrate using wafer bonding and substrate removal techniques <i>C Zhang, D I Lubyshev, W Cai, J E Neal, D L Miller and T S Mayer</i>	25
Comparison of MBE grown InSb on CU substrates using different sacrificial layers <i>M L Seaford, D H Tomich, K G Eyink, W V Lampert, F E Ejeckam and Y-H Lo</i>	29
Modeling MBE RHEED signals using PCA and neural networks <i>T Brown, K Lee, G Dagnall, R Kromann, R Bicknell-Tassius, A Brown, J Dorsey and G May</i>	33
Multicomponent Sb-based solid solutions grown from Sb-rich liquid phases <i>V A Mishurnyi, F de Anda, A Yu Gorbachev, V I Vasil'ev, V M Smirnov and N N Faleev</i>	37

Suppression of dopant redistribution in AlGaAs/GaAs laser-HEMT structures for optoelectronic transmitters grown by molecular beam epitaxy <i>A Gaymann, M Maier, K Köhler, W Bronner, F Grotjahn, J Hornung and M Ludwig</i>	41
Wavelength tunable UV laser stimulated growth of $\text{Al}_x\text{Ga}_{1-x}\text{As}$ by OMVPE <i>A Wankerl, D T Emerson, M J Cook and J R Shealy</i>	45
MBE growth of metamorphic In(Ga)AlAs buffers <i>M Sexl, G Böhm, M Maier, G Tränkle, G Weimann and G Abstreiter</i>	49
Results of 3" and 4" low-gradient s.i. GaAs growth under controlled vapor pressure <i>M Neubert, P Rudolph and M Seifert</i>	53
Impact of growth interruption on interface roughness of MOCVD grown InGaAs/InAlAs studied by photoreflectance spectroscopy <i>C Bru-Chavallier, Y Baltagi, G Guillot, K Hong and D Pavlidis</i>	57
RF sputtered $\text{Cu}_x\text{Cd}_{1-x}\text{Te}$ thin films: a novel semiconductor alloy <i>S López-López, S Jiménez-Sandoval, B S Chao and M Meléndez-Lira</i>	61
Patterned high-index substrates as templates for novel quantum-wire and dot arrays: growth and potential applications <i>R Nötzel, M Ramsteiner, Z Niu, L Däweritz and K H Ploog</i>	65
A new self-limited growth for the fabrication of atomically uniform quantum wires and quantum dots <i>X-L Wang, M Ogura and H Matsuhata</i>	71
Fabrication of InGaAs quantum wire structures by As_2 flux in molecular beam epitaxy <i>T Sugaya, Y Tanuma, T Nakagawa, Y Sugiyama and K Yonei</i>	75
Extremely high conductivities in modulation-doped GaAs and (GaIn)As quantum wells with AlAs/GaAs type-II-superlattice barriers <i>K-J Friedland, R Hey, H Kostial and K H Ploog</i>	79
Fabrication of resonant interband tunneling diode using resistless lithography and selective area epitaxy <i>K Shiraliagi, R Tsui and H Goronkin</i>	83
Ordered incorporation of dopants in GaAs: a new route to overcome solubility limits <i>L Däweritz, P Schützendübe, M Reiche and K H Ploog</i>	87
Low-temperature growth and characterization of silicon delta doped GaInP/GaInAs/GaAs pseudomorphic heterostructures for use in high electron mobility transistors <i>J A Smart, E M Chumbes, L F Eastman and J R Shealy</i>	91

Optimization of group V switching times for InGaP/GaAs heterostructures grown by LP-MOCVD <i>Q Yang, Q J Hartmann, A P Curtis, C Lin, D A Ahmari, D Scott, H C Kuo, H Chen and G E Stillman</i>	95
Solid source molecular beam epitaxy of $\text{Ga}_x\text{In}_{1-x}\text{As}_y\text{P}_{1-y}$ materials for 1.3 μm lasers <i>J N Baillargeon, W-Y Hwang, S N G Chu and A Y Cho</i>	99
Enhanced optical crystal quality of strain-compensated InGaAs/InGaAsP quantum-well structures on GaAs substrates by the introduction of intermediate-strain layers <i>K Hiramoto, M Sagawa, S Fujisaki and T Toyonaka</i>	103
1.3 μm wavelength GaInAsP/InP distributed feedback lasers grown directly on grating substrates by solid source molecular beam epitaxy <i>W-Y Hwang, J N Baillargeon, S N G Chu, P F Sciortino and A Y Cho</i>	109
The growth of mid-infrared emitting InAsSb/InAsP strained-layer superlattices using metalorganic chemical vapor deposition <i>R M Biefeld, A A Allerman, S R Kurtz and J H Burkhardt</i>	113
MOCVD growth of $(\text{Ga}_{1-x}\text{In}_x\text{As}-\text{GaAs}_{1-y}\text{Sb}_y)$ superlattices on InP showing type-II emission at wavelengths beyond 2 μm <i>M Peter, K Winkler, N Herres, F Fuchs, S Müller, K-H Bachem and J Wagner</i>	117
MBE growth and optical investigation of GaSb/AlSb VCSEL structures for the 1.5 μm range <i>J Koeth, R Dietrich and A Forchel</i>	121
Incorporation of thallium in InTlAs and GaTlAs grown by molecular beam epitaxy <i>D I Lubyshev, W Z Cai, G L Catchen, T S Mayer and D L Miller</i>	125
Electronic properties of MBE grown GaAs homointerfaces fabricated using the As cap deposition/removal technique <i>M Passlack, R Droopad, Z Yu, C Overgaard, B Bowers and J Abrokwhah</i>	131
Arsenic precipitation in GaAs for single-electron tunneling applications <i>C-Y Hung, J S Harris Jr, A F Marshall and R A Kiehl</i>	135
GaAs surface passivation with MBE grown GaS thin film <i>N Okamoto, N Hara, M Yokoyama and H Tanaka</i>	139
Simulation of chemical beam epitaxy with triethylgallium and tris(dimethylamino)arsine <i>B Q Shi and C W Tu</i>	143
A comprehensive atomic-level simulator for AlGaAs/GaAs (001) MBE <i>D L Dorsey, K Mahalingam and R Venkat</i>	147

One-step selective growth of GaAs on V-groove patterned GaAs substrates using CBr ₄ and CCl ₄ <i>E K Kim, T-G Kim, C-S Son, S-I Kim, Y K Park, Y Kim, S-K Min and I-H Choi</i>	151
Growth and characterization of thick epitaxial GaAs layers <i>H Samic, J C Bourgoain, B Pajot, R Bisaro, C Grattepain, K Khirouni, M Putero and N Burle</i>	155
Chapter 3: Characterization	
Structural and electrical characterization of epitaxial DyP/GaAs and DyAs/GaAs grown by MBE <i>P P Lee, R J Hwu, L P Sadwick, H Balasubramaniam, B R Kumar, T C Lai, S N G Chu, R Alvis, R T Lareau and M C Wood</i>	159
PIN photodiodes using nitrogen ion implantation on ZnSe/GaAs heterostructure <i>H Hong, W A Anderson, S Nagarathnam, A N Cartwright, E H Lee, H C Chang, M H Na and H Luo</i>	163
Band offset measurement of the ZnS/Si(001) heterojunction <i>B Brar, R Steinhoff, A Seabaugh, X Zhou, S Jiang and W P Kirk</i>	167
(Pd, Ti, Au)-based ohmic contacts to p- and n-doped In _{0.53} Ga _{0.47} As <i>W K Chong, E F Chor, C H Heng and S J Chua</i>	171
PtTiPtAu and PdTiPtAu ohmic contacts to p-InGaAs <i>J S Yu, S H Kim and T I Kim</i>	175
Low-temperature formation of low-resistivity W contact with ultra-thin mixed layer on molecular layer epitaxially-grown GaAs <i>F Matsumoto, J-I Nishizawa, Y Oyama, P Plotka, Y Oshida and K Suto</i>	179
Electrical and optical anisotropy of layered In ₂ Se ₃ epitaxial films <i>T Ohtsuka, T Okamoto, A Yamada and M Konagai</i>	183
Bandgap renormalization studies of n-type GaAs/AlGaAs single quantum wells <i>E D Jones, M Blount, W Chow, H Hou and J A Simmons</i>	187
Magnetoluminescence measurement of Zeeman and exchange interactions of excitons in GaAs/AlGaAs multiple quantum wells <i>Y A Leem, H S Ko, W S Kim, Y S Kim, D H Kim, T Schmiedel, C E Yun, H M Pyo and J C Woo</i>	191
Lateral confinement and inter-wire coupling of exciton in 4–16 nm wide GaAs/AlGaAs quantum wires observed by magentoluminescence <i>W S Kim, Y A Leem, Y S Kim, H S Ko, D H Kim, C E Yun, H M Pyo, T Schmiedel and J C Woo</i>	195
Extremely sharp Er-related luminescence in Er-doped GaP grown by OMVPE with TBP <i>Y Fujiwara, T Ito, H Ofuchi, J Tsuchiya, A Tanigawa, M Tabuchi and Y Takeda</i>	199

Trap-mediated, site-selective excitation of photoluminescence from multiple Er ³⁺ sites in Er-implanted GaN <i>S Kim, S J Rhee, X Li, J J Coleman, S G Bishop and P B Klein</i>	203
Gain spectra measurement of InGaAsP/AlGaAs laser structures for wavelengths near 800 nm using a new variable stripe length method <i>A Oster, F Bugge, G Erbert and H Wenzel</i>	207
Electronic and vibrational Raman scattering in resonance with yellow luminescence transitions in GaN on sapphire substrate <i>D S Jiang, M Ramsteiner, O Brandt, K H Ploog, H Tews, A Graber, R Averbeck and H Riechert</i>	211
Temperature dependence of photoluminescence in Mg-doped GaN epilayers grown by MOCVD <i>E-J Shin, A K Viswanath, J I Lee, N W Song, D Kim, B Kim, Y Choi and C-H Hong</i>	215
Impact of GaN buffer growth conditions on photoluminescence and x-ray diffraction characteristics of MOVPE grown bulk GaN <i>A Eisenbach, D Pavlidis, A Phillippe, C Bru-Chevallier and C Dubois</i>	219
X-ray photoelectron diffraction study of hexagonal GaN(0001) thin films <i>R Denecke, J Morais, J Liesegang and C S Fadley</i>	223
Energy gap bowing and refractive index spectrum of AlInN and AlGaInN <i>J Piprek, T Peng, G Qui and J O Olowolafe</i>	227
Optical and structural characterization of InGaN quantum-well heterostructures grown by metalorganic chemical vapor deposition <i>R D Dupuis, P A Grudowski, C J Eiting, I C Shmagin, R M Kolbas and S J Rosner</i>	231
Optical transitions and dynamic processes in III-nitride epilayers and multiple quantum wells <i>K C Zeng, M Smith, J Y Lin, H X Jiang, A Salvador, G Popvici, H Tang, W Kim, H Morkoc and M A Khan</i>	235
On the nature of radiative recombination processes in GaN <i>C Wetzel, H Amano and I Akasaki</i>	239
STM imaging of Be delta doped layers in GaAs <i>P M Koenraad, M B Johnson, H W M Salemink and J H Wolter</i>	245
Characterization of the interfacial electronic properties of oxide films on GaAs fabricated by in-situ molecular beam epitaxy <i>J S Hwang, W Y Chou, G S Chang, S L Tyan, M Hong, J P Mannaerts and J Kwo</i>	249
Structural and device properties of DFB-LD with lateral undulation of SL-MQW <i>H M Kim, J S Kim, D K Oh, H R Choo, H M Kim and K E Pyun</i>	255
XSTM characterization of GaSb/InAs heterojunctions: observation of white noise in the interface roughness spectrum <i>J Harper, M Weimer, D Zhang, C-H Lin and S S Pei</i>	259

Monolayer scale analysis of ZnSe/GaAs heterointerface structures by x-ray CTR scattering and interference <i>Y Takeda, K Fujita, M Tabuchi, M Funato, S Aoki, Sz Fujita and Sg Fujita</i>	263
Ballistic electron transport in semiconductor superlattices <i>G Strasser, C Rauch, K Kempa and E Gornik</i>	267
Photoluminescence from GaN implanted with isoelectronic phosphorus and bismuth <i>W M Jadwisienczak and H J Lozykowski</i>	271
Magnetoresistance and cyclotron mass in extremely-coupled double quantum wells under in-plane magnetic fields <i>M A Blount, J A Simmons, S K Lyo, N E Harff and M V Weckwerth</i>	275
Band offsets in near-GaAs alloys <i>M F Whitaker, D J Dunstan and M Hopkinson</i>	279
Time-resolved photoluminescence of ZnS_xSe_{1-x} ($0 \leftarrow x \leftarrow 0.12$) epilayers on GaAs grown by MBE <i>E-J Shin, J I Lee, D Kim, J-S Son, J-Y Leem, S K Noh and D Lee</i>	283
Whole wafer characterization of large size GaAs-AlGaAs semiconductor materials prepared by MOCVD TurboDisc TM technology <i>Z C Feng, E Armour, A G Thompson and R A Stall</i>	287
Structural and optical properties of very high-quality GaAs/AlGaAs multiple quantum well structures grown on (111)A substrates by MOVPE <i>A Sanz-Hervás, S Cho, O V Kovalenkov, S A Dickey, A Majerfeld, C Villar, M López, R Melliti, G Wang, P Tronc and B W Kim</i>	291
Study of photoexcited carriers in semi-insulating InP by means of Raman spectroscopy <i>L Artús, R Cruscó, J Ibáñez and G González-Díaz</i>	295
Photocapacitance investigation of stoichiometry-dependent deep levels in InP <i>Y Oyama, J Nishizawa, K Kim and K Suto</i>	299
Photoconduction studies on InGaAs HEMTs <i>F Schuermeyer, D Cheskis, R S Goldman and H H Wieder</i>	303
Hydrogenation effect of InGaP grown on GaAs by molecular beam epitaxy <i>M D Kim, H S Park, T I Kim, J Y Lee, Y H Kwon, D Y Kim and H Y Cho</i>	307
Fourier transform infrared spectroscopy (FTIR), SIMS and Raman scattering of heavily carbon doped MOCVD grown $In_{0.53}Ga_{0.47}As$ <i>A Sibai, F Ducroquet, K Hong, D Cui and D Pavlidis</i>	311
Raman spectroscopy of $InAs_{1-x}Sb_x/InSb$ and $InAs_{1-x}Sb_x/InAs$ superlattices, under hydrostatic pressure <i>S J Webb, R A Stradling and K Nagata</i>	315

Chapter 4: Processing

Growth of $\text{Ga}_2\text{O}_3(\text{Gd}_2\text{O}_3)$ using molecular beam epitaxy technique—key to first demonstration of GaAs MOSFETs <i>M Hong, F Ren, W S Hobson, J M Kuo, J Kwo, J P Mannaerts, J R Lothian, M A Marcus, C T Liu, A M Sergent, T S Lay and Y K Chen</i>	319
Kinetics of AlAs steam oxidation at low pressure and low temperature measured in-situ using a novel furnace design with an integral optical port <i>S A Feld, J P Loehr, R E Sherriff, J Wiemer and R Kaspi</i>	325
Localized intermixing of AlAs and GaAs layers for lithographic control of the lateral oxidation of AlAs <i>A R Massengale, C Y Tai, M D Deal, J D Plummer and J S Harris Jr</i>	329
Improved PL intensity of InGaAs/GaAs SQW with a selectively oxidized AlAs layer <i>T Takamori, A R Pratt and T Kamijoh</i>	333
In-situ monitoring of the selective etching of antimonides in GaSb/AlSb/InAs heterostructures using Raman spectroscopy <i>C Gatzke, S J Webb, K Fobelets and R A Stradling</i>	337
Low-frequency noise in dry and wet etched InAlAs/InGaAs HEMTs <i>H C Duran, L Ren, M Beck, M A Py, M Illegems and W Bächtold</i>	341
Fabrication of integrated twin-guide corner reflector surface-emitting lasers with reactive ion-beam etching <i>S-K Hong and Y-S Kwon</i>	345
Selective and non-selective etching of GaN, AlGaN and AlN using an inductively coupled plasma <i>S A Smith, C A Wolden, M D Bremser, A D Hanser, R F Davis and W V Lampert</i>	349
Focused ion beam assisted ohmic metallizations to p-6H-SiC <i>A A Iliadis, S N Andronescu, V Talyansky, K Edinger, J H Orloff, M S Woods and K A Jones</i>	353

Chapter 5: High-power Semiconductor Devices

Silicon carbide power MOSFET technology <i>J B Casady, A K Agarwal, L B Rowland, S Seshadri, R R Siergiej, D C Sheridan, S Mani, P A Sanger and C D Brandt</i>	359
100V 4H-SiC gate turn off (GTO) thyristor <i>R R Siergiej, J B Cassidy, A K Agarwal, L B Rowland, S Seshadri, S Mani, P A Sanger and C D Brandt</i>	363

Chapter 6: Emitters and Optoelectronics

MOCVD growth of InGaN multiple quantum well LEDs and laser diodes <i>M P Mack, A C Abare, P Kozodoy, M Hanson, S Keller, U K Mishra, L A Coldren and S P DenBaars</i>	367
ECR-MBE growth and high excitation properties of GaInN/GaN heterostructures <i>J Müller, M Lipinski, A Maksimov and A Forchel</i>	371
Optical metastability in InGaN/GaN heterostructures <i>I K Shmagin, J F Muth, R M Kolbas, R D Dupuis, P A Grudowski, C J Eiting, J Park, B S Shelton and D J H Lambert</i>	375
Carrier transport mechanisms in organic electroluminescent devices <i>J-H Xu, J Shen, F So, M Kim and H-C Lee</i>	379
Monolithic integration of a GaInAs PIN photodiode and AlGaAs/GaAs/AlGaAs HEMTs on GaAs substrate <i>W Bronner, W Benz, M Dammann, P Ganser, N Grün, V Hurm, T Jakobus, K Köhler, M Ludwig and E Olander</i>	383
Ion implanted GaAs/InGaAs lateral injection ridge QW laser for OEICs: study of operation mechanisms <i>A A Tager, R Gaska, I A Avrutsky, M Fay, H Chik, A SpringThorpe, Z Husain, J M Xu and M Shur</i>	387
Avalanche multiplication in sub-micron Al _x Ga _{1-x} As/GaAs heterostructures <i>C K Chia, J P R David, G J Rees, S A Plummer, M Hopkinson, R Grey and P N Robson</i>	391
MBE growth of near-infrared InGaAs photodetectors with carbon tetrabromide as a p-type dopant <i>D I Lubyshev, J Neal, W Z Cai, M Micovic, T S Mayer and D L Miller</i>	395
Studies of the effects of multi-stack multiquantum barrier on the properties of 1.3 μm AlGaInAs/InP quantum well lasers <i>J-W Pan, J-I Chyi, Y-K Tu and J-W Liaw</i>	401
Characteristics of native-oxide confined InGaP/(Al _x Ga _{1-x}) _{0.5} In _{0.5} P quantum well visible laser diodes <i>D Sun and D W Treat</i>	405
InGaAs/InP p-i-n heterostructure photodiode arrays on AlGaAs/GaAs waveguide films by solid source molecular beam epitaxy <i>S-H Hsu, F G Johnson, S A Tabatabaei, S Agarwala, J V Hryniwicz, F J Towner, Y J Chen and D R Stone</i>	409
Reduced radiative currents from GaAs/InGaAs and AlGaAs/GaAs p-i-n quantum well devices <i>J Nelson, J Barnes, N Ekins-Daukes, K W J Barnham, B Kluftinger, E S M Tsui, C T Foxon, T S Cheng and J S Roberts</i>	413

The influence of internal mechanical stresses on the GaAs light-emitting diodes <i>V G Sidorov, V I Sokolov and D V Sidorov</i>	417
Chapter 7: Heterojunction Transistors	
Wide bandgap semiconductor RF power devices <i>C E Weitzel</i>	421
High-speed high-power AlGaN/GaN heterostructure field effect transistors with improved ohmic contacts <i>K K Chu, M J Murphy, J Burm, W J Schaff, L F Eastman, A Botchkarev, H Tang and H Morkoç</i>	427
AlGaN/GaN MODFETs with low ohmic contact resistances by source/drain n ⁺ regrowth <i>Y-F Wu, D Kapolnek, P Kozodoy, B Thibeault, S Keller, B P Keller, S P Denbaars and U K Mishra</i>	431
Wide bandgap collectors in GaInP/GaAs heterojunction bipolar transistors with increased breakdown voltage <i>R M Flitcroft, B C Lye, H K Yow, P A Houston, C C Button and J P R David</i>	435
Improved high-frequency performance by composite emitter AlGaAs/GaInP heterojunction bipolar transistors fabricated using chemical beam epitaxy <i>J-W Park, D Pavlidis, S Mohammadi, C Dua and J C Garcia</i>	439
Saturation charge storage measurements in GaInP/GaAs/GaAs and GaInP/GaAs/GaInP HBTs <i>P F Chen, Y M Hsin and P M Asbeck</i>	443
Low-frequency noise characterization of high- and low-reliability AlGaAs/GaAs single HBTs <i>S Mohammadi, D Pavlidis and B Bayraktaroglu</i>	447
High-gain AlGaAs/GaAs HBTs grown by MOCVD <i>R E Welser, N Pan, D P Vu, M A Knowles, I Taulanada, J G Miller and G E Stillman</i>	451
Pd/Ge-based ohmic contacts to n-InGaAs and n-GaAs for heterojunction bipolar transistors <i>I-H Kim, S H Park, T-W Lee, M P Park, B R Ryum, K E Pyun and H-M Park</i>	455
An Au/Pt/Ti/WN _x ohmic contact to n-InGaAs and its application to AlGaAs/GaAs HBTs <i>S H Park, I-H Kim, T-W Lee and M-P Park</i>	459
Real space transfer noise of GaAs p-HEMTs <i>M Feng, D Caruth, S K Hsia and J A Fendrich</i>	463

PdGe on GaAs: a study of the applicability in InGaP/GaAs HBT fabrication <i>D A Ahmari, M L Hattendorf, D F Lemmerhirt, Q Yang, Q J Hartmann and G E Stillman</i>	467
An investigation of breakdown in power HEMTs and MESFETs utilising an advanced temperature-dependent physical model <i>L Albasha, R G Johnson, C M Snowden and R D Pollard</i>	471
Ultra-linear pseudomorphic HEMTs for wireless communications: a simulation study <i>Z Borsosfoldi, D R Webster, I G Thayne, A Asenov, D G Haigh and S P Beaumont</i>	475
GaAs homojunction phototransistor with minority carrier transport assisted by photo-generated carrier profile in the base <i>J Ohsawa, S Yamaguchi, K Saigoh and M Migitaka</i>	479
Metamorphic HFETs with composite $In_{0.8}Ga_{0.2}As/InAs/In_{0.8}Ga_{0.2}As$ channels on GaAs substrate <i>C Karlsson, N Rorsman, S Wang and M Persson</i>	483
A novel high-performance WSi-gate self-aligned N-AlGaAs/InGaAs/N-AlGaAs pseudomorphic double heterojunction MODFET by ion implantation <i>K Nishii, M Nishitsuji, T Uda, T Yokoyama, S Yamamoto, T Kunihisa and A Tamura</i>	487
Novel applications of HEMTs for future 4.2K low-power and low-frequency cryoelectronics <i>Y Jin</i>	491
Influence of backside doping on the nonlinear capacitances of a PHEMT affecting the VCO frequency characteristics <i>H Brech, T Grave, A Werthof, H-J Siweris, T Simlinger and S Selberherr</i>	495
Photoinduced instability in microwave excited GaAs MESFETs <i>E Y Lan, J H Huang, J Blaugh and E Schirmann</i>	499
Optimization of the doping levels in doubly doped InAlAs/InGaAs HEMTs <i>S Kraus, M Sexl, G Böhm, G Tränkle and G Weimann</i>	503
500°C operation of GaAs-based HFET containing low temperature grown GaAs and AlGaAs <i>K M Lipka, P Schmid, N Nguyen, L L Pond, C E Weitzel, U Mishra and E Kohn</i>	507
Ultra-low-power (< 2mW) noise performance of InGaP/GaAs HBT <i>D W Barlage, M S Heins, J H Mu, M T Fresina, D A Ahmari, Q J Hartman, G E Stillman and M Feng</i>	511
DHBT/RTD-based active frequency multiplier for wireless communications <i>H J De Los Santos, K Chui, D H Chow and H L Dunlap</i>	515

Chapter 8: Nanoelectronics and Nanophotonics

Optical and microscopic properties of In _{0.5} Ga _{0.5} As/GaAs highly strained heterostructures <i>A Polimeni, M Henini, L Eaves, S T Stoddart, P C Main, R K Hayden, K Uchida and N Miura</i>	519
Strain tensor, electronic spectra and carrier dynamics in In(Ga)As/GaAs self-assembled quantum dots <i>K Kamath, H Jiang, D Klotzkin, J Phillips, T Sosnowski, T Norris, J Singh and P Bhattacharya</i>	525
Positioning on InAs quantum dots on sub-250 nm facets using selective area epitaxy <i>R Tsui, R Zhang, K Shiralagi and H Goronkin</i>	531
Increased surface ordering on InAs island arrays using a multidot column subsurface structure <i>S A Komarov, G S Solomon and J S Harris Jr</i>	535
Electron transport through tetrahedral-shaped recess (TSR) stacked double quantum dot structures <i>M Shima, Y Sakuma, C Wirner, T Strutz, E Taguchi, T Futatsugi, Y Awano and N Yokoyama</i>	539
Electronic states in quantum dots: Effects of symmetry of the confining potential <i>T Ezaki, Y Sugimoto, N Mori and C Hamaguchi</i>	543
Fabry–Perot and vertical cavity surface emitting InAs quantum dot lasers <i>D Bimberg, N N Ledentsov, M Grundmann, F Heinrichsdorff, V M Ustinov, P S Kop'ev, Zh I Alferov and J A Lott</i>	547
Microcavity lasers: emission from a fully confined photon state <i>J P Reithmaier, M Röhner, F Schäfer, H Zull and A Forchel</i>	553
Subband structure of GaAs coupled quantum wires on V-grooved substrate <i>K Komori, X-L Wang, M Ogura, H Matuhata and A Hamoudi</i>	557
Micromachined tunable vertical cavity lasers as wavelength selective tunable photodetectors <i>F Sugihwo, C-C Lin, J-C Bouteiller, M Larson and J S Harris Jr</i>	561
Characterization of GaAs/AlGaAs mid-infrared emitters <i>L Hvozdara, J N Heyman, G Strasser, K Unterrainer, P Kruck, M Helm and E Gornik</i>	565
Multi-staged, InAsSb mid-infrared lasers and light-emitting diodes, grown by MOCVD <i>S R Kurtz, A A Allerman, R M Biefeld and K C Baucom</i>	569
GaP–Al _x Ga _{1-x} P waveguide Raman lasers and amplifiers for optical communication <i>K Suto, T Kimura, T Saito, A Watanabe and J Nishizawa</i>	573

Atomic force microscope nanoscale lithography for single-electron device applications <i>Y Okada, S Amano, M Kawabe, B N Shimbo and J S Harris Jr</i>	577
Comparison of the effects of different lateral boundary conditions on transport in resonant tunneling diodes <i>A T Hunter and J N Schulman</i>	581
Model of intra and extracavity photodetection for planar resonant cavity light emitting diodes <i>J A Lott and M J Noble</i>	585
Photoluminescence study of the self-organized InAs/GaAs quantum dots grown by gas source molecular beam epitaxy <i>M-C Chen and H-H Lin</i>	589
Resonant interband tunneling through multiple subbands in an InAs/AlSb/GaSb interband tunneling structure <i>J L Huber, M A Reed, G Kramer and H Goronkin</i>	593
Quasi one-dimensional confinement in double-well sidewall gated resonant tunneling transistors <i>V R Kolagunta, D B Janes, M R Melloch and C Youtsey</i>	597
Ultralow-current density RTDs for tunneling-based SRAM <i>J P A Van der Wagt, A C Seabaugh, G Klimeck, E A Beam III, T B Boykin, R C Bowen and R Lake</i>	601
Analysis of heterojunction interband tunneling diodes for MMICs <i>N El-Zein, G Maracas, V Nair, G Kramer and H Goronkin</i>	605
Microwave noise properties for resonant tunneling transistors (RTTs) <i>Y Ando, W Contrata, K Maruhashi and H Miyamoto</i>	609
Photoluminescence study of resonant-tunneling transistor <i>Y Ohno, S Kishimoto, T Mizutani and T Akeyoshi</i>	613
Resonant tunneling in disordered materials such as SiO ₂ /Si/SiO ₂ <i>R Lake, B Brar, G D Wilk, A Seabaugh and G Klimeck</i>	617
Semi-insulating GaAs by controlled introduction of metallic nano-Schottkies <i>L E Wernersson, A Litwin, L Samuelson and W Seifert</i>	621
Chapter 9: Modeling	
Comprehensive simulation of quantum well lasers <i>M S Hybertsen, M A Alam, R K Smith, G A Baraff and M R Pinto</i>	625
Monte Carlo estimation of excess noise factor in thin p ⁺ -i-n ⁺ avalanche photodiodes <i>D S Ong, K F Li, G J Rees, G M Dunn, J P R David and P N Robson</i>	631

Numerical model of a 0.2 μm AlGaAs/GaAs HEMT including electromagnetic effects <i>A Cidronali, G Leuzzi, G Collodi and G Manes</i>	635
NEMO: general release of a new comprehensive quantum device simulator <i>D K Blanks, G Klimeck, R Lake, D Jovanovic, R C Bowen, C Fernando, W R Frensley and M Leng</i>	639
Atomic scale calculations for strain distribution and electronic structure of InAs pyramidal quantum dots on (100) GaAs <i>T Saito, J N Schulman and Y Arakawa</i>	643
Two-dimensional device simulation for PHEMT material and process control <i>Y V Pao and J S Harris Jr</i>	647
Keyword index	651
Author index	659

III-V Nitride-Based Blue LDs with Modulation-Doped Strained-Layer Superlattices

S. Nakamura

R&D Department, Nichia Chemical Industries, Ltd., 491 Oka, Kaminaka, Anan 774, Japan

Abstract. InGaN multi-quantum-well-structure (MQW) laser diodes (LDs) with $\text{Al}_{0.14}\text{Ga}_{0.86}\text{N}/\text{GaN}$ modulation doped strained-layer superlattice (MD-SLS) cladding layers grown on an epitaxially laterally overgrown GaN (ELOG) substrate was demonstrated to have a lifetime of more than 1150 hours under room-temperature continuous-wave operation. The use of the MD-SLS was effective in reducing the operating voltage of the LDs. The ELOG substrate was used to reduce the number of threading dislocations in the InGaN MQW structure. After 2 μm etching of the ELOG substrate, the etch pit density was about $2 \times 10^7/\text{cm}^2$ in the region of the 4- μm -wide stripe window, but almost zero in the region of the 8- μm -wide SiO_2 stripe.

1. Introduction

Short-wavelength-emitting devices, such as blue laser diodes (LDs), are currently required for a number of applications, including full-color electroluminescent displays, laser printers, read-write laser sources for high-density information storage on magnetic and optical media, and sources for undersea optical communications. Major developments in wide-gap III-V nitride semiconductors have recently led to the commercial production of high-brightness blue/green light-emitting diodes (LEDs) and to the demonstration of room-temperature (RT) violet laser light emission in InGaN/GaN/AlGaN-based heterostructures under pulsed and continuous-wave (CW) operations [1]. The lifetime of the InGaN multi-quantum-well (MQW) structure LDs have been improved to 300 hours under RT-CW operation [2]. However, further improvements of the LD characteristics are required to enable commercialization of short-wavelength LDs. At present, one of the problems is that it is difficult to grow a thick AlGaN cladding layer required for optical confinement, due to the formation of cracks during the growth in the layers. These cracks are caused by the stress introduced in the AlGaN cladding layers due to lattice mismatch, and the difference in thermal expansion coefficients between the AlGaN cladding layer and GaN layers. There have been no reports on the use of the AlGaN/GaN strained-layer superlattices (SLSs) for III-V nitride-based LDs to prevent cracking during the growth. Here, we describe the InGaN MQW-structure LDs which have AlGaN/GaN modulation-doped strained-layer superlattices (MD-SLSs) within the range of critical thickness as cladding layers instead of thick AlGaN layers. Modulation doping of the SLSs was performed to reduce the operating voltage of the LDs. As a substrate, the epitaxially laterally overgrown GaN (ELOG) on sapphire was used to reduce the number of threading dislocations of the GaN epilayer, which was reported recently by Usui et al. [3] and later by Nam et al [4].

2. InGaN MQW LDs with MD-SLS cladding layers

III-V nitride films were grown by the two-flow MOCVD method, the details of which have been described elsewhere [1]. The growth was conducted at atmospheric pressure. First, the selective growth of GaN was performed on a 2- μm -thick GaN layer grown on a (0001) C-face sapphire substrate. The 0.1- μm -thick silicon dioxide (SiO_2) mask was patterned to form 4- μm -wide stripe windows with a periodicity of 12 μm in the GaN <1-100> direction. After 10- μm -thick GaN growth on the SiO_2 mask pattern, the coalescence of the selectively grown GaN made it possible to achieve a flat GaN surface over the entire substrate, as shown in Fig.1. We call this coalesced GaN the ELOG. The growth

condition and the SiO_2 mask pattern of the ELOG were previously reported in detail by Kato et al [5]. Figure 1 shows the etched surface morphology of the ELOG substrate. The etching of the GaN was performed by reactive ion etching with Cl_2 plasma [1]. The etching depth was as large as $2 \mu\text{m}$ in order to reveal the etch pit clearly. Many hexagonal etch pits were observed on the $4\text{-}\mu\text{m-wide}$ stripe window, as shown in Fig. 1. The etch pit density was about $2 \times 10^7/\text{cm}^2$ in the region of the $4\text{-}\mu\text{m-wide}$ stripe window. However, the etch pit density was almost zero in the region of the $8\text{-}\mu\text{m-wide}$ SiO_2 stripe.

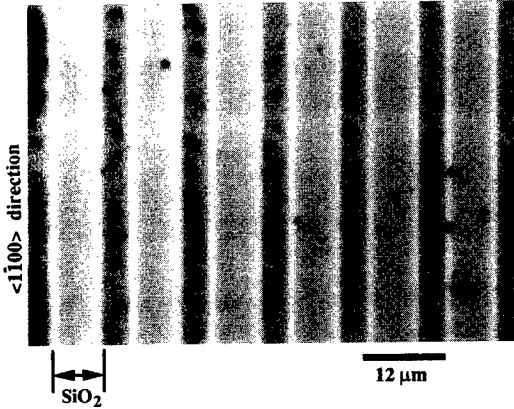


Fig. 1. Etched surface morphology of the ELOG substrate. The SiO_2 stripe width and window width of the ELOG substrate were $8 \mu\text{m}$ and $4 \mu\text{m}$, respectively. The etch pit density was about $2 \times 10^7/\text{cm}^2$ in the region of the $4\text{-}\mu\text{m-wide}$ stripe window.

The InGaN MQW LD structure was grown on the ELOG substrate. The InGaN MQW LD device consisted of a $3\text{-}\mu\text{m-thick}$ layer of n-type GaN:Si , a $0.1\text{-}\mu\text{m-thick}$ layer of n-type $\text{In}_{0.1}\text{Ga}_{0.9}\text{N:Si}$, a $\text{Al}_{0.14}\text{Ga}_{0.86}\text{N/GaN MD-SLS cladding layer}$ consisting of one-hundred-twenty $25\text{-}\text{\AA}$ -thick undoped GaN separated by $25\text{-}\text{\AA}$ -thick Si-doped $\text{Al}_{0.14}\text{Ga}_{0.86}\text{N}$ layers, a $0.1\text{-}\mu\text{m-thick}$ layer of Si-doped GaN, an $\text{In}_{0.15}\text{Ga}_{0.85}\text{N}/\text{In}_{0.02}\text{Ga}_{0.98}\text{N}$ MQW structure consisting of four $35\text{-}\text{\AA}$ -thick Si-doped $\text{In}_{0.15}\text{Ga}_{0.85}\text{N}$ well layers forming a gain medium separated by $105\text{-}\text{\AA}$ -thick Si-doped $\text{In}_{0.02}\text{Ga}_{0.98}\text{N}$ barrier layers, a $200\text{-}\text{\AA}$ -thick layer of p-type $\text{Al}_{0.2}\text{Ga}_{0.8}\text{N:Mg}$, a $0.1\text{-}\mu\text{m-thick}$ layer of Mg-doped GaN, a $\text{Al}_{0.14}\text{Ga}_{0.86}\text{N/GaN MD-SLS cladding layer}$ consisting of one-hundred-twenty $25\text{-}\text{\AA}$ -thick undoped GaN separated by $25\text{-}\text{\AA}$ -thick Mg-doped $\text{Al}_{0.14}\text{Ga}_{0.86}\text{N}$ layers, and a $0.05\text{-}\mu\text{m-thick}$ layer of p-type GaN:Mg . Figure 2 shows the structure of the LDs. The laser cavity was formed within the SiO_2 stripe and parallel to the direction of the SiO_2 stripe. The area of the ridge-geometry LD was $4 \mu\text{m} \times 550 \mu\text{m}$. The cavity length of the LDs was varied between $550 \mu\text{m}$ and $300 \mu\text{m}$. A mirror facet was formed by dry etching, as reported previously [1]. High-reflection facet coatings (50 %) consisting of 2 pairs of quarter-wave $\text{TiO}_2/\text{SiO}_2$ dielectric multilayers were used to reduce the threshold current. A Ni/Au contact was evaporated onto the p-type GaN layer, and a Ti/Al contact was evaporated onto the n-type GaN layer. The electrical characteristics of the LDs fabricated in this way were measured under a direct current (DC) at room temperature (RT).

Figure 3 shows typical voltage-current (V-I) characteristics and the light output power per coated facet of the LD with a cavity length of $550 \mu\text{m}$ as a function of the forward DC current (L-I) at RT. No

stimulated emission was observed up to a threshold current of 90 mA, which corresponded to a threshold current density of 4 kA/cm^2 , as shown in Fig. 3. The operating voltage at the threshold current was 4.6 V. The threshold current and voltage of the LD with a cavity length of 300 μm were 50 mA and 5 V. We were able to reduce the operating voltage using the ELOG substrate and the MD-SLS, in comparison with previous values of the LDs [1]. The operating voltages of the LDs with the same structure, except for the cladding layer which was changed to uniformly Si-doped SLSs consisting of Si-doped $\text{Al}_{0.14}\text{Ga}_{0.86}\text{N}/\text{Si-doped GaN}$, were about 6–7 V. Therefore, the use of the MD-SLSs were effective in reducing the operating voltage of the LDs. Resulting from the good optical confinement, we achieved the lowest threshold current of 16 mA and voltage of 5.5 V with a laser cavity length of 200 μm under RT-CW operation using the AlGaN/GaN MD-SLS cladding layers.

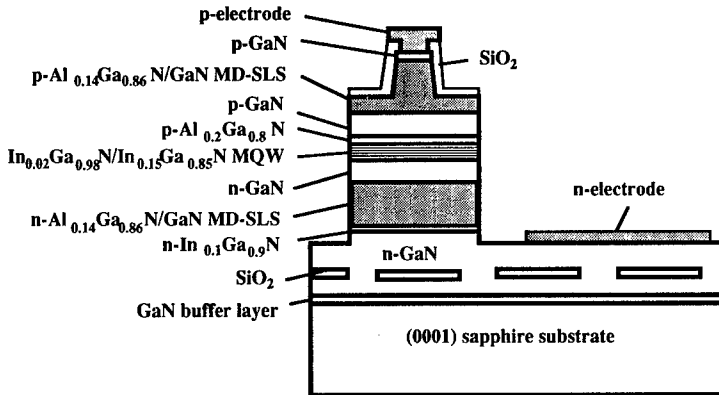


Fig. 2. Structure of the InGaN MQW LDs with MD-SLS cladding layers grown on the ELOG substrate.

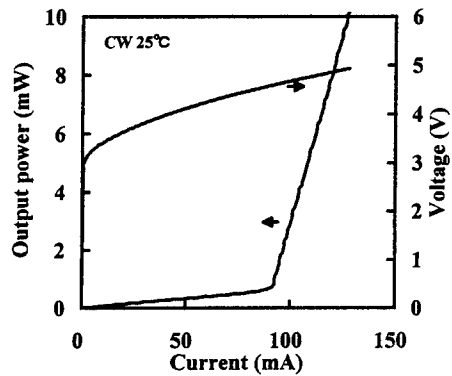


Fig. 3. Typical L-I and V-I characteristics of InGaN MQW LDs measured under CW operation at RT.

Figure 4 shows the results of a lifetime test of CW-operated LDs with a cavity length of 500 μm and 300 μm carried out at RT, in which the operating current is shown as a function of time under a constant output power of 2 mW per facet controlled using an autopower controller (APC). A small increase of the operating current is observed with increasing operating time. The LDs still survive after 1150 hours of operation, which is much longer than that (300 hours) in previous reports [2]. This long lifetime is probably due to the small number of cracks and the low dislocation density resulting from the use of the MD-SLS and the ELOG substrate.

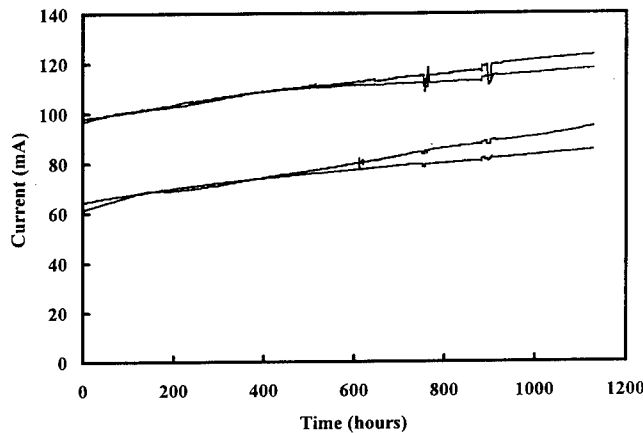


Fig. 4. Operating current as a function of time under a constant output power of 2 mW per facet controlled using an autopower controller. The LDs with a cavity length of 500 μm and 300 μm were operated under DC at RT.

The emission spectra of the LDs with a cavity length of 500 μm were measured under RT CW operation. At a current of 90 mA, longitudinal modes with a mode separation of 0.04 nm were observed. At a current of 100 mA, a single-mode emission was observed at an emission wavelength of 403.7 nm. At currents from 100 mA to 120 mA, only single-mode emission at a wavelength of 403.7 nm was observed.

In summary, InGaN MQW LDs with the MD-SLS cladding layers grown on the ELOG substrate were demonstrated to have a lifetime longer than 1150 hours under RT CW operation. The lifetime test is still continuing after 1150 hours. These results indicate a promising future of the III-V nitride-based short-wavelength LDs.

3. References

- [1] Nakamura S and Fasol G 1997 *The Blue Laser Diode* (Berlin: Springer-Verlag)
- [2] Nakamura S, Senoh M, Nagahama S, Iwasa N, Yamada T, Matsushita T, Sugimoto Y and Kiyoku H 1997 *Jpn. J. Appl. Phys.* 36 L1059-L1061
- [3] Usui A, Sunagawa H, Sakai A and Yamaguchi A 1997 *Jpn. J. Appl. Phys.* 36 L899-L901
- [4] Nam O H, Bremer M D, Zheleva and Davis R F 1997 39th Electronic Material Conference, June 25-27, Colorado USA, D-5
- [5] Kato Y, Kitamura S, Hiramatsu K and Sawaki N 1994 *J. Crystal Growth* 144 133-140

Growth and doping of β -GaN and β -(In,Ga)N films and heterostructures

O. Brandt¹, B. Yang, H. Yang,² J. R. Müllhäuser, and K. H. Ploog

*Paul-Drude-Institut für Festkörperferelektronik, Hausvogteiplatz 5–7,
D-10117 Berlin, Germany*

Abstract. We discuss the growth of cubic GaN and (In,Ga)N films on GaAs by plasma-assisted molecular beam epitaxy. Conditions to be satisfied for the synthesis of single-phase films are pointed out. In the case of the binary compound GaN, strictly stoichiometric growth is required, while the ternary compound (In,Ga)N has to be grown N rich for reducing the amount of In segregating on the growth front. Finally, we discuss our finding of high p-type conductivities in (Be,O)-codoped GaN films in the light of recent theoretical studies of this subject.

1. Introduction

Cubic (β) III-V nitrides are believed to possess potential advantages for the fabrication of blue and green light-emitting diodes and laser diodes as compared to their hexagonal (α) counterparts, particularly, easier cleavage (compatible with the substrate) and a substantially smaller bandgap. A number of researchers, using molecular beam epitaxy (MBE), have synthesized β -GaN of fair quality (see Brandt *et al* 1995 and references therein). Necessary ingredients for an optoelectronic device such as the controlled n-type and p-type doping of β -GaN, as well as the growth of Al and In containing alloys have, however, been investigated just by one group each (Kim *et al* 1994, Lin *et al* 1993, Nakadaira *et al* 1997, Abernathy *et al* 1995, respectively). Since the optical quality of β -GaN is not too far from device requirements, further studies of its doping as well as of its alloys with In and Al are timely for exploring the potential of this material class. In this paper, we briefly summarize the results of our recent studies on the growth and doping of β -GaN and β -(In,Ga)N on GaAs.

2. Experimental

The β -GaN and β -(In,Ga)N films studied in this work are synthesized on semi-insulating GaAs(001) substrates mounted In-free on Mo holders in two different custom-made MBE systems, one of which (M2) is a two-chamber machine equipped with a DC glow-discharge N-plasma source (Riber NPS 200), while the other (M8) is a three-chamber machine with an RF N-plasma source (SVT). Prior to the growth of β -(In,Ga)N, a β -GaN buffer layer is grown under optimized growth conditions (Brandt *et al* 1995, Brandt *et al* 1997). X-ray measurements are performed using a double-crystal diffractometer equipped with a $\text{Cu}_K\alpha_1$ anode and a Ge(004) monochromator. The measurements shown here are taken with a 50 μm detector slit in the $\omega - 2\theta$ mode. Secondary ion-mass spectrometry (SIMS) is performed with a CAMECA 4F utilizing both Cs^+ and O_2^- ions at energies of 10–15 keV. All electrical measurements are done in a four-terminal configuration with the GaAs substrate and buffer layer (if any) etched off.

¹ Corresponding author. Fax:+49-30-20377-201; E-mail: brandt@pdi.wias-berlin.de

² Present address: National Research Center for Optoelectronic Technology (NCOT), Institute of Semiconductors, Chinese Academy of Science, P.O. Box 912, Beijing 100083, China.

3. Results and Discussion

3.1. Growth of β -(In,Ga)N

First, we briefly comment on the question under which conditions epitaxial growth of β -GaN on GaAs is actually achieved. We found (Yang *et al* 96, Brandt *et al* 97) that epitaxy is achieved by using a high N/Ga ratio during the nucleation stage, whereas a low N/Ga ratio invariably results in polycrystalline columnar growth. However, during further growth, the N/Ga ratio at the growth front must be close to unity if the formation of hexagonal domains is to be avoided. Figure 1 shows an expanded portion of the $\omega - 2\theta$ scans for two samples.

Concerning the growth of β -(In,Ga)N, the primary issue we have to deal with is the incorporation of sufficient amounts of In without affecting the crystal quality too much. In both our MBE systems M2 and M8, no measurable incorporation of In is achieved using the growth conditions employed for β -GaN, namely, a N/III ratio close to 1 and a temperature of 680°C. Simply lowering the growth temperature leads first (at about 550°C) to severe roughening of the film and eventually (at about 500°C) to polycrystalline growth. Ex situ investigations of such films by scanning electron microscopy show the presence of densely packed In droplets on the surface, suggesting that In is merely segregating on the growth front under these conditions. This phenomenon is markedly reduced when increasing the N/III (III=Ga+In) ratio to values around 3. However, a connected morphology free of In droplets is achieved only when growth takes place under a N/III ratio of at least 3 and at elevated temperatures around 620°C.

Based on the above results, a series of 150 nm-thick β -(In,Ga)N layers are grown in MBE system M2 on GaAs(001) substrates at 620°C with an effective N/III flux ratio of 3. The GaN buffer layers

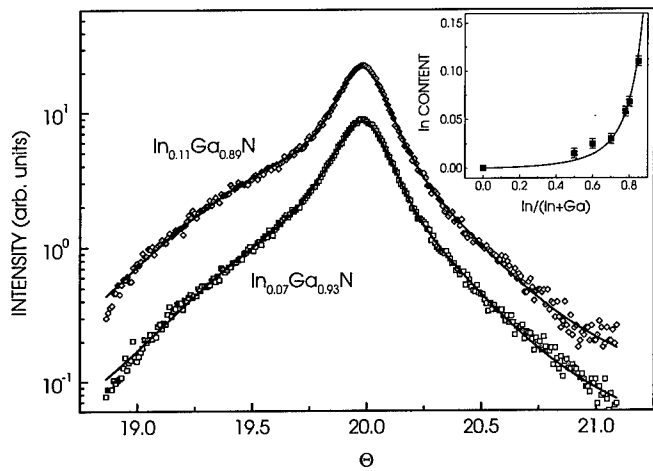


Figure 1. $\omega - 2\theta$ scans of two β -(In,Ga)N/GaN structures grown in M2 with different In content. The solid line is a fit of the profiles with two Pseudo-Voigt functions. The inset shows the In content in several layers vs. the group III flux ratio employed during growth. The solid line is a fit with a segregation-and-desorption model.

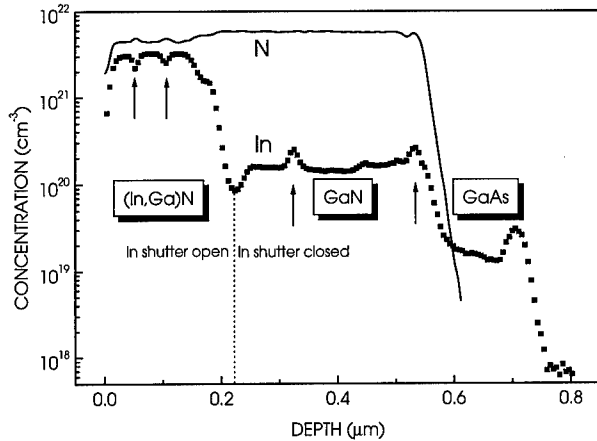


Figure 2. SIMS profile of a β -(In,Ga)N/GaN structure grown in M8. Note the high In concentration with the In shutter closed. The arrows depict growth interruptions. The ordinate refers to the atom density of GaAs.

are 500 nm thick for all of these samples. For determining the dominant modification as well as the In content, both ω and $\omega - 2\theta$ X-ray scans are taken from these samples. No diffraction from either [001]- or [111]-oriented hexagonal domains is detectable in these scans. A low-angle shoulder of the dominant β -GaN (002) reflection at 19.96° is visible in both scans, which we attribute to the (002) reflection from the respective β -(In,Ga)N film. For determining the angular position and the width of this shoulder, the profiles are fit by Pseudo-Voigt functions. The width of the β -(In,Ga)N (002) reflection is around $20-40'$, compared to $10-15'$ for the β -GaN (002) reflection. This broadening corresponds to a substantial inhomogeneous strain within the β -(In,Ga)N layer. To go further, the In content is obtained by calculating the difference of the angular positions assuming validity of Vegard's law and taking the lattice constants of cubic GaN and InN to be 0.451 and 0.498 nm, respectively. The broadening of the β -(In,Ga)N reflection with respect to that of β -GaN then corresponds to a fluctuation in the In content of up to 4%. However, for these samples no InN(002) was observed, so that phase separation is not complete at least for these low In contents.

The inset of Fig. 1 displays the In/(In+Ga) flux ratio dependence of the In content of these β -(In,Ga)N layers. As discussed in detail by Yang *et al* (1997), the strongly nonlinear dependence most likely results from the desorption of an In surface species segregating on the growth front. In fact, the data can be fit well by a simple segregation-and-desorption rate equation model (see Yang *et al* 1997 and references therein) assuming steady-state conditions and complete surface depletion for each grown layer. The only free parameter of the model is the segregation energy, for which we obtain 0.48 eV in the case of the present data. This value is remarkably high, suggesting that In segregation in β -(In,Ga)N is very strong indeed. We stress, however, that segregation of In is very strongly depending on the N/III ratio. Higher N/III ratios than those we were able to use here are clearly necessary to achieve a more efficient In incorporation.

This requirement is easily met when using our second MBE system M8, since the N plasma source

installed there is able to deliver an effective active N flux well in excess of 1 monolayer/s. In fact, the actual In content (up to, at present, 40%) in β -(In,Ga)N layers grown in M8 at the same temperature as that used in M2 (620°C) is close to the nominal one, meaning that In segregation is drastically reduced. Furthermore, the optical quality of these layers is improved with respect to those grown in M2 as broad but intense photoluminescence is detected at room temperature (Müllhäuser *et al* 1997). Figure 2 shows the SIMS depth profile of a β -(In,Ga)N /GaN structure grown in M8 with a nominal In content of 25%. Several interesting observations can be made from this experiment. First of all, the actual In content with the In shutter open is $3.5 \times 10^{21} \text{ cm}^{-3}$, i. e., about 17% and thus only slightly lower than the nominal one. Second, growth interruptions cause a dip in the In concentration profile, demonstrating the efficient depletion of the surface at the temperature used here. Third, the In content in the β -GaN buffer layer, where during growth the In cell was shuttered close but held at the same temperature, is as large as 1% and thus only one order of magnitude lower than with the In shutter open. We attribute this finding, which we found to be strongly dependent on the idling temperature of the In cell, to a "N drag effect" in analogy to the "As drag effect" which has recently been investigated in much detail by Wasilewski *et al* (1997). In short, a fraction of atoms from an idling cell may escape after specular reflections from the shutter into the growth chamber where they may be dragged towards the substrate when intersecting a molecular beam of comparatively large beam equivalent pressure. This phenomenon is machine dependent as it is affected by the geometry of the system, but it is considered to be of great significance for nitride MBE growth since the beam equivalent pressure of the N_2 or NH_3 beam employed there is, in general, very large. Note, finally, that growth interruptions during deposition of the β -GaN buffer layer leads to an accumulation of In onto the surface.

3.2. *p*-type doping—the codoping approach

Conventional wisdom suggests that successful p-type doping of a semiconductor requires the concentration of compensating impurities to be as small as possible. Thus, every attempt is generally undertaken to minimize the background electron concentration in nominally undoped GaN. Furthermore, care has to be taken to avoid unintentional crossdoping by the above mentioned "N drag effect" in a p-n structure. Recently, however, we have accidentally discovered an approach which seems to rely on exactly the opposite principles, namely, on the simultaneous presence of acceptors and donors in almost equal amounts. Indeed, we have measured p-type resistivities as low as $0.02 \Omega\text{cm}$ in β -GaN which are codoped with high concentrations of Be and O (Brandt *et al* 1996). Our qualitative arguments devised to explain this striking result have recently been substantiated by two independent theoretical works (Bernadini *et al* 1997, Yamamoto *et al* 1997). The main results of the calculations of these groups are similar and may be summarized as follows. First, codoping with chemically reactive species considerably enhances the solubility of both species and prevents selfcompensation. Second, ion pairs are predicted to form, pushing the energy levels of the reacting species towards the respective band, thus reducing their activation energy. Third, the formation of ion pairs transforms two Coulomb scattering centers into a single dipole scatterer, thus enhancing the mobility.

Figure 3 shows the SIMS profile of such a (Be,O) codoped structure. The rectifying characteristic of this junction, which could be measured after etching off the (semiinsulating) GaAs substrate, allowed Hall measurements of the top p-type β -GaN layer. This particular sample shows an activated conductivity with a hole concentration and mobility of $2 \times 10^{18} \text{ cm}^{-3}$ and $50 \text{ cm}^2/\text{Vs}$ at room temperature, respectively. Although higher than for the sample reported in our previous work (Brandt *et al* 1996), the resulting resistivity of this sample is still superior to any other reported for GaN.

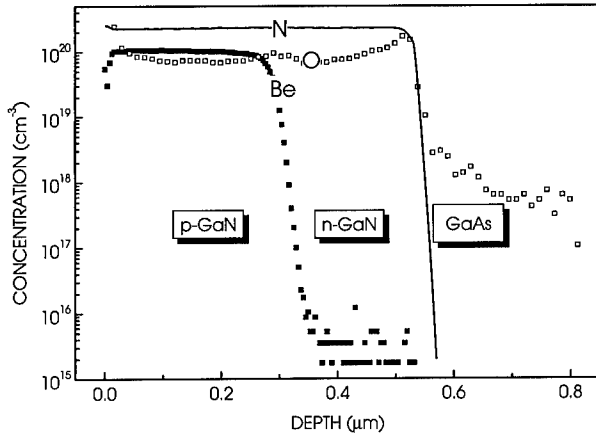


Figure 3. SIMS profile of a (Be,O)-codoped β -GaN/GaAs(001) p-n junction. The N concentration is scaled down for clarity.

Further information is obtained by temperature dependent measurements. Figure 4 shows the temperature dependence of the resistivity of n-type and p-type β -GaN layers. Since the mobility for all these samples is only weakly depending on temperature, the slope of the data at high temperatures roughly corresponds to the activation energy of the dominating impurity. The apparent activation energy

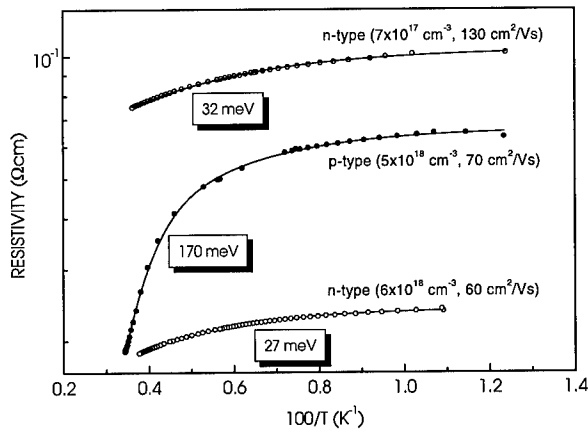


Figure 4. Arrhenius representation of the resistivity of one p-type and two n-type β -GaN layers. The carrier concentration and mobility for each sample are those measured at room temperature. The apparent activation energies labeling the data roughly correspond to those governing the carrier concentration.

of the dominating donor (which most likely is O) in our n-type layers is around 30 meV, close to the value deduced from electronic Raman scattering (Ramsteiner *et al* 1996). The apparent activation energy for the p-type layer of 170 meV is similar to values reported for Mg in α -GaN (Tanaka *et al* 1994, Kim *et al* 1996). This finding shows that the high p-type conductivities in these samples is not a result of a particularly small activation energy, but indeed because of the enhanced hole mobility.

4. Conclusion

We have shown that the growth of β -(In,Ga)N and the p-type doping of β -GaN is principally possible. Both issues, however, require (and deserve) further systematic work before we can start seriously thinking about devices made from cubic nitrides. Particularly, the concept of codoping, while very promising in view of the results already obtained, has to be made technologically controllable for exploiting its potential.

Acknowledgement

We acknowledge financial support of this work by the Bundesministerium für Bildung und Forschung der Bundesrepublik Deutschland.

References

- Abernathy C R and MacKenzie J D (1995) *Appl. Phys. Lett.* **66** 1632.
- Bernadini F, Fiorentini V, and Bosin A (1997) *Appl. Phys. Lett.* **70** 2990.
- Brandt O, Yang H, Jenichen B, Suzuki Y, Däweritz L and Ploog K H (1995) *Phys. Rev. B* **52** R2253.
- Brandt O, Yang H, Kostial H, and Ploog K H (1996) *Appl. Phys. Lett.* **69** 2707.
- Brandt O, Yang H, Trampert A, Wassermeier M, and Ploog K H (1997) *Appl. Phys. Lett.* **71** 473.
- Lin M E, Xue G, Zhou G L, Greene J E and Morkoç H (1993) *Appl. Phys. Lett.* **63** 932.
- Kim J G, Frenkel A C, Liu H, and Park R M (1994) *Appl. Phys. Lett.* **65** 91.
- Kim W, Salvador A, Botchkarev A E, Aktas O, Mohammad S N, and Morkoç H (1996) *Appl. Phys. Lett.* **69** 559.
- Mühlhäuser J, Jenichen B, Wassermeier M, Brandt O, and Ploog K H (1997) *Appl. Phys. Lett.* (to be published).
- Nakadaira A and Tanaka H (1997) *Appl. Phys. Lett.* **70** 2720.
- Ramsteiner M, Menniger J, Brandt O, Yang H, and Ploog K H (1996) *Appl. Phys. Lett.* **69** 1276.
- Tanaka T, Watanabe A, Amano H, Kobayashi Y, Akasaki I, Yamazaki S, and Koike M (1994) *Appl. Phys. Lett.* **65** 593.
- Wasilewski Z R, Rolfe S J, and Wilson R A, (1997) *J. Cryst. Growth* **175/176** 1270.
- Yamamoto T and Katayama-Yoshida H (1997) *Jpn. J. Appl. Phys.* **36** L180.
- Yang B, Brandt O, Jenichen B, Mühlhäuser J, and Ploog K H (1997) *J. Appl. Phys.* (to be published).
- Yang H, Brandt O, Trampert A, and Ploog K H (1996) *Appl. Surf. Sci.* **104/105** 461.

Growth and Effects of Single-Crystalline ZnO Buffer Layer on GaN Epitaxy

T. F. Huang, T. Ueda*, S. Spruytte and J. S. Harris Jr.

Solid State Electronics Laboratory, CIS-X 328, Stanford University, Stanford, CA, 94305, USA

*Matsushita Electronics Corporation, Osaka, Japan

Abstract. Single-crystalline ZnO films have been grown on c-cut sapphire substrates by pulsed laser deposition (PLD) using a KrF laser. The optimum growth conditions are 550 °C and 10^{-2} torr O₂. We observe a sharp and streaked RHEED (Reflection High Energy Electron Diffraction) pattern and atomically smooth surface with a r.m.s. roughness of only 5 Å measured by atomic force microscope. Photoluminescence at 77 K shows a strong near-band-edge peak at 3.34 eV with no deep level emission. Two dimensional growth of GaN by chloride vapor phase epitaxy (VPE) is greatly enhanced compared to earlier results using RF-sputtered ZnO buffer layers. This is a result of better crystalline structure, optical properties and surface flatness of the PLD films. The properties of the VPE-GaN are strongly dependent on ZnO layer thickness. The optimum thickness of ZnO buffer layer is around 25 nm.

1. Introduction

III-V nitride materials have been widely studied for optoelectronic device applications in the blue and ultraviolet regions. Room temperature cw laser operation by current injection has been achieved in GaN-based structures [1]. This structure was fabricated on a highly lattice mismatched sapphire substrate by metal organic chemical vapor deposition (MOCVD) with a dislocation density of 10^8 cm⁻². Moreover, because of the insulating substrate, a substantial series resistance between the active region and the n-type contact results in a high operation voltage, causing heating and a high threshold current density. Among various growth techniques, chloride vapor phase epitaxy (VPE) is very promising to obtain thick GaN films because of its high growth rate. Laser structures grown on a thick VPE-GaN "substrate" would have better crystallinity and lower series resistance than heteroepitaxial growth on sapphire.

Because the physical properties of ZnO are similar to those of GaN, ZnO is a good buffer layer for GaN growth. With a lattice mismatch less than 2% between ZnO and GaN, GaN grown on ZnO buffer layers should have better surface morphology and lower dislocation densities than GaN grown directly on sapphire substrates. The other advantage of a ZnO buffer layer is the possibility of fabricating GaN substrates by etching away the ZnO layer since ZnO can easily be etched by any acid and bulk GaN is extremely hard to produce. One of the most successful thick GaN films was grown by vapor phase epitaxy (VPE) on a sputtered ZnO buffer layer on a sapphire substrate [2]. However, the sputtered ZnO layer was polycrystalline and the effects of the growth condition and thickness of ZnO buffer layers on the growth of GaN were not fully examined. In order to achieve high quality GaN, it is important to optimize the growth and study the properties of the ZnO buffer layer.

In this paper, we report growth of single-crystalline ZnO films with excellent structural and optical properties on c-cut sapphire substrates by pulsed laser deposition (PLD). The properties of ZnO films are characterized by X-ray diffraction (2θ , ω , ϕ scans), reflection high energy electron diffraction (RHEED), photoluminescence (PL), and atomic force microscope (AFM). The strong dependence of ZnO buffer layer thickness on the properties of GaN grown by chloride vapor phase epitaxy (VPE) will also be discussed.

2. Experimental

ZnO films were deposited on c-cut sapphire substrates using a pulsed laser deposition (PLD) apparatus described previously [3]. A KrF excimer laser operating at a wavelength of 248 nm, a pulse duration of 20 ns and a laser fluence of 3 J/cm² was used. The laser repetition rate was 5 Hz and the target-substrate distance was 5 cm. ZnO films were grown under an oxygen partial pressure of 0.01 torr and the background pressure of the system before the introduction of oxygen gas was usually 10⁻⁸ Torr. Targets were prepared by pressing ZnO powders of 99.999% purity and sintering at 1100 °C for three hours. After deposition, the substrates were cooled slowly to room temperature at a rate of 5 °C/min. under 1 torr oxygen.

We employed a chloride VPE system to grow thick GaN layers using GaCl₃ and NH₃ as source materials as described previously [4], using nitrogen as a carrier gas. A notable feature of our system was that the gallium supply was precisely controlled by the temperature of the GaCl₃ cell and the nitrogen flow rate for the cell. The system was simpler than a conventional hydride VPE system in which GaCl (prepared by reaction of liquid Ga and HCl) is used as the Ga source. The growth was carried out at 1000 °C with a (NH₃/GaCl₃) ratio of 500. The growth rate was approximately 6 μm/hr. To prevent thermal desorption of the ZnO buffer layer, the growth was immediately started after the substrate temperature reached the growth temperature.

3. Material Characteristics

3.1 ZnO Buffer Layer

X-ray diffraction and RHEED studies were used to investigate the nature of the epitaxial growth and crystalline quality of the film. At the growth temperatures between 350-650 °C and 0.01 Torr O₂, ZnO films grown on (0001) sapphire substrates show (000c) peaks from x-ray 2θ scans. There are only six peaks observed in the x-ray φ scan of ZnO (10-12) with 60 degree spacing, indicating single crystalline growth despite high lattice mismatch between ZnO and sapphire. The epitaxial relationships are ZnO[0001]/Al₂O₃[0001] and ZnO[10-10]/Al₂O₃[11-20]. The optimum growth temperature is 550 °C with a FWHM of ZnO (0002) peak of 0.35° from x-ray rocking curve scans.

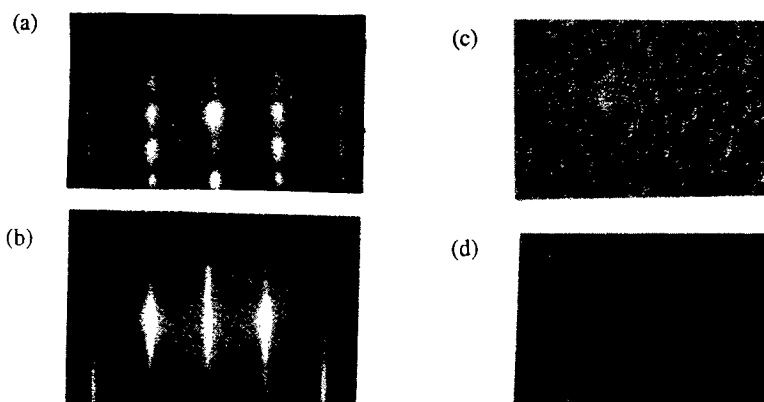
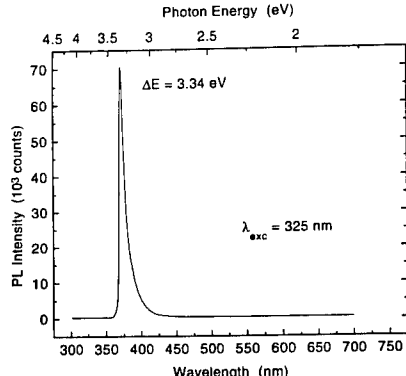


Fig. 1 (a) and (b) are *in situ* RHEED patterns taken along <2110> azimuth of ZnO films grown on c-cut sapphire substrates at 0.01 torr O₂. (c) and (d) are AFM images of the same films.
 (a), (c) at Ts = 350 °C (b), (d) at Ts = 550 °C

In situ RHEED patterns are taken along <2110> azimuth of ZnO films grown at 0.01 torr O₂ and various substrate temperatures. The RHEED gun operates at 14 KV and 1.6 amp. At the growth temperature of 350 °C, a streaky pattern with a regular array of elongated spots indicates that the transmission pattern appears superimposed on the reflection pattern (Fig. 1a). The transmission pattern shown by RHEED is due to the surface roughness of the film, which may occur if the film is grown in a Stranski-Krastanov or Volmer-Weber mode. Another reason for surface roughness may be particulates on the films which are produced by ablating targets during growth. If the surface roughness increases, the RHEED becomes a regular array of spots from transmission through the peaked regions. For ZnO films grown at temperatures lower than 350 °C, extra spots gradually develop, indicating the film is polycrystalline. As the growth temperature increases to 550 °C, a sharp and streaky ZnO RHEED pattern is observed, indicating good crystallinity and atomically smooth surface (Fig. 1b). We observe Kikuchi lines on the RHEED screen which may not be successfully shown on the graph due to the low resolution of the imaging process. The quality of the pattern is comparable with that of MBE-grown ZnO film and is much better than those grown by other techniques.

Surface roughness of ZnO films was examined by scanning electron microscope (SEM) and atomic force microscope(AFM). From SEM, the topography of ZnO films is featureless with very few particulates. By contact-mode AFM, the films are very smooth with only several monolayers of roughness ($c=5.2065 \text{ \AA}$ for ZnO). ZnO film grown at 550 °C shows a r.m.s. roughness of 5 Å, one of the smoothest ZnO film reported by any growth technique (Fig. 1d). ZnO films grown at 350 °C (Fig. 1c) have higher r.m.s. roughness than the film grown at 550 °C. This result agrees with the RHEED observation. At low growth temperature, atoms arriving at the substrate surface may not have enough kinetic energy to move around before the next atoms arrive. Thus, island growth dominates, which results in a rougher surface of the film. This is the main reason that the RHEED pattern for low temperature grown ZnO shows a regular array of elongated spots. With the capability of *in situ* monitoring of the growth in the PLD system by RHEED, we are able to study the crystallinity, roughness and kinetics of growth of freshly grown surfaces.

Figure 2 shows the photoluminescence (PL) spectrum of ZnO grown at 550 °C. The film is excited by He-Cd laser ($\lambda = 325 \text{ nm}$) at 77 K. A strong near band edge peak at 3.34 eV is observed. This has been previously attributed to the annihilation of bound excitons in ZnO [5]. Deep level emission, which usually originates from crystal defects or impurities, is not detectable.



3.2 Effect of Buffer Layer Thickness

We deposited different thicknesses of buffer layers on c-cut sapphire substrates at 550 °C and 10⁻² torr, the optimum growth conditions as described above. Single crystalline GaN films were grown on ZnO buffer layers by vapor phase epitaxy. The thickness of GaN is around 1.5 μm. Crystallinity was verified by x-ray (2θ , ϕ) scans. Two dimensional lateral growth of GaN is greatly enhanced on a single crystalline ZnO buffer layer (Fig. 3). With ZnO buffer layer thickness around 25 nm, the surface of GaN film is relatively flat and featureless by scanning electron microscope. However, a GaN film grown on a 200-nm thick buffer layer exhibits cracks and peeling, which may be improved by optimizing the cooling rate. In addition to better surface smoothness achieved by employing a ZnO buffer layer around 25 nm, the FWHM of x-ray rocking curve of GaN (0002) is reduced to 0.35° while the peak width of GaN film without ZnO buffer layer is three times greater.

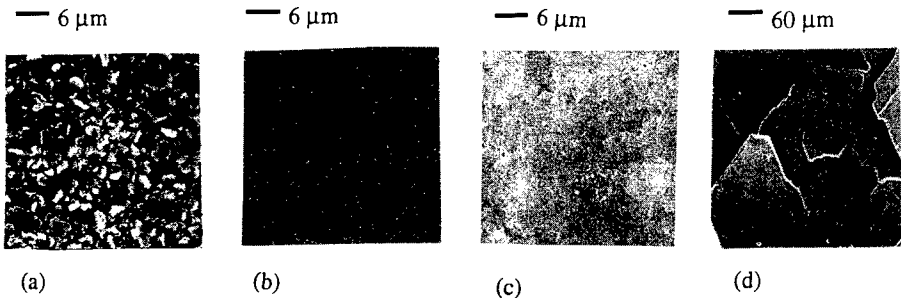


Fig. 3. Surface morphology of VPE-grown GaN films (a) directly on a sapphire substrate, on (b) 25 nm (c) 75 nm (d) 200 nm ZnO buffer layer. Images are taken by SEM.

In conclusion, ZnO buffer layers of high quality, in terms of crystalline structure, optical properties and surface flatness, have been grown by pulsed laser deposition. Single crystalline ZnO film with a sharp and streaky RHEED pattern was deposited at 550 °C and 10⁻² torr O₂. We observed atomically flat surfaces of ZnO films with a r.m.s. roughness of 5 Å. These ZnO films show strong near-band-edge luminescence at 3.34 eV with no deep level emission by PL measurement at 77 K. Surface morphology of VPE-grown GaN is greatly improved by employing a thin layer of ZnO. Strong dependence of GaN properties on ZnO buffer layer thickness is observed and the optimized thickness is around 25 nm.

This work was supported by DARPA through the Optoelectronic Materials Center, contract MDA 972-94-1-003

4. References

- [1] Shuji Nakamura, et al. *Appl. Phys. Lett.* **70**, p1417-9 (1997)
- [2] T. Detchprohm, K. Hiramatsu, H. Amano and I. Akasaki, *Appl. Phys. Lett.* **61**, p2688 (1992)
- [3] S. Schwyn Thöny, K. E. Youden, J. S. Harris Jr. and L. Hesselink, *Appl. Phys. Lett.*, **65**, 2018 (1994)
- [4] H. Lee, M. Yuri, T. Ueda, and J. S. Harris, Jr., *Mat. Res. Soc. Proc.* **423**, 233 (1996)
- [5] S. Bethke, H. Pan and B. W. Wessels, *Appl. Phys. Lett.* **52**, 138 (1988)

GaN/GaAs(111)B grown by molecular beam epitaxy using hydrazine

**V. G. Antipov, A. I. Guriev, V. A. Elyukhin, N. N. Faleev, Yu. A. Kudriavtsev,
A. B. Lebedev, T. V. Shubina, A. S. Zubrilov**

A.F.Ioffe Physical-Technical Institute, St.Petersburg, Russia 194021,

S. A. Nikishin and H. Temkin

Electrical Engineering Department, Texas Tech University, Lubbock, TX 79409, USA

Abstract

Layers of hexagonal GaN were grown on (111)B GaAs substrates by gas source molecular beam epitaxy (GSMBE) using hydrazine as a source of active nitrogen. Nitridation of an AlAs buffer layer was shown to produce a flat layer of AlN. GaN films grown on the AlN surface at growth temperatures above 700°C exhibited quasi two-dimensional growth. Photoluminescence spectra of such GaN layers show narrow band-edge emission and no “yellow” defect band.

1. Introduction

Nitridation of GaAs is used to nucleate epitaxial growth of GaN and related compounds on substrates such as Si [1]. This process, in which GaAs is exposed to a flux of active nitrogen, must be carefully controlled in order to produce smooth surfaces suitable for growth [2-3]. This is in contrast to the nitridation of Al₂O₃ which, at similar temperatures, appears to be more stable. Two-dimensional growth of GaN can be subsequently obtained only after a smooth, nitrided, surface is created. In this work we carry out a detailed growth investigation of hexagonal GaN on (111)B oriented GaAs substrates. The use of hydrazine allows us to generate large active nitrogen fluxes, another factor important in achieving two-dimensional growth. We show that an intermediate layer of AlAs, nitrided under appropriate conditions, results in two-dimensional growth of first AlN and then GaN.

Nitridation of the AlAs layer results in formation of an AlN/GaAs interface which should be a thermodynamically stable two-phase system. Solid state reactions resulting from atomic exchanges at this interface, such as $(Ga - As) + (Al - N) \leftrightarrow (Ga - N) + (Al - As)$, where the dashes indicate chemical bonds, will result in formation of a two-phase AlN-GaAs system rather than the solid solution of $Al_xGa_{1-x}As_yN_{1-y}$ [4,5].

2. Results and discussion

The growth experiments were performed in a custom designed gas source MBE apparatus with a hydrazine (Hy) source, described in detail previously [6]. Substrate temperatures were measured using an optical pyrometer calibrated for a temperature range of $450^{\circ}\text{C} \leq T \leq 1200^{\circ}\text{C}$. Semi-insulating GaAs(111)B substrates were employed for these studies. After a 5 minute degrease in organic solvents the substrates were chemically etched in 5:1:1 hot mixture of $\text{H}_2\text{SO}_4:\text{H}_2\text{O}_2:\text{H}_2\text{O}$ for 40 sec followed by a 3 min rinse in deionized H_2O and then dried with N_2 gas. Half of the samples were bonded with In solder onto a Mo block, the others were mounted using an In-free holder. The substrates mounted in In-free holders were back-metallized for improved heat transfer. The oxide desorption was carried out at $(600 \pm 10)^{\circ}\text{C}$ for 5 min under As_4 flux.

The sample preparation and the growth process were monitored in-situ using RHEED. A clear bulk (1 x 1) RHEED pattern was observed after thermal desorption of the surface oxide layer. A sharp $(\sqrt{19} \times \sqrt{19})$ surface reconstruction, illustrated in Fig.1, was observed after the growth of a thin (~ 500 Å) GaAs layer. The GaAs epitaxial layer was grown at a temperature of $T_{gr} \sim 580^{\circ}\text{C}$ and a rate of $V_{gr} \sim 0.3 \mu\text{m/h}$. The first series of GaN growth experiments were carried out without the deposition of an AlAs buffer. The nitridation of epitaxial GaAs was performed under a hydrazine flux of $J_{Hy} \sim (1-5) \times 10^{14} \text{ mol/cm}^2 \text{ sec}$ for 5-10 min at 450°C . After nitridation, the Ga shutter was opened and a 25 nm thick

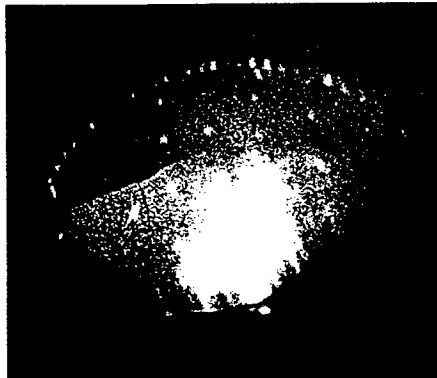


Fig.1 $(\sqrt{19} \times \sqrt{19})$ RHEED pattern

along the $[1\bar{1}0]$ azimuth from GaAs(111)B surface

before AlN buffer layer growth. $T_{\text{substr}} = 580^\circ\text{C}$



Fig.2 Cross-sectional SEM photograph of GaN/GaAs(111)B

film grown without AlN buffer layer. $T_{\text{gr}} = 720^\circ\text{C}$

intermediate layer of GaN was deposited at 450-500°C, with a growth rate of $V_{gr} \sim 0.1 \mu\text{m/h}$. The substrate temperature was then increased to (550 - 670)°C and GaN films with thicknesses in the range of 0.7 - 1.0 μm were grown at $V_{gr} \sim 0.3\text{-}0.4 \mu\text{m/h}$. In all of these experiments the $\text{N}_2\text{H}_4/\text{Ga}$ flux ratio was ~ 250 [1]. In all cases RHEED patterns obtained on such GaN films clearly indicated a three-dimensional growth mode. Higher growth temperatures are limited by the thermal instability of the GaAs substrate, leading to very rough interfaces between GaAs and GaN, see Fig.2.

A second series of GaN layers were grown with an AlN buffer layer. The buffer layers, with thicknesses of about 40 - 50 nm, were prepared by first growing thin layers of AlAs on epitaxial GaAs, at $T_{gr} \sim 580^\circ\text{C}$ and $V_{gr} \sim 0.2 \mu\text{m/h}$. These layers were then nitrided under a hydrazine flux of $\sim 10^{15} \text{ mol/cm}^2 \text{ sec}$ for 10-15 min and at a substrate temperature of 500-550°C. The nitrided surfaces exhibited a (1 x 1) RHEED pattern of elongated spots, consistent with a mixed 2D-3D nature of the surface. An epitaxial layer of AlN, ~ 50nm thick, was then deposited on the nitrided AlAs surface. This was done at $T_{gr} \sim 580^\circ\text{C}$ and a growth rate of $V_{gr} \sim 300 \text{ \AA/h}$. The RHEED pattern of this AlN surface, shown in Fig.3, is consistent with well-developed two-dimensional growth.

GaN layers were grown on AlN buffers, formed by a combination of nitridation and epitaxy, at temperatures ranging from 650-720°C and at $V_{gr} \sim 0.3\text{-}0.4 \mu\text{m/h}$. The AlN buffer remains stable at higher temperatures and the growth temperature of GaN can be increased. RHEED patterns obtained on GaN surfaces, shown in Fig.4, clearly indicate quasi two-dimensional growth. Further optimization of the $\text{N}_2\text{H}_4/\text{Ga}$ flux ratio appears necessary in order to obtain pure 2D mode. RHEED patterns obtained on GaN layers grown directly on GaAs could be interpreted in terms of preferentially oriented three-dimensional domains. Nevertheless, the interfaces between AlN and GaAs layers are quite flat. Fig.5 shows the cross-sectional SEM image of a GaN/AlN/GaAs structure grown at $T_{gr} \sim 720^\circ\text{C}$.



Fig.3 RHEED pattern of AlN layer grown on
nitridated AlAs/GaAs(111)B at $T_{\text{substr}} = 620^\circ\text{C}$,
 $\text{N}_2\text{H}_4/\text{Al} \sim 500$, $e^- \parallel [11\bar{2}0]$ azimuth



Fig.4 RHEED pattern of GaN film grown on
GaAs(111)B surface with AlN buffer layer, $T_{\text{gr}} =$
 720°C , $\text{N}_2\text{H}_4/\text{Ga} \sim 250$. $e^- \parallel [11\bar{2}0]$ azimuth

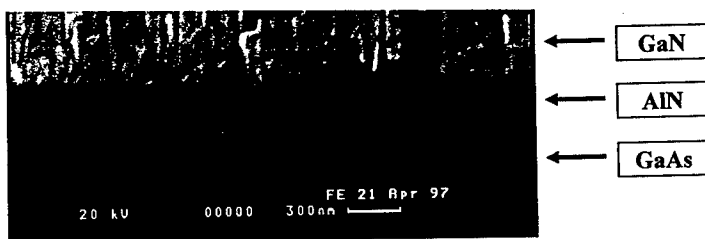


Fig.5 Cross-sectional SEM image of GaN/AlN/GaAs(111)B
structure, T_{gr} of GaN film = 720°C , $\text{N}_2\text{H}_4/\text{Ga} \sim 300$

The optical properties of GaN layers were studied by cathodoluminescence (CL) at 80K. Fig.6 shows CL spectra for two of the GaN/GaAs(111)B films grown at 550°C and 670°C, without the AlN buffer layer. The spectra show the edge band in the 350–400 nm spectral region and a prominent broad, “yellow”, band at $\lambda > 500$ nm. The band-edge emission wavelength of ~380 nm measured in samples grown at low temperature is characteristic of cubic-structure GaN, consistent with our previous results on GaAs(100) [3]. The band-edge emission wavelength shifts to ~360 nm in samples grown at the higher temperature. While this is typical of hexagonal GaN, the width of the peak makes clear assignment difficult [1]. Raman scattering results, not shown here, also support the hexagonal structure identification of high temperature samples.

The CL spectra obtained on GaN samples grown with the AlN buffer layer at temperatures lower than ~670°C are similar to those shown in Fig. 6. The spectra differed only in the lower intensity of the “defect” band. The results obtained for samples mounted with In and in In-free holders were very similar. These samples were also investigated using pulsed excitation with a nitrogen laser operating at 337 nm. The excitation intensity was adjusted to yield PL spectra of the wavelength and width similar to those produced by CL.

The PL spectra of GaN samples mounted with In and grown at temperatures $T_{gr} > 700^\circ\text{C}$ with the optimized AlN buffer layer are very different. Their main features are the complete absence of the “yellow band” and very narrow band-edge emission, less than 20 meV at 77K, Fig.7. Samples of GaN grown directly on GaAs, at temperatures above 700°C, show much wider band-edge emission and strong “yellow” lines. The interpretation of the data shown in Fig.7 is, however, complicated by the non-intentional incorporation of In into the GaN layer. This occurs in case of In-mounted samples. SIMS measurements of these layers show that the In concentration can be as high as 5 at% at the sample’s edge, it decreases towards the center. This explains the red shift in the band-edge emission

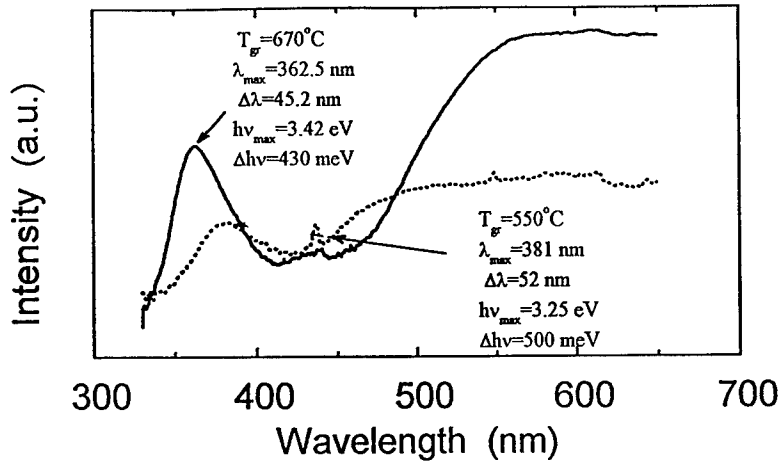


Fig.6. 80K CL spectra of GaN layers grown on GaAs(111)B without AlN buffer layer.

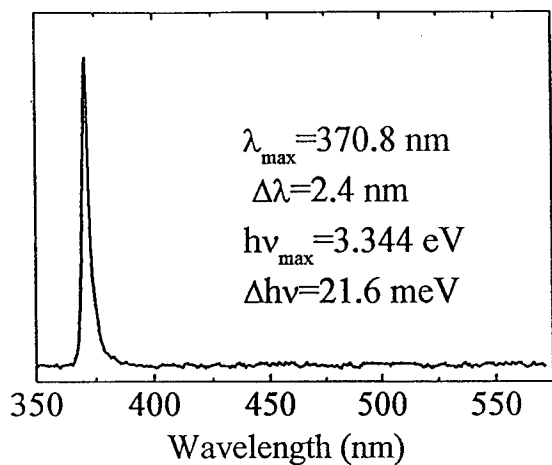


Fig. 7. 77K PL spectra of GaN layers grown on GaAs (111)B with AlN buffer layer. The substrate was bonded with in-solder onto holder.

shown in Fig.7. We believe that the qualitative difference between the spectra shown in Figs.6 and 7 is due to inclusion of the AlN buffer layer and higher growth temperature.

3. Conclusion

Wurtzite phase GaN layer were grown on GaAs(111)B substrates by GSMBE using hydrazine as a nitrogen source. We demonstrate that nitridation of an AlAs buffer layer grown on a clean GaAs(111)B surface provides a smooth AlN/GaAs interface which in turn promotes two-dimensional growth of AlN. The presence of this buffer layer permits the use of higher growth temperatures, up to 720°C. Epitaxial layers of GaN grown with the AlN buffer layer show quasi two-dimensional growth. The PL spectra of the layers grown above 700°C show narrow band-edge emission and a complete absence of the “yellow” defect band.

4. Acknowledgements

This material is based upon work supported by the U.S. Civilian Research and Development Foundation under Award No. RP1-354 and Jack Maddox Foundation. The Ioffe Institutes authors also acknowledge financial support from Russian State Programs “Surface Atomic Structures”, Project No 95-2.21 and RFBR No 97-02-18269(a)

5. References

- [1] Antipov V G, Guriev A I, Elyukhin V A, Kyutt R N, Smirnov A B, Faleev N N, Nikishin S A, Seryogin G A and Temkin H, 1997 Inst. Phys. Conf. Ser. No155 Ch3 327-330
- [2] Kobayashi Y, Scholz F and Kobayashi N 1997 Jpn. J. Appl. Phys. 36A
- [3] Nikishin S A, Antipov V G, Ruvimov S S, Seryogin G A and Temkin H 1996 Appl. Phys. Lett. 69 3227-3229

- [4] Elyukhin V A, Karpov S Yu, Sorokina L P and Fronts K 1982 Soviet Physics, Crystallography 27 668-669
- [5] Onabe K 1982 J. Phys. Chem. Sol. 43 1071-1086
- [6] Antipov V G, Zubrilov A S, Merkulov A V, Nikishin S A, Sitnikova A A, Stepanov M V, Troshkov S I, Ulin V P and Faleev N N 1995 Semiconductors (Russia) 29 946-951

Demonstration of a GaAs-Based Compliant Substrate Using Wafer Bonding and Substrate Removal Techniques

C. Zhang, D. I. Lubyshev, W. Cai, J. E. Neal, D. L. Miller, and T. S. Mayer
 Electronic Materials and Processing Research Laboratory, Department of Electrical Engineering,
 The Pennsylvania State University, University Park, PA 16802

Abstract: A GaAs-based compliant substrate that uses an intermediate AlGaAs-oxide layer to separate thin 150 Å – 1000 Å GaAs compliant layers from a GaAs host substrate is described. The compliant substrates and epitaxial layers of lattice-mismatched $In_{0.15}Ga_{0.85}As$ were studied using atomic force microscopy and double-crystal x-ray diffraction. The surface morphology of the 1000 Å compliant substrate prior to growth had an rms and peak-to-peak roughness of 10 Å and 100 Å. Following growth of 3000 Å $In_{0.15}Ga_{0.85}As$ the root mean square (rms) roughness increased to 50 Å and slip lines were observed in the (110) direction. A comparison of lattice-matched p⁺-n junction diodes grown on a substrate with a 1000 Å compliant layer and a standard GaAs substrate revealed similar dark current-voltage characteristics, which demonstrate the high quality of the compliant substrate.

1. Introduction

Traditionally, the growth of lattice-mismatched materials has relied on compositionally graded buffer layers to relieve strain due to the lattice mismatch between the thick substrate and the epitaxial layers [1]. Unfortunately, these graded buffers are not completely effective in eliminating threading dislocations in the active device layers, which results in a degradation of device performance [2]. Calculations by Lo *et. al.* suggest that thin (< 1000 Å) free-standing substrates can be used to increase the critical thickness of a mismatched overlayer [3]. In this case, the thin substrate can relax before the epitaxial layer relaxes, which allows the growth of active device layers having low dislocation density. One approach that has been used by Ejekam *et. al.* to fabricate pseudo-free standing substrates is based on a so-called twist bond that is formed between a thin GaAs compliant layer and a GaAs substrate when the compliant layer is misoriented relative to the substrate [4]. This approach forms uniformly spaced, weakly bonded areas that permit the substrate to conform to the growing epitaxial layers. In this paper, we demonstrate an alternate approach to fabricating compliant substrates that is based on separating the top GaAs compliant layer from the GaAs host substrate by an intermediate oxide layer formed by the wet oxidation of $Al_{0.9}Ga_{0.1}As$. Previous work using silicon-on-insulator structures suggests that the use of such oxide layers decreases the interaction between the compliant layer and the host substrate and can provide increased flexibility of the compliant layer [5]. The procedure used to prepare a GaAs-based compliant substrate with an intermediate oxide layer is described, and the results of lattice-matched and lattice-mismatched growth of GaAs and InGaAs epitaxial layers on the compliant substrates are presented.

2. Substrate Preparation and Characterization

The substrates investigated in this work contained a thin GaAs compliant layer that was separated from a GaAs host substrate by an intermediate AlGaAs-oxide layer. The samples used to form the host substrate, the AlGaAs-oxide layer, and the upper thin compliant GaAs layer were grown by molecular beam epitaxy (MBE) on (100) semi-insulating GaAs substrates. The structures consisted of a 1000 Å GaAs buffer layer, a 1000 Å $Al_{0.9}Ga_{0.1}As$ layer, and GaAs layers that were either 150 Å or 1000 Å thick. Following the growth, the top GaAs layer was removed from half of each sample and the 1000 Å $Al_{0.9}Ga_{0.1}As$ layer was oxidized in water vapor at 425°C for 10 minutes. It has been demonstrated previously that under these oxidation conditions $Al_{0.9}Ga_{0.1}As$ forms a stable phase of $\gamma-Al_2O_3$ [6]. This intermediate layer was chosen primarily for its ease of wafer bonding to GaAs epitaxial layers and the relatively porous nature of the oxide [6]. The thin 150 Å or 1000 Å GaAs layer on the remaining portion of each sample was wafer bonded at room temperature to the AlGaAs-oxide layer after cleaning and

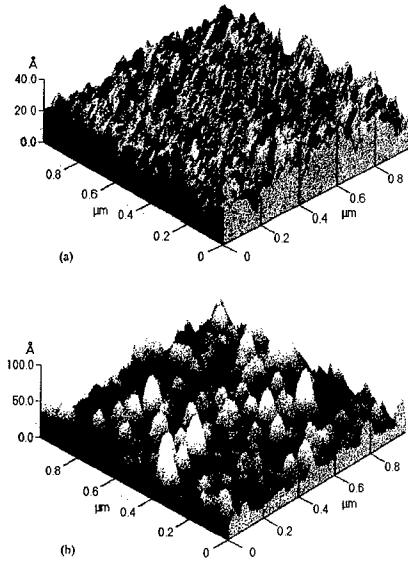


Fig. 1. AFM images of the (a) AlGaAs-oxide layer and the (b) completed 1000 Å compliant substrate prior to growth.

approximately 6 Å and 30 Å. Large area images of this sample also indicated a very uniform surface morphology with no large peaks or valleys in the AlGaAs-oxide layer. The smooth, uniform surface morphology of the AlGaAs-oxide layer facilitated a wafer bond between the oxide and GaAs layers that was able to withstand subsequent mechanical and chemical wafer thinning. Following compliant substrate preparation, the sample with a 1000 Å compliant GaAs layer had an rms roughness less than 10 Å with isolated peaks that were 85–100 Å tall distributed across the surface. We believe that these tall peaks are a result of the incomplete removal of the $\text{Al}_{0.9}\text{Ga}_{0.1}\text{As}$ etch stop layer, which may be eliminated by reducing the aluminum molar fraction of the etch stop layer. These tall features were also observed on samples prepared using a GaAs-to-GaAs direct wafer bond and were not a result of the intermediate oxide layer. In contrast, the sample with a 150 Å compliant GaAs layer had an rms and peak-to-peak roughness of 50 Å and 250 Å. A visual inspection of the surface using an optical microscope revealed that the thin 150 Å GaAs compliant layer was discontinuous, which resulted in the increased surface roughness. This represents a limitation in the thickness of the compliant layer that can be obtained using the intermediate AlGaAs oxide layer described here. By optimizing the oxidation procedure, it may be possible to obtain smoother AlGaAs oxide surfaces and thinner compliant layers.

3. Epitaxial Growth and Device Characterization

In order to assess the quality of the compliant substrates, a lattice-matched GaAs p⁺-n diode was grown on the compliant substrate with a 1000 Å GaAs layer and compared to an identical device grown on a standard GaAs substrate. The structure consisted of a 1.0 μm n⁺-GaAs layer, a 1.5 μm n-GaAs layer, and a 0.5 μm p⁺-GaAs contact layer. Devices with active areas of 100 × 100 μm² were fabricated using a standard mesa-isolated process. Ohmic contacts were formed to the top p⁺-GaAs layer using Ti/Pt/Au

drying the AlGaAs-oxide and GaAs surfaces. To strengthen the room temperature bond, the samples were annealed in a nitrogen ambient at 500°C for 20 minutes. After forming a strong bond between the thin GaAs and AlGaAs-oxide layers, the topmost GaAs substrate and buffer layer were removed by mechanical polishing and wet chemical etching in a citric acid solution, which stops abruptly on the 1000 Å $\text{Al}_{0.9}\text{Ga}_{0.1}\text{As}$ layer [7]. Compliant substrates of 1 × 1 cm² were obtained using this method. Prior to loading the samples into the MBE, the $\text{Al}_{0.9}\text{Ga}_{0.1}\text{As}$ layer was removed in buffered oxide etch leaving only the thin GaAs compliant layer supported on the AlGaAs oxide and host substrate.

The surface morphology of the AlGaAs-oxide layer prior to wafer bonding and the surface of the 1000 Å and 150 Å compliant layers following the GaAs substrate and $\text{Al}_{0.9}\text{Ga}_{0.1}\text{As}$ etch stop removal were studied by atomic force microscopy (AFM) using a Park Scientific Autoprobe M5 AFM. Typical 1 × 1 μm² images of the AlGaAs oxide layer and the completed 1000 Å compliant substrate prior to MBE growth are shown in Fig. 1 (a)–(b). The AlGaAs-oxide layer was very smooth, having a root mean square (rms) and peak-to-peak roughness of

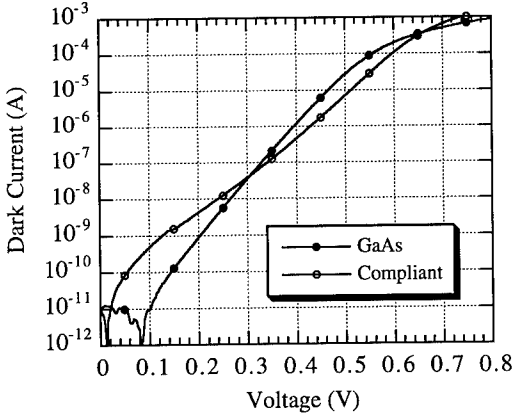


Fig. 2. Typical dark I-V characteristics of GaAs diodes fabricated on a 1000 Å compliant substrate and a standard GaAs substrate.

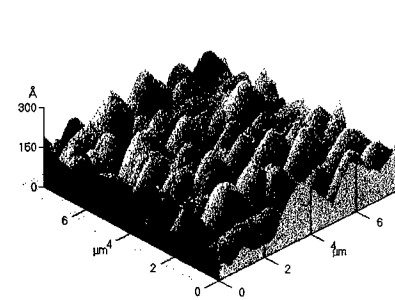


Fig. 3. AFM image of a 1000 Å compliant substrate following the growth of 3000 Å of $\text{In}_{0.15}\text{Ga}_{0.85}\text{As}$.

and to the bottom n^+ -GaAs layer using alloyed Ni/AuGe. The successful fabrication of the mesa-isolated diode demonstrates that the GaAs-AlGaAs oxide compliant substrate is robust and is able to withstand extensive post-processing. Typical dark forward current-voltage (I-V) characteristics of diodes fabricated on the compliant and standard GaAs substrates are shown in Fig. 2. The diode on the standard GaAs substrate had ideal $n = 1$ characteristics over the measured voltage range, while the diode on the GaAs compliant substrate demonstrated non-ideal $n = 2$ characteristics at low forward biases with $n = 1$ characteristics dominating at high forward biases. This non-ideal $n = 2$ current component is typically attributed to recombination in the bulk space-charge region of the diode, and may be a result of the rougher surface morphology of the starting compliant substrate. Although non-ideal behavior was observed for the diodes fabricated on the compliant substrate, the value of the current was comparable to that of the diode grown on the standard substrate indicating the high quality of the compliant substrate.

To study the growth of lattice mismatched materials, 3000 Å of $\text{In}_{0.15}\text{Ga}_{0.85}\text{As}$ (1% lattice mismatch) was deposited by MBE on 1000 Å and 150 Å compliant substrates as well as on a standard GaAs substrate. The substrate temperature during the growth of the $\text{In}_{0.15}\text{Ga}_{0.85}\text{As}$ layer was 450°C. The surface morphology of the $\text{In}_{0.15}\text{Ga}_{0.85}\text{As}$ layers grown on a 1000 Å compliant substrate is shown in Fig. 3. The sample with a 1000 Å compliant GaAs layer had an rms roughness less than 50 Å, with slip lines spaced an average of 0.7 μm apart along the (110) direction. The sample with a 150 Å compliant GaAs layer had a much rougher surface morphology with an rms and peak-to-peak roughness of 130 Å and 650 Å. In this case, no slip lines were observed. This can be attributed to the poor starting surface of the compliant substrate. Double crystal x-ray diffraction measurements of these samples yielded a FWHM of approximately 900 arc-sec with no discernible peak-shift between the layers deposited on the 1000 Å compliant substrate and the standard GaAs substrate.

Lattice-mismatched $\text{In}_{0.20}\text{Ga}_{0.80}\text{As}$ p-i-n diodes were also grown on a 1000 Å compliant substrate. The structure consisted of a 0.7 μm n^+ - $\text{In}_{0.20}\text{Ga}_{0.80}\text{As}$ layer, a 1 μm undoped $\text{In}_{0.20}\text{Ga}_{0.80}\text{As}$ layer, and a 1500 Å p^+ - $\text{In}_{0.20}\text{Ga}_{0.80}\text{As}$ contact layer. Diodes were fabricated using the mesa-isolated process described previously. The forward and reverse dark I-V characteristics of a typical $100 \times 100 \mu\text{m}^2$ device is shown in Fig. 4. Although the dark currents are substantially higher than those calculated theoretically for dislocation-free material [8], the diodes demonstrated a rectifying behavior. The high dark current and soft reverse breakdown voltage suggests that there is still a relatively high density of dislocations present in the active device layers. It has been demonstrated for the growth of

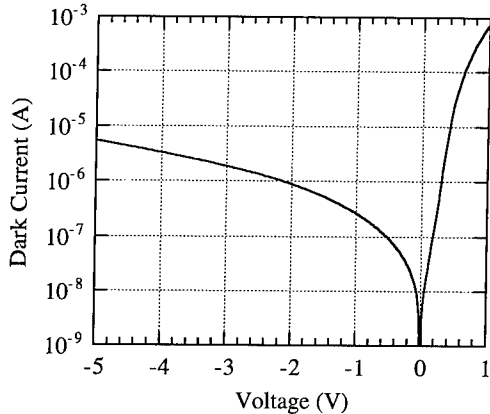


Fig. 4. Typical dark I-V characteristics of $\text{In}_{0.20}\text{Ga}_{0.80}\text{As}$ diodes fabricated on a 1000 Å compliant substrate.

$\text{In}_{0.65}\text{Ga}_{0.35}\text{As}$ layers on $\text{In}_{0.52}\text{Al}_{0.48}\text{As}/\text{InP}$ substrates that the critical thickness of lattice mismatched materials is reduced dramatically when the layers are deposited on intentionally roughened surfaces [9]. Therefore, the rough surface morphology of the starting GaAs-based compliant substrate may also degrade the quality of the lattice-mismatched material by limiting the critical thickness of the $\text{In}_{0.20}\text{Ga}_{0.80}\text{As}$ epitaxial layers.

4. Conclusions

In this paper, we describe the fabrication of a GaAs-based compliant substrate that uses an intermediate AlGaAs-oxide layer to separate thin 150 Å–1000 Å GaAs compliant layers from a GaAs host substrate. Prior to growth, the rms roughness of the substrate with a 1000 Å compliant layer was less than 10 Å with isolated peaks that were 85–100 Å tall. We attribute the

tall peaks to the incomplete removal of the AlGaAs etch stop layer, which may be eliminated by reducing the aluminum molar fraction in the etch stop layer. The thinner 150 Å compliant layer was discontinuous, resulting in a surface with an rms roughness of approximately 50 Å. A comparison of lattice-matched p⁺-n junction diodes grown on a substrate with a 1000 Å compliant layer and a standard GaAs substrate revealed similar dark I-V characteristics, which demonstrate the high quality of the compliant substrate. The fabrication of these devices confirms that the compliant substrate is robust and is able to withstand extensive post-processing. The growth of 3000 Å of $\text{In}_{0.15}\text{Ga}_{0.85}\text{As}$ on the substrate with a 1000 Å compliant layer resulted in a surface with an rms roughness of 50 Å that contained slip lines in the (110) direction. Lattice-mismatched $\text{In}_{0.20}\text{Ga}_{0.80}\text{As}$ p-i-n diodes grown on the 1000 Å compliant substrate were rectifying, however, the magnitude of the dark current suggests the presence of electrically active dislocations in the active layers. Further improvement in quality of the lattice-matched and lattice-mismatched epitaxial layers may be obtained by improving the surface morphology of the starting compliant substrate.

5. Acknowledgments

This work was supported by the ONR Grant # N00014-97-1-0951 and by the NSF CAREER Grant # ECS 9501820. The authors thank T. N. Jackson for his assistance with the AFM studies.

6. References

- [1] Olsen G H, Abrahams M S, Buiocchi C J and Zamerowski T J 1975 *J. Appl. Phys.* **46** (4) 1643-46
- [2] Kochhar R, Hwang W Y, Micovic M, Mayer T S, Miller D L and Lord S 1997 *J. Vac. Sci. Tech. B* **15** (2) 316-320
- [3] Teng D and Lo Y H 1992 *Appl. Phys. Lett.* **62** (1) 43-45
- [4] Ejeckam F E, Lo Y H, Subramanain S, Hou H Q and Hammons B E 1997 *Appl. Phys. Lett.* **70** (13) 1685-87
- [5] Powell A R, Iyer S S and LeGoues F K 1994 *Appl. Phys. Lett.* **64** (14) 1856-58
- [6] Tweten R D, Follstaedt D M, Choquette K D, and Schneider Jr. R P 1996 *Appl. Phys. Lett.*, **69** (1) 19-21
- [7] Tong M, Ballegeer D G, Ketterson A, Roan E J, Cheng K Y and Adesida I 1991 *J. Electron. Mat.* **21** (1) 9-15
- [8] Jones K A 1987 *Introduction to Optical Electronics* (New York: Harper & Row)
- [9] Gendry M, Drouot V, Hollinger G and Mahajan S 1995 *Appl. Phys. Lett.* **66** (1) 40-42

Comparison of MBE grown InSb on CU substrates using different sacrificial layers

M. L. Seaford, D. H. Tomich, K. G. Eyink, W. V. Lampert

Air Force Research Laboratory, Materials Directorate, Wright-Patterson AFB, OH 45433-7750

F. E. Ejeckam, Y.-H. Lo

School of Electrical Engineering, Cornell University, Ithaca, NY 14853

Abstract. InSb epitaxial layers with approximately 15% lattice mismatched to GaAs were grown on a conventional GaAs substrate and compliant universal (CU) substrates using various sacrificial layers. Transmission electron microscopy studies showed dislocation free InSb films grown on the CU substrate using the AlGaAs sacrificial layer, whereas the InSb films on the normal GaAs substrate and the CU substrate with the InGaP sacrificial layer exhibited dislocation densities as high as 10^{11} cm^{-2} . Reciprocal space maps of the (004) peak for the dislocation free InSb layer revealed a large mosaic spread of $\sim 0.25^\circ$. Using atomic force microscopy on the dislocation free InSb layer, the mosaic spread was found to be generated by a periodic surface undulation with a three micron period and 700Å amplitude.

Introduction

Typical growth of semiconductors has been restricted to growth on only a few binary substrates due to strain caused by the lattice mismatch present between the epilayer and the substrate. This strain must be contained in the thin film since the total energy in either layer increases with the thickness of the layer. Growth in which all the total misfit is accommodated by strain in the thin film is termed pseudomorphic.[1] A commonly accepted thickness limit to pseudomorphic growth is the Matthews-Blakeslee critical thickness.[2] In this process, the lattice constant of the thin film will relax to the bulk value generating dislocations and point defects when grown beyond the critical thickness.

If the layer could be uncoupled from the substrate, the strain energy of the film would not increase with thickness and high quality growth would occur independent of film thickness. A substrate capable of allowing growth beyond the pseudomorphic limit has been termed a compliant substrate.[3] Recently Ejeckam et. al.[4] produced a compliant universal (CU) substrate using a twist bonding technology. Using MBE, the ability to grow highly lattice mismatched ($>14\%$), dislocation free materials[5] on a CU substrate has been demonstrated. It is necessary to carefully characterize both the starting and final materials involved in the creation of the CU substrate.

Originally, two different materials were used for the sacrificial layer in the process of creating the CU substrate. The dislocation-free InSb was grown on a compliant substrate that had been formed using AlGaAs sacrificial layers. In this work, we compare and analyze the CU substrate, the sacrificial layers, and the final InSb epitaxial layer.

Experimental

Growth was carried out in a Varian Gen II solid source molecular beam epitaxy system on two different types of substrates under nominally the same conditions. The normal substrate was a nominally on-axis, semi-insulating epi-ready GaAs substrate. The second type of substrate, the CU

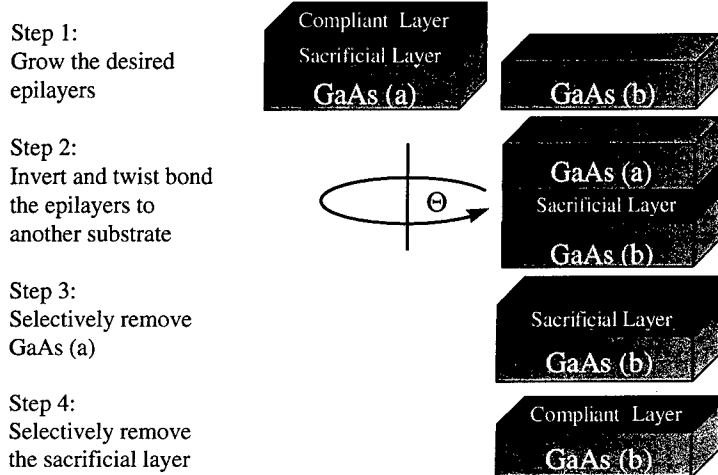


Figure 1. Process for creating a Compliant Universal Substrate

substrate, was created as shown in Figure 1. Two different materials, $In_{0.5}Ga_{0.5}P$ and $Al_{0.7}Ga_{0.3}As$ were used for the 1 μm thick sacrificial layers. The compliant layer was GaAs of less than 100 \AA . The twist bonding process was initially performed at temperatures up to 565°C for approximately one hour. The GaAs(a) was then selectively removed. The quality of the CU substrate was monitored using high resolution x-ray diffraction (HRXRD) reciprocal space maps (RSM) of the sacrificial layers. The sacrificial layer was then chemically removed using HCl acid. The normal and CU substrates were indium bonded to a three inch silicon wafer prior to growth. All substrates were outgassed at 200°C for 20 minutes prior to introduction to the growth chamber. Growth was performed using a cracked Sb source with a cracker temperature believed to produce monomeric Sb at an overpressure of 1×10^{-6} torr. The InSb growth rate was ~1.8 $\text{\AA}/\text{sec}$ for a total thickness of ~6500 \AA for all samples.

After growth, the film was analyzed by HRXRD using a Philips MRD:HR system with a 4 crystal monochromator and a triple crystal detector. Atomic force microscopy (AFM) was also performed on the samples after growth to study the surface morphology of the films. A Digital Instruments Multimode AFM in tapping mode[®] was used for all measurements.

Results and Discussion

The InSb film grown on the CU substrate using the AlGaAs sacrificial layer had a nearly specular surface typical of high quality growth. The growth of InSb on the normal substrate and the CU substrate with the InGaP sacrificial layer produced a visually hazy surface typical of growth beyond the pseudomorphic limit.

Transmission electron microscopy (TEM) of the InSb grown on a normal substrate and the CU substrate with the InGaP sacrificial layer found a high density of dislocations ($>10^{11} \text{ cm}^{-2}$) due to the

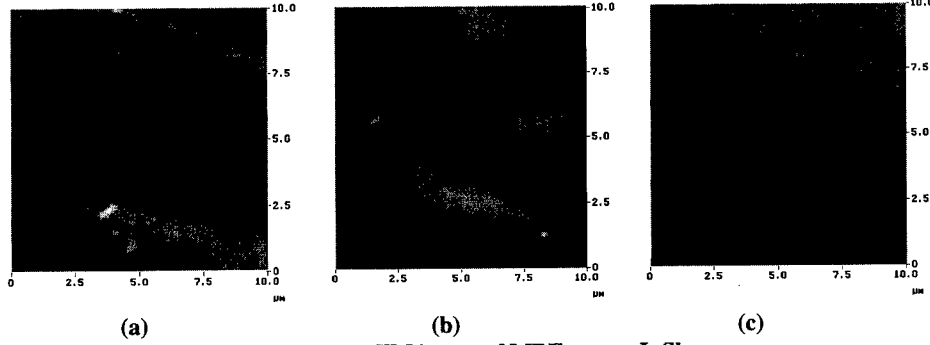


Figure 2. AFM image of MBE grown InSb on
 (a) CU substrate with InGaP Sacrificial Layer
 (b) CU substrate with AlGaAs Sacrificial Layer
 (c) Normal GaAs Substrate

large lattice mismatch. Extensive TEM of the InSb grown on the CU substrate with the AlGaAs sacrificial layer found no dislocation ($< 10^6$ dislocations/cm 2). [5,6]

The HRXRD reciprocal space map (RSM) showed that the peak was spread only 0.1° in the coupled $\Omega/2\theta$ direction, but had a full width half maximum (FWHM) of $\sim 0.25^\circ$ in the Ω direction. This large spread in the Ω direction indicates a mosaic tilt in the crystal of 0.25° . AFM was performed on the InSb growth on the CU substrate (Figure 2b). As can be seen from this micrograph, a rolling surface is observed. This surface has variations in height of $\sim 700\text{ \AA}$ which occur in nearly $3\mu\text{m}$ periods.

Steps were clearly observable for the InSb growth on normal GaAs. Since no steps were observed with AFM on the CU growth using the AlGaAs sacrificial layer, the surface undulation is believed to result from the bending in the thin InSb layer. When the surface height variation is approximated with a periodic function the mosaic spread is calculated to be 0.29° which is consistent with the HRXRD analysis.

The TEM and AFM results clearly indicate that the CU substrates created using the InGaP sacrificial layer failed. The plate-like features seen in Figure 2a revealed that the InSb layer had registered the 40° rotation of the thin compliant layer. In addition, electron diffraction analysis showed that both InSb films grown on CU substrates had the orientation of the thin twist bonded layer ($\sim 40^\circ$ rotation). HRXRD RSM were taken immediately following layer growth (Figure 1, step 1) and prior to removing the sacrificial layer (Figure 1, step 3). The data from the AlGaAs sacrificial layer appears exactly the same before and after twist bonding. However, as shown in Figure 3, the InGaP sacrificial layer quality was noticeably reduced during the bonding process. It is expected that this also damaged the thin compliant layer resulting in the failure of the CU substrate when the InGaP sacrificial layer is used. Lower bonding temperatures were used in an effort to preserve the layer quality. Although, the lower temperatures reduced the damage, a method has not yet been found that will allow the InGaP to be used as the sacrificial layer in the process needed to create the CU substrate.

With the lack of observed dislocations, the $>10\%$ height variation in the epilayer, and the lack of observable terrace features, we believe that voids must form between the epilayer and the CU substrate. At this time, the observed interface roughness at the growth interface is not large enough to account for the InSb surface height variation. We are currently performing cross-sectional studies to analyze this further.

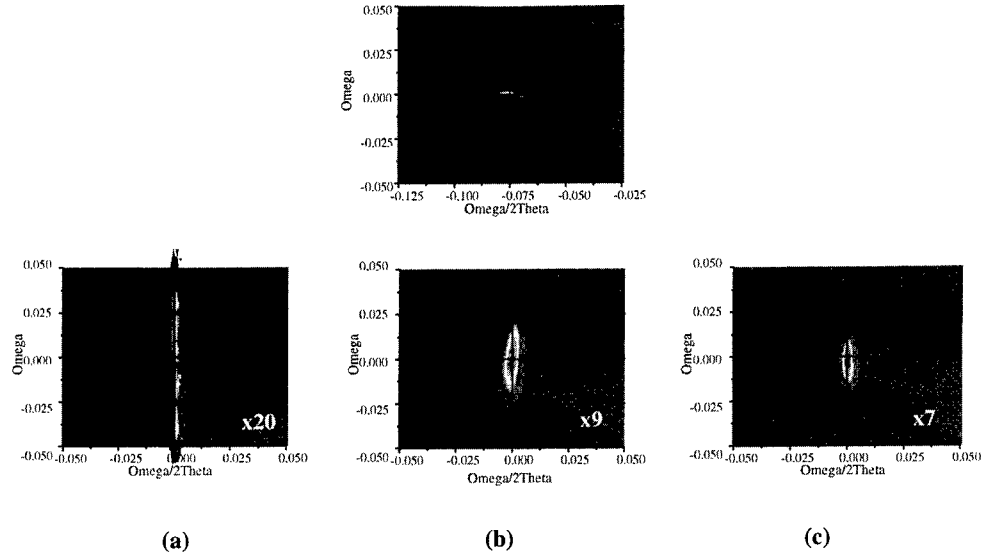


Figure 3. HRXRD - RSM of InGaP sacrificial layers before bonding (top) and after bonding at the different temperatures of (a) 565°C, (b) 505°C, and (c) 415°C
Intensity scaled by (a) x20, (b) x9, and (c) x7 relative to before bonding

Conclusions

We have successfully grown dislocation free InSb on a CU substrate when using AlGaAs sacrificial layers. InGaP sacrificial layers were not found capable of withstanding the bonding process without substantially damaging the resulting CU substrate. HRXRD RSM images of the InSb layer has shown that this growth contains a 0.25° spread in the orientation of the epilayer. AFM has confirmed the presence of a surface undulation with a period of approximately 3 microns and amplitude of 700Å. The geometry of this surface would generate a 0.29° omega variation with a buckling of the InSb layer and void formation at the interface.

References

- [1] F.C. Frank and J.H. van der Merwe 1949 *Proc. R. Soc. London A* **198** 216
- [2] J.W. Matthews and A.E. Blakeslee 1974 *J. Cryst. Growth* **27** 118
- [3] Y.-H. Lo 1991 *Appl. Phys. Lett.* **59** 2311-3
- [4] F.E. Ejeckam, Y.H. Lo, M.L. Seaford, H.Q. Hou, B.E. Hammons *Proc. 1996 IEEE LEOS PDP2.5*
- [5] F.E. Ejeckam, M.L. Seaford, Z.H. Zhu, K.G. Eyink, D.H. Tomich, H.Q. Hou, B.E. Hammons, and Y.H. Lo, 1997 *Proc. 9th IPRM Conf.* 452-4
- [6] F.E. Ejeckam, M.L. Seaford, Y.H. Lo, H.Q. Hou, B.E. Hammons 1997 *Appl. Phys. Lett.* **71** 776-8

Modeling MBE RHEED Signals Using PCA and Neural Networks

T. Brown, K. Lee, G. Dagnall, R. Kromann, R. Bicknell-Tassius, A. Brown, J. Dorsey, G. May

School of ECE, Georgia Institute of Technology, Atlanta, GA 30332-0250, USA

Abstract. This paper introduces a novel technique for constructing an empirical model which relates RHEED intensity patterns to the physical characteristics of MBE grown thin films. A fractional factorial experiment is used to systematically characterize the growth of a five-layer, undoped AlGaAs-InGaAs single quantum well structure on a GaAs substrate as a function of time and temperature for oxide removal, substrate temperatures for AlGaAs and InGaAs layer growth, beam equivalent pressure of the As source and quantum well interrupt time. MBE growth takes place in a Varian Gen-II MBE system using substrate rotation, and RHEED signals are monitored for each experimental trial. RHEED pattern variation is used as an indicator of defect density, x-ray diffraction, and photoluminescence of the grown films. Principal component analysis is used to reduce the dimensionality of the RHEED data set, while maintaining the integrity of the information contained within. The reduced RHEED data set is used to train back-propagation neural networks to model the process responses. These models are quite accurate (about 3% RMSE on training data and less than 10% RMSE for test data), implying that the principal components are a reliable source of input data. Continued development will lead to models which provide a platform upon which to build an automated process control system for MBE growth.

1. Introduction

Molecular beam epitaxy (MBE) is a well-developed technique for growing various compound semiconductor structures. Due to the complexity of growth mechanisms and the large number of adjustable input conditions involved, acceptable process conditions have primarily been derived by trial and error. In addition, the methodology used in most research in MBE growth kinetics has furnished only limited information regarding the effect of variations in process conditions. This can result in the loss of critical data required for process optimization. As process complexity increases, means must be identified for implementing automated process control.

This paper presents a novel technique for constructing an empirical model relating reflection high-energy electron diffraction (RHEED) intensity patterns to the physical characteristics of MBE-grown thin films. A fractional factorial experiment was used to systematically characterize the growth of a five-layer, undoped $\text{Al}_{0.24}\text{Ga}_{0.76}\text{As}-\text{In}_{0.2}\text{Ga}_{0.8}\text{As}$ single quantum well structure on a GaAs substrate as a function of varying process conditions [1]. Growth took place using substrate rotation in a standard 3-chamber Varian Gen-II system with solid source effusion cells. RHEED signals were monitored for each experimental trial, and RHEED pattern variation was used as an indicator of defect density, x-ray diffraction, and photoluminescence (PL) of the grown films. Our process modeling technique uses principal component analysis (PCA) [2] to reduce the dimensionality of the RHEED data, and the reduced RHEED data was used to train back-propagation (BP) neural networks [3] to model the process responses. These models were quite accurate (3% RMS error on training data and less than 10% RMSE for test data), implying that the principal components are a reliable source of input data.

2. Experimental Design

To obtain the data for modeling the MBE RHEED signals, a 2^{6-2} factorial experiment requiring 16 trials was used to characterize the growth of a $\text{Al}_{0.24}\text{Ga}_{0.76}\text{As}-\text{In}_{0.2}\text{Ga}_{0.8}\text{As}$ single quantum well structure on a GaAs substrate (Figure 1). This structure is illustrative of the most common device configurations grown by MBE. Six input factors were examined in this experiment. These factors were time and temperature for oxide removal, substrate temperature for AlGaAs and InGaAs layer growth, beam equivalent pressure of the As source and quantum well interrupt time (Table 1).

Table 1: Experimental Factors and Ranges

No	Factor Description	Range
1	Temperature for oxide removal	580 - 650 °C
2	Time for oxide removal	30 - 300 sec
3	Temperature for AlGaAs growth	580 - 630 °C
4	Temperature for InGaAs growth	450 - 520 °C
5	As source temperature	325 - 340 °C
6	Interrupt time	30 - 90 sec

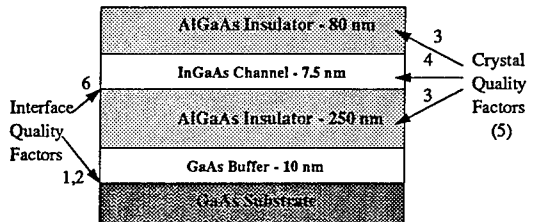


Figure 1 - Single quantum well test structure.

RHEED has long been employed as a tool for in-situ probing the properties of surfaces during MBE. Data relating to surface diffusion, crystal growth mechanisms, and dopant incorporation are examples of information which have been obtained from studies of RHEED intensity oscillations. Even more relevant is the fact that RHEED features have been used in several process control models to calibrate beam fluxes and control alloy composition and thickness of quantum wells and superlattice layers. It is quite likely that RHEED data contains more information about the growth process than could ever be obtained from knowledge of the process set points alone. Therefore, RHEED signals monitored for each of the 16 trials in this experiment were used as indicators of defect density, x-ray diffraction, and PL of the grown films.

3. Process Modeling

Our modeling technique uses PCA to reduce the dimensionality of the RHEED data set, while maintaining the integrity of the information it contains. An example of the raw RHEED intensity data corresponding to a specific set of process conditions appears in Figure 2. Before PCA was performed, the raw data was normalized to a common time scale by block averaging. This yielded 100 RHEED intensity values over time for each of the 16 experimental trials. Dimensionality reduction through PCA was achieved by transforming the normalized RHEED data to a set of principal components (PCs), which are uncorrelated and ordered such that the first few retain most of the variation present in the original data set. After they have been derived, the PCs may be used as predictor variables to estimate the MBE process responses.

The PCs of the RHEED data were used to train BP neural networks to model film defect density,

x-ray and PL. Recently, neural networks have emerged as an attractive method for semiconductor process modeling [3]. Neural networks possess the unique capability of learning arbitrary nonlinear mappings between noisy sets of input and output patterns. Feed-forward neural networks consists of layers of simple processing units which are interconnected such that information is stored in the weight of the connections between them. Network learning is designed to determine an appropriate set of connection strengths which facilitate the activation of these processing units to achieve a desired state that mimics a given set of sampled patterns. An example of the BP network architecture employed appears in Figure 3. Twelve of the experimental trials were used for network training, and data from the remaining trials was used for testing.

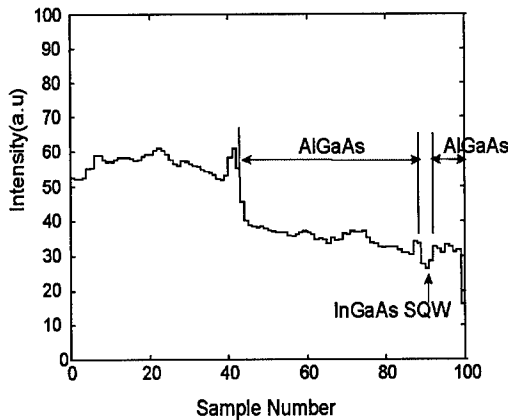


Figure 2 - Sample raw RHEED intensity data.

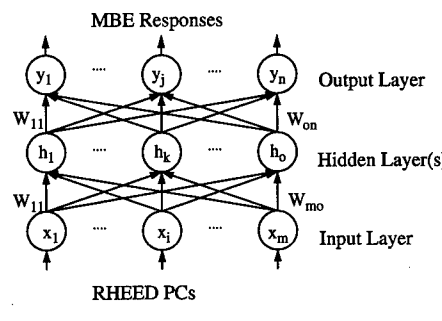


Figure 3 - Neural network architecture.

4. Results and Discussion

The inputs to each of the neural networks consists of the first six PCs of the RHEED data, as they contain 97% of the variance. In this way the PCA achieved a 100:6 data reduction ratio with less than 3% error. Without reducing the dimensionality, a neural network with 100 inputs (one for each sample) would be required to use the RHEED data to predict the MBE responses. This, however, would result in an severely underconstrained problem, since there were only 16 training vectors available from the factorial experiment.

Figure 4 demonstrates the accuracy of the PCA-based neural network models. Models were constructed for defect density, GaAs and AlGaAs x-ray signal full-width-at-half-max (FWHM), x-ray peak separation, InGaAs and AlGaAs PL intensity FWHM, and InGaAs and AlGaAs PL peak position. The neural network models exhibited an average RMSE of 3% on training data and less than 10% for test data (see Table 2). We have demonstrated, therefore, that the PCs of the RHEED signals must contain sufficient information from which to predict the relationship between growth conditions and film quality.

Table 2: Test RMSE for PC-Based Neural Network Models

Response	RMSE
Defect density	0.1572
AlGaAs x-Ray FWHM	0.0519
InGaAs PL FWHM	0.1897
InGaAs PL peak position	0.1078
AlGaAs PL FWHM	0.0731
AlGaAs PL peak position	0.0288
Average	0.0994

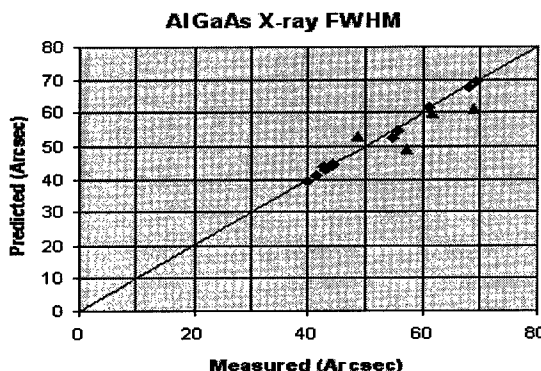


Figure 4 - Neural process model prediction vs. experimental measurements for AlGaAs x-ray FWHM (triangles represent test data).

5. Conclusion

RHEED signals from an MBE growth process have been modeled using PCA and neural networks. PCA was used to reduce the dimensionality of the RHEED data set. The PCs were used to train BP neural networks, and the physical characteristics of MBE-grown thin films were successfully predicted. The continued development of these techniques will lead to models capable of predicting the characteristics of MBE grown thin films via real-time RHEED data analysis, therefore providing a platform on which to build an automated process control system for MBE growth.

References

- [1] Lee, K., Bicknell-Tassius, R., Dagnall, G., Brown, A., and May, G., *Proc. 1996 Internat. Elec. Manufac. Tech. Symp.*, Oct., 1996, pp. 378-385.
- [2] Jolliffe, I., *Principal Component Analysis*, (New York: Springer-Verlag), 1986.
- [3] May, G., *IEEE Spectrum*, 31 (9) 47-51, 1994.

Multicomponent Sb-based solid solutions grown from Sb-rich liquid phases.

V. A. Mishurnyi, F. de Anda, A. Yu. Gorbachev,

IICO UASLP, Alvaro Obregon 64, 78000 San Luis Potosi, SLP, Mexico.

V. I. Vasil'ev, V. M. Smirnov, N. N. Faleev.

A.F.Joffe Physico-Technical Institute, Russian Academy of Science, 26 Polytekhnicheskaya St., 194021, Saint-Peterburg, Russia.

Abstract. We developed the LPE growth technology of InGaAsSb, AlGaAsSb and AlGaInAsSb layers from Sb-rich liquid phases on GaSb substrates. All multicomponent heterostructures were studied by double crystal X-ray diffraction. InGaAsSb layers were grown in both sides of the miscibility gap, near GaSb and near InAs. From a study of the variation of the rocking curves' halfwidth with the supercooling temperature of the In-Ga-As-Sb liquid phases the technological growth conditions were optimized. In the case of AlGaAsSb the GaSb substrate is eroded in contact with a saturated Al-Ga-As-Sb liquid due to the high non equilibrium degree on this system and the erosion increases with Al concentration. One of the techniques to diminish the erosion consists in increasing the initial supercooling but in this system, in the investigated area of compositions, it is impossible because of the low critical supercooling (ΔT_{cr}) of the liquid phase. We have conceived and developed a method to control ΔT_{cr} by adding In to the Al-Ga-As-Sb liquid phase. It was found that when the In concentration increased the ΔT_{cr} also increased. So the transition from the quaternary AlGaAsSb to the pentanary AlGaInAsSb allowed us to decrease the erosion process. It is shown that high quality multi-component Sb-based solid solutions can be grown by the developed technique with Sb as a solvent.

Introduction

InGaAsSb and AlGaAsSb quaternary solid solutions are attractive candidate materials for optoelectronic devices in the near and mid-infrared wavelength range. At the present time InGaAsSb and AlGaAsSb layers are grown by different epitaxial techniques, including MBE and LPE.

Most of the works concerning the LPE growth of these quaternary systems deal with the use of metal-solvents. However, antimonide-based systems can be grown both from metal-rich and from Sb-rich liquid phases. The advantages of using Sb as a solvent for LPE growth [1] are: 1.- When growing AlGaAsSb/InGaAsSb/GaSb structures it is profitable to use the same solvent for all the layers. This can not be done with metal solvents. 2.- It helps to decrease the natural defects concentration normally present in GaSb based systems. 3.- In the case of InGaAsSb it lowers the degree of non - equilibrium between the liquid phase and GaSb substrate.

Growth technology

This work is devoted to the InGaAsSb, AlGaAsSb and AlGaInAsSb LPE growth from Sb solvents. The preliminary data for the composition of the liquid phases was obtained from phase diagrams calculation using the simple solution model [2,3] in the Sb-rich side [4]. The theoretical data were corrected by direct visual observations of liquid phases during slow heating and cooling. The

liquidus temperature T^l and the critical supercooling ΔT_{cr} , when the spontaneous crystallization began, were determined from these experiments for known liquid phase compositions. The epitaxial layers were grown on GaSb (111) B and (100), n- or p-type substrates with carrier concentrations near 10^{17} cm^{-3} . The substrates were etched in $\text{H}_2\text{O}_2 : \text{HF} : \text{C}_4\text{O}_6\text{H}_6$ (tartaric acid) : H_2O [5]. The lattice mismatch measurements of the heterostructures and their crystal perfection were studied by double crystal X-ray diffraction.

$\text{In}_x\text{Ga}_{1-x}\text{As}_y\text{Sb}_{1-y}$ were grown in two composition areas: near GaSb ($0.06 \leq x \leq 0.13$, $0.05 \leq y \leq 0.17$) and near InAs ($0.9 \leq x \leq 0.96$, $0.8 \leq y \leq 0.9$). These areas are on both sides of $\text{In}_x\text{Ga}_{1-x}\text{As}_y\text{Sb}_{1-y}$ miscibility gap [6]. The critical supercooling ΔT_{cr} on the first composition area of solid solutions was about 6-12 °C. The InGaAsSb epitaxial growth was done in the first composition area at a constant temperature of 630-635 °C and at different supercoolings in the range 2 - 7 °C. The typical layer thicknesses were 0.5 - 1.5 μm with a growth time of 5 - 20 s. The use of Sb solvents allowed the growth of $\text{In}_x\text{Ga}_{1-x}\text{As}_y\text{Sb}_{1-y}$ epitaxial layers near InAs on GaSb-substrates by usual LPE technology without the extreme initial temperature differences between the liquid phase and substrate as in the «cold» substrate method reported in [7]. This fact proves that the substitution of metal solvent for Sb increases the substrate stability in contact with an In-Ga-As-Sb liquid phase. The $\text{Al}_x\text{Ga}_{1-x}\text{As}_y\text{Sb}_{1-y}$ and $\text{Al}_x\text{Ga}_{1-x-z}\text{In}_z\text{As}_y\text{Sb}_{1-y}$ solid solutions were grown at similar conditions at the same temperature.

Results and discussions for InGaAsSb solid solutions

The diffraction peaks halfwidths (FWHM) for the best InGaAsSb/GaSb samples were about 11-15 seconds of arc. Moreover, a number of small peaks were observed on the rocking curves superposed to the fundamental Bragg reflections from the layer and the substrate. This is a result of multiple diffraction within the epitaxial layers. The halfwidths of the diffraction peaks for the GaSb substrates ΔQ_1 were always less than ΔQ_2 for the InGaAsSb layers. We investigated the dependence of ΔQ_1 and ΔQ_2 on ΔT which is one of the main technological parameters. For this purpose we have grown InGaAsSb/GaSb structures from identical liquid phases, corresponding to a $\Delta\alpha/\alpha_0$ near 8.2×10^{-4} . It was found that ΔQ_1 and ΔQ_2 first decrease with an increase of ΔT and achieve minimal values of about 11-13 seconds at $\Delta T \sim 5-6$ °C. A further supercooling increase results in a widening of diffraction peaks from both the substrate and the epitaxial layer.

Such behavior could be explained as follows:

In the heteroepitaxial growth process the liquid and solid phases' compositions do not correspond to each other. Therefore immediately after the contact between the liquid and substrate the system is not in equilibrium. There has to be a process taking the system to a quasi-equilibrium situation by means of a particle exchange between both phases. A particles exchange implies a substrate erosion and crystallization from the liquid phase. Both of these two processes take place simultaneously but in different systems one of them can dominate over the other. In the case of InGaAsSb grown on GaSb the substrate erosion process is strong enough. As a result of the substrate's erosion additional atoms of Sb and Ga will go into the liquid phase. Such changes of the composition of the liquid phase will increase the supersaturation degree and cause the crystallization process. Because of these two processes, that bring the system to quasi-equilibrium, a strained transition layer of varying composition and lattice constant will form. These strains will develop not only on the epitaxial layer but also in the substrate region near the interface. Hence the halfwidth of the diffraction peak of the substrate will depend on the transition's layer parameters. Naturally those parameters, principally the thickness, depend on the technological conditions of growth.

Certainly it is necessary to diminish the substrate erosion in order to fabricate a sharp heteroboundary. This can be done by increasing the liquid phase supercooling and therefore reducing the substrate erosion velocity. As a result the thickness of the transition layer will be reduced and as consequence ΔQ_2 will be also reduced indicating a better heterostructure quality. At the same time when the supercooling temperature is optimum, the thickness of the transition layer is a minimum and the crystallographic quality of the epitaxial layers is the best too. The optimum supercooling temperature ΔT_{opt} is about 5 - 6 °C with corresponding minimal halfwidths of the diffraction peaks for both the substrate and the layers. The further increase ΔQ_1 and ΔQ_2 with supercooling is associated most probably with a supersaturation decrease due to a crystallization process in the liquid phase volume before substrate contact.

The FWHM for chemically polished GaSb substrates measured on the same conditions as for the heterostructure were near ΔQ_2 for the best samples. That fact and the additional diffraction maxima on the rocking curves point to a sharp heteroboundary and to a high crystalline quality of InGaAsSb/GaSb structures grown by LPE from the Sb-rich solutions. As a matter of fact distributed feedback InGaAsSb/GaSb heterojunction lasers have been fabricated using this growth technology [8].

Results and discussions for AlGaAsSb and AlGaInAsSb solid solutions

In this work we have investigated the growth process of $Al_xGa_{1-x}As_ySb_{1-y}$ solid solutions with $0.40 < x < 0.45$. For the best AlGaAsSb/GaSb samples grown from Sb in that area of composition the FWHM were 12 - 15 seconds of arc. and a number of small peaks were observed on the rocking curves similar to rocking curves of InGaAsSb/GaSb structures. These peaks confirm a sharp heteroboundary and to a high crystalline quality of the GaAlAsSb/GaSb as in a case of InGaAsSb/GaSb.

However it is necessary to point out that the lattice mismatch reproducibility for AlGaAsSb/GaSb was not good in the investigated area of compositions and growth temperatures. From our point of view, this is connected with the very narrow supercooling interval that it is possible to achieve in the quaternary Sb-rich liquid phases. The critical supercooling ΔT_{cr} value for the quaternary liquid phases was found to be around 4 °C. Note that in metal solvents the critical supercooling is usually larger.

Besides, there is another problem associated with the use of Sb-rich liquid solutions to grow AlGaAsSb/GaSb structures: the big degree of non equilibrium between the GaSb (solid phase) and Al-Ga-As-Sb (liquid phase) system. As a result of that the boundary between the quaternary liquid and the solid phases is unstable, a GaSb substrate is eroded strongly in contact with a saturated liquid phase. If the Al concentration in the liquid solution will increase, the GaSb erosion will increase too. Note, that in the opposite case the GaSb layer can be grown on the AlGaAsSb without noticeable erosion.

It is obvious that in order to produce high quality devices it is necessary to eliminate or minimize the erosion process. This could be done by increasing the initial supercooling used to grow the quaternary layer. Unfortunately this method is not suitable in this case because, as shown above, the critical supercooling in Sb-rich Al-Ga-As-Sb liquid solutions is very low.

It is known that, among other parameters, the critical supercooling (ΔT_{cr}) depends on the specific surface energy of the liquid phase. So it is possible to control ΔT_{cr} by changing the liquid phase composition. One of the suitable elements for that purpose for the Al-Ga-As-Sb system is In because its low segregation coefficient, k_{In} , in comparison with k_{Ga} and k_{Al} . In this case we could expect to change the liquid composition without largely affecting the solid phase. It was found that an increase of In concentration (N_{In}^l) in the liquid phase from 0 to 4 at. % more than doubled ΔT_{cr} . When the N_{In}^l is more than 2 at% the pentanary solid solution $Al_xGa_{1-x-z}In_zAs_ySb_{1-y}$ crystallizes on the GaSb substrate with an In concentration which can be sensed by an electron microprobe ($z \sim 0.01$). The addition of a

fifth component to the solid will increase the lattice mismatch with the GaSb substrate but this effect can be compensated by increasing, again, the As concentration. We have investigated independently the As and In influence at the T^l of the pentanary Al-Ga-In-As-Sb liquid phase. Because the melting points T^{melt} for III-As compounds are higher than T^{melt} for corresponding III-Sb, adding As to the liquid phase will increase T^l . When N_{In}^l increases, T^l decreases because the melting temperatures for InSb and InAs are lower than T^{melt} for Al and Ga arsenides and antimonides. (In the first case N_{Al}^l , N_{Ga}^l and N_{In}^l were kept constant, in the second case N_{Al}^l , N_{Ga}^l and N_{As}^l were kept constant). A comparison of both dependencies shows that the As and In contrary influences on the liquidus temperature are balanced by simultaneously increasing N_{As}^l and N_{In}^l , and so T^l remains the same. But with the added advantage that In addition increases the critical supercooling of the liquid phase. It means that the GaSb erosion process can be depressed by the transition from a quaternary to a pentanary system.

Using these results we have grown single and multilayer heterostructures based on $Al_xGa_{1-x-z}In_zAs_ySb_{1-y}$ ($0.01 < z < 0.04$) lattice matched to GaSb. The smallest FWHM of the diffraction peaks was 12-15 arc. sec. This value and the additional diffraction maxima on the rocking curves are indicatives of high crystalline quality and a sharp heteroboundary of the samples. Also this technology was used to fabricate low threshold current density AlGaInAsSb/InGaAsSb/GaSb heterolasers [9].

Conclusions

In summary we developed and studied the growth technology of InGaAsSb, AlGaAsSb and AlGaInAsSb from Sb-rich solutions. It is shown that high quality heterostructures can be produced by this growth method. We believe that such technology has good perspectives for the production of mid-infrared devices based on solid solutions of the III-V antimonides.

References

- [1] V. A. Mishurnyi, F. de Anda, A. Yu. Gorbachev, V. I. Vasil'ev, N.N. Faleev, Journal of Crystal Growth, 180 (1977) 34.
- [2] M. Illegems and M. B. Panish, J. Phys. Chem. Solids 35 (1974) 409.
- [3] A. S. Jordan and M. Illegems, J. Phys. Chem. Solids 36 (1975) 329.
- [4] V.I. Vasil'ev, V.V. Kuznetsov, V.A. Mishurnyi, Sov. Nonorganical Materials 26 (1990) 23.
- [5] I. E. Berishev, F. de Anda, V. A. Mishurnyi, J. Olvera, N. D. Ilynskaia, V. I. Vasil'ev, J. Electrochem. Soc. 142 (1995) L189.
- [6] L. M. Dolginov, P. G. Eliseev, A. N. Lapshin, L. V. Drujinina, M. G. Mivl'vidskiy, Kristall und Technik 13 (1978) 631.
- [7] E. R. Gertner, A. M. Andrews, L. O. Bubulc, D. T. Cheung, M. J. Ludowise and R. A. Riedel, J. Electron. Mater. 8 (1979) 545.
- [8] V. I. Vasil'ev, N. D. Il'inskaya, D. V. Kuksenkov, V. I. Kychinskii, V. A. Mishurnyi, V. V. Sazonov, V.B. Smirnitskii and N.N. Faleev, Sov. Tech. Phys. Lett. 16 (1990) 67.
- [9] V. I. Vasil'ev, A. G. Deryagin, V. I. Kuchinskiy, A. V. Luney, V. M. Smirnov, Tech. Phys. Lett. 22 (1996) 52.

Suppression of dopant redistribution in AlGaAs/GaAs laser-HEMT structures for optoelectronic transmitters grown by molecular beam epitaxy

A. Gaymann, M. Maier, K. Köhler, W. Bronner, F. Grotjahn, J. Hornung, M. Ludwig

Fraunhofer-Institut für Angewandte Festkörperphysik, Tullastr. 72, 79108 Freiburg, Germany

Abstract. Detailed studies of segregation and diffusion of the dopants Si and Be in MBE grown AlGaAs/GaAs heterostructures for optoelectronic devices are presented. Segregation of Si could be suppressed by lowering the substrate temperature during the growth of a few monolayers after the deposition of the doped layers. Solubility limits of Be were observed to depend on the Al mole fraction. Be diffusion in the laser structures was negligible at doping concentrations below these solubility limits. As an application, transmitter OEICs were fabricated using laser-HEMT structures grown with optimized growth conditions. The devices operated successfully at 15 GBit/s.

1. Introduction

Heterostructures for optoelectronic integrated circuits (OEICs) can be grown by molecular beam epitaxy (MBE) allowing close control of composition, thickness and doping. In our laboratory, AlGaAs/GaAs laser-HEMT structures for monolithic integration have been grown by MBE in one epitaxial run. They consist of a two-sided δ -doped HEMT in combination with a MQW laser structure (Fig. 1). The growth of structures for optical devices requires high growth temperatures in order to achieve good device performance. This generally leads to dopant segregation and diffusion. The performance of the two-sided δ -doped HEMTs, on the other hand, is extremely sensitive to these effects. Thus, other growth parameters including lower substrate temperature are necessary for these HEMT structures. In this paper, we present detailed studies of Si segregation and Be diffusion in AlGaAs/GaAs heterostructures from which optimized growth conditions for optical and electronic structures could be inferred.

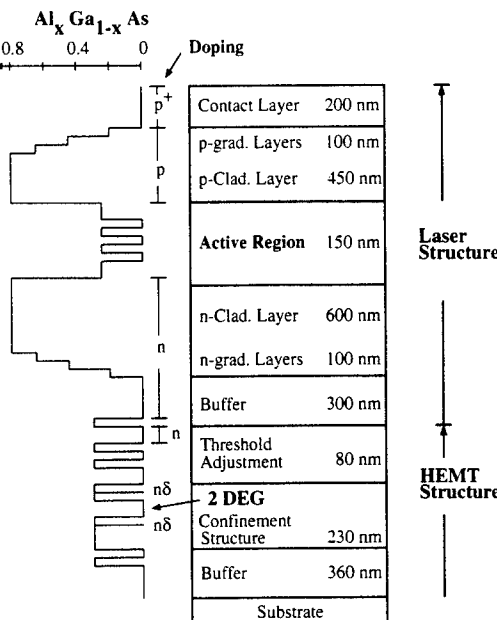


Fig. 1: Layer sequence of the laser-HEMT structure used for monolithic integration (drawings are not in scale).

2. Experimental

All heterostructures were grown by MBE in a Varian Modular Gen II. Si and Be are used as n- and p-type dopants, respectively. Si segregation was studied by comparison of the electrical properties of normal and inverted HEMT structures and by secondary ion mass spectrometry (SIMS) of vertically compact laser structures. Be segregation and diffusion was investigated by SIMS depth profiling of test samples containing Be-doped $\text{Al}_x\text{Ga}_{1-x}\text{As}$ layers of different composition and of laser structures. Lasers and transmitter OEICs were fabricated using the laser-HEMT structures. The lasers were characterized on-wafer by measuring threshold currents and series resistances. The performance of the transmitter OEICs was tested in an optical data transmission experiment.

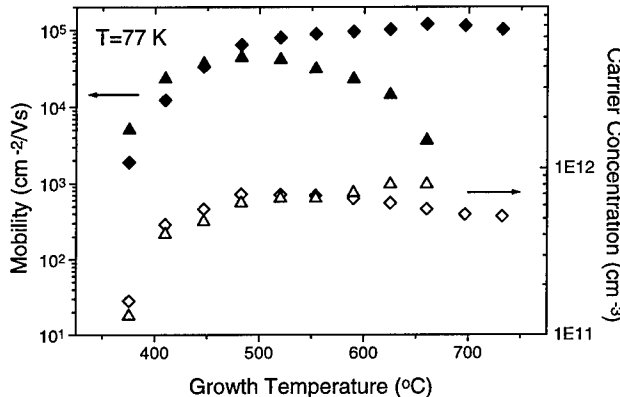


Fig. 2: Hall mobility (full symbols) and carrier concentration (open symbols) at 77 K of HEMT (diamonds) and I-HEMT (triangles) structure versus growth temperature.

3. Results and Discussion

Hall mobility and carrier concentration at 77 K of a conventional and an inverted HEMT (I-HEMT) structure versus growth temperature T_g (pyrometer read-out) are shown in Fig. 2. In the latter case, the undoped GaAs layer which forms the 2DEG is grown after, i.e., on top of the Si doped AlGaAs layer. Channel and spacer thickness are identical for the HEMT and I-HEMT structure. In comparison to the HEMT structure, the mobility of the I-HEMT drops significantly at higher temperatures reaching a value of $3500 \text{ cm}^2/\text{Vs}$ at 660° C . This value is comparable to that of homogeneously doped GaAs with an electron concentration of $10^{17} - 10^{18} \text{ cm}^{-3}$. We attribute the drop in mobility to the segregation of Si towards the GaAs channel [1]. The drop in mobility at low growth temperatures for both structures is due to the reduced crystal quality. The carrier concentration of the I-HEMT structure above 480° C is also influenced by Si segregation: the actual spacer thickness for the I-HEMT decreases with increasing growth temperature leading to a slightly higher carrier concentration (see Fig. 2). The situation is vice versa in the HEMT. Here, the segregation of the dopants leads to an increase of the actual spacer thickness, i.e., the carrier concentration becomes lower with higher growth temperatures. As a result, T_g has to be in the range of 500° C during growth in regions where segregation could deteriorate device performance.

Beryllium diffusion was investigated by SIMS depth profiling within heterostructures containing Be-doped $\text{Al}_x\text{Ga}_{1-x}\text{As}$ layers ($0.3 \leq x \leq 0.8$). At a Be concentration of $2 \times 10^{18} \text{ cm}^{-3}$ we observe Be outdiffusion into the undoped GaAs layers at a growth temperature of 660°C [2]. At a doping concentration of $2 \times 10^{19} \text{ cm}^{-3}$ a strong increase in diffusion occurs for all growth temperatures. The depth profiles show solubility limits for Be in $\text{Al}_x\text{Ga}_{1-x}\text{As}$ layers of approximately $1 \times 10^{19} \text{ cm}^{-3}$ and $2 \times 10^{18} \text{ cm}^{-3}$ at $x = 0.6$ and $x = 0.8$, respectively [2], in agreement with similar findings in AlAs [3].

Based on the results above, various laser structures were grown using our optimized growth parameters. Fig. 3 shows the SIMS depth profile of the laser structure with 600 nm n-cladding layer and 450 nm p-cladding layer. The active region, denoted by the minimum of the Al profile, consists of 3 GaAs quantum wells. The aluminum content of the cladding layers is $x = 0.8$.

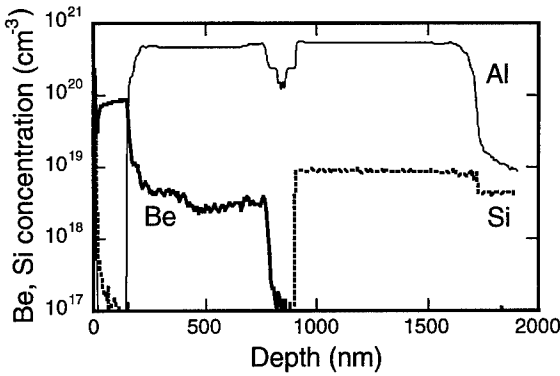


Fig.3: SIMS depth profiles of the laser structure. The active region is denoted by the minimum in the Al profile.

Very sharp dopant profiles for Si and Be were achieved. The dopant concentrations in the active region is below $3 \times 10^{16} \text{ cm}^{-3}$, the detection limit of both Si and Be.

Si segregation into the active region could be suppressed by lowering the growth temperature from 660°C to 590°C for a few monolayers after the growth of the n-doped cladding layer. The latter temperature was the best choice with regard to good optical properties and lowest amount of segregated Si although redistribution of Si starts at even lower temperatures (see Fig.2). The increase in Si concentration at the beginning of the n-cladding layer (right hand side in Fig. 3) is due to the lower growth rate of $\text{Al}_{0.8}\text{Ga}_{0.2}\text{As}$ since the Si beam flux is kept constant during the whole epitaxy. Be was kept from diffusing into the active region by keeping the doping concentration below the solubility limit of $2 \times 10^{18} \text{ cm}^{-3}$ for the first 300 nm $\text{Al}_{0.8}\text{Ga}_{0.2}\text{As}$ cladding layer adjacent to the active region. Additionally, the growth temperature was slightly lower compared to the n-cladding layer and the active region. In the remaining 150 nm of the p-cladding layer the Be doping concentration was raised slightly in order

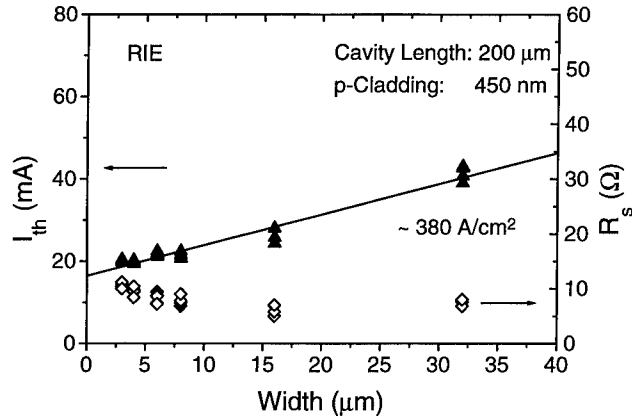


Fig. 4: Threshold current I_{th} (triangles) and series resistance R_s (diamonds) of several lasers vs mesa width. Laser mirrors were fabricated by RIE.

to obtain a lower series resistance. Thus, the selection of the proper doping profile as well as growth parameters allows the growth of complex heterostructures with negligible dopant redistribution.

Laser diodes with fixed cavity length and various widths were processed using the vertically compact laser structures described above. Laser mirrors were fabricated by reactive ion etching (RIE). Threshold currents and series resistances were determined by on-wafer measurements. Fig. 4 shows the results for the structure with 450 nm p-cladding. Although having a high leakage current, lasers with three quantum wells showed a threshold current density of 380 A/cm^2 , as determined by linear regression of the measured current values plotted versus the laser diode width. We attribute this low value to the suppression of Si segregation and Be diffusion into the active region (see Fig. 3). Laser structures with equal layer thicknesses but higher Be doping concentrations showed threshold currents densities exceeding 1000 A/cm^2 . This value was due to a high Be diffusion into the quantum wells as substantiated by SIMS measurements [2].

As an application, transmitter OEICs were fabricated using AlGaAs/GaAs laser-HEMT structures. The two-sided δ -doped HEMT structure was grown at 480°C to prevent Si segregation. The growth temperature and doping profile of the laser structure were described above. Fabry-Perot type MQW lasers were monolithically integrated with driver electronics based on HEMT technology. The high frequency properties were investigated after dicing and mounting the OEICs in an optical data communication set-up. The devices operated successfully at data rates up to 15 Gbit/s.

Acknowledgments

The authors thank J. Schaub and P. Ganser for MBE growth, C. Buchgeister, E. Olander and G. Schilli for processing the lasers and OEICs, and G. Weimann for encouraging support and helpful discussions.

References

- [1] Köhler K 1996 *Appl. Surf. Sci.* 100/101 383
- [2] Gaymann A, Maier M, Bronner W, Grün N and Köhler K 1997 *Mat. Sci. Eng. B* 44 12
- [3] Kopf R F, Schubert E F, Downey S W and Emerson A B 1992 *Appl. Phys. Lett.* 61 1820

WAVELENGTH TUNABLE UV LASER STIMULATED GROWTH OF $\text{Al}_x\text{Ga}_{1-x}\text{As}$ BY OMVPE

A. Wankerl , D.T. Emerson , M.J. Cook & J.R. Shealy
 OMVPE Facility, School of Electrical Engineering, Cornell University, Ithaca NY 14850, USA

Abstract. UV stimulated OMVPE growth of AlGaAs from TMG, TMA and arsine at 500°C was studied using a wavelength tunable pulsed laser in the range from 235 nm to 255 nm. We observe an abrupt wavelength edge at 252 nm, below which the stimulation rate is constant and above which the growth enhancement ceases. We demonstrate a high growth contrast of 3.2 : 1 and show that the growth enhancement is due to photostimulation of the adlayer. The formation of a periodic surface structure agrees with theory and results in growth directions deviating from [100]. Good crystal quality was determined by Raman spectroscopy.

1. Introduction

UV-laser stimulated organometallic vapor phase epitaxy (OMVPE) promises high-resolution in-situ area-selective growth of III-V semiconductors. UV-laser assisted GaAs growth by MOMBE [1], CBE [2] and OMVPE [3-5] has been demonstrated over a wide range of experimental conditions using pulsed laser sources or UV-lamps. Many of these studies have shown significant growth rate enhancements and improved surface morphology [1,3] in the irradiated areas. Significant growth stimulation by laser irradiation during the OMVPE process is only possible in the kinetically limited regime. It can occur via localized thermal heating and thus enhanced pyrolysis, the photodissociation of precursor molecules in the gas phase, or via photo-induced reaction of the chemisorbed adlayer. Among these, adlayer stimulation is most desirable, since it allows for the highest resolution patterning. Several studies have investigated the absorption spectra of gas phase and adsorbed OMVPE precursors [6], and their laser-induced decomposition when adsorbed on GaAs [7] or silica substrates [8]. Although the energy of a single UV photon is sufficient to break bonds of typical precursor molecules, the exact photochemical pathways of both, single molecule dissociation and adlayer reaction stimulation are still poorly understood. This work investigates the wavelength dependence of adlayer photostimulation and the properties of selectively grown AlGaAs.

2. Experiment

UV stimulated growth of AlGaAs and GaAs from trimethylgallium (TMG), trimethylaluminum (TMA) and arsine at 500°C was studied using a wavelength tunable pulsed laser. The raw s-polarized beam was used in all experiments. We operated the excimer-pumped dye laser (Lambda Physik LPX 105i and FL3002) in the wavelength range from 235 nm to 255 nm with Coumarin 102 as the dye. To achieve low pulse energies, the internal pump beam attenuator was used. In this configuration, the system delivered pulse energy densities between 3 and 20 mJ/Pulse cm² at a repetition rate of 10 Hz with a nominal 17 ns (FWHM) pulse duration. The exact pulse energy density was dependent on wavelength and the status of both dye and XeCl excimer pump laser gas. All growths were carried out at 25 torr reactor pressure, a V/III ratio of 76 and an aluminum vapor mole fraction of 46% for AlGaAs. One experiment series varied the wavelength from 235 nm to 255 nm leaving the growth time fixed at 8 minutes. The other series varied the growth time from 2 to 30 minutes at fixed 240 nm wavelength. The layers were characterized by surface profiling, scanning electron microscopy (SEM), atomic force microscopy (AFM) and Raman spectroscopy.

3. Results and Discussion

3.1. Selective Growth Characteristics and Wavelength Dependence

Exposure to the raw laser beam resulted in two spots of enhanced growth, which were identified to originate from the mode structure of the beam itself. They correspond to the two distinct intensity maxima in the beam profile. The location of the quartz window where the laser beam passed through showed a deposit of metallic appearance roughly the size of the overall laser beam. However, two deposit-free spots identical in size and shape to the growth spots on the wafer were embedded in the window deposit. The window deposit for 8 min. exposures was 400 Å and very rough. The rest of the window was free of deposits. Figure 1 shows a representative surface profile across the selectively deposited AlGaAs film on the wafer for a four minute exposure to the 240 nm laser beam and reactants. Both illuminated spots show the same growth rate and the feature height is nearly constant for each spot. We found that longer exposure times lead to less constant feature height (surface roughness on the mesa top). Exposure times less than 15 minutes resulted in a constant stimulated growth rate of 2.6 μm/hr. For longer stimulated growth times the growth rate decreased drastically, indicating a saturation of feature height. The AlGaAs growth rate in the unilluminated areas for all experiments was 1.2 μm/hr, resulting in a growth contrast (total growth in light : growth in dark) of about 3.2 : 1.

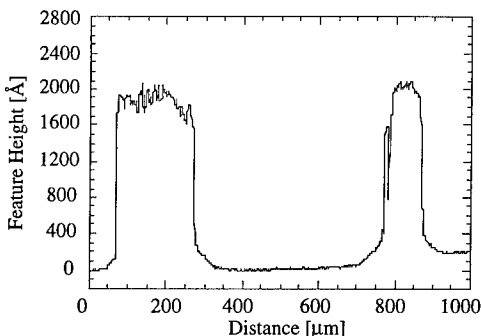


Figure 1. Representative surface profile across the four minute selective AlGaAs deposit. The unstimulated AlGaAs deposit is 800 Å.

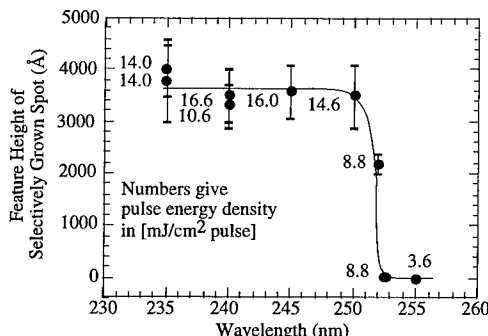


Figure 2. Feature height of selectively deposited AlGaAs as function of laser wavelength. The deposition in the dark was 1600 Å in all cases.

Sasaki et al. [6] investigated the UV absorption spectra of TMG, TMA and arsine, as well as the spectral changes upon adsorption on synthesized silica. Although all spectra exhibit their absorption tail around 250 nm, that of the TMG/AsH₃ co-chemisorbed adlayer extends greatly to longer wavelengths than the vapor phase or physisorbed species. This suggests that chemisorbed adlayer photostimulation without significant gas phase absorption is possible around 250 nm. Figure 2 displays the feature heights of the selectively grown AlGaAs spots as a function of excitation wavelength between 235 nm and 255 nm. It shows an abrupt drop to zero UV growth stimulation around 252 nm. The measured pulse energy density, indicated for each data point, differed slightly between experiments, since it is dependent on wavelength and the conditions of both dye and excimer laser gas. Comparison of the individual data points shows, however, that this variation did not significantly affect the growth contrast. For wavelengths below 250 nm, the stimulated growth rate is approximately constant at 2.6 μm/hr despite the pulse energy density variation from 10.6 to 16.6 mJ/Pulse cm². Across the wavelength edge, the experiments at 252 nm and 252.5 nm had identical pulse energies of 8.8 mJ/Pulse cm², not significantly less than the 10.6 mJ/Pulse cm² experiment at 240 nm. Under our conditions, the stimulated growth rate between 235 nm and 250 nm is thus independent of the photon energy, whereas the photostimulation of the reaction ceases entirely for photon energies smaller than 4.91 eV. Despite zero stimulated growth on

the substrate, the window deposits were observed at wavelengths greater than 252 nm. However, since UV photoassisted OMVPE growth of GaAs from TMG and arsine was observed at 254 nm using a low pressure Hg lamp [4] at 510°C substrate temperature, our measured wavelength edge must be dependent on the reactor parameters. This is supported by experiments with TMG adsorbed on Si and 248 nm excimer laser excitation, which show that the photodissociation process is thermally assisted [9].

3.2. Surface Stimulation

The laser spot surface exhibits over large regions the homogeneous periodic ripple structure as shown by the scanning electron micrograph in figure 3. These rippled surfaces have been reported for pulsed laser annealing [10], growth [5,11] and etching [12] of semiconductors. Sipe et al. [13] have developed a theory for the formation of these periodic patterns by laser irradiation, based on the assumption that the patterns result from inhomogeneous energy absorption just beneath the surface, originally induced by surface roughness. The interference between the incident laser beam and the laser-induced surface propagating electromagnetic wave results in a standing wave pattern, which in turn leads to periodic variations in the intensity of the electromagnetic radiation at the surface. They predict and experimentally confirm [14] the laser polarization dependence of direction and periodicity of these gratings, where the periodicity is a function of wavelength and angle of incidence. We measured the periodicity of the ripple structures on our samples by taking the Fast Fourier Transform of AFM images. Orientation and periodicity agree well with theory. Cross-sectional SEM images of samples grown for eight minutes showed a surface ripple height of 100 nm, 1/4 of the total height of the selectively grown spots. It is believed, that once the surface plasma wave is initiated, the periodic surface structure causes a positive feedback mechanism enhancing the intensity modulation just underneath the surface [14]. This explains the substantial height of the surface ripples and might explain the growth rate drop for longer exposure times as discussed in section 3.1. It also leads to the observed increase in surface roughness as laser stimulated growth time is increased.

Since the generation of these gratings is a surface phenomenon, gas phase photolysis can be excluded as the dominant stimulation mechanism. Furthermore, numerical simulations of laser-induced surface heating under our experimental conditions show that the resulting temperature rise is insignificant towards the observed growth enhancement. Thus, adlayer photolysis constitutes the dominant stimulation mechanism at wavelengths between 235 nm and 255 nm as investigated in this study.

3.3. Structural qualities

The crystal quality of unstimulated and stimulated growth regions were assessed by Raman scattering. The small penetration depth of the Raman probe ($\sim 500 \text{ \AA}$) allows us to sample the top surface. A comparison of the Raman spectra from photostimulated GaAs and AlGaAs samples grown under identical conditions is shown in Figure 4. The spectrum from GaAs grown in the dark exhibits a narrow longitudinal phonon (LO) at 292 cm^{-1} (FWHM $\sim 3 \text{ cm}^{-1}$) confirming that GaAs of good crystal quality is deposited at 500°C. In contrast, the spectrum from the UV stimulated region exhibits in addition to the narrow LO phonon an equally narrow transverse optic (TO) phonon. Although not allowed during scattering from (001) surface of zinc-blende crystals, this mode in general may be activated by crystal damage or deviation of deposition from the (001) direction. The narrow linewidth of the LO phonon rules out crystal damage as the cause of the TO phonon. As seen in the previous section, the deposition in the stimulated growth region predominantly occurs on crystal planes other than (001) due to the formation of the periodic surface ripple structure.

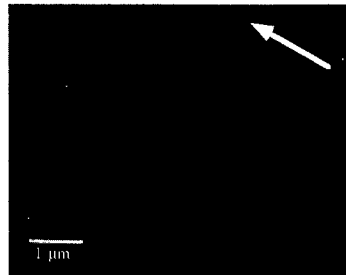


Figure 3. Scanning electron micrographs of laser spot surface showing typical periodic surface structure. The sample was grown at 235 nm laser wavelength. Arrow indicates polarization direction.

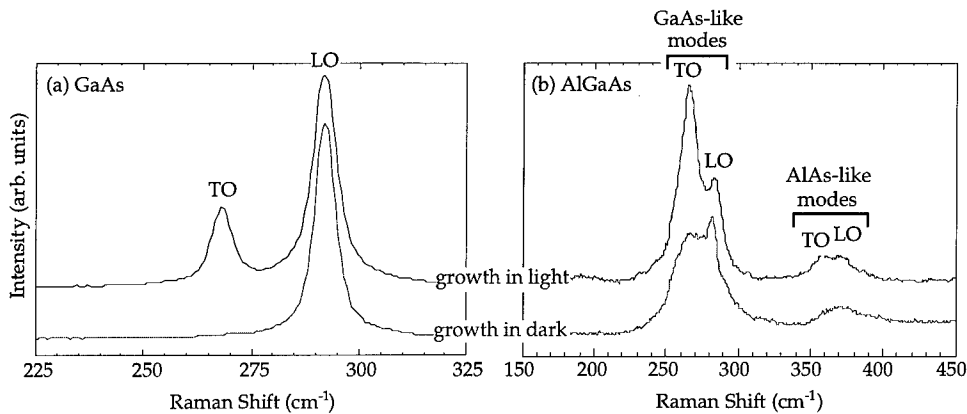


Figure 4. Raman scattering characterization of photostimulated (a) GaAs and (b) AlGaAs.

In the AlGaAs spectra we see both GaAs- and AlAs- like LO and TO phonons. Unlike in the case of GaAs, the TO phonons are comparable in intensity to the LO phonons. Since double crystal x-ray diffraction (DCXRD) measurements of the AlGaAs layer grown in the dark exhibited a narrow linewidth, which confirms good crystal quality, we attribute the presence of the TO modes to alloy related disorder. The enhancement of the TO mode relative to the LO mode for AlGaAs grown in the light, like for the GaAs sample, is due to the deviation from the (001) growth direction.

4. Conclusion

In summary, UV growth enhancement for AlGaAs growth from TMG, TMA and arsine at wavelengths around 240 nm is due to photostimulation of the adlayer reactions. We achieved a high growth contrast of 3.2 : 1 and found that the photostimulation of the adlayer reactions ceases for photon energies less than 4.91 eV under our growth conditions. The generation of the laser-induced surface periodic structure results in growth other than the (100) direction. Despite this significant surface perturbation, the selectively grown features show good crystalline quality.

References:

- [1] Nishizawa J.-I., Abe H., Kurabayashi T. and Sakurai N. 1986 *J. Vac. Sci. Technol. A4* 706
- [2] Farrell T., Armstrong J.V., Joyce T.B., Bullough T.J., Kightly P. and Goodhew P.J. 1992 *J. Cryst. Growth* **120** 395
- [3] Pütz N., Heinecke H., Veuhoff E., Arens G., Heyen M., Lüth H. and Balk P. 1984 *J. Cryst. Growth* **68** 194
- [4] Balk P., Heinecke H., Pütz N., Plass C. and Lüth H. 1986 *J. Vac. Sci. Technol. A4* 711
- [5] Donnelly V.M. and McCaulley J.A. 1989 *Appl. Phys. Lett.* **54** 2458
- [6] Sasaki M., Kawakya Y., Ishikawa H. and Mashita M. 1989 *Appl. Surface Sci.* **41/42** 342
- [7] McCaulley J.A., McCrary V.R. and Donnelly V.M. 1989 *J. Phys. Chem.* **93** 1148
- [8] Nishizawa J., Kokubun Y., Shimawaki H. and Koike M. 1985 *J. Electrochem. Soc.* **132** 1939
- [9] Suzuki H., Mori K., Kawasaki M. and Sato H. 1988 *Mat. Res. Soc. Proc. Vol. 101* 217
- [10] Cullis A.G. 1985 *Rep. Prog. Phys.* **48** 1157.
- [11] Farrell T., Armstrong J.V., Beanland R., Bullough T.J., Joyce T.B. and Goodhew P.J. 1993 *Semicond. Sci. Technol.* **8** 1112
- [12] Kumagai H., Toyoda K., Machida H. and Tanaka S. 1991 *Appl. Phys. Lett.* **59** 2974.
- [13] Sipe J.E., Young J.F., Preston J.S. and van Driel H.M. 1983 *Phys. Rev. B* **29** 1141.
- [14] Young J.F., Preston J.S., van Driel H.M. and Sipe J.E. 1983 *Phys. Rev. B* **29** 1155.

MBE Growth of Metamorphic In(Ga)AlAs Buffers

M. Sexl, G. Böhm, M. Maier¹, G. Tränkle², G. Weimann¹, G. Abstreiter

Walter Schottky Institut, Techn. Univ. München, D-85478 Garching, Germany

¹Fraunhofer Institut IAF, D-79108 Freiburg i. Br., Germany

²Ferdinand Braun Institut, D-12489 Berlin, Germany

Abstract. Metamorphic buffer layers were grown by MBE on GaAs-substrates using linearly graded InAlAs and InGaAlAs buffers to accommodate lattice misfit. The surface morphology was investigated by AFM, the relaxation behavior of the metamorphic buffers are studied by high resolution X-ray diffraction. The degree of relaxation is 86% for the ternary buffer and 90% for the quaternary buffer. Increasing the final In-composition of the buffer up to a value of 0.63, the $\text{In}_{0.52}\text{Al}_{0.48}\text{As}/\text{In}_{0.53}\text{Ga}_{0.47}\text{As}$ layers on top of the metamorphic buffer are unstrained. Transport properties of 2DEG-structures approach those of lattice matched reference samples on InP-substrates.

1. Introduction

Metamorphic buffer layers allow the arbitrary combination of active semiconductor structures with substrates having different lattice constants. These buffers are essential to accommodate the lattice mismatch between the active layers and the substrate in a controllable way, to generate a new substrate with desired lattice constant and moderate dislocation densities. Modulation doped InAlAs/InGaAs-heterostructures, with their inherently high electron densities and mobilities, are the ideal basis for ultrafast, low noise transistors [1]. Their superior device performance can be combined with the advantages of large, less expensive substrates by growth on GaAs-substrates.

In this paper we compare the layer properties of MBE grown metamorphic InAlAs/InGaAs-heterostructures on 3" GaAs-substrates with lattice matched structures on 2" InP-substrates. We study linear graded buffer layer concepts to compensate the lattice misfit using ternary $\text{In}_x\text{Al}_{1-x}\text{As}$ and quaternary $\text{In}_x\text{Ga}_y\text{Al}_{1-x-y}\text{As}$ buffers. High bandgap buffer material is used to avoid parasitic conductance at the interface between the graded buffer and the active layers of transistor structures [2]. With industrial application in mind, the thickness of the buffer layer was kept around one μm .

2. Growth and characterization of metamorphic buffers

The properties of the active layers, e.g. the morphology and the electron mobility in modulation doped structures depend on the composition and growth conditions of the buffer layers. All epitaxial layers were grown by MBE in a Varian Modular Gen II at a constant As_4 flux beam equivalent pressure (bep)

of $2.0 \cdot 10^{-5}$ torr. The growth rates were calibrated by X-ray measurements of lattice matched layers on InP substrates. Because the effusion cell temperatures have to be varied during the growth of linearly graded buffer layers, we have to calibrate the flux-growth rate relation at different cell temperatures. All buffers were grown with a constant grading of 50% In/ μ m. On top of the metamorphic buffers, heterostructures for transport measurements were grown. They consist of 250 nm InAlAs sandwiched between two superlattices followed by an InGaAs-channel with 32 nm and a low Si-doping with a thick spacer of 15 nm, as used on InP-substrates for comparison.

The first metamorphic buffer is a linear grading of InAlAs, starting with In_{0.03}Al_{0.97}As and increasing the In-content up to $x_{In} = 0.52$. The optimum substrate temperature is 420 °C, yielding moderate anisotropic cross hatching with 3 μ m spacing in [01-1], 1.7 μ m spacing in [011]-direction and a mean surface roughness of 5±0.7 nm, indicating the existence of misfit dislocations with a two dimensional layer by layer growth mode [3]. Increasing the growth temperature to 530 °C yields a surface roughness enhanced by a factor of 8, while low temperatures of 350 °C result in rough, three-dimensional surfaces. The surface morphology was improved by using quaternary InGaAlAs buffers. The In-content is increased linearly, the ratio of Ga and Al concentration is adjusted to a constant bandgap of 1.48 eV. Since Ga-adatoms are more mobile than Al-adatoms on the growth surface, lower growth temperatures can be used. We obtained the smoothest morphology using a linear temperature ramp from 350 °C at the beginning of the buffer to 390 °C at the end. The anisotropic cross hatch spacing is also reduced by 10%. Though the effusion cells have to be varied over a wide temperature range (the In-source for about 130 °C), linear grading in the metamorphic buffer is achieved. We verified the exact linear composition by SIMS measurement (Figure 1).

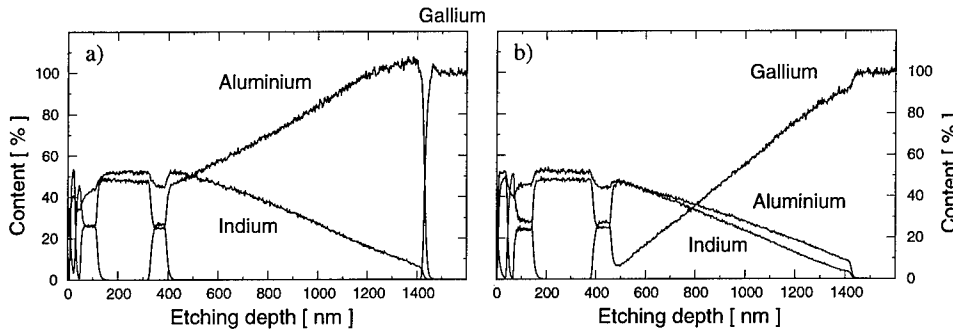


Fig. 1: SIMS measurement of linear graded metamorphic buffers: a) ternary InAlAs, b) quaternary InGaAlAs.

The relaxation behavior of the metamorphic buffers was studied by high resolution X-ray diffraction. A Bartels-type 4-crystal monochromator in the Ge(220) reflection mode was used in the primary beam, whereas in the diffracted beam a three reflection Ge(220) channel-cut analyzer crystal was employed. Reciprocal space maps describe much better the relaxation status and the composition of the metamorphic structures than simple rocking curves. Three different types of linearly graded metamorphic buffers are investigated. Sample A consists of a ternary InAlAs buffer grown at the optimum substrate temperature of 420 °C, sample B has a quaternary InGaAlAs buffer with an In-content up to 52% and sample C was designed according to the design of A. Sacedón [4], based on sample B with an additional overshoot in the In-content of 11% at the end of the buffer. Figure 2 shows the (004) and (224) reciprocal space maps of sample C measured with incident X-rays along [01-1] and [011] direction, respectively. Isointensity lines are plotted in a logarithmic scale in arbitrary units. The weak intensity beneath

the sharp substrate peak shows the reflection of the graded buffer regions. The centrosymmetric reflection of the active layers on top of the buffer is elliptical with main axes parallel and perpendicular to the [hkl] directions, indicating the absence of strain- and composition gradients. However, a broadening results from bulklike defects usually referred to as mosaicity. Both (004) reflections are symmetrical to the dashed line through the origin of the reciprocal space, indicating no macroscopic tilt [5]. From the asymmetric reflection, one can see, that the buffer is nearly completely relaxed up to an In-content of 52%. The parts with higher In-content are pseudomorphic, in good agreement with the relaxation model of Tersoff [6]. The in plane lattice constant on top of the linear graded buffer is equal to the material composition of relaxed $In_{0.52}Al_{0.48}As$, therefore, the reduction of the In-content in the top layers results in unstrained material. The same measurements are made for samples A and B, the results are summarized in Table 1. Both samples are incompletely relaxed. The ternary buffer show a large macroscopic tilt in the [011]-direction, however in the perpendicular direction there is no tilt detected. A superior property of the quarternary buffer compared to the ternary buffer is the absence of tilt and an increased degree of relaxation. In all samples the composition of the active layers is in good agreement with the nominal value of 52%.

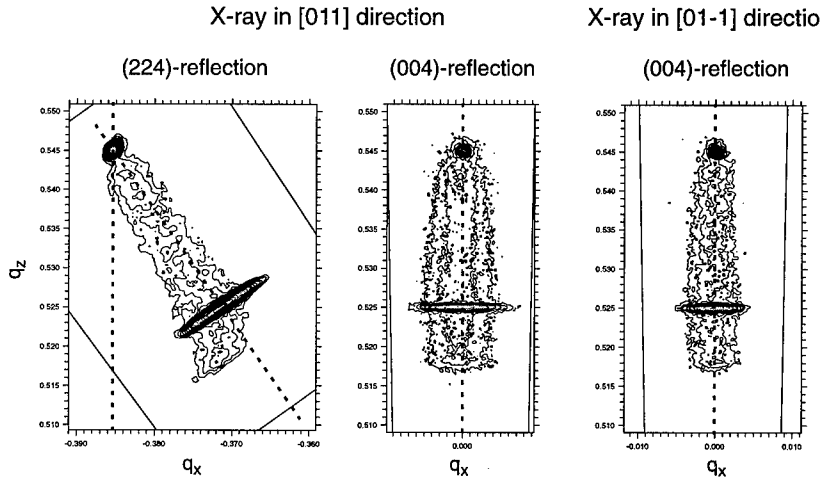


Fig. 2: Reciprocal space mapping of the linear graded metamorphic InGaAlAs buffer (Sample C).

X-rays	[011]-direction			[01-1]-direction
	(004)-reflection	(224)-reflection		(004)-reflection
	tilt	x_{In}	degree of relaxation	tilt
Ternary InAlAs 52%	0.56 °	51.2 %	86.4 %	0.00 °
Quarternary InGaAlAs 52%	0.06 °	53.3 %	89.6 %	0.03 °
Quarternary InGaAlAs 63%	-0.02 °	52.0 %	99.2 %	-0.03 °

Tab. 1: Results of the active layers on top of linear graded metamorphic buffers by reciprocal space mapping.

Interface roughness and its reduction by using different buffer layer structures were studied with respect to transport properties in 2DEG-structures with low carrier density, where interface scattering dominates. The obtained mobilities of otherwise identical structures on the metamorphic buffers discussed above are compared at three different temperatures in Figure 3. The metamorphic buffer with the overshoot in In-content has the best mobility approaching the lattice matched reference on InP-substrate. The carrier density $n_{300K} = 1.3 \cdot 10^{12} \text{ cm}^{-2}$ remains unchanged. The increase in surface roughness as measured by AFM by growing the additional overshoot in In-content is insignificant small.

The observed differences in mobility between metamorphic and lattice matched structures show the effect of scattering by interface roughness and scattering at misfit dislocations in incomplete relaxed active layers.

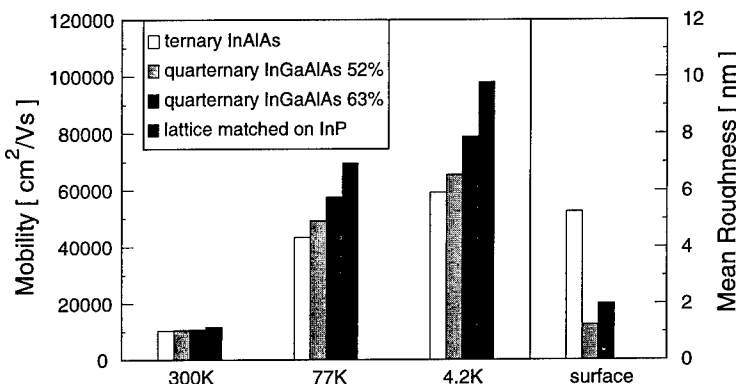


Fig. 3: Mobility and surface roughness of linear graded metamorphic buffers.

3. Conclusion

Grading the metamorphic buffer to an In-content of 0.52 (the value of the active layers) resulted in residual strain. Increasing the final In-composition of the buffer up to a value of 0.63, the $\text{In}_{0.52}\text{Al}_{0.48}\text{As}$ layers on top of the metamorphic buffer are unstrained. Reciprocal space maps of this structure show no macroscopic tilt. Transport properties of 2DEG-structures approach the lattice matched reference values on InP-substrate.

References

- [1] Nguyen L D, Brown A S, Tompson M A, Jelloian L M 1992 *IEEE Trans. Elec. Dev.* 39 2007-2014
- [2] Inoue K, Harmand J C, Matsuno T 1991 *J. Cryst. Growth.* 111 313-317
- [3] Goodhew P J 1994 *J. Phys. Chem. Solids* 55 1107
- [4] Sacedón A, González-Sanz F, Calleja E, Muñoz E, Molina S I, Pacheco F J, Araújo D, García R, Lourenço M, Yang Z, Kidd P, Dunstan D 1995 *Appl. Phys. Lett.* 66 3334-3336
- [5] Koppensteiner E, Bauer G, Kibbel H, Kasper E 1994 *J. Appl. Phys.* 76 3489-3501
- [6] Tersoff J 1993 *Appl. Phys. Lett.* 62 693-695

Results of 3'' and 4'' low-gradient s.i. GaAs growth under controlled vapor pressure

M. Neubert, P. Rudolph, M. Seifert

Institut für Kristallzüchtung (IKZ), Rudower Chaussee 6, D-12489 Berlin, Germany

Abstract. The VCZ technique is promising to grow s.i. GaAs with improved structural quality. Its main idea is to pull the crystals in low temperature gradients to reduce the thermally induced stress. The dislocation density can reproducibly be decreased down to 10^4 cm^{-2} and below in 3'' and 4'' crystals. Within the best samples the radial dislocation density distribution was markedly homogenized (total scatter of a factor of 2 to 3). Electrical parameters of VCZ crystals roughly match those of conventional LEC material.

1. Introduction

The VCZ (vapor pressure controlled Czochralski) technique is a modified LEC (liquid encapsulation Czochralski) method. Its main idea is to grow s.i. GaAs single crystals in lower temperature gradients of about 20 to 30 K/cm. Doing this one is able to i) reduce the non-linearities of the temperature field inside the crystal (thermally induced stress) and therefore the rate of dislocation generation, and ii) increase the homogeneity of the radial and axial distribution of dislocations. Contrary to other methods, the VCZ technique is advantageous to produce low EPD (etch pit density) material with electrical and structural parameters close to those of conventional LEC. This is an essential issue for III-V device producers because nowadays most of the commercially available s.i. GaAs is produced by LEC.

Application of low temperature gradients causes high temperatures of the crystal surface if it emerges from the protective boron oxide melt. To prevent the decomposition of the just grown crystal (arsenic evaporation) it is surrounded by an additional, gas-tight, inner chamber. A pure arsenic evaporation source, placed inside this chamber, produces a certain partial pressure. This keeps the surface of the crystal in equilibrium with the gas phase. A review on VCZ and other low-gradient III-V crystal growth techniques is given in [1].

The present work focuses on further improvements of the structural quality of VCZ s.i. GaAs crystals and their electrical properties.

2. Experimental

In the IKZ labs two pullers (CI 358, LPA Mark 3) are applied to investigate the VCZ technique. The inner chamber is similar constructed in both cases however, the arsenic source is placed in the upper and lower part of the assemblies, respectively. For more details on VCZ please see e.g. [2] and [3].

To analyze the as-grown crystals several techniques were used: standard KOH etching at 400°C for EPD measurements; imaging in specularly reflected light at etch pit facets ([4]) for EPD mapping; standard Hall-technique in van der Pauw geometry for resistivity and carrier mobility; infrared local vibrational mode analysis (LVM) for carbon concentration; near infrared absorption at room temperature for EL2° and photoelastic measurements for residual stress.

3. Results and discussion

3.1 arsenic partial pressure

Developing the VCZ technique a key point was to tighten the inner chamber. This was successfully reached with solid sealing. Today it is possible to maintain the arsenic partial pressure during the whole run (≈ 30 h) with only a low arsenic lost. Thus, the crystals show perfectly mirror-like surfaces without any traces of Ga-rich inclusions or decomposition effects (Fig. 1) as formerly described in [3]. The arsenic partial pressure, required to stabilize the solid GaAs phase, is comparably low at around (0.01-0.05) MPa depending on the crystal surface temperature. Thus, the growing crystal is stabilized near the Ga-saturated solidus of the existence region of GaAs.



Fig. 1 as-grown 3'' (left) and 4'' (right) VCZ GaAs crystals

3.2 axial and radial EPD distribution

The etch pit density has been continuously decreased in the past two years. Best local minima lied at around $2 \times 10^3 \text{ cm}^{-2}$. Photoelastic measurements showed that the residual stresses in the top regions of the crystals are markedly higher than at their tails. However, the dislocation density is roughly uniform from top to tail, e.g. dislocations are generated mainly in the top regions of the crystals prolonging to their ends. Thus, the main attention for decreasing the dislocation density has to be focused to the first-to-freeze part of the crystal. It has been ascertained that the following pre-conditions are advantageous for lowering the EPD:

- Application of new high-tech thermal insulation materials in the furnace to optimize the temperature field inside the growing crystal. This issue was successfully supported by global numerical simulations of the furnace interior.
- Careful adjustment of crystal and crucible rotations respectively, to get a nearly planar solid-liquid interface by influencing the fluid flow in the melt.
- Lowering the height of the boron oxide melt (similar results were recently reported in [5]).
- Flat shape of the seed cone part of the crystal.

In detail, the last two points are also advantageous to homogenize the radial EPD distribution. Fig. 2 shows examples of 3'' and 4'' wafers with very high homogeneity (scatter of a factor of 2-3). In contrary, it has turned out that, at least in the VCZ case, high boron oxide melt and conical crystal top shapes are pre-conditions for the well known w-shaped radial EPD distribution. However, all of those tendencies can only be pointed out for EPD's at around 10^4 cm^{-2} .

Fig. 3 shows the current stage for 4'' crystals. Obviously, the EPD can reproducibly be adjusted at and below 10^4 cm^{-2} within the main parts of the sample area. The very good homogeneity is also clearly illustrated by EPD mappings shown in fig. 4. Unfortunately, there are still some problems with slip line generation near

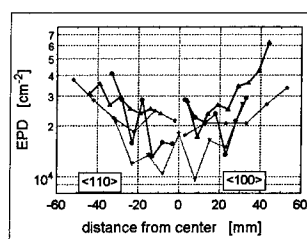


Fig. 2 homogeneous radial EPD distribution in 3'' and 4'' crystals

the edges. However, recent results are promising to overcome this problem.

Cooling-down rates of the just grown crystals are also essential for obtaining low dislocation densities. In the first crystals, grown in the IKZ labs, the EPD was found to increase from top to tail. This effect could be suppressed by considerably lowering the cooling-down rates compared to conventional LEC. The axial EPD distribution became nearly uniform. An explanation can be given by the dynamic theory of dislocations [6]: The *effective* shear stress decreases with the square root of the dislocation density itself. Thus, lower dislocation densities increase the *effective* shear stress and consequently, the dislocation generation rate.

Generally, all types of dislocation arrangements, known from LEC, like cells, lineages and random distribution are also found in VCZ crystals. However, the average cell diameters are larger than in ordinary LEC crystals ($\approx 1\text{ mm}$). Additionally, the cell structure tends to vanish with decreasing dislocation density (less than $1-2 \times 10^4 \text{ cm}^{-2}$) leaving randomly distributed dislocations.

3.3 electrical parameters

With respect to electrical parameters, the crystals have to be sorted into two categories. From economical reasons most of the GaAs was multiple used to study structural properties. The material is still semi-insulating but, it exhibits a large scatter in the electrical behavior due to creeping incorporation of impurities. The specific resistance lies at and above $10^8 \Omega\text{cm}$ while the Hall mobility mostly shows values $\leq 5000 \text{ cm}^2/\text{Vs}$. Thus, it is only sensible to examine material being truly single used. For those as-grown crystals typical parameters are: resistivity $(2-6) \times 10^7 \Omega\text{cm}$, carrier mobility $(5500-7000) \text{ cm}^2/\text{Vs}$. Best values for the normalized standard deviation within a single sample were found to be $<10\%$ for resistivity and Hall mobility, respectively. These values are close to standard LEC material. However, the reproducibility needs to be improved.

3.3.1 carbon content

Carbon incorporated in GaAs (C_{As}) acts as a shallow acceptor and is used to generate n-type semi-insulating material by fully compensating residual shallow donors and partially ionizing EL2. Thus, the carbon concentration is of special interest for s.i. GaAs crystal growth. Its axial distribution is also different for both categories of GaAs as mentioned above. While the carbon content lies at about $(1-2 \times 10^{16} \text{ cm}^{-3})$ in multiple used material, it was found to be approximately $(1-4 \times 10^{15} \text{ cm}^{-3})$ in single used one. In the first case, the carbon concentration decreases towards the ends of the crystals. This is consistent with the segregation coefficient of carbon in GaAs ($k \approx 2$). Single used material shows the opposite behavior. Here we find increasing carbon concentrations towards the crystal tails. This effect can be explained by the well known carbon incorporation from the gas phase

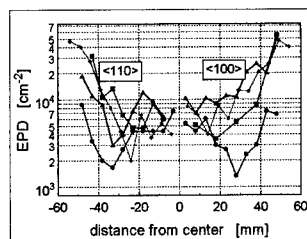


Fig. 3 recent EPD results of 4'' crystals

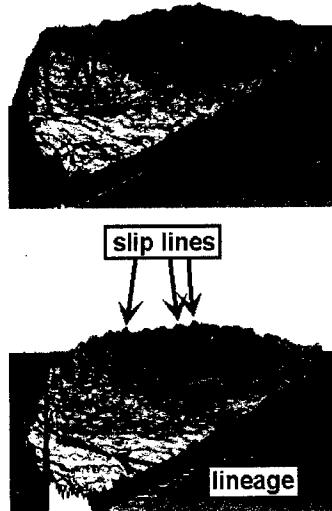


Fig. 4 EPD mapping after [4]

during growth. Additionally, this is supported by the observation that the total carbon concentration increases continuously from run to run in multiple used material.

3.3.2 EL2°

Best values for the normalized standard deviation of EL2° within a single sample were found to be in the range of (3-7)%. This is a very good result for as-grown material (commercial, post growth annealed standard LEC material: ≈5%). But again, reproducibility needs to be improved.

The total content of EL2° shows a larger scatter: $(0.7\text{-}1.5)\times10^{16}\text{ cm}^{-3}$. This may be caused by several reasons like: i) different cooling-down rates after growth (generation of EL2° at around 1100 °C), ii) different melt compositions of multiple used material (Ga enrichment) and iii) the different amount of boron oxide used (the lower the boron oxide hight, the more the arsenic is able to communicate with the GaAs melt i.e. diffuse through the boron oxide)., Unfortunately, this is not yet satisfactorily understood.

4. Summary

It could be shown that the VCZ technique is able to improve the structural quality of 3" and 4" s.i. GaAs markedly by roughly maintaining the electrical properties of conventional LEC material. In some cases the data of commercially available s.i. GaAs (i.e. post growth annealed) were reached by as-grown crystals. However, reproducibility is still too low and has to be improved.

Acknowledgments

The authors are grateful to M. Pietsch and K. Bournot for growing the GaAs crystals, S. Bergmann for EPD analysis, J. Donecker for EPD mapping, W. Ulrici for LVM measurements, N. V. Abrosimov for photoelastic measurements, G. Hempel for Hall measurements, J. Kluge for EL2° investigation and FREIBERGER' (FCM) for valuable discussion and leaving some data. This work was supported by the German Ministry of Education and Science under contract No. 522-4001-01 BM 501/0.

References

- [1] Rudolph P Neubert M Arulkumaran S Seifert M 1997 *Cryst. Res. Technol.* 32 35-50
- [2] Tatsumi M Kawase T Iguchi Y Fujita K Yamada M 1994 *Proc. 8th Conf. on Semiconducting III-V Materials, Warsaw, Poland* 11-18
- [3] Neubert M Seifert M Rudolph P Trompa K Pietsch M 1996 *Proc. 9th Conf. Semicond. and Insulat. Mater. (SIMC'9), Toulouse, France* (IEEE publishing) 17-20.
- [4] Donecker J Rautenstrauch S Bergmann S 1997 *to be presented at DRIP VII Templin, Germany* Proceedings: IOP
- [5] Hashio K Sawada S Tatsumi M Fujita K Akai S 1997 *J. Crystal Growth* 173 33-41
- [6] Alexander H Haasen P 1968 *Solid state physics* (New York: Academic) 27-158

Impact of Growth Interruption on Interface Roughness of MOCVD Grown InGaAs/InAlAs Studied by Photoreflectance Spectroscopy

C. Bru-Chevallier*, Y. Baltagi*, G. Guillot*, K. Hong⁺ and D. Pavlidis⁺

* LPM-INSA Lyon CNRS (UMR5511) - Bât. 502 - 20, Av. A. Einstein - 69621 Villeurbanne Cedex, France

⁺ The University of Michigan, Solid State Electronics Laboratory, Department of Electrical Engineering and Computer Science, 1301 Beal Avenue, MI 48109-2122, USA¹

Abstract The interface quality of InAlAs/InGaAs heterostructures used in High-Electron-Mobility-Transistors (HEMTs) is evaluated as a function of growth interruption time, using photoreflectance spectroscopy on 250Å InGaAs single quantum wells between InAlAs layers. Assessment of the interface roughness is derived from the broadening of the high order quantum confined transitions. The higher the growth interruption time, the smaller the interface roughness as derived from PR measurements. The results are in good agreement with higher electron mobility values measured by Hall effect.

1. Introduction

InGaAs/InAlAs High Electron Mobility Transistors (HEMT) have demonstrated excellent electrical characteristics using MBE grown layers [1,2]. The performance of HEMTs based on metalorganic chemical vapor deposition (MOCVD) can also be good provided that special attention is paid to the growth of low background density InAlAs and a good quality InGaAs-channel/InAlAs-spacer interface. The latter is particularly important for ensuring good transport properties in the two dimensional electron gas channel and is the subject of the studies reported in this paper. A growth interruption time is generally used at the interface, as it is expected to reduce interface roughness; however, it may also introduce undesirable impurities. A compromise has to be found, and for that purpose, photoreflectance (PR) spectroscopy and photoluminescence (PL) measurements were employed in this work to study the interface roughness in 250Å InGaAs single quantum wells (QW), typical of InP-based HEMT designs. Physical parameters derived from PR spectra analysis (energy levels and broadening parameters) are compared with theoretical determinations, and also with complementary Hall effect measurements.

2. Experiment

The evaluated samples consisted of a 250Å InGaAs QW, with InAlAs barriers on InP substrates. The structures were grown by MOCVD at $T_g = 650^\circ\text{C}$ which was found to be the optimum temperature for low background carrier concentration [3]. Different growth interruption times were studied (0s, 5s and 15s) between the moment that group-III sources for InGaAs (Trimethylindium (TMIn) and trimethylgallium (TMGa) are turned off and that when sources for InAlAs (TMIn and trimethylaluminium (TMAI)) are turned on. The indium concentration in the barrier AlInAs layer was measured by double X-ray diffraction and estimated to be about 51%.

Room temperature PR measurements are performed using a standard experimental set up [4], using a 150W quartz tungsten halogen lamp as the probe beam, and an HeNe laser as the pump beam. PL measurements are performed at low temperature (10K) using an Ar-ion laser as the excitation source and a cooled Germanium photodetector.

¹ Work supported by URI (DAAL03-92-G-0109) and NSF/CNRS (INT-9217513)

3. Results and discussion

3.1 Photoluminescence results

The photoluminescence spectra recorded at low temperature (10K) are plotted for the three samples in figure 1. The shape of the PL peak from the quantum well is typical of that of doped structures, with a high energy feature corresponding to recombinations between electrons and localized holes at the interface [5]. The full width at half maximum ΔE of the PL peak is roughly equal to $E_F - E_I$, which is related to the 2D electron gas density n_s by [6]:

$$\Delta E \approx E_F - E_I = \frac{\hbar^2 n_s}{4 \pi m^*} \quad (1)$$

where \hbar is the Planck constant and m^* the electron effective mass. Using this expression, the electron gas density in the quantum well has been estimated in each sample. Results are given in table 1 together with those obtained from room temperature Hall measurements. Both techniques give the same order of magnitude and do not exhibit significant variations as the growth interruption time is varied. The high residual carrier concentration is commonly observed in MOCVD grown AlInAs layers.

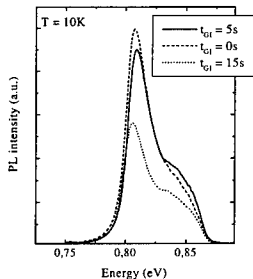


Table 1: Electron gas density estimated from PL and from Hall measurements.

Growth interruption time (s)	FWHM (meV)	n_s (cm ⁻²) (PL)	n_s (cm ⁻²) (Hall)
0s	69	$1.5 \cdot 10^{12}$	$2.4 \cdot 10^{12}$
5s	68	$1.5 \cdot 10^{12}$	$2.3 \cdot 10^{12}$
15s	72	$1.6 \cdot 10^{12}$	$3 \cdot 10^{12}$

Fig. 1: Low-temperature (10K) PL spectra of the samples for different growth interruption times: 0s, 5s, 15s.

Hall measurements give values of electron gas density nearly twice as high as PL technique. This is attributed to the fact that the Hall effect is sensitive to an average electron density in the structure, and is influenced not only by the 2D gas but also by the bulk AlInAs layer and namely by electrons at the substrate interface. The total PL intensity is reduced by a factor of ten for the longer growth interruption time (15s), whereas it does not change significantly for an interruption time of 5s. This indicates that growth interruption favors the incorporation of non-radiative impurities at the interface only when the growth interruption time exceeds 10s.

3.2 Photoreflectance results

A typical PR spectrum recorded at room temperature for the 15s growth interruption time sample is plotted in figure 2. Several transitions are clearly resolved for energies larger than 0.8eV and are attributed to allowed optical transitions E_iH_j between quantum confined electron E_i and heavy hole H_j levels in the InGaAs quantum well. At energies lower than 0.8eV, a large and wide signal is recorded, which is typical of the PR spectra in doped structures [7], and which prevents the lower confined transition E_jH_i lying be-

low the Fermi level being seen. The PR peak which arises near 1.35eV comes from the InP substrate, and the 1.5eV PR peak is attributed to the AlInAs barrier layer. This energy gap is higher than the gap commonly observed in $\text{Al}_{0.48}\text{In}_{0.52}\text{As}$ lattice matched to InP [8], and this indicates an Al-rich alloy in good agreement with DDX measurements ($x_{\text{In}} = 51\%$). The AlInAs PR feature is very large, it is an indication for modulation composition in this alloy [9].

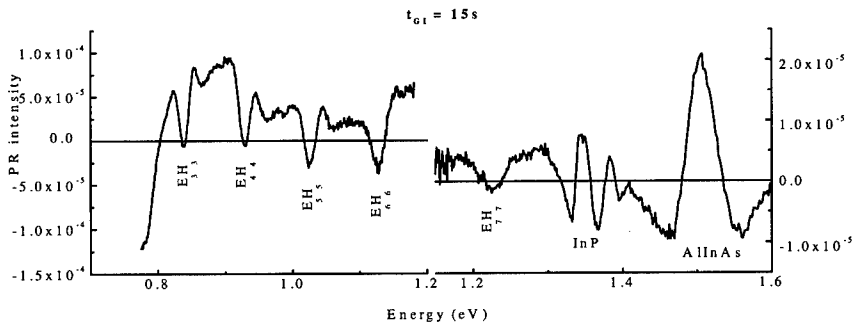


Fig. 2: Room temperature PR spectra of samples for 15s growth interruption time.

The PR transitions corresponding to the quantum confined levels in the quantum well are fitted using the First Derivative Functional Form of the dielectric function, which is appropriate in the case of confined systems [10]. We have used a mathematical model based on a Gaussian absorption profile, with four adjustable parameters (energy, broadening parameter, amplitude and phase) to fit each quantum well PR feature in the spectra. The transition energies are in good agreement with theoretical predictions for a quantum well slightly larger (26nm) than the nominal thickness (25nm) with 51% indium composition in AlInAs barriers. The broadening parameter Γ_n of the quantum confined transition was found to increase with the quantum index n of the transition. For the high order quantum transitions ($n = 4$ to 6), a decrease of Γ_n is observed as soon as a growth interruption is performed. The decrease is all the more important as the growth interruption time is longer (up to 15s).

3.3 Discussion

In the InGaAs/InAlAs system, a Gaussian absorption profile is assumed. We take into account the two main inhomogeneous scattering phenomena responsible for the broadening (Γ) of optical transitions: the alloy disorder (Γ_0) and the interface roughness (Γ_1). Each of this phenomenon being Gaussian, the resulting broadening parameter can be expressed as follows:

$$\Gamma = \sqrt{\Gamma_0^2 + \Gamma_1^2} \quad (2)$$

In an ideal infinite quantum well the quantum confined energy levels can be expressed as a function of quantum well width L_{QW} , electron effective mass m^* and quantum index n . If some interface roughness is suspected, then L_{QW} is supposed to vary by ΔL_{QW} and this implies a broadening of energy levels ΔE_n . The level broadening Γ_1 due to interface roughness (equal to ΔE_n) is proportional to the square of quantum index n . Therefore, high quantum index transitions are expected to be more sensitive to interface roughness than lower transitions. Moreover, the parabola coefficient is proportional to ΔL_{QW} which is the amplitude of interface roughness. The general expression for Γ_n can then be expressed as follows:

$$\Gamma_n = \sqrt{\Gamma_0^2 + K n^4} \quad (3)$$

where K is a proportionality coefficient containing quantitative information about interface roughness.

We have plotted in figure 3 for the 15s growth interruption sample the evolution as a function of n, of Γ_n as determined from PR spectra. The solid lines is the theoretical curve from equation (3) fitted to experimental results. The evolution of Γ is well fitted by this theoretical expression even though the model of an ideal infinite quantum well is not real.

Figure 4 shows the evolution of the K coefficient with growth interruption time. A clear decrease is shown for high growth interruption times. This suggests the reduction of interface roughness by growth interruption at the interface. This trend is in good agreement with the evolution of mobility as a function of t_{GI} which is also plotted and exhibits an increase for large growth interruption times.

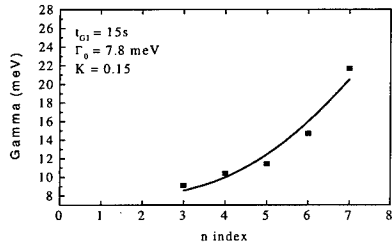


Fig. 3: Evolution of broadening parameters of QW transitions as a function of quantum index n, for 15s growth interruption time.

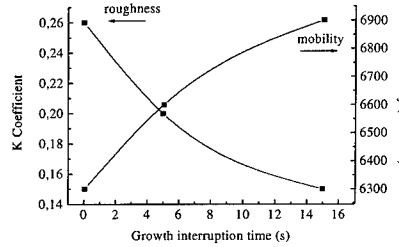


Fig. 4: Evolution of K coefficient and mobility as a function of growth interruption time.

4. Conclusions

InGaAs single quantum wells in InAlAs barriers have been grown by MOCVD with different growth interruption times at the well interfaces. Low temperature PL showed the existence of a 2D electron gas in the well, and allowed the estimation of gas density in agreement with Hall measurements. A large growth interruption time (15s) introduces non-radiative impurities at well interfaces. Despite the high residual doping level of the layers, room temperature PR measurements were performed, and showed that the broadening parameter of quantum confined transitions varies quadratically with quantum index n. Growth interruption times up to 15s were shown to reduce interface roughness. The results are in good agreement with an increase of Hall mobilities as the growth interruption time is increased.

References

- [1] Nguyen L D, Brown A S, Thompson M A and Jelloian L M 1992 *IEEE Trans. on Electr. Dev.* 39 2007-2014
- [2] Smith P M 1995 *Proc. 7th Int. Conf. on InP and Rel. Mat* 68-72
- [3] Ducroquet F, Guillot G, Hong K, Hong C H, Pavlidis D and Gauneau M 1993 *Proc. Mat. Res. Soc. Symp.* 325 235-239
- [4] Bottka N, Gaskill D K, Sillmon R S, Henry R and Glosser R 1988 *J. Electron. Mater.* 17 161-170
- [5] Zhang Y-H, Cingolani R and Ploog K 1991 *Phys. Rev. B* 44 5958-5961
- [6] Tabata A, Benyattou T, Guillot G, Georgakilas A, Zekentes K and Halkias G 1993 *Appl. Surf. Sci.* 63 182-186
- [7] Yin Y, Qiang H, Pollak F H, Streit D C and Wojtowicz M 1992 *Appl. Phys. Lett.* 61 1579-1581
- [8] Gaskill D K, Bottka N, Aina L and Mattingly M 1990 *Appl. Phys. Lett.* 56 1269-1271
- [9] Bearzi E, Benyattou T, Bru-Chevallier C, Guillot G, Harmand J C, Marty O, Pitaval M 1996 *Proc. Mat. Res. Soc. Symp.* 417 271-275
- [10] Huang Y S, Qiang H, Pollak F K, Lee J and Elman B 1991 *J. Appl. Phys.* 70 3808-3814

RF sputtered $\text{Cu}_x\text{Cd}_{1-x}\text{Te}$ thin films: a novel semiconductor alloy

S. López-López*, **S. Jiménez-Sandoval†**, **B.S. Chao‡** and **M. Meléndez-Lira***

*Departamento de Física, Centro de Investigación y de Estudios Avanzados del Instituto Politécnico Nacional, Apartado Postal 14-740, México D.F. 07000, México

†Laboratorio de Investigación en Materiales, Centro de Investigación y de Estudios Avanzados del Instituto Politécnico Nacional, Apartado Postal 1-1010, Querétaro, Qro. 76001, México

‡Energy Conversion Devices, Inc., 1675 West Maple, Troy, Michigan 48084, USA

Abstract. An investigation of the structural, chemical and optical properties of a novel metal-semiconductor alloy based on CdTe and Cu is presented. The samples were prepared as thin films in a magnetron rf sputtering system at various substrate temperatures. On the basis of chemical analyses carried out by Auger spectroscopy and energy dispersive X-ray analysis, it was concluded that a novel semiconducting alloy had been created: $\text{Cu}_x\text{Cd}_{1-x}\text{Te}$. It was also determined that the crystalline structure and optical band gap of CdTe was not severely affected by the inclusion of Cu atoms for values of x up to 8.0 at.%. On the other hand, it was observed that the transport properties changed drastically since in some cases the resistivity of the films decreased by seven orders of magnitude with respect to pure CdTe films grown in similar conditions. The copper concentration had influence on the mean grain-size of the polycrystalline films and on the appearance of the hexagonal phase.

1. Introduction

The search for new materials is one of the areas in materials science where intensive efforts are devoted nowadays. Within this field, semiconducting materials play a central role because of their own standpoint in the development and improvement of electronic and opto-electronic devices. Among the II-VI compounds, cadmium telluride (CdTe) has been the base of important ternary semiconductors such as $\text{Hg}_x\text{Cd}_{1-x}\text{Te}$, $\text{Zn}_x\text{Cd}_{1-x}\text{Te}$, which are of interest for infrared technology, and $\text{Mn}_{1-x}\text{Cd}_x\text{Te}$, which plays a central role among the family of diluted magnetic semiconductors.

In this work we present the results of an investigation carried out to develop thin films of a novel semiconductor material based on CdTe and Cu: $\text{Cu}_x\text{Cd}_{1-x}\text{Te}$. From simple chemical arguments, the inclusion of copper atoms into the CdTe lattice as a substituting element for cadmium is appealing because of the following considerations: a) the ionic radii are 0.97 and 0.96 angstroms for Cd^{+2} and Cu^{+1} , respectively, b) the electronic configuration of copper is $\text{Ar}3d^{10}4s^1$ which favors the formation of the s-p hybrid in the Cu-Te bond as it occurs in the case of the Cd-Te bond and c) the electronegativities of cadmium and copper have similar values having a ratio of 0.9. It will be shown below that the incorporation of copper into CdTe, for the concentrations used in this work, affects mostly the transport properties while the structural and optical parameters remain nearly unaltered. It must be mentioned that copper-doped CdTe samples have previously been prepared and studied, with the emphasis being placed on diffusion processes [1], copper-induced defects [2] and the change in transport properties when it is doped with copper [3]. Typical copper concentrations in previous studies have been in the 10^{15} - 10^{18} cm^{-3} range.

2. Experimental details

The $\text{Cd}_{1-x}\text{Cu}_x\text{Te}$ thin films were produced in a Plasma Sciences CrC-100 rf planar magnetron sputtering system. The sputtering chamber had a base pressure of about 5×10^{-6} Torr. The substrates were made from Corning glass 7059 and were situated at 6.5 cm from a 2"-target. The target was elaborated by compressing an appropriate mixture of -325-mesh powders of high purity CdTe and Cu at 20 ton/cm². The copper concentrations used to fabricate the targets were 5, 10 and 15 molar %. The argon pressures in the vacuum chamber were fixed at 4 mTorr and the radiofrequency power was in the 80-85 W range. The substrate temperatures (T_s) were set at 20, 120 and 180°C for different runs. The thicknesses of the films varied between 1.5 to 4.0 μm depending upon deposition times.

The surface morphology of the films was studied by atomic force microscopy which showed that the grain size was homogeneous. The crystalline structure was analyzed by carrying out X-ray diffraction scans performed over 14 hours, giving an excellent signal-to-noise ratio so that the weak intensity peaks could easily be identified. A silver dot was pasted onto the film surfaces to serve as a reference so that peak shifts due to instrumental effects could be corrected for. Because of this, we are confident that the accuracy of the d-spacings is better than one-hundredth of an angstrom.

The chemical composition was determined from Auger and energy dispersive X-ray analysis (EDX). The band gap was obtained from both photoreflectance and optical absorption measurements carried out at room temperature.

3. Results and discussion

The concentrations of Cu, Cd and Te in the films were measured by Auger spectroscopy and EDX. The results obtained by these two techniques were similar and are presented in Table 1 for some representative samples. From Table 1, it is observed that the Te concentration remains close to 50 at.%, while the other 50 at.% is complemented by both Cd and Cu. Therefore, one may conclude that an alloy of the type $\text{Cd}_{1-x}\text{Cu}_x\text{Te}$ was deposited. This conclusion is further supported by the experimental results presented below which also indicate that Cu atoms substitute for Cd in the CdTe lattice. To the best of the authors' knowledge this is the first report on a semiconducting *alloy* based on CdTe and Cu.

X-ray diffraction patterns were measured for the whole set of samples. In Fig.1 typical diffraction patterns of some samples are shown. In these patterns the peaks labeled with an asterisk correspond to Ag dots used for calibration. Pure CdTe crystallizes in the cubic zincblende structure, although in the case of CdTe thin films the hexagonal (wurtzite) phase has also been observed, as this is a metastable crystallographic phase for CdTe. The X-ray patterns indicate that the films are polycrystalline and highly oriented along the (111) cubic/(002) hexagonal direction. In all cases, the full width at half maximum (FWHM) of the peaks increased with copper content, indicating that the grain size decreased with increasing amount of copper in the film, see Table 1. By using the Scherer relation, it was found that the mean grain size was in the 21.2-42.4 nm range for as-grown films.

The peaks related to the hexagonal phase were more intense for films grown at lower substrate temperatures and higher copper concentrations. Special attention was paid to the X-ray diffraction traces of the $\text{Cu}_x\text{Cd}_{1-x}\text{Te}$ films at the (111) reflection region of the cubic CdTe phase. The positions of these peaks were all corrected for instrumental errors, and yielded the values of d-spacings and FWHMs listed in Table 1. Samples S2 and S3 possessed the narrowest line widths among the group. The spacing d of film S3 agreed incredibly well with that of a polycrystal of pure CdTe, for which the line width

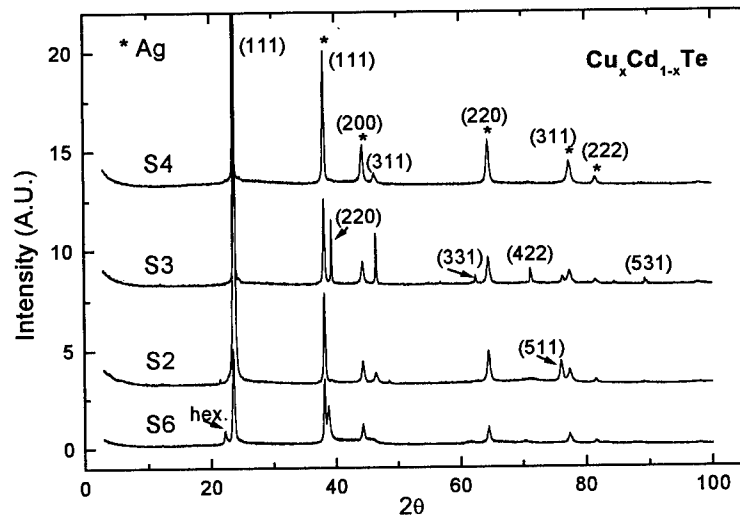


Fig. 1. X-ray patterns of representative $\text{Cu}_x\text{Cd}_{1-x}\text{Te}$ films. The peaks have been indexed according to the zincblende structure of CdTe. The growth parameters and important X-ray data are given in Table 1.

was 0.21 and $d=3.742 \text{ \AA}$. This corresponds to $d=a_0/\sqrt{3}$ for $a_0=6.481 \text{ \AA}$, which is the single crystal lattice constant of CdTe. The d-spacings of the rest of the samples, see Table 1, are higher and indicative of an increment in the lattice parameter with respect to that of CdTe single crystals. It is believed that the thermal treatment carried out on sample S3 improved its crystalline characteristics by increasing the crystallite size, by reducing the defect density and by releasing those areas of the film subject to stress in such a way that its d-spacing coincides with that of a CdTe single crystal. It was also observed in the diffraction patterns that the peaks of samples S2 and S3 are sharp and well defined, which is an indication of superior crystalline characteristics. It is important to note that no copper segregation effects were observed in the annealed sample, even after more than six months of

Table 1. Growth parameters, composition and X-ray data of the $\text{Cu}_x\text{Cd}_{1-x}\text{Te}$ films

Sample	Copper concentration in target (molar %)	T_g (°C)	Film composition (at.%)			(111)cubic / (002)hexag. peak d (Å)	FWHM
			Cd	Cu	Te		
S1	0	180	49.6	--	50.4	3.758	--
S2	5	120	49.1	0.8	50.1	3.754	0.14
S9	5	180	47.8	1.4	50.8	--	--
S3	5	180+TT*	47.6	1.8	50.6	3.743	0.15
S4	10	180	42.9	8.0	49.1	3.759	0.26
S6	15	23	44.7	6.5	48.8	3.774	0.33

*This case refers to a sample grown at 180°C which received a thermal treatment after growth for 3 hours at 350°C in an inert atmosphere

storage, which is evidence about the stability of copper in CdTe for concentrations around 1.8 at.%. Sample S2, which also presented good crystalline characteristics, had a copper content of 0.8 at.%

Finally, some extremely weak traces of Cu_xTe were found at 2θ=12°. These cases were predominantly evident in samples grown at T_s<180 °C. Some correlation was also found between the appearance of Cu_xTe phases and the observation of peaks related to the hexagonal phase. It may be speculated in this case, that the Cu_xTe phases would take a certain amount of Te out of CdTe so that the remaining part became slightly Cd rich. This condition is known to favor the appearance of the hexagonal phase in CdTe [4].

The band gap (E_g) of the films was obtained by two different methods: photoreflectance and optical absorption spectroscopies. The absorption spectra were analyzed by fitting the region around E_g to a model of direct transitions between parabolic bands. In the case of photoreflectance, E_g was obtained by using the three-point method [5]. These two techniques provided E_g values which differed in less than 0.02 eV for the same samples. It was observed that E_g of the alloys are lower than those of the CdTe films grown in the same conditions by no more than 50 meV, and that this difference is a minimum (~10 meV) for samples grown at T_s=180 °C. This result suggests that the incorporation of copper into the CdTe lattice does not affect drastically the magnitude of the electronic band gap of CdTe.

Preliminary electrical measurements indicated that the films were p-type. The samples measured yielded resistivity values which ranged from 5.2 × 10³ to 1.0 × 10⁻² Ω-cm depending upon growth conditions and copper content. These values contrast positively with those of sputtered CdTe films for which resistivity values of the order of 10⁷ Ω-cm are typically found.

4. Conclusions

A novel semiconducting alloy Cu_xCd_{1-x}Te was prepared by rf sputtering for copper concentrations in the 0.8-8.0 at.% range. The best structural properties were found for films with x<0.02. Excellent crystalline quality was found in a sample with x=0.018 which received a thermal treatment after growth. It was determined that the incorporation of copper into CdTe improves significantly the transport properties, while the structural and optical parameters remain nearly unchanged.

Acknowledgments

This work was partially supported by the National Council of Research and Technology (CONACYT) of Mexico under grant No. 211085-5-1564E. S.J.S. wishes to thank God for allowing him to participate in this work.

References

- [1] Jones E D, Stewart N M and Mullin J B 1992 *J. Crystal Growth* 117 244-48
- Chou H C, Rohatgi A, Jockerst N M, Thomas E W and Kamra S 1996 *J. Electron. Mater.* 25 1093-98
- [2] Babentsov V N, Rashkovetskii L V, Sal'kov E A and Tarbaev N I 1992 *Sov. Phys. Semicond.* 26 608-12
- [3] Von Windheim J A and Cicivera M 1992 *J. Phys. Chem. Solids* 53 31-38
- [4] Spinulescu-Carnaru I 1966 *Phys. Stat. Sol.* 15 761-65
- [5] Aspnes D E 1973 *Surface Science* 37 418-42

Patterned high-index substrates as templates for novel quantum-wire and dot arrays: Growth and potential applications

Richard Nötzel, Manfred Ramsteiner, Zhichuan Niu, Lutz Däweritz, and Klaus H. Ploog

Paul-Drude-Institut für Festkörperferelektronik, Hausvogteiplatz 5-7, D-10117 Berlin, Germany

Abstract. On patterned GaAs (311)A substrates lateral GaAs/(AlGa)As quantum wires are formed by MBE at the fast growing sidewall of mesa stripes along [01-1]. This new growth mode develops a smooth, convex surface profile without faceting. The wires exhibit narrow PL linewidths, high PL efficiency and strong confinement up to room temperature. For a given mesa height the wires can be vertically stacked in three-dimensional arrays. Strained (InGa)As quantum wires reveal strongly enhanced optical nonlinearity due to internal piezoelectric fields. In different structures (InGa)As islands can be positioned selectively on the patterned substrate. Finally, in atomic hydrogen assisted MBE step bunching across the GaAs wires forms arrays of quantum dots whose μ -PL spectra are dominated by one single sharp line.

1. Introduction

The natural formation of nanometer-scale structures on high-index semiconductor surfaces during MBE [1] and MOVPE [2] has opened new pathways for the realization of quantum-wire and dot arrays. Even higher flexibility in the formation of nanostructures can be realized by growth on patterned high-index substrates where new phenomena in the selectivity of growth occur. Moreover, patterning provides an additional degree of freedom for the control of the size and, most important, allows the precise positioning of the nanostructures desired for applications in devices.

2. Formation of sidewall quantum wires on patterned GaAs (311)A substrates

On patterned GaAs (311)A substrates a new growth mode is found to produce lateral, quasi-planar quantum-wire structures (Fig. 1). The wire formation relies on the preferential migration of Ga atoms

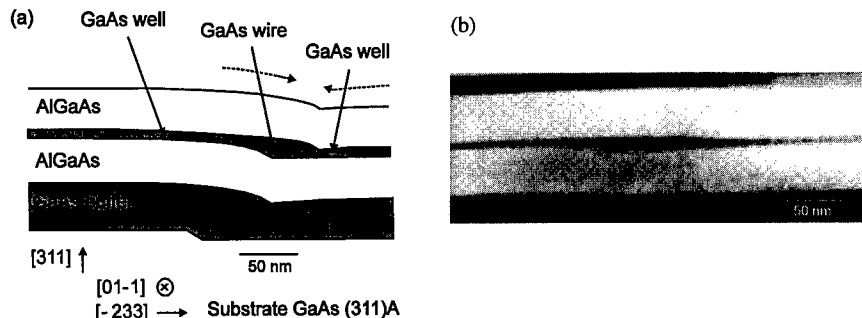


Fig. 1. (a) Schematic of the sidewall quantum wires on patterned GaAs (311)A substrates. The broken arrows indicate the preferential migration of Ga atoms. The cross-sectional TEM image shows the lateral quantum-wire structure connected with a 6 nm thick quantum well and clad by 50 nm thick $\text{Al}_{0.5}\text{Ga}_{0.5}\text{As}$ barrier layers.

from the mesa top as well as the mesa bottom towards the sidewall of 10-20 nm high mesa stripes along [01-1] (i.e., the direction of migration is opposite to the case of patterned GaAs (100) and (111) substrates) which develops a fast growing sidewall with a convex curved, unfaceted surface profile revealing no roughening of the surface morphology compared to the flat parts of the mesa [3].

This unique growth mode on patterned GaAs (311)A substrates is understood by comparing it with the selectivity of growth on other patterned high-index GaAs (n11)A&B substrates depicted schematically in Fig. 2 [3]. The upper line denotes the orientation of the substrate and the lower line that of the facets developing at the sidewalls of the mesa stripes along [01-1]. The dashed lines point on the side in the

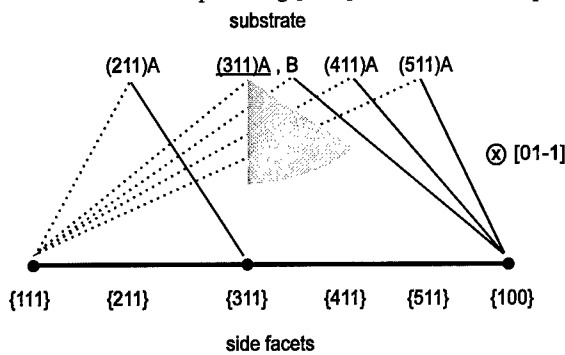


Fig. 2. Diagram of the facet formation on patterned GaAs (n11) substrates.

sector towards the next (111) plane and the solid lines on the opposite side in the sector towards the next (100) plane. In the first sector all planes develop slow growing (111) facets, whereas in the second one mesa stripes on (411)A and (511)A planes develop slow growing (100) facets and that on the (211)A plane a slow growing (311)A side facet. This identifies the (311)A plane as the slowest growing plane in the sector towards the next (100) plane. Consequently, in this sector mesa stripes on patterned GaAs (311)A substrates develop a fast growing, unfaceted sidewall with a convex curvature. The evolution of a (100) side facet for patterned GaAs (311)B substrates is attributed to the higher chemical reactivity of (n11)B planes to enhance the growth rate compared to that of (100) planes.

3. Optical properties of sidewall quantum wires on patterned GaAs (311)A substrates

As expected from the high structural perfection of the wires, the optical properties reveal narrow photoluminescence (PL) linewidths, high PL efficiency (linewidths and efficiency of the wires are always comparable to those of the quantum well), and strong lateral confinement of carriers in the wire region up to room temperature. The two-dimensional quantum confinement of excitons in the wires is confirmed by the transition from two-dimensional to magnetic confinement with increasing magnetic field (Fig. 3). The PL peak position of the wire shows a distinct changeover from weak (two-dimensional quantum confinement) to strong (magnetic confinement) magnetic field dependence at about 2 T which corresponds to a cyclotron diameter of about 40 nm, in good agreement with the geometrical width of the wire [3]. Moreover, clear one-dimensional subbands have been resolved in near-field PL excitation spectroscopy with energy spacings of 12 meV ($\equiv 1/2 k_B T$ at 300 K) [4].

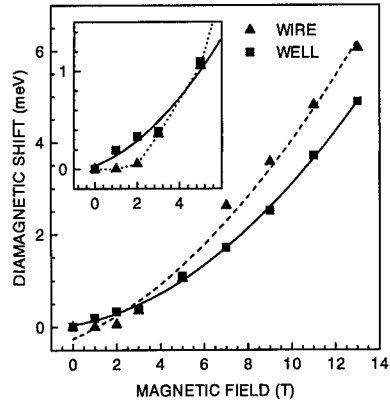


Fig. 3. Dependence of the PL peak energy of the wire and the adjacent well on the magnetic field.

The energy position of the cathodoluminescence (CL) line of the wire can be controlled in a wide range by the initial mesa height reflecting a higher thickness of the wire for higher mesas (see Fig. 4). Therefore, the mesa height prepared by etching is an additional parameter to control the shape and electronic properties of the present wire structure that has no equivalent in V-groove or ridge-type structures.

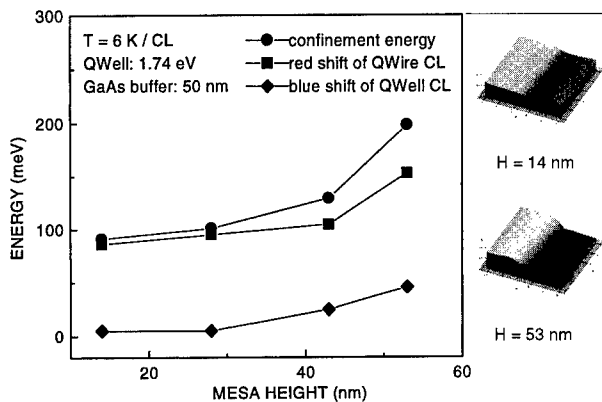


Fig. 4. Dependence of the CL peak energies of the wire and well at the sidewall, and the corresponding confinement energy in the wire on the initial mesa height H . The PL of the 6 nm GaAs/50 nm (AlGa)As quantum well in the flat parts of the mesa is centered at 1.74 eV. The thickness of the GaAs buffer layer is 50 nm. The insets show the atomic force microscopy (AFM) images of the sample surface for $H = 14$ and 53 nm.

The in-plane density of the wires can be easily increased by reducing the mesa widths and spacings. Most important for device applications is, however, that for a given mesa height the wires can also be vertically stacked in growth direction without any increase in interface roughness and wire width fluctuations. This is confirmed by spatially resolved CL spectroscopy (Fig. 5) showing no increase of

the CL linewidth of a stack of three planes of wires compared to that of a single one thus indicating a self-limiting growth mechanism with well defined lateral growth [3].

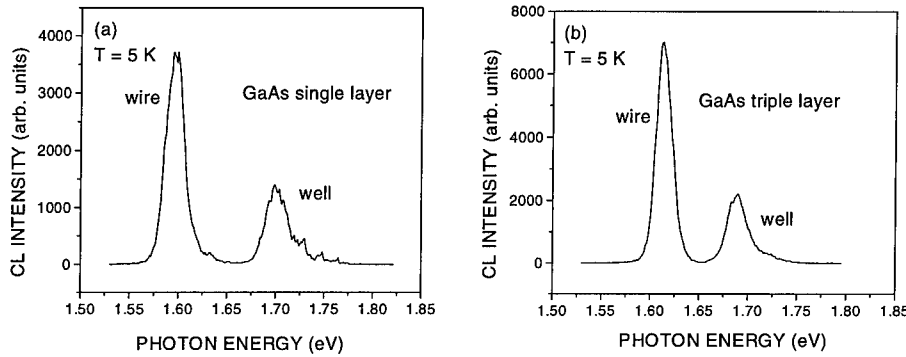


Fig. 5. CL spectra excited at the sidewall of (a) a single quantum wire and (b) a stack of three quantum wires. The thickness of the quantum well connected with the quantum wires is only 2 nm to increase the sensitivity to interface roughness and wire width fluctuations.

4. Strained systems

Strained $\text{In}_{0.2}\text{Ga}_{0.8}\text{As}$ sidewall quantum wires exhibit a blue shift of the PL of 17 meV with increasing excitation power which strongly exceeds that of the adjacent quantum well of 1-2 meV (Fig. 6) [5]. The blue shift is reduced from 7 meV for an In composition of 0.1 to zero for unstrained GaAs wires.

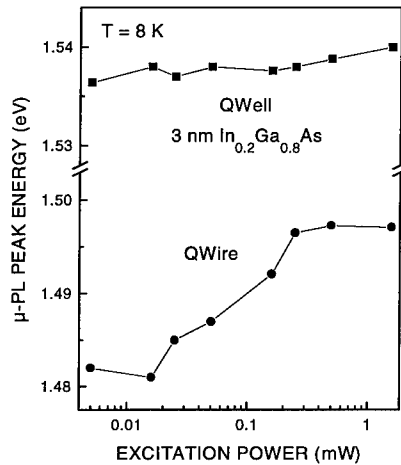


Fig. 6. Dependence of the PL peak energy of the strained (InGa)As sidewall quantum wire and adjacent quantum well on the excitation power.

Full modulation is already obtained for an increase of the excitation power by only one order of magnitude. This enhanced optical nonlinearity is assigned to additional lateral optical band gap modulation in the quantum wire due to internal piezoelectric fields [6] which allows the fabrication of optical modulators operating with high modulation depth at low incident power.

For strained layers, at the onset of the two-dimensional to three-dimensional growth mode transition, (InGa)As island are formed only on the mesa top and bottom. Despite the shallow profile, the curved surface along the sidewall is smooth with a well defined boundary for island formation. This indicates the possibility to selectively position (InGa)As islands on patterned GaAs (311)A substrates (Fig. 7).

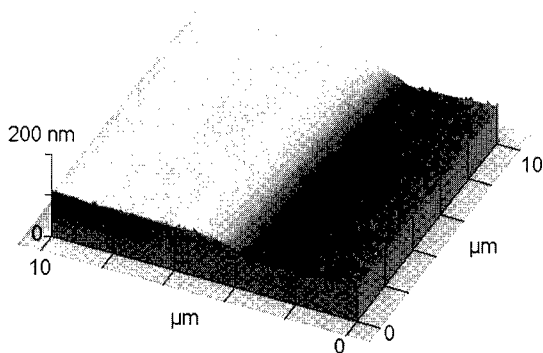


Fig. 7. AFM image of (InGa)As islands on patterned GaAs (311)A substrates. The mesa height is 30 nm.

5. Atomic hydrogen assisted MBE on patterned GaAs (311)A substrates: Formation of highly uniform quantum-dot arrays

In atomic hydrogen assisted MBE of GaAs on GaAs (311)A substrates distinct quasi-periodic step arrays running along [-233] are naturally formed by step bunching with a lateral periodicity around 40 nm, i.e., similar in size to the width of the quantum wire on patterned substrates oriented along the perpendicular [01-1] direction. The step bunches, 2-3 nm in height are maintained over the curved sidewall without displacement, thus generating a periodic thickness modulation of the GaAs/(AlGa)As wire structure to produce an array of quantum dots along the sidewall. The three-dimensional quantum confinement of excitons in the dots is revealed by pronounced splitting of the μ -PL spectra into sharp lines [7,8]. In contrast to the PL from the corrugated quantum well (denoted by QWell in Fig. 8) in the flat parts of the mesa structure governed by strong three-dimensional exciton localization at random interface fluctuations along the step bunches (reflected in the statistic distribution of the sharp lines over the broad envelope of the quantum well emission), the spectral range of the emission from the quantum dots (QDot) in μ -PL is much narrower than the linewidth of the average spectra. The spectra are dominated by one single sharp line without background emission over an energy range exceeding 40 meV. The measured linewidth of the PL from the dots is limited by the spectral resolution of about 60 μ eV. The spectra remain almost unchanged when the diameter of the optical probing area is increased from 2 to 16 μ m corresponding to several ten to several hundred dots. Therefore, combining the self-organizing periodic surface corrugation in atomic hydrogen assisted MBE with the wire formation in patterned growth yields arrays of quantum dots along the sidewall with excellent uniformity over areas which are already large enough to be accessed for further processing.

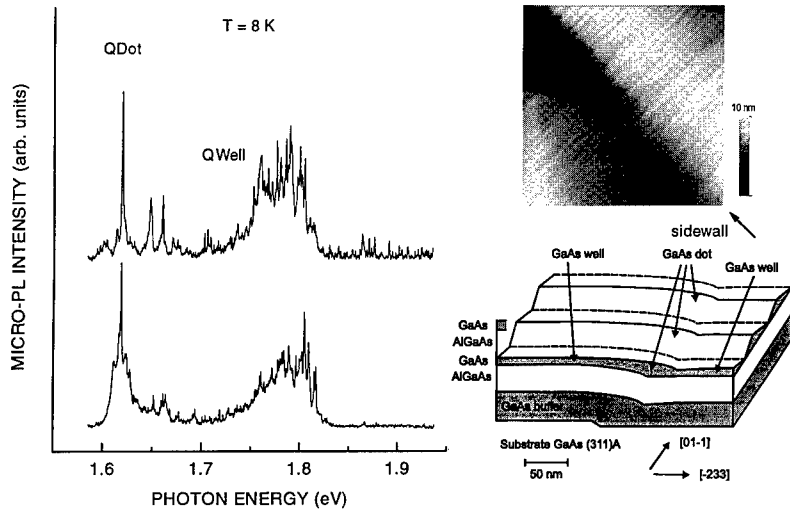


Fig. 8. μ -PL spectra at two positions at the sidewall and AFM top view of the quantum-dot array. The mesa height is 20 nm. QDot denotes the emission from the quantum-dot array along the sidewall and QWell that from the adjacent quantum well. The insets show the AFM top view of the corrugated GaAs layer at the sidewall and a schematic illustration of the final GaAs/(AlGa)As quantum-dot structure.

6. Conclusion

Lateral quantum wires have been formed by MBE on patterned GaAs (311)A substrates at the fast growing sidewall of mesa stripes along [01-1]. The high structural perfection of the wires is demonstrated in narrow PL linewidths, high PL efficiency, and efficient confinement of carriers up to room temperature. To increase the active volume the wires can be vertically stacked in growth direction. Strong enhancement of the optical nonlinearity is found in strained (InGa)As sidewall quantum wires. Finally, in atomic hydrogen assisted MBE distinct natural step arrays are generated across the wire to produce an ordered array of quantum dots whose spectra in μ -PL are dominated by one single sharp line.

References

- [1] Nötzel R, Ledentsov N, Däweritz L, Hohenstein M and Ploog K 1991 *Phys. Rev. Lett.* **67** 3812
- [2] Nötzel R, Temmyo J and Tamamura T 1994 *Nature* **369** 131
- [3] Nötzel R, Menniger J, Ramsteiner M, Schönher H P, Däweritz L and Ploog K H 1996 *Appl. Phys. Lett.* **68** 1132; *Jpn. J. Appl. Phys.* **35** L297; *J. Appl. Phys.* **80** 4108
- [4] Richter A, Süptitz M, Lienau Ch, Elsaesser T, Ramsteiner M, Nötzel R and Ploog K H 1997 *Phys. Rev. Lett.* **79** 2145
- [5] Nötzel R, Ramsteiner M, Niu Z, Schönher H P, Däweritz L and Ploog K H 1997 *Appl. Phys. Lett.* **70** 1578
- [6] Ilg M, Ploog K and Trampert A 1994 *Phys. Rev. B* **40** 17111
- [7] Brunner K, Abstreiter G, Böhm G, Tränkle G and Weimann G 1994 *Phys. Rev. Lett.* **73** 1138
- [8] Gammon D, Snow E S, Shanabrook B V, Kratzer D S and Park D 1996 *Science* **273** 87

A New Self-limited Growth for the Fabrication of Atomically Uniform Quantum Wires and Quantum Dots

Xue-Lun Wang, Mutsuo Ogura and Hirofumi Matsuhata

Electrotechnical Laboratory, 1-1-4 Umezono, Tsukuba 305, Japan

Abstract. A new self-limited growth based on the control of surface migration of Ga atoms during flow rate modulation epitaxial growth of GaAs on patterned substrates is demonstrated. By the use of this new growth technique, atomically uniform GaAs quantum wires and quantum dots can be realized easily, despite the existence of pattern size fluctuations in the initial substrate induced by pattern preparation processes.

1. Introduction

Atomically uniform semiconductor quantum wires (QWRs) and quantum dots (QDs) with sufficiently high densities are highly required for the realization of high-performance optical and electronic devices utilizing novel quantum effects predicted in these low dimensional quantum nanostructures [1]. Although a variety of fabrication techniques have been developed in the last decade for the realization of high quality QWRs and QDs [2-4], the structure uniformity is still a severe problem impeding the observation of the predicted quantum effects. In this paper, we propose and demonstrate a completely new self-limited growth observed in selective growth on patterned substrate by flow rate modulation epitaxy (FME) [5] which is a modified metalorganic vapor phase epitaxy (MOVPE) technique and has been successfully applied to the fabrication of high quality QWRs [6-7]. By the use of this new self-limited growth, atomically uniform quantum nanostructures can be achieved easily even on substrates with large pattern size fluctuations.

2. Experimental Results

This new technique is based on the control of surface migration of Ga atoms during FME growth on patterned substrate. Figure 1 shows the typical gas flow sequence of FME growth. A typical FME growth cycle consists of 4 gas supply periods: Ga flow (triethylgallium: TEGa), H₂ purge, As flow (asine: AsH₃), and H₂ purge. It is worth to mention that, unlike the conventional atomic layer epitaxy (ALE), a very small amount of AsH₃ is supplied throughout the growth to prevent the desorption of As species and the impurity incorporation during Ga flow and H₂ purge periods.

Another important difference of FME with respect to ALE is that, in the case of growth on flat substrate, the FME method has no self-limiting effects because the Ga materials are supplied in the form of completely decomposed Ga atoms. If the amount of Ga species supplied in one growth cycle exceeds 1 monolayer (ML), the excess Ga atoms will form droplets on the substrate surface. However, we recently recognized that, in the case of growth on patterned substrate, the FME growth can have self-limiting effect.

We next describe the experimental demonstration of this new self-limiting effect. For this purpose,

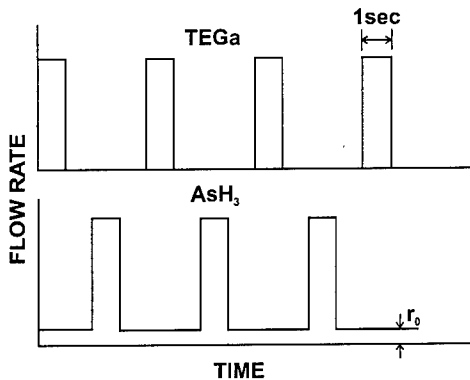


Fig. 1. Typical gas flow sequence of FME growth

AlGaAs/GaAs vertically-stacked multiple QWRs were grown on [0 $\bar{1}1$] oriented V-grooved GaAs substrates with a V-groove period of 2 μm [Fig.2(a)] at 630 °C using a low pressure (76 Torr) MOVPE system. Only the GaAs wire layers were grown by FME, while all the other layers were grown by the conventional MOVPE. The AlGaAs barrier layers between GaAs wire layers were kept thick enough to completely recover the shape of the V-groove bottom distorted by the growth of GaAs wire layer. Figure 2(b) shows the transmission electron microscopy (TEM) image of a 6-QWR sample. Figure 3 gives the growth rate of QWR at the V-groove center and that of the (001) mesa top quantum well measured from the

TEM image as a function of TEGa flow rate, where the growth thickness per FME cycle is expressed by the (001) facet ML thickness (2.83 Å). The growth rate of the QWR region (solid circle) does not increase linearly with the increase of TEGa flow rate, but is composed of several regions in which the QWR growth stops automatically independent of TEGa flow rate, in other words, is self-limited. The TEGa flow rate range of these self-limited growth regions becomes to be wider and the growth rate difference between adjacent regions becomes to be larger with increasing TEGa flow rate. Moreover, the growth rate changes rapidly from one to the other self-limited regions. The self-limiting effect of the QWR growth can also be clearly confirmed from the TEM image of the 6-QWR sample given in Fig.2(b). This sample was grown in the widest self-limited growth region (~ 1.36 ML/cycle), with the TEGa flow rate being increased by an amount of about 30 % from the first to the sixth QWR. Despite of the increase of TEGa flow rate, exactly the same shape was obtained for all these QWRs, while the thickness of the (111)A side wall showed clear increase with the increase of TEGa flow rate. On the other hand, the (001) mesa top growth rate increases approximately linearly with the increase of TEGa flow rate and showed quite large dispersion from wafer to wafer.

3. Discussion

The above results represent a completely new type of self-limited growth which could not be explained by the existing self-limiting mechanism. We next consider the mechanism responsible for this new self-limited growth. In selective growth on patterned substrate, the Ga atoms migrate from facets with longer migration length to facets shorter migration length over a distance shorter than the average Ga migration length due to the difference of Ga migration length on different facets, and the equilibrium distribution of Ga atoms is mainly determined by the difference in migration length and the detailed geometry of the patterned substrate. As a result, the local growth rates of facets with shorter migration length will be selectively enhanced and this leads to the formation of quantum nanostructures [8]. On the other hand, the Ga migration length also changes greatly depending on the surface conditions even on the same crystalline facet [9]. In FME growth, due to the extremely low AsH₃ partial pressure during TEGa flow and H₂ purge periods, most of the Ga atoms are considered to remain un-bonded

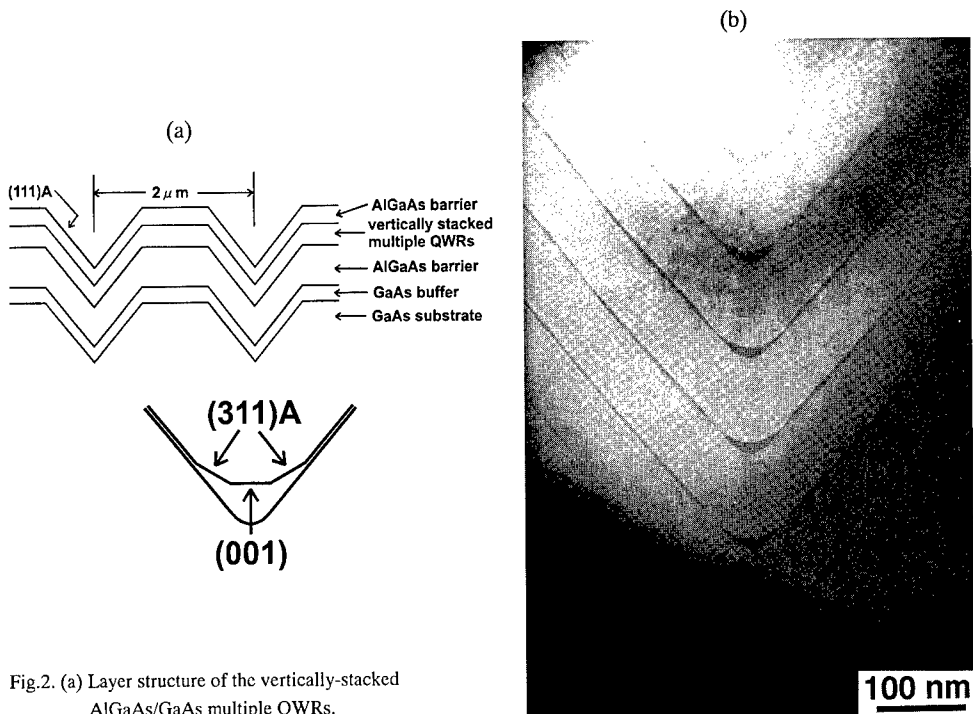


Fig.2. (a) Layer structure of the vertically-stacked AlGaAs/GaAs multiple QWRs.
 (b) Cross-sectional TEM image of a 6-QWR sample.

with As atoms until the start of the AsH_3 flow period. Surface reconstruction into stable microstructures is highly preferred on such surfaces toward the minimization of surface free energy by reducing the number of dangling bonds at some specific Ga compositions [10]. We propose that various stable surface reconstructions were formed at the V-groove bottom in the self-limited growth regions. The Ga migration length on the reconstructed stable surface is expected to be significantly prolonged compared with the case of un-reconstructed surface. Therefore, the excess Ga atoms at the V-groove bottom will migrate to the (001) mesa top or (111)A side wall facets and hence the growth of QWR will stop automatically until the formation of a new surface reconstruction. We call this new self-limited growth as *surface migration induced self-limited growth* in the sense that it is based on the control of surface migration of Ga atoms to distinguish it from the conventional ALE growth.

The significant meaning of this new self-limited growth for the fabrication of quantum nanostructures is obvious. If we do growth in the well-developed self-limited growth regions, atomically uniform QWRs or QDs can be fabricated easily even if there exist some fluctuations in the pattern size of the initial substrate which are inevitable due to the limited accuracy of the pattern preparation processes. In practice, the absence of size fluctuation between different wires at least for QWRs grown on 2 μm pitch substrates has been confirmed by a micro-PL characterization [11]. In this

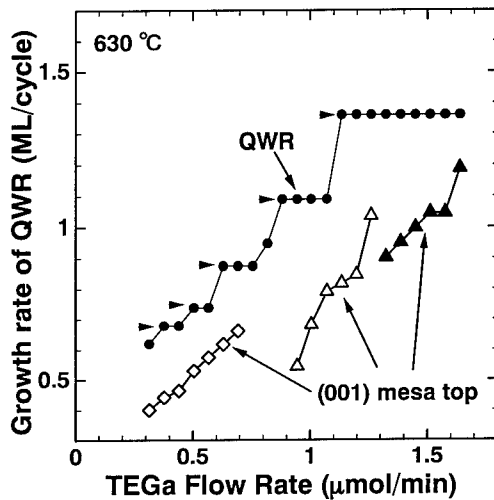


Fig.3. Growth rate of QWR at the V-groove center (solid circle) and that of the (001) mesa top quantum well (open square, open triangle, and solid triangle) as a function of TEGa flow rate.

experiments, the micro-PL spectrum which comes from a single QWR showed the same overall linewidth as that of the macro-PL spectrum. Quantum nanostructures grown by this new technique are considered to be very suitable for the exploration of various new quantum effects which are hidden by size fluctuations in the conventional structures and also for the realization of high-performance devices.

4. Conclusion

A new self-limited growth based on the control of surface migration of Ga atoms during FME growth on patterned substrate was demonstrated. By the use of this new self-limited growth, atomically uniform semiconductor QWRs and QDs can be realized easily on substrates prepared by the conventional lithography and wet chemical etching techniques.

Acknowledgements

The authors would like to thank Dr. Tsunenori Sakamoto and Dr. Keizuo Shimizu for their encouragement on this work.

References

- [1] Arakawa Y and Sakaki H 1982 *Appl. Phys. Lett.* **40** 939-941
- [2] Kapon E, Hwang D M and Bhat R 1989 *Phys. Rev. Lett.* **63** 430-433
- [3] Pfeiffer L N, West K W, Störmer H L, Eisenstein J P, Baldwin K W, Gershoni D and Spector J 1990 *Appl. Phys. Lett.* **56** 1697-1699
- [4] Leon R, Petroff P M, Leonard D and Fafard S 1995 *Science* **267** 1966-1967
- [5] Kobayashi N, Makimoto T and Horikoshi Y 1985 *Jpn. J. Appl. Phys.* **24** L962-L964
- [6] Wang X L, Ogura M and Matsuhata H 1995 *Appl. Phys. Lett.* **66** 1506-1508
- [7] Wang X L, Ogura M and Matsuhata H 1995 *Appl. Phys. Lett.* **67** 3629-3631
- [8] Kapon E 1994 *Epitaxial Microstructures* (New York: Academic)
- [9] Osaka J, Inoue N, Mada Y, Yamada K and Wada K 1990 *J. Cryst. Growth* **99** 120-123
- [10] Biegelsen D K, Bringans R D, Northrup J E and Swartz L -E 1990 *Phys. Rev. B* **41** 5701-5706
- [11] Bellessa J, Voliotis V, Grousson R, Wang X L, Ogura M and Matsuhata H 1997 *Appl. Phys. Lett.* (in press)

Fabrication of InGaAs Quantum Wire Structures by As₂ Flux in Molecular Beam Epitaxy

Takeyoshi SUGAYA¹, Yasuhiko TANUMA², Tadashi NAKAGAWA¹,
Yoshinobu SUGIYAMA¹ and Kenji YONEI²

¹*Electrotechnical Laboratory, 1-1-4, Umezono, Tsukuba 305 Japan*

²*Shibaura Institute of Technology, 3-9-14, Shibaura, Minato-ku Tokyo 108, Japan*

Abstract. InGaAs/InAlAs quantum wire structures on V-grooved substrates have been fabricated under As₂ flux by molecular beam epitaxy. Under As₂ flux, a smaller number of In atoms migrate than those under As₄ flux to the V-groove bottom from the sidewall surface. The InAlAs layer on the V-grooved InP substrates grown under As₂ flux preserves the V-shape, whereas the V-shape cannot be preserved and the quantum wire structures cannot be fabricated under As₄ flux. The InGaAs quantum wires grown under As₂ flux have good optical property.

1. Introduction

Semiconductor quantum wires, in which carriers are confined to one dimension, have been extensively studied for the application to novel optoelectronic devices. As a promising method to fabricate the quantum wire structures, a selective growth of III-V semiconductors on non-planar substrates has been studied. A large number of works of the GaAs or InGaAs quantum wire structures fabricated by the selective growth on non-planar substrates using metalorganic chemical vapor deposition (MOCVD) as well as molecular beam epitaxy (MBE) have been reported [1-5]. The fabrication of GaAs quantum wire structures on V-grooved substrate and its application to a laser structure have been reported by MOCVD [1]. The InGaAs quantum wires having InP barrier layers on V-grooved InP substrate were also fabricated by MOCVD [2].

For the MBE, InGaAs quantum wire structures have been fabricated on the (411)A ridge structures which is formed during the growth at high temperature ($>580^{\circ}\text{C}$) [5]. In the case of the conventional InGaAs/InAlAs MBE using As₄ flux, V-grooved substrate cannot be applied because of the strong migration of In atoms which destroys the V-groove shape during the InAlAs buffer layer, or barrier layer, formation [6]. The InGaAs quantum wire structures cannot be fabricated on the V-grooved substrate in the MBE using As₄ flux. In our previous works, a suppression of the surface diffusion of Ga atoms under As₂ flux have been demonstrated. In this paper, we report the preserving V-shape grooves due to the suppression of In migration under the As₂ flux. Also we report the successful formation of the InGaAs/InAlAs quantum wire structures on the V-grooved InP substrates with As₂ flux at the temperature of 475°C .

2. Experiment

To investigate the difference of In migration under As₂ and As₄ flux, InAs layers were grown on non-planar InAs substrates with As₂ or As₄ flux. The non-planar structures were prepared by photolithography followed by chemical etching in an etchant based on citric acid for 30s. The depth of the etching was about 1000nm. Line-and-space patterns were formed along [110]

direction. After thorough degreasing, the substrates were loaded into MBE chamber and cleaned with atomic hydrogen at 400°C for 10min [7]. The growth rate of InAs was 500nm/h. During the growth, the beam pressure of In was 3×10^{-5} Pa, and those of As₄ and As₂ were 4×10^{-4} Pa, respectively. These values were measured with an ionization gauge at the substrate position. The As₂ flux was generated by cracking As₄ molecules.

To grow InGaAs quantum wire structures, the non-planar structure with V-grooves consisting of (211)A sidewalls and (001) flat surfaces was prepared on a (001) InP substrates by chemical etching in HCl:CH₃COOH:H₂O₂(1:2:1 by volume) for 2min. The atomic hydrogen cleaning was performed at 350°C for 5min. The growth rates of InAlAs and InGaAs were 360nm/h and 350nm/h, respectively. The compositions of InAlAs and InGaAs layers were lattice-matched to InP on the flat (001) surfaces. The growth temperatures were 475°C with no substrate rotation. Two samples were made, one with the InAlAs barrier layer grown with the As₄ source, and the other with the As₂ source. The beam pressures of In, Ga and Al were 1×10^{-5} Pa, 6×10^{-6} Pa and 2×10^{-6} Pa, respectively, and those of As₄ and As₂ were 4×10^{-4} Pa. The thicknesses of InGaAs quantum wire layer, and first and second barrier layers of InAlAs were 4nm, 500nm and 200nm, respectively. These thicknesses were obtained on the flat (001) substrate. Scanning electron microscopy (SEM) observations and photoluminescence (PL) measurements of these structures were performed.

3. Results and Discussions

Figure 1 demonstrates the effect of As₂ flux for the InAs growth on the patterned substrates. The thickness of the grown InAs is 500nm. The layers in Figs.1(a) and 1(b) are grown under As₄ and As₂ flux, respectively. In Fig.1(a), the increase in the growth rate of InAs near the edge of the sidewall is observed. This is due to the migration of In atoms from the sidewall to the (001) surface [8]. The increase in the growth rate is not observed in Fig.1(b). This phenomenon clearly shows that fewer In atoms migrate from the sidewall to the (001) surface under As₂ flux. The mechanism of the difference in surface diffusion is due to the difference in the interaction kinetics of group- III atoms and As₄ or As₂, which occurs on all planes as reported previously [9].

For the growth of quantum wires in the V-grooves, the formation of a barrier layer, while maintaining the sharp groove, is necessary. This requirement is fulfilled by the smaller migration of

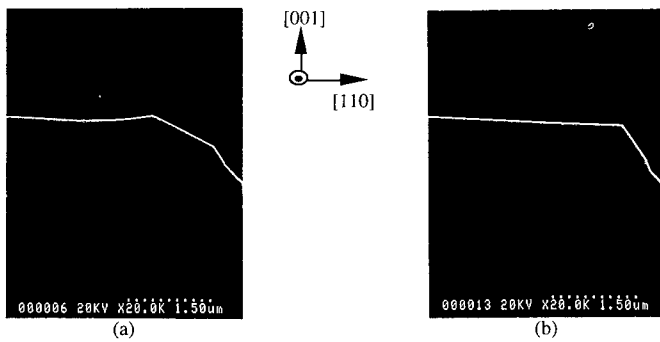


Fig.1 Cross-sectional views of InAs layers grown on patterned substrates. The InAs layers of (a) and (b) were grown with As₄ and As₂, respectively. The thickness of grown layer was 500nm.

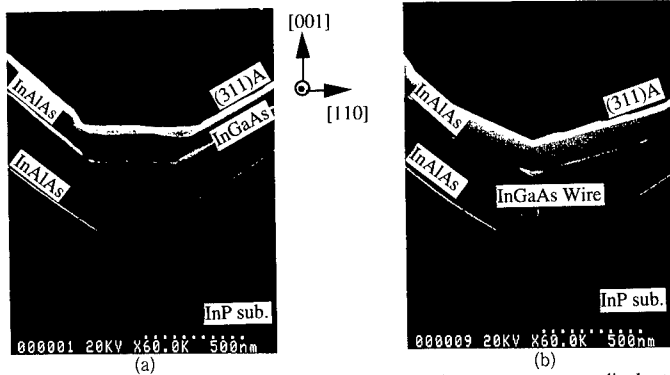


Fig.2 Cross-sectional views of InGaAs/InAlAs quantum wire structures perpendicular to [1-10]. The InAlAs barrier layers of (a) and (b) were grown with As₄ and As₂, respectively. The InGaAs quantum wire was fabricated only with As₂ flux.

group-III atoms under As₂ flux as shown in Fig.1. Figure 2 shows the effects of As₂ flux for the fabrication of InGaAs/InAlAs quantum wires on the V-grooved InP substrates. The InAlAs barrier layers in Fig.2(a) and Fig.2(b) were grown by As₄ and As₂, respectively. The InGaAs quantum wires for both samples were grown under As₄ flux to enhance the migration of the group-III atoms. Although the V-grooves before the barrier layer growth are identical for these two samples, they differ in their profile after the first barrier layer growth. For the As₄-grown sample, the V-shape disappears as shown in Fig.2(a) and no quantum wire is formed. The As₂-grown sample preserves the initial profile and distinct quantum wire structure is obtained as shown in Fig.2(b). These phenomena are caused by the difference in the surface diffusion of In atoms under As₄ and As₂ fluxes as shown in Fig.1. The larger numbers of In atoms migrate to the bottom of V-groove from the sidewall surfaces under As₄ flux and the V-shape is destroyed. Under the As₂ flux, because the migration of In atoms is small, the V-shape is preserved.

Figure 3 shows the photoluminescence spectra of other two samples, one has the InGaAs quantum wire structures and the other has not any InGaAs wires as shown in the inset. The PL measurement was performed at 15K using Ar⁺ laser ($\lambda=514.5\text{nm}$) and Ge photodetector. The diameter of excited area was 200μm and the numbers of excited V-grooves was about 50. The quantum wire has a triangular cross section with 12nm×80nm side dimensions by SEM observation. The broken line in Fig.3 is a spectrum for the sample which have flat bottom regions and no InGaAs quantum wire structures. It has only one peak at around 1150nm which originates from quantum wells on flat (001) ridge and bottom regions. The solid line in Fig.3 is a spectrum for the sample which have InGaAs quantum wire structures. The PL peak at around 1320nm originates from the quantum wires because this peak is not observed from the sample without the quantum wires. The transition energy of the quantum wires is 0.939eV and the energy difference from the InGaAs bulk transition grown at the V-groove bottom is 105meV. The theoretical value of the transition energy of the quantum wires is 0.910eV, which is obtained by a model of the parabolic quantum-wire potential-well [10] and is in agreement with the result of the PL measurement. The full width at half maximum of the quantum wires peak is 38meV. This result indicates that the InGaAs quantum

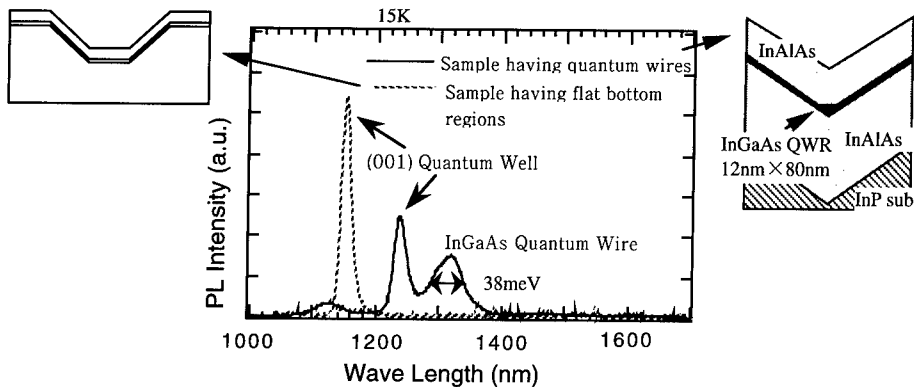


Fig.3 PL spectra of two samples, one has InGaAs quantum wires and another has not any InGaAs wires.
PL peak around 1320nm originates from InGaAs wires.

wire structures have good optical quality. The peak at around 1240nm in the solid line originates from (001) ridge quantum wells, in which the thickness of the well becomes thicker than that of the broken line. That is due to the migration of In and Ga atoms from the sidewall surfaces to (001) ridge surfaces which is narrower than that of the broken line's sample. The weak broad peak at around 1120nm may be due to (311)A quantum wells, or some impurities or defects in the InAlAs layer grown on the sidewalls. Cathodoluminescence measurements confirmed above positional assignment. Although InGaAs and InAlAs layers are lattice-matched to InP on (001) flat region, the precise composition in the wire region and the surrounding barriers are not clear at present. The compositional change in the larger area grown on the patterned InP was reported previously [4]. Further studies are required to determine precise composition in the wire region.

4. Conclusions

In summary, we successfully fabricated the InGaAs quantum wire structures having InAlAs barrier layer grown with As₂ flux on V-grooved substrates by MBE. Under As₂ flux, a smaller number of In atoms migrate to the (001) surface and the bottom of V-groove from the sidewall surfaces than those under As₄ flux. The growth of InAlAs on the V-grooved substrate could not preserve the V-shape under As₄ flux, whereas the shape was preserved under As₂ flux. The InGaAs quantum wires were fabricated only under As₂ flux, and the quantum wires had good optical quality.

References

- [1] Kapon E, Simhony S, Bhat R and Hwang D M 1989 *Appl. Phys. Lett.* 55 2715-2717
- [2] Tsukamoto S, Nagamune Y, Nishioka M and Arakawa Y 1992 *J. Appl. Phys.* 71 533-535
- [3] Wang X L and Ogura M 1995 *Appl. Phys. Lett.* 66 1506-1508
- [4] Sugaya T, Nakagawa T and Sugiyma Y 1996 *IEICE Transactions on Electronics* E79-C 1568-1572
- [5] Fujikura H and Hasegawa H 1996 *J. Electron. Mater.* 25 619-625
- [6] Fujikura H, Iwa-ana T and Hasegawa H 1994 *Jpn. J. Appl. Phys.* 33 919-924
- [7] Sugaya T and Kawabe M 1991 *Jpn. J. Appl. Phys.* 30 402-404
- [8] Hata M, Isu T, Watanabe A and Katayama Y 1990 *J. Vac. Sci. Technol. B8* 692-696
- [9] Sugaya T, Nakagawa T, Sugiyma Y, Tanuma T and Yonei K 1997 *Jpn. J. Appl. Phys.* in press
- [10] Kapon E, Kash K, Clausen Jr. E M, Hwang D M and Colas E 1992 *Appl. Phys. Lett.* 60 477-479

Extremely High Conductivities in Modulation-doped GaAs and (GaIn)As Quantum Wells with AlAs/GaAs Type-II-Superlattice Barriers

K.- J. Friedland, R. Hey, H. Kostial and K. H. Ploog

Paul-Drude-Institut für Festkörperelektronik, Hausvogteiplatz 5-7, D-10117 Berlin, Germany

Abstract We present a new structure to reduce impurity scattering in remotely doped GaAs and (GaIn)As single quantum wells by using heavy-mass X-electrons in the short-period AlAs/GaAs superlattice barriers to smooth the potential fluctuations of the ionized Si dopants. In 10-nm GaAs SQW electron mobilities as high as $120 \text{ m}^2/\text{Vs}$ at electron densities of $1.2 \cdot 10^{16} \text{ m}^{-2}$ are obtained in the one-subband conductivity mode without any parallel conductance. In the case of (GaIn)As SQW the reduction of the impurity scattering manifests itself in the increase of the single particle relaxation time. The design limits to achieve these ultra-high conductivities in terms of layer sequence and growth parameters are discussed.

1. Introduction

Two-dimensional electron gases (2DEG) with ultrahigh conductivity are important for both fundamental research and for applications in low-noise and high-frequency devices [1]. However, remote impurity scattering (RIS) at the randomly distributed dopants becomes one of the main limitations for achieving high conductivities. We have proposed a new concept to reduce RIS in GaAs single quantum wells (SQW) with high carrier concentration and thereby significantly increased the mobility, i.e. by means of the $n \times \mu$ – product, the conductivity [2]. In this presentation we review the applicability of our concept for GaAs as well as for (InGa)As SQW.

2. Concept to reduce remote impurity scattering

To get enhanced conductivity the fluctuations of the scattering potential (FSP) caused by the randomly distributed remote dopants have to be smoothed. For this purpose we use barriers consisting of short period AlAs/GaAs superlattices (SPSL) instead of ternary (AlGa)As. The superlattice period is chosen short enough to get the X-like conduction-band states the lowest energy states in the AlAs sequence of the SPSL. At high enough doping concentration these states become occupied with heavy-mass X-electrons which are located close to the doping layer (Fig.1). The heavy-mass of the carriers provides a high screening capability. Additionally, their Bohr-radius a_B as well as their nominal distance from the doping layer is smaller or nearly equal to the average distance between the Si-dopant atoms. Therefore, the X-electrons can be very easily localized at the minima of the fluctuating potential, hence smoothing the FSP. As a result, with X-electrons in the SPSL the mobility of the electrons in the GaAs SQW can be considerably increased.

3. Configuration of layer structure

The structures were grown by solid-source molecular beam epitaxy on GaAs (001) substrates. The free carriers in the 10 nm GaAs or (InGa)As SQW are provided by remote δ -doping with Si. The

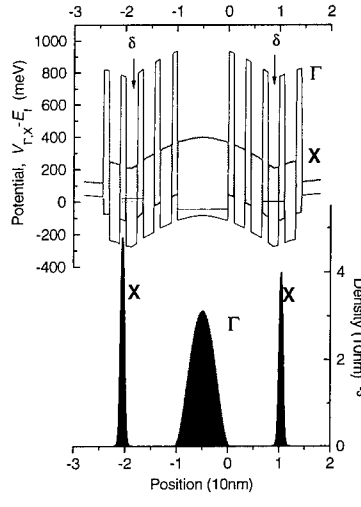


Fig. 1 Calculated potential and charge distribution of a GaAs SQW clad by GaAs/AlAs SPSL[3]. δ marks the position of the do-ping layer $N\delta \approx 1.6 \cdot 10^{16} \text{ m}^{-2}$.

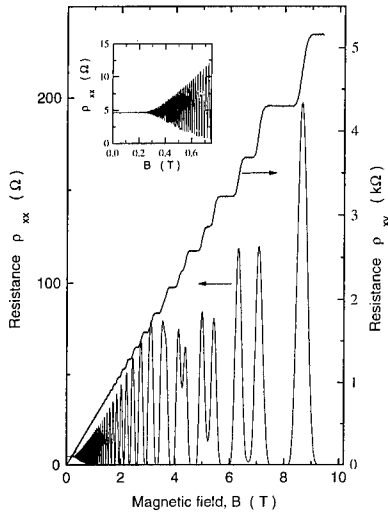


Fig. 2 Magnetic field dependence of ρ_{xx} and ρ_{xy} at $T=0.33 \text{ K}$ in GaAs SQW with X-electrons on both sides of the QW sample, $N^{\delta}=2.5 \cdot 10^{16} \text{ m}^{-2}$

barriers of the SQW consist of several periods of 4ML AlAs / 8ML GaAs SPSL. As indicated in Fig. 1, on both sides of the SQW single Si δ -doping sheets with a doping concentration of N^d were inserted into a GaAs layer of the SPSL at a spacer distance d_s . The low-temperature magnetotransport properties were studied on samples with Hall-bar geometry including a Ti/Au gate electrode to change the electron density.

4. Magnetotransport measurements

To demonstrate the applicability of our concept we show in Fig. 2 the dependence of the components of the resistivity tensor ρ_{xx} and ρ_{xy} on the magnetic field in a GaAs SQW at low temperature. Very high mobilities $\mu \approx 120 \text{ m}^2/\text{Vs}$ at high electron densities n up to $1.2 \cdot 10^{16} \text{ m}^{-2}$ have been obtained. The single-subband occupation is manifested by the one-frequency Shubnikov-de-Haas (SdH) oscillations of the corresponding σ_{xx} component of the conductivity tensor. At temperatures of $T = 0.3 \text{ K}$ and 77 K we found the maximum value of the product $n \times \mu = 1.4 \cdot 10^{18} (\text{Vs})^{-1}$ and $4.2 \cdot 10^{17} (\text{Vs})^{-1}$, respectively. These values are comparable to the highest conductivities in experiments with SQW's at low temperatures, $T < 1 \text{ K}$ [4,5]. However, our $n \times \mu$ -product at $T=77 \text{ K}$ is several times higher than so far reported for 2DEGs [6]. In the (InGa)As SQW the alloy scattering is dominating. However, to achieve very high electron densities in these SQWs the spacer distance d_s must be low and RIS may become important. To demonstrate the suppression of RIS by X-electrons even in (InGa)As SQWs we show in Figs. 3a,b the results of low-temperature magnetotransport measurements. In sample S1 (Fig. 3a) X-electrons are present on both sides of the SQW, while in sample S2 (Fig. 3b) the X-electrons on the surface side of

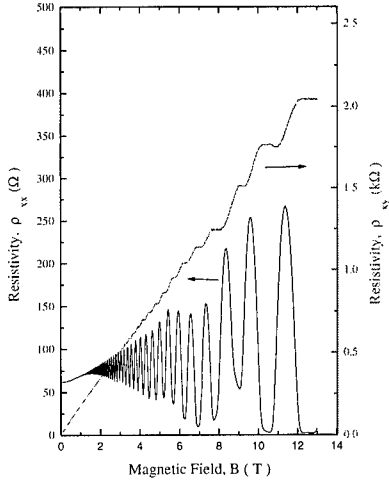


Fig. 3a Magnetic field dependence of ρ_{xx} and ρ_{xy} at $T=0.33$ K in $\text{In}_{0.2}\text{Ga}_{0.8}\text{As}$ SQW with X-electrons on both sides of the QW sample S1, $N^{\delta}=4\cdot10^{16} \text{ m}^{-2}$, $n_{SdH}=3\cdot10^{16} \text{ m}^{-2}$ and $0.7\cdot10^{16} \text{ m}^{-2}$ for the first and second 2D sublevel, respectively.

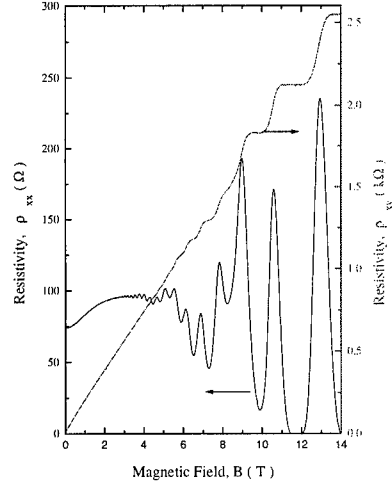


Fig. 3b Magnetic field dependence of ρ_{xx} and ρ_{xy} at $T=0.33$ K in $\text{In}_{0.2}\text{Ga}_{0.8}\text{As}$ SQW with X-electrons removed from one side of the QW sample S2, $n_{SdH}=2.9\cdot10^{16} \text{ m}^{-2}$ and $0.6\cdot10^{16} \text{ m}^{-2}$ for the first and second 2D sublevel, respectively.

the SQW are removed by etching a thin surface layer. Careful analysis of the SdH oscillations reveals two occupied subbands n_0 and n_1 with similar occupation in both samples. The Hall mobilities $\mu_H = \rho_{xy}(0)/\rho_{xx}(0)$ which we expect to be mainly determined by alloy scattering are similar in the two samples, too. Significant differences are seen in the amplitude of the SdH oscillations which contains information about the single-particle relaxation time τ_s . In comparison to sample S2, τ_s is higher by a factor of 4.5 in sample S1, containing X-electrons on both sides of the SQW. This indicates a stronger reduction of the RIS by X-electrons in the barrier. Although the low-temperature mobility is lower in the case of the (GaIn)As QW compared to the GaAs QW due to alloy-scattering, the high carrier density of $4\cdot10^{16} \text{ m}^{-2}$ is promising to provide high conductivity at high field applications of device structures.

5. Design Limits and Durability

There are strict design conditions for which we get reduced RIS in our modulation-doped GaAs QW. The concept is effective only if dopant segregation and intermixing of the SPSL barrier are avoided. This is important, i.e., if we want to be flexible in placing the dopant sheet at discrete separations to the well. For instance, by reducing the SPSL period from 12 ML to 6 ML the carrier concentration is not effected, but the mobility decreases by a factor of about 8. This mobility reduction is probably caused by intermixing and dopant segregation. It is known that a unidirectional segregation of Ga from GaAs into AlAs at the GaAs/AlAs interface exists[7]. This Ga segregation leads to an intermixing of

the SPSL components. The intermixing process develops inhomogeneously depending on the actual defect structure of the surface (terrace-step structure). The process will be more pronounced the smaller the individual SPSL layers are. As a consequence the dopant segregation towards the SQW interface in the growth direction is enhanced leading to an increase of RIS. Additionally, strong intermixing can lift the type II SPSL character. Growing the whole structure at a constant substrate temperature of 580°C also leads to a loss of the extremely high electron mobility because of similar reasons. Therefore, the achievement of smooth SQW interfaces and the suppression of dopant segregation in combination with intermixing effects must be balanced by an adequate choice of growth temperatures.

With optimized structure design and growth conditions the remotely doped SQWs with SPSL barriers presented here are less sensitive to interfaces and steps introduced by patterning of the underlying template (substrate) prior to MBE growth. We have demonstrated this unique durability by fabricating the GaAs SQW structure as described before on patterned substrates. The measured low-temperature carrier concentration of $1 \times 10^{16} \text{ m}^{-2}$ and mobility of $50 \text{ m}^2/\text{Vs}$ evidence a minor degradation only. This durability of the structure is very promising to realize three-dimensional architectures (e. g. back-gating, parallel conducting channels, etc.) in advanced electron devices

6. Conclusions

In conclusion, we have shown that the impurity scattering in remotely doped GaAs and (InGa)As SQW can be reduced effectively by the presence of heavy-mass X-electrons in the direct vicinity of the doping atoms in the barrier. These X-electrons exhibit an extremely high screening capability and are able to smooth the potential fluctuations, caused by the random distribution of the dopants. At low temperatures they are localized and do not contribute to the conductivity. This opens new possibilities for device applications. The high electron conductivity may be decreased by dopant segregation in combination with intermixing effects in ultra-short period superlattices. With an adequate choice of the growth procedure these detrimental effects can be minimized.

Acknowledgements

The authors wish to thank M. Hoericke for MBE wafer growth.

References

- [1] G. Traenkle, H. Rothfritz, R. Mueller and R. Weimann, J. Crystal Growth **120**, 240 (1992).
- [2] K.-J. Friedland, R. Hey, H. Kostial, R. Klann and K. H. Ploog, Phys. Rev. Lett. **77**, 4616 (1996).
- [3] K.-J. Friedland and R. Zimmermann unpublished. The calculations are performed by the one-dimensional self-consistent solution of the Schrödinger and Poisson equations in the effective mass approximation, including exchange and correlation interaction energy.
- [4] L. N. Pfeiffer, K. W. West, J. P. Eisenstein, K. W. Baldwin and P. Gammel, Appl. Phys. Lett. **61**, 1211 (1992).
- [5] B. E. Kane, L. N. Pfeiffer and K. W. West, Appl. Phys. Lett. **67**, 1262 (1995).
- [6] M. Blumina, I. O. Lelong, R. Sarfaty and D. Fekete, J. Appl. Phys. **75**, 357 (1994).
- [7] W. Braun and K. H. Ploog, J. Appl. Phys. **75**, 1993 (1994).

Fabrication of Resonant Interband Tunneling Diode Using Resistless Lithography and Selective Area Epitaxy

Kumar Shiraliagi, Raymond Tsui, and Herbert Goronkin

Phoenix Corporate Research Laboratories, Motorola, Inc., 2100 East Elliot Road, M/S-EL308, Tempe, Arizona 85284 USA

Abstract. InAs and InAs/GaSb/AlSb based resonant interband tunneling diodes are grown selectively in open windows on patterned GaAs substrates. The patterning is carried out by using a recently discovered resistless process wherein the GaAs surface is modified in the light exposed regions into forming a stable gallium oxide mask that can withstand InAs selective growth conditions. The one-step process used here replaces multi-step processes typically used to pattern the silicon nitride or oxide conventionally used as a mask for selective growth. It brings about many advantages such as cleanliness, reduction in cycle time, and improved compatibility with cluster tools.

1. Introduction

Selective area epitaxy (SAE), in which a substrate is patterned with a mask to enable the growth of epitaxial material in the open windows, has been a useful technique in fabricating novel devices [1]. Materials such as GaAs, InP, and InGaAs have been selectively grown using MOCVD and CBE on patterned substrates [2,3]. The selective growth of InAs has also been reported on a nitride patterned GaAs substrate [4]. InAs selective growth opens up possibilities of novel devices and the complex device integration of resonant tunneling diodes (RITDs) and FETs into such devices as resonant interband tunneling FETs (RITFETs) [5]. InAs, with its narrow bandgap (0.36eV), high electron mobility, and close lattice matching to GaSb and AlSb, enables the fabrication of these structures. In the past, selective InAs growth (and growth of other compounds) has been reported on silicon nitride and oxide patterned wafers and a number of challenges. The quality of the mask, particularly the cleanliness of a mask patterned using photoresist, is a significant factor in determining the selectivity of the grown material. Conventionally, silicon nitride is deposited on GaAs wafers by plasma enhanced chemical vapor deposition and patterned using photolithography and reactive ion etching. After pattern transfer, the resist mask is removed using an oxygen plasma. Prior to loading the wafers into the CBE system, they are cleaned in a dilute NH₄OH solution. Any particulates present on the mask surface, even on an atomic scale, can act as nucleating sites for atoms during growth and result in poor selectivity. Growth on top of the nitride, under these circumstances, appears as polycrystalline material. Complex multi-step cleaning processes are used to ensure an atomically clean surface in order to grow selective InAs.

In this paper we discuss how many of these patterning and growth related issues are resolved using the recently discovered resistless process of patterning GaAs wafers. Selective RITDs are fabricated utilizing this technique as described in this paper. Details on substrate patterning and the selective growth of InAs as compared to the conventional approach, and the results of the fabrication and electrical characterization of RITDs are presented.

2. Experimental procedures

In the resistless process, a conventional chrome-on-glass mask is placed on an epi-ready GaAs substrate and exposed to collimated UV light, which can be 185 nm light that is typically used in ozone cleaners or 248 nm light [6]. The substrate was exposed for a total of three minutes under room ambient conditions.

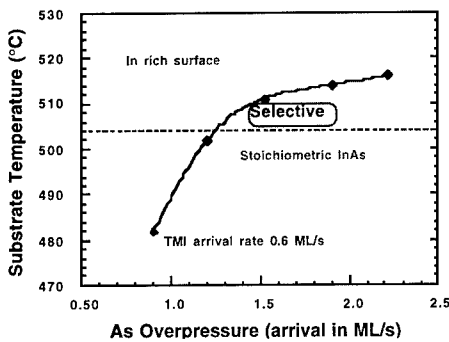


Fig. 1. Phase diagram showing the maximum temperature where InAs can be grown under group V stable conditions for increasing arsenic arrival rates and a constant In arrival rate of 0.6 ML/s. The dotted line indicates the boundary of selective growth.

flux. The substrate was subsequently cooled to approximately 500 °C and selective InAs growth performed. Trimethylindium (TMI) and arsine were used as sources for the growth of InAs. Solid Ga, Al and Sb were used for the growth of antimonides in the RITD device structure.

3. Results and discussions

The quality of the mask plays a very important role in our ability to grow InAs selectively because of the small available growth window. This can be understood by examining the phase diagram in Fig. 1 which shows the V/III ratios required for the growth of InAs at varying substrate temperatures. The area below the curve represents the region where stoichiometric InAs grows under a group V stable (2x4) reconstruction as determined by RHEED. The curve is shown for an In arrival rate of 0.6 ML/s. Even at temperatures lower than 450 °C, there is a finite group V desorption rate from the InAs surface and hence As flux greater than that of the arrival rate of In is needed to keep the surface stable. As the substrate temperature increases for the same arrival rate of In, an increasing amount of As is needed to prevent the surface from turning In rich. At temperatures higher than 520 °C, the high As over-pressure needed may push the chamber pressures to impractical values. Thus, in reality, temperatures close to 510 °C or below represent an acceptable upper limit.

On the other hand, selective InAs growth on patterned GaAs substrates is possible only at temperatures higher than 500°C. At lower temperatures the adatoms on the mask are not able to overcome the activation barrier for desorption and hence nucleation begins, resulting in polycrystalline InAs. Thus, the temperature window where InAs can be grown selectively is about 10-15°C. At substrate temperature close to 500 °C, sufficient arsenic over-pressure is needed to grow InAs under As

The native oxide on GaAs substrates in the form of gallium arsenic oxide $\approx 10\text{ \AA}$ thick is modified into a more stable gallium oxide $\approx 15\text{ \AA}$ thick as measured by an ellipsometer [7]. In vacuum, the native oxide desorbs at 580 °C whereas the modified oxide has a higher desorption temperature of ≈ 645 °C. In comparison to a multi-step conventional process using photoresist, extremely clean patterned substrates can be obtained in just one step.

Epitaxial growth was performed in a Fisons V90-H CBE system on 3" UV patterned (100) n^+ GaAs substrates. A 15 KeV reflection high energy electron diffraction (RHEED) system at an electron beam angle of about 1.5° was used to determine growth conditions and growth rates. Surface temperature was measured using an IRCON infrared optical pyrometer. Arsine was injected through a cracker cell that was operated at 900 °C for complete dissociation of arsine into dimeric arsenic. The native oxide was first desorbed by heating the substrate to above 580 °C and annealing it for 10 minutes under an arsenic

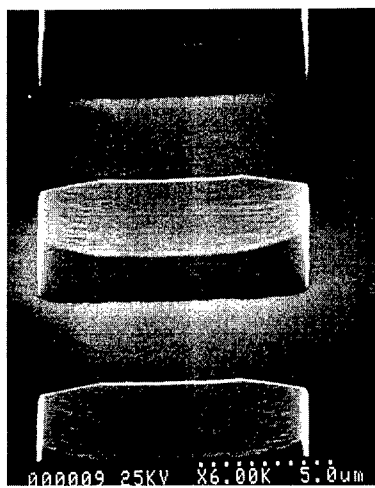


Fig. 2. Scanning electron microscope image of 10 μm square mesas of 1 μm thick selective InAs grown on a resistlessly patterned GaAs substrate.

stable conditions; at the same time, too high a V/III ratio will render the surface hazy as a result of three-dimensional InAs growth on a GaAs substrate. These boundaries define a narrow window for the SAE of InAs as indicated by the shaded region marked 'selective' in Fig. 1. This understanding further elucidates the need to measure surface temperature accurately in order to carry out InAs SAE. The surface temperature, as measured by the pyrometer is a function of a number of factors such as type of substrate, type of mask, area of pattern coverage, InAs thickness, doping, and other hot sources radiating in the chamber. Some of these factors, such as the narrow bandgap of the growing material that absorbs radiation more efficiently and results in an increase in temperature as layer gets thicker, are unique to InAs SAE. These factors are not significant while growing selective GaAs. Other factors, as discussed below, are sensitive to the mask. The conventional nitride mask used for SAE tends to result in a higher measured temperature as a result of a difference in emissivity from that of the epilayer. The offset is a function of the area of the surface covered by the mask. In addition, the hot sources present inside the CBE chamber generate light which are reflected from the masked and unmasked areas and the nitride mask tends to reflect light different from that of InAs and accurate temperature measurement and compensation can be difficult. Surface roughness or a small amount of nucleation on the mask can also reflect heat from the sources into the pyrometer showing an increase in temperature. It is important to absolutely prevent any nucleation on the surface since this will cause a pseudo temperature rise which when corrected for, will throw growth into a positive feed back loop ruining selectivity. Temperature correction during SAE of InAs has to take into account all of these above mentioned factors; inappropriate temperature correction will result in poor selectivity.

The thin, very clean gallium oxide mask, with an emissivity close to that of the substrate, eliminates a few of these problems and makes the selective growth process easier and better controlled. The elimination of photoresist on the surface helps keep the surface extremely clean, preventing any extraneous material from affecting selectivity. Fig. 2 shows 10 μm square mesas of InAs grown on resistlessly patterned (100) GaAs substrates. The layers correspond to a bulk InAs thickness of 1 μm in the [100] direction. Along the [011] direction, vertical sidewalls with clear (011) facets are seen. Extremely smooth (101) facets are obtained for 45° oriented features. In the [011] direction, distinct Ga-terminated (111)A and (311)A facets are obtained. The facets are a result of the net growth rate in each crystallographic direction, which in turn is a function of the V/III ratios, substrate temperature, shadowing effects due to orientation of the lines, epitaxial layer thickness and the source substrate geometry. No deterioration in the mask is observed during the selective growth of InAs.

4. Device results

The cross-sectional schematic of a selective RITD is shown in Fig. 3. It consists of a 1 μm thick $2 \times 10^{18} \text{ cm}^{-3}$ Si doped InAs layer, on top of which is the active region consisting of a 6.5 nm GaSb layer sandwiched between 2.5 nm AlSb and 10 nm unintentionally doped InAs [6], and 200 nm of doped InAs which acts as the top contacting layer.

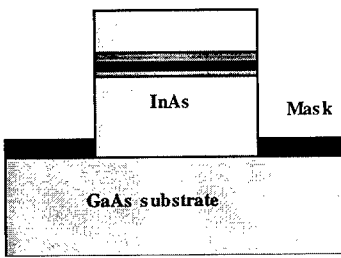


Fig. 3. Cross-section schematic of an RITD structure fabricated.

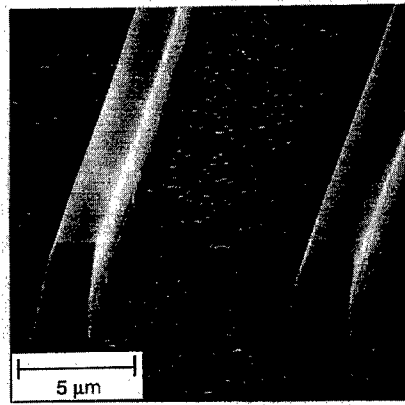


Fig. 4. Scanning electron microscope image of a InAs/AlSb/GaSb selective RITD grown on resistlessly patterned GaAs substrate.

The selective growth of InAs was carried out under conditions described in the previous section on a resistlessly patterned n⁺ GaAs substrate.

A scanning electron microscope picture of the structure is shown in Fig. 4. Even though the InAs below the active region was grown selectively, the AlSb in the active region was non-selective and this gave rise to the subsequent nucleation of InAs on top of the AlSb, seen as small polycrystalline deposits on top of the oxide. Ohmic contacts are evaporated and a quick InAs wet etch is performed to remove the polycrystalline InAs deposited on the mask. However, it is possible to use InAs directly to contact the RITD in integrated device structures, without the need for contact metal evaporation. The room temperature I-V characteristics of the RITD are shown in Fig. 5. The peak to valley current ratio (PVCR) is a parameter typically used to evaluate resonant tunneling devices. Room temperature PVCRs in the 10-15 range have been obtained, and these results are comparable to the conventional RITDs fabricated by etching layers grown on planar substrates and to those grown selectively using a nitride patterned GaAs substrates [2,6].

5 . Summary

GaAs substrates are patterned without using any photoresist in a simplified one-step process. Extremely clean surfaces are obtained with a thin gallium oxide mask and this simplifies the selective growth process of InAs as compared to growth on a conventional nitride patterned GaAs. SAE of InAs was utilized to demonstrate RITDs with characteristics comparable to those seen in conventional RITDs that are processed on planar substrates. Selective growth results in well defined crystallographic facets and the thin gallium oxide mask can be used further to obtain a higher degree of device integration and more complicated device structures that are not easily possible with post growth patterning.

Acknowledgments

This work was performed in part under the management of FED (the R&D Association for Future Electron Devices) as a part of the R&D of Basic Technology for Future Industries supported by NEDO (New Energy and Industrial Technology Development Organization, Japan). Thanks to Sue Allen, John Tresek, Ruth Zhang, Diana Convey, and Theresa Hopson for help with sample processing and characterization.

References

- [1] H. Heinecke, 1994 J. Crystal Growth 136 18-28.
- [2] W.T. Tsang 1992 J. Crystal Growth 120 1-24.
- [3] R. Bhat, 1992 J. Crystal Growth 120 362-368, and references therein.
- [4] K. Shiraliagi, M. Walther, R. Tsui, and H. Goronkin 1996 J. Crystal Growth 164 334-338.,
- [5] J. Shen, S. Tehrani, H. Goronkin, G. Kramer 1996 SPIE Proc. Series 2694, (SPIE, Bellingham,) 90-98.
- [6] K. Shiraliagi, R. Tsui, H. Goronkin 1997 paper W 10, 39th Electronics Materials Conference, Fort Collins CO.
- [7] K. Shiraliagi, N. Saha, R. Tsui, and H. Tompkins, 1997 Electrochemical Society Proc. of The Twenty-Sixth State of the Art Program on Compound Semiconductors, 97-1, 54-57.

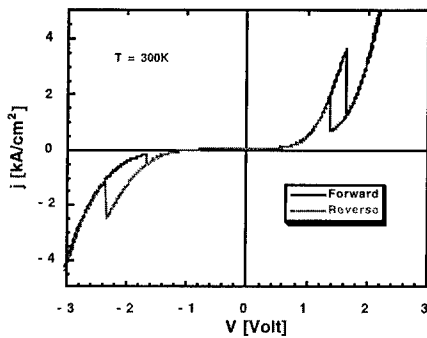


Fig. 5. Room temperature IV characteristics of a selective RITD showing PVCR.

Ordered incorporation of dopants in GaAs: A new route to overcome solubility limits

L. Däweritz, P. Schützendübe, M. Reiche, and K.H. Ploog

Paul-Drude-Institut für Festkörperelektronik, D-10117 Berlin, Germany

Abstract. An analysis of atomic configurations during Si incorporation in GaAs by MBE has been performed using RHEED and reflectance difference spectroscopy (RDS). It provides a direct explanation for the different findings of the maximum sheet electron concentration in Si-delta doped GaAs reported in literature.

1. Introduction

An important issue for Si δ -doping of GaAs as well as for very heavily doped bulk-type material is the saturation mechanism of the free carrier concentration. Different mechanisms of structural or of electronic type might be operative [1,2]. The structural mechanism involves the Si incorporation kinetics that can be varied by the structure of the initial surface and by the Si deposition conditions.

2. Experiment

Si was deposited at conditions of high adatom mobility on singular and on toward (111)Ga misoriented GaAs(001)(2×4) surfaces. RHEED and RDS data were measured simultaneously. The recorded RDS signal is the real part of the reflectance anisotropy $\Delta r / r = 2 (r_{[\bar{1}10]} - r_{[1\bar{1}0]}) / (r_{[\bar{1}10]} + r_{[1\bar{1}0]})$.

3. Results and discussion

3.1. Free carrier concentration

The effect of Si deposition conditions on the carrier concentration is apparent from the data of Fig. 1a. The samples of curve 1 were prepared by pulsed deposition (5.8×10^{12} atoms cm^{-2} in 60 s, interruptions of 90 s) at 590°C and by GaAs overgrowth at 540°C and an As₄ pressure yielding the (2×4) α structure [3]. Data for δ -doping at 590°C during continuous Si supply and GaAs overgrowth [4] are displayed in curve 2. Curve 3 [5] represents conventional δ -doping at lower temperature and higher As surface coverage than used in this work. In contrast to conventional δ -doping there is no rapid decrease in the carrier concentration for pulsed Si deposition at 590°C and GaAs overgrowth at 540°C. Comparison of the corresponding SIMS profiles reveals that the distribution of segregated Si atoms is narrower with pulsed Si supply than with continuous Si supply. Consequently, the differences in the maximum sheet carrier concentration cannot be explained by a concentration dependent reduction of the electrical activity of incorporated Si atoms due to the solubility limit and random distribution on lattice sites.

3.2 Dopant incorporation model

Insight into the Si surface distribution is given by monitoring the reconstruction during Si supply. Fig. 2 shows a RHEED-intensity linescan plot taken in the [110] azimuth for pulsed Si supply on the vicinal surface. During deposition of 0.4 ML Si the half-order streak due the initial (2×4) structure splits into

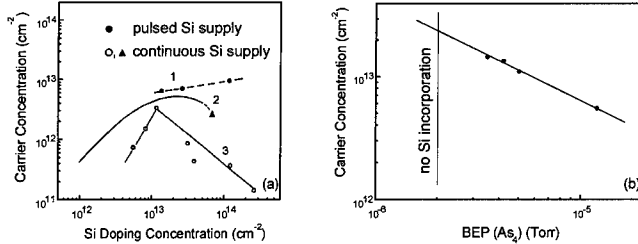


Fig. 1. Sheet carrier concentration vs. Si sheet doping concentration (a) and vs. As_4 pressure during GaAs overgrowth (b) for pulsed δ -doping at 590°C on vicinal GaAs(001)2° and overgrowth at 540°C - curve 1. Curve 2 [4] refers to δ -doping with continuous Si supply at 590°C (control experiment represented by triangle) and curve 3 [5] to conventional δ -doping on the singular surface. Si concentration in (b) $1.4 \times 10^{14} \text{ cm}^{-2}$.

asymmetric third-order streaks due to (3×2) domains [6] until symmetric third-order streaks due to an ordered (3×2) structure appear. In the present case the (3×2) symmetry is maintained up to 1.2 ML Si. Using the difference function approach between RD spectra of Si-covered and bare surfaces we have found that differently terminated surfaces of the same symmetry exist [7]. The δ RD spectrum for 0.3 ML Si (Fig. 3a) is characterized by a negative shoulder at 2 eV due to Ga dimers [8] and a minimum at 4 eV. Comparison with the RD spectrum from vicinal Si(001)(2×1) [9] allows to identify the latter as optical anisotropy due to Si dimers on the $(3\times 2)\alpha$ surface (Fig. 4c). The δ RD spectrum for 0.7 ML Si (Fig. 3b) is dominated by a minimum at 4.3 eV combined with a maximum at 3.7 eV. Comparison with the RD spectrum for As-terminated Si(001):As(1×2) [10] reveals that the 4.3 eV feature is an As dimer related transition. The $(3\times 2)\beta$ structure is thus terminated by As dimers (Fig. 4d).

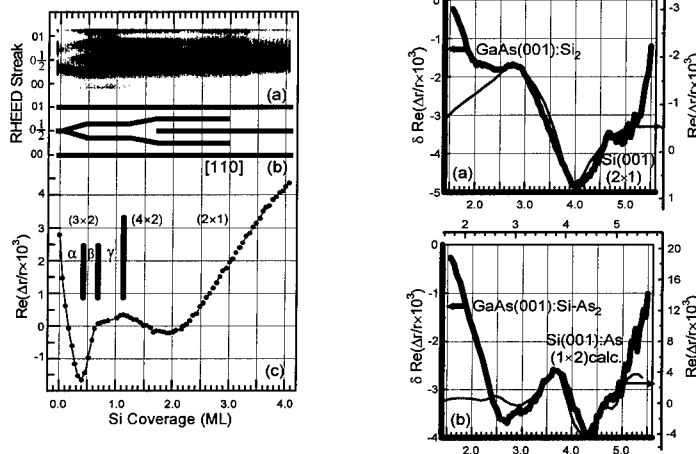


Fig.2. RHEED-intensity linescan plot (a,b), and 3.8 eV RDS transient (c) vs. Si coverage. The RHEED plot includes the fractional order spots between the 00 and 01 streaks. GaAs(001)2°, 590°C , pulsed Si supply, 1×10^{-6} Torr As_4 .

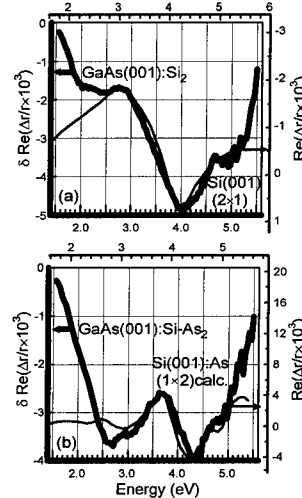


Fig.3. δ RD spectra (thick lines) for (a) 0.3 and (b) 0.7 ML Si and their comparison with the RD spectrum (thin line) for Si(001)(2×1) [9] and Si(001):As(1×2) [10], respectively.

These findings lead to the Si incorporation model depicted in Fig. 4b,c,d for deposition on GaAs(001) with a $(2\times 4)\alpha$ structure which is characterized by a complete Ga plane in the second layer [11]. The existence of Si dimers already in early incorporation stages is evident from the clear 4 eV feature in 8RD spectra for 0.02 ML Si, the lowest coverage measured. During Si incorporation on top of As, the As atoms marked by a cross undimerize and rearrange themselves, thereby bridging the trench and creating new adsorption sites for Si. The exposed Ga atoms dimerize if neighboured. In the ideal case, after deposition of 1/3 ML Si this process results in the $(3\times 2)\alpha$ structure which is highly anisotropic since the bond directions of the Si dimers and of the Ga dimers as well as the missing atom rows are all aligned along [110]. Above 0.3 ML the combined incorporation of Si and As atoms leads to the $(3\times 2)\beta$ structure with As-dimer rows on top of Si in the second layer. In the ideal case, this structure is completed with 2/3 ML Si deposition. Since the As-dimer bonds are now perpendicular to the missing atom rows, the optical anisotropy is reduced.

The change in anisotropy at the $(3\times 2)\alpha$ to $(3\times 2)\beta$ transition is reflected as sharp minimum in the RDS transient recorded at 3.8 eV (Fig. 2c). The coverage required for this minimum provides a quantitative measure for the number of available Si incorporation sites. As the 3.8 eV RDS transients for continuous Si deposition on singular and vicinal surfaces with 1° and 2° misorientation of Fig. 5a show, the misorientation has a strong influence on the incorporation. The first minimum in the transients, due to completion of the $(3\times 2)\alpha$ structure, is shifted from 0.7 ML for the singular to 0.35 ML for the 2° misoriented surface. The stability range of the considered GaAs(001) $(2\times 4)\alpha$ structure is narrow, this structure is probably not an equilibrium phase [11]. The usually observed (2×4) reconstruction on the singular surface corresponds to the $\beta 2$ structure with two As dimers per unit mesh in the topmost layer, a missing Ga row in the second layer and an additional As dimer in the third layer [12]. The unoccupied Ga sites in the trenches provide incorporation sites for 0.25 ML Si. As shown in an STM study [13] for the same deposition parameters, the Si indeed preferentially occupies these vacant second layer Ga sites, and adjacent Si atoms are eventually covered with As, bridging the missing dimer trenches. Thus the combined filling of the trenches and the completion of the $(3\times 2)\alpha$

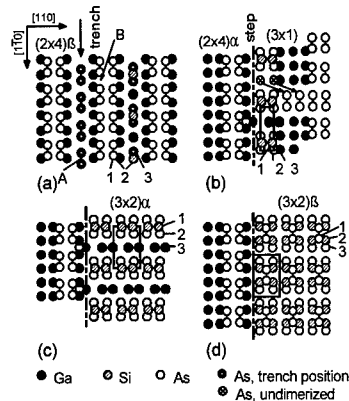


Fig. 4. Surface configurations during Si incorporation (a) in trenches of the $(2\times 4)\beta 2$ structure and (b) on top layer As dimers of the $(2\times 4)\alpha$ structure; (c) fully developed $(3\times 2)\alpha$ and (d) fully developed $(3\times 2)\beta$ structure.

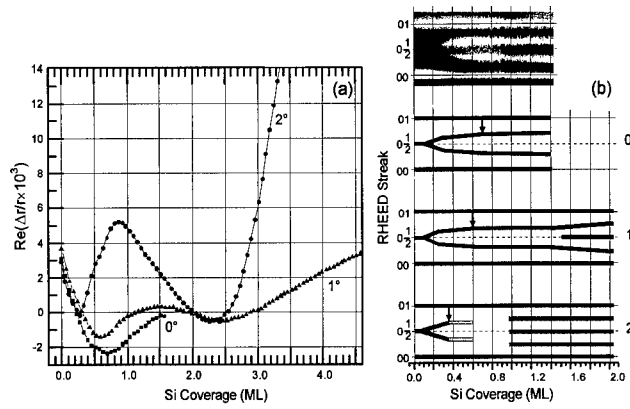


Fig. 5. 3.8 eV RDS transients (a) and RHEED-intensity linescan plots (b) for continuous Si deposition on GaAs(001) with different misorientation toward $(111)Ga$; 5×10^{10} Si cm $^{-2}$ s $^{-1}$, 560°C, 2×10^{-6} Torr As $_4$.

structure (Fig. 4a,c) requires the deposition of (1/4+1/3) ML Si. This value agrees well with the first minimum in the RDS transient for the singular surface. The minimum is shifted to a lower coverage for 1° misorientation and reaches 1/3 ML for 2° misorientation as expected for a (2×4) α -reconstructed surface. Obviously the misorientation steps stabilize this structure. The RHEED recordings (Fig. 5b) confirm the conclusion that with increasing misorientation the completion of the (3 × 2) α structure is shifted to lower Si coverages. Simultaneously the ordering of the structures increases with the misorientation. Whereas for the singular surface, in principle, over the whole coverage range only asymmetric fractional-order streaks are developed, for the 2° misoriented surface the fractional-order streaks become completely symmetric above 0.35 ML. This suggests a higher degree of ordering also at lower coverages and thus the preferred nucleation along the step edges.

The main difference between δ -doping at conventional conditions and at high adatom mobility on a vicinal surface is that in the first case Si is randomly incorporated on Ga sites in trenches of the (2×4) reconstructed surface, whereas in the latter case these sites are not available. This and ordering phenomena at high adatom mobility explain the increase of carrier concentration saturation by shifting the onset of Si cluster formation (with Si on Ga as well as on As sites) to higher concentrations.

3.3. Overgrowth and segregation

The sheet carrier density increases when the As₄ pressure during GaAs overgrowth is reduced (Fig. 1b). It drops, however, dramatically when the surface becomes (4×2) reconstructed. The underlying Si segregation process can be monitored by recording the specular beam RHEED intensity which is inversely proportional to the Si induced kink density in the As-dimer rows [3]. First real-time RDS experiments revealed that during Si segregation on the surface besides As dimers also Ga dimers exist.

4. Conclusions

Using RHEED and RDS for a detailed analysis of atomic processes during incorporation of Si atoms on GaAs(001) we have shown that in dependence on the misorientation and structure of the initial GaAs(001) surface the Si-induced reconstructions nucleate at randomly distributed sites or highly ordered at step induced sites. These subtle differences in the incorporation kinetics provide a direct explanation for the different findings of the maximum sheet electron concentration in Si-delta-doped GaAs reported in the literature. The ordered incorporation of dopants on lattice sites under strict MBE growth control allows to push the upper limit of the sheet carrier density in GaAs well above 10¹³ cm⁻².

References

- [1] Zrenner A, Koch F, Williams R L, Stradling R A, Ploog K and Weimann G 1988 *Semicond. Sci. Technol.* **3** 1203-9
- [2] Peng Z and Horikoshi Y 1996 *Jpn. J. Appl. Phys.* **35** L1151-4
- [3] Däweritz L et al. 1996 *phys. stat. sol. (b)* **194** 127-44
- [4] Köhler K, Ganser P and Maier M 1993 *J. Crystal Growth* **127** 720-3
- [5] Ashwin M J, Fahy M, Harris J J, Newman R C, Sansom D A and Addinal R 1993 *J. Appl. Phys.* **73** 633-9
- [6] Fahy M R, Ashwin M J, Harris J J, Newman R C and Joyce B A 1992 *Appl. Phys. Lett.* **61** 1805-7
- [7] Däweritz L, Schützendorf P, Reiche M and Ploog K H 1997 *Surf. Sci.* **385** L917-21
- [8] Kamiya I, Aspnes D E, Florez L T and Harbison J P 1992 *Phys. Rev. B* **46** 15894-904
- [9] Yasuda T, Mantese L, Rossow U and Aspnes D E 1995 *Phys. Rev. Lett.* **74** 3431-4
- [10] Kipp L, Biegelsen D K, Northrup J E, Swartz L-E and Bringans R D 1996 *Phys. Rev. Lett.* **76** 2810-3
- [11] Northrup J E and Froyen S 1994 *Phys. Rev. B* **50** 2015-8
- [12] Garreau Y, Sauvage-Simkin M, Jedrecy N, Pinchaux R and Veron M B 1996 *Phys. Rev. B* **54** 17638-46
- [13] Avery A R, Sudijono J L, Jones T S and Joyce B A 1995 *Surf. Sci.* **340** 57-70

Low temperature growth and characterization of silicon delta doped GaInP/GaInAs/GaAs pseudomorphic heterostructures for use in high electron mobility transistors

J.A. Smart, E.M. Chumbes, L.F. Eastman, and J. R. Shealy

Cornell University OMVPE Facility, 20 Thornwood Drive, Ithaca New York 14850, USA

Abstract: Flow Modulation Organometallic Vapor Phase Epitaxy (OMVPE) was used to synthesize selectively doped GaInP/GaInAs/GaAs pseudomorphic heterostructures. Transport properties of the two dimensional electron gas (2DEG) were optimized with various buffer formation schemes, techniques for single sided doping, and the channel and spacer layer thicknesses. GaAs buffers were deposited at 550°C and 635°C, while GaInP layers were grown at 550°C to promote atomic disordering. Achieving high 2DEG densities involved incorporating several delta doping supply layers separated by thin GaInP regions. Mobilities as high as $5100 \text{ cm}^2 \text{ volt}^{-1} \text{ sec}^{-1}$ with associated 2DEG densities of $2.6 \times 10^{12} \text{ cm}^{-2}$ were obtained at room temperature. Effects of vicinal substrates on mobilities was determined with conduction paths parallel and perpendicular to steps seen in AFM images. Finally, RF results are presented on devices with $0.25\mu\text{m} \times 100\mu\text{m}$ gate geometry.

1. Introduction

High electron mobility transistors (HEMTs) are very promising devices for high speed digital circuits [1] and low-noise amplifiers [2]. Electron confinement with $\text{Ga}_x\text{In}_{1-x}\text{P}$ produces lower channel sheet resistance compared to the conventional $\text{Al}_x\text{Ga}_{1-x}\text{As}$ barrier material. Advantages of GaInP include a smaller donor binding energy, the lack of electronically active donor related deep levels (*DX-centers*), and oxidation problems associated with the AlGaAs alloy. Disordered GaInP barriers latticed matched to GaAs also provide larger conduction band offsets compared to $\text{Al}_{0.22}\text{Ga}_{0.78}\text{As}$ (250 to 180meV). Even greater conduction band offsets are possible with pseudomorphic $\text{Ga}_{0.65}\text{In}_{0.35}\text{P}$ barriers (380meV), increasing the 2DEG density in the channel [3]. Simultaneously solving Poisson and Schrödinger's equations using C-band code [4] predicts a 2DEG density of $2.4 \times 10^{12} \text{ cm}^{-2}$ in the n=1 state of the $\text{Ga}_{0.65}\text{In}_{0.35}\text{As}$ channel. In the past, attempts to achieve this density involved decreasing the growth rate of the supply layer, doping of the channel [5], or adding aluminum to the barrier material [6]. Our initial efforts on a continuously doped supply layer grown at a reduced rate of 17Å/min produced a 2DEG density of only $3.4 \times 10^{11} \text{ cm}^{-2}$. Single sided delta doping with undoped channels was used to obtain the required electron concentration. We have optimized growth parameters of the GaAs buffers, GaInAs channel, GaInP spacer, and delta doped supply layers.

2. Experimental Procedure

Layers were grown at 550°C in a vertical barrel OMVPE reactor held at 76 torr using the precursors, triethylgallium (TEG), trimethylindium (TMI), arsine, and phosphine [7]. For the supply layer doping, silane diluted 200ppm in hydrogen was used at $0.67\mu\text{moles}/\text{min}$. GaAs buffer layers consisted of an initial 6000Å deposited at 100Å/min followed by 500Å at 35Å/min. The growth rate for $\text{Ga}_{0.65}\text{In}_{0.35}\text{As}$ and $\text{Ga}_{0.65}\text{In}_{0.35}\text{P}$ were 95Å/min and 70Å/min, respectively. The complete HEMT structure is shown in Figure 1a. The 2DEG resides in 75 Å thick GaInAs quantum well channel separated from the delta doped supply layer by an undoped 45Å thick GaInP spacer. Details of the multiple delta doped regions

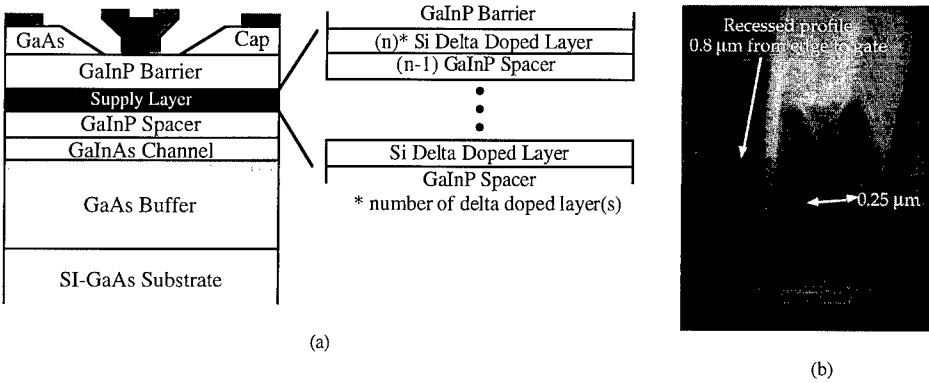


Figure 1. HEMT structure, (a) is a schematic of the structure with detail on the delta doping scheme employed, (b) is a SEM micrograph of an end view of a $0.25\mu\text{m} \times 100\mu\text{m}$ gate with source drain separation of $5\mu\text{m}$.

are shown in the inset for clarity. On top of the delta doped region, an additional layer (160 Å thick) of undoped GaInP was used under the Schottky gate while a 250 Å n+ GaAs layer is used for the ohmic source/drain contacts.

Devices were fabricated using a three-level process which required both optical and e-beam lithography. Isolation mesa's of 1000\AA were defined using a non-selective acetic acid based etchant, while ohmic contacts for the source and drain incorporated a Ni/Au/Ge/Au metallization. Recessed gate structures with gate lengths of $0.25 \mu\text{m}$ and widths of either $50 \mu\text{m}$, $75 \mu\text{m}$, $100 \mu\text{m}$ or $150 \mu\text{m}$ were written using e-beam lithography. A Ti/Pd/Au metallization was used as the mushroom-shaped Schottky gate contact shown in the SEM image presented in Figure 1b [3].

3. Results and Discussions

Three GaAs buffer designs were investigated motivated by the desire to improve the channel breakdown voltage. It was found that the quality of the 2DEG (mobility and sheet density) was strongly influenced by the growth temperature of the buffer used. Two growth temperatures were investigated: at 635°C, step flow growth was observed on GaAs layers on non-vicinal substrates, producing background carrier concentrations of $5 \times 10^{14} \text{ cm}^{-3}$, while growth at 550°C results in rough surfaces ($\pm 3\text{nm}$) with unintentional electron concentrations as high as $1-2 \times 10^{16} \text{ cm}^{-3}$. The latter buffer significantly degrades device isolation and reduces breakdown voltages. Unfortunately, it is necessary to grow disordered GaInP for large ΔE_c , requiring temperatures $\leq 550^\circ\text{C}$. Exploiting the advantages of a high temperature buffer, the temperature was reduced for the active portion of the HEMT structure. Carrier concentrations derived from CV measurements are shown in Figure 2 for buffers grown entirely at 550°C compared to growing first at 635°C, then at 550°C. To further reduce charge in the GaAs buffer, V/III ratios were lowered. Exploring V/III ratios in the range 1.0 to 10.0, maximum mobility and sheet density were achieved at a V/III of 2.25. Mobility reductions as large as 15% were seen at V/III ratios below 2.25 due to surface roughening. In the range from 2.25 to 10.0, no significant changes were seen in the room temperature transport properties.

The $\text{Ga}_{0.65}\text{In}_{0.35}\text{As}$ pseudomorphic channel was varied from 40\AA to 120\AA , the critical thickness of this layer being 75\AA . A 13% reduction in mobility along with a 21% decrease in sheet density was seen on 40\AA compared to 75\AA channels as a result of weaker carrier confinement. Channels beyond the near optimum critical thickness resulted in a reduction of the mobility by as much as 60 %. The inset of Figure 2 shows the measured 2DEG profile displaying a FWHM of 92\AA which agrees well with the C-band calculated value of 84\AA .

Room temperature mobilities were used to evaluate effects of spacer thickness as seen in Figure 3. The mobility decreases with thinner spacers due to increased ionized impurity scattering while the thicker results in parallel conduction within the supply layer. A spacer of 100Å produced the highest mobility of $5400 \text{ cm}^2 \text{ volt}^{-1} \text{ sec}^{-1}$, but at a less than desired 2DEG density. Maximum channel conductance was obtained at a spacer thickness of 45Å with a mobility of $5100 \text{ cm}^2 \text{ volt}^{-1} \text{ sec}^{-1}$ and the required 2DEG density of $2.6 \times 10^{12} \text{ cm}^{-2}$.

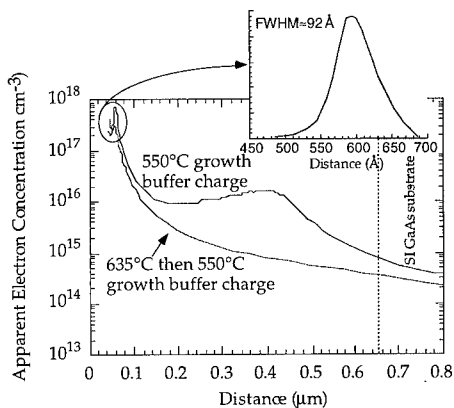


Figure 2. CV derived carrier concentrations for different buffer formation schemes. Inset shows 2DEG profile.

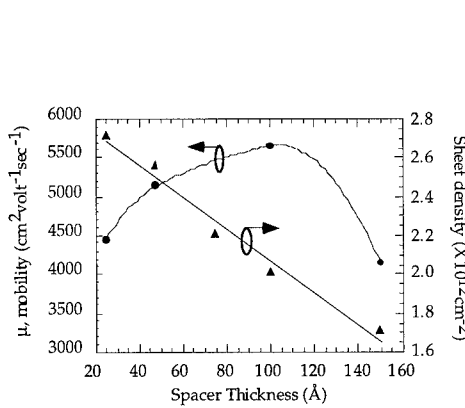


Figure 3. Effects on 300K mobilities and 2DEG densities for variations in spacer layer thickness.

Growth was suspended just after deposition of the channel to determine effects of (100) vicinal surfaces on the growth front. Substrates were either on-axes ($\pm 0.1^\circ$), 3° or 6° miscut surfaces towards the $<111>\text{B}$. Growth on vicinal surfaces is known to promote alloy disordering in GaInP which, in the case of the 3° miscut, produced an enhancement in the carrier confinement as observed in CV profiles (not shown). AFM images for each case are shown in Figure 4. Strain induced steps are seen on the non-vicinal substrate with height of $\leq 30\text{\AA}$. Step bunching is present on the vicinal surfaces in the direction of the miscut with step heights of 120\AA and 200\AA for the 3° and 6° miscut, respectively. It was discovered that the bunching originates in the buffer layers and propagates throughout the structure and results in a reduction of the room temperature mobilities. This measured decrease with increasing degree of miscut is from 5000 , 2670 , and $2100 \text{ cm}^2 \text{ volt}^{-1} \text{ sec}^{-1}$ for on-axis, 3° and 6° samples. Similar mobilities were observed with conduction parallel or perpendicular to the direction of the step bunching.

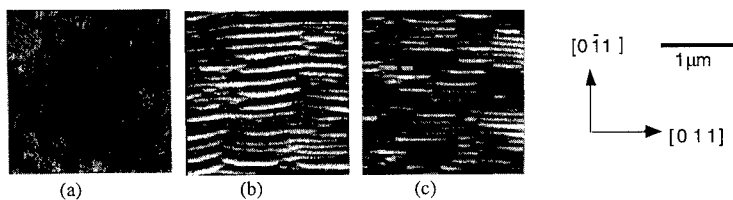


Figure 4. AFM images of the GaInAs channel on (a) 0° , (b) 3° miscut, (c) 6° miscut. Scan areas are $2.5\mu\text{m}^2$

Delta doping was done in the supply layer with varying dopant exposure times from 30sec to 600sec. With silane concentrations of 200ppm, the 2DEG densities saturates at $1.65 \times 10^{12} \text{ cm}^{-2}$ after 600sec. To achieve the higher electron density needed, multiple delta doped layers were incorporated

between thin (2-3 monolayers) GaInP layers as depicted in Figure 1(a). A two minute exposure time was chosen, and up to eight separate layers were deposited. The 2DEG density increased linearly from $3.5 \times 10^{11} \text{ cm}^{-2}$ for one delta doped layer to $2.8 \times 10^{12} \text{ cm}^{-2}$ for eight layers. This high a density could not be reached employing a continuously doped layer of the same thickness.

RF performance is shown in Figure 5 for devices with gate dimensions of $0.25 \mu\text{m} \times 100 \mu\text{m}$. This transistor had low source-drain isolation of roughly $40 \text{ k}\Omega$. Poor isolation is believed to be caused by insufficient etching of the device mesa - parasitic RF conduction occurs in the relatively large pads used to accommodate the co-planar microwave probes. Maximum transconductance of 252 mS/mm was measured. Frequency response gives $f_t = 25.5 \text{ GHz}$ and $f_{max} = 59.5 \text{ GHz}$ compared to state-of-the-art values of $f_t = 67.4 \text{ GHz}$ and $f_{max} = 188.4 \text{ GHz}$ [3]. Other factors influencing the RF performance include the source/drain ohmic contacts ($R_s \sim 1 \Omega \text{ mm}$) due to insufficient silane doping in the GaAs cap.

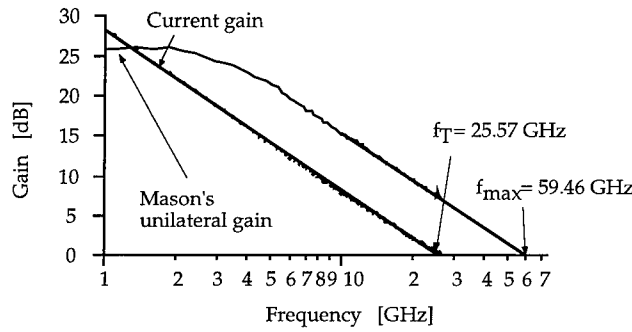


Figure 5. RF response from HEMT with gate geometry of $0.25 \mu\text{m} \times 100 \mu\text{m}$.

4. Conclusions

HEMT structure utilizing a stress compensated pseudomorphic $\text{Ga}_{0.65}\text{In}_{0.35}\text{P}/\text{Ga}_{0.65}\text{In}_{0.35}\text{As/GaAs}$ heterostructure were studied. GaAs buffer layer formation required a high temperature (635°C) growth segment and at a reduced V/III ratio of 2.25 to minimize unintentional charge detrimental to device performance and isolate the electron traps in the Si substrate. Channel and spacer layer thicknesses were optimized at 72 \AA and 45 \AA respectively. Single sided delta doping was successfully implemented using up to eight planar doping layers separated by 2-3 monolayers of GaInP within the supply layer. This provided the needed 2DEG density of $2.6 \times 10^{12} \text{ cm}^{-2}$ with associated mobility of $5100 \text{ cm}^2 \text{ volt}^{-1} \text{ sec}^{-1}$. RF performance on transistors ($0.25 \mu\text{m}$ gate length) with an unoptimized process yielded an $f_t = 25.5 \text{ GHz}$ and $f_{max} = 59.5 \text{ GHz}$.

References

- [1] Abe M, Mimura T, Kobayashi N, Suzuki M, Kosugi M, Nakayama M, Odani K, and Hanyu I 1989 *IEEE Trans. Electron Devices* 36, 2021.
- [2] Asai S, Joshi K, Hirachi Y, and Abe M 1987 *IEEE MTT-S Digest* 1019.
- [3] Pereiaslavets B, Bachem K H, Braunstein J, and Eastman L, 1996 *IEEE Trans. Electron Devices* 43 1659.
- [4] C-band is a one-dimensional charge-control simulator written by M. C. Foisy at Cornell University in 1989
- [5] Geiger D, Mittermeier E, Dickman J, Geng C, Winterhof R, Scholz F, and Kohn E 1995 *IEEE Electron Device Lett.* 16 259.
- [6] Bachem K H, Fekete D, Pletschen W, Rothmund W, and Winkler K *Journ. Cryst. Growth* 1992 124 817.
- [7] Pitts B L, Matragrano M J, Emerson D T, Sun B, Ast D T, and Shealy J R *Inst. Phys. Conf.* 1993 136 619

Optimization of group V switching times for InGaP/GaAs heterostructures grown by LP-MOCVD

**Q. Yang, Q. J. Hartmann, A. P. Curtis, C. Lin*, D. A. Ahmari, D. Scott,
H. C. Kuo, H. Chen and G. E. Stillman**

Department of Electrical and Computer Engineering, University of Illinois, Urbana,
IL 61801-2355

* Department of Materials Science and Engineering, Materials Research Laboratory,
University of Illinois, Urbana, IL 61801

Abstract. We studied the effect of group V switching times on the formation of interfacial layers in InGaP/GaAs heterostructures grown by LP-MOCVD using low temperature photoluminescence (PL), double crystal x-ray diffraction (DCXRD) and high resolution transmission electron microscopy (HR-TEM). Due to the severe substitution process of P by As, the quality of InGaP-to-GaAs interface was very sensitive to switching times. By optimizing the switching conditions, we were able to minimize the interfacial layers to one monolayer (ML) of $In_{0.5}Ga_{0.5}As$ at the GaAs-to-InGaP interface and 1 ML of $In_{0.65}Ga_{0.15}P_{0.15}As_{0.85}$ at the InGaP-to-GaAs interface. Heterojunction bipolar transistors (HBTs) grown using this switching scheme showed excellent etch selectivity as well as dc characteristics.

1. Introduction

InGaP lattice matched to GaAs has been intensively studied recently due to its wide range of device applications [1-4]. The InGaP/GaAs material system is a particularly good candidate for high speed HBTs because of its superior band alignment and high chemical etching selectivity compared to AlGaAs/GaAs[5]. For InGaP/GaAs HBTs, it is especially important to have an abrupt interface at the emitter-base junction to reduce recombination in the space-charge region at the emitter/base interface. It is also important for the InGaP-to-GaAs interface from the emitter to the cap layer to be free from quaternary formation. If a thick quaternary layer forms, difficulties in using selective wet chemical etches may be encountered including inability to initiate etching or non-uniform etching.

In this article, we present a study optimizing the switching sequence for lattice matched InGaP/GaAs heterostructures grown by LP-MOCVD. The optimum switching is determined through both optical (low temperature PL) and structural (DCXRD rocking curve and HR-TEM) characterization techniques.

2. Experiment

All of the InGaP/GaAs heterostructures used in this switching study were grown in an Emcore vertical flow MOCVD reactor. The chamber pressure was kept at 76 Torr. The thermal couple temperature was 600°C. TMGa and TMIn were used as group III precursors and pure AsH₃, and PH₃ were used as group V precursors. These samples were grown on 2° misoriented GaAs substrates with a V/III ratio of 145. The growth rates for InGaP and GaAs were kept constant at 3 μm/h and 1.8 μm/h respectively.

The general switching sequence used in the experiment is shown in Fig 1. After switching off the group III precursors, an AsH₃ overpressure is maintained for t_1 seconds. PH₃ is then introduced for t_2 seconds before the group III precursors are introduced. A similar scheme is used for the InGaP-to-GaAs interface.

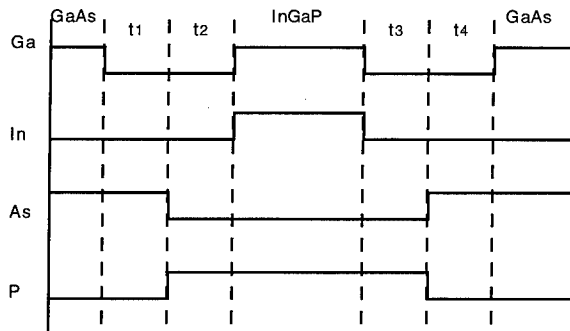


Figure 1. Switching sequence of InGaP/GaAs heterostructure grown by LP-MOCVD.

Single heterostructures of GaAs-to-InGaP with a 1000 Å GaAs buffer and 3000 Å InGaP were grown to characterize interface abruptness using low temperature PL when varying t_1 and t_2 . Similar structures with a 1 μm InGaP buffer and 3000 Å GaAs were grown to study the effect of switching times on InGaP-to-GaAs interface by optical investigation. Quantum well structures were also grown for DCXRD measurements. The structures consisted of a 3000 Å InGaP buffer and 30 periods of 250 Å InGaP barriers and 80 Å GaAs wells. The switching times were optimized individually by varying one and keeping the rest constant. HR-TEM lattice images were taken with optimized and non-optimized switching schemes in order to directly examine the extent of the interfacial layer.

Finally, large area HBTs were fabricated with both optimized and non-optimized switching schemes. DC measurements were performed on these devices to demonstrate the effect of the different switching schemes on device performance.

3. Results and discussion

Four GaAs-to-InGaP samples were grown with t_1 values of 0, 3, 12 and 60 seconds. t_2 was fixed at 3 seconds. Low temperature PL (4 K) was performed on these samples. For each sample, a GaAs excitonic peak at 1.512 eV and a band-to-acceptor peak at 1.49 eV were observed [6]. The intensity of these peaks was used to evaluate the interface quality. For samples with t_1 of 0, 3 and 60 seconds, the intensity for both the excitonic peak and the band-to-acceptor peak was very low. The PL intensity was the highest for t_1 equal to 12 seconds. This indicates the lowest level of non-radiative recombination and thus the most abrupt interface among these samples. Three other sets of samples were grown to study t_2 , t_3 and t_4 using the same method as above. The optimum values for t_1 , t_2 , t_3 and t_4 were determined to be 12, 3, 12 and 0 seconds, respectively. The switching times suggest that a growth pause under AsH₃ (PH₃) overpressure for a GaAs (InGaP) surface is necessary to produce a smooth As (P) terminated surface. In addition, the residual AsH₃ is removed from the chamber when GaAs growth is finished and before initiating InGaP growth. Because the substitution of As by P is not severe at the GaAs-to-InGaP interface PH₃ can be introduced for 3 seconds while removing AsH₃. However, because the substitution of P by As is much more efficient, AsH₃ overpressure should be avoided on P terminated surfaces.

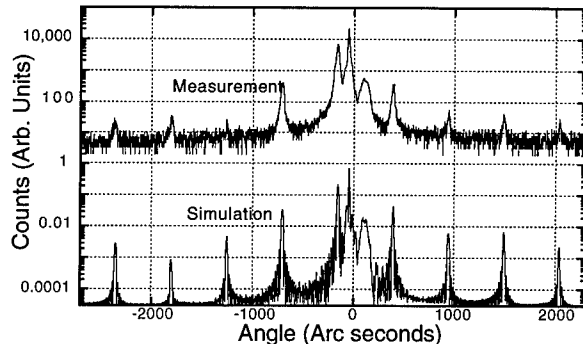


Figure 2. X-ray scan and simulation of a 30 period InGaP/GaAs MQWs with optimized switching condition.

The effects of switching on interface quality were also studied by DCXRD measurements of 30 period InGaP/GaAs superlattices. Each sample had 30 periods of 80 Å GaAs wells and 250 Å barriers. A dynamic simulation was performed on the x-ray data using commercially available software by Bede Scientific to determine the interfacial layer composition and thickness. Figure 2 shows the x-ray rocking curve of the superlattice grown using the optimized switching times. Sharp satellite peaks indicate abrupt interfaces [7]. The broad peak on the right side of the GaAs substrate peak was caused by the presence of the InGaP buffer layer. The simulation suggests that the GaAs-to-InGaP switch results in only 1 ML of $In_{0.5}Ga_{0.5}As$ which is expected at this interface as In and Ga are introduced on an As terminated surface. The ability to model this interfacial layer as a ternary rather than a quaternary layer also indicates the substitution of As by P was negligible. The InGaP-to-GaAs switch results in only 1 ML of $In_{0.65}Ga_{0.35}P_{0.15}As_{0.85}$. This suggests the substitution process of P by As was so fast that most of the P atoms at the surface were instantly replaced by As when it arrived at the surface. The high In concentration also suggests that In has an appreciable memory effect compared to Ga[8].

HR-TEM measurements were conducted on a sample with the optimized switching scheme. In Fig 3, fluctuations on the order of 1 ML are present for the sample. From this we can conclude that by optimizing the switching scheme, 1 ML abruptness can be achieved for both interfaces.

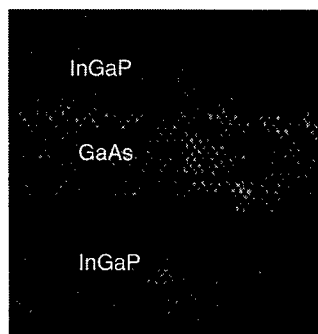


Figure 3. HR-TEM lattice image of a InGaP/GaAs QW with the optimized switching.

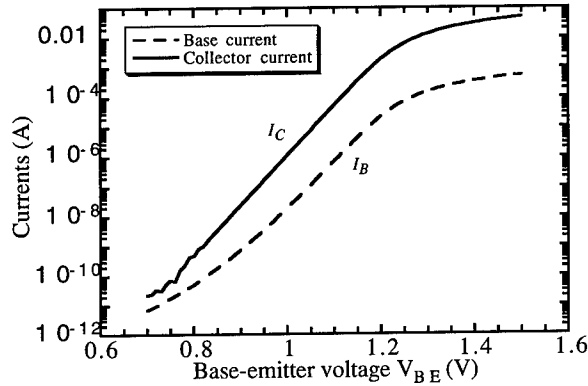


Figure 4 Gummel plot of InGaP/GaAs HBT using optimized switching parameters.

Finally, InGaP/GaAs HBTs were grown with both the optimized switching and a non-optimized switching at the base-emitter junction in order to directly compare the effect of the switching scheme on device performance. The HBT with the optimized switching has a dc current gain, $\beta=82$ at $I_C=1$ mA and a base sheet resistance of $R_{sb}=265 \Omega/\text{sq}$. The HBT with non-optimized switching at the base-emitter junction has a $\beta=62$ at $I_C=1$ mA and $R_{sb}=280 \Omega/\text{sq}$. The ideality factor improved from 1.12 to 1.08 by optimizing the switching at the base-emitter junction.

4. Conclusion

The switching times for growing InGaP/GaAs heterostructures were optimized by 4 K PL study of single interface structures and verified with HR-TEM and DCXRD measurements of the superlattices grown with the same switching sequences. Single ML interfacial layers were obtained at both GaAs-to-InGaP and InGaP-to-GaAs interfaces. InGaP/GaAs HBTs were grown using the optimized switching scheme. Excellent selective chemical etching was obtained at both the base-emitter junction and the emitter-cap interface. Optimized switching at the base-emitter junction significantly improves the current gain.

References

- [1] A. W. Hanson, S. A. Stockman and G. E. Stillman Electron Dev. Lett. **14**, 25 (1993).
- [2] M. Ishikawa, Y. Ohba, H. Sugawara, M. Yamamoto and T. Nakanisi Appl. Phys. Lett. **48**, 207 (1986).
- [3] J. M. Olson, S. R. Kurtz, A. E. Kibbler and P. Faine Appl. Phys. Lett. **56**, 623 (1990).
- [4] B. Pereiaslavets, G. H. Martin, L. F. Eastman, R. W. Yanka, J. M. Ballingall, Braunstein, K. H. Bachen and B. K. Ridley IEEE Trans. Electron. Dev. **44**, 1341 (1997).
- [5] H. Kroemer J. Vac. Sci. Technol. B, **1**, 126 (1983).
- [6] B. J. Skromme, T. S. Low, and G. E. Stillman Proceeding of Int. Symp. GaAs and Related compounds, Albuquerque, NM, 1982.
- [7] C. Ferrari and P. Franzosi J. Appl. Phys. **65**, 1544 (1989).
- [8] X. He and M. Razeghi Appl. Phys. Lett. **61**, 1703 (1992)

Solid Source Molecular Beam Epitaxy of $\text{Ga}_x\text{In}_{1-x}\text{As}_y\text{P}_{1-y}$ Materials for $1.3 \mu\text{m}$ Lasers

J. N. Baillargeon, W.-Y. Hwang, S. N. G. Chu, and A. Y. Cho

Bell Laboratories, Lucent Technologies, 600 Mountain Avenue, Murray Hill, NJ 07974

Abstract. Growth of lattice matched 1.12Q and 1.3Q $\text{Ga}_x\text{In}_{1-x}\text{As}_y\text{P}_{1-y}$ was performed with all solid source molecular beam epitaxy. Different P and As valved cracking cell designs were investigated to enhance photoluminescence (PL) emission uniformity. With appropriately constructed cells, the variation in the PL emission wavelength across a two inch diameter wafer could be made as small as $\sim 1\%$ at $1.3 \mu\text{m}$ and 0.6% at $1.12 \mu\text{m}$. Multi-quantum well laser diodes fabricated with strained wells and lattice matched barriers show a transparency current density as low as 71 A/cm^2 per well and greater than 0.5 W/A efficiencies.

1. Introduction

All solid source molecular beam epitaxy (MBE) is a safe, high precision growth technique. Until just a few years ago growth of III-V compounds and devices by MBE, exclusively with all solid sources, was limited to the arsenides and antimonides. Reproducible growth of quaternary compounds containing phosphorus was not possible without use of hydrides or metalorganic sources, even though polycrystalline InP and GaP sources were capable of supplying phosphorus vapor.¹ Red phosphorus could not be utilized because the derived beam flux was highly unstable, even though it had been used successfully for growth of red-emitting AlGaInP laser diodes.² The beam flux instability was a consequence of a seemingly random red to white phosphorus phase transformation. The three temperature zone valved phosphorus cell, recently developed, permits amorphous red phosphorus to be used as a starting source. More specifically, *in-situ* generation of high vapor pressure α -white phosphorus from amorphous red phosphorus allows the production of an ultra-stable P_2 beam flux.³ Subsequently, reproducible stoichiometric growth of $\text{Ga}_x\text{In}_{1-x}\text{As}_y\text{P}_{1-y}$ layers and heterojunction devices is now possible with all solid sources, provided both As and P valved cracking cells are employed. High electron mobility transistors,⁴ heterojunction bipolar transistors,⁵ Fabry-Perot lasers⁶⁻⁹ and distributed feedback laser diodes¹⁰ have all been demonstrated using valved arsenic and phosphorus sources. As solid source valved cracker cell technology continues to mature, it will become increasingly relevant to MBE electronic and photonic device production.

2. Experimental

Uniformity is of prime importance to the manufacture of devices. Different As and P valved cell designs were studied for the purpose of improving the emission wavelength uniformity. Spatially uniform beam fluxes are the most important requisite for achieving good composition uniformity. Particular attention was paid to the construction of the cracking head section of each valved cell. Minimization of the beam flux transient is essential for obtaining proper multi-quantum well (MQW) device performance, but at least with respect to phosphorus, this must not be realized at the expense of cracking efficiency.

Modification of the cracking portion of the cells required changes to the flux control valve and/or heater geometry. For the arsenic cell, this entailed retracting the control valve so that it was contained entirely within the heated region, the addition of a small amount of baffling, and a diffuser at the end of the cracking tube. This is the VC-IV As cell, which is an altered VC-III. Modifications to the phosphorus cell cracker section included changing the in-line heater to a radial heater, adding 400 cm² of a non-baffling Ta surface and end diffuser. The phosphorus valve was also modified to increase its conductance. More specific design details will be given elsewhere.

Of interest here is the uniformity of quaternary material near 1.12 μm (1.12Q), used for separate confinement (SCH) and barrier layers, and 1.3 μm, the QW emission wavelength. The growth system used was a Riber 2300 with 2 inch capability. Column III sources were supplied via standard effusion cells. The column V fluxes were extracted from standard and modified Riber KPC series phosphorus, and Riber VAC series and EPI VC series arsenic valved cells. Quaternary layer growth was performed at 500 °C on (100) n-type InP, for both PL emission uniformity experiments and MQW laser structures. InP buffer and cladding layers were grown at 470 °C. Temperature was measured with an optical pyrometer and the values quoted are relative to a measured InP oxide desorption temperature of 490 °C. MQW lasers were grown by fixing the P flux and modulating the As flux during SCH, barrier and QW layer growth. Growth interrupt times of 12s were used at the SCH, QW and barrier interfaces to allow for stabilization of the As beam. Both n- and p- type dopant levels were held constant at 1 × 10¹⁸ cm⁻³ within the confinement regions of the laser, using Si and Be sources, respectively.

3. Results

The PL emission wavelength uniformity as a function wafer position, for three separate lattice matched quaternary layer growths (on InP), are shown in Fig. 1. Each layer is 0.8 μm thick. Curve I was obtained using standard (unmodified) KPC40 and VC-III cell combination. The variation in wavelength is 56 nm (~4%). A maximum wavelength variation, shown by Curve II, of 19 nm was obtained with

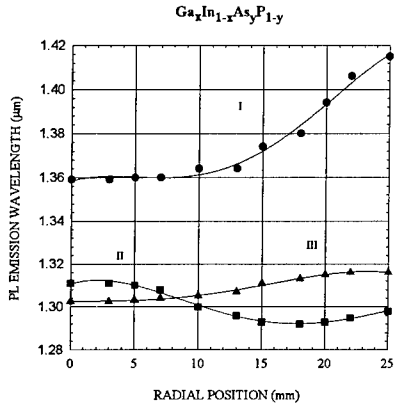


Fig. 1 PL wavelength as a function of wafer position for lattice matched layers obtained with three different As and P valved cell design combinations. The best uniformity achieved was 14.5 nm, ~1%.

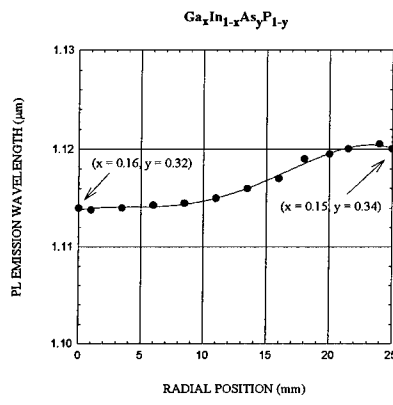


Fig. 2 PL emission wavelength as a function of wafer position for typical lattice matched SCH and barrier layer material. The uniformity is 6.5 nm, 0.6%.

unmodified KPC250 and Riber VAC500 combination. Curve III, having a best wavelength uniformity of 14.5 nm, or ~1%, was achieved with modified KPC250 and VC-IV cells. Shown, in Fig. 2, is the emission uniformity for typical SCH and barrier layer material, also grown with the modified KPC250/VC-IV combination. The wavelength uniformity here is 0.6%, or 6.5 nm. The variation in the As/P mole fraction indicated in the figure is believed due almost entirely to the variation in the In/Ga mole fraction. The relative abundance of In and Ga adatoms strongly influences the As and P incorporation rates.¹¹ Equally important, the run-to-run wavelength variation for the quaternary improved slightly, from 13 nm to 10 nm.

Epitaxial quaternary material can exhibit strong phase separation within the region bounded by 1.25 μm and 1.36 μm . The degree of spinodal decomposition occurring as the layer grows is intrinsically dependent upon growth temperature. In general, quaternary material tends to phase separate into GaP and InAs rich regions on the growth surface, which incorporate into the layer. The resultant spatial segregation induces non-uniform biaxial strain and energy shift to the band gap. This is a particularly important consideration when $\text{Ga}_x\text{In}_{1-x}\text{As}_y\text{P}_{1-y}$ is used for QW material. With respect to structural integrity, spinodal decomposition can impart a roughening to the QW-barrier interfaces. In the case of a MQW laser diode, rough interfaces will degrade device performance, primarily by increasing the internal losses of the structure. Higher growth temperatures produce layers with a smaller degree of phase separation, improved morphology, reduced PL spectral widths, higher PL intensities and less shift to the band edge emission. For these reasons, SCH, barrier and QW layers are grown between 500 - 510°C, rather than at 470 °C along with the InP cladding material.

Threshold current density data as a function of inverse cavity length for lasers with different well strain, -0.5% (tensile) and 0.73% (compressive), are shown in Fig. 3. Individual data points represent an average of three devices. The structure has nine-QWs and was designed for 1.3 μm fiber-to-the-home application. For both lasers, the n-type InP cladding layer thicknesses are 0.6 μm , the p-type InP cladding layers are 1.4 μm . Barrier and SCH region thicknesses are 100 Å and 550 Å per side $\text{Ga}_{0.14}\text{In}_{0.86}\text{As}_{0.32}\text{P}_{0.68}$, respectively. Barriers, SCH and QWs are unintentionally undoped. The

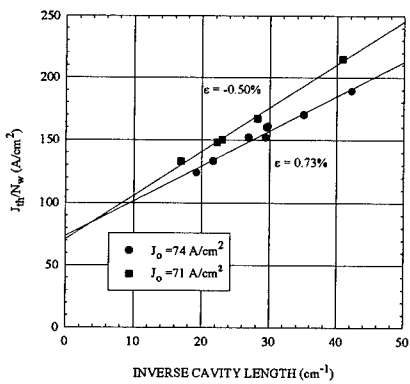


Fig. 3 Average threshold current density as a function of inverse cavity length for lasers with -0.5% and 0.73% well strain. The transparency current density is 71 and 74 A/cm^2 , respectively

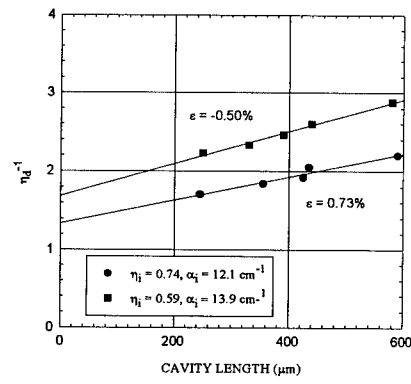


Fig. 4 Inverse differential quantum efficiency as a function of cavity length for lasers with -0.5% and 0.73% well strain. Internal losses and quantum efficiency are provided.

entire structure was grown with a fixed P beam equivalent pressure (BEP) of 8.3×10^{-6} Torr. During growth of the active region, the As BEP was modulated between 1.4×10^{-6} Torr (for barriers and SCH regions) and 5.4×10^{-6} Torr (0.73%, 75Å - $\text{Ga}_{0.24}\text{In}_{0.76}\text{As}_{0.72}\text{P}_{0.38}$ wells), or 5.2×10^{-6} Torr (-0.5%, 100Å - $\text{Ga}_{0.26}\text{In}_{0.72}\text{As}_{0.42}\text{P}_{0.58}$ wells). Both structures have nearly the same transparency current density of $\sim 70 \text{ A/cm}^2$ per well, and show similar threshold current dependencies with cavity length. A per well transparency current density as low as 55 A/cm^2 has been obtained for the same structure utilizing 9- lattice matched, $\text{Ga}_{0.26}\text{In}_{0.74}\text{As}_{0.57}\text{P}_{0.43}$ wells. The corresponding differential quantum efficiencies (DQE), shown in Fig. 4, were measured for the laser diodes of Fig. 3. Data points represent an average of three devices. The devices with the highest DQE have compressive strain wells, as expected. Internal losses for that structure are 12 cm^{-1} and the internal quantum efficiency is 74%. For the typical 300 μm cavity device with 9 compressive wells, an average power slope efficiency of 0.53 W/A is realized. The tensile strained well devices show a slightly lower slope efficiency of 0.44 W/A for the same cavity length. These values are state-of-the-art.

References

- [1] A. Y. Cho, M. P. Panish, and Hayashi, *Gallium Arsenide and Related Compounds, Inst. of Physics* **9**, 18 (1970).
- [2] H. Ashi, Y. Kawamura, M. Ikeda, and H. Okamoto, *J. Appl. Phys.* **52**, 2852 (1981).
- [3] J. N. Baillargeon, A. Y. Cho, F. A. Thiel, R. J. Fischer, P. J. Pearah, and K. Y. Cheng, *Appl. Phys. Lett.* **65**, 207 (1994).
- [4] W. E. Hoke, P. J. Lemonias, D. G. Weir, H. Y. Hendriks, L. J. Chou, and K. C. Hsieh, *J. Vac. Sci. Technol.* **B14**, 2233 (1996).
- [5] T. P. Chin, J. C. P. Chang, J. M. Woodall, W. L. Chen, G. I. Haddad, C. Parks, and A. K. Ramdas, *J. Vac. Sci. Technol.* **B13**, 750 (1995).
- [6] J. N. Baillargeon, K. Y. Cheng, and A. Y., Cho, *Proceedings of the 15th North American Conference on Molecular Beam Epitaxy*, September, 1995 (College Park, MD).
- [7] J. N. Baillargeon, K. Y. Cheng, A. Y. Cho, and S.N.G. Chu, *J. Vac. Sci. Technol.* **B14**, 2244 (1996).
- [8] M. Toivonen, P. Savolainen, H. Asonen, and M. Pessa, *J. Crystal. Growth* **175**, 37 (1997).
- [9] F. G. Johnson, O. King, F. Seiferth, S. Horst, D. R. Stone, R. D. Whaley, M. Dagenais, and Y. J. Chen, *J. Crystal Growth* **175**, 46 (1997).
- [10] W.-Y. Hwang, J. N. Baillargeon, S. N. G. Chu, P. Sciortino, and A. Y. Cho, *9th International Conference on Molecular Beam Epitaxy*, September 1996 (Malibu, CA).
- [11] J. N. Baillargeon, A. Y. Cho, and K. Y. Cheng, *J. Appl. Phys.* **79**, 7652 (1996).

Enhanced optical crystal quality of strain-compensated InGaAs/InGaAsP quantum-well structures on GaAs substrates by the introduction of intermediate-strain layers

Kiyohisa Hiramoto, Misuzu Sagawa, Sumiko Fujisaki and Takashi Toyonaka¹
 Central Research Laboratory, ¹Telecommunications Division, Hitachi Ltd.
 1-280, Higashi-koigakubo, Kokubunji-shi, Tokyo 185, Japan

To improve the crystal quality of hetero-interfaces in InGaAs/InGaAsP strain-compensated quantum-well structures on (001) GaAs substrates, we added layers with intermediate levels of strain between the well and barriers. Photoluminescence measurements confirmed that the crystal quality of the hetero-interfaces was improved by adding these intermediate layers. The greatest improvement was attained with an intermediate layer thickness of 4 monolayers and a strain at about the midpoint between that of QWs and barriers. The mean time to failure of fabricated 0.98-μm laser diodes (LDs) with such intermediate-strain layers was found to be about five times longer than that of LDs without the intermediate-strain layer.

1. INTRODUCTION

Strain-compensated (SC) quantum-well (QW) structures have attracted much attention as the active layers of semiconductor laser diodes (LDs) [1-3]. It has been reported that the maximum number of QWs and the maximum strain that QWs can tolerate without misfit dislocation can be increased by strain compensation [3]. This has improved device properties [1-3]. However, strain-compensation has been reported to cause deterioration in the crystal quality of QW structures when the difference between strain in wells and strain in barriers is too large [4]. This is thought to be due to deterioration of crystal quality in the hetero-interfaces of the wells and barriers, caused by the introduction of opposite strains in the barriers and in the wells. In this paper we study the effect of strain compensation on the crystal quality of the hetero-interfaces by using time-resolved photoluminescence (PL) measurement. To improve the crystal quality in the hetero-interfaces of wells and barriers in SC-QW structures, we added layers between the wells and barriers that have intermediate levels of strain (hereafter referred to as intermediate-strain layers), thus reducing the difference in strain at the hetero-interfaces. We used low-temperature (77 K) photoluminescence measurement to investigate the effects of these layers on the crystal quality of the hetero-interfaces. We also fabricated two types of 0.98-μm LDs with a strain-compensated InGaAs/InGaAsP QW active layer, one with intermediate-strain layers and the other without these layers. We examined the effect of intermediate-strain layers on the reliability of the LDs.

2. EXPERIMENT

We grew SC-QW structures consisting of compressive-strain InGaAs wells and InGaAsP barriers on (001) GaAs substrates by using metal-organic vapor phase epitaxy (MOVPE). The growth temperature was 650°C and the growth pressure was 40 torr. Triethylgallium (TEGa), trimethylindium (TMIn), arsine (AsH₃), and phosphine (PH₃) were used as source materials. Low-temperature PL measurements were done at 77 K using the 514.5-nm line of an argon-ion laser. The time-resolved photoluminescence measurements were done at 77 K using 3 ps pulses (output wavelength: 800 nm) produced at a rate of 80 MHz by a Ti:sapphire laser pumped by an argon-ion laser. The lattice mismatch ($\Delta a/a$) between the GaAs substrate and the InGaAsP barrier was measured by X-ray diffraction.

For the PL measurements, a 50-nm-thick GaAs buffer layer, a 200-nm-thick In_{0.48}Ga_{0.52}P layer lattice-matched to the GaAs, an active layer, and an In_{0.48}Ga_{0.52}P layer were grown successively on the GaAs substrates.

Figure 1 shows the SC-QW structure for time-resolved photoluminescence (PL) measurement. Five-nm-thick InGaAsP layers were inserted between the InGaP layers and the active layers to avoid InGaP/GaAs interfaces. The QW was In_{0.2}Ga_{0.8}As layer compressively strained on the GaAs substrate with a lattice-mismatch of about 1.4%. The InGaAs layer was 7-nm thick. Three types of barriers were examined: tensile-strain In_{0.18}Ga_{0.82}As_{0.55}P_{0.45} ($\Delta a/a$: 0.3%) barriers,

tensile-strain In_{0.13}Ga_{0.87}As_{0.55}P_{0.45} ($\Delta a/a$: 0.6%) barriers, and unstrained In_{0.22}Ga_{0.78}As_{0.55}P_{0.45} barriers. The

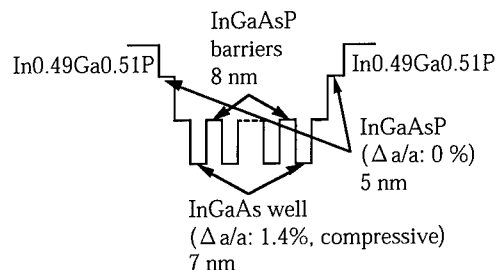


Fig. 1. Schematic diagram of a strain-compensated quantum-well structure; $\Delta a/a$ shows the lattice mismatch between the layers and the GaAs substrate. The vertical direction shows comparative bandgap energies.

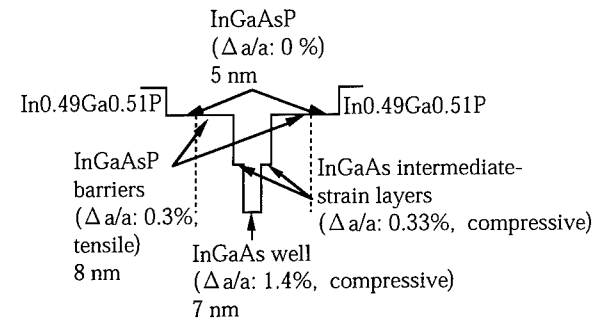


Fig. 2. Schematic structure of a strain-compensated quantum-well structure; $\Delta a/a$ shows the lattice mismatch between the layers and the GaAs substrate. The vertical direction shows comparative bandgap energies.

composition of the barriers was determined by measurements of PL and X-ray diffraction. The barrier thickness was 8 nm. Figure 2 shows the SC-QW structure for low-temperature PL measurements. Five-nm-thick InGaAsP layers were also inserted between the InGaP layers and the active layers. The QW was In_{0.2}Ga_{0.8}As layer compressively strained on the GaAs substrate with a lattice-mismatch of about

1.4%. The InGaAs layer was 7 nm thick. The barriers were tensile-strain In_{0.03}Ga_{0.97}As_{0.78}P_{0.22} ($\Delta a/a$: 0.6%) layers. The barrier thickness was 8 nm. The intermediate-strain layers were InGaAs layers with thicknesses of 0, 2, 4 and 8 monolayers (MLs). The $\Delta a/a$ of these layers was 0.3, 0.45 and 0.6%.

3. RESULTS AND DISCUSSIONS

3.1 time-resolved photoluminescence measurement

Figures 3 (a), (b), and (c) show the dependence of time-resolved PL time decay of the QW structures on the number of QWs: (a) for unstrained In_{0.22}Ga_{0.78}As_{0.55}P_{0.45} barriers, (b) for tensile-strain In_{0.18}Ga_{0.82}As_{0.55}P_{0.45} ($\Delta a/a$: 0.3%) barriers, and (c) for tensile-strain In_{0.13}Ga_{0.87}As_{0.55}P_{0.45} ($\Delta a/a$: 0.6%) barriers. In the case of unstrained barriers (Fig. 3 (a)), there is only one lifetime for SQW and 4QWs. For 7QWs and 10QWs, another fast decay appears. In the case of 7QWs and 10QWs, there was crosshatching on the grown surfaces. This fast decay, then, is related to the crystal defects caused by the stack of strain. In the case of strained barriers (Fig. 3 (b) and (c)), this fast decay appears even for SQW although, because of strain compensation, there was no crosshatching even on the surfaces of 15QWs.

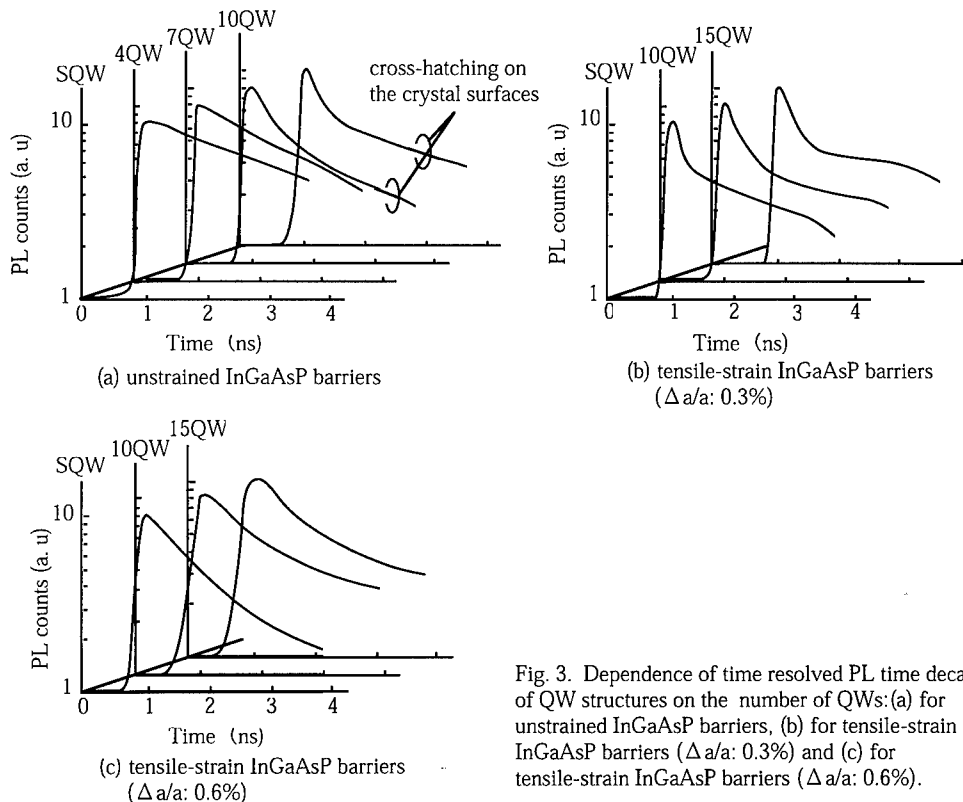


Fig. 3. Dependence of time resolved PL time decay of QW structures on the number of QWs: (a) for unstrained InGaAsP barriers, (b) for tensile-strain InGaAsP barriers ($\Delta a/a$: 0.3%) and (c) for tensile-strain InGaAsP barriers ($\Delta a/a$: 0.6%).

Figure 4 shows the dependence of time-resolved PL time decay on the strain of barriers. As can be seen, time decay for strained barriers is much faster than that for unstrained barriers. This implies that, although it is possible to improve overall crystal quality of strained QW structure by strain compensation, some deterioration in crystal quality will probably occur at the hetero-interfaces.

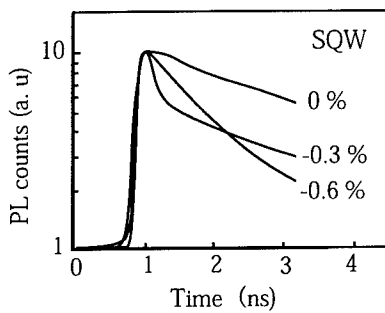


Fig. 4. Dependence of time-resolved PL time decay of SQW structures on the strain of barriers.

3.2 low-temperature (77 K) photoluminescence measurement

Figure 5 shows the dependence of the peak PL intensity of the QW structures on the thickness of the intermediate-strain layers. In this case, the $\Delta a/a$ of the intermediate-strain layers was 0.3%. The PL intensity reached a maximum when the thickness of the intermediate layer

was 2 monolayers (MLs). Figure 6 shows the dependence of the PL full-width at half maximum (FWHM) of the QW structures on the thickness of the intermediate-strain layers. The $\Delta a/a$ of the intermediate-strain layers was 0.3%. The PL FWHM reached a minimum when the thickness was 4 or more MLs. These results show that the crystal quality of the hetero-interfaces of wells and barriers in SC-QW structures is improved by adding intermediate-strain layers. When the thickness of intermediate-strain layers is 8 MLs, the PL intensity is smaller than the PL intensity of 2 or 4 MLs. This is thought to be due to deterioration of crystal quality because of total amount of strain of the stacked layers. The PL

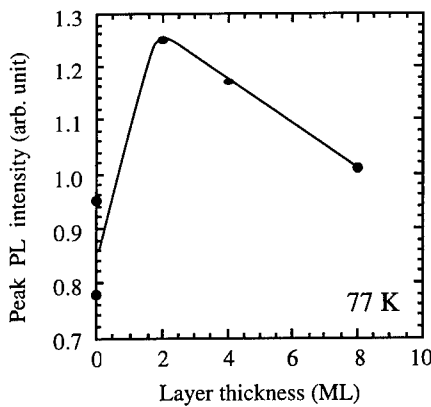


Fig. 5. Dependence of peak PL intensity of strain-compensated quantum-well structures on the layer thickness of intermediate-strain layers (ML: monolayer, 2.83 Å). The $\Delta a/a$ of the intermediate-strain layer was 0.3%.

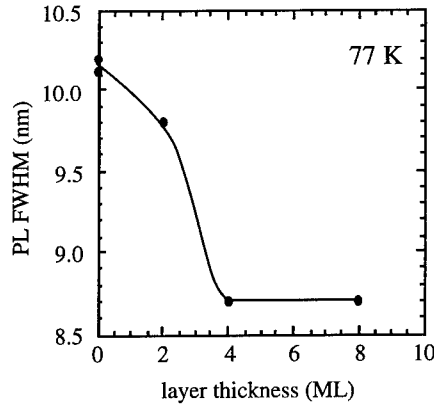


Fig. 6. Dependence of PL full-width at half maximum (FWHM) of strain-compensated quantum-well structures on the thickness of intermediate-strain layers (ML: monolayer, 2.83 Å). The $\Delta a/a$ of the intermediate-strain layer was 0.3%.

FWHM is not small for a thickness of 2 MLs as it is for thicknesses of 4 or 8 MLs. When the thickness is 2 MLs, the uniformity of the intermediate-strain layers is thought to be insufficient. The quality of the hetero-interfaces is best when the thickness of the intermediate layers is 4 MLs.

Figures 7 and 8 shows the dependence of the peak PL intensity and FWHM of the QW structures on the strain of intermediate-strain layers. The values for the QW without intermediate-strain layers are shown by arrows. The thickness of the intermediate-strain layer was fixed to 4MLs. As can be seen in these figures, the peak PL intensity is best and FWHM is smallest when the strain of the intermediate-strain layer is 0.45%. This value is close to the midpoint of the strain of wells and barriers and shows that the crystal quality of the QW structure is best when the difference of strain at the hetero-interfaces is smallest.

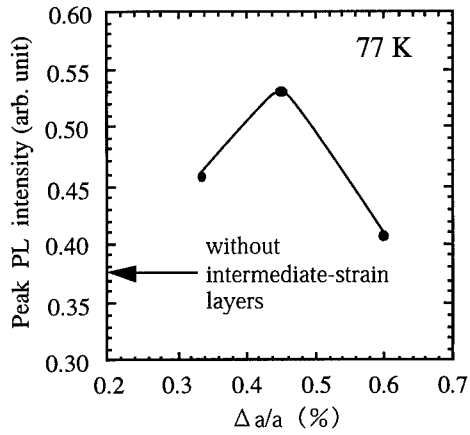


Fig. 7. Dependence of peak PL intensity of strain-compensated quantum-well structures on $\Delta a/a$ of intermediate-strain layers. The thickness of the intermediate-strain layer was 4MLs.

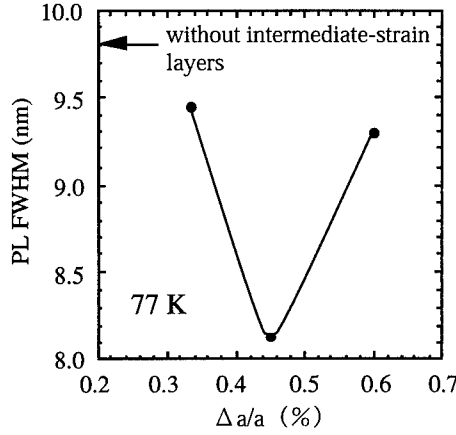


Fig. 8. Dependence of peak PL intensity of strain-compensated quantum-well structures on $\Delta a/a$ of intermediate-strain layers. The thickness of the intermediate-strain layer was 4MLs.

3.3 Reliability of laser diodes

To study the effect of intermediate-strain layers on the reliability of 0.98- μm LDs, we fabricated two types of LDs: one with intermediate-strain layers ($\Delta a/a$: 0.3%, 4 MLs) and the other without intermediate-strain layers. For both structures, the active layers had a single quantum well. The LD structures are described elsewhere [5]. The percentage increase in the drive current at a constant optical-power output of 150 mW of fabricated 0.98- μm LDs with the intermediate-strain layers was about five times smaller than the increase of those without these layers. The mean time to failure (MTTF) of LDs with intermediate-strain layers is thus about five times longer than those without intermediate-strain layers. This improvement in reliability can be attributed to the improvement in crystal quality of hetero-interfaces of SC-QW structures by the introduction of strain-intermediate layers.

4. SUMMARY

Time-resolved PL measurements showed that the PL decay of InGaAs/InGaAsP SC-QW structures is much faster than that of InGaAs/InGaAsP QW structures which have unstrained barriers. This implies that strain compensation may cause the crystal quality of the hetero-interfaces to deteriorate because of the large difference of strain in the barriers and wells. To improve the crystal quality of the hetero-interfaces, we added layers with intermediate levels of strain between the well and barriers. PL measurements confirmed that the crystal quality of the hetero-interfaces was improved by adding these intermediate layers, and the greatest improvement was attained with an intermediate layer thickness of 4 monolayers and the strain of mid-st of that of QWs and barriers. The mean time to failure of fabricated 0.98- μm laser diodes (LDs) with such intermediate-strain layers was found to be about five times longer than that of LDs without the intermediate-strain layer.

REFERENCES

- [1] C. P. Seltzer, S. D. Perrin, M. C. Tatham, and D. M. Cooper: Electron. Lett. 28, No. 1 (1992) 63.
- [2] D. Varga, O. Kjebon, U. Ohlander, K. Streubel, J. Wallin, S. Lourdudoss, T. Klinga, B. Broberg, and G. Landgren: Proceedings of 6th Int. Conf. on InP and. Rel. Mat., Paper WP22 (1994) 473.
- [3] T. Takiguchi, K. Goto, M. Takemi, A. Takemoto, T. Aoyagi, H. Watanabe, Y. Mihashi, S. Takamiya, and S. Mitsui: Proceedings of 7th Int. Conf. on Metalorganic Vapor Phase Epitaxy, Paper P3-6 (1994) 276.
- [4] A. Kasukawa, N. Yokouchi, N. Ymanaka, and N. Iwai: Electron. Lett. 31, No. 20 (1995) 1749.
- [5] M. Sagawa, K. Hiramoto, T. Toyonaka, T. Kikawa, S. Fujisaki, and K. Uomi: IEEE Journal of Selected Topics in Quantum Electronics 3, No. 2 (1997) 666.

1.3 μm Wavelength GaInAsP/InP Distributed Feedback Lasers Grown Directly on Grating Substrates by Solid Source Molecular Beam Epitaxy

W.-Y. Hwang, J. N. Baillargeon, S. N. G. Chu, P. F. Sciortino, and A. Y. Cho

Bell Laboratories, Lucent Technologies, 600 Mountain Ave., Murray Hill, NJ 07974

Abstract. Successful growth of GaInAsP/InP multi-quantum well lasers directly on a distributed feedback (DFB) grating substrate using all solid source molecular beam epitaxy (MBE) was demonstrated. A 500 Å thick 1.12 μm wavelength GaInAsP planarization layer was first grown on the DFB gratings at an elevated temperature to create a smooth surface for subsequent layer growth. Transmission electron micrograph showed smooth interfaces after the growth of this GaInAsP planarization layer. Low threshold current density and high quantum efficiency were obtained from these index-coupled DFB lasers grown by solid source MBE.

1. Introduction

Distributed feedback (DFB) lasers operating at 1.3 and 1.55 μm wavelengths employing GaInAsP/InP materials are crucial components for wide-band single-mode optical fiber communications. This is because of their closely controlled and stable single longitudinal mode operation even at high output power range. Fabrication of a high quality DFB laser structure requires growth on a corrugated crystal surface with precise control of material composition and layer thickness. Although all presently utilized growth techniques can achieve high quality layers on planar surfaces, growth on grated or patterned substrates is far more challenging.¹⁻³ Typically, a DFB laser can be constructed by growing a laser structure directly on a grated substrate or by making gratings on a grown laser structure and followed by a second step overgrowth. When growing a DFB laser structure directly on a grated InP substrate, the growth surface must be mechanically smooth and dislocation free after only a few hundred angstroms of the quaternary is deposited. Metalorganic chemical vapor deposition (MOCVD) is presently the most successful and dominate growth technique for fabricating DFB lasers. Recently, MBE growth of high quality GaInAsP layers and high performance GaInAsP/InP lasers have been achieved by using all solid sources.³⁻⁶ This technology subsequently enables the growth investigation of DFB lasers on InP grating surfaces.

2. Experiments

The growth of GaInAsP/InP index-coupled DFB lasers were carried out with a Riber 2300 MBE system using elemental In, Ga, Si, and Be, and P₂ and As₂ supplied via solid phosphorous and arsenic valved sources. The valved P₂ cell used is a three temperature zone Riber model KPC40 with a modified cracker head. The As₂ flux is supplied via an EPI VC-IV valved cell with two temperature

zones. Growth temperatures were measured with an IRCON 6000 series optical pyrometer that was calibrated to a surface oxide desorption temperature of 460 °C with S-doped InP. First order gratings, with a periodicity of 0.202 μm, were optically patterned parallel to the [0̄1̄1] direction using holographic photolithography for the 1.3 μm wavelength DFB lasers. Wet chemically etching in HBr:HNO₃:H₂O (1:1:20) for one minute was then used to define the grating on the InP surface. The etched depth of the V-grooves with (111)A side-walls was about 600 Å. A planar InP substrate was also placed adjacent to the grated InP substrate for each growth. Samples were affixed to the molybdenum block using indium. Both of the grated and planar InP wafers were etched in H₂SO₄:H₂O₂:H₂O (10:1:1) solution for 40 seconds before loading into the MBE system.

Before initiating the growth, the S-doped InP substrates were heated at 470°C for 10 min under a P₂ flux of 1.0×10^{-5} Torr to desorb the native oxide. The substrate temperature was then ramped from 470 °C to 510 °C in two minutes for growth of the Ga_{0.15}In_{0.85}As_{0.32}P_{0.68} ($\lambda_{PL} = 1.12$ μm, denoted as 1.12Q) quaternary planarization layer, Si-doped at 8×10^{17} cm⁻³. An As₂ flux of 8.0×10^{-7} Torr was used in addition to the P₂ flux during this substrate temperature ramping in order to preserve a proper grating depth. The higher growth temperature for the 1.12Q planarization layer is crucial for producing a flat surface for the subsequent growth of the MQW laser structure.⁶ After the planarization layer, a 1200 Å thick InP lower cladding layer (Si-doped at 8×10^{17} cm⁻³) was then grown, followed by a 800 Å thick undoped 1.12Q separate confinement layer, an undoped active region, a 800 Å thick undoped 1.12Q separate confinement layer, a 1.2 μm thick InP (Be doped at 1×10^{18} cm⁻³) upper cladding layer and finally a 500 Å thick Ga_{0.47}In_{0.53}As (Be doped at 4×10^{19} cm⁻³) contact layer. The active region consists of six (nine), 75 Å thick GaInAsP quantum wells and five (eight), 100 Å thick 1.12Q barrier layers. A growth interruption of 10 seconds was used at the interfaces between barriers and wells. The growth temperatures of the InP cladding layers and the active regions were 460 °C and 490 °C, respectively. Between the growth of the planarization layer and the InP lower cladding layer, a growth interruption of 90 seconds was employed to reduce the substrate temperature from 510 °C to 460 °C. The growth rates for InP, 1.12Q, and GaInAsP quantum wells were 1.20, 1.41, and 0.71 μm/h, respectively. A P₂ flux of 1.0×10^{-5} Torr was used for the growth of all layers except the GaInAs p-contact layer. The As₂ beam fluxes used for the growth of 1.12Q and quantum wells were 8.0×10^{-7} and 5.8×10^{-6} Torr, respectively. These group V fluxes were measured by an ionization gauge located in the beam path. Broad area stripe lasers (80 μm wide) were fabricated without any facet coating or lateral current confinement.

3. Results and Discussion

The transmission electron micrograph of a 6 quantum well DFB laser is shown in Fig. 1. The preserved grating depth is about 300 Å and smooth interfaces were obtained between all epitaxial layers. When a deeper grating depth is required, a larger initial grating depth and a lower oxide desorption temperature can be used. For example, when performing the oxide desorption at 465°C for 10 minutes from a 600 Å deep grating, the preserved grating depth is about 550 Å. The threshold current densities per-well as a function of inverse cavity length under pulsed operation are plotted in Fig. 2(a) for both lasers grown simultaneously on the grated and planar substrates. The transparency current density of the lasers grown simultaneously on grated and planar substrates are 68 and 94 A/cm² per well, respectively. From Fig. 2(a), one can observe that lasers grown on grated and planar

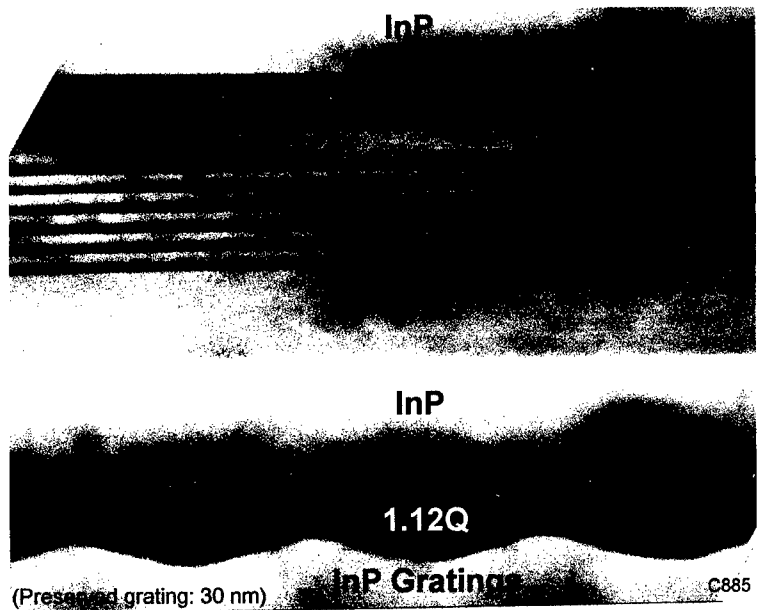


Fig.1 The transmission electron micrograph of a 6-quantum-well $1.3 \mu\text{m}$ DFB laser. The preserved grating depth in this sample is about 300 \AA . Smooth interfaces are observed after the growth of a 1.12Q planarization layer.

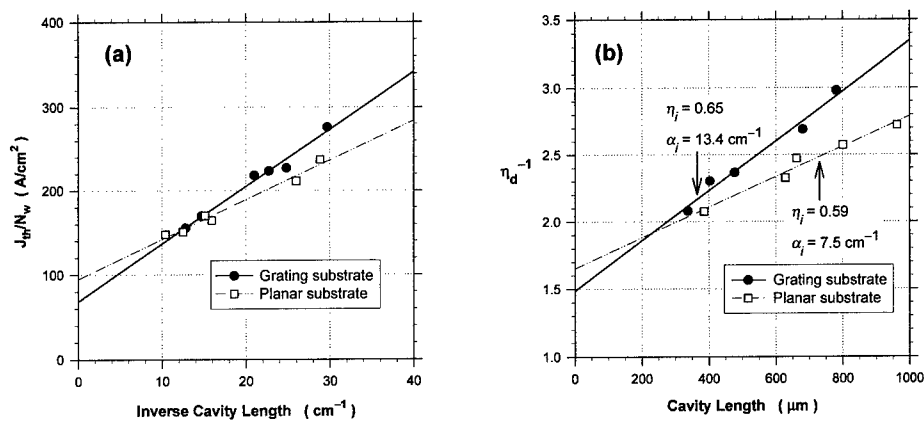


Fig.2 The threshold current density per-well as a function of the inverse cavity length, (a) and the inverse external quantum efficiency as a function of the cavity length (b) for $1.3 \mu\text{m}$ lasers grown simultaneously on a DFB grating substrate and a planar substrate. Each data point represents the average of 3 lasers with the same cavity length.

substrates with the same cavity length showed similar threshold current densities. The inverse external quantum efficiency as a function of the laser cavity length for these DFB lasers are shown in Fig. 2(b). The internal quantum efficiency, η_i , and internal loss, α_i , for these 6-quantum-well lasers are 0.65 and 13.4 cm^{-1} for the grated substrate and 0.59 and 7.5 cm^{-1} for the planar substrate, respectively. The transparency current density, η_i and α_i of the 9-quantum-well DFB lasers are 61 A/cm^2 per well, 0.67 and 15.2 cm^{-1} , respectively. These results indicate that the properties of the lasers grown on the grated substrate are similar to that of the lasers grown on the planar substrate. The emission spectra of an uncoated DFB laser is shown in Fig. 3 with a side mode suppression ratio of more than 20.

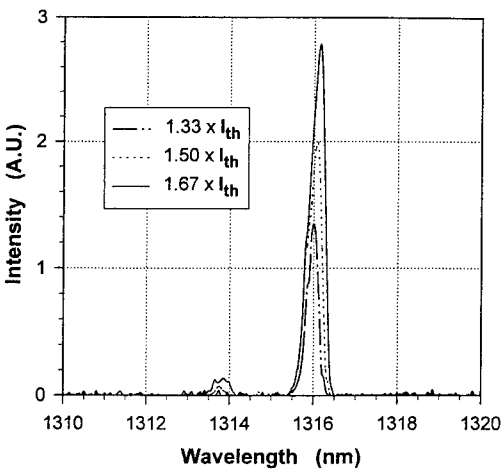


Fig. 3 The emission spectra of an uncoated DFB laser at three different current injection levels are shown.

4. Conclusion

Successful growth of GaInAsP/InP multi-quantum well (MQW) lasers directly on DFB grating substrates using all solid source MBE was achieved. After desorbing the surface oxide at 470°C , a 500 \AA thick 1.12Q planarization layer was first deposited on the DFB gratings at an elevated temperature to create a smooth surface for subsequent layer growth. Transmission electron micrographs show smooth interfaces after growth of the GaInAsP planarization layer. Low threshold current density and high quantum efficiency were obtained from these index-coupled MQW DFB lasers. Broad area lasers show room-temperature transparency current densities as low as 61 and 68 A/cm^2 per well for 9-well and 6-well DFB lasers, respectively. The measured internal quantum efficiency and internal loss for 9-well (6-well) DFB lasers are 0.67 (0.65) and 15.2 (13.4) cm^{-1} , respectively.

References

- [1] B. Elsner, R. Westphalen, K. Heime, and P. Balk, *J. Crystal Growth* 124, 326 (1992)
- [2] O. Kayser, *J. Crystal Growth* 107, 989 (1991)
- [3] P. Legay, F. Alexandre, J. L. Benchimol, and J. C. Harmand, *J. Crystal Growth* 150, 394 (1995)
- [4] J. N. Baillargeon, A. Y. Cho, and K. Y. Cheng, *J. Appl. Phys.* 79, 7652 (1996)
- [5] M. Toivonen, P. Savolainen, H. Asonen and M. Pessa, *Journal of Crystal Growth* 175, p. 37, 1997
- [6] W.-Y. Hwang, J. N. Baillargeon, S. N. G. Chu, P. F. Sciortino, and A. Y. Cho, *9th International Molecular Beam Epitaxy Conference*, August, 1996 (Malibu, CA)

The Growth of Mid-Infrared Emitting InAsSb/InAsP Strained-Layer Superlattices Using Metal-Organic Chemical Vapor Deposition

R. M. Biefeld, A. A. Allerman, S. R. Kurtz, and J. H. Burkhart
 Sandia National Laboratory, Albuquerque, New Mexico 87185-0601

Abstract. We describe the metal-organic chemical vapor deposition of InAsSb/InAsP strained-layer superlattice (SLS) active regions for use in mid-infrared emitters. These SLSs were grown at 500 °C, and 200 torr in a horizontal quartz reactor using trimethylindium, triethylantimony, AsH₃, and PH₃. By changing the layer thickness and composition we have prepared structures with low temperature (≤ 20 K) photoluminescence wavelengths ranging from 3.2 to 5.0 μm. Excellent performance was observed for an SLS light emitting diode (LED) and both optically pumped and electrically injected SLS lasers. An InAsSb/InAsP SLS injection laser emitted at 3.3 μm at 80 K with peak power of 100 mW.

1. Introduction

Chemical sensor and infrared countermeasure technologies would become viable with the availability of high power, mid-infrared (3-6 μm) lasers and light emitting diodes (LEDs) operating near room temperature. However, the performance of mid-infrared emitters has been limited by nonradiative recombination processes (usually Auger recombination), which overwhelm radiative recombination in narrow bandgap semiconductors. Auger recombination can be suppressed in “band-structure engineered”, strained InAsSb heterostructures. In order to reduce Auger recombination in mid-infrared (2-6 μm) lasers, several narrow bandgap III-V, strained-layer superlattices (SLSs) have been explored using metal-organic chemical vapor deposition (MOCVD) and molecular beam epitaxy (MBE) [1-13]. In both type I and type II SLS laser active regions, holes are confined to compressively strained layers, producing a low in-plane, effective mass ($|3/2, \pm 3/2\rangle$) hole ground state. In compressively strained InAsSb SLSs, it is necessary to maximize the light-heavy ($|3/2, \pm 1/2\rangle - |3/2, \pm 3/2\rangle$) hole splitting to suppress Auger recombination. For example, we have investigated the electronic properties of InAsSb/InGaAs SLSs, and we find that the light-heavy hole splitting (≈ 30 meV) is insufficient to achieve maximum suppression of Auger recombination[1,12-15]. InAsSb SLSs incorporating barrier layers with larger valence band offsets are required to maximize the light-heavy hole splitting through quantum confinement. In this work, we report the properties of InAsSb/InAsP SLS materials and devices. Incorporating InAsP as a barrier layer in the active region will introduce a larger valence band offset than either of the offsets between InAs or InGaAs and InAsSb. Compared with other compressively strained InAsSb devices, initial tests on InAsSb/InAsP SLS lasers and LEDs show state-of-the-art performance. We report on the synthesis of these materials by MOCVD and their use in improved 3-6 μm, mid-infrared optoelectronic heterojunction emitters.

2. Experimental

This work was carried out in a previously described MOCVD system [16,17]. The InAsSb/InAsP SLSs were grown on n-type InAs substrates at 500 °C, and 200 torr in a horizontal quartz reactor using trimethylindium (TMIn), triethylantimony (TESb), 100 % AsH₃ for the InAsSb layers, 10 % AsH₃ in hydrogen for the InAsP layers, and 100 % PH₃. The InAsSb layers were grown using a V/III ratio of 15 to 21 and an TESb/(AsH₃+TESb) ratio of 0.29 to 0.41 at a growth rate of 2.5 Å/second. A 5 to 15 second purge, with reactants switched in and out of the chamber, was used for different samples. The InAsP layers were grown using a V/III ratio of about 217 and an AsH₃/(AsH₃+PH₃) ratio of 0.015 to

0.025 with an identical growth rate of 2.5 Å/second. The strain balanced SLSs were lattice matched to InAs with $\Delta a/a < 0.0004$ with the InAsSb layers in compression and the InAsP layers in tension relative to the InAs substrate. The SLS composition and strain were determined by x-ray diffraction.

We used ethyldimethylamine alane (EDMAA), TESb and 10% arsine (AsH_3) in hydrogen as the sources for Al, Sb and As respectively, for the growth of $AlAs_xSb_{1-x}$ cladding layers. Triethylgallium (TEGa), arsine and TESb were used to grow a 400 to 2500Å GaAsSb cap on all samples to keep the $AlAs_xSb_{1-x}$ layer from oxidizing and to serve as a semi-metal electron injector for the emitter structures.[10, 13] Hydrogen was used as the carrier gas at a total flow of 8 slpm.

Infrared photoluminescence (PL) was measured on all samples at 14 K up to 300 K using a double-modulation, Fourier-transform infrared (FTIR) technique which provides high sensitivity, reduces sample heating, and eliminates the blackbody background from infrared emission spectra. Injection devices (both LEDs and lasers) also were characterized with double modulation FTIR.

3. Results And Discussion

The growth rate of the InAsSb/InAsP SLSs was found to be proportional to the TMIn flow into the reaction chamber and independent of the TESb, PH_3 , and AsH_3 flow. The variation of the Sb composition for the InAsSb layer as a function of TESb /($AsH_3 + TESb$) ratio in the vapor is shown in Figure 1. The Sb composition could be varied between 0.12 to 0.23 while maintaining approximately constant layer thicknesses for both the InAsSb and InAsP layers.

The PL peak wavelength dependence on Sb composition of the InAsSb layer in the SLSs is shown in Figure 2. For a change of composition from $x = 0.12$ to 0.23 the PL peak changes from 3.6 to 5.0 μm. Room temperature photoluminescence, also shown in Figure 2, was observed from 4.2 to 5.8 μm. The variation of PL wavelength versus thickness of the InAsSb well is shown in Figure 3. The wavelength could be varied from 3.2 to 3.8 μm for a change in thickness from 45 to 108 Å. For layers thicker than approximately 90 Å the x-ray diffraction patterns broadened, indicating the presence of dislocations. The crystal quality of the SLSs was excellent with 3 to 4 orders of x-ray diffraction satellite peaks typically observed. The intensity of the PL peak and the surface morphology of the layers was found to be strongly dependent on the purge time between the growth of the layers of the SLS and whether or not AsH_3 was present during the purge. We investigated purge times from 0 to 30 seconds with and without AsH_3 in the reactor during the purges. The optimum growth conditions are a purge of 15 seconds duration with AsH_3 in the reactor.

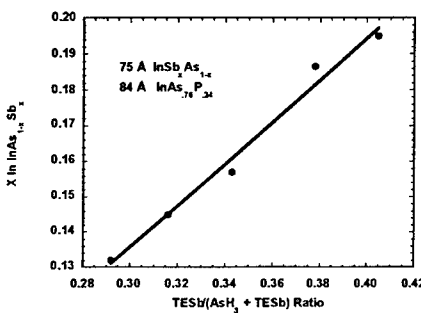


Figure 1. Incorporation of Sb into the InAsSb layer as a function of TESb /($AsH_3 + TESb$) ratio in the vapor phase for the InAsSb/InAsP SLSs.

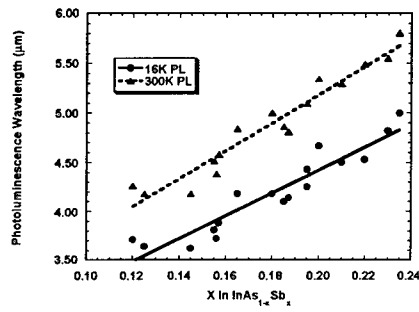


Figure 2. Photoluminescence at 300 K and 16 K from 40 period 78-87 Å InAs_{1-x}Sb_x / 81-89 Å InAs_{0.76}P_{0.24} SLSs grown on InAs for different Sb contents in the InAsSb layer.

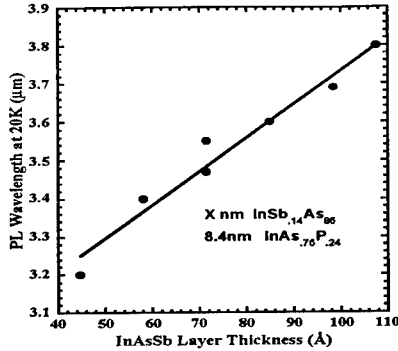


Figure 3. Low temperature PL ($< 20\text{K}$) from 20 period $\text{InAs}_{0.86}\text{Sb}_{0.14}$ / 84 Å $\text{InAs}_{0.76}\text{P}_{0.24}$ SLS's grown on InAs for different InAsSb layer thicknesses.

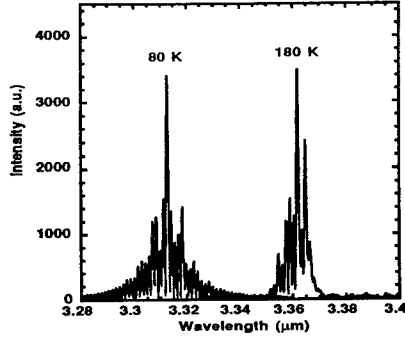


Figure 4. Electrically injected, pulsed laser emission spectra at 80 and 180 K for a 10 period $\text{InAs}_{0.89}\text{Sb}_{0.11}$ / $\text{InAs}_{0.74}\text{P}_{0.26}$ (87 Å / 84 Å) SLS active region.

An LED was constructed with a 0.7 μm thick, n-type, $\text{InAs}_{0.88}\text{Sb}_{0.12}$ / $\text{InAs}_{0.75}\text{P}_{0.25}$ (80 Å / 82 Å) SLS active region. As for the previously published MQW structures, [10] a semi-metal layer consisting of a 500 Å thick GaAsSb (p-type) and a 500 Å thick InAs (n-type) heterojunction provided electrical injection for the LED. A 1 mm² piece of the wafer was mounted onto a header with a parabolic collector. The top contact of the LED was a 0.02" diameter Ti/Au dot. Operating the device at 1 kHz, 50% duty cycle, 200 mA average current, the average output power of the LED was 80 μW at 300 K. At 80 K the output power of the LED was 24x that observed at 300 K. The output power of our SLS device (300 K) was 5-6x that measured with the same current for LPE-grown, InAsSb alloy, commercial LEDs [18].

The electrically injected laser structure consisted of 2.5 μm of not intentionally doped p-AlAsSb ($5 \times 10^{16} \text{ cm}^{-3}$) top and bottom claddings, a p-GaAsSb / n-InAs semi-metal electron injector, and a 10 period InAsSb/InAsP SLS active region separated from the claddings by 3000 Å of InAs. Gain-guided, stripe lasers were fabricated with Ti/Au metallizations. The facets were uncoated. Under pulsed operation, lasing was observed in forward bias with 40x1000 or 80x1000 micron stripes. Devices were tested with 100 nsec pulse widths at 10 kHz (0.1 % duty-cycle). Several longitudinal modes were observed in the 3.3-3.4 μm range, shown in Figure 4 for 80 K and 180 K operation. The wavelength of our laser shifts from 3.31 μm to 3.36 μm due to the decrease in bandgap over the 80-180K temperature range. At 80 K, peak powers of 100 mW could be obtained with a maximum average power of 0.5 mW. The temperature dependence of the SLS laser threshold is described by a characteristic temperature, $T_0 = 39$ K, over the entire temperature range.

An optically pumped laser was grown on an InAs substrate with a 2.5 μm thick AlAs_{0.16}Sb_{0.84} lower cladding. The active region was a 1.0 μm thick, $\text{InAs}_{0.89}\text{Sb}_{0.11}$ / $\text{InAs}_{0.77}\text{P}_{0.23}$ (83 Å / 87 Å) SLS. The SLS laser was pumped with a Q-switched Nd:YAG (1.06 μm, 20 Hz, 10 nsec pulse, focused to a 200 μm wide line), and emission was detected with an FTIR spectrometer operated in a step-scan mode. Due to the low rep-rate of the pump, approximately a 4 hour scan was required to obtain an interferogram with resolution $\geq 2 \text{ cm}^{-1}$. Laser emission was observed from cleaved bars, 1000 μm wide, with uncoated facets. A lasing threshold and spectrally narrowed, laser emission was seen from 80 K through 240 K, the maximum temperature where lasing occurred. The PL linewidth is ≈ 25 meV at 80K, but above threshold, the laser emission narrowed to 3-5 meV depending on the sample. The laser emission linewidth is limited by inhomogeneities in the material and the presence of multiple, unresolved

longitudinal modes; similar behavior was observed in optically pumped type II, GaInSb/InAs lasers [7,9]. The wavelength of our laser shifts from 3.57 μm to 3.85 μm due to the decrease in bandgap over the 80-240K temperature range. At 80 K, peak powers >100 mW could be obtained. The temperature dependence of the SLS laser threshold is described by a characteristic temperature, $T_0 = 33$ K, over the entire range.

4. Conclusions

We have evaluated InAsSb/InAsP SLSs as active regions for MOCVD-grown, mid-infrared lasers and LEDs. X-ray and optical characterization of the SLSs indicate very high crystalline quality for the MOCVD-grown material and electronic properties consistent with our model of the SLS. Excellent performance was observed for an SLS LED, an electrically injected laser, and an optically pumped laser. The semi-metal injected, broadband LED emitted at 4 μm with 80 μW of power at 300K, 200 mA average current. The electrically injected laser emitted at 3.36 μm at 180 K with peak powers of 100 mW at 80 K and a characteristic temperature of 39 K. The optically pumped laser displayed 3.86 μm emission at 240 K, the maximum operating temperature of the laser, and a characteristic temperature of 33 K. InAsSb/InAsP SLS laser operating temperature, characteristic temperature, and threshold power values are state-of-the-art for InAsSb lasers at $\approx 4 \mu\text{m}$. With nominal improvements in materials and processing and the further development of multi-stage active regions, MOCVD-grown InAsSb devices should be able to satisfy the system requirements for use in chemical sensor and infrared countermeasure technologies in the near future.

Acknowledgments

We thank J. A. Bur for technical support. Our work was supported by the US Dept. of Energy under contract No. DE-AC04-94AL85000. Sandia is a multiprogram laboratory operated by Sandia Corporation, a Lockheed Martin Company, for the United States Department of Energy.

References

- [1] Kurtz S R, Biefeld R M, Allerman A A, Howard A J, Crawford M J and Pelczynski M W 1996 *Appl. Phys. Lett.* 68 1332-1333.
- [2] Choi H K and Turner G W 1995 *Appl. Phys. Lett.* 67 332 -334.
- [3] Zhang Y-H 1995 *Appl. Phys. Lett.* 66 118-120.
- [4] Biefeld R M, Allerman A A and Pelczynski M W 1996 *Appl. Phys. Lett.* 68 932-934.
- [5] Kurtz S R, Biefeld R M, Dawson L R, Baucom K C and Howard A J 1994 *Appl. Phys. Lett.* 64 812-814.
- [6] Garbuzov D Z, Martinelli R U, Menna R J, York P K, Lee H, Narayan S Y and Connolly J C 1995 *Appl. Phys. Lett.* 67 1346-1348.
- [7] Chow D H, Miles R H, Hasenberg T C, Kost A R, Zhang Y-H, Dunlap H L and West L 1995 *Appl. Phys. Lett.* 67 3700-3702 .
- [8] Choi H K, Turner G W, Manfra M J and Connors M K 1996 *Appl. Phys. Lett.* 68 2936-2938.
- [9] Malin J I, Meyer J R, Felix C L, Lindle J R, Goldberg L, Hoffman C A, Bartoli F J, Lin C H, Chang P C, Murry S J, Yang R Q and Pei S S 1996 *Appl. Phys. Lett.* 68 2976-2978.
- [10] Allerman A A, Biefeld R M, and Kurtz S R 1996 *Appl. Phys. Lett.* 69 465-467.
- [11] Menna R J, Garbuznov D Z, Martinelli R U and Olsen G H (*to be published*).
- [12] Kurtz S R, Allerman A A and Biefeld R M 1997 *Appl. Phys. Lett.* 70 3188-3190.
- [13] Biefeld R M, Allerman A A and Kurtz, S R 1997 *J. Crystal Growth* 174 593-598.
- [14] Kurtz S R, Biefeld R M and Howard A J 1995 *Appl. Phys. Lett.* 67 3331-3333.
- [15] Hjalmarson H P and Kurtz S R 1996 *Appl. Phys. Lett.* 69 949-951.
- [16] Biefeld R M, Baucom K C and Kurtz S R 1994 *J. Crystal Growth*, 137 231-233.
- [17] Biefeld R M 1986 *J. Crystal Growth* 75 255-263.
- [18] Our device was compared with a 4.2 μm LED obtained from RMC Ltd., Moscow, Russia.

MOCVD Growth of $(\text{Ga}_{1-x}\text{In}_x\text{As} - \text{GaAs}_{1-y}\text{Sb}_y)$ Superlattices on InP showing Type-II emission at Wavelengths beyond 2 μm

M. Peter, K. Winkler, N. Herres, F. Fuchs, S. Müller, K.-H. Bachem, J. Wagner

Fraunhofer-Institut für Angewandte Festkörperphysik, Tullastrasse 72
D-79108 Freiburg, Germany

We report on $(\text{Ga}_{1-x}\text{In}_x\text{As} - \text{GaAs}_{1-y}\text{Sb}_y)$ superlattices grown strain-compensated on (100) InP:Fe substrates using metal organic chemical vapor deposition. Low temperature photoluminescence measurements show a spatially indirect type-II recombination of electrons in the conduction band of the $\text{Ga}_{1-x}\text{In}_x\text{As}$ and holes in the valence band of the $\text{GaAs}_{1-y}\text{Sb}_y$ layers at 2.20 μm . Type-II emission was observed up to room-temperature with 300 K emission centered at 2.30 μm . The valence and conduction band offsets between strain-compensated $\text{Ga}_{0.42}\text{In}_{0.58}\text{As}$ and $\text{GaAs}_{1-y}\text{Sb}_y$ ($y \approx 0.2$ to 0.3) layers were estimated to 0.21 eV and 0.33 - 0.39 eV, respectively.

Introduction

$\text{Ga}_{1-x}\text{In}_x\text{As}$ and $\text{GaAs}_{1-y}\text{Sb}_y$ can be grown both lattice matched and strained on InP. While $\text{Ga}_{1-x}\text{In}_x\text{As}$ is a well established material system less work has been reported on $\text{GaAs}_{1-y}\text{Sb}_y$. This is mainly due to the wide miscibility gap of $\text{GaAs}_{1-y}\text{Sb}_y$ and the resulting difficulties in the preparation of high-quality epitaxial layers. In spite of this difficulties $\text{GaAs}_{1-y}\text{Sb}_y$ has been grown successfully throughout the whole compositional range with non-equilibrium growth techniques like molecular beam epitaxy (MBE) [1] and metal-organic chemical vapor deposition (MOCVD) [2].

Sai-Halasz et al. [3] and Klem et al. [4] grew $(\text{Ga}_{1-x}\text{In}_x\text{As} - \text{GaAs}_{1-y}\text{Sb}_y)$ superlattices (SL) lattice matched on InP-substrate using MBE. The $(\text{Ga}_{1-x}\text{In}_x\text{As} - \text{GaAs}_{1-y}\text{Sb}_y)$ system is known to show spatially indirect type-II recombination of electrons in the conduction band of the $\text{Ga}_{1-x}\text{In}_x\text{As}$ and holes in the valence band of the $\text{GaAs}_{1-y}\text{Sb}_y$ [3,4,5]. Calculations based on the Model Solid Theory [6,7] predict that this emission is expected at wavelengths between 2 μm (lattice-matched) and 3 μm (strain-compensated, $\text{Ga}_{1-x}\text{In}_x\text{As}$ compressively strained). This property makes $(\text{Ga}_{1-x}\text{In}_x\text{As} - \text{GaAs}_{1-y}\text{Sb}_y)$ SLs a promising system for mid-IR LEDs and laser diodes based on InP-substrate.

Experimental

We report on the growth of strain-compensated $(\text{Ga}_{1-x}\text{In}_x\text{As} - \text{GaAs}_{1-y}\text{Sb}_y)$ SLs on (100) InP:Fe substrates using MOCVD. The SLs were sandwiched between $\text{Ga}_{0.28}\text{In}_{0.72}\text{As}_{0.6}\text{P}_{0.4}$ confinement layers with thicknesses varying from 110 to 300 nm. All samples were grown at a pressure of 100 mbar using hydrogen as a carrier-gas. TMGa, TMIn and AsH_3 were used as precursors for $\text{Ga}_{1-x}\text{In}_x\text{As}$, TMGa, TBAs and TESb for $\text{GaAs}_{1-y}\text{Sb}_y$. The SL was grown at a substrate temperature of 530°C. InP cladding and $\text{Ga}_{0.28}\text{In}_{0.72}\text{As}_{0.6}\text{P}_{0.4}$ confinement layers were grown at 640°C using TMIn, TMGa, AsH_3 and PH_3 as precursors.

Sample	Nominal Sample Structure		HRXRD			FT-PL	
	n_{period}	d^{GaInAs} (nm)	d^{GaAsSb} (nm)	d^{SL} (nm)	$(\Delta d/d)_{\perp}$	$E_g^{\text{type-II}}$ (eV)	E_g^{GaInAs} (eV)
#8	10	26.0	4.0	30.0	$2.8 \cdot 10^{-4}$	0.562	0.772
#7	10	15.6	5.3	20.9	$-6.3 \cdot 10^{-3}$	0.551	-
#9	10	8.6	5.3	13.9	$-2.7 \cdot 10^{-3}$	0.566	-
#10	10	11.5	10.4	21.9	$-3.1 \cdot 10^{-3}$	0.588	-
#15	10	8.8	3.4	12.2	$1.1 \cdot 10^{-3}$	0.615	-
#16	20	4.0	2.2	6.2	$-3.1 \cdot 10^{-3}$	0.708	-

Tab. 1: Number of periods n_{period} , nominal thicknesses of the $\text{Ga}_{1-x}\text{In}_x\text{As}$ and $\text{GaAs}_{1-y}\text{Sb}_y$ layers, total thickness of a single period d^{SL} , lattice mismatch $(\Delta d/d)_{\perp}$ and low temperature (10 K) PL peak positions of $(\text{Ga}_{1-x}\text{In}_x\text{As} - \text{GaAs}_{1-y}\text{Sb}_y)$ SL on (001) InP substrates. The $\text{Ga}_{1-x}\text{In}_x\text{As}$ and $\text{GaAs}_{1-y}\text{Sb}_y$ layer thicknesses were deduced from d^{SL} taking nominal thickness ratios into account.

All samples have been investigated by high resolution X-ray diffractometry (HRXRD). X-ray rocking curves were taken around the 002 and 004 reflection of the (100) InP substrate to determine the SL period d^{SL} and the average lattice mismatch $(\Delta d/d)_{\perp}$ perpendicular to the substrate surface. The surface of all samples was investigated by Nomarski interference microscopy and selected samples have been examined by atomic force microscopy (AFM) to obtain the surface-roughness. Temperature dependent Fourier-transform photoluminescence spectroscopy (FT-PL) was used to characterize the samples which were mounted in a variable temperature cryostat. The 1.064 μm line of a Nd:YAG laser was used for optical excitation with a power density of about 10 W/cm^2 .

Results and Discussion

A series of $(\text{Ga}_{1-x}\text{In}_x\text{As} - \text{GaAs}_{1-y}\text{Sb}_y)$ SLs surrounded by $\text{Ga}_{0.28}\text{In}_{0.72}\text{As}_{0.6}\text{P}_{0.4}$ confinement layers, was grown strain-compensated on InP. Within this series the thicknesses of the $\text{Ga}_{1-x}\text{In}_x\text{As}$ and $\text{GaAs}_{1-y}\text{Sb}_y$ layers were varied (see Tab.1). The Sb concentration y of all $\text{GaAs}_{1-y}\text{Sb}_y$ layers was kept constant at nominally $y = 0.42$, while the In concentration x in the $\text{Ga}_{1-x}\text{In}_x\text{As}$ was adjusted in order to obtain strain balancing relative to the InP substrate.

The surface morphology of all samples is excellent. RMS-roughnesses of less than 0.3 nm averaged over a $2 \mu\text{m} \times 2 \mu\text{m}$ area were measured by AFM. Fig. 1 shows a X-ray rocking curve of a nominal $10 \times \text{Ga}_{0.46}\text{In}_{0.54}\text{As}$ (26nm)/ $\text{GaAs}_{0.58}\text{Sb}_{0.42}$ (4nm) SL (sample #8) around the 002 reflection of the (100) InP substrate. SL diffraction peaks up to the 19th order give evidence of the high structural quality of the layers. The average lattice mismatch of the SL is $(\Delta d/d)_{\perp} = 2.8 \cdot 10^{-4}$ indicating a good lattice match to InP.

Fig. 2 shows normalized low-temperature PL spectra (10 K) of the $(\text{Ga}_{1-x}\text{In}_x\text{As} - \text{GaAs}_{1-y}\text{Sb}_y)$ SLs (see Tab. 1). The dominant peak in all spectra arises from spatially indirect type-II recombination of electrons in the conduction band of the $\text{Ga}_{1-x}\text{In}_x\text{As}$ and holes in the valence band of the $\text{GaAs}_{1-y}\text{Sb}_y$. The SL of sample #8 is very asymmetric in its individual layer thicknesses with $d^{\text{GaInAs}}/d^{\text{GaAsSb}} = 26 \text{ nm} : 4 \text{ nm}$. This sample shows besides the type-II emission at 0.562 eV (2.20 μm) also the spatially direct type-I recombination within the $\text{Ga}_{1-x}\text{In}_x\text{As}$ layer at 0.772 eV (1.61 μm). At higher temperatures this peak vanishes while the type-II emission was observed up to room-temperature. The 300 K emission is centered at 2.30 μm . The $\text{Ga}_{1-x}\text{In}_x\text{As}$ and $\text{GaAs}_{1-y}\text{Sb}_y$ layer composition and the thickness ratio $d^{\text{GaInAs}}/d^{\text{GaAsSb}} = 2.3$ is identical in sample #15 and #16, while the SL period d^{SL} has been reduced from

12.2 nm (#15) to 6.2 nm (#16) with the number of periods doubled in sample #16. Therefore the volume of the SL stack was kept constant while the number of interfaces was doubled. Due to the enhanced wavefunction overlap the PL intensity of sample #16 was more than a factor of two larger than that of sample #15. The 93 meV blue-shift of the type-II emission from 0.615 eV (#15) to 0.708 eV (#16) is caused by an increase in confinement energies with the smaller period of the SL.

From the PL of sample #8 it is possible to give a rough estimate of the band alignment of strained $\text{GaAs}_{1-y}\text{Sb}_y$ relative to $\text{Ga}_{1-x}\text{In}_x\text{As}$ and InP. Assuming the low-temperature band-gap energy of $\text{Ga}_{1-x}\text{In}_x\text{As}$ to be $E(x) = 1.519 + 1.584 x + 0.475 x^2$ [8] and including the splitting of the valence band due to tetragonal strain [9], an In concentration $x \approx 0.58$ is obtained from the PL spectrum of sample #8. Confinement effects in the conduction band of the 26 nm wide $\text{Ga}_{1-x}\text{In}_x\text{As}$ layer have been neglected. Based on the average lattice mismatch $(\Delta d/d)_\perp = 2.8 \cdot 10^{-4}$ and the nominal thickness ratio $d^{\text{GaInAs}} : d^{\text{GaAsSb}} = 26 \text{ nm} : 4 \text{ nm}$ the actual Sb concentration y in the $\text{GaAs}_{1-y}\text{Sb}_y$ layer can be estimated to 0.2. A slight variation of this ratio, such as e.g. $d^{\text{GaInAs}} : d^{\text{GaAsSb}} = 24.3 \text{ nm} : 5.7 \text{ nm}$, results in an increase of the Sb concentration to $y = 0.3$. The composition dependence of the band-gap energy of $\text{GaAs}_{1-y}\text{Sb}_y$ is given by $E(y) = 1.519 + 1.2 y + 1.2 y^2$ [8]. Taking strain effects into account [9] one obtains a low-temperature band-gap for $\text{GaAs}_{1-y}\text{Sb}_y$ of $E_g = 0.98 \text{ eV}$ ($y = 0.2$) or $E_g = 0.89 \text{ eV}$ ($y = 0.3$). From the difference between the type-I and the type-II emission energies a valence band offset between $\text{Ga}_{1-x}\text{In}_x\text{As}$ and $\text{GaAs}_{1-y}\text{Sb}_y$ ($y = 0.2$ to 0.3) of 0.21 eV is obtained. These values result in a conduction band offset between $\text{Ga}_{1-x}\text{In}_x\text{As}$ and $\text{GaAs}_{1-y}\text{Sb}_y$ of 0.33 eV to 0.39 eV. Assuming a valence band discontinuity $Q_V = \Delta E_V / (\Delta E_V + \Delta E_C) = 0.6$ for $\text{Ga}_{1-x}\text{In}_x\text{As}$ relative to InP [6,7,10] the valence band discontinuity Q_V of $\text{GaAs}_{1-y}\text{Sb}_y$ relative to InP is found to be between 1.1 and 1.3.

For calibration purposes a sample with a 60 nm thick layer of $\text{GaAs}_{1-y}\text{Sb}_y$ was grown pseudomorphically strained on InP substrate. The Sb content was determined by HRXRD as $y = 0.42$.

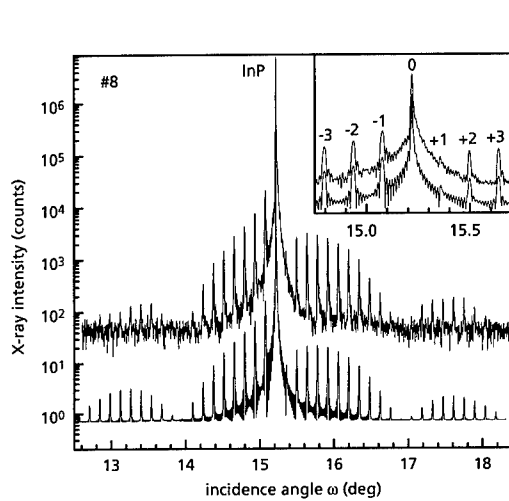


Fig. 1: HRXRD reflection profile of a $10 \times (\text{Ga}_{1-x}\text{In}_x\text{As} - \text{GaAs}_{1-y}\text{Sb}_y)$ SL (sample #8) around the 002 reflection of InP (upper profile: measurement, lower profile: simulation). The inset shows a magnification of the region around the InP-substrate peak.

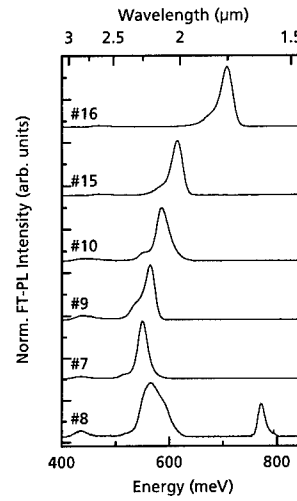


Fig. 2: 10K PL spectra of $(\text{Ga}_{1-x}\text{In}_x\text{As} - \text{GaAs}_{1-y}\text{Sb}_y)$ SL structures with varying $\text{Ga}_{1-x}\text{In}_x\text{As}$ and $\text{GaAs}_{1-y}\text{Sb}_y$ thicknesses ($\lambda_{\text{exc}} = 1.064 \mu\text{m}$, $P_{\text{exc}} \approx 10 \text{ W/cm}^2$).

Though exactly the same nominal growth parameters were used for the $(\text{Ga}_{1-x}\text{In}_x\text{As} - \text{GaAs}_{1-y}\text{Sb}_y)$ SL the Sb incorporation is significantly lower in the SL structure than in the thick $\text{GaAs}_{0.58}\text{Sb}_{0.42}$ layer. The Sb incorporation into $\text{GaAs}_{1-y}\text{Sb}_y$ is known to depend strongly on the V:III ratio [2,11,12]. It is likely that the V:III ratio during the growth of the SL stack is larger than during the growth of a single $\text{GaAs}_{1-y}\text{Sb}_y$ layer ($V:\text{III} = 1.6$), since the $\text{Ga}_{1-x}\text{In}_x\text{As}$ layers of the SL were grown with a V:III ratio of 70. Thus the Sb concentration into the $\text{GaAs}_{1-y}\text{Sb}_y$ layers of the SL might be less than 42% due to a higher As background in the MOCVD reactor. This also explains why most SLs are compressively strained, i.e. $(\Delta d/d)_\perp < 0$ (see Tab. 1) even though strain compensation is expected on the basis of the bulk calibration data.

Klem et al. [4] used low-temperature PL to derive values for the conduction and valence band offsets in $(\text{Ga}_{1-x}\text{In}_x\text{As} - \text{GaAs}_{1-y}\text{Sb}_y)$ SLs lattice matched to InP. Direct band-gaps of $E_g^{\text{GaAsSb}} = 0.80$ eV and $E_g^{\text{GaInAs}} = 0.81$ eV and a type-II band-gap $E_g^{\text{type-II}} = 0.43$ eV were found which result in band offsets between $\text{Ga}_{1-x}\text{In}_x\text{As}$ and $\text{GaAs}_{1-y}\text{Sb}_y$ of $\Delta E_{CB} = 0.37$ eV and $\Delta E_{VB} = 0.43$ eV. Sai-Halasz et al. [3] investigated $\text{Ga}_{0.45}\text{In}_{0.55}\text{As}$ (3.7 nm) / $\text{GaAs}_{0.45}\text{Sb}_{0.55}$ (3.1 nm) SLs by absorption spectroscopy at 10 K and obtained $E_g^{\text{type-II}} = 0.27$ eV, $\Delta E_{VB} = 0.54$ eV and $\Delta E_{CB} = 0.65$ eV ($E_g^{\text{GaAsSb}} = 0.81$ eV and $E_g^{\text{GaInAs}} = 0.92$ eV). It is difficult to compare the results of the present study with the data reported in Ref. 3 and Ref. 4 since all investigated SLs have the different nominal compositions.

In conclusion, $(\text{Ga}_{1-x}\text{In}_x\text{As} - \text{GaAs}_{1-y}\text{Sb}_y)$ SLs were grown by MOCVD strain compensated onto InP. All samples showed excellent surface morphology with RMS-roughnesses less than 0.3 nm. The SL period was varied from 6.2 nm to 30 nm. X-ray rocking curves of all samples show well resolved SL diffraction peaks. FT-PL measurements reveal strong type-II emission beyond 2 μm at 10 K, which persists up to room temperature. Assuming a valence band discontinuity Q_V between $\text{Ga}_{0.42}\text{In}_{0.58}\text{As}$ and InP of 0.6 [6,7,10], the valence and conduction band offsets between $\text{Ga}_{0.42}\text{In}_{0.58}\text{As}$ and $\text{GaAs}_{1-y}\text{Sb}_y$ ($y \approx 0.2$ to 0.3) are estimated to be 0.21 eV and between 0.33 eV and 0.39 eV, respectively. The Sb incorporation into the $(\text{Ga}_{1-x}\text{In}_x\text{As} - \text{GaAs}_{1-y}\text{Sb}_y)$ SL was found to be smaller than in thick $\text{GaAs}_{1-y}\text{Sb}_y$ layers grown with identical growth parameters. This is due to the growth of $\text{Ga}_{1-x}\text{In}_x\text{As}$ layers in-between the $\text{GaAs}_{1-y}\text{Sb}_y$ layers which results in a higher As background in the MOCVD reactor chamber and therefore reduces the Sb incorporation into the SL.

Acknowledgments

We would like to thank K. Schwarz and H. GÜLICH for expert technical assistance in the FT-PL and the HRXRD measurements, respectively.

References

- [1] J. Waho, S. Ogawa, S. Maruyama, Jpn. J. Appl. Phys. **16**, 1875 (1979)
- [2] M.J. Cherng, G.B. Stringfellow, R.M. Cohen, Appl. Phys. Lett. **44**, 677 (1984)
- [3] G.A. Sai-Halasz, L.L. Chang, J.-M. Welter, C.-A. Chang, L. Esaki, Solid State Commun. **27**, 935 (1978)
- [4] J.F. Klem, S.R. Kurtz, A. Datye, J. Crystal Growth **111**, 628 (1991)
- [5] M.Peter, K. Winkler, M. Maier, N. Herres, J. Wagner, D. Fekete, K.H. Bachem, Appl. Phys. Lett. **67**, 2639 (1995)
- [6] C.G. Van de Walle, Phys. Rev. B **39**, 1871 (1988)
- [7] M.P.C.M. Krijn, Semicond. Sci. Technol. **6**, 27 (1991)
- [8] Landolt-Börnstein Bd. 22a, ed. O. Madelung, Springer Berlin, 1987
- [9] D.A. Dahl, Solid State Commun. **61**, 825 (1987)
- [10] R. Weihofen, G. Weiser, Ch. Starck, R.J. Simes, Phys. Rev. B **51**, 4296 (1995)
- [11] N. Watanabe, Y. Iwamura, Jpn. J. Appl. Phys. **35**, 16 (1996)
- [12] J. Shin, T.C. Hsu, Y. Hsu, G.B. Stringfellow, J. Crystal Growth **179**, 1 (1997)

MBE Growth and Optical Investigation of GaSb/AlSb VCSEL Structures for the $1.5\mu\text{m}$ Range

J. Koeth, R. Dietrich and A. Forchel
 Universität Würzburg, D-97074 Würzburg, Germany

We have investigated the growth of VCSELs based on the GaAlSb material system by solid source molecular beam epitaxy. Laser structures with different numbers of mirror layers have been analyzed by reflectivity experiments. We observe a systematic narrowing of the cavity resonance with increasing number of mirror layers down to a FWHM of 0.9 meV (50 K). The dependence of the FWHM of the cavity resonance on the number of mirror layers and the temperature dependence of the resonance energy are found to be in good agreement with results of transfer matrix theory calculations.

1 Introduction

Recently there has been an increasing interest in the GaSb material system caused by the search for novel emitters and detectors for the near and mid infrared. The most important material system for wavelengths in the range of telecommunication InGaAsP shows severe limitations for devices operating at wavelengths beyond $1.6\mu\text{m}$ as far as vertical cavity surface emitting lasers (VCSELs) are concerned. VCSEL structures are of particular interest for massively parallel optical transmission systems. In these structures a vertical cavity is formed by Bragg mirror layer stacks of materials with different refractive index. Low threshold lasers can be obtained for properly tuned cavities and Bragg mirror stacks with reflectivities in excess of 99.99%. Due to the rather small refractive index difference in the InGaAsP system this requires the growth of very thick ($11.5\mu\text{m}$, 45 InP/GaInAsP pairs [1]) lasers or the use of hybrid mirror laser structures [2].

Heterostructures based on GaAlSb permit to use a very large refractive index difference of up to 0.7 between the binary materials and therefore constitute very good candidates for VCSEL fabrication at telecommunication wavelengths and beyond. In the present paper we report the growth and the reflectivity characterization of these structures.

2 Growth of GaAlSb VCSELs

The present VCSEL structures were grown in an Eiko EV-100 S MBE with eight solid source Knudson cells. In order to grow layers with different Al contents the system is equipped with two Al Sources. As and Sb are provided by solid sources. The growth temperature was controlled by a pyrometer and especially at lower temperatures by a thermocouple. Prior to the growth of the buffer layer the surface oxide of the GaAs substrates was removed by heating the samples for one minute at 620°C under As pressure. The growth temperatures of the GaSb and $\text{Ga}_{0.86}\text{Al}_{0.14}\text{Sb}$ layers were about 500°C . For AlSb layers the substrate temperature was raised to 540°C . Growth rates for GaSb of about $1.07\mu\text{m}/\text{h}$, $1.17\mu\text{m}/\text{h}$ for $\text{Ga}_{0.86}\text{Al}_{0.14}\text{Sb}$ and of $0.45\mu\text{m}/\text{h}$ for AlSb were used.

Fig. 1 shows schematically the layout of a typical VCSEL structure. On top of a nominally undoped (100) oriented GaAs substrate a 300 nm thick GaAs buffer layer is deposited. On top of the buffer layer lies the bottom mirror with up to 15 alternating layers of AlSb (119 nm thick) and

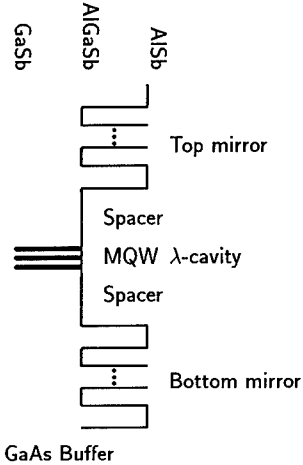


FIG. 1: Schematic bandstructure of a GaSb/AlSb VCSEL as presented here. The bottom mirror consists of up to 15 and the top mirror of 14 mirror pairs. The active region is a 9 nm multi quantum well (MQW).

of $\text{Ga}_{0.86}\text{Al}_{0.14}\text{Sb}$ layers (93 nm thick). Due to the large lattice mismatch of 7 % between GaSb and AlSb and GaAs the lower mirror contains a high density of misfit dislocations. On the lower Bragg reflector a one λ -cavity of $\text{Ga}_{0.86}\text{Al}_{0.14}\text{Sb}$ is grown, which includes in its center three GaSb quantum wells (thickness 9 nm), serving as active layers in the devices. The upper Bragg reflector includes similar mirror stacks as the bottom one. Due to the additional reflectivity at the surface, we typically grow the upper reflector with one mirror pair less than the lower one. $\text{Ga}_{0.86}\text{Al}_{0.14}\text{Sb}$ is used for the cavity and the low band gap/high refractive index sections of the mirrors in order to avoid absorption of the light emitted by the quantum wells. The complete structure is covered by a thin GaSb cap layer (5 nm) to avoid degradation due to Al oxidation.

3 Reflectivity Studies

VCSEL structures with different numbers of mirror pairs were characterized by reflectivity measurements using a standard halogen lamp as a light source. As a detector a LN_2 cooled Ge photoconductor connected to a lock-in amplifier was used. The reflectivity of the samples was calibrated with respect to that of an Au-coated mirror. For temperature dependent measurements the samples were mounted inside a variable temperature cryostat, which permitted investigation between 2K and room temperature.

Fig. 2a shows reflectivity spectra measured on a VCSEL structure containing 15 mirror pairs at the bottom Bragg reflector and 14 at the top. The spectra show a large stopband of about 100 meV between approximately 0.77 eV and 0.875 eV. In the center of the stopband a very sharp cavity resonance is observed. The FWHM of the cavity resonance at 50 K is 0.9 meV. With increasing temperature the stopband and the cavity resonance shift to lower energy due to the temperature dependence of the refractive indices of the cavity and mirror materials. Simultaneously the depths

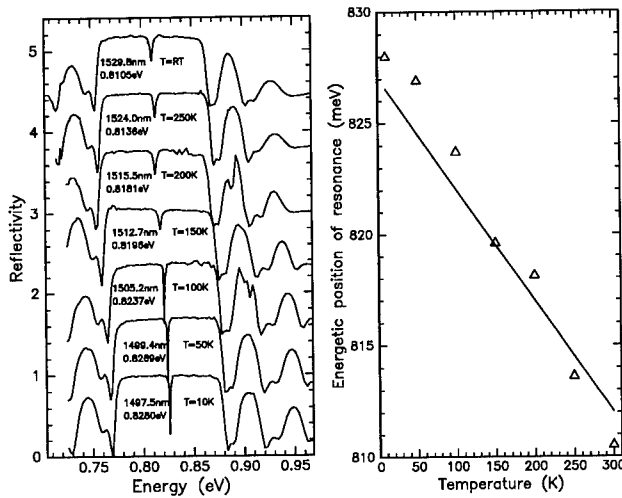


FIG. 2: a) Reflectivity spectra for several temperatures. The measured structure contains 15 bottom and 14 top mirrors. It has a large stopband of 100 meV and a narrow FWHM of the resonance peak of about 0.9 meV at a temperature of 50 K. b) Comparison of the measured values with transfer matrix theory.

of the resonance decreases and FWHM increases which arises due to differences in the temperature dependences of the refractive indices of cavity and mirrors.

Fig. 2b shows a comparison of the temperature dependence of the cavity resonance as determined from experiment with transfer matrix theory. Due to the rather weak temperature dependence of the refractive indices the shift of the cavity resonance between He and room temperature observed experimentally amounts only 18 meV.

In order to modell the data a values of

$$dn/dT = 1.14 \cdot 10^{-4} K^{-1}$$

has been used for the temperature dependence of the refractive index and the room temperature value of n [3]. For GaSb we used values of

$$1/n \cdot dn/dT = 9.7 \cdot 10^{-5} K^{-1}$$

from [4]. The value of the refractive index of $Ge_{0.86}Al_{0.14}Sb$ and of its temperature dependence have been interpolated linearly from the values for the binary systems. As can be seen from the good agreement of the experimental data and the calculated curve the observed temperature dependence of the resonance position can be described quantitatively by the calculations.

Fig. 3a shows on an enlarged scale the energetic region of the cavity resonance taken from reflectance spectra of samples with a varying number of mirror pairs. For the VCSEL structure

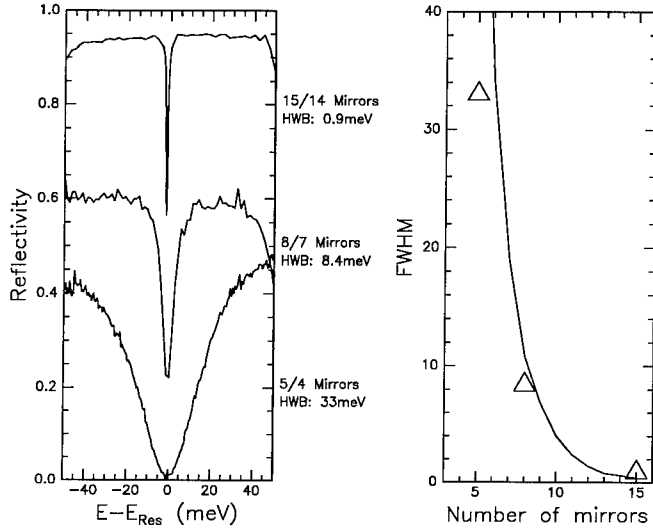


FIG. 3: a) Dependency of the FWHM from the number of mirror pairs. b) The solid line in the plot on right hand was calculated using matrix theory.

containing 5 bottom and 4 top mirror pairs (bottom trace in the figure) the cavity resonance has a very large halfwidths of 33 meV. As the number of mirror pairs is increased the FWHM decreases dramatically. For a VCSEL with 8 bottom and 7 top mirror pairs the resonance FWHM is 8.4 meV, which decreases to 0.9 meV for the structure with 15 and 14 mirror pairs in the top and bottom Bragg reflectors. The narrowing of the cavity resonance reflects the increase of the quality factor of the cavity with an increasing number of mirror pairs. Fig. 3b shows a comparison of the measured values of the FWHM of the resonances at 300 K with the results of transfer matrix calculations. The values of the refractive indices at 300 K were obtained as described above. We observe a very good agreement between the experimental results and the calculation.

References

- [1] F. S. Choa, K. Tai, W. Tsang, and S. N. G. Chu, *Appl. Phys. Lett.* **59**, 2820 (1991).
- [2] D. I. Babić *et al.*, *IEEE Photon. Technol. Lett.* **7**, 1225 (1995).
- [3] D. K. Ghosh, L. K. Samanta, and G. C. Bhar, *Infrared Phys.* **26**, 111 (1986).
- [4] Landolt-Börnstein, *Semiconductors: Physics of Group IV Elements and III-V Compounds*, Vol. III/17a of *New Series*, 1 ed. (Springer-Verlag, Berlin, Heidelberg, New York, 81).

Incorporation of Thallium in InTlAs and GaTlAs Grown by Molecular Beam Epitaxy

D. I. Lubyshev, W. Z. Cai, *G. L. Catchen, T. S. Mayer, D. L. Miller

Electronic Materials and Processing Research Laboratory, Department of Electrical Engineering,
The Pennsylvania State University, University Park, PA 16802

*Electronic Material and Processing Research Laboratory, Department of Nuclear Engineering,
The Pennsylvania State University, University Park, PA 16802

Abstract. Thallium incorporation in GaTlAs and InTlAs was systematically studied in solid source MBE by RHEED, Auger Electron Spectroscopy and X-ray diffraction as function of thallium concentration, substrate temperature and III/V flux ratio. Low temperature growth exhibits a (2x2) thallium-induced structure and also shows surface thallium accumulation. No evidence of binary TlAs formation was found. Auger electron spectroscopy measurements show limited thallium solubility in GaTlAs and InTlAs. X-ray diffraction measurements show the successful growth of epitaxial layers of TlGaAs with a molar fraction of Tl=0.05 and a second metal phase on the surface.

1. Introduction:

A new family of thallium-based III-V semiconductor compounds such as InTlP, InTlAs and InTlSb has been proposed recently as an alternative low band gap material system [1,2]. According to theoretical calculations, the stable zinc-blend binary compounds TlP, TlAs and TlSb, lattice mismatched less than 2% to InP, InAs and InSb, are semimetals with negative band gaps, similar to HgTe. Therefore these thallium alloys may be analogous to HgCdTe, spanning the far- and mid-infrared spectral regions. It has been predicted that the alloys $\text{In}_{0.33}\text{Tl}_{0.67}\text{P}$, $\text{In}_{0.85}\text{Tl}_{0.15}\text{As}$ and $\text{In}_{0.91}\text{Tl}_{0.09}\text{Sb}$ each reach a bandgap of 100 meV and are nearly lattice-matched to InP, InAs, and InSb, respectively, with $\delta a/a < 1\%$. However, there is currently little information about phase diagrams for these alloys [3], and there have been few reports of attempts to grow them. TlP, InTlP and InGaTlP have been grown successfully by gas-source molecular beam epitaxy [4,5] and also the $\text{In}_{1-x}\text{Tl}_x\text{Sb}$ system has been studied for $0 < x < 1$ in metal-organic chemical vapor deposition [6,7].

Thallium is a volatile material with a high equilibrium vapor pressure at low temperatures by molecular beam epitaxy (MBE) standards ($P = 10^{-6}$ torr at 350°C [8]), which stimulates thallium reevaporation from the grown surface even at low substrate temperatures. The covalent radius of the thallium valence -3 ion (0.095 nm) is bigger than the radius of either Ga or In (0.062 and 0.081 nm). This large covalent radius can enhance the accumulation and segregation of thallium on the growing surface, from which it can re-evaporate. This combination of segregation to the surface and re-evaporation can make it difficult to incorporate significant amounts of thallium into the layer. Fortunately, the molecular beam epitaxy technique can grow thermodynamically metastable compounds under strongly non-equilibrium conditions by using a very low substrate temperature and a large III/V element flux ratio.

In this work, we have studied thallium incorporation in InTlAs and GaTlAs grown by solid-source MBE. The thallium behavior was determined by reflection high-energy electron diffraction (RHEED), Auger electron spectroscopy (AES) and x-ray rocking-curve measurements. InTlAs was grown over InAs buffer layer, while GaTlAs was grown on both GaAs and InAs.

2. Experimental procedure:

We grew epitaxial layers using conventional solid-source MBE with As₄ and elemental column III metal sources. The incorporation of thallium in TlAs, InTlAs and GaTlAs was studied by the growth of epitaxial films over InAs and GaAs buffer layers on (100)-oriented surfaces. The substrate temperature was varied from 450°C to 150°C. The growth rate of InAs and GaAs was determined by observing RHEED oscillations and was set to 1.0 ML/s. The fluxes of Tl, Ga, In and As₄ were measured by a molecular beam flux monitor (ion gauge) which was rotated into the substrate position. The growth temperature was measured by a thermocouple located near to the substrate, calibrated from the temperatures of superstructure transitions on GaAs and InAs in ultrahigh vacuum [9] and also from the temperature of native oxide evaporation from GaAs.

The surface concentration of thallium was estimated from AES spectra taken *in situ*. The lattice parameter of the epitaxial films was determined by X-ray diffraction rocking curves of (400) and (511) reflections. Surface morphology was observed using optical microscopy with Nomarski contrast.

3. Attempts to grow the binary compound TlAs:

Substrate temperatures ranging from 450°C to 150°C, as well As/Tl beam flux ratios from 1500 to 100 were employed for synthesis of TlAs over InAs and GaAs. These beam flux ratios correspond to a much larger excess of arsenic than is typically used for the growth of GaAs or InAs. Reevaporation caused a rapid decrease of thallium sticking coefficient at temperatures above 350 °C. In this temperature range, the surface reconstruction of both GaAs and InAs transformed under a Tl flux from c(4x4) to (2x2), but we found no evidence of TlAs formation.

Reduction of substrate temperature to the range below 350 °C caused thallium to accumulate on the surface in form of metallic droplets. During epitaxial growth at these temperatures, the brightness of the RHEED pattern decreased monotonically with time, and the surface became covered by thallium droplets. The size and density of Tl droplets increased as substrate temperature was reduced and as the length of time increased during which Tl was deposited. It is interesting to note that reduction of the substrate temperature to 150 °C, which is less than the thallium melting point of 305°C, still results in thallium droplet formation. We suggest that this phenomenon be caused by a very high surface mobility of thallium adatoms.

To further clarify the interaction of thallium with arsenic flux on the InAs and GaAs surfaces, we deposited about ~ 0.5 ml of thallium in the absence of arsenic flux on these epitaxial surfaces at 300°C. This coverage of Tl converted the surface reconstruction from c(4x4) to (2x2) for both GaAs and InAs. We observed a strong reduction of the diffuse background in the RHEED patterns for these surfaces, which is typical of (4x2) metal-stabilized structures on GaAs and InAs. Cooling these samples in ultrahigh vacuum from 300°C to room temperature did not result in any observed changes in surface reconstruction. Maintaining this thallium stabilized-surface in an arsenic flux in the temperature range 300°C-20°C also caused no change in surface structure. The exposure of this surface to an arsenic flux at room temperature for a long time resulted only in arsenic accumulation. Increasing the substrate temperature to above 350°C rapidly converted the Tl-induced (2x2) structure to C(4x4) for GaAs and to (2x4) for InAs. RHEED patterns observed on InAs under Tl deposition are shown in Fig. 1a and Fig.1b. The surface structure after thallium desorption is shown in Fig.1c. Based on these measurements, we suggest that thallium on GaAs and InAs surfaces does not react with As₄ flux at temperatures below 350°C and is easily sublimed from these surfaces at temperatures above 350°C.

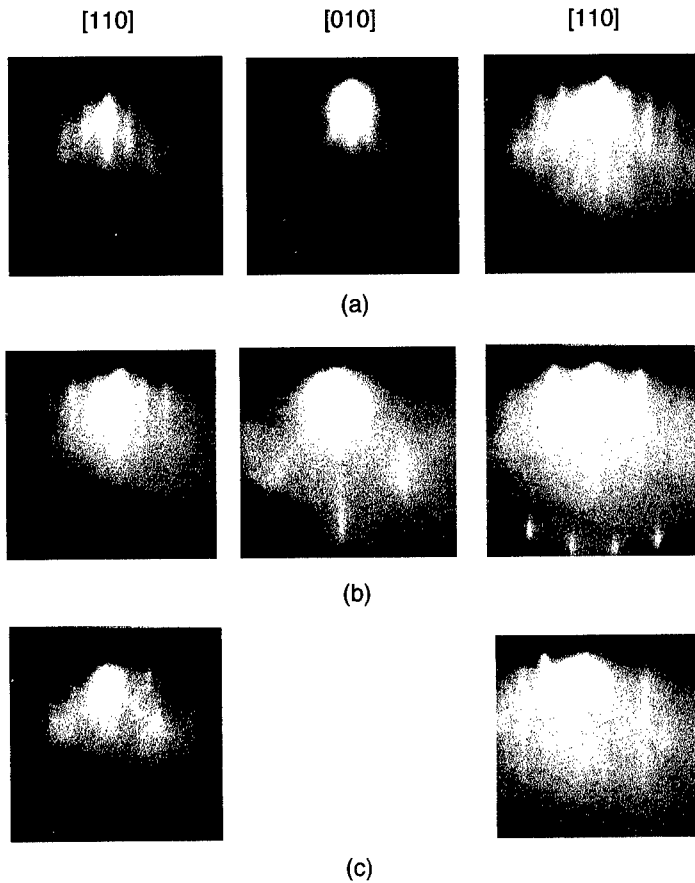


Fig.1. RHEED pattern of InAs surface, taken in along the [110], [010] and [110] azimuths: a)- before thallium deposition, b)- after deposition of 0.5 ml of Tl at 300°C and c)- after Tl desorption at 350°C

4. The growth of InTlAs and GaTlAs:

In an initial attempt to determine the solubility of thallium in InAs and GaAs, these compounds were grown on Tl-rich surfaces at 300 °C, a temperature at which no thallium reevaporation takes place. The surface concentration of thallium was measured *in situ* by AES following deposition of InAs and GaAs layers of increasing thicknesses. The AES measurements show a monotonic decrease of the thallium surface concentration as a function of InAs or GaAs deposition time (see Fig.2). Assuming that the surface thallium initially present either rides along the surface or is incorporated into the growing layer, we determined that the fractional solubility limit of thallium in InTlAs and GaTlAs at 300 °C is 0.006 and 0.009 respectively.

To synthesize InTlAs and GaTlAs with larger fractional Tl compositions, lower substrate temperatures were used. A series of samples was grown at $T_s = 180$ °C, 220 °C and 245 °C with a thallium molecular beam flux of about ~3% of the Ga or In beams (Tl source temperature 480 °C).

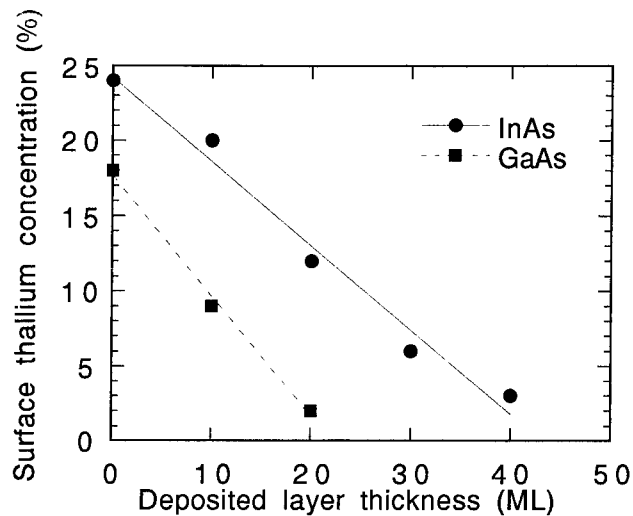


Fig.2. Thallium surface concentration dependence determined by AES as a function of deposited thickness of InAs and GaAs.

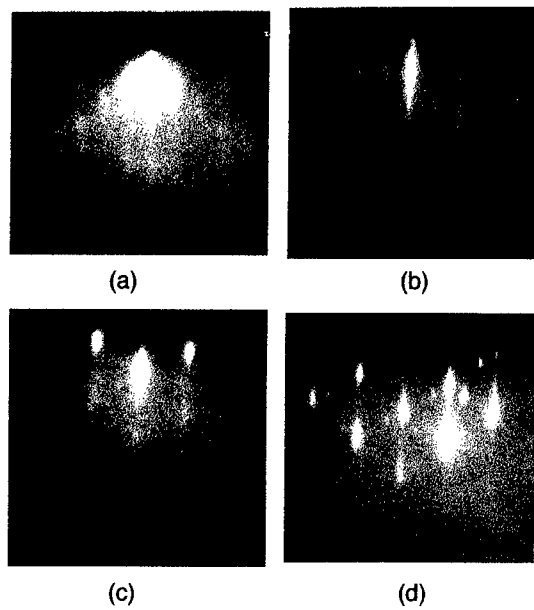


Fig.3. RHEED pattern of GaTlAs taken along the [110] azimuth a) before growth, b) after 5 min growth, c) after 20 min growth and d) after 30 min growth.

RHEED patterns and subsequent optical microscopy showed a rapid segregation of thallium on the growing surface in the form of Tl droplets when Tl/Ga or Tl/In ratios exceeded 0.03.

The evolution of the RHEED pattern of GaAs:Tl at 180 °C is shown in the Fig. 3. An initial arsenic-stabilized c(4x4) structure converted to a (2x2) Tl-induced structure during approximately the first five minutes of growth. As growth continued, the intensity of the RHEED pattern decreased due to thallium accumulation and surface roughening. Microtwin crystal formation was detected after deposition about 0.6 μm of GaTlAs. When growth took place at higher Ts, we observed only the transition to the Tl-induced structure and subsequent reduction of RHEED intensity due to Tl droplet accumulation, but no microtwins. Qualitatively similar RHEED behavior was observed during the growth of InTlAs.

The evolution of surface morphology as function of growth temperature for GaTlAs and InTlAs is shown in Fig.4. All epitaxial films have a thickness of 0.7 μm. No thallium droplets were found on GaTlAs surfaces grown at $T_s=180^\circ\text{C}$, but they were present on InTlAs grown at that temperature. At T_s increased, the size of droplets and the average distance between them expanded, which reflects an increase in the thallium surface diffusion length.

Fig.5 shows double-crystal X-ray diffraction (400) rocking curves for GaTlAs layers grown on GaAs substrates at $T_s=180^\circ\text{C}$, 220°C and 245°C . The peaks from the ternary alloys are clear visible, indicating thallium incorporation into the film. The peak separation is 623 arc sec for samples grown at $T_s=180^\circ\text{C}$, 617 arc sec for $T_s=220^\circ\text{C}$, and 160 arc sec for the sample grown at 245°C . The rapid reduction in peak separation as T_s increases reflects the redistribution of thallium away from incorporation into the solid and toward formation of Tl droplets. We estimate the maximum Tl molar fraction to be 2.5% in GaTlAs, based on a predicted TlAs lattice constant of 0.618 nm [1]. An increase of Tl/Ga flux ratio to ~0.06 (thallium source temperature 500 °C) caused an increase in Tl

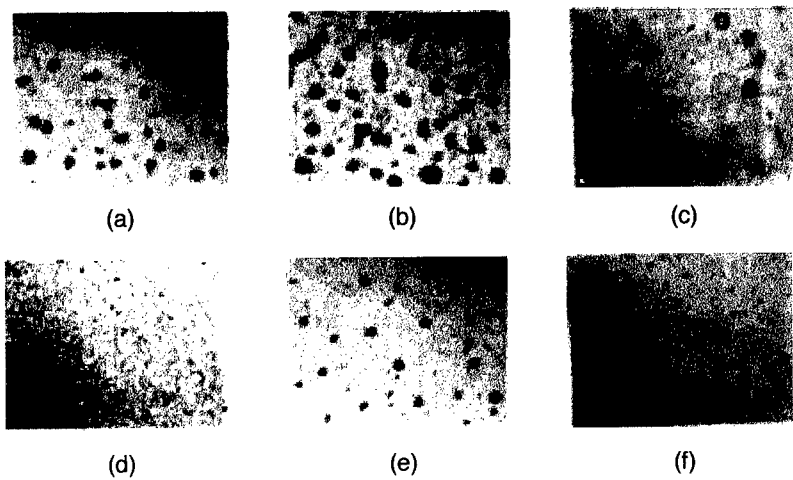


Fig.4. Surface morphology (x1000 with Nomarski contrast) of GaTlAs and InTlAs grown at three substrate temperatures: a) GaTlAs grown at $T_s=180^\circ\text{C}$, b) $T_s=220^\circ\text{C}$, c) $T_s=245^\circ\text{C}$, d) InTlAs grown at $T_s=180^\circ\text{C}$, e) $T_s=220^\circ\text{C}$, f) $T_s=245^\circ\text{C}$.

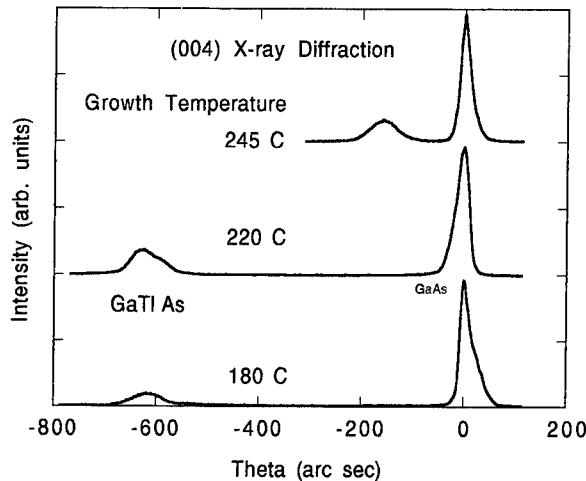


Fig.5. X-ray diffraction (400) rocking curves for GaTlAs, grown a)- at $T_s = 180^\circ\text{C}$, b)- at $T_s = 220^\circ\text{C}$ and c)- at 245°C .

droplet density and also an increase in peak separation in X-ray rocking curves to 1260 arc sec, which corresponds to a Tl molar fraction 0.05 in GaTlAs.

Since predicted lattice constant of TlAs is close to one of InAs, this makes difficult to apply X-ray technique for characterization of InTlAs. The bandgap determination of InTlAs and GaTlAs by photoluminescence and transmission measurements is stills in progress and will subject of separate paper.

5. Conclusion:

Using conventional solid source MBE with As_4 , we were not able to synthesize the binary compound TlAs. We have, however, grown GaTlAs and InTlAs for the first time using conventional solid source MBE. X-ray diffraction showed the successful growth of GaTlAs with a Tl molar fraction of 0.05. The typical MBE growth conditions for GaTlAs and InTlAs lie in a two-phase region, bounded by the ternary alloy GaTlAs (or InTlAs), and the liquid $\text{Ga}(\text{In})+\text{Tl}+\text{As}$. Thallium incorporation in the solid films suffers from the metal phase accumulation on the surface due to the very low stability of TlAs relative to the liquid phase and also due to differences between the atom covalent radii of Tl and Ga or In.

References:

- [1] M. van Shilfgaarde and A. Sher 1994, *Appl. Phys. Lett.* **65**, 2714 - 6
- [2] M. van Shilfgaarde A. Chen, S. Krishnamurthy , A. Sher, 1993 *Appl. Phys. Lett.* ,**62** ,1857-9.
- [3] T.B. Massalski, *Binary Alloy Phase Diagramms*, Vol. 1, 2 nd ed., ASM International, Materials Park, 1990, 350
- [4] H. Asahi, K. Yamamoto, K. Iwata, S. Gonda, K. Oe, 1996, *Jpn. J. Appl. Phys.* **35**, , L876-9
- [5] H. Asahi, M. Fushida, K. Yamamoto, K. Iwata, H. Koh, K. Asami, S. Gonda, K. Oe, 1997, *J. Crystal Growth*, **175**, 1195.
- [6] K. T. Huang, R. M. Cohen, G. B. Stringfellow, 1995, *J. Crystal Growth*, **156**, 320-6
- [7] P. T. Staveteing, Y. H. Choi, G. Labeyrie, E. Bigan and M. Razeghi, 1994, *Appl. Phys. Lett.*, **64**, 460-2
- [8] L. I. Maissel, *Handbook on thin film technology*, Ney York 1970, 1-17
- [9] V.V. Preobrazhenskii, D. I. Lubyshev and V. P. Migal, *Poverhnost*, 1989, 9, 156

Electronic Properties of MBE Grown GaAs Homointerfaces Fabricated Using the As Cap Deposition/Removal Technique

M. Passlack, R. Droopad, Z. Yu, C. Overgaard, B. Bowers, and J. Abrokwah

Motorola Phoenix Corporate Research Laboratories, 2100 East Elliot Road, Tempe, AZ 85284, USA

Abstract. High quality interfaces are the workhorse of the semiconductor industry. Structural and electronic interface properties have a significant impact on device performance. This paper investigates the effect of the As cap deposition/removal process on electronic interface properties. The electronic interface properties were investigated by photoluminescence power spectroscopy. It was found that the As cap deposition/removal process with wafer storage in air causes significant degradation of the electronic interface properties ($N_{it} \geq 10^{11} \text{ cm}^{-2}$) although structural degradation of the GaAs surface could not be observed. Thus, the impact on electronic interface properties needs to be considered when designing electronic or optoelectronic devices using the As cap deposition/removal process.

1. Introduction

For compound semiconductors such as GaAs, the fabrication of abrupt and atomically ordered interfaces is routinely performed using *in situ* overgrowth. Alternatively, the As cap deposition/removal technique was suggested to add flexibility to a variety of processes used in the compound semiconductor industry [1]. The latter technique is based on *in situ* deposition of an As cap layer which protects the wafer surface in the fabrication facility. Following wafer processing and/or storage, the As cap is thermally desorbed under As over pressure or in ultra-high vacuum (UHV) prior to overgrowth. While the thermal desorption of the As cap is preferentially done under As over pressure, the process of thermally desorbing the As cap was also investigated under UHV conditions. Previous *in situ* studies established that the As cap desorption technique can provide surface properties such as surface atomic order and roughness which are comparable to those of as-grown surfaces (e.g., [2]). Although electronic interface properties have a significant impact on device performance, there have been no reports on electronic properties of interfaces which were fabricated using the As cap deposition/removal technique.

In this article, we investigate the electronic properties of GaAs homointerfaces grown by molecular beam epitaxy (MBE) using the As cap deposition/removal technique. Interface properties such as surface recombination velocity S and interface state density N_{it} are reported and compared to those observed for *in-situ* grown GaAs homointerfaces.

2. Wafer Fabrication

The epitaxial layers were grown by MBE on 2-in n^+ (100) GaAs wafers. The layer sequence is shown in Fig. 1 for (a) the structure using the As cap deposition/removal process and (b) a standard reference structure. For the structure depicted in Fig. 1(a), the epitaxial growth was interrupted after completion of the

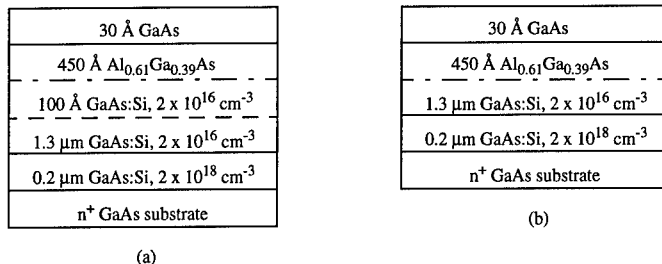


Fig. 1. Test structures using (a) the As cap deposition/removal process, and (b) a standard reference structure. The dashed and dashed-dotted lines indicate the GaAs homointerface and the AlGaAs-GaAs heterointerface, respectively.

1.3 μm thick GaAs active layer, an As cap was deposited under various conditions and the wafers were stored in ultra-high vacuum or air for 3 to 10 days. The deposition/storage conditions for the As cap layer are summarized in Table 1. Subsequently, the wafers were loaded into the growth chamber, the As cap was desorbed under As over pressure when the substrate temperature T_s was raised to 600 °C, and the layers above the dashed line in Fig. 1(a) were grown at $T_s = 600$ °C. The As desorption was monitored by reflection high-energy electron diffraction (RHEED). The standard reference structure shown in Fig. 1(b) was fabricated without growth interruption.

The doping concentration of the GaAs epitaxial layers was measured by an electrochemical profiling technique. The $\text{Al}_x\text{Ga}_{1-x}\text{As}$ thickness and composition were determined by x-ray diffraction, and the As cap layer thickness was verified by cross-sectional scanning electron microscopy (SEM).

Table 1. Parameters of As cap deposition/removal

Wafer #	As deposition conditions			As layer Thickness (Å)	Storage Conditions		RHEED after As desorption
	Substrate Temperature T_s *	Deposition Time t_s	As Species		Time (days)	Ambient	
298	90 °C	15 min	As ₄	n/d	3	UHV	streaky (2x4)
313	90 °C	15 min	As ₄	n/d	7	Air	streaky (2x4)
314	36 °C	15 min	As ₄	n/d	7	Air	streaky (2x4)
327	50 °C	15 min	As ₂	n/d	4	Air	streaky (2x4)
351	33 °C	60 min	As ₄	371	4	Air	streaky (2x4)
367	-1 °C	60 min	As ₄	1400	3	Air	streaky (2x4)
384	0 °C	150 min	As ₂	23800	3	Air	streaky (2x4)

n/d: not determined, * Thermocouple reading

3. Characterization of Electronic Interface Properties

We have introduced a photoluminescence power spectroscopy (PL-PS) technique as a standard tool to study interface recombination velocity S and to monitor the interface quality during device fabrication. The optoelectronic PL-PS method comprises the measurement of the photoluminescence spectra and the integrated intensity I_{PL} over a wide range of laser excitation power density P_0 . The subsequent analysis of the measured I_{PL} versus P_0 is based on a numerical Poisson and continuity equation solver for semiconductor heterostructures and provides the dependence of the internal quantum efficiency η on P_0 , the recombination velocity S and related quantities of interest such as interface state density N_{it} (in units of cm^{-2}) [3]. The technique is in particular advantageous for (i) systems with relatively small band discontinuities such as $\text{Al}_x\text{Ga}_{1-x}\text{As-GaAs}$ where capacitance-voltage measurements are impractical or inconclusive [3], and (ii) semiconductors with a small effective density of states such as GaAs ($N_C = 4.7 \times 10^{17} \text{ cm}^{-3}$). The latter advantage is illustrated in Fig. 2 which shows a simulated PL depth profile for an $\text{Al}_{0.61}\text{Ga}_{0.39}\text{As-GaAs}$ structure. Because of the strong degeneracy of the $0.2 \mu\text{m}$ thick buffer layer and the substrate ($N_D = 2 \times 10^{18} \text{ cm}^{-3}$), the PL signal emitted from the structure stems primarily ($\approx 88\%$) from the lightly doped epitaxial layer and substrate effects are virtually excluded. Also, the impact of the non-radiative lifetime of the epilayer is only marginal. Thus, the quantum efficiency depends mainly on two parameters only, namely (i) the radiative lifetime of the GaAs epilayer, and (ii) the nonradiative carrier lifetime at the interface [3]. The first parameter is easily determined from the doping concentration of the epilayer and the second parameter is used to fit the simulated results to the measurement.

The standard reference structure shown in Fig. 1(b) is designed such that S at the AlGaAs-GaAs interface (dashed-dotted line) can be inferred [3]. The structure depicted in Fig. 1(a) exhibits a second interface (dashed line), the GaAs homointerface which was fabricated using the As cap deposition/removal process. Since the homo- and heterointerfaces in Fig. 1(a) are separated by a distance which is

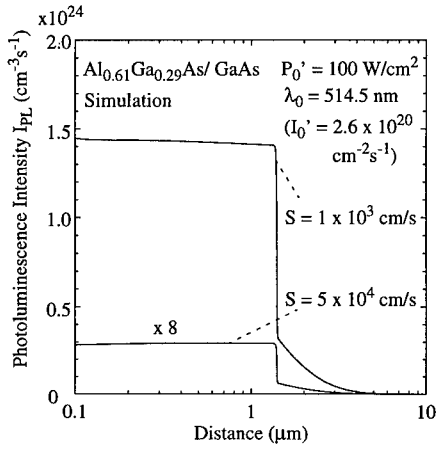


Fig. 2. Simulated PL depth profile of an $\text{Al}_{0.61}\text{Ga}_{0.29}\text{As-GaAs}$ structure. The GaAs surface is located at a distance of 100 nm .

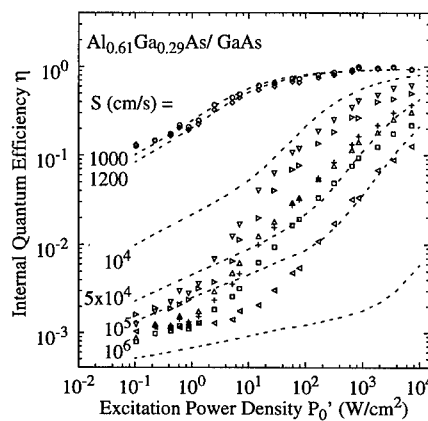


Fig. 3. Internal quantum efficiency as a function of excitation power density. The symbols show the measurement results; the dashed lines represent the simulation results with S as a parameter. The symbols are explained in Tab. 2.

much shorter than the minority carrier diffusion length ($L_{Dh} \approx 5 \mu\text{m}$), both interfaces virtually act as one source of interface nonradiative recombination S . Fig. 3 shows the measured and simulated internal quantum efficiency η as a function of excitation power density P_0 . The excitation wavelength λ_0 is 514.4 nm. Virtually identical results ($1000 \leq S \leq 1200 \text{ cm/s}$) have been obtained for the standard reference structure (diamonds) and the structure using the As cap deposition/removal process *and* UHV storage (circles). This clearly indicates that the GaAs homointerface is of better quality than the AlGaAs-GaAs heterointerface in this case and device performance will not be affected. However, the GaAs homointerface dominates $S (> 10^4 \text{ cm/s})$ for all structures using the As cap deposition/removal technique *and* air storage. Neither the deposition of a thicker As layer of up to $2.38 \mu\text{m}$ thickness (triangles left) or using As_2 instead of As_4 (squares and triangles left) improved the homointerface. The corresponding N_{it} at the GaAs homointerface for the latter structures is higher than 10^{11} cm^{-2} . The uniformity across a wafer and the wafer-to-wafer reproducibility are also affected as outlined in Table 2 which summarizes the results of the interface analysis. Note that the RHEED patterns observed on the UHV and air stored samples were virtually identical after As cap desorption indicating identical structural surface properties such as atomic order and roughness.

Table 2. Electronic interface properties

Wafer #	Symbol in Fig. 3	$S (\text{cm/s})$	$N_{it} (\text{cm}^{-2})$	Uniformity	Comments
309	Diamond	1000 - 1200	10^9 range	$\pm 2\%$	In-situ reference
298	Circle	1000 - 1200	10^9 range	$\pm 2\%$	As cap, UHV
313	Triangle up	$\approx 5 \times 10^4$	$> 10^{11}$	$\pm 20\%$	As cap, Air
314	Triangle down	$\geq 10^4$	$\geq 10^{11}$	$\pm 20\%$	As cap, Air
327	Square	$\approx 5 \times 10^4$	$> 10^{11}$	$\pm 20\%$	As cap, Air
351	Plus	$\approx 5 \times 10^4$	$> 10^{11}$	$\pm 20\%$	As cap, Air
367	Triangle right	$\geq 10^4$	$\geq 10^{11}$	$\pm 20\%$	As cap, Air
384	Triangle left	$\geq 10^5$	$> 10^{11}$	$\pm 20\%$	As cap, Air

4. Conclusions

In conclusion, the As cap deposition/removal process *and* storage in air causes significant degradation ($N_{it} \geq 10^{11} \text{ cm}^{-2}$) of the electronic interface properties of GaAs homointerfaces although identical, streaky RHEED pictures have been observed for wafers stored in UHV or air. Thus, the impact on electronic interface properties needs to be considered when designing electronic or optoelectronic devices using the As cap deposition/removal process.

References

- [1] Kowalczyk S P, Miller D L, Waldrop J R, Newman P G, and Grant R W 1981 *J.Vac.Sci.Technol.* 19, 255
- [2] Fan Y, Karpov I, Bratina G, Sorba L, Gladfelter W, and Franciosi A 1996 *J.Vac.Sci.Technol.* B14, 623-631
- [3] Passlack M, Hong M, Schubert E F, Zydzik G J, Mannaerts G P, Hobson W S, and Harris T D 1997 *J. Appl. Phys.* 81, 7647-7661

Arsenic Precipitation in GaAs for Single-Electron Tunneling Applications

C.-Y. HUNG, J. S. HARRIS, JR., A. F. MARSHALL*, AND R. A. KIEHL

Solid State Electronics Laboratory, CIS-X 328, Stanford University, Stanford, CA, 94305, USA

*Center for Materials Research, Stanford University, Stanford, CA 94305, USA

Abstract. Compositional control of precipitate position by preferential precipitation in a GaAs well sandwiched between low-temperature grown AlGaAs arsenic supply layers is examined for single-electron tunneling applications, where closely spaced particles a few nanometers in diameter are required. Control of small particles formed at low annealing temperatures where positional control is expected to be more difficult is examined. The use of a superlattice supply layer to intentionally increase the arsenic diffusion from the AlGaAs into the GaAs well is also examined. The results suggest useful directions for realizing controlled precipitation at scales of interest for single-electron tunneling applications.

1. Introduction

Nanometer-scale arsenic particles can be formed in GaAs by molecular beam epitaxy at low growth temperatures and subsequent high temperature annealing [1,2]. It has been shown that the position of particles in the growth direction can be controlled by composition while the lateral position can be controlled by strain produced by a surface stress structure. One-dimensional arrays of arsenic particles have recently been demonstrated by combining these effects in a patterned self-assembly process [3].

We are studying applications of this self-assembly technique to the fabrication of single-electron tunneling devices in which the arsenic particles serve as small metallic islands separated by GaAs tunneling barriers. For such applications, closely spaced particles a few nanometers in diameter are required, which is one order of magnitude smaller than used in Ref [3]. In this paper, we focus on issues concerning the effectiveness of compositional control for these applications. First, we examine the use of an arsenic supply layer comprised of an AlGaAs/GaAs superlattice (SL) to intentionally increase the diffusion of arsenic into the GaAs well. This experiment follows up on a previous report by Melloch et al for a short-period (5 nm) AlGaAs/GaAs LT superlattice layer in which virtually no precipitates formed [4]. Those authors suggested that precipitation is energetically unfavorable in such a SL because the layer thicknesses are less than the critical size for nucleation and that this leads to the diffusion of arsenic to adjacent layers. Second, we examine control of small particles (~ 4 nm). The diameter of arsenic precipitates in GaAs decreases with decreasing annealing temperature [4]. At the same time, the control of precipitate position is expected to be weaker at lower temperatures, due to the rapid decrease in the diffusion coefficient. Hence, in this case we examine compositional control as a function of annealing time.

2. Film Growth and Analysis Techniques

The films used in this work were grown in a Varian GEN. II MBE system on a two-inch diameter substrate. The grown rates were typically 0.15 $\mu\text{m}/\text{hr}$ and 0.27 $\mu\text{m}/\text{hr}$ for GaAs and AlGaAs, respectively. The ratio of group V to group III beam equivalent pressures used was 36, as measured with an ion gauge at the substrate growth position. A 200 nm thick epi-GaAs buffer layer was first grown to eliminate the defects from the substrate. Then, MBE grown structures containing three 200 °C low-temperature (LT) layers: 200 nm of AlGaAs, 10 nm of GaAs, and 50 nm of AlGaAs; followed by a thin InGaAs cap grown at 450 °C. For our purposes, the low temperature grown AlGaAs layers serve as "arsenic supply layers" for the thin GaAs well where preferential precipitation is desired. Samples were

capped by a SiN layer deposited at 350 °C by chemical vapor deposition and annealed at high temperature in the ambient of nitrogen and forming gas. Rapid thermal anneals (RTA) and furnace (quartz tube) anneals were used for the short-time anneal and long-time anneal, respectively. The distribution of arsenic precipitates in the structure was examined by transmission electron microscopy (TEM) in <110> cross section. The specimens were prepared by mechanical polishing, dimpling, and then standard Ar milling until perforation. All samples were examined in Philips CM20 and EM430 electron microscopes.

3. Results and Discussion

Precipitation in a structure with 5 nm period $\text{Al}_{0.8}\text{Ga}_{0.2}\text{As}/\text{GaAs}$ SL supply layers was compared to that in a control structure with uniform $\text{Al}_{0.4}\text{Ga}_{0.6}\text{As}$ supply layers after an 850 °C / 30 s anneal. The mole fraction in the SL supply layer was chosen to provide the same average mole fraction as the uniform supply layer. The cross-sectional <110> TEM image for the uniform supply layer sample in Fig. 1(a) shows precipitate-free regions ~40 nm wide around the GaAs well and a strong preferential precipitation in the well. In contrast, no precipitate-free regions were found in the SL structure, as shown in Fig. 1(b). The precipitate distribution is uniform with a high density of As precipitates formed in the AlGaAs/GaAs SL supply layer beneath the well, in contrast to earlier results for similar SL layers. A possible cause for the difference between the two sets of results is the higher AlAs mole fraction in the present superlattice ($\text{Al}_{0.8}\text{Ga}_{0.2}\text{As}$ vs $\text{Al}_{0.3}\text{Ga}_{0.7}\text{As}$). Because of the high mole fraction, arsenic diffusion into the well may be suppressed in our SL by a competing mechanism whereby the $\text{Al}_{0.8}\text{Ga}_{0.2}\text{As}$ layers act as arsenic diffusion barriers [5]. If this is the case, SL supply layers with an optimal, lower AlAs mole fraction should be useful in obtaining the desired enhancement in preferential precipitation.

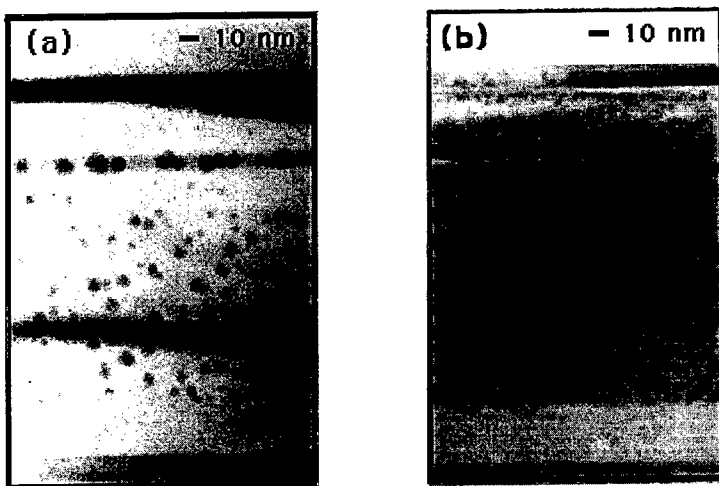


Fig. 1 Cross-sectional TEM showing precipitate distribution for a GaAs well surrounded by (a) uniform $\text{Al}_{0.4}\text{Ga}_{0.6}\text{As}$ supply layers and (b) $\text{Al}_{0.8}\text{Ga}_{0.2}\text{As} / \text{GaAs}$ superlattice supply layers. Both structures have the same average composition. The annealing cycle was 850 °C / 30 s.

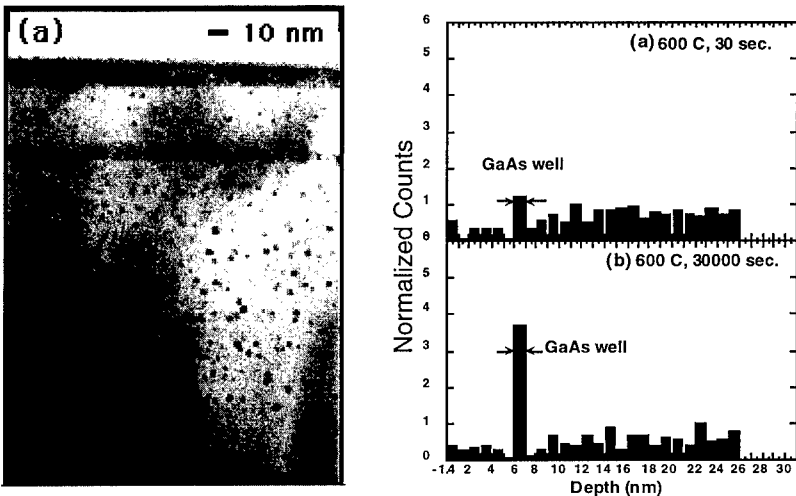


Fig. 2 (a) Cross-sectional TEM showing preferential precipitation in a GaAs well surrounded by Al_{0.4}Ga_{0.6}As supply layers for an annealing cycle of 600 °C / 30,000 s. Histograms showing the effect of annealing time on the precipitate distribution. The annealing time is 600 °C for (b) 30 seconds and (c) 30,000 s.

In the second experiment, samples were annealed at a low temperature of 600 °C, where small precipitates with diameters of approximately 4 nm form. Precipitate profiles were compared for 30 and 30,000 s anneals. In contrast to the strong compositional control seen in Fig. 1(a) for large precipitates (~14 nm) formed after a 30 s anneal at 850 °C, only a weak control was observed for 30 s at 600 °C, as shown in the histogram of Fig. 2(b). Increasing the annealing time by a factor of 1000, however, produces a significant improvement in preferential precipitation, as shown in the histogram and the <110> cross-sectional TEM image in Figs. 2 (a) and (c). These results demonstrate that strong compositional control can be obtained for small precipitates formed at low annealing temperatures, provided that the annealing time is sufficiently long.

Some comparisons can be made between the diffusion lengths involved in these experiments and those estimated from earlier work. Diffusion in these structures is a complicated process in that LTG GaAs and AlGaAs results in the incorporation of a high density of vacancies and other defects with concentrations greatly exceeding equilibrium values in addition to the large fraction of arsenic antisite defects. These enhance the diffusion process in LTG III-V materials and affect the rate of excess arsenic clustering. In addition, due to the annihilation of the supersaturated vacancies during the anneal, the density of vacancies decreases with time. Thus, there is strong time dependence for the diffusion mechanism for the LTG III-V materials. The time- and temperature-dependent diffusion length L_D for the interdiffusion of Al and Ga described by

$$L_D^2(t) = D_1 \tau \exp\left(-H_m/k_B T\right) \left[1 - \exp\left(\frac{-t}{\tau}\right)\right]$$

has been estimated from experimental data for interdiffusion in nonstoichiometric AlAs/GaAs quantum wells [6,7]. In the above formula, D₁ is the diffusion constant contributed from the supersaturated concentration of group III vacancies, 1/τ is the rate for the annihilation of the supersaturated vacancies, and H_m is the migration enthalpy for the group III vacancies. According to Lahiri et al observations [6], H_m has a value of 1.8±0.2 eV. Fitting their data with a temperature dependent τ and temperature independent D₁ we obtain : D₁ = 9.65x10⁻⁸ cm²/s and τ = 184 seconds at T = 600 °C and τ = 43 seconds

at $T = 850^\circ\text{C}$. Although D_1 would be different in the case of As antisite diffusion, the diffusion length for As antisites should have a proportional relationship with L_D since the diffusion of arsenic antisites during arsenic precipitation is also dominated by the motion of group III vacancies. Using the formula of L_D , the ratio of $L_D(600^\circ\text{C}, 30,000\text{s}) / L_D(850^\circ\text{C}, 30\text{s})$ is found to be 0.2, meaning that the diffusion lengths of excess arsenic for the $600^\circ\text{C} / 30,000\text{s}$ case would be expected to be about 1/5 of that for the $850^\circ\text{C} / 30\text{s}$ case. While an accurate quantitative estimate of diffusion lengths is not possible from our experimental data, comparison of Figs. 1 (a) and 2 (a) and of the histograms for the two cases indicates that this estimate is in line with our results.

4. Conclusion

We have examined compositional control of precipitate position by preferential precipitation in a GaAs well sandwiched between low-temperature grown AlGaAs arsenic supply layers for potential use in fabricating closely spaced particles a few nanometers in diameter. Our results show that, despite the reduced diffusion at low annealing temperatures, strong compositional control can be obtained for small precipitates provided that the annealing time is sufficiently long. This suggests that it should be possible to scale self-assembly processes based on controlled precipitation to the small particle regime. It was found that a superlattice containing high AlAs mole-fraction layers is not effective as an arsenic supply layer, apparently because of the reduced arsenic diffusion through high mole-fraction barriers. The desired enhancement in preferential precipitation may be possible, however, with optimized superlattice parameters.

Acknowledgments

This work was supported by ONR/DARPA through contract N00014-96-1-0983. Support from Fujitsu Laboratories, Ltd. is also gratefully acknowledged.

References

- [1] Melloch M R, et al. 1990 *Appl. Phys. Lett.* 57 1531-33
- [2] Mahalingam K, et al. 1991 *Journal od Vac. Sci. and Technol. B9* 2328-2332
- [3] Kiehl R A, et al. 1996 *Appl. Phys. Lett.* 68 478-480
- [4] Melloch M R, et al. 1992 *Mat. Res. Soc. Symp. Proc.* 241 113-124
- [5] Yin L-M, et al 1992 *Mater. Res. Soc. Symp. Proc.* 241 181
- [6] Lahiri I, et al. 1996 *Appl. Phys. Lett.* 69 239-241
- [7] Melloch M R, et al. 1996 *Critical Reviews in Solid State and Mat. Sci.* 21 189-263

GaAs Surface Passivation with MBE Grown GaS Thin Film

Naoya Okamoto, Naoki Hara, Mitsunori Yokoyama, and Hitoshi Tanaka

Fujitsu Laboratories Ltd. 10-1 Morinosato-Wakamiya, Atsugi, Kanagawa 243-01, Japan

Abstract. We report on the successful GaAs surface passivation with GaS thin film grown by MBE employing the single precursor, tertiarybutyl-galliumsulfide-cubane ($[(t\text{-Bu})\text{GaS}]_4$). GaAs bandgap PL intensity increased by passivating with GaS and has been maintained for a year. Furthermore, we investigated the relationship between the interface state density and the GaAs surface reconstruction before GaS passivation. The PL intensity for c(4x4)As was largest among the surface reconstructions investigated. Also, a minimum interface state density as low as $5 \times 10^{10} \text{ eV}^{-1}\text{cm}^{-2}$ was obtained for an Al/GaS/n-GaAs MIS structure of c(4x4)As. In addition, we demonstrated the feasibility of GaS passivation for device applications.

1. Introduction

In the field of III-V compound semiconductors, MISFETs such as Si MOS devices have not yet been made practical. This is caused by the poor quality of insulator/semiconductor structures because of a large state density that is generated at the interface. Therefore, although GaAs has a high potential, i.e., a higher electron mobility than Si, it is not enough to draw performance in the views of power consumption and circuit integration. Hence, trials to reduce the interface state density were performed using various methods [1-3]. Among them, cubic GaS near-epitaxially grown on GaAs using the single precursor, tertiarybutyl-galliumsulfide-cubane ($[(t\text{-Bu})\text{GaS}]_4$), by MOCVD is an attractive passivation material [4-6]. However, the vapor pressure of the precursor is very low, and the sublimation temperature of 225°C is too high for the precursor of MOCVD. Therefore, we regard MBE as superior to MOCVD for GaS growth on GaAs using this precursor. In this paper, we report on the successful GaAs surface passivation with MBE grown GaS thin film employing the single precursor. Furthermore, we demonstrate the feasibility of GaS passivation for device applications.

2. Experiment

Our equipment consisted of a conventional MBE and our own designed gas handling system. The single precursor, $[(t\text{-Bu})\text{GaS}]_4$, which is a stable white powder, was loaded in a PBN crucible. We used an $(\text{NH}_4)_2\text{S}_x$ solution for *ex-situ* S-termination. Furthermore, trisdimethylaminoarsine (TDMAAs) and bisdimethylaminochloroarsine (BDMAAsCl) were used as GaAs surface cleaning gasses. We also used ditertiarybutylsulfide (DTBS) as the *in-situ* S-terminating gas. We used *epiready* GaAs (100) substrates and MOCVD grown n-GaAs epitaxial layers. During GaS growth, the substrate temperature (T_s) was kept at 400 to 420°C and the cell temperature was 70 to 120°C. The GaS growth rates were 30 to 50 nm/h. We observed the GaAs surface reconstructions by RHEED. GaS/undoped GaAs structures were evaluated by PL measurements at room temperature (RT). We estimated the interface

state density of Al/GaS/n-GaAs MIS structures by Terman's method [7] of the 100 kHz C-V characteristics at RT.

3. Results and Discussion

3.1 Long-term stability of GaAs bandgap PL intensity of GaS passivated GaAs

First, we used $(\text{NH}_4)_2\text{S}_x$ pre-treated (55 °C, 15 minutes) and untreated GaAs semi-insulating substrates. GaS films were grown on these wafers after being heated in the growth chamber without As overpressure at a Ts of 575 °C for 10 minutes. Figure 1 shows the long-term stability of the GaAs bandgap PL intensity of 90 nm-thick GaS/undoped GaAs. By passivating with GaS, the PL intensity increased about 40 and 20 times, for $(\text{NH}_4)_2\text{S}_x$ pre-treatment and only thermal cleaning without As, respectively, compared with that of untreated GaAs. This indicates that GaS passivation suppresses non-radiative recombination due to the interface state. Furthermore, the PL intensity of GaS-passivated GaAs has not been seen to degrade over the period of a year. However, the PL intensity of GaS-removed GaAs gradually degraded. These results imply that GaS is a long-term, stable passivation material for GaAs.

By Terman's method, the interface state density of a MIS structure for thermal cleaning without As was estimated to be $2 \times 10^{11} \text{ eV}^{-1}\text{cm}^{-2}$ near the GaAs midgap. However, this value is still too large to be applicable to MISFETs. According to SIMS analysis, a high density (mid 10^{13} cm^{-2}) of impurities (especially oxygen) existed at the interface of a GaS/GaAs structure for thermal cleaning without As. As a result, the residual impurities interfered with the reduction of the interface state density.

So far, we performed GaAs surface cleaning by TDMAAs and BDMAAsCl [8]. In this case, wafers were cleaned at a Ts of 500 °C using 0.5 sccm TDMAAs for 15 minutes. After TDMAAs cleaning, the wafers were etched by a gas mixture of 0.1 sccm BDMAAsCl and 0.4 sccm TDMAAs at a Ts of 500 °C for five minutes, corresponding to an etching depth of about 5 nm. This method can reduce the interfacial oxygen density of a GaS/GaAs structure by two orders of magnitude over thermal cleaning without As.

3.2 Relationship between interface state density and GaAs surface reconstruction

After cleaning GaAs surfaces by TDMAAs and BDMAAsCl, we controlled the GaAs surface reconstructions such as c(4x4)As, (2x4)As, and (2x1)S using TDMAAs and DTBS. We will describe the details of the preparation methods for surface reconstruction elsewhere [9]. Figure 2 shows the

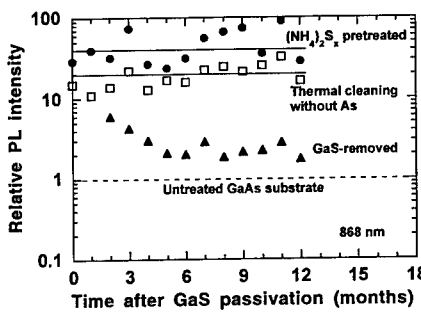


Fig. 1. GaAs PL intensity of GaS/GaAs structures.
PL intensity is normalized to that of untreated GaAs.

surface reconstruction dependence of the GaAs bandgap PL intensity of GaS/undoped GaAs structures. The relative PL intensity was plotted after normalizing to the maximum PL intensity of an untreated GaAs substrate. We observed that the PL intensity for c(4x4)As was the largest among the surface reconstructions we investigated. We had expected that *in-situ* S-termination would increase the PL intensity the most, because S molecules/atoms generated from DTBS must passivate the GaAs surface more completely than GaS molecules generated from [(t-Bu)GaS]₄. However, the *in-situ* S termination by DTBS did not further improve the PL intensity.

Next, we fabricated an Al/GaS/n-GaAs MIS structure on MOCVD grown n-GaAs layers (500 nm, $9 \times 10^{16} \text{ cm}^{-3}$). The GaS thickness was 50 nm, and the capacitor area was $3.14 \times 10^4 \text{ cm}^2$. Figure 3 shows the high-frequency C-V characteristics of the MIS structure for c(4x4)As. The solid and dashed lines show the experimental data and an ideal curve, respectively. We obtained an interface state density as low as $5 \times 10^{10} \text{ eV}^{-1} \text{ cm}^{-2}$ near the midgap for c(4x4)As. Whereas, for (2x4)As, it was $1.8 \times 10^{11} \text{ eV}^{-1} \text{ cm}^{-2}$. Apparently the optimum surface reconstruction was c(4x4)As. These results correspond to the PL results shown in Figure 2. Also, the surface potential calculated from the capacitance at a zero bias voltage was about 50 meV at the depletion, which implies a very small band-bending due to the elimination of Fermi level pinning at the Al/GaS/n-GaAs interface.

3.3 GaS/GaAs MISFET

The bandgap of MOCVD grown GaS was reported to be above 3.5 eV [6]. We fabricated a GaS/GaAs MISFET to confirm the effects of GaS passivation. The surface reconstruction of the MESFET structure before the GaS growth was controlled to be c(4x4)As. We grew a 25 nm-thick GaS film on a MOCVD grown MESFET wafer, which consisted of an n-GaAs active layer (160 nm, $3 \times 10^{17} \text{ cm}^{-3}$) and an undoped AlGaAs buffer layer. The sheet resistance of the MESFET wafer was determined to be $1.6 \text{ k}\Omega/\square$ by eddy current measurements. By passivating with GaS, the sheet resistance decreased to $1 \text{ k}\Omega/\square$. This was attributed to the remarkable reduction of the depletion layer width from the surface. We fabricated a MISFET and a MESFET with the same process for a direct comparison. These FETs consisted of a WSi gate and source/drain contacts formed by alloyed AuGe/Au. The gate

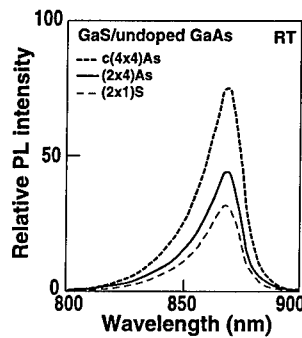


Fig. 2. Dependence of PL intensity for GaS/undoped GaAs on surface reconstructions before GaS passivation.

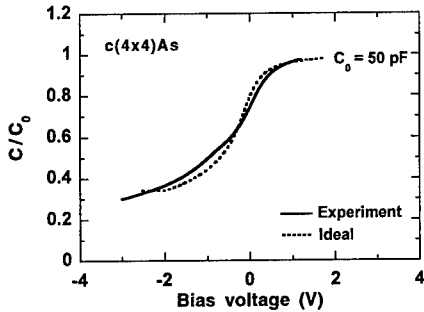


Fig. 3. 100 kHz C-V characteristics of Al/GaS/n-GaAs MIS structure for c(4x4)As.

widths were 10 μm and the gate lengths were 0.8 μm . The gate turn-on voltage (V_f), which is defined as the voltage at which the leakage current density exceeds 1 $\mu\text{A}/\mu\text{m}$, was 0.4 V for the MESFET. However, the V_f of the MISFET increased up to 1.4 V. Figure 4 shows the drain current versus drain-source voltage characteristics of the MISFET and the MESFET. The gate bias (V_g) was varied from 0 to -3 V in 0.5 V steps. The threshold voltage (V_{th}) of the MISFET was -2.7 V, while that of the MESFET was -1.5 V. The both transconductances were 60 to 70 mS/mm. The saturated drain current of the MISFET at a V_g of 0 V was larger than that of the MESFET, and did not change even when increasing V_g to a forward voltage. This result is further evidence that the surface band-bending was flat.

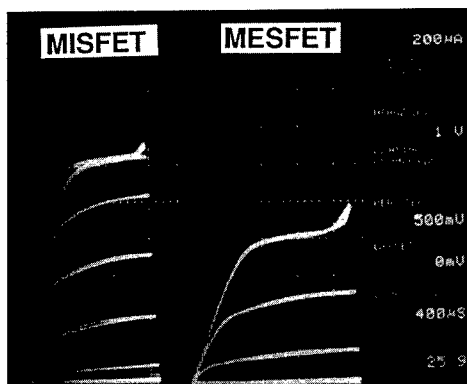


Fig. 4. Drain current vs. drain-source voltage characteristics of GaS/GaAs MISFET and GaAs MESFET.

4. Conclusion

We demonstrated a successful GaAs surface passivation with MBE grown GaS thin film using the single precursor, [(t-Bu)GaS]₄. By GaS passivation, the GaAs bandgap PL intensity increased and has remained steady for a year. Among the various GaAs surface reconstructions before GaS passivation, the highest PL intensity and the lowest interface state density ($5 \times 10^{10} \text{ eV}^{-1}\text{cm}^{-2}$) were obtained with c(4x4)As. Furthermore, we demonstrated the feasibility of GaS passivation for device applications.

Acknowledgements

The authors are grateful to T. Takahashi and T. Tanaka for their discussions, and would like to thank K. Fukuzawa, T. Kurihara, K. Atsuta, and T. Sato for technical assistance. We also thank H. Nishi and M. Takikawa for their encouragement.

References

- [1] Passlack M, Hong M, Mannaerts J.P, Opila R.L, Chu S.N.G, Moriya N, and Ren F 1997 *IEEE Trans. Electron Devices* **44** 214.
- [2] Kodama S, Koyanagi S, Hashizume T and Hasegawa H 1995 *J. Vac. Sci. Technol. B* **13** 1794.
- [3] Chen Z, Park D.G, Stengal F, Mohammad S.N and Morkoc H 1996 *Appl. Phys. Lett.* **69** 230.
- [4] MacInnes A.N, Power M.B, Barron A.R, Jenkins P.P and Hepp A.F 1993 *Appl. Phys. Lett.* **62** 711.
- [5] Tabib-Azar M, Kang S, MacInnes A.N, Power M.B, Barron A.R, Jenkins P.P, and Hepp A.F 1993 *Appl. Phys. Lett.* **63** 625.
- [6] Jenkins P.P, MacInnes A.N, Tabib-Azar M and Barron A.R 1994 *Science* **263** 1751.
- [7] Terman L.M, 1962 *Solid State Electron.* **5** 285.
- [8] Okamoto N and Tanaka H 1997 submitted to *J. Vac. Sci. Technol.*
- [9] Okamoto N and Tanaka H 1997 submitted to *Jpn. J. Appl. Phys.*

Simulation of Chemical Beam Epitaxy with Triethylgallium and Tris(dimethylamino) Arsine

B. Q. Shi^{a)} and C. W. Tu^{b)}

a) Department of AMES/Chemical Engineering

b) Department of Electrical and Computer Engineering
University of California, San Diego, La Jolla, CA 92093

Abstract. A reaction model for the epitaxial growth of GaAs by chemical beam epitaxy using triethylgallium and tris(dimethylamino) arsine is presented. The model is developed by properly combining surface decomposition mechanisms of the two metalorganic species. Computer simulations based on the model are carried out to make comparison with the experimental observations for this growth system. The model is shown to provide very good agreement with the growth kinetics observed.

1. Introduction

The mechanism of GaAs growth using the ultra-high vacuum (UHV) technique of metalorganic molecular beam epitaxy (MOMBE) with solid arsenic and triethylgallium (TEGa) has been extensively investigated in recent years. Robertson et al. [1] proposed a stepwise mechanism for TEGa decomposition, estimated the relative magnitudes of the kinetic parameters, and fitted these parameters to observed GaAs growth rates. The data for the incident flux in monolayer per second (ML/s) corresponding to one mass flow controller (MFC) setting was obtained by including the flux as a fitting parameter along with the kinetic parameters. The incident fluxes at other flow rates were then derived by scaling as were done experimentally. Donnelly and Robertson [2] extended Robertson's previous model by including new reactions and Arrhenius parameters reported in UHV studies. Foord et al. [4-6] developed a numerical model of GaAs MOMBE growth with TEGa and As₂. Their model included physical effects, which had been partially or totally neglected in earlier studies, involving site-blocking effects, lateral interactions between adsorbed species and a role for chemisorbed As in inhibiting growth. The most important criterion used by them in the determination of the kinetic parameters for TEGa decomposition was that they simulate satisfactorily the temperature programmed desorption (TPD) and other experimental surface-science data of Murrell et al. [4].

Tris(dimethylamino) arsine (TDMAAs) is believed to be a promising alternative to the toxic, gaseous arsine [7]. Epitaxy of III-V semiconductors with TDMAAs has shown that it possesses unique and superior characteristics for lowering background carbon incorporation, improving electrical properties of semiconductors and *in situ* etching [8-9]. In this paper we report a reaction model of chemical beam epitaxy of GaAs with TEGa and TDMAAs.

2. Triethylgallium and Tris(dimethylamino) arsine surface decomposition

The reactions chosen to describe TEGa decomposition on a GaAs(100) surface and assumptions in chemical physics for deriving reaction rates are identical to those outlined by Foord et al. [6]. The arguments presented by them for developing their model were based on surface spectroscopic data.

The coverage terms for reactions (4) and (6) of their report are modeled as $\theta_{\text{DO}}\theta_{\text{E}}/(1-\theta_{\text{DEGa}})$ and $\theta_{\text{DO}}(1-\theta)/(1-\theta_{\text{DEGa}})$ in our model respectively, where θ_{E} , θ_{DEGa} and θ_{DO} are dimensionless surface coverage [10-11] of ethyl radicals, DEGa and nearest neighbor pairs formed by adsorbed DEGa and non-DEGa species respectively with θ being the dimensionless total surface coverage. The reaction kinetic parameters for TEGa decomposition are taken from their report [6], which were derived from temperature programmed desorption data of TEGa.

Shi and Tu [7] recently reported a kinetic model for TDMAAs decomposition on a Ga(100) surface. They demonstrated that the model can explain well the behavior of desorption data from surface science studies of TDMAAs thermal decomposition on a GaAs(100) surface. The kinetic parameters were derived based on TPD data reported in literature. The kinetic model is incorporated into the reaction model we are reporting.

3. Reaction schemes for TEGa and TDMAAs interactions on GaAs surfaces

Co-dosing experiments carried out by Salim et al. [13] with TDMAAs and trimethylgallium or deuterium-labeled trimethylgallium ($\text{Ga}(\text{CD}_3)_3$) revealed that methane and methylarsenic were major reaction products in addition to nitrogen-containing species, specifically methylmethylenimine ($\text{H}_2\text{C}=\text{NCH}_3$) and dimethylamine ($\text{HN}(\text{CH}_3)_2$). Since the recombination reaction of an ethyl radical with a hydrogen atom is included in the TEGa decomposition model, the effect of TDMAAs as a hydrogen atom provider on GaAs growth is thus explicitly taken into account with the TDMAAs decomposition model we developed. Evidence of desorption of ethyl-arsenic radicals was found using mass spectroscopy during GaAs growth with TEGa [14], but these species were present in concentrations several orders of magnitude lower than ethylene (C_2H_4). Reactions between adsorbed arsenic atoms and ethyl radicals are ignored in our model.

Before Salim et al.'s work [13], it had been hypothesized that CBE GaAs growth with TMGa and TDMAAs involves a simple transfer of methyl from TMGa to the dimethylamine, leading to the formation of the stable compound, trimethylamine ($\text{HN}(\text{CH}_3)_3$). But no trimethylamine was detected as a surface reaction product in their experimental investigation. Based on their finding we suppose that interactions between dimethylamino ligands of TDMAAs and TEGa or its decomposition products including ethyl radicals are not important and assumed not to occur.

The GaAs growth rate is equated to the rate at which adsorbed TEGa species become converted to surface Ga. It is also assumed in our model that with every Ga atom incorporated into the lattice of a substrate, an adsorbed arsenic atom is also incorporated into the lattice, yielding an empty surface site. Apart from the role as a provider of surface hydrogen atoms which TDMAAs species play, they affect the growth rate also by occupying surface sites and therefore inhibiting TEGa adsorption and decomposition processes. TDMAAs decomposition is also dependent on the growth rate since Ga incorporation into the lattice depletes adsorbed arsenic atoms and TDMAAs surface decomposition critically depends on the number of surface sites available.

4. Simulation, experiment and comparison

Experimental growth rates were measured by means of *in situ* intensity oscillations of reflection high-energy electron diffraction (RHEED). In our experiment, TEGa is introduced into the growth chamber

through a vapor source mass flow controller, while TDMAAs is carried by hydrogen and injected into the chamber through a leak valve. Detailed experimental procedures have been reported elsewhere [8]. The absolute TDMAAs fluxes in ML/s were determined by measuring group-V induced growth rates when the substrate temperature was somewhere between 420 °C and 470 °C. The incident flux of TEGa in ML/s corresponding to one flow rate was obtained by treating the flux as a fitting parameter to reproduce the profile of growth rate vs. substrate temperature, while incident fluxes at other flow rates were then calculated by means of linear scaling.

Fig. 1 shows the simulated variation of the growth rate with the substrate temperature corresponding to the growth conditions of Tu et al. [8]. Also displayed are the experimental data points reported by them. The TDMAAs flux used, 1.7 ML/s, was read from Fig. 4 of their paper. An incident flux of 1.45 ML/s corresponding to TEGa MFC setting at 0.5 sccm was found to agree well with the experimental data. As described above, the kinetic parameters of this reaction model were all obtained based on data from surface-science desorption studies. Yet, with the TEGa incident flux as the only adjusting parameter, variation of the GaAs growth rate with the substrate temperature is reproduced.

Fig. 2 gives simulated growth rates under a different set of incident fluxes of TEGa and TDMAAs. The TDMAAs ML/s flux, 0.79 ML/s, was determined experimentally as discussed above. With TEGa MFC setting at 0.3 sccm, a linear scaling gives us the value of the absolute TEGa incident flux, which is 0.87 ML/s. We can see from Fig. 2 that even without any adjustable parameters, the simulated growth rate as a function of substrate temperature agrees very well with the experimental data.

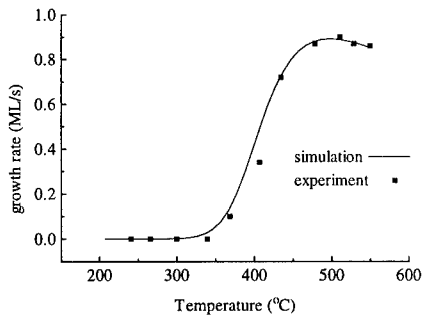


Fig. 1. growth rate as a function of substrate temperature. TEGa = 0.5 sccm and TDMAAs = 1.7 ML/s

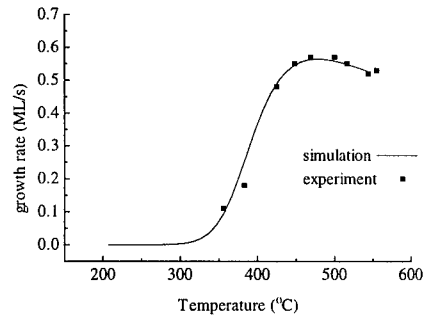


Fig. 2. growth rate as a function of substrate temperature. TEGa = 0.3 sccm and TDMAAs = 0.79 ML/s.

Fig. 3 displays coverage of surface species under incident fluxes of Fig. 1. The surface coverage of the parent molecules (TEGa and TDMAAs) is very small because they dissociate immediately once chemisorbed onto a GaAs(100) surface. The intermediate decomposition products $\text{Ga}(\text{C}_2\text{H}_5)_2$ and $\text{As}(\text{N}(\text{CH}_3)_2)_2$ also decompose quickly and thus exhibit small surface concentrations. Surface species which have relatively longer lifetimes are chemisorbed As atoms, ethyl radicals and mono-dimethylamino arsine ($\text{AsN}(\text{CH}_3)_2$). The coverage of $\text{AsN}(\text{CH}_3)_2$ and As is significant up to 420 °C. Since the TEGa decomposition chemistry depends on the number of surface sites available, the agreement in the growth rate with experiment as shown in Figs. 1 and 2 implies that this reaction

model delineates the underlining surface chemistry well and that the TDMAAs kinetic model can well be applied to simulate epitaxial growth in addition to its ability to reproduce the behavior of desorption data from surface science studies of TDMAAs thermal decomposition.

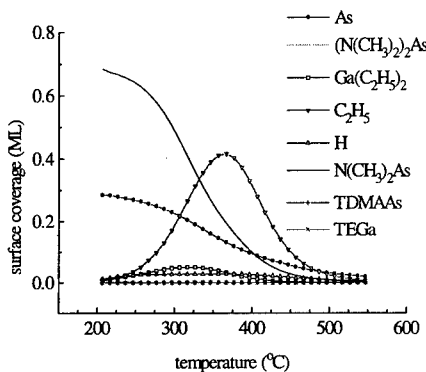


Fig. 3. Surface coverage as a function of substrate temperature during GaAs growth.

5. Summary

We have reported a GaAs CBE reaction model. This model is different from the GaAs epitaxial growth models which have been reported in literature in that it involves surface decomposition and interaction of two metalorganic species, each of which possesses complicated surface decomposition kinetics. We have demonstrated that properly combining reaction mechanisms derived from surface-science desorption studies enables us to predict well the growth rate without adjustable parameters.

6. Acknowledgment

This work is partially supported by the Air Force Wright Laboratory.

7. References

- [1] Robertson Jr. A, Chiu T H, Tsang W T and Cunningham J E 1988 *J. Appl. Phys.* **64** 877-887
- [2] Donnelly V M and Robertson Jr. A 1993 *Surface Science* **293** 93-106
- [3] Liang B W and Tu C W 1990 *Appl. Phys. Lett.* **57** 689-
- [4] Murrell A J, Wee A T S, Fairbrother D H, Singh N K, Foord J S, Davies G J and Andrews D A 1990 *J. Appl. Phys.* **68** 4053-
- [5] French C L and Foord J S 1992 *J. Crystal Growth* **120** 63-70
- [6] Foord J S, French C L, Levoguer C L and Davies G J 1993 *Phil. Trans. R. Soc. Lond. A* **344** 507-520
- [7] Shi B Q and Tu C W 1997 submitted to *J. Electr. Mat.*
- [8] Tu C W, Dong H K and Li N Y 1995 *Materials Chemistry and Physics* **40** 260-266
- [9] Dong H K 1995 *Ph. D Thesis* (University of California at San Diego)
- [10] Fowler R and Guggenheim E A 1952 *Statistical Thermodynamics* (Cambridge: University Press)
- [11] Goymour C G and King D A 1973 *J. Chem. Soc. Faraday I* **69** 749-760
- [12] Xi M, Salim S, Jensen K F and Bohling D A 1994 *Mat. Res. Soc. Symp. Proc.* **334** 169-
- [13] Salim S, Lu J P, Jensen K F 1992 *J. Crystal Growth* **124** 16-
- [14] Kimura K, Horiguchi S, Kamon K, Mashita M, Mihara M and Ishii M 1987 *Jpn. J. Appl. Phys.* **26** 419-
- [15] Gear C W 1971 *Numerical Initial Value Problems in Ordinary Differential Equations* (Englewood Cliffs, N. J.: Prentice-Hall)
- [16] Hou H Q, Liang B W, Chin T P, and Tu C W 1991 *Appl. Phys. Lett.* **59** 292-294
- [17] Arthur J R 1974 *Surface Sci* **43** 449-

A Comprehensive Atomic-Level Simulator for AlGaAs/GaAs (001) MBE

D. L. Dorsey and K. Mahalingam

Materials and Manufacturing Directorate, Air Force Research Laboratory, WL/MLPO Bldg 651, 3005 P St
Ste 6, Wright Patterson AFB, OH 45433-7707, USA

R. Venkat

Dept. of Electrical and Computer Eng., Univ. of Nevada, Las Vegas, Las Vegas, NV, 89154-4026, USA

Abstract. A comprehensive, quantitatively accurate, atomic-level simulator for AlGaAs/GaAs (001) MBE has been developed. The kinetic Monte Carlo method was applied within the solid-on-solid approximation, explicitly accounting for deposition, desorption and surface diffusion of both the group III and group V species. In contrast to previous efforts, the kinetic parameters of the model (neighbor interaction energies) were determined by matching model results to gallium desorption transients measured by desorption mass spectrometry (DMS) during GaAs/AlGaAs/GaAs heterointerface formation. The model reproduces these complex transients, and predicts the stoichiometry profile near the GaAs/AlGaAs heterointerface.

1. Introduction

The advent of quantum well-based devices has put increasing demands on the structural and stoichiometric control of semiconductor thin-film materials grown by Molecular Beam Epitaxy (MBE). Of particular interest is the structure of the heterointerfaces within these materials. In general, it is desired that these be atomically abrupt. However, even the precise on-off flux control provided by MBE does not guarantee atomically abrupt interfaces, due to growth-driven surface roughening and layer intermixing. In this work, we have developed a model for both GaAs and AlGaAs MBE growth. The model was then used to explore the effect of various MBE growth strategies on the atomic-level abruptness of the GaAs/AlGaAs interface.

2. Model

A kinetic Monte Carlo (kMC) model of III-V MBE growth was developed for this study. In contrast to most previous efforts [1,2], the kinetics of arsenic, including deposition, physisorption, desorption and diffusion were included. An innovation of this work is that the kinetic parameters of the model were determined by matching predicted gallium desorption profiles with those obtained by experiment for high-temperature GaAs and AlGaAs growth.

Our initial efforts consisted of matching the experimentally determined Ga desorption behavior during GaAs growth at temperatures high enough for significant Ga desorption. Using the conventional approach to kMC modeling of III-V MBE [1] yielded poor agreement with experiment. We determined that a previously unconsidered mechanism was responsible for this disparity. In the earlier work, only typical GaAs MBE conditions were considered, meaning that high arsenic surface coverages were always assumed. At high temperatures and/or low arsenic fluxes, much lower arsenic surface coverages are evident. This leads to the possibility of a physisorbed state for the group III component, defined as the condition where a group III adatom is located at a group III-terminated site. Gallium adatoms in this state would have both much higher diffusion rates and much higher desorption rates. This was implemented in the model by allowing physisorbed atoms a temperature-dependent number of diffusive hops to find a

chemisorption site (a group V-terminated site) before desorbing. Excellent agreement with experiment was obtained after this mechanism was included.

Following this work, the model was extended to the AlGaAs system. Kinetic parameter values from the GaAs work were directly adopted for the case of AlGaAs, thereby reducing the number of adjustable parameters used to fit the desorption data for the case of AlGaAs growth. Another mechanism was introduced to account for the experimentally observed vertical exchange between Al and Ga [3]. This was implemented in the model by immediately exchanging any depositing or diffusing Al atom which comes in contact with a Ga-terminated site.

Taking the typical kMC approach, all processes except deposition (atom arrival) were taken to be thermally activated with an activation energy related to the configuration dependent binding energy of the atom in question. The binding energy is determined by summing the nearest neighbor (Ga-As, Al-As) interaction energies and the next-nearest neighbor (Ga-Ga, Al-Al, Al-Ga, As-As) interaction energies for all nearest and next nearest neighbors present. The following values were determined (by fit to DMS data) for these interaction energies: Ga-As 0.85eV; Al-As 0.97eV; Ga-Ga 0.17eV; Al-Al 0.25eV; Al-Ga 0.21eV and As-As 0.12eV. Additional model details are available elsewhere [4,5].

3. Gallium Desorption Behavior

The complex behavior of the DMS-measured gallium desorption signal during growth of an AlGaAs layer at 990K is shown in Figure 1. In attempting to match this experimental data two different versions of the model were explored. Model I includes the Al-Ga exchange mechanism and uses the interaction parameter values listed above. Model II does not include exchange, and uses a smaller value for the Al-Ga interaction energy (0.17eV). Both models show good agreement with the experimental results. Analyzing these results yields a qualitative picture of the physics of Ga desorption during AlGaAs MBE.

In examining the causes for the various features of the Ga desorption signal, it is important to keep in mind that the model predicts that the arsenic surface coverage (plot not included due to space considerations) changes in near step-like fashion upon opening or closing the Al shutter. Specifically, when the Al shutter is opened, the decrease in the V/III flux ratio causes a nearly instantaneous decrease

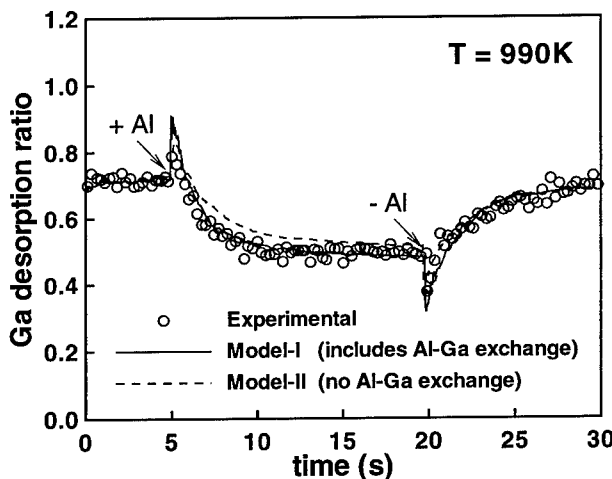


Figure 1. Comparison of kMC model results with DMS measurements for Ga desorption during growth of an AlGaAs layer at 990K.

in the As surface coverage to a new steady-state value. When the Al shutter is closed, a near step increase back to the original value for GaAs is realized.

When the Al shutter is opened, two mechanisms cause the immediate sharp increase in the desorbed Ga signal. First, the influx of Al atoms increases the Ga surface concentration, as the exchange reaction pumps Ga atoms to the surface. This increase in the surface Ga population results in a corresponding increase in the Ga desorption rate. The results of Model II, however, show that the exchange reaction is not required to duplicate the upward spike in desorption rate. The operative mechanism here is the reduction in the As surface coverage that accompanies the decrease in the V/III flux ratio. This exposes more Ga atoms to the surface, increasing the Ga desorption rate.

After the spike in the Ga desorption rate, there is a gradual decrease to a new steady-state value. Again there are two possible mechanisms for this gradual decrease. In Model I, as more Al accumulates on the surface, the desorption activation energy of Ga increases, because the Al-Ga interaction energy is higher than that for Ga-Ga. In Model II, this effect is not present as these interaction energies are set at the same value. What is occurring in Model II is that the increased Al surface concentration is "screening" Ga atoms, thereby reducing the desorption rate. This screening mechanism is not as prevalent in Model I as the exchange mechanism acts to "bury" a large fraction of the incoming Al atoms.

When the Al shutter is closed, the immediate drop in the Ga desorption rate is caused by the increase in As surface coverage, and by the fact that the exchange mechanism is no longer pumping Ga atoms to the surface. The recovery of the Ga desorption rate to the initial value of that for GaAs occurs in two stages. The first is a fast increase due to the reduction in the surface Al content. This lasts until the surface Al content is reduced to zero, about one second after the shutter is closed for the case in Figure 1. The second phase is a slow accumulation of surface Ga until a steady-state value is reached.

4. Heterointerface Formation

The gradual variations in the Ga desorption signal which are evident in Figure 1 are expected to cause a compositional grading near the heterointerface. The results above indicate that the change in V/III flux ratio is the primary cause for these effects. We postulate that maintaining a constant V/III flux ratio during growth of the GaAs/AlGaAs heterointerface may result in a more "step-like" profile for the gallium desorption rate. The kMC model results examining this case are shown in Figure 2.

For both models I and II the upward spike in the desorption rate at +Al is effectively eliminated, and the time to reach a steady-state Ga desorption rate is much reduced. Note that the steady-state desorption

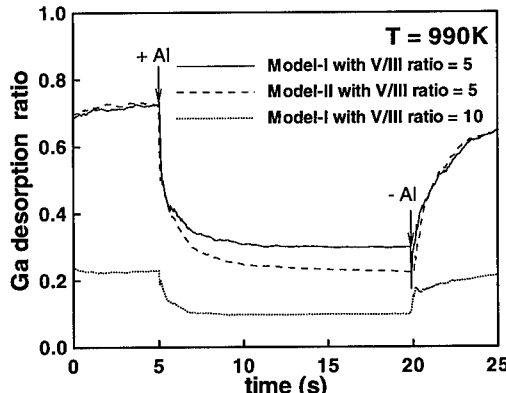


Figure 2. Effect of maintaining a constant V/III flux ratio on the predicted desorbed gallium signal during growth of a GaAs/AlGaAs/GaAs structure at high temperature.

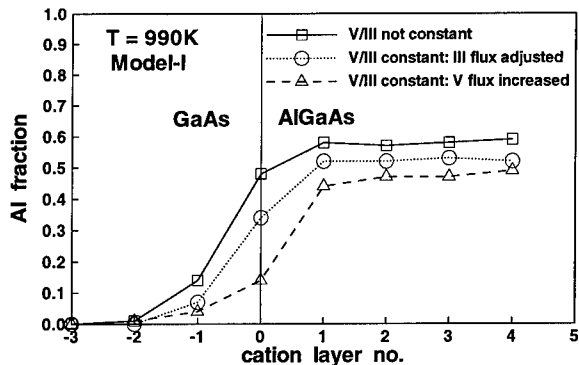


Figure 3. Stoichiometry profile of the GaAs/AlGaAs heterointerface as a function of various growth strategies.

rate is significantly lower (~0.3) than in the previous case (~0.5). One reason for this behavior is that the As surface coverage (not plotted) remains nearly constant throughout the entire simulation. The higher As surface coverage during growth of the AlGaAs layer suppresses the Al-Ga exchange mechanism (less exposed Ga). Furthermore, the higher As flux causes a nearly instantaneous increase in the gallium incorporation rate, leading to a sharp drop in the desorption rate to the new steady-state value.

Upon closing the Al shutter, there is still a rapid initial increase in the desorbed Ga signal, which again is related to the Al surface concentration quickly dropping to zero. Beyond this the recovery to the steady-state value remains slow, as the Ga surface population slowly accumulates to its previous value.

The effect of these strategies on the abruptness of the heterointerface is shown in Figure 3. Note that the ideal stoichiometry profile is an Al fraction of zero on and to the left of the interface line, with a uniform value to the right of the line. The standard approach leads to a significant Al content within what should be the GaAs layer, largely due to the Al-Ga exchange mechanism. The Al content is reduced within the "GaAs" layer when the strategy of maintaining a constant V/III flux ratio is used. The best result is obtained when the As flux is increased. This leads to a higher As surface coverage which suppresses the exchange mechanism.

5. Conclusions

We have developed an atomic-level model for MBE growth of the GaAs/AlGaAs/GaAs system which is quantitatively accurate with regard to the gallium desorption behavior at high temperatures. The model results clearly show that the complex Ga desorption behavior during the growth of AlGaAs layers are predominately a result of the step changes in the V/III flux ratio upon opening and closing the Al shutter. Based on model predictions, maintaining a constant V/III flux ratio during growth of the GaAs/AlGaAs heterointerface should result in a more abrupt GaAs/AlGaAs interface.

6. References

- [1] Madhukar A and Ghaisis S V 1988 *CRC Crit. Rev. in Solid State and Mat. Sci.* 14 1-130
- [2] Smilauer P and Vvedensky D D 1993 *Phys. Rev. B* 48 17603-17608
- [3] Braun W, Trampert A, Daueritz L and Ploog K H 1997 *J. Crystal Growth* 175/176 156-161
- [4] Mahalingam K, Dorsey D L, Evans K R and Venkat R 1997 *J. Crystal Growth* 175/176 211-215
- [5] Mahalingam K, Dorsey D L, Evans K R and Venkat R 1997 *Appl. Phys. Lett.* 70 3143-3146

One-Step Selective Growth of GaAs on V-groove Patterned GaAs Substrates Using CBr₄ and CCl₄

Eun Kyu Kim, Tae-Geun Kim, Chang-Sik Son*, Seong-Il Kim, Young K. Park,
Yong Kim, Suk-Ki Min, and In-Hoon Choi*

Semiconductor Materials Research Center, Korea Institute of Science and Technology,
P.O. Box 131, Cheongryang, Seoul 130-650, Korea

*Division of Materials Science and Engineering, Korea University, Seoul 132-701, Korea

Abstract. With carbon tetrabromide (CBr₄) and carbon tetrachloride (CCl₄) supplied, well-defined selective GaAs epilayers were successfully grown on V-groove and mesa patterned GaAs substrates by one-step atmospheric pressure metalorganic chemical vapor deposition. It appeared that the selectivity of the grown epilayers showing huge lateral growth rate enhancement depended on supplying gases. Inside a V-groove, the selectively grown GaAs epilayers exhibited a triangular and a round shape with supplying CBr₄ and CCl₄, respectively. The selective growth was also done on the side walls of a mesa. In contrast, no growth was observed outside V-groove and on the top of the mesa. This kind of selective epitaxial technology has promising features for well-defined quantum structures and lateral *p-n* junction.

1. Introduction

The ratio of the lateral epitaxial growth rate to the vertical one on a patterned substrate can be controlled slightly by variation of growth temperature and the V/III ratio during metalorganic chemical vapor deposition (MOCVD) [1]. However, the minor controllability in the lateral growth rate ratio has been a limitation for fabrication of some desired optoelectronic device structures. To obtain better lateral growth control, various selective epitaxy (SE) techniques were investigated, such as the regrowth on masked layers and the regrowth after fine lithography and dry etching, which have been most often used to form these nanoscale structures [2-4]. The SE is a direct approach to form quantum structures and novel optoelectronic devices, since it enables us to control the lateral direction of the device structures.

In this study, we report one-step selective epitaxial growth on patterned GaAs substrates with CBr₄ and CCl₄ supplied during MOCVD growth. It is suggested that the obtained selective GaAs epilayer can not only have application to much efficient optical confinement structures but also reduce the number of the device fabrication processes.

2. Experiment

The V-groove and mesa patterns were fabricated along the [011] direction on exactly (100) oriented semi-insulating GaAs substrates by standard photolithography. GaAs epilayers were grown on patterned GaAs substrates by atmospheric pressure MOCVD with a vertical quartz reactor. After growth of undoped GaAs buffer layers on the patterned GaAs substrates, CBr₄ and CCl₄-doped GaAs epilayers were grown. For identifying the growth behavior of GaAs epilayers, AlGaAs marker layers were inserted not only between a GaAs substrate and a GaAs buffer layer, but also between a GaAs buffer layer and a CBr₄ or CCl₄-doped GaAs epilayer. Trimethylgallium (TMG) and AsH₃ (10 %

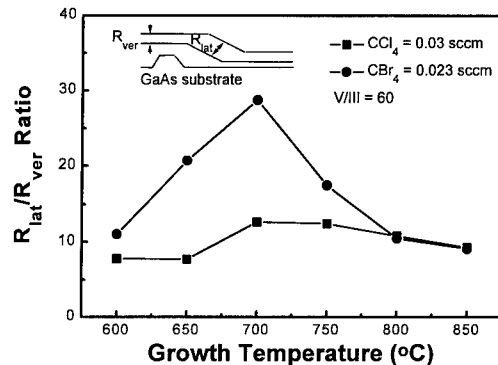


Fig. 1. The growth rate ratio of lateral (R_{lat}) over vertical (R_{ver}) as a function of growth temperature.

diluted with pure hydrogen) were used as the gas sources. CBr₄ or CCl₄ gases were flowed during the epitaxial growth which is normally p-type dopant and can bring out the lateral growth enhancement of GaAs epilayers. Growth temperature and the V/III ratio were fixed at 680 °C and 60, respectively. CBr₄ and CCl₄ were supplied at 0.023 and 0.03 sccm, respectively. Pd-diffused H₂ gas was used as the carrier gas. Total flow rate was 5,000 sccm. The cross-sectional micrographs of the samples were observed by a field emission scanning electron microscopy (FE-SEM).

3. Results and discussion

In our previous work [5-8], it was reported that the lateral growth rate of the GaAs epilayer on a mesa remarkably increased by supplying CBr₄ and CCl₄, as shown in Fig. 1. CCl₄ and CBr₄ were usually used as effective p-type sources. This figure shows the growth rate ratio of lateral (R_{lat}) over vertical (R_{ver}) as a function of growth temperature with CBr₄ and CCl₄ supplied. It is noticeable that in the case of CBr₄ the $R_{\text{lat}}/R_{\text{ver}}$ is as high as 29 at about 700 °C. When CBr₄ is used, the growth rate enhancement is about twice than that of CCl₄ at 700 °C. The lateral growth rate increases with increase in temperature up to 700 °C, but it decreases at higher growth temperatures. The selective growth in this work was performed at a given growth condition which was selected to obtain the highest lateral growth enhancement, i.e., growth temperature and the V/III ratio were fixed at 680 °C and 60. CBr₄ and CCl₄ were supplied at 0.023 and 0.03 sccm, respectively.

Figure 2(a) shows a round-shaped selective CCl₄-doped GaAs epilayer, which was grown on the inside of a [011] oriented V-groove (the facet of the sidewall is a Ga-rich plane). In the region of undoped-GaAs buffer layer, the R_{lat} inside the V-groove was about 3.5 μm/hr, which was twice that of the R_{ver} outside the V-groove. In the region of a CCl₄-doped GaAs epilayer, a large lateral growth enhancement ($R_{\text{lat}} \sim 4 \mu\text{m}/\text{hr}$) was exhibited in the inside region of V-groove, whereas no growth was observed outside the V-groove. This peculiar selectivity also occurred in the region of a single mesa. Figure 2(b) shows a round-shaped selective CCl₄-doped GaAs epilayer which was grown on the both side walls of a single mesa, which showed a larger lateral growth rate enhancement ($R_{\text{lat}} \sim 10 \mu\text{m}/\text{hr}$) than that of the V-groove, and also showed almost no growth on the top region of the mesa.

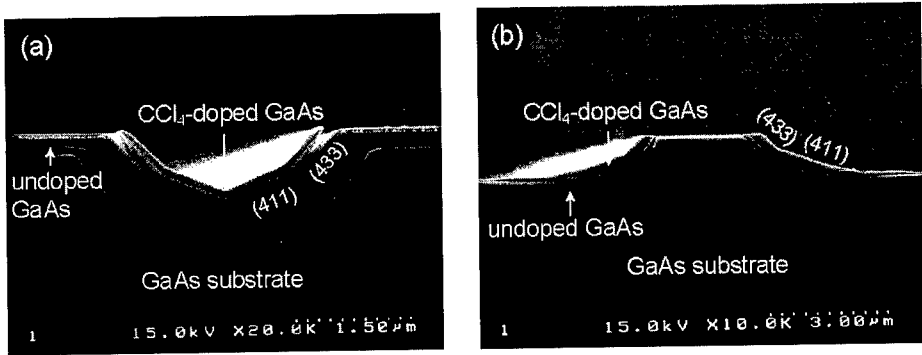


Fig. 2. Cross-sectional SEM micrographs of round-shaped CCl₄-doped GaAs epilayers selectively grown on patterned GaAs substrates having [011] oriented either V-groove (a) or mesa (b).

As shown in Figs. 2(a) and (b), the (411)A and (433)A facet planes are clearly visible on the side walls of the V-groove or the mesa of the buffer epilayer. These facets are maintained in CCl₄-doped GaAs epilayers.

Figure 3(a) shows a triangular-shaped selective CBr₄-doped GaAs epilayer, which was grown on the inside of a [011] oriented V-groove. In the region of undoped-GaAs buffer layer, the lateral growth rate (inside the V-groove) was twice that of the vertical. In the region of CBr₄-doped GaAs epilayer, a huge lateral growth enhancement was exhibited inside V-groove, whereas no growth was observed outside the V-groove. For the case of CBr₄, the inside region of V-groove was completely filled up, and thus the top of the epilayer was flattened. Figure 3 (b) shows a bird-wing shaped selective CBr₄-doped GaAs epilayer on the side walls of a single mesa. As shown in Figs. 3(a) and (b), the (433)A and (411)A facet planes are clearly visible on the side walls of the V-groove and mesa, respectively.

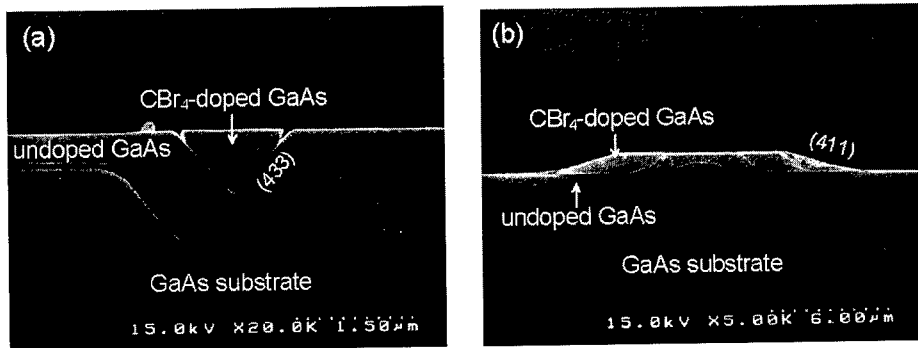


Fig. 3. Cross-sectional SEM micrographs of triangular shaped CBr₄-doped GaAs epilayers selectively grown on patterned GaAs substrates having [011] oriented either V-groove (a) or mesa (b).

The selectivity obtained by supplying CBr_4 was higher than that of CCl_4 . The CBr_4 -doped GaAs epilayer was completely filled up (Fig. 3 (a)), whereas the CCl_4 -doped GaAs partially filled up the inside of the V-groove region (Fig. 2 (a)). Higher selectivity in the case of CBr_4 would be attributed to the higher lateral growth enhancement when CBr_4 is used than that of CCl_4 . This trend in efficiency of selectivity would be correlated with the difference in the strength of the chemical bonds between the carbon nucleus and Cl and Br ligands. Br ligands bound more weakly to carbon than Cl enhance the decomposition rate of the surface-adsorbed chemical species [9], and therefore the lateral growth rate is enhanced more in the case of CBr_4 than that of CCl_4 . It was also suggested that the lateral gas phase diffusion of column III species (particularly Ga species) involved the decomposition products from CBr_4 and CCl_4 and etching effects due to Cl or Br complex were occurring at the same time during the MOCVD growth. Although very thin (<10 nm) layers outside a V-groove and on the top of a mesa may be etched away during the stain etching with $\text{KOH} : \text{K}_3\text{Fe}(\text{CN})_6 : \text{H}_2\text{O}$ solution, it is very interesting that the vertical growth rate is too small to be observed with the technique of this paper. This technique can realize the true SE by one-step growth, and thus would enhance the quality of quantum confined devices fabricated on patterned substrates. Further studies should be required to clarify the selective epitaxial growth and realize the quantum structures and lateral *p-n* junction structures.

4. Conclusion

One-step selective GaAs epilayers were fabricated on V-groove and single mesa of patterned GaAs substrates by atmospheric pressure MOCVD with CBr_4 and CCl_4 being supplied. The selectivity obtained using CBr_4 was higher than that of CCl_4 . Triangular-shaped CBr_4 -doped GaAs epilayers were also selectively grown on a V-groove and mesa, showing a huge lateral enhancement on both sidewalls, whereas there was no growth outside V-groove and on the top of the mesa. In the CCl_4 -doped case, round-shaped GaAs epilayers were also selectively grown on a V-groove and mesa, showing large lateral growth enhancement on the side walls and no growth outside V-groove and on the top of the mesa.

Acknowledgments

This work was partially supported by the KOSEF-SPRC and the MOST(Contract No. 2N15920).

References

- [1] Hersee S D, Barbier E and Blondeau R 1986 *J. Cryst. Growth* **77** 310.
- [2] Kim T G, Kim E K, Min S K and Park J H 1996 *Appl. Phys. Lett.* **69** 955.
- [3] López M, Tanaka N, Matsuyama I and Ishikawa T 1996 *Appl. Phys. Lett.* **68** 658.
- [4] Finnie P, Buchanan M, Laclell C and Roth A P 1996 *J. Cryst. Growth* **160** 220.
- [5] Kim Y, Park Y K, Kim M S, Kang J M, Kim S I, Hwang S M and Min S K 1995 *Appl. Phys. Lett.* **67** 1871.
- [6] Kim S I, Kim M S, Kim Y, Son C S, Hwang S M, Min B D, Kim E K and Min S K 1996 *Appl. Phys. Lett.* **69** 815.
- [7] Son C S, Kim S I, Kim Y, Lee M S, Kim M S, Min S K and Choi I H 1996 *J. Cryst. Growth* **165** 222.
- [8] Son C S, Kim S I, Kim Y, Park Y K, Kim E K, Min S K and Choi I H 1997 *J. Appl. Phys.* **82** 1205.
- [9] de Lyon T J, Buchanan N I, Kirchner P D, Woodall J M, Scilla G J and Cardone F 1991 *Appl. Phys. Lett.* **58** 517.

Growth and Characterization of Thick Epitaxial GaAs Layers

H. Samic¹, J.C. Bourgoin², B. Pajot², R. Bisaro³, C. Grattepain³,
 K. Khirouni⁴, M. Putero⁵ and N. Burle⁵

¹Saobracajni Fakultet, Skenderija 35, 71000 Sarajevo (Bosnia Herzegovina)

²Groupe de Physique des Solides, Université Paris 7, C.N.R.S., Tour 23, 2 place Jussieu,
 75251 Paris Cedex 05 (France)

³Laboratoire Central de Recherche, Thomson-CSF, Domaine de Corbeville, 91404 Orsay Cedex (France)

⁴Laboratoire des Semiconducteurs, Faculté des Sciences de Monastir, Route de Kairouan, 5000 Monastir
 (Tunisia).

⁵Laboratoire Matériaux Organisation et Propriétés (MATOP), C.N.R.S., Faculté des Sciences de Saint-Jérôme, Case 151, 13397 Marseille Cedex 20 (France).

Abstract. We present an economical and non polluting vapor phase technique, allowing the growth of practically all III-V and II-VI compounds, using water as reactant. This technique will be illustrated here in the case of GaAs. We show that GaAs can be grown at very high growth rates. This has been used to obtain thick layers. We demonstrate that these layers exhibit good structural, electrical and optical properties when grown, at least, up to $5\text{ }\mu\text{m}$ per minute. Since doping can be mastered, millimeter thick layers can be grown in a reasonable time, opening new applications for epitaxial GaAs layers such as high power electronics, nuclear detection and optics.

1. Introduction

Gallium Arsenide epitaxial layers are used for micro-electronic applications. However, they could also be used in other fields such as high power electronics, optics, nuclear detection, etc., if they could be grown thick enough because the conventional bulk materials exhibit electrical characteristics which are often not sufficiently homogeneous, while epitaxial layers exhibit in principle perfect homogeneity.

The aim of this communication is to present a particular, non polluting, vapor phase epitaxy technique which allows to reach very high growth rates, up to $50\text{ }\mu\text{m min}^{-1}$, and thus to obtain millimeter thick layers in a reasonable time. We will describe the structural, optical and electrical properties of layers, several hundred microns thick, grown by this technique as well as the variation of their properties with the growth rate.

2. The growth technique

The vapor phase technique considered here has already been used (for a review on this technique, see ref. [1]). It is universal in the sense that it can use the same reactant to grow all III-V (even nitrides) and II-V compounds. It is based on the decomposition of a source material with a reactant, followed by mass transport in the vapor phase of the temperature and concentration gradients, ending with the reverse reaction on the substrate. The reactant, water, is cheap, easy to find and non polluting. In practice, as schematized in Figure 1, water at a level of the order of a few hundred ppm, in H_2 at atmospheric pressure, decomposes the source. The gaseous products of decomposition are transported to the substrate, placed face to face at a short distance (of the order of a few millimeters) where the

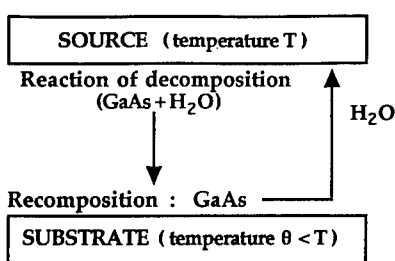


Fig. 1 – Principle of the reactions inducing the growth.

reverse reaction occurs. The growth rate (deduced from the layer thickness grown for a given time) is adjusted independently by the source and substrate temperatures and the water partial pressure. In the work reported here the source and substrates are conventional semi-insulating Czochralski grown wafers.

Because the transport is nearly 100 % efficient and not limited by diffusion, very high growth rates can be achieved. This is illustrated in Figure 2 where we show that growth rates up to 10 $\mu\text{m min}^{-1}$, i.e. 500 times faster than that of conventional techniques, can be obtained. We used this specific potentiality of the technique, usually called Close Space Vapor Transport (CSV), to grow layers of several hundred of microns thick. Here, we shall describe the structural, optical and electronic properties of layers grown on (001) oriented GaAs substrates which are either n⁺ doped or semi-insulating wafers originating from Czochralski grown materials.

3. STRUCTURAL CHARACTERIZATION

Optical observation shows that, as the thickness of the layer increases, the surface becomes more and more faceted, i.e. pyramids with (111) oriented faces appear and grow in number and size. The occurrence of these facets depends on the growth rate. It reaches a maximum in the 0.5 to 1 $\mu\text{m min}^{-1}$ range and decreases abruptly when the substrate temperature is above 750° C.

X-ray topography demonstrates that the layers are free of dislocations except on the edges where they are induced, from the substrates, by the mechanical system which holds them. However, when layers exhibit small localized regions associated with surface defects, short dislocations or stacking faults are observed.

Double X-ray diffraction, which probes the surface layer (up to a depth of 20 μm), exhibits a single peak whose width is slightly broader (20 to 40 arc.s.) than that of a few μm thick layer (12 arc.s.). This is attributed to the disorder induced by the large concentration of As antisites, related to EL2 defects, whose concentration depends on the growth rate (see below). The variation of the lattice parameter $\Delta a/a$ is of the order of 10⁻⁵ to 10⁻². We did not find any correlation between $\Delta a/a$ and the growth rate nor with the substrate temperature.

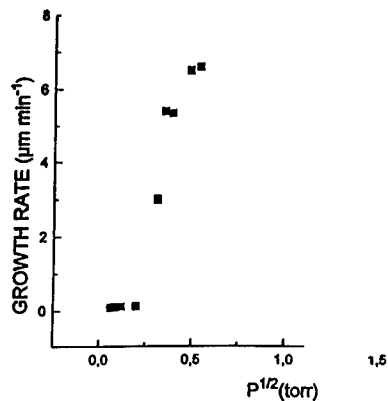


Fig. 2 – Variation of the growth rate versus the partial pressure of water for a substrate temperature of 800° C and a source temperature of 900° C.

4. Optical characterization

Absorption in the 0.8 – 1.5 eV range, eventually performed after surface polishing, gives a spectrum similar to that of a Czochralski grown material. The band edge exhibits a tail typical of the presence of EL2 defects. In order to evaluate this concentration, we used the absorption around 1 μm which has been calibrated for the measurement of this concentration [2,3]. In the case of Figure 3 corresponding to a 170 μm thick layer grown at 800° C, at a rate of 5.8 $\mu\text{m}.\text{min}^{-1}$, this calibration indicates an EL2 concentration of $4 \times 10^{17} \text{ cm}^{-3}$. As reported in ref. [4], the concentration increases with the growth rate and allows to obtain semi-insulating layers [5] because undoped layers are predominantly p-type (see below).

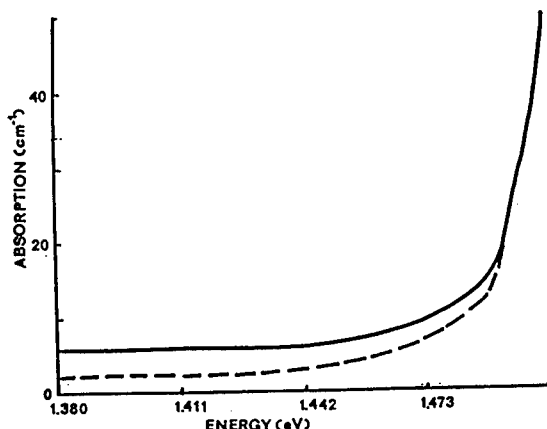


Fig. 3 – Optical absorption spectrum of a 170 μm thick layer grown at 800° C with a rate of 5.8 $\mu\text{m}.\text{min}^{-1}$. The dashed line corresponds to the absorption of the substrate.

As to photoluminescence, it demonstrates good quality of the layers grown with rates lower than 5 $\mu\text{m}.\text{min}^{-1}$. Indeed, luminescence spectra exhibit the band exciton line, and lines associated with donor-acceptor recombination as well as several phonon replica. The acceptor impurities involved in these lines are Si_{As} and Ga_{As} in agreement with analysis performed by secondary ion mass spectroscopy (SIMS). These latter measurements show that Si is present at a concentration ranging from 10^{15} to 10^{16} cm^{-3} , while S is at a concentration ten times lower (the correlation between the impurity concentrations in the source and the layers will be developed elsewhere). The dominant acceptor is C, in the range 10^{16} – 10^{17} cm^{-3} . These concentrations seem to be related neither with the substrate temperature, nor with the growth rate. But they are, as expected, directly related to the impurity content of the source material.

5. Electrical characterization

Hall effect measurements are in agreement with the SIMS analysis and the photoluminescence observations. The layers, originating from semi-insulating, undoped, Czochralski materials are p-type at

level ranging from few 10^{15} cm^{-3} to few 10^{16} cm^{-3} . The temperature dependence of the mobility indicates that the layers contain a small concentration of charged defects or impurities. In the range 100 – 300 K the mobility increases linearly with $T^{-3/2}$ (see Fig. 4) which means that it is limited by phonons. Below typically 100 K, the mobility is a decreasing function of the temperature (see Fig. 5) as a result of scattering with charged defects.

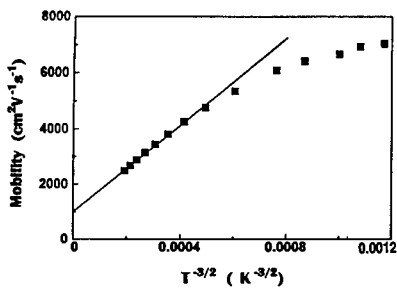


Fig. 4 – Hole mobility versus $T^{-3/2}$ in a $62 \mu\text{m}$ thick layer grown at 750°C with a growth rate of $1.7 \mu\text{m} \cdot \text{min}^{-1}$.

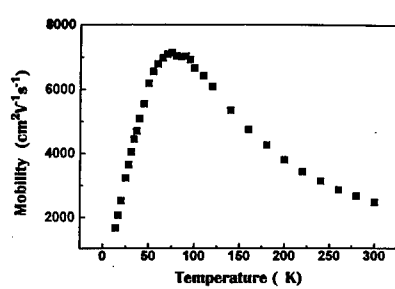


Fig. 5 – Temperature dependence of the hole mobility of the same layer as in Fig. 4 showing the low temperature range.

Finally, a search for deep charged impurities has been performed by SIMS : Cr, Mn, Fe and Ni, are at a level of 10^{13} cm^{-3} or below; O exists at larger concentration ($\sim 10^{17} \text{ cm}^{-3}$), but it is known that it does not give rise to any deep level.

6 . Conclusion

We have demonstrated that it is possible to grow very thick epitaxial layers of GaAs which exhibit good electronic and optical properties. We shall demonstrate elsewhere (for a preliminary work, see ref. [6]) that these layers can be p- and n-types doped, allowing their use in high power electronics.

Acknowledgments

The materials used as source and substrate were provided by Y. Otoki (Advanced Research Center Hitachi Cable Ltd., Japan).

References

- [1] Bourgoin J C and Samic H 1996 in Properties of Gallium Arsenide, Emis Datareview serie n° 16 (INSPEC Publ.) eds. Brozel M R and Stillman G E p. 639
- [2] Martin G M 1981 *Appl. Phys. Lett.* 39 747
- [3] Skowronski M, Lagowski J and Gatos H C 1986 *J. Appl. Phys.* 59 2451
- [4] Samic H and Bourgoin J C Proc. Int. Conf. on Defects in Semiconductors (Portugal, 1997), *to be published*.
- [5] Castenedo R, Mimila-Arroyo J and Bourgoin J C 1990 *J. Appl. Phys.* 68 6274
- [6] Sandoval H, Mimila-Arroyo J and Bourgoin J C 1995 *J. Appl. Phys.* 77 5418

Structural and Electrical Characterization of Epitaxial DyP/GaAs and DyAs/GaAs grown by MBE

P.P. Lee^a, R.J. Hwu^b, L.P. Sadwick^{a,b}, H. Balasubramaniam^b, B.R. Kumar^b, T.C. Lai^b
S.N.G. Chu^c, R. Alvis^d, R.T. Lareau^e, and M.C. Wood^e

^aDepartment of Materials Science & Engineering, University of Utah, Salt Lake City, UT 84112

^bDepartment of Electrical Engineering, University of Utah, Salt Lake City, UT 84112

^cLucent Technologies, 600 Mountain Avenue, Murray Hill, NJ 07974

^dAdvanced Micro Devices, 3625 Peterson Avenue, Santa Clara, CA 95054

^eUS Army Research Labs, 2800 Powder Mill Road, Adelphi, MD 20783

Abstract. Details of the structural and electrical properties of epitaxial DyP/GaAs and DyAs/GaAs are reported. Both DyP and DyAs have been grown by solid source MBE with growth temperatures ranging from 500 to 600°C and growth rates between 0.5 and 0.7 $\mu\text{m}/\text{hr}$. DyP epilayers are n-type with measured electron concentrations on the order of 3 to $4 \times 10^{20} \text{ cm}^{-3}$, room temperature mobilities of 250 to 300 cm^2/Vs , and a barrier height of about 0.81 eV to GaAs at room temperature. DyAs epilayers are also n-type with concentrations of 1 to $2 \times 10^{21} \text{ cm}^{-3}$, and mobilities between 25 and 40 cm^2/Vs . DyP is stable in air with no signs of oxidation even after months of exposure.

1. Introduction

The ability to grow thermally stable Schottky/Ohmic contacts and buried, epitaxial metallic or semi-metallic layers on semiconductors has many potential applications in novel device structures. One promising approach for achieving thermally stable contacts is to select a high melting point elemental metal-phosphide or metal-arsenide binary compound that displays metallic characteristics and is chemically inert. Two attractive material systems that offer strong promise in this area are dysprosium phosphide/gallium arsenide (DyP/GaAs) and dysprosium arsenide/gallium arsenide (DyAs/GaAs).

This paper reports the structural and electrical characterizations of DyP and DyAs on GaAs as well as GaAs/DyP/GaAs and GaAs/DyAs/GaAs heterostructures. DyP and DyAs have only one stable phase with a NaCl crystal structure and have lattice constants of 5.6534 Å and 5.7894 Å, respectively. The lattice mismatch between DyP and GaAs is less than 0.01% at room temperature.

2. Results and Discussion

Fig. 1 shows the selected area diffraction pattern of GaAs and DyP epilayers on a GaAs substrate. The diffraction pattern indicates an epitaxy of the two layers with the substrate. Fig. 2 shows a high-resolution lattice image of the same sample looking at the buried DyP layer and the GaAs capping interface. No pinholes were observed in the DyP layers. In spite of the good growth of DyP on GaAs, the GaAs layer grown on top of the DyP is usually twinned. Most of the top GaAs layer is epitactically aligned with DyP/GaAs but there are areas where (111) GaAs grows on (001) DyP. This phenomenon has also been observed in the GaAs/ErAs/GaAs structure where the GaAs layer grown on top of ErAs is usually heavily twinned with most of the twin boundaries lying parallel to {111} planes [1].

Fig. 3 shows the selected area diffraction pattern of DyAs epilayer on GaAs substrate. The diffraction pattern also indicates an epitaxy of DyAs with the substrate. However, the cross-section images review the threading dislocation as well as twinning and stacking faults in the DyAs layer. This is expected due to the larger lattice mismatch between DyAs and GaAs. The difference in the crystal structures between DyP or DyAs (rock salt) and GaAs (zinc blende) seemed to affect the growth of GaAs/DyP/GaAs and GaAs/DyAs/GaAs heterostructures.

The Auger electron spectroscopy (AES) profile of the GaAs/DyP/GaAs sample is shown in Fig. 4. The AES profile indicates abrupt interfaces with no significant impurities present in any of the layers. For GaAs/DyAs/GaAs, although the interface appears to be abrupt, unlike GaAs/DyP/GaAs, a certain amount of oxygen is observed at the DyAs and the capping GaAs interface. DyAs is reactive to a certain degree to oxygen, however, it is less reactive when compared to ErAs, which is highly reactive even in a UHV environment, resulting in significant oxygen and carbon contaminations on the surface [2]. The atomic force microscopy (AFM) analysis of DyP/GaAs revealed smooth surfaces with RMS roughness between 4 and 8 Å. The surface roughness of DyAs, on the other hand, was between 10 and 15 Å, and may be due to the lattice mismatch between DyAs and GaAs.

The resistivity values of DyP as determined by four-point probe and Hall measurements were found to be consistent and were in the range of 6.5×10^{-5} to 1.5×10^{-4} Ω·cm as seen in Fig. 5. Hall measurements indicated that DyP films were n-type with electron concentrations on the order of 3×10^{20} to 4×10^{20} cm⁻³.

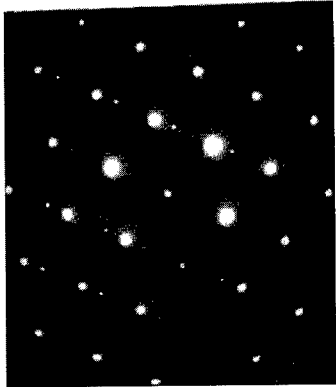


Fig. 1. Selected area diffraction pattern from GaAs substrate with GaAs/DyP epilayers.

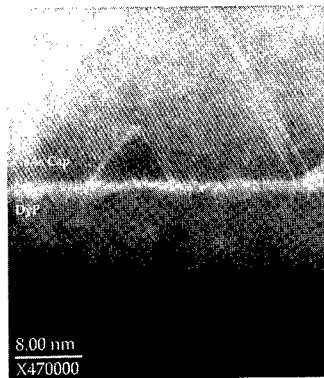


Fig. 2. Selected area cross-section HRTEM image of GaAs/DyP interface.



Fig. 3. Selected area diffraction pattern from GaAs substrate with DyAs epilayer.

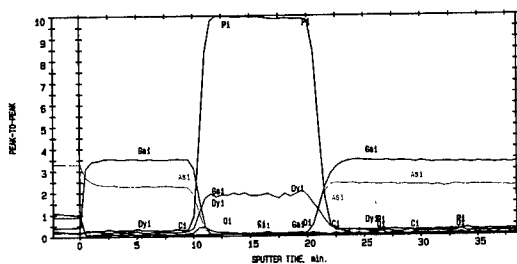


Fig. 4. AES profile of GaAs/DyP/GaAs sample.

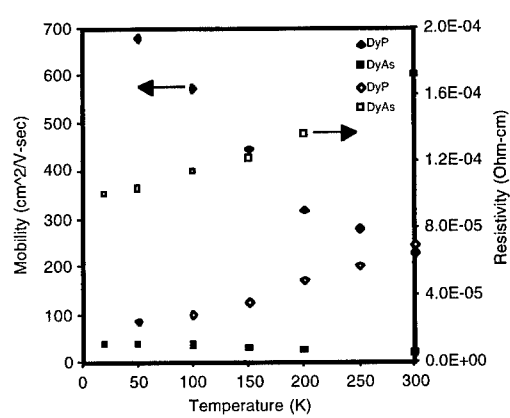


Fig. 5. Resistivity and Mobility of DyP and DyAs obtained from Hall measurements.

The room temperature mobility was between 250 and 300 cm²/V·s and increased with a decrease in temperature.

I-V measurements were performed on DyP/GaAs and indicated a Schottky behavior. The barrier height, measured by *I-V* measurements, was found to be approximately 0.81 eV. Variable temperature *I-V* measurements, using DyP as the Schottky contact and patterned Cu₃Ge as the Ohmic contact, indicated that the contacts performed efficiently up to a temperature of 200°C.

For DyAs, Hall measurements were performed between 20 K and 300 K and the resistivity was found to be in the region of 1.0×10^{-4} to 1.5×10^{-4} Ω·cm as seen in Fig. 5. DyAs was also found to be n-type with carrier concentration on the order of 1×10^{21} to 2×10^{21} cm⁻³ and mobilities between 25 and 40 cm²/V·s, and showed an increase with a decrease in temperature as shown in Fig. 5. According to *I-V* measurements, DyAs was found to form a poor Ohmic contact to n-GaAs.

3. Conclusions

We have demonstrated the epitaxial growth of DyP and DyAs on GaAs as well as GaAs/DyP/GaAs and GaAs/DyAs/GaAs heterostructures using solid source MBE. The epilayers were characterized by TEM, AES, Hall measurements, and *I-V* and *C-V* measurements. DyP was found to be stable in air with no signs of oxidation even after months of exposure. *I-V* measurements show that DyP forms a Schottky contact to GaAs with a barrier height of about 0.81 eV. This contact is stable up to about 200°C. DyAs was found to form a poor Ohmic contact to n-GaAs.

Acknowledgments

The authors would like to thank T. Block and D.C. Streit of TRW for their helpful discussion. This research was supported by the National Science Foundation under grant number ECS 9502891.

References

- [1] Zhu J G, Carter C B, Palmstrøm C J, and Mounier S 1990 *Appl. Phys. Lett.* **56** 1323-6
- [2] Palmstrøm C J, Tabatabaie N, and Allen Jr. S J 1988 *Appl. Phys. Lett.* **53** 2608-11

PIN Photodiodes using Nitrogen Ion Implantation on ZnSe/GaAs Heterostructure

H. HONG, W. A. Anderson, S. Nagarathnam, A. N. Cartwright, E. H. Lee, H. C. Chang, M.H. Na, and H. Luo

State University of New York at Buffalo, Center for Advanced Photonic and Electronic Materials, Bonner Hall, Amherst, NY. 14260, USA

Abstract. PIN photodiodes were fabricated by nitrogen ion implantation on undoped 0.5, 1.0, 1.5, and 2.0 μm thick ZnSe/n-ZnSe/n⁺GaAs(100) grown by molecular beam epitaxy (MBE). To obtain the p-layer, nitrogen ions at multiple energies and ion doses were implanted at room temperature to obtain a quasi-uniform doping profile. The activation of implanted ions was achieved by post-annealing in a N-ambient at 500 °C for 5min. Optical studies were performed by photoluminescence (PL) spectroscopy at 10 K, which indicated donor-acceptor pairs at an energy of 2.7 eV and its phonon replicas with 30 meV intervals. The circular PIN diodes with 1 mm diameter active area showed an ideality factor of 1.19 and reverse bias breakdown voltage of 10 V for 0.5 μm thick undoped ZnSe. Moreover, good linearity with light intensity, low dark current and high photocurrent were seen. A photocurrent/dark current ratio of more than 10⁴ for an illumination of 100 mW/cm² at a reverse bias of 1V through a 200 Å thick metal layer was seen for the 0.5 μm thick layer. A responsivity of 0.025 A/W was obtained at a wavelength of 460 nm through the metal contacts.

1. Introduction

ZnSe, a wide and direct bandgap material, is an attractive material for optoelectronic devices. Especially, photodetectors operating in the visible and ultraviolet regions could be important for many space and medical application. To realize these devices, highly doped p-type layers are necessary. Highly doped p layers using a nitrogen source during MBE/MOCVD growth are difficult to obtain due to compensation between nitrogen and intrinsic impurities[1,2]. Ion implantation is attractive as a doping method because of its controllability and repeatability. Continuing on our previous nitrogen ion implantation study on Zn(S)Se[3], PIN photodiodes were fabricated by this method with various i-layer thicknesses. This could result in new applications in radiation detectors using ZnSe due to its large bandgap (low dark current), high resistivity and low capacitance[4].

2. Experimental

Sample growth using molecular beam epitaxy (MBE) was carried out in a Riber MBE 32P system. Elemental sources of Zn and Se were used for the ZnSe growth. Cl-doped 1.0 μm thick n-type ZnSe films and 0.5 μm , 1.0 μm , 1.5 μm , and 2.0 μm thick undoped ZnSe epilayers were grown on n⁺GaAs(100) at 300 °C. To form the p-type ZnSe, nitrogen ion implantation was performed at room temperature using multiple ion energy and dose with various conditions as shown in Table 1. Of special note is condition E, where nitrogen was implanted at a single energy level of 50 KeV with an

Table 1. Implantation Data for N-ion Implanted PIN Diodes

Experiment #	Samples	Thickness of Undoped Layer (μm)	Implantation Condition	
			Ion Energy (KeV)	Ion Dose (cm^{-2}) $\times 10^{13}$
1	A	0.5	20, 40, 90, 130, 180	1, 2, 6, 20, 100
	B	0.5		
2	C	1.0	20, 40, 90, 130, 180	4, 5, 8.5, 11, 12
	D	1.5		
3	E	2.0	50	1000

ion dose of 10^{16} cm^{-3} to achieve a shallow p+ layer. Post implant annealing was performed at a temperature of 500°C for 5 min in a N_2 ambient [3]. Optical activation of the implanted species as a p-type dopant was examined by 10 K photoluminescence (PL) on as-grown and implanted/activated samples. For electrical study, Au:Ge/Ni ohmic contacts were deposited on the n⁺GaAs side and 1 mm diameter circular Pd Schottky contacts were evaporated on top of the N-ion implanted ZnSe. The current-voltage with/without illumination, temperature dependent carrier transport, high frequency capacitance-voltage, deep level transient spectroscopy (DLTS), and spectral response were employed for characterization.

3. Results and Discussion

As the first experiment, optical and electrical tests were performed on N-ion implanted PIN diodes having a 0.5 μm thick undoped ZnSe/ZnSe:Cl/n⁺GaAs structure. PL measurements at 10 K were carried out on as-grown and implanted samples after annealing. As seen in Fig. 1, the as-grown sample showed a strong free exciton (FX) at an energy of 2.803 eV and free-to-bound exciton (BX) at an

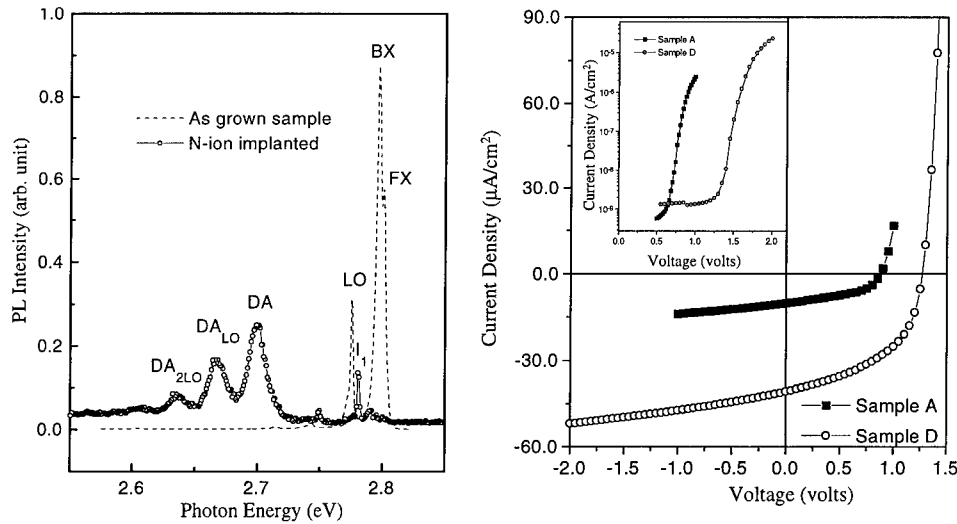
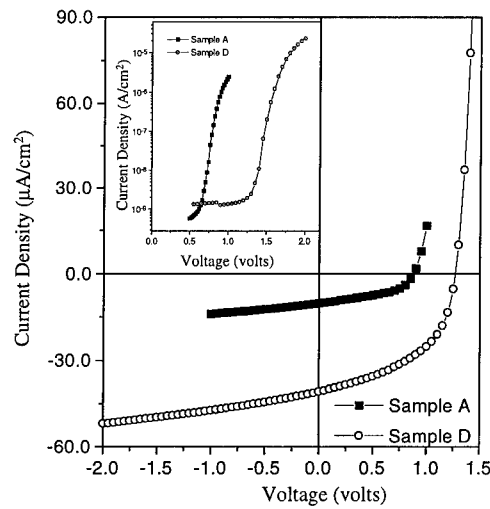


Fig. 1 10 K PL of as-grown and Ion Implanted sample A

Fig. 2 Dark and photo I-V of PIN diodes A and D with 100 Å thick 1 mm diameter contacts



energy of 2.79 eV similar to that seen in a typical undoped ZnSe spectra[5]. However the PL spectra of the N-ion implanted sample showed donor-acceptor pair (DAP) transitions at the energy of 2.7 eV with three longitudinal optical (LO) phonon replicas at every 30 meV on the lower energy side and suppressed FX and BX peaks which indicate p-type doping.

Dark and photo current-voltage data for diodes A and D (Table 1), differing in the undoped layer thickness, is shown in Fig. 2. The ideality factor of diode A was 1.19 at lower forward bias (< 0.8 V) indicating the diffusion dominated transport mechanism in this structure contrary to the expected recombination dominated transport, probably a result of a very thin intrinsic layer. However, the ideality factor of diode D was 1.9, indicating recombination in the carrier transport mechanism. A dark current ~ 40 pA at a reverse bias voltage of 5 V was seen for diode A. The ratio of photo to dark current of the PIN diode was 10^4 and photocurrent (applied zero bias) of diode A was $10 \mu\text{A}/\text{cm}^2$. A breakdown voltage of 10 V for diode A and 60 V for diode D were observed.

Data for 1 MHz capacitance-voltage (C-V) characteristics of PIN diodes A and D are shown in

$$|N_A - N_D| = \frac{2}{q\epsilon_s A^2 (d(1/C^2)/dV)} \quad (1)$$

Fig. 3. Using Eq (1), the background carrier concentration was $\sim 10^{15} \text{ cm}^{-3}$ and built-in potential ($1/C^2=0$) of ~ 3 V was extracted. Thickness of the depletion layer for the given condition of implantation was estimated as 0-0.2 μm for A and 1.0-1.2 μm for D diode, respectively by TRIM. From the C-V plot, the thickness of the depletion layer was estimated $> 0.3 \mu\text{m}$, indicative of spatial variation of the net acceptor concentration due to the compensation by incorporated chlorine.

DLTS studies were performed to examine traps in the material and this is shown in Fig. 4. A hole trap at an energy of 710 meV above the valence band with a 10^{-14} cm^2 capture cross section is seen. This trap position was found in N-doped MBE grown ZnSe [6] due to Zn vacancies or residual impurities on Zn site.

Room temperature spectral response of photodiode A at four reverse bias voltages in Fig. 5 shows

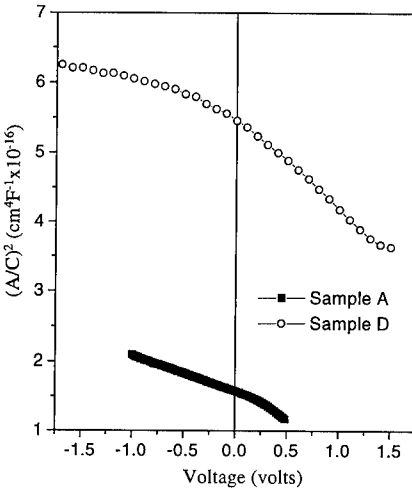


Fig. 3 1 MHz C-V characteristics of PIN diodes A and D

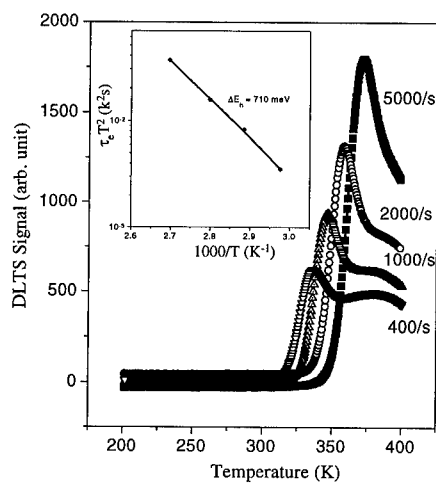


Fig. 4 DLTS signal of PIN diode A

a strong absorption at the wavelength of 460 nm, equivalent to a bandgap energy of 2.67 eV. Also, the spectral response showed the field-assisted transition (Franz-Keldysh effects) below the cut-off wavelength. A responsivity of 0.025 (A/W) was obtained without anti-reflecting coating and through 200 Å thick metal layers. Only 20 % of the optical power was transmitted into ZnSe through 100 Å thick metal layers. Spectral responsivity is increased with reverse bias voltage due to increasing dark current and better carrier separation. In the short wavelength region, the responsivity decreased due to surface recombination and limitation of the light source.

To improve the device performance, the thickness of the undoped layer of the PIN structure was increased to 1.0, 1.5, and 2 μm. With these structures, an ideality factor of ~2 was obtained indicating the carrier transport dominated by recombination. The background carrier concentration was $\sim 10^{15} \text{ cm}^{-3}$, and the C-V characteristics showed that the undoped layer was fully depleted as the capacitance remained constant in higher reverse bias. Also, the breakdown voltage was increased by increasing the thickness of the undoped layer. Especially, the 2.0 μm thick undoped ZnSe/ZnSe:Cl/n-GaAs structure was designed for a shallow p+-layer and thicker intrinsic layer. The spectral response was improved significantly with this design.

4. Conclusions

PIN photodiodes having low dark current and low capacitance were realized by using N-ion implantation as a doping method for the p-layer on undoped ZnSe epilayers having different thickness. These PIN diodes by ion implantation are reproducible. PIN diodes have an ideality factor of 1.19 for the 0.5 μm thick undoped ZnSe sample and ideality factor of 1.9 ~ 2.0 for the undoped ZnSe having thickness greater than 1 μm. This study shows the possible application of ZnSe PIN diodes as photodetectors having low dark current and high breakdown voltage.

5. References

- [1] Fan Y et al 1994 Appl. Phys. Lett. 65 1001-1003
- Chen A. L et al 1994 Appl. Phys. Lett 65 1006-1008
- [2] Laks D.B. et al 1993 Physica B 185 118-127
- [3] Hong, H et al 1997 J. Appl. Phys.(to be published)
- [4] Verger L and et al 1997 J. Elec. Matrls.26 738-744
- [5] Ohkawa K et al 1992 J. Crystal Growth 117 375-384
- Gutowski J et al 1990 Phys. Stat. Sol (a) 120 11-59
- [6] Hu B. et al 1993 Appl. Phys. Lett. 63 358-360

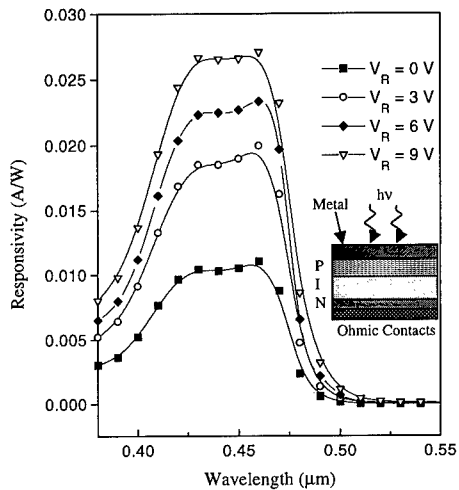


Fig. 5 Spectral Response of PIN photodiode A at several value of applied reverse bias (not corrected for reflection and absorption in the metal)

Band offset measurement of the ZnS/Si(001) heterojunction

B. Brar, R. Steinhoff, A. Seabaugh, X. Zhou,* S. Jiang,* and W. P. Kirk*

Raytheon TI Systems, Dallas, TX 75243.

*NanoFAB Center, Texas A&M University, College Station, TX 77843-4242
EMail: brar@resbld.csc.ti.com

Abstract. High-quality ZnS layers on silicon have recently been realized by initiating MBE growth on a vicinal Si (001) surface that has been terminated with a single monolayer (ML) of As. We report the first measurement of the electronic transport properties of the ZnS/As(1ML)/n-Si(001) heterostructure. Temperature-dependent current-voltage measurements show that the transport is characterized by an activation energy of 1.00 ± 0.04 eV for the Si/ZnS conduction band offset. A similar activation energy of 1.02 ± 0.04 eV is obtained for the opposite bias polarity, corresponding to transport over the Al/ZnS Schottky barrier.

1. Introduction

The realization of high-quality compound semiconductors that are lattice-matched to a silicon (Si) substrate will promote the development of band-gap-engineered devices in Si technology. One candidate for a barrier material is zinc sulfide (ZnS), which has an energy band gap of 3.6 eV and a zinc-blende (cubic) crystal structure with a lattice constant of 5.42 Å. By comparison, silicon has a bandgap of 1.12 eV and a diamond (cubic) crystal structure with a lattice constant of 5.431 Å. The band offset of a molecular beam epitaxy (MBE) grown ZnS/Si(111) heterojunction was measured by Maierhofer et al. [1], using photoelectron spectroscopy. They reported a valence-band offset of $\Delta E_v = 0.7$ eV and a conduction-band offset of $\Delta E_c = 1.7$ eV. The large band offsets in a straddled band line-up suggest that ZnS is an excellent choice for use as an insulating barrier that is lattice-matched to silicon. Recently, high-quality ZnS layers on silicon have been realized by initiating MBE growth on a vicinal Si (001) surface that has been terminated with a single monolayer (ML) of As [2]. In the present paper, we report the first electronic transport properties of the ZnS/As(1 ML)/n-Si(001) heterostructure.

2. Growth and Experiment

The samples were grown in a VG80S MBE chamber on phosphour-doped ($1\text{--}10 \Omega\text{-cm}$) vicinal Si substrates (100 surface with a 4° off-cut towards $[0\bar{1}1]$). Details of the ZnS growth can be found in reference [2]. Briefly, growth was initiated with a 200 nm thick not-intentionally doped silicon buffer layer at a growth temperature of 620°C . The sample was then annealed at 850°C to produce a double-stepped Si surface, as confirmed by reflection high-energy electron diffraction. After the substrate was cooled to room temperature, more than 1 ML of As was deposited. The excess (beyond 1 ML) As was then removed with a 600°C anneal. Finally, 200 nm of ZnS was grown from a solid ZnS source at a substrate temperature of 50°C followed by a 10 minute anneal at 320°C . Both Al and Au contacts were e-beam evaporated and patterned on the sample. Metal covered the entire wafer surface except a $10 \mu\text{m}$

spacer region, which isolated 15, 150, and 1500 μm diameter circular devices. In the case of Al, the rings were etched in Al-leach; in the case of Au, a lift-off process was used to define the device. The large-area greater surface outside of these circles was grounded in the electrical measurements.

3. Results and Discussion

Figure 1 is a plot of the J - V characteristics of the 150 μm diameter device for selected temperatures. The bias was swept in two different directions (arrows indicate the sweep direction). The magnitude of the voltage was swept from 0 to 2 to 0 V at a rate of ~ 1 V/min. The hysteresis predominant at lower temperatures is presumably related to the charging time of slow traps in the ZnS barrier. The voltage dependence of the current at fixed temperature indicates a nearly symmetric device. The non-exponential dependence on applied bias (large non-ideality factor) is typical for a heterostructure barrier that does not change with applied voltage. Figure 2 is an Arrhenius plot constructed from the forward-sweep data in Fig. 1 to determine the activation energy E_c for the conduction mechanism. At lower temperatures, where the curves in Fig. 2 flatten out, the current measured is presumably through defect-assisted transport (e.g., via grain boundaries or traps in the ZnS) with a relatively small thermal activation energy. At higher temperatures, the data indicate a thermally-activated process with a well-defined activation energy. The activation energy is obtained at each bias point by fitting the data to a conventional thermionic emission model $J = J_0 \cdot T^2 \exp(-E_{ac}/kT)$ [3], and plotted in Fig. 3 as a function of the applied bias. Note that an activation energy obtained from the Arrhenius plot is the extrapolated value at zero temperature, and is only accurate to within $kT \approx 40$ meV. Since the detail at low bias in Fig. 3 is smaller than this, it is not analyzed.

The activation energy may be related to the band offset by determining the chemical potential as a function of voltage and temperature. For a metal (with $E_F \gg kT$), the chemical potential is independent of both of these parameters, and the value of 1.02 ± 0.04 eV obtained from Fig. 3 for negative biases, is

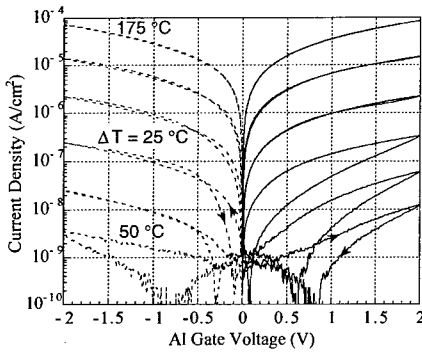


Fig. 1. Temperature dependence of the current densities through Al/ZnS/As(1ML)/Si diodes. The temperature is varied from 50 °C to 175 °C in 25 °C steps.

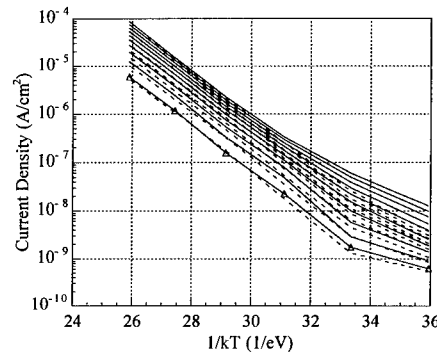


Fig. 2. I-V Arrhenius plot to extract activation energies in Al/ZnS/As(1ML)/Si diodes. Solid lines are positive gate biases (from 0.2 V to 2.0 V in 0.2 V steps) and the dashed lines are negative gate biases.

the Al/ZnS Schottky barrier height. For a non-degenerate semiconductor with fully-ionized donors, however, charge neutrality in the bulk forces $(E_c - E_F)/kT$ to remain constant as the temperature changes, and the extrapolated E_F at $T = 0$ is approximately E_c . Therefore, the activation energy of 1.00 eV measured for small positive gate voltages is approximately the conduction band offset ΔE_c . This value is considerably lower than the value of 1.7 ± 0.2 eV obtained by photoelectron spectroscopy between ZnS and non-As-terminated Si(111) [1]. This difference in the conduction band offset is partly due to the substrate orientation. Also, some of the difference may be due to a modification of the interface dipole charge caused by the As monolayer.

To understand the bias (in)dependence of the extracted activation energy we performed capacitance-voltage (C - V) measurements on the above devices. The C - V data were noisy and hysteretic. Also the data for the devices characterized above showed no evidence of electron accumulation at the ZnS/Si interface. The hysteresis in the C - V signified field-driven transfer of charge within the ZnS, i.e. mobile ions or trapped electrons in the ZnS. Electron traps in the ZnS would account for the lack of image-force barrier lowering in Fig. 3, which should be roughly 50 meV when 2 V is applied across the ZnS. If traps were in the ZnS, and the ZnS charged negatively when current flowed, then the electric field at the ZnS/Si interface (causing barrier reduction) would have been smaller than the trap-free case. Our inability to measure an accumulation capacitance in these devices is consistent with our hypothesis that there is no significant electric field at the ZnS/Si interface even under bias (shown schematically in Fig. 3).

To confirm that the activation energy represents an interface property and not a bulk transport property of the ZnS, additional metal/ZnS/As(1ML)/Si devices were fabricated in an identical manner, but with Au electrodes. Previous work has determined the Au/ZnS Schottky barrier height to be 1.2 eV larger than the Al/ZnS Schottky barrier height [4]. Temperature dependent measurements on these Au/ZnS/As(1ML)/Si-n showed that, consistent with our interface-barrier-limited current model, a large ($\sim 20x$) reduction in current was observed as plotted in Fig. 4 (only forward sweep data are shown). The asymmetry in the J - V characteristic is also consistent with our model of Schottky emission. A well-

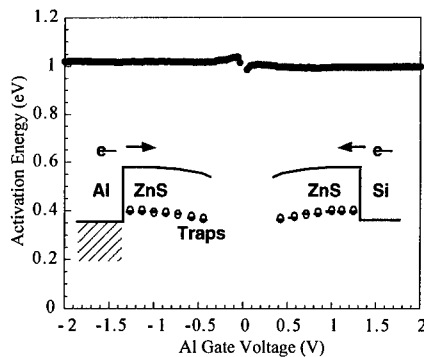


Fig. 3. Extracted activation energies in Al/ZnS/As(1ML)/Si diodes.

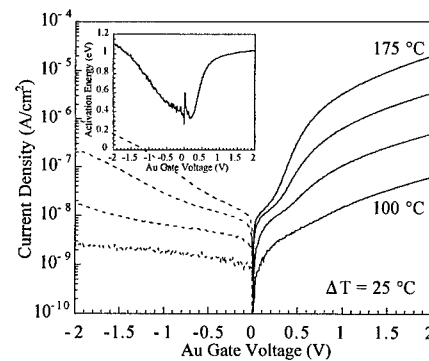


Fig. 4. Temperature dependence of the current densities through Au/ZnS/As(1ML)/Si diode. The inset shows the extracted activation energies as a function of bias.

defined activation energy (see inset of Fig. 4) exists only for positive gate voltages greater than approximately 0.6 V where it starts to level-off around 1.0 eV. This value for the ZnS/Si barrier height agrees with the value for devices with Al electrodes. For negative biases, defect transport processes dominate any bulk emission over the large Au/ZnS barrier height. Figure 4 shows that these defect processes do not have a single well-defined activation energy.

4. Conclusions

The Al/ZnS/As(1ML)/Si-n heterostructure was found to be characterized by a ZnS/Si conduction band offset $\Delta E_C = 1.00 \pm 0.04$ eV, and a Al/ZnS Schottky barrier height of 1.02 ± 0.04 . C-V measurements, I-V hysteresis, and the lack of a reduction in the barrier height due to image force lowering (expected to be ≈ 50 meV at a bias of 2 V) suggests that there are traps in the ZnS that charge negatively under bias. Figure 5 is a schematic of the proposed energy band diagram for the Al/ZnS/As(1ML)/Si-n heterostructure. The approximately 1 eV ZnS barrier heights to Al and Si, being much larger than kT at room temperature, are encouraging for the use of ZnS as an insulating epitaxial barrier for Si devices.

Acknowledgments

The authors gratefully acknowledge several stimulating discussions with Drs. R. Lake, G. Wilk, and T. Moise, and the excellent technical support of P. Stickney. This research has been supported in part by DARPA Contract No. F49620-96-C-0006, AFOSR Grant No. F49620-96-1-0242, and NSF Grant No. ECS-9306293.

References

- [1] C. Maierhofer, S. Kulkarni, M. Alonso, T. Reich, and K. Horn, *J. Vac. Sci. Techn.*, vol. B9, pp. 2238, 1991.
- [2] L. T. Romano, R. D. Bringans, X. Zhou, and W. P. Kirk, *Phys. Rev. B*, vol. 52, pp. 11202, 1995; and X. Zhou, S. Jiang, and W.P. Kirk, *J. Appl. Phys*, vol. 82 (1997).
- [3] S. M. Sze, *Physics of Semiconductor Devices*. 2nd Ed. New York: John Wiley & Sons, 1981.
- [4] M. Aven and C. A. Mead, *Appl. Phys. Lett*, vol. 7, 1965.

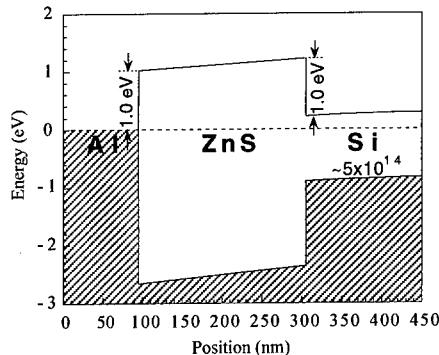


Fig. 5. Zero-bias energy band diagram for Al/ZnS/As(1ML)/Si structure.

(Pd, Ti, Au)-Based Ohmic Contacts to p- and n-doped In_{0.53}Ga_{0.47}As

W. K. Chong, E. F. Chor, C. H. Heng and S. J. Chua

Centre for Optoelectronics, Department of Electrical Engineering, National University of Singapore, 10 Kent Ridge Crescent, Singapore 119260, Singapore.

Abstract. The electrical characteristics and stability of Pd, Ti/Pd, Ti/Pd/Au and Pd/Ti/Pd/Au ohmic contacts to p- and n-doped In_{0.53}Ga_{0.47}As have been investigated. A thin contacting Pd layer has been found to be crucial to the formation of a low resistance contact to p⁺-InGaAs. On the contrary, a Ti contacting layer is desirable in contacts to n⁺-InGaAs. Pd(100Å)/Ti(200Å)/Pd(200Å)/Au(2000Å) has yielded a lowest specific contact resistance (ρ_c) of $9.61 \times 10^{-6} \Omega\text{-cm}^2$ to p⁺-InGaAs after a 350°C-20s anneal and has demonstrated sufficient stability as contact to the thin base region of InP-based HBTs. The lowest ρ_c of $2.54 \times 10^{-7} \Omega\text{-cm}^2$ to n⁺-InGaAs was achieved by Ti(200Å)/Pd(200Å)/Au(2000Å) after a 400°C-20s anneal.

1. Introduction

Two commonly used metallization schemes for InP-based heterojunction bipolar transistors (HBTs) were Ti/Pt/Au for n⁺-InGaAs and Pt/Ti/Pt/Au for p⁺-InGaAs [1-3]. Unfortunately, the evaporation of Pt requires a high temperature over a prolonged duration owing to its high melting point (1769°C) and low vapor pressure (0.14μmHg). These could cause problems such as in-situ “out-gassing” of impurities within the evaporation chamber and the hardening of photoresist. On the other hand, Pd, a metal that possesses electrical properties similar to Pt, for example resistivity (Pd : 9.93μΩ·cm; Pt : 9.85μΩ·cm) and workfunction (Pd : 4.99eV; Pt : 5.32eV), has a lower melting point of 1552°C and a much higher vapor pressure of 26μmHg. These mean easier and faster evaporation at a lower temperature compared with Pt which imply the above-mentioned problems could be alleviated. In addition, since both Pd and Pt are group VIII transition metals, they are not expected to have very different physical and chemical properties. Consequently, it may be beneficial to replace Pt by Pd in a contact system. Furthermore, several Pd-based metallization schemes [4-7] have been reported to yield a specific contact resistance (ρ_c) of the order of $10^{-5} \Omega\text{-cm}^2$ to p⁺-InGaAs. Some of these contacts have also demonstrated good thermal stability of 5 to 6 hours at 400°C [4]. In this work, we aimed to investigate the feasibility of replacing Pt by Pd in the Ti/Pt/Au and Pt/Ti/Pt/Au contact systems to p- and n-doped In_{0.53}Ga_{0.47}As. We have also included the Pd and Ti/Pd contacts in our studies with the objective of understanding the role of each constituent of the multi-layer contact systems.

2. Experiment

The epilayer structure used comprises a 600Å p⁺-InGaAs layer, a 1μm n⁺-InGaAs layer and a 0.5μm n⁺-InGaAs layer followed by a 0.3μm i-InGaAs buffer layer, grown lattice matched on an InP substrate by means of molecular beam epitaxy (MBE). The p⁺-InGaAs layer is Be-doped to a concentration of $5 \times 10^{18} \text{ cm}^{-3}$ while the n⁺-InGaAs layer is Si-doped to a concentration of $5 \times 10^{19} \text{ cm}^{-3}$. The p⁺- and n⁺-

InGaAs epilayers constitute a p⁺n junction and its current-voltage (IV) characteristic was used to assess if a metal contact to p⁺-InGaAs has enough stability for implementation on the thin base region of a HBT. If the penetration of the contact metal or the reaction zone between the metal and the underlying InGaAs exceeds 600Å, the IV characteristic of the p⁺n junction will deteriorate to a linear relationship. The specific contact resistances (ρ_c 's) to the p⁺- and n⁺-InGaAs layers were measured by means of the transmission line model (TLM) structure. The desired metals were electron beam evaporated sequentially onto the sample, in a single pump down, after a base chamber pressure of 5×10^{-7} Torr has been attained. Prior to loading into the evaporation chamber, samples were treated with 10% NH₄OH for 1 minute to remove the native oxide on the surface. A total of five metal contacts were prepared : Pd(1700Å), Ti(700Å)/Pd(700Å), Ti(200Å)/Pd(200Å)/Au(2000Å), Pd(50Å)/Ti(200Å)/Pd(200Å)/Au(2000Å) and Pd(100Å)/Ti(200Å)/Pd(200Å)/Au(2000Å), where the first metal in each sequence is in contact with semiconductor. Contacts were deposited simultaneously on p⁺- and n⁺-InGaAs. Alloying of contacts was carried out using rapid thermal annealing (RTA), in forming gas ambient, at temperature ranging from 250°C to 450°C and for duration between 10s and 50s. Anneal temperatures higher than 450°C were not used because the decomposition of InGaAs was no longer negligible.

3. Results and Discussion

All the contacts were ohmic as-deposited with smooth surface morphology. The adhesion of contacts to InGaAs was good except for Pd which peeled off easily after a 400°C-20s anneal. The presence of Ti seems to improve the adhesion as no peeling was observed for Ti/Pd, Ti/Pd/Au and Pd/Ti/Pd/Au. The ρ_c of the following contacts : Pd(1700Å), Ti(700Å)/Pd(700Å), Ti(200Å)/Pd(200Å)/Au(2000Å) and Pd(100Å)/Ti(200Å)/Pd(200Å)/Au(2000Å) to p⁺- and n⁺-InGaAs are shown in Fig.1 as a function of the RTA temperature. Anneal duration is 20s. The missing data at 400°C and higher temperature were caused by one of the following reasons : contacts have peeled off or shorting of metal through the 600Å p⁺-InGaAs layer. In the latter, although ρ_c can be measured, it does not truly represent the contact resistance to p⁺-InGaAs. As shown in Fig.1, Pd and Pd/Ti/Pd/Au render a lower minimum ρ_c to p⁺-InGaAs than Ti/Pd and Ti/Pd/Au for the anneal temperature range of 250°C to 400°C. It may be inferred that the presence of a contacting Pd layer is instrumental to the formation of a low ρ_c to p⁺-InGaAs. Similar observations were reported by P. Ressel et al [6] and H. Okada et al [8]. P. Ressel et al studied Pd/Pt and Ti/Pt contacts to p⁺-InGaAs and obtained a lower ρ_c for the former. H. Okada et al investigated Ti/Pt/Au and Pt/Ti/Pt/Au contacts to p⁺-GaAs and found that the latter gave a lower ρ_c . The minimum ρ_c 's achieved for Pd and Pd/Ti/Pd/Au to p⁺-InGaAs are $2.18 \times 10^{-6} \Omega\text{-cm}^2$ (after a 300°C-20s anneal) and $9.61 \times 10^{-6} \Omega\text{-cm}^2$ (after a 350°C-20s anneal) respectively, as shown Fig.1. For contacts to n⁺-InGaAs, the lowest ρ_c of $2.54 \times 10^{-7} \Omega\text{-cm}^2$ is obtained with Ti/Pd/Au after a 400°C-20s anneal. This is in contrast to the results for p⁺-InGaAs where contacts with Pd adjoining the semiconductor exhibited a lower ρ_c . It may be concluded that different contacting layers are needed to achieve low ρ_c to p⁺-InGaAs and n⁺-InGaAs - Pd for p⁺-InGaAs and Ti for n⁺-InGaAs. It is worth noting that these observations are in line with the common contacts used in InP-based HBTs - Ti/Pt/Au to n-InGaAs and Pt/Ti/Pt/Au to p-InGaAs - which we try to replace by Ti/Pd/Au and Pd/Ti/Pd/Au respectively.

With an anneal temperature of 400°C or higher, the IV characteristic of the p⁺n junction, with Pd or Ti/Pd/Au as contact, became ohmic. This indicated that either the contact metal has diffused deeper than 600Å into p⁺-InGaAs or the reaction zone between the metal and the underlying p⁺-InGaAs

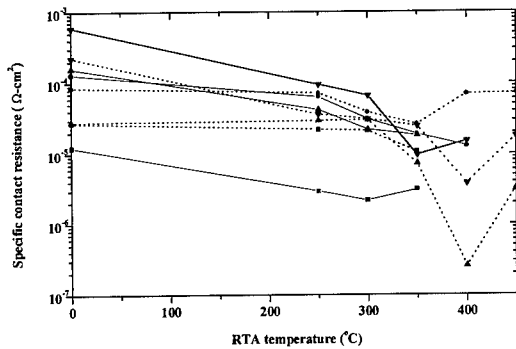


Fig. 1 Variation of ρ_c as a function of RTA temperature for contacts to p^+ -InGaAs (—) and n^+ -InGaAs (---) : (a) ■ - Pd(1700Å), (b) ● - Ti(700Å)/Pd(700Å), (c) ▲ - Ti(200Å)/Pd(200Å)/Au(2000Å) and (d) ▼ - Pd(100Å)/Ti(200Å)/Pd(200Å)/Au(2000Å). The anneal duration is 20s.

has exceeded the same thickness. On the other hand, p^+n junctions with a Pd(100Å)/Ti/Pd/Au contact survived a 400°C-20s anneal although those with a Pd(50Å)/Ti/Pd/Au contact did not. The thickness of the contacting Pd is therefore observed to be an important parameter. The shorting of the Pd and Pd(50Å)/Ti/Pd/Au contacts indicates that the amount of Pd present must be carefully controlled in order to achieve good thermal stability for the Pd/Ti/Pd/Au contact. The improved thermal stability of Pd(100Å)/Ti/Pd/Au over Ti/Pd/Au is similar to that of Pt/Ti/Pt/Au over Ti/Pt/Au reported by H. Okada et al [8]. Both Pt and Pd exhibit a similar behaviour as a barrier to the in-diffusion of metals. In the case of Ti/Pt/Au contact, Ti has been shown to form a complicated reaction zone of up to 800Å with InGaAs [9] and this is most likely the reason for the shorting of the Ti/Pd/Au contact. After a 450°C-20s anneal, all the contacts shorted through the p^+n junction. The surface morphology also became rough and the colour turned pale. Rough surface morphology was also observed by P. Leech et al [5] for Pd/Zn/Pd/Au contacts and their AES depth profiles showed a significant out-diffusion of In, Ga and As signifying the decomposition of InGaAs.

Fig.2 shows the variation of ρ_c with the anneal duration at a RTA temperature of 350°C for Ti(200Å)/Pd(200Å)/Au(2000Å), Pd(50Å)/Ti(200Å)/Pd(200Å)/Au(2000Å) and Pd(100Å)/Ti(200Å)/Pd(200Å)/Au(2000Å) to p^+ - and n^+ -InGaAs. The optimum anneal duration is observed to be about 20s for contacts to p^+ -InGaAs, regardless of the contacting layer. The minimum ρ_c of $9.61 \times 10^{-6} \Omega \cdot \text{cm}^2$ was attained by Pd(100Å)/Ti/Pd/Au. The same contact also yielded the lowest ρ_c of $1.51 \times 10^{-6} \Omega \cdot \text{cm}^2$ to n^+ -InGaAs but after a longer anneal of 40s. It can be seen in Fig.2 that for contact to n^+ -InGaAs, the thicker the contacting Pd layer, the lower is the ρ_c and the longer is the required anneal duration. This seems to indicate that the reaction between Pd and n^+ -InGaAs proceeds with time and more reaction leads to a lower ρ_c . After a further 350°C-15min anneal, ρ_c 's of Pd(100Å)/Ti/Pd/Au to n^+ - and p^+ -InGaAs degraded to the order of $10^{-4} \Omega \cdot \text{cm}^2$. Although ρ_c has increased, Pd(100Å)/Ti/Pd/Au did not short through the p^+n junction. It may therefore be concluded that the contact has sufficient stability for further thermal processing, such as the deposition of SiN_x at 350°C for 15 mins. Pd(100Å)/Ti/Pd/Au has also demonstrated the possibility of a common contact to n^+ - and p^+ -InGaAs : a reasonably low ρ_c of less than $2.5 \times 10^{-5} \Omega \cdot \text{cm}^2$ was obtained for both types of InGaAs after a 350°C-20s anneal, as shown in Fig.2.

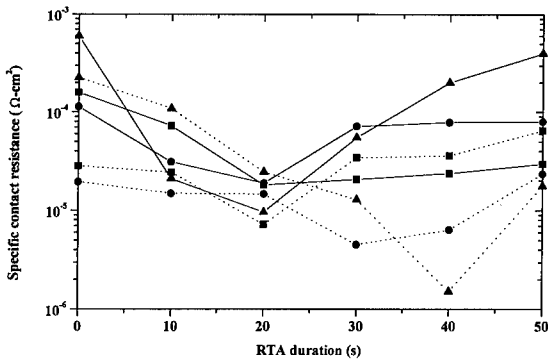


Fig. 2 Variation of ρ_c as a function of RTA duration for contacts to p^+ -InGaAs (—) and n^+ -InGaAs (----) :
 (a) ■ - Ti(200Å)/Pd(200Å)/Au(2000Å), (b) ● - Pd(50Å)/Ti(200Å)/Pd(200Å)/Au(2000Å) and (c) ▲ -
 Pd(100Å)/Ti(200Å)/Pd(200Å)/Au(2000Å). The RTA temperature is 350°C.

4. Conclusion

Our investigations have demonstrated promising results of replacing Pt by Pd in the Ti/Pt/Au and Pt/Ti/Pt/Au contacts. Ti(200Å)/Pd(200Å)/Au(2000Å) has shown to be very suited for n^+ -InGaAs with a minimum ρ_c of $2.54 \times 10^{-7} \Omega \cdot \text{cm}^2$ while Pd(100Å)/Ti(200Å)/Pd(200Å)/Au(2000Å) has yielded not only a low ρ_c of $9.61 \times 10^{-6} \Omega \cdot \text{cm}^2$ but also adequate thermal stability for use as contact to the thin p^+ -InGaAs base region of InP-based HBTs. In addition, Pd(100Å)/Ti(200Å)/Pd(200Å)/Au(2000Å) has provided the possibility of a single metal system to both n^+ - and p^+ -InGaAs with a ρ_c of less than $2.5 \times 10^{-5} \Omega \cdot \text{cm}^2$.

Acknowledgement

This work was supported by Academic Research Grant RP950671 and MINDEF-NUS Joint R&D Programme (GR 6476). Thanks are due to Mr R. Akkipeddi for growing the epilayer structure.

References

- [1] Kurishima K *et al* 1994 *IEEE Trans. Electron Dev.* 41 1319-1325
- [2] Willen B *et al* 1995 *IEEE Electron Dev. Lett.* 16 479-481
- [3] Sawdai D *et al* 1995 *Inst. Phys. Conf. Series* 145 621-626
- [4] Leech P *et al* 1995 *J. Appl. Phys.* 77 3908-3912
- [5] Leech P *et al* 1994 *J. Appl. Phys.* 76 4713-4718
- [6] Ressel P *et al* 1992 *Electronics Lett.* 28 2237-2238
- [7] Shantharama L G *et al* 1990 *Electronics Lett.* 26 1127-1129
- [8] Okada H *et al* 1991 *Jap. J. Appl. Phys.* 30 L558-560
- [9] Chu S N G *et al* 1990 *J. Appl. Phys.* 67 3754-3760

PtTiPtAu and PdTiPtAu ohmic contacts to p-InGaAs

J. S. YU, S. H. Kim, T. I. Kim

Samsung Advanced Institute of Technology, P.O. Box 111, Suwon, Korea 440-600

Abstract. 10nm layers of Pt and Pd were employed as an interlayer between Ti(30nm)Pt(80nm)Au(200nm) metallization and p-InGaAs doped at $1\sim4\times10^{19}\text{cm}^{-3}$. For the annealing temperatures of 300–500°C, the PtTiPtAu and the PdTiPtAu metallizations exhibited consistently lower contact resistivities than the TiPtAu metallization. The effective barriers height of the PtTiPtAu contacts (0.11eV) was estimated to be lower than those of the PdTiPtAu contacts (0.14eV) and the TiPtAu contacts (0.16eV). The high work function Pt lowered the barrier height. The Pd, on the other hand, formed a favorable interfacial compound when as-deposited, thereby reducing the contact resistivity.

1. Introduction

In a majority of InP based optoelectronic devices, $\text{In}_{0.53}\text{Ga}_{0.47}\text{As}$ doped over $1\times10^{19}\text{cm}^{-3}$ is used as a p-type contact layer since it has the smallest band gap among InP lattice-matched materials. As for the p-type contact metals, the TiPtAu metallization is, by far, the most popular. This metallization scheme together with appropriate annealing was reported to yield very low contact resistivities in the region of $10^{-7\sim-8}\Omega\text{cm}^2$ [1~3]. However, the InGaAs layers were invariably doped extremely high i.e. $>1\times10^{20}\text{cm}^{-3}$. The only exception was Katz et al [4]; they reported a contact resistivity of $3.4\times10^{-8}\Omega\text{cm}^2$ with InGaAs doped at $1.5\times10^{19}\text{cm}^{-3}$. In our experience, the contact resistivity of TiPtAu contacts to p-InGaAs doped at $1\times10^{19}\text{cm}^{-3}$ was mere $4.5\times10^{-5}\Omega\text{cm}^2$ while the same metallization formed ohmic contacts to p-GaAs in the region of $0.4\sim1.1\times10^{-6}\Omega\text{cm}^2$. The high contact resistivity with p-InGaAs should be related to the way the Fermi level pins in InGaAs - near the conduction band edge [5]. The n-type barrier height is nearly zero. For p-type, it is nearly the same as the entire band-gap, making it difficult to form low resistivity ohmic contacts.

The schottky barrier height, Φ_b between a p-type semiconductor and a metal is the difference in their respective work functions, Φ_s and Φ_m .

$$\Phi_b = \Phi_s - \Phi_m$$

When a metal with high work function is used, the barrier height is reduced as the band bending becomes small. Therefore, it would be possible to lower the contact resistivity. In this paper, the role of two high work function metals, Pt ($\Phi_m=5.65\text{eV}$) and Pd ($\Phi_m=5.12\text{eV}$), was investigated as an interlayer between p-InGaAs and TiPtAu metallization. The work function of Ti is 4.33eV.

2. Experiment

$1.3\mu\text{m}$ $\text{In}_{0.53}\text{Ga}_{0.47}\text{As}$ layers were grown on Fe-doped semi-insulating InP using metalorganic vapour phase epitaxy (MOVPE). Three different Zn doping concentrations - $1\times10^{19}\text{cm}^{-3}$, $2\times10^{19}\text{cm}^{-3}$, $4\times10^{19}\text{cm}^{-3}$ were prepared to study the current transport mechanism. Prior to metal deposition, the InGaAs layers were treated with buffered oxide etchant for 10 seconds to remove oxides. The basic metallization scheme was Ti(30nm)Pt(80nm)Au(200nm), but a 10nm Pt or Pd interlayer was included between the TiPtAu metallization and the InGaAs. The results were compared to the one with no interlayer. The

metallizations were electron-beam evaporated at a base vacuum better than 3×10^{-7} mbar. The TLM pads, each 100 μm wide and 300 μm long were patterned using a standard photolithographic technique and lift-off. The spacings between the pads were 10, 15, 20, 30, 40, 60, 80 μm . The contacts were heat-treated using a rapid thermal annealer between 300~500°C for 30 seconds in a nitrogen ambient.

3. Results and Discussion

The mean contact resistivities of the three metallizations are plotted as a function of annealing temperature for the three different doping concentrations in Fig. 1. For $1 \times 10^{19}\text{cm}^{-3}$, none of the metallizations exhibited contact resistivities below $1 \times 10^{-5}\Omega\text{cm}^2$. Doping concentrations greater than $2 \times 10^{19}\text{cm}^{-3}$ were required to achieve contact resistivities in the region of $10^{-6}\Omega\text{cm}^2$.

When a Pd or Pt interlayer was included in the metallization, the contact resistivity was reduced for a given doping concentration. The PtTiPtAu contacts generally yielded the lowest contact resistivity, but when as-deposited, the contact resistivity of the PdTIPtAu contacts was the lowest. The TiPtAu contact had to be annealed above 400°C in order to achieve appreciable reduction in contact resistivity. The PtTiPtAu contacts required a lower annealing temperature i.e. at around 300°C and the optimum annealing temperature was 350~400°C depending on doping concentration. The PdTIPtAu produced the lowest as-deposited contact resistivity and could effectively be used non-alloyed provided that the doping concentration is greater than $2 \times 10^{19}\text{cm}^{-3}$. The decrease in contact resistivity upon subsequent annealing was small, the contact resistivity remaining within $3 \sim 4 \times 10^{-6}\Omega\text{cm}^2$ over 300~500°C for the doping concentration of $2 \times 10^{19}\text{cm}^{-3}$ (Fig. 1b). Compared to the previously reported PdPt non-alloyed contacts, for which the optimum annealing temperature was tightly confined around 300°C [1], the PdTIPtAu contacts should satisfy wider processing requirements and have superior long term reliability.

The reduction in contact resistivities when the doping concentration was increased from $1 \times 10^{19}\text{cm}^{-3}$ to $2 \times 10^{19}\text{cm}^{-3}$ was about one order. However, the reduction when the doping was increased from $2 \times 10^{19}\text{cm}^{-3}$ to $4 \times 10^{19}\text{cm}^{-3}$ was only about half for the PtTiPtAu contacts and even less for the other contacts. If the tunnelling is the dominant current transport mechanism, the contact resistivity should proportional to $\exp(1/\sqrt{n})$, where n is the doping concentration [6]. To estimate the extent of tunnelling, the characteristic energy, E_{∞} was calculated and compared to kT , where k is the Boltzmann's constant and T is temperature in Kelvin.

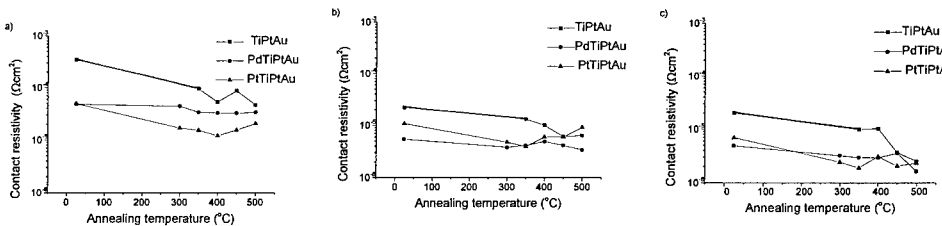


Fig. 1 Mean contact resistivities of the three metallizations are plotted as a function of annealing temperature. The doping concentration of InGaAs are a) $1 \times 10^{19}\text{cm}^{-3}$, b) $2 \times 10^{19}\text{cm}^{-3}$ and c) $4 \times 10^{19}\text{cm}^{-3}$

E_{∞} is defined as below.

$$E_{\infty} = \frac{q \cdot \hbar}{2} \sqrt{\frac{n}{(m^* \cdot \epsilon)}}$$

q is the electronic charge; \hbar is the Planck's constant divided by 2π ; m^* is the effective mass of tunnelling hole; and ϵ is the dielectric constant of InGaAs. Using $m^*=0.46m_0$ and $\epsilon=13.1\epsilon_0$ [7], the E_{∞}/kT values were calculated to be 1.85 for $n=1\times 10^{19}\text{cm}^{-3}$, 2.61 for $n=2\times 10^{19}\text{cm}^{-3}$ and 3.70 for $n=4\times 10^{19}\text{cm}^{-3}$. Tunnelling is dominant only if $E_{\infty}/kT \gg 1$, which was not the case here. For p-type InGaAs doped at low 10^{19}cm^{-3} , the current transport mechanism is likely to be thermionic field emission. Assuming that the metal-semiconductor interface is identical microstructurally regardless of doping concentration for a given annealing temperature, isothermal contact resistivity was plotted against $\exp(1/\sqrt{n \cdot \coth(E_{\infty}/kT)})$ for each metallization in Fig. 2. The PtTiPtAu metallization conformed to the thermionic field emission model well except that annealed at 500°C. In the cases of the TiPtAu contacts, the as-deposited specimens and those annealed below 400°C deviated from the model at the high doping concentration. As for the PdTiPtAu, the contacts annealed below 450°C gave poorer fits. However, the overall fit was better than the tunnelling model.

The log slope of contact resistivity against $\exp(1/\sqrt{n \cdot \coth(E_{\infty}/kT)})$ is a function of the barrier height. The gradients of the slopes did not decrease as annealing temperature increased, indicating that the reduction in contact resistivity did not involve changes in barrier height. From the average gradient of each metallization, the effective barrier height was calculated. The PtTiPtAu contacts had the lowest barrier height of 0.11eV followed by 0.14eV of the PdTiPtAu contacts and 0.16eV of the TiPtAu contacts. From the difference in the effective barriers, it can be concluded, for the PtTiPtAu contacts, that the high work function Pt interlayer had the desired effect of lowering the contact resistivity but for the PdTiPtAu contacts, it was less conclusive.

While the current transport mechanism may indeed be of thermionic field emission, other factors such as microstructural reactions at the metal-semiconductor interface may play an important role in the case of the PdTiPtAu contacts. When transmission electron microscopy was performed on the as-deposited PdTiPtAu contacts, an interfacial layer was observed (Fig. 3). The layer thickness was approximately 50nm, thin enough for most optoelectronic applications. Although the exact composition was not identified, there have been reports that Pd forms metastable compounds with the semiconductor i.e. $Pd_xInGaAs$ [8]. This compound is supposed to be metastable, but, to break it down, a third species is required to interact with Pd. Ti seemed stable in this respect.

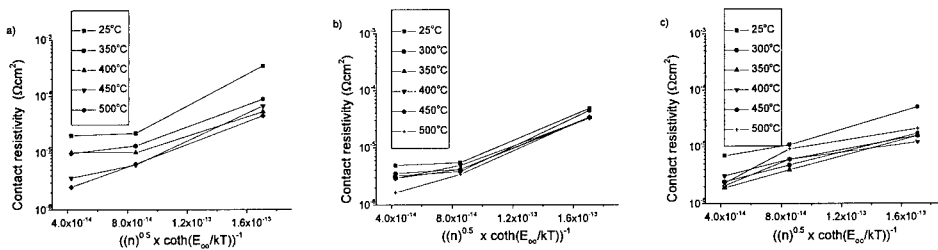


Fig. 2 Contact resistivity variation of each metallization with InGaAs doping concentration is plotted according to the thermionic field emission model a)TiPtAu b)PdTiPtAu c) PtTiPtAu

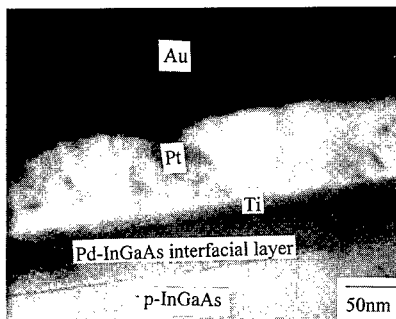


Fig. 3. Cross Sectional TEM micrograph of the as-deposited PdTiPtAu contacts to p-InGaAs

The layer was found to be intact when annealed at 350°C. This may explain why the contact resistivity varied little with annealing temperature. As for the PtTiPtAu contacts, the as-deposited metal-semiconductor interfaces was clean, but an interfacial layer was also observed when annealed at 350°C. The thickness was approximately the same as that of the PdTiPtAu contacts. It was concluded that the reduction in contact resistivity upon annealing was related to changes in contact microstructures.

4. Conclusions

The role of Pt and Pt interlayers in the TiPtAu contacts to p-InGaAs was studied as a function of annealing temperature and of the p-InGaAs doping concentration. The Pt lowered the effective barrier height due to its high work function. As for the Pd, the effective barrier height alone could not explain the improvement in contact resistivity. The formation of a favorable interfacial compound even when as-deposited should also be taken into account.

5. References

- [1] Ressel P, Vogel K, Frizsche D and Mause K 1992 *Electron. Lett.* 28 2237-8
- [2] Stareev G, Umbach A, Fidorra F and Roehle H 1991 *Third Int. Conf. on InP and Related Materials*, 264-267
- [3] Franz G and Amann M, 1993 *J. of Electrochem. Soc.* 140 847-50
- [4] Katz A, Dautremont-Smith W, Chu S, Thomas P, Kozi L, Lee L, Riggs V, Brown R, Napholtz S and Jilko J 1989 *Appl. Phys. Lett.* 54 2306-8
- [5] Rhoderick E and Williams R 1988 *Metal-Semiconductor Contacts*, 2nd Edition, Oxford Science Publications, Oxford Press
- [6] Yu A, 1970 *Solid-State Electron.* 13 239-47
- [7] Bhattacharya P 1993 *Properties of lattice-matched and strained Indium Gallium Arsenide*, An INSPEC publication, the Institution of Electrical Engineers
- [8] Ressel P, Strusny H, Trapp M and Fritzsche D 1994 *Appl. Phys. Lett.* 65 1174-6

Low Temperature Formation of Low Resistivity W Contact with Ultra Thin Mixed Layer on Molecular Layer Epitaxially-Grown GaAs

Fumio Matsumoto^a, Jun-ichi Nishizawa^a, Yutaka Oyama^{b,a}, Piotr Plotka^a, Yoshiyuki Oshida^b, and Ken Suto^{b,a}

^a Semiconductor Research Institute of Semiconductor Research Foundation, Kawauchi Aoba, Sendai 980, Japan

^b Dep. of Materials Science, Graduate School of Engineering, Tohoku University, Aramaki Aoba, Sendai 980-77, Japan

Abstract. The precursor for the W CVD on GaAs used is W(CO)₆. The contact resistance in W/GaAs is obtained by the transmission line measurements of patterned W on heavily doped GaAs grown by MLE. The dependence of the contact resistance on the surface treatment prior to the W CVD is also studied. Barrier height of W/GaAs structure is measured by the temperature dependence of I-V characteristics in reference to the contact resistance. The W/GaAs interface is analyzed using SIMS and RBS. Contact resistance of non-alloyed structure achieved are $3 \times 10^7 \Omega\text{cm}^2$ for n-type GaAs and below $5 \times 10^8 \Omega\text{cm}^2$ for p-type respectively. From the physical analyses, the mixed layer in W/GaAs interface is estimated less than 20Å.

1. Introduction

In recent years, the active region of the fast semiconductor devices is localized in atomic scale and the thin layered structure is required with atomic accuracy(AA). In such fast devices, the metal/semiconductor contacts limit net operating speed. In addition, the conventional alloyed contact cannot be applied for such thin layered structures. Therefore, low resistivity metal/semiconductor contact formed at low temperature with thin mixed layer has been urgently required. W/GaAs contacts were found stable up to 500°C. This temperature is higher than used for selective regrowth with the molecular layer epitaxy (MLE) for the 100Å channel GaAs static induction transistor (SIT) [1]. Sputtering was commonly used for W deposition. However, it can result in generation of defects in thin active semiconductor layers.

In this report we present CVD W suitable for ultra-thin devices. The contact resistance in W/GaAs is shown as a function of surface stoichiometry by using the transmission line measurements (TLM) on heavily doped GaAs grown by MLE. Barrier height of W/GaAs is studied in reference to lowering the contact resistance. The W/GaAs interface and the impurity profiles in MLE GaAs layers are measured by secondary ion mass spectrometry (SIMS). Rutherford backscattering spectroscopy (RBS) is used to study the structural properties of W/GaAs interface.

2. Experiments

The precursor for the W deposition on GaAs used is W(CO)₆. The W layers were deposited in the MLE reactor [2]. Prior to the W CVD, oxides were removed from GaAs surface, in the deposition chamber, by exposing to AsH₃ below 480°C. Oxides are chemically reduced with this process rather than physically evaporated[3]. Immediately after oxide reduction, W(CO)₆ was injected continuously at 360°–400°C with the pressure of 15 mTorr. GaAs surfaces were heated with a halogen lamp located over the wafer.

The contacts to n-type MLE GaAs layers doped with Te on semiinsulating undoped (100) GaAs were studied. The MLE layers were grown with triethylgallium (TEG) and AsH₃ precursors. Diethyltellurium (DETe) was used for doping. P type MLE layers were doped with Zn from diethylzinc (DEZn) or with C from trimethylgallium[4]. W/GaAs contacts were evaluated by a transmission line method (TLM) with the SiN patterned structure. By using SiN remote-plasma

deposition and two-step etching process, the process-induced defects in W/GaAs interface were safely avoided in TLM fabrication process. Wet etching with $\text{NH}_4\text{OH}:\text{H}_2\text{O}_2:\text{H}_2\text{O}$ was used for patterning of the W layers.

The Schottky barrier heights of W/GaAs contacts were estimated by using temperature dependence of the I-V characteristics. By the following equation, the barrier heights ϕ_b were calculated.

$$J_s = A^* T^2 \exp(-\phi_b/kT)$$

where J_s is the saturation current density, A^* is the effective Richardson constant, T is the measurement temperature, k is the Boltzmann constant, V_a is the applied voltage, ϕ_b is the Schottky barrier height.

The impurity profiles in MLE layers were obtained by SIMS. A primary sputtering beam of Cs and O ion with 1keV for negative and positive SIMS were used, respectively. W/GaAs interface profiles were analyzed by time of flight (TOF) SIMS, in which the sputtering beams of Ar^+ of 1keV were used to minimize a mixing effect for high depth resolution.

RBS measurements were carried out by the 1.5MeV He^+ irradiation. W/GaAs samples used for RBS measurements were the same as those for the barrier height measurements. Random spectra were measured by tilting the crystal surface 7° off to the <100> axis. Plane channeling was safely avoided. Angular dependence of the backscattering yield was also measured. He^+ dose for each angular step used was 200nC.

3. Results and Discussion

The deposition could be observed only for pressures higher than 1×10^{-3} Torr, for the entire tested range of temperature 360° - 400°C. Deposition rate was about 3 Å/min on GaAs, like reported for pyrolytic decomposition[5]. However, we can not exclude some photolytic reaction[6]. Although the GaAs substrates were not intentionally illuminated, the light of the halogen heater lamp contained near-UV wavelengths. The W layers on GaAs observed with Nomarski and SEM microscopes appeared mirror-like. The layers on SiN had a grain structure, similar to the one reported previously[5]. The difference in layer morphology between SiN and GaAs suggests a catalytic properties of the GaAs clean surface.

Fig.1 shows the relation of the carrier concentration in MLE layers with Te concentration measured by SIMS. The carrier concentration gradually increased over $1\times 10^{19}\text{cm}^{-3}$ Te concentration, and beyond $4\times 10^{20}\text{cm}^{-3}$, decreased rapidly. In this figure, the specific contact resistance ρ_c is also shown as a function of Te concentration. ρ_c strongly depended on Te concentration and had a minimum at the peak of the carrier concentration. For heavily doped semiconductors the tunneling becomes predominant, and ρ_c is determined by the factor, $\exp(\phi_b/N_D^{1/2})$. The dependence was different from the tunneling theory. It can be related to excess Te atoms adjacent to W/GaAs interface. The lowest ρ_c was $3\times 10^7\Omega\text{cm}^2$. This is the lowest reported value for doping concentration in the range of 10^{19}cm^{-3} . Similar values were reported by Patkar, *et al* [7], for molecular beam epitaxial (MBE) GaAs doped with Si as the low temperature grown cap. The MLE layers, reported here, were doped uniformly and no passivation layers were necessary. The fabrication process used was

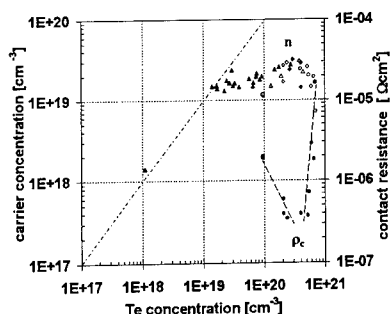


Fig.1 Te concentration dependence of the carrier concentration in MLE layer and the specific contact resistance for W/GaAs

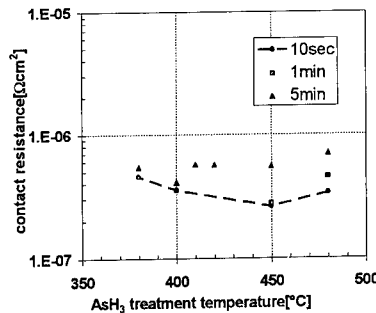


Fig.2 AsH₃ treatment temperature dependence of the specific contact resistance. AsH₃ pressure was 8×10^{-4} Torr.

close to that used for device fabrication, including SiN PE CVD and ozone ashing for semiconductor cleaning. Using uniformly doped top layers of GaAs is advantageous for such an application. In addition, all processes reported here for the CVD W contacts were done at the temperature below 480°C, which is required for ultra-thin devices[1] to prevent their thermal degradation. To achieve ρ_c of $3 - 4 \times 10^7 \Omega\text{cm}^2$, it was also necessary to apply AsH₃ treatment temperature below 480°C for oxide reduction prior to the W CVD, as shown in Fig.2. In all experiments, the CVD temperature did not exceed that of AsH₃ treatment. The lowest ρ_c was obtained with the AsH₃ treatment at 450°C 10 s.

The average value of the ρ_c for the W contacts to C-doped p-GaAs was $2 \times 10^8 \Omega\text{cm}^2$ at acceptor concentration $3 \times 10^{19} \text{ cm}^{-3}$ as shown in Fig.3. The low ρ_c value and low mobility of p-type layers result in large uncertainty of this value. The measured values were from almost 0 to $5 \times 10^8 \Omega\text{cm}^2$. At that low ρ_c values, the main source of error was an absolute accuracy of distance measurements between the TLM contacts, which was 0.1 μm in our laboratory. The ρ_c extraction accuracy is lost, if a transfer length $L = (\rho_c / R_s)^{1/2}$ becomes comparable to the contact distance measurement accuracy, where R_s is a sheet resistance value. The obtained ρ_c for C dopant was about 1/10 smaller than expected from the hole concentration measured in the MLE layer and literature reports, shown in Fig.3. One possible reason for this is oxide free interface of our layers. The results of Stareev[8], who obtained a low ρ_c value for $N_A = 2 \times 10^{20} \text{ cm}^{-3}$ after sputter, in-situ, cleaning and annealing, indicate importance of this factor. The ρ_c value for Zn dopant was 10 times larger, $1 \times 10^9 \Omega\text{cm}^2$, at the same acceptor concentration average of $3 \times 10^{19} \text{ cm}^{-3}$, than for C. The W contact resistance to the Zn-doped MLE layers corresponds well with the reported ρ_c values(Fig.3). To explain the difference between the W contacts to C-doped and to Zn-doped layers requires further investigation.

Fig.4 shows the dependence of Schottky barrier heights ϕ_b on the surface treatment condition prior to the W deposition. The surface treatment was carried out at 480°C for 30 min under various AsH₃ pressure. W deposition was carried out at 380°C for 30 min. The surface treated without AsH₃, in vacuum 5×10^{-9} Torr, gives the lowest ϕ_b , 0.58 eV by I-V characteristics. ϕ_b increases up to 0.8 eV with AsH₃ pressure at 1×10^{-3} Torr. The ideal factor of the Schottky barrier diode on the surface treated without AsH₃ is 1.05, and that with higher AsH₃ pressure, 1.01, indicates that the interface crystal quality depends on the surface treatment prior to the W deposition. From experiments on pin diodes regrown with MLE on AsH₃ treated interfaces, it was also concluded[3], this treatment affects crystal structure in layers adjacent to the interface. This can explain the dependence of the ρ_c value on the treatment temperature though ϕ_b is as high as 0.75 eV. Possible mechanisms include depletion of the surface layers from dopant atoms by their evaporation or exchange reactions, as well as modification of the barrier height by crystal structure changing.

Fig.5 shows the angular dependence of backscattering yield of RBS from the surface W, W/GaAs interfacial region and the bulk region of GaAs. Dip curve was obtained from the W/GaAs SBD mentioned previous paragraph, which W layer is deposited on the GaAs surface heat-treated in vacuum for 30 min just prior to the deposition. As shown in Fig.5, the angular dependence of backscattering yield from the surface W shows clear dip almost at the same angle, where the

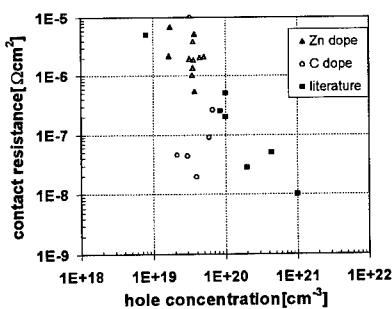


Fig.3 Carrier concentration dependence of the specific contact resistance to p-MLE GaAs

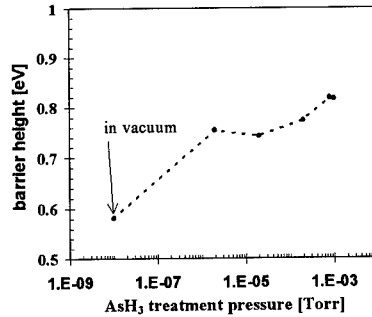


Fig.4 AsH₃ pressure dependence of Schottky barrier height in surface treatment. Temperature is 480°C and time is 30min.

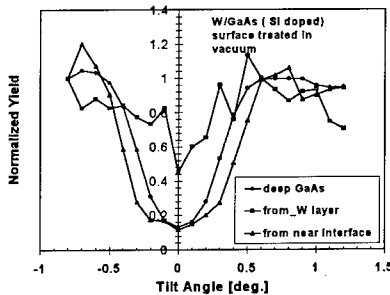


Fig.5 Angular dependence of backscattering yield of RBS from the surface W, the W/GaAs interface and the bulk GaAs

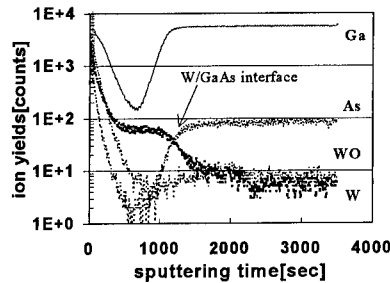


Fig.6 TOF-SIMS profile of W/GaAs. Surface treatment was carried out at 450°C for 10 sec with $\text{AsH}_3:8 \times 10^{-4}$ Torr. W was deposited at 380°C for 30min.

underlying GaAs shows <100> axial channeling. Therefore, the W atoms deposited on GaAs show <100> aligned when the GaAs surface is heat-treated in vacuum at 480°C for 30min just prior to the W deposition. As shown previously, the SB height was lowered when the GaAs surface was heat-treated in vacuum at 480°C compared with that heated under AsH_3 exposure of 1×10^3 Torr. Whereas the atomic structure of deposited W/GaAs is not clear yet, it is considered that the barrier height of W/GaAs structure is closely related with the atomic alignment of W on GaAs.

In Fig.6, the W/GaAs interface profile measured by TOF-SIMS is shown. W to GaAs interface was clearly separated, and the mixed layer in the interface was estimated less than 20Å. But strange profile was seen on the surface of W. Ga, As and O piled up. And in the W film, O yields reduced, and also C (not shown). It is possible to explain these results by a surface instability or a matrix effect, but it is necessary to study details further more.

4. Conclusion

In summary, CVD of W from $\text{W}(\text{CO})_6$ on MLE n-type layers, doped with Te, gives contact resistance $\rho_c = 3 \times 10^{-7}$ Ωcm^2 and mirror-like layer morphology. The native oxides can be reduced with AsH_3 prior to the CVD. The AsH_3 treatment and CVD temperatures should not exceed 480°C. The CVD W contacts to p-GaAs MLE layers doped with C give ρ_c in the low range of $10^8 \Omega\text{cm}^2$, while for the Zn dopant, only $1 \times 10^6 \Omega\text{cm}^2$ was obtained. The low contact resistance is obtained for electrically active dopant concentration about one tenth lower than expected from literature reports. The mixed layer in the interface was estimated less than 20Å. The conditions used for GaAs MLE and W CVD are suitable for self-aligning constructions of ultra-thin devices with regrown epitaxial layers.

Acknowledgement

Authors would like to acknowledge Dr. T.Kurabayashi for useful discussion and TOF-SIMS measurement, and Mr. H.Kikuchi, Mr. T.Hamano, Mr. M.Henmi and Mr. K.Ito for MLE layer growth, W CVD and sample processing.

References

- [1] Plotka P, et al 1994 *Applied Surface Sci.* 82/83 91-96
- [2] Nishizawa J, et al 1989 *J. Electrochem. Soc.* 136 478-484
- [3] Oyama Y, et al 1994 *Applied Surface Sci.* 82/83 41-45, Nishizawa J, et al 1996 *Surface Science* 348 105-114
- [4] Kurabayashi T and Nishizawa T 1994 *Applied Surface Sci.* 82/83 97-102
- [5] Kaplan L H and d'Heurle F M 1970 *J. Electrochem. Soc.* 117 693-700
- [6] Solanki R, et al 1981 *Appl. Phys. Lett.* 38 572-574
- [7] Patkar MP, et al 1995 *Appl. Phys. Lett.* 66 1412-1414
- [8] Stareev G, 1983 *Appl. Phys. Lett.* 62 2801-2803

Electrical and Optical Anisotropy of Layered In_2Se_3 Epitaxial Films

Tomohiko Ohtsuka, Tamotsu Okamoto*, Akira Yamada and Makoto Konagai

Department of Electrical and Electronic Engineering, Tokyo Institute of Technology

*Research Center for Quantum Effect Electronics, Tokyo Institute of Technology

2-12-1, Ookayama, Meguro-ku, Tokyo 152, JAPAN

Tel +81-3-5734-2662 Fax +81-3-5734-2897 E-mail: ohtsuka@solid.pe.titech.ac.jp

abstract. In_2Se_3 epitaxial films with layered structure were successfully grown on (001)GaAs substrates by molecular beam epitaxy (MBE). The layered In_2Se_3 films whose c-axis was oriented in only one direction were obtained by using slightly misoriented (001)GaAs. Furthermore, electrical and optical anisotropy were observed in the layered In_2Se_3 films. Conductivity of the layered In_2Se_3 epitaxial films in a-axis was found to be much larger than that in c-axis. Besides, absorption coefficient of the layered In_2Se_3 films for the light polarized toward c-axis was found to be larger than that toward a-axis.

1. Introduction

III_2VI_3 compound semiconductors such as Ga_2Se_3 and In_2Se_3 have unique properties originated from their crystal structures. For example, Ga_2Se_3 has a defect zincblende structure. This structure is basically a zincblende structure, but 1/3 of cation sites are vacant. Up until now, we investigated the molecular beam epitaxial (MBE) growth of Ga_2Se_3 films on (001)GaAs and (001)GaP substrates, and it was found that a spontaneous superstructure was formed by the ordering of the native Ga vacancies and that the large optical anisotropy was observed in the vacancy-ordered Ga_2Se_3 films [1-6].

On the other hand, In_2Se_3 has two types of crystal structure, i.e., layered structure (α -phase) and defect wurtzite structure (γ -phase). The layered structure consists of rather loose stack of covalently bonded layers, including five atomic layers of Se-In-Se-In-Se [7]. The layered structure is considered to be a kind of spontaneous superstructure. Therefore, unique properties such as electrical and optical anisotropy are to be expected. Meanwhile, the defect wurtzite structure is basically a wurtzite structure but 1/3 of cation sites are vacant. In this structure, it was reported that the In vacancies took screw arrangement and that large optical rotary power was observed [7-9].

Until now, we investigated the MBE growth of In_2Se_3 films and epitaxial films with the layered structure based on the zincblende structure were successfully grown on exact (001)GaAs substrates. [10]. However, the c-axis direction of the layered In_2Se_3 films was perpendicular to two directions: $[1\bar{1}1]$ and $[1\bar{1}\bar{1}]$ direction. In this paper, we reported the growth of the layered In_2Se_3 epitaxial films on slightly misoriented (001)GaAs substrates for the control of the c-axis orientation. Furthermore, we report on electrical and optical anisotropy of the layered In_2Se_3 epitaxial films for the first time.

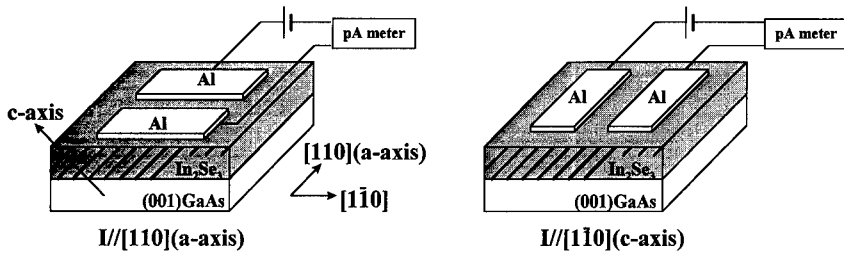


Fig.1 Measurement system for conductivity of the layered In_2Se_3 films.

2. Experimental Procedure

In_2Se_3 films were grown by MBE technique on SI-(001)GaAs substrates slightly misoriented toward $[1\bar{1}0]$ by 2° to control c-axis orientation. Growth temperature was varied in a range of 400°C to 480°C . In beam equivalent pressure (BEP) was fixed at 4×10^{-7} Torr and VI/III ratio was kept at 10. Before being inserted into the MBE system, the GaAs substrates were degreased, and chemically etched in a 3:1:1 $\text{H}_2\text{SO}_4:\text{H}_2\text{O}_2:\text{H}_2\text{O}$ solution at 60°C for 1.5min. After acid etching, the GaAs substrates were heated at 570°C for 15min in the growth chamber to remove surface oxides. Growth rate was around 600nm/h. Surface morphology and cross-sectional image were observed by scanning electron microscopy (SEM). We measured conductivity in both directions toward $[110]$ (a-axis of the layered In_2Se_3) and $[1\bar{1}0]$ (c-axis). Measurement system was shown in Fig.1. Two Al electrodes with a gap of around $80\mu\text{m}$ were formed on the In_2Se_3 films by vacuum evaporation technique. Besides, we measured wavelength dependence of photoconductivity of the In_2Se_3 films for the lights polarized toward $[110]$ and $[1\bar{1}0]$.

3. Results and Discussion

3.1 Molecular Beam Epitaxial Growth of the layered In_2Se_3 films on slightly misoriented (001)GaAs substrates

First of all, we attempted the growth of the layered In_2Se_3 epitaxial films on slightly misoriented (001)GaAs substrates for the control of the c-axis orientation. Fig.2 shows surface morphology, (110)cross-sectional image and schematic drawing of (110) cross-sectional view of the layered In_2Se_3 epitaxial film on slightly misoriented (001)GaAs substrate. In the surface morphology, a lot of lines parallel to the $[110]$ direction are observed. This suggests that a-axis of the layered In_2Se_3 is parallel to $[110]$ direction. Furthermore, in the cross-sectional image, the c-axis direction of the layered In_2Se_3 epitaxial film is found to be perpendicular to one direction: $[1\bar{1}1]$ direction. From this result, it was successfully demonstrated that the orientation of the layered In_2Se_3 epitaxial films could be controlled by the substrate orientation.

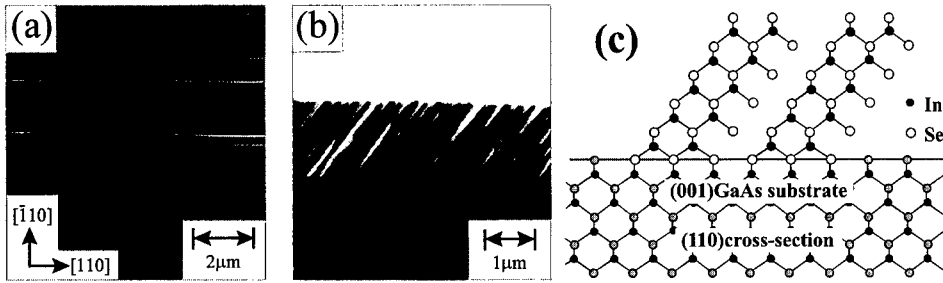


Fig.2 (a)Surface morphology, (b)(110)cross-sectional image of the layered In_2Se_3 film on slightly misoriented (001)GaAs substrate, and (c)schematic drawing of (110)cross-sectional view of the layered In_2Se_3 film.

3.2 Electrical Anisotropy of Layered In_2Se_3 Epitaxial Films

Fig.3 shows dark conductivity of the layered In_2Se_3 films measured at room temperature (RT). The films were grown for 1h and the thickness was around 600nm. The conductivity of the layered In_2Se_3 epitaxial films was independent of the growth temperature. However, an anisotropic feature was observed in the conductivity. The conductivity in [110] (a-axis) direction is much larger than that in [1T0] (c-axis) direction for any film. This result indicates that the mobility in a-axis direction is much higher than that in c-axis. The anisotropy of the conductivity is probably attributed to the carrier confinement by van der Waals gaps of the layered structure.

3.3 Optical anisotropy of Layered In_2Se_3 Epitaxial Films

Fig.4(a) shows wavelength dependence of photoconductivity of the layered In_2Se_3 epitaxial film measured at RT. The film was grown at 430°C for 1h. The conductivity was measured in a-axis direction. The wavelength dependence of photoconductivity of the polycrystalline In_2Se_3 film with the defect wurtzite structure on glass substrate is also shown in Fig.4(b). The film was grown at 500°C and the film thickness was around 3 μm. In the layered In_2Se_3 film, the photoconductivity increases at around 900nm. From the spectra, the bandgap of the layered In_2Se_3 is roughly estimated as around 1.4eV, which is almost the same as the reported bandgap [11,12]. A peak located at around 880nm is due to the absorption in the GaAs substrate. On the contrary, the photoconductivity of the polycrystalline γ - In_2Se_3 film increases at shorter wavelength than that of the layered In_2Se_3 films. This result indicates that the bandgap of In_2Se_3 with defect wurtzite structure is larger than that of the layered In_2Se_3 . It was reported that the bandgap of the γ - In_2Se_3 was 2.0eV [13], but it is roughly estimated as around 1.7eV from Fig.4(b). Furthermore, in the layered In_2Se_3 film, photoconductivity for [1T0] polarization is higher than that for [110] polarization in a range of 700nm to 900nm. This result suggests that absorption coefficient for the light polarized toward c-axis is larger than that toward a-axis in the layered In_2Se_3 film.

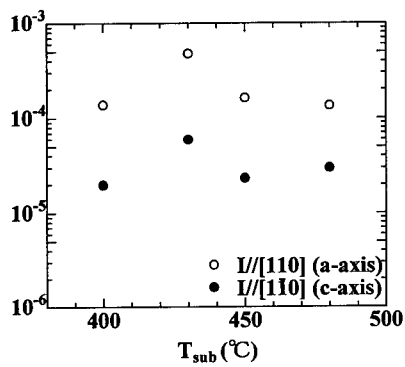


Fig.3 Dependence on the growth temperature of the dark conductivity of the layered In_2Se_3 films.

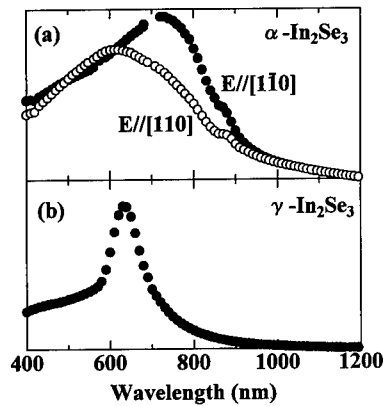


Fig.4 Wavelength dependence of photoconductivity of the In_2Se_3 films; (a) layered epitaxial film (α -phase), (b) polycrystalline film with defect wurtzite structure (γ -phase).

4. Conclusion

In_2Se_3 epitaxial films with layered structure were successfully grown on (001)GaAs substrates by molecular beam epitaxy (MBE). The layered In_2Se_3 films whose c-axis was oriented in only one direction were obtained by using slightly misoriented (001)GaAs. Furthermore, electrical and optical anisotropy were observed in the layered In_2Se_3 films. Conductivity of the layered In_2Se_3 epitaxial films in a-axis was found to be much larger than that in c-axis. Besides, absorption coefficient of the layered In_2Se_3 films for the light polarized toward c-axis was found to be larger than that toward a-axis.

References

- [1] Teraguchi N et al. 1991 *Appl. Phys. Lett.* 59 567
- [2] Teraguchi N et al. 1991 *J. Crystal Growth* 115 798
- [3] Okamoto T et al. 1992 *Jpn. J. Appl. Phys.* 31 L143
- [4] Okamoto T et al. 1993 *J. Electron. Mater.* 22 229
- [5] Okamoto T et al. 1994 *J. Crystal Growth* 138 204
- [6] Okamoto T et al. 1995 *Jpn. J. Appl. Phys.* 34 5984
- [7] Ye J 1995 "Structural Studies on the Defect Wurtzite Type III₂VI₃ Compound Semiconductors and Their Application to Giant Activity Azimuth Rotator", *Doctoral Thesis at Tokyo Institute of Technology*
- [8] Ye J et al. 1996 *Philosophical Magazine* A73 169
- [9] Ye J et al. 1995 *App. Phys. Lett.* 67 3066
- [10] Okamoto T et al. 1997 *J. Crystal Growth* 175/176 1045
- [11] Becla P et al. 1982 *Optica Applicata* 12 143
- [12] Julien C et al. 1986 *Thin Solid Films* 137 27
- [13] Yudasaka M et al. 1987 *Thin Solid Films* 146 65

Bandgap Renormalization Studies of n-type GaAs/AlGaAs Single Quantum Wells

E. D. Jones, M. Blount, W. Chow, H. Hou, and J. A. Simmons
 Sandia National Laboratories
 Albuquerque, NM 87185, USA

Bandgap energy renormalization due to many body effects has been studied in a series of n-type 8-nm-wide GaAs/AlGaAs single quantum wells using magnetoluminescence spectroscopy at 1.4K. The 2D-carrier densities varied between 1 and $12 \times 10^{11} \text{ cm}^{-2}$. At the maximum 2D-carrier density, the bandgap energy reduction compared to an undoped specimen was found to be about 34 meV.

1. Introduction

In the last several years, there has been much focus on bandgap energy renormalization resulting from many body effects [1-11]. For structures relying on the electronic bandgap in heavily doped quantum wells, e.g., high-power injection lasers, many body effects can lead to bandgap renormalization energies approaching 20 to 40 meV, i.e., for GaAs/AlGaAs systems, the bandgap energy can change as much as a 2%. For precise laser wavelength control, a knowledge of the bandgap energy versus carrier density is mandatory.

In this paper, we present a study of the bandgap renormalization as a function of the 2D-carrier density for a series of modulation doped n-type 8-nm-wide GaAs/AlGaAs single quantum wells. We use an unambiguous method for obtaining accurate bandgap energies by measuring the photoluminescence spectrum as a function of magnetic field. With the application of external magnetic fields, Landau energy levels are formed and the energy of the PL transition for each Landau level energy is shifted linearly. Extrapolating the magnetoluminescence “Fan” diagram to zero magnetic field yields the true bandgap energy without complications of spectral shifts in the zero-field PL line shape [12].

2. Experimental

The modulation doped GaAs/AlGaAs SQW structures were prepared using metal organic vapor phase epitaxy. All samples were grown on semi-insulating (100) GaAs substrates. An undoped 1- μm -thick GaAs epilayer was grown on top of the substrate and on top of this GaAs-epilayer, a single 8-nm-wide GaAs quantum-well was placed between 100-nm-wide $\text{Al}_{0.30}\text{Ga}_{0.70}\text{As}$ barriers, followed by an unintentionally doped 5 nm thick GaAs cap layer. The top AlGaAs barrier layer was delta-doped 30 nm from the GaAs quantum well, with silicon densities in the range between 0.5 and $2.5 \times 10^{18} \text{ cm}^{-3}$. For absolute calibration of the bandgap energy reduction, an unintentionally doped structure was also prepared in the same manner. The growth temperature for all layers and structures was 750C.

The magnetoluminescence measurements were made at 1.4K, and the magnetic field varied between 0 and 14 tesla. The luminescence measurements were made with an Argon-ion laser operating at 514.5 nm and an IEEE-488-based photon counting data acquisition system. The direction of the applied magnetic field is parallel to the growth direction, i.e., the resulting Landau orbits are in the plane of the GaAs quantum well. The laser excitation and sample PL signal were respectively brought in and carried

out along the same 100- μm -diameter optical fiber. The fiber tip was placed directly on the sample and the resulting maximum laser power density on the sample was about 1 W/cm².

The 2D-carrier densities were determined by two different methods, magnetoluminescence and low temperature transport measurements. The magnetoluminescence method notes when each Landau level and hence each interband transition disappears from the PL spectrum. The transport method relies on an analyses of Shubnikov-deHaas oscillations in the conductivity, but essentially provides the same information as PL method by recording the magnetic field and filling factor v when the Fermi energy lies half-way between two adjacent Landau levels, one filled and one empty. These two different measurement techniques for gave similar results for the 2D-carrier density.

3. Results and Discussion

The 1.4-K zero-field PL spectrum for a $N_{2D} = 8.2 \times 10^{11} \text{ cm}^{-2}$ sample (#EMC-2218) is shown in Fig. 1. The bandgap energy $E_{\text{gap}} = 1557.6 \text{ meV}$ is indicated in the figure and it is apparent that the energy of the peak intensity of the PL spectrum at 1563 meV is shifted above the bandgap value, i.e., the spectral shift is 6 meV. The PL line shape for degenerate quantum wells will not be discussed here, but the reader is referred to [12] where it has been treated in detail. The high energy shoulder near 1590 meV is due to transitions near the Fermi energy E_f . Also shown in the figure is the energy $E' = 1585.7 \text{ meV}$ for the undoped structure where the effective Rydberg for an 8-nm-wide quantum well [13] has been added to the observed PL energy. Thus, for this sample, where $N_{2D} = 8.2 \times 10^{11} \text{ cm}^{-2}$, the bandgap energy reduction is nearly 20 meV.

A free particle, with mass m and charge e , moving in a magnetic field B forms quantized states, Landau levels, with an energy $E = (n + 1/2)(e\hbar B/mc) \equiv (n + 1/2)\hbar\omega$ (cgs units) where n is the Landau level index, \hbar is Planck's constant over 2π , c is the velocity of light, and $\hbar\omega$ is the quantized cyclotron

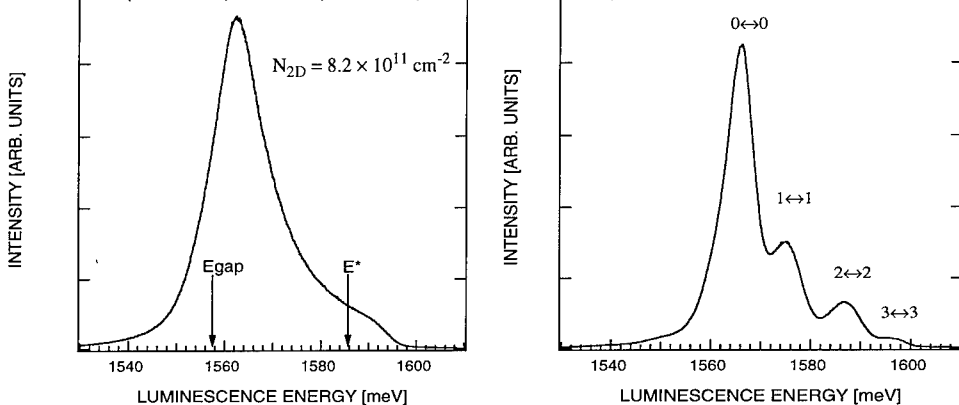


Figure 1. Zero-field 1.4K PL spectrum for an 8-nm-wide n-type GaAs/AlGaAs single QW. The bandgap energy for the undoped quantum well is labeled E' and $E_{\text{gap}} = 1557.6 \text{ meV}$ is bandgap energy from the magnetoluminescence "Fan" diagram shown in Fig. 3.

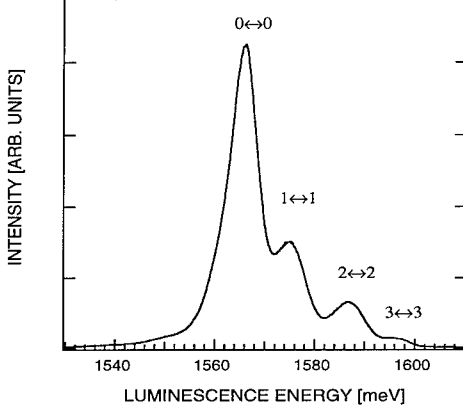


Figure 2. The magnetoluminescence spectrum at 8 tesla and 1.4K for the zero-field spectrum shown in Fig. 1. The 2D-carrier density is $N_{2D} = 8.2 \times 10^{11} \text{ cm}^{-2}$. The Landau transition indices $n_c \leftrightarrow n_v$ for each transition are indicated above their respective peak energies.

energy. The distribution function for a degenerate 2D-electron gas (conduction-band states for a n-type material) is based on Fermi-Dirac statistics, but because of the very small 2D-density of photo-induced hole-states, the distribution for the valence-band holes are governed by Maxwell-Boltzmann statistics. For temperatures where kT is much larger than valence-band cyclotron energy $\hbar\omega_v$, the $n_v = 0, 1, 2, \dots$ valence-band Landau levels are populated and all magnetoluminescence transitions between the n_c and n_v Landau levels obey the $\delta n_{cv} \equiv (n_c - n_v) = 0$ selection rule. Because of heavy-hole light-hole valence-band mixing for an 8-nm-wide GaAs quantum well, the ground state in-plane valence-band masses are "heavy" (and nonparabolic) and hence the condition that $kT > \hbar\omega_v$ is satisfied at 1.4K [14]. The interband PL transition energy E is thus given by

$$E(n) = E_{gap} + \left(n + \frac{1}{2} \right) \left(\frac{e\hbar B}{\mu c} \right), \quad (1)$$

where E_{gap} is the bandgap energy, μ is the reduced mass ($\mu^{-1} = m_c^{-1} + m_v^{-1}$) where m_c and m_v are respectively the conduction or valence-band effective masses.

Figure 2 shows a magnetoluminescence spectrum at 8 tesla and 1.4K for the sample whose zero-field spectrum is shown in Fig. 1. As can be seen, the zero-field spectrum breaks up into a series of peaks whose energies are given by Eq. (1). The Landau transition indices $n_c \leftrightarrow n_v$ for each peak are indicated in the figure. A "Fan" diagram can be generated by plotting the energy of each Landau transition energy (See Fig. 2) as a function of magnetic field and this result is shown in Fig. 3. The Landau transition indices $n_c \leftrightarrow n_v$ are indicated and the lines drawn through the data are best fits of Eq. (1) to the data. The ratio of the slopes are nearly 1:3:5:7 as predicted by Eq. (1). The bandgap energy E_{gap} can be uniquely determined from a straight line zero-field extrapolation of the lines shown in Fig. 2 with the result, $E_{gap} = 1557.6$ meV.

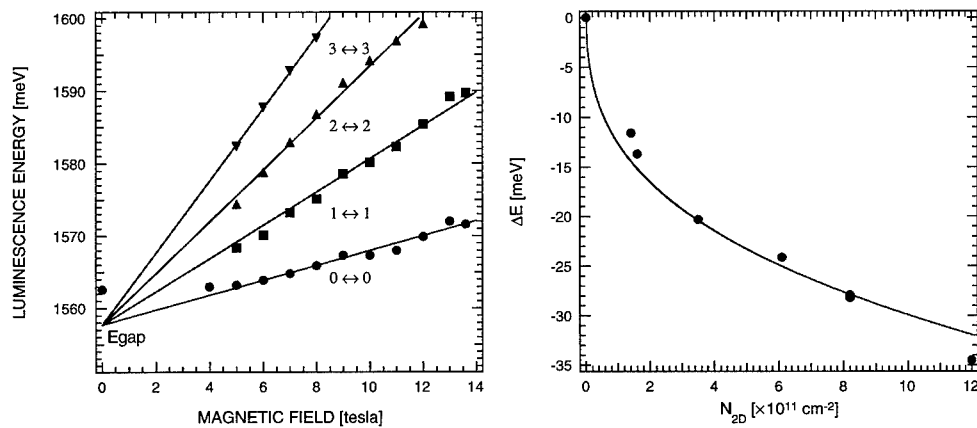
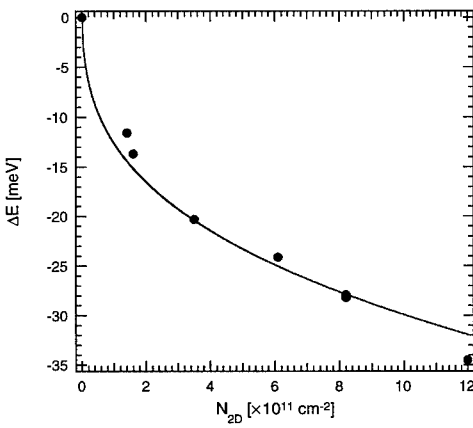


Figure 3. Magnetoluminescence "Fan" diagram for the 1.4K, $N_{2D} = 8.2 \times 10^{11} \text{ cm}^{-2}$, data. The Landau transition indices $n_c \leftrightarrow n_v$ for each transition are indicated. The lines are a best of Eq. (1) to the data and the bandgap energy is 1557.6 meV. The slope ratio of the lines is nearly 1:3:5:7.

Figure 4. The energy difference ΔE between the undoped bandgap energy and the renormalized bandgap energy due to many body corrections. The curve through the data is given by Eq. (2).



For all of the n-type samples, magnetoluminescence “Fan” diagrams similar to the one shown in Fig. 3 can be made using the above described procedures. The bandgap energy reduction ΔE for each sample can then be calculated by subtracting the magnetoluminescence determined bandgap energy E_{gap} from the undoped bandgap energy E^* shown in Fig. 1.

From Schmidt-Rink et. al. [2,5], the size of the bandgap energy renormalization due to many body effects can be calculated from the expression

$$\Delta E = -3.1 \left(N a_0^2 \right)^{1/3} E^*, \quad (2)$$

where ΔE is the difference in energy between the bandgap energy of the undoped and n-type samples, N is the 2D-carrier density, a_0 is the bohr radius, and E^* is the exciton binding energy. For an 80-Å QW, $E^* \sim 9$ meV and $a_0 \sim 125$ Å. We thus expect $\Delta E \sim -3.2 \times 10^{-3} N^{1/3}$.

Figure 4 shows the result of plotting ΔE as a function of the 2D-carrier density N_{2D} . The solid line drawn through the data is a result of a best fit curve given by

$$\Delta E = -3.22 \times 10^{-3} N_{2D}^{1/3} \text{ meV}. \quad (3)$$

The best fit curve given (Eq. (3)) is in good agreement the estimated $\Delta E \sim -3.2 \times 10^{-3} N^{1/3}$.

In conclusion, we have shown that the magnetoluminescence technique allows a direct determination of the bandgap energy for degenerate quantum well samples. Furthermore, the complications of spectral shifts to the PL-peak intensity are avoided by this method. Finally, agreement with previously reported measurements was found for the dependence of the bandgap energy reduction on the 2D-carrier density.

Sandia is a multiprogram laboratory operated by Sandia Corporation, a Lockheed Martin Company. This work is supported by the Division of Material Science, Office of Basic Energy Science, for the United States Department of Energy under Contract DE-AC04-94AL85000.

References

- [1] Kleinman D A and Miller R C 1985 *Phys. Rev. B* 32 2266-2272
- [2] Schmitt-Rink S and Ell C 1985 *J. Lumin.* 30 585-
- [3] Tränkle G, Leier H, Forchel A, Haug H, Ell C and Weimann G 1987 *Phys. Rev. Lett.* 58 419-422
- [4] Delalande C, Bastard G, Orgonasi J, Brum J A, Liu H W, Voos M, Weimann G and Schlapp W 1987 *Phys. Rev. Lett.* 59 2690-2692
- [5] Schmitt-Rink S, Chemla D S and Miller D A B 1989 *Adv. Phys.* 38 89-
- [6] Potemski M, Maan J C, Ploog K and Weimann G 1990 *Surf. Sci.* 229 380-383
- [7] Jalabert R and Das Sarma S 1990 *Surf. Sci.* 229 405-409
- [8] Reinecki T L, Broido D A, Lach E, Kulakovskii V, Forchel A and Gruetzmacher D 1990 *Superlattices and Microstructures* 7 437-440
- [9] Potemski M, Maan J C, Ploog K and Weimann G 1990 *Solid State Communications* 75 185-188
- [10] Cingolani, R, La Rocca G C, Kalt H and Ploog K, Potemski M and Maan J C 1991 *Phys. Rev. B* 43 9662-9671
- [11] Priest A N, Nicholas R J, Najda S P, Duggan G and Kean A H 1997 *Physica* (to be published)
- [12] Lyo S K and Jones E D 1988 *Phys. Rev. B* 38, 4113-4119
- [13] Green R L and Bajaj K K 1985 *Phys. Rev. B* 31 6498-6502
- [14] Jones E D, Lyo S K, Klem J F and Schirber J E 1991 *Inst. Phys. Conf. Ser. No* 120 407-412

Magnetoluminescence Measurement of Zeeman and Exchange Interactions of Excitons in GaAs/AlGaAs Multiple Quantum Wells

Y.A. LEEM,* H.S. Ko,* W.S. Kim,* Y.S. Kim,* D.H. Kim,* T. Schmiedel,[#]
C.E. Yun,[@] H.M. Pyo,[@] and J.C. Woo*

* Department of Physics, Seoul National University, Seoul 151-742, Korea

National High Magnetic Field Laboratory, Tallahassee, FL 32306, USA

@ Wireless Comm. Res. Labs., Korea Telecom., Seoul 137-792, Korea

Abstract. The Zeeman splitting and diamagnetic shift of heavy-hole exciton in GaAs/Al_{0.25}Ga_{0.75}As multi-quantum wells (MQW) were investigated for various barrier widths by magnetoluminescence up to 30 T at 4.2 K. It is obtained that the diamagnetic shift is independent to the barrier width (L_B), but the effective g-factor becomes smaller as L_B decreases for a fixed QW width. Also reported is the fine splitting due to the exchange interaction for $L_B \leq 50$ Å.

1. Introduction

Spin interaction of exciton confined in quasi-two-dimensional (quasi-2-D) system such as coupled quantum well (QW) has been of great interest in recent years.[1,2] However, most of the reports related to coupled QW are concentrated on the double QWs[3,4,5] and little known is the spin interaction in coupled 2-D system. In this work, multiple QWs (MQWs) was chosen in the study of spin interaction of coupled QWs, because double QW has additional complication with symmetric and antisymmetric sublevels and its magnetic field (B) dependence is difficult to analyze. Also, we have concentrated on the barrier width (L_B) dependence in order to investigate the coupling effect and role of quantum barrier.

The samples used in this work are undoped GaAs/Al_{0.25}Ga_{0.75}As MQWs of a fixed well-width (L_z) of 38 monolayer (ML) (100 Å) and of different L_B of 10, 14, 18, 22, 28 and 38 ML. (The MQW samples are identified by L_z/L_B , e.g., 38/10 for the first one.) For comparison, single QW (SQW) of $L_z = 38$ ML, and MQW of $L_z = 18$ ML and $L_B = 18$ ML are also

prepared. All the samples are grown by MBE at $T_G = 600$ °C and are confirmed to have very flat heterointerface and low carrier density (usually lower than 10^{14} cm⁻³). The magnetoluminescence spectroscopy is performed with an Ar⁺ laser excitation in Faraday configuration with the field up to 30T at LHe temperature. From the observed L_B dependence of the effective g-factor and exchange splitting in small L_B samples, the coupling effects and the barrier contribution on spin-spin interaction and excitonic interaction are discussed.

2. Data and Results

Typical spectra are shown in Fig. 1 for the 38/18 sample. As B increases, the blue shift is observed, which often is called diamagnetic shift and defined $\epsilon_D = E(B) - E(0)$, where $E(B)$ is the peak photon energy at B . Along with this shift, the two kinds of splittings have been observed. One kind is the splitting whose separation increases almost linearly to the field. This splitting has been observed in all the samples, and is identified with Zeeman splitting (ϵ_Z). The other kind is a fine splitting (ϵ_X), which is invariant to the field. It is only distinguishable for the samples with small L_B , that is for 38/10, 38/14 and 38/18. The cause of this splitting will be discussed later.

The diamagnetic shift is best fit with $\epsilon_D = \beta B^2$ for $B \leq 6$ T, and $\epsilon_D = \alpha B + \epsilon_0$ for $B > 6$ T, where ϵ_0 is a constant. The linear increase of ϵ_D in the high field is due to the domination of Landau shift. Typical Zeeman and fine splittings are summarized in Fig. 2 for 38/10, 38/14 and 38/18 samples. The Zeeman splitting for $B \geq 8$ T is best fit with $\epsilon_Z = \mu_B g_{eff} B + c$, where μ_B is Bohr magneton and c is a constant. The constant c is introduced, since the Zeeman splitting is quadratic at small B .[6] The effective g-factor found to be constant for $B \geq 10$ T(See Fig. 3), and this indicates that the spin-field is dominant.[1] The field dependences of ϵ_D and ϵ_Z are summarized in terms of α , β and g_{eff} in Table 1 along with ϵ_X .

For the samples of $L_z = 38$ ML, α and β are the same within the experimental error (0.1 meV). This implies that the effective reduced mass m^* is invariant to L_B and little affected by the interwell coupling, because both α and β are inversely proportional to m^* with $\alpha \propto 1/\omega_c = e/m^*$ and $\beta = (\epsilon^2/8m^*)\langle x^2+y^2 \rangle$. The smaller α and β observed from 18/18 than those of $L_z =$

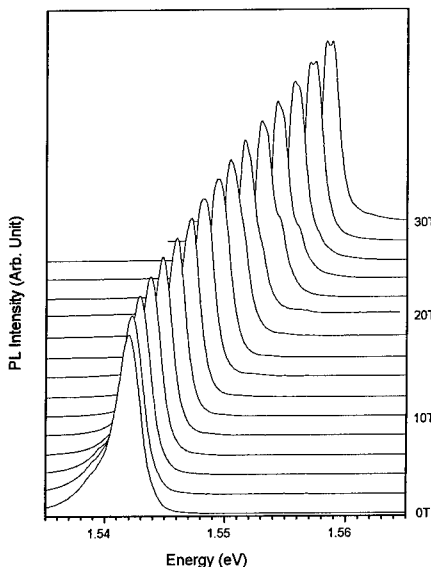


Fig. 1 Magnetoluminescence of 38/18 MQW

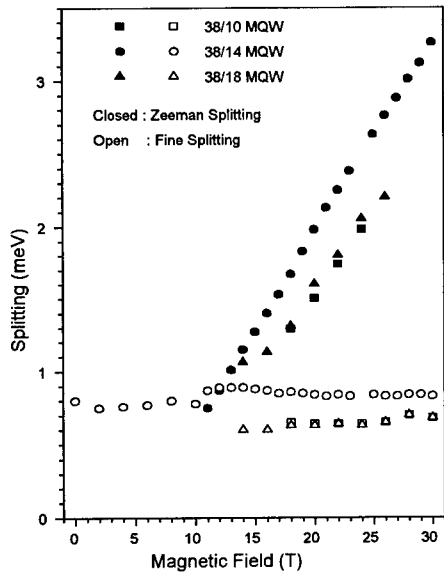


Fig. 2 Zeeman and fine splittings for
38/10, 38/14, and 38/18 MQWs

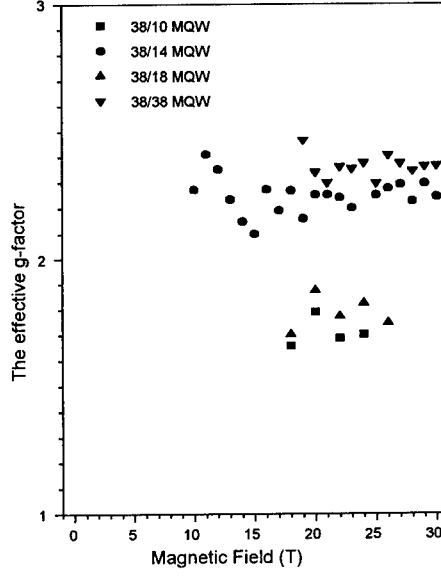


Fig. 3 The effective g-factors for 38/10,
38/14, 38/18, and 38/38 MQWs

38ML samples are consistent with the increase of m^* by low-D confinement.

It is the L_B -dependence of Zeeman splitting that should be noticed. The g_{eff} seems to increase as L_B increases (except 38/18). The magnitude of g_{eff} is known to be influenced by the bandgap energy, valence band mixing of heavy-hole (hh) and light hole (lh) and the penetration of the wavefunctions to the barrier. Since there is little bandgap change by L_B and no B dependence of g_{eff} is observed, the possibilities of the first two are ruled out. If we assume that the wave function penetration to the AlGaAs barrier increases as L_B decreases, the g_{eff} is expected to become smaller.[2] The g_{eff} can be estimated from $g_{e(M)} = \gamma_w g_{e(hh)}^{\text{GaAs}} + \gamma_B g_{e(hh)}^{\text{AlGaAs}}$, where γ_w and γ_B are the weighing factors related to the penetration and $g_{e(hh)}^{\text{GaAs}}$ and $g_{e(hh)}^{\text{AlGaAs}}$ are g-factors of electron (heavy-hole) of QW and quantum barrier materials respectively. The g_{eff} of $L_B = 38$ ML SQW is observed to be 2.37, which is even larger than 38/38. The observed g_{eff} of this isolated system also supports the penetration model.

The fine splitting observed in small L_B samples can be interpreted with the exchange interaction of the electron-hole pair. The observed magnitude of the splitting, 0.6–0.8 meV is smaller by approximately 1/2 than the theoretically predicted value for QW[7] but about 2 times larger than the bulk.[8] The exchange splitting may be quenched under the strong negative crystal field perturbation of axial symmetry. But, as the axial symmetry is lifted with the penetration, the electron-hole exchange coupling would be enhanced. In large B , the oscillator

Table 1 : The summary of the diamagnetic shift, Zeeman splitting and the fine splitting.

Sample		38/10	38/14	38/18	38/22	38/28	38/38	18/18
Diamagnetic shift	β (meV/T ²)	0.04	0.04	0.04	0.04	0.04	0.04	0.03
Landau shift	a (meV/T)	0.63	0.64	0.63	0.64	0.64	0.63	0.50
Zeeman splitting	g_{eff}	1.71	2.25	1.78	2.30	2.33	2.35	2.57
Fine splitting	ϵ_x (meV)	0.6	0.8	0.6	--	--	--	--

strength of electron and hole becomes large, which is evident from the narrowing of the spectral linewidth. The enhancement of the oscillator strength will also enhance the probability of exciton formation via interwell coupling, if the penetration effect becomes significant.

3. Discussion

Conclusively, the spin-field and spin-spin interactions in coupled quasi-2-D system have been investigated by magneto-photoluminescence spectroscopy on MQW samples of varying the barrier widths in the magnetic field $B \leq 30$ T at LHe temperature. The effective g-factor is observed to become smaller as L_B decreases, and a distinct fine splitting from spin-spin exchange interaction is obtained in MQWs of narrow L_B . As the role of the barrier becomes increasing with increasing wavefunction penetration, the coupling effect becomes significant to the spin-field and spin-spin interactions of the exciton.

Acknowledgement

Sincere thanks are expressed to K.H. Yoo and D.W. Kim for their helpful discussions. This work is supported in part by Korea Telecom and MOE BSRI96-2421.

References

- [1] Heberle A P, Rühle W W and Ploog K 1994 *Phys. Rev. Lett.* 72 3887-3890
- [2] Hannak, R M, et. al 1995 *Solid State Comm.* 93 313-317
- [3] Perry C H, et. al. 1990 *J. Appl. Phys.* 67 4920-4922
- [4] Zhao Q X, et. al 1994 *Phys. Rev.* B50 4476-4481
- [5] Bayer M, et. al 1996 *Phys. Rev.* B54 8799-8808
- [6] Wang H, Jiang M, Merlin R, and Steel D G 1992 *Phys. Rev. Lett.* 69 804-807
- [7] Zhao Q X and Westgaard T 1991 *Phys. Rev.* B44 3726-3735
- [8] Willmann F, Suga S, Dreybrodt W and Cho K 1974 *Solid State Comm.* 14 783-786

Lateral Confinement and Inter-wire Coupling of Exciton in 4-16 nm Wide GaAs/AlGaAs Quantum Wires Observed by Magnetoluminescence

**W.S. Kim,* Y.A. Leem,* Y.S. Kim,* H.S. Ko,* D.H. Kim,* C.E. Yun,[@]
H.M. Pyo,[@] T. Schmiedel[#] and J.C. Woo***

* Department of Physics, Seoul National University, Seoul 151-742, Korea

@ Wireless Comm. Res. Labs., Korea Telecom, Seoul , 137-792, Korea

National High Magnetic Field Laboratory, Tallahassee, FL 32306-4005, U.S.A.

Abstract. The result on magnetoluminescence study of the exciton in GaAs/Al_{0.5}Ga_{0.5}As quantum wire (QWR) superlattice grown on vicinal GaAs substrate are reported. For 30 T, the diamagnetic shift is 7.8 meV for QWR of 4 nm wide, while it is 11 meV for QWR of 8 nm or wider. For 4 nm QWR, the diamagnetic shift remains the same up to 17 T for the magnetic field parallel and angled to the growth direction. But, it saturates in the angles geometry at 17 T where the cyclotron diameter becomes comparable to QWR width. If the lateral confinement model is introduced in the formation of exciton in QWR, the saturation can be interpreted as the breaking of inter-wire coupling.

1. Introduction

The excitonic state in quantum wire (QWR) has recently been attracting interest not only as a fundamental issue in physics but also for potential device applications. Even though the exciton bound to imperfection and impurity can be formed in the quasi-one dimensional (1-D) structure, the electron-hole interaction and the dimensionality of the exciton in pure and near-perfect QWR are still little known.

A direct and efficient means of investigating the dimensionality of exciton is to study electron-hole interaction under magnetic field (**B**), since **B** introduces additional confinement in the direction as well as the orbit of the electronic motion. In this work, magneto-optical properties of QWR have been examined by photoluminescence (PL) and PL excitation (PLE) for various QWR widths, while applying **B** in perpendicular and angled geometry to the QWR plane.

2. Experiment

The structures of GaAs/Al_{0.5}Ga_{0.5}As QWR superlattice samples used in this work are listed in Table 1. They have been prepared by migration enhanced epitaxial method (MEE) on vicinal GaAs substrates disoriented toward [110] by 2°, 1° and 0.5°.[4] The growth temperature was 620°C at barrier layer and 600°C elsewhere. The wire region grown by a sequence of 1/2 monolayer (ML) of lateral GaAs and Al_{0.5}Ga_{0.5}As was sandwiched between Al_{0.5}Ga_{0.5}As 50 nm barriers. No modulation of RHEED intensity oscillation has been observed which is evidence of step flow growth. The QWR structure has been confirmed by atomic force microscopy (AFM), transmission electron microscopy (TEM) and polarization dependence of PLE.

Magneto-PL (MPL) was performed using an Ar+ laser, and the PLE by dye laser with Rhodamine 6G for QWR-1 and DCM for the other three. The MPL was performed up to 30 T at liquid helium temperature for $B \parallel z_s$ and angled 20° from the parallel geometry, where z_s is the growth direction.

Table 1 : Summary of sample structures and zero field PL

Sample Number	QWR-1	QWR-2	QWR-3	QWR-4
Substrate misoriented angle	2°	1°	1°	0.5°
wire width (nm)	4	8	8	16
QWR size	barrier width (nm)	4	8	16
wire height (nm)	5	8	16	8
PL peak position (eV)	1.942	1.913	1.903	1.885
FWHM (meV)	7	17	14	16

3. Result and Discussion

The positions and linewidth of zero field PL peaks are summarized in Table 1. The AFM image of QWR-4 is shown in Fig. 1, and the zero-field PL and PLE spectra in Fig. 2. The anisotropic polarization of PLE and the microscopic results show that all the samples have well-defined 1-D structure.

The diamagnetic shifts for $B \parallel z_s$ are summarized in Fig. 3. In low B (<10 T), the shifts are well fit with $\Delta E = \beta B^2$, where β is interpreted as an effective exciton area in 2-D excitonic

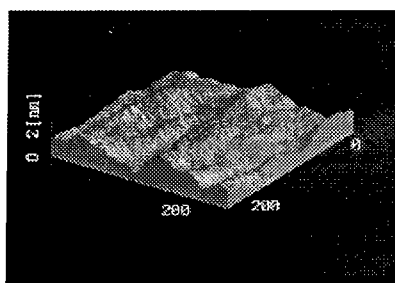


Fig. 1 : AFM image of QWR-4

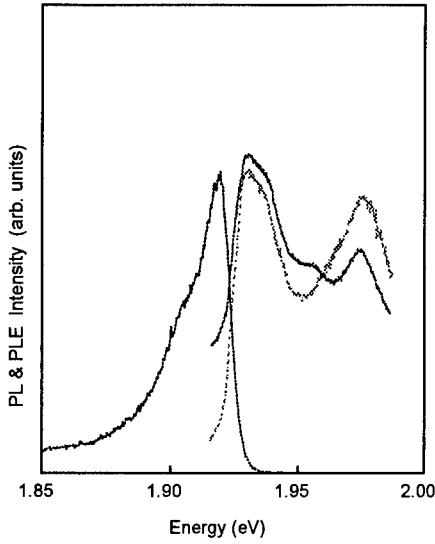


Fig. 2 : PL (dot) and polarization dependent PLE of QWR-3, dashed (solid) line is parallel to the wire.

model.[5] We obtained β to be 16×10^{-3} meV/T² for QWR-1, and $(22 \pm 1) \times 10^{-3}$ meV/T² for QWR-2, 3, and 4, which correspond to the effective excitonic diameter (D_x) of 7 and 8 nm, respectively. It is noticed that D_x for QWR-1 is larger than the QWR width, while they are smaller for the rest of the samples. The shifts are almost linear to B for B>10T, which is indicative that Landau shift dominates in the high field. But, the linear constant of QWR-1 (0.3 meV/T) differs from those of the other three (0.4 meV/T). The difference between QWR-1 and the others is also observed in the linewidth (see Table 1).

When B is applied at a 20° angle, the shifts for QWR-2, 3, and 4 keep increasing linearly as in the parallel case. But, in the QWR-1 sample, the shift saturates at B>17T.

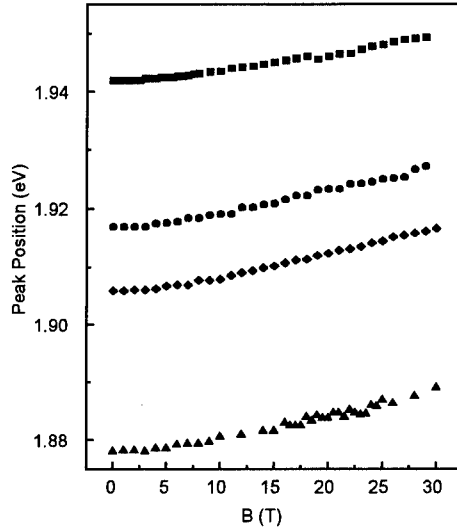


Fig. 3 : PL peak position of QWR-1, 2, 3, 4 (square, circle, diamond and triangle respectively)

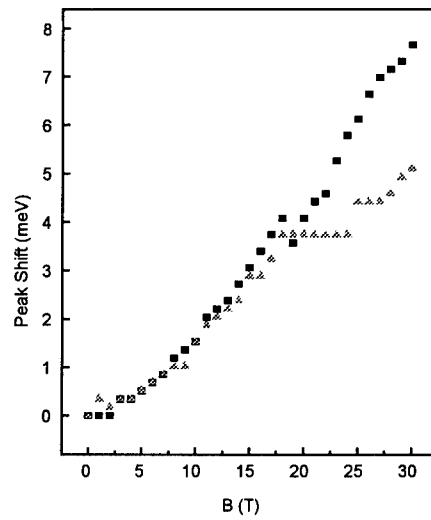


Fig. 4 : Diamagnetic shift of QWR-1, square (triangle) is parallel (angled) geometry

(See Fig. 4) This clearly indicates that the exciton formation in QWR-1 differs from the rest. It has been reported that the transition from 1-D to 2-D occurs between QWR widths of 6 and 8 nm (QWR superlattice grown on 1.4° and 2° tilted substrates, respectively),[2][3] and 1-D lateral confinement does not occur in QWR of 7nm or narrower.[6] The anomalous diamagnetic shift observed $B>17$ T in QWR-1 is somewhat consistent with these claims. Tilting under high magnetic field forces exciton decoupling. So, a 2-D excitonic coupling such as inter-wire interaction is more plausible to be more proper than the 1-D lateral confinement model. Since electron wave function is spread over QWRs, even though the hole is confined by the lateral potential of QWR,[4] the overlap of exciton wave function between neighboring QWRs is increased as the lateral size of QWR is decreased and the inter-QWR interaction can play a significant role in the exciton formation in narrow QWR superlattices such as QWR-1.

4. Conclusion

In summary, the diamagnetic shift has a 2-D excitonic behavior even in the narrow wire width sample when $B \parallel z_s$. However, we have observed that the diamagnetic shift of QWR-1 behaves like an exciton confined in a quantum dot, if the magnetic field is strong enough that the cyclotron diameter becomes smaller than the separation of neighboring QWRs when the plane of cyclotron motion is angled with the QWR plane. This provides a direct evidence that the exciton formation in the QWR of 4 nm in width and 4 nm in inter-QWR interval is dominated by inter-wire coupling.

Acknowledgments

This work is supported in part by Korea Telecom and MOE BSRI96-2421.

References

- [1] Miller M S, Weman H, Pryor C E, Krisnamurthy M, Petroff P M, Kroemer H and Merz J L 1992 *Phys. Rev. Lett.* 68 3464-3467
- [2] Ando H, Saito H, Chavez-Pirson A, Gotoh H, Kobayashi N 1996 *Appl. Phys. Lett.* 69 1512-1514
- [3] Bloch J, Bockelmann U and Laruelle F 1994 *Europhys. Lett.* 28 501-1994
- [4] Petroff P M, Gossard A C, Wiegmann W 1984 *Appl. Phys. Lett.* 45 620-622
- [5] Someya T, Akiyama H and Sakaki H 1995 *Phys. Rev. Lett.* 74 3664-3667
- [6] Nagamune Y, Tanaka T, Kono T, Tsukamoto S, Nishioka M, Arakawa Y, Uchida K and Miura N 1995 *Appl. Phys. Lett.* 66 2502-2504

Extremely Sharp Er-Related Luminescence in Er-Doped GaP Grown by OMVPE with TBP

**Y. Fujiwara, T. Ito, H. Ofuchi, J. Tsuchiya, A. Tanigawa, M. Tabuchi and
Y. Takeda**

Department of Materials Science and Engineering, Graduate School of Engineering
Nagoya University, Furo-cho, Chikusa-ku, Nagoya 464-01, Japan

Abstract. We have successfully observed radiant Er-related low-temperature photoluminescence (PL) dominated by numerous extremely sharp emission lines due to the intra-4f shell transitions of Er^{3+} ions in Er-doped GaP (GaP:Er) grown by OMVPE with TBP. The intensity of the emission lines depended strongly on the growth temperature, the Er concentration and the reactor pressure, indicating coexistence of various Er-related luminescence centers in the samples. The fluorescence-detected EXAFS analysis on the samples revealed clearly that the majority of Er atoms doped are substitutionally incorporated into Ga sites in the GaP lattice. Effects of In-addition to GaP:Er have also been investigated.

1. Introduction

Er-doped III-V semiconductors have attracted increasing attention because they can potentially have a great impact on optical communication systems operating near $1.5 \mu\text{m}$ that is the range of minimum transmission loss in silica-based fibers [1]. The intra-4f shell transitions from the first excited state ($^4\text{I}_{13/2}$) to the ground state ($^4\text{I}_{15/2}$) of the Er^{3+} ions result in emission near $1.5 \mu\text{m}$. Er-doped GaP is an interesting material because the thermal quenching of the Er-related luminescence is much smaller than in GaAs and InP [2]. However, there have been few studies on GaP doped with Er by OMVPE, although the epitaxial doping of Er is a necessity for fabrication of practical devices with confinement structures for light and carriers.

In this paper, we report the successful observation of numerous extremely sharp Er-related emission lines in OMVPE-grown GaP:Er, and systematic study on effects of growth conditions on the Er-related luminescence. Preliminary EXAFS results of Er local structures are also described.

2. Sample Preparation

The low-pressure growth system with a vertical quartz reactor was utilized in this work. Details of the growth system was described previously [3]. TMGa and TBP were used as source materials for GaP growth. $\text{Er}(\text{MeCp})_3$ (tris(methylcyclopentadienyl)erbium) as the Er source was maintained at 100°C and introduced in the reactor by H_2 flow through the Er source cylinder. The substrate for the growth was undoped GaP with a surface orientation of (100). The growth rate for all the samples was $1 \mu\text{m}/\text{h}$.

3. Results and Discussion

3.1. PL measurements

The luminescence properties of the samples were characterized by PL measurements. The PL measurements were carried out with the samples directly immersed into liquid He at 4.2 K. The photoexcitation source was a cw mode He-Cd laser with a beam diameter of 1 mm and an incident power of 30 mW. The luminescence of the sample was dispersed with a 1.25 m grating monochromator and detected by a Ge pin photodiode cooled by liquid N₂. Not all spectra were calibrated for the spectral response of the measurement system.

A characteristic Er-related emission was successfully observed in all the samples. Figures 1 and 2 show Er-related PL spectra as functions of the growth temperature, Er flow rate and reactor pressure. A series of PL spectra are dominated by tens of extremely sharp emission lines. The FWHM of each emission line is 0.2 - 0.3 meV, close to the spectral resolution (about 0.19 meV) in this study. This is the first report on the observation of such sharp emission lines in GaP doped with Er by OMVPE.

The intensities of the emission lines exhibit apparent dependence on the growth conditions, while Er concentration, determined by SIMS measurements using Cs⁺ as a primary ion, in the samples grown with the same Er flow rate remained almost constant against the growth temperature and the reactor pressure. This observation indicates that there coexist several Er-related luminescence centers with different atomic configurations in the samples, and that relative concentrations of the luminescence centers depend significantly on the growth conditions. As for the growth temperature dependence of the PL spectra, several emission lines appear in the high energy region at the high growth temperature and those in the low energy region at the low growth temperature. Similar behaviors were previously

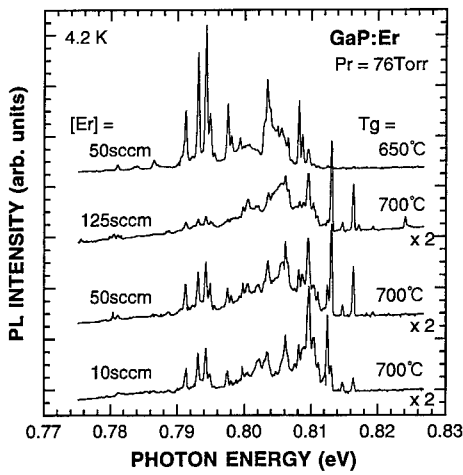


Fig. 1 Growth temperature and Er flow rate dependences of the Er-related PL spectra in Er-doped GaP.

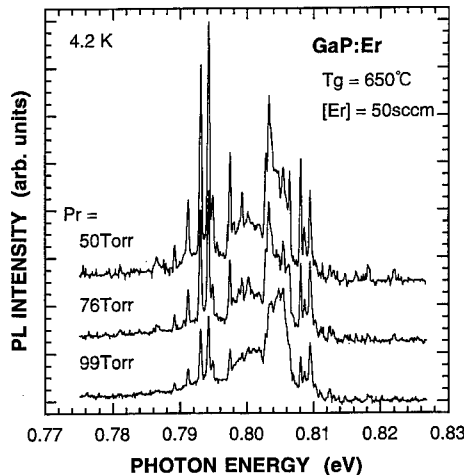


Fig. 2 Reactor pressure dependence of the Er-related PL spectra in Er-doped GaP.

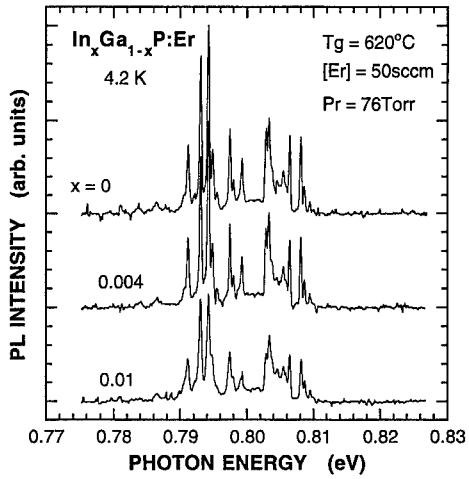


Fig. 3 In composition dependence of the Er-related PL spectra in Er-doped InGaP grown on GaP substrates.

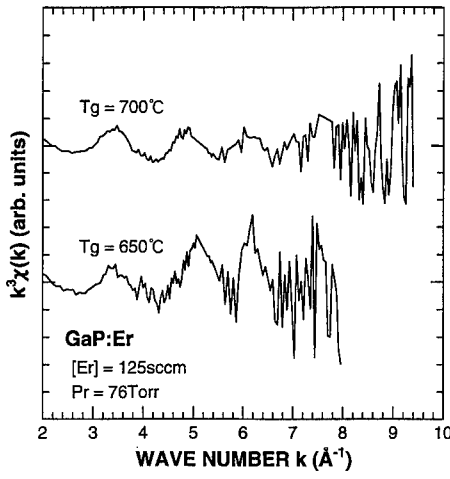


Fig. 4 EXAFS $k^3\chi(k)$ spectra of Er in Er-doped GaP grown at 650 and 700°C , respectively, with the Er flow rate of 125 sccm.

observed in Er-doped InP [4, 5]. These results indicate that there are several optically active Er centers with similar microscopic structures in each P-based III-V semiconductor.

Effects of In-addition to GaP:Er for a gradual change in the host environment have also been investigated to understand deep-level properties of Er, which play an important role in excitation mechanism of the 4f electrons [6]. Figure 3 shows the In composition dependence of the Er-related PL spectra in Er-doped InGaP grown on GaP substrates. The PL intensity decreases gradually with increasing In composition, i.e., decreasing band gap of InGaP, while the photon energy of the emission lines is invariant. Hogg *et al.* reported that the intensities of some emission lines observed in Er, O-codoped GaAs increase gradually with hydrostatic pressure and they concluded that the traps due to the luminescence centers responsible for the emission lines are resonant with the conduction band or the valence band [7]. Therefore, it is speculated that the traps combined with the Er-related luminescence centers existing in GaP:Er might be resonant traps.

3.2. Fluorescence-detected EXAFS measurements

In order to investigate atomic configurations around Er atoms doped in GaP:Er, EXAFS measurements have been performed successfully in a series of GaP:Er at the beam line BL12C at the Photon Factory at Tsukuba using synchrotron radiation from the 2.5 GeV storage ring. Details of the measurement system was described previously [8, 9].

The EXAFS $k^3\chi(k)$ spectra of Er for the samples grown at 650 and 700°C , respectively, with the Er flow rate of 125 sccm are shown in Fig. 4. Preliminary EXAFS analysis reveals clearly substitutional incorporation of the majority of Er atoms into Ga sites in the GaP lattice in both samples. This

observation is quite different from in Er-doped InP in which the incorporation sites of Er atoms depend strongly on the growth temperature, i.e., the majority of Er atoms have a rocksalt crystal arrangement with P atoms in samples grown at temperatures higher than 580 °C, exhibiting a low efficiency of luminescence, while the majority of Er atoms are substitutionally incorporated into In sites in the InP lattice in samples grown at temperatures lower than 550 °C, exhibiting a high efficiency of luminescence [5, 8]. Furthermore, the Debye-Waller factor (0.137 Å) in the 700 °C sample is much larger than that (0.093 Å) in the 650 °C sample, suggesting that there is a significant variation in atomic configurations around substitutional Er atoms in the 700 °C sample.

Combined with the PL results, it is concluded that in GaP:Er, the luminescence centers responsible for the sharp emission lines are related to similar substitutional Er atoms and have different microscopic structures due to the existence of native defects or impurities around the Er atoms.

4. Conclusions

Radiant Er-related luminescence dominated by numerous extremely sharp emission lines due to the intra-4f shell transitions of the Er³⁺ ions has been successfully observed in GaP:Er grown by OMVPE with TBP. The intensities of the emission lines exhibit apparent dependence on the growth temperature, the Er concentration and the reactor pressure, indicating coexistence of various Er-related luminescence centers in the samples. Preliminary EXAFS analysis reveals clearly substitutional incorporation of the majority of Er atoms into Ga sites in the GaP lattice, independent of the growth temperature. These results indicate that the luminescence centers responsible for the sharp emission lines involve similar substitutional Er atoms and have different microscopic structures with native defects or impurities around the Er atoms.

Acknowledgments

This work was performed as a part of the project (Project No. 95G221) accepted by the Photon Factory Program Advisory Committee. The authors would like to thank Professors T. Ohyama and H. Nakata of Osaka University for PL measurements. The authors wish to acknowledge Tri Chemical Laboratory Inc. for the Er source. This work was supported in part by the Grant-in-Aid for Scientific Research (C) No. 08650009 and for Scientific Research of Priority Areas, Spin Controlled Semiconductor Nanostructures No. 09244209 from the Ministry of Education, Science and Culture.

References

- [1] For example, Coffa S, Polman A and Schwartz R N 1996 *Rare Earth Doped Semiconductors II, Materials Research Society Symposium Proceedings* vol. 422 (Materials Research Society, Pittsburgh)
- [2] Wang X Z and Wessels B W 1994 *Appl. Phys. Lett.* 64 1537-9
- [3] Fujiwara Y, Furuta S, Makita K, Ito Y, Nonogaki Y and Takeda Y 1995 *J. Cryst. Growth* 146 544-8
- [4] Fujiwara Y, Ito Y, Nonogaki Y, Matsubara N, Fujita K and Takeda Y 1995 *Proc. 18th Inter. Conf. Defects in Semiconductors, Mater. Sci. Forum* vol. 196-201 (Switzerland, Trans Tech Publications) 621-6
- [5] Fujiwara Y, Matsubara N, Tsuchiya J, Ito T and Takeda Y 1997 *Jpn. J. Appl. Phys.* 36 2587-91
- [6] Taguchi A, Takahei K and Horikoshi Y 1994 *J. Appl. Phys.* 76 7288-95
- [7] Hogg R A, Takahei K and Taguchi A 1996 *Extend. Abst. (The 57th Autumn Meeting, 1996)*; The Japan Society of Applied Physics, 7a-D-4
- [8] Tabuchi M, Kawamura D, Fujita K, Matsubara N, Yamada N, Ofuchi H, Ichiki S, Fujiwara Y and Takeda Y 1996 *Rare Earth Doped Semiconductors II, Materials Research Society Symposium Proceedings* vol. 422 (Materials Research Society, Pittsburgh) 155-60
- [9] Ofuchi H, Tsuchiya J, Matsubara N, Tabuchi M, Fujiwara Y and Takeda Y 1997 *Appl. Surf. Sci.* 117/118 781-4

Trap-mediated, Site-Selective Excitation of Photoluminescence from Multiple Er³⁺ Sites in Er-implanted GaN

S. Kim, S.J. Rhee, X. Li, J.J. Coleman, and S.G. Bishop

Microelectronics Laboratory, University of Illinois at Urbana-Champaign, Urbana, IL 61801

P.B. Klein

Naval Research Laboratory, Washington, DC 20375-5347

ABSTRACT. Site-selective photoluminescence (PL) and photoluminescence excitation (PLE) spectroscopy have been carried out at 6 K on the ~1540 nm $^4I_{13/2} \rightarrow ^4I_{15/2}$ emissions of Er³⁺ in Er-implanted MOCVD GaN. The PLE spectroscopy has detected several independent, site-selective excitation mechanisms which demonstrate the existence of four different Er³⁺ sites in Er-implanted GaN. Each of these four Er³⁺ sites exhibits a distinctive PL spectrum characteristic of that center's environment when pumped by the appropriate wavelengths of below-gap light. Two of the site-selective Er³⁺ PL spectra pumped by trap-mediated excitation bands dominate the Er³⁺ PL spectrum excited by above-gap light. The PLE spectra demonstrate that the Er³⁺ PL spectra are excited by below gap absorption attributable to both implantation damage-induced defects and defects and impurities characteristic of the as-grown GaN. The temperature dependence of the Er³⁺ PL spectra was studied to examine thermal quenching properties of these site-specific Er³⁺ PL centers.

INTRODUCTION

The recent suggestion that the thermal quenching of intra-4f shell emissions from Er³⁺ in semiconductor hosts decreases with increasing band gap has spurred research on Er-doped GaN [1-3]. Our PL and PLE spectroscopy demonstrates the existence of at least four different Er³⁺ sites in Er-implanted wurtzite GaN, which can be selectively excited by appropriate wavelengths of below-gap excitation [4-5]. The above-gap excitation for each is also examined here; this excitation is important regarding future GaN:Er devices since it emulates the e-h pair pumping occurring in forward biased p-n junctions. PLE spectroscopy on the broad damage-induced PL band in the Er-implanted GaN has been performed to determine whether these defect-related radiative recombination centers are pumped by the same absorption bands observed in the PLE spectra of the site-selective Er³⁺ PL bands. In an effort to understand thermal quenching properties of these site-specific Er³⁺ PL centers, studies of the temperature dependence of the Er³⁺ PL spectra have been carried out.

EXPERIMENTAL PROCEDURE

GaN films (3 μm thick) were grown on sapphire substrates by atmospheric pressure metalorganic chemical vapor deposition (MOCVD) [6]. For preparation of Er-doped samples, Er ions were implanted with an energy of 280 keV and with implantation dosage of $4 \times 10^{13} \text{ cm}^{-2}$ into as-grown films at room temperature. The implanted samples were annealed at 900 °C for 30 minutes under a continuous flow of nitrogen gas. PLE and PL spectroscopy were carried out on the Er-implanted GaN at temperatures ranging from 6 K to 295 K. The PL spectra were excited with light from a variety of sources including an Ar laser, a He-Cd laser, and a He-Ne laser, a tunable CW Ti:sapphire laser, a frequency-doubled, mode-locked Ti:sapphire laser, and a xenon lamp. The PLE spectra were excited with a xenon lamp dispersed by a double grating monochromator and the tunable Ti: sapphire laser. All of the PLE spectra were corrected for the spectral response of the tunable excitation systems. The luminescence was analyzed by a 1-m single grating monochromator and detected by a cooled Ge PIN detector.

RESULTS AND DISCUSSION

Figure 1 shows the four different Er^{3+} PL spectra obtained from Er-implanted GaN. A distinct Er^{3+} PL center, which gives rise to the simple-structured PL spectrum referred to as the “4f-pumped” spectrum (Fig. 1a), was excited by a set of sharp PLE peaks due to the $\sim 810 \text{ nm } ^4\text{I}_{15/2} \rightarrow ^4\text{I}_{9/2}$ internal 4f-band absorption of the Er atoms [5]. Two of the site-selective Er^{3+} PL bands (the “red-pumped” and “blue-pumped” spectra, as shown in Figs. 1b and 1c, respectively) were pumped by broad, deep, defect-related bands in the “red” and “blue” spectral ranges (see Fig. 2d). The fourth site-selective PL spectrum (referred to as the “violet-pumped” PL spectrum in Fig. 1d) was pumped by a $\sim 3.1 \text{ eV}$ “violet” absorption band (see Fig. 2d). The excitation of three of the site-selective Er^{3+} PL bands involves trap-mediated absorption rather than direct intra-4f shell absorption, with subsequent nonradiative transfer of the energy to nearby Er^{3+} luminescence centers. The fact that only one of the four Er^{3+} luminescence centers is excited directly by intra 4f band absorption indicates that the Er^{3+} site giving rise to this “4f-pumped” spectrum is present at a much higher concentration than the other three Er^{3+} sites.

The same Er-implanted GaN sample was also excited by above-gap light. Careful comparison of the above-gap-pumped spectrum (Fig. 1e) with the four Er^{3+} PL spectra pumped site-selectively with below-gap

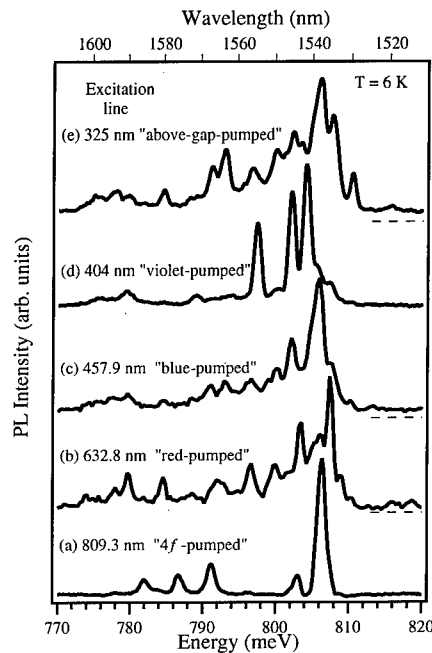


Fig. 1 PL spectra of GaN:Er excited selectively by various laser lines

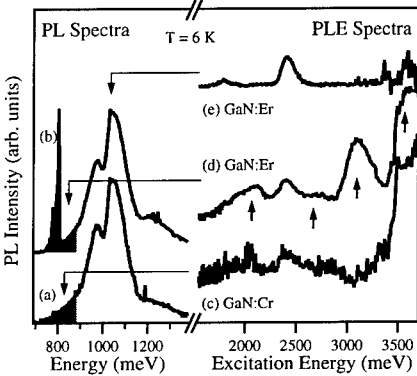


Fig. 2 The PL spectra, excited by 515 nm light, for Cr-implanted (a) and Er-implanted (b) GaN, the PLE spectra (c) and (d) for the integrated PL intensity for wavelengths longer than 1400 nm in Figs. 2(a) and 2(b), respectively, and the PLE spectrum (d) detected at the peak position of the highest intensity in the damage-induced emission shown in Figs. 2(a) and 2(b).

light reveals that the above-gap-pumped spectrum comprises an admixture of the “red-pumped” and “blue-pumped” PL spectra, indicating that trap-mediated excitation dominates above-gap pumping of Er^{3+} emission in GaN:Er. The “4f-pumped” and “violet-pumped” PL spectra are apparently not strongly excited by above-gap pump light. This observation illustrates that only a relatively small concentration of the optically active Er^{3+} centers may be strongly pumped by optically excited free carriers and that a significant fraction of the optically active Er^{3+} sites are not strongly pumped by optically excited free carriers.

Figures 2(a) and 2(b) show 6K PL spectra obtained from Cr-implanted and Er-implanted GaN, respectively. Both samples exhibit identical broad (~ 800 - 1200 nm) damage-induced defect PL spectra [4]. In addition, the sharply structured 1540 nm and 980 nm PL bands characteristic of Er^{3+} are observed in the Er-implanted sample. The PLE spectra [Figs. 2(c) and 2(d)] plot the integrated PL intensity for wavelengths longer than 1400 nm for both of these samples; the PLE spectrum of the broad defect PL bands is shown in Fig. 2(e). These PLE spectra reveal that not all of the broad

site-selective PLE can be attributed to damage-induced defect absorption. Only the dominant PLE band in the PLE spectrum of the broad damage-induced PL (Fig. 2e), which peaks at about 515 nm, is clearly evident in the PLE spectra of some of the Er^{3+} luminescence centers. In addition, the broad damage-induced PL exhibits a weaker "deep red" PLE band which may contribute a portion of the broad "red" PLE bands of the Er^{3+} luminescence. Clearly, the PLE spectrum of the damage-induced PL shows no evidence of the $\sim 3.1 \text{ eV}$ PL peak just below the GaN bandedge in Fig. 2d (believed to be associated with an Er-related trap), and it exhibits little or no excitation response in the blue and red spectral ranges above and below, respectively, the strong 515 nm PLE band.

Figure 3 shows the Er^{3+} PL spectra excited at 515 nm at 6 and 295 K. Careful study of these spectra reveals that the PL spectrum obtained at 6 K comprises an admixture of the predominant peaks of the "red-pumped" and "blue-pumped" spectra (as shown in Figs. 1b and 1c, respectively) and that the PL spectrum obtained at 295 K contains only the predominant peaks of the "blue-pumped" spectrum taken at 6 K. The predominant peaks of the "blue-pumped" spectrum experience less thermal quenching than those of the "red-pumped" spectrum and their peak positions are independent of temperature.

The temperature dependence of the Er^{3+} PL intensity measured separately for each of the six PL spectra is shown in Fig. 4. The "violet-pumped" and "blue-pumped" spectra exhibit similar temperature dependences, reaching a reduction of about a factor of two in integrated intensity at 295 K. The integrated intensities of the "red-pumped" and "4f-pumped" spectra are reduced by a factor of ~ 10 at 295 K. The predominant peaks of the "violet-pumped", "blue-pumped", and "4f-pumped" spectra obtained at 6 K are present at temperatures ranging from 6 K to 295 K, while the predominant peaks of the "red-pumped" spectrum obtained at 6 K are absent in the "red-pumped" spectra obtained at temperatures higher than 150 K which contain the same predominant peaks of the "blue-pumped" spectrum. The predominant peaks seen in the "red-pumped" spectrum experience the most rapid thermal quenching among the six spectra. It should be emphasized that because the PL and PLE bands of the "red-pumped" and "blue-pumped" Er^{3+} spectra have significant overlap, it is not possible to achieve complete separation of the two bands in the site-selective experiments. This means that there is some "cross-talk" between the thermal quenching curves. For example, the thermal quenching curve of the "blue-pumped" PL exhibits an obvious dip in the 50–100 K range where the overlapping "red-pumped" spectrum is being rapidly quenched.

It is apparent that trap-mediated energy transfer mechanisms dominate the excitation of Er^{3+} in ion-implanted GaN. Optically-injected free carriers are captured at traps, or the traps are excited directly by the absorption of extrinsic, below-gap light. The energy stored in the traps is transferred by a non-

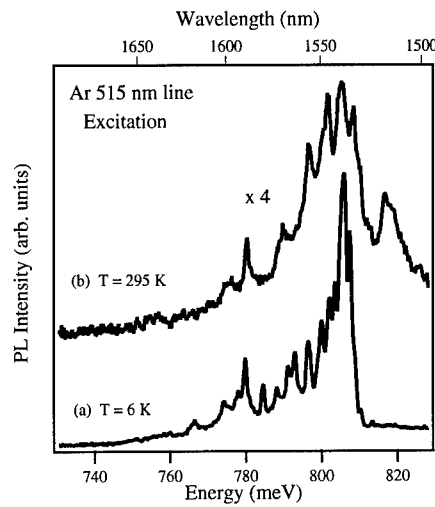


Fig. 3 The PL spectra excited at 515 nm at 6 K (a) and 295 K (b).

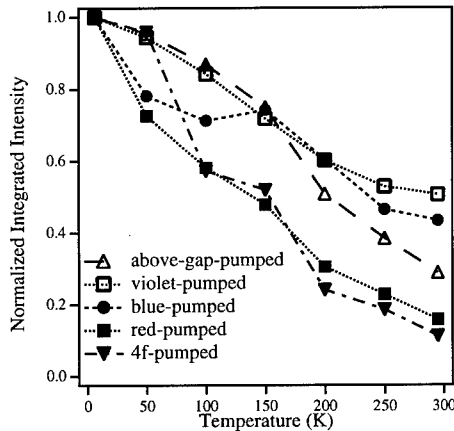


Fig. 4 The temperature dependence of the integrated intensity for various PL spectra.

radiative mechanism to nearby Er³⁺ centers, inducing ground state-to-excited state transitions within the Er³⁺ 4f-shell. Subsequently, the Er³⁺ centers relax radiatively to their ground states [7]. There are two processes by which the Er³⁺ PL intensity can be thermally quenched during the course of trap-mediated excitation [8]: 1) thermal ionization (de-trapping) of the optically excited traps before their energy is transferred to Er³⁺ centers; 2) subsequent to excitation of the Er³⁺ by energy transfer from the traps, the Er³⁺ may undergo non-radiative de-excitation by energy transfer to either the exciting traps or to other traps coupled to the Er³⁺. The first process will decrease the Er³⁺ PL intensity without affecting the luminescence lifetime. The second process will decrease both the Er³⁺ PL intensity and the luminescence lifetime. Studies of the temperature dependence of the Er³⁺ PL lifetimes are planned to provide insights concerning these thermal quenching mechanisms. Clearly, the rate of thermal quenching will depend strongly upon the depth or stability of the traps which mediate the non-radiative excitation and de-excitation processes. Speaking qualitatively, the quenching mechanisms discussed above might be far more important in narrower band gap materials such as GaAs (or Si) in which trap depths are much smaller than in wide band gap semiconductors such as GaN.

CONCLUSIONS

Site-selective PL and PLE spectroscopy of the 1540 nm $^4I_{13/2} \rightarrow ^4I_{15/2}$ Er³⁺ emission in Er-implanted GaN has demonstrated the existence of four different Er³⁺ sites in this sample. Three of the Er³⁺ sites are excited by trap-mediated processes and the fourth site is pumped by direct intra-4f shell absorption. Two of the Er³⁺ sites excited by trap-mediated mechanisms dominate the above-gap-pumped spectrum, indicating that only the Er³⁺ sites coupled to traps having large cross-section for carrier capture are strongly excited by above-gap pump light. A comparison of the damage-induced PLE spectrum with the PLE spectra of the four distinct Er³⁺ luminescence centers reveals that not all of the broad site-selective Er³⁺ PLE can be attributed to damage-induced defect absorption. Broad optical absorption bands due to defects and impurities characteristic of the as-grown GaN films also contribute to the site-selective PLE of Er³⁺. Studies of the temperature dependence of the Er³⁺ PL spectra suggest that the trap-mediated energy transfer processes that dominate the excitation of Er³⁺ in ion-implanted GaN also control the thermal quenching rates for the different Er³⁺ PL centers.

ACKNOWLEDGMENTS

This work was supported by NSF under the Engineering Research Centers Program (ECD 89-43166), DARPA (MDA972-94-1-004), and the JSEP (0014-90-J-1270).

REFERENCES

1. P. N. Favennec, H. L'Haridon, M. Salvi, D. Moutonnet, and Y. Le Guillou, Electron. Lett. **25**, 718 (1989); A. J. Neuhalfen and B. W. Wessels, Appl. Phys. Lett. **60**, 2657 (1992).
2. R. G. Wilson, R. N. Schwartz, C. R. Abernathy, S. J. Pearton, N. Newman, M. Rubin, T. Fu, and J. M. Zavada, Appl. Phys. Lett. **65**, 992 (1994).
3. E. Silkowski, Y. K. Yeo, R. L. Hengehold, B. Goldenberg, and G. S. Pomrenke, Mater. Res. Soc. Symp. Proc. **422**, 69 (1996).
4. S. Kim, S. J. Rhee, D. A. Turnbull, E. E. Reuter, X. Li, J. J. Coleman, and S. G. Bishop, Appl. Phys. Lett. **71**, 231 (1997).
5. S. Kim, S. J. Rhee, D. A. Turnbull, X. Li, J. J. Coleman, and S. G. Bishop, Mater. Res. Soc. Symp. Proc. **468**, 131 (1997).
6. X. Li, D. V. Forbes, S. Q. Gu, D. A. Turnbull, S. G. Bishop, and J. J. Coleman, J. Electron. Mater. **24**, 1711 (1995).
7. D. L. Dexter, J. Chem. Phys. **21**, 836 (1953).
8. R. A. Hogg, K. Takahei, and A. Taguchi, J. Appl. Phys. **79**, 8682 (1996); J. H. Shin, G. N. van den Hoven, and A. Polman, Appl. Phys. Lett. **67**, 377 (1995).

Gain spectra measurement of InGaAsP/AlGaAs laser structures for wavelengths near 800 nm using a new variable stripe length method

A. Oster, F. Bugge, G. Erbert, and H. Wenzel

Ferdinand-Braun-Institut für Höchstfrequenztechnik, Rudower Chaussee 5, D-12489 Berlin, Germany

Abstract: Gain spectra are determined by a new variable stripe length method using current injection. The amplified spontaneous emission of laser structures with contact stripes of different length is measured in dependence on the current density. From these spectra -resolved in TE and TM polarization- the corresponding gain spectra are extracted and the maximum modal net gain, the transparency current density and the internal losses are determined. Laser structures for wavelengths near 800 nm with InGaAsP active regions of different thicknesses and compositions are analyzed. With decreasing thickness and increasing compressive strain in the Al-free quantum well, the transparency current density is reduced and the TM gain is suppressed compared to the TE gain. Under high excitation conditions the gain from the first subband transition saturates and the wavelength of the gain maximum shifts to smaller values due to the additional occupation of higher subbands.

1. Introduction

The optical gain of the active region of a semiconductor laser determines many of its operating properties. Hence, the knowledge of the gain in dependence on the wavelength and the current density is very important for device development and optimization. A common technique for measuring the modal gain is the variable stripe length (VSL) method [1]. Doped samples as used for laser structures or undoped samples are optically excited by a laser beam focused to a stripe with variable length. The amplified spontaneous emission (ASE) emitted from the sample edge is measured and the modal net gain spectra are extracted. Measuring without feedback -in contrast to the method of Hakki and Paoli [2]- this method is not limited by the laser threshold and can be done up to high excitation densities. It is difficult however, owing to the unknown carrier density in the active region, to correlate the gain spectra obtained at different optical pump intensities with laser parameters. In addition, the sample under examination sees other excitation and bias conditions than an active laser diode.

In this letter we present a new method to determine the modal gain. We use the VSL method with current injection in metal contact stripes. The gain extracted from the measured electroluminescence can be directly related to laser properties. We compare the spectral gain curves and the transparency current density of InGaAsP/AlGaAs laser structures with Al-free SQWs of different thickness and strain with wavelengths near 800 nm.

2. Sample preparation and measurement method

For the gain measurement, metal contact stripes with different length are deposited on the complete epitaxial laser structure. The laser structures for the emission around 800 nm have a 17 nm (sample A) or 12 nm (sample B) thick lattice matched $\text{In}_{0.17}\text{Ga}_{0.83}\text{As}_{0.7}\text{P}_{0.3}$ SQW embedded in 0.5 μm thick $\text{Al}_{0.65}\text{Ga}_{0.35}\text{As}$ waveguide and 1.8 μm thick $\text{Al}_{0.7}\text{Ga}_{0.3}\text{As}$ cladding layers grown by MOVPE on GaAs

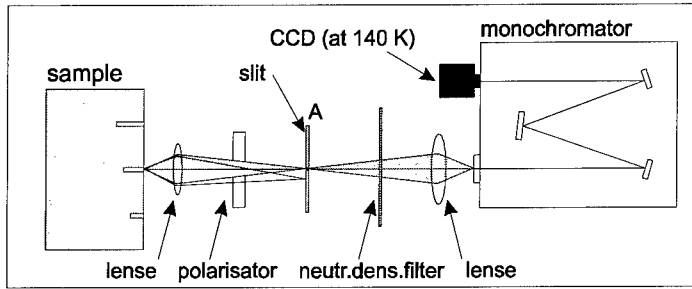


Fig. 1: optical setup for gain measurements

substrates. Sample C has a 13 nm thick compressively strained $\text{In}_{0.27}\text{Ga}_{0.73}\text{As}_{0.6}\text{P}_{0.4}$ SQW surrounded by the same AlGaAs layers as in samples A and B. The contacts for the gain measurements are 80 to 440 μm long and 25 μm wide. The GaAs contact layer and 1.4 μm of the cladding layer are etched off outside the metal contacts to achieve current confinement. To avoid feedback effects and the formation of Fabry-Perot modes both facets are antireflection coated ($R < 1\%$) and there is a large unexcited highly absorbing area behind the contact stripes. Thus the resonator quality is sufficiently low and the measurement can be done up to high current densities. For comparison 50 μm wide broad area (BA) lasers are processed from the same wafer and are cleaved with resonator lengths between 0.6 and 2 mm.

ASE spectra of ten stripes with different lengths are measured at various current densities with the experimental setup sketched in Fig. 1. The ASE intensity is detected polarization-dependent by a cooled CCD camera at the rear of a monochromator with a resolution of $\Delta\lambda = 0.5 \text{ nm}$. The modal net gain is extracted from the stripe length dependence of the ASE intensity under the same excitation density at each wavelength. Using broad area (BA) contact stripes the slit at plane A (Fig. 1) is necessary for the spatial filtering of off-axis modes with higher losses [3].

3. Results and discussion

Modal net gain spectra of sample A are shown in Fig. 2a for current densities j between 0.3 and 1.3 kA/cm^2 for TE (solid lines) and TM polarization (dotted lines). For the same current density, the TE gain is higher than the TM gain, mainly due to the better optical confinement of the TE mode - polarized in the SQW plane- compared to that of the TM mode. The maximum of the gain curves of this nearly unstrained SQW is at the same wavelength for both polarizations and shifts to shorter wavelengths with increasing j due to bandfilling. Note, that in this thick SQW there are several allowed subband transitions which can not be spectrally resolved. Thermal effects can be neglected using 10 μs long pulses with a duty cycle of 1:625. The dashed-dotted lines in Fig. 1 are guides to the eye to illustrate the wavelength shift of the gain maxima.

At transparency, where the material gain g_{mat} vanishes, the photon energy is equal to the difference of the quasi-Fermi energies of electrons and holes. Because there is a common quasi-Fermi level for heavy and light holes under stationary conditions, transparency is the same for TE and TM polarization [4]. The modal gain g_{mod} can be written as $g_{\text{mod}} = \Gamma \cdot g_{\text{mat}} - \alpha_i$, where the confinement factor Γ is different for TE and TM. Assuming that the internal losses α_i are identical for both polarizations,

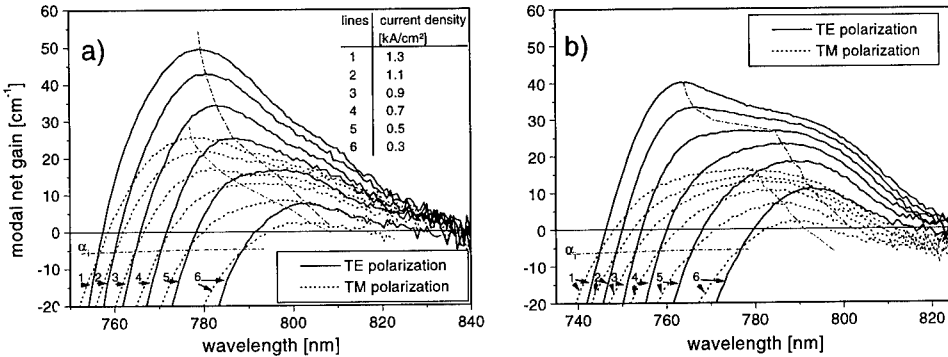


Fig. 2: TE and TM polarized modal net gain of In_{0.17}Ga_{0.83}As_{0.7}P_{0.3} SQWs
a) sample A (17 nm), b) sample B (12 nm thick)

the TE and TM modal net gain can only be equal at transparency. So the value of the intersection at the short wavelength side yields directly the value of the internal losses. The internal losses of $\alpha_i = 5 \text{ cm}^{-1}$ of sample A agree well with the result of the measurement of the external efficiency of BA lasers with resonator lengths of $L = 0.64 \dots 2 \text{ mm}$ from the same wafer. The losses slightly increase with current density, which can be explained by an increased free carrier absorption.

The maximum modal net gain g_{\max} , obtained from the spectra of Fig. 2, is drawn against the current density in Fig. 3. g_{\max} of sample A (full squares in TE, open squares in TM polarization) increases with j up to high values without saturation. From the logarithmic fit $g_{\max} = \Gamma \cdot G_0 \cdot \ln(j/j_r)$ the transparency current density j_r and the product $\Gamma \cdot G_0$ can be obtained, where G_0 is the gain parameter. The fitting of g_{\max} for j between 150 and 700 A/cm² yields $\Gamma \cdot G_0 = 18.5 \text{ cm}^{-1}$ and $j_r = 193 \text{ A/cm}^2$. These values agree well with results extrapolated from the $\ln(j_r) - 1/L$ curve obtained from the threshold current densities j_r of the BA lasers ($\Gamma \cdot G_0 = 19 \text{ cm}^{-1}$ and $j_r = 200 \text{ A/cm}^2$). Taking the calculated confinement factor $\Gamma = 0.034$ into account the gain parameter $G_0 = 540 \text{ cm}^{-1}$ is obtained for the TE mode, the corresponding values for the TM mode are $\Gamma = 0.020$ and $G_0 = 650 \text{ cm}^{-1}$.

Fig. 3 also shows g_{\max} of sample B (circles) with the thinner SQW, but the same composition as sample A. The transparency current density is reduced to 140 A/cm². For $j \geq 0.35 \text{ kA/cm}^2$ $g_{\max}(j)$ in TE polarization saturates before it increases again more rapidly for $j \geq 0.9 \text{ kA/cm}^2$. The kink in the $g_{\max} - j$ curve is connected with an abrupt shift of the wavelength of g_{\max} by about 20 nm, which is clearly visible in the gain spectra of sample B in Fig. 2b, measured and drawn in the same way as in Fig. 2a. For high excitation densities the second electron subband is occupied and the maximum of the gain is at the wavelength of the transition from the second electron subband. The same phenomenon has been observed at InGaAsP lasers grown on InP [5]. In TM polarization, g_{\max} is reduced compared to sample A and the wavelength of g_{\max} is shifted by about 3 nm towards shorter wavelengths compared to the TE first subband transition at the same j . Due to the enhanced quantum confinement the light hole band is shifted below the heavy hole band.

The spectral shape of the TE modal net gain of sample C with a 0.55 % compressively strained SQW looks like sample B with almost the same SQW thickness: saturation of the first subband transition and switching to the second one at $j = 0.8 \text{ kA/cm}^2$. The compressive strain lowers the valence band density of states and so the transparency current density is again reduced to 110 A/cm².

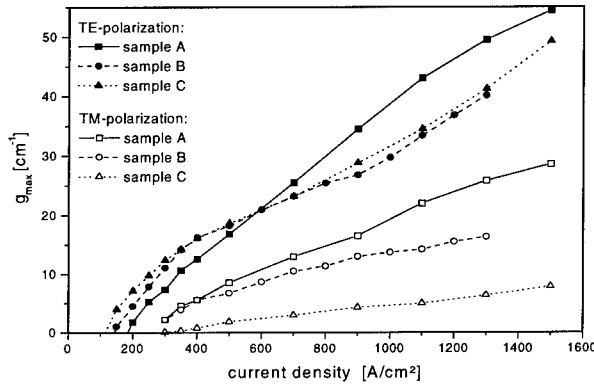


Fig. 3: Modal peak gain versus current density for all samples in TE (full signs) and TM (open signs) polarization

In addition, the light hole band is splitted off the heavy hole band due to the strain. For that reason the wavelength shift of g_{\max} between TE and TM is twice as high as in sample B. The total gain in TM polarization is strongly reduced to only 7 cm^{-1} at $j = 1.3 \text{ kA/cm}^2$ as shown in Fig. 3 (open triangles).

4. Summary

A new method for spectrally resolved gain measurements was introduced. We measured TE and TM polarized gain spectra of an AlGaAs laser structure with different InGaAsP SQWs and obtained the transparency current density and the internal losses. The maximum of the gain spectra of an almost unstrained 17 nm thick SQW increases nearly linear and shifts to shorter wavelengths with the current density. The TE gain is about twice as high as the TM gain. A 12 nm thick unstrained SQW shows gain saturation of the first subband transition. At high current densities the maximum of the gain is at the wavelength of the transition from the second electron subband. 0.55 % compressive strain in a 13 nm thick SQW reduces the transparency current density from 140 A/cm^2 -in the thin unstrained sample- to 110 A/cm^2 and suppresses the TM against the TE polarization.

5. Acknowledgment

The authors would like to thank K. Vogel and P. Ressel for sample processing, and G. Tränkle and M. Weyers for useful discussion.

References

- [1] Shaklee K L and Leheny R F 1971 *Appl. Phys. Lett.* **18** 475-477
- [2] Hakki B W and Paoli T L 1975 *J. of Appl. Phys.* **46** 1299-1306
- [3] Oster A, Erbert G and Wenzel H 1997 *Electr. Lett.* **3** 864-866
- [4] Avrutin E A, Chebunin I A, Eliashevitch I A, Gurevich S A and Shtengel G E 1993 *Sem. Sci. Techn.* **8** 80-87
- [5] Zielinski E, Keppler F, Haussler S, Pilkuhn M H, Sauer R and Tsang W T 1989 *J. Quantum Electron.* **25** 1407-1403

Electronic and vibrational Raman scattering in resonance with yellow luminescence transitions in GaN on sapphire substrate

D.S. Jiang ^(a,b), M. Ramsteiner ^(a), O. Brandt ^(a), K.H. Ploog ^(a), H. Tews ^(c), A. Graber ^(c), R. Averbeck ^(c), and H. Riechert ^(c)

^(a) Paul Drude Institute for Solid State Electronics, D-10117 Berlin, Germany

^(b) Institute of Semiconductors, CAS, Beijing 100083, China

^(c) Siemens Corporate Research and Development, D-81730 Munich, Germany

Abstract. We analyze low-temperature Raman and photoluminescence spectra of MBE-grown GaN layers on sapphire. Strong and sharp Raman peaks are observed in the low frequency region. These peaks, which are enhanced by excitation in resonance with yellow luminescence transitions, are attributed to electronic transitions related to shallow donor levels in hexagonal GaN. It is proposed that a low frequency Raman peak at 11.7 meV is caused by a pseudo-local vibration mode related to defects involved in yellow luminescence transitions. The dependence of the photoluminescence spectra on temperature gives additional information about the residual impurities in these GaN layers.

1. Introduction

GaN is a promising semiconductor material with wide energy gap. Recently, molecular beam epitaxy (MBE) and metal-organic vapor phase epitaxy have been successfully employed to grow high efficiency III-V nitrides blue and green light emitting diodes and lasers. Despite this great technological progress, some fundamental properties of GaN, including the behavior of residual impurities, are still not well understood.

Impurity-induced electronic Raman excitations in MBE-grown cubic GaN on GaAs have been reported first by Ramsteiner et al. [1]. These Raman peaks are located in the energy range between 18.5 and 30 meV and are enhanced for excitation in resonance with yellow luminescence transitions. Two peaks at 23.4 and 29.4 meV have been attributed to electronic Raman scattering (ERS) caused by internal shallow donor transitions [1,2]. Here, we analyze low temperature Raman spectra of MBE GaN layers, grown on sapphire. It is found that hexagonal GaN layers on sapphire also show strong and sharp Raman peaks in the low frequency region. We confirm that these peaks are in accordance with a model of electronic transitions related to shallow donors in GaN. In addition, the peak at 11.7 meV is attributed to a defect-induced pseudo-local vibrational mode. In connection with the temperature dependence of photoluminescence (PL) spectra, the residual defects in MBE-grown GaN are tentatively assigned to be related to Si.

2. Experimental

The hexagonal GaN samples were grown on (0001)-oriented sapphire substrates by MBE employing an RF nitrogen plasma source. The growth conditions were identical to those which have been

used for fabricating blue and green light-emitting diodes [3]. The nominally undoped layers are predominantly hexagonal and n-type with a carrier concentration of the order of 10^{17} cm^{-3} (mobility of about $300 \text{ cm}^2/\text{Vsec}$). The Raman spectra were measured with a Dilor triple grating monochromator system. Some measurements were made by using a low-temperature confocal micro Raman equipment in which the light spot is focused by a microscope to a diameter of about $2 \mu\text{m}$.

3. Results and Discussion

The analysis of the frequency positions and polarization selection rules of the optical phonon lines proves the GaN layers on sapphire to be predominantly hexagonal [4]. The temperature dependence of the carrier density obtained by Hall-effect measurements reveals an activation energy in the range of 25 to 35 meV.

Low-frequency Raman peaks appear only in part of the investigated hexagonal GaN layers. However, a clear dependence on certain growth parameters was not yet found. Generally five resonantly enhanced Raman peaks are observed in the range between 11.5 meV and 31.0 meV, namely, at 11.7, 18.3, 23.4, 27.1, and 30.7 meV. They are denoted as β , A^* , ϕ , B^* , and ϵ in Fig. 1, respectively. The notation of peaks A^* and B^* follows the literature [1] where these peaks have been observed in Raman spectra of GaN layers grown on GaAs. They were tentatively attributed to intra-shallow donor electronic transitions in hexagonal GaN domains within the predominantly cubic matrix. The detection of strong peaks A^* and B^* in GaN grown on sapphire substrates strongly supports the assignment of these peaks to the hexagonal phase of GaN. Furthermore, this observation rules out both N in GaAs and As in GaN as the possible origin of these low frequency peaks as it was proposed in Ref. [5].

The assignment of the low-frequency peaks to electronic transitions is based on the following arguments. They are observed only in part of the samples investigated and are thus not intrinsic to GaN but must be related to defects. Their energy positions are compatible with the energy separation between the ground and excited states of shallow donors in GaN. An Arrhenius plot of the peak intensity yields an activation energy close to that of shallow donors, suggesting that the decrease in the Raman peak intensity with increasing temperature, as shown in Fig. 2, is related to the thermal population of the donor's ground state. In addition, a resonance enhancement with a pronounced maximum of the scattering probability located at about 2.35 eV is observed, which is close to the energy of the yellow luminescence band at 2.1–2.2 eV (see Fig. 3). The resonance effect is explained as being due to transitions via defect states involved in the yellow luminescence recombination process, as proposed for cubic GaN on GaAs [1]. The yellow band luminescence transitions, which are supposed to occur between shallow donors and deep acceptors, provide real intermediate states for the resonant Raman process. The energy shift is presumably related to the Stokes-shift expected for the deep acceptor in absorption and emission.

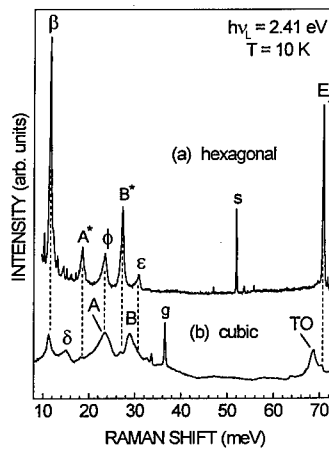


Fig.1. Low temperature Raman spectra of a hexagonal GaN-on-sapphire sample (a) and of a predominantly cubic GaN-on-GaAs sample (b). The excitation energy is 2.41 eV. The optical phonon lines of the sapphire (s) and GaAs (g) are indicated.

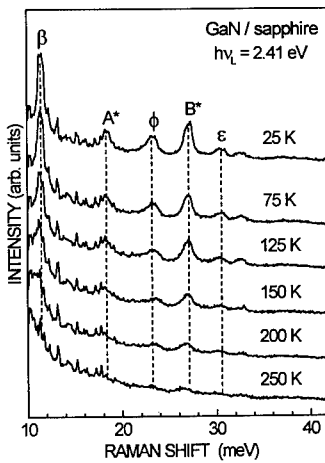


Fig. 2. Raman spectra of the hexagonal GaN-on-sapphire sample for different temperatures as indicated in the figure. The excitation energy is 2.41 eV.

phonon modes, which also causes the broadening of the Raman peak with increasing temperature (see Fig. 2). The resonance enhancement for excitation at about 2.4 eV indicates that the defects involved contribute to the electronic states which are responsible for the yellow luminescence band [9].

From their energy position peaks ϕ and ϵ can be assigned to be the hexagonal counterparts of peaks A and B (see Fig. 1) which have been attributed to the 1s-2s and 1s-3s transitions of shallow donors in cubic GaN in Ref.[1]. The derived binding energy of 33 meV is in agreement with the value expected from effective mass theory (EMT) for hexagonal GaN [6]. Peaks A* and B*, on the other hand, could be tentatively attributed to the corresponding transitions of a second donor with a binding energy of 27.5 meV [1]. However, assuming peaks β , A* and B* to be caused by lowest-energy electronic transitions of different donors the corresponding binding energies estimated by EMT, including a central cell correction, are 20, 26.5 and 35.5 meV, respectively. In fact, these three binding energies, derived from electrical and optical measurements, have already been reported for different donors in GaN [6-8]. Actually, these donors have not necessarily to be hydrogenic.

Because of the very low energy of peak β we may alternatively attribute this particular peak to a defect-induced pseudo-local vibrational mode. In this case, the decrease in intensity of peak β at higher temperatures might be explained by the enhanced damping of vibrations via their coupling to lattice

A preliminary secondary ion mass spectroscopy (SIMS) analysis was performed for the GaN layers on sapphire. Comparing samples which show weak and strong low-energy Raman peaks, respectively, a higher content of residual Si is found for the latter ones. This result suggests that Si might be responsible for at least part of the observed Raman processes. Different ionization energies between 12 and 35 meV, obtained from Hall effect measurements, have been related to the Si donor in hexagonal GaN [7,8]. In addition, it was proposed that there is a relationship between Si doping and the yellow luminescence [8].

Temperature-dependent PL spectra of our hexagonal GaN samples (Fig. 4) show that above 50 K, the free exciton (FX) peak appears at an energy of 3.479 eV and becomes dominant with further increasing temperature, accompanied by a gradual disappearance of the (D_0 , X) bound exciton [10]. The binding energy of (D_0 , X) of 3.5 meV (see also Ref. [6]) implies a donor ionization energy of 35 meV according to Haynes rule. At temperatures above 60 K, a peak at 3.29 eV gradually replaces the donor-acceptor-pair (DAP) luminescence peak at about 3.265

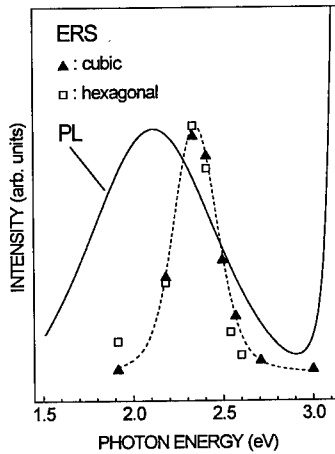


Fig. 3. Intensity of electronic Raman scattering (ERS) as a function of the incident photon energy for cubic and hexagonal GaN samples as well as a spectrum of the yellow band luminescence at 10 K.

eV. The peak at 3.29 eV is attributed to free electron to acceptor (FB) transitions [11]. Such a behavior was also observed in Si doped GaN [7]. The separation of the DAP and FB peaks represents the lower bound of the donor binding energy of about 25 – 30 meV in agreement with the measured activation energy of the carrier concentration in our samples. However, further work is necessary to identify the chemical nature of the residual impurities or defects.

4. Conclusions

In summary, we have observed low-frequency Raman peaks in MBE-grown GaN layers on sapphire which are enhanced when the excitation energy is in resonance with the yellow luminescence band. It has been confirmed that these peaks are related to the hexagonal phase. The arguments of attributing Raman peaks in cubic GaN to electronic excitations of intra-shallow donor transitions have been found to be also suitable for hexagonal GaN. An additional peak at 11.7 meV has been assigned to a quasi-local vibration. Si seems to be the most likely candidate for being related to these low-frequency Raman peaks. Further investigations are being carried out in order to elucidate the origin of the residual donors.

References

- [1] Ramsteiner M, Menniger J, Brandt O, Yang H and Ploog K H 1996 *Appl. Phys. Lett.* **69** 1276
- [2] Ramsteiner M, Menniger J, Brandt O, Yang H and Ploog K H 1997 *Appl. Phys. Lett.* **70** 910
- [3] Tews H, Averbeck R, Gruber A and Riechert H 1996 *Electronics Lett.* **32** 2004
- [4] Azuhata T, Sota T, Suzuki K and Nakamura S 1995 *J. Phys.: Cond. Mat.* **27** L129
- [5] Siegle H, Loa I, Thurian P, Eckey L, Hoffmann A, Broser I and Thomassen C 1997 *Appl. Phys. Lett.* **70** 909
- [6] Meyer B K, Volm D, Gruber A, Alt H C, Detzprohm T, Amano A and Akasaki I 1995 *Sol. State Commun.* **95** 597; Fischer S, Volm D, Kovalev D, Averboukh B, Gruber A, Alt H C and Meyer B K 1997 *Mat. Sci. Eng. B* **43** 192
- [7] Goetz W, Johnson M, Chen C, Liu H, Kuo C and Imler W 1996 *Appl. Phys. Lett.* **68** 3144
- [8] Hacke P, Maekawa A, Koide N, Hiramatsu K and Sawaki N 1994 *Jpn. J. Appl. Phys.* **33** 6443
- [9] Yu P Y, Pilkuhn M H and Evangelisti F 1987 *Sol. State Commun.* **55** 371
- [10] Merz C, Kunzer M, Kaufmann U, Akasaki I and Amano H 1996 *Semicond. Sci. Technol.* **11** 712
- [11] Dingle R and Illegems M 1971 *Sol. State Commun.* **9** 175

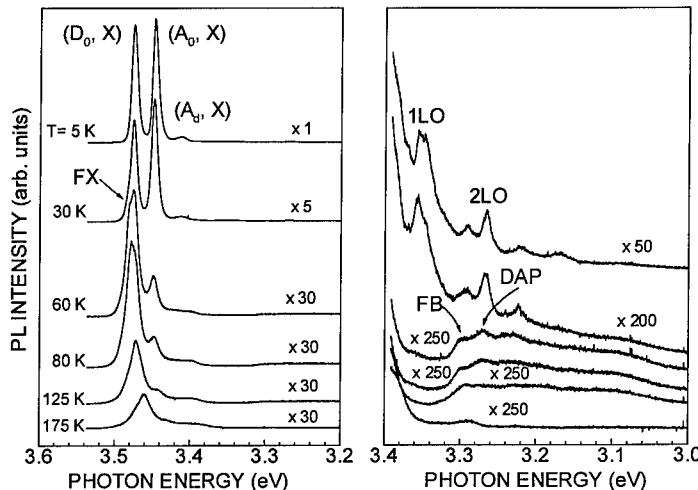


Fig.4. PL spectra of the hexagonal GaN-on-sapphire sample at different temperatures.

Temperature dependence of photoluminescence in Mg-doped GaN epilayers grown by MOCVD

**Eun-joo Shin, A. Kasi Viswanath, Joo In Lee, Nam Woong Song, Dongho Kim,
Baeyong Kim*, Yoonho Choi*, Chang-Hee Hong***

Spectroscopy Laboratory, Korea Research Institute of Standards and Science, Daedok
Science Town, Taejon 305-600, Korea, *Optoelectronics Group, L.G. Corporate Institute
of Technology, Seoul 137-140, Korea

Abstracts. High quality magnesium doped GaN epitaxial layers on sapphire substrate were achieved by the rotating disk MOCVD. Energy levels of these acceptors were investigated by temperature dependent photoluminescence measurements. Magnesium concentration was varied from $< 1 \times 10^{19}$ to higher than $5 \times 10^{19} \text{ cm}^{-3}$. In the samples with lower magnesium concentration we have observed free excitonic transitions and the donor-acceptor pair transition with its phonon replicas. For the samples with higher magnesium concentration the spectra were dominated by acceptor related transitions. In this study, we could not see any deep level luminescence even in highly Mg-doped GaN and free excitonic transitions were observed in doped materials. These facts show the high quality of samples.

1. Introduction

In spite of achieving several important practical optoelectronic devices based on p-type Mg-doped GaN, the photoluminescence (PL) study of these materials has not been done in detail so far. In this work we report the temperature dependent PL studies on Mg-doped GaN with various Mg concentration which was varied from $< 1 \times 10^{19}$ to higher than $5 \times 10^{19} \text{ cm}^{-3}$. The understanding of the radiative recombination processes in Mg-doped GaN can provide a fundamental basis for the optimum design of optical devices.

2. Experiment

The epilayers of Mg-doped GaN of about 4 μm thickness were grown on (0001) sapphire substrate by the rotating disk MOCVD. The substrate was preheated for 10 minutes at 1050 $^{\circ}\text{C}$ and then cooled under ammonia flow to 520 $^{\circ}\text{C}$ for the deposition of GaN nucleation layer. The GaN epilayer was grown at 1010 $^{\circ}\text{C}$ and has shown FWHM of about 250 to 270 arc sec for (0002) reflections by high resolution x-ray diffraction. The sample was thermally annealed in the nitrogen atmosphere for 20 minutes at 700 $^{\circ}\text{C}$. A He-Cd laser (325 nm) was used as an excitation source for the cw PL experiments. The PL signal was dispersed by a 1-meter monochromator (McPHERSON) and detected by a photomultiplier tube (Hamamatsu) and a Lock-in amplifier (Princeton Applied Research). The sample was mounted in a closed-cycle liquid-helium cryostat (Janis) for low temperature measurements.

3. Results and Discussion

Fig. 1 shows the temperature dependent PL spectra for Mg-doped GaN epilayers of which Mg concentration is less than $1 \times 10^{19} \text{ cm}^{-3}$. We observed a strong line at 3.276 eV and satellites on the low energy side at 3.184, and 3.092 eV. The main line at 3.276 eV is attributable to the donor-to-acceptor pair (DAP) transitions. The separation between two consecutive lines is about 92 meV which corresponds to A1(LO) mode of GaN. And from the similar decay profiles for these three peaks, the lines at 3.184 and 3.092 eV are assigned as the first and second phonon replica of the DAP transitions. At present we do not know exactly the nature of donors in our samples. The donor may be nitrogen vacancies. We can also see high energy peaks around 3.48 eV which are due to free excitons and bound excitons. As the temperature increases the DAP transitions were observed to move to higher energy by few meV. This behavior is attributable to the enhancement of more closely spaced pairs by a higher thermal ionization rate for the donors when the temperature is raised. Above 200 K the luminescence due to DAP was found to be quenched. We could also notice that the free exciton emission intensity increases relative to DAP transitions as the temperature increases.

Fig. 2 shows the PL spectrum in the excitonic transition region at 12 K where FX(A), FX(B), DX and AX represent the free exciton A, free exciton B, donor bound exciton and acceptor bound exciton transition, respectively. The spectrum for doped samples shown in Fig. 2 has exactly the same features as those found in undoped GaN [1]. The assignment of these transitions has been made from the temperature dependent PL measurements.

Fig. 3 shows the PL spectra of samples with Mg concentration of 1 to $5 \times 10^{19} \text{ cm}^{-3}$ after annealing. We can see well resolved peaks at 3.276, 3.184, 3.092 and 3.00 eV which are attributed to zero phonon, first phonon, second phonon and third phonon replica of DAP transitions in the annealed

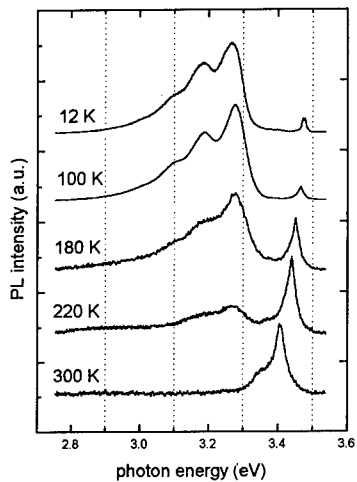


Fig. 1. Temperature dependent PL spectra for Mg-doped GaN epitaxial layers grown on (0001) sapphire substrate. Mg concentration is less than $1 \times 10^{19} \text{ cm}^{-3}$.

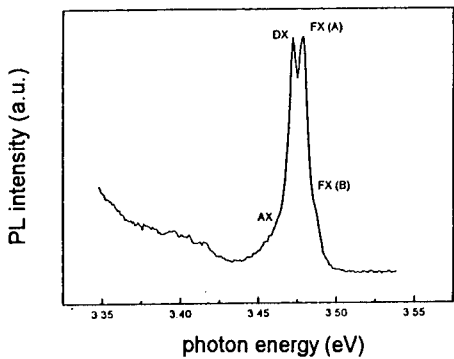


Fig. 2. Excitonic region PL spectrum for Mg-doped GaN at 12 K. Mg concentration is less than $1 \times 10^{19} \text{ cm}^{-3}$.

sample compared to as-grown (which is not shown here). And in the annealed sample we observed that the PL intensity has increased to a large extent. As the temperature increases the DAP transition is thermally quenched. The thermal quenching of DAP is followed by an increase in the new band around 3.1 eV at 90 K. This peak could be observed up to room temperature and has shifted to ~ 2.96 eV and is considered to be related to the shallow acceptor. At 220 K we can see another peak at ~ 2.91 eV which has become stronger than ~ 2.96 eV transitions. This is regarded as due to another acceptor level which is a little bit deeper than the other shallow level. This transition picks up intensity as the

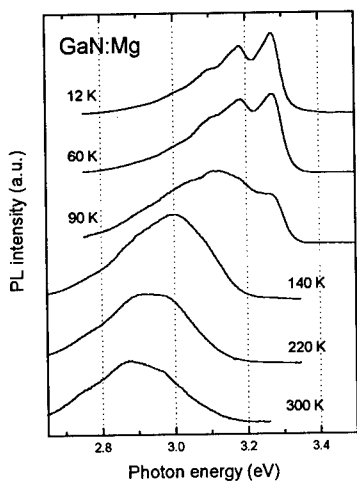


Fig. 3. Temperature dependent PL spectra for Mg-doped GaN after annealing. Mg concentration is in the range of 1 to $5 \times 10^{19} \text{ cm}^{-3}$.

temperature increases as seen in Fig. 3. The increase in intensity of this peak with temperature is explained by the favorable population of deeper levels at higher temperature.

Fig. 4 shows the PL spectrum of highly Mg-doped GaN at 12 K. Very deep level transitions at 1.0, 1.2, 1.8 and 2.2 eV have been reported by several workers [2,3] and deep level has been reported to be at 2.43 eV [4] and was attributed to Mg at the nitrogen site. However we did not observe very deep level in our PL measurements even for the high Mg concentration of $5 \times 10^{19} \text{ cm}^{-3}$. The absence of such very deep level in our samples indicates that complex centers of Mg do not exist in our samples, and that the samples are of high quality. We suggest that, controlling the crystal growth in such a way that the acceptors take the substitutional positions of Ga and not any other sites like the substitutional position of nitrogen or interstitial positions will give the desired characteristics. We believe that Mg occupies the substitutional site of Ga in GaN lattice for acceptors.

4. Summary

Good quality magnesium doped GaN epitaxial layers with higher impurity concentrations were achieved by rotating disk vertical MOCVD. Temperature dependence of PL for various Mg concentrations has been reported. When Mg concentration was less than $1 \times 10^{19} \text{ cm}^{-3}$ donor-acceptor pair transitions were observed and free excitonic transitions were observed in doped GaN. As Mg concentration increases the spectra were dominated by acceptor related transitions. We could not see any deep level luminescence from complex Mg centers or yellow luminescence from defects. This facts along with the observation of free excitons shows that the samples are of good quality.

References

- [1] Viswanath A K *et al.* 1997 *Phys. Rev. B* submitted
- [2] Hacke P *et al.* 1996 *Appl. Phys. Lett.* 68 1362
- [3] Gotz W *et al.* 1996 *Appl. Phys. Lett.* 68 3470
- [4] Myoung J M *et al.* 1996 *Appl. Phys. Lett.* 69 2722

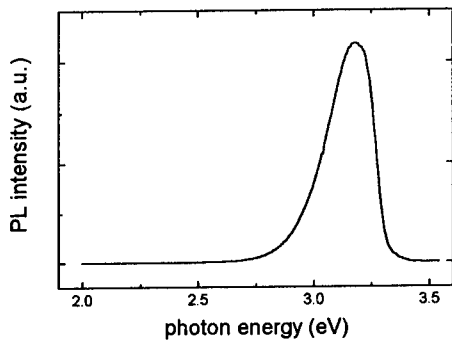


Fig. 4. PL spectrum for Mg-doped GaN at 12 K. Mg concentration is higher than $5 \times 10^{19} \text{ cm}^{-3}$.

Impact of GaN Buffer Growth Conditions on Photoluminescence and X-ray Diffraction Characteristics of MOVPE Grown Bulk GaN

A. Eisenbach¹⁾, D. Pavlidis¹⁾, A. Philippe²⁾, C. Bru-Chevallier²⁾, and C. Dubois²⁾

¹⁾ Solid State Electronics Laboratory, Department of Electrical Engineering and Computer Science, The University of Michigan, 1301 Beal Avenue, Ann Arbor, MI 48109-2122, USA, e-mail: eisenbac@umich.edu

²⁾ Laboratoire de Physique de la Matière, Institut National des Sciences Appliquées de Lyon, Bâtiment 502, 20, Avenue Albert Einstein, 69621 Villeurbanne Cedex, France

Abstract. Properties of metalorganic vapor phase epitaxy (MOVPE) grown GaN bulk layers with varying GaN buffer growth conditions are characterized by low-temperature (6K) photoluminescence (LT-PL) and X-ray diffraction (XRD). Full width at half-maximum (FWHM) of the near-bandedge emission of undoped layers is between 4.9 and 10meV, exhibiting no distinct dependence on buffer growth conditions. PL as well as photoreflectance measurements allowed the identification of neutral-donor bound exciton (D_0X) emission at ~3.48eV, and free A and B exciton emission lines at ~6 and ~15meV higher energies, respectively. UV/yellow luminescence integrated intensity ratio and XRD FWHM show clear dependence on buffer growth conditions. Decreasing buffer thickness results in increasing PL intensity ratio and decreasing XRD FWHM. For thicker buffers, increasing the temperature ramping time between buffer and bulk growth also improves optical layer quality. Si-doped GaN was grown with carrier concentrations between $9 \times 10^{17} \text{ cm}^{-3}$ and $2 \times 10^{19} \text{ cm}^{-3}$. The PL peak position decreases with increasing carrier concentration and its FWHM increases due to donor banding effects.

1. Introduction

III-N compound semiconductors have attracted wide attention, largely due to the demonstration of blue light emitters [1], and their potential in high-temperature and high-power applications [2]. Despite the large differences in lattice constant and thermal expansion coefficients with regard to nitrides, sapphire has been the substrate of choice for device applications, made possible only through the introduction of low-temperature grown GaN or AlN buffer layers [3,4]. A wide variety of GaN buffer growth conditions, e.g. thickness, growth temperature, etc., have been reported to result in device quality MOVPE grown GaN layers on sapphire substrates (e.g. [1,2]). This is, however, in most cases growth system specific and only few reports are published on specific trends of buffer growth conditions on bulk layer quality [5-8]. This paper addresses such issues and reports on the impact of GaN buffer growth conditions on GaN bulk quality as characterized by LT-PL and single-crystal XRD.

2. Experimental

The GaN layers were grown by low-pressure MOVPE (60torr) on c-plane (0001) sapphire in a modified EMCORE GS3200 system. TMGa and NH₃ were used as precursors, Si₂H₆ for Si-doping, and H₂

as carrier gas. Bulk growth temperature was 1040°C, bulk growth rate was 2.5μm/hr (TMGa=136μmol/min) at V/III=1650, and bulk layer thickness was constant 1.25μm. The GaN buffers (TMGa=17μmol/min and V/III≈5000) were grown at temperatures between 500 and 550°C, growth time was varied between 150 and 630sec, corresponding to buffer thicknesses of ~80-400Å, and the temperature ramping time between buffer and bulk growth was varied between 4 and 25min. The GaN layers were characterized by single crystal (θ-2θ) XRD. LT-PL measurements have been performed at 6K using an Argon laser by COHERENT, combined with a monochromator to select the 334nm emission line from its spectrum. Output power was kept constant at 15mW, and the samples have been mounted on the cold fingers of a liquid helium cooled cryostat equipped with a temperature controller.

3. Results

All GaN layers exhibit smooth, shiny surfaces and are clear and transparent. XRD FWHM is typically ~250arcsec. During this study, background carrier concentration was in the mid 10^{17}cm^{-3} range with mobilities between 30 and 110cm²/Vs corresponding to non-optimized buffer growth conditions.

6K PL FWHM of the bandedge emission of undoped layers is between 4.9 and 10meV, exhibiting no distinct dependence on buffer growth conditions. However, the UV/yellow luminescence integrated intensity ratio shows clear dependence on buffer growth conditions. Figure 1 shows representative UV bandedge PL spectra for samples grown with constant buffer growth temperature $T_b=500^\circ\text{C}$ and different buffer growth times. The main peak at 3.482eV is usually identified as the neutral-donor bound exciton peak (D_0X), blue-shifted by 13meV due to strain from the 3.469eV [9] measured on very thick (and presumably completely relaxed) GaN layers. These spectra clearly exhibit 3 additional peaks besides the main peak. The shoulder on the low energy side of the exciton peak at 3.468eV is attributed to the radiative recombination of an exciton bound to an acceptor [10]. The two peaks at the high energy side at 3.488 and 3.497eV, which are separated by 6 and 15meV from the D_0X peak, respectively, are in good agreement with previous reports and can be interpreted as free A and B exciton [9-15]. In samples where the exciton lines were not well resolved in the PL spectra, photoreflectance measurements also allowed the identification of free A and B exciton lines at 5 and 14meV above D_0X energy in excellent agreement with the PL results. Free C exciton was only weakly resolved and its energy is estimated to be 30-35meV above D_0X energy.

3.1 Impact of buffer growth time

Samples have been grown with different buffer growth times to determine the effect of buffer thick-

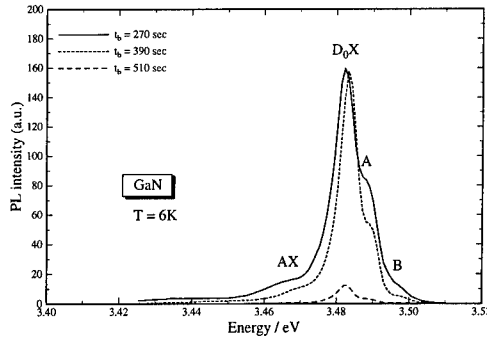


Fig. 1: PL spectra at 6K showing acceptor bound, neutral-donor bound and free A and B exciton peaks.

ness. In Fig. 2, the UV/yellow luminescence integrated intensity ratio and the XRD FWHM are plotted as a function of buffer growth time with buffer growth temperature and ramping time between buffer and bulk growth as parameters. (Intensity ratios between different series are not to scale.) This figure clearly indicates improved layer quality with decreasing buffer layer thickness. Except for very thin buffer and long ramping time (25min), the UV/yellow luminescence integrated intensity ratio increases and the XRD FWHM decreases as the buffer thickness is reduced. This dependence is in general independent of buffer growth temperature and temperature ramping time between buffer and bulk growth. However, for thin buffers, a shorter ramping time seems to be favorable (circles vs. squares in Fig. 2). This might indicate, that the optima of ramping time and buffer thickness depend on each other. For a thicker buffer layer, the optical layer quality improves clearly with longer ramping times as can be seen in Fig. 3.

3.2 PL measurements of highly Si-doped samples

Si-doped GaN has been grown with carrier concentrations between $9 \times 10^{17} \text{ cm}^{-3}$ and $2 \times 10^{19} \text{ cm}^{-3}$. Hall mobility for these layers is between $182 \text{ cm}^2/\text{Vs}$ at $n=10^{18} \text{ cm}^{-3}$ and $133 \text{ cm}^2/\text{Vs}$ at $n=2 \times 10^{19} \text{ cm}^{-3}$, respectively. Carrier concentrations as high as $n=5 \times 10^{19} \text{ cm}^{-3}$ have been achieved, however, surface morphology and mobility start degrading for carrier concentrations higher than $2 \times 10^{19} \text{ cm}^{-3}$. A recent publication for MBE-grown Si-doped GaN on GaAs reports drastic broadening of the PL linewidths up to 105 meV at 6K for $n=10^{19} \text{ cm}^{-3}$ [15]. Figure 4 shows the shift of the main PL peak position and its FWHM as a function of the Si_2H_6 flow. In the semi-logarithmic plot,

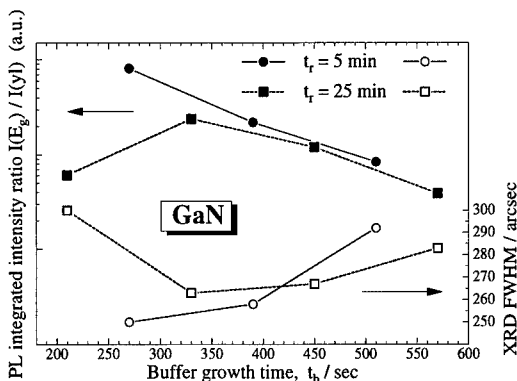


Fig. 2: UV/yellow luminescence integrated intensity ratio and XRD FWHM as a function of buffer growth time. (Intensity ratio between different series not to scale.)

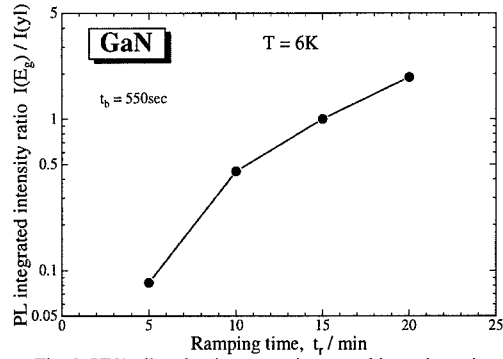


Fig. 3: UV/yellow luminescence integrated intensity ratio as a function of ramping time between buffer and bulk growth.

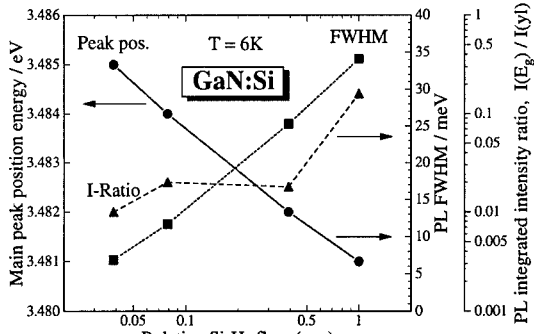


Fig. 4: Main PL peak position and its FWHM as a function of the Si_2H_6 flow.

the peak position decreases linearly with increasing Si flow, which could be attributed to a gradual shift from donor-bound exciton transitions to free hole-to-donor transitions [15]. The line broadening with increased doping level is in our case much less severe (34meV at $n=1.9\times10^{19}\text{cm}^{-3}$) than reported in [15] and is obviously associated with donor banding effects that will begin to occur for $N_d>10^{18}\text{cm}^{-3}$ due to the Bohr radius of electrons in GaN of $\sim23\text{\AA}$ [15].

4. Conclusions

Overall, we report on trends of PL and XRD of GaN bulk layers with buffer growth conditions. GaN characteristics are studied under various buffer growth conditions, e.g. thickness, growth temperature, and ramping time between buffer and bulk GaN growth. 6K PL FWHM of the bandedge photoluminescence is usually around $4.9\text{-}10\text{meV}$, exhibiting no distinct dependence on buffer growth conditions. Neutral-donor bound exciton, free A and B exciton peaks could be identified in PL and photoreflectance measurements. Layer quality as estimated by XRD FWHM and UV/yellow luminescence integrated intensity ratio improves with thinner buffers and/or longer temperature ramping times between bulk and buffer growth. Si-doped GaN layers have been grown with carrier concentrations between $9\times10^{17}\text{cm}^{-3}$ and $2\times10^{19}\text{cm}^{-3}$. The peak position decreases linearly with increasing Si flow, which could be attributed to a gradual shift from donor-bound exciton transitions to free hole-to-donor transitions. The line broadening with increased doping level is obviously associated with donor banding effects.

Acknowledgments

The authors would like to thank M. Yoder and C. Wood for encouragement and support of this work which has been supported by ONR Contract No. N00014-92-J-1552 and NSF/CNRS (INT-9217513)

References

- [1] Nakamura S, Senoh M, Nagahama S, Iwasa N, Yamada T, Matsushita T, Sugimoto Y and Kiyoku H 1997 *Appl. Phys. Lett.* **70** 1417-9
- [2] Binari S C, Doverspike K, Kelner G, Dietrich H B and Wickenden A E 1997 *Solid-State Electr.* **41** 177
- [3] Amano H, Kito M, Hiramatsu K and Akasaki I 1989 *Jpn. J. Appl. Phys.* **28** L2112
- [4] Nakamura S, Mukai T and Senoh M 1992 *J. Appl. Phys.* **71** 5543
- [5] Uchida K, Watanabe A, Yano F, Kouguchi K, Tanaka T and Minagawa S 1996 *J. Appl. Phys.* **79** 3487
- [6] Kuznia J N, Khan M A and Olson D T 1993 *J. Appl. Phys.* **73** 4700
- [7] Doverspike K, Rowland L B, Gaskill D K and Freitas Jr J A 1995 *J. Electron. Mater.* **24** 269
- [8] Turnbull D A, Li X, Gu S Q, Reuter E E, Coleman J J and Bishop S G 1996 *J. Appl. Phys.* **80** 4609-14
- [9] Monemar B 1974 *Phys. Rev. B* **10** 676
- [10] Lagerstadt O and Monemar B 1974 *J. Appl. Phys.* **45** 2266
- [11] Harris C I, Monemar B, Amano H and Akasaki I 1995 *Appl. Phys. Lett.* **67** 840
- [12] Shan W, Schmidt T J, Yang X H, Hwang S J, Song J J and Goldenberg B 1995 *Appl. Phys. Lett.* **66** 985
- [13] Nanaiwae K, Itoh S, Amano H, Itoh K, Hiramatsu K and Akasaki I 1990 *J. Cryst. Growth* **99** 381
- [14] Dingle R, Sell D D, Stolkowski S E and Illegems M 1971 *Phys Rev.* **4** 1211
- [15] Orton J W, Lacklison D E, Andrianov A V, Cheng T S, Dewsnip D J, Foxon C T, Jenkins L C and Hooper S E 1997 *Solid-State Electr.* **41** 219-22

X-Ray Photoelectron Diffraction Study of Hexagonal GaN(0001) Thin Films

R. Denecke^{1,2}, J. Morais¹, J. Liesegang*, C. S. Fadley^{1,2}

¹Materials Sciences Division, Lawrence Berkeley National Laboratory, Berkeley, CA 94720, USA

²Department of Physics, University of California - Davis, Davis, CA 95616, USA

*On leave from Department of Physics, La Trobe University, Bundoora, 3086 Australia

Abstract. We report on the first scanned-angle x-ray photoelectron diffraction measurements on GaN(0001) in the wurtzite structure, as grown on sapphire substrates using LPCVD. These as-grown samples reveal forward scattering peaks in agreement with a theoretical calculation using a multiple scattering cluster calculation. From the combination of experiment and theoretical calculation and from a simple intensity ratio argument the surface polarity for these samples could be determined to be N. The surface contamination by O and C does not exhibit any clear structure. The data also indicate that C is on average closer to the GaN surface than O.

1. Introduction

GaN is a promising material for the fabrication of blue light-emitting diodes (LEDs) and lasers due to its large and direct bandgap. The electronic properties depend, however, strongly on the geometric structure and the quality of the samples. There exist two different phases of GaN: a hexagonal wurtzite structure which is the stable structure (called α -GaN), and a zinc-blende structure which can only be achieved by epitaxial growth (the β -GaN phase). Since the normally used technique of X-ray diffraction (XRD) is more a bulk probe and is furthermore not element-specific, it can only determine the overall structure of a given epitaxial sample, and is not able to determine the actual positions of the atoms with respect to the surface. Therefore the use of element-specific x-ray photoelectron diffraction (XPD) promises to give a more detailed view of the near-surface structure, including the nature of the surface polarity, which can be Ga or N, or some mixture of these two growth orientations. This is especially important since surface morphology investigations have revealed a columnar growth for a wide range of growth conditions [1]. So an additional question is whether or not contaminants like O or C are preferentially incorporated in the films in the interstitial regions between the columns.

2. Experiment

The samples we used have been grown using low-pressure chemical vapor deposition (LPCVD). The substrate for the wurtzite structure films was the c-plane (0001) of sapphire, on which layers of about 2-3 μm thickness have been grown without a buffer layer. With XRD the overall quality of the layers has been checked and the presence of a (0001) oriented α -GaN could be confirmed [2]. Looking at the sample surface with a light microscope showed the aforementioned hexagonal columns.

The photoemission measurements have been performed using a standard X-ray source (Al K_α , $h\nu = 1486.6 \text{ eV}$, Mg K_α , $h\nu = 1253.6 \text{ eV}$) and a VG ESCALAB electron analyzer, which has been modified so as to permit automated XPD measurements [3]. This system is equipped with a two-axis

goniometer, enabling us to rotate the sample on two perpendicular axes so as to cover essentially the full 2π solid angle of emission directions above the surface. The sample for the data shown here was as-grown, meaning that it was not treated in the UHV chamber. Prior to introducing it to the chamber the sample was cleaned using a standard chemical cleaning procedure [4]. XPD measurements were then begun directly after a system bakeout and the attainment of a base pressure of $\sim 1 \times 10^{-10}$ Torr range. We have measured the Ga 3p and N 1s core levels at kinetic energies of 1382 eV and 856 eV, respectively, together with the O 1s and C 1s levels at 722 eV and 1203 eV, respectively, to monitor the surface contamination. The diffraction patterns have been measured with starting angle steps of 3° for both azimuthal (ϕ) and polar (θ) angles. However, the azimuthal angle step was adjusted throughout the measurements to ensure an equal sampling of solid angle. In order to cut the measuring time we used the expected three-fold symmetry of the GaN (0001) surface. Overall measurement times were several days, but the relative intensities of all component (Ga, N, O, and C) were found to be stable from start to finish.

3. Results

Fig. 1a) shows full 2π photoelectron diffraction patterns for all four core levels measured. Shown is the so-called χ -function for each core level as a function of emission angle (ϕ, θ). It is obtained from the measurements via a linear background subtraction and an integration of the intensity over the width of a given peak in an energy distribution curve. Furthermore, an isotropic function I_0 due to unscattered intensity has been subtracted from the measured intensity $I(\phi, \theta)$: $\chi(\phi, \theta) = (I(\phi, \theta) - I_0) / I_0$.

One clearly observes strong diffraction peaks for Ga 3p and N 1s emission in a nearly six-fold pattern. Most of these maxima result from scattering along high symmetry directions of the crystal and are mainly brought about by the highly forward peaked nature of the scattering factors at such high kinetic energies. Therefore, these peaks are referred to as forward scattering maxima. Comparing this with the O 1s and C 1s diffraction patterns shows immediately that C and O do not have any ordered scatterers in between them and the detector, as they have basically featureless patterns with no forward scattering maxima. The weak three-fold symmetry in the C 1s pattern is probably artifactual, and arises from the three-fold symmetry operation used to obtain the full diffraction pattern. Just from a simple analysis of the angle of the forward scattering peaks one can thus confirm the overall hexagonal structure of the GaN epilayer.

A more quantitative understanding of the structure can be obtained by comparing these patterns with single-scattering or multiple-scattering diffraction calculations. Using the unit-cell crystal structure as reported in the literature and a cluster with 12 atomic layers and about 150 atoms we performed multiple-scattering calculations based on a Rehr-Albers approach [5]. The results are shown in Fig. 1b). We show the diffraction patterns for both Ga 3p and N 1s emission and for a surface with N polarity. Both patterns here are three-fold symmetric, which is the symmetry of the GaN(0001) cluster as seen in the surface-sensitive XPD experiment. As the experiment is six-fold symmetric, this suggests the presence of two domain types rotated by 60° with respect to one another in different hexagonal columns. With this in mind, the agreement between experiment and theory is fairly good. There is also an ongoing discussion about whether the surfaces are Ga or N-polar [6]. Although not shown here, a comparison of experiment with theory using R-factor analysis yields much less agreement for the Ga-polar surface, strongly suggesting a N polarity of the sample under study.

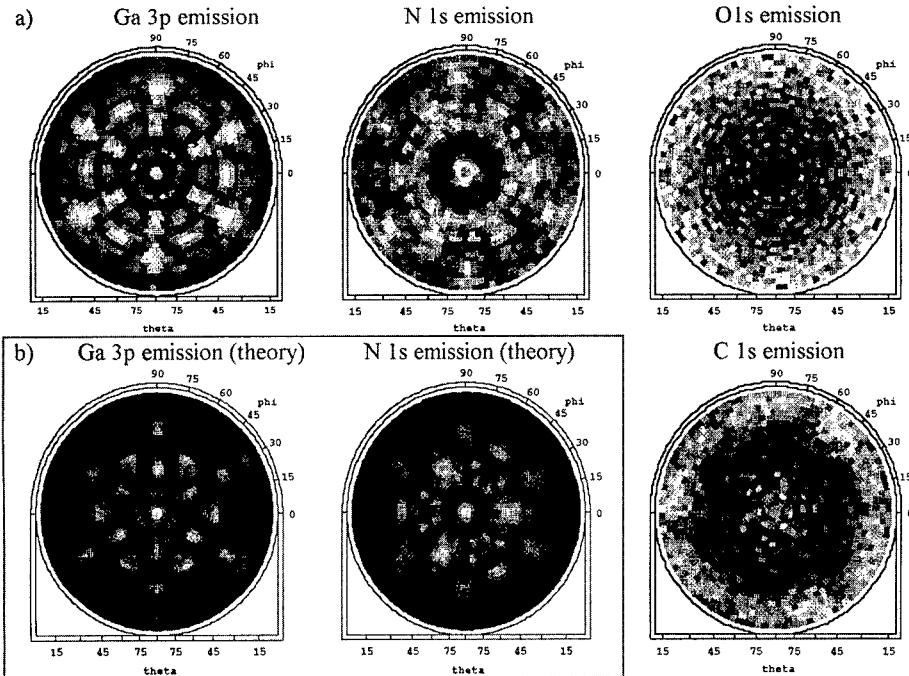


Fig.1: a) Experimental photoelectron diffraction patterns (χ -functions) for the four core levels Ga 3p, N 1s, O 1s and C 1s, as excited with Al or Mg K α radiation, respectively. Data obtained over 120° in azimuth have been three-fold symmetrized to yield the full pattern. b) Theoretical photoelectron diffraction patterns for a N-polar GaN cluster using a multiple scattering cluster calculation scheme. Shown are χ -functions for Ga 3p and N 1s emission corresponding to a). Light colors correspond to high intensity, dark colors to low intensity.

In order to further reveal the relative positions of the Ga and N, as well as the contaminant O and C atoms, one can use a rather simple analysis of the diffraction patterns. Since the photoelectron sampling depth varies with polar takeoff angle θ , due to the finite electron escape depth, Λ_e , according to $\Lambda_e \sin\theta$, plotting azimuthally-averaged intensity ratios of the different core levels as a function of polar angle is a way to get such information. Therefore we have plotted in Fig. 2 the ratio of these azimuthally-averaged intensities for various combinations of the measured core levels. First of all, the baseline of the ratio Ga 3p/N 1s is very flat, in agreement with the nearly uniform distribution of these atoms in the overall crystal. At first sight, it is a little surprising that there is no enhancement of the N 1s relative intensity at low takeoff angles, in view of our conclusion of N termination based on the XPD patterns. However, this can be explained by the slightly bigger escape depths for the Ga 3p photoelectrons, which have a higher kinetic energy as compared to the N 1s photoelectrons. So this data is not in contradiction to the above finding of N termination of the surface.

Considering now the contaminant peaks, we find that the O 1s/Ga 3p (O 1s/N 1s) and C 1s/Ga 3p (C 1s/N 1s) ratios show a dramatic increase for low takeoff angles, indicating that O and C are primarily surface contaminants. The lack of any increase in this ratio for near-normal emission also suggests that

not much O or C is present in the interstitial regions between columns, although this might be a reasonable initial conjecture. Finally, the increase in the O 1s/C 1s ratio for low takeoff angles suggests that O is present in the outermost regions of the contaminant layer and that C is on-average closer to the GaN surface (e.g. as adsorbed CO).

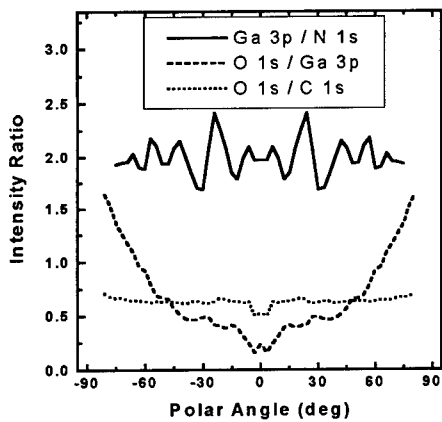


Fig. 2: Ratios of azimuthally-averaged intensities from the diffraction patterns of Fig. 1a) plotted versus polar angle. Shown are the ratios Ga3p/N1s (solid line), O1s/Ga3p (dotted line), and O1s/C1s (dashed line). Ratios have not been corrected for the different escape depths of the photoelectrons and the different photoemission cross sections.

4. Conclusions

We have performed the first x-ray photoelectron diffraction (XPD) measurements on an as-grown wurtzite GaN(0001) sample. We obtained diffraction patterns which show the expected crystal structure for the bulk material. A comparison of experiment with multiple scattering cluster calculations further shows the best overall agreement for a N-polar surface. An analysis of various azimuthally-averaged peak intensity ratios also permits concluding that both O and C are present as surface impurities, without being significantly incorporated into the interstitial regions between hexagonal columns, and that C is on average closer to the surface than O. These results illustrate the potential of XPD for a more detailed study of the different annealing and cleaning procedures and their effect on the surface structure, and such work is now in progress.

5. Acknowledgments

We would like to thank C. Wetzel and E. E. Haller for providing the samples and introducing us to this topic, R. X. Ynunza for helping with the experiments, S. Ruebush for usage of azimuthal-averaging and smoothing routine, and Y. Chen for the use of his program for calculating diffraction patterns. Work has been supported by ONR (Contract N00014-94-1-0162), DOE, BES, Mat. Sci. Div. (Contract DE-AC03-76SF00098), CNPq (Brazil), and DFG (Germany).

6. References

- [1] T. Sasaki, J. Crystal Growth **129**, 81 (1993)
- [2] S. Koynov, M. Topf, S. Fischer, B. K. Meyer, P. Radojkovic, E. Hartmann, Z. Lilienthal-Weber, J. Appl. Phys. **82**, 1890 (1997)
- [3] J. Osterwalder, M. Sagurton, P. J. Orders, C. S. Fadley, B. D. Hermsmeier, D. J. Friedman, J. Electr. Spectr. Relat. Phenom. **48**, 55 (1989); Y. J. Kim, Ph.D. thesis (University of Hawaii, 1995).
- [4] V. M. Bermudez, J. Appl. Phys. **80**, 1190 (1996)
- [5] J. J. Rehr and R. C. Albers, Phys. Rev. B **41**, 2974 (1993).
- [6] M. Asif Khan, J. N. Kuznia, D. T. Olson, R. Kaplan, J. Appl. Phys. **73**, 3108 (1993)

Energy Gap Bowing and Refractive Index Spectrum of AlInN and AlGaInN

J. Piprek¹, T. Peng, G. Qui, and J. O. Olowolafe

University of Delaware, College of Engineering, Newark, DE, 19716, USA

Abstract. High-quality polycrystalline AlInN films are deposited by low-temperature magnetron reactive sputtering. The energy band gap is measured across the entire compositional range and strong band gap bowing is observed. Within the transparency wavelength region, the effect of AlInN composition on the refractive index spectrum is strongest at shorter wavelength. Taking these measurements into account, non-linear interpolation formulas are employed to predict band gap and refractive index of quaternary AlGaInN for arbitrary compositions.

1. Introduction

Semiconductor compounds of group-III elements (Al, Ga, In) and nitrogen are heavily investigated for applications in blue light emitting devices. Besides binary GaN, those devices mainly employ the ternary compounds AlGaN and GaInN. The third ternary alloy AlInN is less explored but its investigation is of substantial interest. The knowledge of AlInN properties enables predictions for quaternary AlGaInN compounds.

2. Measurements of polycrystalline AlInN films

AlInN thin films are prepared by magnetron reactive sputtering at low temperatures of about 200°C [1]. Compared to a previous report [2], we obtain a larger variation of Al content including AlN and InN. Rutherford backscattering spectroscopy gives the $\text{Al}_x\text{In}_{1-x}\text{N}$ film composition within an uncertainty of ± 0.05 in x value [1]. The film thickness is about 1000 nm. The X-ray diffraction spectrum indicates a high-quality polycrystalline structure [1]. The shift of the diffraction peaks with composition proves the solubility between AlN and InN, i.e., the sputtered AlInN alloys are stoichiometric materials sharing the wurzite structure. Phase separation is not observed.

Optical transmission is measured for wavelengths $\lambda = 100 \text{ nm} - 800 \text{ nm}$. The plot of the absorption coefficient vs. photon energy confirms direct band gap transitions [3]. Grain boundary effects are excluded from our band gap analysis. The band gap E_g is given as function of the lattice constant in Fig. 1. The typical linear interpolation of binary data is shown for comparison. In perfect agreement with [2] a strong energy gap bowing is found for $\text{Al}_x\text{In}_{1-x}\text{N}$ alloys, which might be attributed to the atomic size difference between Al and In. This result is confirmed by the close match of our binary data with typical values for crystalline AlN and InN (see Fig. 1). Thus, the ternary compound AlInN seems to provide poor carrier confinement when used as lattice matched cladding layer on typical active region materials.

¹present address: Department of Electrical and Computer Engineering, University of California, Santa Barbara, CA 93106-9560, electronic mail: piprek@opto.ucsb.edu

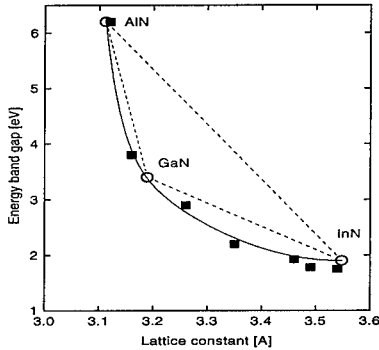


Fig. 1: Measured direct band gap bowing of $Al_xIn_{1-x}N$ (filled squares) in comparison to linear interpolations between typical numbers of crystalline binary materials (open circles). The solid line corresponds to Eq. (1).

The refractive index n of the AlInN films is determined within the transparency range from the interference pattern of the reflectivity spectra [3]. The dependence of $n(\lambda)$ on alloy composition is shown in Fig. 2. The short wavelength limit is given by the band gap. With higher In content, the band gap shrinks and the spectrum $n(\lambda)$ shows the expected shift towards longer wavelength, i.e., the effect of AlInN composition on the refractive index spectrum is strongest at shorter wavelength.

3. Interpolation for quaternary AlGaN compounds

This investigation of AlInN, together with previous knowledge of AlGaN and GaInN properties, enables predictions for quaternary compounds $Al_xGa_yIn_{1-x-y}N$. The ternary band gap bowing delivers the basis to estimate band gap and refractive index of quaternary compounds. Including values for crystalline AlN and InN, our measurement can be approximated phenomenologically by

$$E_g(Al_xIn_{1-x}N) = 1.9 + 2x^2 + 2.3x^{15} \quad (1)$$

(solid line in Fig. 1). A typical bowing equation like (2) or (3) does not provide reasonable agreement. For the other two ternary compounds other authors [4,5] measured weak energy gap bowing

$$E_g(Ga_xIn_{1-x}N) = 3.4x + 1.9(1-x) - x(1-x) \quad (2)$$

$$E_g(Ga_xAl_{1-x}N) = 3.4x + 6.2(1-x) - 0.5x(1-x) \quad (3)$$

Those ternary interpolation formulas are usually employed to predict the band gap of the quaternary compound

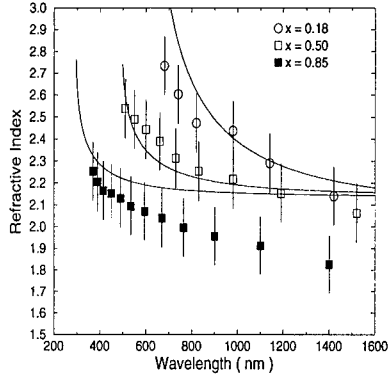


Fig. 2: Measured refractive index spectrum in the transparency region for three different compositions of $\text{Al}_x\text{In}_{1-x}\text{N}$ (dots) including error bars. The solid lines are corresponding results of the theoretical model.

$$E_g(\text{Al}_x\text{Ga}_y\text{In}_z\text{N}) = \frac{xyE_g(\text{Al}_u\text{Ga}_{1-u}\text{N}) + yzE_g(\text{Ga}_v\text{In}_{1-v}\text{N}) + zxE_g(\text{In}_w\text{Al}_{1-w}\text{N})}{xy + yz + zx} \quad (4)$$

with

$$z = 1 - x - y, \quad u = \frac{1 + x - y}{2}, \quad v = \frac{1 + y - z}{2}, \quad w = \frac{1 + z - x}{2}. \quad (5)$$

The result is plotted in Fig. 3 (dashed line) for $\text{Al}_x\text{Ga}_y\text{In}_{1-x-y}\text{N}$ lattice matched to GaN ($x=0.823(1-y)$). Despite almost identical values at the compositional endpoints $y=0$ ($x=0.82$) and $y=1$ ($x=0$), there is considerable bowing in between up to $E_g=4.2$ eV at $y=0.26$ ($x=0.61$). This indicates that quaternary compounds could be used as lattice matched carrier confinement layers.

Our refractive index model follows the approach of Adachi [6]. Neglecting the small valence-band split-off in AlGaInN, we obtain for photon energies $h\nu$ below the band gap energy E_g [7]

$$n^2(\text{Al}_x\text{Ga}_y\text{In}_{1-x-y}\text{N}) = a \left(\frac{h\nu}{E_g}\right)^{-2} \left[2 - \sqrt{1 + \left(\frac{h\nu}{E_g}\right)} - \sqrt{1 - \left(\frac{h\nu}{E_g}\right)} \right] + b \quad (6)$$

(Eq. (1) in [7] contains a typing error). The band gap $E_g(x, y)$ is given by Eq. (4). The fit parameters $a(x, y)$ and $b(x, y)$ are determined from comparison to measurements. Using our refractive index measurements on AlInN, the fit gives

$$a(\text{Al}_x\text{In}_{1-x}\text{N}) = 13.55x + 53.57(1 - x) + 92x(1 - x) \quad (7)$$

$$b(\text{Al}_x\text{In}_{1-x}\text{N}) = 2.05x - 9.19(1 - x) - 40x(1 - x) \quad (8)$$

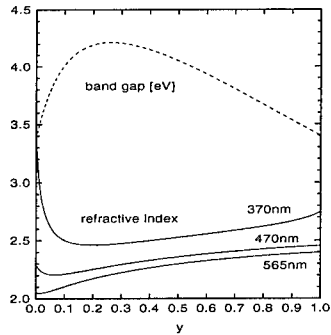


Fig. 3: Calculated band gap (dashed) and refractive index (solid) at different wavelengths for quaternary compounds $Al_xGa_yIn_{1-x-y}N$ lattice matched to GaN.

(see solid lines in Fig. 2). Deviations from the measurements might be caused by grain boundary effects in our polycrystalline material. For AlGaN and GaInN, linear interpolation between the fit results for binary materials is employed ($a, b = 9.31, 3.03$ for GaN; $53.57, -9.19$ for InN; $13.55, 2.05$ for AlN) [7]. A formula equivalent to Eq. (4) is used to obtain $a(x, y)$ and $b(x, y)$ of quaternary compounds. The solid lines in Fig. 3 show the calculated refractive index for $Al_xGa_yIn_{1-x-y}N$ lattice matched to GaN. Three standard wavelengths (ultraviolet, blue, green) are chosen corresponding to 3.35 eV, 2.64 eV, and 2.19 eV photon energy, respectively. At 370 nm, the refractive index rises strongly with y approaching zero. In all other cases, the quaternary refractive index is lower than the GaN value ($y=1$). Thus, optical waveguiding within GaN active regions could be supported by lattice matched cladding layers of AlGaN or AlInN.

4. References

- [1] Qiu G, Olowolafe J O, Peng T, Unruh K M, Swann C P and Piprek J 1996 *Proc. Mat. Res. Soc. Symp., Boston* 301-6
- [2] Kubota K, Kobayashi Y and Fujimoto K 1989 *J. Appl. Phys.* 66 2984-8
- [3] Peng T, Piprek J, Qui G, Olowolafe J O, Unruh K M, Swann C P, and Schubert E F 1997 *Appl. Phys. Lett.* to be published Oct. 27
- [4] Osamura K, Nakajima K, and Murakami Y 1972 *Solid State Comm.* 11 617-21
- [5] Itoh K, Amano H, Hiramatsu K, and Akasaki I 1991 *Jap. J. Appl. Phys.* 30 1604-8
- [6] Adachi S 1982 *J. Appl. Phys.* 53 5863-9
- [7] Peng T and Piprek J 1996 *Electron. Lett.* 32 2285-6

Optical and Structural Characterization of InGaN Quantum-Well Heterostructures Grown by Metalorganic Chemical Vapor Deposition

R. D. Dupuis, P. A. Grudowski, and C. J. Eiting

Microelectronics Research Center, The University of Texas at Austin, Austin TX 78712 USA

I. C. Shmagin and R. M. Kolbas

Electrical and Computer Engineering Department, North Carolina State University, Raleigh NC 27695 USA

S. J. Rosner

Hewlett-Packard Laboratories, 3500 Deer Creek Road, Palo Alto CA 94304 USA

Abstract. We describe the optical and structural properties of InGaN multiple-quantum-well (MQW) heterostructures grown by metalorganic chemical vapor deposition on (0001) sapphire substrates. These structures consist of $In_xGa_{1-x}N$ quantum wells and $In_yGa_{1-y}N$ barrier layers with GaN or AlGaN cladding layers. A comparison of the 300K photoluminescence spectra of these samples indicates that the emission from the quantum well structure is not strongly affected by the high-temperature overlayer growth of GaN or AlGaN films. X-ray diffraction scans show superlattice peaks and indicate that the MQW's are fully strained.

1. Introduction

The III-N compound semiconductors have been extensively studied as a result of the rapid progress in the growth of high-performance InAlGaN-based blue and green light-emitting diodes (LED's)^{1,2} and blue and violet injection laser diodes (LD's).³ Detailed studies of the growth of the binary compound GaN have been extensively reported by a variety of authors.⁴ In contrast, while high-quality InGaN ternary alloy films were first reported in 1991⁵, the optical and structural properties of InGaN quantum wells are not as well documented in the literature.

In this work, we have studied the growth of $In_xGa_{1-x}N/In_yGa_{1-y}N$ multiple-quantum-well (MQW) heterostructures grown on GaN heteroepitaxial films grown on (0001) sapphire substrates. Some of these structures have been grown with GaN cladding layers while, for comparison, others have been grown with AlGaN cladding layers. We report the results of a study of the X-ray diffraction rocking curves and asymmetric reciprocal space maps and the 300K PL peak intensity and linewidth when AlGaN cladding layers are incorporated into the MQW structure.

2. Epitaxial structures

The structures used in this study are grown by low-pressure metalorganic chemical vapor deposition (MOCVD) in an EMCORE Model D125 rotating disk reactor at a growth pressure $P_G \sim 76$ Torr and a rotation rate of 800 RPM. The Column III organometallic precursors employed are trimethylgallium (TMGa), trimethylaluminium (TMAI), and trimethylindium (TMIn); the hydride ammonia (NH_3) is used as the Column V source. The source for *n*-type doping is a mixture of SiH_4 in H_2 . The GaN films are grown in H_2 at $T_G \sim 1050^\circ C$ using a V/III ratio $\sim 2,600$ and growth rates $R_G \sim 50$ nm/min for GaN. $Al_{0.05}Ga_{0.95}N$ films are grown at the same growth temperature but using lower Column III molar flows resulting in $R_G \sim 14$ nm/min. The InGaN films are grown at lower temperatures ($T_G \sim 750-830^\circ C$), and a higher V/III ratio $\sim 16,000$. The InGaN layers are grown in a predominantly N_2 ambient⁶ at $R_G \sim 8.4$ nm/min, as has been described previously.⁷

3. Photoluminescence studies

Room-temperature (300K) PL measurements have been made on the MQW structures using a continuous-wave argon-ion laser operating at a wavelength of 275 nm and providing excitation levels $\sim 2.5 \text{ W/cm}^2$ at the sample surface. The spectra reported here have not been corrected for system response.

4. X-ray diffraction characterization

In this work, a Philips X'Pert MRD X-ray diffraction system has been used to determine the alloy composition of "bulk" InGaN layers as well as the "average" composition and periodicity for InGaN MQW and superlattice (SL) structures.⁸ For these measurements, we have employed the (0006) diffraction in the ω - 2θ mode. For thick layers, the lattice parameter in the " a -axis" (in the 0001 plane) for "completely relaxed" $\text{In}_x\text{Ga}_{1-x}\text{N}$ alloys was assumed to follow Vegard's Law. However, thin InGaN films may not be completely relaxed and therefore, the degree of strain in the film is an important question to be answered. We have employed asymmetric reciprocal space mapping to determine the degree of relaxation present in selected InGaN MQW structures.

5. Results and discussion

5.1 InGaN thick heteroepitaxial layers

The alloy composition of thick (80-200 nm) InGaN-GaN single-heterostructure (SH) and double-heterostructure (DH) "calibration layers" (doped with Si) has been determined by measurement of the 300K PL spectra. We also estimated the average In alloy composition from the X-ray rocking curve data, assuming a fully relaxed film.⁹ Generally, these composition values agree well with the values determined by the 300K PL data.

The 300K PL from the InGaN:Si bulk double-heterostructure samples show intense emission related to the bandedge with a FWHM as low as ~ 99 meV for a peak wavelength of $\lambda \sim 403$ nm. We have optically pumped some of these structures and have obtained 77K "vertical-cavity" stimulated emission from an ~ 60 nm-thick InGaN-GaN SH.¹⁰

5.2 InGaN MQW-GaN heterostructures

The 300K PL emission from a five-period of $\text{In}_{0.13}\text{Ga}_{0.87}\text{N}/\text{In}_{0.03}\text{Ga}_{0.97}\text{N}$ (3.5 nm/7.0 nm) MQW heterostructure having a 1.5 μm -thick GaN lower cladding layer and an ~ 20 nm-thick high-temperature GaN "cap" layer is shown in Figure 1 (a). The peak wavelength is $\lambda_p \sim 403.5$ nm, the FWHM value is ~ 176 meV (23.1 nm), and the MQW/yellow band intensity ratio is ~ 173 .

The alloy compositions and thicknesses of the $\text{In}_x\text{Ga}_{1-x}\text{N}$ quantum wells and $\text{In}_y\text{Ga}_{1-y}\text{N}$ barrier layers in the MQW structures are estimated from the peak positions of the 0 th-order and the $n = -1$ and -2 superlattice (SL) peaks in (0006) ω - 2θ scans, and the intended layer thicknesses estimated from growth times. Shown in Figure 2 (a) are the results for an InGaN-GaN MQW showing the three negative superlattice peaks from which we calculate the period and compositions. In general, good agreement was found between the measured and expected values of the compositions and period.

To further analyze the strain and mosaicity of these MQW heterostructures, we have performed two-dimensional reciprocal-space mapping (RSM) of the InGaN MQW wafers. Recently, Li, et al., reported such measurements for a three-period MQW structure having $\text{In}_{0.06}\text{Ga}_{0.94}\text{N}$ QW's and GaN barriers (period $A = 51$ nm). Their results demonstrated that, to the resolution of this technique, such structures are essentially fully strained.¹¹ We have performed similar asymmetric (105) RSM analyses of

$\text{In}_{0.13}\text{Ga}_{0.87}\text{N}/\text{In}_{0.03}\text{Ga}_{0.97}\text{N}$ five-period MQW structures (period $\Lambda = 10.5$ nm) with GaN “cladding layers. From the vertical alignment of the diffraction isointensity contours for the GaN film and the InGaN MQW, we conclude that these ternary-ternary MQW's with GaN cladding layers are coherently strained.¹²

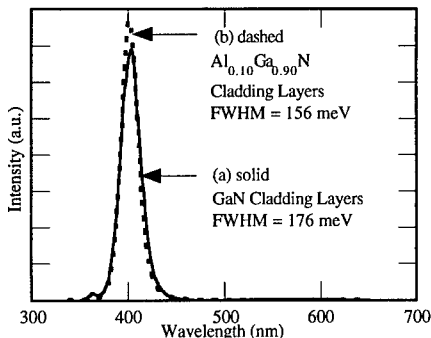


Figure 1: 300K PL spectra for InGaN MQW structure with (a) GaN and (b) AlGaN cladding layers.

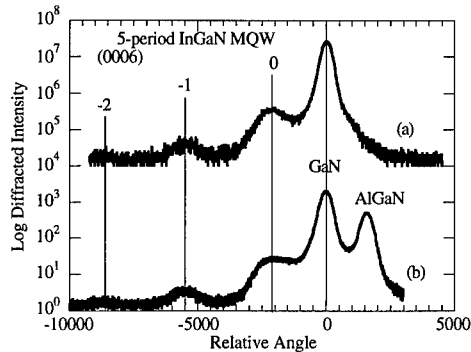


Figure 2: (0006) X-ray diffraction data on InGaN MQW's (a) with and (b) without AlGaN cladding layers

5.3 AlGaN-InGaN MQW-AlGaN-GaN heterostructures

It is important to determine the effect of the high-temperature overgrowth of GaN and AlGaN cladding layers on InGaN MQW's. This is especially of concern for diode laser structures which typically have ≥ 0.75 μm of AlGaN and GaN overlayers grown at high-temperature, resulting in a significant high-temperature “anneal” for the InGaN MQW structure grown at low-temperature. It can be expected that a significant change in the interface and bulk properties of the InGaN QW's and barriers can occur during this high-temperature cycle, possibly contributing to the formation (or destruction) of spatial inhomogeneities in InGaN alloys.¹³ Other similar effects can arise from the additional strain provided by the incorporation of AlGaN cladding layers.

To evaluate the effect of the incorporation of AlGaN cladding layers, we have grown InGaN MQW structures similar to those of Figure 1 (a) but having a 0.25 μm -thick lower $\text{Al}_{0.05}\text{Ga}_{0.95}\text{N}$ cladding layer and an ~20 nm-thick upper cladding layer of the same alloy composition. The 300K PL from this structure is shown in Figure 1 (b). We observe a relatively narrow MQW-related emission from this sample having a peak emission at $\lambda_p \sim 402$ nm, a FWHM value ~ 151 -156 meV (19.7-20.2 nm), and a MQW/yellow band intensity ratio ~ 385 . The emission from our MQW wafers generally exhibits FWHM values in the meV range 149-160 meV for peak wavelengths ~ 400 -405 nm.

To determine the alloy composition and thickness of the MQW structure, we have measured the (0006) ω - 2θ scans as shown in Figure 2 (b). The period and compositions are identical to those determined for the MQW with GaN cladding layers shown in Figure 2 (a). To evaluate the degree of strain present in InGaN MQW/AlGaN structures, we have examined RSM's employing the (105) asymmetric reflection of an $\text{In}_x\text{Ga}_{1-x}\text{N}/\text{In}_y\text{Ga}_{1-y}\text{N}$ MQW with AlGaN cladding layers grown on a 1.5 μm GaN buffer layer.¹⁴ From this measurement, it is clear that all of the layers are fully strained on the GaN buffer layer. Thus the incorporation of the AlGaN (or GaN) cladding layers does not seem to result in relaxation of the MQW structure.

We expect that for a light-emitting device, there will exist an optimal number of wells and also quantum-well and barrier thicknesses and compositions, as well as an optimum choice for the AlGaN compositions and thicknesses. From our previous PL study, the optimal MQW structure for QW's in

this thickness range ($3.5 \text{ nm} \leq t_{QW} \leq 4.2 \text{ nm}$) and alloy composition ($x \sim 0.13$) has been determined to contain five wells' so we have used this MQW "active region" in this study. From the fact that we do not see an increased FWHM value or significant change in the peak emission wavelength of the PL spectra with the incorporation of AlGaN cladding layers, we conclude that the increased strain resulting from these layers does not contribute to pronounced roughening of the interfaces or the modification of the interface abruptness. TEM analysis of these structures is currently underway and is expected to support these conclusions.

5. Conclusions

In conclusion, we have grown $\text{In}_x\text{Ga}_{1-x}\text{N}/\text{In}_y\text{Ga}_{1-y}\text{N}$ MQW heterostructures by MOCVD on GaN heteroepitaxial GaN layers deposited on (0001) sapphire substrates and have shown somewhat enhanced 300K luminescence properties of MQW's having AlGaN cladding layers. No degradation of the luminescent properties of the MQW's is observed resulting from increased strain due to the increased lattice mismatch due to the AlGaN cladding layers. X-ray diffraction studies show superlattice peaks and also indicate that the MQW's are fully strained.

6. Acknowledgments

We acknowledge useful technical discussions with Drs. R. F. Karlicek and C. P. Kuo. We thank D. E. Dupuis for assistance in manuscript preparation. This work was partially supported by NSF under grant DMR-93-12947 and by the NSF Science and Technology Center Program under grant CHE-89-20120, the State of Texas Advanced Technology Program, the Army Research Office under DAHA04-93-G-0317, by the Office of Naval Research under contract N00014-95-1-1302, and by ARPA under contract MDA972-95-3-0008. Additional support by Ford Motor Company is also gratefully acknowledged.

7. References

- ¹ I. Akasaki and H. Amano, *J. Electrochem. Soc.* **141**, 2266 (1994).
- ² S. Nakamura, M. Senoh, N. Iwasa, and S. Nagahama, *Jap. J. Appl. Phys.* **34**, L797 (1995).
- ³ S. Nakamura, M. Senoh, S. Nagahama, N. Iwasa, T. Yamada, T. Matsushita, H. Kiyoku, and Y. Sugimoto, *Jap. J. Appl. Phys.* **35**, L74 (1996).
- ⁴ See for example, the papers in "Gallium Nitride and Related Materials", Materials Research Society Symp. Proc. Vol. 395, Ed. F. A. Ponce, R. D. Dupuis, S. Nakamura, and J. A. Edmond (Materials Research Society, Pittsburgh PA, 1996).
- ⁵ N. Yoshimoto, T. Matsuoka, T. Sasaki, and A. Katsui, *Appl. Phys. Lett.* **59**, 2251 (1991).
- ⁶ C. Yuan, T. Salagaj, W. Kroll, R. A. Stall, M. Schurman, C.-Y. Hwang, Y. Li, W. E. Mayo, Y. Lu, S. Krishnankutty, and R. M. Kolbas, *J. Electron. Mater.* **25**, 749 (1996).
- ⁷ P. A. Grudowski, C. J. Eiting, J. Park, B. S. Shelton, D. J. H. Lambert, and R. D. Dupuis, *Appl. Phys. Lett.* **71**, to be published.
- ⁸ S. Nakamura, T. Mukai, M. Senoh, and S. Nagahama, *J. Appl. Phys.* **74**, 3911-3915 (1993).
- ⁹ K. Osamura, S. Nakajima, and Y. Murakami, *J. Appl. Phys.* **46**, 3432 (1975).
- ¹⁰ I. Shmagin, J. F. Muth, R. M. Kolbas, R. D. Dupuis, P. A. Grudowski, C. J. Eiting, J. Park, B. S. Shelton, and D. J. H. Lambert, *Appl. Phys. Lett.* **71**, to be published.
- ¹¹ W. Lei, P. Bergman, I. Ivanov, W. X. Ni, H. Amano, and I. Akasaki, *Appl. Phys. Lett.* **69**, 3390 (1996).
- ¹² C. J. Eiting, P. A. Grudowski, and R. D. Dupuis, *J. of Metals*, to be published, Sept. 1997.
- ¹³ S. Nakamura, M. Senoh, S. Nagahama, N. Iwasa, T. Yamada, T. Matsushita, Y. Sugimoto, and H. Kiyoku, *Appl. Phys. Lett.* **69**, 1477 (1996).
- ¹⁴ P. A. Grudowski, C. J. Eiting, and R. D. Dupuis, *Proceedings of the Second International Conference on Nitride Semiconductors*, submitted for publication.

Optical Transitions and Dynamic Processes in III-Nitride Epilayers and Multiple Quantum Wells

K. C. Zeng, M. Smith, J. Y. Lin, and H. X. Jiang^(a)

Department of Physics, Kansas State University, Manhattan, KS 66506-2601

A. Salvador, G. Popovici, H. Tang, W. Kim, and H. Morkoc

Materials Research Laboratory and Coordinated Science Laboratory, University of Illinois at Urbana-Champaign, Urbana, Illinois 61801

M. A. Khan

Department of Electrical and Computing Engineering, University of South Carolina, Columbia, SC 29208

Abstract. Fundamental optical transitions in GaN and InGaN epilayers, InGaN/GaN and GaN/AlGaN multiple quantum wells (MQWs) grown both by metal-organic chemical vapor deposition and reactive molecular beam epitaxy have been studied by picosecond time-resolved photoluminescence spectroscopy. The exciton binding energies and radiative recombination lifetimes of the free excitons and bound excitons have been obtained. Effects of well thickness on the optical properties of $In_xGa_{1-x}N/GaN$ and $GaN/Al_xGa_{1-x}N$ MQWs have also been studied.

1. Introduction

GaN based devices offer great potential for applications such as UV-blue lasers, solar-blind UV detectors, and high-power electronics. Researchers in this field have made extremely rapid progress toward materials growth as well as device fabrication.¹ The commercial availability of super-bright blue light emitting diodes (LED) and the demonstration of the room temperature blue lasers based on the GaN system are clear indicative of the great potential of this material system.^{2,3} Recently, there has been much work concerning the fundamental optical transitions in GaN.⁴⁻⁷ It is expected that all optoelectronic devices based on GaN will take advantages of multiple quantum well (MQW) structures of GaN/AlGaN and InGaN/GaN. Thus a better understanding of the fundamental optical transitions in nitride epilayers and MQWs is needed.

2. Experimental

Samples used in this work include GaN and $In_xGa_{1-x}N$ epilayers and $In_xGa_{1-x}N/GaN$ and $GaN/Al_xGa_{1-x}N$ MQWs grown both by metal-organic chemical vapor depositions (MOCVD) and by reactive molecular beam epitaxy (MBE). Their structures and parameters are summarized in Table I. All samples studied were of wurtzite structure grown on sapphire (Al_2O_3) substrates with AlN buffer layers.

Low temperature time-resolved PL spectra were measured by using a picosecond laser spectroscopy system with an average output power of about 20 mW, a tunable photon energy up to 4.5 eV, and a spectral resolution of about 0.2 meV.^{4,5} A micro-channel-plate photomultiplier tube (MCP-PMT) together with a single photon counting system was used to collect time-resolved PL data and the overall time resolution of the detection system was about 20 ps.

3. Results and Discussions

3.1 GaN epilayers. Figure 1 shows four low-temperature (10 K) photoluminescence (PL) spectra obtained for samples A, B, C, (MOCVD) and sample G (MBE). For high purity epilayer grown by MOCVD (sample A), two emission lines with energy peak positions at about 3.485 eV and 3.491 eV are identified as due to the recombination of the ground state of free A and B excitons [A(n=1) and B(n=1)].⁸ The narrow linewidths of these two emission bands are clear indication of its high crystalline quality of sample A. Our results show that the energy separation between the A and B valance bands is about 6 meV with the assumption that A and B exciton binding energies are comparable.⁵ An emission line due to the recombination of the first excited state of the A-exciton A(n=2), which is about 14.3 meV above the A(n=1) emission line, is also observable in sample A at T>40 K. For an as-grown sample with a higher

Growth Method	Sample	Materials	x	Structure	Type	Carrier Concentration (cm ⁻³)
MOCVD	A	GaN		Epilayer	n	5×10^{16}
	B	GaN			n	2.4×10^{17}
	C	GaN		Epilayer	p	1×10^{17}
	D	In _x Ga _{1-x} N	0.12	Epilayer	n	
	E	25 Å In _x Ga _{1-x} N/GaN	0.15	MQW		
	F	90 Å In _x Ga _{1-x} N/GaN	0.15	MQW		
MBE	G	GaN		Epilayer	Insulating	
	H	25 Å GaN/Al _x Ga _{1-x} N	0.07	MQW		
	I	50 Å GaN/Al _x Ga _{1-x} N	0.07	MQW		

Table I. Structures and parameters of GaN, InGaN epilayers, InGaN/GaN and GaN/AlGaN MQW samples used in this work. Well thicknesses of MQWs are also indicated.

native donor concentration (sample B), the dominant emission line occurs at 3.476 eV and is due to the recombination of the excitons bound to neutral donors, called I₂.⁹ The shoulder at about 3.484 eV in sample B is due to the free A exciton (n=1) recombination. Thus the binding energy of the neutral-donor-bound exciton is about 8-9 meV. For Mg doped p-type epilayer (sample C), the dominant emission line at 3.459 eV is due to the recombination of neutral-acceptor-bound excitons, called I₁.¹⁰ A value of about 26 meV is thus obtained for the binding energy of the neutral-acceptor-bound exciton in GaN. For a MBE grown high quality and purity epilayer (sample G), three emission lines at 3.483 eV, 3.489 eV, and 3.498 eV are observable, which correspond to the transitions of the ground state of A- and B-excitons and the first excited state of the A-exciton (n=2), respectively.⁴ The energy difference between the first and the ground states of the excitons thus gives the binding energy of the A exciton, E_b=(4/3)x(3.498-3.483) eV = 20 (meV). The energy separation between the A and B valence bands obtained from sample G (6 meV) is consistent with that obtained from sample A. The slight energy difference in the peak positions of the A(n=1) and B(n=1) emission bands for sample A and G (3.485 eV vs. 3.483 eV and 3.489 eV vs. 3.491 eV) may be due to a slight difference in strain in these two different samples.

3.2 InGaN epilayers. Figure 2(a) shows a PL emission spectrum for a MOCVD grown InGaN epilayer (sample D) measured at 10 K. By comparing with the PL spectra of GaN epilayers (Fig. 1(a) and Fig. 1(d)), the emission peak position is clearly shifted toward lower energy due to In incorporation. Another effect is that the emission linewidth of the InGaN epilayer is more than one order of magnitude larger than those of GaN epilayers due to alloy disorder. The emission peak position in sample D is at about 3.193 eV with a full linewidth at half maximum (FWHM) of about 55 meV, which is due to the recombination of localized excitons. In an alloy, the exciton localization is caused by energy fluctuations in the band edge induced by alloy disorder and the linewidth is correlated with the exciton localization energy.

3.3 InGaN/GaN MQWs. The MQW sample with well thickness of 25 Å (sample E shown in Fig. 2(b)) emits an exciton line at 3.211 eV. The emission linewidth seen in MQWs is broader than that in the InGaN epilayer. Quantum confinement is also evident by comparing the PL spectrum of MQWs (sample E) shown in Fig. 2 (b) with that of InGaN epilayer (sample D) shown in Fig. 2(a). For MQWs with large well thicknesses, e.g. L_w= 90 Å (sample F shown in Fig. 2(c)), a dominant emission at 2.963 eV is observed. From the fact that the energy position of this emission line is below the exciton emission line in InGaN epilayers, we attribute it to an impurity related transition. Since the growth conditions for 25 and 90 Å MQWs are identical, our results indicate that the 90 Å well thickness is above the critical thickness of the InGaN/GaN MQW system. Above the critical thickness, strain is relieved by the creation of large density of misfit dislocations, which leads to the dominance of the impurity transition.

3.4. GaN/AlGaN MQWs. As shown in Fig. 3, in GaN/Al_xGa_{1-x}N MQWs, the dominant emission lines always result from the well region at low temperatures. Comparing the PL spectra shown in Fig. 3(a) and

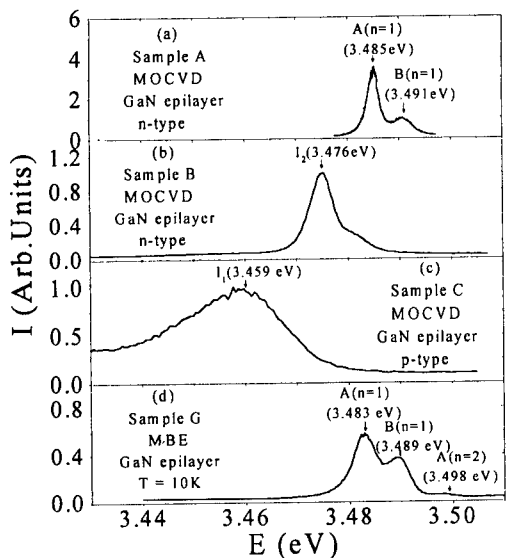


Fig.1. PL emission spectra of GaN epilayers measured at T = 10 K.

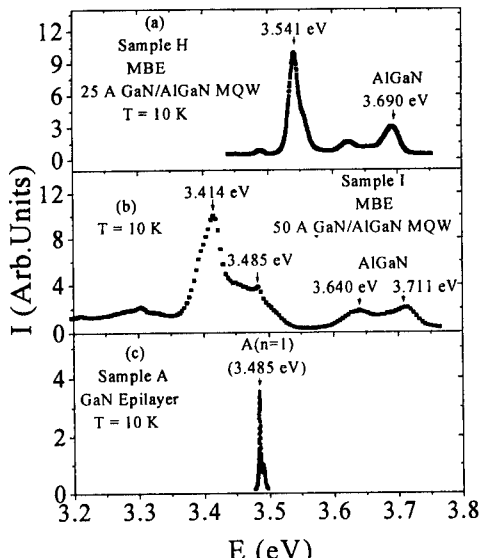


Fig.3. PL emission spectra of GaN/Al_xGa_{1-x}N MQWs (a) and (b), and GaN epilayer (c) measured at T = 10 K.

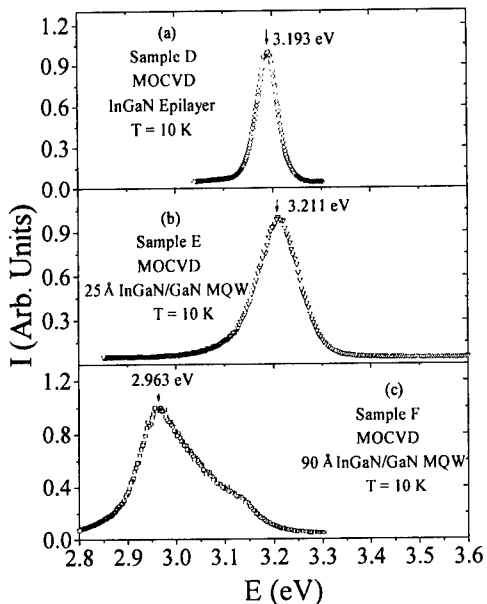


Fig. 2. PL emission spectra of In_xGa_{1-x}N/GaN MQWs (b) and (c), and In_xGa_{1-x}N epilayer (a) measured at T=10 K.

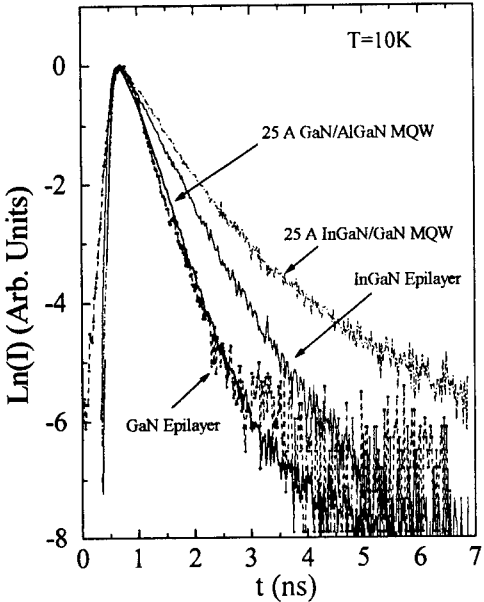


Fig. 4. PL temporal responses measured at the spectral peak positions for MBE and MOCVD samples: GaN and In_xGa_{1-x}N epilayers, GaN/Al_xGa_{1-x}N and In_xGa_{1-x}N/GaN MQWs .

3(c), the exciton emission line resulting from the 25 Å MQWs (sample H) is blue shifted by 56 meV with respect to the GaN epilayer (sample A). Comparing the PL spectra shown in Fig 3(b) and 3(c), the dominant emission line in the 50 Å MQWs is 71 meV below the exciton emission line (sample I). Our results for GaN/AlGaN MQWs can be summarized as follows: (i) the optical transitions in MQWs with narrow well widths ($L_w < 40 \text{ \AA}$) are blue shifted with respect to the GaN epilayer, however, no such blue shift was evident for the MQW samples with well thickness greater than 40 Å and (ii) the band-to-impurity transitions are the dominant emission lines in MQWs of large well thicknesses ($L_w > 40 \text{ \AA}$).

3.5. Recombination lifetimes. Recombination lifetimes of various emission lines in GaN and InGaN epilayers and InGaN/GaN and GaN/AlGaN MQW samples used here have been measured. Fig. 4 shows PL temporal responses of exciton emission lines in GaN and $\text{In}_x\text{Ga}_{1-x}\text{N}$ epilayers, GaN/Al_xGa_{1-x}N and In_xGa_{1-x}N MQWs measured at their respective spectral peak positions. In general, the exciton lifetimes in MQWs are enhanced compared with those in epilayers. The typical exciton lifetime is around 0.3 ns in GaN epilayers and 0.6 ns in InGaN epilayers. Moreover, the exciton recombination lifetime in GaN/AlGaN MQWs of narrow well thickness (< 40 Å) increases linearly from about 0.3 ns to about 0.45 ns as temperature increases from 10 to 60 K, which is a hallmark of radiative recombination in MQWs.¹¹

4. Summary

Our results have revealed that the optical transitions at low temperatures are dominated by I₂ (I₁) in n-type (p-type) epilayers and free exciton transitions in high quality and purity GaN epilayers. The binding energies of free and bound excitons have been determined. The dominant optical transitions in In_xGa_{1-x}N/GaN and GaN/Al_xGa_{1-x}N MQWs are localized excitons at low temperatures due to alloy disorder and/or well width fluctuation. Quantum confinement effect has been observed for MQWs of narrow well widths. Exciton lifetimes in different materials and structures have been measured and compared.

Acknowledgements: The research at Kansas State University is supported by ARO and ONR/BMDO (monitored by Dr. John Zavada and Dr. Yoon S. Park), DOE (96ER45604/A000), and NSF (DMR-9528226). The research at the University of Illinois is supported by ONR, AFOSR and BMDO and monitored Max Yoder, Yoon S. Park, C. Wood, G. L. Witt, and K. P. Wu.

References

- (a) Jiang@phys.ksu.edu
- [1] H. Morkoc, S. Strite, G. B. Gao, M. E. Lin, B. Sverdlov, and M. Burns, *J. Appl. Phys.* **76**, 1363 (1993); S. N. Mohammad, A. Salvador, and H. Morkoc, *Proc. IEEE*, **83**, 1306 (1995).
- [2] S. Nakamura, M. Senoh, N. Iwasa, and S. Nagahama, *Jpn. J. Appl. Phys.* **34**, L797 (1995).
- [3] S. Nakamura, M. Senoh, N. Iwasa, S. Nagahama, N. Iwasa, T. Yamada, T. Matsushita, H. Kiyoku, and Y. Sugimoto, *Appl. Phys. Lett.* **68**, 2105 (1996).
- [4] M. Smith, G. D. Chen, J. Z. Li, J. Y. Lin, H. X. Jiang, A. Salvador, W. K. Kim, O. Aktas, A. Botchkarev, and H. Morkoc, *Appl. Phys. Lett.* **67**, 3387 (1995).
- [5] G. D. Chen, M. Smith, J. Y. Lin, H. X. Jiang, S. H. Wei, M. Asif Khan, and C. J. Sun, *Appl. Phys. Lett.* **68**, 2784 (1996).
- [6] C. I. Harris, B. Monemar, H. Amano, and I. Akasaki, *Appl. Phys. Lett.* **67**, 840 (1995).
- [7] D. C. Reynolds, D. C. Look, W. Kim, Ö. Aktas, A. Botchkarev, A. Salvador, H. Morkoc, and D. N. Talwar, *J. Appl. Phys.*, **80**, 594 (1996).
- [8] M. Smith, G. D. Chen, J. Y. Lin, H. X. Jiang, M. Asif Khan, C. J. Sun, Q. Chen, and J. W. Yang, *J. Appl. Phys.* **79**, 7001 (1996).
- [9] G. D. Chen, M. Smith, J. Y. Lin, H. X. Jiang, M. Asif Khan, and C. J. Sun, *Appl. Phys. Lett.* **67**, 1653 (1995).
- [10] M. Smith, G. D. Chen, J. Y. Lin, H. X. Jiang, M. Asif Khan, and C. J. Sun, *Appl. Phys. Lett.* **67**, 3295 (1995).
- [11] M. Smith, J. Y. Lin, H. X. Jiang, A. Salvador, A. Botchkarev, W. K. Kim, and H. Morkoc, *Appl. Phys. Lett.* **69**, 2453 (1996).

On the nature of Radiative Recombination Processes in GaN

Christian Wetzel, Hiroshi Amano and Isamu Akasaki

High Tech Research Center, Meijo University, Tempaku-ku, Nagoya 468, Japan

Abstract A mechanism for efficient radiative light emission in GaN is presented. Stokes shifted emission was found to propagate almost exclusively along the c-plane when excited deep behind this surface. Onset of stimulated emission is observed. Emission intensity increases with the magnitude of the Stokes shift which in turn increases with film thickness, i.e. reduced biaxial stress conditions. We propose a model for the levels nature based on the strong oscillator of the heavy hole A-transition and its crystal field coupling to the small density of states associated the light hole B-transition. Highest emission is found for bulk-like stress conditions where the valence band top is found to be formed by the light hole mass.

1. Introduction

Identification and optimization of the light emission process in wide gap GaN [1] and its alloys with InN and AlN is a major task of optical spectroscopy. Record breaking device efficiencies of light emitting diodes and laser structures and their rapid improvement over time indicate features very unique to this wurtzite semiconductor system. Among several surprising properties of the nitrides an apparent contradiction between improvements of structural properties resulting in a decreasing luminescence efficiency has become common knowledge.

Large lattice mismatch between nitrides and possible substrates results in a variety of biaxial stress conditions expressed in the ratio of lattice constants c and a . This additional parameter directly affects the electronic bandstructure in the top of the valence band controlling optical and transport properties. Most of GaN characterization and development has been performed on thin epitaxial films using sapphire or 6H-SiC as a substrate. While bulk-like GaN has been obtained only in small crystal sizes its polarization and orientation dependent characterization provides the key elements to establish the electronic band structure and its stress behavior.

2. Experimental

2.1 Samples and Equipment

Stress relaxed bulk GaN crystals from hydride vapor phase epitaxy (HVPE) employing a ZnO buffer technique [2] at a size of 3 mm x 2 mm x 400 μm have been investigated. Lattice constants from X-ray diffraction are 3.1890 \AA (a) and 5.1850 \AA (c). The crystals are highly oriented with mirror-like c - and a -plane surfaces. For comparison a 20 μm high temperature vapor phase epitaxy (VPE) GaN film on 6H-SiC [3], a 10 μm hydride VPE (HVPE) GaN film and a 2 μm metal organic chemical vapor phase deposition (MOCVD) GaN film on sapphire are presented. All samples are nominally undoped. From Raman spectroscopy [4] of the $A_1(\text{LO})$ phonon mode a free electron concentration of $\sim 3 \times 10^{17} \text{ cm}^{-3}$ was

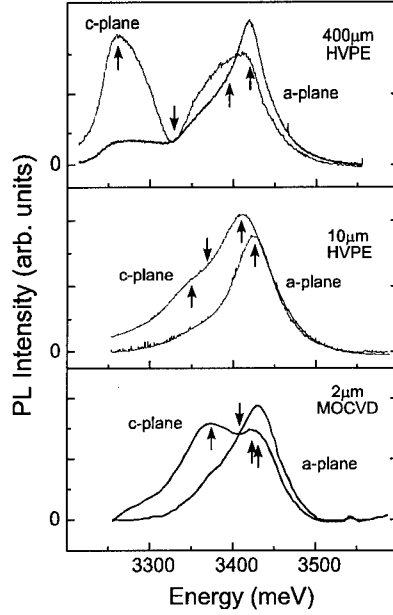
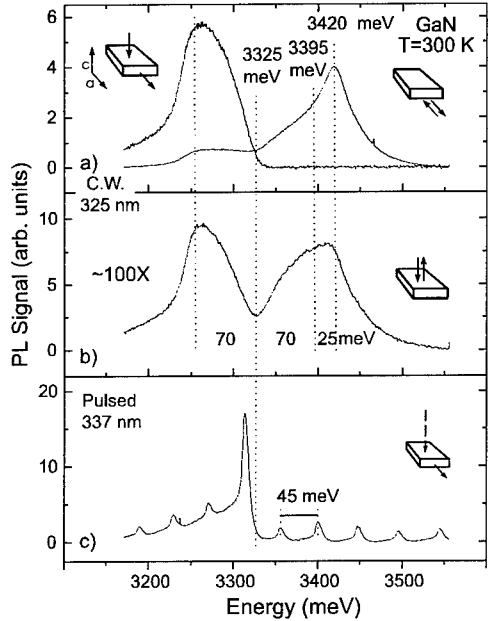


Figure 1. Directional PL of 400 μm bulk GaN. a) From the a -plane edge excited on the a -surface (right), and excited on the c -plane surface offset from the edge by $\sim 300 \mu\text{m}$. b) c -plane luminescence at much weaker intensity. c) a -plane edge emission under high density excitation.

Figure 2. Directional PL of GaN films with different thickness ($T=300\text{K}$). Paired peaks dominate in c -plane emission and splitting increases with thickness.

derived. Photoluminescence was excited using 20 mW of an 325 nm HeCd laser and a 1 mJ pulsed N² 337 nm laser. Photoreflectance was excited by a Xe lamp, modulated resonantly by the HeCd laser and a mechanical chopper, dispersed by a 25 cm monochromator and detected by a photomultiplier tube. All components are centrally software controlled. All data presented were taken at room temperature.

2.2 Oriented Photoluminescence

Photoluminescence (PL) ($T= 300\text{K}$) of the c -plane surface of bulk GaN is shown in Fig. 1b). It consists of a two-peak structure with V-shaped minimum centered approximately at half the splitting energy. Compared to other samples the intensity is very weak only. Turning to the emission off the a -plane the situation changes dramatically (Fig. 1a), (right hand spectrum). Total intensity is approximately 100 times higher and for photoexcitation onto the a -plane the upper wing clearly dominates leaving only a weak terrace like remnant of the lower wing. Changing the location of the photoexcitation to the c -plane and increasing the distance to the edge of detection by up to 500 μm the spectrum changes to convert all the intensity into the lower wing (Fig. 1a), (left hand spectrum). Propagation is therefore strongly limited to the c -plane. This part of the emission is subject of highest interest. Under pulsed high density excitation an onset of stimulated emission occurs in the lower wing (Fig. 1c) (c -plane

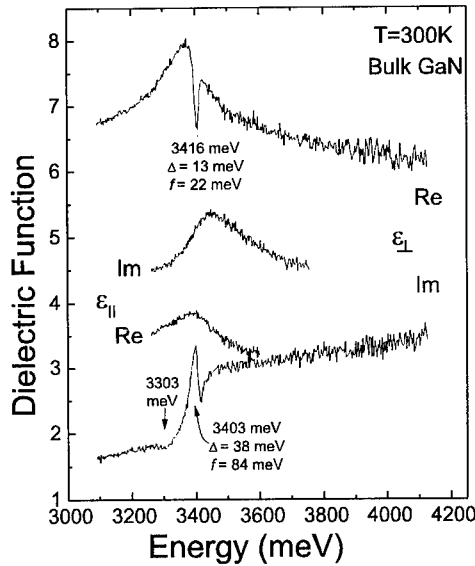


Figure 3. Dielectric function of bulk GaN for both polarizations. A clear oscillator structure interacting with a resonant background in both polarizations is observed in $\epsilon_{\perp c}$. Real part of $\epsilon_{\parallel c}$ is larger than imaginary part.

excitation and a -plane detection, offset $\sim 300 \mu\text{m}$) [1,5]. Note that all characteristic energies like upper and lower edges of the wings, as well as the minimum in-between are kept constant in all spectra.

PL under weak excitation densities off a - and c -plane in the 10 μm and 2 μm GaN films are compared in Fig. 2. The features of a single strong mode in a -plane emission and the double peak structure for c -plane emission are observed in all studied samples. For decreasing film thickness the respective splitting decreases. There is a consistent deviation of the higher maximum in both detection geometries. Intensities could be determined qualitatively finding the a -plane emission significantly increases with film thickness as (1:10:100).

2.3 Ellipsometric Spectroscopy

Spectroscopic ellipsometry to derive absolute values of the complex dielectric function in the vicinity of the bandgap was performed for $E \perp c$, $\epsilon_{\perp c}$ from reflection of the c -plane and for $E \parallel c$, $\epsilon_{\parallel c}$ from reflection of the a -plane (Fig. 3). It is

due to the large thickness of the bulk crystal that data could be taken from the a -plane edge. Using a Brewster angle geometry a high degree of σ -polarization could be achieved. Clear features in the imaginary part of $\epsilon_{\perp c}$ mark the transversal energy of a strong oscillator at 3403 meV interacting with a continuum at higher energies as seen by the pronounced longitudinal mode in the real part at 3416 meV. This feature shows characteristics of excitons in highest purity semiconductors at low temperatures. Here, however, this sharp structure is observed at room temperature in 400 μm GaN obtained from high growth rate vapor phase epitaxy. It is this unusual feature that we ascribe to the unique properties of efficient light emission processes. In addition interaction with other modes are obvious from the additional minimum at 3303 meV, below the transversal mode. In $\epsilon_{\parallel c}$ no sharp features are observed in this region of the spectrum. Note that here the imaginary part of $\epsilon_{\parallel c}$ is larger than the real part, a situation typically encountered on the *high* energy side of the main oscillator, i.e. at the optical bandgap.

2.4 Photoreflection Spectroscopy

A higher sensitivity to the dielectric function is obtained by photoreflection where the spectroscopically measured reflection is modulated by chopped 20 mW of a 325 nm HeCd Laser. Normalized to the DC component polarized $\delta R / \delta P_{325\text{nm}} \times 1/R$ for $\epsilon_{\perp c}$ (Fig. 4). Interpretation in the bulk sample can be supported by computation of the reflection R_{calc} at normal incidence from the ellipsometric data. Assuming that only the bandgap energy is changed by the photo modulation a

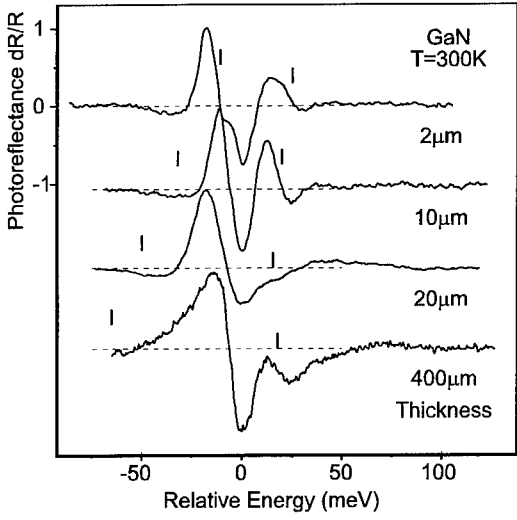


Figure 4. Photoreflectance of c -plane GaN. In direction of increasing thickness one mode approaches the central minimum and another crosses through the maximum away to the low energy side.

observed on either side indicated by vertical bars. In direction of increasing thickness one mode approaches the central minimum and another crosses through the maximum away to the low energy side. In parallel the upper line approaches gradually the center double structure. Peak positions are collected in Fig. 5.

3. Interpretation

Wurtzite belongs to the C_{6v}^4 space group and the C_{6v} point group. In Γ the valence band maxima are of Γ_9 , Γ_7 , and Γ_7 symmetry. This sequence from higher to smaller electron energy has been found from excitonic features at temperatures below 10 K in biaxially compressed GaN as typically grown on sapphire substrate [6]. The conduction band minimum is of Γ_7 symmetry. In addition to the spin orbit coupling that splits the valence band maximum in sphalerite (zincblende) degeneracy of heavy and light hole bands is further lifted by the crystal field in wurtzite. This additional parameter of the bandstructure corresponds to the second lattice constant of the unique c -axis. A fixed relation between c/a for GaN single layers of variable thickness has been established [2] reflecting the biaxial stress conditions. As a function of c/a the level splitting described by the spin orbit splitting energy Δ_{so} and the crystal field splitting energy Δ_{cf} exhibits an anticrossing behavior of the respective bands. Experimental values $\Delta_{\text{cf}} = 22 \pm 2$ meV, $\Delta_{\text{so}} = 11 \pm 5$ meV were found in small bulk-like crystals [7] and theory values are found as large as $\Delta_{\text{cf}} = 73$ meV and $\Delta_{\text{so}} = 16$ meV [8]. Electric dipole interband transitions for $E \perp c$, $\epsilon \perp c$ light propagating in $k \parallel c$ is allowed between pairs (conduction band cb, valence band vb) cb: $\Gamma_7 \rightarrow$ vb: Γ_9 (A), cb: $\Gamma_7 \rightarrow$ vb: Γ_7 (B), and cb: $\Gamma_7 \rightarrow$ vb: Γ_7 (C), whereas for $E \parallel c$, $\epsilon \parallel c$, light

numerical derivative $\delta R/R_{\text{calc}}/\delta E \times 1/R_{\text{calc}}$ reproduces very well all the structures in the photoreflection data. It is common to use models where several degrees of freedom for each expected oscillator are used to describe photoreflection data. Here, however we are concerned not only with single oscillators such as excitons at low temperature but instead with continua of states. We therefore use a visual inspection of data sets and collect the extrema locations as measured.

Photoreflection spectra of GaN samples with various thicknesses are combined in Fig. 4. Samples are arranged in the sequence of total GaN thickness and for the ease of interpretation spectra are offset in energy to align the overall minimum position. Taking the central oscillation as a reference two satellite modes are observed on either side indicated by vertical bars. In direction of increasing thickness one mode approaches the central minimum and another crosses through the maximum away to the low energy side. In parallel the upper line approaches gradually the center double structure. Peak positions are collected in Fig. 5.

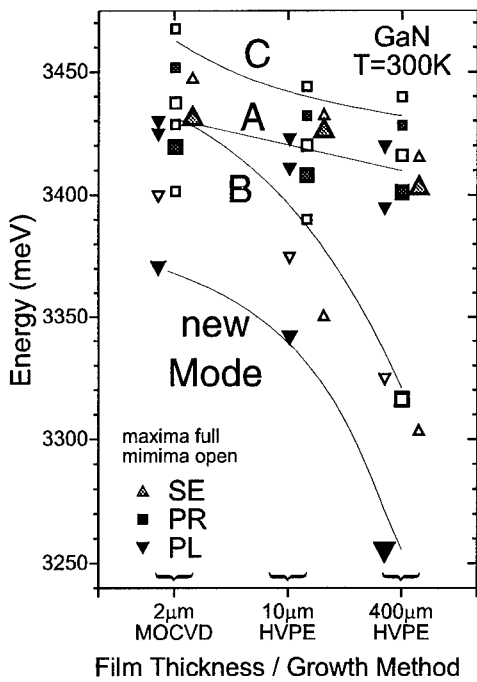


Figure 5. Maxima and minima as measured in PL, photoreflectance and ellipsometry. After crossing through the dominant oscillator one mode exhibits a large Stokes shift for thicker films. Large symbols mark dominant peaks.

Remains to be solved the elemental question concerning the nature of the strong luminescence level Stokes shifted below the optical absorption edge providing the optical gain for stimulated emission. The observed splitting of levels A, B, and C can be described in the picture of Fano resonances [9]. A single oscillator in transition A interacts with strength V with a continuum above transition B characterized by the light hole mass m_{lh} (Inset of Fig. 6). Both A and B each interact with the conduction band by oscillator strengths T_A and T_B , respectively.

The band of transition B has an effective upper limit at the energy of transition C [8]. In a schematic model calculation we assume the values: strengths $T_B / T_A = 0.3$, mode A at 3500 meV, B extending from 3330 to 3500 meV and variable coupling strength $V \in \{1, 2, 3 \dots 10\}$. Depending on T_A , T_B and the matrix element V coupling them in the given energetical sequence oscillator strength from A and B is removed and projected to an energy below the optical bandgap. The new level draws its strength and polarization from both the continuum above B and the two dimensional oscillator in A. Its level is determined directly by the coupling of A and B which is the quantity of the crystal field coupling.

We find that propagation of this new mode is strongly limited to the c -plane minimizing emission in conventional easily implemented PL geometry.

propagating in $k \perp c$ only transitions B and C are allowed. Bandstructure calculations of the effective valence band masses along the corresponding k -axes find $m_{lh} = 1.65$ (A), $m_{lh} = 0.15$ (B), and $m_{ch} = 1.10$ (C) [8]. The highest energy derivative density of states has therefore to be attributed to the A-transition (see Fig. 5).

Considering all the features an assignment of the modes to A, B, and C transitions and transition ranges is possible. Most importantly is the observation of oscillator strength corresponding to transition range B below the strong mode of A. This results in a level/transition sequence in 400 μm bulk GaN from HVPE at room temperature of Γ_7 (B), Γ_9 (A), and Γ_7 (C). The so identified modes are compared with the PL results (Fig. 5). While small energetical changes are observed in the vicinity of the strong A oscillator, large level shifts occur on the low energy side. The dominant PL mode exhibits an even faster shift than the B-mode feature in the ellipsometric and photoreflective data. Furthermore transition B corresponds to the minimum in the c -plane luminescence equivalent to the characteristic edge in a -plane luminescence. We conclude that transition B determines the optical bandgap and higher wing emission from deep behind surface a is reabsorbed above B (Fig. 1).

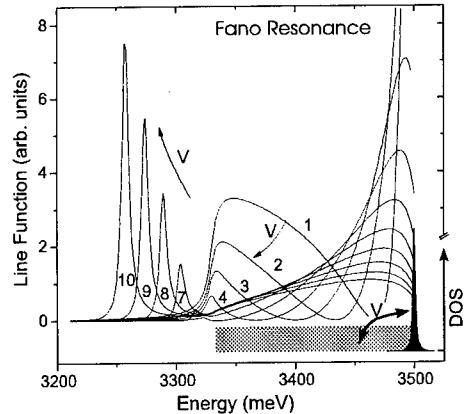


Figure 6. Schematic model of interaction of oscillator above continuous density of states with limited width (Fano resonance). Dependent of coupling strength some oscillator strength is projected beyond the limits of the initial gap defining a Stokes shifted band.

4. Results

In 400 μm bulk GaN from HVPE we observe a strong oscillator in $\varepsilon \perp c$ associated with heavy hole Γ_9 edge of transition A. This room temperature feature corresponds to excitons in two-dimensional systems at low temperatures. Top of the valence band is formed by the light hole Γ_7 of transition B. Interaction of both produces an additional Stokes shifted mode in the transparent energy range of the gap. Its propagation is ideally limited to the c -plane consistent with π polarization, $E \parallel c$ at the recombination site. Forming the valence band edge the light hole mass may provide low transparency densities, low inversion thresholds and a dispersion symmetrical to the conduction band edge. Onset to stimulated emission is observed for largest Stokes shift.

Acknowledgement

Work funded by the Japanese Society for the Promotion of Science (Research for the Future Program).

References

- [1] Amano H, Asahi T, Kito M, and Akasaki I 1991 *J. of Lumin.* **48&49** 889
- [2] Detchprohm T, Amano H, Hiramatsu K, and Akasaki I 1992 *Appl. Phys. Lett.* **61** 2688
- [3] Fischer S, Wetzel C, Hansen WL, Bourret-Courchesne ED, Meyer BK, and Haller EE 1996 *Appl. Phys. Lett.* **69** 2716
- [4] Wetzel C, Walukiewicz W, Haller EE, Ager JW III, Grzegory I, Porowski S, and Suski T 1996 *Phys. Rev. B* **53** 1322-6
- [5] Wetzel C, Fischer S, Walukiewicz W, Ager JW III, Haller EE, Grzegory I, Porowski S, and Suski T (Eds Ponce F, Dupuis RD, Nakamura S, and Edmond JA) 1996 *Mater. Res. Soc. Symp. Proc.* **395** 417
- [6] Gil B, Briot O, and Aulombard RL 1995 *Phys. Rev. B* **52** 17028
- [7] Dingle R, Sell DD, Stokowski SE, and Illegems M 1971 *Phys. Rev. B* **4** 1211
- [8] Suzuki M and Uenoyama T 1997 *Solid-State Electron.* **41** 271; Suzuki M Thesis (Osaka University 1997)
- [9] Fano U 1961 *Phys. Rev.* **124** 1866; Klein MV in *Light Scattering in Solids I*, (Ed. Cardona M, Springer, Topics in Applied Physics **8**, 1983) p169

STM imaging of Be delta doped layers in GaAs

P.M. Koenraad, M.B. Johnson^{†‡}, H.W.M. Salemink[†], and J.H. Wolter

COBRA Inter-University Research Institute, Department of Physics,
Eindhoven University of Technology, P.O.Box 513, 5600 MB Eindhoven.

[†] Department of Physics and Astronomy, University of Oklahoma
440 W. Brooks, Norman, Oklahoma, 73019 USA

[‡] IBM Research Division, Zurich Research Laboratory,
8803 Rüschlikon, Switzerland

Abstract. We have imaged Be delta-doped layers in GaAs with atomic resolution using cross-sectional scanning tunneling microscopy (STM). In the samples, grown at low temperature (480 °C), we observe that the width of doping layers for concentrations up to $1 \cdot 10^{13} \text{ cm}^{-2}$ is smaller than 1 nm, while for higher doping concentrations we find that the doping layer thickness increases strongly with doping concentration. This broadening is symmetrical about the intended doping plane. We believe that this broadening of the doping layer at high doping concentrations is due to Coulombic repulsion between individual Be ions. The effect of Coulombic repulsion can also be observed in the spatial distribution of the dopant atoms in the plane of the doping layer.

1. Introduction

As the size of electronic devices decreases, better control over the growth is required. With present day growth techniques like MBE, CBE etc. atomically sharp interfaces can be obtained. However, in small novel devices not only the layer structure has to be controlled on the atomic scale, also the dopant atoms have to be confined to a few atomic layers. The technique of confining dopant atoms to, ideally, a single atomic layer is referred to as delta doping. Moreover, in these devices the local doping concentrations has to be increased too in order to have sufficient free carriers available. Thus there is a large amount of interest in the physics and applications of delta doping layers in semiconductors.

Delta doped layers have been studied using many techniques[1-6]. Unfortunately, all these techniques have a limiting depth resolution of a few nm. Several authors [7,8] have recently shown that individual ionized dopants can be observed in cross-sectionally cleaved III-V semiconductors surfaces with STM. It is a strong advantage of STM that individual atoms at a surface are observed so that there is not some kind of averaging in one or two directions as is the case with other techniques. Because the (110) cross-sectional surface is perpendicular to the (001) growth surface by means of this technique one can study the spreading of the doping layer as well as the distribution of the dopant atoms within the dopant plane [9].

2. Experimental details

The GaAs structure we have studied was grown at 480 °C with a growth rate of about 1 μm/h (\approx monolayer/sec) on a (001) p⁺ substrate with alignment 0.0 ± 0.2 °. The Be delta-doped layers were obtained by doping the growth surface during a growth interrupt lasting from 10 s up to 360 s, while the surface was under an As flux. In this way, a stack of four doping layers was produced with doping concentrations of $3 \cdot 10^{12} \text{ cm}^{-2}$, $1 \cdot 10^{13} \text{ cm}^{-2}$, $3 \cdot 10^{13} \text{ cm}^{-2}$ and $1 \cdot 10^{14} \text{ cm}^{-2}$, respectively. 25 nm of undoped GaAs was grown between the individual doping layers. This stack of four delta doping layers was repeated 3 times in the structure where each stack was separated by a doped 2.5 nm Al_{0.2}Ga_{0.8}As

marker layer. The intended doping concentration was checked by SIMS measurements and the electric activity of the dopant atoms in the layers by etching CV profiling. The STM measurements were performed in an UHV environment ($p \approx 1 \cdot 10^{-11}$ torr) on freshly in situ-cleaved samples.

3. Results

In Fig. 1 we show a large scale As related image across a full stack of four delta doped layers. The white hillocks which are due to individual ionized doping atoms are clearly visible [6]. Ionized Be closest to the cleaved surface appear brightest while deeper lying dopants appear weaker. We are able to observe ionized dopant atoms up to a depth of about 1.5 nm below the cleaved surface.

From expanded images like in Fig. 1 the position of the Be atoms was determined with atomic resolution in both the [001] and the [110] direction. Fig. 2 shows the spreading of the dopants in the [001] growth direction. The spreading is given in bilayer units where one bilayer consists of a single As layer and a single Ga layer. A Gaussian fit was used to quantitatively determine the spreading of the dopants.

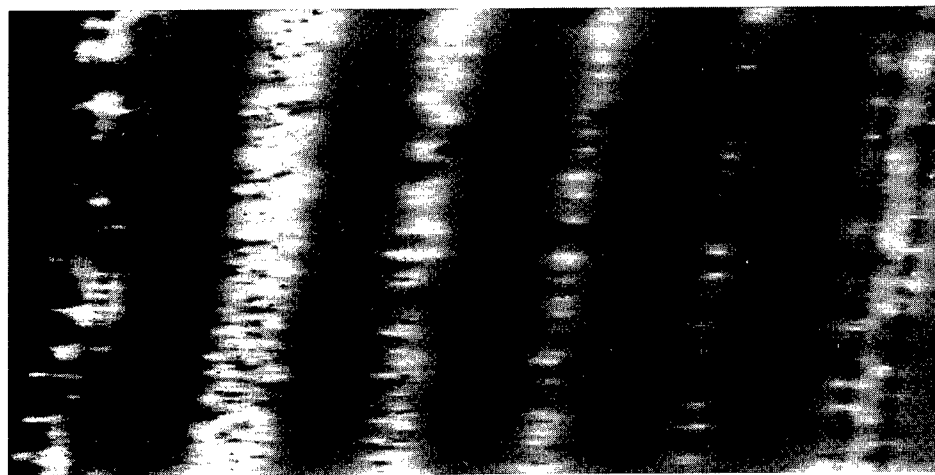


Fig. 1. STM image of Be-delta doped layers. Large scale (300*120 nm², compressed) As related image of one of the stacks consisting each of four delta-doped layers. Tunneling conditions: sample bias = 1.0 V and tunnel current 20 pA. The grey-scale range is 0.08 nm with a [001] corrugation of approximately 0.03 nm. Electrically active Be dopants appear as white hillocks of approximately 2.5 nm in diameter and up to 0.05 nm high.

4. Discussion

The unprecedented resolution in Fig. 1 shows the potential of X-STM for the study of delta-doped layers. No other technique is able to get a similar atomic resolution as demonstrated here for the case of X-STM. The results show a near single atomic layer thickness for the doping layers with the lowest doping concentration whereas a considerable broadening is observed for the layers with the higher doping concentration. We also observed a small, about 2 bilayers, shift of the dopant plane from the

intended doping position towards the growth surface. This shift is probably due to the field induced drift from the surface depletion field which exists at the surface of the semiconductor [10]. However, this surface depletion field cannot be responsible for the broadening of the dopant layers at high doping concentrations because we observe a symmetric broadening of the doping layer centred around the intended dopant plane. We believe that this broadening is due to the mutual Coulomb repulsion between the individual Be ions. This drift/diffusion process is active in the absence of the surface depletion field as can be seen from the ongoing drift/diffusion during growth of the sample. This is confirmed in Fig. 2 where we show that in the different stacks of delta layers the thickness of the dopant layer depends on the time at growth temperature.

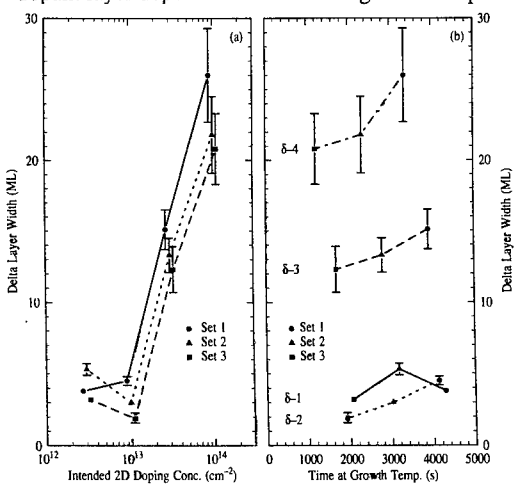


Fig. 2. Layer width as a function of the intended doping concentration and the time at growth temperature for the three stacks of doping layers. Data from stack 1 (circle), stack 2 (triangle) and stack 3 (square) are shown.

One of the most exciting possibilities of X-STM is the fact that we are able to study the distribution of the dopants in the plane of the doping layer. The study of the in plane distribution can be used to check if any ordering of the dopants is occurring. A convenient way of showing the presence of structure in a particle distribution is the radial distribution function (frequency plot of the pair distance for all available pairs in the set of particles). In Fig 3 we show the radial distribution function of the doping layers with doping concentrations of $1 \cdot 10^{13} \text{ cm}^{-2}$ and $3 \cdot 10^{13} \text{ cm}^{-2}$, respectively. In the case of a totally random distribution one would observe a flat radial distribution function, $g(r) = 1$. Fig 3 clearly shows that close pairs of dopant atoms are much less common. The distribution of the ionized Be atoms thus has the character of a so called strongly interacting gas.

We believe that the absence of the close pairs is due to the mutual repulsion of the two ionized dopants. This is the same Columbic repulsion that spreads the dopants out in the growth direction. Thus it might be difficult to obtain a long range order in the dopant distribution, because the same effect that orders in the in-plane dimensions pushes the dopants off the plane in the growth direction. To achieve order it may be important to use longer growth interrupts because during this time the drift/diffusion of the dopants is highly anisotropic with motion on the growth surface being far more likely. In the future, it will be very interesting to see what the influence of the structure in the ionized dopant distribution is on the mobility of free carriers that scatter on these ionized impurities. In the ideal case of perfect long range order producing a Wigner crystal of ionized Be atoms, the scattering of the free carriers on the impurity distribution is absent.

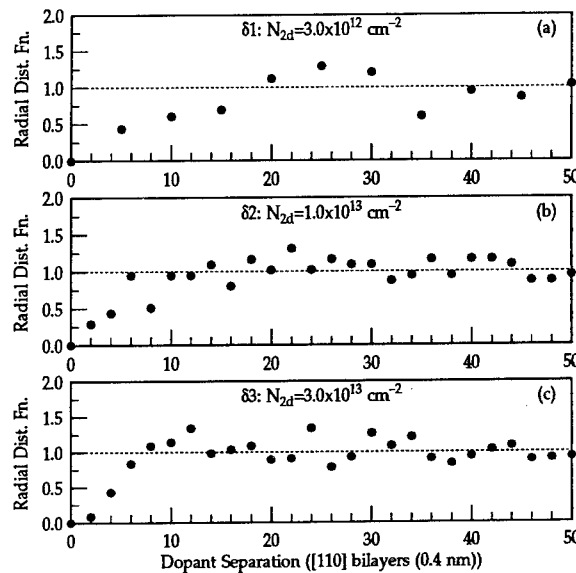


Fig. 3. Radial distribution function for the delta layers with doping concentrations of (a) $3 \cdot 10^{12} \text{ cm}^{-2}$, (b) $1 \cdot 10^{13} \text{ cm}^{-2}$ and (c) $3 \cdot 10^{13} \text{ cm}^{-2}$ respectively as determined from the XSTM images (circle). The radial distribution function for a random distribution is shown by the dotted line.

5. Conclusions

Using STM we have shown that the width of the doping layers for concentrations up to $1 \cdot 10^{13} \text{ cm}^{-2}$ is smaller than 1 nm. In doping layers with a higher doping concentration we find that the doping layer thickness increases strongly due to Coulombic repulsion between individual Be ions. The Coulombic repulsion can also be observed in the spatial distribution of the dopants in the plane of the doping layer.

References

- [1] E.F. Schubert, J.M. Kuo, and R.F. Kopf 1989 Journ. of Electronic Materials 19, 521
- [2] J.J. Harris, J.B. Clegg, R.B. Beall, J. Castagné, K. Woodbridge, and C. Roberts 1991 Journ. of Crystal Growth 111, 239
- [3] P.M. Koenraad 1996 chapter 17 in "Delta Doping of Semiconductors" Ed. by E.F. Schubert, Cambridge University Press, UK, 304
- [4] A. Ourmazd, J. Cunningham, W. Jan, J.A. Rentschler, and W. Schroeter 1990 Appl. Phys. Lett. 56, 854
- [5] J. Wagner, M. Ramsteiner, W. Stolz, M. Hauser, and K. Ploog 1989 Appl. Phys. Lett 55, 978
- [6] L. Hart, M.R. Fahy, R.C. Newman, and P.F. Fewster 1993 Appl. Phys. Lett. 62, 2218
- [7] M.B. Johnson, O. Albrektsen, R.M. Feenstra, and H.W.M. Salemink 1993 Appl. Phys. Lett. 63, 2923
- [8] J.F. Zheng, X. Liu, N. Newman, E.R. Weber, D.F. Ogletree, and M. Salmeron 1994 Phys. Rev. Lett. 72, 1490
- [9] M.B. Johnson, P.M. Koenraad, H.W.M. Salemink, W.C. van der Vleuten, and J.H. Wolter 1995 Phys. Rev. Lett. 75, 1606
- [10] E.F. Schubert, G.H. Gilmer, R.F. Kopf, and H.S. Luftman 1993 Phys. Rev. B 46, 15078

Characterization of the Interfacial Electronic Properties of Oxide Films on GaAs Fabricated by In-Situ Molecular Beam Epitaxy

J. S. Hwang, W. Y. Chou, G. S. Chang and S. L. Tyan

Department of Physics, National Cheng Kung University, Tainan, Taiwan, R.O.C.

M. Hong, J. P. Mannaerts, and J. Kwo

Bell Laboratories, Lucent Technologies, Murray Hill, New Jersey 07974

Abstract. We have used room temperature photoreflectance spectroscopy to study interfacial electronic properties of various oxide-GaAs heterostructures. The samples, Air-, Al_2O_3 - Ga_2O_x , and $\text{Ga}_2\text{O}_3(\text{Gd}_2\text{O}_3)$ -GaAs, were fabricated by *in-situ* molecular beam epitaxy. Build-in electric fields are 48, 44, and 38 kV/cm for Air-, Al_2O_3 - Ga_2O_x -GaAs samples, respectively, corresponding to the interfacial state density (D_{it}) of 2.4, 2.2, and $1.9 \times 10^{11} \text{ cm}^{-2} \text{ eV}^{-1}$, respectively. For the $\text{Ga}_2\text{O}_3(\text{Gd}_2\text{O}_3)$ -GaAs sample, the build-in electric field is negligibly small, indicating a very low interfacial state density. Estimated by the low field limit criterion, D_{it} is less than $1 \times 10^{11} \text{ cm}^{-2} \text{ eV}^{-1}$. Our results are consistent with the previous data obtained using capacitance-voltage measurements in quasi-static/high frequency modes.

1. Introduction

The dielectric or insulating film has played an important role in the fabrication of conventional and low dimensional field-effect metal-insulator conductor devices.[1]-[5] However, for the high mobility materials such as GaAs and its related compounds, which are the mostly commonly used for low power, high speed devices, the insulating film providing low interface state density and stable device operation is still not available. Many efforts have been made on the searching of such dielectric film including Si_3N_4 , SiO_2 , Al_2O_3 , and Ga_2O_3 deposited in combination with dry, wet and photochemical surface treatment.[6]-[9] Recently, M. Passlack *et al.*[10] of Bell laboratory have reported a new approach to grow, by *in-situ* molecular beam epitaxy, a $\text{Ga}_2\text{O}_3(\text{Gd}_2\text{O}_3)$ -GaAs structure with interface state density in the low $10^{10} \text{ cm}^{-2}\text{eV}^{-1}$ range at midband energy and an interface recombination velocity of 4500 cm/s.[10]-[12] A capacitance-voltage (C-V), capacitance-time (C-T), conductance-voltage (G-V) and steady state photoluminescence (PL) measurements[13] were employed in their investigations on the electronic interface properties.

In this letter, we present results of our studies on the electronic properties of the oxide-semiconductor interface by contactless and nondestructive photoreflectance (PR). Four samples, Air-, Al_2O_3 - Ga_2O_x , $\text{Ga}_2\text{O}_3(\text{Gd}_2\text{O}_3)$ -GaAs (bare sample surface) were studied. From the observed Franz-Keldysh oscillations (FKOs) of the PR spectra we were able to estimate the interface electric fields and deduce the densities of interface states.

2. Experiment

Samples were grown using a multiple-chamber UHV system.[10] A typical growth sequence entailed different oxide films being deposited on 1.5 μm of n-type GaAs buffer layer ($1.6 \times 10^{16} \text{ cm}^{-3}$) which had been previously grown on a highly doped n-type (100) GaAs substrate. The oxide films, Al_2O_3 - Ga_2O_x , and $\text{Ga}_2\text{O}_3(\text{Gd}_2\text{O}_3)$ -GaAs were deposited using molecular beams of aluminum and

Table 1. The sample structure, dielectric film thickness, the values of the interface field F_{in} , and the density of interface states D_{it} .

Dielectric film	Thickness (Å)	F_{in} (kV/cm)	$D_{it}(10^{11} \text{ cm}^{-2}\text{eV}^{-1})$
Air	×	48	2.4
Al_2O_3	700	44	2.2
Ga_2O_x	600	38	1.9
$\text{Ga}_2\text{O}_3(\text{Gd}_2\text{O}_3)^*$	400	<21	<1.0

* Estimated from the low field limit criterion, $|\hbar\Omega^3/\Gamma^3| < 1/3$

gallium-oxide. Single crystals of Al_2O_3 , Ga_2O_3 , and $\text{Gd}_3\text{Ga}_5\text{O}_{12}$ were used as source materials and evaporated by e-beam technique. According to the report by Passlack *et al.*,[10] the use of $\text{Gd}_3\text{Ga}_5\text{O}_{12}$ was motivated by the unavailability of single Ga_2O_3 crystal and led to the first successful deposition of gallium oxide molecules forming extremely uniform nonstoichiometry $\text{Ga}_2\text{O}_3(\text{Gd}_2\text{O}_3)$ films on GaAs. Samples with different dielectric film materials and thickness are listed in Table 1.

A standard PR apparatus was used in this study.[14] The probe beam consisted of a tungsten lamp and a quarter meter monochromator. A He-Ne laser served as the pump beam. The detection scheme consisted of a Si photodetector and a lock-in amplifier. The probe and pump beams were defocus on the sample to reduce the photovoltaic effect. All measurements were performed at room temperature and at a modulation frequency of $f=200$ Hz.

3. Theory

In PR, the electric field of the sample is modulated through the changes in the surface photovoltage induced by the absorption of the photons above the band gap. When an electric field is applied to a sample, electrons and holes are accelerated by the field. The electro-optic energy, $\hbar\Omega$, is defined as [15] :

$$(\hbar\Omega)^3 = (\hbar F e)^2 / 2\mu \quad (1)$$

where F is the electric field and μ is the reduced interband electron and hole pair effective mass in the direction of the electric field. The line shape of the PR spectrum in the low field limit $|\hbar\Omega^3/\Gamma^3| < 1/3$, where Γ is the broadening parameter, can be fitted to [16],[17]:

$$\Delta R/R = \text{Re}[A e^{i\theta} (E - E_g + i\Gamma)^{-m}] \quad (2)$$

where A is the amplitude, θ the phase angle, E the incident photon energy, E_g the interband transition energy and m is a parameter depending on the type of the critical point (for three dimensional critical point $m=5/2$). If an electric field exists and is not in the low field limit, the analysis of the PR spectrum is based on the so-called high field limit of electroreflectance. Under this limit, the PR spectra near the fundamental absorption edge exhibit FKO's above the band gap energy. The extrema in the FKO's are given by [18],[19]:

$$n\pi = \phi + \frac{4}{3} [(E_n - E_g) / \hbar\Omega]^{3/2} \quad (3)$$

where n , ϕ , E_n and E_g are the index of the n^{th} extrema, an arbitrary phase factor, the photon energy of the n^{th} oscillation and the energy band gap, respectively.

4. Results and Discussion

Fig. 1 shows the PR spectra for all samples at room temperature. Spectra of the three samples Air-, Al_2O_3 - and Ga_2O_x -GaAs contain the FKO features (labeled A-D in Fig. 1) with different periods exhibited above the energy gap of GaAs (1.42 eV) for each spectrum. It indicates that electric fields of different strengths exist at the interface regions of the samples and the electric fields are not in the low field limit. No FKO feature appears in the spectrum of $\text{Ga}_2\text{O}_3(\text{Gd}_2\text{O}_3)$ -GaAs inferring that the electric field in this sample is too low to create any FKO and the only feature in the spectrum corresponds to the fundamental band to band transition. The broadening parameter Γ obtained by fitting its spectrum to Eq. (2), is approximately 13 meV. The electric field F corresponds to the low field limit criterion, $|\hbar\Omega|^3/\Gamma^3 < 1/3$, which at this broadening parameter is less than 2.1×10^4 V/cm. In Fig. 2, the quantity $(4/3\pi)(E_n - E_g)^{3/2}$ is plotted as a function of the index n , where E_g is estimated by the "three point method". The solid lines represent linear fits to Eq. (3). The slope of the solid line yields the electro-optic energy $\hbar\Omega$ which in turn gives the built-in electric field F . The effective masses of the electron and heavy hole used here are $0.065 m_0$ and $0.34 m_0$ respectively in GaAs, where m_0 is the free electron mass. The calculated value of F are also included in Table 1.

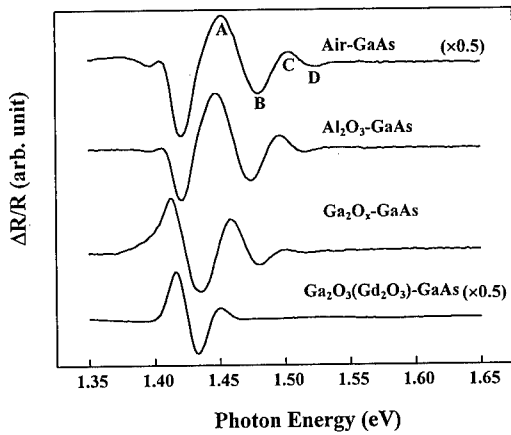


Fig. 1 The PR spectra for samples Air-, Al_2O_3 -, Ga_2O_x -, $\text{Ga}_2\text{O}_3(\text{Gd}_2\text{O}_3)$ -GaAs, at room temperature.

The mechanism of the built-in electric field can be interpreted by simple model of parallel plate capacitor. The band bending region, which supplies the PR signal is sandwiched between the negative charges in the interface states (surface states for Air-GaAs structure) and the positive charges in the thin depletion layer in the n-type GaAs. The electric field of the capacitor is given by :

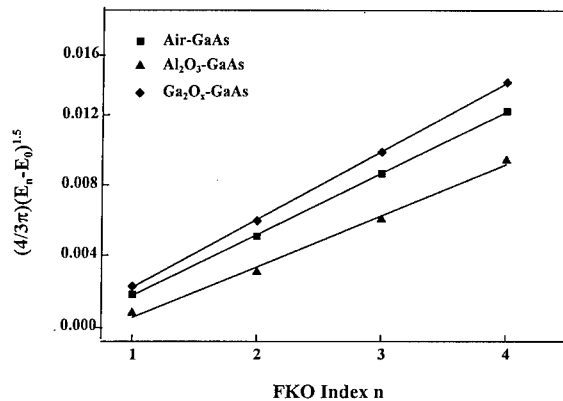


Fig. 2 The quantity, $(4/3\pi)(E_n - E_g)^{3/2}$, as a function of index n (FKO extrema)

$$F = \sigma_i / \epsilon \epsilon_0 = e D_{ii} / \epsilon \epsilon_0 \quad (4)$$

where σ_i , ϵ , ϵ_0 , e and D_{ii} represent the surface charge density, relative dielectric constant, free space permittivity, free electron charge and the density of occupied interface states, respectively. Once the electric field is obtained from the FKO's, the interface charge density σ_i and thus the occupied interface state density D_{ii} can be calculated from Eq. (4). The results are included in Table 1. The density of interface states of Ga₂O₃(Gd₂O₃)-GaAs reported by M. Passlack *et al.*[10], measured by the quasi-static/high frequency technique, ranges from 2×10^{10} to 5×10^{12} cm⁻²eV⁻¹ at various band gap energies which is comparable with the value of less than 1.0×10^{11} cm⁻²eV⁻¹ averaged over the band gap energies estimated by the low field limit criterion in photoreflectance spectroscopy. For Air-, Al₂O₃-, and Ga₂O_x-GaAs, the densities of interface states are 2.4, 2.2, 1.9×10^{11} cm⁻²eV⁻¹ respectively. Passlack *et al.* also reported a density of interface states of Al₂O₃-GaAs to be around 10^{12} cm⁻²eV⁻¹ measured by capacitance-voltage technique which is also comparable with the result obtained by PR technique.

5. Conclusion

In conclusion, the contactless and nondestructive technique of photoreflectance has been used to characterize the electronic interface properties of a series of oxide-GaAs structures fabricated by in-situ molecular beam epitaxy. We found that the densities of interface states measured by PR technique is consistent with the results obtained from quasi-static/high frequency technique. The built-in electric field and the density of interface states of Ga₂O₃(Gd₂O₃)-GaAs structure are very small due to the fact that the nonstoichiometry film is extremely uniform deposited on GaAs.

Acknowledgement

This work was supported by National Science council of the Republic of China under contract No NSC. 86-2112-M-006-010 and NSC. 86-2112-M-006-008.

References

- [1] Spicer W E *et al* 1988 J. Vac. Sci. Technol. B 6 1245
- [2] Hung L S *et al* 1992 Appl. Phys. Lett. 60 201
- [3] Viktorovitch P *et al* 1991 Appl. Phys. Lett. 58 2387
- [4] Shigekawa H *et al* 1991 Appl. Phys. Lett. 59 2986
- [5] Dagata J A *et al* 1991 Appl. Phys. Lett. 59 3228
- [6] Capasso F and Williams G F 1982 J. Electrochem. Soc. 129 821
- [7] Offsey S D *et al* 1986 Appl. Phys. Lett. 48 477
- [8] Sandroff C J *et al* 1987 Appl. Phys. Lett. 51 33
- [9] Herman J S and Terry F L 1992 Appl. Phys. Lett. 60 716
- [10] Passlack M *et al* 1995 IEDM
- [11] Hong M *et al* 1996 J. Vac. Sci. Technol. 14 2297
- [12] Passlack M *et al* 1997 IEEE Tran. Electr. Devices 44 214
- [13] Passlack M *et al* 1995 J. Appl. Phys. 77 2
- [14] Shen H *et al* 1987 Rev. Sci. Instrum. 58 1429
- [15] Hwang J S *et al* 1994 Appl. Phys. Lett. 64 3314
- [16] Shen H *et al* 1973 Phys. Rev. B7 4605
- [17] Shen H *et al* 1986 Appl. Phys. Lett. 48 653
- [18] Hwang J S and Tyan S L 1992 J. Vac. Sci. Technol. A10 3176
- [19] Hwang J S *et al* 1991 Solid State Commun. 80 891

Structural and Device Properties of DFB - LD with Lateral Undulation of SL - MQW

Hyung Mun Kim, Jeong Soo Kim, Dae Kon Oh, Heung Ro Choo, Hong Man Kim, and Kwang Eui Pyun

Optoelectronics Section, Electronics and Telecommunications Research Institute
Yusong P.O. Box 106, Taejon, 305-600, Korea

Abstract. The InGaAsP/InGaAs strained-layer multiple quantum well (SL-MQW) structures for 1.3 μm or 1.55 μm distributed feedback laser diodes (DFB-LD) have been grown by low-pressure metalorganic vapor phase epitaxy. We observed the lateral undulation or deformation of SL-MQW grown on sawtooth-patterned substrates before the fabrication of DFB-LD, and it was dependent upon the initial growth conditions, AsH₃ partial pressure and heat-up time, prior to the 1st active layer growth. It is mainly due to the excess accumulation of strain in a given growth condition. The structural qualities of SL-MQW are analyzed in-depth using DCXRC, PL, TEM, SEM, and OM. We will discuss the effect of undulation or deformation on the device properties, such as I-V, I-L, differential quantum efficiency, internal loss, and characteristic temperature.

1. Introduction

The 1.3 μm or 1.55 μm InGaAsP/InP strained-layer multiple quantum well distributed feedback laser diodes have been extensively studied as light sources for long-haul, high-speed optical communication systems [1]. Recently, lateral thickness modulations have been observed in the strain-compensated InGaAsP/InGaAsP MQW [2-4], the strained-compensated GaInAs/GaInAs MQW [5], and InGaAs/GaAs superlattices structures [6], grown on no patterned substrates. Ponchet et al. reported that tensile layer growth appeared to be responsible for starting of the modulation in the strain-compensated structure[2]. One may observe the undulation or deformation of SL-MQW layers in the growth of 1st active layers on the patterned substrates prior to the fabrication of DFB-LD. Such phenomenon deteriorates the device performances, such as thermal stability and reliability of DFB-LD.

In this report, we observe that this undulation or deformation of the layer grown on the sawtooth-patterned substrate is dependent upon the initial growth conditions, AsH₃ partial pressure and heat-up time, prior to the 1st active layer growth. We report the optimum initial growth conditions for removing such a lateral undulation or deformation of SL-MQW layers, and discuss the influence of undulation or deformation on the device performance.

2. Experiments

The epitaxial layers used in this study were grown on (100) InP substrates with 1st-order

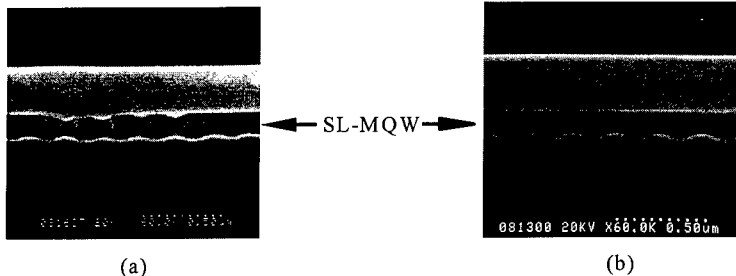


Fig. 1 SEM cross-sectional views of (a) undulation and (b) no undulation of SL-MQW layers.

corrugation grating using low-pressure metalorganic vapor phase epitaxy (LP-MOVPE). The layer structure consists of compressively strained InGaAs wells and lattice-matched InGaAsP barriers (10 periods of MQW) emitting at 1.55 μm , and 1.24- μm InGaAsP waveguide layers. For double crystal X-ray rocking curve (DCXRC) measurement, symmetric (004) reflection RCs were obtained a high resolution double-crystal diffractometer (Bede DCC 300) equipped with a rotating-anode CuK α radiation and a Si(220) channel-cut collimator. The structural qualities of SL-MQW are analyzed using DCXRC, PL, TEM, SEM, and OM, and will discuss the effect of undulation or deformation on the device properties (I-V, I-L, differential quantum efficiency, etc), after the fabrication of high speed DFB-LD.

3. Results and Discussion

We observed the lateral undulation or deformation of SL-MQW DFB-LD structure grown on patterned InP substrates with the initial growth conditions of both AsH₃ partial pressure of 1.5×10^{-3} Torr and heat-up time of 5 min, as seen in a SEM photograph (Fig. 1(a)). In Fig. 2(a), it shows rough surface morphology for the layer with undulation of SL-MQW. From the double crystal X-ray rocking in Fig. 3(a), satellite peaks of SL-MQW layers around InP substrate peak are very broad and not clear, indicating the very poor epitaxial quality of MQW, due to the dislocations generated at the concave of MQW, as reported by Jang et al.[7]. Dislocations appeared as early as the fifth period of MQW in TEM bright field image[8], and it is mainly due to the excess accumulation of strain. We could not detect PL signal for the sample of layer undulation due to the poor layer quality. This undulation was removed by controlling the AsH₃ partial pressure and heat-up time as shown in Fig. 1(b), and the

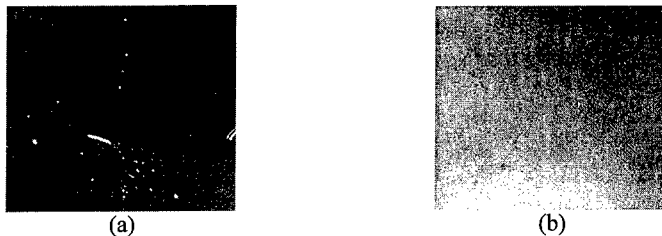


Fig. 2 Surface morphologies of (a) undulation and (b) no undulation of SL-MQW layers.

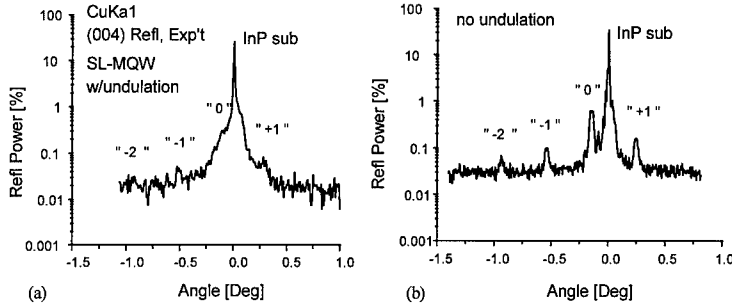


Fig. 3 Double Crystal X-ray Rocking Curves : (a) undulation and (b) no undulation of SL-MQW layers. Satellite peaks of SL-MQW layers with undulation are very weak due to the dislocations.

sample exhibited specular surface morphology in Fig. 2(b). We found the optimum initial growth conditions, such as AsH₃ partial pressure of 9×10^{-4} Torr and 3 min heat-up time. In the DCXRC of sample with no layer undulation in the Fig. 3(b), several satellite peaks are sharp and comparable to the peaks of Fabry-Perot LD structure. Unlike the layer undulation, the clear and sharp PL spectrum was observed, showing good layer quality.

Figure 4 shows typical static characteristics, such as I-V, I-L, and differential quantum efficiency (or, slope efficiency (SE)), of DFB-LD fabricated with undulation and no undulation of SL-MQW. The differential quantum efficiency was 8% for the sample of layer undulation (Fig. 4(a)), while for the sample of no layer undulation, quantum efficiency increased to 16% in Fig. 4(b). For the sample of layer undulation, the characteristic temperature (T_c) of ~ 48 K was obtained from the measured I-L curves at heat sink temperatures $20 \sim 80^\circ\text{C}$ for laser diode having 300 μm cavity length (Fig. 5). However, T_c was the range of 51 \sim 57 K for the sample of no layer undulation. The internal quantum efficiency and the internal losses were extracted from the dependence of external efficiency with cavity length. Internal loss and internal quantum efficiency of the undulated DFB-LD were 26.7 cm^{-1} and 43.4 %, respectively, while for no layer undulation they were 19.8 cm^{-1} and 58 %, showing better device properties.

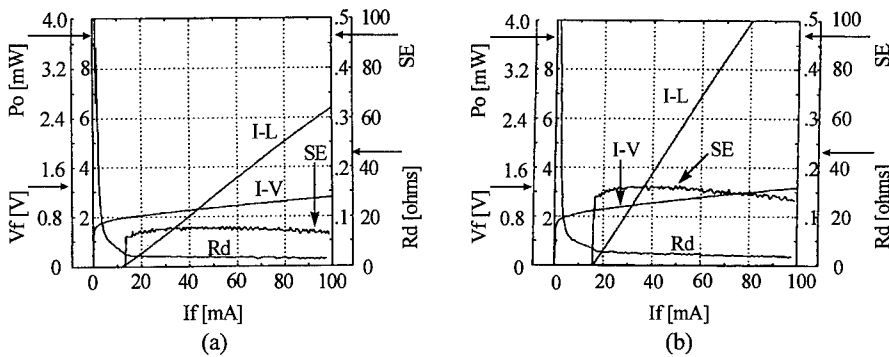


Fig. 4 Static Characteristics of DFB-LD : (a) undulation and (b) no undulation of SL-MQW layers.

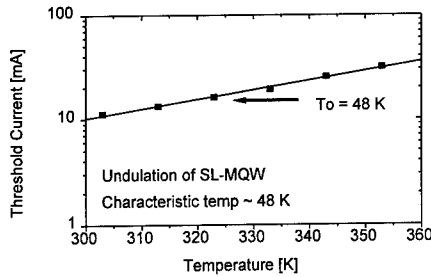


Fig. 5 Characteristic temperature of DFB-LD with undulation of SL-MQW.

4. Conclusion

The InGaAsP/InGaAs SL-MQW structures for 1.3 μm or 1.55 μm distributed feedback laser diodes have been grown by LP-MOVPE. The lateral undulation or deformation of SL-MQW layers grown on sawtooth-patterned InP substrates has been observed, and it was dependent upon AsH₃ partial pressure and heat-up time prior to the 1st active layer growth. Based upon our results, the optimum initial growth conditions, in order to remove such an undulation or deformation of SL-MQW layers, were AsH₃ partial pressure of 9×10^{-4} Torr and 3 min heat-up time. The differential quantum efficiency was 8% for the sample of layer undulation, while for the sample of no layer undulation, quantum efficiency increased to 16%, indicating better device properties. Characteristic temperatures of ~ 48 K and ~ 57 K were obtained for undulation and no undulation of SL-MQW, respectively.

5. Acknowledgments

Authors would like to acknowledge Dong Cheol Kim for his technical assistance. This work was supported by the B-ISDN Project of the Korea Telecommunication under the supervision of the Ministry of Information and Communication, and the Ministry of Science and Technology.

6. References

- [1] H.P.Mayer et al. 1995 in Proceeding of ECOC '95, Brussels, Belgium, paper WeA.3.1, pp.529-536
- [2] A.Ponchet and A. Rocher 1993 J. Appl. Phys. **74** (6) 3778 - 3782
- [3] R.W.Glew et al. 1994 J. Crystal Growth **145** 764 - 770
- [4] Y.Shimose, T.Kikugawa, and H.Nagai 1995 Proceeding of the 7th Conf. on IPRM '95, Sapporo, Japan, paper WP35, 210-212
- [5] A.D.Smith et al. 1994 Appl.Phys.Lett. **65** (18) 2311-2313
- [6] Z.H.Ming et al. 1995 Appl.Phys.Lett. **66** (2), 165-167
- [7] Dong Hoon Jang et al. 1995 Appl.Phys.Lett. **66** (23) 3191 - 3193
- [8] Hyung M. Kim et al. 1997 Proceedings of the 9th Conf. on IPRM '97, Hyannis, USA, paper TuB5
268 - 271

XSTM Characterization of GaSb/InAs Heterojunctions: Observation of White Noise in the Interface Roughness Spectrum

J. Harper and M. Weimer

Department of Physics, Texas A&M University, College Station, Texas 77843-4242

D. Zhang, C.-H. Lin, and S. S. Pei

Space Vacuum Epitaxy Center, University of Houston, Houston, Texas 77094-5507

Abstract. We report the appearance of a white-noise component in the anion roughness spectrum of the GaSb/InAs interface under MBE growth conditions routinely employed for type-II quantum well and interband cascade lasers. Real-space imaging with cross-sectional scanning tunneling microscopy (XSTM) reveals that the white-noise power due to anion cross incorporation within the layers (As in GaSb and Sb in InAs) is less than the white-noise background appearing in the roughness spectrum, indicating an excess of interface defects.

1. Introduction

Improved control of the interfaces between nearly-lattice-matched 6.1 Å materials (InAs, GaSb, and AlSb) is important for a number of applications, including the optimization of type-II quantum-well (QW) and interband cascade (IC) lasers operating in the mid-IR [1-3].

We present new cross-sectional scanning tunneling microscopy (XSTM) results exploring the relationship between two fundamental materials issues in the mixed-anion GaSb/InAs system: bulk cross incorporation and the interface roughness spectrum. In particular, we observe a new, white-noise component in the roughness spectrum at the GaSb-on-InAs interface under conditions routinely employed for the growth of mid-IR lasers. We associate this phenomenon with point defects in the anion sublattice which occur within the layers as well as at the interface. We demonstrate the point defects appearing within the GaSb layers are due to As cross incorporation and, following earlier work, ascribe those in the InAs layer to Sb incorporation. The spectral density associated with cross incorporation cannot fully account for the white noise observed at the GaSb/InAs interface, indicating the presence of additional interface-specific defects.

2. Experiment

Two model structures were employed for the experiments reported here: the first was designed to facilitate studies of the effect of growth order on interface properties and the second the role of anion cross incorporation (specifically As incorporation in GaSb). The respective layer sequences are illustrated in Fig. 1.

All growths were performed in a Riber 32 MBE system equipped with a valved, cracked As source and an EPI 175 Sb cracker. In the first structure, the As valve remained open at the optimal setting for growth of InAs while the source was shuttered during deposition of the antimonide layers. In the second structure, the As source was shuttered as before but the valve setting readjusted during antimonide

.	
.	
InAs	40 Å
AlSb	38 Å
GaSb	200 Å
GaSb spacer	500 Å
.	
.	
AlSb	38 Å
InAs	40 Å
GaSb	280 Å
InAs	90 Å
AlSb	86 Å
GaSb	700 Å 25 mils
InAs	90 Å
AlSb	86 Å
GaSb	600 Å 50 mils
InAs	90 Å
AlSb	86 Å
GaSb	500 Å 100 mils
InAs	90 Å
AlSb	86 Å
GaSb	400 Å 200 mils
InAs	90 Å
AlSb	86 Å
GaSb	300 Å 200 mils

Figure 1. Layer sequences employed to study the effect of growth order (structure 1, left), and cross-incorporation (structure 2, right, with As valve settings in mils) on interface properties. Growth direction is toward the top of the page.

growth as indicated in Fig. 1. Both structures were grown at a temperature of 440 °C on top of a 0.3 μm GaSb buffer layer previously deposited on a *p*-GaSb substrate. Details of the growth procedures can be found in reference [4].

The samples were cleaved under UHV conditions ($\leq 5 \times 10^{-11}$ Torr) in a separate STM chamber, and the exposed (110) surfaces imaged with Pt-Ir tips at typical sample biases of -2.5 V and tunnel currents of 100 pA.

3. Results and Discussion

To assess the interface quality in these MBE-grown structures, we derive the roughness spectrum from *atomic-resolution* interface profiles (Fig. 2). Because of the pronounced electronic contrast arising from

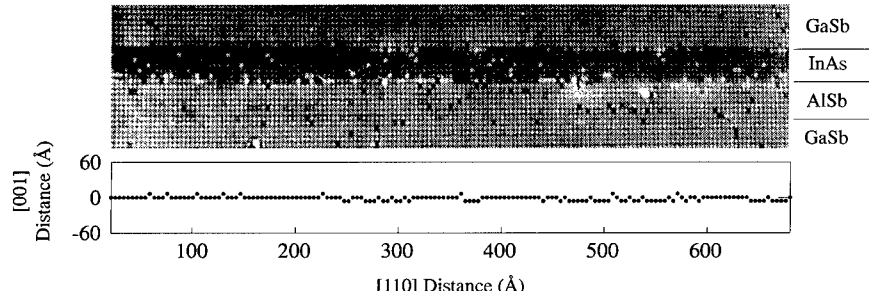


Figure 2. (Top) Representative XSTM image of the anion sublattice from the upper portion of structure 1. Growth direction is toward the top of the page. (Bottom) Corresponding profile at the GaSb/InAs interface, discretized in units of the surface mesh.

the valence-band offset between the respective materials, the GaSb/InAs interface readily lends itself to this kind of analysis.

Following earlier XSTM studies [5-7], we examine interface segments with minimum lengths $\sim 500 \text{ \AA}$ and use the surface mesh (4.2 \AA along the interface and 6.1 \AA across the interface) as a grid for discretizing our atomic-resolution profiles (Fig. 2). The resulting spectral density, obtained by averaging ten such profiles from structure 1, is plotted versus spatial frequency in Fig. 3.

Previous XSTM studies of antimonide-based heterojunctions [5,7] have concluded that the roughness spectrum is Lorentzian [8], reflecting the interface kinks due to terrace/island structure at the GaSb/InAs growth front. Inspection of Fig. 3, however, indicates our data is comprised of two components: a Lorentzian at low wave vectors that smoothly joins to a constant background at high wave vectors. As shown by the solid line in Fig. 3, the functional form

$$|A_q|^2 L = \frac{2\Delta^2(\Lambda/2\pi)}{\left\{1 + q^2(\Lambda/2\pi)^2\right\}} + \text{Constant} \quad (1)$$

provides an excellent fit to the observed spectrum, producing reasonable values for the roughness amplitude Δ ($1.7 \pm 0.1 \text{ \AA}$) and correlation length Λ ($79.0 \pm 10.1 \text{ \AA}$) associated with the Poisson-distributed interface kinks. We interpret the constant offset in the spectral density ($20.5 \pm 1.5 \text{ \AA}^3$) as a “white-noise” background due to random, uncorrelated *point defects*. These defects appear as isolated, single-cell discontinuities in the raw interface profiles (Fig. 2).

The XSTM data shown in Fig. 2 suggests one possible origin for these interfacial defects. There are a number of anion defects *within* the layers that appear either as isolated dark sites in the case of GaSb or as bright sites in the case of InAs. The bright sites in InAs have been previously interpreted as substitutional Sb [5]; the appearance of dark sites in GaSb is similarly consistent with the hypothesis of substi-

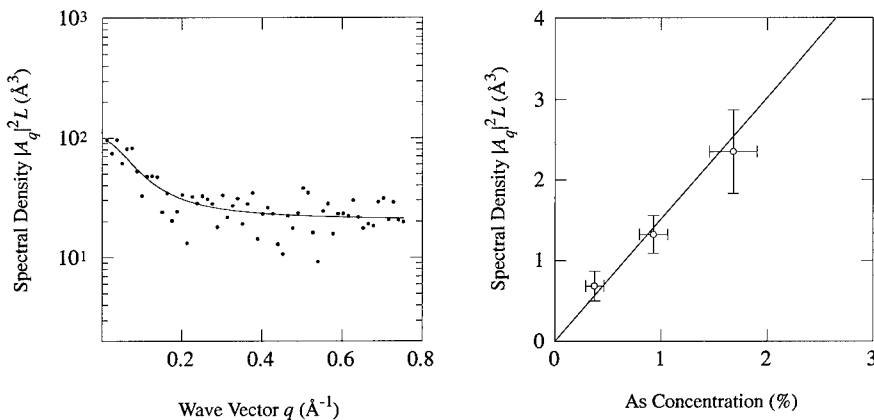


Figure 3. (Left) GaSb/InAs interface roughness spectrum using atomic-resolution interface profiles from structure 1. Solid line is a fit to Eq.(1). (Right) White-noise spectral density as a function of As concentration obtained from bulk profiles through the GaSb layers in structure 2. Solid line is an extrapolation of the spectral density due to a single defect.

tutional As, presumably from *background incorporation* during MBE growth. Atomic-resolution XSTM images from our second structure confirm this hypothesis by demonstrating a linear correlation between the GaSb layer defect density and the As-cracker valve settings indicated in Fig. 1.

Bulk cross incorporation will contribute to the roughness exhibited by our interface profiles, since a dark or bright substitutional defect may introduce single-cell discontinuities prejudicing our assignment of atoms to the InAs and GaSb layers, respectively. We can ascertain the influence this has on our results by examining an ensemble of *bulk profiles* (of standard length) through the GaSb layers in structure 2 and analyzing them in the same manner as our interface data. We find the associated “roughness” spectrum is “white”, and that the spectral density scales linearly with As defect density as shown in Fig. 3.

The scaling emphasized in Fig. 3 allows us to predict the spectral density associated with bulk cross incorporation in structure 1. So doing, we find that the combined Sb-in-InAs (4.5 %) and As-in-GaSb (2 %) defect concentrations account for less than half the interfacial white-noise observed in Fig. 2. This deficit indicates the presence of additional, *interface-specific* defects whose character and origin are still under investigation.

4. Conclusions

We have used XSTM to examine the microstructure of epitaxial GaSb/InAs interfaces formed under conditions routinely employed in the growth of mid-IR lasers. Atomic-resolution images reveal the presence of point defects in the anion sublattice that introduce a white-noise component to an otherwise Lorentzian interface roughness spectrum. We have identified arsenic cross incorporation as a source of bulk defects within the GaSb layers and quantified its influence on the interface roughness spectrum. When the combined effect of anion cross incorporation in both GaSb and InAs layers is properly accounted for, we find an excess white-noise spectral density which we attribute to interface-specific defects. The precise origin of these defects is not yet known.

Acknowledgement

This work was supported by a grant from the National Science Foundation, Division of Materials Research (DMR-9633011).

References

- [1] R. Q. Yang and S. S. Pei, *J. Appl. Phys.* **79**, 8197 (1996).
- [2] C. H. Lin, P. C. Chang, S. J. Murry, D. Zhang, *et al.*, *J. Electron. Mater.* **26**(5), 440 (1997).
- [3] C. H. Lin, R. Q. Yang, D. Zhang, S. J. Murry, *et al.*, *Electron. Lett.* **33**(7), 598 (1997).
- [4] C. H. Lin, S. J. Murry, D. Zhang, P. C. Chang, *et al.*, *Journal of Crystal Growth*, **175/176**, 955 (1997).
- [5] R. M. Feenstra, D. A. Collins, and T. C. McGill, *Superlattices and Microstructures*, **15**(2), 215 (1994).
- [6] S. L. Skala, W. Wu, J. R. Tucker, J. W. Lyding, *et al.*, *J. Vac. Sci. Technol. B* **13**(2), 660 (1995).
- [7] A. Y. Lew, S. L. Zuo, E. T. Yu, and R. H. Miles, *Appl. Phys. Lett.* **70**(1), 75 (1997).
- [8] S. M. Goodnick, D. K. Ferry, C. W. Wilmsen, Z. Liliental, D. Fathy, and O. L. Krivanek, *Phys. Rev. B* **32**, 8171 (1985).

Monolayer Scale Analysis of ZnSe/GaAs Heterointerface Structures by X-Ray CTR Scattering and Interference

Y. Takeda, K. Fujita, and M. Tabuchi

Department of Materials Science and Engineering, Graduate School of Engineering, Nagoya University, Nagoya 464-01, Japan

M. Funato, S. Aoki, Sz. Fujita, and Sg. Fujita

Department of Electronic Science and Engineering, Graduate School of Engineering, Kyoto University, Kyoto 606-01, Japan

Abstract. By x-ray CTR (crystal truncation rod) scattering and x-ray interference in ZnSe/GaAs heterostructures, Zn, Se, Ga and As distributions and crystal structures near the heterointerfaces were analyzed to the one monolayer level non-destructively. In Zn-initiated growth of ZnSe, several monolayers depth of interdiffusion of Ga/Zn and abrupt change of As and Se were observed. In Se-initiated growth, distribution of Ga-vacancy was observed, which means Ga_2Se_3 formation near the interface.

1. Introduction

Binary II-VI compound ZnSe has been grown on binary III-V compound GaAs because of close matching of lattice constants (ZnSe: 5.668 Å and GaAs: 5.653 Å) and availability of large area GaAs as the substrate for epitaxial growth (e.g. Gunshor and Nurmikko 1997). However, the difference in the valence of ZnSe and GaAs often nucleates stacking faults at the heterointerface, creates interfacial dipoles and highly doped regions and/or new phases such as Ga_2Se_3 by the mutual interdiffusion of host atoms near the heterointerface (e.g. Gunshor and Nurmikko 1997). Those interface structures should change depending on growth conditions of ZnSe on GaAs. Even though ZnSe/GaAs is a very important heterovalent structures, very little is known on the atom distributions at and near the heterointerface, which determine the electronic and energy structures at the interface.

We have conducted the x-ray CTR (crystal truncation rod) scattering measurement to reveal the atomic distribution at and near the heterointerface of ZnSe/GaAs grown by OMVPE with Zn-initiated and Se-initiated growth of ZnSe at 450°C. X-ray CTR is a rod (or a needle depending on the x-ray beam size) that appears around a Bragg diffraction spot in \mathbf{k} -space. It is caused by the abrupt truncation of a crystal at the surface and finite penetration depth of the x-ray (Robinson 1986, Kashiwagura et al. 1987). We have demonstrated that the x-ray CTR scattering with x-ray interference effect is a very powerful technique to reveal the layer structure, even the crystal structure in the layer, of the heteroepitaxially grown samples in the atomic scale and that a proper design of the layer structure enhances the CTR signal by one order of magnitude (Takeda et al. 1995, Tabuchi et al. 1995, Tabuchi et al. 1996a, b, Tabuchi et al. 1997, Fujita et al. 1997, Takeda et al. 1997).

In this paper, we report the measurement of x-ray CTR scattering and x-ray interference in ZnSe/GaAs heterostructures and non-destructive analysis of Zn, Se, Ga and As distributions and crystal structures near the heterointerfaces to the one monolayer level. Clear difference in the spectra in Zn-initiated growth and Se-initiated growth of ZnSe on GaAs was observed, and hence clear difference in the interface structures in Zn-initiated and Se-initiated growth was obtained from the analysis.

2. Experiments

2.1 Sample preparation

The samples were prepared by an atmospheric pressure OMVPE (Funato et al. 1997). TEGa and TBAs were used for the growth of GaAs and DEZn and DMSe were used for the growth of ZnSe. 3~5 nm-thick ZnSe layers were grown on GaAs (001) substrates with 150 nm-thick undoped GaAs buffer layers. Growth temperature was 700°C for GaAs, once lowered to 200°C to purge the precursor for GaAs out of the reactor and then raised to 450°C to grow ZnSe. Prior to the ZnSe growth, GaAs surface was exposed to a Zn flux (Zn-initiated growth) or a Se flux (Se-initiated growth) for 2~60 s.

2.2 X-ray scattering measurement

X-ray CTR spectrum measurement was conducted at the beam line BL6A₂ of the Photon Factory at Tsukuba using synchrotron radiation from the 2.5 GeV storage ring. The wavelength of the x-ray was set at 1.600 Å. The CTR spectrum extending from 004 Bragg point was recorded by a Weissenberg camera with IP (imaging plate) as a detector.

3. Results and discussion

To analyze the interface structures a model structure as shown in Fig. 1 was created from which a theoretical CTR spectrum was generated using a kinetic theory (Robinson 1986). In the model, those parameters such as n_{Zn} (number of Zn monolayers), n_{Se} (number of Se monolayers), d_{Zn} (distribution distance of Zn into Ga sublattices), d_{Se} (distribution distance of Se into As sublattices), d_{Ga} (distribution distance of Ga into Zn sublattices), d_{As} (distribution distance of As into Se sublattices), $x_{i\text{Zn}}$ (Zn composition at Zn/Ga interface), $x_{i\text{Se}}$ (Se composition at Se/As interface), $x_{h\text{Zn}}$ (Zn composition in ZnSe layer), $x_{h\text{Se}}$ (Se composition in ZnSe layer), and Ga-vacancy concentration which appears to form Ga_2Se_3 were considered. The distribution functions were assumed to be expressed as, e.g., in the case of Se distribution, $x_{h\text{Se}} = x_{i\text{Se}} \{1 - \text{erf}(n/d_{\text{Se}})\}$, where erf is the error function and n is the number of monolayer from the interface, i.e., the distance from the interface in units of monolayer. Other conventional parameters such as the surface roughness $\langle\Delta z^2\rangle$ and the lattice distortion are also considered as usual (e.g. Tabuchi 1996b). The values of these parameters were obtained at the best fit of the theoretical curve to each of the experimental spectra.

Figure 2 (a) shows the measured (background subtracted) CTR spectra by solid circles. Each spectra are shifted by two orders of magnitude for clarity and the bottom one is plotted at the real intensity. The horizontal axis is the index l of (001). Upper two spectra are from the samples with the Se-initiated growth and lower three spectra are from the samples with the Zn-initiated growth. Clear difference in both the lower index side and the higher index side of the spectra is observed for the Zn-initiated growth and the Se-initiated growth. The sharp drop around $l=4.02$ reached almost zero intensity in all the spectra. In Fig. 2 (a), the best-fit curves to the spectra without assuming Ga-vacancy are also drawn with thin dotted lines. Data around the Bragg peak ($l=4\pm0.01$) were not used for the fitting because the intensity may be too strong for the kinetic theory.

Figure 2 (b) shows the best-fit curves to the upper two spectra in Fig. 2 (b), i.e., of the

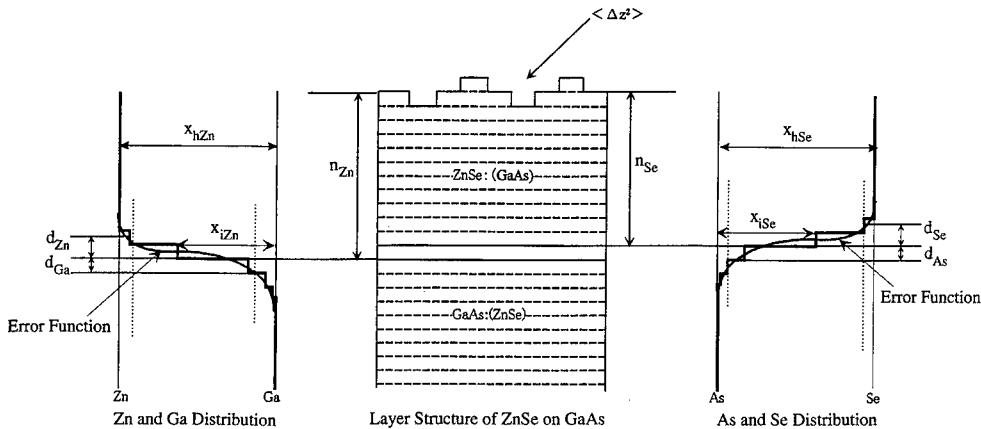


Fig. 1 Model structure for ZnSe/GaAs with Zn/Ga and Se/As interdiffusion near the interface. Central figure is the model layer structure with ZnSe on top of GaAs. Left curve is the distribution of Zn and Ga, and the right curve is the distribution of As and Se. The distribution curves were assumed to be the error function with distance from the interface as the variable. The symbols are explained in the text.

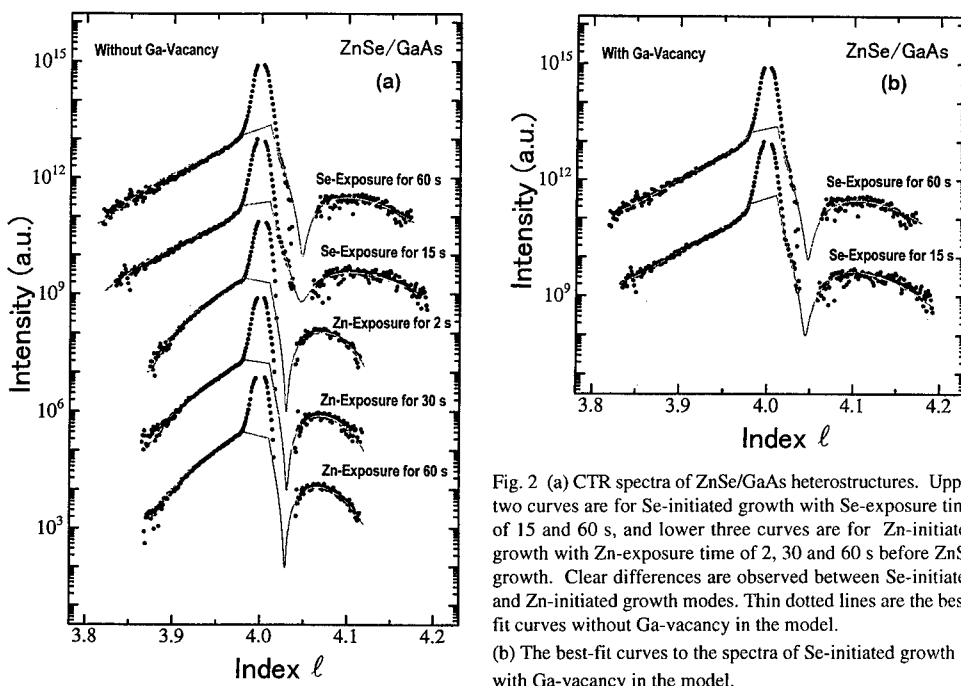


Fig. 2 (a) CTR spectra of ZnSe/GaAs heterostructures. Upper two curves are for Se-initiated growth with Se-exposure time of 15 and 60 s, and lower three curves are for Zn-initiated growth with Zn-exposure time of 2, 30 and 60 s before ZnSe growth. Clear differences are observed between Se-initiated and Zn-initiated growth modes. Thin dotted lines are the best-fit curves without Ga-vacancy in the model.

(b) The best-fit curves to the spectra of Se-initiated growth with Ga-vacancy in the model.

Se-initiated growth. In this theoretical curve Ga-vacancy was introduced, and much better fitting near the dip and in the lower index region was obtained.

The results of the analysis are summarized as follow: 1) In the Zn-initiated growth, it was found that the compositions of Zn and Ga at the II/III interface were 0.5 and 0.5, which means that there are no Ga-vacancy in the Zn-initiated growth. 2) In the Zn-initiated growth, several monolayers of diffusion of Ga into ZnSe and that of Zn into GaAs were observed, while As and Se distributions changed quite abruptly at the interface. 3) Considering the donor-like pair Ga-Se in the ZnSe layer and the acceptor-like pair Zn-As in the GaAs layer, dipoles were found to be formed very near the interfaces. 4) In the Se-initiated growth the Ga-vacancy distribution was found to result in a better curve-fitting to the CTR spectra. 5) The Ga-vacancy which is considered to form Ga_2Se_3 was found to distribute into the ZnSe layer for several monolayers.

4. Summary

X-ray CTR scattering measurements were conducted on ZnSe/GaAs samples grown by OMVPE with Zn-initiated and Se-initiated growth mode. Obviously different spectra for these two growth modes were observed. From the analysis of the spectra, Ga, As, Zn, Se, and Ga-vacancy distributions in these samples were obtained in the atomic scale. In the Zn-initiated growth mode, several monolayers of interdiffusion of Ga/Zn and abrupt change of As and Se were observed. In the Se-initiated growth mode, distribution of Ga-vacancy was observed, which means formation of Ga_2Se_3 near the interface.

Acknowledgments

This work was performed as a part of the project (Proposal No. 95G314) accepted by the Photon Factory Program Advisory Committee. This work was supported in part by the Grant-in-Aid for Scientific Research (A) No. 07555100 from the Ministry of Education, Science and Culture.

References

- [1] Fujita K, Tsuchiya J, Ichiki S, Hamamatsu H, Matsumoto N, Tabuchi M, Fujiwara Y and Takeda Y 1997 *Appl. Surf. Sci.* 117/118 785-9
- [2] Funato M, Aoki A, Fujita Sz and Fujita Sg (1997) *Japan. J. Appl. Phys.* 36 L4-7
- [3] Gunshor R L and Nurmiikko A V 1997 *II-VI Blue/Green Light Emitters: Device Physics and Epitaxial Growth* (San Diego: Academic Press)
- [4] Kashiwagura N, Kashihara Y, Sakata M, Harada J, Wilkins S W and Steven A W (1987) *Japan. J. Appl. Phys.* 26 L2026-9
- [5] Robinson I K 1986 *Phys. Rev.* B33 3830-6
- [6] Tabuchi M, Takeda Y, Sakuraba Y, Kumamoto T, Fujibayashi K, Takahashi I, Harada J and Kamei H 1995 *J. Cryst. Growth* 146 148-52
- [7] Tabuchi M, Fujibayashi K, Yamada N, Hagiwara K, Kobashi A, Kamei H and Takeda Y 1996a *Inst.. Phys. Conf. Ser.* 145 227-32
- [8] Tabuchi M, Yamada N, Fujibayashi K, Takeda Y and Kamei H 1996b *J. Electron. Mat.* 25 671-5
- [9] Tabuchi M, Fujibayashi KY, Yamada N, Takeda Y and Kamei H 1997 *J. Appl. Phys.* 81 112-5
- [10] Takeda Y, Sakuraba Y, Fujibayashi Y, Tabuchi M, Kumamoto T, Takahashi I, Harada J and Kamei H 1995 *Appl. Phys. Lett.* 66 332-4
- [11] Takeda Y, Fujita K, Matsubara N, Yamada N, Ichiki S, Tabuchi M and Fujiwara Y 1997 *J. Appl. Phys.* 82 635-8

Ballistic electron transport in semiconductor superlattices

G. Strasser, C. Rauch, K. Kempa* and E. Gornik

Solid State Electronics, TU Vienna, Floragasse 7, A-1040 Vienna, Austria

*Department of Physics, Boston College, Chestnut Hill, MA 02167

Abstract. An investigation of the electric field dependent transport through superlattice and multiple superlattice minibands is presented. A decrease of the miniband transmission with increasing electric field is observed in agreement with the results of a calculation based on a transfer matrix method. This observed behavior gives direct evidence for coherent transport through an undoped and biased GaAs/AlGaAs superlattice. The transconductance in 'broken gap' superlattices is used to probe interminiband transition rates above and below the optical phonon frequency.

1. Introduction

The electrical field dependent electron transport in undoped, biased GaAs/Ga_{0.7}Al_{0.3}As superlattices (SLs) and multiple superlattice structures (MLs) has been investigated. The ballistic hot electron spectroscopy technique [1,2] allows to measure the transmission through superlattice states under well defined bias conditions. The localization of electron wave functions of extended superlattice states as a function of the electric field in the superlattice [3, 4] is directly evident as a decreasing transmission.

Additionally, multiple superlattices were designed to measure transition probability between minibands. In these samples electrons can only pass through the multiple SL structure by a decay process, the direct nondissipative way is blocked. By measuring the transmission as a function of minigap size, transition probabilities and miniband (MB) lifetimes are derived.

2. Experimental Setup

A three terminal device [1] is used to probe the superlattice transmittance [2]. An energy tunable hot electron beam is generated by a tunneling barrier, passes the superlattice after traversing a thin highly doped n-GaAs base layer and an undoped drift region. Having the possibility to control the injected current independently from the superlattice bias field, the transmittance of the superlattice can be measured directly for a given superlattice bias. The calculated conduction band energy diagram of a typical hot electron transistor including band bending is sketched in figure 1 for a given bias condition. The injected tunable electron beam has a normal energy distribution of about 15 meV in width [5]. The collector current is measured as a function

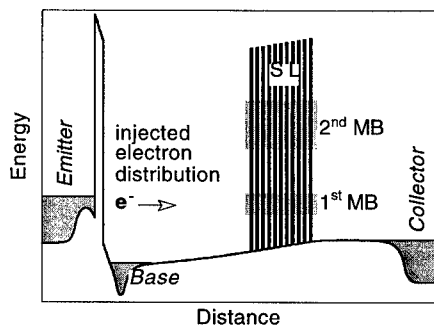


Figure 1: Schematic conduction-band diagram of the three terminal device, negative bias applied to the SL. conduction band energy diagram of a typical hot electron transistor including band bending is sketched in figure 1 for a given bias condition. The injected tunable electron beam has a normal energy distribution of about 15 meV in width [5]. The collector current is measured as a function

of the injection energy. The measured transfer ratio $\alpha=I_C/I_E$ is directly related to the transmission through the miniband under bias conditions.

3. Samples

The structures were grown by molecular beam epitaxy on a semi-insulating GaAs substrate: a highly doped n⁺-GaAs collector contact layer ($n=1\times 10^{18} \text{ cm}^{-3}$) is followed by a superlattice and the drift region, slightly n-doped ($n\sim 5\times 10^{14} \text{ cm}^{-3}$) in order to avoid undesired band bending. To reduce quantum mechanical confining effects originating from the quantum well formed by the emitter barrier and by the superlattice the drift region is chosen to be at least 200 nm in width. This is followed by a highly doped ($n=2\times 10^{18} \text{ cm}^{-3}$) n⁺-GaAs layer (base) of 13 nm width. On top of the base layer a 13 nm undoped Ga_{0.7}Al_{0.3}As barrier is grown followed by a spacer and a n⁺-GaAs layer, nominally doped to $n=3\times 10^{17} \text{ cm}^{-3}$, in order to achieve an estimated narrow normal energy distribution of the injected electrons of about 15 meV. It should be noted that the width of the injected electron beam limits the energy resolution of the experiment. Finally, an n⁺-GaAs contact layer ($n=1\times 10^{18} \text{ cm}^{-3}$) is grown on top of the heterostructure to form the emitter.

Different types of SLs were embedded into the hot electron transistor structure. All SL structures have 5 periods and are given in table 1.

sample No.	superlattice 1		superlattice 2		superlattice 3	
	barrier (Å)	well (Å)	barrier (Å)	well (Å)	barrier (Å)	well (Å)
single SL #1	25	65				
multiple SL #2	35	42.5	25	120	15	85
multiple SL #3	40	44	40	55	40	68

Table 1: Description of the single and multiple superlattice structures embedded into the three terminal device

The devices were fabricated using wet chemical etching of 20x20 μm^2 mesas. The ohmic contacts are formed using a standard AuGe/Ni alloy. All measurements are performed at liquid helium temperatures. The doping profiles were verified using a CV-etch profiler. For the single SL #1 a simple Kronig-Penney calculation gives the lowest miniband lying between 46 meV and 68 meV, and the second between 182 meV and 276 meV [6].

4. Results and Discussion

The static transfer ratio $\alpha=I_C/I_E$ of the single 5 period superlattice structure (SL #1) is measured as a function of emitter bias in a common base configuration for different collector biases (see Fig. 2). No collector current is observed up to the first transparent state of the first miniband, indicating that there is no significant leakage current between base and collector. The bold solid line represents the transfer ratio at flat band condition ($U_{BC}=0$). The sharp increase of the transfer ratio

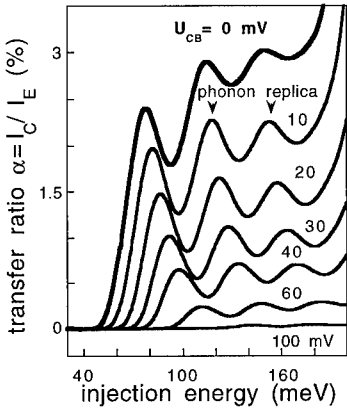


Figure 2: Transfer ratio at 4.2K versus injection energies of a single superlattice sample at different bias conditions.

applied electric field) has reached about half of the total superlattice length.

The experiment shows a symmetric decrease of the transmission for both bias directions indicating that the transport is purely ballistic and that no scattering is evident. This is in agreement with the result of a calculation based on a transfer matrix method using an envelope function approximation shown as solid line in Fig. 3. This experiment demonstrates for the first time clear evidence of coherent transport through electric field modified superlattice states.

The next step is to look at the transport through a superlattice where a transition between states is enforced by the presence of a “broken gap” SL. Two samples with different combinations of five period SLs were designed. In Fig. 5 the basic idea is indicated: electrons injected into the miniband on the left-hand side can only pass through the multiple SL structure by a decay process.

Figure 5 shows the transfer ratio versus injection energy of two different samples. Since the energy gap between the second and the lowest MB of sample #2 is of the order of the optical phonon energy, the inter-MB transition rate is mainly governed by LO-phonon emission. Sample #3 is designed in such a way that the gap between the MB is smaller the

at about 45 meV coincides very well with the lower edge of the first miniband which is calculated to be 46 meV. The peak due to ballistic transport through the first miniband is broader than the expected miniband width (22 meV) due to a superposition of the miniband and the injector width. Before the sharp rise at the second miniband position 2 phonon replica are seen separated by 36 meV, the origin of these replica is explained in greater detail in Ref. [2].

Figure 3 shows the transfer ratio of sample SL #1 as a function of positive and negative superlattice bias. An increased electric field leads to a decrease of the extend of the individual wavefunctions. The observed behavior is therefore in good agreement with a simple estimate for the quenching of the superlattice transmission which should occur when the localization length $\lambda \approx \Delta/eF$ (Δ is the miniband width, and F the

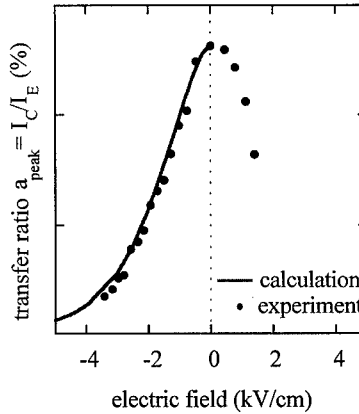


Figure 3: Measured (dots) and calculated (line) transfer ratio versus electric field.

optical phonon energy. The transfer ratio of #3 is found to be smaller by a factor of 20, thus giving a lifetime in the upper miniband 20 times larger than the optical phonon lifetime in the order of 10 ps.

The applied currents lead to current densities of less than one electron in the superlattice ($20 \times 20 \mu\text{m}^2$ mesa), making electron-electron scattering events very unlikely. Only 2 to 3% of the carriers are scattered in sample #3 in the overlapping region and contribute to the transmission current compared to the transmission of sample #2. Most of the electrons bounce back and are collected in the base region. However by biasing sample #3 with an electric field the superlattice transition energies are

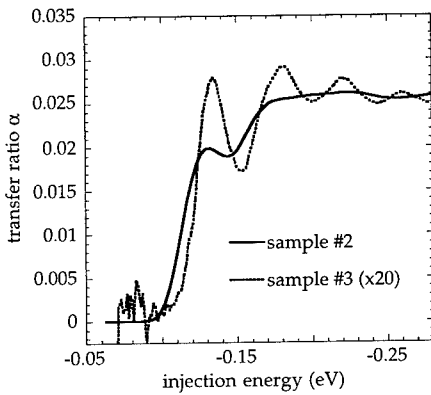


Figure 5: Transfer ratios of multiple SL #2 and #3.

decreases the transfer ratio similar to the case of the single SL sample #1 due to electric field induced localization.

Acknowledgment:

This work was partly supported by the Austrian Ministry of Science and Traffic, the Gesellschaft für Mikroelektronik, and the European Research Office of the US Army.

References:

- [1] Heiblum M, Nathan M I, Thomas D C, Knoedler C M, 1985 *Phys.Rev.Lett* 55 p 2200
- [2] Rauch C, Strasser G, Unterrainer K, Gornik E, Brill B, 1997 *Appl.Phys.Lett.* 70 p 649
- [3] Wannier G H, 1959 *Elements of Solid State Theory* (Cambridge University Press, London) p 190
- [4] Esaki L, Tsu R, 1970, *IBM J Res Dev* 14, p 61
- [5] Strasser G, Rauch C, Boxleitner W, Gornik E, to be published
- [6] Bastard G, 1983 *Phys.Rev.Lett* 24 p 5693

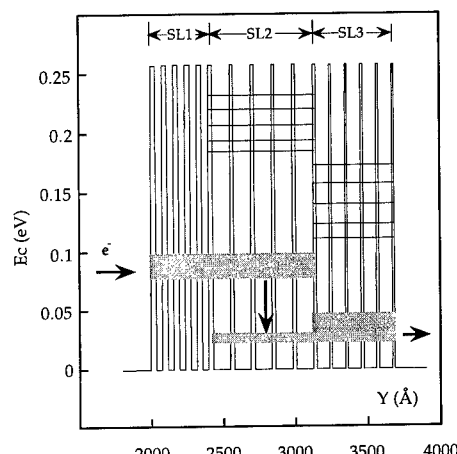


Figure 4: Bandstructure of multiple SL sample #2; arrows indicate the electron injection.

increased leading to an increase in the transfer ratio of more than one order of magnitude. When the increasing separation of the states in the minibands reaches transition energies close to the energy of optical phonons, fast interminiband transitions become possible, leading to a strong increase in the transfer ratio. Further increase of the applied voltage

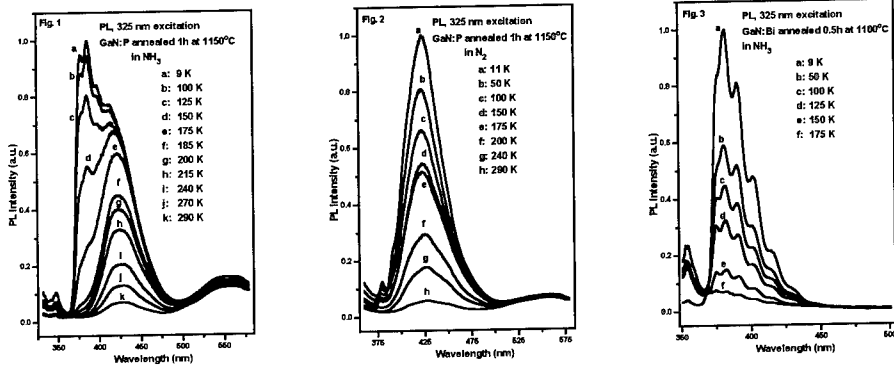
Photoluminescence from GaN Implanted with Isoelectronic Phosphorus and Bismuth.

W.M. Jadwisienczak and H.J. Lozykowski,

School of Electrical Engineering & Computer Science, and Condensed Matter & Surface Sciences Program, Ohio University, Stocker Center, Athens, OH, 45701

Photoluminescence spectra, excitation spectra and decay kinetics of epitaxial GaN layers grown by MOCVD on sapphire substrates and implanted by isoelectronic impurities P and Bi were investigated. Post implant annealing up to 1150 °C, and different duration time was done in a tube furnace under flowing NH₃ or N₂, using proximity cap method to recover implantation damages. The PL of GaN: P shows strong emission peaked at 423 nm - 428 nm with modulated structures that depend on annealing condition. The PL of GaN: Bi shows a luminescence transitions, observable at wide temperature range from 9 K to 300 K. Further, we develop the luminescence models that describe the recombination and quenching processes.

It is well known that isoelectronic impurities in semiconductors produce bound states in the forbidden gap, binding an electron or a hole. An isoelectronic center can form bound states because of a short range central-cell potential. The primary factors affecting the binding potential are the electronegativity and the size differences between the impurity and the host ion which it replaces. The Pauling's electronegativity of N, P and Bi are 3.04, 2.19 and 2.02 respectively. From experimental data the isoelectronic impurity potential is attractive to a hole or electron according to the electronegativity rule that states that impurities may bind a hole (electron) if its electronegativity is smaller (larger) than that of the host atom it substitutes. It is found experimentally that only very large atoms or very small atoms produce isoelectronic traps because they create large lattice distortion induced by the substitution. To create a large binding potential, the substituted atom must generate a noticeable change in the local properties of the lattice [1,2]. After an isoelectronic trap has captured an electron or a hole, the isoelectronic trap is negatively or positively charged, and by Coulomb interaction it will capture a carrier of the opposite charge creating a bound exciton. If the isoelectronic trap remains as a stable charged state after trapping an electron (hole) without producing a bound exciton, the trapped electron (hole) will recombine radiatively with a hole (or an electron) located at a distant acceptor (or donor). In this paper we discuss the isoelectronic traps in GaN semiconductors introduced by implanted P [3a,b] and Bi ions replacing the nitrogen. Photoluminescence spectra, excitation spectra, and PL kinetics of a high quality epitaxial GaN layers grown by MOCVD at CREE and EMCORE on sapphire substrates and implanted by isoelectronic impurities P and Bi were investigated. Post implant annealing at temperatures of up to 1150 °C, and at different duration of time was done in a tube furnace under flowing NH₃ or N₂, and a in rapid thermal annealing system in ambient of N₂ using the proximity cap method to recover implantation damages. The PL of GaN: P showed a strong emission peaked at 423 nm - 428 nm with modulated structures that depend on annealing conditions Fig.1,2. The PL of GaN: Bi shows a modulated luminescence spectra Fig.3 observable at wide temperature ranges from 9 K to 300 K (due to interference). The PL of GaN: P annealed at 1150 °C in NH₃ exhibits strong pair-type luminescence transitions overlapped with emissions of an exciton bond to the P isoelectronic trap which became dominant at 150 K Fig.1. From Fig.1 we obtained experimental evidence that under above bandgap excitation, there exists the pair type emission involving P isoelectronic traps and neutral donors and the emission band due to the recombination of excitons bound to phosphorus isoelectronic traps. With increasing temperature the pair emission decrease and vanished at 175 K, but the emission of excitons bound to a P isoelectronic trap is observed till room temperature. The new pair spectra are different from the ordinary donor- acceptor pair spectra, because an isoelectronic hole trap is neutral before the hole capture. The recombination process of an electron from an separate neutral donor with



Temperature dependance of PL GaN:P: Fig.1 annealed in NH₃, Fig.2 in N₂, and Fig.3 GaN:Bi annealed in NH₃.

a hole trapped on an isoelectronic trap is different from the normal donor-acceptor pair recombination. The recombination energy of an electron and hole bound to a donor - P isoelectronic pair does not have the Coulomb interaction term and is given by [4]:

$$\hbar\omega = E_g - E_l - (E_d + E_p) - m\hbar\omega_{phn} \quad (1)$$

where E_l and E_d are the binding energies of holes at isoelectronic traps and electrons at donors, and E_p is the electrostatic polarization interaction energy. The binding energy of the electron to the donor can be increased by interaction with the positive hole trapped at the neutral P isoelectronic trap. For a pair separation larger than the sum of radii of trapped electron and hole states, the interaction energy is

$$E_p = -[9 e^2/(4 \epsilon R_D)](R_D/r)^4 \quad (2)$$

where R_D is the ground state radius of the donor, r is the pair separation, and ϵ is the low frequency dielectric constant. From equations 1 and 2 it is seen that the transition energy will decrease if the donor ionization energy is increased ($E_d + E_p$). The energy shift due to the change of pair separation should increase with increasing excitation intensity. The shift should be toward lower energy with the increase of excitation intensity indicating that the isoelectronic-trap - donor pair transition energy decreases with decreasing pair separation. The magnitude of the energy shift calculated from equation 2 is $E_p \approx 0.16$ meV. This shift is much smaller and opposite to the ordinary donor-acceptor pair radiative transition energy shift. The intensity of the isoelectronic P (hole trap)- donor pair luminescence decreases quickly with increasing temperature Fig. 1a-d, and at 150 K spectrum d the dominant luminescence is attributed to P isoelectronic trap-bound exciton (P- BE) recombinations.

To optimize the PL intensity of GaN: P we investigated the development of the luminescence as the function of the post-implantation annealing process. The characteristic spectra of phosphorus (P) isoelectronic impurities were first observed after the annealed temperature reached 900 °C, and their intensity increased at each anneal at higher temperatures up to 1150 °C, at that temperature we stop the annealing process to avoid decomposition of the GaN samples. The variation of the emission peak positions

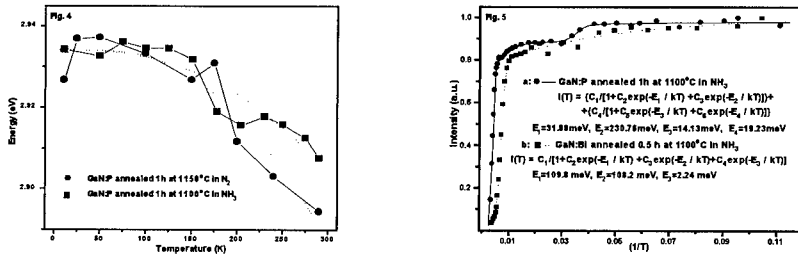


Fig.4 Temperature dependance of the emission peaks for GaN: P annealed in NH₃ ■ and in N₂ ●.
Fig.5 Temperature quenching of the PL of GaN: P and GaN: Bi.

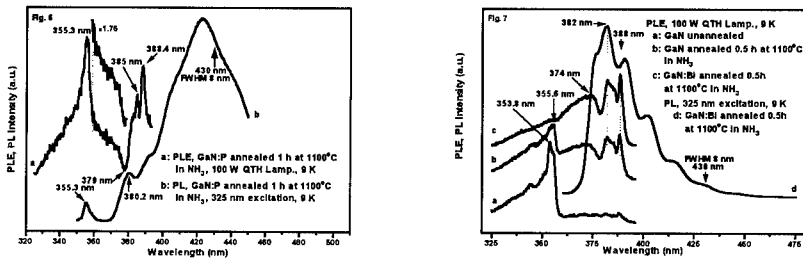


Fig.6 The PL emission and excitation spectra of GaN: P.
Fig.7 The PL emission and excitation spectra of GaN, GaN: Bi.

with temperatures for the spectra from Fig.1 is shown in Fig.4. The band emission of the exciton bound to P-isoelectronic trap is anomalous in variation of the emission peak position with temperature as shown in Fig.4. The maximum shift in that range of temperature is about 29 meV. Generally the peak position decreases as temperature increase, although not quite as fast as the bandgap which decreases in this same temperature range by 66 meV. In contrast GaN: Bi emission peaks not change position with temperature. The temperature dependency of the PL integral intensity for GaN: P, (Bi) annealed in NH₃ are plotted in Fig.5. The activation energies derived from best fit to equations shown considerable variation in the values of activation energies E_a determined from a larger number of samples.

The example of low-temperature photoluminescence excitation spectrum (PLE) from GaN: P epi-layer monitored at 430 nm, uncorrected for the spectral variation in the excitation intensity, is shown in Fig.6,7. Below the exciton peaks we can see a broad excitation band. This excitation band is attributed as the characteristic excitation band of the P-isoelectronic band appearing at 425 nm (2.917 eV). For this emission band peaking at 425 nm, the estimated zero-phonon line position, unobservable because of strong phonon coupling, is at the long-wavelength end of the excitation band at 379 nm (3.2709 eV).

Let us take the energy difference between the bandgap for GaN and the estimated zero-phonon line position to be a measure of the trapped exciton's binding energy [6]. This gives us a value of 232 meV. The binding energy for the exciton, localized at the P-isoelectronic trap 232 meV, is consistent with the value of a thermal dissociation energy ~230meV, obtained from the fitting of PL quenching shown in Fig.5a. The modulated D-A pairs like spectra visible on the short wavelength side of the emission spectrum of GaN: P (Fig.1) is attributed to recombination of the electron on the shallow native donor with a hole on

a phosphorus isoelectronic center (D-Iso pair). Taking the donor energy $E_d = 35.5$ meV [5], and zero-phonon line at 382 nm (Fig. 1) we obtained for the binding energy for the exciton localized at the P-isoelectronic trap 222 meV. This value is consistent with estimation of the binding energy for the exciton localized at the P-isoelectronic center. For the isolated P, Bi isoelectronic impurities the binding energy of a hole by short range potential can be described [7] by a three dimensional spherical potential well model with the potential depth $-V_0$ and the radius ρ_1 . The binding energy of an exciton to an isolated P impurity, a P pair or n-atomic P clusters is essentially equal to the binding energy of a hole to these clusters. To extend this model to the n atomic P clusters it is assumed that each P, Bi atoms in a cluster contribute the same potential well leading to a total potential well with unchanged depth and n times enlarged volume. The potential well is approximated by a spherical one with the same volume having the effective radius

$$\rho_n = n^{1/3} \rho_1$$

The binding energy for an exciton bound to an n atomic P cluster is given by

$$\epsilon_n = [(\hbar^2 \beta_n^2) / (2m^* \rho_n^2)] \quad (3a)$$

Where m^* is free (effective) mass of an electron. The β_n^2 must be calculated from the transcendental equation:

$$\beta_n = \{2m^* V_0 / \hbar^2 - \beta_n^2\}^{0.5} \operatorname{Cot} [\rho_n \{2m^* V_0 / \hbar^2 - \beta_n^2\}^{0.5}] \quad (3b)$$

Using above equations we can fit the experimental binding energy ϵ_1 for isolated P impurity but the two parameters' V_0 and ρ_1 in this simple model cannot be determined uniquely. If the experimental binding energies are known for isolated P impurity ϵ_1 and for phosphorus pair ϵ_2 , the two parameters can be found uniquely. In GaN the distances between like atoms is 0.3189 nm. Taking as m^* the free electron mass, and $\rho_1 = 3.6 \times 10^{-10}$ m, we can calculate the potential V_0 to fit experimental binding energy ϵ_1 . For the experimental binding energy 232 meV, the exciton localized at the P isoelectronic trap the two parameters are: $\rho_1 = 3.6 \times 10^{-10}$ m, and $V_0 = 1.397$ eV.

Acknowledgment.

The work was supported by the BMDO Contract No. N00014-96-1-0782, Ohio University P. Stocker Found and Ohio University CMSS Program.

- [1] A. Baldereschi 1973 J. of Lumin. 7 79
- [2] P. J. Dean 1973 J. of Lumin. 7 51
- [3] a) J.I. Pancove and J.A. Hutchby 1976 J. Appl. Phys. 47 5387,
b) R.D Metcalfe, D. Wickenden and W.C Clark 1978 J. of Lumin. 16 405-15
- [4] J. Dean, J.D. Cuthbert, and R.T. Lynch 1969 Phys.Rev. V.179 754
- [5] B.K. Meyer, D. Volum, A. Gruber, H.C. Alt, T. Detchprohm, A. Amano, and I. Akasaki 1975 Solid State Communications 95 597
- [6] D.M. Roessler 1970 J. Appl. Phys. 41 4589-4604
- [7] O. Goede, W. Heimbrodt, and R. Muller 1981 phys. stat. sol.(b) 105 543-550

Magnetoresistance and Cyclotron Mass in Extremely-Coupled Double Quantum Wells Under In-Plane Magnetic Fields*

M. A. Blount,[†] J. A. Simmons, S. K. Lyo, N. E. Harff, and M. V. Weckwerth

Sandia National Laboratories, Albuquerque, New Mexico 87185 USA

Abstract. We experimentally investigate the transport properties of an extremely-coupled AlGaAs/GaAs double quantum well, subject to in-plane magnetic fields (B_{\parallel}). The coupling of the double quantum well is sufficiently strong that the symmetric-antisymmetric energy gap (Δ_{SAS}) is larger than the Fermi energy (E_F). Thus for all B_{\parallel} only the lower energy branch of the dispersion curve is occupied. In contrast to systems with weaker coupling such that $\Delta_{SAS} < E_F$ we find: (1) only a single feature, a maximum, in the in-plane magnetoresistance, (2) a monotonic increase with B_{\parallel} in the cyclotron mass up to 2.2 times the bulk GaAs mass, and (3) an increasing Fermi surface orbit area with B_{\parallel} , in good agreement with theoretical predictions.

1. Introduction

Coupled double quantum well (DQW) systems have shown interesting transport properties under the application of an in-plane magnetic field, B_{\parallel} . Due to the presence of inter-well tunneling, B_{\parallel} causes the dispersion curves of the individual QWs to shift in k -space, and a partial energy gap to open at their anticrossing point, whose width is given by the symmetric-antisymmetric gap Δ_{SAS} of a balanced DQW at $B_{\parallel}=0$. The Fermi surface (FS) of this unusual system thus continuously evolves from two concentric circular orbits at $B_{\parallel}=0$, to a large hour-glass shaped orbit and a much smaller lens-shaped orbit at higher B_{\parallel} . In contrast to the constant density of states (DOS) exhibited by a single 2D electron layer, this system exhibits additional singularities in the DOS at the upper and lower edges of the anticrossing gap. [1] Because the energy position of the anticrossing gap depends on B_{\parallel} , the DOS singularities can be made to pass through the chemical potential μ , producing two large features, a minimum followed by a maximum, in the in-plane magnetoresistance. [2] Simmons *et al.* [3] previously measured the cyclotron mass m_c of electrons in the lens orbit by adding a small perpendicular magnetic field B_{\perp} and measuring the dependence of the Shubnikov-de Haas (SdH) oscillations on temperature T . The lens m_c was found to decrease strongly with B_{\parallel} , in agreement with theoretical calculations. [4] Lyo has also predicted that, in contrast to the lens orbit, electrons in the hourglass orbit will exhibit an m_c that *increases* with B_{\parallel} . [4] However, Simmons *et al.* were unable to reliably determine the m_c of electrons in the large area hourglass orbit over a significant field range, since the hourglass SdH oscillations were obscured by the much stronger SdH oscillations arising from the small area lens orbit.

In this work, we investigate the transport properties of an *extremely* coupled DQW: whereas in almost all DQW systems previously studied Δ_{SAS} was smaller than the Fermi energy E_F , in this work $\Delta_{SAS} > E_F$. Thus at $B_{\parallel} = 0$ the upper energy branch (or anti-symmetric sub-band) is entirely unoccupied. As a result, *for all B_{\parallel} only the lower energy branch, or hour-glass orbit, is occupied*, enabling its transport properties to be readily determined. This system displays markedly different behavior than a system with both branches occupied. (While Millard *et al.* [5] have recently studied a system with only lower branch occupation, the extreme built-in density imbalance between the two QWs makes interpretation of the data much less straightforward.) In contrast to Ref. 3, we find (1) a single peak in the in-plane

magnetoresistance at high B_{\parallel} , (2) an enhancement by more than a factor of two in the cyclotron mass of electrons in the lower branch, and (3) a steadily increasing FS orbit area. These results agree with the predictions of Lyo for a system with only the lower branch occupied.

2. Samples and experimental method

Our sample was grown by molecular beam epitaxy and consisted of two identical 125 Å GaAs quantum wells separated by a 10 Å $\text{Al}_{0.3}\text{Ga}_{0.7}\text{As}$ barrier. Self-consistent Hartree calculations on this structure without gate bias yielded a Δ_{SAS} of 8.5 meV. A metallic top gate was placed over the DQW in order to control the total density n . At gate voltage $V_G = 0.0$ V, the total mobility was $9.4 \times 10^3 \text{ cm}^2/\text{Vs}$, and n was $1.2 \times 10^{11} \text{ cm}^{-2}$, corresponding to an E_F of 4.3 meV. At $V_G = 0.5$ V the total mobility increased to $2.2 \times 10^4 \text{ cm}^2/\text{Vs}$, and n became $2.9 \times 10^{11} \text{ cm}^{-2}$, increasing E_F to 10.3 meV. Due to the conduction band minima offset, the upper-lower branch energy difference E_{u-l} became 12.8 meV. These values of E_F are both below the calculated E_{u-l} , therefore the upper energy branch is expected to be unoccupied for all B_{\parallel} . Fourier analysis of the SdH oscillations in a pure B_{\perp} show only one frequency component, verifying that only one energy branch is occupied. An in-situ sample tilting stage was used to introduce both B_{\parallel} and B_{\perp} components, enabling measurements of m_e . Magnetoresistance measurements were made via standard four terminal low frequency lock-in techniques at temperatures between 0.3 and 10 K.

3. Measurement results and discussion

3.1 In-plane magnetoresistance

Fig. 1(a) shows the in-plane magnetoresistance R_{xx} of the sample as a function of B_{\parallel} for $V_G = 0.0$ V and $B_{\perp} = 0$. While previous work [3] on samples with $\Delta_{\text{SAS}} < E_F$ showed two features, a large minimum followed at higher B_{\parallel} by a smaller maximum, this extremely coupled sample exhibits only a single feature, a large maximum, occurring at $B_{\parallel} = 10.8$ Tesla. The occurrence of only a maximum in the in-plane magnetoresistance can be understood by considering the action of B_{\parallel} on the shape of the dispersion

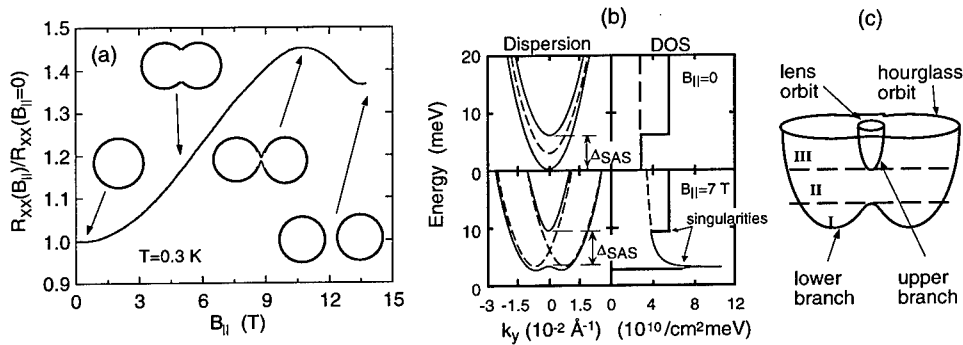


Fig. 1. (a) In-plane magnetoresistance of the extremely coupled DQW. Insets show sketches of the Fermi surface for different characteristic regions. (b) Sketch of dispersion (left) and density of states (right) for $B_{\parallel}=0$ (top) and $B_{\parallel} \approx 7$ T (bottom). (c) Sketch of dispersion, with the three different Fermi surface cases depending on the position of μ .

curve. Fig. 1(b) shows a sketch of both the dispersion and DOS for our density-balanced coupled DQW, for the two cases $B_{\parallel}=0$ and $B_{\parallel}\approx 7$ T. At $B_{\parallel}=0$, the symmetric (lower energy branch) and antisymmetric (upper energy branch) dispersions each form identical paraboloids offset by DSAS. The DOS at $B_{\parallel}=0$ is thus constant for each branch. The primary effect of a finite B_{\parallel} is to induce a linear shift $\Delta k_y = eB_{\parallel}/\hbar$ in the canonical momenta of electrons in one QW relative to those in the other, where d is the distance between the electron layers and B_{\parallel} is in the x -direction. The shifted dispersion curves then form an anticrossing gap of width Δ_{SAS} , yielding a highly non-parabolic dispersion. New singularities in the DOS appear at the upper and lower edges of this gap. The shape of the FS is given by the intersection of μ with the dispersion, as illustrated in Fig. 1(c). Three distinctly different cases occur, depending on the energy range in which μ falls: two separated Fermi circles (I); an hour-glass shaped orbit only (II); and both an hour-glass orbit and a much smaller lens-shaped orbit enclosed within it (III). As B_{\parallel} is increased, the gap rises in energy relative to μ . For samples with $\Delta_{\text{SAS}} < E_F$, the FS changes from case III to case II, and finally to case I. The magnetoresistance features occur at the two transitions between these three cases. When the upper edge of the energy gap crosses μ , a magnetoresistance minimum occurs. This is because a step decrease in the DOS exists at this point, causing an abrupt decrease in the available scattering states as electrons empty out of the lens orbit. [1,2] At higher B_{\parallel} the lower edge of the energy gap crosses μ . Because the lower gap edge is a saddle point in the dispersion, a logarithmic singularity in the DOS exists here, all of whose states have zero Fermi velocity. Electrons are thus rapidly scattered into these non-current-carrying states, producing a magnetoresistance maximum. In the extremely coupled DQW investigated here, however, $\Delta_{\text{SAS}} > E_F$. Thus μ never resides in region III, causing the upper energy branch to be unoccupied for all B_{\parallel} and yielding only a single feature in the magnetoresistance, a maximum corresponding to the lower gap edge crossing μ .

Using the model of Ref. 2 and assuming balanced densities in the two QWs, we estimate the B_{\parallel} at which we expect the maximum to occur. The lower edge of the anticrossing gap will cross μ when the momentum offset Δk_y is such that the undistorted QW dispersion curves cross at an energy $E_F + \Delta_{\text{SAS}}/2$. Hence $eB_{\parallel}/\hbar = 2[2m^*(E_F + \Delta_{\text{SAS}}/2)]^{1/2}/\hbar$. Using $d = 135$ Å, this yields a position of $B_{\parallel} = 11.9$ T, differing by only 10% from the experimental value.

3.2 Cyclotron mass

In order to measure m_c , the sample was rotated to $\theta=10^\circ$ from a purely B_{\parallel} so as to introduce a small B_{\perp} . For several different T , sweeps of total field B_T were then performed, resulting in simultaneous variation of $B_{\perp} = B_T \sin\theta$ and $B_{\parallel} = B_T \cos\theta$. The mass measurement was performed for both $V_G=0.0$ V and 0.5 V. Following Simmons *et al.* [3], m_c was extracted from the T -dependence of the SdH oscillation amplitude using a form of the Ando formula, $\Delta R(T)/\Delta R(T_0) = T \sinh[\beta T_0(m_c/m_0)/B_{\perp}] / T_0 \sinh[\beta T(m_c/m_0)/B_{\perp}]$. Here $\Delta R = R(B_{\perp}) - R(B_{\perp}=0)$, T_0 is the base temperature, $\beta = 2\pi^2 k_B m_0 / \hbar e$ and m_0 is the free electron mass.

Fig. 2(a) shows fits of this expression to the measured $\Delta R(T)/\Delta R(T_0)$ for $B_{\parallel} = 4.2$ and 9.7 T, at $V_G=0.5$ V, with m_c the only fit parameter. At 4.2 T the extracted value of $m_c = 0.069 m_0$ is very close to that of bulk GaAs, $m_{\text{GaAs}}^* = 0.067 m_0$. However, at 9.7 T we find that m_c has increased to $0.113 m_0$, or ~ 1.7 times m_{GaAs}^* . Repeating this procedure for several SdH extrema, in Fig. 2(b) we show m_c as a function of B_{\parallel} for the two V_G values. For $V_G=0.5$ V, m_c increases monotonically to ~ 1.7 times m_{GaAs}^* , while for $V_G=0$ V m_c reaches a value over 2.2 times m_{GaAs}^* . This is contrast to previous work, in which the lens orbit m_c decreased monotonically with B_{\parallel} , and the hourglass orbit m_c could not be fully determined. In the present work the absence of the lens orbit enables the ready determination of the hourglass m_c over a broad field range. Our data agrees well with the theory of Lyo for a DQW with only lower-branch occupation, as shown by tight-binding calculations for our sample (solid lines). [4]

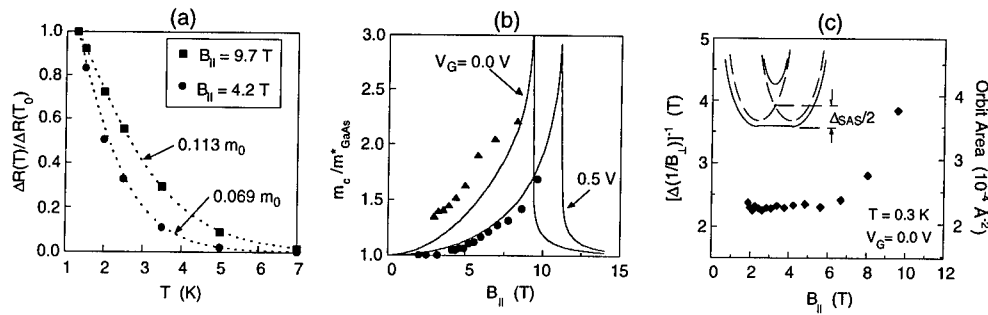


Fig. 2. (a) Amplitude of SdH oscillations vs. temperature at $B_{\parallel}=4.2$ and 9.7 T. Dotted lines show fits to the Ando formula, yielding $m_e=0.069$ and $0.113 m_0$ respectively. (b) Summary of mass data vs. B_{\parallel} for $V_G=0$ V (triangles) and 0.5 V (circles). Lines show theory. (c) Area of hourglass orbit vs. B_{\parallel} . Inset shows condition under which saddle point begins to form.

Although we could not reliably extract m_e for $B_{\parallel} > 10$ T, we expect that at higher B_{\parallel} the lower gap edge would cross μ , causing m_e to return to the bulk GaAs value. This has been observed in Ref. 5.

3.3 Fermi surface orbit area

We also measured the B_{\parallel} -dependence of the area in k -space of the hourglass orbit, given experimentally by $A = (2\pi e/\hbar)[\Delta(1/B_{\perp})]^{-1}$, where $\Delta(1/B_{\perp})$ is the reciprocal spacing of the extrema of the SdH oscillations. In Fig. 2(c) we plot A as a function of B_{\parallel} for $V_G=0$. The data shows a nearly constant area until about 7 T, after which it increases rapidly. At 9.7 T, A reaches a value over 60% larger than at 2 T. This increase in A with B_{\parallel} is in agreement with our picture of a system with lower branch occupation only. The hourglass orbit is elongated by the action of B_{\parallel} , causing a corresponding increase in the area. Again, this is in contrast to the previous measurements of Simmons *et al.*, [3] which allowed measurement of only the lens orbit area, since its strong oscillations obscured those of the hourglass orbit. In that work, the lens orbit area was shown to decrease with B_{\parallel} . We note that the hourglass orbit's area remaining relatively constant until ~ 7 T is also consistent with a large Δ_{SAS} : although the orbit will change shape at small values of B_{\parallel} , its area will not change significantly until the saddle point begins to develop. Roughly, this will occur when the momentum offset Δk_y is such that the two undistorted QW dispersion curves cross at an energy $\Delta_{\text{SAS}}/2$ above the dispersion minimum. That is, $\Delta k_y = edB_{\parallel}/\hbar = 2[m^*\Delta_{\text{SAS}}]^{1/2}/\hbar$. For $\Delta_{\text{SAS}}=8.5$ meV, this expression yields 8.5 T, in fair agreement with the data.

References

- * Sandia is a multiprogram laboratory operated by Sandia Corporation, a Lockheed-Martin Company, for the U. S. Dept. of Energy under Contract DE-AC04-94AL85000.
- [†] Also at Department of Physics and Astronomy, University of New Mexico, Albuquerque New Mexico 87131 USA
- [1] Lyo S K 1994 *Phys. Rev. B* 50 4965.
- [2] Simmons J A *et al.* 1994 *Phys. Rev. Lett.* 73 2256.
- [3] Simmons J A *et al.* 1995 *Phys. Rev. B* 51 11156
- [4] Lyo S K 1995 *Phys. Rev. B* 51 11160.
- [5] Millard I S *et al.* 1997 *J. Phys.: Condens. Matter* 9 1079.

Band Offsets in Near-GaAs Alloys

M.F. Whitaker, D.J. Dunstan and M. Hopkinson*

Department of Physics, Queen Mary and Westfield College, University of London, Mile End Road, London E1 4NS, UK.

*Department of Electronic and Electrical Engineering, University of Sheffield, Mappin Street, Sheffield S1 3JD, UK.

Abstract. We determine the band offset ratio of GaAs/GaXAs heterostructures, where X is any alloying element (e.g. In, Al, P, Sb), by studying GaXAs/AlGaAs superlattices. Photoluminescence is measured at both ambient and high pressure from GaAs and GaXAs quantum wells and this yields the band offset ratio of the GaXAs/GaAs interface. To confirm the technique, the band offset ratio of GaAs/AlGaAs is determined in this paper using this general method, and the result agrees well with previously published data obtained more directly.

1. Introduction

With the increasing diversity of heterostructures used in advanced semiconductor devices and the need to characterise their electronic band structures, a general method for determining band-offset ratios is becoming important. The general method demonstrated here can be applied to any GaXAs/GaAs interface, where X is an alloying element (e.g. In, Al, P, Sb), and can also be extended to a wider range of compounds and alloys. We have previously reported the band offsets of InGaAs/GaAs using InGaAs/AlGaAs superlattices [1]. Here we determine the band offset ratio of GaAs/AlGaAs heterostructures directly by comparing GaAs/AlGaAs and AlGaAs/AlGaAs superlattices.

In 1986, using a direct but not generally applicable method, Wolford et al [2] reported the band offset ratio of GaAs/AlGaAs to be 68 : 32 and Venkataswaran et al [3] reported it to be 70 : 30 ($Q_c : Q_v$). In this paper we apply our general method to GaAs/AlGaAs and find good agreement, thus demonstrating the validity of the general method.

2. Experimental Details

The samples were grown by molecular beam epitaxy (MBE) at the EPSRC III-V Central Facility in Sheffield. One sample consisted of 20 repeats of an 80Å GaAs quantum well in 150Å Al_{0.30}Ga_{0.70}As barriers. The other was identical to the first apart from having Al_{0.10}Ga_{0.90}As alloy quantum wells. To achieve the Al_{0.10}Ga_{0.90}As quantum well, a short period superlattice was grown, consisting of 1 × Al_{0.30}Ga_{0.70}As + 2 × GaAs monolayers. Relatively thick quantum wells were used so that the corrections for quantum confinement would be small.

The experiments were carried out in a miniature diamond anvil cell at 10K using our standard techniques [4]. The cell was loaded with argon as the pressure transmitting medium and a piece of In_{0.53}Ga_{0.47}As was used for pressure calibration. Photoluminescence was excited by a few mW of 514nm argon ion laser radiation.

3. Results and Discussion

Photoluminescence was measured at ambient pressure from both the GaAs quantum wells and the $\text{Al}_{0.10}\text{Ga}_{0.90}\text{As}$ quantum wells. From figure 1, the difference in energy between the $\text{Al}_{0.10}\text{Ga}_{0.90}\text{As}(\Gamma-\Gamma)$ transition and the $\text{GaAs}(\Gamma-\Gamma)$ transition, $E_3 - E_1$, is the total band offset energy, ΔE_g , in a GaAs/AlGaAs heterostructure. The pressure was increased to above Γ -X crossover so the photoluminescence transitions occurred between the $\text{Al}_{0.30}\text{Ga}_{0.70}\text{As}$ X level in the barrier and the Γ valence band level in the quantum well. The difference in energy between the two transitions, $\text{Al}_{0.30}\text{Ga}_{0.70}\text{As}(X)-\text{Al}_{0.10}\text{Ga}_{0.90}\text{As}(\Gamma)$ and $\text{Al}_{0.30}\text{Ga}_{0.70}\text{As}(X)-\text{GaAs}(\Gamma)$, or $E_4 - E_2$ as shown in figure 1, is the band offset energy in the valence band, ΔE_v . The band offset in the conduction band, ΔE_c , is simply the difference between ΔE_g and ΔE_v .

Because of the sub-linearity of band-gaps with pressure we have plotted our data as a function of unit cell density, calculated using the Murnaghan equation [5], (see figure 2). Linear plots against pressure and against lattice constant are commonly used, but it was found that different workers' data sets were best reconciled if plotted against density [6].

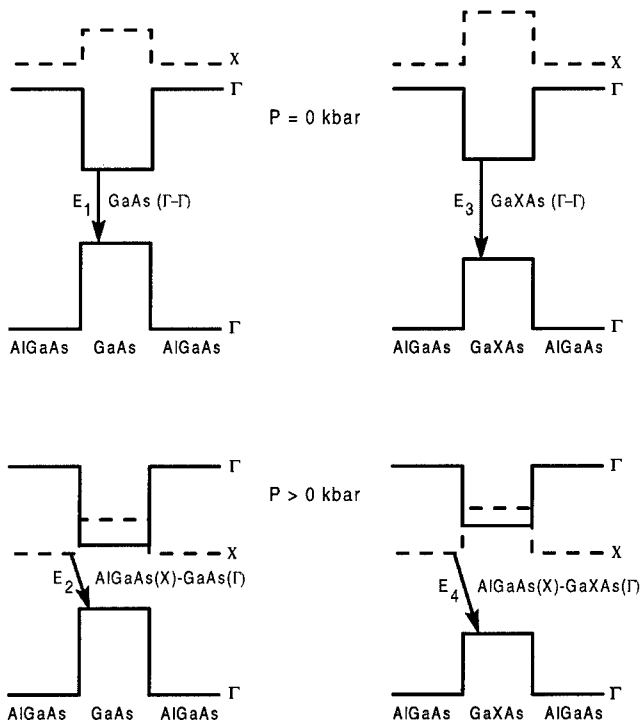


Fig.1: Photoluminescence transitions at ambient pressure and at a pressure above Γ -X crossover, for a GaAs/AlGaAs sample and a GaXAs/AlGaAs sample, ($X = \text{Al}_{0.10}$). The total band offset energy for GaAs/AlGaAs is $E_3 - E_1$, and the valence band offset energy is $E_4 - E_2$. Confinement energies are omitted for clarity.

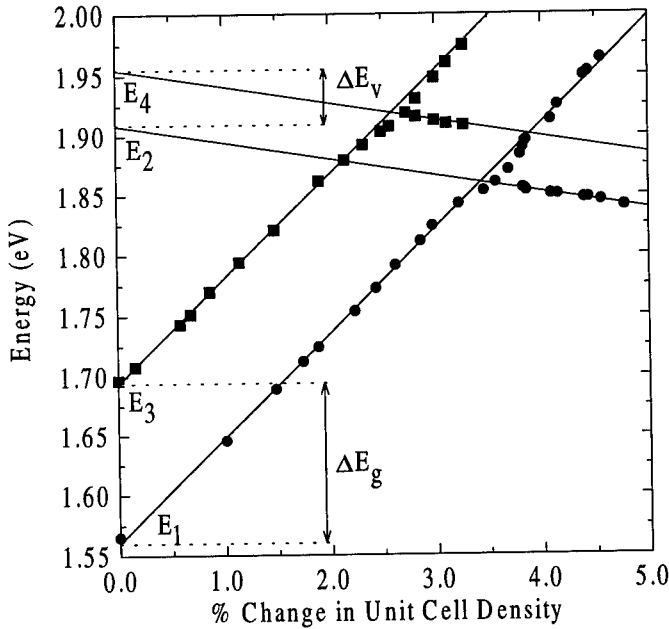


Fig.2: The photoluminescence peak energies of the GaAs/Al_{0.30}Ga_{0.70}As (circles) and Al_{0.10}Ga_{0.90}As/Al_{0.30}Ga_{0.70}As (squares) samples, plotted as a function of percentage change in unit cell density. The energies $E_4 - E_2 = \Delta E_v$ and $E_3 - E_1 = \Delta E_g$ which give the band offset ratio, are shown.

At ambient pressure strong photoluminescence peaks, with linewidths of a few meV, were observed from the quantum wells of the two samples. The difference in energy between these two peaks is the difference between the Al_{0.10}Ga_{0.90}As and GaAs band gap, ΔE_g , (shown on figure 2). Pressure was then applied until the Γ level in the quantum wells crossed with the X level in the barrier. The photoluminescence was observed to quench strongly, and the emission peak began to move slowly to longer wavelength. Also observed were some weak defect related bands which limited the range over which the indirect X- Γ emission could be followed. The valence band offset, ΔE_v , of the GaAs/Al_{0.10}Ga_{0.90}As, shown in figure 2, is the difference between the indirect transition energies of the two samples extrapolated back to 0kbar. The straight line fits in the plot are calculated by using a least squares fitting routine over the initial linear portion of the plot before any perturbation from the crossing with the X level. The pressure under which the two samples are measured is subject to a significant experimental error, so the fits to the Γ related emission have been rescaled to give the same slope, as have the fits to the X related data.

From the fits in figure 2, $E_2 = 1.909\text{eV} \pm 3\text{meV}$ and $E_4 = 1.955\text{eV} \pm 3\text{meV}$. The errors are determined from the intercept error given by the least squares fit. Correcting for small valence band confinement energies of $E_{2v} = 7.9\text{meV}$ and $E_{4v} = 7.6\text{meV}$, the valence band offset is

$$\Delta E_v = (E_4 - E_{4v}) - (E_2 - E_{2v}) = 47 \pm 5 \text{ meV}$$

Similarly, E_1 is $1.561\text{eV} \pm 2\text{meV}$ and E_3 is $1.694\text{eV} \pm 1\text{meV}$. Thus the direct energy difference at Okbar, with additional corrections for confinement energies in the conduction band of $E_{1c} = 62.7\text{meV}$ and $E_{3c} = 53.3\text{meV}$, gives a total band offset energy of

$$\Delta E_g = (E_3 - E_{3c} - E_{3v}) - (E_1 - E_{1c} - E_{1v}) = 143 \pm 2 \text{ meV}$$

so the conduction band offset is simply

$$\Delta E_c = \Delta E_g - \Delta E_v = 96 \pm 5 \text{ meV}$$

yielding a band offset ratio of $Q_c : Q_v = 67 : 33 \pm 3$ which is in excellent agreement with the previous reported results of $68 : 32$ [2] and $70 : 30$ [3].

An additional source of error is introduced if the fits to the X related data are not forced to have the same slope. In this case, extrapolations of the separate fits to Okbar gives $E_2 = 1.909\text{eV}$ and $E_4 = 1.962\text{eV}$ and a band offset ratio of $62 : 38$, so that alternatively, an average result of $65 : 35 \pm 5$ is obtained.

4. Conclusions

We present data demonstrating the validity of this general method for obtaining band offsets for any pair of near-GaAs alloys. A band offset ratio for GaAs/AlGaAs, using AlGaAs barriers, was determined to be $67 : 33$ ($Q_c : Q_v$), in excellent agreement with previously reported results. The main source of error in the technique is still the difficulty in identifying the weak X-related transitions above crossover, and the consequent uncertainty in the extrapolation to Okbar. Additional error is also introduced by the need for using two different samples which have to be measured in separate experiments. Both errors will be eliminated when growth problems have been overcome so that the X-related zero phonon line and phonon replicas are clearly visible, and the two different sample structures can be incorporated into one structure.

Once the difficulties of growing suitable structures have been overcome, the general method is directly applicable to GaAsSb/GaAs, GaInAsP/GaAs etc. If suitable "marker" barrier X levels are identified, the method would extend to near-InP compounds and many others. While the necessary GaXAs growth may be problematic we have shown that short period superlattices can be adequate substitutes.

Acknowledgements We would like to thank the EPSRC for financial support, and Dr M. Missous and Dr L. Gonzalez for valuable collaboration in the growth and design of suitable samples.

References

- [1] M.F. Whitaker, D.J. Dunstan, M. Missous and L. Gonzalez, Phys. Stat. Sol. (b) **198**, 349 (1996).
- [2] D.J. Wolford, T.F. Keuch, J.A. Bradley, M.A. Gell, D. Ninno and M. Jaros, J. Vacuum Sci. Technol. B **4**, 1043 (1986).
- [3] U. Venkateswaran, M. Chandrasekar, H.R. Chandrasekar, B.A. Vojak, F.A. Chambers and J.M. Meese, Phys. Rev. B **33**, 8416 (1986).
- [4] I.L. Spain and D.J. Dunstan, J. Phys. E **22**, 923 (1989).
- [5] F. Murnaghan, Proc. Nat. Acad. Sci. U.S.A. **30**, 244 (1944).
- [6] M.D. Frogley, J.L. Sly and D.J. Dunstan (to be published).

Time-resolved photoluminescence of ZnS_xSe_{1-x} ($0 < x < 0.12$) epilayers on GaAs grown by MBE

Eun-joo Shin, Joo In Lee, Dongho Kim, Jeong-Sik Son*, Jae-Young Leem*, Sam Kyu Noh*, Donghan Lee[†]

Spectroscopy Laboratory, Korea Research Institute of Standards and Science, Daedok Science Town, Taejon 305-600, Korea, *Thin Film Laboratory, Korea Research Institute of Standards and Science, Daedok Science Town, Taejon 305-600, Korea, [†]Department of Physics, Chungnam National University, Taejon 305-764, Korea

Abstracts. We have reported steady-state and time-resolved PL studies of ZnS_xSe_{1-x} epilayers grown on GaAs substrate by molecular beam epitaxy with various sulfur compositions around the lattice matching composition ($0 < x < 0.12$). We have investigated the PL decay dynamics of ZnS_xSe_{1-x} epilayers, and found that the decay time of the ZnS_xSe_{1-x} epilayer with sulfur composition closely lattice-matched with the substrate is longer than that of any other lattice-mismatched one. This is interpreted as indicating that the crystalline defects induced by lattice mismatch with the substrate mainly act as nonradiative recombination centers and consequently reduce the PL lifetimes of the epilayers. These studies suggest that the lattice mismatch has a strong correlation with PL lifetimes of the ZnS_xSe_{1-x} epilayers.

1. Introduction

The steady-state and time-resolved photoluminescence (PL) studies of ZnS_xSe_{1-x} epilayers on GaAs substrate grown by molecular beam epitaxy around the lattice matching composition ($0 < x < 0.12$) are discussed. The primary focus of this work is on determining the influence of crystal defects mainly induced by lattice mismatch on the PL lifetimes for ZnS_xSe_{1-x} epilayers grown on GaAs. Little is known about the excitonic recombination lifetime in ZnS_xSe_{1-x} epilayers. To our knowledge, we have firstly observed the PL decay times of ZnS_xSe_{1-x} epilayers through time-resolved PL measurements.

2. Experiment

The ZnS_xSe_{1-x} /GaAs structures under investigation were grown in a dual-chamber RIBER 32P MBE system. Undoped GaAs buffer layers with a thickness of 500 nm were grown at 560 °C on (100)-oriented GaAs substrate. The undoped ~ 0.6 μm thick ZnS_xSe_{1-x} ($0 < x < 0.12$) epilayers were deposited at 300 °C on the GaAs buffer. The sulfur composition was determined by double-crystal X-ray diffractometry (DCXD). Time-correlated single photon counting (TCSPC) system has been employed to study the exciton dynamics of the ZnS_xSe_{1-x} epilayers. The excitation source is a picosecond dual-jet dye laser (Coherent 702) with a cavity dumper (Coherent 7220) at 3.8 MHz pumping rate. The instrumental response function of our TCSPC system was typically 55 ps, which gives about 10 ps time resolution through deconvolution technique.

3. Results and Discussions

Fig. 1(a) shows the PL spectra of the $\text{ZnS}_x\text{Se}_{1-x}$ epilayers grown on GaAs substrate with various sulfur compositions ($0 < x < 0.12$) at 12 K. The two peaks of free exciton (FE) and donor bound exciton (DBE) emissions with different intensities were observed for each sample. The full width at half maximum (FWHM) of DBE and FE emission bands of each sample are nearly 3.5 meV, indicating that the crystallinity of the epilayers is similar to each other. The origins for free and bound exciton emissions were identified through the temperature and excitation dependent PL measurements shown in Fig. 1(b) and (c). As the temperature increases, the bound excitonic PL lines disappear (near 70 K) because the binding energy of the exciton bound to the impurity is smaller than the free exciton binding energy. The measured energy difference between FE and DBE emission is nearly the same for each sample (5 ~ 6 meV) and can be considered to be the binding energy of DBE which corresponds to the exciton emissions bound to neutral donors weakly. The excitation intensity dependent PL spectra show that the intensity of FE emission was found to increase more than that of DBE with increasing the excitation intensity. The temperature and laser excitation intensity dependent PL measurements were carried out using the 325 nm line of a cw He-Cd laser and various neutral density filters. In addition we observed that the PL intensity of DBE emission became weaker as sulfur composition x increases. Hence the enhancement of the FE emission for the sample with higher sulfur composition is likely attributable to the localization of free excitons due to an increase in alloy fluctuation. The potential fluctuation of alloy disorder could create the free excitons in a localized state. These excitons may have low probability to meet nonradiative decay centers, and result in large oscillator strengths for optical transitions.

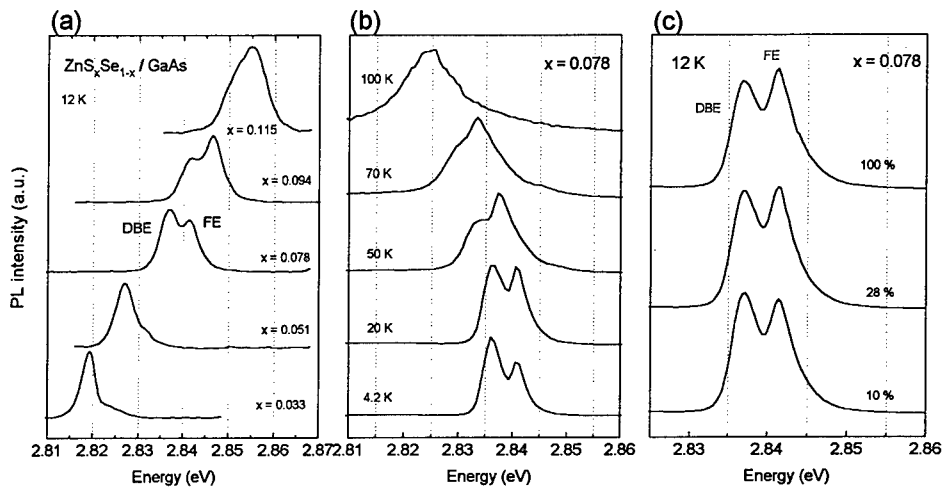


Fig. 1. (a) PL spectra of the $\text{ZnS}_x\text{Se}_{1-x}$ epilayers on GaAs substrate with various sulfur compositions ($0 < x < 0.12$) at 12 K. DBE and FE represent the donor bound exciton and free exciton emissions, respectively. (b) Temperature dependent PL spectra of $\text{ZnS}_x\text{Se}_{1-x}$ epilayers ($x = 0.078$) (c) Laser excitation intensity dependet PL spectra of $\text{ZnS}_x\text{Se}_{1-x}$ epilayers ($x = 0.078$)

Fig. 2 illustrates the PL decay profiles for both free exciton and donor bound exciton emissions observed in the ZnS_xSe_{1-x} ($x = 0.062$) epilayer at 12 K. The PL decay times for DBE and FE emissions of ZnS_xSe_{1-x} ($x = 0.062$) epilayer were found to be around 140 and 130 ps, and the risetimes of about 90 and 30 ps, respectively. In the case of an $\sim 1 \mu\text{m}$ thick ZnS_xSe_{1-x} epilayer ($x = 0.062$) with the same PL FWHM value, the measured PL decay times were around 250 and 210 ps for DBE and FE emissions, respectively. The faster PL decay time of $\sim 0.6 \mu\text{m}$ thick epilayer as compared with that of $\sim 1 \mu\text{m}$ thick sample is probably associated with the surface recombination effect [1]. It has to be pointed out that the measured PL decay time does not provide a direct measurement of radiative lifetime, and represents an effective carrier lifetime (τ_{eff}) for free excitons and bound excitons. It can be expressed as a combination of radiative (τ_R) and nonradiative (τ_{NR}) recombination lifetimes with the decay rate given by $1/\tau_{\text{eff}} = 1/\tau_R + 1/\tau_{\text{NR}}$. For the cases where the nonradiative decay rate is larger than the radiative one, the measured decay time follows the characteristic of the nonradiative processes such as multiphonon emission or capture of free excitons at defects and impurities. The risetime of PL contains information concerning the dynamics of the formation of excitons from the initially photogenerated electron-hole pairs. Since the excitation energy ($\sim 4.2 \text{ eV}$) is above the band gap of the ZnS_xSe_{1-x} epilayers ($\sim 2.9 \text{ eV}$), we can anticipate a finite rise of the FE emission due to the relaxation of excitons with excess energies. In addition, we have observed the longer risetime of the DBE emission than that of the FE whose energy is only $5 \sim 6 \text{ meV}$ apart from the DBE emission. The slow rise of the DBE emission probably reflects the relaxation of the FE into the DBE energy by nonradiative relaxation processes such as interaction with acoustic phonons.

In Fig. 3(a) the sample with $x = 0.051$ composition was observed to have the longer decay time, $\sim 170 \text{ ps}$, than those with $x = 0.033$ and 0.094 for which decay times are around 110 and 120 ps, respectively. The composition dependent decay times of DBE and FE emissions for the ZnS_xSe_{1-x}

($0 < x < 0.12$) epilayers are summarized in Fig. 3(b). The ZnS_xSe_{1-x} epilayer is known to be lattice-matched with GaAs substrate for the composition x of ~ 0.055 at room temperature [2,3] and of ~ 0.08 at growth temperature around 340°C [4,5]. And it was reported that the lattice matching sulfur composition x at 11 K is almost the same as that at room temperature as expected from the thermal expansion coefficients [4]. As illustrated in Fig. 3(b), the decay time of the ZnS_xSe_{1-x} epilayer with $x = 0.051$, which is close to the lattice matching sulfur composition, is slower than that of any other sample. There are pre-existing defects originated from the II-VI/III-V interface during the growth.

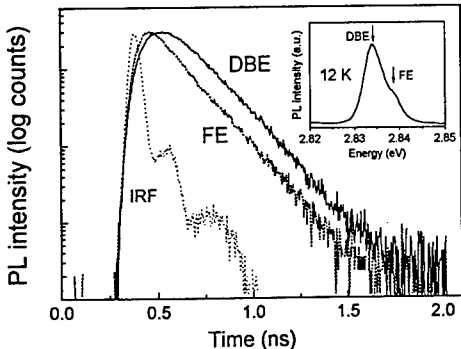


Fig. 2. PL decay profiles for DBE and FE emissions observed in the ZnS_xSe_{1-x} epilayers ($x = 0.062$) at 12 K.

But the defects such as misfit dislocations caused by the lattice mismatch would be dominant in the PL decay for ZnS_xSe_{1-x} epilayer, where its thickness ($\sim 0.6 \mu\text{m}$) is larger than the critical thickness ($\sim 0.2 \mu\text{m}$) [4,6] from which the strain starts to relax by nucleation of misfit dislocations. This suggests

that the longer PL lifetimes for the $\text{ZnS}_x\text{Se}_{1-x}$ epilayers with sulfur composition closely lattice-matched with GaAs substrate arises from the decrease of crystalline defects which are mainly induced by the lattice mismatch. On the other hand, the crystal defects such as stacking faults and misfit dislocations provide nonradiative deactivation centers for the decay of excitonic emission in the lattice-mismatched $\text{ZnS}_x\text{Se}_{1-x}$ epilayers

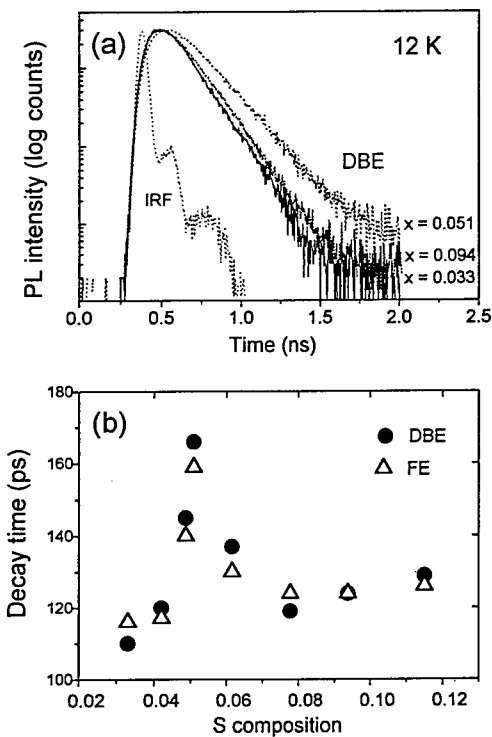


Fig 3.(a) PL decay profiles for DBE emission in the $\text{ZnS}_x\text{Se}_{1-x}$ epilayers with various sulfur compositions of $x = 0.033, 0.051$ and 0.094 at 12 K . (b) Sulfur composition dependence of decay times for DBE and FE emissions in the $\text{ZnS}_x\text{Se}_{1-x}$ epilayers on GaAs substrate at 12 K .

4. Summary

The steady-state and time-resolved photoluminescence (PL) studies of $\text{ZnS}_x\text{Se}_{1-x}$ epilayers on GaAs substrate grown by molecular beam epitaxy around the lattice matching composition ($0 < x < 0.12$) are discussed. The fast decay for both free exciton and bound exciton emissions suggest that the exciton lifetimes in the $\text{ZnS}_x\text{Se}_{1-x}$ epilayers are governed by nonradiative relaxation processes. The PL lifetime is longer for the sample with sulfur composition which is closely lattice-matched with the substrate than for any other lattice-mismatched one. It is considered that the crystalline defects such as misfit dislocations induced by lattice mismatch with the substrate mainly act as nonradiative recombination centers and consequently reduce the PL lifetimes of the epilayers. As a result of our empirical assignments, we have deduced that a precise lattice matching is needed to obtain crystals which have a longer PL lifetime in the $\text{ZnS}_x\text{Se}_{1-x}/\text{GaAs}$ system.

References

- [1] Zhao Y -G *et al.* 1996 *Appl. Phys. Lett.* **68** 696
- [2] Jeon H *et al.* 1991 *Appl. Phys. Lett.* **59** 3619 ; Okuyama H *et al.* 1992 *Electron. Lett.* **28** 1798
- [3] Matsumura N *et al.* 1988 *J. Crystal Growth* **86** 311
- [4] Matsumura N *et al.* 1989 *J. Crystal Growth* **95** 525
- [5] Matsumura N *et al.* 1990 *Jpn. J. Appl. Phys.* **29** L221
- [6] Wolf K *et al.* 1995 *J. Cryst. Growth* **152** 34

Whole Wafer Characterization of Large Size GaAs-AlGaAs Semiconductor Materials Prepared by MOCVD *TurboDiscTM* Technology

Z. C. Feng, E. Armour, A. G. Thompson, and R. A. Stall

EMCORE Corporation, 394 Elizabeth Avenue, Somerset, NJ 08873, USA

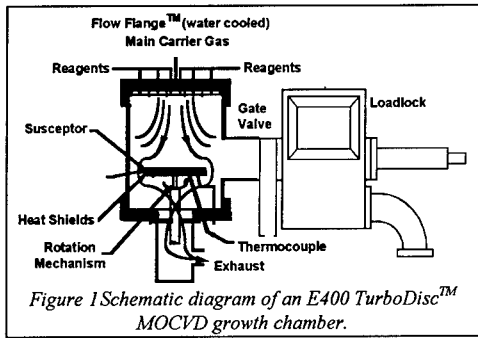
Abstract. GaAs-AlGaAs III-V compound semiconductor materials and structures have many applications for electronic and optoelectronic devices. Large diameter wafers from epitaxial growth of these materials with high quality and high uniformity are in great demand. Non-destructive and whole wafer characterizations are very necessary for these materials in mass production industry environment. In this study, we demonstrate the low pressure MOCVD growth and non-destructive materials characterization on 100 mm (4") diameter wafer epitaxial films of GaAs, AlGaAs, and quantum well structures. A series of mapping distributions of the film thickness, sheet resistivity, and PL spectra within a run and run to run are illustrated. Uniformities of our epitaxial film thickness, sheet resistivity, major PL band peak wavelength and width are better than 1-4%, characteristic of the grown materials with high crystalline quality and uniformity. These wafer scale material characterizations were tightly coupled with the epitaxial growth processes for the optimization of growth and processing parameters.

1. Introduction

GaAs-based III-V compound semiconductor materials and structures have many applications in electronic and optoelectronic devices working over a wide wavelength range from visible to infrared (IR). Mass production and large-scale wafer epitaxial growth of these materials with high quality and high uniformity are in great demand. Further developments in modern electronics and optoelectronics require the production of different types of III-V material and microstructure wafers with high uniformity over the entire wafer area, coupled with the ability to maintain a wafer-to-wafer repeatability within a run and run-to-run, the ability to maximize the yield per wafer and the minimization of the costs of mass production. To meet these challenges, EMCORE Corporation has developed and applied the advanced *TurboDiscTM* technology, which utilizes a vertical growth configuration and a high speed rotating disk reactor (RDR) for the metalorganic chemical vapor deposition (MOCVD) of large area and multiple wafer growth of various semiconductor, ferroelectric, oxide and superconductor materials [1-5 and refs. in]. To achieve these goals, we face a new challenge on the necessity for whole wafer non-destructive material characterization. Whole wafer scale and non-destructive characterizations are quite different from single point and destructive measurements, and are more difficult and important in compound semiconductors than in silicon case. As a flexible technique, whole wafer characterization ability has become an important part of advanced growth technology development.

In this study, we describe our efforts to establish several mapping techniques, present some results on whole wafer mappings and demonstrate the non-destructive material characterization of 100 mm (4") wafer size epitaxial films of binary GaAs, ternary AlGaAs and microstructures. These data show that the grown materials are of high crystalline quality and uniformity. For example, uniformities of our epitaxial film sheet resistivity, major PL band peak wavelength and band width

are typically better than 1-4%. These wafer scale material characterizations were tightly combined with the epitaxial growth processes and helped to greatly improve the quality and uniformity of the large scale wafer epitaxial films, thereby guaranteeing the success, high yield and high efficiency of mass production for modern electronic and optoelectronic materials and structures using *TurboDiscTM* MOCVD and technology.

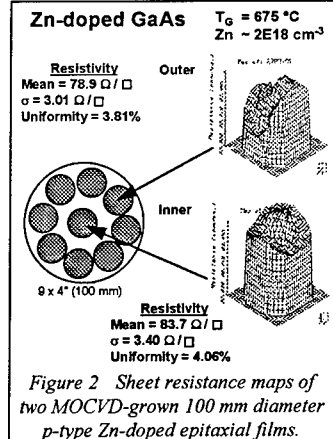


2. Experimental

2.1 Growth Technology

GaAs-based materials in this study were grown using an EMCORE Enterprise 400 (E400) system with a 16" wafer carrier and in the vertical growth configuration, as shown in Figure 1. A high speed rotating disk holds a susceptor with a diameter of 400 mm in this model. Nine wafers of 100 mm (4") diameter or equivalent, such as 38x2", 17x3", 4x150 mm or 1x300 mm, wafers are handled per run. The

loadlock system allows fully automated transfer of platters into and out of the reaction chamber without breaking vacuum. The system design was made according to the hydrodynamic symmetry and rotating disk reactor (RDR) flow dynamics, which ensures growth to be laterally uniform, abruptly switchable, and robust against variations in process parameters [1,4,5]. High purity trimethylgallium (TMGa) and trimethylaluminum (TMAI) metalorganic sources were used to supply Ga and Al, respectively, and AsH₃ was used for P. High purity H₂ was used as the carrier gas. More growth details can be found in Refs. 1-5.



2.2 Characterization Techniques

Sheet resistivity mapping was performed by a Lehighton eddy current sheet resistivity non-destructive mapper. A 55 point 3-dimensional (3D) map is created as a function of position on the wafer. Fourier transform infrared (FTIR) reflectance and map distribution were measured by a Bio-Rad 175C and a PIKE mapper. Room temperature (RT) photoluminescence (PL) mapping was done using a Philips SPM-200 mapper using a He-Ne laser (633 nm) in this study.

3. Results and Discussion

3.1 Sheet Resistance

Sheet resistance mapping has become a routine characterization at EMCORE for epitaxial films. Doping distributions over large area epitaxial wafers can be studied by Lehighton sheet resistance maps. The effects and sheet resistivity distributions of n-type Si doping in 2" InGaAs/InP and 4" epitaxial

GaAs have also been presented [2,4]. Here we present new results on p-type zinc doping, which is generally more difficult than n-type doping. Figure 2 exhibits the sheet resistivity maps of two 4" (100 mm) Zn-doped GaAs epi-wafers from nine wafers in one growth run. As can be seen, nine 4" wafers were grown in the same single run with one wafer sitting in the center of the platter and eight wafers in the outer region. Our results show that by using a high speed rotating disk and optimizing process parameters, including the pressure, rotation speed, flow ratios etc., all the eight wafers located on the symmetrical locations in the outer region of the platter have almost identical films grown on. This means that all the eight outer 4" wafers have an average sheet resistivity of $78.9 \Omega/\square$ and a standard deviation (S-D), σ , of $3.01 \Omega/\square$ with an uniformity of 3.8%. The inner wafer possesses a slightly different average value of $83.7 \Omega/\square$ and σ of $3.4 \Omega/\square$ with an uniformity of 4.1%. It has been reported that the Zn doping concentration is related to the substrate growth temperature [6]. Therefore, the good Zn-doping uniformity is also an indication of good growth temperature uniformity over the entire 4" wafer region.

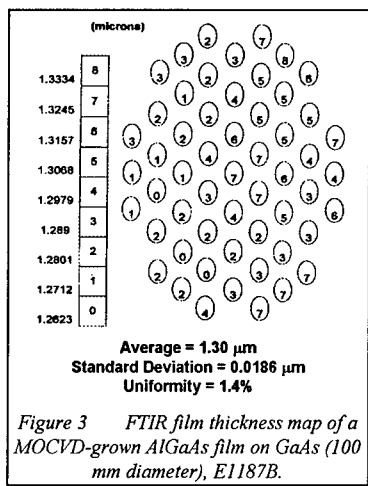


Figure 3 FTIR film thickness map of a MOCVD-grown AlGaAs film on GaAs (100 mm diameter), E1187B.

3.2 FTIR Thickness Map

Fig. 3 shows an example of a thickness mapping distribution, determined by Fourier transform infrared (FTIR) technique, of an AlGaAs film grown on a 100 mm diameter GaAs substrate, E1187B. An average film thickness of $1.30 \mu\text{m}$ and a uniformity of 1.4% have been obtained, indicating a good epi-film thickness control.

3.3 Photoluminescence Mapping

PL has been used in the compound semiconductor industry as a major characterization tool, since it provides information on both alloy composition and crystalline properties. PL maps directly predict the distributions and uniformity of the composition and crystalline quality of epitaxial compound films. It can also serve for the quantum well structures.

Figure 4 (a) shows the structural diagram of a GaAs-AlGaAs single quantum well (SQW) structure, E809. This SQW consists of a 56 \AA wide GaAs well with 1000 \AA $\text{Al}_x\text{Ga}_{1-x}\text{As}$ ($x \sim 30\%$) barrier layers, an upper clapping layer of 2500 \AA n^+ Si-doped (1E18) $\text{Al}_y\text{Ga}_{1-y}\text{As}$ ($y \sim 60\%$) with a 100 \AA GaAs cap and a lower cladding layer of 2000 \AA un-doped $\text{Al}_y\text{Ga}_{1-y}\text{As}$ ($y \sim 60\%$), grown on 1000 \AA Si-doped (1E18) GaAs on a semi-insulating 100 mm diameter GaAs substrate. Fig. 4 (b) exhibits the RT PL map of $\lambda(\text{peak})$ with an average value of 800.4 nm and a S-D of 0.50 nm (a uniformity better than 0.1%). Fig. 4 (c) shows an average FWHM of 24.1 nm and a S-D of 0.82 nm . The FWHM uniformity of the main PL band for this SQW wafer is 3.4%. The intensity uniformity is about 10% (not shown here). The QW PL peak position is directly related to the quantum well width and barrier composition [7]. The high uniformity in peak PL wavelength and FWHM predicts the high uniformity of the quantum well width and barrier alloy composition, and good control of the structural interfaces. Further quantitative analysis is in progress.

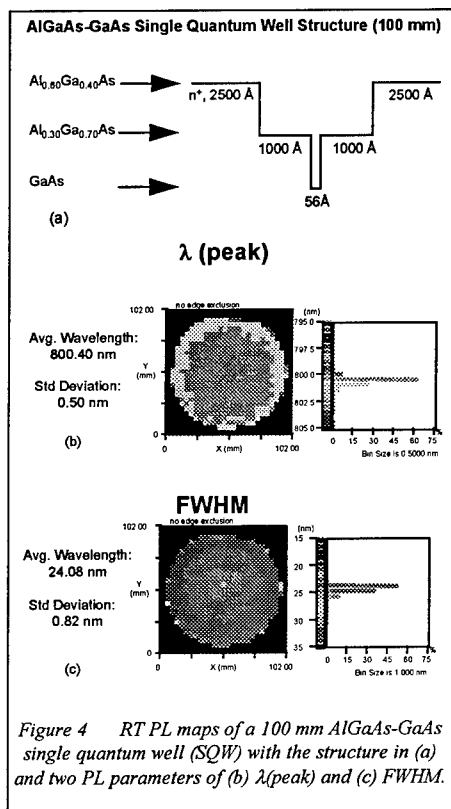


Figure 4 RT PL maps of a 100 mm AlGaAs-GaAs single quantum well (SQW) with the structure in (a) and two PL parameters of (b) λ (peak) and (c) FWHM.

4. Conclusion

We have demonstrated whole wafer characterization by applying several non-destructive techniques, including sheet resistance, FTIR-determined film thickness and room temperature (RT) photoluminescence (PL) for semiconductor epitaxial materials of 100 mm (4") diameter GaAs, AlGaAs and quantum well structures prepared by *TurboDisc™* MOCVD technology. Good results have been obtained. Zn doped 100 mm p-type epitaxial GaAs possesses a sheet resistivity uniformity of 3-4%. $\text{Al}_x\text{Ga}_{1-x}\text{As}$ film has a film thickness uniformity of 1.4%. RT PL maps show the AlGaAs-GaAs single quantum well structure with a peak wavelength of $800.4 \pm 0.5 \text{ nm}$ (uniformity better than 0.1%) and a FWHM uniformity of 3.4%. The success of these achievements are based upon the advanced MOCVD *TurboDisc™* technology [5 and references therein] and the close feedback of the characterization information with the adjustment and optimization of various growth parameters and conditions [1-4]. Other non-destructive and wafer scale characterization techniques, using such as double crystal X-ray diffraction, Raman scattering, photoreflectance and ellipsometry spectroscopy etc., are under investigation and development.

5. References

- [1] Tompa G S, McKee M A, Beckham C, Zawadzki P A, Colabella J M, Reinert P D, Capuder K, Evans G H, Stall R A and Norris P E 1988 *J. Crystal Growth* **93**, 220-227.
- [2] McKee M A, Norris P E, Stall R A, Tompa G S, Chern C S, Noh N, Kang S S and Jasinski T J 1991 *J. Crystal Growth* **107**, 445-451.
- [3] Liu H, Zawadzki P A and Norris P E 1993 *Thin Solid Films* **225**, 105-108.
- [4] Tompa G S, Breiland W G, Gurary A, Zawadzki P A, Evans G H, Esherick P, Kroll B and Stall R A 1994 *Microelectronics J.* **25**, 757-765.
- [5] Thompson A G 1997 *Materials Lett.* **30**, 255-263.
- [6] Chang C Y, Chen L P and Wu C H 1987 *J. Appl. Phys.* **61**, 1860-1863.
- [7] Feng Z C, Perkowitz S, Cen J, Bajaj K K, Kinell D K and Whitney R L 1995 *IEEE J. Selected Topics in Quantum Electronics* **1**, 1119-1125.

Structural and Optical Properties of Very High Quality GaAs/AlGaAs Multiple Quantum Well Structures Grown on (111)A Substrates by MOVPE

A. Sanz-Hervás^a, Soohaeng Cho, O. V. Kovalenkov^b, S. A. Dickey, and A. Majerfeld^c

Dept. of Electrical and Computer Engineering, CB425, University of Colorado, Boulder, CO 80309, USA.

C. Villar, and M. López

Dpto. de Teoría de la Señal y Comunicaciones e Ingeniería Telemática, ETSIT, Universidad de Valladolid, Real de Burgos, 47011 Valladolid, Spain.

R. Melliti, G. Wang, and P. Tronc

Ecole Supérieure de Physique et Chimie Industrielles, Laboratoire d'Optique Physique, 10 rue Vauquelin, 75231 Paris Cedex 05, France.

B. W. Kim

Electronics and Telecommunications Research Institute, P.O. Box 106, Yusong, Taejon, 305-600 Korea.

Abstract. We report an investigation of the structural and optical properties of the first high quality GaAs/AlGaAs multi-quantum-well structures grown on (111)A substrates by the metallorganic vapor phase epitaxial process at the relatively low temperature of 600 °C. By high-resolution x-ray diffractometry it is shown that the structure analyzed has a good crystal quality and period reproducibility. The structural and optical properties were also investigated by photoluminescence and photoreflectance spectroscopies. A photoluminescence linewidth of 12.3 meV at 11 K indicates that the well length (105 Å) fluctuation over 10 periods is at most ± 3 monolayers. A detailed analysis of the photoreflectance spectrum at 11 K permits an excellent identification of all the allowed and also weakly allowed optical transitions expected for this structure, further demonstrating that the heterointerfaces are abrupt and smooth.

1. Introduction

The epitaxial growth of AlGaAs/GaAs multilayers along the <111> crystallographic directions has received considerable interest in the last few years due to their special fundamental optical and electrical properties and their possible application to novel optoelectronic devices [1]. A strong anisotropy is present in the valence band which leads to a large heavy hole effective mass in the <111> directions. A reduced threshold current density for <111> lasers as compared with the same [001] devices has been reported [2].

^a On leave from Dpto. de Tecnología Electrónica, ETSIT, UPM, Ciudad Universitaria, 28040 Madrid, Spain.

^b On leave from A. F. Ioffe Physical-Technical Institute, 194021 St.-Petersburg, Russia.

^c Corresponding author.

Some researchers have achieved the growth of high quality AlGaAs/GaAs heterostructures on (111)A and (111)B GaAs by molecular beam epitaxy (MBE) [3,4] using high growth temperatures, however, this is a serious obstacle for the growth of the strained InGaAs/GaAs/AlGaAs material system necessary for the fabrication of laser devices along the <111> axes. Recently, the growth by MBE of high quality single-quantum-wells (SQWs) on the (111)A face at 520 °C has been reported [5]. Several works have been published on the growth by metallorganic vapor phase epitaxy (MOVPE) of GaAs and AlGaAs single layers on (111)A and (111)B substrates. It has been observed that the optimum growth conditions to obtain good surface morphology are very limited [6-8] or require high growth temperatures (>800 °C) [9,10]. In a previous paper we demonstrated the feasibility of growing AlGaAs/GaAs SQWs on (111)A GaAs at a relatively low substrate temperature (660 °C) [11]. In this work we present the fabrication, structural and optical characterization of high quality AlGaAs/GaAs multi-quantum-wells (MQWs) grown at an even lower temperature (600 °C).

2. Experimental

AlGaAs/GaAs QW structures were grown in a horizontal quartz MOVPE reactor operated at atmospheric pressure. We used nominally exactly-oriented (111)A and 2°-off (100) towards [110] semi-insulating GaAs substrates, which were placed side by side during each growth run. We used 100% AsH₃, trimethylgallium and trimethylaluminum as precursors. The MQW structure reported in this paper consists of an unintentionally doped AlGaAs/GaAs MQW of 10 periods grown on top of a 0.3 μm buffer. The growth temperature was 600 °C and the V/III molar ratios were 68 for the GaAs and 52 for the AlGaAs layers, respectively.

High-resolution x-ray diffractometry (HRXRD) was used to assess the crystal quality of the samples and to obtain structural information. The measurements were carried out in a Bede D³ diffractometer ($\lambda = \text{Cu K}\alpha_1$). For the (111)A MQW we recorded the crystal truncation rods around the 333 and {224}± reciprocal points using $\theta/\kappa\theta$ scans to improve the signal-to-noise ratio of the measurements, where the angular ratio κ depends on the reflection. The experimental scans were fitted by theoretical profiles calculated through an improved simulation model [12].

Photoluminescence (PL) measurements at 11 K were performed using the 5145 Å line of an Ar⁺ laser with an excitation intensity of 0.001-2 W/cm² and a double pass monochromator. The photoreflectance (PR) measurements at 300 K and 11 K were made by using the beam from a tungsten light source passed through a double pass monochromator as the probe beam, while a chopped Ar⁺ laser beam tuned to 5145 Å was used as the pump beam. The reflectance signal was detected by a Si diode with a longpass filter (Corning 3-68) placed at the collection lens to cut off the laser beam. Both optical intensities were kept low (1 mW for the laser).

3. Results and discussion

Under Normarski contrast microscopy the (111)A sample showed a defect-free surface with some hardly visible corrugation. The (100) 2°-off sample showed a mirror-like surface. According to HRXRD the (111)A sample has a good crystal quality with clear satellite peaks due to the MQW periodicity. We could deduce the Al fraction in the barriers $x_b = 28.8 \pm 0.5 \%$, and the well and barrier thicknesses

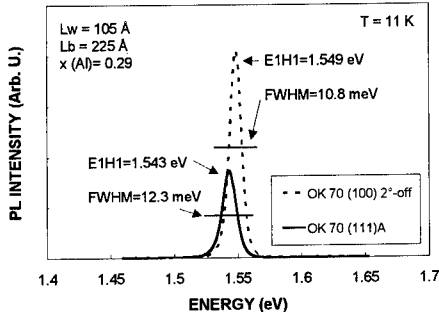


Figure 1. 11 K PL spectra of a 10-period AlGaAs/GaAs MQW grown on (100) 2°-off and (111)A GaAs.

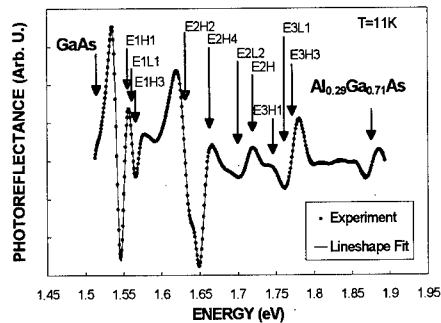


Figure 2. 11 K PR spectrum of the 10-period AlGaAs/GaAs MQW on (111)A GaAs.

$L_w = 105 \pm 5 \text{ \AA}$ and $L_b = 225 \pm 5 \text{ \AA}$, respectively. By HRXRD it was also determined that the nominal orientation of the substrates was correct within $\pm 0.3^\circ$.

Figure 1 shows the 11 K PL emission from the (111)A and the (100) 2°-off samples grown side-by-side. It can be seen that the FWHM is 12.3 meV and 10.8 meV for the (111)A and the (100) samples, respectively. The FWHM for (111)A is slightly lower than the best value recently reported for an MBE AlGaAs/GaAs MQW with only 5 periods [4]. The FWHM value indicates a well thickness variation across the 10-period MQW of ± 3 monolayers at most.

The 11 K PR spectrum for the (111)A AlGaAs/GaAs MQW and the best theoretical fit are displayed in Figure 2. The PR energies are identified with all the allowed transitions for this structure (up to E3-HH3) and five weakly allowed transitions, which proves the high optical quality of the MQW. The eigenvalues for the structure were calculated assuming a band gap energy for the $\text{Al}_x\text{Ga}_{1-x}\text{As}$ barriers corresponding to the AlGaAs transition energy at 1.878 eV of the PR spectrum. This energy represents an Al fraction $x_b = 29\%$ according to ref. [13], which is very close to the value obtained from HRXRD. The eigenvalues that best agreed with the experimental transitions are listed in Table 1 and were obtained for $L_w = 105 \text{ \AA}$, in perfect accord with the HRXRD value. An exciton binding energy of 8 meV was subtracted from all the theoretical eigenvalues [14]. In the computations the GaAs effective masses employed were $m_e = 0.067m_0$, $m_{hh} = 0.952m_0$, and $m_{lh} = 0.079m_0$, and the AlGaAs effective masses were $m_e = 0.087m_0$, $m_{hh} = 1.002m_0$, and $m_{lh} = 0.093m_0$ [15]. The conduction- and valence-band discontinuities used were $\Delta E_c = 245 \text{ meV}$, and $\Delta E_v = 120 \text{ meV}$, respectively. There is an excellent agreement, within ± 3 meV, between the experimental and the calculated transitions energies. The PR results indicate an overall well width fluctuation of ± 1 monolayer, which is even lower than the fluctuation previously obtained from the PL FWHM.

4. Conclusions

We have reported the growth of high quality AlGaAs/GaAs MQWs on (111)A GaAs by MOVPE at low temperature (600 °C). The HRXRD study proves the good crystal quality and periodicity of the MQW. The sample exhibited a single PL peak with a FWHM of 12.3 meV at 11 K, the narrowest value reported for a MQW on {111} GaAs, which corresponds to a well length fluctuation of at most

Table 1. Comparison between the experimental energy transitions deduced from the best fit to the 11 K PR spectrum for the 10-period AlGaAs/GaAs MQW on (111)A GaAs and the theoretical eigenvalues for the structure.

Spectral feature	PR energy (eV)	Calculation * (eV)	Spectral feature	PR energy (eV)	Calculation * (eV)
Al _{0.29} Ga _{0.71} As	1.878	—	E2-HH4	1.669	1.669
E2-HH3	1.771	1.768	E2-HH2	1.635	1.635
E3-LH1	1.764	1.764	E1-HH3	1.565	1.565
E3-HH1	1.745	1.745	E1-LH1	1.561	1.561
E2-HH6	1.722	1.722	E1-HH1	1.543	1.543
E2-LH2	1.703	1.704			

* After deducting an exciton energy of 8 meV

±3 monolayers. The PR spectrum shows all the allowed and also weakly allowed transitions for the structure, further demonstrating the excellent interfacial quality of the MQW. The theoretically calculated transition energies are in excellent agreement, within ±3 meV, with the observed PR transitions using a well width of 105 Å, in full agreement with the HRXRD value. This also indicates a thickness fluctuation of ±1 monolayer. Finally, the low growth temperature (600 °C) achieved indicates a good prospect for the growth of InGaAs/GaAs/AlGaAs structures for the fabrication of laser devices.

Acknowledgments

The work at the University of Colorado was supported by the Electronics and Telecommunications Research Institute, Taejon, Korea, the NATO grant CRG-960094, and the NSF grant INT-9315393.

References

- [1] Sánchez-Rojas J L, Sacedón A, Calleja E, Muñoz E, Sanz-Hervás A, de Benito G and López M 1996 Phys. Rev. B 53 15469-15472.
- [2] Hayakawa T, Suyama T, Takahashi K, Kondo M, Yamamoto S and Hijikata T 1988 Appl. Phys. Lett. 52 339-341.
- [3] Viña L and Wang W I 1986 Appl. Phys. Lett. 48 36-37.
- [4] Chin A and Lee K 1996 Appl. Phys. Lett. 68 3437-3439.
- [5] Watanabe T, Yamamoto T, Vaccaro P O, Ohnishi H and Fujita K 1996 Microelectronics Journal 27 411-421.
- [6] Reep D H and Ghandi S K 1983 J. Crystal Growth 61 449-457.
- [7] Umemura M, Kuwahara K, Fuke S, Sato M and Imai T 1992 J. Appl. Phys. 72 313-315.
- [8] Fuke S, Umemura M, Yamada N, Kuwahara K and Imai T 1990 J. Appl. Phys. 68 97-100.
- [9] Ando S, Chang S S and Fukui T 1991 J. Crystal Growth 115 69-73.
- [10] Dzurko K M, Hummell S G, Menu E P and Dapkus P D 1990 J. Electronic Materials 19 1367-1372.
- [11] Mao E, Dickey S A, Majerfeld A, Sanz-Hervás A and Kim B W 1997 Microelectronics Journal 28 in press.
- [12] Sanz-Hervás A, Aguilar M, Sánchez-Rojas J L, Sacedón A, Calleja E, Muñoz E, Villar C, Abril E J and López M 1997 J. Appl. Phys. 82 in press.
- [13] Casey H C and Panish M B 1978 Heterostructure Lasers Part A p. 187 (New York: Academic).
- [14] Viña L, Muñoz L, Calle F, Mestres N, Calleja J M and Wang W I 1992 Phys. Rev. B 46 13234-13243.
- [15] Los J, Fasolino A and Castellani A 1996 Phys. Rev. B 53 4630-4648.

Study of photoexcited carriers in semi-insulating InP by means of Raman spectroscopy

L. Artús[†], R. Cuscó[†], J. Ibáñez[†], and G. González-Díaz[‡]

[†] Institut Jaume Almera (C.S.I.C.), Solé i Sabaris s.n., 08028 Barcelona, Spain

[‡] Dept. Electricidad y Electrónica, Facultad de Física, Universidad Complutense, 28040 Madrid, Spain

Abstract. We present a study of photoexcited plasmons in semi-insulating, Fe-doped InP at room temperature and at 80 K by means of Raman spectroscopy. Two peaks are detected in the frequency region of the LO mode. Whereas the low-energy peak does not change with incident laser power, the high-energy peak shifts to higher energies with increasing laser power, and therefore is assigned to the L^+ branch of the LO-plasmon coupled mode. The LO and the L^+ modes could be resolved at room temperature for high incident power, and were clearly resolved at 80 K for all the incident powers studied. The Raman spectra were fitted using a L^+ lineshape model based on the Lindhard-Mermin dielectric function, in which contributions from electron, heavy-hole and light-hole intraband transitions as well as heavy-hole-light-hole interband transitions were taken into account. The fitting procedure allows us to determine the photoexcited plasma density as a function of the incident laser power.

1. Introduction

Recently, there has been a great interest in InP due to its applications to a wide range of high-performance electronic and optoelectronic devices. The capability to design InP-based devices lies in the thorough understanding of the carriers behaviour.

Light scattering by single-particle and collective excitations of photoexcited carriers has been extensively studied in GaAs [1]. By contrast, only a few articles on Raman scattering by photoexcited carriers in InP have been published so far, some of which report time-resolved measurements using high-power pulsed lasers for generating the e-h plasma [2, 3]. The observation of light scattering by a photoexcited plasma in InP under cw laser excitation was first reported by Nakamura and Katoda [4]. In lightly doped n -InP they observed a shift of the L^+ branch of the LO-plasmon coupled modes (LOPCM) to higher frequency with increasing laser power. The shift was attributed to the generation of photoexcited carriers, whose density was estimated to be about $3 \times 10^{17} \text{ cm}^{-3}$ for a laser power density of 1200 W cm^{-2} . In a more recent paper, Boudart *et al* [5] have reported Raman measurements on undoped semiconducting (SC) InP and semi-insulating (SI) InP:Fe. For the SC InP, the L^+ modes were clearly resolved from the LO mode arising from the depletion zone, and exhibited the expected shift to higher frequencies with increasing power density. However, they could not resolve the L^+ and LO modes in SI InP, and therefore the presence of L^+ modes in photoexcited SI InP could not be demonstrated. Quite recently, the results

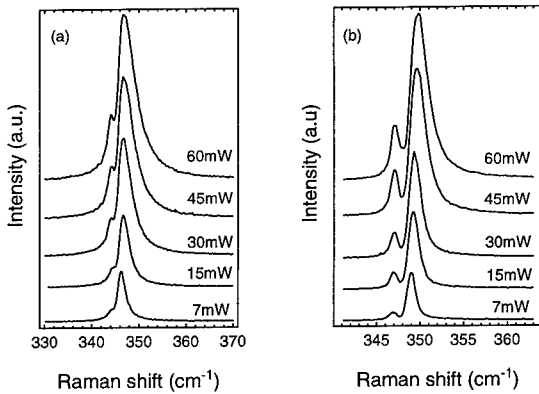


Figure 1. Polarized Raman spectra of semi-insulating InP:Fe for different incident laser power (a) at room temperature and (b) at 80 K.

of polarized Raman measurements close to the $E_0 + \Delta E_0$ resonance have been published [6]. These results appear to be in conflict with previous data, as frequency shifts of only 0.2 cm^{-1} are reported for the L^+ peak, even with very high exciting laser-power densities. In contrast, L^+ shifts in excess of 20 cm^{-1} have been observed by other authors for similar laser-power densities [4, 5].

Up to date, no experimental evidence of L^+ modes in SI InP under cw laser excitation has been reported. In this work we study the Raman scattering of SI InP for a range of incident cw laser power, and show that, even at low laser power densities, the photoexcited e-h plasma couples with the LO phonons giving rise to the observation of a L^+ peak.

2. Experiment

The experiments were performed on LEC grown, semi-insulating (Fe-doped to approximately $5 \times 10^{16}\text{ cm}^{-3}$) InP samples supplied by Sumitomo. We used the 528.7-nm line of an argon-ion laser as excitation source which was focused onto a spot area of about $5.3 \times 10^{-4}\text{ cm}^2$. The Raman signal was analyzed using a T64000 Jobin-Yvon spectrometer equipped with a charge-coupled device detector cooled with liquid nitrogen. The triple-additive configuration of the spectrometer was used, with $100\text{-}\mu$ entrance slit, which gives a spectral resolution better than 1 cm^{-1} . The polarized Raman measurements were performed on a (001) face in the $\langle Z|XY|\bar{Z} \rangle$ configuration. The low-temperature measurements were performed at 80 K in a TBT Air-Liquide liquid nitrogen cryostat. The power loss through the optical window of the cryostat was measured and taken into account in the determination of the incident power on the sample.

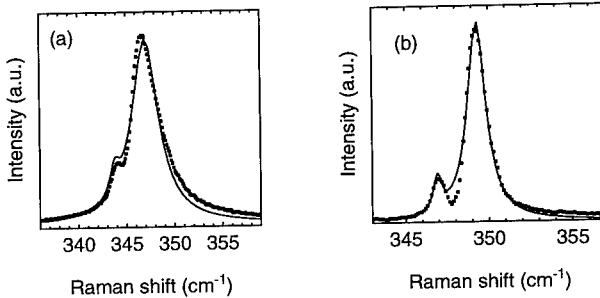


Figure 2. Lindhard-Mermin lineshape fit (solid line) to the experimental Raman spectrum (dots) of InP:Fe measured with an incident laser power of 15 mW (a) at room temperature and (b) at 80 K.

3. Results and discussion

Figure 2 (a) shows the Raman spectra measured at room temperature for different incident laser powers. A strong peak at 346 cm⁻¹ and a shoulder at 344 cm⁻¹ can be observed in the room-temperature spectra taken with 7 mW shown in Fig. 2 (a). With increasing incident power, the dominant peak shifts slightly to higher energies and broadens, while the shoulder is observed at the same frequency position, and for higher incident powers becomes resolved as a peak at 344 cm⁻¹. In the $\langle Z|XY|\bar{Z} \rangle$ configuration the deformation-potential mechanism is allowed for both the LO and the LOPCM modes [7]. We assign the high-energy dominant peak to scattering by coupled LO-photoexcited electron-hole plasma modes. The LO-L⁺ splitting is even better resolved by performing the measurements at 80 K, as can be seen in Fig. 2 (b).

The density of the photoexcited plasma can be estimated by fitting a suitable LOPCM lineshape model to the experimental data. In our experimental geometry, only deformation potential and electro-optical mechanisms contribute to Raman scattering [7]. The corresponding Raman cross-sections are evaluated using the fluctuation-dissipation theory of Hon and Faust [8] and expressed in terms of the electric susceptibility of the plasma, which includes contributions from electron, heavy-hole and light-hole intraband transitions as well as heavy-hole-light-hole interband transitions. The intraband contributions to the susceptibility are calculated in the random phase approximation including collision-damping corrections using the Lindhard-Mermin formalism [9]. The inter-valence-band terms are evaluated following Wan and Young [10]. This lineshape model, which contains two free parameters, the photoexcited plasma density and a phenomenological damping constant, was fitted to the experimental spectra. Figure 3 shows the results of the model calculation for the spectra corresponding to a power density excitation of 28 W cm⁻² (a) at room temperature and (b) at 80 K. From the fit we estimate the electron-hole density in the plasma to be about 4×10^{16} cm⁻³. In the range of power densities studied, the photoexcited electron-hole density changes only by about 1.5×10^{16} cm⁻³. This is due to the presence of Fe deep impurity levels [11] which are very effective in capturing and recombining the photoexcited carriers [5].

4 Conclusions

We have shown that LO-plasmon coupled modes are observed in SI InP:Fe under cw laser excitation even at low incident-power density. High-resolution measurements are necessary to resolve the LO and the L^+ peaks, thus allowing the accurate determination of the LO mode energy. A lineshape model based on the Lindhard-Mermin dielectric function, which takes into account the intraband electron, heavy-hole, and light-hole, as well as the interband heavy-hole-light-hole transitions, provides a good fit to the measured spectra. From fits of this model to the spectra the photoexcited carrier density can be determined.

References

- [1] Abstreiter G, Cardona M, and Pinzuk A 1984 *Light Scattering in Solids IV* Cardona M and Güntherodt G (eds.) *Topics in Applied Physics Vol. 54* (Berlin: Springer-Verlag).
- [2] Young J F and Wan K 1987 *Phys. Rev. B* 35 2544-7
- [3] Tsen K T, Halama G, Sankey O F, Tsen S C Y, and Morkoc H 1989 *Phys. Rev. B* 40 8103-6
- [4] Nakamura T and Katoda T 1984 *J. Appl. Phys.* 55 3604-7
- [5] Boudart B, Mari B, and Prevot B 1993 *Mater. Sci. Eng. B* 20 109-12
- [6] Kernohan E T M, Phillips R T, Bairamov B H, Ritchie D A, and Simmons M Y 1996 *Sol. State Commun.* 100 263-7
- [7] Olego D and Cardona M 1981 *Phys. Rev. B* 24 7217-32.
- [8] Hon D T and Faust W L 1973 *Appl. Phys.* 1 241-56
- [9] Mermin N D 1970 *Phys. Rev. B* 1 2362-3
- [10] Wan K and Young J F 1990 *Phys. Rev. B* 41 10772-9
- [11] Eaves L, Smith A V, Williams P J, Cockayne B, and MacEwan W R 1981 *J. Phys. C* 14 5063-8

Photocapacitance Investigation of Stoichiometry-dependent Deep Levels in InP

Yutaka Oyama^{a,b,c}, Jun-ichi Nishizawa^{b,c}, Kyo Kim^a and Ken Suto^{a,b,c}

^a Dep. of Materials Science, Graduate School of Engineering, Tohoku University, Aramaki Aoba, Sendai 980-77, Japan

^b Semiconductor Research Institute, Kawauchi Aoba, Sendai 980, Japan

^c Telecommunication Advancements Organization, SENDAI Research Center, Nagamachi Aoba, Sendai 980, Japan

Abstract. The photocapacitance measurements under constant capacitance condition is applied to *n*- and *p*-type InP crystals prepared by 4h-annealing at 700°C under controlled phosphorus vapor pressure. Samples used are InP bulk crystals grown by the conventional LEC method. Vapor pressure controlled-zone melting grown InP and LPE-grown InP are also investigated. The phosphorus vapor pressure dependence of the deep level density is shown. And the excitation photocapacitance method is also applied to show the precise optical transition mechanism of these deep levels. From these results, the defect formation mechanism is discussed in view of the deviation from the stoichiometric composition of InP.

1. Introduction

The most important factor to be controlled in compounds is the deviation from the stoichiometric composition[1]. Whereas InP is one of the most promising semiconductor material for the application of ultra-fast electronic devices, opto-electronic devices and so on, the deviation from the stoichiometric composition is more serious compared with Ga-As based compounds. Many reports on the deep levels have been published[2]. However, the results are far from crucial conclusion of the effects of stoichiometry on the defects in InP.

In this paper, the photocapacitance (PHCAP) measurements under constant capacitance condition is applied to various *n*- [3]and *p* -InP[4] crystals prepared by 4h-annealing at 700°C under controlled phosphorus vapor pressure followed by rapid cooling. Vapor pressure controlled-zone melting grown InP and LPE-grown InP are also investigated by PHCAP. The phosphorus vapor pressure dependence of the deep level density is shown. And the excitation photocapacitance method is also applied to show the precise optical transition of these deep levels.

2. Experiments

2.1 Sample preparation

The starting crystals used for annealing were LEC grown *n*-and *p*-InP. Carrier concentration of undoped crystal is $1.2\text{-}1.5 \times 10^{16} \text{ cm}^{-3}$ and that of Sn doped InP is $2.2 \times 10^{16} \text{ cm}^{-3}$. Carrier concentration of *p*-InP doped with Zn is $3 \times 10^{17} \text{ cm}^{-3}$. InP is placed in one end of a dumbbell-type quartz ampoule and 6N-red phosphorus in the other end. After sealing in vacuum, heat treatment was carried out at 700°C for 4h under controlled phosphorus vapor pressure. Phosphorus vapor pressure at the phosphorus zone, P_p , is determined from the temperature of red phosphorus [5]. The phosphorus vapor pressure at the crystal zone, P , was determined from the following equation.

$$P = P_p (T/T_p)^{1/2} \quad (1)$$

where T and T_p are the temperature of InP crystals and red phosphorus, respectively. After annealing, the ampoule was rapidly cooled by dipping into the water at nominal room temperature.

2.2 Photocapacitance measurements

PHCAP measurement by constant capacitance method is applied at 77K to determine the level densities and their energy levels. Metal-semiconductor contact diodes were made by Au-evaporation as a barrier metal. Monochromatic light was fed into the depletion layer of the sample diodes. Deep levels was made to be neutral before each light irradiation. For this purpose, forward bias injection was carried out in the dark before each light irradiation. After light irradiation, bias voltage (ΔV_{ph}) changes to keep the junction capacitance constant according to the ionization of the levels. However, the depletion layer thickness is kept constant regardless of the change of ion density. The change of ion density, ΔN_t , is given by the following equation.

$$\Delta V_{ph} = (\epsilon/2C^2)\Delta N_t \quad (2)$$

where C is the constant capacitance of the sample diode, ϵ is the dielectric constant and ΔV_{ph} is the change of bias voltage. Precise description of the PHCAP will be referred elsewhere[6].

3. Results and Discussion

3.1 n-type LEC InP crystal

Figure 1 shows the ion density PHCAP spectrum of undoped *n*-InP crystal before annealing. V_{dark} is attributed to the thermally ionized level density in the dark. Net ion density induced by the light irradiation is obtained by $\Delta V_{ph} = V_{ph} - V_{dark}$, where V_{ph} is the bias voltage after light irradiation. In Fig. 1, it is shown that the ion density shows gradual increase at $\sim 0.4\text{eV}$ and then increase at 0.63eV . The decrease of ion density at 0.74eV is induced by the neutralization of ionized deep level. In the wavelength region of $0.9\text{-}1.1\text{eV}$, another ionization is observed at 1.1eV . In case of undoped *n*-InP, almost the same deep levels are observed even after 4h-annealing at 700°C .

Figure 2 shows the change of deep level density as a function of the phosphorus vapor pressure. It is shown that the $E_c-0.63$, 1.1eV and $0.74\text{eV}+E_v$ level density decreases with increasing vapor pressure in the range below 100 Torr. Then, the level densities increase when the vapor pressure exceeds 1000 Torr.

Ion density PHCAP spectrum of S-doped InP crystal with the carrier concentration of $5 \times 10^{17}\text{cm}^{-3}$ does not show the ionization at 0.63eV nor the neutralization at 0.74eV . Group VI impurity S will occupy the P-sublattices. Therefore, the doped impurity S will also reduce the V_p concentration. It is considered that these deep levels are stoichiometry-dependent and are related most possibly with at least the V_p . It is also considered that the annealing under extremely high vapor pressure induces non-equilibrium defects in the lattice. Indeed, in the case of GaAs, it is noticed that high-pressure annealing induces not only the interstitial arsenic atom-related point defects but structural defects like stacking faults and extended dislocations. In such highly degraded lattices, it is considered that both the excess phosphorus composition-related defect and the vacancy-related defects are generated.

Excitation PHCAP method is applied to determine the precise energy level position at 40K. After 1.40eV

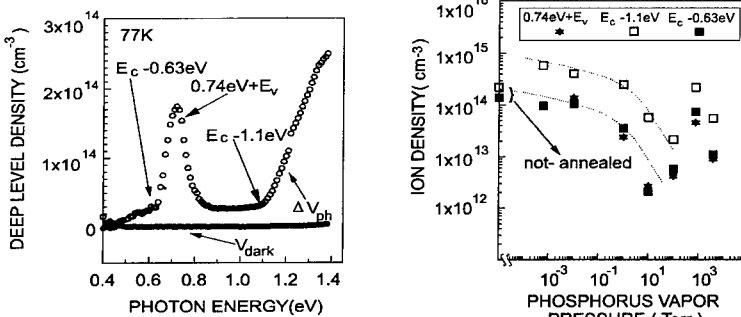


Fig.1 Ion density PHCAP spectrum of intentionally-undoped *n*-InP crystal before annealing

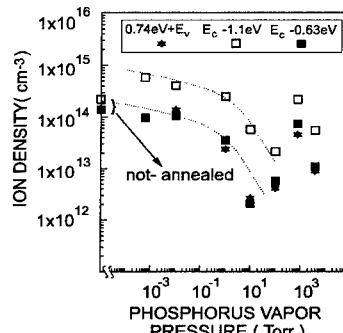


Fig.2 Phosphorus vapor pressure dependence of the deep level density in intentionally-undoped *n*-InP prepared by 4h-annealing at 700°C

light irradiation, the ion density PHCAP spectrum was measured from long wavelengths. It is shown that the decrease of ion density is induced at 0.43 and 0.45eV. This decrease of ion density is caused by the neutralization of ionized deep levels. The precise optical transition of deep levels in *n*-InP will be shown later with those in *p*-InP. In case of Sn-doped *n*-InP, the ion density PHCAP spectrum shows almost no ionized levels at around 0.63eV. However, after 4h-annealing at 700°C, Ec-0.63eV and 0.74eV+Ev levels are induced. The vapor pressure dependence of these deep levels shows gradual decrease in the range of $6 \times 10^{-6} \sim 1 \times 10^{-1}$ Torr. Above 1×10^{-1} Torr, the ion densities shows slight increase with increasing vapor pressure. Under the application of high vapor pressure, Sn-doped *n*-InP crystal is seriously degraded after annealing by the crystallographic inspection.

3.2 *p*-type InP LEC crystal doped with Zn

Figure 3 shows the ion density PHCAP spectrum of *p*-InP crystals prepared by 4 h-annealing at 700°C. It is shown that 1.05 eV+Ev level is detected before and after annealing. In addition, the deep level is detected at 0.74 eV above the valence band when *p*-InP crystals are annealed under lower vapor pressure of 1-100 Torr. It is already shown that PHCAP results revealed the electron capture at 0.74eV above the valence band even in undoped *n*-InP crystals. It is also shown that the 0.74eV+Ev level density in *n*-InP decreases with increase of vapor pressure in the range below <100 Torr. It means that the photoresponse at 0.74 eV+ Ev in Zn- doped *p*-InP corresponds to the electron capture at 0.74 eV in *n*-InP. Therefore, it is concluded that the phosphorus vapor pressure dependence of the 0.74eV+Ev level density shows good correspondence between *n*- and *p*-InP crystals respectively. It is considered that 0.74eV+Ev level is at least related to V_P. 1.05 eV+ Ev level density increases monotonically with increase of vapor pressure. In view of vapor pressure dependence and the effect of impurity doping, 1.05 eV level may be due to defect- impurity complex with close relation to either In vacancy or P interstitial.

The excitation PHCAP was also carried out to 1.05eV+Ev level. After the primary light irradiation, ion density PHCAP spectrum was measured repeatedly from the long wavelength by changing the primary excitation light wavelength. After 1.08 eV light irradiation, neutralization is induced at 0.51 eV below the conduction band. From these results, schematic drawing of the optical transition

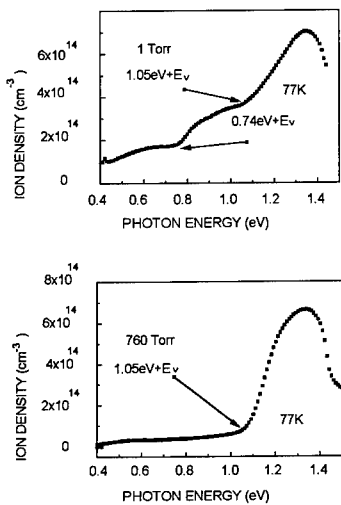


Fig.3 Ion density PHCAP spectra of intentionally Zn doped p-InP prepared by 4h-annealing at 700°C

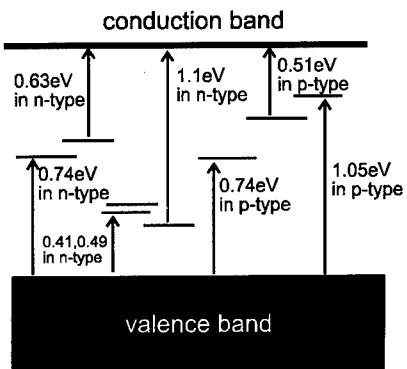


Fig.4 Schematic drawings of the optical transition process of stoichiometry-dependent deep levels in LEC-grown InP prepared by 4h-annealing at 700°C

process in InP is shown in Fig.4.

3.3 Vapor pressure controlled InP crystal growth

The vapor pressure control technology has been extensively applied to the liquid phase epitaxy (LPE) and bulk crystal growth of InP by the pressure controlled zone melting method. Contrary to the conventional method, LPE growth has been carried

out by the temperature difference method under controlled vapor pressure (TDM-CVP)[7]. Figure 5 shows the ion density PHCAP spectrum of LPE-grown n-type InP under controlled vapor pressure. As shown in Fig.5, almost no deep level is detected in the spectral range below 1.1eV. This indicates that the high quality LPE InP with stoichiometric composition can be grown by the pressure controlled LPE method.

Figure 6 shows the ion density PHCAP spectrum of InP bulk crystal by the pressure controlled zone melting method. From our previous results, it has been shown that the electron concentration shows its minimum and the Hall mobility shows its maximum under a specific phosphorus vapor pressure of ~22.7 atm[8]. As shown in Fig.6, the PHCAP method revealed deep donors at 0.46, 0.86 and 1.1eV below the conduction band and ~1.0eV above the valence band respectively. These deep levels are quite different from those observed in conventional LEC InP except Ec-1.1eV level. In addition, the level density is extremely low compared with the LEC InP. Therefore, vapor pressure control technology has a possibility to obtain high quality bulk crystals with stoichiometric composition.

4. Conclusion

PHCAP measurements revealed stoichiometry-dependent deep levels at Ec-0.63eV, 0.74eV+Ev, Ec-1.1eV in both intentionally-undoped and Sn doped n-type InP, and 0.74eV+Ev and 1.05eV+Ev levels have been revealed in Zn-doped p-type InP respectively. 0.74eV+Ev level was detected commonly in both n-and p-type InP when annealed under lower phosphorus vapor pressure. From the results, it is considered that Ec-0.63eV, 0.74eV+Ev and Ec-1.1eV levels relate at least with V_P. 1.05eV+Ev level in p-InP is considered to be related with excess phosphorus composition. Vapor pressure control has been extensively applied to the LPE and bulk crystal growth of InP. PHCAP results indicates that the high quality crystals with stoichiometric composition will be obtained by the vapor pressure control during crystal growth.

References

- [1] Y.Watanabe, J.Nishizawa and I.Sunagawa, 1951 Kagaku, **21**, 140.
- [2] ex. Y.Yamazoe, Y.Sasai and T.Nishino, 1981 Jpn. J. Appl. Phys., **20**, 347.
- [3] J.Nishizawa, Y.Oyama, K.Suto and K.Kim, 1996 J. Appl. Phys., **80**, 1488.
- [4] J.Nishizawa, K.Kim, Y.Oyama and K.Suto, 1997 J. Appl. Phys., **81**, 3151.
- [5] R.E.Honig and D.A.Kramer, 1969 RCA Rev., **30**, 285.
- [6] J.Nishizawa, Y.Oyama and K.Dezaki, 1990 J. Appl. Phys., **67**, 1884.
- [7] J.Nishizawa, H.Tadano and Y.Okuno, 1975 J. Crystal Growth, **31**, 215.
- [8] J.Nishizawa and Y.Oyama, 1994 Mater. Sci. Eng., **R12**, 273.

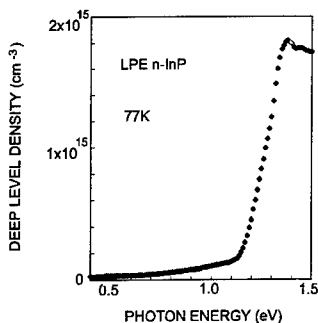


Fig.5 Ion density PHCAP spectrum of LPE-grown n-type InP epitaxial layer.

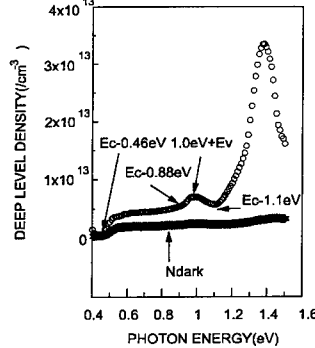


Fig.6 Ion density PHCAP spectrum of n-type InP bulk crystal grown by the vapor pressure controlled zone melting method.

Photoconduction Studies on InGaAs HEMTs

Fritz Schuermeyer^{a)}, David Cheskis^{b)}, R.S.Goldman^{c)}, and H.H.Wieder^{d)}

a) Wright Laboratory, WL/AADD, WPAFB, OH, 45433-7322; b) Anadigics, Warren, NJ;
c) UM, Ann Arbor, MI; d) UCSD, San Diego, CA

Abstract. Photoconduction measurements made on $In_{0.53}Ga_{0.47}As$ channel HEMTs indicate that the threshold energy for photoconduction corresponds to the bandgap of the quantum well and the absorption edge of the substrate. Many interband transitions are observed which can be correlated with the electronic subbands of the quantum well. Strong confinement of photogenerated holes is associated with a large modulation of the HEMT threshold voltage.

1. Introduction

Photoelectric measurements based on induced photoluminescence, (PL) and photoconductivity, (PC) are standard techniques used for the evaluation of semiconductors. PC measurements were extended by Schuermeyer (1996) to include GaAs-based fully fabricated high electron mobility transistors (HEMTs). Such measurements are considered desirable because fundamental material properties can be affected by the device processing procedures and the electronic properties of such devices depend on the voltages applied to their terminals. PC procedures can be used for these purposes with radiation incident on the substrate side of HEMTs if their substrates are transparent for radiation which is absorbed in their conductive channel quantum wells.

There are fundamental differences between PL and PC spectroscopic techniques applied to quantum confined charge carriers. In emission spectroscopy the charge carriers relax to their lowest energy states and recombine by means of radiative transitions; their spectral response consists of a few narrow lines whose width is broadened by their thermal distribution. The PC spectral response is not affected by thermal broadening provided that the Fermi levels and quasi-Fermi levels are far removed from the electron and hole subbands; this occurs in deeply depleted HEMTs. Therefore more transitions can be resolved by means of such absorption spectroscopic measurements (Tanaka 1996, Kotera 1996) than by means of photoemission measurements. PC measurements can even be made at room temperature. However, their absorption spectra have step-like characteristics. Differentiating the PC response versus photon energy yields spectral lines at the risers of the steps; the linewidths of the spectra indicate the quality of the quantum wells. The PC spectral response characteristics provide information about the energy profile of GaAs-based HEMTs (Schuermeyer 1997) and indicate, as well, that the photogenerated charge is amplified by the HEMTs due to hole storage in the channel. These holes modify the HEMT threshold voltage and consequently they also affect its effective drain current.

2. Experiment and Interpretation

Details of the apparatus used for the on-wafer, non-destructive, PC measurements have been described previously (Schuermeyer 1996). Chopped monochromatic radiation, obtained from a 50W tungsten/iodine source incident on a grating monochromator, is applied to the substrate side of HEMT by means of an optical fiber; its source, gate and drain contacts were shielded. A thermopile and a Ge detector were used

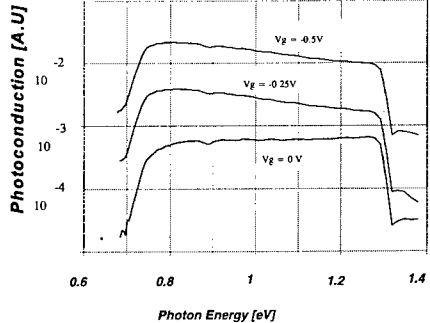
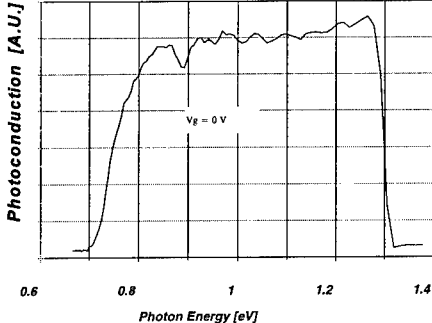


Figure 1 Photoconduction spectra of InP-based HEMT

Figure 2 Photoconduction spectrum at a gate voltage $V_g = 0 \text{ V}$

to calibrate the energy dependence of the incident radiation intensity. The DC as well as the AC drain currents induced by the chopped light were recorded as functions of the photon energy and gate voltage.

The photon energy dependence of PC spectra, measured at room temperature, on a HEMT with an $\text{In}_{0.53}\text{Ga}_{0.47}\text{As}$ channel, an $\text{In}_{0.52}\text{Al}_{0.48}\text{As}$ barrier layer, and a $0.25 \mu\text{m}$ buffer, grown on an InP substrate, (Goldman 1996a) is shown in Figure 1. Each of the 3 curves shown here has a threshold energy at $\sim 1.3 \text{ eV}$, consistent with the InP absorption edge, and a second threshold at $\sim 0.7 \text{ eV}$ consistent with the bandgap of $\text{In}_{0.53}\text{Ga}_{0.47}\text{As}$. The strong dependence on the applied gate voltage, V_g , similar to that observed on GaAs-based HEMTs, is attributed to amplification of photo-generated charges by the transistor. Figure 2 shows the structural features of the $V_g = 0 \text{ V}$ curve, between its two thresholds. The spectra observed in the vicinity of 0.9 eV are produced by the tungsten-iodine light source rather than by the transistor. Figure 3 shows the energy dependence of the derivative of the other PC signals of Figure 2: a well developed peak at $\sim 740 \text{ meV}$ and oscillations at higher energies with an interval between peaks of $\sim 55 \text{ meV}$. The exact location and the intensity of these peaks varied slightly from device to device. Figure 3 also shows the consistency between spectra measured, between 1 and 1.3 eV , on the same device, under the same conditions, after an elapsed period of several days. These spectra represent, therefore, the PC response of the HEMTs and are not random noise.

The spectra in Figure 3 are considered to represent electronic transitions to the subbands of the quantum well channel. The relevant energy levels of these subbands were calculated by means of procedures, such as described by Weisbuch (1987, p. 11), assuming a quantum well width of 50 nm , an effective electron mass ratio, $m'/m_0 = 0.041$ and a heterobarrier of 510 meV . These calculations yielded a total of 12 subbands whose energies with respect to the valence band maximum are indicated in Figure 4 by triangles. Figure 4 also shows these energy levels as Gaussian functions of equal weight with a standard deviation of 12 meV . The calculations effectively simulate the experimentally obtained data. Above 1 eV we observe 4 bands which appear evenly spaced by $\sim 65 \text{ meV}$ in good agreement with experiment. At lower energies the subbands are closely spaced and cannot be resolved as discrete levels. However, their overlap produces an increase in the resultant signal, similar to those observed experimentally. We have considered possible alternative explanations for the oscillatory PC signals above 1 eV such as might be caused by interference effects. We reject this assumption because the separation between peaks suggests a fundamental wavelength of $25 \mu\text{m}$, in vacuum, and $7 \mu\text{m}$, in the semiconductor, assuming its index of refraction to be $n=3.5$.

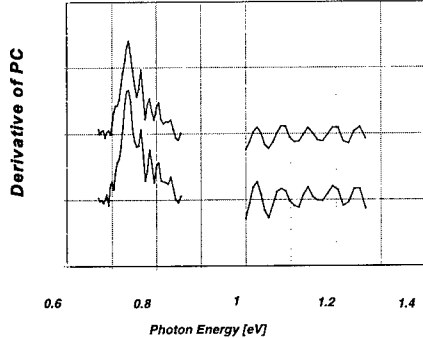


Figure 3 Derivative of photoconduction spectrum shown in Figure 2. The two spectra indicate reproducibility of minor details.

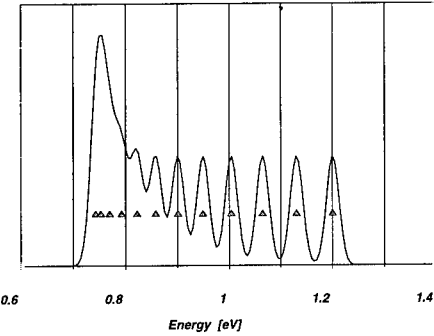


Figure 4 Display of theoretically derived electron subbands

Figure 5 shows the photocurrent I_p , transconductance of the HEMT, and the threshold shift dependence on the gate voltage, measured with a drain voltage, $V_d = 20\text{mV}$ for an incident photon energy of 800meV . The data shown in Figure 5 are similar to those obtained on GaAs-based HEMTs and are attributed to the amplification of the photogenerated charge by the transistor. The modulation of the threshold voltage (Schueremeyer 1997) shown here indicates excellent hole confinement in the channel; the range is considerably greater than that observed in GaAs-based devices, limited between 5 an 10 mV and remaining constant in the depletion range.

We have made similar PC measurements on an $\text{In}_{0.53}\text{Ga}_{0.47}\text{As}/\text{In}_{0.52}\text{Al}_{0.48}\text{As}$ HEMT, made of a heterostructure, grown by MBE, on a GaAs substrate with a compositionally step- graded $\text{In}_x\text{Ga}_{1-x}\text{As}$ buffer (Cheskis 1996). In order to inhibit the generation and the propagation of lattice defects generated by the lattice mismatch between the substrate and the HEMT we use a compositionally step-graded $\text{In}_x\text{Ga}_{1-x}\text{As}$ buffer (Goldman et al. 1996a) between the substrate and the $\text{In}_{0.53}\text{Ga}_{0.47}\text{As}$ channel.

Each one of 5 buffer steps is $\sim 200\text{ nm}$ -thick and the In concentration increases from the substrate by $\sim 10\%$, per step. The PC response vs photon energy of this specimen, shown in Figure 6, indicates a threshold at $\sim 1.4\text{ eV}$ consistent with the GaAs absorption edge while the other threshold at $\sim 0.7\text{ eV}$

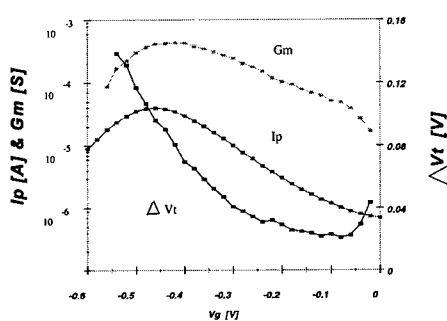


Figure 5 Transconductance, photocurrent and modulation of threshold voltage

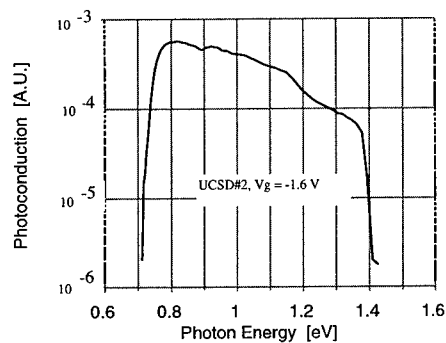


Figure 6 Photoconduction spectrum of a GaAs-based HEMT

Table I

HEMT on	n_s/cm^2 (300K)	μ cm^2/Vs (300K)	n_s/cm^2 (1.6K)	μ cm^2/Vs (1.6K)	I_{ds} (mA/mm) (300K)	g_m (mS/mm) (300K)	f_t (GHz) (300K)
InP-based substrate	1.4×10^{12}	13,600	1.4×10^{12}	102,000	200	240	19
GaAs-based substrate	2.7×10^{12}	12,600	2.5×10^{12}	64,000	520	300	20

corresponds to that of the $\text{In}_{0.53}\text{Ga}_{0.47}\text{As}$ channel. From the derivative of the PC spectra measured for $V_g = -1.6\text{V}$ we find a single transition peak at $\sim 0.75\text{eV}$ in contrast to the closely spaced transitions associated with the peak of the InP-based HEMTs. Furthermore, at higher energies the spacing between the peaks is $\sim 200\text{meV}$. These results may be due to a much narrower quantum well with fewer electronic subbands in the GaAs-based device than in the InP-based device. The effects of the absorption in the buffer layer on the PC spectrum have not been evaluated, as yet. The charge transport properties of the heterostructures used to fabricate the HEMTs are shown in Table I. A nearly complete strain relaxation in the buffer is required (Goldman et al. 1996b) to provide a room temperature electron mobility of the GaAs-based HEMT comparable to that of the lattice matched InP-based HEMT. However, in the cryogenic regime (1.6 K), the former has only half the electron mobility of the latter, attributed to a high density of occupied ionized acceptor centers associated with dislocations present in the quantum well.

The room temperature saturated drain current, I_{ds} , the transconductance, g_m , and the gain-bandwidth product, f_t , of the identical configuration $1.0 \times 50 \mu\text{m}^2$ HEMTs are also shown in Table I (Cheskis 1995). The larger g_m is, obviously, associated with the higher n_s of the GaAs-based sample although the f_t values are nearly the same, probably because the electron velocity in the $\text{In}_{0.53}\text{Ga}_{0.47}\text{As}$ channel is nearly the same in both transistor types.

3. Conclusions

The photoconductive responses of representative $\text{In}_{0.53}\text{Ga}_{0.47}\text{As}/\text{In}_{0.52}\text{Al}_{0.48}\text{As}$ HEMTs grown on InP and on GaAs substrates were evaluated at room temperature within the spectral range delimited by the absorption edges of their substrates and their conductive channels. The calculated spectral response is in good agreement with the experimentally measured transitions to the subbands of their quantum wells and the fundamental interband transition (e1-hh1) energy is the same in both transistor types.

References

- Schuermeyer, F et al. 1996 , Inst. Phys. Conf. Ser. No 145:Chapter 5,pp791-796
- Schuermeyer, F et al. 1997, Inst. Phys. Conf. Ser. No 155: Chapter 6,pp 495-498
- Tanaka, K et al. 1996, Inst. Phys. Conf. Ser. No 145: Chapter 3,pp 455-458
- Kotera, N et al. 1996, Inst. Phys. Conf. Ser. No 145: Chapter 3,pp 393-396
- Goldman, R S, Kavanagh, K L, Wieder, H H, Robbins, V M, Ehrlich, S N, and Feenstra, R M, 1996a, J..Appl.Phys.80, p. 6849
- Weisbuch C. 1987. In Semiconductors and Semimetals, Willardson R.K. and Beer A.C. Editors, Vol. 24, pp. 1 - 133
- Goldman, R S, Kavanagh, K L, Wieder, H H and Ehrlich, S N,1996b, J. Vac.Sci.Techol.B14,p.3035
- Cheskis, D.J, 1995, "Pseudomorphic and Strain-Relaxed InGaAs Channel Modulation-doped Field-Effect Transistors on GaAs and InP substrates," University of California, San Diego, PhD Dissertation, (unpublished)

Hydrogenation Effect of InGaP Grown on GaAs by Molecular Beam Epitaxy

M. D. Kim, H. S. Park, and T. I. Kim

Samsung Advanced Institute of Technology, P.O.Box 111, Suwon 440-600, KOREA

J. Y. Lee, Y. H. Kwon, D. Y. Kim, and H. Y. Cho

Department of Physics, Dongguk University, Seoul 100-715, Korea

Abstract. Hydrogenation effects on electrical properties of n-type and undoped InGaP epi layers lattice matched to GaAs was investigated. It was found that the hydrogenation under a proper condition can be resulted in a Au/n-InGaP Schottky diode with a good rectifying characteristics as well as an effective defect passivation. These improvement were thought to be resulted from the atomic hydrogen diffused into InGaP neutralized Si donor and passivated recombination centers near the surface.

1. Introduction

InGaP lattice matched to GaAs is an attractive alternative to AlGaAs in optoelectric devices. Due to many useful properties such as its wide band gap, low concentration of deep traps and large valence band discontinuity, this material system appears to have good potential to applications for laser diodes[1,2], field effect transistor[3], and heterojunction bipolar transistors[4].

Hydrogen can be introduce into semiconductors during the device process such as chemical vapor deposition(CVD), thermal annealing, exposure to a hydrogen containing plasma, and wet etching process. In many cases, its incorporation into crystalline semiconductors is unintentional, and can cause changes in the electrically active dopant profile in the near surface region. Since atomic hydrogen in semiconductors results in electrical passivation of impurity states, deep levels as well as unreconstructed surface dangling bonds, the hydrogen incorporation in crystalline semiconductors has attracted considerable interest.

In this paper, hydrogenation effect on electrical properties of Si doped n-type and undoped InGaP epi layers grown on GaAs was investigated. It was found that the hydrogenation under a proper condition can be resulted in a Au/n-InGaP Schottky diode with a good rectifying characteristics as well as an effective defect passivation.

2. Experiments

Undoped and Si-doped n-type $In_{0.48}Ga_{0.52}P$ epilayers were grown on 2-in.-diam semi-insulating (100)GaAs substrates by molecular beam epitaxy (MBE) using a special phosphorus solid source with a fast acting valve and a cracking section(Riber KPC 250). The P_2 beam equivalent pressure(BEP) used in this work were typically about 6.5×10^{-6} Torr. The growth rate of InGaP was $0.8 \mu\text{m/h}$. The room temperature electron concentrations in the n-type sample was about $8 \times 10^{16} \text{ cm}^{-3}$. In order to investigate the hydrogenation effect, two type specimens were prepared by CVD-processed. One deposited SiO_2 film by plasma enhanced chemical vapor deposition (PECVD) using at a substrate temperature 200°C . The PECVD was performed with a power of 0.33 W/cm^2 . The film thickness

was 100 nm and deposition rate was 20 nm/min. The other type of sample was prepared at 200 °C by the hydrogen plasma exposure(HPE) in remote plasma chemical vapor deposition(RPCVD) system. The hydrogen pressure during the exposure was 5 mTorr and the substrate temperature was sustained by IR lamps.

Au Schottky diodes with a diameter of 0.5 mm were prepared using a thermal evaporator. The active carrier concentration, its profile vs. junction depth and current density were obtained using an 1 MHz capacitance-voltage and current-voltage measurement system controlled by a microcomputer. Also, the characteristics of deep levels existing in the active layer were studied by optical deep level transient spectroscopy(ODLTS).

3. Results and discussion

Figure 1 shows the reverse biased I-V curves of Au/n-InGaP Schottky diodes before and after hydrogen plasma exposure in CVD at 200 °C. As shown in this figure, the leakage current in the Schottky diode hydrogenated at 200 °C for 2 h decreased from 10^{-5} A/cm² to 10^{-7} A/cm² at - 3 V, and the breakdown voltage was increased to above 30 V, while in the untreated Schottky diode those were about 10^{-4} A/cm² and - 4 V, respectively. Here, the breakdown voltage was defined as the voltage when the leakage current density reached 1×10^{-4} A/cm² under reverse bias. As can be seen in this figure, in the CVD processed-diode which was fabricated after removed of the passivated SiO₂, the leakage current was five times lower and the breakdown voltage was 20 % higher than those of the untreated diodes. These improvement in the rectifying characteristics were thought to be due to hydrogen atoms diffusing during the CVD process.

Figure 2 was the forward biased I-V characteristics for the Schottky diodes. In the forward characteristics, the ideal factors (*n*) of the untreated and the CVD-processed samples were about 1.05 and that of the hydrogenated specimen was 1.15. The saturation current of the hydrogenated sample increased two orders of magnitude compared to the untreated and the CVD-processed diodes. As a hydrogenation result, we found that hydrogenation under a proper condition can result in good rectifying characteristics of a Au/n-InGaP Schottky diode. The increase in breakdown voltage and the decrease in leakage current of the hydrogenated diode were resulted from the increase in Schottky diode barrier height during hydrogenation. In other words, the atomic hydrogen diffused into InGaP during HPE neutralized Si donors as well as deep levels near the surface. Thereby giving rise to the increase in effective barrier height and the decrease in recombination centers. To confirm the hydrogen incorporation to Si donors, high frequency C-V (1 MHz) measurements were performed. In the as-grown sample, the donor carrier concentration was about 8.0×10^{16} cm⁻³. In the CVD-processed sample, the concentration was lower by 4.5×10^{16} cm⁻³ at 2200 Å. In the hydrogenated sample at 200 °C for 2 h, the concentration was five times lower than that of the as-grown sample. This indicated that the CVD-processed samples could contain the hydrogen atoms near the surface and the diffused hydrogen during the CVD process can passivated the electrical activity of Si-donor in InGaP.

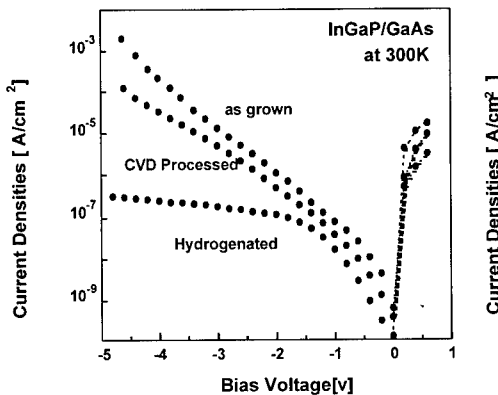


Fig. 1 The reverse biased I-V characteristics of the Schottky diodes made by Au contacts on as-grown, CVD processed, and hydrogenated n-type InGaP.

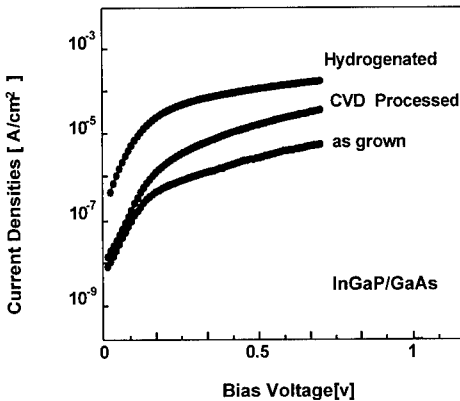


Fig. 2 The forward biased I-V characteristics of the Schottky diodes made by Au contacts on as-grown, CVD processed, and hydrogenated n-type InGaP.

In order to investigate deep levels in the hydrogenated InGaP, ODLTS measurements were performed. The rate window of the spectra was fixed to 18.48 s^{-1} . The InGaP samples were heat-treated at $350\text{ }^\circ\text{C}$ for 5 min in N_2 ambient after metallization. Figure 3 shows the changes of deep levels by the hydrogen plasma exposure at $200\text{ }^\circ\text{C}$ for undoped InGaP. In the pre-hydrogenated sample, four deep levels, denoted as P1, P2, P3, and P4, respectively were observed. By using the DLTS signal analysis method, it was confirmed that the four signals represented deep level defects located at 0.25 eV , 0.31 eV , 0.43 eV , and 0.62 eV from a conduction band edge. The concentration of P1 and P2 in undoped InGaP decreased with increasing $P_2\text{ BEP}$, suggesting that these traps may be associated with the crystal defects in the P deficient lattice sites such as the phosphorus vacancies(V_p). Also, the origin of P3 and P4 signals were attributed to phosphorus vacancies V_p and/or a transformed defect from V_p such as a Ga_p or In_p antisite[5]. After hydrogenation at $200\text{ }^\circ\text{C}$ for 2 h, the relative intensities of all traps decreased in about 10 times and only two signals corresponding to P3 and P4 traps around 180 K and 280 K remained as main defects.

Figure 4 shows the behavior of deep levels for hydrogenated n-type InGaP. Like the undoped sample, the three deep levels, P1, P2, and P3, after hydrogenation, decreased rapidly. After hydrogenation, the decrease of deep level defects was believed to be due to the neutralization of their active states related to the phosphorus vacancies by the atomic hydrogen. Since vacancy defects always have dangling bonds, they can easily bond together with hydrogen atoms[6]. In generally, the hydrogen atom can effectively passivates vacancy defects. This indicated that electron traps in InGaP have been formed due to complexes of vacancies and other impurities.

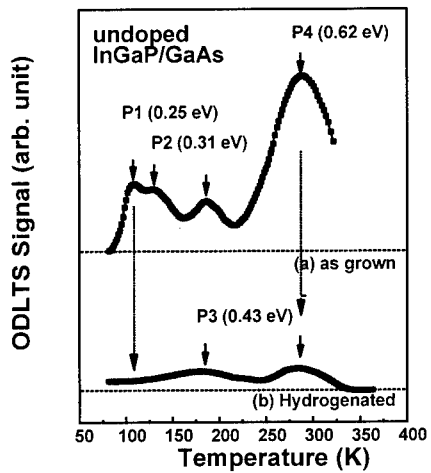


Fig. 3 ODLTS measurements on undoped InGaP as-grown (a) and hydrogenated (b) samples.

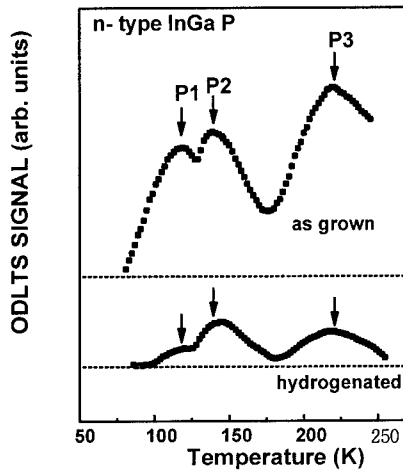


Fig. 4 ODLTS measurements on Si doped as-grown (a) and hydrogenated (b) n-type InGaP.

4. Conclusion

The increase in break down voltage and the decrease in leakage current in the hydrogenated diode are thought to be resulted from the increase of the diode barrier height during hydrogenation. That is, the atomic hydrogen diffused into InGaP by HPE neutralizes Si donor as well as deep levels near the surface, giving a rise to the increase of the effective barrier height and the decrease of recombination centers.

References

- [1] M. Ishikawa, Y. Ohba, H. Sugawara, M. Yamamoto, and T. Nakanishi, *Appl. Phys. Lett.* 48, 207(1986).
- [2] H. Asahi, Y. Kawamura, and H. Nagai, *J. Appl. Phys.* 54, 6958(1983).
- [3] Y. J. Chan, D. Pavlidis, M. Razeghi, and F. Omnes, *IEEE Trans. Electron Devices* ED-37, 2141(1990).
- [4] T. Kobayashi, K. Taira, F. Nakamura, and H. Kawai, *J. Appl. Phys.* 65, 4898(1989).
- [5] Z. C. Huang, C. R. Wie, J. A. Varriano, M. W. Koch, and G. W. Wicks, *J. Appl. Phys.* 77, 1587(1995).
- [6] S. J. Peaton, J. W. Corbett, and T. S. Shi, *Appl. Phys. A43*, 153(1987).

Fourier Transform Infrared Spectroscopy (FTIR), SIMS and Raman Scattering of Heavily Carbon Doped MOCVD Grown $\text{In}_{0.53}\text{Ga}_{0.47}\text{As}$.

A. Sibai*, F. Ducroquet*, K. Hong[†], D. Cui[†] and D. Pavlidis[†].

*Laboratoire Physique de la Matière, INSA de Lyon - CNRS- UMR 5511; 20 avenue Albert Einstein, 69621 Villeurbanne Cedex, France.

[†]The University of Michigan, Department of Electrical Engineering and Computer Science, 1301 Beal Avenue, Ann Arbor, MI 48109-2122, USA.

Abstract: InGaAs layers were grown on InP substrates by MOCVD using CBr_4 sources and $3 \times 10^{19} \text{ cm}^{-3}$ doping was achieved upon annealing and de-passivation from hydrogen. The impact of annealing was investigated by FTIR, SIMS and Hall measurements. The results show the presence of the $\text{H} - (\text{C}_{\text{As}})_2$ complex and a loss of hydrogen upon annealing which is estimated to be ~33% by FTIR and ~50% by SIMS. These results are consistent considering the fact that FTIR refers only to C-H bonds. In and As variations near the surface and some carbon concentration variation upon annealing is also reported.

I. Introduction

Heavily doped p-type $\text{In}_x\text{Ga}_{1-x}\text{As}$ ($x = 0.53$) is very attractive for electronic and optoelectronic applications such as, Heterojunction Bipolar Transistors (HBTs), heterojunction lasers and p-i-n diodes. Carbon doping offers a valuable alternative to traditionally used group II elements, such as Zn and Be due to its low diffusivity and high degree of incorporation. Most of the work to date has been carried out by growth techniques other than Metalorganic Chemical Vapor Phase Epitaxy (MOCVD). Results presented so far using MOCVD employed primarily CCl_4 as carbon source [1] and demonstrated some limitations imposed by the presence of large amounts of hydrogen which reduce carbon incorporation and passivate the incorporated atoms. Annealing appears to be in certain cases necessary in order to activate the incorporated acceptor atoms and obtain a high level of p-doping. Little is known on the hydrogen passivation process and the characteristics of such layers. We report the growth of C-In_{0.53}Ga_{0.47}As by MOCVD, using CBr_4 rather than CCl_4 as carbon source and analyze its characteristics using Fourier Transform Infrared Spectroscopy (FTIR), Secondary Ion Mass Spectrometry (SIMS) and Raman spectroscopy.

II. Basic considerations of C-incorporation in III-Vs

Extensive reports have been made on C-GaAs and its passivation with hydrogen [2][3] but much less has been reported on its ternary compounds [4]. Studies of these materials by infrared and Raman Spectroscopy have revealed Localized Vibrational Modes (LVM) of (C - H) pairs and carbon isolated acceptors. Carbon acceptors in InGaAs can manifest five different cluster configurations, depending on the number of In Nearest Neighbors (NN), $\text{C}_{\text{As}}\text{Ga}_4$, $\text{C}_{\text{As}}\text{InGa}_3$, $\text{C}_{\text{As}}\text{In}_2\text{Ga}_2$, $\text{C}_{\text{As}}\text{In}_3\text{Ga}$, and CIn_4 , with T_d , C_{3v} , C_{2v} , C_{3v} , and T_d symmetry.

The introduction of Hydrogen passivates the carbon acceptors and form a C-H complex, with hydrogen occupying the bond centered site, between the carbon and one of its NN atoms. High resolution IR and Raman spectra of GaAs at He liquid temperature (HeLT) revealed the presence of a high frequency stretch mode at 2635 cm^{-1} which was assigned to a C-H complex [4][5]. Moreover, the frequencies 2635, 2626, 2617, 2608 and 2558 cm^{-1} were observed in $\text{Al}_x\text{Ga}_{1-x}\text{As}$ with $0 < x < 1$ [6]. These lines provided information on the Al (NN) complex with zero, one, two or three Al (NN). The 2635 cm^{-1} line has also been observed in InGaAs for $x < 0.1$ [7]. The difference in line number appears to depend on the technique and parameters used for growth. A 2688 cm^{-1} line has also been observed at (HeLT), in GaAs and AlGaAs [8][9]. Extensive work on this line, concluded that it is due to the formation of an aligned carbon - hydrogen complex [$\text{H} - (\text{C}_{\text{As}})_2$] involving two carbon atoms aligned in the [110] direction, when the growth direction is [100]. Moreover, some of these

complexes but not necessarily all, incorporate at least one hydrogen and the di-carbon split interstitial appears to act as a donor [9]. Dissociation and defect cluster formation combined with eventual presence of interstitial C and deep donor presence can consequently impact the performance of devices such as HBTs. It is therefore important to understand the local structure of C_{As} in InGaAs before and after annealing.

We report a similar investigation on the local structure of C acceptors in In_xGa_{1-x}As with x = 0.53. SIMS, Raman, FTIR and Hall measurements were performed for this purpose. Annealing led to de-passivation of the carbon acceptors and its impact has also been investigated. The results show the presence of the di-carbon defect [H-(CAs)₂] aligned in the plane perpendicular to the (100) growth axis.

III. MOCVD Growth Study of C-In_{0.53}Ga_{0.47}As using CCl₄ and CBr₄ Sources

The investigated C-InGaAs layer was 2.5 μm thick and was grown directly on Fe-doped SI InP (100) substrate, using our EMCORE LP-MOCVD system [1]. TMIn, TMGa and 100% AsH₃ were used for group III and group V elements respectively. The V/III ratio was 5 to 20. Studies of the CBr₄ source efficiency as a function of growth temperature showed a much smaller sensitivity of indium incorporation efficiency to temperature compared with growth in the presence of CCl₄. Since the incorporation of both H and C increases as the growth temperature decreases, the latter was set to 450°C which is a good trade-off for reduced H incorporation and maximum doping.

The maximum doping level achieved with the above described approach was 7 × 10¹⁹ cm⁻³ and 3 × 10¹⁹ cm⁻³ for CCl₄ and CBr₄ sources respectively. Studies of the mobility vs. hole concentration characteristics for InGaAs grown using the above two sources showed similar values as those obtained using other growth techniques such as MBE and Gas-Source MBE. SIMS and Hall analysis suggested that the Hydrogen reduction taking place upon annealing is smaller than the occurring increase of p-doping. A possible explanation for this is the presence of an additional mechanism related to carbon displacement from group III to group V site [1]. The investigated samples consisted of "as-grown" InGaAs, annealed InGaAs and a reference InP substrate.

IV. Fourier Transform Infrared Spectroscopy Characteristics of C-In_{0.53}Ga_{0.47}As

FTIR measurements were performed at room temperature, using a Nicolet 800 FTIR spectrometer at 4 cm⁻¹ resolution in the 400 - 4000 cm⁻¹ range. Tests took place with and without polarizer, at different angles of incidence, in the transmission and reflection modes, before and after annealing of the sample. The absorption spectra of the InGaAs are shown in Fig.1 and reveal a wide peak centered at 2666 cm⁻¹. Taking into account the difference in frequency between (HeLT) and room temperature spectra, this peak is to be compared with the 2688 cm⁻¹ line observed in GaAs and AlGaAs. The latter suggests that the observed peak may be assigned to a [H-(CAs)₂] complex as previously reported for GaAs.

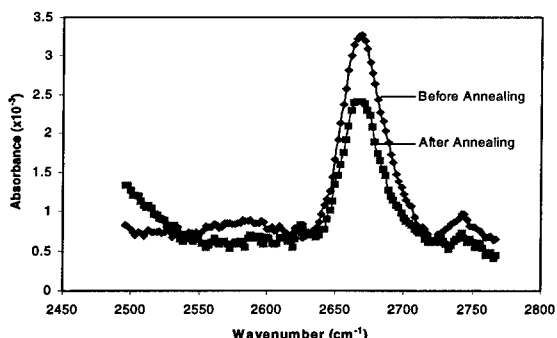


Fig. 1 FTIR spectra of C-InGaAs before and after annealing in the 2600 cm⁻¹ region

Annealing at 600°C in an inert atmosphere for 10 secs, led to a decrease in the intensity of the 2666 cm^{-1} peak. The integrated absorbances for both spectra before and after annealing ($A_1 = 0.0921 \text{ cm}^{-1}$, $A_2 = 0.0612$), show that 33% of the complex centers dissociate upon annealing. Assuming that the carrier concentration increase upon annealing is solely related to dissociation of C-H complexes, this suggests that 50% of the passivated carbon atoms could be freed upon annealing.

Study of the isolated carbon (C - Ga) or (C - In) bond in the low energy range turned out to be difficult due to the apparent Fe segregation and diffusion in the InP substrate taking place at the process temperature and upon annealing [9]. Nevertheless, in the narrow window, between 515 and 600 cm^{-1} , where the InP muliphonons and Fe impurities contributions are absent, a very weak peak was observed at 545 cm^{-1} . The nature of this line can be better understood by consideration of the lines associated with the isolated carbon (C-Ga) bond and observed in C-GaAs and C-AlGaAs between 500 and 600 cm^{-1} . By analogy to the correlation reported between the 576 cm^{-1} and 2688 cm^{-1} lines in GaAs [10], it is suggested that the 545 cm^{-1} is likely to be correlated to the 2666 cm^{-1} line observed in our InGaAs samples.

V. Hall and SIMS Characterization of C- $\text{In}_{0.53}\text{Ga}_{0.47}\text{As}$

Hall measurements showed a strong increase in carrier concentration after annealing with a doping increase from $2.0 \times 10^{18} \text{ cm}^{-3}$ to $6.9 \times 10^{18} \text{ cm}^{-3}$, while the mobility remained almost constant showing a small variation from 60 to 63 cm^2/Vs . This suggests the presence of a hydrogen passivation mechanism which is purely associated with a neutralization effect (partially neutralized $[\text{H} - (\text{CA}_3)_2]$ complexes).

SIMS depth profiles made it possible to obtain information on the concentration of the different elements present in the InGaAs layer. SIMS measurements were performed with a Cameca - IMS 4f apparatus, with oxygen as primary beam. The samples (before and after annealing), were introduced together, and measured simultaneously, after 24 hours degassing, in order to overcome the interference from residual hydrogen in the chamber, and ensure the use of same parameters and conditions for the evaluating the sample profile. Typical results are shown in Fig.2 and demonstrate a variation in the concentration of In and As over the top one micron of the layer. The layer appears in this region as «In rich» and «As poor» and the results suggest the presence of stoichiometry variations near the surface.

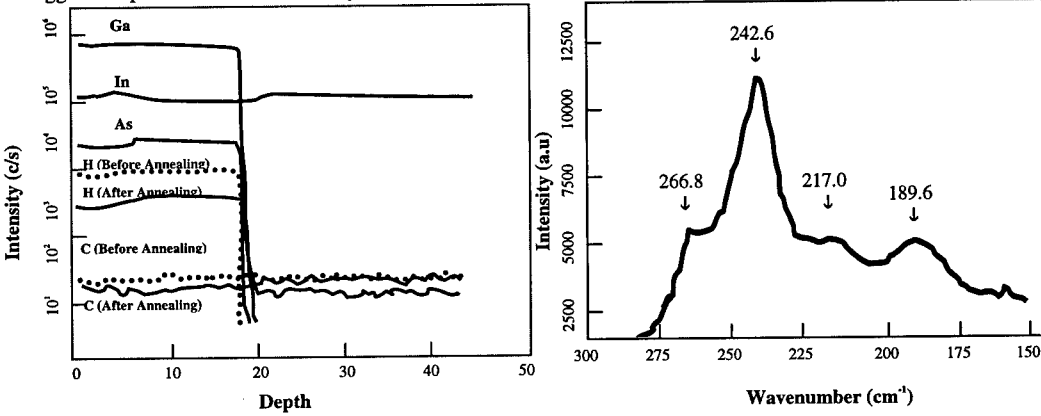


Fig. 2 SIMS characteristics of C-InGaAs after annealing Fig. 3 Raman spectrum of C-InGaAs upon annealing

Hydrogen depth profiles of the samples before and after annealing showed a 50% decrease in hydrogen concentration (proportional to the ionic current) upon annealing. This agrees with the above reported FTIR results which predicted a smaller decrease of 33% as expected in such a measurement which is solely related to changes in C-H bonds. The remaining elements except carbon, appeared to remain stable upon annealing.

Care was taken to ensure very stable and reliable conditions for SIMS measurements. As explained earlier, samples were characterized simultaneously before and after annealing and degassing took place over extended periods of time. The observed 20% carbon loss in C-InGaAs upon annealing (on a linear scale) is higher than the 5 to 10% uncertainty of the SIMS measurement. There is consequently at least 10% of carbon concentration change, possibly by outdiffusion [11]. Moreover, the decrease in Carbon concentration upon annealing is linear, showing a maximum variation of ~10% at the top of the layer and almost zero variation near the InGaAs/InP substrate interface.

VI. Raman Spectroscopy of C-In_{0.53}Ga_{0.47}As

Raman measurements have been performed at room temperature with a Dilor spectrometer using the 514.5 nm Argon laser line at 2 cm⁻¹ resolution. Fig. 3 shows the Raman spectrum of the InGaAs layer before annealing. InGaAs is expected to manifest two modes behavior in Raman spectra. The observed peaks at 267, 244, 217 and 190 cm⁻¹ are, however, very wide and convoluted to be analyzed precisely. Moreover, the C-H peak which is expected at 2666 cm⁻¹ due to the stretch mode of H - (CAs)₂ pairs complexes is absent. Only phonons bands are visible, as well as, a peak at 244 cm⁻¹ which has been attributed to disorder alloy and becomes narrower after annealing. The presence of an InAs peak at 217 cm⁻¹, suggests a lack of stoichiometry i.e. In rich conditions and is in agreement with the previously discussed SIMS results.

Finally, the very wide peak at 190 cm⁻¹ is not an InGaAs phonon band. This peak could be attributed to an AlAs disorder induced scattering activated mode [12]. SIMS spectra obtained after this observation confirmed the presence of very low concentration of Al in the InGaAs layer and support this hypothesis.

VII. Conclusion

C-doped InGaAs was grown by MOCVD on InP (100) substrates using a CBr₄ source and doping levels of 3×10^{19} cm⁻³ have been achieved. The presence of an aligned [H - (CAs)₂] complex is evidenced at the growth surface of C-In_xGa_{1-x}As layers for x=0.53 by FTIR measurements. Further evidence of the passivation mechanism taking place by hydrogen incorporation in the layer is expected by performing liquid Helium temperature IR measurements, with higher resolution, in order to resolve the observed peak.

SIMS measurements provided information on the total loss of hydrogen which occurs in the layer upon annealing. They have also revealed a variation of In and As concentration near the surface and a change of C-concentration upon annealing. Raman characterization suggested some lack of stoichiometry and the presence of AlAs induced scattering. The evolution of hydrogen content is obviously related to the annealing temperature and thermal budget used. Further studies along these lines would yield optimum conditions for carbon acceptor activation, and will help understanding of the dissociation mechanism of complexes present in the layer.

References:

- [1] K.Hong and D. Pavlidis, J. Electr. Mater., 25, 449, (1995).
- [2] D.M. Kozuch, M.Stavola, S.J. Pearton, C.R. Abernathy and W.S. Hobson, J. Appl. Phys., 73, 3716, (1993).
- [3] C. R. Abernathy and W.S. Hobson, J. Mater. Sci. 7, 1, (1996).
- [4] B.R. Davidson, R.C. Newman, T.J. Bullough and T.B. Joyce, Phys. Rev., B48, 17106, (1993).
- [5] Wagner, K.H. Bachem,B.R. Davidson, R.C. Newman, T.J. Bullough and T.B. Joyce, Phys. Rev B51, 4150, (1995).
- [6] R.E. Pritchard, R.C. Newman, J. Wagner, F. Fuchs, R. Jones S. Oberg, Phys. Rev. B50,10628, (1994).
- [7] M.J. Ashwin, R.E. Pritchard, R.C. Newman, T.B. Joyce, T.J. Bullough, J. Wagner, C. Jeynes, S.J. Breuer, R. Jones, P.R. Briddonand S. Oberg,J. Appl. Phys., 80, 6754, (1996).
- [8] Y Cheng, M.Stavola, C.R. Abernathy, S.J. Pearton and W.S. Hobson. Phys. Rev., B49, 2469, (1994).
- [9] B.R. Davidson, R.C. Newman, H. Fushimi, K. Wada,H. Yokohama and N. Inoue, J. Appl. Phys. 81,7255, (1997).
- [10] H. Kamada, S. Shinoyama and A. Katsui, J. Appl. Phys. 55,2881,(1984).
- [11] K. Woodhouse, R.C. Newman, R. Nicklin, R.R. Bradley and M.J.L. Sangster, J. Cry. Growth, 120,323, (1992)
- [12] S. Emura, T. Nakagawa and S. Gonda, J. Appl. Phys. 62, 4632,1987.

Raman spectroscopy of $\text{InAs}_{1-x}\text{Sb}_x/\text{InSb}$ and $\text{InAs}_{1-x}\text{Sb}_x/\text{InAs}$ superlattices, under hydrostatic pressure

S. J. Webb and R. A. Stradling

Department of Physics, Imperial College, Prince Consort Road, London SW7 2BZ, UK

K. Nagata

Department of Applied Physics, Fukuoka University, Fukuoka 814-01, Japan

Abstract

The high pressure phase transitions of $\text{InAs}_{1-x}\text{Sb}_x/\text{InSb}$ and $\text{InAs}_{1-x}\text{Sb}_x/\text{InAs}$ superlattices are investigated using Raman spectroscopy. Both component layers of the superlattices undergo a phase transition at the same pressure. In the $\text{InAs}_{1-x}\text{Sb}_x/\text{InAs}$ system, this pressure is the same as that of bulk InAs, independent of the Sb content of the alloy layer. In the $\text{InAs}_{1-x}\text{Sb}_x/\text{InSb}$ system, the transition pressure is either that of the $\text{InAs}_{1-x}\text{Sb}_x$ alloy, or it is the mean of the transition pressures of both constituent layers. The mechanisms which could cause the differences in transition pressures are discussed.

1. Introduction

In a previous paper we reported Raman spectra of $\text{InAs}_{1-x}\text{Sb}_x$ alloys under hydrostatic pressure [1]. The phonon peak positions shifted monotonically to higher frequency with increasing pressure, until the phase transition pressure was reached. The phase transition pressure was 75 kbar for pure InAs, and decreased almost linearly as the Sb content (x) was increased. An $\text{InAs}_{0.58}\text{Sb}_{0.42}/\text{InSb}$ superlattice changed phase at a pressure equal to the mean of the transition pressures of its constituent layers. This paper extends those studies, by investigating the phase transition pressures of $\text{InAs}_{1-x}\text{Sb}_x/\text{InSb}$ superlattices with $x > 0.4$, and $\text{InAs}_{1-x}\text{Sb}_x/\text{InAs}$ superlattices with $x < 0.38$.

2. Experiment

All the superlattice samples were grown by molecular beam epitaxy (MBE) on GaAs substrates. Buffer layers of composition $\text{InAs}_{1-x/2}\text{Sb}_{x/2}$, and 1 μm thick, accommodated the lattice mismatch between the epilayer and the substrate. The samples were grown at 450°C, a temperature for which phase separation is unlikely to occur [2]. Each superlattice consisted of 100 periods, and the thickness of each layer was 100 Å (i.e. a period of 200 Å), giving a total superlattice thickness of 2 μm . The top layer of each sample was the binary compound (InAs or InSb). The compositions of the alloy layers were determined by x-ray diffraction.

High pressures were generated using a miniature diamond anvil cell [3], with a 4:1 (by volume) mixture of methanol and ethanol as the pressure transmitting medium. The pressure in the cell was measured by the ruby fluorescence method [4]. Raman spectra were taken using a Renishaw Raman

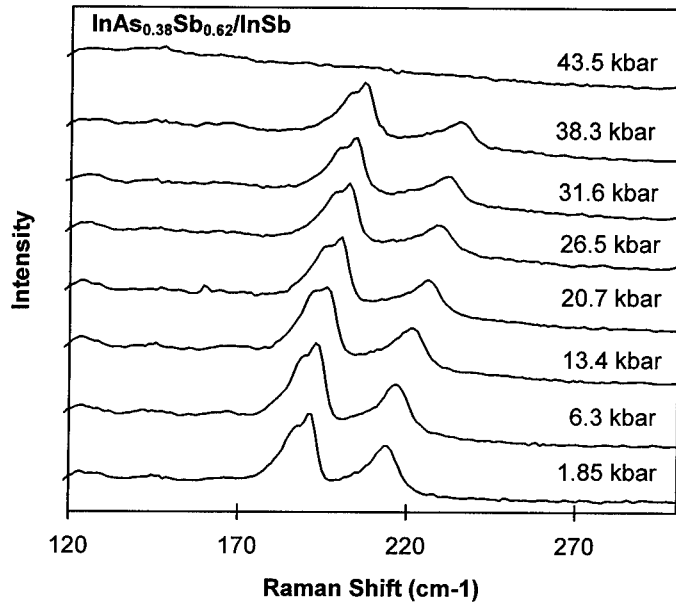


Figure 1: Raman spectra of $\text{InAs}_{0.38}\text{Sb}_{0.62}/\text{InSb}$ superlattice at various pressures

Microprobe, and the excitation source was a HeNe laser, giving a wavelength of 633nm. Taking into account optical losses from both the spectrometer and the diamond anvil cell, the laser power at the sample is estimated to be less than 1mW.

3. Results and Discussion

Raman spectra from an $\text{InAs}_{0.38}\text{Sb}_{0.62}/\text{InSb}$ superlattice, at a series of pressures, are shown in Figure 1. The peak at higher frequency (about 211cm⁻¹ at atmospheric pressure) is the InAs-like LO mode from the alloy layer. At lower frequency, there is a peak with a shoulder on the low frequency side. The peak is thought to be the InSb mode from the binary layer, while the shoulder is the InSb-like mode from the alloy layer. The frequency of the InSb-like mode in an $\text{InAs}_{1-x}\text{Sb}_x/\text{InSb}$ superlattice is expected to be lower than its bulk frequency, due to the tensile strain in the InAsSb layers.

The Raman modes from both the binary and alloy layers remain visible up to the phase transition pressure (P_t), suggesting that all the superlattice layers transform simultaneously. The phase transition is identified by the disappearance of the Raman peaks, as the lattice structure changes to a high pressure orthorhombic phase [5]. The surface morphology of the sample also changes; when viewed under an optical microscope, the surface takes on a wrinkled appearance. If the pressure increments are sufficiently small, P_t can be determined to an accuracy of $\pm 1\text{-}2\text{kbar}$. Measurement of

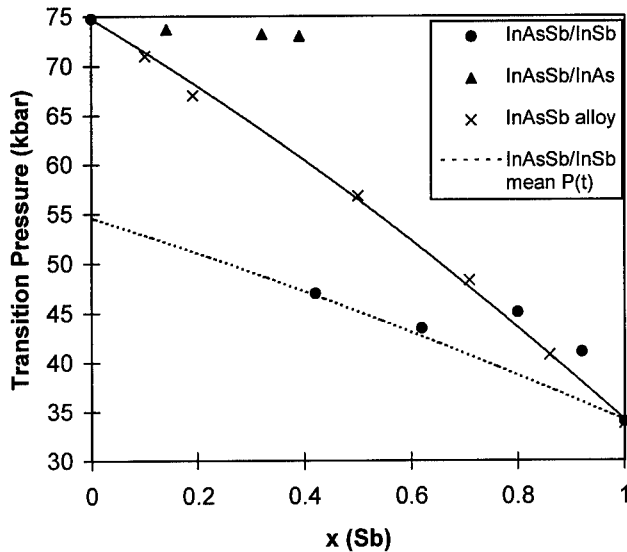


Figure 2: Phase transition pressures of superlattice samples

ruby fluorescence from pieces of ruby at different positions in the gasket hole indicates that the pressure varies by less than ± 1 kbar.

The phase transition pressures of all the superlattice samples are shown in Figure 2. Also shown are the results for $\text{InAs}_{1-x}\text{Sb}_x$ alloys, from reference 1. All of the $\text{InAs}_{1-x}\text{Sb}_x/\text{InAs}$ superlattices transform at a pressure close to the transition pressure of bulk InAs (75 kbar). The $\text{InAs}_x\text{Sb}_{1-x}$ layers are therefore ‘superpressed’ beyond their normal transition pressures, by as much as 12 kbar in the case of the $x=0.38$ sample. The two $\text{InAs}_{1-x}\text{Sb}_x/\text{InSb}$ samples with lowest values of x transform at the mean of the transition pressure of their constituent layers (this mean pressure is indicated by a dotted line on the diagram). The transition pressures of the other two are approximately equal to the bulk transition pressures of their alloy layers, resulting in a superpressing of the InSb layers of about 11 kbar for $x=0.80$. The samples are therefore behaving in two distinct ways: either they transform at the mean P_t of their layers, or the higher P_t layer dominates. These two groups will be referred to, respectively, as ‘mean P_t ’ and ‘high P_t ’ samples.

It is thought that a superlattice can undergo a phase transformation by the motion of alternate $\{111\}$ planes of atoms to new lattice locations [6]. Since these planes intersect both types of superlattice layer, the higher P_t layer can hinder their motion, and prevent the lower P_t layer from transforming. The lower P_t layer can therefore be ‘superpressed’ beyond its bulk transition pressure. In the mean P_t samples, the lower P_t layer can overcome this resistance, causing the whole superlattice to transform at an average P_t . In the high P_t samples it cannot, so the higher P_t layer is able to constrain the lower P_t layer, until the higher P_t layer transforms. It can be seen from Figure 2 that for

$\text{InAs}_{1-x}\text{Sb}_x/\text{InSb}$, the mean P_t samples have lower Sb contents, and are therefore more highly strained, than the high P_t samples. The increased compressive strain in the lower P_t layers could be providing the extra energy needed for them to overcome the resistance of the higher P_t layers.

The $\text{InAs}_x\text{Sb}_{1-x}/\text{InSb}$ sample with $x=0.62$ is a ‘mean P_t ’ sample. However, the $\text{InAs}_x\text{Sb}_{1-x}/\text{InAs}$ sample with $x=0.38$ is similarly strained (with a lattice mismatch of about 2.5%), and it changed phase at the P_t of bulk InAs, i.e. it is a ‘high P_t ’ sample (as were all of the $\text{InAs}_x\text{Sb}_{1-x}/\text{InAs}$ samples studied here). This suggests that the InAs layers are more effective at preventing the lower P_t layers from changing phase, possibly because the P_t of bulk InAs is significantly higher than the P_t ’s of the $\text{InAs}_x\text{Sb}_{1-x}$ alloys (in the range of x studied here). Therefore, even in the more highly strained $\text{InAs}_x\text{Sb}_{1-x}/\text{InAs}$ samples, the lower P_t layers cannot overcome the resistance of the InAs layers, and the higher P_t layers determine the superlattice P_t .

4. Conclusions

The behaviour of $\text{InAs}_x\text{Sb}_{1-x}/\text{InSb}$ and $\text{InAs}_x\text{Sb}_{1-x}/\text{InAs}$ superlattices, under high pressures, is investigated by Raman spectroscopy. The superlattice layers with the higher P_t impede the phase transition in the lower P_t layers. In the more highly strained $\text{InAs}_{1-x}\text{Sb}_x/\text{InSb}$ superlattices, compressive strain can cause the lower P_t layers to partially overcome this resistance, making the superlattice transform at the mean P_t of its constituent layers. All of the $\text{InAs}_{1-x}\text{Sb}_x/\text{InAs}$ samples changed phase at pressures close to the P_t of bulk InAs.

References

- [1] Nagata K, Webb S J and Stradling R A, *Phys. Stat. Sol. (b)* **198**, [527], (1996)
- [2] Ferguson, Norman A G, Seong T Y, Thomas R H, Phillips C C, Stradling R A and Joyce B A, *Appl. Phys. Lett.* **59**, 3324, (1991)
- [3] Dunstan D J and Scherrer W, *Rev. Sci. Instrum.* **59** (4), 627, (1988)
- [4] Piermarini G J, Block S, Barnett J D, and Forman R A, *J. Appl. Phys.* **46**, 2774, (1979)
- [5] McMahon M I and Nelmes R J, *Phys. Stat. Sol. (b)*, **198**, 389 (1996)
- [6] Dunstan D J, Prins A D, Gil B and Faurie J P, *Phys. Rev. B*, **44** (8), 4017 (1991)

Growth of $\text{Ga}_2\text{O}_3(\text{Gd}_2\text{O}_3)$ Using Molecular Beam Epitaxy Technique - Key to First Demonstration of GaAs MOSFETs

M. Hong, F. Ren, W. S. Hobson, J. M. Kuo, J. Kwo, J. P. Mannaerts, J. R. Lothian, M. A. Marcus, C. T. Liu, A. M. Sergent, T. S. Lay*, and Y. K. Chen

Bell Laboratories, Lucent Technologies, Murray Hill, New Jersey USA

Abstract. This article reviews our recent research efforts on GaAs passivation by the growth of a novel oxide made of Ga_2O_3 and Gd_2O_3 . The oxide-GaAs interface has a low interfacial state density of 10^{10} $\text{cm}^{-2}\text{eV}^{-1}$, comparable to that of SiO_2 -Si interface. A multi-chamber UHV system, including molecular beam epitaxy (MBE) growth chambers, has been used to fabricate $\text{Ga}_2\text{O}_3(\text{Gd}_2\text{O}_3)$ -GaAs device wafers. The growth of $\text{Ga}_2\text{O}_3(\text{Gd}_2\text{O}_3)$, in combining a conventional ion implantation process, enables us to demonstrate the first enhancement-mode GaAs metal-oxide-semiconductor field-effect-transistors (MOSFETs) with inversion.

1. Introduction

Today's integrated circuit is based upon Si MOSFETs technology. The primary reason is the ability to produce a superb interface between Si and SiO_2 , which has a low interfacial state density, and is thermodynamically stable. It is well known, however, that electrons move faster in GaAs, an important aspect to build high-speed circuits. Furthermore, semi-insulating substrates, not available in silicon, can be used to reduce cross-talk between high-speed signal lines in dense GaAs circuits. Present GaAs transistors use a metallic Schottky gate contact placed directly on a highly doped GaAs channel (called MESFETs), rather than on an oxide as in the MOS configuration. The Schottky gate induces unavoidable leakage currents, which severely limits the integration level of GaAs MESFETs. The lack of a stable dielectric film with a low interfacial state density (D_{it}) precluded the development of GaAs MOSFETs.

Unlike SiO_2 -Si, oxidation of GaAs surface produces poor-quality oxides. Efforts in searching for thermodynamically stable insulators providing a low interface state density for GaAs were taken as early as in 1960s. Thermal, anodic, and plasma surface oxidation techniques produced highly resistive films but could not provide the oxide-GaAs interfaces with low interfacial state density. [1,2] Deposition of different insulator materials on GaAs, including Si_3N_4 , SiO_2 , Al_2O_3 , and Ga_2O_3 has been used, in combination with dry, liquid, and photochemical semiconductor surface treatments.[1-4] These efforts produced limited improvements of electronic properties of the interfaces, with D_{it} at best in the range of $\sim 10^{12} \text{ cm}^{-2} \text{ eV}^{-1}$.

Recently, we have effectively passivated GaAs surfaces using a novel oxide of $\text{Ga}_2\text{O}_3(\text{Gd}_2\text{O}_3)$ prepared from our multi-chamber UHV system. [5-6] GaAs MOS diodes were fabricated, and accumulation and inversion in p- and n-channels were established. An interfacial state density as low as $2-3 \times 10^{10} \text{ cm}^{-2} \text{ eV}^{-1}$ was demonstrated, [7] which is comparable to that of SiO_2 -Si. In 1996, using $\text{Ga}_2\text{O}_3(\text{Gd}_2\text{O}_3)$ as a gate dielectric and a conventional ion implantation process, enhancement-mode GaAs MOSFETs with inversion have been implemented on semi-insulating GaAs substrates in n- or p- channel configurations.[8]

In the following, first, the requirements for obtaining low interfacial state density are discussed. We then describe the multi-chamber ultra high vacuum (UHV) system which was used to evaporate $\text{Ga}_2\text{O}_3(\text{Gd}_2\text{O}_3)$ and to grow the device materials. Structural and compositional characteristics of the *in-situ* fabricated oxide-GaAs interfaces were studied, followed by the discussion of the electronic properties. We then present fabrication and demonstration of enhancement-mode GaAs MOSFETs. We also discuss the more recent results on depletion-mode GaAs MOSFETs and enhancement-mode InGaAs MOSFETs.

2. Important parameters for achieving low interfacial state density

From the vast amount of work over the last 30 years, in order to achieve low interfacial state density in oxide-GaAs heterostructures, the following requirements have to be considered: (i) low surface exposure, in particular, the exposure to oxygen to be completely avoided or kept to a very low level, (ii) exclusion of chemical reactions between deposited oxides and GaAs, (iii) oxide deposition in an As free environment, and (iv) no introduction of interfacial states by electronic structures of deposited oxides. We believe, as will be discussed next, that a multi-chamber UHV system is a proper approach to achieve most of these requirements.

3. Film growth using multi-chamber UHV system

Fig. 1 shows our multi-chamber UHV system that includes two MBE growth chambers (a solid source GaAs based III-V chamber and an arsenic-free oxide deposition chamber) and other functional chambers. These chambers are linked together by several transfer modules with a background pressure of 10^{-10} torr. UHV is needed to minimize surface exposure, particularly to avoid oxidation, and to achieve an atomically ordered and chemically clean GaAs surface before the oxide deposition. Thus, neither contamination nor oxidation occurred on wafer surfaces during wafers transfer, and prior to the oxide deposition. The oxide deposition in an As free environment is preferred, because excess As on GaAs surface may cause high interfacial state density.

Samples were first loaded in the III-V chamber for either epi growth or surface cleaning by desorbing native oxides, which was monitored using reflection high energy electron diffraction (RHEED). Once an As-stabilized GaAs surface reconstruction of (2x4) was maintained, the wafers were then transferred to the second growth chamber for deposition of $\text{Ga}_2\text{O}_3(\text{Gd}_2\text{O}_3)$ or other oxides. The background pressure of the oxide chamber was below 10^{-9} Torr. $\text{Ga}_2\text{O}_3(\text{Gd}_2\text{O}_3)$ films were deposited by electron-beam evaporation of a single-crystal $\text{Gd}_3\text{Ga}_5\text{O}_{12}$ source at substrate temperatures in the range of 350-600 °C.

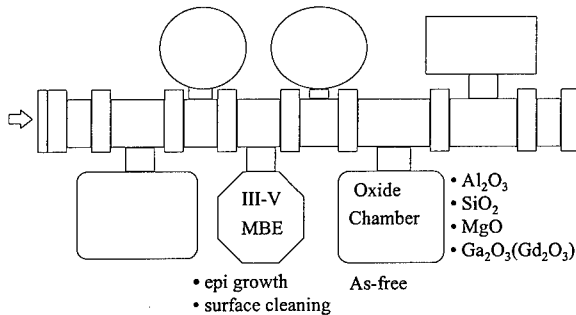


Fig. 1 Schematic of *in-situ* fabrication system, including solid-source III-V MBE, oxide chamber, and other functional chambers.

4. Structural characteristics of $\text{Ga}_2\text{O}_3(\text{Gd}_2\text{O}_3)$ -GaAs interfaces

The as-deposited $\text{Ga}_2\text{O}_3(\text{Gd}_2\text{O}_3)$ films are amorphous as studied by transmission electron microscopy (TEM), and RHEED. From studies of Rutherford backscattering spectrometry (RBS) and Auger analysis, the ratio of Gd_2O_3 to Ga_2O_3 depends on the deposition conditions such as substrate temperatures. The interfacial depth profiles of $\text{Ga}_2\text{O}_3(\text{Gd}_2\text{O}_3)$ -GaAs investigated by x-ray photoelectron spectroscopy (XPS) showed only the presence of Ga_2O_3 , Gd_2O_3 , and GaAs. Chemical reaction products, in particular As_2O_3 and As_2O_5 are not detectable. [7] Consequently, the chemical reaction $\text{As}_2\text{O}_3 + 2\text{GaAs} \rightarrow \text{Ga}_2\text{O}_3 + 4\text{As}$ ($\Delta G = -62$ kcal/mol) resulting in As formation and degradation of electronic interface properties is excluded. XPS was also employed to study the structural properties of other *in-situ* fabricated oxide-GaAs samples, such as MgO-, Al_2O_3 -, and SiO_2 -GaAs. The results are similar to that of $\text{Ga}_2\text{O}_3(\text{Gd}_2\text{O}_3)$ -GaAs interface, namely, no observation of As_2O_3 and As_2O_5 . However, as will be discussed in the next section, Fermi level is pinned at the interfaces for these oxide-GaAs structures, but not at the $\text{Ga}_2\text{O}_3(\text{Gd}_2\text{O}_3)$ -GaAs interface.

5. Electronic properties of $\text{Ga}_2\text{O}_3(\text{Gd}_2\text{O}_3)$ -GaAs interfaces characterized using photoluminescence

Interfacial recombination velocity (S), although not being directly related to an actual velocity, is related to the rate at which excess carriers recombine at the interface. For PL and recombination velocity studies, two reference samples of no oxide deposition (bare surface) and $\text{Al}_{0.45}\text{Ga}_{0.55}\text{As}$ -GaAs were fabricated, with identical GaAs epitaxial layer and substrate. Standard steady-state PL measurements using an argon ion laser at a high injection level of 1100 W/cm^2 were used to qualitatively characterize the MgO-, Al_2O_3 -, SiO_2 -, $\text{Ga}_2\text{O}_3(\text{Gd}_2\text{O}_3)$ -, and $\text{Al}_{0.45}\text{Ga}_{0.55}\text{As}$ -GaAs interfaces as well as the bare surface. [9,10] The results reveal two distinctively different classes of interfaces where the first group includes $\text{Ga}_2\text{O}_3(\text{Gd}_2\text{O}_3)$ - and $\text{Al}_{0.45}\text{Ga}_{0.55}\text{As}$ -GaAs, and the second comprises the other oxide-GaAs interfaces. Based on the internal quantum efficiency measured for incident light power densities, the interfacial recombination velocity has been inferred using a self-consistent numerical heterostructure device model. [9,10] The best fit of the simulations to the measured data has been obtained at $S = 4000\text{-}5000$, and 1000 cm/s for $\text{Ga}_2\text{O}_3(\text{Gd}_2\text{O}_3)$ -GaAs and reference $\text{Al}_{0.45}\text{Ga}_{0.55}\text{As}$ -GaAs structures. The $\text{Ga}_2\text{O}_3(\text{Gd}_2\text{O}_3)$ -GaAs interfacial recombination velocity is consistent with the low interface state density in the mid $10^{10} \text{ cm}^{-2} \text{ eV}^{-1}$ range, as measured from the C-V method. [7]

We notice that Al_2O_3 -, SiO_2 -, and MgO-GaAs structures are characterized by a Fermi level pinned at the interface and an interface recombination velocity which is comparable to that of the bare GaAs surface ($\sim 10^7 \text{ cm/sec}$). The fundamentally different electronic properties observed at various *in-situ* fabricated oxide-GaAs interfaces are due to the specific chemical bonding associated with the interfacial atoms of GaAs and the deposited oxide molecules. Evidently, in addition to (a) clean and atomically ordered GaAs surface and (b) no As_xO_y at the oxide-GaAs interface, the attainment of low interfacial recombination velocity, hence low interfacial state density, also requires no introduction of GaAs gap states by the deposited oxide molecules.

6. Interfacial roughness and formation of inversion and accumulation

Metal-oxide-semiconductor (MOS) capacitors were characterized by C-V measurements at frequencies ranging from quasi-static to 1MHz. The inferred midgap interfacial state density is in the low $10^{10} \text{ cm}^{-2} \text{ eV}^{-1}$ range as reported in Ref. 7. The observation of inversion and accumulation depends strongly on the interfacial roughness of $\text{Ga}_2\text{O}_3(\text{Gd}_2\text{O}_3)$ -GaAs heterostructures. Figs. 2 and 3 show the x-ray reflectivity and the corresponding C-V characteristics for a $\text{Ga}_2\text{O}_3(\text{Gd}_2\text{O}_3)$ film 8.8 nm thick deposited on Si doped GaAs (10^{18} cm^{-3}). In the x-ray reflectivity method of film metrology, the specular reflectivity of x-ray from a film surface is measured as a function of incidence angle. By analyzing these data, one can measure the thickness, density, and roughness of a single film on a substrate. The oxide-GaAs interfacial roughness was measured to be 0.24

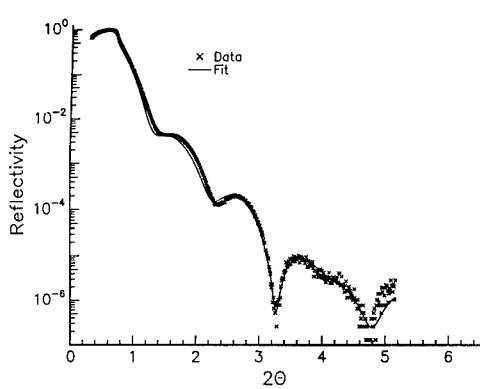


Fig. 2 X-ray reflectivity as a function of the incident angle for a $\text{Ga}_2\text{O}_3(\text{Gd}_2\text{O}_3)$ film 8.8 nm thick on GaAs.

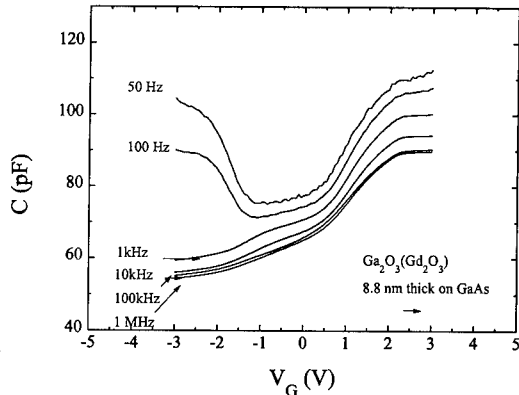


Fig. 3 Capacitance as a function of the bias voltage for the sample in Fig. 2. Frequency varies from 50 Hz to 1 MHz.

nm. The C-V measurement in Fig. 3 was performed under dark. For negative voltage, an inversion layer of holes forms at the interface. The inversion carriers follow the a.c. signal at 100 Hz at dark, and at 1 kHz under light (not shown). For an oxide-GaAs sample with an interfacial roughness of 0.8 nm, the inversion carriers only barely follow the a.c. signal at 100 Hz.

7. Demonstration of enhancement-mode GaAs MOSFET with inversion

The process sequence and a cross-sectional view of a GaAs enhancement-mode device are shown in Figs. 4 and 5. As described above in section 3, native oxides on GaAs were thermally desorbed at substrate temperatures of 580–600°C under an As overpressure. The wafers were then *in-situ* (under UHV) transferred into the oxide chamber where $\text{Ga}_2\text{O}_3(\text{Gd}_2\text{O}_3)$ was deposited at a substrate temperature of 535°C. Selective area ion implantation was used for ohmic, well, and channel regions. The implant activation anneal was carried out at 800°C and 860°C for 5 min for p- (Zn) and n- (Si) implants, respectively. HCl:H₂O mixtures were used for the oxide etching. AuBe/Pt/Au and Ge/Ni/Au-Ge/Mo/Au were used for p- and n-metallization, respectively. The interconnection and gate contact formation were achieved using e-beam evaporated Ti/Pt/Au metallization and lift-off process.

Figure 6 (a) and (b) illustrates the drain I-V curves of p- and n-channel devices with a geometry of $4 \times 50 \mu\text{m}^2$. [11] For p-MOSFET, the gate voltage varies from -9 to 0 V in steps of -1 V with a threshold voltage (V_T) of -0.5 V. The saturation drain current is proportional to $(V_g - V_T)^2$, which is a characteristic of an enhancement-mode device. An extrinsic transconductance of 0.2 mS/mm, which is limited by the large gate length and parasitic resistance, is obtained at V_{ds} of 2 V and V_g of -9 V. From the variation of drain conductance g_D versus gate voltage at small drain voltage, the effective mobility μ_{eff} was derived to be 20 cm²/Vs. The measured μ_{eff} is an order of magnitude lower than the bulk hole mobility, which is most likely caused by interfacial scattering. Similar device characteristics were also observed for n-MOSFET. Before the oxide growth, a rough wafer surface caused by prior device processing, was observed using *in-situ* RHEED. With the gate oxide 40 nm thick, a symmetrical gate breakdown voltage of 12.4 V is obtained. The gate breakdown is consistent with the breakdown field of 3.6 MV/cm, as measured on a large-area MOS diode.

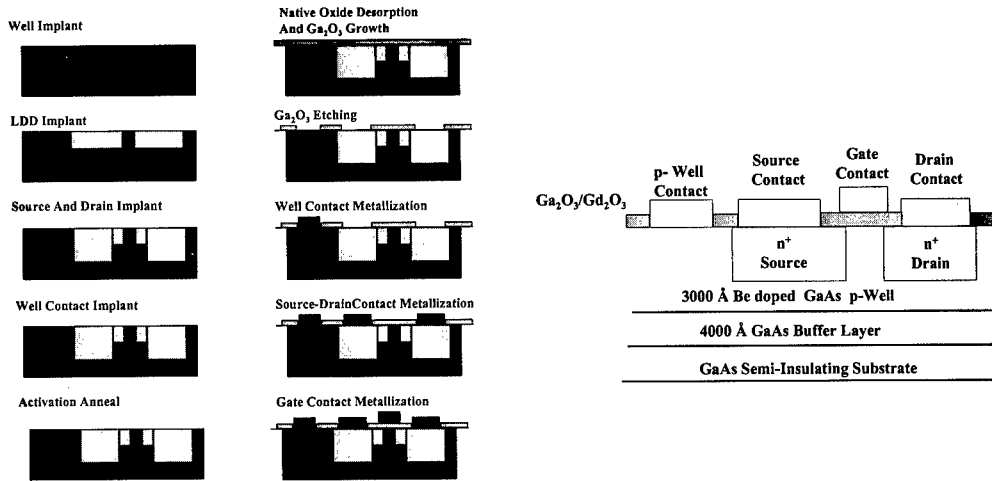


Fig. 4 Processing sequence of enhancement-mode GaAs MOSFETs.

Fig. 5 Cross-sectional view of an enhancement-mode p-channel GaAs MOSFET.

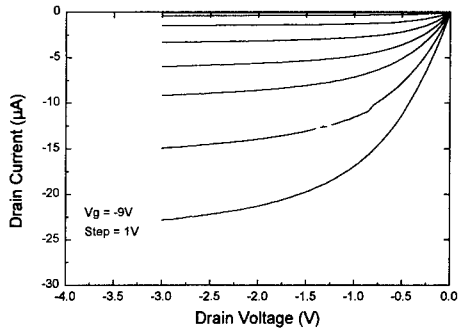


Fig. 6(a) Drain I-V characteristics of an enhancement-mode GaAs p-MOSFET with a gate geometry of $4 \times 50 \mu\text{m}^2$.

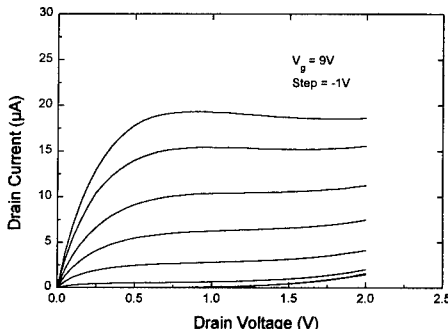


Fig. 6(b) Drain I-V characteristics of an enhancement-mode GaAs n-MOSFET with a gate geometry of $4 \times 50 \mu\text{m}^2$.

8. Depletion-mode GaAs MOSFETs and enhancement-mode InGaAs MOSFETs

$\text{Ga}_2\text{O}_3(\text{Gd}_2\text{O}_5)$ as the gate dielectric has also been applied to fabricate depletion-mode GaAs MOSFETs and enhancement-mode InGaAs lattice matched to InP. For depletion-mode GaAs MOSFET, an $1 \mu\text{m} \times 100 \mu\text{m}$ device shows good I-V characteristics with pinch off of the device occurring at $V_g = -2.5\text{V}$. The operation of the device in the accumulation regime is well established. Maximum transconductance is 100 mS/mm and

maximum drain current density is 315 mA/mm. The device also shows a very small output conductance. The microwave results show that unity current gain cutoff frequency (f_T) is 14 GHz and maximum available gain cutoff frequency (f_{max}) is 35 GHz.

For enhancement-mode InGaAs, an extrinsic transconductance of 190 mS/mm was obtained. There is no drain-current drifting or hysteresis observed for the devices with gate length larger than 2 μm . The effective mobility of 470 cm^2/Vs is derived from the variation of drain conductance, g_D , versus gate voltage at small drain voltage (~ 0 V). The current gain cutoff frequency and the maximum frequency of oscillation of 6.8 and 7.8 GHz were obtained, respectively.

9. Conclusions

Deposition of the novel oxide, a mixture of Ga_2O_3 and Gd_2O_3 , on clean and atomically ordered GaAs using *in-situ* MBE technique has produced a low interfacial state density. With $\text{Ga}_2\text{O}_3(\text{Gd}_2\text{O}_3)$ as the gate dielectric and an ion-implant technology, the first enhancement-mode GaAs MOSFETs were fabricated. The process discussed in the paper is compatible with the present commercial GaAs MESFET technology. The reason why $\text{Ga}_2\text{O}_3(\text{Gd}_2\text{O}_3)$ provides a low interfacial state density to GaAs, but not the other oxides, is still under investigation. Nevertheless, the results presented here show that the *in-situ* deposition of $\text{Ga}_2\text{O}_3(\text{Gd}_2\text{O}_3)$ has opened the possibility for the applications of III-V MOSFET technologies.

References

*Institute of Electro-Optical Engineering, National Sun Yat-Sen University, Kaohsiung, Taiwan

- [1] Wilmsen C W and Szpak S, 1977, *Thin Solid Films*, 46, 17 and references therein.
- [2] A review can be found in *Physics and Chemistry of III-V Compound Semiconductor Interfaces*, edited by C. W. Wilmsen (Plenum, New York, 1985).
- [3] Hasegawa H, Ishii H, Sawada T, Saitoh T, Konishi S, Liu Y, and Ohno H, 1988, *J. Vac. Sci. Technol. B*, 6, 1184-1192.
- [4] Aydil E S and Gottscho R A, 1994, *Mater. Sci. Forum*, V148-149, 159.
- [5] Hong M, Passlack M, Mannaerts J P, Kwo J, Chu S N G, Moriya N, Hou S Y, and Fratello V J, 1996, *J. Vac. Sci. Technol. B*, 14, 2297-2300.
- [6] Hong M, 1995, *J. Crystal Growth* 150, 277.
- [7] Passlack M, Hong M, Mannaerts J P, Opila R L, Chu S N G, Moriya N, Ren F, and Kwo J, 1997, *IEEE Trans. Electr. Devices*, 44, 214.
- [8] Ren F, Hong M, Hobson W S, Kuo J M, Lothian J R, Mannaerts J P, Kwo J, Chen Y K, and Cho A Y, 1996, *IEDM technical digest* p.943.
- [9] Passlack M, Hong M, Mannaerts J P, Kwo J, and Tu L W, 1996, *Appl. Phys. Lett.*, 68, 3605-3607.
- [10] Hong M, Passlack M, Noh D, Kwo J, and Mannaerts J P, 1996, ed by Ren F et al, *State-of-the-art program on compound semiconductors XXIV*, 36.
- [11] Ren F, Hong M, Hobson W S, Kuo J M, Lothian J R, Mannaerts J P, Kwo J, Chu S N G, Chen Y K, and Cho A Y, 1997, *Solid State Electronics*, in print.

Kinetics of AlAs Steam Oxidation at Low Pressure and Low Temperature Measured In-Situ Using a Novel Furnace Design with an Integral Optical Port

S.A. Feld*, J.P. Loehr, R.E. Sherriff, J. Wiemer, and R. Kaspi

Avionics Directorate, Wright-Patterson Air Force Base, Ohio 45433

*Wright State University, Dayton, Ohio 45435

Oxidation of AlGaAs layers has become a critical processing step in the fabrication of high-performance vertical-cavity surface-emitting lasers (VCSELs). The low refractive index of the oxide provides for high-contrast distributed Bragg reflector (DBR) mirrors, while the high oxide resistivity makes it ideal for defining VCSEL current apertures. We have integrated a glass viewport into a low-pressure (5 Torr) cold-walled oxidation chamber to allow in-situ optical monitoring of the oxidation reaction, enabling superior control and reproducibility. Real-time, in-situ optical measurements of AlAs oxidation rates were performed and we compare the results with a standard model. Oxide-semiconductor DBRs were also fabricated and we present reflectivity measurements on these samples.

1. Introduction

Recently, native oxides of AlAs/GaAs alloys have become popular for the fabrication of vertical-cavity surface-emitting lasers (VCSELs)[1,2]. The low refractive index of the oxide allows fabrication of high-contrast distributed Bragg reflector (DBR) mirrors using only a few quarter-wave layers[3], while the high oxide resistivity makes it ideal for defining VCSEL current apertures. Unfortunately, when the oxidation reaction is conducted in a conventional tube furnace it is hard to control, making it difficult to reproducibly define the small features necessary for high-quality VCSELs.

2. Oxidation furnace design

To improve our control over the reaction we have designed and constructed a custom oxidation furnace (Figure 1). A window in the reaction chamber permits real-time in-situ optical monitoring of the oxidation. To prevent water vapor from condensing on the cold window and obscuring the sample, the reaction chamber is operated at low pressure (5 Torr). This low pressure also allows us to immediately halt the reaction by evacuating the chamber. In addition, we dramatically reduce the oxidation rate by keeping the sample at low temperature (325-400°C). The combination of optical monitoring, rapid shutoff, and slow oxidation greatly increases our control over the reaction and allows us to define small features precisely and reproducibly.

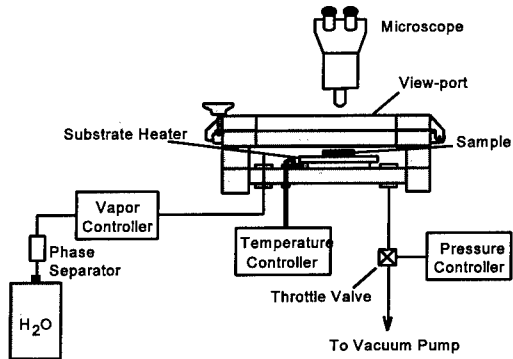


Figure 1. Schematic diagram of the oxidation system

3. Oxidation kinetics

Using our in-situ monitoring capability we directly measure the oxidation distance as a function of time. Using a long working distance microscope and an infrared camera, magnified images of the sample can be obtained during the oxidation (Figure 2).

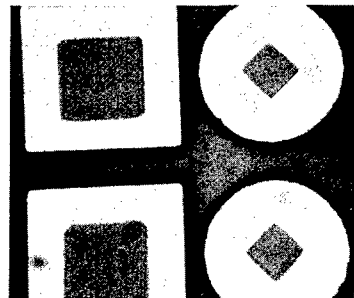


Figure 2. Infrared image of partially oxidized DBR structures showing the clear contrast between oxidized regions and unoxidized regions.

These images can be analyzed to determine the oxidation distance as a function of time (Figure 3). The data have been shifted in time to coincide at the origin. This time delay is believed to be due to oxidation of the surfaces in air during the time between the preparation of the samples and their introduction into the oxidation chamber. Despite care to reproducibly prepare the samples, the delay time does not seem to vary in a systematic manner. A standard oxidation model, of the form[4]:

$$x(t')^2 + Ax(t') = Bt', \quad \text{or} \quad x(t') = \frac{A}{2} \sqrt{1 + \frac{t'}{(A^2/4B)} - 1}$$

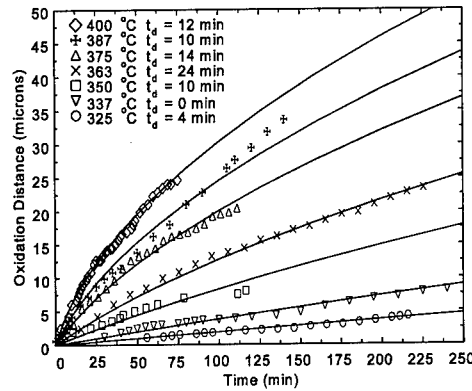


Figure 3. Oxidation distance as a function of time for several temperatures. The measured and fitted curves have been shifted in time by the delay values t_d to coincide at the origin. All oxidations were carried out at a water vapor pressure of 5 Torr and a flow of 500 sccm.

can be well-fit to the data in figure 3. Here the coefficients A and B are temperature dependent and have the form:

$$A(T) = A_0 e^{-E_{aA}/kT}, \text{ and } B(T) = B_0 e^{-E_{aB}/kT}.$$

A least-squares fit to the data gives $A_0 = 7.8 \times 10^{-6} \mu\text{m}$, $B_0 = 1.07 \times 10^8 \mu\text{m}^2 \text{ min}$, $E_{aA} = -0.846 \text{ eV}$, and $E_{aB} = -0.912 \text{ eV}$. Unfortunately, due to the small range of temperatures studied in this experiment, we cannot attach great statistical significance to these parameters despite the close agreement between the measured and fitted curves.

4. Reflectivity measurements

To verify that these oxides have suitable optical and mechanical properties for DBR mirror fabrication, we also measured the reflectance of DBR layer stacks after low-temperature oxidation. Since the low oxidation rate makes it impractical to oxidize large features, we constructed an imaging system capable of measuring the reflectance of small ($\sim 20 \mu\text{m}$) features. A schematic diagram of the system is shown in Figure 4.

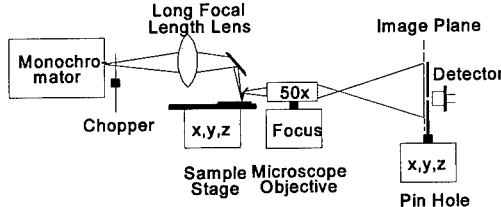


Figure 4. Schematic diagram of the small-area reflectivity measurement system.

Typical reflectivity spectra obtained from the system are shown in figure 5. A calculated spectrum of the unoxidized sample is fitted to the measured spectrum to extract the thickness of the layers prior to oxidation. After oxidation, the sample is re-measured and the calculated spectrum is again fitted to determine layer thickness after oxidation. From this analysis, a layer shrinkage of approximately 2.5% is obtained for the oxidized AlAs layers.

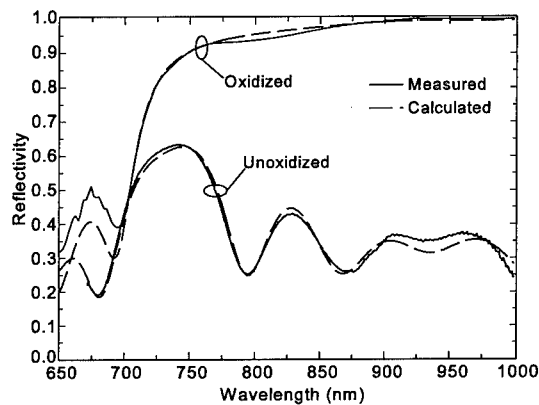


Figure 5. Measured and calculated reflectivity spectra of unoxidized and oxidized DBR structures.

5. Conclusion

We have constructed and tested an oxidation system with an integrated view-port. This enables real-time monitoring of the oxidation reaction and allows precise control over the fabrication of oxidized structures. Testing of the oxidized structures using a custom reflectivity measurement system shows that high quality distributed Bragg reflectors can be fabricated using the oxidation system.

6. References

1. K. D. Choquette, R. P. Schneider, Jr., K. L. Lear, K. M. Geib, "Low threshold voltage vertical-cavity lasers fabricated by selective oxidation", *Elect. Lett.*, vol. 30, p. 2043-2044, 1994.
2. B. J. Thibeault, E. R. Hegblom, P. D. Floyd, R. Naone, Y. Akulova, L. A. Coldren, "Reduced optical scattering loss in vertical-cavity lasers using a thin (300Å) oxide aperture", *IEEE Photonics Tech. Lett.*, vol. 8, pp. 593-595, 1996.
3. D. L. Huffaker, D. G. Deppe, "Low threshold vertical-cavity surface-emitting lasers based on high contrast distributed Bragg reflectors", *Appl. Phys. Lett.*, vol. 70, pp. 1781-1783, 1997.
4. B. E. Deal, A. S. Grove, "General relationship for the thermal oxidation of silicon", *J. Appl. Phys.*, vol. 36, pp. 3770-3778, 1965.

Localized Intermixing of AlAs and GaAs Layers for Lithographic Control of the Lateral Oxidation of AlAs

A.R. Massengale, C.Y. Tai*, M.D. Deal*, J.D. Plummer*, and J. S. Harris, Jr.

Solid State Electronics Laboratory, CIS-X 329, Stanford University, Stanford, CA, 94305-4075, USA

*Integrated Circuits Laboratory, CIS-X 331, Stanford University, Stanford, CA 94305-4075, USA

Abstract. We present a method to achieve lithographic control of the lateral oxidation of AlAs layers. The technique uses impurity induced layer disordering (IILD) in buried, heavily Si-doped layers to introduce Ga atoms into the AlAs layers to be oxidized. By selectively patterning the wafer surface and combining point defect generation mechanisms from the uncapped surface and in the highly Si-doped layers, this intermixing may be localized. Because lateral oxidation rates are heavily dependent on Al mole-fraction, lateral oxidation stop layers can thus be formed. Results are discussed for several types of capping conditions, and SUPREM simulations of the two-dimensional disordering process are presented.

1. Introduction

Several types of devices now utilize the stable native oxide of AlAs [1] to confine electrical and/or optical fields. Among these, edge-emitting lasers, VCSELs, and Collector-Up HBTs rely on the selective lateral oxidation of high Al mole-fraction AlGaAs to create apertures of unoxidized material. Because the size of these apertures is critical to device performance, lithographic control of the oxidation process would be highly advantageous. By decreasing the dependence on variables such as temperature, Al mole-fraction, layer thickness, sample preparation, and furnace conditions, yields may be improved and systems of more than one device enabled. By forming oxidation stop layers, it is also possible to create devices in which the aperture is not concentric with the mesa from which the oxidation proceeds.

Lateral oxidation rates of Al(Ga)As have been shown to be highly dependent on Al mole-fraction [2]. The ability to locally intermix Al and Ga atoms, introducing Ga atoms into the AlAs layers to be oxidized, is one manner in which to control the oxidation process. There are several mechanisms which induce intermixing of Al and Ga atoms in the column III matrix [3]. In terms of localized disordering, these methods can be loosely divided into two groups. In the first, vertical columns, perpendicular to the surface of the wafer are disordered according to patterning on the top of the wafer [4]. In the second, selected buried layers are disordered, parallel to the surface of the wafer, according to dopant type and doping level [5]. The method described here is a combination of these two techniques [6].

In this method, selected regions of the wafer surface are capped with silicon nitride. Highly Si-doped AlAs layers are buried in the epitaxial structure. Upon annealing at high temperatures, the wafer sees two competing mechanisms of point defect generation. In the buried highly Si-doped AlAs layers, a very high concentration of column III vacancies exists. (The dominant point defect in heavily Si-doped material has been found to be the triply negative column III vacancy, V_{III}^3 . The concentration of these vacancies, relative to their concentration in an intrinsic region of the same material, is $(n/n_i)^3$ [7].) In the regions underneath the nitride (a neutral surface), the AlAs layers disorder due to this high column III vacancy concentration. In the uncapped areas, the wafer loses As from the surface and the downward flux of As-poor point defects (Ga interstitials, IGa , and/or As vacancies, V_{As}) acts to reduce the column III vacancy concentration, slowing the disordering process.

2. Experiment and Results

2.1 Epitaxial Structures and Experimental Procedure

Molecular beam epitaxy was used to grow two test structures. The first structure (structure A), consists of two 25Å GaAs layers, doped $5 \times 10^{18} \text{ cm}^{-3}$, placed one-third and two-thirds of the way into a 750Å AlAs layer doped $1 \times 10^{18} \text{ cm}^{-3}$, such that each GaAs layer has 250Å of AlAs above and below it. Two more 25Å GaAs layers lie above and below the AlAs, which lies 2500Å below the surface [8]. The second structure (structure B) contains two 500Å AlAs layers. The top layer is doped $5 \times 10^{18} \text{ cm}^{-3}$, lies 3000Å down from the top surface of the wafer, and is surrounded above and below by 500Å of GaAs doped $5 \times 10^{18} \text{ cm}^{-3}$. The second AlAs layer lies 3000Å below the first, is doped $5 \times 10^{17} \text{ cm}^{-3}$, and is surrounded by GaAs doped $5 \times 10^{17} \text{ cm}^{-3}$ above and below.

CVD silicon nitride was deposited and subsequently patterned on both of these structures. Wafers were annealed for two hours at 875°C in a 1" tube furnace under flowing nitrogen. Following the anneal, PECVD nitride was deposited to serve as an etch mask. After a wet etch, the samples were oxidized at 425°C for 30 minutes.

2.2 Experimental Results (Structure A)

The first anneal utilized a GaAs wafer as a proximity cap on top of the patterned CVD nitride. These samples did not lose enough As to slow the disordering process outside the nitride, and thus the oxidation proceeded at the same decreased rate everywhere. At the edge of the sample however, slightly more As was lost, and a 2.5 to 1 ratio in oxidation rates was observed. Two techniques using Si wafers as proximity caps were also tried. In the first, small pieces of Si wafer, stacked two high, were placed adjacent to the sample. A Si "bridge" was then placed over the sample, and the sample was annealed. The result of this type of anneal varied over the wafer surface, regions seeing the most nitrogen flow appeared very rough. The left side of figure 2 represents such a sample. In this picture, the etched mesa is a rectangle and the patterned nitride is a circle, intentionally misaligned. After oxidation, we have converted a rectangular mesa into a circular aperture, clearly showing a difference in oxidation rate between the capped and uncapped regions. In the second, a direct Si cap was employed. The direct Si cap yielded the most specular surface after annealing. The right side of figure 3 shows a circular outer mesa and an intentionally misaligned SiN_x inner mesa. The mesa was overoxidized approximately 1.5 times yet the process still yielded a circular aperture. The ratio of oxidation rates nearby was 1 to 10. Note the improved surface relative to the indirectly capped sample.

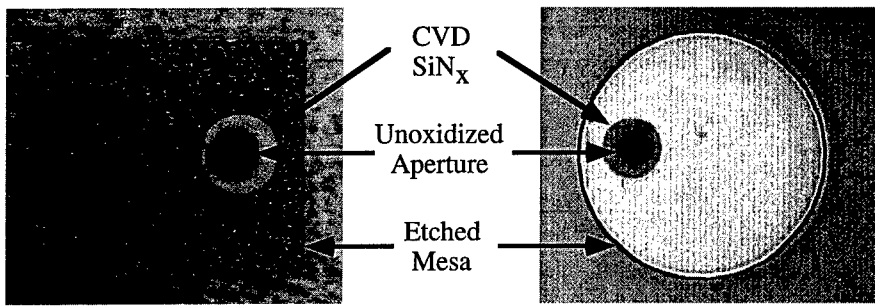


Fig. 1 Optical micrographs of, *left*, a rectangular mesa ($50 \times 58 \mu\text{m}^2$) oxidized to a circular aperture. This sample was capped indirectly with a Si wafer. *Right*, a circular mesa (52 µm in diameter) oxidized to a misaligned circular aperture. This sample was capped directly with a Si wafer.

2.3 Experimental Results (Structure B)

Structure B was annealed using an indirect Si wafer as a cap. Because the concentration of column III vacancies is proportional to the cube of the electron concentration, a large number of vacancies exist in the regions doped $5e18 \text{ cm}^{-3}$ with Si. In the regions outside the nitride cap, this vacancy concentration is mitigated by the downward flux of As-poor point defects, and the top AlAs layer disorders less. Underneath the cap, the vacancy concentration remains high, and here the highly doped AlAs layer disorders the most. This can be seen in Figure 2 where the oxidation of the top layer proceeds further where it does not run into the region underneath the cap. The lower layer is less, though still, affected by the injection of point defects from the surface. Because the vacancy concentration is much less in the $5e17 \text{ cm}^{-3}$ Si-doped regions, the lower AlAs layer will disorder less. Figure 2 shows that the lower oxidized-AlAs layer extends much further than the upper oxidized-AlAs layer. Note however that this layer does disorder slightly, as is evidenced in the slightly different oxidation depths in the regions outside and underneath the nitride cap.

The ability to disorder a particular Al(Ga)As layer(s) while leaving other Al(Ga)As layers relatively undisturbed is potentially useful in various types of devices. Besides changing the concentration of the Si doping in the layers not to be intermixed, changing the species of the n-type dopant can be used [9]. For p-type doping, carbon has been shown to retard Al-Ga interdiffusion [10].

2.4 Simulation Results (Structure B)

The localized disordering of AlAs described above is a highly three-dimensional process. In order to gain a better understanding of variables affecting the disordering process, we have carried out two-dimensional process simulations using SUPREM-IV.GS [11]. In these simulations of structure B, the aluminum diffusion constant depends on the anneal temperature and local Fermi level, and is based on empirical data [12]. Ga interstitials are injected at a constant rate from the uncapped portions of the wafer, while the injection rate is set to zero underneath the nitride. (Physically, the injection rate may be varied by changing the anneal temperature, the capping conditions, or the semiconductor material at the surface of the wafer [6].) As we vary the rate at which these interstitials are injected, the distance which the less disordered AlAs layer encroaches underneath the cap changes. This can be seen in Figure 3 where we plot contours of constant aluminum concentration for three injection rates: $1e13$, $1e14$, and $1e15$ gallium interstitials / $\text{cm}^2 \text{ s}$.

The innermost line in the upper AlAs layers in Figure 3 represents an aluminum mole-fraction of 0.98. If we compare the distance to which these lines extend underneath the edge of the nitride cap (parts (b) and (c)), the picture qualitatively confirms our understanding of the disordering process: the higher the injection rate, the less the extent of the intermixing. Because the injection of gallium interstitials and their diffusion is a two-dimensional process, the higher the injection rate at the surface, the greater the flux that extends laterally underneath the cap to diminish the interdiffusion of Al and Ga here.

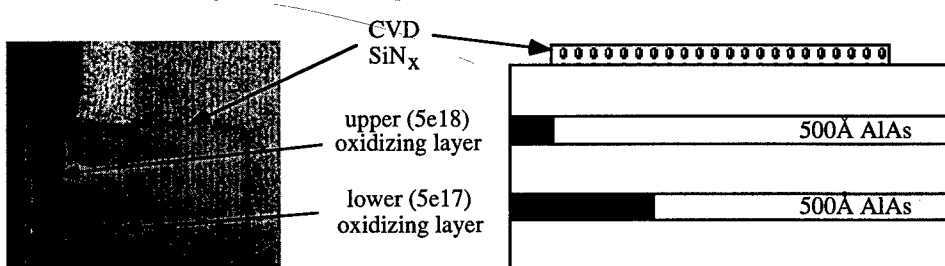


Fig. 2 Optical micrograph (*left*) and schematic (*right*) of two AlAs layers oxidized following localized disordering. The top layer is Si-doped $5e18 \text{ cm}^{-3}$ (disorders more) and the bottom layer is Si-doped $5e17 \text{ cm}^{-3}$ (disorders less).
The square is $86 \mu\text{m}$ on a side.

In comparing (a) to (b) and (c), it is interesting to note that a $1e13 / \text{cm}^2 \text{s}$ flux is insufficient to keep the top AlAs layer from disordering, and the mole-fraction of this layer is below 0.9 everywhere. Conversely, the higher gallium interstitial flux in parts (b) and (c) is sufficient to keep the lower and more lightly doped AlAs layer from disordering, where the lower flux in (a) is not.

3. Conclusions

Localized impurity induced layer disordering can be used to form effective oxidation stop layers, and thus introduce lithographic control to the lateral oxidation of AlAs. Wafer capping conditions during the anneal play a large role in the rate at which As-poor point defects are injected down from the surface. This rate in turn is important in determining what the final aluminum profiles will look like.

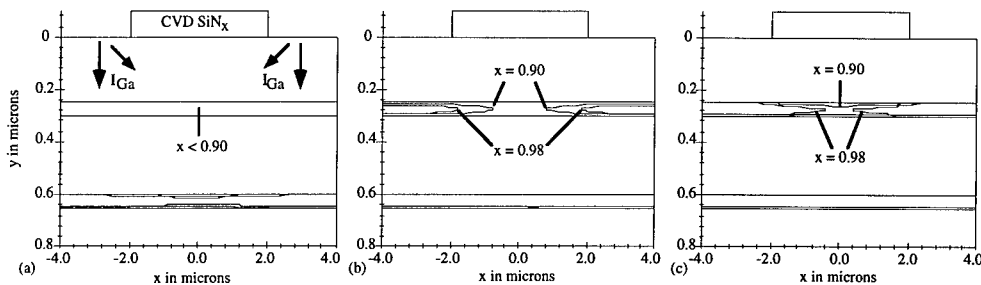


Fig. 3 Results of SUPREM-IV.GS simulations modeling the localized disordering process. Contours are of constant aluminum concentration, with lines plotted for mole-fractions 0.90 and 0.98. Samples were annealed for two hours at 875°C, with the gallium interstitial injection rate varied. The injection rates were (a) $1e13 / \text{cm}^2 \text{s}$ (b) $1e14 / \text{cm}^2 \text{s}$ and (c) $1e15 / \text{cm}^2 \text{s}$.

4. Acknowledgments

The authors would like to acknowledge the help of Rouel Fernandez, Tetsuzo Ueda, Dr. Decai Sun and Dr. Robert Thornton. This work is supported by ARPA/UNM through contract MDA972-94-1-0003.

5. References

- [1] Dallesasse J M et al. 1990 *Appl. Phys. Lett.* 57 2844-2846
- [2] Choquette K D et al. 1994 *Electron. Lett.* 30 2043-2044
- [3] Deppe D G and Holonyak N Jr 1988 *J. Appl. Phys.* 64 R93-R113
- [4] Guido L J et al. 1987 *J. Appl. Phys.* 61 1372-1379
- [5] Beernink K J et al. 1995 *Appl. Phys. Lett.* 66 2522-2524
- [6] Beernink K J et al. 1996 *Appl. Phys. Lett.* 68 284-286
- [7] Tan T Y et al. 1991 *Critical Reviews in Solid State and Materials Sciences* 17 47-106
- [8] Massengale A R et al. 1997 *Electron. Lett.* 33 1087-1089
- [9] Thornton R L et al. 1996 *Tech. Dig. 54th Device Research Conference* 92-93
- [10] Guido L J et al. 1990 *J. Appl. Phys.* 67 2179-2182
- [11] Hansen S E and Deal M D eds. 1993 *SUPREM-IV.GS Two Dimensional Simulation for Silicon and Gallium Arsenide* (Integrated Circuits Laboratory Stanford University)
- [12] Tai C Y 1997 *Ph.D. Thesis* Stanford University (to be published)

Improved PL intensity of InGaAs/GaAs SQW with a selectively oxidized AlAs layer

T. Takamori, A. R. Pratt, and T. Kamijoh

Semiconductor Technology Laboratory, R & D Group, Oki Electric Industry Co., Ltd.
550-5 Higashiasakawa, Hachioji, Tokyo 193, Japan.

Abstract. Data is presented on room temperature photoluminescence (PL) intensity measurements of InGaAs/GaAs single quantum wells (SQW's) adjoining a selectively oxidized AlAs layer. A drastic PL intensity reduction was observed for a sample with a direct interface between the GaAs barrier and the oxidized AlAs layer. Samples in which an AlGaAs layer was inserted between the SQW and the AlAs showed no such PL intensity reduction after oxidation provided the thickness of the AlGaAs layer was greater than 20 nm. The results provide important information for the design of oxide based optoelectronic devices operated at room temperature.

1. Introduction

Selective wet oxidation of AlAs/GaAs multilayers has been intensively studied in recent years.[1, 2] It has already been used in optical devices such as ultra-low threshold surface-emitting lasers in which a oxide layer forms a buried current aperture.[3-5] Furthermore, the high refractive index step in these oxide/semiconductor multilayers is expected to be useful for forming wavelength-size microcavities.[6-8] However, to date there is insufficient information available on the optical characterization of selectively oxidized material which will be important for device designing.[9-11]

In this paper, we present data on the optical properties of InGaAs/GaAs single quantum wells (SQW's) adjacent to a selectively oxidized AlAs layer. Photoluminescence (PL) intensities at room temperature, which gives direct information for practical device applications, were compared before and after oxidation using samples carefully designed to minimize the interference effect caused by the large refractive index step between oxide and semiconductor. Although a drastic reduction

in PL intensity was observed in a sample with a direct interface between the SQW and oxidized AlAs, a 20-nm-thick AlGaAs interface layer was found to effectively isolate the generated carriers from the interface and yield a PL efficiency after oxidation identical to that of the as grown materials. A study of the temperature dependence of the PL intensity also showed a similar tendency supporting the above results.

2. Experiments

A schematic diagram of the sample structure used in this work is shown in Fig. 1. The samples were grown undoped by molecular beam epitaxy on (100)-oriented undoped GaAs substrates. Four InGaAs/GaAs SQW samples were used each with an AlAs layer to be oxidized underneath the QW. The Indium content and well width of the SQW were nominally 20% and 7 nm, respectively, which resulted in emission wavelengths at room temperature in the range 980 to 1000 nm. One sample has a direct interface between the SQW and the AlAs, while the other three samples have a thin $\text{Al}_{0.38}\text{Ga}_{0.362}\text{As}$ interface layer with different

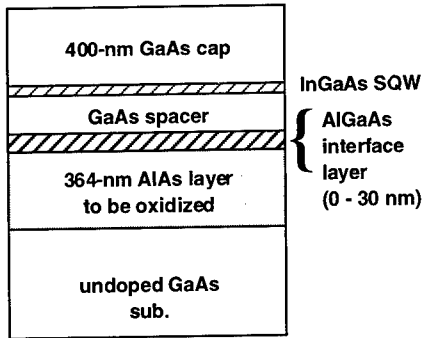


FIG. 1. Schematic diagram of the sample structure. The spacer layer thickness is 136 nm for the sample without AlGaAs, and those for the samples with AlGaAs are adjusted to keep the separation between SQW and oxide layer constant.

thickness (10, 20 and 30 nm) at the oxide interface.

In order to evaluate the PL intensity before and after oxidation the samples were designed to minimize the interference effect caused by the large refractive index step at the GaAs spacer and oxidized AlAs (refractive index changes from 2.9 to 1.55 at 0.98 μm after oxidation). Therefore, the AlAs thickness was chosen to be 364 nm to form a $\lambda/2$ antireflective layer at the SQW emission wavelength after oxidation, taking account the thickness shrinkage and the index change. The thickness of the GaAs spacer layer in the sample without the AlGaAs interface layer was 136 nm, which corresponds to an optically $\lambda/2$ -thick layer. For the three samples with the AlGaAs interface layer, the GaAs spacer thickness was adjusted, trying as far as possible to keep the optical separation of the InGaAs and AlAs constant ($\sim\lambda/2$). Numerical calculations using a standard matrix method[12] showed the expected change in the PL intensity produced by the interference effect to be less than 15 % even after considering a $\pm 5\%$ thickness variation. Selective oxidation was performed in a standard way,[13] using chemical

etching ($\text{H}_2\text{SO}_4:\text{H}_2\text{O}_2:\text{H}_2\text{O} = 4:1:1$) to form nominally 47- μm square mesas and oxidation at 400°C for 1 hour in flowing nitrogen gas bubbled through deionized water at 80°C. The samples were characterized before and after oxidation using room temperature PL, excited using an Ar ion laser (514.5 nm) with a power density of 0.5 W/cm^2 . In order to perform the temperature dependent PL measurements, the samples were mounted in a closed cycle helium cryostat where the temperature could be maintained between 12 and 300K.

3. Results

We first confirmed that the quality of the SQW itself remains unaffected after the oxidation process by low temperature (77 K) PL measurements; the luminescence efficiency and the full width at half maximum of the spectra (FWHM: typically 5–8 meV) were identical before and after oxidation for all four samples. The room temperature PL spectra for the sample without the AlGaAs interface layer on the other hand, showed substantial reduction after oxidation, corresponding to a one tenth reduction in the luminescence efficiency, which is shown in Fig. 2, indicating an efficient non-radiative pathway is present after oxidation. If the active layer in an optical device has such an interface to an oxide layer, high performance is hardly expected because the injected carriers are efficiently trapped at the interface. This drastic intensity reduction can be improved by isolating the QW from the oxide/semiconductor interface by placing the AlGaAs interface layer between the GaAs spacer and the oxidized AlAs. This interface layer is expected to be unoxidized, taking advantage of the fact that the oxidation rate strongly depends on the aluminum content.[3]

Figure 3 shows the PL spectra recorded before and after oxidation for the sample grown with a 20-nm interface layer. As can be seen in the figure, PL spectra before and after oxidation are

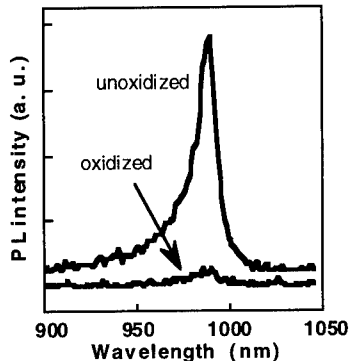


FIG. 2. Unnormalized room temperature PL spectra before and after oxidation of the samples without the AlGaAs layer. The unoxidized spectra have been shifted relative to the oxidized spectra for clarity.

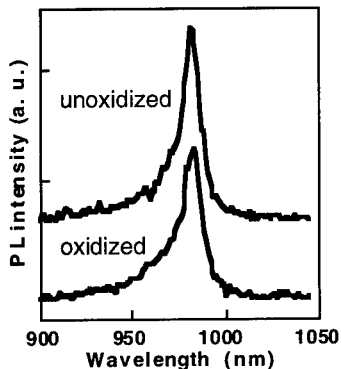


FIG. 3. Unnormalized room temperature PL spectra recorded before and after oxidation of the QW samples with a 20 nm AlGaAs interface layer.

almost identical in their intensities and FWHMs, indicating that the emission from the SQW is insensitive to the oxide/semiconductor interface. The integrated PL intensity after oxidation (normalized to that before oxidation) are plotted in Fig. 4 as a function of the AlGaAs layer thickness. It is evident that for the samples grown with an AlGaAs interface layer of 20 nm or larger, the PL from the SQW is clearly unaffected by the oxidation process.

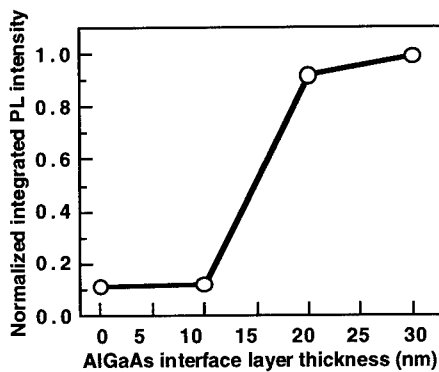


FIG. 4. Variation of the spectrally integrated PL intensity after oxidation as a function of the AlGaAs interface layer thickness. The integrated PL intensities have been normalized to that of the as grown material.

Similar results were obtained in the temperature dependent PL measurements. The integrated PL intensities are plotted against inverse temperature for the samples without the AlGaAs interface layer (Fig. 5) and with a 30-nm-thick AlGaAs interface layer (Fig. 6). In each figure, the oxidized material is compared to the material before oxidation. As can be seen in the figures, the sample with a direct interface between the GaAs spacer and oxidized AlAs showed a lower quenching temperature (defined as the temperature above which the PL intensity starts decreasing) after oxidation, while the data is identical, before and after oxidation, for the sample with a 30-nm-thick AlGaAs interface layer.

The results obtained above can be explained as follows; carriers generated in the GaAs layer and which thermally escape from the SQW are effectively blocked by the wider bandgap AlGaAs interface layer (≥ 20 nm), and therefore the electron wave function does not overlap the non-radiative centers believed to be located at the oxide/semiconductor interface; while in the sample with the 10 nm interface layer the isolation is not sufficient and carriers in the GaAs are still efficiently trapped by the deep non-radiative centers.

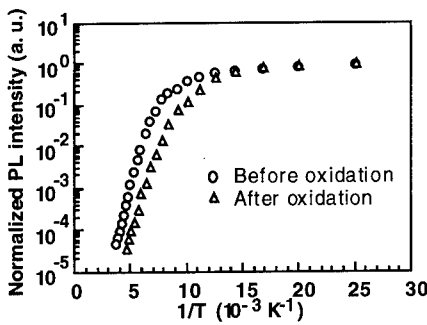


FIG. 5. Variation of the PL intensity versus T^{-1} recorded before and after oxidation of the samples without AlGaAs layer. The solid lines are guides for the eye.

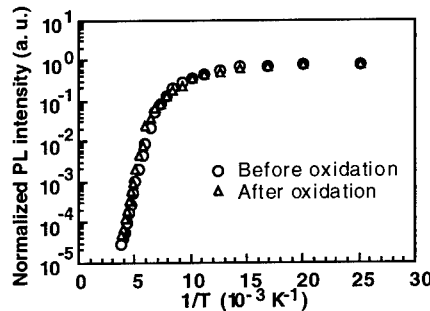


FIG. 6. Variation of the PL intensity versus T^{-1} recorded before and after oxidation of the samples with 30-nm-thick AlGaAs layer. The solid line is a guide for the eye.

4. Conclusion

In conclusion, we have presented data on the effects of selective wet oxidation in a series of InGaAs/GaAs SQW's adjacent to an AlAs layer. Room temperature PL intensities, which provides direct information for practical device applications, were compared before and after oxidation using a sample structure carefully designed to minimize

the interference effect caused by the large refractive index step between the oxide and semiconductor. A 20-nm-thick $\text{Al}_{0.38}\text{Ga}_{0.62}\text{As}$ interface layer placed between the SQW and the oxidized AlAs was found to preserve the room temperature PL intensity after oxidation, while an efficient non-radiative recombination channel is detected in an oxidized sample with a direct interface between the SQW and oxidized AlAs and also in a sample with a 10-nm-thick AlGaAs interface layer. These results should play an important role in the design of oxide based optoelectronic devices operated at room temperature.

References

- [1] Kish F A, Caracci S J, Holonyak N, Jr., Dallesasse J M, Hsieh K C, Ries M J, Smith S C and Burnham R D 1991 *Appl. Phys. Lett.* 59 1755
- [2] Sugg A R, Chen E I, Richard T A, Holonyak N, Jr. and Hsieh K C 1993 *Appl. Phys. Lett.* 62 1259
- [3] Choquette K D, Schneider R P, Lear K L and Geib K M 1994 *Electron. Lett.* 30 2043
- [4] Huffaker D L, Deppe D G, Kumar K and Rogers T J 1994 *Appl. Phys. Lett.* 65 97
- [5] Lear K L, Choquette K D, Schneider J R P, Kilcoyne S P and Geib K M 1995 *Electron. Lett.* 31 208
- [6] MacDougal M H, Zhao H, Dapkus P D, Ziari M and Steier W H 1994 *Electron. Lett.* 30 1147
- [7] Twesten R D, Follstaedt D M, Choquette K D and Schneider R P, Jr. 1996 *Appl. Phys. Lett.* 69 19
- [8] Graham L A, Deng Q, Deppe D G and Huffaker D L 1997 *Appl. Phys. Lett.* 70 814
- [9] Kash J A, Pezeshki B, Agahi F and Bojarczuk N A 1995 *Appl. Phys. Lett.* 67 2022
- [10] Takamori T, Takemasa K and Kamijoh T 1996 *Appl. Phys. Lett.* 69 659
- [11] Shi S S, Hu E L, Zhang J-P, Chang Y-I, Parikh P and Mishra U 1997 *Appl. Phys. Lett.* 70 1293
- [12] Huang Z, Lei C, Deppe D G, Lin C C, Pinzone C J and Dupuis R D 1992 *Appl. Phys. Lett.* 61 2961
- [13] Dallesasse J M, Holonyak N, Jr., Sugg A R, Richard T A and El-Zein N 1990 *Appl. Phys. Lett.* 57 2844

In-situ monitoring of the selective etching of antimonides in GaSb/AlSb/InAs heterostructures using Raman spectroscopy

C. Gatzke, S. J. Webb, K. Fobelets[†] and R. A. Stradling

Department of Physics, Imperial College, Prince Consort Road, London SW7 2BZ

[†]Department of Electrical and Electronic Engineering, Imperial College, Exhibition Road, London SW7 2BT

Abstract. The in-situ real-time monitoring of the selective etching of semiconductor structures with a Raman microprobe system is demonstrated for the first time. The technique that is applied to GaSb/AlSb/InAs heterostructures allows the accurate timing of the etching as well as a study of the chemistry of the etching process and can be applied to many problems in processing of compound semiconductors. During etching of AlSb a surface layer rich in Sb builds up that slows down the etch rate whereas GaSb is etched without producing this residue layer. The origin of the antimony layer is explained.

1. Introduction

Fabrication of devices from semiconductor heterostructures often involves selective etching as a crucial step. For quantum devices it is important to be able to control the etching process because epitaxial layers can be as thin as a few nanometers. Raman spectroscopy is a very powerful method in this context because it can provide very rapid compositional analysis of the material near the surface of a sample. Moreover, the use of a microprobe with a lateral resolution in the micrometer region allows a local analysis of material properties compatible with the dimensions of state-of-the-art devices.

In this paper we demonstrate the in-situ monitoring of selective etching in InAs/AlSb/GaSb heterojunctions. There has been much recent interest in this materials system for devices such as resonant tunnelling diodes, high electron mobility transistors and quantum wires. A common application of selective etching in the processing of these structures is the selective removal of the antimonides to allow contacting to InAs. Positive photoresist developer Microposit MF319 which is a hydroxide solution has been reported to be an etchant that removes both GaSb and AlGaSb with high selectivity over InAs [1]. We find that MF319 also etches AlSb. However, the chemical mechanism underlying this etching has not been fully understood as yet.

2. Samples and Experiment

The etching of a number of MBE grown samples is studied. Sample IC594 is a thick 1μm GaSb film. Sample IC522 consists of 800nm of AlSb sandwiched between a thin 6.5nm GaSb cap and a 400nm GaSb buffer. IC582 consists of a 12nm GaSb cap, 15nm AlSb barrier, 15nm InAs quantum well, 20nm AlSb barrier and a GaSb buffer layer. All samples were grown on GaAs substrates.

Raman spectra are collected using a Renishaw Raman Microprobe. All spectra are unpolarised, and taken in back-scattering geometry, with the 514 nm line of an Ar⁺ laser as the excitation source. The experiment is carried out at room temperature. The samples are etched in MF319 while Raman spectra are taken through the etchant. A CCD camera records the Raman signal, and sequential 60 second long exposures are used. To maintain the etching process the etchant has to be continuously

stirred. Remarkably, it is possible to obtain spectra through the liquid with satisfactory signal to noise ratios even though the agitation leads to a random change of focus of the probing laser beam.

3. Results and Discussion

Fig. 1 and 2 show representative sequences of in-situ Raman spectra of the etching of the heterostructure samples. Raman spectra of the etching of sample IC594 are shown in fig. 1. The two peaks at about 230 and 240 cm^{-1} correspond to the TO and LO modes of GaSb, respectively. The spectrum does not change until the GaSb is etched down to the GaAs after about 56 minutes, and the LO mode of GaAs appears at about 290 cm^{-1} . When sample IC522 is etched in MF319 the 6.5nm GaSb cap disappears completely during the second minute (fig. 2). The AlSb layer underneath the cap is visible even before etching as the penetration depth in GaSb (about 8 nm) is larger than the cap thickness. After removal of the cap an additional peak appears that has to be attributed to products of the etching of AlSb. This broad peak centred around 150 cm^{-1} can be identified as amorphous Sb (cf. [2-3]). While the signal from AlSb disappears within 2 minutes after the GaSb cap is removed, the a-Sb peak increases reaching maximum intensity after 6 minutes, and remains unchanged for the next 10 minutes. After a total etching time of 20 minutes all a-Sb is removed and the GaSb epilayer underneath the AlSb becomes visible. It is essential that the etchant is stirred continuously. Without this agitation the etching comes to a halt. The a-Sb layer (probably mixed with oxides) protects the AlSb underneath and prevents further etching.

However, agitation restarts the etching process by dissolving this residue. Note that, as in fig. 1, no Sb is observable while GaSb is being etched. After additional 20 minutes a peak from the GaAs

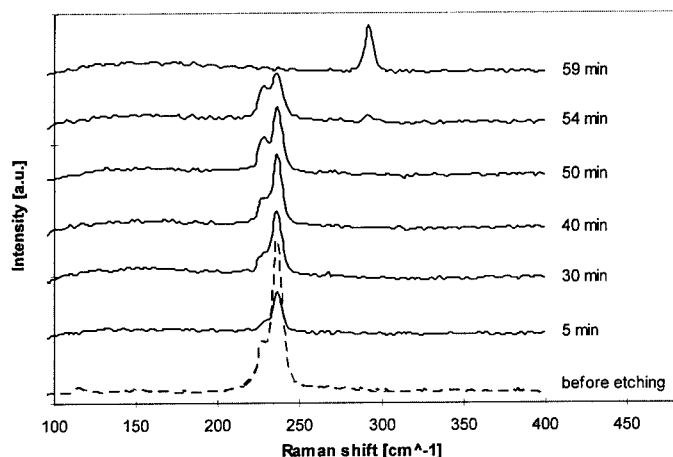


Figure 1 Raman spectra of 1 μm GaSb film grown on a GaAs substrate (sample IC594) etched in photoresist developer MF319. The lowest line shows the spectrum of the unetched sample. The upper line are spectra taken in-situ through the stirred etchant. The acquisition time for each of the scans is 1 minute, e.g. the spectrum labelled "5 min" is acquired between 4 and 5 minutes after the etching is started.

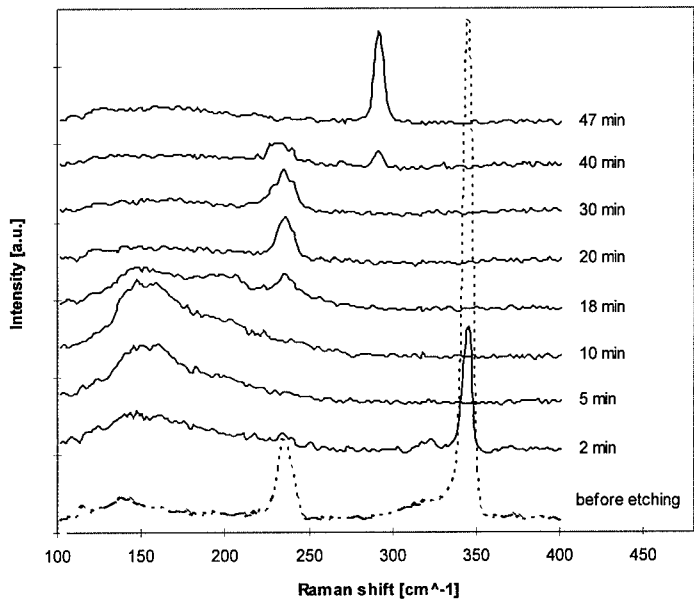


Figure 2 Raman spectra of a sample of $0.8\mu\text{m}$ AlSb sandwiched between a 6.5nm GaSb cap and a $0.4\mu\text{m}$ GaSb buffer (IC522) etched in photoresist developer MF319 (see fig. 1 for explanations)

substrate adds to the signal from GaSb. Finally, all GaSb disappears.

The initial stages of the etching of sample IC582 is very similar to that of IC522 (no figure). The 12 nm GaSb cap is removed after 8 minutes; then, the spectra show the appearance of a-Sb. After an overall etching time of 30 minutes the a-Sb feature reduces and the InAs LO mode becomes observable. Afterwards the Raman spectra do not change for at least 60 minutes which is consistent with MF319 etching being stopped at InAs.

To understand the difference in the etching of GaSb and AlSb that is apparent in the Raman spectra we have to examine the chemistry of the etching process. In general, the chemical reaction underlying wet etching of a $\text{A}_{\text{III}}\text{B}_{\text{V}}$ semiconductor is believed to consist of three steps: (i) decomposition of the compound into ions, (ii) reaction with OH^- ions of the etchant to A_2O_3 and B_2O_3 and (iii) solution of the oxides in the etchant. Our experiment shows that, in the case of etching of AlSb, a surface layer rich in Sb is built whereas when GaSb is etched no elemental Sb appears. This difference in the etching behaviour can be explained by the difference in reaction heat between Al and Ga which is also responsible for the fact that AlSb disintegrates under ambient atmosphere whereas GaSb is stable. Al immediately oxidises on contact with OH^- ions. Sb reacts much more slowly so there are atoms left over without reaction partners and an a-Sb layer is built on the AlSb surface. This is similar to the observation that when $\text{A}_{\text{III}}\text{B}_{\text{V}}$ material is oxidised there is in many cases a higher proportion of A-oxide than B-oxide which can lead to an enrichment of elemental B in the oxide [4]. In contrast, when GaSb is etched the reactivities of the III and the V elements are more balanced and most Sb oxidises and is dissolved in the etchant. No elemental Sb is left behind.

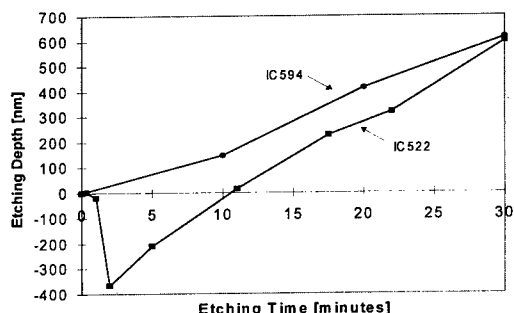


Figure 3 Etching depth for etching of IC522 and IC594 in photoresist developer MF319

A measurement of the etching depth using a Dektak stepper confirms the different etching of GaSb and AlSb (fig. 3). For GaSb the etch rate is constant at 0.3 nm/s. This rate is also inferred from the series of Raman spectra in fig. 1. For AlSb the situation is very different. During the first 30 seconds of etching sample IC522 the thickness of the region which is exposed to the etchant is reduced. Then, it *increases* rapidly by more than 300 nm. It is only after the first 2 minutes that this increase is stopped and we observe a steady reduction of the thickness with an initial rate of 0.7 nm/s. From the Raman spectra in fig. 2 we see that this process is linked to the removal of the thin GaSb cap, the appearance of a-Sb from AlSb and finally its removal.

The combined information from the thickness measurement and the Raman spectra leads to the following explanation of the process. Once the AlSb gets into contact with the etchant it disintegrates very rapidly. The Al reacts to aluminium oxide which is thicker than the semiconductor monocrystal. This leads to the increase of the film thickness shown in fig. 3. The Sb is left behind as a residue which slows down etching and is apparent in the Raman spectra in fig. 2.

4. Conclusions

A new technique of in-situ Raman spectroscopy of wet etching is described and demonstrated for the selective etching of antimonides. We show that the technique allows the real-time monitoring of the etching and an improved analysis of the chemistry of the etching process. It is found that during the etching of AlSb a-Sb is present at the semiconductor surface whereas GaSb is etched without this residue. The reason for the different etching behaviour are the different reaction heats of Ga and Al.

References

- [1] Yoh K, Kiyomi K, Nishida A and Inoue M 1992 *Jpn. J. Appl. Phys.* 31, 4415
- [2] Lannin J S 1977 *Phys. Rev. B* 15, 3863
- [3] Resch-Esser U, Frotscher U, Esser N, Rossow U, Richter W 1994 *Surf. Sci.* 307-309, 597
- [4] Guglielmacci J M, Charfi F and Joullie A 1981 *Thin Solid Films* 76, 69

Low frequency noise in dry and wet etched InAlAs/InGaAs HEMTs

H. C. Duran, L. Ren¹, M. Beck¹, M. A. Py¹, M. Illegems¹, and W. Bächtold

Laboratory for Electromagnetic Fields and Microwave Electronics, Swiss Federal Institute of Technology
Zürich, ETH-Zentrum, CH-8092 Zürich, Switzerland

Tel.: ++41 - 1 - 632 76 25 Fax: ++41 - 1 - 632 11 98 email: duran@ifh.ee.ethz.ch

¹Institute of Micro and Optoelectronics, Swiss Federal Institute of Technology Lausanne, CH-1015
Lausanne, Switzerland

Abstract. The low frequency noise of lattice-matched InP-based HEMTs gate recess etched with CH₄/H₂ RIE and phosphoric-acid based wet etchants was studied at different gate and drain biases in a temperature range of 77 K to 340 K. The measurements showed a significantly lower normalized drain current 1/f noise for the dry etched HEMTs in all bias conditions. Varying the temperature, four electron traps could be identified in the drain current noise spectra for both dry and wet etched devices. No additional traps were introduced through the dry etching step. The concentration of the main trap in the Schottky layer is one order of magnitude lower for the dry etched HEMTs probably due to hydrogen trap passivation. The kink effect in the dry etched HEMTs was observed to be reduced significantly compared with wet etched devices which gives further evidence of trap passivation during dry etching.

1. Introduction

During the past several years significant improvements have been presented for the high frequency and noise performance of High Electron Mobility Transistors (HEMTs). At the present time InP based HEMTs exhibit the highest cut-off frequencies and the lowest microwave noise of all three terminal semiconductor devices. Therefore InP HEMTs are very attractive for integrated microwave and millimeter wave applications [1]. The low frequency noise behavior of these devices is of significant importance for nonlinear circuits such as oscillators and mixers. Thus, achieving low 1/f and G-R noise levels is critical for sensitive circuit applications.

Reproducible transistor parameters are essential for mm-wave circuits. The precise definition of the gate recess in HEMT devices is important to ensure uniform device parameters. For small feature sizes, wet etching techniques suffer from surface wetting problems which reduce the uniformity of the devices. Dry etching techniques can provide more controllable etching characteristics [2]. However, the Reactive Ion Etching (RIE) process may introduce surface damage through ion bombardment, preferential etching of surface elements and hydrogen passivation of donors and traps. These defects can have detrimental effects on the noise performance of dry etched transistors. Concerning the microwave channel noise, no significant difference between dry and wet etched InP HEMTs could be observed [3]. Up to now, only little work has been done on the low frequency noise properties of dry etched HEMTs. In this work, we investigate the influence of methane/hydrogen RIE of InP-based HEMTs on the low frequency drain noise spectra and compare the spectra of dry and wet etched devices.

2. Experiment

HEMTs have been fabricated on lattice-matched InGaAs/InAlAs heterostructures. For the dry etched devices, the gate recess was etched using a selective CH₄/H₂ reactive ion etching (RIE) process, see [4]

for further details. The InAlAs Schottky layer of the HEMT structure acted as an etch stop layer with a selectivity of more than 100 thus ensuring uniform device parameters. The length of the fabricated T-gates was 0.2 μm . For direct comparison, HEMTs with gate recesses etched with a solution of $\text{H}_3\text{PO}_4:\text{H}_2\text{O}_2:\text{H}_2\text{O}$ 1:1:150 were processed. The drain current noise was measured at different drain and gate biases in the frequency range from 1 Hz to 100 kHz using a computer-controlled setup based on a HP 3562A dynamic signal analyzer. The temperature was varied from 77 K to 340 K using a cryostat.

3. Results

In Fig. 1, the normalized low-frequency drain current noise spectra are shown at room temperature for dry and wet etched devices at a drain bias of 15 mV, i.e. in the linear region of device operation. It is clearly seen that the dry etched device exhibits lower noise, i.e. lower 1/f and generation-recombination (G-R) noise compared with the wet etched device. In order to be sure that the observed difference in the current 1/f noise is not only due to better charge-control characteristics for the dry etched case, the Hooge parameters a_{ch} [5] have been calculated and are shown in Fig. 2. For any gate bias, the dry etched devices exhibit lower Hooge parameters, hence less 1/f noise.

Varying the temperature in the range of 77 K - 340 K, four discrete Lorentzian components could be identified in the low-frequency drain current noise spectra. The Arrhenius plot of the deep level traps is shown in Fig. 3. The activation energies of the detected traps were as follows: $E_1: E_c = 0.50 \text{ eV}$, $E_2: E_c = 0.31 \text{ eV}$, $E_3: E_c = 0.22 \text{ eV}$, $E_4: E_c = 0.18 \text{ eV}$. All traps that appear in the wet etched devices are also visible in the dry etched HEMTs. There are no additional traps detectable after dry etching which is an indication for a low damage dry etching process. The traps E_1 , E_2 and E_3 are probably located in the Schottky layer and origin from defects introduced during MBE growth [6]. From analytical modeling of the transfer characteristics, the concentration of the dominant trap E_1 was estimated to be $5 \times 10^{15} \text{ cm}^{-3}$

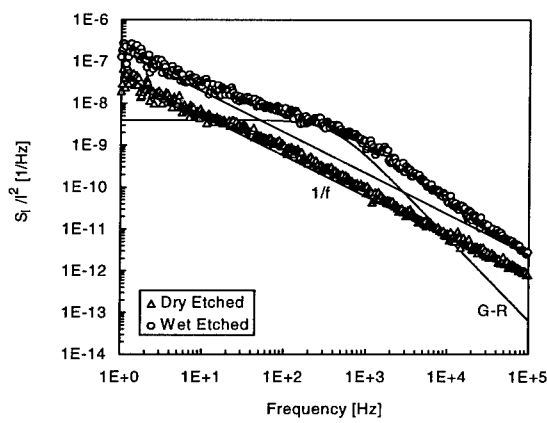


Fig. 1: Normalized low frequency drain current noise spectra of dry and wet etched HEMTs in the linear region ($U_{ds} = 15 \text{ mV}$) at $T = 300 \text{ K}$.

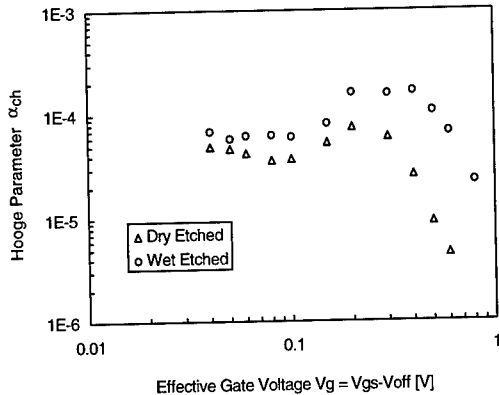


Fig. 2: Gate bias dependence of the Hooge parameter α_{ch} for dry and wet etched HEMTs at room temperature.

for the wet etched devices. The trap concentration in the dry etched HEMTs is about one order of magnitude lower. We attribute the reduction of the trap concentration to hydrogen deep level trap passivation during methane/hydrogen RIE [7].

The kink effect in InP-based HEMTs is commonly believed to be associated with deep-level traps in the InAlAs layers or at interfaces [8]. In Fig. 4, the output characteristics of dry and wet etched HEMTs are shown. For the wet etched devices, the kink appears for drain-source voltages between 0.4 and 0.8 V. It can clearly be seen that the kink effect is reduced considerably in the dry etched HEMTs. We attribute this mainly to the passivation of electron traps during the dry etching step.

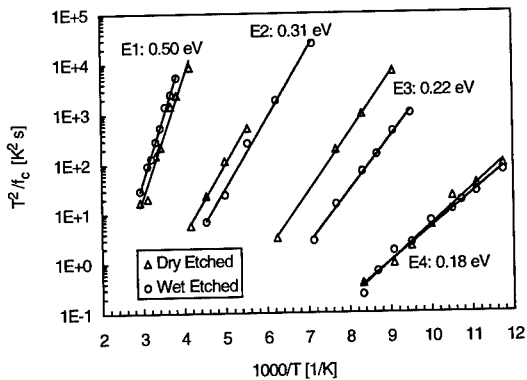


Fig. 3: Arrhenius plot of G-R noise components in dry and wet etched HEMTs ($U_{ds} = 15$ mV).

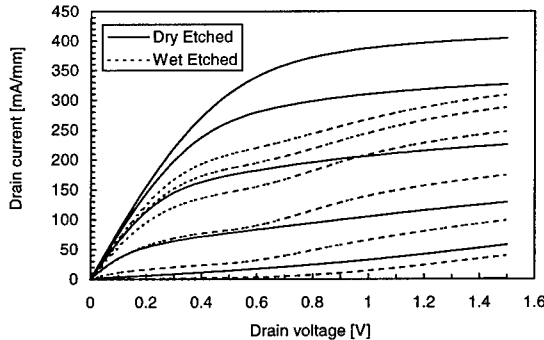


Fig. 4: Output characteristics of dry and wet etched HEMTs. The gate voltage was varied in steps of 0.2 V with a largest bias of 0.4 V.

4. Conclusions

We present the low frequency noise performance of dry and wet etched InP-based HEMTs. The 1/f drain current noise is considerably lower in the dry etched devices. Examining the G-R components in the noise spectra, we found the same four discrete traps in both device types. No additional traps have been introduced during the dry etching step which is an indication of a low damage process. The trap density in the dry etched HEMTs was one order of magnitude lower compared with the wet etched ones. We attribute this differences to hydrogen passivation of deep level traps. Comparing the output characteristics, the dry etched HEMTs showed a largely reduced kink effect. The suitability of dry etched HEMTs for high frequency applications due to their higher uniformity compared with wet etched ones and their low microwave noise has already been shown [3]. Regarding the observed lower 1/f and G-R noise components, our results show that RIE gate recess etching is a very promising technique for low frequency noise sensitive applications like oscillators and mixers.

5. References

- [1] Smith P M Liu S-M J Kao M-Y Ho P Wang S C Duh K H G Fu S T and Chao P C 1995 *IEEE Microwave and Guided Wave Lett.* 5 230-232
- [2] Adesida I and Agarwala S 1993 *J. Vac. Sci. Technol. B* 11 2258-2263
- [3] Duran H C Klepser B-U H and Bächtold W 1996 *IEEE Electron Device Lett.* 17 482-484
- [4] Duran H C Patrick W and Bächtold W 1995 *J. Vac. Sci. Technol. B* 13 2386-2389
- [5] Hooge F N Kleinpenning T G M and Vandamme L K J 1981 *Rep. Prog. Phys.* 44 479-532
- [6] Claverie A Yu K M Swider W Weber Z L O'Keefe M Kilaas R Pamulapati J and Bhattacharya P K 1992 *Appl. Phys. Lett.* 60 989-991
- [7] Cheung R Thoms S McIntyre I Wilkinson C D W and Beaumont S P B 1988 *J. Vac. Sci. Technol. B* 6 1911-1915
- [8] Kruppa W and Boos J B 1995 *IEEE Trans. Electron Devices* 42 1717-1723

Fabrication of Integrated Twin-Guide Corner Reflector Surface-Emitting Lasers with Reactive Ion-Beam Etching

Sung-Kwon Hong and Young-Se Kwon

Department of Electrical Engineering, Korea Advanced Institute of Science and Technology,
373-1 Kusong-dong, Yusong-gu, Taejon 305-701, KOREA

Abstract. We demonstrate InGaAs/AlGaAs/GaAs single quantum well surface-emitting laser (SEL) with integrated twin-guide structure (ITG). Integrated twin-guide lasers have been designed with normal-mode analysis at $\lambda=980\text{ nm}$ to achieve maximum coupling efficiency. Then, we have utilized corner reflectors (CR's) on ITG structure and angled beam deflectors tilted 45° with respect to the surface plane. The corner reflectors and the 45° beam deflectors were made by RIBE in order to have high power surface-emitting lasers (SEL's). Corner reflectors were formed for ITG's active layer and 45° angled deflectors were located at the end of the output waveguide. ITG-CR-SEL's were characterized with near-field intensity.

1. Introduction

Surface-emitting lasers (SEL's) are attractive devices for optical interconnection and two-dimensional laser array for optical communication. Several different structures for SEL's have been reported, such as vertical-cavity SEL's (VCSEL's), distributed Bragg grating SEL's, and in-plan lasers with 45° beam deflectors. Recently, high-power and low-threshold folded cavity SEL's (FCSEL's) have been fabricated using the dry etching techniques. Considering the output beam power, in-plan laser SEL's are more favorable than VCSEL's[1,2].

For this reason, in this work, we have fabricated surface-emitting lasers (SEL's) with corner reflectors (CR's) and external 45° beam deflectors. Integrated twin-guide (ITG) structure was proposed in the late 70s for applications to opto-electronic integrated circuits (OEIC's). But, at that time the fabrication technique was not fully developed for the efficient coupling efficiency to output waveguide. Nowadays, metalorganic chemical vapor deposition (MOCVD) can give precise epitaxy controllability, reproducibility, and very high uniformity by using *in situ* monitoring techniques[3]. In addition to the epitaxy, the dry etching techniques, such as reactive ion etching (RIE), electron cyclotron resonance (ECR) etching or reactive ion-beam etching (RIBE), have been also well developed for compound semiconductors[4,5]. By using these dry etching techniques, the angled beam deflector can be formed with a good surface morphology.

As compared with the other SEL's, ITG-CR-SEL's have some advantages: 1) there's no unguided region.; 2) it has a flexibility of bending the output light beam.; 3) it's possible to integrate this device with others for OEIC's. The ITG structure with CR's can operate as laser diode, detector or external modulator depending on the characteristics of applied voltages. By locating these structures on the network of waveguides, complex OEIC's can be implemented.

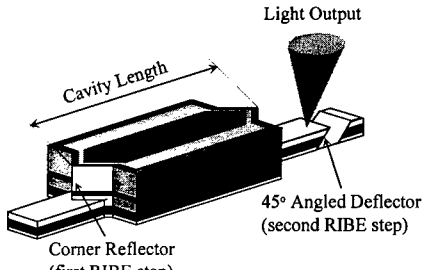


Fig. 1 Schematic view of the fabricated ITG-CR-SEL with an angled deflector.

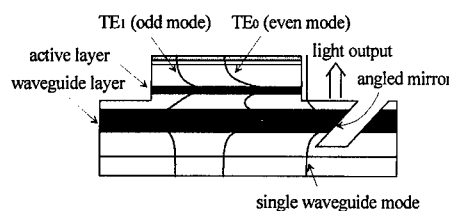


Fig. 2 Cross sectional view of ITG-CR-SEL laser structure.

2. Simulation and Experiments

ITG laser structure with etched facets has been designed by normal-mode analysis for InGaAs-AlGaAs-GaAs graded index separated confinement heterostructure (GRINSCH) single quantum well laser. The structure was optimized in order to obtain a maximum coupling efficiency into the output waveguide under the phase matching condition fulfilled at a wavelength of 980 nm [6]. The layer structure and the material parameters are listed in Table I. According to our calculation results, the coupling length was 93 μm , and the coupling efficiency to the output waveguide was 98%.

Corner reflector was used for the formation of the etched facets of ITG laser. Since a corner reflector has a high reflectivity and a low scattering loss, low threshold current can be achieved [7]. 45° beam deflectors were located at the end of the external output waveguide to deflect the light power to surface normal. Fig. 1 illustrates the schematic view of the fabricated ITG-CR-SEL, consisting of a twin-guide layers, two corner reflector, and an external 45° beam deflectors. In this structure, lasing light is coupled to the waveguide layer below the active layer as a result of the evanescent coupling. Fig. 2 shows the cross sectional view of ITG-CR-SEL.

InGaAs-AlGaAs-GaAs materials were grown in AIXTRON 200 low-pressure MOCVD with a

Table I. Structure Parameters of the ITG Laser.

Layer	Composition	Refractive index*	Thickness
p-ohmic contact	p+-GaAs	3.5122	2000Å
cladding	P-Al _{0.5} Ga _{0.5} As	3.2381	1.2 μm
GRINSCH	Al _{0.5} Ga _{0.5} As \rightarrow GaAs	3.2381 \rightarrow 3.5122	1500Å
active (SQW)	In _{0.2} Ga _{0.8} As/GaAs	3.5258/3.5122	70Å/100Å
GRINSCH	GaAs \rightarrow Al _{0.5} Ga _{0.5} As	3.5122 \rightarrow 3.2381	1500Å
separation	N- Al _{0.5} Ga _{0.5} As	3.2381	5500Å
waveguide	N- Al _{0.2} Ga _{0.7} As	3.3608	5270Å
cladding	N- Al _{0.5} Ga _{0.5} As	3.2381	1.2 μm
buffer	n-GaAs		1.0 μm
substrate	n-GaAs		

* refractive index at $\lambda = 980 \text{ nm}$ from Ref. [8].

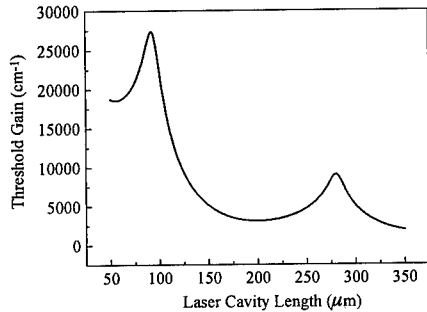


Fig. 3 Simulation result for the threshold current density of ITG laser.

tailored reactor for *in situ* laser reflectometry with which we could obtain growth thickness accuracy within $\pm 1\%$ error. The ITG laser structure consisted of 70-Å In_{0.2}Ga_{0.8}As- 100-Å GaAs GRINSCH SQW laser, as listed in Table I. A SiO₂-Ti-NiCr (2000 Å/ 300 Å/ 1000 Å) layer was deposited by e-beam evaporator for a current blocking layer. This evaporated layer was also used as a dry-etch masking material. The deposition of a Ti-Au-NiCr (500 Å/ 2000 Å/ 1000 Å) layer by thermal-evaporation followed the current stripe opening process for p-contact metal on the current blocking layer. The cavity length was 280 μm at which the coupling efficiency had a maximum value, and the cavity width was 20 μm.

Both corner reflectors and angled deflectors were formed by RIBE. In order to precisely control the etching depth with 100 Å resolution, etching process was also monitored by the *in situ* laser reflectometry. RIBE was performed in Ar-Cl₂ gas mixture with an 1000 eV ion-source power for corner reflectors. The etching depth was 1.93 μm which corresponded to 2000 Å below the top of the separation layer. After deposition of the Cr for mask material, the external 45° beam deflectors at the output waveguide layer was made by second step RIBE under 1100 eV ion-source power. The angled beam deflector could be achieved by tilting the substrate 45° in RIBE. After the deflector etching, the Cr mask material was removed. Then, the wafer was lapped down to about 100 μm, and a AuGe-Ni-Au was deposited on the bottom of the wafer as n-contact material.

3. Results and Discussion

As shown in the SEM photograph of Fig. 4, the reverse mesa etched beam deflector is tilted by about 45°. For the effective output coupling to surface, the external output waveguide should have a proper cladding layer thickness. The upper cladding layer thickness was 3500 Å and the vertical etching depth of 45° beam deflector was 1.35 μm. Atomic force microscope (AFM) was utilized for an investigation of the etched surface morphology and the effect of pinnacles at the reflectivity. The scanned area was 1.2 × 1.2 μm². We could obtain the arithmetic average surface roughness of 75.8 Å, as shown in Fig. 5. This value is an evidence that the pinnacles are at the outside of 45° beam deflector, so that they are not thought to affect the reflectivity. In Fig. 6, a near-field intensity of ITG-CR-SEL from the 45° beam deflector is illustrated. The full width at half maximum (FWHM) in the lateral and the transverse direction were 18 μm and 1.3 μm, respectively.



Fig. 4 SEM photograph of an ion beam-etched 45° beam deflector.

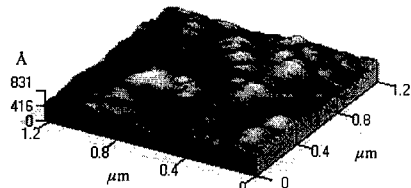


Fig. 5 AFM image of the ion beam-etched surface.

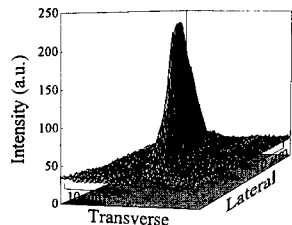


Fig. 6 Near-field intensity from the beam deflector at threshold current

4. Conclusions

We report the fabrication of integrated twin-guide corner reflector surface-emitting InGaAs-GaAs lasers. Dry-etching technique was utilized for the formation of corner reflector and the 45° beam deflector. The dry-etched surface roughness was estimated as 75.8 Å. ITG-CR-SEL has a potential for the implementation of optoelectronic devices.

Acknowledgments

This work was financially supported by Korea Science and Engineering Foundation (KOSEF) through Opto-Electronics Research Center (OERC).

References

- [1] H. P. Lee, A. Scherer, E. D. Beebe, W. P. Hong, R. Bhat, and M. A. Koza 1992 *Electron. Lett.* **28** 580-582
- [2] Y. Cheng, G. M. Yang, and P. D. Dapkus 1995 *IEEE Photon. Technol. Lett.* **7** 1104-1106
- [3] H. Q. Hou, H. C. Chui, K. D. Choquette, B. E. Hammons, W. G. Breiland, and K. D. Geib 1996 *IEEE Photon. Technol. Lett.* **8** 1285-1287
- [4] Z. J. Fang, G. M. Smith, D. V. Forbes, and J. J. Coleman 1994 *IEEE Photon. Technol. Lett.* **6** 10-12
- [5] K. Hamamoto, H. Chida, T. Miyazaki, and S. Ishikawa 1995 *IEEE Photon. Technol. Lett.* **7** 602-604
- [6] H. Ribot, P. Sansonetti, and A. Carencio 1990 *IEEE J. Quantum Electron.* **26** 1930-1941
- [7] B. B. Jian 1996 *IEEE Photon. Technol. Lett.* **8** 1609-1611
- [8] J. H. Shin and Y. H. Lee 1994 *J. Appl. Phys.* **76** 8048-8050

Selective and non-selective etching of GaN, AlGaN, and AlN using an inductively coupled plasma

S. A. Smith*, C. A. Wolden, M. D. Bremser, A. D. Hanser, and R. F. Davis

Department of Materials Science and Engineering, North Carolina State University, Raleigh, North Carolina 27695-7919

W. V. Lampert

Materials Directorate, Air Force Research Laboratory, Wright Patterson Air Force Base, OH 45433-7750

* Permanent address: Materials Directorate, Air Force Research Laboratory, Wright Patterson Air Force Base, OH 45433-7750

The etching behavior of gallium nitride (GaN) has been systematically examined in an inductively coupled plasma (ICP) using Cl₂ and Ar as the reagents. Design of experiments (DOE) software was used to optimize the etch rate as well as determine any interactions between the parameters (ICP power, DC bias, and pressure). Interactions were found between the ICP power and pressure and also between the ICP power and DC bias. There were no interactions between the DC bias and pressure. Selective etching of GaN relative to AlN and Al_{0.28}Ga_{0.72}N was achieved at low DC biases. At -20 V, the GaN etch rates were 38 times greater than AlN and a factor of 10 greater than Al_{0.28}Ga_{0.72}N.

1. Introduction

The etching of GaN and the alloy Al_xGa_{1-x}N has been a challenge for researchers due to the strong Ga-N and Al-N bonds as well as the chemical inertness of these materials. Different plasma sources, namely capacitively coupled, inductively coupled (ICP), and electron cyclotron resonance (ECR) have been employed to etch these materials. Capacitively coupled plasma sources such as that in reactive ion etchers (RIE) have produced low etch rates and non-vertical sidewalls etching these materials due in part to low plasma densities and high operating pressures.[1] High density plasma discharges such as (ECR) and (ICP) have distinct advantages over RIE systems that in addition to having higher plasma densities, they employ lower operating pressures and dc biases that are controlled separately from the plasma source. As a result, higher etch rates, vertical sidewalls, and lower etching induced damage occurs.

The etch selectivity of GaN relative to AlN and Al_xGa_{1-x}N is of significant interest for the fabrication of Al_xGa_{1-x}N based heterostructure devices. One example is the etch penetration through a GaN capping layer to the Al_xGa_{1-x}N recessed gate in a high electron mobility transistor. Etching of the latter material should be minimal.

In this paper we report a systematic study of ICP etching of GaN as a function of DC bias, ICP power, and pressure using a Cl₂/Ar chemistry. To minimize the number of experiments, design of experiments (DOE) software was used to optimize the etch rates with respect to these parameters. Selectivity of GaN relative to AlN and Al_xGa_{1-x}N is also discussed as a function of DC bias at low dc biases.

2. Experiment

2.1 System description

The ICP system was a custom built, 41 cm diameter by 58 cm tall, loadlocked stainless steel chamber. The RF power was coupled through a 32.4 cm diameter quartz window at the top of the chamber. The inductive source was a planar, 4 turn, 23 cm diameter copper coil which was connected to an RF Power

Products 2 kW RF generator operating at 13.56 MHz via an autotuning matching network. Gas was fed into the chamber through a stainless steel shower ring positioned level with the bottom of the quartz window. A water-cooled wafer chuck was mounted on a motor driven vertical translation stage which had 30.5 cm of travel. This allowed samples to be transferred between the loadlock chamber and the processing zone. A second 500 W RF source was connected to the wafer chuck to apply a controllable DC bias to the substrate. The substrate cooling water was maintained at 16°C to prevent the baking of photoresist during etching. The chamber was evacuated by an Alcatel 900 l/s turbomolecular pump which attained a base pressure of 10^{-7} torr.

A magnetic bucket containing 240 Nd-Fe-B magnets was mounted on the outside perimeter of the chamber to increase the plasma density by confining the electrons to a central volume within the chamber. This reduced electron losses due to collisions with the chamber walls. The ions were also confined due to electrostatic coupling with the electrons. The former were not directly affected by the magnetic field.

2.2 Sample preparation

The GaN, AlN, and $\text{Al}_{0.28}\text{Ga}_{0.72}\text{N}$ samples used for this study were epitaxially grown on 6H-SiC-(0001) substrates via metalorganic vapor phase epitaxy (MOVPE) using trimethylaluminum (TMA) and triethylgallium (TEG) as the Al and Ga sources, respectively, and NH_3 as the nitrogen source.[2, 3] An $\approx 100\text{nm}$ AlN buffer layer was deposited on the SiC substrates prior to the growth of the GaN and the $\text{Al}_{0.28}\text{Ga}_{0.72}\text{N}$. Preparation of the samples for etching employed the sequence of applying a Ni coating, patterning with photoresist, and dipping into HNO_3 to etch the Ni and into acetone to remove the photoresist. Just prior to entry into the etching system, the samples were dipped into HCl for 10 minutes to remove oxygen and carbon contaminants. Samples were attached to a 7.6 cm diameter anodized aluminum transport plate using vacuum grease which was mounted onto the wafer chuck. After entry into the system a base pressure of $\leq 5 \times 10^{-7}$ torr was attained before the etching experiments were initiated.

3. Results

3.1 Etch rate optimization

For this study three parameters were optimized: the ICP power, DC bias, and pressure were varied, while the gas flows and concentrations were held constant at 20 sccm Cl_2 and 5 sccm Ar. The ranges for the 3 varied parameters were as follows: ICP power = 100-1100 W, DC bias = 50-450 V, and pressure = 1-11 mtorr. Previous experiments had shown that changing the gas flow rates and concentration minimally affected the etch rates (<20%). The etch depths were measured using a Dektak profilometer on at least three different points on each sample.

To determine the effects of interactions between parameters and their affect on etch rate and to optimize the etch rate SAS JMP statistical software was employed which reduced the total number of experiments from 150 to 20. A central composite design was chosen as it uses five levels of each parameter and accounts for any curvature in the response. Past experiments have shown that none of the parameters behave linearly with the etch rate. Table I shows the design matrix of the parameters which were varied and the resultant etch rates. As can be seen from this table, there are 15 different experiments with the center point repeated 6 times.

Figure 1 is a plot of contours of GaN etch rate derived from the data in Table I. In this type of plot, and in the case of Figure 1, one parameter (pressure) was varied while the other two are on the x (ICP power) and y (DC bias) axes. The individual contours are of equal response and have a step increase of 1000 Å/min between lines. This type of analysis can be very useful when a process window must be identified when there are multiple responses.

A plot of the interaction profiles between the different parameters are shown in Figure 2. The interaction plots between the DC bias and pressure reveal that there is no interdependence between them; whereas, the ICP power and pressure are highly dependent on each other. It was observed that the

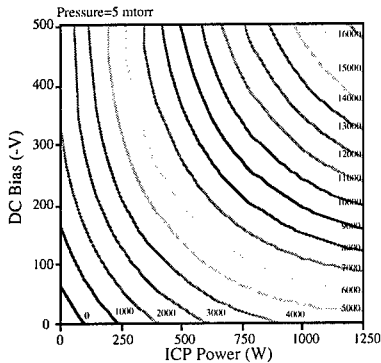


Figure 1. Contour plot derived from the data in Table I of etching rate of GaN as a function of ICP power and DC bias at 5 mtorr. The contours signify etch rate in Å/min.

optimum pressure for etching increased with increasing ICP power. There is also a dependence between the DC bias and the ICP power.

The predictions by the DOE software were checked experimentally at 5 different points and can be seen in Figure 3. The parameters were as follows: (1) ICP=1100 W, Bias=-428 V, Pressure=6 mtorr, (2) ICP=960 W, Bias=-174 V, Pressure=9 mtorr, (3) ICP=1750 W, Bias=-600 V, Pressure=12 mtorr, (4) ICP=370 W, Bias=135 V, Pressure=2 mtorr, (5) ICP=270 W, Bias=410 V, Pressure=4 mtorr. With the exception of sample 3, all of the points were within original input parameter ranges previously stated. Sample 3 was well outside of the original ranges; however, there was only a 8.6% difference between the actual and predicted etch rates. The highest error was found for sample 5 at 20%.

Table I - Design matrix for etch rate optimization of GaN thin films.

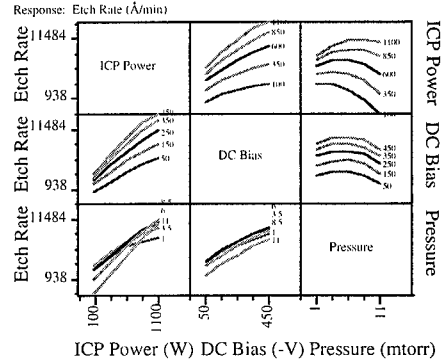


Figure 2. Interaction profiles that show the interdependence between ICP power, DC bias, and pressure on the etch rate of GaN.

Run	ICP Power(W)	DC Bias(-V)	Pressure(mtorr)	Etch Rate(Å/min)
1	303	131	3	3730±40
2	303	131	9	1940±90
3	600	250	6	7760±80
4	303	369	3	6380±140
5	303	369	9	3960±60
6	600	250	6	7770±60
7	897	131	3	7050±100
8	897	131	9	7200±200
9	600	250	6	7790±90
10	897	369	3	10920±360
11	897	369	9	9520±380
12	600	250	6	7680±50
13	100	250	6	940±20
14	1100	250	6	11480±330
15	600	250	6	7840±80
16	600	50	6	2120±210
17	600	450	6	10630±250
18	600	250	6	7630±90
19	600	250	1	5020±140
20	600	250	11	5650±160

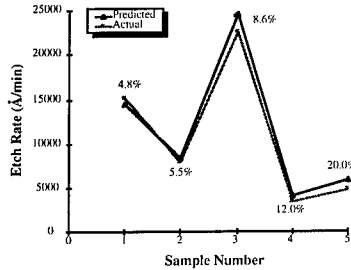


Figure 3. Comparison of experimental and predicted GaN etch rate from studies used to test the accuracy of the DOE model. See text for parameters.

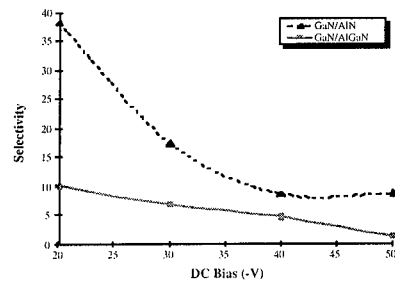


Figure 4. The selectivity of GaN relative to $\text{Al}_{0.28}\text{Ga}_{0.72}\text{N}$ and AlN as a function of DC bias. Values of selectivity were obtained from the GaN/AlN and GaN/ $\text{Al}_{0.28}\text{Ga}_{0.72}\text{N}$ etch rate ratios.

3.2 Selective etching

Selective etching of GaN relative to AlN and $\text{Al}_{0.28}\text{Ga}_{0.72}\text{N}$ was achieved at low DC biases. All materials were etched concurrently to insure an accurate comparison. The experimental parameters were 500 W ICP power, 5 mtorr pressure, and a -20 to -50 V variable DC bias. Figure 4 shows the selectivity of GaN as ratios of the etch rate of this material to that of AlN and $\text{Al}_{0.28}\text{Ga}_{0.72}\text{N}$. At -50 V, the selectivity between GaN and AlN was 8.5; whereas, it was only 1.2 between the GaN and $\text{Al}_{0.28}\text{Ga}_{0.72}\text{N}$. The greatest selectivities for GaN were found at a bias of -20 V, a factor of 38 over AlN and approximately 10 over $\text{Al}_{0.28}\text{Ga}_{0.72}\text{N}$. These differences in etch rates are consistent with the different bond energies between Ga-N and Al-N of 8.92 eV/atom and 11.52 eV/atom, respectively.[4] A second factor is the lower volatility of AlCl_x relative to GaCl_x . Since lower DC biases were used to attain the selective etching, there is a tradeoff between the selectivity and the total etch rate.

3.3 Summary

Dry etching of GaN has been investigated in an ICP system produced in the authors' laboratories using Cl_2 and Ar as the process gases. Design of experiments software was used to both optimize the parameters and to determine the interactions between the different parameters. Interactions were observed between the ICP power and pressure as well as the ICP power and the DC bias. There was no interaction between the DC bias and the pressure. Selective etching of GaN relative to AlN and $\text{Al}_{0.28}\text{Ga}_{0.72}\text{N}$ was achieved at low DC biases. Selectivities of 38 between GaN and AlN and 10 between GaN and $\text{Al}_{0.28}\text{Ga}_{0.72}\text{N}$ were obtained at a DC bias of -20V. These results are of potential interest for the fabrication of $\text{Al}_x\text{Ga}_{1-x}\text{N}$ based heterostructure devices. Research is ongoing to quantify the effects of plasma induced damage and to better understand the underlying mechanisms.

This work was supported by the Office of Naval Research under contract No. N00014-96-1-0765. Colin A. Wolden acknowledges support as an NRC/ARO postdoctoral fellow. Scott A. Smith wishes to acknowledge Claude Woods from the University of Wisconsin for help in the design of the ICP system and the U.S. Air Force PALACE Knight program.

4. References

- [1] Lin ME, Fan ZF, Ma Z, Allen LH, and Morcoç H 1994 *Appl. Phys. Lett.* 64 (7) 887.
- [2] Bremser MD, Perry WG, Zheleva T, Edwards NV, Nam OH, Parikh N, Aspnes DE, and Davis RF 1996. *MRS Internet J. Nitride Semicond. Res.* 1 (8)
- [3] Hanser AD, Wolden CA, Perry WG, Therrien R, and Davis RF (not yet published).
- [4] Shul RJ, Briggs RD, Pearton SJ, Vartuli CB, Abernathy CR, Lee JW, Constantine C, and Barratt C 1996 MRS Boston, MA 969.

FOCUSED ION BEAM ASSISTED OHMIC METALLIZATIONS TO p-6H-SiC

**A. A. Iliadis, S. N. Andronescu, V. Talyansky¹, K. Edinger, J. H. Orloff, M. C. Woods², and
K. A. Jones²**

Electrical Engineering Department, University of Maryland, College Park, Maryland 20742

1. Center for Superconductivity, Department of Physics, University of Maryland, College Park,
MD 20742

2. Army Research Laboratory, 2800 Powder Mill Road, Adelphi, MD 20783-1197

Abstract. This work deals with the development of high temperature, low resistance ohmic metallizations to p-type 6H-SiC, using a novel approach of focused ion beam (FIB) surface-modification and in-situ direct-write metal deposition for ohmic contact formation without annealing. FIB(Ga) surface-modification and in-situ deposition of Pt, Mo and W showed minimum contact resistance values of 1.3×10^{-4} Ohm cm² to 7.3×10^{-3} Ohm cm², depending on metal and FIB conditions. These contact resistance values of the direct FIB deposited non-annealed contacts, compare well with reported values for conventionally deposited and annealed contacts to SiC. Ex-situ E-beam deposition of Pt on FIB surface-modified and unmodified areas showed a substantial increase (one order of magnitude) in the contact resistance values of the unmodified contacts.

1. Introduction

The formation of low resistance high quality ohmic contacts to SiC, is critical to the operation of the devices, especially in the high temperature/high power operation regime. The problem is particularly difficult in the case of p-type ohmic contacts, where deposited and annealed contacts on moderately to highly doped 6H-SiC material reach at best contact resistance values between 10^{-3} and mid 10^{-4} Ohms cm² [1][2], while for very highly doped (10^{19} cm⁻³) material one report indicates a value of 10^{-5} Ohms cm² for Al/Ti contacts annealed at 1000 °C [3]. Other systems examined so far are based on Ti and W with some Pt and Au combinations, that may have better stability under extended high temperature operation. In general the contacts may deteriorate due to interface reactions that include silicide and carbide formation, interdiffusion, and surface oxidation [4][5]. Clearly, for the development of viable high temperature/high power SiC device technology, the quality of p-type ohmic metallizations needs to be studied further and improved.

In this work we report a new approach to ohmic contact formation based on focused ion beam (FIB) surface-modification and concurrent in-situ FIB direct-write metal deposition. In addition, FIB surface-modification and ex-situ metal deposition (E-beam), was also employed for comparison. Our approach of surface-modification using focused ion beams is aiming at lowering surface barriers, while at the same time increasing surface doping by Ga ion implantation to enhance tunneling and further improve contact resistance. Metallization is achieved concurrently by focused ion beam in-situ direct-write metal deposition of various metals [6]. For the present work we report contact resistance values from the direct-write

deposition of Platinum (Pt), Molybdenum (Mo), and Tungsten (W), as well as Pt deposition by E-beam on FIB surface-modified and unmodified p-type 6H-SiC.

2. Experimental Details

The SiC samples used in this study are p-type epitaxial layers on n-type 6H-SiC substrates purchased from CREE Corporation, with doping levels in the $2 \times 10^{18} \text{ cm}^{-3}$ range. Two focused ion beam (FIB) systems using Ga ion beams, have been employed in this study. One is a FEI system with ion beam energy of 30 KeV where the Pt and Mo direct-write deposition was performed, and the other is a MICRION system with ion beam energies up to 50 KeV, where the W direct-write deposition and surface-modification for ex-situ Pt E-beam deposition were performed. The Pt was E-beam deposited on FIB surface-modified and unmodified areas, to assess the effects of the FIB surface-modification process on contact resistance. The transmission line model (TLM) for contact resistance measurements was used on both the FIB direct-write metal patterns (Fig. 1), and the ex-situ E-beam deposited Pt that was patterned by standard photolithographic techniques. The measurements provide the specific contact resistance values, r_c , for the contacts, which we refer to as the contact resistance values for simplicity. Auger depth profiling is used to examine the metal/interface system and correlate it with the observed electrical properties.

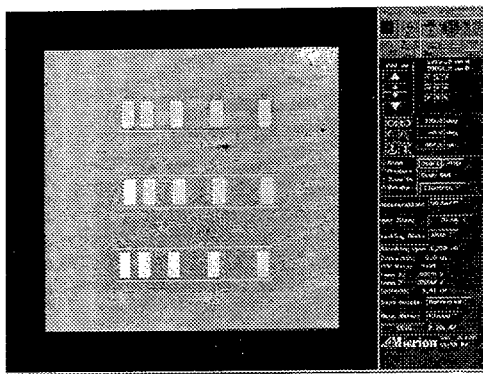


Fig. 1. W FIB direct-write TLM pattern.

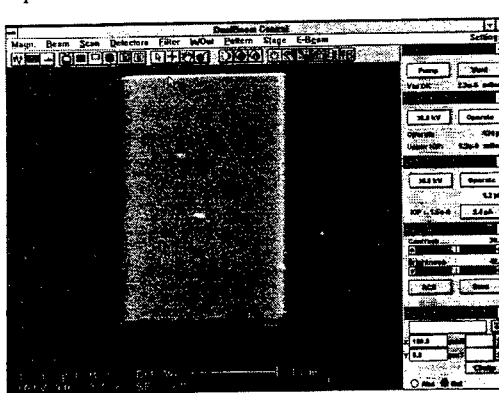


Fig. 2. Mo FIB direct-write contact definition.

3. Experimental Results and Discussion

The FIB direct-write deposition of Mo was performed at ion beam energies of 30 KeV and produced well defined metal films with thicknesses around $1\mu\text{m}$, shown here in Fig. 2.

The TLM contact resistance measurements of contacts made at two different ion beam currents of 6,000 pA and 12,200 pA, gave contact resistance values $r_c = 3.3 \times 10^4 \text{ Ohm cm}^2$ and $1.3 \times 10^4 \text{ Ohm cm}^2$ respectively (Fig. 3). The lowest r_c value is observed for the highest beam current direct-write deposition. Although Mo has not been reported before as a p-type contact on 6H-SiC, the value of r_c obtained here, is comparable to

those reported for W/Pt/Au [2] and better than the values reported for Al/Ti [3] that have been annealed.

The FIB direct-write deposition of Pt was also performed at 30 KeV and at the same high beam current of 12,200 pA, but the r_c values from the TLM measurements (7.3×10^{-4} Ohm cm 2) were higher than those of Mo.

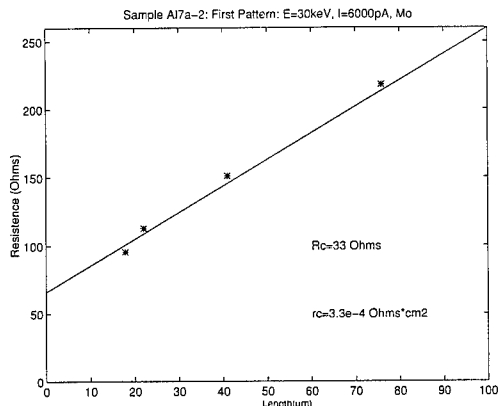


Fig. 3. Mo FIB direct-write r_c measurement.

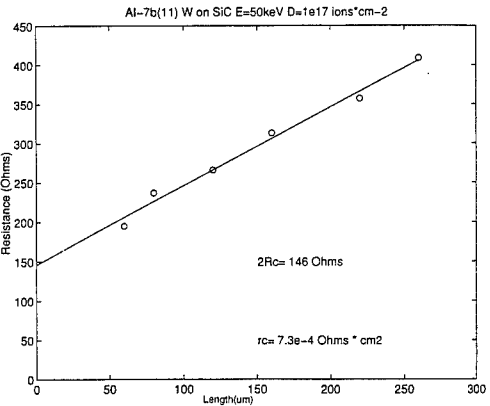


Fig. 4. W FIB direct-write r_c measurement.

The direct-write deposition of W was performed at ion beam energies of 50 KeV and with ion doses of $D=1.0 \times 10^{17}$ ions/cm 2 and $D=3.0 \times 10^{17}$ ions/cm 2 . TLM contact resistance measurements gave $r_c = 7.3 \times 10^{-4}$ Ohm cm 2 and 1.1×10^{-3} Ohm cm 2 for the low and high doses respectively (Fig. 4). These values are higher than those of Mo and Auger depth profiling was performed on the W and Mo contacts to evaluate the interface.

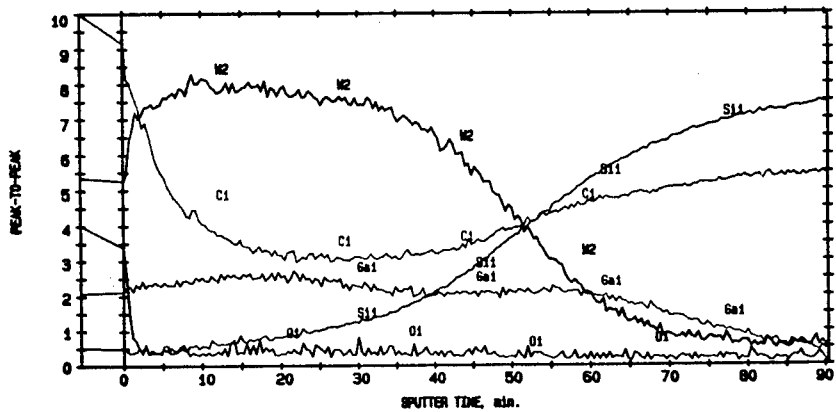


Fig. 5. Auger Depth Profile of W contacts.

Fig. 5 shows the Auger depth profile of the W contacts. As can be seen in the profile, a considerably diffused interface results from this FIB direct-write deposition at 50 KeV, with significant concentration of Ga in the metal and significant penetration into the SiC substrate. Si outdiffusion is also evident, while C levels in

the metal films are high due to the FIB deposition process, and possibly to a lesser extend, to the outdiffusion from the substrate.

In contrast the Auger profile from the Mo contacts, shown in Fig. 6, produces at 30 KeV a much less diffused interface with limited Ga penetration within a surface layer, and a Si outdiffusion that, except from a surface peak, remains nearly constant through the metal film. The high C levels observed also in these films, are the subject of further investigation of the FIB deposition process, aiming at reducing such levels.

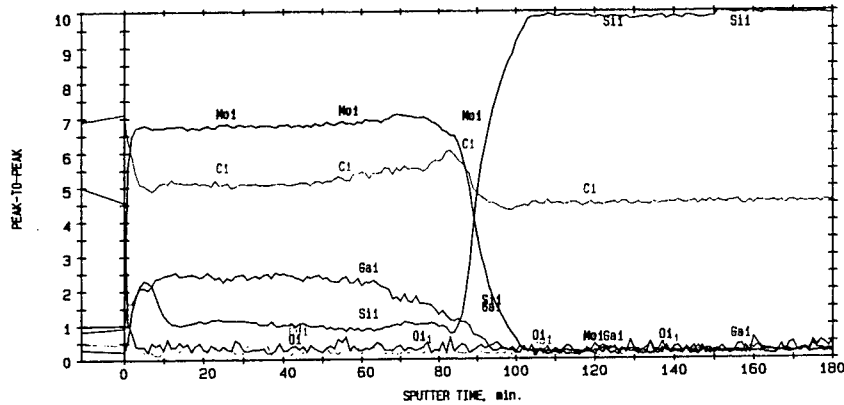


Fig. 6. Auger Depth Profile of Mo FIB direct-write contacts.

In order to develop an initial understanding of the effects of the FIB surface-modification process, Pt was deposited by E-beam on FIB surface-modified and unmodified areas of p-type 6H SiC, and r_c (Fig. 7) was measured.

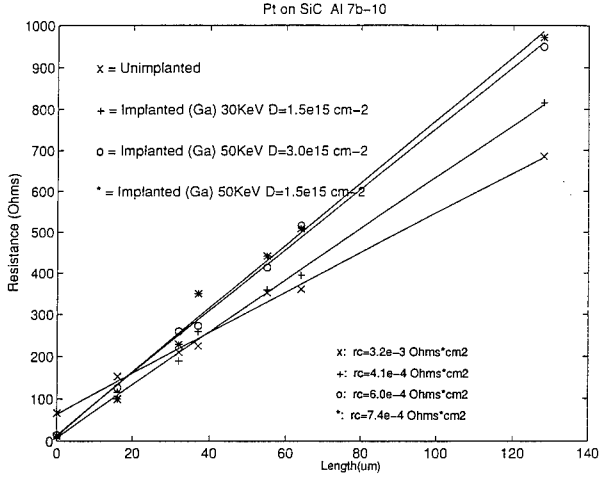


Fig. 7. r_c measurements from E-beam Pt deposition on surface-modified and unmodified areas.

Three FIB surface-modified areas were produced side by side at 30 KeV and a moderate dose of 1.5×10^{15} ions/cm², and at 50 KeV and two different doses of 1.5×10^{15} ions/cm² and 3.0×10^{15} ions/cm².

The FIB surface-modified areas produced r_c values of 4.1×10^{-4} Ohm cm² at 30 KeV and 7.4×10^{-4} Ohm cm² and 6.0×10^{-4} Ohm cm² at 50 KeV for low and high doses respectively. In contrast the unmodified contacts produced r_c values of 3.2×10^{-3} Ohm cm², which is nearly an order of magnitude higher than the surface-modified contacts.

4. Conclusions.

A novel approach to ohmic contact formation using FIB surface-modification and Ga implantation with FIB direct-write metal deposition, is reported here for Mo, Pt, and W metallizations.

Of the three different FIB direct-write metallizations, Mo, reported here for the first time, is shown to have the lowest contact resistance value at 1.3×10^{-4} Ohm cm², while Pt and W showed higher values. Auger depth profiling revealed considerable intermixing at the W contact interface, with substantial Ga penetration, Si outdiffusion and C concentrations in the metal, in contrast with the Mo interface, which appeared significantly less intermixed, with limited Ga penetration into the substrate.

Ex-situ E-beam deposition of Pt on FIB surface-modified and unmodified areas, clearly showed a substantial (one order of magnitude) improvement in the contact resistance values of the surface-modified areas as compared with the unmodified areas, which validated the FIB process.

Furthermore, moderate energies (30 KeV) and moderate doses (1.5×10^{15} ions/cm²) of ion beams, appear to produce lower values of contact resistance. Experiments are under way to examine the stability of these contacts under thermal treatment, and provide a better understanding of the processes and parameters involved.

Acknowledgements. This research was funded by the Army Research Laboratory under Cooperative Agreement No. DAAL01-95-2-3530. The views and conclusions presented here are those of the authors and should not be interpreted as representing the official policies, either expressed or implied of the Army Research Laboratory or the U.S. Government.

References

- [1] O. Nennowitz, L. Spiess and V. Breternitz, Appl. Surf. Sci. 91, pp 347-351 (1995)
- [2] J. S. Shor, R. A. Weber, L.G. Provost, D. Goldstein and A. D. Kurtz, MRS Proc. Vol 242, pp 573-581 (1992)
- [3] J. Crofton, P. A. Barnes, J. R. Williams and J. A. Edmond, Appl. Phys. Lett. 62, pp 384-386 (1993)
- [4] H. Morkoc, S. Strite, G. B. Gao, M. E. Lin, B. Sverdlov and M. Burn, J. Appl. Phys. 76, pp 1363-1396, (1994)
- [5] F. Goesmann, R. Schmid-Fetzer, Mat. Sci and Eng. B34, pp 224-231 (1995)
- [6] P. Blauner, Y. Butt, J. Ro, C. Thompson, and J. Melngailis, J. Vac. Sci. Tech. B7, pp 1816-1818 (1989).

Silicon Carbide Power MOSFET Technology

**J.B. Casady, A.K. Agarwal, L.B. Rowland, S. Seshadri, R.R. Siergiej,
D.C. Sheridan, S. Mani, P.A. Sanger, and C.D. Brandt**

Northrop Grumman Science & Technology Center
1350 Beulah Road
Pittsburgh, PA 15235-5080

Abstract. 4H-SiC UMOSFETs and DMOSFETs have been fabricated and tested with measured blocking voltages (1400 V and 900 V, respectively). Although these breakdown voltages were reasonable, obtaining sufficient channel mobility ($50 \text{ cm}^2/\text{Vs}$) to enable devices with practical current densities has thus far proven elusive owing to the poor quality of the SiC-SiO₂ interface. DMOS structures suffer from a non-self aligned process, and gate oxide present over rough implanted and annealed SiC surfaces. Thus surface scattering effects and interface state density remain high, lowering carrier mobility. In addition, UMOS devices also suffer from poor inversion layer mobility due to the difficulties of forming high quality oxide on the sidewalls of the vertical trenches. In this paper we will explore these and other design and processing trade-offs.

1. Introduction

SiC power MOSFETs offer several potential advantages over Si power MOSFETs in the areas of switching (faster with lower losses), operating temperature, and blocking voltage. These advantages are a consequence of SiC's inherent material advantages including wide bandgap (3.2 eV for 4H-SiC), high electric breakdown strength (2.2 MV/cm) and high thermal conductivity ($\sim 3 \text{ W/cm}\cdot\text{K}$) [1]. While the advantages of SiC power MOSFETs over Si power MOSFETs (both UMOS and DMOS type structures) have been long known [2], processing issues [3-5] including poor SiC-oxide interfaces and premature breakdown of the gate oxide, have prevented these devices utility for commercial systems.

2. Fabrication of SiC power MOSFET structures

Here we report on both the 4H-SiC UMOSFET and 4H-SiC DMOS structures. The 4H-SiC UMOSFET was fabricated with a 12 μm thick drain-drift layer ($N_D \sim 2 \times 10^{15} \text{ cm}^{-3}$) and a 90 nm gate oxide, as shown by the cross-sectional view of the device in Figure 1. The gate oxide consisted of a thin-layer of thermally grown SiO₂ followed by a thicker-layer of deposited SiO₂ to ensure a more uniform gate oxide across the bottom and sidewalls of the trench. Nickel was used for the drain and source metallizations, with TLM measurements yielding a specific contact resistance of $5-7 \times 10^{-6} \Omega\cdot\text{cm}^2$. The channel length was nominally set to 4 μm from the as-grown channel epitaxial layer.

4H-SiC DMOS structures were also fabricated using a lightly doped n-type 10 μm thick drain-drift layer. These devices used multiple ion implants (high-dose nitrogen implants for source regions, high-dose aluminum implants for body contact, and high-energy aluminum or boron implants for formation of the p-wells) to fabricate a planar power MOSFET in SiC. After activating the implants with a standard high-temperature anneal in an inert ambient, the gate oxidation was performed in pyrogenic steam at 1150°C, followed by LPCVD polysilicon deposition for the gate, and subsequent patterning of the polysilicon. Finally, ohmic contacts were formed to the drain, source, and body terminals completing a standard four terminal MOSFET structure. Completed device cross-section of the DMOS is also shown in Figure 1.

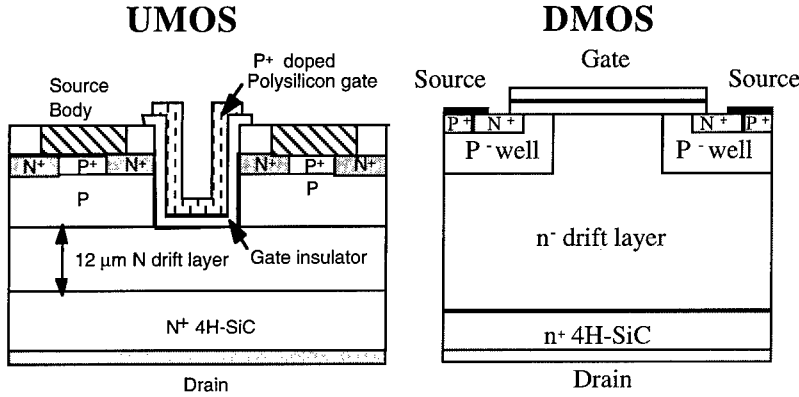


Figure 1: Vertical SiC UMOS cross-section with 12 μm thick drift layer and 4 μm channel length on left and 4H-SiC DMOS power FET structure is shown on right.

3. Device Characteristics and Discussion

Forward blocking characteristics of the 4H-SiC MOSFETs were measured by wafer level probing under high dielectric strength FluorinertTM to prevent surface flashover. The drain and gate bias were supplied by dual computer-controlled Keithley 237 power supplies (maximum voltage of 1100 V). The blocking voltages of the vertical 4H-SiC DMOS and 4H-SiC UMOS FET are shown in Figure 3a) and 3b), respectively. In Figure 2, this DMOSFET blocked 900 V, while a similar UMOSFET blocked 1100 V, which was the maximum voltage available from the power supply. Further testing using a Tektronix 371A curve tracer resulted in measuring a maximum blocking voltage of approximately 1400 V for the UMOS, as shown in Figure 3.

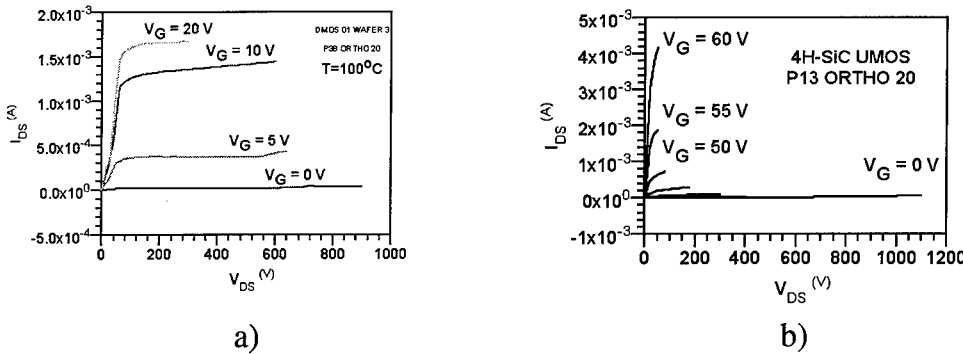


Figure 2: a) 4H-SiC DMOS blocking 900V at 100°C under FluorinertTM (left) and b) 4H-SiC UMOS blocking 1100 V at room temperature under FluorinertTM (right).

Under a moderate gate bias of 32 V (3.55 MV/cm) at room temperature, the channel mobility of the UMOS was only $1.5 \text{ cm}^2/\text{V}\cdot\text{s}$, while increasing the temperature to 100°C increased the channel mobility to $7 \text{ cm}^2/\text{V}\cdot\text{s}$ at a gate bias of only 26 V (2.9 MV/cm). This data can be explained by interface traps located at the SiC-oxide interface which release charge carriers at higher temperatures resulting in increased conduction for a given bias.

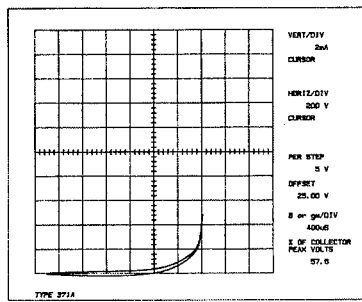


Figure 3: 4H-SiC UMOS blocking 1400 V at room temperature under FluorinertTM (6.75x10⁻⁴ cm² active area).

Initial results of the 900 V DMOS devices also have channel mobility exhibiting the same temperature effects of interface traps as was noted in the UMOSFET. Both the UMOSFET and DMOSFET were operated from room temperature to 300°C with higher currents and transconductance values obtained at higher temperatures. No catastrophic device failures occurred from the high-temperature operation although device reliability tests have not yet been performed.

In Figure 4a), the characteristic I-V family of curves is shown for a 4H-SiC UMOSFET at an ambient temperature 100°C, as well as the linear region ($V_{DS} = 100$ mV) small-signal transconductance for a similar UMOSFET at different temperatures. From the characteristic family of curves, a specific on-resistance of 74 $\text{m}\Omega\cdot\text{cm}^2$ can be extracted, which is higher than expected due to the high channel resistance. From Figure 4b), an increase in small-signal transconductance with temperature can be observed. The linear region g_m is defined below in Equation (1), where W is the gate width, L is the gate length, μ is the *effective* electron inversion layer mobility in the channel, and C_{ox}' is the oxide capacitance per unit area. The increased drain current and small-signal transconductance found at higher temperatures are counter intuitive. One would expect increased acoustic phonon scattering at higher temperatures acting to decrease both parameters via mobility degradation at high temperatures.

$$g_{m,lin} = (W/L) \mu C_{ox} V_{DS} \quad (1)$$

Increasing μ with temperature can explain the increased $g_{m,lin}$ at higher temperatures, since all other parameters in Equation (1) are independent of temperature. Thus, μ is not limited by acoustic phonon scattering at these temperatures, but by other physical mechanisms. The most plausible temperature related mechanism which explains the increasing μ with temperature is thermal and bias-dependent activation of a high number of filled interface traps beneath the conduction band at the SiC-SiO₂ interface. In depletion-mode SiC MOSFETs, the normally expected decrease in μ with temperature has been found [6], which is consistent with our explanation since in depletion-mode devices carriers are not confined to the interface, and thus the mobility would not be dominated by interface traps for those devices.

Comparisons between the UMOS and DMOS FET structures in SiC are still preliminary, but the highest channel mobility's reported in SiC DMOS structures ($26 \text{ cm}^2/\text{V}\cdot\text{s}$) [4] are a factor of two higher

than the highest reported values for SiC UMOSFETs [5]. The higher μ found in DMOS is to be expected since the etched surface directly above the UMOS channel is considerably roughened which acts to increase surface scattering of carriers, and since the oxide-SiC interface is found to be optimal on planar silicon-face surfaces as opposed to the vertical trench surfaces in the UMOS. However, μ of the DMOS, while improved over the UMOSFET (confirmed elsewhere [4,5]) is still low as a consequence of surface roughening caused by implant damage, and a non-optimal interface.

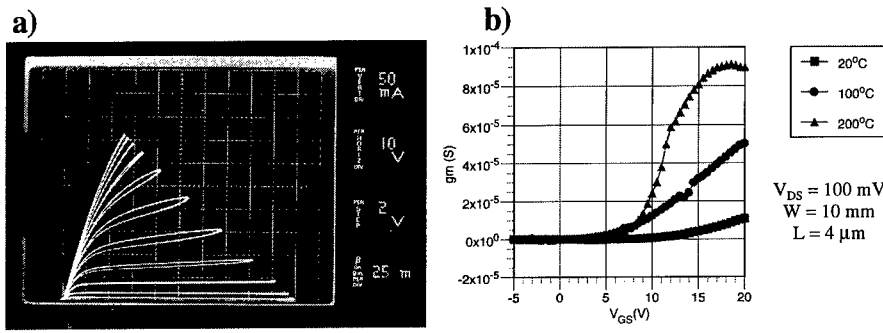


Figure 4: Low-voltage characteristics of 4H-SiC UMOSFETs shown by a) drain-to-source current as a function of drain-to-source voltage and gate-to-source voltage and b) small-signal linear region transconductance as a function of temperature for a similar UMOSFET.

4. Conclusions

4H-SiC vertical power MOSFETs have been fabricated and preliminary analysis has been reported. Both UMOS and DMOS structures experimentally demonstrated high (1400 and 900 V, respectively) blocking voltages. A significant impediment to optimized device performance is the poor SiC-SiO₂ interface, which currently results in channel mobility below the theoretical values for SiC. The increasing values of I_{DS} and transconductance with temperature suggest the possible presence of high densities of interface traps immediately below the conduction band which release trapped carriers during biased high-temperature operation.

8. Acknowledgments

Work funded by ONR contract No. N00014-95-C-0132 and U.S. Air Force Contract No. F33615-92-C-2275 (Subcontract No. 353941BA to Hamilton Standard. Authors are grateful for technical support and encouragement from A. Goodman and G. Campisi of ONR, as well as C. Severt of U.S.A.F. WPAFB.

References

- [1] Casady J B and Johnson R W 1996 *Solid-St. Elect.* 39 1409-1422
- [2] Bhatnagar M and Baliga B J 1993 *IEEE Trans. Elect. Dev.* 40 645-655
- [3] Agarwal A K, Siergiej R R, Seshadri S, White M H, McMullin P G, Burk A A, Rowland L B, Brandt C D, and Hopkins R H 1996 *Mat. Res. Soc. Symp. Proc.* 423 87-92
- [4] Shenoy J N, Cooper J A Jr. and Melloch M R 1997 *IEEE Elect. Dev. Lett.* 18 93-95
- [5] Palmour J, Singh R, Lipkin L A, and Waltz D G 1996 *Trans. 3rd Intl. High Temp. Elect. Conf.*, 2, XVI-9-XVI-14
- [6] Casady J B, Cressler J D, Dillard W C, Johnson R W, Agarwal A K, and Siergiej, R R 1996 *Solid-St. Elect.* 39 777-784

1000V 4H-SiC Gate Turn Off (GTO) Thyristor

R. R. SIERGIEJ, J. B. Casady, A. K. Agarwal, L. B. Rowland, S. Seshadri, S. Mani, P. A. Sanger, and C. D. Brandt

Northrop Grumman Science & Technology Center
1350 Beulah Road
Pittsburgh, PA 15235-5080

Abstract. 4H-SiC GTO devices were designed, fabricated and evaluated on the basis of blocking voltage, current density and forward drop. Interdigitated designs with device pitches ranging from 26 to 48 μm and circular devices with diameters from 0.5 to 1.5 mm were fabricated. We measure 600 V forward blocking voltage, and 4 A (1500 A/cm^2) forward current on 680 μm diameter involute 4H-SiC GTOs fabricated with a 14 μm base layer. Interdigitated devices of smaller areas ($\sim 6.5 \times 10^{-4} \text{ cm}^2$ active area) measure 1000 V forward blocking for a 14 μm epitaxial base layer. By combining 8 interdigitated devices in parallel, a maximum current of 20 A was achieved which corresponds to a current density of 3500 A/cm^2 (compared to 200 A/cm^2 maximum for a Si GTO). Current density as a function of forward drop was evaluated over the temperature range of 25 $^\circ\text{C}$ to 390 $^\circ\text{C}$

1. Introduction

SiC power devices have recently made significant progress towards both high-voltage and high-current capabilities as SiC material and device processing technologies have matured. Advances in three and four terminal SiC power devices include 900 V, 2 A and 700 V, 6 A thyristors [1], 700 V GTOs [2], 1100 V UMOSFETs [3], 900 V DMOSFETs [4], and 2600 V DMOSFETs [5]. The advantages of these transistors over silicon-based devices in terms of switching speed, high-temperature operation, and blocking voltage are as a direct result of SiC's inherent material advantages. These include wide bandgap (3.2 eV for 4H-SiC), high electric breakdown strength (2.2 MV/cm) and high thermal conductivity ($\sim 3 \text{ W/cm}\cdot\text{K}$) [6,7]. Here we present some of our most recent work on the 4H-SiC GTO structure (shown in Figure 1) including our first reported results on circular GTO devices with diameters ranging from 0.5 to 1.5 mm, and interdigitated designs with pitches ranging from 26 to 48 μm . Preliminary results include 600 V forward blocking voltage, a maximum of 4 A (1500 A/cm^2) forward current on 680 μm diameter involute 4H-SiC GTOs, and 1000 V forward blocking for interdigitated devices of smaller areas ($\sim 6.5 \times 10^{-4} \text{ cm}^2$ active area).

2. Fabrication of SiC power GTO structures

The 4H-SiC GTO was fabricated with a thick, lightly doped, base layer approximately 14 μm thick, on top of p- and n-type buffer layers as reported elsewhere [2]. Nickel was used to contact the implanted n⁺ gate material, with TLM measurements yielding a specific contact resistance of $1 \times 10^{-5} \Omega\cdot\text{cm}^2$. The anode p⁺ contact was formed using an Al/Ti alloy with a specific contact resistance of $1 \times 10^{-3} \Omega\cdot\text{cm}^2$. All photolithography was performed using a MANN DSW 4800 g-line (436 nm) stepper, with all metal layers defined after lift-off using a standard bi-level resist process. The GTO cross-section is shown in Figure 1.

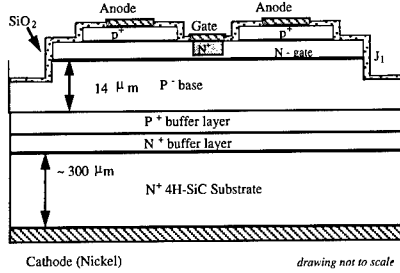


Figure 1: Cross-section of an inverted asymmetrical 4H-SiC GTO with 14 μm thick blocking layer.

3. Device Characteristics and Discussion

Measurements of static D.C. operation were performed by grounding the anode and applying a negative bias to the cathode. Initial 25°C *on-wafer* measurements of the completed 4H-SiC involute GTO (680 μm diameter) reveal 600 V anode to cathode forward blocking, and anode to cathode (I_{AK}) forward conduction of 4 A ($\sim 1500 \text{ A/cm}^2$ normalized to the anode area) as shown in Figure 2a. Increased current capability is expected once these devices are packaged with proper heat sinking. The device was turned on by gate currents in excess of 500 μA . Smaller interdigitated devices were capable of 1000 V blocking which is shown in Figure 2b, for a GTO with interdigitated anode and gate (26 μm pitch, 10 fingers, 250 μm gate length). Devices of this geometry are referred to as P26LIN10 devices. The forward blocking curve in Figure 2b is measured at room temperature using Fluorinert™ with no gate drive(off condition). By combining 8 interdigitated devices in parallel, a maximum current of 20 A is achieved which corresponds to a current density of 3500 A/cm^2 (compared to 200 A/cm^2 maximum of a Si GTO). To examine the forward current density with respect to forward voltage drop, a P26LIN10 was probed on a hot chuck up to 390°C. The results of this test are shown in Figure 3 for current densities of up to $\sim 3500 \text{ A/cm}^2$, normalized to the anode area. The experimental data shown in Figure 3 also includes the voltage drop from the measured 1 Ω series probe resistance. The voltage drop across the probes is 1 V at the peak current density of 3500 A/cm^2 .

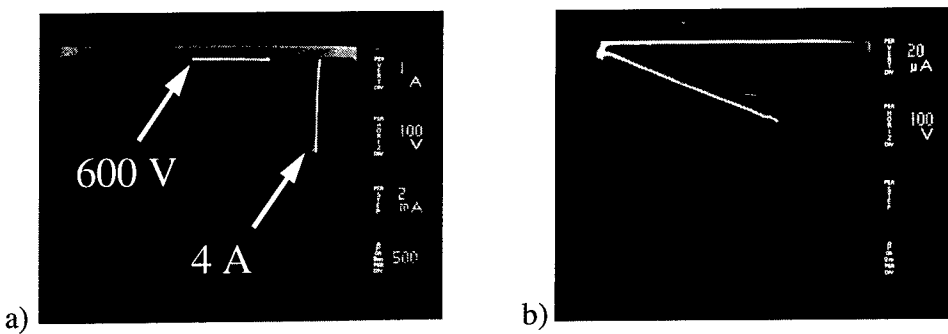


Figure 2: Room temperature I-V characteristics of a) 680 μm diameter involute structure 4H-SiC GTO with forward blocking voltage of 600 V and forward current of up to 4 A (1500 A/cm^2 normalized to anode area). In b) the room temperature forward blocking (V_{AK}) of an interdigitated 4H-SiC GTO cell (26 μm pitch, 10 fingers, 250 μm finger length) is shown to be 1000 V.

Correcting for series probe resistance effects, an approximate forward voltage drop of 4.4 V at room temperature and 3.6 V at 390°C can be expected for these GTO's operating with a current density of 1000 A/cm². To further reduce the forward voltage drop, reduction in contact resistances are being explored. The forward voltage drop decreases at elevated temperatures as expected from the ideal diode equation, and secondly due to a reduction of the p-type layer resistivity as a consequence of increased dopant ionization.

Light emission can be used to sample current distribution in SiC p/n junction devices. For example in Figure 4, one such example is shown for a 0.68 mm diameter involute GTO structure. The outside circle corresponds to the mesa isolated blocking junction, where the involute fingers shown are resulting from the isolated gate-to-anode p/n junction. Blue light emission appears uniform from which we deduce a uniform current distribution in the device.

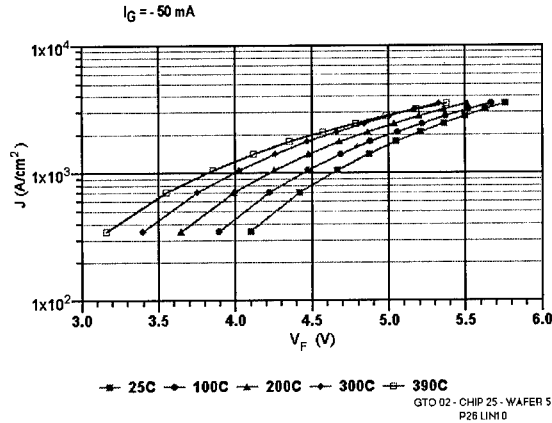


Figure 3: Forward current density as a function of temperature for a 4H-SiC GTO (interdigitated gate-anode, 26 μm pitch, 10 finger device) with current normalized to anode area. Maximum current shown for this device is 1 A ($\sim 3500 \text{ A/cm}^2$). Measured data shown here includes voltage drop across the probe resistance of approximately 1 Ω , which would correspond to a 1 V reduction in the peak forward drop shown above.

4. Conclusions

4H-SiC vertical power GTOs have been fabricated and preliminary analysis has been reported. Blocking voltages of 1000 V were obtained from small-area devices, whereas larger 0.68 mm diameter circular devices were capable of blocking up to 600 V. Forward current of up to 4.2 A was probed in the larger devices, 20 A was obtained through a parallel combination of 8 devices, and currents up to 1 A (3500 A/cm^2) were evaluated as a function of forward voltage drop and temperature for the smaller devices. At a current density of 1000 A/cm², neglecting the series probe resistance, forward voltage drop was approximately 4.4 V at room temperature to 3.6 V at 390°C.

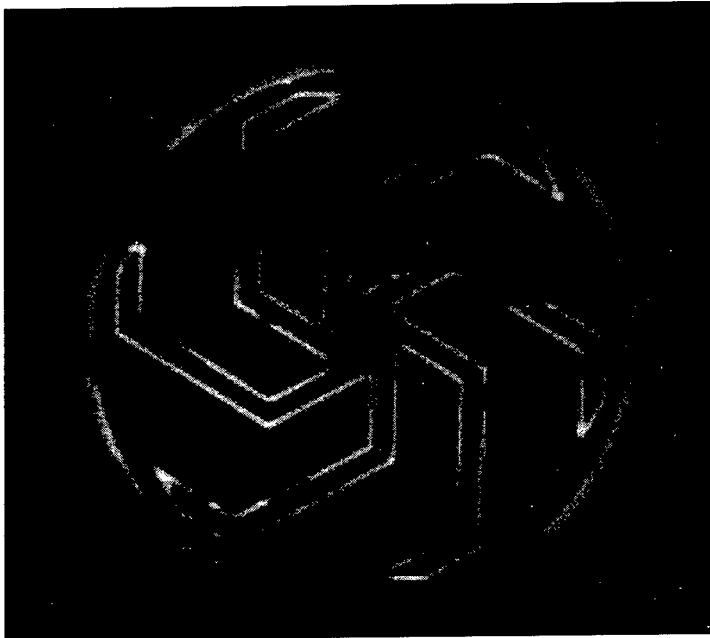


Figure 4: Light emission from a 0.68 mm diameter 4H-SiC GTO structure with forward current conduction. Light emitting from the outside circle corresponds to the mesa isolated p/n blocking junction, while light emitted from the involute fingers is a result of the mesa isolated gate-to-anode junction.

5. Acknowledgments

This work was funded by DARPA, Air Force TRP SiC Power Device Consortium (Northrop Grumman, DARPA, Silicon Power Corporation, EPRI, Baltimore Gas and Electric, and Rutgers University); Dr. E. Brown and Dr. J. Scofield contract monitors. Authors are grateful to C.F. Seiler and W. Urban for process development, as well as the technicians of the Advanced Electronic Structures and Central Processing Laboratories at Northrop Grumman.

References

- [1] Palmour J, Singh R, Lipkin L A, and Waltz D G 1996 *Trans. 3rd Int'l. High Temp. Elect. Conf.* 2 XVI(9-14)
- [2] Agarwal A K, Casady J B, Rowland L B, Seshadri S, Valek W F, and Brandt C D 1997 *IEEE Elect. Dev. Lett.* submitted
- [3] Agarwal A K, Casady J B, Rowland L B, Valek W F, White M H, and Brandt C D 1997 *IEEE Elect. Dev. Lett.* submitted
- [4] Casady J B, Agarwal A K, Rowland L B, and Brandt C D 1997 *Tech. Digest 55th Int'l. IEEE Device Research Conf.*
- [5] Spitz J, Melloch M R, Cooper J A Jr., and Capano M, 1997 *to be published in Proc. of the Int. Conf. on Silicon Carbide, III-Nitrides and Related Materials*
- [6] Bhatnagar M and Baliga B J, 1993 *IEEE Trans. Elect. Dev.* 40 645-655
- [7] Casady J B and Johnson R W 1996 *Solid-St. Elect.* 39 1409-1422

MOCVD Growth of InGaN Multiple Quantum Well LEDs and Laser Diodes

M. P. Mack,* A. C. Abare, P. Kozodoy, M. Hanson, S. Keller, U.K. Mishra, L.A. Coldren and S.P. DenBaars
 Electrical and Computer Engineering Department, University of California, Santa Barbara, California 93106.
 *Wright Labs, WL/AADD

Abstract: The MOCVD growth of InGaN/GaN multiple quantum well (MQW) structures for blue LEDs and lasers has been investigated. (1) The structural and optical properties of the layers have been characterized by x-ray diffraction and photoluminescence. (2) By incorporating an MQW structure as the active region in a GaN p-n diode, high-brightness light emitting diodes (LEDs) have been produced. Under a forward current of 20 mA, these devices emit 2.2 mW of power corresponding to an external quantum efficiency of 4.5%. (3) Room temperature (RT) pulsed operation of blue (420 nm) nitride based multi-quantum well (MQW) laser diodes grown on c-plane sapphire substrates with threshold current densities as low as 19 kA/cm² were observed for 5x800 μm² lasers with uncoated reactive ion etched (RIE) facets

1. Introduction

High performance light emitting diodes (LEDs) that operate in the ultraviolet to green portion of the spectrum and laser diodes that operate from the 400 nm to 440 nm have been realized recently through the use of GaN and its alloys with In and Al. Early devices were constrained by difficulty obtaining p-type films, however the discovery of post-growth activation procedures for these films has led to rapid progress in nitride-based LEDs and lasers(Amano et al., 1989, Nakamura et al., 1991). For the optimization of super-bright LEDs and laser diodes an understanding of the electroluminescence of the InGaN multiple quantum well (MQW) structure is crucial. The growth and characterization of such MQW stacks has been a subject of intense research for some time (Itoh et al., 1991, Koike et al., 1996, Singh et al., 1996) but little data has been published on the characteristics of spontaneous emission from such structures. Recently, Nakamura and co-workers have published impressive results on the room-temperature CW operation of a laser diode with a MQW InGaN active region, achieving a laser output power of 10 mW at a current of 100 mA (Nakamura et al., 1997). In this work, we report on the growth and characterization of InGaN/GaN MQW layer structures with varying dimensions. We also report on the characteristics of an LED grown with an MQW active region, which exhibits very high output power and excellent color purity. Finally, we report, for the first time, on measurements of blue-MQW-InGaN LEDs and lasers.

2. MQW Growth Study

2.1 MQW Growth Study Experiment

InGaN/GaN MQW stacks were grown on c-plane sapphire substrates by metalorganic chemical vapor deposition. The MOCVD growth conditions and resulting material quality for GaN and InGaN have been discussed earlier.(Keller et al., 1996, Keller et al., 1995). The MQW stacks consisted of 14 periods of $\text{In}_{0.2}\text{Ga}_{0.8}\text{N}$ wells with GaN barriers and were grown on top of a 2 μm GaN buffer. The indium composition was determined by a bulk reference sample. Two studies were performed: in one set of growths the barrier width was varied and the well width was held constant at 22 Å. In the other set, the well width was varied and the barrier width was held constant at 43 Å.

2.2 MQW Growth Study Results

Figure 1 and Figure 2 shows the photoluminescence (PL) and x-ray diffraction (XRD) rocking curve data obtained from each sample in the well-width study. Superlattice peaks are evident in the XRD data, indicating the presence of abrupt heterojunction interfaces and a high degree of coherency along the growth direction. The superlattice peak spacing was used to obtain the thickness of the wells and barriers. The PL data shows strong quantum well emission with a narrow linewidth. 25-36 Å wells

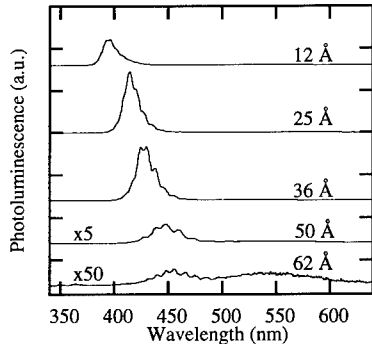


Figure 1: PL spectra for MQWs with varying well widths

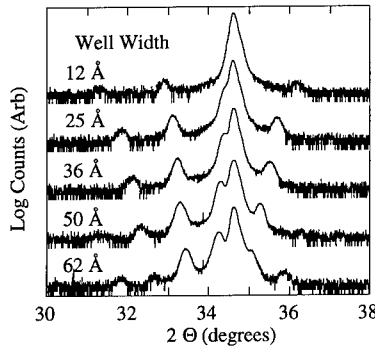


Figure 2: X-ray for MQWs with varying well widths

are seen to give optimal luminescence qualities. In comparison the 12 Å wells have a wider emission linewidth and reduced emission intensity due to interface roughness effects. Increasing the well width beyond 50 Å also results in an increased linewidth and decreased emission intensity. The mechanism for this trend is likely a combination of effects such as degradation of the InGaN material during subsequent high-temperature growth, piezoelectric field inducing spatial separation of electrons and holes, and possibly compositional fluctuation. The wavelength increases with well width as expected with quantum confinement. The behavior deviates from simple theory due to piezoelectric fields and compositional fluctuation.

The results of the barrier width study are less dramatic. As the barrier width is increased to about 50 Å, the emission linewidth decreases and the peak intensity improves. Expanding the barrier width beyond 50 Å appears to saturate this effect. From these preliminary studies we conclude that thin InGaN quantum wells (25–36 Å) with thick GaN barriers (>50 Å) give optimal photoluminescence properties. Further studies on the growth and characterization of MQW structures are being pursued; the results will be published in a separate paper.

3. LED

3.1 LED Experiment

The electroluminescence properties of the multi-quantum-well layers were tested in an LED structure (Figure 3). Devices were fabricated with a mesa size of $6 \times 10^{-4} \text{ cm}^2$. Ni/Au was used for the p-contact and Ti/Al for the n-contact. The devices were then packaged in the standard LED lamp form. When tested under a DC current of 20 mA, the emission is seen to peak at approximately 445 nm and a narrow emission linewidth of 28 nm was obtained. The output power at this current level was 2.2 mW. The power saturates at 8 mW under a DC current of approximately 100 mA; this saturation is attributed to heating effects causing a drop in quantum efficiency. The external quantum efficiency reaches its peak value of 4.5% at a driving current of 20 mA.

3.2 LED Results

By testing the LED under pulsed conditions the effect of heating can be greatly reduced. Current pulses of width 3 μs and duty ratio 3×10^{-4} were used during high current testing. As Figure 4 demonstrates, output

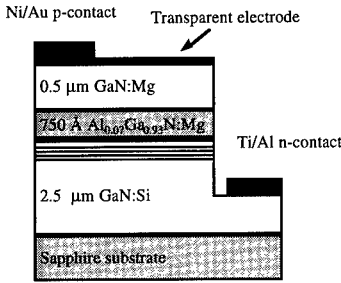


Figure 3: LED device structure. The active region consists of 5 periods of 25 Å In_{0.25}Ga_{0.75}N and 40 Å GaN.

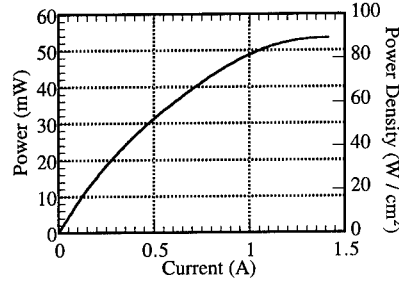


Figure 4: L-I curve for MQW LED under DC current. The quantum efficiency is 4.5%.

power saturation was not observed under these conditions until a driving current of 1.4 A was applied. At this current level, the output power was 53 mW, to our knowledge the highest reported for an InGaN LED. In contrast, commercially available SQW InGaN LEDs tested under the same conditions saturate at a current of 600 mA with an output power of 25 mW. We attribute the very high power level achieved in this LED to the use of a MQW structure, which reduces the degree of carrier overflow and non-radiative recombination.

4. Laser Diode

4.1 Laser Diode Experiment

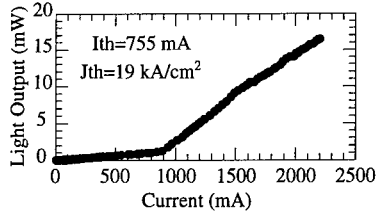
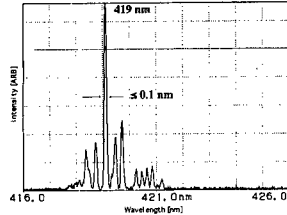
The optimized MQWs were incorporated into the laser structure with 10 QWs and 0.4 μm upper and lower Al_{0.1}Ga_{0.9}N cladding layers and 0.1 μm Mg doped GaN contact layer. The lasers facets were formed by Cl₂ reactive ion etching of 125 μm wide mesas of various lengths ranging from 400 μm to 2,000 μm. P-contact stripes were subsequently formed in the center of these large mesas with widths ranging from 3 μm to 20 μm. The n and p-contacts were formed by electron beam evaporation of Ti/Al/Ni/Au and Ni/Au respectively. Fabricated lasers were tested under pulsed operation with a duty cycle of about 0.025%.

4.2 Laser Diode Results

A typical light vs. current (LI) curve is shown in Figure 5. We obtain a for a threshold current density of 19 kA/cm² for a 5 μmx800 μm laser bar with uncoated facets at room temperature.

The highest differential efficiency was 1.1%. Output powers of these devices were limited by heating during the pulses. Nevertheless, peak powers as high as 17.6 mW were obtained. Most devices gave outputs in excess of 10 mW. Device yield was well above 50%. The emission above threshold was strongly TE polarized with an extinction ratio in excess of 60. Spectra were collected above and below threshold using an optical spectrum analyzer with a resolution of 0.1 nm. A strong, well-defined mode spectrum appears at threshold as shown in Figure 6. The resolution is not sufficient to resolve the expected individual mode spacing for the cavity lengths tested. As a result the width of the observed peaks corresponds to the analyzer resolution. The lasing spectrum does, however, show an envelope modulation with a peak spacing around 0.35 nm similar to that observed by Nakamura et al. (Nakamura and Fasol, 1997) The origin of this modulation is still unclear.

A lifetime test was done on a single 10 μmx400 μm device operated above threshold in pulsed mode in excess of 6 hours before failing catastrophically between 6 and 8 hours due to shorting of the p-n junction.

Figure 5: Typical LI curve for $5\mu\text{m} \times 800\mu\text{m}$ laserFigure 6: Above threshold spectrum for $400\mu\text{m}$ long device with a $5\mu\text{m}$ stripe width

Conclusions

We have investigated the luminescence properties of InGaN/GaN multi-quantum-well structures grown by MOCVD. Photoluminescence measurements performed on MQW stacks indicate that optimal emission qualities are obtained using thin quantum wells and thick barriers. The structural quality of the films is confirmed by x-ray diffraction measurements showing prominent superlattice peaks. The MQW stack has been incorporated as the active region in an LED and laser. The resulting LED device demonstrates very high output power, narrow linewidth, and excellent color purity. The LED output power saturation under DC conditions is attributed to heating, a problem which is exacerbated by the poor thermal conductivity of the sapphire substrate. Under pulsed conditions heating may be avoided and very high output powers are achieved. The laser incorporating the optimized MQW lasers under RT pulsed operation. The output is thermally limited by heating during the pulses.

Acknowledgments

We gratefully acknowledge support for this research from the DARPA (N00014-96-1-0738), monitored by Dr. Anis Husain and ARO (DAAH04-95-1-0329) monitored by Dr. Jon Zavada.

References

- Amano, H., Kito, M., Hiramatsu, K. and Akasaki, I. (1989) *Japanese Journal of Applied Physics, Part 2 (Letters)*, **28**, L2112-2114.
- Itoh, K., Kawamoto, T., Amano, H., Hiramatsu, K. and Akasaki, I. (1991) *Japanese Journal of Applied Physics, Part 1 (Regular Papers & Short Notes)*, **30**, 1924-1927.
- Keller, B. P., Keller, S., Kapolnek, D., Jiang, W. N., Wu, Y. F., Masui, H., Wu, X., Heying, B., Speck, J. S., Mishra, U. K. and DenBaars, S. P. (1995) In *7th Biennial Workshop on Organometallic Vapor Phase Epitaxy*, Vol. 24 Fort Meyers, FL, USA, pp. 1707-1709.
- Keller, S., Keller, B. P., Kapolnek, D., Abare, A. C., Masui, H., Coldren, L. A., Mishra, U. K. and Den Baars, S. P. (1996) *Applied Physics Letters*, **68**, 3147-3149.
- Koike, M., Yamasaki, S., Nagai, S., Koide, N., Asami, S., Amano, H. and Akasaki, I. (1996) *Applied Physics Letters*, **68**, 1403-1405.
- Nakamura, S. and Fasol, G. (1997) *The blue laser diode : GaN based light emitters and lasers*, Springer, Berlin, New York.
- Nakamura, S., Senoh, M. and Mukai, T. (1991) *Japanese Journal of Applied Physics, Part 2 (Letters)*, **30**, L1708-1711.
- Nakamura, S., Senoh, M., Nagahama, S. I., Iwasa, N., Yamada, T., Matsushita, T., Sugimoto, Y. and Kiyoku, H. (1997) *Applied Physics Letters*, **70**, 1417-1419.
- Singh, R., Doppalapudi, D. and Moustakas, T. D. (1996) *Applied Physics Letters*, **69**, 2388-2390.

ECR-MBE growth and high excitation properties of GaInN/GaN heterostructures

J. Müller, M. Lipinski, A. Maksimov[†], A. Forchel

Technische Physik, University of Würzburg, Am Hubland, D-97074 Würzburg, Germany

[†]permanent address: Institute of Solid State Physics, Russian Academy of Science, Chernogolovka

Abstract. We have developed a method to reduce plasma self biasing effects during ECR-MBE growth of GaN based on an external magnet positioned on axis to the ECR-source. With this method it is possible to increase the growth rate up to $0.7\text{ }\mu\text{m/h}$ by using high microwave powers (up to 200 W) to increase the density of excited nitrogen. With this method we have realized GaN and GaInN/GaN QW-structures with high optical efficiency. The GaN-layers show strong excitonic emission with line widths below 5 meV and no yellow luminescence. Optically pumped stimulated emission in stripe excitation geometry (threshold pumping intensity $\sim 1\text{ MWcm}^2$) was realized up to room temperature.

1. Introduction

Due to their direct bandgap the group-III-nitrides are a very attractive material system for the realization of optical emitters from the UV far into the visible range ($E_g, \text{AlN} \sim 6.2\text{ eV}$ - $E_g, \text{InN} \sim 1.9\text{ eV}$) [1]. Highly efficient light emitting diodes based on InGaN/GaN-QW-structures are commercially available and room temperature lasing has been demonstrated with similar structures [2,3].

Despite several advantages of MBE most of the commercially available devices are fabricated up to now by MOVPE. This is partly due to the problem to produce activated nitrogen in MBE systems. This is typically done by cracking nitrogen molecules (N_2) into radicals (N^*) in plasma sources developed for plasma processing. One very severe drawback of this method is the production of charged particles such as electrons and differently activated ions which lead to the formation of electrostatic potentials and subsequently to ion damage during the MBE growth. This paper reports on a novel method for ECR-MBE which allows to reduce the plasma self biasing effects and to increase the source efficiency significantly. The method is described in detail and cw- and high excitation photoluminescence results from GaN and GaInN/GaN-QW-structures realized by this method will be presented.

2. Experimental setup

Fig. 1 shows a schematical sketch of the MBE system. Group-III elements (Al, Ga, In) and dopands (Si, Mg) are evaporated from solid sources. An ECR source mounted at the bottom of the chamber is used to produce active nitrogen. The sample stage, which is electrically isolated with respect to ground or the electrodes of the beam flux ion gauge, can be used with an electrical setup shown in Fig. 1 to determine plasma parameters. The key element of our setup

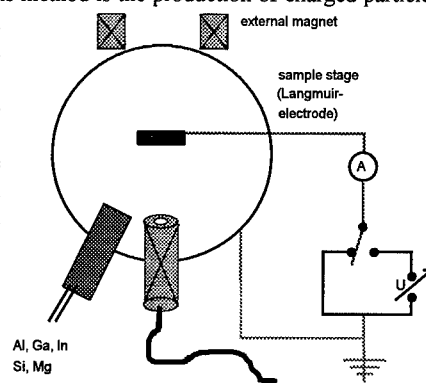


Fig. 1 ECR MBE setup for the growth of GaN with an external on axis magnet to reduce plasma self bias effects

to reduce plasma effects is an external magnet positioned on the top of the chamber, on axis with the ECR-source.

2.1 Reduction of plasma effects

Fig. 2 shows the dependence of the current collected at the sample stage (ampere-meter grounded) on the current of the external magnet for ECR operation at about 194 W of microwave power and a nitrogen flux of about 0.5 sccm. Without magnetic field ($I_{\text{ext}} = 0 \text{ A}$) a relatively strong negative current of about 3.5 mA is collected at the sample stage. This is due to electrons produced in the plasma discharge, which are strongly guided towards the sample stage by the field lines of the internal ECR-magnet. The corresponding negative charge density around the sample stage forms an attractive potential for positive

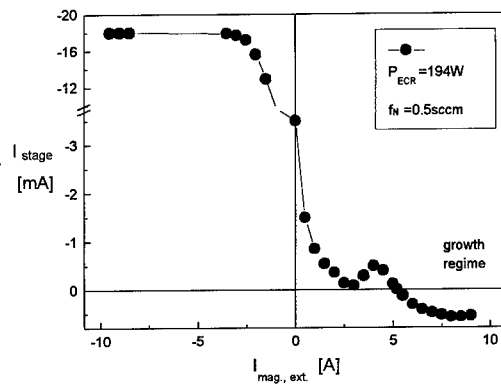


Fig. 2 Dependence of the net current collected at the sample stage during ECR-operation from the current of the external magnet.

ions which are also produced in the plasma discharge. The ions are thus accelerated towards the wafer during epitaxial growth and are responsible for ion damage in the GaN-layers. Such effects are known as plasma self biasing effects.

To reduce these effects it is thus necessary to remove the negative net charge from the sample region. According to Fig. 2 this can be realized by applying positive currents to the external magnet (\equiv opposite direction of magnetic field of external magnet and internal ECR magnet). The collected net current can be reduced significantly and saturates at small positive values possibly due diffusing positive nitrogen ions. This situation corresponds nearly to a complete removal of the plasma self biasing effect. For negative external magnet currents the current collected at the sample stage is strongly increased and saturates at values around -18 mA. This corresponds to a focusing of the total electron current towards the sample stage. This value or the current at zero external current can be regarded as a measure for the activation of the plasma.

The measurement of the current collected at the sample stage, which is produced by the plasma discharge, allows to determine the spatial distribution of the charges in the MBE chamber. In a numeric calculation we thus calculated the potential drop between ECR discharge region and sample stage, which is a measure for the ion energy, for different external magnet currents:

Without external magnetic field, a relatively strong potential drop between discharge region and sample stage of about 15 eV is obtained. For a negative external magnet current of -5 A, which corresponds to a focusing of the emission characteristics of electrons towards the sample stage ($I_{\text{stage}} \sim 18 \text{ mA}$), we obtain an increase of the ion energy to about 30 eV.

For increased external magnet currents (low charge density at the sample stage) the potential drop and therefore the ion energy is significantly reduced. Finally negligible values below 1 eV are obtained for external currents of about +5 A. This regime is thus chosen for the activation of nitrogen for the growth of GaN and GaInN with high microwave powers (150-200 W) with growth rates between $0.3 \mu\text{m/h} - 0.75 \mu\text{m/h}$. Without the external magnet setup GaN-layers with high optical quality, comparable to those described in this paper, could only be realized with low microwave power ($\sim 60 \text{ W}$) resulting in low growth rates below 50 nm/h. Higher microwave power ($> 80 \text{ W}$) caused plasma induced damage in the structures so that no radiative recombination could be detected when no external magnetic field was applied.

3. Growth of GaN and InGaN/GaN -QW and cw-photoluminescence (PL) results

Sapphire is chemically cleaned ($H_2O_4:H_3PO_4$) and then mounted into an In-free sample holder. Homogeneous sample heating up to wafer temperatures of about 870°C is realized by a backside coating of the wafers. After mounting into the load lock the samples are outgassed at 650°C before being transferred into the growth chamber. Growth was carried out with and without low temperature AlN buffer layers. The deposition of GaN is carried out at wafer temperatures of about 820°C. The beam equivalent pressure of Ga is typically around $5 \cdot 10^{-7}$ Torr. To obtain a sufficiently high density of excited nitrogen the ECR source is operated at high microwave powers up to 200 W with nitrogen fluxes of about 1-2 sccm. The growth rate for the GaN layers is between 0.3 and $0.75 \mu\text{m}/\text{h}$.

Fig. 3 shows a PL spectrum of a GaN layer with an AlN buffer layer deposited at 550°C on c-plane sapphire. The microwave power used for the activation of nitrogen was 150 W and the growth rate was about $0.5 \mu\text{m}/\text{h}$. The PL shows only excitonic recombination with a FWHM of less than 5 meV which demonstrates the high quality of the layers. Yellow luminescence is typically not observed in such layers.

For the growth of GaInN/GaN-structures the wafer temperature is significantly lowered to about 620-640°C during the deposition of the GaInN layers because of the high desorption rate of the In at elevated temperatures. To increase the In/Ga ratio in these layers the total group-III flux is reduced resulting in growth rates of about 0.15 - $0.2 \mu\text{m}/\text{h}$ during the growth of GaInN/GaN-

structures.

Fig. 4 shows the PL of two different GaInN/GaN film structures with different active layer thicknesses of 40 nm and 4 nm deposited with identical In/Ga ratios. As a reference we plotted also the emission of a GaN structure in Fig. 4. For the layer with thick GaInN layers we observed very efficient radiative recombination in the blue green at 2.6 eV. The recombination is most likely due to localized states e.g. In-rich clusters. If we reduce the layer thickness to a few nm (4 nm GaInN/GaN film structure in Fig. 4) the luminescence shifts strongly to the UV at 3.2 eV while high optical efficiency is preserved.

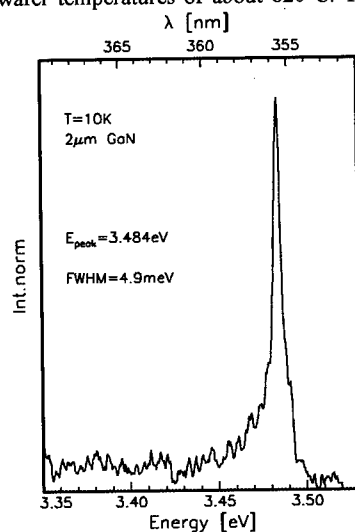


Fig. 3 Near bandedge luminescence of a GaN layer at 10 K.

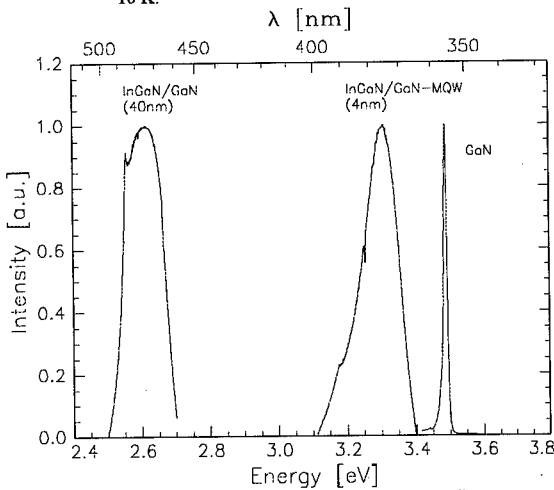


Fig. 4 PL recombination of three different samples: pure GaN, GaInN/GaN film structures with 40nm and 4nm GaInN films at 10 K.

4. Optically pumped stimulated emission of GaN

To investigate high excitation properties of the GaN layers we carried out optical pumping experiments with a pulsed nitrogen laser in stripe excitation geometry [5]. The laser is focused with a cylindrical lens onto the GaN sample. When the pumping creates optical amplification in the GaN layers intense amplified spontaneous emission can be detected from the edge of the sample in rectangular direction with respect to the excitation beam. Characteristic signs for stimulated emission are a significant line narrowing above the threshold and an exponential dependence of the stimulated emission intensity on the excitation length $[I(L) \sim \{exp(gL)-1\}$, g - optical gain coefficient, L - excitation length [5]].

Fig. 5 shows high excitation luminescence spectra of an GaN layer in stripe excitation geometry for different excitation lengths at room temperature ($L = 100 - 300 \mu m$). The pumping pulse intensity is approximately 1 MW/cm^2 .

At the lowest excitation length we mainly observe spontaneous emission with a FWHM in the order of 100 meV. When the excitation stripe length is increased from $100 \mu m$ to $130 \mu m$ a sharp feature appears in the spectrum due to the onset of amplification. When the slit length is increased further up to $300 \mu m$ the sharp feature grows rapidly and dominates the entire luminescence band. The FWHM of the stimulated emission line is about 30 meV i.e. much narrower than the corresponding spontaneous emission band at short excitation length. The optical gain determined from the above experiment is around 100 cm^{-1} . Detailed numerical line shape calculations determine a threshold carrier density of about 10^{19} cm^{-3} at room temperature.

The realization of stimulated emission at room temperature at low threshold pumping intensity indicates a high crystalline quality resulting in a low density of nonradiative recombination centers and weak optical absorption due to defects in the layers.

Regarding the high microwave power (200 W) used for the deposition of the GaN-layer these results confirm that the external magnet in on-axis position efficiently removes plasma self biasing effects and the resulting ion damage to a negligible amount. Additionally the layer was deposited at a high growth rate of about $0.3 \mu m/h$ which is one of the highest growth rates for which room temperature stimulated emission has been reported up to now for GaN layers deposited with plasma assisted MBE [6].

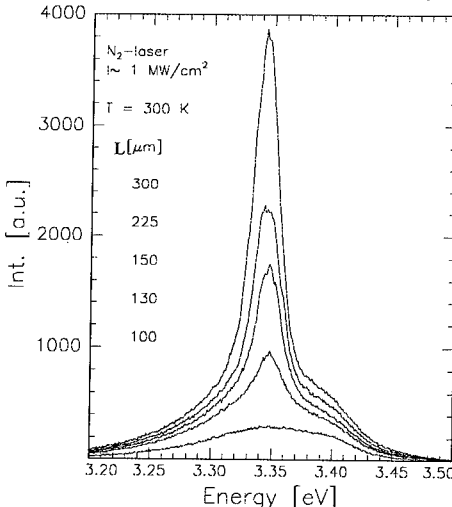


Fig. 5 Optical recombination traces of a GaN layer at RT optically pumped in stripe excitation geometry for different excitation lengths L.

- [1] S. Strite and H. Morkoc 1992, J. Vac. Sci. Technol. B **10**, 1237 and references therein
- [2] S. Nakamura, T. Mukai and M. Senoh 1994, Appl. Phys. Lett. **64**, 1687
- [3] S. Nakamura, M. Senoh, S. Nagahama, N. Iwasa, T. Yamada, T. Matsushita, H. Hiroyuki and Y. Sugimoto 1996, Jpn. J. Appl. Phys. **35**, L217
- [4] A. Ohtani, K.S. Stevens, M. Kinniburgh, R. Beresford 1995, J. of Cryst. Growth, **150**, 902
- [5] K. L. Shalee, R. F. Leheny 1971, Appl. Phys. Lett. **18**, 475
- [6] O. Gluschenkov, J. M. Myoung, K. H. Shim, K. Kim, Z. G. Figen, J. Gao and J. G. Eden 1996, Appl. Phys. Lett. **70**, 811

Optical Metastability in InGaN/GaN Heterostructures

I. K. Shmagin, J. F. Muth, and R. M. Kolbas

Electrical and Computer Engineering Department, North Carolina State University, Raleigh, NC
27695-7911

**R. D. Dupuis, P. A. Grudowski, C. J. Eiting, J. Park, B. S. Shelton, and
D. J. H. Lambert**

Microelectronics Research Center, The University of Texas at Austin, Austin, TX, 78712-1100

Abstract. Optical metastability was studied in an InGaN/GaN single heterostructure. It was observed that an exposure to a high intensity ultraviolet (UV) light temporarily changes the optical properties of the InGaN/GaN epitaxial layer. The photo-induced changes were used to create high contrast optical patterns on the sample at room temperature and 77 K. The photo-induced patterns were viewed under low-intensity illumination with UV light from the same light source.

1. Introduction

Persistent optical and electrical effects have been studied in Nitride based III-V wide band gap semiconductors. Deep levels are responsible for persistent photoconductivity in p- and n-type GaN.[1, 2, 3] Optical metastability in bulk GaN single crystals has been observed [4] and optical memory effects have been seen in GaN epitaxial thin films that have distinct morphological features [5]. Optical data storage was realized in InGaN/GaN single heterostructures.[6] Reconfigurable optical properties were also reported in InGaN/GaN multiple quantum wells.[7] In general persistent effects in the nitride system seem to last much longer than in other semiconductors due to the larger band gap.

2. Experimental Procedure

$\text{In}_x\text{Ga}_{1-x}\text{N}/\text{GaN}$ single heterostructures were grown by low-pressure ($P_{\text{tot}}=76$ Torr) metalorganic chemical vapor deposition (MOCVD) on c-plane sapphire substrates using trimethylgallium, trimethylindium, and ammonia. The structure used in this study consisted of a 60 nm thick undoped $\text{In}_x\text{Ga}_{1-x}\text{N}$ ($x=0.14$) layer deposited on top of a 1.5 μm thick GaN layer. Further details of the growth process can be found elsewhere.[8]

Photoluminescence and transmission spectroscopy were used for optical characterization of the sample. A CW Ar-ion laser and frequency-tripled (280 nm operating wavelength; 250 fs pulse duration) output of a

Ti:sapphire laser were used as the excitation sources for photoluminescence measurements. The measurements were conducted at room (RT) and liquid nitrogen (77 K) temperatures.

To write patterns on the sample the frequency tripled output of the Ti:sapphire laser was focused to a spot approximately 200 μm in diameter. The peak power density was 4 MWatts cm^{-2} . The focused beam was manually translated across the surface of the sample using the X- and Y- micrometer screws on the lens mount. The read out was accomplished by defocusing the laser beam in order to illuminate the entire sample (approximately 3 mm in diameter). The photo-induced patterns were observed under an optical microscope in the defocused laser light. A long-pass dielectric filter with 400 nm cut-off wavelength was used in the eyepiece of the microscope to protect the viewer's eyes from the UV light. The surface of the sample revealed no signs of damage or cracking and was free of morphological features as viewed under the optical microscope.

3. Results and Discussion

The room temperature CW photoluminescence from the InGaN/GaN single heterostructure was centered at 408 nm and had full width at half maximum (FWHM) of 18 nm. The indium composition of the $\text{In}_x\text{Ga}_{1-x}\text{N}$ was calculated to be $x \approx 0.14$ from the photoluminescence data. The 77 K pulsed photoluminescence emission intensity increased and FWHM narrowed down to 3 nm at the input power densities above the threshold. This abrupt increase in the output emission intensity and line narrowing are indicative of the onset of stimulated emission.

It was observed that exposure to the high intensity UV light temporarily changes the photoluminescence properties of the InGaN/GaN single heterostructure. The photoinduced effect can be observed as a change in the color of the output emission under "read" conditions. At room temperature the output emission from the sample looks purple prior to the exposure. When the patterns are written as described above, the written area appears yellowish to the eye. The difference between the colors of output emission between the exposed areas and the unwritten areas of the sample is detected as high-contrast patterns, as shown in Fig. 1. The photograph is reproduced in black and white which enhances the contrast ratio between the written and unwritten areas. The photo-induced lines appear discontinuous because the laser beam was translated across the sample manually. The contrast ratio was found to be dependent on the total fluence deposited on the sample, as was determined by varying the exposure times. No photo-induced patterns or surface damage were observed under incandescent light. No signs of etching were detected on the sample with the written pattern on it under the optical microscope after the sample was submerged in HCl for approximately 30 minutes. After this process the patterns were still observed under UV excitation. The photo-induced patterns were written and read using a CW Ar-ion laser as well.



Fig. 1. The pattern "TEST" was written on the InGaN/GaN SH at room temperature with a focused UV laser source. The writing was made visible by illuminating the entire sample ("read" conditions). The sample completely self-restored after about 4 hours at room temperature.

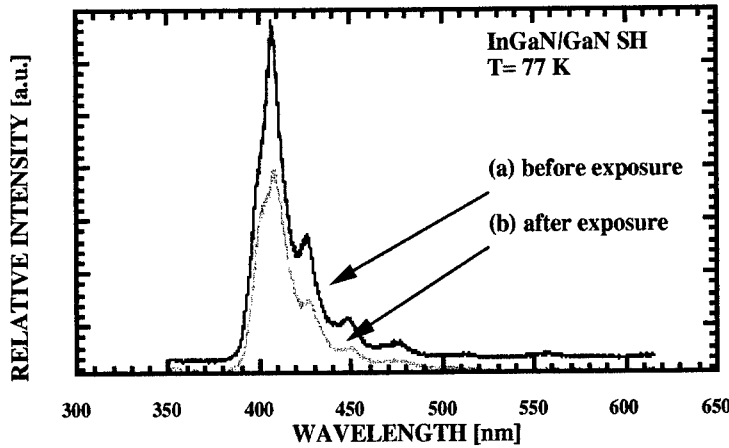


Fig. 2. 77 K photoluminescence spectra before (a) and after (b) the patterns were written. The integrated intensity decreases after the part of the sample was exposed to a high-intensity UV light.

The photo-induced patterns completely self-erased after the sample was left under incandescent light at room temperature. The retention time for the InGaN/GaN single heterostructure was estimated to be approximately 4 hours at room temperature [6]. The retention time appeared to be dependent on the exposure time used to "write" the patterns. A lower total fluence resulted in the weaker contrast lines and shorter retention time, while the higher exposure levels resulted in high contrast patterns that had longer retention times. Preliminary results indicate that the retention time is much longer at 77 K. After the photo-induced patterns disappear information can be rewritten on the same area of the sample as the previous patterns without a change in the efficiency and retention time.

77 K pulsed photoluminescence spectra from the InGaN/GaN single heterostructure before and after patterns were written are shown in Fig. 2 (a) and (b), respectively. The output emission spectrum from the InGaN/GaN single heterostructure prior to writing had a peak position at 407 nm. The long-wavelength shoulder of the spectrum is modulated due to interference effects in the epitaxial layer. After a part of the sample was exposed to the intense UV excitation described as "write" conditions, the integrated output intensity from the sample decreases, as shown in Fig. 2 (b). The change in the emission spectrum is detected by the human operator as a high contrast pattern.

The preliminary data described above is consistent with a creation and/or filling of defects in the InGaN. These defects have a long retention time, which is indicative of a large lattice relaxation mechanism associated with the defects.

References

- [1] Hisch M T, Wolk J A, Walukiewicz W, and Haller E E 1997 *Appl. Phys. Lett.*, **71**, 1098-1100
- [2] Beadie G, Rabinovich W S, Wickenden A E, Koleske D D, Binari S C and Freitas J A Jr., 1997 *Appl. Phys. Lett.*, **71**, 1092-1094
- [3] Qiu C H and Pankove J I, 1997 *Appl. Phys. Lett.* **70**, 1983-1985
- [4] Shmagin I K, Muth J F, Kolbas R M, Balkas C M, Sitar Z and Davis R F, 1997 *Appl. Phys. Letts.*, **71**, 455-457
- [5] Joshkin V A, Roberts J C, Piner E L, Behbehani M K, McIntosh F G and Bedair S M, 1997 *App. Phys. Lett.*, **71**, 234-236
- [6] Shmagin I K, Muth J F, Kolbas R M, Grudowski P A, Eiting C J, Park J, Shelton B S, Lambert D J H, and Dupuis R D, to be published 1997 *Appl. Phys. Lett.*, **71**,
- [7] Shmagin I K, Muth J F, Kolbas R M, Mack M P, Abare A C , Keller S, Coldren L A, Mishra U K, and DenBaars S P, to be published 1997 *Appl. Phys. Lett.*, **71**
- [8] Dupuis R D, Grudowski P A , Eiting C J, Park J, Shelton B S and Lambert D J H, to be published 1997 *ICSC-24*

Carrier Transport Mechanisms in Organic Electroluminescent Devices

Ji-Hai Xu, JUN SHEN, Franky So*, Matthew Kim*, and H.-C. Lee*

Department of Electrical Engineering and Center for Solid-State Electronics Research, Arizona State University
and Phoenix Applied Research Center, Motorola*

Abstract. The current-voltage relationships in organic electroluminescent devices are derived for the following two cases: (i) double-carrier injection trap-charge limited (TCL) regime, and (ii) TCL conduction with internal photodetrapping. Several experimental observations are explained based on our equations. Location of the recombination zone is predicted.

1. Introduction

Electroluminescent (EL) devices based on organic thin films, such Alq, have shown promising properties for low power, flexible, cost-competitive display applications [1-5]. Red, green, and blue light emitting devices are readily available. Devices with luminous efficiency greater than 15 lm/W and lifetime greater than 10,000 hours have been demonstrated. Like its inorganic counterparts, a typical organic electroluminescent device (OED) consists of a hole transport layer, an electron transport layer, and a recombination region. Typically, ITO is used as the hole injection electrode and a low work function metal layer (e.g., Mg) is used as the electron injection electrode. At present, Alq has been most widely used as the EL layer because of its temperature stability and EL efficiency.

The typical current-voltage (J-V) characteristics of an Alq-based OED are shown in Fig. 1. As can be seen, the J-V characteristics exhibit four regions: (a) a linear region ($J \sim V$) at low voltage (<2 V); (b) a $J \sim V^2$ ($I \sim V$); (c) a $J \sim V^{1/2}$ region; and (d) a series-resistance dominated region (J changes toward linear-voltage dependence). Various models have been proposed to explain these characteristics. The main ones are: (a) the thermionic emission model; (b) the Fowler-Nordheim tunneling model; and (c) the trap-charge limited (TCL) model. Models (a) and (b) relate to metal-organic contacts and model (c) relates to the bulk organic layers. In this paper, we will mainly discuss the bulk TCL theories and present results of our study on this subject.

2. Results and Discussions

Typical organic materials used for OED's (e.g. Alq) can be categorized as semiconductors according to their band gap values (~3 eV). On the other hand, it would not be too wrong to label them insulators either, because they have very low carrier mobility (~ 10^{-4} cm²/V.s, or smaller) and large concentrations of traps

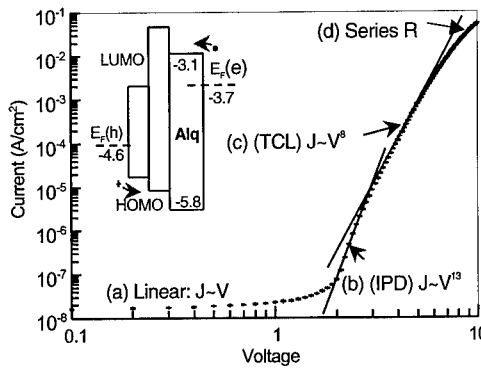


Fig. 1. Typical energy alignments in an Alq-based organic electroluminescent diode. The numerical values represent the currently-believed relative energy positions (in eV) in reference to vacuum of the highest occupied molecular orbital (HOMO), the lowest unoccupied molecular orbital (LUMO), the Fermi levels of hole ($E_f(h)$) and electron ($E_f(e)$) injecting electrodes. The additional layers (unlabeled) besides Alq are the hole injecting and transporting layers.

($\sim 10^{19}$ cm $^{-3}$). Due to the large trap concentration, the current-voltage dependence in organic layers deviates significantly from the linear ohmic form and has been proposed to be trap-charge limited (TCL).

2.1. Double-carrier injection in trap-charge-limited conduction

The single-carrier TCL transport has been extensively studied [6]. With the assumption of an exponential trap energy distribution, the current-voltage characteristics are given by [7]

$$J_{e,h} = e\mu_{e,h} N_{\text{eff}} \left(\frac{\varepsilon}{eH}\right)^l \frac{V_{e,h}^{l+1}}{L_{e,h}^{2l+1}}, \quad (1)$$

where μ is the mobility, N_{eff} is the density of states in the carrier band, ε is the permittivity, H is the total trap density, L is the thickness of the organic layer, and $l = T_c/T$ with T_c being the characteristic temperature of the trap distribution. The subscript e or h denotes the quantity being either for electrons or holes. Such a current-voltage power-law relationship has been observed and confirmed by many experiments.

In the TCL double-carrier injection case, however, a current-voltage expression has not been derived, to the best of our knowledge. Simple single-carrier injection formula J_e [Eq.(1)] has been used so far to approximate the total current [3-5, 8-10]. Because of the fact that the electron mobility (μ_e) is much larger than the hole mobility (μ_h) in the Alq material ($\mu_e \approx (5\pm2) \times 10^{-5}$ cm 2 /V.s [11] and $\mu_h \sim 0.01\mu_e$ [12]), it is commonly believed that the electrons would travel all the way to the interface between Alq and the hole transport layer and recombine with holes in the immediate vicinity (a few monolayers) of that interface. Furthermore, it is also intuitively thought that the double-carrier injection current should be approximately equal to the single-carrier injection current under otherwise the same conditions [3-5, 8-10]. However, experiments often showed that the double-carrier injection current is one to two orders of magnitude larger than the single-carrier injection current [13]. Apparently, a current-voltage expression taking into account of both carriers is needed to properly understand the OED characteristics.

The double-carrier injection problem for a trap-free insulator has been studied first by Parmenter and Ruppel [14]. They have shown that the current can be written in the form

$$J = \varepsilon \mu_{\text{eff}} \frac{V^2}{L^3}, \quad (2)$$

with the effective mobility μ_{eff} being defined by

$$\mu_{\text{eff}} = \frac{4}{9} \mu_0 v_e v_h \left[\frac{(1.5(v_e+v_h)-1)!}{(1.5v_e-1)!(1.5v_h-1)!} \right]^2 \left[\frac{(v_e-1)!(v_h-1)!}{(v_e+v_h-1)!} \right]^3, \quad (3)$$

where $\mu_0 = \varepsilon K/2e$ is called the recombination mobility with K being the recombination rate; $v_e = \mu_e/\mu_0$ and $v_h = \mu_h/\mu_0$. For inorganic solids, we generally have $v_e \gg 1$ and $v_h \gg 1$, and Eq. (3) can then be reduced to $\mu_{\text{eff}} = (2/3)[2\pi\mu_e\mu_h(\mu_e+\mu_h)/\mu_0]^{1/2}$.

Although the current-voltage relationship [Eq. (2)] has the same form as the Child's law [6] in the single-carrier trap-free injection case, the current magnitude can be quite different because of the μ_{eff} prefactor. For most inorganic materials, the electron mobility is much larger than the hole mobility ($\mu_e \gg \mu_h$). Under such a condition, the effective mobility in Eq. (3) is given by $\mu_{\text{eff}} = (2/3)\mu_e[2\pi\mu_h/\mu_0]^{1/2}$ and the current becomes $J_{\text{double}} \sim (\mu_h/\mu_0)^{1/2} J_{\text{single}}$, where $J_{\text{single}} = \varepsilon \mu_e V^2/L^3$ according to the Child's law [6]. If $\mu_h/\mu_0 = 10^4$, we have $J_{\text{double}} \sim 100 J_{\text{single}}$. In the other words, the current in a double-carrier injection device can be much larger than in a single-carrier injection device at the same applied voltage. This result is the direct consequence of relatively large carrier mobility and small recombination rate in the inorganic materials. When electrons and holes are injected from the electrodes, they overlap throughout the sample, partially

cancelling the electric field strength. This is the so called the injected plasma limit [15]. However, for organic materials, such as Alq, the above picture does not apply because the opposite limit is true, namely, $v_e \ll 1$ and $v_h \ll 1$. In this limit, the effective mobility in Eq. (3) becomes $\mu_{\text{eff}} = \mu_e + \mu_h$. For Alq, $\mu_e \gg \mu_h$, so $\mu_{\text{eff}} \approx \mu_e$ according to Eq. (3), *i.e.*, the double-carrier injection current would have the same order of magnitude as the electron-only SCL current. This result, though intuitively straightforward, is inconsistent with the experimental data of OED's which clearly show that the algebraic sum of the electron-only and hole-only SCL currents is much less than the observed current in the two-carrier device [13].

The reason why Parmenter and Ruppel's results can not be used to explain the OED experimental data is that the traps are not included in their theory. With assumptions made possible by the very low mobility in OED's, it is possible to obtain an analytical expression for the double-carrier injection TCL current. We will derive such a solution as follows.

Let us consider the TCL current in an OED. Because of the low mobility, the effective carrier recombination rate is relatively large and the carrier recombination zone is limited to a very thin plane in the device, *i.e.*, the space-charge overlap is very small in this system, in contrast to the injected plasma limit as in most inorganic materials [15]. The recombination zone can then be described using the phenomenological parameters such as voltage drop (V) crossing the thin recombination zone and the thickness (L_r) of this zone. The sum of the segmental thicknesses or voltages should be equal to the respective total values of the organic layer:

$$V = V_e + V_r + V_h, \quad L = L_e + L_r + L_h, \quad (4)$$

where the subscripts e, h, and r stand for electron-, hole-dominated TCL, and recombination regions, respectively. Using Eqs. (1) and (4), the current continuity condition ($J = J_e = J_h$), as well as the constant field approximation [6], we obtain the double-carrier injection TCL current-voltage characteristic in terms of the total thickness (L) and the total voltage drop (V) as:

$$J = eN_{\text{eff}} \left(\frac{\epsilon}{eH} \right)^l (\mu_e^{1/l} + \mu_h^{1/l})^l \frac{(V - V_d)^{l+1}}{(L - L_r)^{2l+1}}, \quad (5)$$

$$L_h = \left(\frac{\mu_h}{\mu_e} \right)^{1/l} L_e. \quad (6)$$

For $V \gg V_d$ and $L \gg L_r$ (typical case in OED's), we have $J \propto V^{l+1}$, which has the same form as in the single-carrier injection case. However, because of the prefactor $\mu_{\text{eff}} = (\mu_e^{1/l} + \mu_h^{1/l})^l$, the current magnitude can again be significantly different from the single-carrier injection case. This result is also in disagreement with the usual belief that $\mu_{\text{eff}} \sim \mu_e + \mu_h$ for organic devices with two separate TCL currents. Compared to the sum of the two single-carrier injection currents, the double-carrier injection current is enhanced by a factor of $[1 + (\mu_h/\mu_e)^{1/l}]^l / (1 + \mu_h/\mu_e)$. For trap-free case ($l = T_c/T = 1$), this factor is unity and there is no current enhancement at all. On the other hand, for an OED with a large density of traps (corresponding to $l \gg 1$), this factor can be very large. For example, with $\mu_h/\mu_e = 0.01$, the enhancement factor is about 35 for $l = 8$ and 132 for $l = 10$, respectively, which explains the larger double-carrier injection currents observed in OED's [13]. This enhancement arises from trap-related effect. It is important to note that even though the ratio (μ_h/μ_e) is much smaller than unity, its $1/l$ -th ($\sim 1/8$) power can not be ignored in evaluating the current.

Another importance of our theory is its ability to predict the location of the recombination zone (Eq. (6)). As mentioned previously, the electrons in Alq are considerably more mobile than holes because $\mu_e \gg \mu_h$. So, one would intuitively expect that it is much harder for holes to move into the bulk of Alq, and the recombination zone will be very close to the hole transporter/Alq interface. However, according to Eq. (6), the location of the recombination zone depends on both l and μ_h/μ_e . For small l and small μ_h/μ_e , the zone is

indeed close to that interface; whereas for very large l , the location of the zone is in the middle of Alq, almost independent on the ratio of μ_h/μ_e . For example, for $l = 8$ and $\mu_h/\mu_e = 0.01$, we have $L_h = 0.56 L_e$ according to Eq. (6). Thus for a 1000 Å-Alq device, the recombination zone is located at about 360 Å away from the hole transporter/Alq interface, *i.e.*, the recombination zone is located significantly inside the bulk of Alq, against the common belief. Again, such a shift of the recombination zone into the bulk organic layer is related to the trapping effect. This new revelation of the intricate differences between double-carrier injection and single-carrier injection processes in the TCL conduction process is very important in designing OED structures. For example, knowing the location of the recombination zone, one can maximize the efficiency or tune the emission spectrum by delta-doping at the zone or other means.

2.2. Internal photo-detrappling

To explain the $J \sim V^{13}$ dependence (region (b) in Fig. 1), we noticed that at the onset of region (b), the OED begins to illuminate. The illumination intensity (I) is almost strictly linear in current (J). The emitted light can in term be re-absorbed internally by the organic layer by releasing trapped carriers. We call this process internal photo-detrappling (IPD). The IPD process can increase the free-to-trapped carrier ratio and thus the current. By assuming $I = \alpha J$, we derived the new J - V expression under IPD condition:

$$J = \left[\frac{\epsilon}{H} (\mu_e + \mu_h) \right]^l N_{eff} \left(\frac{\alpha A(\lambda)}{v\sigma} \right)^{l-1} \frac{(V - V_r)^{2l}}{(L - L_r)^{3l}}, \quad (7)$$

where $A(\lambda)$ is the photodetrapping rate constant, σ is the capture cross section of the trap, v is the carrier thermal velocity. Apparently, region (b) in Fig. 1 can be very well explained by the above result. The transition from (b) to (c) in Fig. 1 is probably due to the light saturation effects observed in insulators [6].

3. Conclusions

We have derived analytical current-voltage relationships for TCL double-carrier injection OED's with or without the IPD process. Special effects on current magnitudes and locations of the recombination zone are discussed.

References

- [1] C. W. Tang and S. A. VanSlyke, *Appl. Phys. Lett.*, **51**, 913 (1987).
- [2] C. W. Tang, S. A. VanSlyke, and C. H. Chen, *J. Appl. Phys.*, **65**, 3610 (1989).
- [3] P. E. Burrows and S. R. Forrest, *Appl. Phys. Lett.*, **64**, 2285 (1993).
- [4] Z. Shen, P.E. Burrows, V. Bulovic, D. Z. Garbuzov, D. M. McCarty, M. E. Thompson, and S. R. Forrest, *Jpn. J. Appl. Phys.*, **35**, L401 (1996).
- [5] P. E. Burrows, Z. Shen, V. Bulovic, D. M. McCarty, S. R. Forrest, J. A. Cronin, and M. E. Thompson, *J. Appl. Phys.*, **79**, 7991 (1996).
- [6] M. A. Lampert and P. Mark, *Current injection in Solids* (Academic, New York, 1970).
- [7] P. Mark and W. Helffrich, *J. Appl. Phys.*, **33**, 205 (1962).
- [8] R.N. Marks, D.D. C. Bradley, R.W. Jackson, P.L. Burns, and A.B. Holmes, *Synthetic Metals* Vol.55-57 (1993) pp.4128-4133
- [9] H. Antoniadis, M. Abkowitz, B.R. Hsieh, S.A. Jenekhe and M. Stolka, *MRS Fall Meeting*, Boston, 1993
- [10] P.W. Blom, M.J. M. de Jong, and J.J. M. Vleggaar, *Appl. Phys. Lett.* vol. 68 (1996) pp. 3308
- [11] C. Hosokawa, H. Tokailin, H. Higashi, and T. Kusumoto, *Appl. Phys. Lett.*, **60**, 1220 (1992).
- [12] R. G. Kepler, P. M. Beeson, S. J. Jacobs, R. A. Anderson, M. B. Sinclair, V. S. Valencia, and P. A. Cahill, *Appl. Phys. Lett.*, **66**, 3618 (1995).
- [13] I. D. Parker, *J. Appl. Phys.* **75**, 1659 (1994).
- [14] R. H. Parmenter and W. Ruppel, *J. Appl. Phys.* **30**, 1548 (1959).
- [15] L. M. Rosenberg and M. A. Lampert, *J. Appl. Phys.*, **41**, 508 (1970).

Monolithic integration of a GaInAs PIN photodiode and AlGaAs/GaAs/AlGaAs HEMTs on GaAs substrate

**W. Bronner, W. Benz, M. Dammann, P. Ganser, N. Grün, V. Hurm, T. Jakobus,
K. Köhler, M. Ludwig, E. Olander**

Fraunhofer-Institut für Angewandte Festkörperphysik, Tullastr. 72, D-79108 Freiburg, Germany

Abstract. A monolithic integrated optoelectronic receiver for a wavelength of $1.55\text{ }\mu\text{m}$ consisting of a GaInAs PIN diode and a transimpedance AlGaAs/GaAs HEMT amplifier has been fabricated. The available technology includes three etch processes, five metal lift-off processes, an oxygen implantation for device isolation, two dielectric layers of SiN and an electroplated gold interconnection layer. The gate levels for enhancement and depletion FETs were carried out using e-beam lithography with gate lengths of $0.3\text{ }\mu\text{m}$. The responsivity of the photodiodes is 0.40 A/W , and the photoreceiver has a -3 dB bandwidth of 6.9 GHz . Clear and open eye diagrams for a 10 Gbit/s optical data stream have been obtained. At this data rate the sensitivity of the photoreceiver is better than -17.5 dBm ($\text{BER}=10^{-9}$). The yield of this circuit is better than 80 \% realized on 2^{nd} wafers.

1. Introduction

Data transmission over long distances requires transmitters and receivers for wavelengths of either 1.3 or $1.55\text{ }\mu\text{m}$. Monolithic integration of such devices results in compactness, and high speed operation. Most detectors reported so far for these wavelengths have been processed on InP substrates. An alternative approach is the use of GaAs substrates and the advantage of a well-established AlGaAs/GaAs HEMT device technology. Recently we reported on the first 10 Gbit/sec long wavelength photoreceiver grown on GaAs, combining AlGaAs/GaAs HEMTs and GaInAs metal semiconductor metal (MSM) photodiodes [1, 2]. We have now successfully integrated InGaAs PIN photodiodes using a similar technology.

2. Technology

2.1 MBE Growth

The vertical structure is grown on a semi-insulating GaAs substrate in a single molecular beam epitaxy run. The structure includes the $\text{Ga}_{0.47}\text{In}_{0.53}\text{As}$ PIN structure on top of the HEMT structure. The layer sequence of the HEMT structure consists of the electron channel δ -doped on both sides in the electrical confinement and the threshold adjustment for enhancement and depletion transistors [3]. Between the HEMT and the PIN structure a 3 nm AlGaAs etch stop layer and a 300 nm GaAs sacrificial layer are grown. These two layers are used to uncover the HEMT structure during the fabrication process by etch techniques. A compositionally graded buffer beginning with $\text{Al}_{0.51}\text{Ga}_{0.49}\text{As}$ and ending with $\text{Al}_{0.48}\text{In}_{0.57}\text{As}$, having a total thickness of 600 nm , was grown to accommodate the lattice mismatch between GaAs and $\text{Ga}_{0.47}\text{In}_{0.53}\text{As}$ [4]. During the buffer growth the effusion cell temperatures of Ga and In are continuously varied while the Al and As fluxes are kept constant. Finally, the PIN structure consisting of 300 nm n-doped $\text{Ga}_{0.47}\text{In}_{0.53}\text{As}$ ($\text{Si}: 5 \times 10^{18}\text{ cm}^{-3}$), an undoped absorption layer of 400 nm

$\text{Ga}_{0.47}\text{In}_{0.53}\text{As}$ and 300 nm p-doped $\text{Ga}_{0.47}\text{In}_{0.53}\text{As}$ ($\text{Be}: 2 \times 10^{19} \text{ cm}^{-3}$) is grown (Figure 1). The heterostructure shows mirror-like optical surface quality. The cross-hatched morphology observed in an interference contrast microscope indicates the existence of misfit dislocations with a two dimensional growth still present [4]. The surface roughness is in the range of 7 to 10 nm. The whole structure for the photodiodes including the buffer layer was designed to be vertically compact and not do exceed a thickness of to 2 μm to avoid problems during further processing with contact lithography. The PIN structure was also grown lattice matched on InP for comparison of the photodiode performance.

2.2 Device Fabrication

Fabrication of the photoreceiver begins with the Ti/Pt/Au metal layer for the p-contacts of the photodiodes. This layer also includes alignment marks for all subsequent process steps. Photodiode mesas are structured in two masking steps using a combination of wet and dry etching techniques. A non selective wet etch solution based on phosphoric acid is first used to reach the n-doped $\text{Ga}_{0.47}\text{In}_{0.53}\text{As}$ layer. This process step requires an exact control of composition and temperature of the solution and also of etching time. With the second mask the same solution is used to remove all the remaining layers of the PIN structure and is interrupted within the GaAs sacrificial layer while a highly selective dry etch stops at the AlGaAs layer on top of the HEMT structure. A Ni/Ge/Au metallization is used as n-contact for the PIN diodes and is processed together with the source and drain regions of the HEMTs. Alloying of the contacts takes place on a hotplate at 400°C for one minute. The devices are isolated from each other by an oxygen implantation. Ti/Pt/Au transistor gates with a length of 0.3 μm are defined by electron beam lithography and are processed using reactive ion etching, metal evaporation, and lift-off technique. Great care has to be taken during the gate recess etch process to protect the PIN mesas against damage at the mesa edge. Further processing includes NiCr thin film resistors, a first interconnection metal (Au), a silicon oxynitride dielectric layer and an electroplated air-bridge layer to interconnect PIN diodes and electronic circuits (Figure 1).

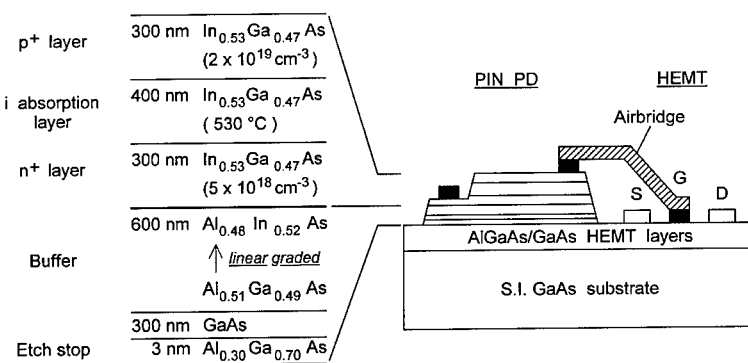


Fig. 1: Schematic drawing of a 1.3 - 1.55 μm wavelength GaInAs PIN photodiode integrated with an AlGaAs/GaAs HEMT. The left part shows the MBE structure of the PIN diode. The integration of the different devices is sketched in the right part of the figure.

MIM capacitors can be realized between these two interconnection metals. The dielectric layer also serves as an anti-reflection coating for the photodiodes. All mask levels with the exception of the gates are processed by optical contact lithography. For the metal layers image reversal resist and lift-off technique is used.

3. Characterization and results

3.1 PIN diodes

The InGaAs photodiodes were characterized by irradiation with light of $1.55\text{ }\mu\text{m}$ wavelength from a calibrated laser diode. Within the saturation region a linear dependence of the photodiode current on the incident power was found. The responsivity is 0.40 A/W at -2 V bias (operating condition of the photoreceiver). The dark current is less than 10 nA and the breakdown voltage is greater than 5 V . The frequency response of the diodes was determined for two light sensitive area diameters: $20\text{ }\mu\text{m}$ and $10\text{ }\mu\text{m}$. The -3 dB bandwidths are 14.9 GHz and greater than 20 GHz , respectively. The respective capacitances are 234 fF and 109 fF , this implies that the photodiodes are limited by the RC time constant of the capacitance and the load resistance. The characteristics of the same photodiodes grown on InP substrate, which have been fabricated for comparison, are nearly identical.

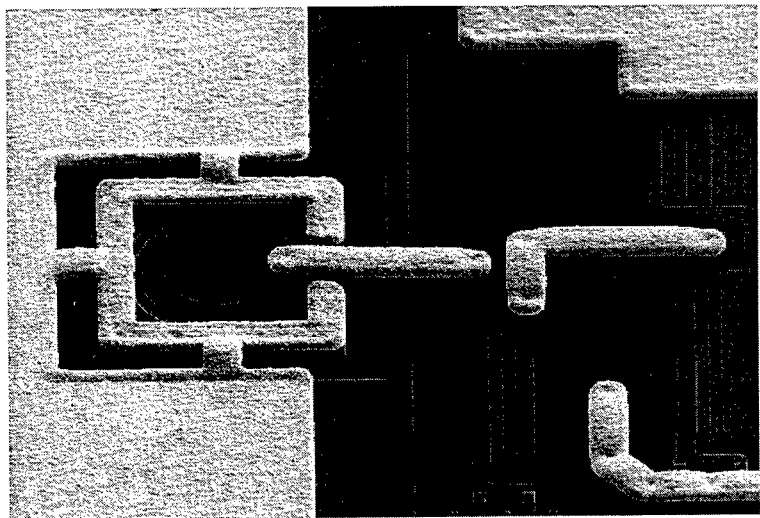


Fig. 2: SEM picture of a monolithically integrated photoreceiver. A PIN diode with $20\text{ }\mu\text{m}$ diameter (left) is shown together with a part of the transimpedance amplifier.

3.2 Photoreceiver

A photoreceiver consisting of a PIN diode, a transimpedance amplifier, a second amplifier stage, and a two-stage differential amplifier was fabricated (figure 2). The chip size is $1.0 \times 1.0\text{ mm}^2$. For the

photoreceiver a -3 dB bandwidth of 6.9 GHz was measured. It is limited by the RC time constant of the photodiode capacitance, the amplifier input capacitance and the feedback resistance within the transimpedance amplifier stage. The response to pulse modulated optical signals was tested by means of a pulse pattern generator. Eye diagrams of the two output voltages show that the photoreceiver operates successfully at a data rate of 10 Gbit/s (see figure 3). The bit error rate as a function of the received optical power leads to a sensitivity of better than -17.5 dBm (BER = 10^{-9}). On all processed 2“ wafers we achieved a yield for this device better than 80 %.

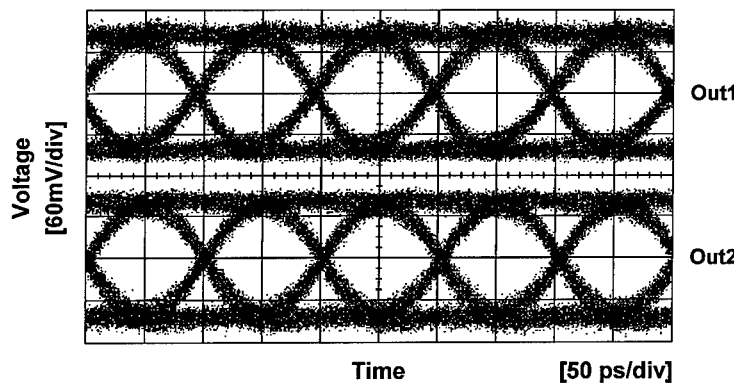


Fig. 3: Eye diagrams of the two photoreceiver output voltages for 10 Gbit/s optical pulse input at a wavelength of 1.55 μ m, (NRZ $2^{15}-1$ pattern length PRBS, optical input power -4 dBm).

4. Conclusion

We have fabricated the first long wavelength PIN-HEMT photoreceiver grown on GaAs operating at a data rate of 10 Gbit/s. Responsivity, dark current and bandwidth are the same for PIN diodes grown on GaAs or on InP substrate. However, the technology described here has more advantages. The use of GaAs substrates allows very easy the transition to larger wafer size of 3“ or 4“. With the quaternary buffer layer the indium content of the absorption structure is variable therefore the PIN structure can be ‘tailored’ for a large range of different wavelengths. The excellent performance and yield of the GaAs-based process offers the possibility to realize optoelectronic integrated circuits with even higher complexity and functionality.

References

- [1] Hurm V, Benz W, Berroth M, Bronner W, Fink T, Haupt M, Köhler K, Ludwig M, Raynor B and Rosenzweig J, 1996 *Electron. Lett.* 32 (4), 391
- [2] Hurm V, Benz W, Berroth M, Bronner W, Fink T, Haupt M, Köhler K, Ludwig M, Raynor B and Rosenzweig J, 1996 *Conf. Proc. IPRM'96*, 435
- [3] Köhler K, Ganser P, Bachem K H, Maier M, Hornung J and Hülsmann A, 1990 *Inst. Phys. Conf. Ser.* 112, 521
- [4] Haupt M, Köhler K, Ganser P, Emminger S, Müller S and Rothmund W, 1996 *Appl. Phys. Lett* 69 (3), 412

Ion Implanted GaAs/InGaAs Lateral Injection Ridge QW Laser for OEICs: Study of Operation Mechanisms

A.A. Tager¹, R. Gaska², I.A. Avrutsky¹, M. Fay¹, H. Chik¹, A. SpringThorpe³, Z. Husain³, J.M. Xu¹, and M. Shur⁴

¹University of Toronto, Dept. of Electrical & Computer Engineering, Toronto, Ontario, M5S 1A4, Canada.

²University of Virginia, Dept. of Electrical Engineering, Charlottesville, VA; currently with APA Optics Inc., MN.

³Nortel Technology, Nepean, Ontario, Canada.

⁴Rensselaer Polytechnic Institute, Dept. Electrical, Computer, and Systems Engineering, Troy, NY.

Abstract. We have fabricated and characterized lateral current injection (LCI) ridge-waveguide lasers with implanted contacts. Comprehensive optical and electrical measurements have been performed over a wide temperature range (10K to 300K) on two sets of lasers with differing ridge widths and active region structures. Several new phenomena unique to the LCI mechanism have been observed and explained, including a positive differential resistance kink at threshold, and an inverse temperature-dependence of quantum efficiency and threshold current at cryogenic values. Electron/hole mobility disparity, local carrier non-pinning above threshold due to photon-assisted carrier diffusion, and intrinsically higher current densities have been experimentally identified as the major factors governing LCI laser characteristics. The results have important implications for optimum LCI laser design and ultimate performance.

The lateral current injection (LCI) laser, with *n* and *p* contacts on the same side of the wafer and current flowing along the quantum wells (QWs), has considerable advantages over more traditional vertical current injection (VCI) devices: it is inherently more suitable for planar OEIC, offers greater integrated electronics compatibility, and frees the vertical dimension for control (e.g. gating) of laser operation and for novel functionalities. However, wider use of LCI lasers has been impeded by their inferior lasing efficiency compared to that of the best VCI lasers, and in part by the technological difficulties associated with double regrowth and/or impurity diffusion processes employed so far for LCI contact formation [1-3]. Our theoretical studies have shown that the ultimate performance of *ion-implanted* ridge LCI lasers, compatible with OEIC technology, can be superior to that of VCI devices, if designed in accordance with the distinct operational physics of LCI devices. However, such a design requires in-depth investigations of the complicated lateral bipolar transport in LCI lasers.

Here, we report on the fabrication and characterization of what we believe is the first working ion-implanted LCI ridge-waveguide laser. We investigated the use of ion implantation for *p*⁺- and *n*⁺-contact region formation, and performed the first comprehensive analysis of a number of operational features (mechanisms) intrinsic and unique to the LCI laser. These include: (i) the disparity in in-plane transport of electrons and holes and the consequences for modal gain, threshold, and quantum efficiency; (ii) the issues of lateral carrier confinement and local non-pinning due to photon-assisted

diffusion; and (iii) the nature and device consequences of high current density (but low current) operation.

The laser structures (Fig.1) were grown on semi-insulating GaAs by MBE. After ridge formation, *n*- and *p*-contacts were formed respectively via implantation of Si and co-implantation of Be and P (with P providing both control of Be diffusion and better QW intermixing). The implants were annealed simultaneously at a temperature optimized for maximum Si activation. Annealing time was chosen to intentionally out-diffuse Be into the active QW region under the ridge, which is a design counter-measure to mobility disparity, suggested by our theoretical studies [4,5].

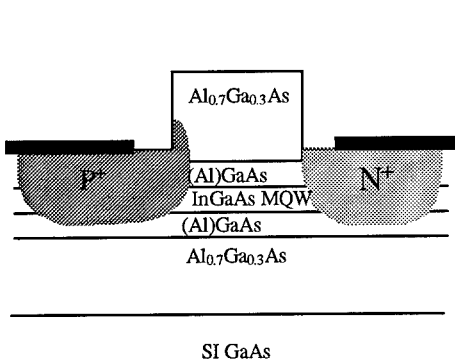


Fig.1 The ridge-waveguide LCI laser design.
Asymmetry in doping profile is due to larger
diffusivity of Be.

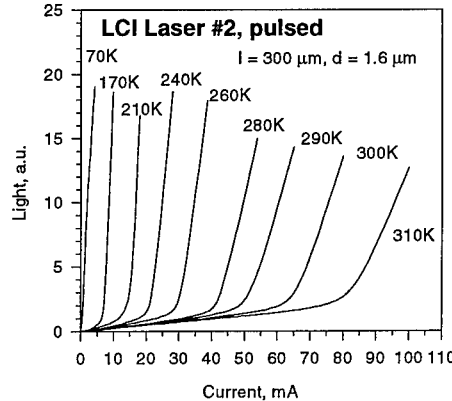


Fig.2 Light-current characteristics of a 2 μm ridge laser

Two structures, with different waveguide-active MQW regions, were grown and processed as described above: the undoped structure LCI#1 employed two 60 \AA In_{0.2}Ga_{0.8}As QWs sandwiched between two 150 \AA GaAs waveguides and separated by a 120 \AA GaAs barrier layer; and structure LCI#2 had a *p*-doped (Be $5 \times 10^{17} \text{ cm}^{-3}$) active region consisting of 3 In_{0.05}Ga_{0.95}As QWs separated by 100 \AA Al_{0.2}Ga_{0.8}As barriers, and sandwiched between two 400 \AA Al_{0.2}Ga_{0.8}As wave-guiding layers. The *p*-doping was intended to provide an additional supply of holes along the active region, in order to partly compensate for lower hole mobility and make the lateral gain profile more uniform.

A set of lasers was fabricated from each wafer, with ridge width *d* ranging from 0.6 to 10 μm for LCI#1; and from 0.6 to 2.6 μm for LCI#2. To probe and quantify lateral transport effects, *L-I* (Fig.2), electrical, spectral and far-field characteristics in cw and pulsed regimes were measured at temperatures from 10K to 310K.

For both laser sets, optimum ridge width was found to be ~1-1.5 μm , with threshold current *J_{th}* increasing for both wider and narrower devices; however, optimum ridge width is likely dependent on the degree of QW intermixing, and hence bandgap broadening, in the contact regions. By measuring the *L-I* slope below threshold as a function of ridge width *d*, we found that the increase in *J_{th}* for narrower devices is caused by decreasing injection efficiency and increasing electron escape to the *p*-contact

region as d becomes smaller than the ambipolar diffusion length ($\sim 1.2 \mu\text{m}$ at 273K for our structures). This leakage was found to be the main cause of quantum efficiency deterioration at high temperatures for both sets of lasers, with much more severe effects for the LCI#1 lasers (Fig.3,4). However, leakage was greatly reduced for the LCI#2 lasers by employing a wide p-doped active region with higher barriers, yielding lasing at temperatures above 300K. In pulsed regime, 300 μm long LCI#2 lasers of ridge-width 1.6 μm at room temperature had a 45 mA threshold. The lasers from both sets suffered from a large contact resistance, which impeded cw lasing at room temperature and must be optimized. At cryogenic temperatures, however, their characteristics (230 μA cw threshold and $\sim 0.3 \text{ W/A/facet}$ slope efficiency for above-mentioned LCI#2 lasers) were comparable to those of the best ridge-waveguide VCI lasers of similar dimensions at the same temperature.

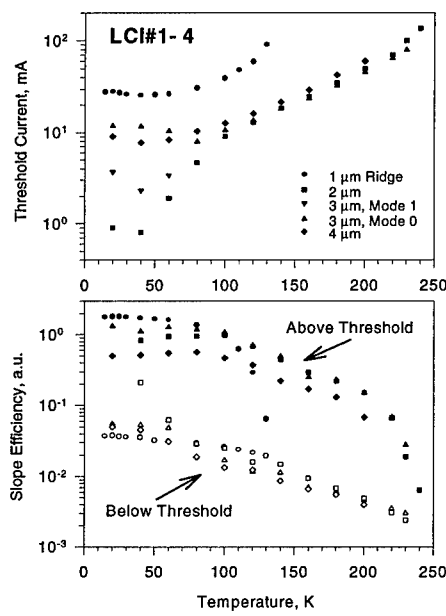


Fig.3 LCI#1 laser threshold current and slope efficiency vs. temperature for different ridge widths.

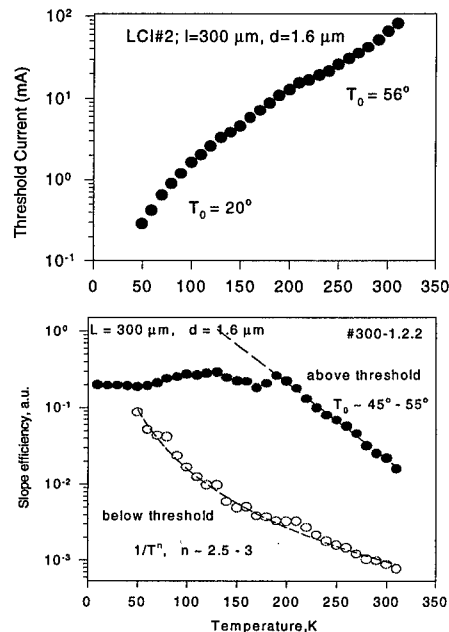


Fig.4 LCI#2 laser threshold current and slope efficiency vs. temperature for different ridge widths.

Investigations over a wide temperature range enable the identification of key factors affecting LCI laser performance which are responsible for reducing external laser quantum efficiency as temperature increases. Behavior was found to differ from that of vertical injection devices in several major aspects, including a positive kink at threshold in dV/dI vs. I (Fig.5) associated with the finite resistance of the active region (as opposed to the negative kink for VCI lasers); first-order mode lasing preceding fundamental mode lasing for wider ridges (Fig.6); rising quantum efficiency and decreasing threshold as

temperature increases for $T < 40\text{-}60\text{K}$ (Fig.4); and fast efficiency roll-off for $T > 200\text{K}$. Moreover, behavior varied qualitatively in different temperature ranges (Fig.3,4): the probable dominant factor at low T ($< 100\text{K}$) is the temperature dependence of diffusion coefficient and mobility, and at high T ($> 200\text{K}$) is electron escape (leakage) from the active region.

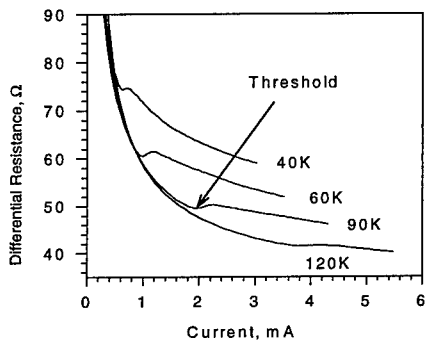


Fig.5 Temperature evolution of the cw electrical characteristics of LCI lasers.

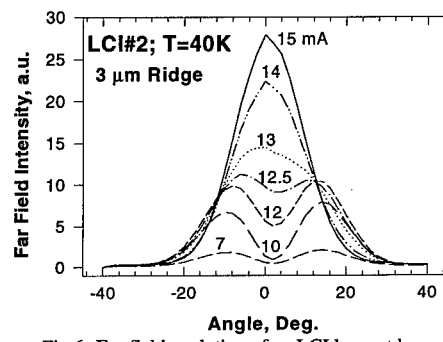


Fig.6 Far-field evolution of an LCI laser at low temperature

Analysis of threshold current and emission efficiency in laser and LD regimes, together with far-field and electrical characteristics, indicate a strong temperature-dependent influence of lateral carrier nonuniformity on laser characteristics, with continuing changes in carrier profile above threshold (local carrier non-pinning effect). These phenomena, together with high operation current density and insufficient lateral carrier confinement, explain the increased carrier leakage found in the LCI lasers. Analysis and comparison with theoretical results show that a thick and narrow active region, high MQW intermixing in the contact regions (or buried LCI structures), and possibly heavier doping of the $p+$ lateral cladding layers are required, in order to overcome the observed negative effects and arrive at an LCI laser competitive in performance with VCI counterparts.

In conclusion, we fabricated two sets of ion implanted LCI lasers with differing active regions and ridge width. The laser structures with higher barriers, better confinement factor and p-doping of active region demonstrated significantly lower current leakage and lased at room temperature. The lasers' threshold and electrical characteristics, together with spectral and far-field results for varying ridge width, are compared with theoretical model predictions. The observed new behaviors have significant implication on optimum LCI laser design and ultimate performance.

References

- [1] Furuya A, Makuchi M, Wada O, and Fujii T 1988 *IEEE J. Quantum Electron.* **24** 2448-2453.
- [2] Kawamura Y, Noguchi Y, and Iwamura H 1993 *Electron. Lett.* **29** 102-104.
- [3] Yang W, Gopinath A, and Hibbs-Brenner M 1995 *IEEE Photon. Technol. Lett.* **7** 848-850.
- [4] Suda D A, Lu H, Makino T, and Xu J M 1995 *IEEE Photon. Technol. Lett.* **7** 1122-1124.
- [5] Sargent E H, Tan G L, and Xu J M 1997 *IEEE J. of Selected Topics on Quantum Electron.*, **3** 507-512.

Avalanche multiplication in sub-micron $\text{Al}_x\text{Ga}_{1-x}\text{As}/\text{GaAs}$ heterostructures

C. K. Chia, J. P. R. David, G. J. Rees, S. A. Plimmer, M. Hopkinson, R. Grey and P. N. Robson.

Dept. of Electronic and Electrical Engineering, Univ. of Sheffield, Mappin street, Sheffield S1 3JD, U.K.

Abstract. The electron and hole multiplication characteristics (M_e and M_h , respectively) in thin ($\sim 0.1\text{-}0.2\text{ }\mu\text{m}$) $\text{Al}_x\text{Ga}_{1-x}\text{As}(500\text{\AA})/\text{GaAs}(500\text{\AA})$ heterostructures, with $0.3 \leq x \leq 0.6$, in a p-i-n configuration have been determined experimentally. At low electric fields, M_e and M_h are very different as they are primarily determined by the ionisation characteristic of the latter half material, in the directions of their transport, due to dead space effects. However as the electric field increases the feedback of the opposite carrier type causes ionisation in the other half of the structure as well. Eventually M_e and M_h become similar and converge to that of the equivalent alloy.

1. Introduction

Heterostructures are now commonly used in Avalanche Photodiodes to enhance the breakdown or to improve the gain bandwidth product [1]. However, to the best of our knowledge, no one has studied carrier transport across a heterointerface at the high electric fields ($F=300\text{-}1000\text{kV/cm}$) in an avalanching device. To investigate this, we have designed a series of single $\text{Al}_x\text{Ga}_{1-x}\text{As}/\text{GaAs}$ heterostructures in a p-i-n configuration and studied the effect of the band edge discontinuity by measuring accurately the carrier multiplication down to very low values.

2. Experiment

The structures were grown by MBE on (001) n^+ GaAs substrates in a p^+in^+ configuration. Two different types of heterostructure were grown. For heterostructure type A, a thin n^+ AlAs etch-stop layer ($0.1\text{-}\mu\text{m}$) was first grown on top of an n^+ GaAs buffer, followed by a $1\text{-}\mu\text{m}$ thick Si doped GaAs n^+ layer. Subsequently, the i-region, consisting of a 500\AA GaAs and a 500\AA $\text{Al}_x\text{Ga}_{1-x}\text{As}$ undoped layer were grown. The growth was completed by a $1\text{-}\mu\text{m}$ thick Be doped $\text{Al}_x\text{Ga}_{1-x}\text{As}$ p^+ cladding layer capped by a 100\AA p^+ GaAs contact layer. Heterostructure type B was the complimentary layer to type A, i.e., after the $0.1\text{-}\mu\text{m}$ AlAs etch-stop layer, a $1\text{-}\mu\text{m}$ thick $\text{Al}_x\text{Ga}_{1-x}\text{As}$ n^+ cladding layer was grown, followed by the 500\AA $\text{Al}_x\text{Ga}_{1-x}\text{As}$ and the 500\AA GaAs undoped layers, and finally a $1\text{-}\mu\text{m}$ thick GaAs p^+ top contact layer. Three pairs of such structures were grown with Al content of 0.30, 0.45 and 0.60, allowing us to investigate the effect of electron transport across a direct and indirect $\text{Al}_x\text{Ga}_{1-x}\text{As-GaAs}$ interface. The exact Al composition for each layer was determined from high resolution X-ray rocking curves, obtained using a double crystal diffractometer. The thicknesses of the $\text{Al}_x\text{Ga}_{1-x}\text{As}$ and GaAs heterostructure layers were obtained by fitting to the pendellösung fringes of the rocking curves using a commercial program. These results were then used to estimated the thicknesses of the undoped $\text{Al}_x\text{Ga}_{1-x}\text{As}$ and GaAs regions from the growth times.

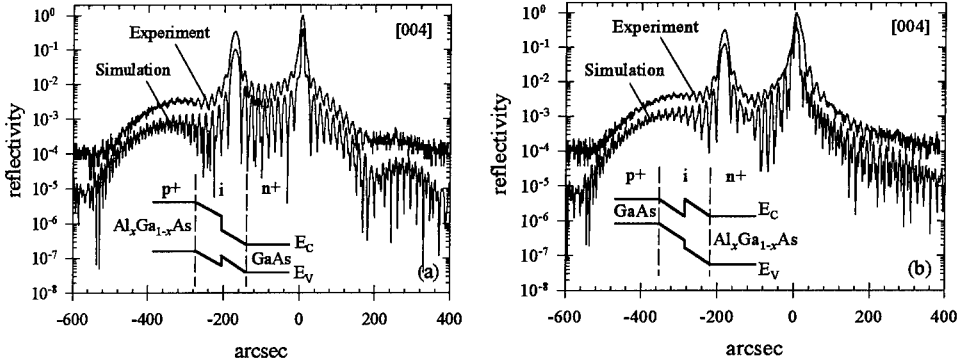


Figure 1. Simulated X-ray rocking curves fitted to experimental results. The Al compositions were (a) 45%, (b) 47%. Inset shows the (a) type A, (b) type B band structure.

Fig. 1 shows the typical rocking curves of the Al-45% heterostructures; the estimated undoped $\text{Al}_x\text{Ga}_{1-x}\text{As}$ and GaAs layer thicknesses are shown in Table 1. Circular mesa diodes of radius 50 μm , 100 μm and 200 μm with top annular contacts, for optical access, were then fabricated using conventional photolithography techniques. Capacitance-voltage profiles were obtained using a Hewlett-Packard 4275A multi-frequency LCR meter. The doping values and i-region thickness were then deduced using a carrier transport model incorporating Fermi-Dirac statistics as a simulation tool. Good agreement was found for the w determined using X-ray and C-V techniques. A summary of the parameters obtained from these techniques is listed in Table 1.

The electron and hole photomultiplication characteristics (M_e and M_h respectively) as a function of electric field were obtained using the technique described by Stillman and Wolfe [2]. A 442nm He-Cd laser was focused to a fine spot via a microscope lens onto the top p⁺ cladding layer of the mesa diode. The short wavelength used results in near total absorption of the light in the $\text{Al}_x\text{Ga}_{1-x}\text{As}$ p⁺ layer and minority carrier photo-electrons diffuse toward the high field region resulting in pure electron injection. The incident laser is modulated by an optical chopper and the resulting photocurrent is measured using a phase sensitive lock-in amplifier.

Table 1. Summary of relevant parameters determined from X-ray and C-V measurements.

Layers	X-ray			C-V			
	Al content x	Al _x intrinsic	GaAs intrinsic	p $/\text{cm}^{-3}$	n $/\text{cm}^{-3}$	i $/\text{cm}^{-3}$	w
Al30%/GaAs *	0.285	480 \AA	495 \AA	1.5×10^{18}	1.7×10^{18}	1.0×10^{15}	1016 \AA
Al45%/GaAs *	0.450	520 \AA	500 \AA	1.8×10^{18}	1.9×10^{18}	1.0×10^{17}	1026 \AA
Al60%/GaAs *	0.600	548 \AA	500 \AA	1.3×10^{18}	2.1×10^{18}	1.0×10^{17}	1080 \AA
GaAs/Al30%**	0.290	452 \AA	500 \AA	1.5×10^{18}	1.6×10^{18}	1.0×10^{15}	997 \AA
GaAs/Al45%**	0.470	490 \AA	505 \AA	1.9×10^{18}	1.6×10^{18}	1.7×10^{15}	1075 \AA
GaAs/Al60%**	0.640	524 \AA	429 \AA	1.8×10^{18}	1.9×10^{18}	1.6×10^{15}	1052 \AA
GaAs ***	-	-	-	1.4×10^{18}	1.1×10^{18}	1.0×10^{15}	1044 \AA
Al 30% ***	0.310	-	-	2.0×10^{18}	2.5×10^{18}	1.0×10^{15}	1060 \AA
Al 60% ***	0.610	-	-	2.7×10^{18}	2.8×10^{18}	1.0×10^{15}	880 \AA

* Heterostructure type A ** Heterostructure type B *** Homostructures

For heterostructures type A with a top $\text{Al}_x\text{Ga}_{1-x}\text{As}$ cladding layer, top illumination with an 820nm semiconductor laser penetrates to the n^+ GaAs layer and gives nearly pure hole injection into the high field region from the 1- μm n^+ GaAs layer. Although there will be some absorption in the 500 \AA GaAs intrinsic region, resulting in mixed injection, we estimate that it represents only 5% of the total absorption length (1- μm) and most of the carriers causing the primary photocurrent will be holes. To confirm this, via holes were selectively etched onto the back of the type A $\text{Al}_{0.3}\text{Ga}_{0.7}\text{As}/\text{GaAs}$ heterostructure devices and pure hole injection was effected by illuminating the n^+ GaAs layer with the 442nm laser. Identical M_h characteristics were obtained. M_h values for the other two type A heterostructures were therefore obtained more simply and reliably by top illuminating the devices with the 820nm laser. For type B heterostructures, only M_e could be obtained by top illumination since the p^+ absorption layer was GaAs.

3. Results and discussion

To help interpret the results obtained from the heterostructures, photomultiplication measurements were also undertaken on a series of $\text{Al}_x\text{Ga}_{1-x}\text{As}$ homojunction p-i-n's with 'i' regions $w=0.1\text{-}\mu\text{m}$ and Al content of 0, 0.30 and 0.60. M_e was found to be only slightly larger than M_h in these structures. Fig.2 shows M_e and M_h as a function of electric field for the $\text{Al}_x\text{Ga}_{1-x}\text{As}/\text{GaAs}$ heterostructures plotted on a $\ln(M-1)$ axis.

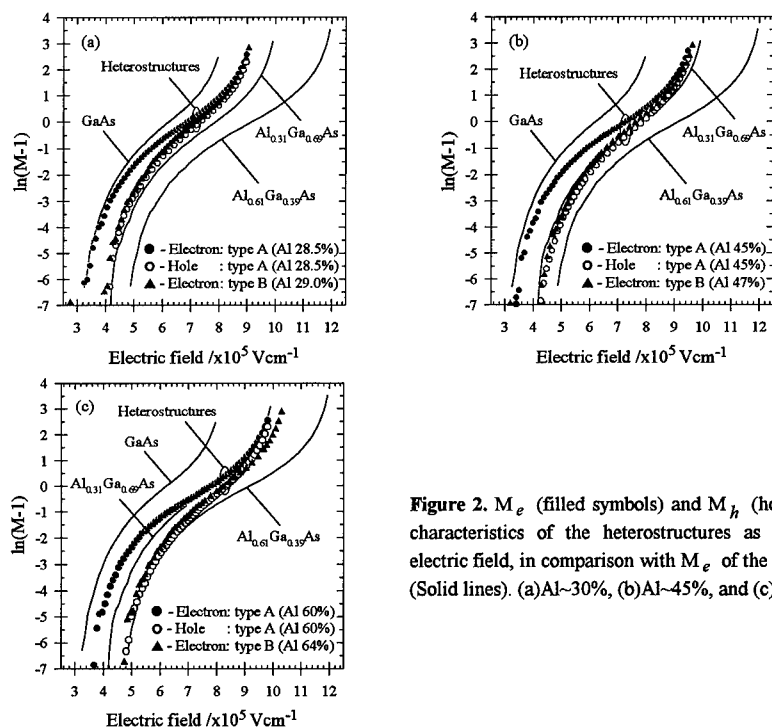


Figure 2. M_e (filled symbols) and M_h (hollow symbols) characteristics of the heterostructures as a function of electric field, in comparison with M_e of the homojunctions (Solid lines). (a) Al~30%, (b) Al~45%, and (c) Al~60%

M_e from similar 0.1- μm dimension $\text{Al}_x\text{Ga}_{1-x}\text{As}$ homojunction p-i-n structures are also plotted for comparison. The results from all the type A heterostructures show that at low fields, M_e (in which injected electrons pass from $\text{Al}_x\text{Ga}_{1-x}\text{As}$ to GaAs) is similar to that of the GaAs homojunction structure. Conversely, M_h (in which injected holes pass from GaAs to $\text{Al}_x\text{Ga}_{1-x}\text{As}$) is similar to that of the $\text{Al}_x\text{Ga}_{1-x}\text{As}$ homojunction structure. As the electric field increases however, M_e and M_h both diverge from these homojunction characteristics and converge towards those of the equivalent average alloy for the active region. This suggests that at low electric fields the dead space (the mean distance carriers need to attain the ionisation threshold energy) is very significant in these thin structures and M_e and M_h are very different as they are primarily determined by the ionisation properties of the latter half material in the directions of their transport in the high field region. However as the electric field increases the feedback of the opposite carrier type causes ionisation in the other half of the structure as well, eventually M_e and M_h become similar near breakdown, converging to the values measured in devices with the equivalent alloy composition in the 'i'-region. M_e obtained from the type B structures is found similar to M_h obtained from the type A structures for all electric fields up to breakdown. The M_e characteristic for the type B $\text{Al}_{0.64}\text{Ga}_{0.36}\text{As}/\text{GaAs}$ structure, shown in Fig. 2(c), breaks down at a slightly higher electric field than the type A $\text{Al}_{0.60}\text{Ga}_{0.40}\text{As}/\text{GaAs}$ structure due to the higher average Al composition in the former.

Any enhancement of electron ionisation due to the conduction band edge discontinuity at the interface should manifest itself as an increase in M_e in the type A heterostructures. However our measurements show that M_e in these type A structures never exceed M_e of homojunction GaAs at any electric field. This suggests that the conduction band edge discontinuity contributes very little to the ionisation process. One of the possible reasons is that the higher phonon scattering rate in the first 500 \AA $\text{Al}_x\text{Ga}_{1-x}\text{As}$ layer compensates for the excess energy gained from the conduction band edge discontinuity and consequently no advantage is obtained. Conversely in the type B heterostructures, any advantage in electrons gaining energy more rapidly (relative to the $\text{Al}_x\text{Ga}_{1-x}\text{As}$) in the first 500 \AA GaAs is compensated by the energy they lost in surmounting the potential barrier at the interface.

4. Conclusions

No evidence shows that the conduction band edge discontinuity enhances the electron ionisation or multiplication process in these heterostructures because M_e in the type A heterostructures never exceeds M_e of homojunction GaAs at any electric field. At low electric fields, M_e in these heterostructures shows homojunction like behaviour while at high fields M_e converges to that of the equivalent alloy of the i-region. For the active region thicknesses and fields used in these experiments, there is no evidence to suggest that any significant difference between the electron and hole ionisation coefficients can be engineered in a periodic $\text{Al}_x\text{Ga}_{1-x}\text{As}/\text{GaAs}$ structure.

References

- [1] Kagawa T, Asai H and Kawamura Y 1991 *IEEE Photonics Technology Lett.* 3 815-817
- [2] Stillman G E and Wolfe C M 1977 *Semiconductors and Semimetals* (New York: Academic)

MBE Growth of Near-Infrared InGaAs Photodetectors with Carbon Tetrabromide as a p-Type Dopant

D. I. Lubyshev, J. Neal, W. Z. Cai, M. Micovic, T. S. Mayer, and D. L. Miller
 Electronic Materials and Processing Research Laboratory, Department of Electrical Engineering,
 The Pennsylvania State University, University Park, PA 16802

Abstract: The carbon doping of $In_xGa_{1-x}As$ was systematically studied as a function of carbon tetrabromide flux and indium molar fraction. The efficiency of carbon incorporation in InGaAs lattice matched with InP was the same as GaAs and showed a maximum attainable doping level of $2 \times 10^{20} \text{ cm}^{-3}$. The increase of indium molar fraction showed autocompensation and a switch of conductivity from p-to-n-type, at an In molar fraction of 80%. $In_{0.75}Ga_{0.25}As$ photodetectors were fabricated using carbon as a dopant. The figures of merit of the p-i-n photodetectors showed parameters close to those of beryllium doped devices. CBr_4 can be used as an effective p-type doping precursor in solid-source Molecular Beam Epitaxy in $In_xGa_{1-x}As$ with indium molar fraction up to 80%.

1. Introduction

Increasingly, carbon is being used to replace beryllium and zinc as a p-type dopant in gallium arsenide (GaAs) and indium gallium arsenide (InGaAs) based devices because of its low diffusivity at high doping levels [1-4]. For example, the use of carbon as the p-type base dopant in AlGaAs/GaAs and lattice-matched InAlAs/InGaAs heterojunction bipolar transistors (HBTs) has resulted in devices with excellent dc and rf performance and improved reliability [5]. Despite potential reliability advantages, carbon has not been used as a p-type dopant in $In_xGa_{1-x}As$ -based devices with $x \geq 0.53$ due to its amphoteric nature and reduced incorporation efficiency at high indium molar fractions [6,7]. Additional difficulties associated with the use of carbon in InGaAs arise from a reduction in free carrier concentration due to hydrogen passivation of carbon acceptors in metalorganic molecular beam epitaxy (MOMBE) [8], and a growth rate reduction and compositional variation due to preferential removal of indium atoms from the growth surface during carbon doping with carbon tetrabromide (CBr_4) and carbon tetrachloride (CCl_4) in chemical beam epitaxy (CBE) and MOMBE [9-13].

In this paper, we study the incorporation of carbon in InGaAs using a conventional solid source molecular beam epitaxy (MBE) system with CBr_4 as a dopant source. The dependence of the carrier concentration on CBr_4 flux was determined, and its effects on the growth mechanism and surface morphology were observed. The doping efficiency and amphoteric behavior of carbon was investigated as a function of indium molar fraction in $In_xGa_{1-x}As$ for $0.53 \leq x \leq 1$. To determine the effectiveness of using CBr_4 in device applications with indium molar fraction exceeding $x = 0.53$, lattice-mismatched $In_{0.75}Ga_{0.25}As$ photodetectors grown on an InP substrate using carbon and beryllium as a p-type dopant were compared.

2. Experimental Procedure

The incorporation of carbon in InGaAs was investigated by growing a series of samples with 5000 Å $In_xGa_{1-x}As$ ($0.53 \leq x \leq 1$) layers doped using CBr_4 . All of the epitaxial layers were grown in a Varian GEN II MBE system on (100) InP substrates that were mounted using indium on a molybdenum substrate holder. The CBr_4 vapor was delivered into the MBE system through a gas injector mounted on one of the cell ports, as reported previously[14]. The flux was varied with a leak valve placed between CBr_4 bottle and the gas injector. A run-vent configuration was used to reduce the transients in the CBr_4 flux. Because monitoring CBr_4 flux with the beam flux monitor in the MBE chamber is complicated by the high background arsenic pressure, the vent ion pump current values were used to set the CBr_4 flux. During the growth of the epilayers, the substrate temperature was maintained at 460°C as measured by an

optical pyrometer. The growth rate of the InGaAs was 0.8 $\mu\text{m}/\text{hour}$, which was calibrated using reflection high-energy electron diffraction (RHEED) intensity oscillations. To obtain the most efficient carbon incorporation, the minimum III/V ratio required to maintain a (2×4) arsenic-stabilized structure was used. The molar fraction of the ternary InGaAs alloy was established using RHEED oscillations and later confirmed by double crystal x-ray diffraction measurements. Free carrier concentration and Hall mobility in the epitaxial layers were evaluated by Van der Pauw measurements.

The effectiveness of using CBr_4 as a p-type dopant in $\text{In}_{x}\text{Ga}_{1-x}\text{As}$ -based devices with $x > 0.53$ was investigated by comparing the optical and electrical performance of $\text{In}_{0.73}\text{Ga}_{0.27}\text{As}$ p-i-n photodetectors grown using carbon and beryllium. The structure for both photodetectors included an n^+ -buffer layer, a 1 μm undoped $\text{In}_{0.73}\text{Ga}_{0.27}\text{As}$ active region, and a 150 nm p^+ -cap layer as shown in Fig. 1. The growth of the buffer layers for all samples was initiated by depositing 300 nm of lattice-matched $n^+\text{-In}_{0.52}\text{Al}_{0.48}\text{As}$ followed by 200 nm of lattice-matched $n^+\text{-In}_{0.53}\text{Ga}_{0.47}\text{As}$ on an InP substrate at a substrate temperature of 490°C. After the growth of the lattice matched layer, the substrate temperature was reduced to 400°C, and a n^+ -linearly graded buffer layer (LGLB) was deposited. The indium composition in the LGLB was increased from 53% to 73% in a series of 50 steps over a thickness of 1.0 μm [15]. The LGLB was then capped with three sets of five-period 10 nm $\text{In}_{0.73}\text{Ga}_{0.27}\text{As} / 10 \text{ nm } \text{In}_{0.73}\text{Al}_{0.27}\text{As}$ superlattices with 80 nm $\text{In}_{0.73}\text{Ga}_{0.27}\text{As}$ layers separating the superlattices. After the final $\text{In}_{0.73}\text{Al}_{0.27}\text{As}$ layer of the last two superlattices were deposited, the Ga and In shutters were closed and the substrate temperature was raised to 510°C for 20 minute in-situ anneals of the graded buffer layer [16]. Prior to the growth of the p-i-n active region, the substrate temperature was lowered to 450°C. The active region of the photodetector consisted of a 1.0 μm unintentionally doped $\text{In}_{0.73}\text{Ga}_{0.27}\text{As}$ absorption layer, a 50 nm $p^-\text{-In}_{0.73}\text{Ga}_{0.27}\text{As}$ layer, a 50 nm $p^-\text{-In}_{0.73}\text{Al}_{0.27}\text{As}$ window layer, and a 50 nm $p^-\text{-In}_{0.73}\text{Ga}_{0.27}\text{As}$ contact layer.

Photodetectors with active areas ranging from $50 \times 50 \mu\text{m}^2$ to $300 \times 300 \mu\text{m}^2$ were fabricated for room temperature spectral response and dark I-V measurements. Because the samples were grown using an indium mount, the backside $n^+\text{-InP}$ ohmic contacts were formed with alloyed indium. Mesas were defined by photolithography and were etched to the undoped active layer using a 1:2:40 $\text{H}_3\text{PO}_4:\text{H}_2\text{O}_2:\text{H}_2\text{O}$ solution. Ti/Pt/Au contacts were deposited on the top of the mesa structure by electron-beam evaporation and lift-off. A layer of polyimide served as an interlayer dielectric, and Ti/Au bonding pads were formed using thermal evaporation and lift-off. Devices were placed in TE9 packages for optical and electrical characterization.

3. Experimental Results

The dependence of $\text{In}_{0.53}\text{Ga}_{0.47}\text{As}$ carrier concentration on CBr_4 flux in comparison with GaAs is shown in Fig. 2. These data demonstrate that the efficiency of carbon incorporation is directly proportional to the CBr_4 flux. A maximum doping level of approximately $2 \times 10^{20} \text{ cm}^{-3}$ was obtained, which was limited by the conductance of the leak valve. This doping level in $\text{In}_{0.53}\text{Ga}_{0.47}\text{As}$ is approximately two times higher than previously reported for this material grown by MBE [14].

To investigate the CBr_4 etching effect on surface morphology and ternary alloy composition, GaAs and InAs was grown using high CBr_4 fluxes at substrate temperatures of 600°C and 460°C, respectively. CBr_4 affected the growth mechanism of both GaAs and InAs at doping levels higher than $6 \times 10^{19} \text{ cm}^{-3}$. The shape of the RHEED shown in Fig. 3 (a) is evidence of a transition from a 2-D to a multi-level growth mode. The reduced stripe length on the RHEED pattern is indicative of surface roughening on the atomic scale. At the CBr_4 flux corresponding to doping density of $2 \times 10^{20} \text{ cm}^{-3}$, a 3% reduction of growth rate was observed for both GaAs and InAs. When the substrate temperature was reduced to 520°C, RHEED oscillations due to CBr_4 etching of GaAs were observed as shown in Fig. 3 (b). The fact that growth rate reduction was the same for both GaAs and InAs suggests that there should not be a compositional change in InGaAs due to preferential removal of In atoms. The etching which we

Layer	Material	Doping (cm^{-3})	Thickness (nm)
p ⁺ -Contact	In _{0.73} Ga _{0.27} As:(C or Be)	5×10^{18}	50
p ⁺ -Window	In _{0.73} Al _{0.27} As:(C or Be)	5×10^{18}	50
p ⁺ -Active	In _{0.73} Ga _{0.27} As:(C or Be)	5×10^{17}	50
i-Absorption	In _{0.73} Ga _{0.27} As	Undoped	1000
20 minute, 510°C Anneal			
n ⁺ -Buffer	In _{0.73} Ga _{0.27} As:Si	5×10^{17}	80
n ⁺ -Buffer	In _{0.73} Al _{0.27} As:Si	5×10^{17}	10
n ⁺ -Buffer	In _{0.73} Ga _{0.27} As:Si	5×10^{17}	10
Linearly Graded Buffer	In _x Ga _{1-x} As:Si ($0.53 < x < 0.73$)	5×10^{18}	1000
Lattice Matched Buffer	In _{0.53} Ga _{0.47} As:Si	5×10^{18}	300
n ⁺ -Substrate	InP:S	$2-5 \times 10^{18}$	

$3 \times \left\{ \begin{array}{l} \text{n}^+ - \text{Buffer} \\ \text{n}^+ - \text{Buffer} \\ \text{n}^+ - \text{Buffer} \end{array} \right. \quad \left. \begin{array}{l} \text{Linearly Graded} \\ \text{Buffer} \\ \text{Lattice Matched} \\ \text{Buffer} \end{array} \right\} \quad 5 \times \left. \begin{array}{l} \text{n}^+ - \text{Substrate} \end{array} \right.$

Fig. 1. Lattice-mismatched In_{0.73}Ga_{0.27}As p-i-n device structure grown by MBE with carbon and beryllium as p-type dopants.

observed was considerably less than what was observed in MOMBE [11-13], probably because solid-source MBE requires a lower total flux of CBr₄ for given doping density.

The dependence of free carrier concentration in In_xGa_{1-x}As layers as a function of indium molar fraction is shown in Fig. 4. The hole concentration was constant ($p = 6 \times 10^{18} \text{ cm}^{-3}$) for In molar fractions from $x = 0.53$ to 0.7 and then decreased dramatically to $p = 6 \times 10^{17} \text{ cm}^{-3}$ for $x = 0.8$. The layers with $x = 0.9$ and 1.0 demonstrate n-type conductivity with electron concentration and mobility of $5 \times 10^{16} \text{ cm}^{-3}$ and $2500 \text{ cm}^2/\text{V}\cdot\text{s}$. This dependence is qualitatively similar to that observed in CBE and MOMBE[17,18], where p-to-n conversion was observed at $x = 0.3$ and 0.8, respectively. The increase of maximum indium molar fraction for p-n conversion in our case can be attributed to the coherent surface kinetic process in MBE by comparison to CBE and MOMBE. This verifies that carbon introduced from CBr₄ can be used as an effective p-type dopant in MBE growth of In_xGa_{1-x}As with molar fractions exceeding $x = 0.7$.

4. Device Characterization

Double crystal x-ray diffraction was performed on the as-grown material to verify the In composition and the lattice relaxation of the In_{0.73}Ga_{0.27}As active layers. Photodetectors fabricated from these materials had cutoff wavelengths of approximately 2.25 μm , which is consistent with the indium composition determined from the x-ray diffraction data. The maximum response that was obtained at a wavelength of 1.9 μm was 0.75 A/W, which was limited by the thin 1 μm absorption region.

The room temperature dark current as a function of voltage is shown in Fig. 5 for typical mesa-isolated photodetectors fabricated on samples that used carbon and beryllium as a p-type dopant. Typical room temperature dark current densities at a 1 V reverse bias were 7 mA/cm² and 4 mA/cm² for the carbon and beryllium doped devices. Although the low-bias dark current of the carbon doped devices is a factor of two higher than that of the beryllium doped devices, both values of dark current are comparable to commercially available photodetectors of this indium composition processed using a planar process. Such small differences in dark current are consistent with the sample-to-sample variations we

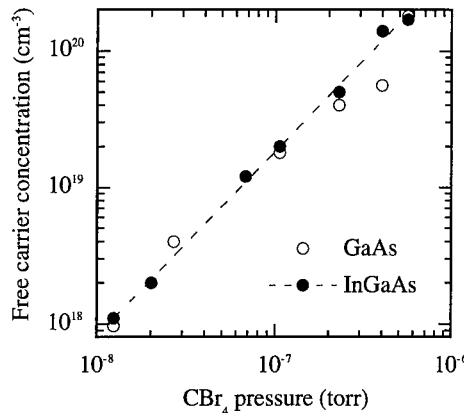


Fig. 2. Hole Concentration in In_{0.53}Ga_{0.47}As as a function of CBr₄ flux.

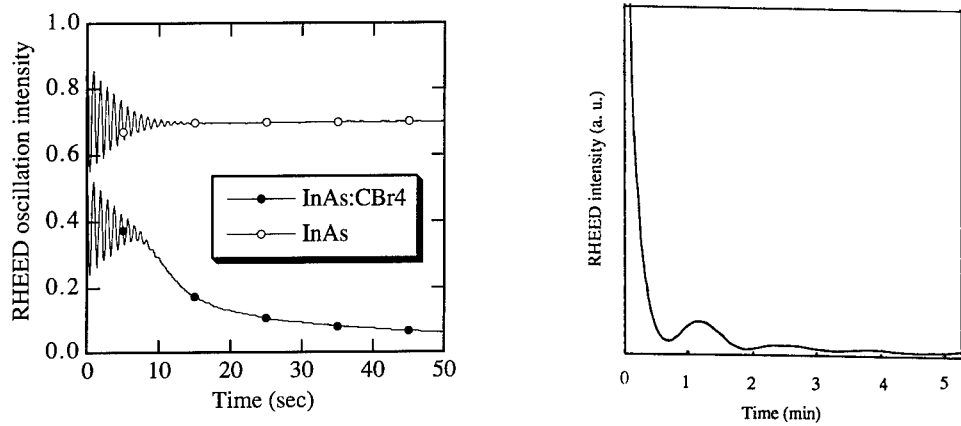


Fig. 3 RHEED intensity oscillation (a) during the growth of InAs with and without CBr_4 flux (b) from a GaAs surface being etched under CBr_4 flux.

have seen using beryllium. At larger reverse biases, the dark current of both samples is reduced substantially over earlier reports [15] due to the use of an in-situ anneal following the growth of the compositionally graded buffer layer. It has been demonstrated previously that the dark currents of samples that contain an in-situ anneal show a large reduction in the generation current at low biases and a delay in the onset of tunneling at high biases [19].

Additional photodetector figures of merit including the shunt impedance area product (R_0A) and the reverse breakdown voltage were also measured. The slope of the room temperature dark current-voltage (I-V) characteristics for voltages between -5 mV and $+5$ mV was used to determine values of the R_0A for these devices. Typical values of R_0A on the carbon and beryllium samples were 25 and $28 \Omega\text{-cm}^2$. Finally, the reverse breakdown voltage, which was defined as the voltage corresponding to a reverse current of 1 mA, of the carbon and beryllium photodetectors were 20 and 21 V. These results demonstrate that carbon can be used as an efficient replacement for beryllium in $\text{In}_x\text{Ga}_{1-x}\text{As}$ -based devices with $x < 0.8$.

6. Conclusions

In this paper, we investigated the incorporation of carbon in InGaAs using a conventional solid source MBE with CBr_4 as a p-type dopant. Lattice-mismatched $\text{In}_{0.73}\text{Ga}_{0.27}\text{As}$ photodetectors grown using carbon and beryllium as a p-type dopant were compared to determine the effectiveness of using CBr_4 in device applications were $x > 0.53$. We established that free carrier concentration in InGaAs is directly proportional to the CBr_4 flux over the concentration range ($10^{18} - 2 \times 10^{20} \text{ cm}^{-3}$) that was studied. A growth rate reduction of 3% was measured by RHEED oscillations on both GaAs and InAs at doping level of $2 \times 10^{20} \text{ cm}^{-3}$, which suggests that there will not be a compositional change in the ternary alloy when doping with CBr_4 . The free carrier concentration dependence on In molar fraction for $\text{In}_x\text{Ga}_{1-x}\text{As}$ ($x = 0.53 - 1.0$) grown on the (100) InP surface shows that CBr_4 -derived carbon can be used as an effective acceptor for $x < 0.8$ in solid source MBE. Electrically, the p-i-n $\text{In}_{0.73}\text{Ga}_{0.27}\text{As}$ photodetectors fabricated using carbon and beryllium had similar characteristics. The typical room temperature dark current density at a 1 V reverse bias for the carbon doped photodetectors was 7 mA/cm^2 , which is

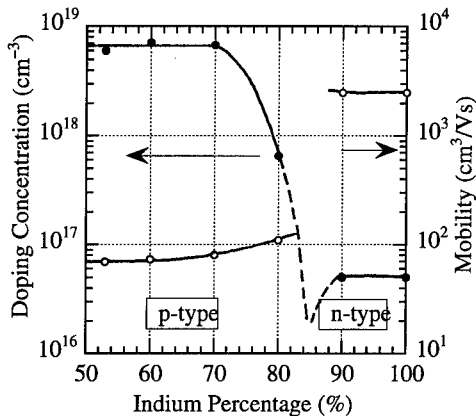


Fig. 4. Indium molar fraction dependence of carbon carrier concentration in $\text{In}_x\text{Ga}_{1-x}\text{As}$ grown on (100) InP substrates.

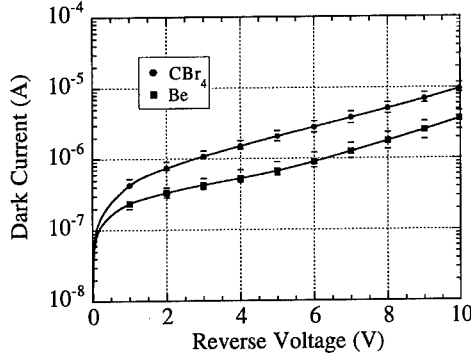


Fig. 5. Typical reverse I-V characteristics for beryllium and carbon doped $\text{In}_{0.73}\text{Ga}_{0.27}\text{As}$ p-i-n photodetectors.

comparable to commercially available devices fabricated using a planar process. The reverse breakdown voltages and large $R_o A$ products of 20V and $25\Omega\text{-cm}^2$ also indicate that device quality $\text{In}_x\text{Ga}_{1-x}\text{As}$ can be grown using carbon as a p-type dopant.

7. Acknowledgments

This work was supported by an ONR STTR Phase II with Sensors Unlimited, Inc., and AFSOR SBIR Phase II with QED, Inc.

8. References

- [1] Malik, R J , Nottenburg, R N , Schubert, E F , Walker, J F , and Ryan, R W 1988 *Appl. Phys. Lett.* **53** 2261
- [2] Konagai, M, Yamada, M, Akatsuka, T, Saito, K, and Tomkumitsu, E 1989 *J. Crystal Growth* **95** 167
- [3] Keutsch, T J , Tischler, M A , Wang, P J , Scilla, G , Potemski, R , and Cardone, F 1988 *J. Appl. Phys.* **53** 1377
- [4] Abernathy, C R , Pearton, S J , Caruso, R , Ren, F , and Kovalchick, J 1989 *Appl. Phys. Lett.* **55** 1750
- [5] Ren, F, et. al. 1991 *J. Appl. Phys.* **59** 3613
- [6] Ito, H, and Ishibashi, T 1991 *Jpn. J. Appl. Phys.* **30** L944
- [7] Kamp, M, Contini, R, Werner, K, Heinecke, H, Wyers, M, Luthi, H and Balk, P 1989 *J. Crystal Growth* **95** 144
- [8] Stockman, S.A , Hanson, A W , and Stillman, G E 1992 *Appl. Phys. Lett.* **60** 2903
- [9] Hamm, R A , Chandrasechar, S , Lunardi, L and Geva, M 1995 *J. Crystal Growth* **148** 1
- [10] Joyce, T B , Westwater, S P , Goodhew, P J , and Pritchard, R E 1996 *J. Crystal Growth* **164** 371
- [11] Watanabe, N, Nitto, T, and Ito, H 1994 *J. Crystal Growth* **145** 929
- [12] Ito, H, Kurushima, K and Watanabe, J 1996 *J. Crystal Growth* **158** 430
- [13] Stockman, S, Hanson, A, Colomb, C, Fresina, M, Baker, E, and Stillman, G 1994 *J. Electron Mater.* **23** 791
- [14] Hwang, W Y , Miller, D L , Chen, Y K , and Humphrey, D A 1993 *J. Vac. Sci. Tech.* **B12** 1193
- [15] Kochhar, R , Hwang, Y H , Micovic, M , Mayer, T S , and Miller, D L 1997 *J. Vac. Sci. Tech.* **15** 1
- [16] Micovic, M, Cai, W, Ren, Y, Neal, J, Nelson, S, Mayer, T S, and Miller, D L 1997 *MRS Symp. Proc.* **450** 219
- [17] Ro, J R , Park, S J , Kim, S B , and Lee, E H 1996 *J. Crystal Growth* **164** 377
- [18] Tokumitsu, E, et. al. 1992 *J. Crystal Growth* **120** 301
- [19] Ren, Y, Micovic, M, Cai, W, Mohney, S, Lord, S M , Miller, D L , and Mayer, T S to be published

Studies of the Effects of Multi-Stack Multiquantum Barrier on the Properties of 1.3 μm AlGaInAs/InP Quantum Well Lasers

Jen-Wei Pan, Jen-Inn Chyi, Yuan-Kuang Tu*, and Jy-Wang Liaw*

Department of Electrical Engineering, National Central University,
Chung-Li, Taiwan, 320, Republic of China

*Telecommunication Labs, Chunghwa Telecom., Co., Ltd.
Yang-Mei, Taiwan, 326, Republic of China

Abstract. The optical confinement factor, far-field angle, and threshold current of 1.3 μm AlGaInAs/InP separate confinement heterostructure (SCH) laser with two-stack AlInAs-(AlGa)InAs multiquantum barriers (MQB) are theoretically studied. The internal quantum efficiency for the laser with MQB is decreased by 13 % in contrast to 24 % for the laser without MQB in the temperature range of 298-348 K. The characteristic temperature can be improved by 10 K. Experimental results for the 1.3 μm AlGaInAs/InP laser with MQB are also presented and compared.

1. Introduction

Multiquantum barrier (MQB) structure has shown great potential on decreasing the threshold current and raising the characteristic temperature of quantum well lasers[1-3]. The significant improvement on the laser performance is mainly attributed to the enhanced barrier height induced by the MQB which greatly reduces carrier leakage. Since the mobility of electron is higher than that of hole, MQB structure is usually used at the p-type guiding layer as an electron barrier for long wavelength laser[4]. However, any minor structural change in the MQB may lead to a large variation in the optical confinement factor, far-field pattern, and internal quantum efficiency. In order to have an in-depth understanding on the effects of MQB, 1.3 μm AlGaInAs/InP separate confinement heterostructure (SCH) lasers with AlInAs-(AlGa)InAs multi-stack MQBs are theoretically studied. The optical confinement factor, and vertical far-field angle, and the temperature dependence of threshold current are investigated and compared with the conventional step-index SCH lasers.

2. Electron Reflectivity of MQBs

The schematic conduction band diagram of a two-stack $\text{Al}_{0.48}\text{In}_{0.52}\text{As-(Al}_x\text{Ga}_{1-x})_{0.48}\text{In}_{0.52}\text{As}$ MQB structure is shown in Fig.1. and is expressed as $(12,5)\times 4 + (11,11)\times 4$, where the first and second terms in parenthesis are the widths of barrier and well in the unit of monolayer (ML), respectively. In this work, two types of $\text{Al}_{0.48}\text{In}_{0.52}\text{As-(Al}_x\text{Ga}_{1-x})_{0.48}\text{In}_{0.52}\text{As}$ ($x = 0, 0.7$) MQBs are investigated and denoted as MQBx and MQBy, respectively. The two-stack MQB is part of the p-type guiding layer and serves as an electron barrier. The total thickness of this guiding layer is set to be 0.15 μm . The electron reflectivity's of the two-stack MQBs and conventional step-index structures are shown in Fig.2. The classic barrier height U_0 in this work is defined as the

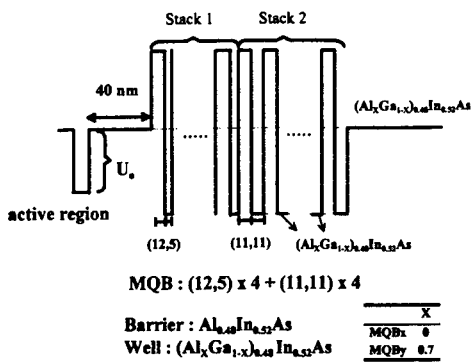


Fig.1 Schematic conduction band diagram of multi-quantum barriers with various Al compositions in the well.

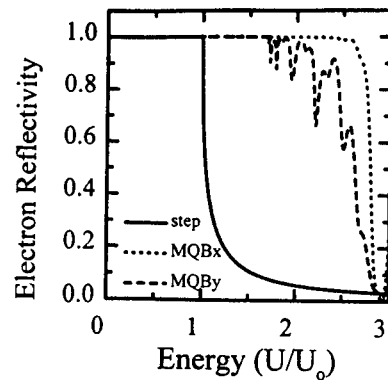


Fig.2 Electron-wave reflectivities of the conventional step-index, MQBx, and MQBy structures.

conduction band continuity ΔE_c between $(\text{Al}_{0.35}\text{Ga}_{0.65})_{0.34}\text{In}_{0.66}\text{As}$ and $(\text{Al}_{0.7}\text{Ga}_{0.3})_{0.48}\text{In}_{0.52}\text{As}$, which is 0.26 eV. The effective barrier heights calculated by transfer matrix method for MQBx and MQBy are enhanced to be $1.7 U_o$ and $2.5 U_o$, respectively. The detailed simulated characteristics are shown in ref.[4-5].

3. Laser Performance

The active region of the lasers studied in this work consists of six 5.5-nm compressively strained $(\text{Al}_{0.35}\text{Ga}_{0.65})_{0.34}\text{In}_{0.66}\text{As}$ quantum wells and five 10-nm $(\text{Al}_{0.7}\text{Ga}_{0.3})_{0.48}\text{In}_{0.52}\text{As}$ barrier layers. The thickness' of the cladding and guiding layers are 2 μm and 0.15 μm , respectively. The calculated optical confinement factor Γ and vertical far-field angle for each laser are listed in Table I. It is found that the far-field angle of the laser with AlInAs-GaInAs MQB is only slightly larger than that of the conventional laser and the opposite is observed for the laser with AlInAs-AlGaInAs MQB. Since lower average refractive index of the guiding layer leads to a lower optical confinement factor and a smaller far-field angle, the far-field angle of the laser with MQB can be therefore tailored by varying the materials of the MQB while maintaining a high electron barrier.

The calculated internal quantum efficiency η_i represents the ratio of spontaneous emission of the active region to that of the active region and guiding layer[4,6]. The internal quantum efficiency as a function of temperature for each laser is shown in Fig.3. For the conventional step-index laser, the internal quantum efficiency is calculated to be 85 % at room temperature. The carrier density populated in the barriers increases significantly at high temperatures, i.e. varies approximately with $T^{3/2}$ in contrast to T^1 for the carrier density in the quantum well[7]. It thus facilitates the recombination at the guiding layer and deteriorates the slope efficiency at high temperature. The internal quantum efficiency is thus decreased by 24 % as the temperature increases from 298 K to 348 K. On the other hand, for the lasers with MQB structure, the carrier density at the p-type guiding layer is significantly reduced as a result of the enhanced barrier height induced by MQB. The carrier density at the n-type guiding layer

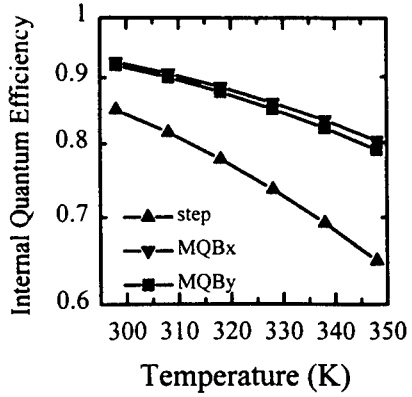


Fig.3 Internal quantum efficiencies as a function of temperature for the lasers with the conventional step-index, MQBx, and MQBy structures.

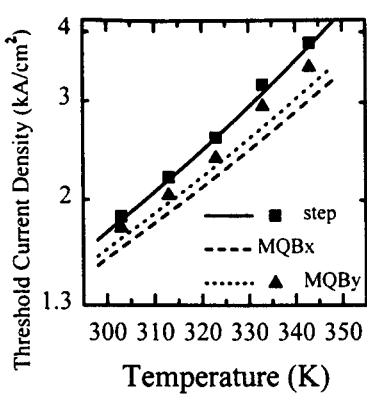


Fig.4 Threshold current densities as a function of temperature for the lasers with the conventional step-index, MQBx, and MQBy structures. The filled squares and triangles are the experimental results.

therefore dominates the internal quantum efficiency. It is found that the lasers with MQB structures exhibit the same internal quantum efficiencies (~92 %) at room temperature. Compared with the laser with MQBy, a higher internal quantum efficiency for the laser with MQBx is obtained at high temperatures, since the larger optical confinement factor reduces threshold carrier density per well and consequently the carrier leakage. In the temperature range of 298–348 K, the internal quantum efficiencies for the lasers with MQBx and MQBy are decreased by 13 % and 14 %, respectively. Obviously, the internal quantum efficiency and its temperature dependence of the lasers with MQB structures are significantly improved.

The threshold gain G_{th} used in this calculation is assumed to be 48 cm^{-1} at room temperature, for a laser with a cavity length and width of $300 \mu\text{m}$ and $50 \mu\text{m}$, respectively, and uncoated mirror facets. Its temperature dependence is also assumed to be $0.045 \text{ cm}^{-1}/\text{T}$ [7]. Based on the previous results [8], the transparency current density J_{tr} at room temperature and its characteristic temperature are 120 A/cm^2 and 105 K , respectively. The threshold current density J_{th} for MQW lasers can thus be expressed as $J_{th} = (M J_{tr}) / (\eta_i \exp(G_{th}/TG_o))$, where M is the number of quantum well in the active region and G_o is the gain parameter (1200 cm^{-1}). [9] The threshold current density of each laser structure is shown in Fig.4. The threshold current densities of the

Table 1 Optical confinement factor and vertical far-field angle for the lasers with the conventional step-index, MQBx, and MQBy structures.

	confinement factor	far-field angle
conventional SCH	5.8 %	38.2°
MQBx	5.95 %	40.2°
MQBy	5.68 %	37.1°

Table 2 Experimental characteristic temperatures for the lasers with the conventional step-index, MQBy structures.

Laser structure	Characteristic Temperature	
	30-50 °C	30-70 °C
with MQBy	68 K	60 K
without MQB	60 K	56 K

lasers with MQB structures are calculated to be about $1.64\text{-}1.7 \text{ kA/cm}^2$ and are slightly improved as compared to 1.84 kA/cm^2 of the conventional step-index SCH laser at 303 K. Although the resultant effective barrier height for the laser with MQBx is 1.47 times that for the laser with MQBy, it is found that the characteristic temperatures for both lasers with MQB structures are about the same values of 64 K. However, the characteristic temperature of the laser without MQB is only 55 K. This indicates that, by using the MQB at the p-type guiding layer, improvements on the threshold current and characteristic temperature can be expected. In addition to the theoretical calculations, two types of $1.3 \mu\text{m}$ AlGaInAs/InP laser structures grown by molecular beam epitaxy are experimentally studied: (a) MQBy and (b) conventional step-index SCH. These devices are $50 \mu\text{m}$ -wide broad area ridge lasers with $300 \mu\text{m}$ cavity length and uncoated facets. The threshold current densities of these lasers at 303 K are 1.78 kA/cm^2 and 1.86 kA/cm^2 , respectively. These values are comparable to the calculated results. The characteristic temperatures for these lasers are listed in Table II. It is found that the improvement on the characteristic temperature is not as significant as expected. This phenomenon might be attributed to the noticeable change on the electron reflectivity of the MQB under high bias condition[10]. The increased leakage current due to the reduced barrier height of the MQB thus enhances the temperature sensitivity of the laser. Using more stacks of MQBs at the p-type guiding layer to enhance barrier height is an effective approach. On the other hand, MQBs for holes may be as important since hole injection into the n-type guiding layer becomes significant at high temperatures as suggested by recent report [11].

4. Conclusions

We have theoretically studied the effects of two-stack MQB on the properties of $1.3 \mu\text{m}$ AlGaInAs/InP SCH quantum well lasers. It is found that lower threshold current and smaller far-field angle can be achieved simultaneously by using proper MQB structure. The characteristic temperature can also be improved by as much as 10 K. Experimental results for the $1.3 \mu\text{m}$ AlGaInAs lasers show good agreement for threshold current density. In order to improve the characteristic temperature, more stacks of MQBs for holes and electrons are necessary.

References

- [1] Takagi T and Iga K 1992 *IEEE Photon. Technol. Lett.* 4 1322-1324
- [2] Kishino K, Kikuchi A, Kaneko Y and Nomura I 1991 *Appl. Phys. Lett.* 58 1822-1824
- [3] Usami M, Matsushima Y and Takahashi Y 1995 *IEEE J. Selected Topics in Quantum Electron.* 244-248
- [4] Fukushima T, Shimizu H, Nishikata K, Hirayama Y and Irikawa M 1995 *Appl. Phys. Lett.* 66 2025-2027
- [5] Chyi J I, Wang S K, Gau J H, Shieh J L and Pan J W, 1996 *IEEE J Quantum Electron.* 32 441-447
- [6] Fukushima T, Namegaya T, Ikegami Y, Nakayama H, Matsumoto N, Kasukawa A and Shibata M 1994 *Optical and Quantum Electron.* 26 S843-855
- [7] Zah C E, Bhat R , Pathak B N, Favire F, Lin W, Wang M C, Andreadakis N C, Hwang D M, Koza M A, Lee T P, Wang Z, Darby D, Flander D and Hsieh J J 1994 *IEEE J Quantum Electron.* 30 511-523
- [8] Pan J W and Chyi J I, 1996 *IEEE J Quantum Electron.* 32 2133-2138
- [9] Liu D C, Lee C P, Tsai C M, Lei T F, Tsang J S, Chiang and Tu Y K, 1994 *J Appl. Phys.* 73 8027-8034
- [10] Takagi T, Koyama F and Iga K 1991 *Appl. Phys. Lett.* 59 2877-2879
- [11] Sei S, Oohasi H, Sugiura H, Hiroto T and Yokoyama k 1995 *Appl. Phys. Lett.* 67 1054-1056

Characteristics of native-oxide confined InGaP/(Al_xGa_{1-x})_{0.5}In_{0.5}P quantum well visible laser diodes

Decai Sun and D. W. Treat

Xerox Palo Alto Research Center, 3333 Coyote Hill Rd. Palo Alto, CA 94304, USA

Abstract. We report 670 nm native-oxide confined GaInP-(Al_xGa_{1-x})_{0.5}In_{0.5}P quantum well visible laser diodes. The devices are fabricated from a compressively strained GaInP/(Al_xGa_{1-x})_{0.5}In_{0.5}P QW double heterostructure laser structure. A real refractive index-guided waveguide is formed by converting part of the p-Al_{0.5}In_{0.5}P cladding layer above the QW active region into an AlO_x oxide. Laser diodes of 4 μm wide ridge waveguide operate with threshold currents below 15 mA and differential quantum efficiencies over 60%.

1. Introduction

Red laser diodes are being widely used in applications such as laser printing, bar code scanning and optical data storage. In applications which need a stable single transverse mode beam at a power level over tens of milliwatts, a buried ridge waveguide structure has been commonly used[1]. In this type of diode, n-GaAs is selectively grown over a bare ridge to form a buried waveguide structure which can suppress high-order mode oscillation through optical absorption in the n-GaAs region. Although high power red lasers with good beam quality have been realized from these diodes, the drawback of this approach is the requirement of one or more regrowth steps, complicating the fabrication. Additionally, these diodes have relatively high loss and low quantum efficiency. It is very desirable to fabricate single transverse mode visible laser diodes with a simpler process.

Recently there has been strong interest in using native oxides converted from Al-based III-V alloys to form optical waveguides and current confinement apertures in the fabrication of both edge emitting and vertical cavity surface emitting laser diodes[2, 3]. Oxidation of (Al_xGa_{1-x})_{0.5}In_{0.5}P alloys in visible laser structures has been reported in fabrication of single and coupled stripe array devices, where the native oxides were used for forming device isolation and non-absorbing windows [4, 5]. These devices demonstrated high output powers, but also high threshold currents due to wide active region and weak optical confinement. Low threshold, single transverse mode visible lasers have not been reported using the oxidation technique. In this letter, we report high performance native-oxide confined narrow waveguide laser diodes for single transverse mode operation. The diodes were fabricated by oxidizing Al_{0.5}In_{0.5}P to form a native oxide for optical and electrical confinement. Low threshold and high efficiency diodes have been achieved.

2. Device fabrication

Native oxide confined visible laser diodes were fabricated from a compressively strained Ga_{0.4}In_{0.6}P/(Al_xGa_{1-x})_{0.5}In_{0.5}P quantum well (QW) separate confinement heterostructure, which was grown by low pressure organometallic vapor phase epitaxy (OMVPE) on a n⁺ GaAs substrate. The active region consisted of an 80 Å wide Ga_{0.4}In_{0.6}P QW layer, confined by a pair of 1200 Å thick

$(Al_{0.6}Ga_{0.4})_{0.5}In_{0.5}P$ confinement layers. The active region was sandwiched between a pair of p- and n- $Al_{0.5}In_{0.5}P$ 1 μm thick cladding layers. A p⁺- $Ga_{0.5}In_{0.5}P$ 500 \AA thick barrier reduction layer was grown on top of the p- $Al_{0.5}In_{0.5}P$ cladding layer followed by an 1000 \AA GaAs p⁺-GaAs cap layer.

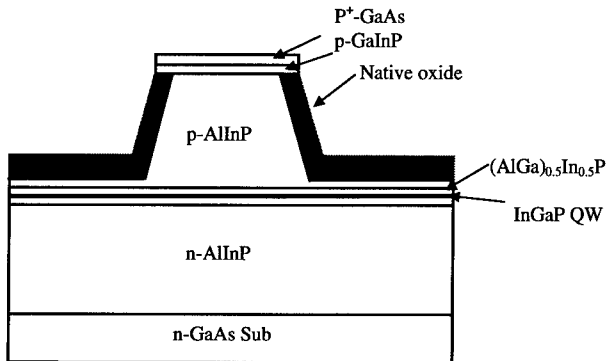


Fig. 1 Cross section view of the oxide confined red laser

After growth, a layer of 800 \AA SiN_x was deposited on the crystal surface. The SiN_x layer was then patterned into 4 μm wide stripes. These stripes were used as an etching mask for wet-chemical etching to define the ridge waveguide by etching away the GaAs cap layer, the GaInP barrier reduction layer and the upper 0.65 μm thick p- $Al_{0.5}In_{0.5}P$ cladding layer. After etching, the wafer was loaded into an open tube furnace, which was saturated with H₂O vapor by an N₂ carrier gas bubbling through 95 °C deionized water. It was oxidized at 530 °C for four hours. After oxidation, the cross section of the waveguides was examined in a scanning electron microscope. A layer of 0.3 μm thick native oxide surrounded the p- $Al_{0.5}In_{0.5}P$ ridge and above the active region as shown in the cross section view of the device. The oxide surface looked very smooth under an optical microscope. Following the oxidation, SiN_x stripes were removed in a plasma etcher. 125 μm wide Ti(200 \AA)/Au (3500 \AA) metal stripes were directly deposited on top of the waveguides using the lift-off technique, and AuGe metal was deposited on the back of the substrate after thinning.

3. Results and discussion

The diodes were bonded p-side up on heat sinks for test under pulsed and CW operations. The light output (L-I) characteristic of a 500 μm long diode under CW operation is shown in Fig. 2. The diode had a threshold current of 14.6 mA and a differential quantum efficiency of 35%/facet. Compared with the buried ridge diodes fabricated from the same structure, the oxide confined waveguide lasers showed a reduction of the threshold current density by a factor of almost 2, and over 50% increase in the external differential quantum efficiency. The improvement in the threshold and quantum efficiency is very beneficial in reducing thermal heating during CW operation. The maximum power was 32 mW/facet, limited by catastrophic optical damage. Higher power could be achieved if the diode facets are coated.

Under pulsed operation (0.1% duty cycle and 0.1 μs pulse width), the maximum power from another diode reached 92 mW/facet before failure as shown in Fig. 2. A preliminary burn-in test of

the diodes at 10 mW/facet in CW operation showed that the devices were stable, with no evidence of short-term degradation.

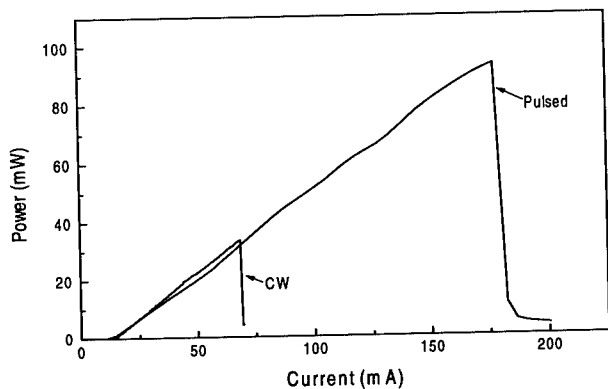


Figure 2 L-I curve of the oxide confined visible laser

The emission spectrum of the laser diode, measured by an 1.5 meter high resolution spectrometer at the driving current of 20 mA, is shown in Fig. 3. The spectrum is quite narrow, with a few longitudinal modes dominating, indicating that the cavity is strongly index-guided. We calculated the effective index step in the lateral direction of the waveguide. The results show that the index step is as high as 3×10^{-2} when the oxide is right above the confinement region assuming that the refractive index of the native oxide is 1.6. It is noticed that the spectral peak shifted from 6722 Å to 6728 Å, as the current was increased from 15 to 30 mA. The small wavelength shift indicated that the thermal heating in the active region was very small due to low threshold and high efficiency, although the diode was mounted p-side up.

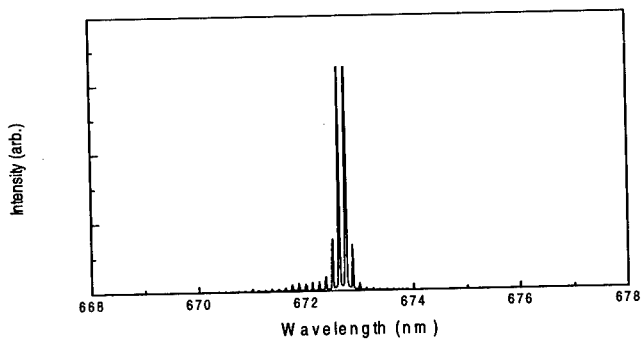


Figure 3 Emission spectrum of the oxide confined laser at 20 mA

The far-field pattern of the diode was measured under CW operation at different power levels. The far-field patterns parallel to the junction plane are shown in Fig. 4. The laser operated in a single

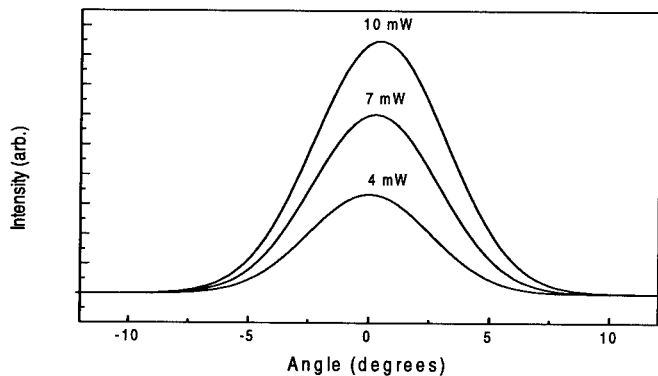


Figure 4 The far field patterns of the oxide confined laser parallel to the junction plane

transverse mode. The full widths at half-maximum (FWHM) of the far field parallel and perpendicular to the junction plane were 6° and 42° , respectively. The characteristic temperature T_0 of the laser diodes was measured under the pulsed mode in the range 10 to 100°C . The T_0 was calculated to be 150 K for the temperature range from 10 to 45°C , and 110 K from 50 to 100°C .

4. Summary

Native oxide confined ridge waveguide visible laser diodes have been fabricated from an $\text{In}_{0.6}\text{Ga}_{0.4}\text{P}/(\text{Al}_x\text{Ga}_{1-x})_{0.5}\text{In}_{0.5}\text{P}$ single quantum well laser structure, by oxidizing the upper p- $\text{Al}_{0.5}\text{In}_{0.5}\text{P}$ cladding layer. The laser diode showed excellent performance, with very low threshold currents of 15 mA and differential quantum efficiencies over $35\%/\text{facet}$ under CW operation in single transverse mode.

The authors wish to thank P. Floyd and R. Thornton for helpful discussions. This work was supported in part by the Department of Commerce Advanced Technology program under Grant No. 70NAN82H1241.

References

- [1] I. Yoshida, T. Katsuyama, J. Hashimoto, and H. Hayashi, Jpn. J. Appl. Phys. Vol. 34, pp. 803-4808, 1995
- [2] S. J. Caracci, F. A. Kish, N. Holonyak, Jr., and S. A. Maranowski, Appl. Phys. Lett. Vol. 61, pp. 321-323, 1992
- [3] Y. Cheng, P. D. Dapkus, M. H. Macdougal, and G. M. Yang, IEEE Photon. Techno. Lett. Vol. 8, pp.176-178, 1997
- [4] S. A. Maraowski, F. A. Kish, S. J. Caracci, N. Holonyak, Jr., J. M. Dallesasse, D. Bour, and D. W. Treat, Appl. Phys. Lett. Vol. 61 pp. 1688-1690, 1992
- [5] F. A. Kish, S. J. Caracci, N. Holonyak, Jr., and . Maraowski, Appl. Phys. Lett. Vol. 59, pp. 2883-2885, 1991

InGaAs/InP p-i-n Heterostructure Photodiode Arrays on AlGaAs/GaAs Waveguide Films by Solid Source Molecular Beam Epitaxy

Shih-Hsiang Hsu[†], F. G. Johnson*, S. A. Tabatabaei*, Sambhu Agarwala*, John V. Hryniecicz[†], F. J. Towner[‡], Y. J. Chen[†], and D. R. Stone*

[†]Department of Computer Science and Electrical Engineering

University of Maryland Baltimore County
1000 Hilltop Circle, Baltimore, MD 21250

*The Laboratory for Physical Sciences
College Park, MD 20740

[‡]Quantum Epitaxial Designs, Bethlehem, PA 18015

Abstract: The first solid-source molecular beam epitaxial growth of $\text{In}_{0.53}\text{Ga}_{0.47}\text{As}$ photodetector structure on top of an AlGaAs/GaAs waveguide for monolithic 1.55 μm receiver applications has been demonstrated using a single, thin InP buffer layer to suppress dislocations. Mesa-type detector arrays were made by chemically assisted ion beam etching. Utilizing a novel dense array fabrication technique, we demonstrated the integration of InGaAs optoelectronic devices with AlGaAs/GaAs waveguide films grown on a GaAs substrate. These heterostructure photodiode arrays, which can be readily integrated with GaAs optoelectronic and electronic components, also show high photoresponsivity (0.7A/W without any antireflection coating), and exhibit a bandwidth in excess of 7 GHz.

The monolithic integration of photodetectors with both passive and active optical waveguide components and electronic circuits has numerous applications in long distance fiber-optic communication systems and local area networks [1]. Presently, GaAs is the most well developed compound semiconductor material for electronic devices and is one of the preferred substrate materials for opto-electronic integrated circuits (OEIC) even at 1.55 μm . Although the epitaxial growth of InGaAs based opto-electronic devices on InP is well developed, the electronic part of the technology on InP substrates is not as advanced as that of GaAs. Therefore, it is highly desirable to develop techniques for monolithic integration of InGaAs photodiode devices operating in the 1.0 - 1.6 μm wavelength range with AlGaAs/GaAs waveguides and electronic circuits on GaAs substrates. The technique we report here to produce an array of $\text{In}_{0.53}\text{Ga}_{0.47}\text{As}$ mesa-type photodiodes on an AlGaAs/GaAs waveguide, grown by solid source molecular beam epitaxy (MBE) and etched by ultrahigh vacuum chemically assisted ion beam etching (CAIBE) [2], will permit the fabrication of monolithic OEIC receiver modules. These diodes exhibit low dark current, low capacitance, high photoresponsivity, and a bandwidth greater than 7 GHz.

To epitaxially grow InGaAs layers on GaAs, thick or multistage InP buffer layers grown by metal-organic chemical vapor deposition (MOCVD) [3,4] have been reported to avoid dislocation propagation due to the large lattice mismatch (~3.8%) between InP and GaAs. The thick (over 9 μm) buffer layer used by Kimura et al. [3] is not well suited for monolithic integration due to processing difficulties. We show that a thin InP layer (1.7 μm) grown by conventional solid-source MBE serves as

hetero- and homo- structure $\text{In}_{0.53}\text{Ga}_{0.47}\text{As}$ p-i-n photodiode layers to be overgrown. In the current work, the substrate temperature of the $\text{In}_{0.53}\text{Ga}_{0.47}\text{As}/\text{InP}$ during growth was approximately 480°C , and the growth rates were approximately 1 monolayer/s. Two independent, valved effusion cells were used to supply As_2 ($T_{\text{cracker}} = 900^\circ\text{C}$) and P_2 ($T_{\text{cracker}} = 1000^\circ\text{C}$) from elemental arsenic and white phosphorus sources, respectively. The heterostructure p-i-n photodiodes were etched by CAIBE ($T_{\text{substrate}} = 260^\circ\text{C}$, 3 sccm Cl_2 and 500 eV Ar ion beam), as shown in Fig. 1. For comparison, photodiodes were also etched with selective wet-chemistry [5] (1 H_2SO_4 : 1 H_2O_2 :10 H_2O for $\text{In}_{0.53}\text{Ga}_{0.47}\text{As}$ and 1 HCl :1 H_2O for InP). In earlier work, reactive ion etching (RIE) at high self bias voltage (up to 1 kV) was used to achieve high anisotropy [6]. This RIE process causes extensive damage and re-deposition on the sidewalls leading to unacceptably high leakage currents and requires special sidewall surface treatments after etching. In the present work, the CAIBE process with a lower ion energy (500 eV Ar⁺) beam plus chlorine gas was utilized to reduce the surface damage, immediately followed by a short in-situ chlorine gas etch to remove the damaged layer. The additional etch depth after using a chlorine gas flow for 20 seconds at 260°C was estimated to be about 0.1 μm [7]. A Ti(300Å)/Pt(2000Å) metallization was used as the etching mask. The Ti overlayer has a lower ion beam etch rate than Pt (53% rate ratio Ti/Pt, data from Commonwealth Scientific Corporation), so it protects the underlying Pt p-metal contact from being sputtered away during the etch. The $\text{In}_{0.53}\text{Ga}_{0.47}\text{As}$ etch rate was 0.74 $\mu\text{m}/\text{min}$ and the ion beam current density was estimated to be 0.6 mA/cm² from the Faraday cup measurement. The n-metal, Au/Ni/Ge/Au/Ge/Ni, contact was accomplished by a lift-off process. After contact fabrication, the PIN detector array was encapsulated using PI2711, which is a negative acting photo-sensitive polyimide, cured in a 350°C furnace for 40 minutes [8]. The final metal, Au/Ti (3000/300Å), was deposited to form a $50\ \Omega$ coplanar waveguide contact array as shown in Fig. 2. The 150 μm pitch ground-signal-ground (GSG) Cascade-Allessi coplanar waveguide probes were applied to acquire the high-speed data.

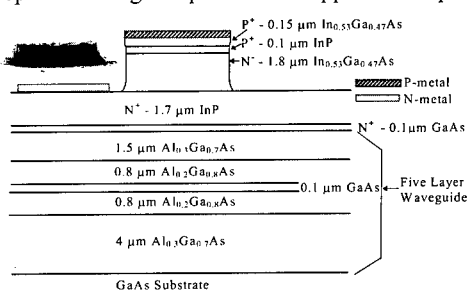


Fig. 1: Schematic cross sections of $\text{InP}/\text{In}_{0.53}\text{Ga}_{0.47}\text{As}/\text{InP}$ double heterostructure grown on a five layer AlGaAs/GaAs waveguide, including scanning electron microscope (SEM) picture for 2.6 μm CAIBE etched mesa-type photodiode.

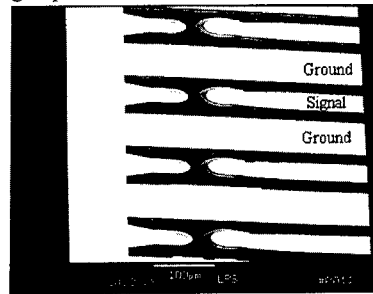


Fig. 2: The etched mesa photodiode array planarized by polyimide for high speed testing.

Fig. 3 shows the dark current versus applied voltage for heterostructure devices processed by CAIBE and by wet etching, measured by a Hewlett-Packard (HP) 4145B semiconductor parameter analyzer after encapsulation. The dark currents achieved at room temperature were 37 nA and 25 nA, respectively, for CAIBE and wet etch diodes at a -5V bias, on a 30 μm diameter mesa. This shows that

analyzer after encapsulation. The dark currents achieved at room temperature were 37 nA and 25 nA, respectively, for CAIBE and wet etch diodes at a -5V bias, on a 30 μm diameter mesa. This shows that dry-etched diodes have only a small residual process-induced damage. Our dry-etched diode result is better than that reported by Seto et al. [6], in which the dark current of reactive-ion etched equivalent photodiode was ~ 100 nA. It should be added that unlike lattice-mismatched diodes in the present work, those in ref. 6 were grown lattice-matched to the InP substrate and a wet-etching step was used subsequent to the RIE mesa etch to remove the etch-induced damage. For wet-etched mesa, the dark current of an InGaAs photodiode grown on a GaAs substrate with a fairly thick InP buffer layer [4] is typically two orders of magnitude larger than that on InP [8]. The dark current obtained in the present work (both wet- and dry-etched diodes) is consistent with this report. Our dark current data from thin buffer (1.7 μm) detectors are comparable to that of thicker buffer (4 μm) devices on GaAs substrates [4] and also suitable for high bit rate applications. The thin buffer layer is especially beneficial for the subsequent processing with improved prospects for integration with devices and circuits in the underlying GaAs based material. The dark current vs. diode area exhibits a linear curve, which indicates that lattice-mismatch-induced dislocation traps, generation-recombination, and minority carrier diffusion are the dominant sources of dark current, not surface leakage. The photoresponsivity and quantum efficiency performance of our p-i-n detectors were 0.7 A/W and 56% respectively at 1.55 μm without any antireflection coating.

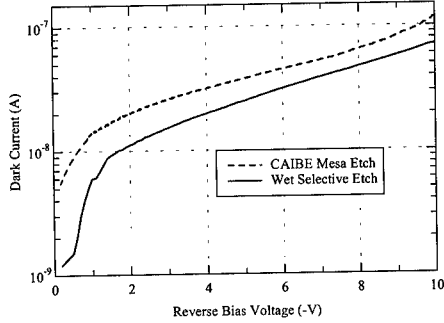


Fig. 3: The dark current versus reverse bias voltage of an InGaAs photodiode.

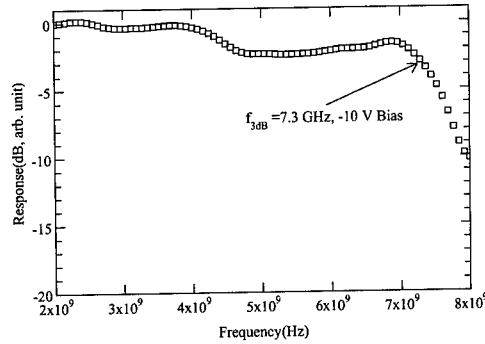


Fig. 4: The frequency response of a 30 μm diameter diode with a 1.8 μm thick i-region,

Device capacitance values were obtained from the S_{11} parameter, measured by a calibrated HP8510C network analyzer from 50 MHz to 10 GHz. A capacitance of 0.1 pF, for a 30 μm diameter InGaAs photodiode, was measured at 2 GHz. The pad capacitance was 0.19 pF with planarized polyimide. The slope of the voltage vs. (capacitance per unit area) $^{-1/2}$ curve shows that the absorbing $\text{In}_{0.53}\text{Ga}_{0.47}\text{As}$ layer is unintentionally doped n-type at $\sim 1.5 \times 10^{15} \text{ cm}^{-3}$. The frequency response of 30 μm diameter diodes was measured using an 8 GHz externally modulated single mode distributed feedback (DFB) 1.55 μm laser diode. A 3dB bandwidth of over 7 GHz was measured as shown in Fig. 4., which was limited by the intrinsic transit time of the PIN structure and not by the RC time constant of photodiodes and the equivalent circuit.

In conclusion, we have fabricated and characterized an $\text{In}_{0.53}\text{Ga}_{0.47}\text{As}/\text{InP}$ PIN photodiode array on an AlGaAs/GaAs waveguide grown by solid-source MBE. The dark currents observed for CAIBE and wet etched devices are comparable, indicating small residual dry-etched induced damage,

and adequate for high bit rate applications. A novel process for air bridges has also been applied to detector arrays for ultrahigh speed testing. These photodiode arrays, which are readily integratable with GaAs optoelectronic and electronic components, also show high quantum efficiency, and a bandwidth in excess of 7 GHz.

Acknowledgments: We thank O. King, T. Filemyr, G. A. Porkolab, Y. P. Ho, W. Lin, H. Li, M. H. Shih, and S. Didde for fruitful technical assistance and discussions. This project is supported by the Joint Program for Advanced Electronic Materials at the Laboratory for Physical Sciences.

References:

- [1] Deri R J 1993 *IEEE Photon. Technol. Lett.* 11 1296-1313
- [2] Hryniecic J V, Chen Y J, Hsu S H, Lee C H, and Porkolab G A 1997 *J. Vac. Sci. Technol. A* 15 616-621
- [3] Kimura T, Kimura T, Ishimura E, Uesugi F, Tsugami M, Mizuguchi K, and Murotani T 1991 *J. Crystal Growth* 107 827-831
- [4] Dentai A G, Campbell J C, Joyner C H, and Qua G J 1987 *Electron. Lett.* 23 38-39
- [5] Hsu S H, Johnson F G, Liu Y C, Towner F J, Tabatabaei S A, Agarwala A, Hryniecic J V, Ho Y P, Lin W, Chen Y J, Dagenais M, and Stone D R 1997 *CLEO '97 Tech. Digest* CThX1
- [6] Seto M, Deri R J, Schiavone L M, Bhat R, Soole J B D, Schumacher H, Andreadakis N C, and Koza M 1991 *Electron. Lett.* 27 911-913
- [7] Panepucci R, Youtsey C, Turnbull D A, Gu S Q, Caneau C, Bishop S G, and Adesida I 1995 *J. Vac. Sci. Technol. B* 13 2752-2756
- [8] Tabatabaei S A, Porkolab G A, Agarwala S, Johnson F G, Merritt S A, Hsu S H, Seiferth F, Whaley R D, Dagenais M, Chen Y J, and Stone D R 1997 accepted by *Materials Research Society*, Spring Meeting, San Francisco
- [9] Porkolab G A, Chen Y J, Tabatabaei S A, Johnson F G, King O, Dagenais M, Frizzell R E, Beard W T and Stone D R 1997 accepted for publication of *J. Vac. Sci. Technol. B*

Reduced radiative currents from GaAs/InGaAs and AlGaAs/GaAs p-i-n quantum well devices

J. Nelson, J. Barnes, N. Ekins-Daukes, K.W.J. Barnham, B. Kluftinger, E.S.M. Tsui, C.T. Foxon^b, T.S. Cheng^b, J.S. Roberts^c

Solid State Experimental Group, Blackett Laboratory, Imperial College, Prince Consort Road, London, SW7 2BZ, UK

^b University of Nottingham, University Park, Nottingham, NG7 2RD, UK

^c University of Sheffield, Mappin Street, Sheffield, S1 3JD, UK

Abstract: Calibrated electroluminescence spectra of GaAs/InGaAs and AlGaAs/GaAs single and double quantum well (QW) p-i-n devices, at various temperatures (200-300K) and applied biases ($V_{app} = 0.8\text{-}1.5V$), have been compared to theory to extract the quasi-Fermi level separation, $\Delta\phi_f$, in the QWs and where possible in the host material. Emission from the host material for the GaAs/InGaAs cell is well fitted with $\Delta\phi_f = V_{app}$ at all biases and temperatures. In contrast, emission from the QW in both GaAs/InGaAs and AlGaAs/GaAs cases requires a value of $\Delta\phi_f$ which is a few tens of meV less than V_{app} . We attribute the variations in $\Delta\phi_f$ to irreversible thermally assisted escape from the QWs and detail some preliminary results from double QW samples.

1. Introduction

Many semiconductor applications, such as modulators, lasers [1] and quantum well solar cells [2] use quantum wells (QWs) within a p-i-n structure. To understand the radiative current, it is important to know how the electron and hole quasi Fermi level separation, $\Delta\phi_f$, varies and how it depends on the applied bias, V_{app} . This current, an unavoidable loss even in perfect material, is of fundamental importance for QW lasers [3] and for the limiting efficiency of QW solar cells [4]. We have recently proposed a method of extracting the value of $\Delta\phi_f$ from calibrated QW emission spectra [5] and we apply it to room temperature electroluminescence (EL) spectra from single QWs and, for the first time, to double QW p-i-n devices.

2. Experiment and Theory

The samples were a GaAs/InGaAs single QW grown by MOVPE (sample 1) and three samples in a set of AlGaAs/GaAs single and double QW samples grown by MBE (samples 2, 2p and 2n). All the samples were p-i-n photodiodes, made into 1mm diameter cylindrical mesa structures, with a 545 μm diameter optical window. Sample 1 had a 0.5 μm p layer, 0.24 μm i region containing a single 107Å In_{0.16}Ga_{0.84}As quantum well in the centre and a 2 μm n region, with a 430 Å front Al_{0.8}Ga_{0.2}As window layer to reduce surface recombination. The Al_{0.34}Ga_{0.66}As samples had a 0.15 μm p layer, 0.31 μm i region and a 0.46 μm n region, plus a short period superlattice between the n and i regions to clean up the first QW interface. Sample 2 contained a single 140Å GaAs quantum well in the centre of the i region, whilst samples 2p and 2n had in addition a second, 20Å, QW placed either nearer the p region (2p) or nearer the n region (2n), separated from the wide well by 40Å. All the QWs were characterized

by low temperature photocurrent measurements [6,7]. The front surface was either coated with a single layer of SiN AR coating (sample 1) or had a thin 170Å layer of GaAs (samples 2, 2p and 2n). Background dopings in all samples were estimated to be around 10^{15} cm^{-3} .

The samples were mounted in a closed cycle cryostat and their emission calibrated following the method of ref. [5]. Carriers were excited only in the QW using either a Ti-Sapphire cw laser at 880nm, 0.9mW (sample 1) or a 1mW solid state cw diode laser operating at 782nm (AlGaAs samples), which in the case of the double QWs excites carriers only in the wider 140Å QW. For each sample, photoluminescence (PL) was measured at low temperatures (15-20K), where we had previously determined non-radiative processes to be small (<20%). All emissions were measured by a cooled CCD camera attached to a 30cm monochromator. Equating the maximum integrated PL at forward bias to the generation rate (equivalent to the reverse bias saturation photocurrent (PC)), all further luminescence from each sample was then expressed in absolute units. Electroluminescence (EL) spectra were measured from each sample over the temperature range 200-300K. Due to the sensitivity of the CCD, several decades of intensity could be measured before encountering the series resistance limit.

The theory will be described in detail elsewhere [8] but a brief summary may assist the reader. The EL spectra are calculated using the generalized Planck equation [9] assuming detailed balance and using a calculated absorption spectra for the QW [10]. The radiative current (J_{rad}) is calculated by integrating the emission over the surface of the device, exploiting azimuthal symmetry and following the detailed balance method of [11]:

$$J_{\text{rad}} = q \frac{2n^2}{h^3 c^2} \int_0^\infty \frac{E^2}{e^{(E-q\Delta\phi_f)/kT}-1} \int_s^{\theta_c} \int_0^{\theta_c} a(E, \theta, s) \cos\theta (2\pi \sin\theta d\theta) ds dE$$

Here h , c , k , T and q have their usual meanings and θ_c is the critical angle for internal reflection from the relevant (front or rear) surface S . $a(E, \theta, s)$ represents the probability of photon emission for photon energies E greater than the bandgap, which is equal, in the detailed balance scheme, to the absorptivity. Published values are used for the refractive index (n) and GaAs absorption coefficient [12,13], allowing J_{rad} to be calculated as a function of temperature and $\Delta\phi_f$.

3. Results and Discussion

Figure 1 shows an experimental spectrum from sample 1 at 300K, compared to theory for $\Delta\phi_f = V_{\text{app}}$ and $\Delta\phi_f = V_{\text{app}} - 0.023\text{eV}$. Note the QW emission is overestimated if $\Delta\phi_f = V_{\text{app}}$ and is fitted only

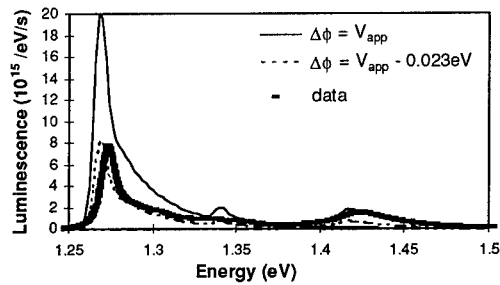


Figure 1: Experimental data for sample 1 at 300K, 1.00V compared to theory.

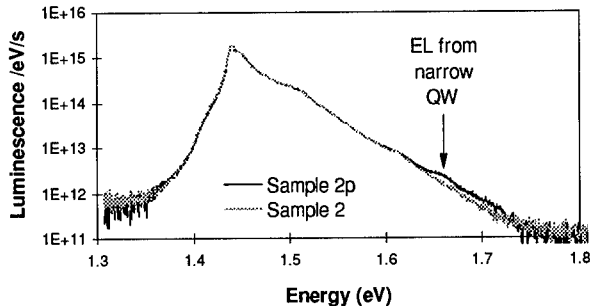


Figure 2: Experimental data from samples 2 and 2p at 1.12V, 300K showing emission from the second, narrow quantum well at energies \sim 1.65eV.

with the reduced value of $\Delta\phi_f$. However, the emission from the host material, emitted from one absorption length from the surface of the device (i.e. in the p region), requires $\Delta\phi_f = V_{app}$.

Figure 2 shows typical spectra from samples 2 and 2p showing the emission from the second, smaller well at 1.65 eV. Modelling the wide QW in all the AlGaAs samples requires a reduced $\Delta\phi_f$ as is seen in sample 1. (No signal is seen from the host material due to the large difference in bandgaps.) The numerical values are given in Table 1 and due to some bias dependence in the value of $\Delta\phi_f$ for the AlGaAs samples, bias values below the series resistance limit are averaged to give the values shown. In all cases the wide QW requires a reduced value of $\Delta\phi_f$ which for sample 2 approaches V_{app} as the temperature is reduced as for sample 1, indicating a thermal escape process may be removing carriers from the QW, and so reducing $\Delta\phi_f$.

Modelling the signal from the 20Å QW in samples 2n and 2p is more difficult, as the narrow QW emission is only visible at the highest temperature (300K). In sample 2p a value of $\Delta\phi_f$ greater than the applied bias is required, whilst for sample 2n, a value close to V_{app} is needed. Previous studies [7,14] on these samples have shown that for sample 2p, holes can tunnel very efficiently from the wide to the narrow QW, whilst for sample 2n escape times are slower. It is possible that the strong tunnelling (and so non-temperature dependent) component to the escape times between the two structures accounts for the differences in the value of $\Delta\phi_f$ for both QWs compared to sample 2.

Other possible explanations for the reduction in $\Delta\phi_f$ for the wide QWs include uncertainties in

Table 1: $\Delta(\Delta\phi_f) = V_{app} - \Delta\phi_f$ required to fit the samples studied in this paper. Note a negative (positive) value indicates a value of $\Delta\phi_f$ greater (smaller) than the applied voltage V_{app} . (Typical errors: 3 mV for wide QW, 5mV for narrow QW)

	Sample 1 (GaAs/InGaAs)	Sample 2 (SQW)	Sample 2n (DQW)		Sample 2p (DQW)	
T(K)	$\Delta(\Delta\phi_f)$ in QW - $\Delta(\Delta\phi_f)$ in host	$\Delta(\Delta\phi_f)$ in QW	$\Delta(\Delta\phi_f)$ in wide QW	$\Delta(\Delta\phi_f)$ in narrow QW	$\Delta(\Delta\phi_f)$ in wide QW	$\Delta(\Delta\phi_f)$ in narrow QW
300	23 meV	15 meV	11 meV	6 meV	16 meV	-15 meV
250	14 meV	6 meV	12meV	-	8meV	-
200	6 meV	8 meV	14meV	-	15meV	-

the absorption spectra, but within the uncertainties acceptable in well width and alloy composition to explain the observed excitonic transition, the luminescence is still overestimated by $\Delta\phi_f = V_{app}$. Also, carrier recombination in the neutral p region, where the GaAs signal originates in sample 1, would reduce $\Delta\phi_f$, whilst in practice the very good agreement between $\Delta\phi_f$ and V_{app} gives us confidence in our calibration method. Our future work will involve studying samples 2n and 2p further plus other samples (where the two QWs are separated by 150Å) to explain the precise values of $\Delta\phi_f$. Further samples with different i region thicknesses may also be studied to determine if this has an effect on the value of $\Delta\phi_f$.

4. Conclusions

We have presented calibrated EL spectra from both single and double quantum well samples and compared data to theory. We find that in all cases, emission from a single quantum well is described by a reduced $\Delta\phi_f$ in the QW relative to the host material. Initial results from double quantum well samples show that depending upon the position of the second well, $\Delta\phi_f$ may be either close to or greater than the applied bias. Combined with the temperature dependence of $\Delta\phi_f$ these results suggest an escape process may be responsible for reducing the effective population within the QW and this agrees qualitatively with differences previously seen in escape times from the different samples.

Acknowledgments

We would like to thank Malcolm Pate for processing the samples, Ian Ballard for assistance with the CCD camera and Steve Webb for the loan of the 782nm solid state laser used in the experiments. We would also like to acknowledge the financial support of the Engineering and Physical Science Research Council, the Greenpeace Environmental Trust and the Royal Commission for the Exhibition of 1851 (JB).

References

- [1] e.g. Blood P *et al.*, Fletcher ED and Woodbridge K, 1985 *Appl. Phys. Lett.*, 47 193
- [2] Barnham K W J and Duggan G, 1990 *J. Appl. Phys.*, 67 3490-3493
- [3] Evans PA *et al.*, 1994 *Semicond. Sci. Techno.*, 9 1740-1743
- [4] Nelson J *et al.*, 1995 *Proc. of 13th Photovoltaics and Solar Energy Conference*, I 150-153
- [5] Tsui ESM *et al.*, 1996 *J. Appl. Phys.* 80 4599-4603
- [6] Barnes J *et al.*, 1996 *J. Appl. Phys.* 79 7775-7779
- [7] Barnes J, PhD thesis, University of London 1994
- [8] Nelson J *et al.*, to be published in 1997 *Proc. of 14th Photovoltaics and Solar Energy Conference* and in 1997 *J. Appl. Phys.*
- [9] e.g. Würfel P, 1982 *J. Phys. C: Solid State Phys.*, 15 3967-3985
- [10] Paxman M *et al.*, 1993 *J. Appl. Phys.*, 74 614-621
- [11] Araujo GL *et al.*, 1994 1997 *Proc. of 14th Photovoltaics and Solar Energy Conference*, 1481-1484
- [12] Aspnes DE, *Properties of GaAs* (INSPEC) Institution of Electrical Engineers, London, 2nd Edition 1990
- [13] Aspnes DE *et al.*, 1986 *J. Appl. Phys.*, 60 754
- [14] Thucydides G *et al.*, 1997 *Semicond. Sci. Techno.*, 12 35-41

The Influence of Internal Mechanical Stresses on the GaAs-Light-Emitting Diodes

V.G.Sidorov, V.I.Sokolov*, D.V.Sidorov

Semiconductor Physics and Nanoelectronic Department, St.Petersburg State Technical University, 29 Politehnicheskaya Str., St.Petersburg, 195251, Russia

*A.F.Ioffe Physico-Technical Institute, Russian Academy of Science, St.Petersburg, Russia

Abstract. The influence of internal mechanical stresses on design and performance of GaAs-LEDs is for the first time in detail investigated. The LED-structures were grown by liquid phase epitaxy from the melts doped with impurities of Si or Si and Sn simultaneously. The bending of crystal planes, internal friction, distribution of dislocations, and microhardness in p-n-junction regions have been measured. The value of internal mechanical stresses changes depending on concentration of doping impurities. When the internal mechanical stresses reach their minimum the LEDs perform the maximum value of quantum efficiency and maximum time of failure. The double Si and Sn doping is more effective. The qualitative model of all observed phenomena is offered.

1. Introduction

Internal mechanical stresses (IMS) are the most general and ineluctable component of the defect structure of all types of semiconductor devices. The origin of the IMS predetermines the construction of semiconductor devices. The value and distribution of stresses over the surface and through the bulk of crystal depend on the concentrations of the doping impurities and are mostly determined by the peculiarity of the technological cycle.

The IMS are mainly caused by local deformation of the interatomic bonds what leads to the deformation of the crystal zone structure and may vary its properties in a very wide range. The presence of noncompensated gradients of IMS in semiconductor devices makes their defect structure unstable in general and determines a lot of degradational effects caused by IMS relaxation during storing and usage of the devices. The influence of IMS on GaAs-LEDs' external quantum efficiency and their degradational behavior has been investigated. The results of the investigation are suggested for discussion.

2. Experimental

The GaAs p-n-structures doped with Si or Si and Sn simultaneously have been used as the samples for the experiment. The structures have been grown in a single technological cycle of liquid phase epitaxy from a limited volume of Ga-rich GaAs melt-solution on substrates of (100)GaAs doped with Sn or Te. The thickness of substrates was between 300 μm and 350 μm . The thickness of n-and p-epitaxial layers was nearly equal and varied from 20 μm to 60 μm . The melt-solution was cooled down with two speeds 0.5°C/min and 7°C/min. Concentration of Si in the liquid phase varied from 0.1% to 1.1% of weight. The Si and Sn simultaneously doped structures were grown at constant concentration of Si in liquid phase whereas the concentration of Sn were varied from zero up to 8% of weight.

For all samples the following characteristics have been measured: bending radius of structure - R; distribution of microhardness - H and density of dislocations - N_d ; internal friction spectra at a frequency of 6 Hz; concentration of deep levels - N_t in p-n-junctions; external quantum efficiency of the electroluminescence β_{ex} ; dependence of the β_{ex} on the exploitation time of the LEDs. Measurement data are presented at Fig.1 and Fig.2.

The values of microhardness and density of dislocations are given for sample areas where electroluminescence is generated. These areas are situated in p-layer of structures at distances of 3-15 μm from p-n-junction [1]. Microhardness of layers was determined relatively to the microhardness of the substrates in purpose of reducing the influence of substrate elastic properties.

The internal friction is integral method of defect structure investigation in solids[2]. The internal friction spectra have the resonance maxima at the melting point of Ga, Sn and 470K. From this spectra we determine the quantity of metallic Ga (W_{Ga}) and metallic Sn (W_{Sn}) in sample. Ga and Sn were caught by the growing epitaxial layer from melt-solution and appear to be inclusion of the second phase [3]. The internal friction peak at 470K (Q) correlate with the bending radius of the structure (Fig.1a and Fig.1c). When $R^1 = 0$, Q reaches its maximum value. Consequently Q may be characteristic of mechanical stresses in GaAs-epitaxial layers.

3. Discussion

During GaAs growth from the melt-solution doped with Si the defect structure of the epitaxial layers is formed in the following way. There are several processes that go simultaneously in the growing layer: doping with Si, enriching with As-vacancies (V_{As}), and capturing of excessive Ga (Ga_i). The increased cooling rate of melt-solution is faster the last process goes (Fig.1g). The local deformations of crystal lattice caused by V_{As} and Ga_i defects have different signs (atomic volume of vacancy is negative) and compensate to each other (Table 1), and therefore give mechanical stability to the crystal. Along with Ga_i some quantity of Ga captured by film will occupy the antisite positions Ga_{As} . It also increases the mechanical stability of the crystal lattice since the local deformation for Ga_i and Ga_{As} defects have the same sign.

Table 1. Structural characteristics of the elements.

Element	Atomic weight, gm/mole	X-ray density, gm/cm ³	Atomic volume, cm ³
Si	28.08	2.332	12.04
Ga	69.72	5.908	11.8
Ga in GaAs	-	5.317	15.0
As	74.92	5.77	12.98
As in GaAs	-	5.317	12.2
α -Sn	118.7	5.77	20.5

The values of the defect concentrations V_{As} , Ga_i and Ga_{As} depend on the Si concentration. Si in GaAs may occupy the both type of vacancies creating defects Si_{Ga} and Si_{As} though somehow always prefers the vacancies in the Ga sublattice [4]. If the concentration of Si is low the excessive Ga mostly occupies the interstitial position in crystal, expanding the crystal lattice and bending the structure toward the epitaxial layer (Fig.1a). If the Si concentration grows up the concentration of Ga_{As} defects also grows

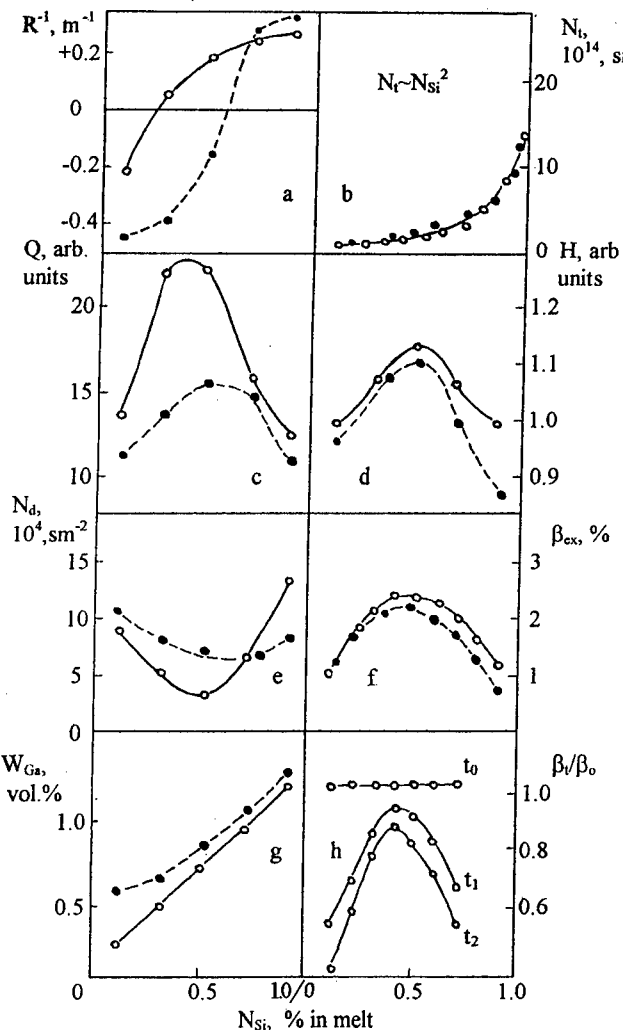


Fig.1. GaAs-LEDs characteristics at different Si concentrations
 a-crystal planes curvature; b-deep level concentrations;
 c-mechanical quality; d-microhardness; e-density of dislocations;
 f-external quantum efficiency; g-Ga concentration;
 h-changing of external quantum efficiency with time during
 the accelerated test

Melt-solution cooling rate: 0.5°C/min ;  7°C/min

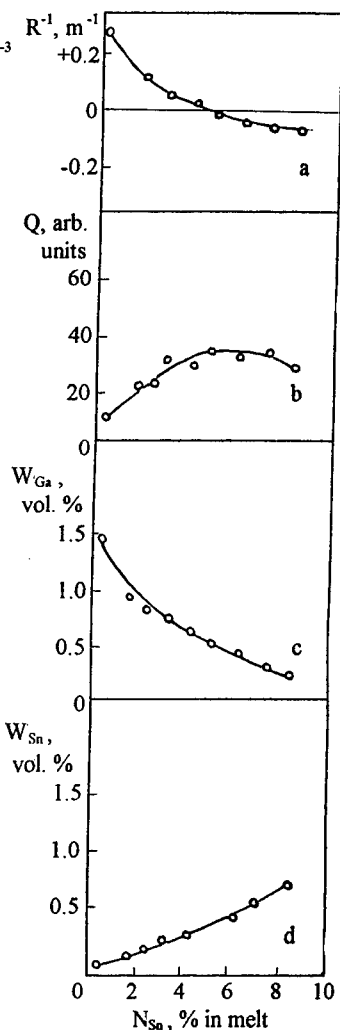


Fig. 2. GaAs-LEDs characteristics at different Si concentrations
 a-crystal planes curvature;
 b-mechanical quality;
 c-Ga concentration;
 d-Sn concentration

up and the excessive Ga makes less influence on crystal lattice. Along with the increase of Si concentration in melt-solution its concentration in As-vacancies grows up. The unstable structural clusters $\text{Si}_{\text{Ga}}[\text{Si}_{\text{As}}(\text{Ga}_{\text{As}})_3](\text{Ga}_{\text{As}})_{12}$ may be formed. These clusters may collapse forming the inclusions of metallic Ga. Si though may be considered as a beginning of the Ga metallic phase. The concentration of Ga inclusions grows up along with Si concentration growth (Fig.1g). The collapse of clusters cause the shrinkage of crystal lattice because the atomic volume of Ga in metallic phase is much less then its atomic volume in GaAs (Table 1). Shrinkage of the epitaxial layer causes the bending of structure to the opposite direction (Fig.1a).

The described phenomena may be observed in the entire investigated range of Si concentrations. There is an optimum concentration of Si when there is no bending of the epitaxial structure. Then local areas described above balance to each other what reduces the gradients of IMS to their minimum values. It makes the crystal structure of the epitaxial layers relatively the most perfect (Fig.1c). The maximum values of microhardness (Fig.1d) and minimum values of dislocation density (Fig.1e) confirm the most relative firmness of crystal lattice.

The defect structure of the epitaxial layers determines the properties of LEDs made on their base. The LEDs with optimum Si concentrations reveal the maximum quantum efficiency of electroluminescence β_{ex} (Fig.1f) and the minimum degradational speed of this characteristic (Fig.1h).

The deep levels N_t that are responsible for nonemitting recombination (energy of activation $E_t = E_v + 0.44$ eV; cross section of main charge carries $\sigma_t = 10^{-17} \text{ cm}^2$ at $T=300\text{K}$) may be formed by $[\text{Si}_{\text{Ga}}-\text{Si}_{\text{As}}]$ complex whose concentration is proportional to square of Si concentration in melt (Fig.1b).

We expected that doping of melt-solution with impurity whose atomic volume is bigger then the atomic volumes of Ga, As, and Si (for example Sn) must cause the efficient compensation of IMS in GaAs epitaxial layers. This effect was observed the most clearly at big concentrations of Si. For instance, at $N_{\text{Si}} = 1,1\%$ of weight in liquid phase the calculated Sn concentration - N_{Sn} that compensates the IMS in epitaxial layers is about 4% of weight in melt-solution. The experimental N_{Sn} concentration that corresponds to the minimum of bending in structures was equal to the calculated one (Fig.2a). In this case the concentration of Ga inclusions decreases by 2-3 times (Fig.2c), mechanical perfectness (Q) of structures increases by 4-5 times (Fig.2b), and microhardness increases at 10%. At the same wave lenght of emission ($\lambda=1\mu\text{m}$) that corresponds to $N_{\text{Si}} = 1,1\%$ of weight the quantum efficiency of LEDs' luminescence β_{ex} increases at 20-100% and time of failure increases by 10 times.

References

- [1] Korolev V L and Sidorov V G 1988 *Phis. Tech. Poluprovod.* 22 1827-30
- [2] Zener C 1948 *Elasticity and Anelasticity of Metals* (Chicago)
- [3] Mitrohin V T, Yaroslavtsev N P, Izmailov N V, Rembeza S I, and Lisovenko V D 1985 Patent of USSR #1179183 GO1N25/02 (USSR)
- [4] Spitzer W G and Panish M 1969 *J. Appl. Phys.* 40 4200-6

Wide Bandgap Semiconductor RF Power Devices

C. E. Weitzel

Phoenix Corporate Research Laboratories
Motorola, Inc., MS-EL508
2100 E. Elliot Rd.
Tempe, AZ 85284 USA

Abstract. AlGaN HFET's have achieved the highest f_{max} 97 GHz. 4H-SiC MESFET's have achieved the highest power densities, 3.3 W/mm at 850 MHz (CW) and at 10 GHz (pulsed). On the other hand, 4H-SiC SIT's have achieved the highest output power, 450 W (pulsed) at 600 MHz and 38 W (pulsed) at 3 GHz. Moreover a one kilowatt, 600 MHz SiC power module containing four SIT's with a total source periphery of 94.5 cm has been demonstrated.

1. Introduction

In recent years, wide bandgap semiconductors, silicon carbide and gallium nitride, have received increased attention because of their potential for a wide variety of high-power, high-frequency devices [1-3]. Their unique material properties, high electric breakdown field and high saturated electron drift velocity, are what gives these materials their tremendous potential in the high-frequency power device arena. The data in Table 1 allows a comparison of the basic material properties of silicon, gallium arsenide, 4H silicon carbide, and gallium nitride. Another SiC polytype 6H is not included in this comparison because its lower electron mobility [4] yields devices with inferior performance compared to 4H devices. Wide bandgap semiconductor devices will have superior high voltage performance to Si and GaAs devices primarily because of their higher breakdown field. In addition planar GaN heterojunction devices could have superior performance to planar SiC devices if the excessive heating of present GaN devices fabricated on sapphire substrates can be overcome. Two possible solutions to the heating limitation is the use of a SiC substrate in place of a sapphire substrate or flip chip packaging. The two SiC high-frequency devices that have demonstrated the most impressive RF power performance are MESFET's (MEtal Semiconductor Field Effect Transistor) and SIT's (Static Induction Transistor). The AlGaN HFET's (Heterojunction FET) have demonstrated the most impressive performance in the gallium nitride material system. This paper will review the exciting achievements that have been made in the area of wide bandgap semiconductor high power RF devices.

Table 1. Material properties of silicon, gallium arsenide, silicon carbide, and gallium nitride.

Property	Units	Silicon	GaAs	4H-SiC	GaN
Bandgap	eV	1.11	1.43	3.2	3.4
Dielectric Const	ϵ_r	11.8	12.8	9.7	9
Breakdown Field ($N_d = 1 \times 10^{17} \text{ cm}^{-3}$)	V/cm	6×10^5	6.5×10^5	35×10^5	35×10^5
Saturated Velocity	cm/sec	1×10^7	1×10^7	2×10^7	1.5×10^7
Electron Mobility	$\text{cm}^2/\text{V}\cdot\text{sec}$	1350	6000	800	1000
Hole Mobility	$\text{cm}^2/\text{V}\cdot\text{sec}$	450	330	120	300
Therm Conductivity	$\text{W}/\text{cm}\cdot^\circ\text{K}$	1.5	0.46	4.9	1.3

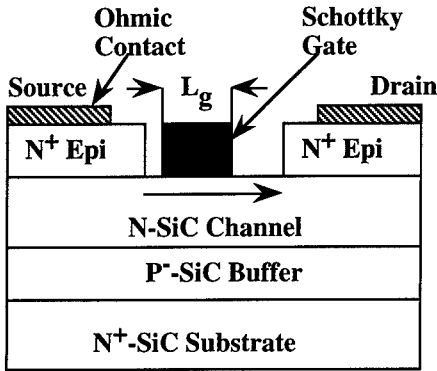


Fig. 1. Cross section of a SiC MESFET. Electrons flow laterally from source to drain confined to the n-type channel by the P⁺ buffer layer and controlled by the Schottky gate.

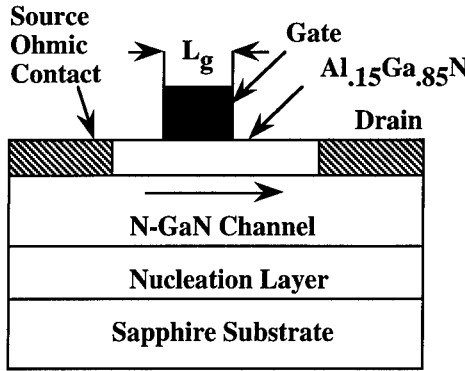


Fig. 2. Cross sectional view of an AlGaN HFET. Electrons flow laterally from the source to drain confined by the nucleation layer and controlled by the gate.

2. Device Structures

2.1 MESFET's and HFET's

SiC MESFET's are lateral devices with source and drain ohmic contacts on the top surface of the wafer (Fig 1). These contacts are typically placed on top of an N⁺ epitaxial layer to reduce contact resistance and are separated by a more lightly doped (1×10^{17}) n-type channel region [5]. The majority carriers flow in the channel (arrow) from source to drain and are controlled by a negative potential applied to the Schottky gate contact. Typically device isolation is achieved with a P⁺ buffer layer on a conducting N⁺ SiC substrate. More recently high resistivity substrates have been used in place of the P⁺ buffer layer to reduce bond pad capacitance and thereby to achieve higher cut-off frequency devices.

AlGaN HFET's (Fig 2) are also lateral devices, but contain a more complex material structure than the SiC MESFET. First, because GaN substrates are not readily available, the GaN epitaxial channel layer is grown on a sapphire substrate with an interposed nucleation layer [6,7]. Wider bandgap Al_{1.15}Ga_{.85}N is grown on the channel layer forming a quantum well at the interface. The very high sheet carrier density $1 \times 10^{13} \text{ cm}^{-2}$ in the quantum well gives the AlGaN HFET very high current carrying capability and high transconductance. Both of which are very attractive for high frequency power devices.

2.2 SIT's

In contrast to FET's, SiC SIT's are vertical devices (Fig 3) with a source ohmic contact on the top and a drain ohmic contact on the back of the wafer. Between these two N⁺ regions is an N⁻ SiC epitaxial drift layer (1×10^{16}) whose doping is one of the factors that determines the device's breakdown voltage, pinch-off voltage, and transconductance. Trenches are etched to define the channel region and Schottky gate contacts are formed on the bottom and along the sidewalls of the trench. Majority carriers flow from the source contact to the drain contact through the n-type channel region. Two arrows are shown to indicate that the SIT structure [8] actually consists of two vertical channel regions each controlled by a different gate electrode. Therefore the SIT can be visualized as two vertically oriented MESFET's placed back-to-back. By applying a negative voltage to the gate contacts the current flow in each of the two channel can be modulated and even decreased to zero when the depletion regions under each gate contact meet in the middle of the channel.

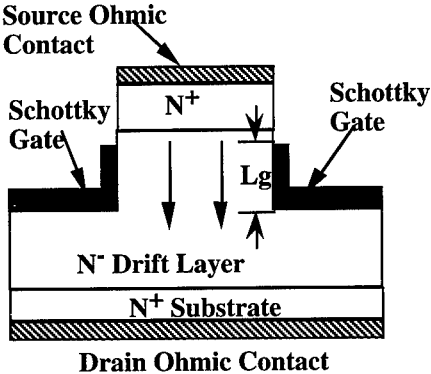


Fig. 3. Cross sectional view of an RF SiC static induction transistor (SIT). Electrons flow vertically from the source to drain subject to Schottky gate control.

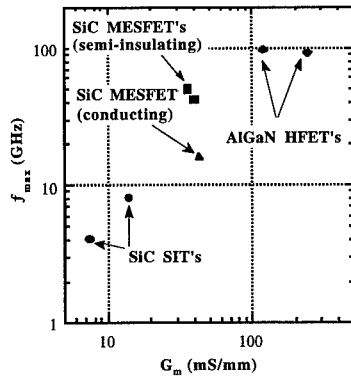


Fig. 4. f_{\max} of SiC SIT's, SiC MESFET's and AlGaN HFET's.

3. High Frequency Performance

The high frequency performance of a transistor is characterized by two parameters f_T and f_{\max} . f_T is the unity current gain cutoff frequency and f_{\max} is the maximum frequency of oscillation. To first order the values of these two figures of merit [9] are determined by the transconductance G_m , gate-source capacitance C_{gs} , gate-drain capacitance C_{gd} , output conductance G_{ds} , source resistance R_s , and gate resistance R_g of the transistor,

$$f_T = \frac{G_m}{2\pi(C_{gs} + C_{gd})} \quad (1)$$

$$f_{\max} = \frac{f_T}{2\sqrt{G_{ds}(R_s + R_g) + 2\pi f_T C_{gd} R_g}} \quad (2)$$

The high frequency performance of RF devices can be compared by plotting f_{\max} versus transistor transconductance G_m (Fig 4). Eqs. 1 and 2 can be used to help understand the large differences in G_m and f_{\max} that are seen when comparing SiC SIT's, SiC MESFET's, and AlGaN HFET's. Of these three device types the SIT's have the lowest G_m and f_{\max} primarily because of the large channel thickness which is determined by lithography, etching, and minimum source contact size. The typical double channel region is 2 μm thick with a doping density of $1 \times 10^{16} \text{ cm}^{-3}$ [10]. The actual channel thickness and doping determine whether the device operates in the SIT mode, FET mode, or mixed mode. The mixed mode is preferred over the SIT mode because of higher G_m and lower G_{ds} both of which contribute to higher f_{\max} [11]. SIT's with air bridged source contacts to reduce C_{gs} and C_{gd} have achieved an f_{\max} of 8 GHz [12].

Because FET's are lateral devices with channel thicknesses determined by epitaxial growth or quantum wells, their G_m 's are necessarily higher than those of SIT's. These higher G_m 's lead directly to higher frequency performance (Fig 4). SiC MESFET's fabricated on conducting substrates have achieved f_{\max} 's as high as 16.3 GHz [13]. SiC MESFET's on semi-insulating substrates have achieved even higher frequency performance ($f_{\max} > 42$ GHz) because the semi-insulating substrate

has helped reduce some of the FET's parasitic capacitances C_{gs} [14,15]. In the last year AlGaN HFET's have achieved the highest f_{max} 's ever reported for wide bandgap semiconductor devices. These high frequencies can be directly attributed to the quantum well channels of these devices. Quantum well channel confinement results in very high G_m 's (> 100 mS/mm) and the resulting very high f_{max} 's (> 90 GHz) [16,17].

4. RF Power Performance

The theoretical power capability of an RF FET's is limited by the knee voltage, drain breakdown voltage, and maximum drain current [18] and is calculated by,

$$P_{max} = \frac{I_{dson} (V_b - V_{knee})}{8} \quad (3)$$

where P_{max} is the maximum RF power, I_{dson} is the maximum drain current, V_b is the drain breakdown voltage, and V_{knee} is the knee voltage as shown below in Fig 5. I_{dson} is the drain current with a small positive voltage on the gate electrode. The allowable positive gate voltage (≈ 1 V) will depend on the channel doping and the work function of the gate metal. The positive gate voltage is limited by the onset of forward Schottky diode current. Although Eq. 3 applies specifically to FET's the same approach would apply equally well to other electronic devices. Therefore this discussion is also valid for a SIT which is operated in the SIT mode, the MESFET mode, or mixed mode even though the I-V characteristics may be somewhat different from those shown in Fig. 5. The DC load line shown in Fig. 5 would be used in a Class A RF amplifier with the drain voltage $V_d = (V_b + V_{knee})/2$. The slope of the load line is $1/R_L$ where R_L is the value of the resistance placed across the output of the FET.

The output power of SiC MESFET's and AlGaN HFET's is maximized by achieving the highest I_{dson} and V_b while minimizing V_{knee} . I_{dson} can be increased and V_{knee} can be reduced by raising the channel doping, but as mentioned earlier, this will lower the breakdown voltage V_b . Therefore a design tradeoff must be made. Power amplifier efficiency is also important and can be improved by reducing V_{knee} . One of the advantages of SiC MESFET's and AlGaN HFET's compared to Si and GaAs based devices is their higher breakdown voltage. This higher breakdown voltage is a direct result of the wider bandgap of SiC and GaN, see Table 1.

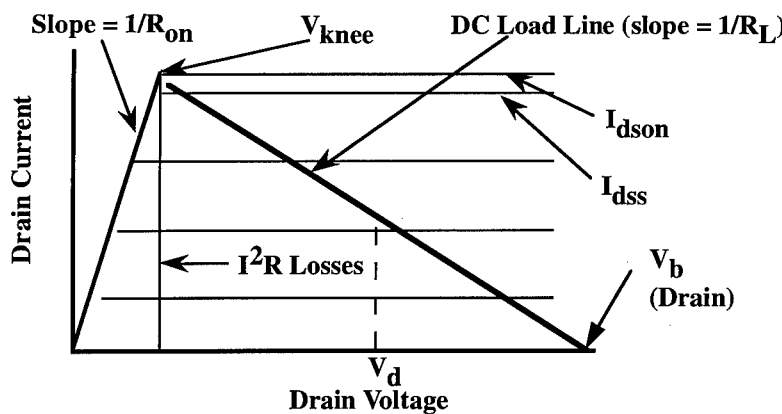


Fig 5. Piecewise linear MESFET drain characteristic.

The same considerations apply to SiC SIT's for maximizing output power. However being a vertical device the SIT structure offers advantages in achieving higher breakdown voltage than the FET's. The breakdown voltage in a FET is limited not only by the doping of the channel, but also by the surface breakdown between gate and drain. The SIT breakdown voltage is not limited by this surface component and therefore, for the same channel doping density would have a higher drain breakdown voltage than the MESFET. This gives the SIT an advantage for high voltage applications. On the other hand, as mentioned earlier, the channel doping of the SIT is usually lower than the MESFET. As a result the I_{dson} of the SIT is smaller than that of either the SiC MESFET or AlGaN HFET.

Some of these differences are apparent in the experimental data that has been reported to date. Table 2. SiC MESFET's have achieved the highest power density of 3.3 W/mm which was achieved using a conducting substrate with $V_d = 50$ V at a frequency of 850 MHz [19] and using a semi-insulating substrate with $V_d = 45$ V at a frequency 10 GHz [20]. However it should be pointed out that the 850 MHz result was achieved during CW (continuous wave) operation whereas the 10 GHz result was pulsed. A device operated under pulsed conditions experiences less self-heating and therefore is able to deliver more RF power than a device operated under CW conditions, everything else being equal. These two results do, however, illustrate the significant increase in frequency performance that can be achieved by using a semi-insulating rather than a conducting substrate. The highest total power reported for a single SiC MESFET is 15 W at 2.1 GHz V[15]. Unfortunately the power density of this device 0.83 W/mm at 30 V is approximately the same as that achieved with commercially available Si LDMOS FET's at 48 V [21]. The highest reported power density for an AlGaN HFET is 2.56 W/mm with $V_d = 25$ V at 10 GHz [17]. Unfortunately this device was fabricated on a sapphire substrate whose poor thermal conductivity probably severely limited its power performance. In spite of this the 2.56 W/mm at 25 V shows that the AlGaN HFET technology could offer strong competition to SiC RF power devices as the thermal limitations are resolved. Although FET's have been demonstrated with the highest power densities, the highest output power devices have been a UHF SIT which achieved 450 W pulsed at 600 MHz [22] and an S-Band SIT which achieved 38 W pulsed at 3 GHz [12] both with $V_d = 90$ V. Moreover a one kilowatt, 600 MHz SiC power module containing four SIT's with a total source periphery of 94.5 cm has been demonstrated [22].

Table 2. RF power performance of SiC MESFET's, SiC SIT's, Si LDMOS FET's and AlGaN HFET's.

Device	I_{dss} (mA/mm)	V_d (V)	Frequency (GHz)	Duty Cycle	Power Density (W/mm)	Total Power (W)	Ref.
MESFET (4H-SiC)	225	50	0.85	CW	3.3	1.1	[18]
MESFET (4H-SiC)	300	54	1.8	CW	2.8	0.9	[5]
MESFET (4H-SiC)		30	2.1	CW	0.83	15	[15]
MESFET (4H-SiC)		45	10	Pulsed	3.3	6.35	[20]
AlGaN HFET	350	25	10	CW	2.56	0.26	[17]
Si LDMOS FET		48	0.85	CW	0.87	80	[21]
SIT (4H-SiC)		90	0.6	Pulsed	1.3	450	[22]
SIT (4H-SiC)	65	90	3	Pulsed	1.2	38	[12]
SIT Module		90	0.6	Pulsed	1.058	1000	[22]

5. Conclusions

Impressive RF power performance has been demonstrated by three radically different wide bandgap semiconductor power devices, SiC MESFET's, SiC SIT's, and AlGaN HFET's. At this time each of these devices excels in different aspects of power performance. AlGaN HFET's have achieved the highest f_{max} 97 GHz. 4H-SiC MESFET's have achieved the highest power densities, 3.3 W/mm at 850 MHz (CW) and at 10 GHz (pulsed). On the other hand, 4H-SiC SIT's have achieved the highest output power, 450 W (pulsed) at 600 MHz and 38 W (pulsed) at 3 GHz. Moreover a one kilowatt, 600 MHz SiC power module containing four SIT's with a total source periphery of 94.5 cm has been demonstrated. As these device technologies mature they will play important roles in RF power generation.

Acknowledgements

The author would like to acknowledge the support of the management and technical staff of Motorola's Phoenix Corporate Research Laboratories and especially Karen Moore for many helpful discussions.

References

- [1] Trew R J, Yan J and Mock P M 1991 *Proc. IEEE* 79 598-620
- [2] Weitzel C E, Palmour J W, Carter Jr. C C, Moore K, Nordquist K J, Allen S, Thero C and Bhatnagar M 1996 *Trans. IEEE Electron Devices* 43 1732-1741
- [3] Mohammad S N, Salvador A A and Morkoc H 1995 *Proceedings of the IEEE* 83 1306-1355
- [4] Schaffer W J, Negley G H, Irvine K G and Palmour J W 1994 *Diamond, SiC, and Nitride Wide Bandgap Semiconductors* 339 (Material Research Society) 595-600
- [5] Weitzel C E, Palmour J W, Carter, Jr. C H and Nordquist K 1994 *IEEE Electron Device Letters* 15 406-408
- [6] Wu Y -F, Keller B P, Keller S, Kapolnek D, Denbaars S P and Mishra U K 1996 *54th Device Research Conference Digest* 60-61
- [7] Shur S M and Khan M A 1997 *MRS Bulletin* XXII 44-50
- [8] Nishizawa J, Terasaki T and Shibata J 1975 *IEEE Trans. Electron Devices* ED-22 185-197
- [9] Ohkawa S, Suyama K and Ishikawa H 1975 *FUJITSU Scientific & Technical Journal* 151-173
- [10] Agarwal A K, Augustine G, Balakrishna V, Brandt C D, Burk A A, Chen L S, Clarke R C, Esker P M, Hobgood H M, Hopkins R H, Morse A W, Rowland L B, Seshadri S, Siergiej R R, Smith Jr. T J and Sriram S 1996 *IEDM Technical Digest* 225-230
- [11] Clarke R C, Agarwal A K, Siergiej R R, Brandt C D and Morse A W 1996 *54th Device Research Conference Digest* 62-63
- [12] Siergiej R R, Morse A W, Esker P M, Smith Jr. T J, Bojko R J, Rowland L B and Clarke R C 1997 *55th Device Research Conference Digest* 136-137
- [13] Moore K, Weitzel C, Nordquist K, Pond III L, Palmour J, Allen S, Tsvetkov V K, Macko S and Carter Jr.C 1995 *15th Biennial IEEE/Cornell University Conference on Advanced Concepts in High Speed Semiconductor Devices and Circuits* 12-13
- [14] Sriram S, Augustine G, Burk A A, Glass R C, Hobgood H M, Orphanos P A, Rowland L B, Smith T J, Brandt C D, Driver M C and Hopkins R H 1996 *IEEE Electron Device Letters* 17 369-371
- [15] Allen S T, Sadler R A, Alcorn T S, Palmour J W and Carter Jr. C H 1997 *IEEE MTT-S Digest* 57-60
- [16] Khan M A, Chen Q, Shur M S, Dermott B T, Higgins J A, Burn J, Schaff W J and Eastman L F 1996 *IEEE Electron Device Letters* 17 584-585
- [17] Wu Y -F, Keller B P, Keller S, Nguyen N X, Le M, Nguyen C, Jenkins T J, Kehias L T, Denbaars S P and Mishra U K 1997 *55th Device Research Conference Digest* 142-143
- [18] Weitzel C E 1996 *Silicon Carbide and Related Materials 1995* (Inst. Phys. Pub., Bristol) 142 765-768
- [19] Moore K E, Weitzel C E, Nordquist K J, Pond III L L, Palmour J W, Allen S and Carter Jr. C H 1997 *IEEE Electron Device Letters* 18 69-70
- [20] Sriram S, Smith T J, Rowland L B, Burk Jr. A A, Augustine G, Balakrishna V, Hobgood H M and Brandt C D 1997 *55th Device Research Conference Digest* 138-139
- [21] Cardullo M and Davidson B 1997 *Wireless Systems Design* June 28-30 and private communications
- [22] Morse A W, Esker P M, Clarke R C, Brandt C D, Siergiej R R and Agarwal A K 1996 *IEEE MTT-S Digest* 677-680

High Speed High Power AlGaN/GaN Heterostructure Field Effect Transistors with Improved Ohmic Contacts

**Kenneth K. Chu, Michael J. Murphy, Jinwook Burm[‡], William J. Schaff,
and Lester F. Eastman**

School of Electrical Engineering and National Nanofabrication Facility, Cornell University,
Ithaca, NY 14853, USA

[‡]Lucent Technologies, Murray Hill, NJ 07974, USA

Andrei Botchkarev, Haipeng Tang, and Hadis Morkoç

Materials Research Laboratory and Coordinated Science Laboratory, University of Illinois
at Urbana-Champaign, Urbana, IL 61801, USA

Abstract. Ti/Al/Ti/Au ohmic contacts with low contact resistance (as low as $0.24 \Omega \text{ mm}$) were used in fabricating short gate length modulation-doped field effect transistors on MBE-grown AlGaN/GaN layers. Maximum drain current achieved was above 1 A/mm with a transconductance of 182 mS/mm . RF measurements showed a maximum f_T of 35.9 GHz and an f_{MAX} of 57.0 GHz , both achieved with $0.15 \mu\text{m}$ gate length. Simple analysis showed an electron saturation velocity of $1.3 \times 10^7 \text{ cm/s}$ in our device structure. Maximum gate-drain breakdown voltages for these devices were measured to be 30 to 35 V .

1. Introduction

There has been increased interest in nitride-based heterostructure field effect transistors (HFET's) for use in high power applications. The large conduction band discontinuity allows for high electron sheet densities and thus high maximum drain currents, while the large energy bandgap gives extremely high breakdown voltages. Indeed AlGaN/GaN HFET's have shown drain currents above 1.1 A/mm [1] and breakdown voltages over 200 V [2]. On the other hand, good electron mobility (in excess of $1,500 \text{ cm}^2/\text{V s}$) and high saturation velocity ($2 \times 10^7 \text{ cm/s}$) have also allowed GaN based HFET's to achieve f_T as high as 46.9 GHz and f_{MAX} over 100 GHz [3].

Recent advances in nitride HFET fabrication technology include the lowering of ohmic contact resistance from relatively high values ($>2 \Omega \text{ mm}$) [3],[4] to $0.5 \Omega \text{ mm}$ or lower utilizing the Ti/Al based contacts [2],[5]. Since the good RF performance as demonstrated in reference [3] was obtained with relatively high values of contact resistance, this work was focused on the fabrication of high frequency AlGaN/GaN HFET's using improved ohmic contacts. Emphasis was also put on retaining a high breakdown voltage despite the high electron sheet density and short gate lengths used in these devices.

2. Layer structure and Device Fabrication

The AlGaN/GaN HFET layer structure used in this study was that of a modulation-doped field effect transistor (MODFET). The wafer was MBE-grown and included (from bottom to top) a sapphire substrate, $0.1 \mu\text{m}$ of AlN nucleation layer, $1.5 \mu\text{m}$ of undoped GaN, 20 \AA of undoped AlGaN spacer, 20 \AA of Si-doped AlGaN layer ($N_d = 7 \times 10^{19} \text{ cm}^{-3}$) and 110 \AA of undoped AlGaN barrier. The Al mole fraction used in all the AlGaN layers was 0.3. Hall measurements showed a mobility of $405 \text{ cm}^2/\text{V s}$ and an electron sheet density of $1.67 \times 10^{13} \text{ cm}^{-2}$.

Before the actual fabrication of the transistors, different ohmic metallization schemes were tested on another chip of the same wafer to optimize the ohmic contacting step. Different metal systems were

deposited and annealed at 800°C, while their contact resistances were monitored as a function of annealing time. 800°C was chosen instead of the usual annealing temperature of 900°C to minimize any surface damage induced by annealing. Among the different metal systems used, Ti/Al/Ti/Au (200 Å/ 1000 Å/ 450 Å/ 550Å) and Pd/Al/Ti/Au (200 Å/ 1000 Å/ 450 Å/ 550Å) gave the best results. Minimum contact resistance for the Ti/Al/Ti/Au system was 0.60 Ω mm with a specific contact resistance of $3.44 \times 10^{-6} \Omega \text{ cm}^2$, while the Pd/Al/Ti/Au system achieved 0.25 Ω mm and $5.95 \times 10^{-7} \Omega \text{ cm}^2$. However, adhesion of the Pd/Al/Ti/Au contact to the nitride surface had to be improved. Also, it was noteworthy that the sheet resistance of the material stayed constant at 1030 Ω per square through the 120 s of 800°C annealing, suggesting that the surface damage (nitrogen desorption) induced by the anneal was minimal.

HFET's were then fabricated using the Ti/Al/Ti/Au ohmic system. The transistor fabrication process included mesa isolation, ohmic contact formation, connection pad deposition and gate metallization. After annealing the ohmic metal at 800°C for 60 s, a low contact resistance of 0.24 to 0.4 Ω mm was measured with TLM patterns. This variation of contact resistance was attributed mainly to non-uniformity of the wafer, as the wafer was not rotated during growth. T-shaped gates were defined by electron beam lithography and formed by evaporating Pt/Au (400Å/ 2600Å) or Ni/Au (200Å/ 2800Å). Using SEM, the gate lengths were estimated to be varying from 0.15 to 0.28 μm, a direct result from variation of the exposure dose. Nominal gate-drain spacings were 0.75 and 1 μm.

3. Device performance

Shown in Figure 1(a) is the DC current-voltage characteristics of the fabricated transistors. The maximum drain current was above 1 A/mm, a result of the high electron sheet density of the material. (Measurement was stopped at 1 A/mm due to the current compliance of the measurement system.) Maximum DC transconductance was 182 mS/mm. Linear and steep current-voltage characteristics at low drain biases signify the excellent quality of the ohmic contacts. Total drain-source resistance was measured to be 2.6 Ω mm.

As seen in Figure 1(a), there was a non-zero output conductance, particularly for lower current levels. This was attributed to short-channel effects created by the short gate length and the absence of a backside barrier to the conduction channel. At higher current levels the output conductance was reduced and even became negative. This was due to the additional effect of carrier mobility lowering with increasing temperature.

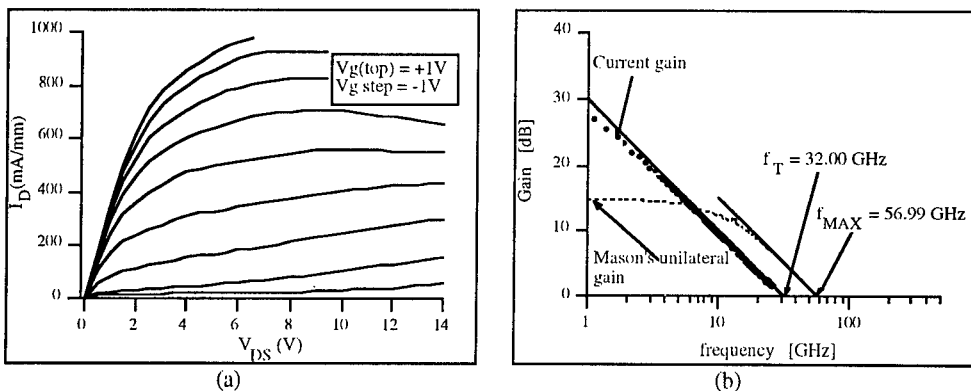


Figure 1. (a) DC characteristics of the AlGaN/GaN MODFET's showing drain current over 1 A/mm, and (b) RF performance of a 75 μm periphery device

Despite a thin barrier, good ohmic contacts and high electron sheet density, the measured static transconductance (g_m) was only 182 mS/mm, 13% lower than the result obtained in another layer structure with the same AlGaN barrier thickness [6]. One possible reason is electrons trapped in the AlGaN barrier (in traps or at the conduction band minimum of the donor layer) which would then have a screening effect on the gate potential, reducing the effectiveness of charge modulation by the gate.

Figure 1(b) gives the RF performance of a 75 μm periphery device. An f_T of 32.0 GHz and an f_{MAX} of 57.0 GHz were achieved. A similar device with a 100 μm periphery demonstrated an f_T of 35.9 GHz and an f_{MAX} of 54.8 GHz. SEM studies showed a gate length of 0.15 μm for these devices. Although the ohmic contact was greatly improved compared to devices in reference [3], the RF performance was not as good. This could be attributed to a different layer structure and longer gate lengths utilized.

An estimate of the electron saturation velocity (v_{sat}) in our structure can be obtained from the RF data as follows. For a field effect transistor, total time delay for electron transit (τ_{total}) can be given by

$$\tau_{\text{total}} = \frac{1}{2\pi f_T} = \tau_{\text{RC}} + \tau_g + \tau_{\text{gd}} \quad (1)$$

where τ_{RC} is the RC time constant for charging the gate capacitances, τ_g is the transit time of electrons under the gate and τ_{gd} is the delay time for electrons to traverse the gate-drain separation. They are in turn given by

$$\tau_{\text{RC}} = (R_g + R_s)(C_{\text{gs}} + C_{\text{gd}} + C_{\text{gpad}}) \quad (2)$$

$$\tau_g = \frac{L_{\text{g,eff}}}{v_{\text{sat}}} \quad (3)$$

$$\tau_{\text{gd}} = \frac{L_{\text{gd}} + L_{\text{transfer}}}{2v_{\text{sat}}} \quad (4)$$

where R_g is the gate access resistance, R_s is the source resistance, and C_{gs} , C_{gd} and C_{gpad} are gate-source, gate-drain and gate pad capacitances respectively. $L_{\text{g,eff}}$ is the effective gate length which includes the fringing field effect. L_{gd} is the physical gate-drain separation and L_{transfer} is the ohmic contact transfer length. The factor of 2 in equation (4) comes from the fact that here an induced current is passing through a region with a relatively constant field [7], as is the case of bipolar transistors where the collector depletion transit delay takes on a similar expression [8]. For a rigorous mathematical treatment readers are referred to reference [9].

Substituting the appropriate values from various DC measurements and RF parameter extraction, we have an estimate of the electron saturation velocity in our structure:

$$v_{\text{sat}} = 1.3 \times 10^7 \text{ cm/s}$$

which is about 60% of the theoretical value obtained from Monte Carlo calculations [10]. As material quality and processing techniques continue to improve, this saturation velocity value is expected to increase towards the theoretical maximum.

4. Considerations as a power device

For these transistors to be useful as power devices, they must have a high maximum drain current together with a high breakdown voltage at pinch-off. Maximum drain current was high and above 1 A/mm, but these devices showed only a modest gate-drain breakdown voltage of 30 to 35 V, much less than some of the best results achieved in GaN based field effect transistors (> 200 V for large gate-drain spacing) [2]. This was the result of a relatively high gate leakage current on the gate at pinch-off. Because of the high sheet charge density in the layer structure, there would be a very high electric field underneath the gate in pinch-off conditions, giving rise to increased tunneling. Any additional field that comes from drain bias and field crowding effects for very short gates further worsen the situation. Indeed a recent experiment by the authors on the same layer structure showed an average gate-drain

breakdown voltage of 22.6 V for 0.15 μm -gates, 33.8 V for 0.3 μm -gates and 51.6 V for 1 μm -gates for the same gate-drain separations. Furthermore, the breakdown voltage variation with gate-drain spacing was small (as opposed to common observation), suggesting that the major breakdown mechanism occurred close to the gate, possibly tunneling in this case, and was not very sensitive to changes in gate-drain separation. Another plausible reason for high gate leakage would be surface states or carrier traps in the barrier that lead to conduction paths which were not accounted for in our original transistor design. With a better layer structure design, i.e. lower sheet charge density, this high gate leakage current is expected to be eliminated and transistors should show a much higher breakdown voltage.

5. Conclusions

We have demonstrated high frequency AlGaN/GaN MODFET's with improved ohmic contacts. With a contact resistance as low as 0.24 $\Omega \text{ mm}$, over 1 A/mm of drain current and 182 mS/mm of transconductance were obtained. RF measurements revealed $f_T = 35.9$ GHz and $f_{MAX} = 57.0$ GHz. However, these devices suffered from a relatively low gate-drain breakdown voltage of 30 to 35 V. Pending more detailed analysis, the gate leakage current that lowered the breakdown voltage was attributed to tunneling through the AlGaN barrier and/or conduction through traps and surface states. With improved layer structure design and processing techniques, AlGaN/GaN HFET's will reach their full potential as high frequency and high power devices.

Acknowledgements

This work was supported by ONR/MURI (Contract Monitor, Dr. K. Sleger), and was performed in part at the Cornell Nanofabrication Facility (a member of the National Nanofabrication Users Network) which is supported by the National Science Foundation under Grant ECS-9319005, Cornell University, and industrial affiliates.

References

- [1] H. Morkoç *et al.*, 1997 GaN Workshop.
- [2] Y. F. Wu, S. Keller, P. Kozodoy, B. P. Keller, P. Parikh, D. Kapolnek, S. P. Denbaars, and U. K. Mishra, *IEEE Elec. Dev. Lett.*, vol. 18, pp. 290-292, 1997.
- [3] J. Burm, K. Chu, W. J. Schaff, L. F. Eastman, M. A. Khan, Q. Chen, J. W. Yang, and M. S. Shur, *IEEE Elec. Dev. Lett.*, vol. 18, pp. 141-143, 1997.
- [4] M. A. Khan, M. S. Shur, and Q. Chen, *Appl. Phys. Lett.*, vol. 68, pp. 3022-3024, 1996.
- [5] Z. Fan, S. N. Mohammad, W. Kim, O. Aktas, A. E. Botchkarev, and H. Morkoç, *Appl. Phys. Lett.*, vol. 68, pp. 1672-1674, 1996.
- [6] S. N. Mohammad, Z. F. Fan, A. Salvador, O. Aktas, A. E. Botchkarev, W. Kim, and H. Morkoç, *Appl. Phys. Lett.*, vol. 69, pp. 1420-1422, 1996.
- [7] P. Asbeck, private communication.
- [8] S. M. Sze, *High-Speed Semiconductor Devices*, Wiley Interscience, 1990.
- [9] R. L. Pritchard, *Electrical Characteristics of Transistors*, McGraw-Hill, 1967.
- [10] J. Kolnik, I. H. Oguzmanm, K. F. Brennan, R. Wang, P. P. Ruden, Y. Wang, *J. Appl. Phys.*, vol. 78, pp. 1033-1038, 1995.

AlGaN/GaN MODFETs with Low Ohmic Contact Resistances by Source/Drain n⁺ Re-growth

Y.-F. Wu, D. Kapolnek, P. Kozodoy, B. Thibeault, S. Keller, B.P. Keller, S.P. Denbaars and U.K. Mishra

Department of Electrical & Computer Engineering, University of California, Santa Barbara, CA 93106

Abstract: n⁺ regrown source-drain regions have been used for AlGaN/GaN MODFETs to obtain a low-resistance ohmic contact and clear-cut ohmic boundaries which will potentially facilitate fabrication of deep submicron-gate devices. The process consists: 1. Formation of the SiO₂ re-growth mask by E-beam evaporation and lift-off; 2. Removal of the AlGaN layer in the ohmic region by RIE; 3. n⁺ GaN re-growth in the MOCVD reactor; 4. Ohmic metal deposition and annealing. A transfer ohmic contact resistance of 0.44 Ω-mm was achieved. Much improved device performance was obtained with the new ohmic scheme over the conventional scheme with the same metalisation.

1. Introduction

As a candidate for future power devices in microwave and millimeter frequencies, the GaN-channel FET has been consistently improving its performances as represented by an f_t of 50 GHz and a CW power density of 2.6 W/mm at 10 GHz^[1]. Low ohmic contact resistances are required to achieve a high power efficiency and high cut-off frequencies. Although a transfer contact resistance of 0.4 ~ 0.6 Ω-mm for AlGaN/GaN MODFETs can be obtained with the multi-layer ohmic scheme^[2], the high annealing temperature of 900 °C results in an ohmic alloy with large edge roughness of 0.3 ~ 0.4 μm, making implementation of deep sub-micron devices difficult^[3]. Here we report a new ohmic scheme using n⁺ source and drain re-growth which yielded both a low contact resistance and clear-cut ohmic boundaries with a lower annealing temperature.

2. Device fabrication and performance

The epi-layer structure for this study is shown in Fig.1 (a). The growth by metal organic chemical vapor deposition (MOCVD) started with a 200 Å GaN nucleation layer. This was followed by a 0.4 μm unintentionally doped (UID) GaN layer ($n \sim 4 \times 10^{16} \text{ cm}^{-3}$). The Al_{0.15}Ga_{0.85}N gating layer consisted of a 30 Å UID spacer, a 150 Å Si doped donor layer ($n \sim 3 \times 10^{18} \text{ cm}^{-3}$) and a 120 Å UID cap. The background doping density of the UID Al_{0.15}Ga_{0.85}N was $\sim 1 \times 10^{18} \text{ cm}^{-3}$.

Two samples with the same nominal structure were used for a direct comparison of the n⁺ regrown contact method with the conventional one. The process flow of the n⁺ re-growth method is shown in Fig.1. First, a 4000 Å SiO₂ pattern was deposited by electron beam (E-beam) evaporation. With this as a mask the Al_{0.15}Ga_{0.85}N layer and 1000 Å of GaN in the source and drain regions were removed by Cl₂ reactive-ion-etching (RIE). Then the wafer was transferred into the MOCVD reactor and 6000 ~ 8000 Å of n⁺ GaN (Si doped to $2 \times 10^{18} \text{ cm}^{-3}$) was regrown. Over-growth was avoided by

choosing the proper orientation (please see reference [4] for details). Fig.2 shows the scanning electron microscope (SEM) image of the regrown source/drain regions. Inspection indicated that the roughness of the n⁺ GaN edge duplicated that of the SiO₂ boundary. The SiO₂ was removed with HF after the re-growth and the rest of the process was the same as for the conventional GaN MODFET: Ti/Al (200Å/2000Å) was evaporated and annealed at 670 °C. Mesa isolation was done by RIE with photo-resist as the mask. Finally, Ni/Au (200Å/4800Å) was deposited as the gate metal.

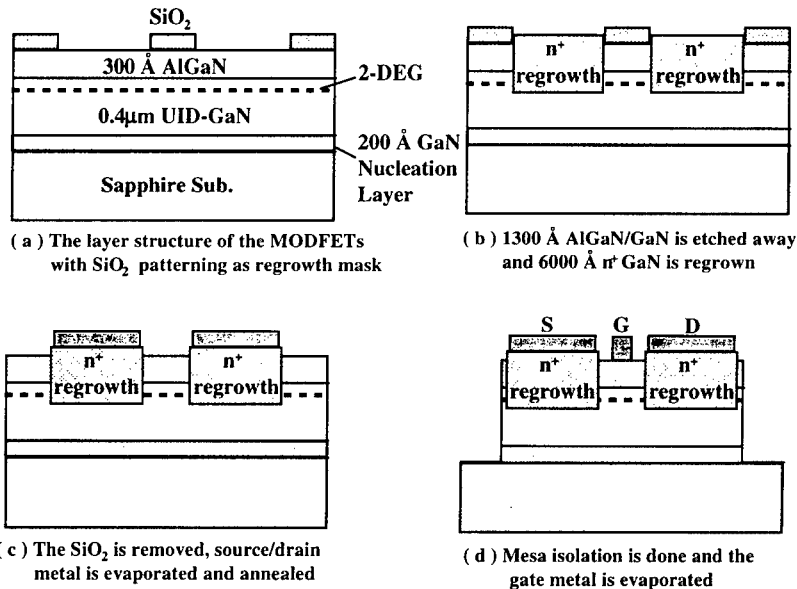


Fig.1 Process flow of the GaN MODFETs with n⁺ regrown ohmic contacts.

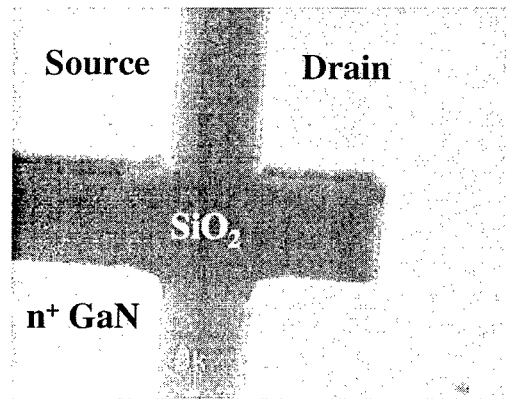


Fig.2 An SEM image of the n⁺ regrown source/drain regions with the SiO₂ mask ($L_{sd}=4\mu m$).

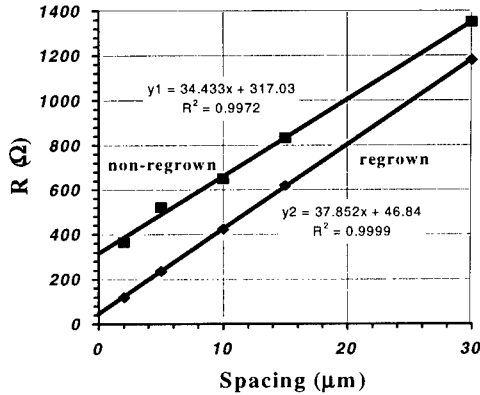


Fig.3 Linear curve fits of the TLM measurement results for determining contact resistances

(1. conventional method: $R_c=3.0 \Omega\text{-mm}$; 2. n^+ regrowth method: $R_c=0.44 \Omega\text{-mm}$).

On-wafer, 19 μm square, TLM patterns with separations from 2 to 30 μm were used for the contact-resistance measurement. Fig.3 shows the results of both methods. A typical transfer contact resistance of 0.44 Ω-mm was achieved with the regrown ohmic contact, not far from the 0.2 Ω-mm value generally obtained with GaAs MESFETs. Compared with the 3 Ω-mm value using the conventional scheme, the new method showed an improvement by a factor of 7. The MODFET output IV characteristics are shown in Fig.4. The new scheme resulted in a much lower knee voltage of ~ 3 V, a higher transconductance of 170 mS/mm and a better current-gain cut-off frequency of 10 GHz, as compared with the values of 7 V, 130 mS/mm and 7 GHz accordingly for the conventional scheme (gate-lengths were both 1.2 μm). The breakdown voltages for both devices with a gate-drain separation of 1 μm are ~ 100 V, showing no degradation due to the re-growth process.

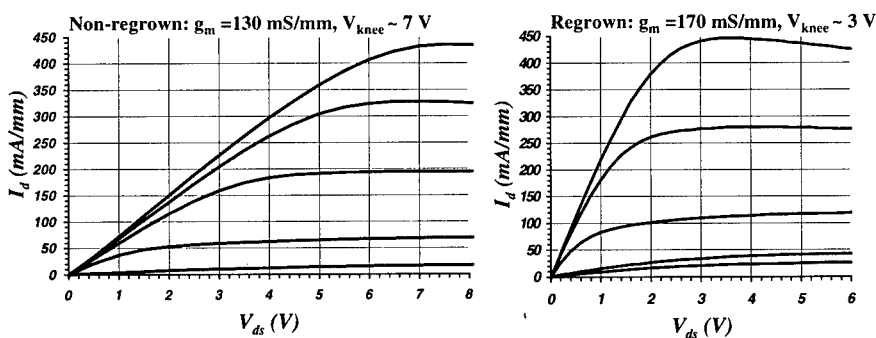


Fig.4 Comparison of the output characteristics of the MODFETs with two ohmic contact schemes
(V_{gs} start: +1.5V, step: -1V).

3. Conclusion

we have developed a new ohmic contact scheme for AlGaN/GaN MODFETs with n⁺ re-growth, which yielded a low transfer ohmic contact resistance of 0.44 Ω-mm. Since the n⁺ ohmic region is defined by E-beam evaporated SiO₂ through lift-off, a clear-cut ohmic edge can be achieved which potentially facilitates fabrication of deep sub-micron devices.

Acknowledgment

This work was supported by ONR/MURI (contract monitor: Dr. K. Sleger) and AFOSR (contract monitor: Dr. G. Witt).

^[1] Y.-F. Wu, B.P. Keller, S. Keller, N.X. Nguyen, M. Le, C. Nguyen, T.J. Jenkins, L.T. Kehias, S.P. Denbaars, and U.K. Mishra, "High speed and high power AlGaN/GaN MODFETs", presented in the 55th Device Research conference, Colorado State University, June 23-25, 1997.

^[2] Z. Fan, S.N. Mohammad, W. Kim, O. Aktas, A.E. Botchkarev, and H. Morkoc, "Very low resistance ohmic contact to n-GaN", *App. Phys. Lett.* 68 (12), 1672-1674, 18 March 1996.

^[3] J. Burm, K. Chu, W.J. Schaff, L.F. Eastman, M.A. Khan, Q. Chen, J. W. Yang, and M.S. Shur, "0.12-μm gate III-V nitride HFET's with high contact resistances", *IEEE Electron Device Letters*, Vol. 18, No.4, 141-143, April 1997.

^[4] D. Kapolnek, S. Keller, R. Vetur, R.D Underwood, P. Kozodoy, S.P. DenBaars and U.K. Mishra, "Anisotropic epitaxial lateral growth in GaN selective area epitaxy", *Appl. Phys. Lett.* 71 (9), 1 Sept. 1997.

Wide Bandgap Collectors in GaInP/GaAs Heterojunction Bipolar Transistors with Increased Breakdown Voltage

R.M. Flitcroft, B.C. Lye, H.K. Yow, P.A. Houston, C.C. Button, J.P.R. David.

Department of Electronic and Electrical Engineering, The University of Sheffield, Mappin Street, Sheffield S1 3JD, UK.

Abstract. $\text{Al}_{0.11}\text{Ga}_{0.89}\text{As}$ in the base, adjacent to the collector has been used to eliminate the conduction band spike and demonstrate double HBTs with high breakdown voltages, BV_{CEO} and BV_{BCO} , of 44V (current gain of 20) and 54V respectively with a 1 μm thick GaInP collector doped to $2 \times 10^{16}\text{cm}^{-3}$ without any voltage dependence on the gain. The inferred electron lifetime in the AlGaAs base was found to be approximately ten times smaller than the equivalently doped GaAs. Analysis of the Kirk effect yielded an estimate of the effective velocity in the GaInP collector of $4.3 \times 10^6\text{cms}^{-1}$ at room temperature. A graded AlGaAs base and graded transition from GaInP at the base/collector junction to AlInP demonstrated a record breakdown voltage, $BV_{BCO}=74\text{V}$, for the same collector doping and thickness. Electron impact ionisation coefficients were measured for use in an Ebers-Moll model to predict breakdown voltage.

1. Introduction

A high breakdown voltage and good frequency and current handling near saturation are both required for high power and power added efficiency [1] in GaInP/GaAs high-power microwave HBTs. Lattice matched GaInP or AlInP as the collector material increases the breakdown voltage compared to GaAs but both have an undesirable conduction band spike at the junction with the GaAs base which compromises the device performance close to saturation. An n⁻ spacer layer at the base/collector junction and/or a high delta-doped layer in the conduction band spike, to depress the spike and encourage tunnelling, respectively, have been tried but may lead to premature space charge storage effects at high collector current densities or Zener breakdown if the delta-doped region is not positioned accurately in the spike and with the correct amount of dopant.

In this paper, we present a novel approach to eliminate the conduction band spike using AlGaAs as the base material, which has been shown recently to have a zero conduction band offset with GaInP for a composition of $\text{Al}_{0.11}\text{Ga}_{0.89}\text{As}$ [2]. This structure has enabled us to assess the effective saturation velocity under high space-charge injection conditions. Direct comparisons were made of the GaAs and AlGaAs bases using magneto-transport measurements. Impact ionisation measurements made directly on the HBTs, have enabled accurate predictions of breakdown voltages over a range of collector material, doping levels, thicknesses and temperature to be made.

2. Experiment

The DHBT structures were grown in an MR350 (MR Semiconductors Ltd) low pressure (150 Torr) horizontal MOVPE reactor. A 0.5 μm thick GaAs subcollector doped to $n=3 \times 10^{18}\text{cm}^{-3}$ grown on an n⁺ GaAs substrate was followed by a 1 μm thick collector of $\text{Ga}_{0.52}\text{In}_{0.48}\text{P}$ or $\text{Al}_{0.52}\text{In}_{0.48}\text{P}$ with a 250Å

region graded from $\text{Ga}_{0.52}\text{In}_{0.48}\text{P}$ at the collector base junction to $\text{Al}_{0.52}\text{In}_{0.48}\text{P}$. The collector was doped to either $1 \times 10^{15} \text{ cm}^{-3}$ or $2 \times 10^{16} \text{ cm}^{-3}$ with the graded layer in the case of the $\text{Al}_{0.52}\text{In}_{0.48}\text{P}$ collector doped to $2 \times 10^{17} \text{ cm}^{-3}$ to maintain a zero electron blocking spike at zero bias. The $0.08\mu\text{m}$ thick C-doped ($p=1$ to $5 \times 10^{19} \text{ cm}^{-3}$) base layer was linearly graded $\text{Al}_x\text{Ga}_{1-x}\text{As}$ ($x=0.11$ at the collector to $x=0.21$ at the emitter) and had a $\text{Ga}_{0.52}\text{In}_{0.48}\text{P}$ emitter layer ($0.25\mu\text{m}$ thick) doped to $n=5 \times 10^{17} \text{ cm}^{-3}$ on top. Two further $0.05\mu\text{m}$ thick layers of $\text{Ga}_{0.52}\text{In}_{0.48}\text{P}$ and GaAs completed the structure with doping of $n=3 \times 10^{18} \text{ cm}^{-3}$ and $n=5 \times 10^{18} \text{ cm}^{-3}$, respectively. The source materials were AsH_3 and PH_3 (both 100%) and TMGa, TMIn and TMAI. 10ppm disilane in He and 450ppm CCl_4 in H_2 were used for the n and p-doping respectively. Growth was carried out at 700°C except for the base which was grown at 620°C to ensure high C incorporation. The $120\mu\text{m} \times 120\mu\text{m}$ devices were fabricated using a standard double mesa process with InGe/Au and Pd/Zn/Pd/Au used for the n and p type contacts respectively.

The collector doping was determined by C-V measurements, and magneto-transport experiments were performed to determine the minority carrier mobility in the base [3]. Impact ionisation coefficients were measured directly on the HBTs using the injected emitter current into the collector depletion region to initiate multiplication [4].

3. Results and Discussion

Figure 1 compares the output characteristics of DHBTs with (a) an $\text{Al}_{0.11}\text{Ga}_{0.89}\text{As}$ base with a GaInP collector and (b) an $\text{Al}_{0.11}\text{Ga}_{0.89}\text{As}$ base with a AlInP collector including a 250\AA linear compositional graded region at the base-collector interface, to a GaAs base and a GaInP collector. The very effective elimination of the conduction band spike by interfacing the $\text{Al}_{0.11}\text{Ga}_{0.89}\text{As}$ composition at the collector side of the base with GaInP at the collector is clearly demonstrated by the absence of any significant

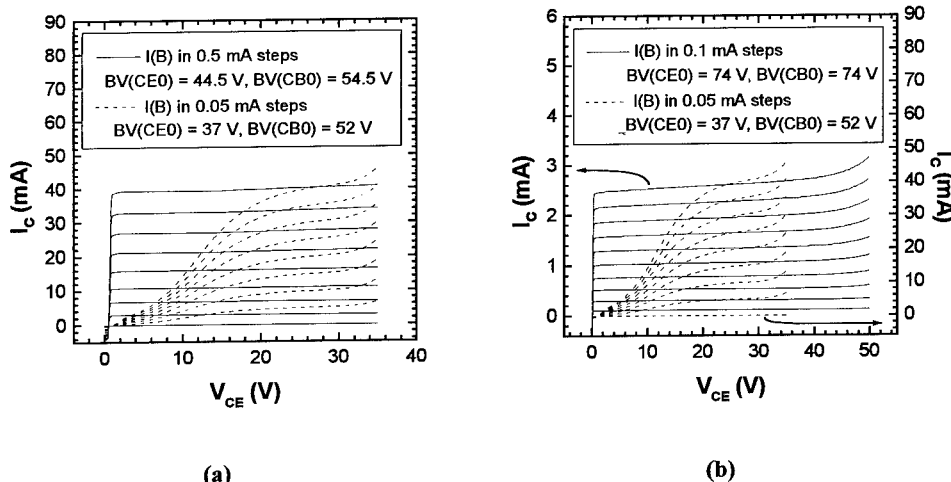


Figure 1: DHBT output characteristics of (a) GaInP and (b) AlInP collectors with AlGaAs bases compared to a GaInP collector with a GaAs base (broken line).

voltage dependence of gain with the AlGaAs base. In the GaAs base device the low current gain at $V_{CE} < 20V$ is due to excess base charge storage resulting from the conduction band spike at the collector. The breakdown voltages, BV_{CEO} and BV_{BCO} , were measured separately on a curve tracer to give values of 44V and 54V respectively with a 1 μm thick GaInP collector doped to $2 \times 10^{16} cm^{-3}$ and a current gain of 20 (case (a)). The AlInP collector device demonstrated a record breakdown voltage, $BV_{CEO} \approx BV_{BCO} = 74V$, for the same collector doping and thickness with a current gain of 8. The difference in these current gains is mainly due to a base doping concentration difference.

Magneto-resistance measurements on the AlGaAs base, together with the DC current gain, yielded electron lifetimes ten times less than equivalently doped GaAs which would affect (reduce) f_{max} . However, the built-in field offsets this to a degree by reducing the base transit time by a factor of 2.4 which would enhance f_t . The graded base enhances the gain by this factor compared to a non-graded base with the same average Al and doping concentration.

The Kirk effect was used to determine the important effective electron saturation velocity in GaInP. Because of the lack of a conduction band discontinuity in our structures, the effect of field reversal at the base-collector junction [5] could be clearly observed without being masked by the blocking effect of the spike. The well known Kirk effect equation applies in this case:

$$J_K = qv_s \left(N_c + \frac{2\epsilon V_{CB}}{qW_c^2} \right) \quad (1)$$

where J_K is the collector current at the onset current gain reduction, q the electronic charge, v_s the effective collector velocity, N_c the collector doping density ($1 \times 10^{15} cm^{-3}$ in this case), ϵ the dielectric constant in the collector, V_{CB} the collector-base junction bias including the built-in potential, the applied bias and voltage across the collector and base series resistance due to the collector and base current flow respectively, and W_c is the base width. The potentials across the base and collector resistances tend to reverse and forward bias the base-collector junction respectively and a good knowledge of both is required to solve (1) for v_s . The observed onset of current gain reduction is due to the build-up of electron space charge in the collector causing the field to reverse at the base-collector junction [5],

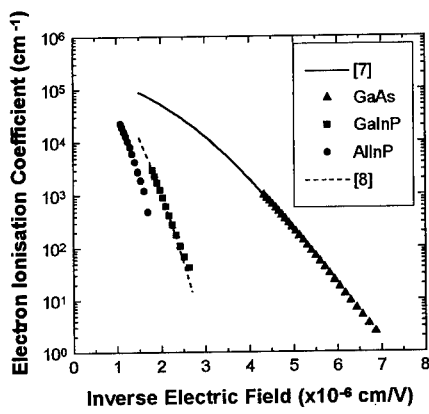


Figure 2: Electron ionisation coefficients measured on a range of collector materials.

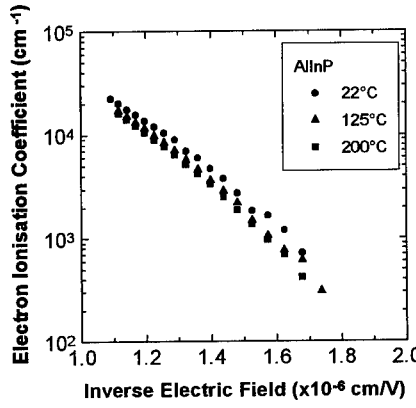


Figure 3: Variation of electron ionisation coefficients with temperature.

resulting in an increase in the electron storage in the base. Note that base pushout, where holes from the base move into the collector to neutralise the electron space charge, does not occur in this structure due to the blocking action of the valence band discontinuity. Equation (1) was solved for v_s using measured and estimated values of the collector and base series resistances to calculate V_{CB} . Using pulsed (200ns) emitter-base bias with a 0.5×10^{-3} duty cycle yielded $v_s = 4.3 \times 10^6 \text{ cms}^{-1}$. This value is in good agreement with that reported ($4.4 \times 10^6 \text{ cms}^{-1}$) from the dependence of cut-off frequency with collector depletion width [6] but may represent a lower limit because of current crowding effects in these large devices.

Measured electron ionisation coefficients for GaAs, GaInP and AlInP and are shown in figure 2. The temperature dependencies for AlInP are shown in figure 3. Such data were included in a comprehensive Ebers-Moll model which contains a wide range of temperature dependent effects and figure 4 illustrates the calculated output characteristics at two temperatures. The ionisation data exhibited here enables breakdown characteristics to be predicted for a wide range of materials, temperatures, and doping and thicknesses of collectors.

4. Conclusions

$\text{Al}_{0.11}\text{Ga}_{0.89}\text{As}$ in the base layer of an HBT, next to the collector, eliminates the conduction band spike in GaInP and AlInP collectors, demonstrating the usefulness of these structures for high power-added efficiency devices. The AlGaAs base material has a reduced gain compared to GaAs for a given doping density, but this effect can be partially offset by employing grading in the base. The effective saturation velocity for GaInP has been estimated to be $4.3 \times 10^6 \text{ cms}^{-1}$; somewhat less than that for GaAs but still useful for lower frequency applications. Electron impact ionisation coefficients have been measured directly on the HBTs and can be successfully used to predict breakdown behaviour in HBTs covering a range of collector materials, thicknesses and doping densities.

Acknowledgments: This work was funded by the UK Engineering and Physical Sciences Research Council (EPSRC).

References

- [1] Gao G, Morkoc H, and Chang M C F 1992 *IEEE Trans. Electron Dev.* 39 1987-1997
- [2] Kim K-S, Cho Y-H, Choe B-D, Jeong W G, and Lim H 1995 *Appl. Phys. Lett.* 67 1718-1720
- [3] Betser Y, and Ritter D, 1996 *IEEE Trans. Electron Dev.* 43 1187-1192
- [4] Zanoni E et al 1992 *IEEE Electron Dev. Lett.* 13 253-255
- [5] Cottrell P E and Yu Z 1990 *IEEE Electron Dev. Lett.* 11 431-433
- [6] Liu W, Henderson T, Beam E, and Fan S K 1993 *Electron. Lett.* 29 1885-1887
- [7] Bulman G E, Robbins V M, and Stillman G E 1985 *IEEE Trans. Electron. Dev.* 32 2454-2466
- [8] Ghin R et al 1997 *Appl. Phys. Lett.* 70 3567-3569

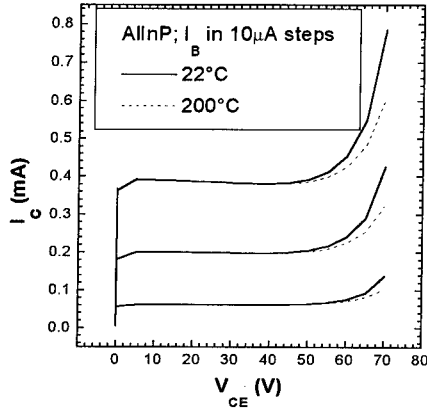


Figure 4: Ebers-Moll calculated output characteristics (AlInP collector) using the measured ionisation data.

Improved High Frequency Performance by Composite Emitter AlGaAs/GaInP Heterojunction Bipolar Transistors Fabricated using Chemical Beam Epitaxy

J.-W. Park¹⁾, D. Pavlidis¹⁾, S. Mohammadi¹⁾, C. Dua²⁾, J. C. Garcia²⁾

¹⁾Department of Electrical Engineering and Computer Science, The University of Michigan, Ann Arbor, MI 48109-2122 USA

²⁾Thomson-CSF, Laboratoire Central de Recherches, Domaine de Corbeville, 91404 Orsay, Cedex, France

Abstract. A new emitter design based on composite AlGaAs/GaInP approach is described which allows significant reduction of C_{BE} and improved high frequency performance. Self-aligned composite AlGaAs/GaInP and traditional emitter design HBTs were fabricated on CBE layers grown with TBA/TBP precursors. C_{BE} of composite emitter HBTs is significantly lower than for traditional designs and does not show significant variation with collector current. This leads to enhanced f_T characteristics for composite emitter HBT designs and confirms the theoretical expectations. The C_{BE} achieved with the new designs was by at least 4 times lower than that of conventional transistors and resulted in 20% enhancement of cutoff frequency.

1. Introduction

GaInP/GaAs Heterojunction Bipolar Transistors (HBTs) offer significant advantages over AlGaAs/GaAs devices such as large valence band discontinuity and excellent etching selectivity as demonstrated by the authors[1] and other laboratories [2], [3]. Excellent microwave properties have been obtained using GaInP HBTs [3] and Chemical Beam Epitaxy (CBE) using TBA/TBP precursors has been reported for material growth of such devices [4]. A common limitation in high speed performance of HBTs has been their relatively large base-emitter capacitance(C_{BE}) which is limited by mobile carrier transport in the emitter region [5]. Mobile carrier transport takes place in traditional HBT designs by diffusion and results in charge accumulation in the emitter and thus increased C_{BE} . To reduce the impact of this effect, a composite AlGaAs/GaInP emitter design was employed. A compositionally graded AlGaAs layer forms an electron launcher at the interface with the GaInP layer which injects the electrons at a high kinetic energy towards the remaining part of the emitter, thus resulting in lower free carrier concentration and smaller C_{BE} , especially at high current drive(J_C). Although the dynamic resistance of the HBT also increases with J_C , the C_{BE} increase in traditional designs plays a predominant role, dominating therefore the emitter time constant (τ_E). This paper addresses experimentally the new emitter design based on the earlier reported composite AlGaAs/GaInP approach [5] which allows significant reduction of C_{BE} and thus improved high frequency performance.

2. Layer Structure and Device Fabrication

The new emitter HBT design consists of a compositionally graded $5 \times 10^{17} \text{ cm}^{-3}$, 380Å thick AlGaAs (Al : 0 → 0.22) layer followed by undoped 100Å thick GaInP which serves in reducing the spike created in the conduction band of the AlGaAs/GaInP heterointerface. A $5 \times 10^{16} \text{ cm}^{-3}$, 400Å thick emitter layer is used below the undoped GaInP and the p-doped base. To better evaluate the advantages of the new emitter design and validate the proposed approach, an abrupt junction GaInP/GaAs traditional HBT was also fabricated for comparison. The emitter design of the traditional HBT consists starting from the emitter cap, of an n+ ($1 \times 10^{19} \text{ cm}^{-3}$) GaInP, 700Å thick layer followed by n ($3 \times 10^{17} \text{ cm}^{-3}$), 2000Å thick GaInP. A common design feature of the two HBT structures is a GaInP etch stop layer between the GaAs collector and subcollector. This can be used to form a laterally etched undercut and leads to reduction of the C_{BC} capacitance and thus cutoff frequency enhancement. The GaInP/GaAs HBT layers were grown by CBE. Group III atoms were provided by TEGa and TMIn. Precracked tertiarybutylarsine and phosphine (TBA,TBP) and uncracked tridimethylaminoarsine (tDMAAs) were employed as Group V sources. Uncracked hydrogen sulfide (H_2S) and TMGa were used for n- and p- doping respectively. The employed growth approach resulted in very high level of reproducibility of growth parameters and very low defect densities as expected earlier on by the authors [6]. Self-aligned HBTs with single $2 \times 30 \mu\text{m}^2$ emitter fingers were fabricated on the above layers. The key process features are as follows; Ti/Pt/Au non-alloyed emitter and collector ohmic contacts; Pt/Ti/Pt/Au non-alloyed base contacts, GaInP emitter etch by HCl and pillar/airbridge fabrication using Ti/Al/Ti/Au. GaAs collector undercut as necessary for C_{BC} was achieved by a wet etching solution consisting of $\text{NH}_4\text{OH} : \text{H}_2\text{O}_2 : \text{H}_2\text{O}$. Fig. 1 shows the cross-section of a completed HBT with laterally etched undercut.

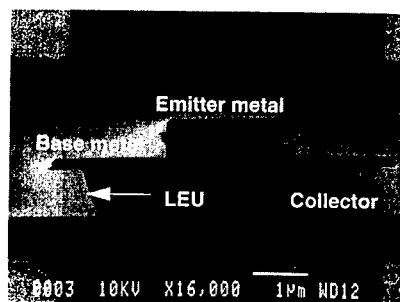


Fig. 1. Cross-section of the device profile with laterally etched collector.

3. DC and Microwave Performance

Typical DC characteristics of the composite emitter and the traditional emitter device are presented in Fig. 2(a). DC gain of 30 and 28, base ideality factors of 1.72, 2.26 and collector ideality factors of 1.26, 1.27 and a collector-emitter breakdown voltage of above 13.5V are obtained for the composite emitter and traditional emitter device respectively. The offset voltage (V_{offset}) of both devices was

about same (0.15V). The microwave properties of HBTs were measured in common-emitter configuration using on wafer tests and an HP8510B network analyzer. The power and current gain versus frequency characteristics of the composite emitter HBT are shown in Fig. 2(b). The current gain cutoff frequency (f_T) extrapolated from the measured $|H_{21}|$ using a -6dB/Oct slope rule was 60GHz for the composite emitter design HBT, and 43GHz for the traditional emitter design HBT. The maximum oscillation frequency (f_{max}) from Mason's U was 75GHz for the composite design, and 60GHz for the traditional design at $V_{CE}=2V$, $I_C=18.1mA$ and $V_{CE}=2V$, $I_C=16.5mA$ for the composite and traditional designs respectively.

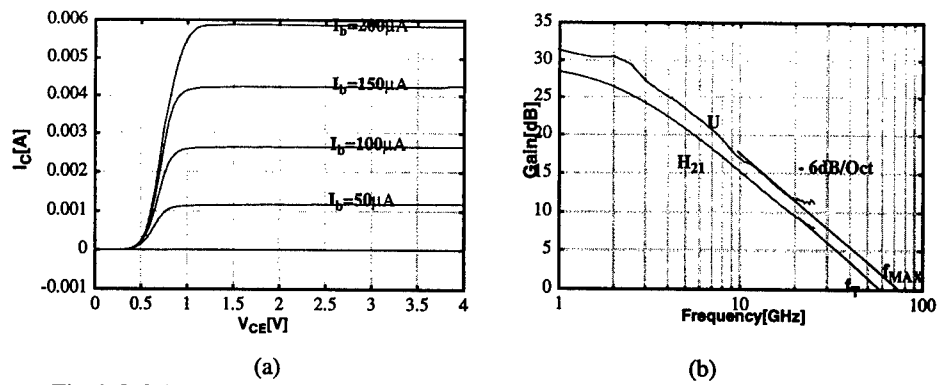


Fig. 2. DC (a) and Microwave (b) characteristics of the composite emitter HBTs, $V_{ce}=2V$, $I_C=18.1mA$. (Emitter size : $2 \times 30\mu m^2$)

The HBT equivalent circuit parameters were extracted from S parameter data using our previously reported analytic approach [7]. The total delay time (τ_d) and forward transit time ($\tau_F = \tau_B + \tau_C$) were calculated analytically from the impedance block elements of the HBT equivalent circuit. The relations below summarize the approach used [7], [8]:

$$\tau_d = \tau_E + \tau_B + \tau_C + \tau_C' = \text{ang}([Z_{12}-Z_{21}]/[Z_{22}-Z_{21}]) \quad (1)$$

$$\tau_F = \tau_B + \tau_C = -\tan^{-1}(\text{Re}[\alpha Z_{BC}]/\text{Im}[\alpha Z_{BC}]) \quad (2)$$

where $\tau_E \sim C_{BE}R_{BE}$, $\tau_C' = C_{BC}R_C$

The calculated τ_d , τ_F as function of frequency from the extracted small signal parameters were as follows; In case of the composite emitter design, a τ_d of 2.33psec, a τ_F of 2.2psec were achieved which leads to an emitter delay time($\tau_E = \tau_d - \tau_F - \tau_C'$) of only 0.071psec; $\tau_C' = C_{BC}R_C$ was in this case 0.059psec. On the other hand, the total delay time (τ_d) of the traditional design was 3psec while its forward transit time (τ_F) was 1.66psec. The resulting emitter delay time (τ_E) for the traditional design was consequently 0.485psec. These results indicate that the emitter delay time of the composite design is much shorter than that of traditional design HBTs. Thus the composite design leads to enhancement of cutoff frequency which in the case of the tested devices is of the order of 20%. The C_{BE} and f_T

dependence on J_C manifests distinct features for composite and traditional emitter designs as shown in Fig. 3 for a $2 \times 30\mu\text{m}^2$ single emitter device. In particular, the C_{BE} of composite emitter HBTs is significantly lower than that of traditional designs and presents a weak J_C dependence. This feature is representative of the new design and as expected from theory leads to enhanced f_T performance. Best microwave performance for composite emitter HBTs was $f_T=60\text{GHz}$ and $f_{max}=75\text{GHz}$ for a $2 \times 30\mu\text{m}^2$ emitter geometry. In summary, we have applied CBE growth technology using TBA/TBP precursors to the demonstration of self-aligned composite emitter AlGaAs/GaInP designs and showed the superior properties of such designs for reduced emitter-base capacitance and enhanced f_T performance.

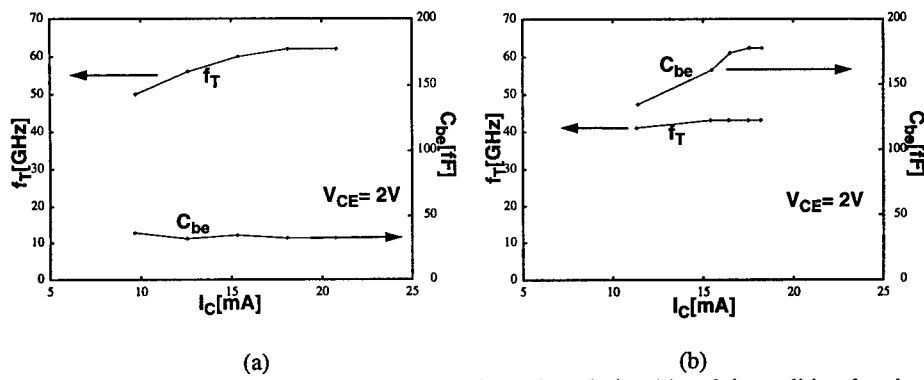


Fig. 3. Comparison of C_{BE} and f_T of the composite emitter design (a) and the traditional emitter Design (b) HBTs.

Acknowledgement

Work supported by CNET France Telecom/DRI (Contract No. 94 6M 917), Thomson-CSF and ARO/URI (Contact No. DAAL03-92-6-0109).

References

- [1] Y. J. Chan, D. Pavlidis, M. Razeghi, F. Omnes, *Int. Symp. on GaAs and Related Compounds*, 1989, p891.
- [2] T. Takahashi, S. Sasa, A. Kawano, T. Iwai and T. Fuji, *Intl. El. Dev. Meeting*, 1994 p. 331.
- [3] D. A. Ahmadi, M. T. Fresina, Q. J. Hartman, D. W. Barlage, P. J. Mares, M. Feng, and G.E. Stillman, *IEEE Electron Device Letters*, 1996, vol.17, No. 5 p226.
- [4] G.I. Ng, D. Pavlidis, J.C. Garcia, *Conf. on Indium Phosphide and Related Materials*, 1994.
- [5] J. Hu, Q. M. Zhang, R. K. Surridge, J. M. Xu and D. Pavlidis, *IEEE Electron Device Letters*, 1993, vol. 14, No12, p563.
- [6] J. C Garcia, C. Dua, S. Mohammadi and D. Pavlidis, *38th Electr. Mat. Conf. Santa Barbara, CA* 1996 p EE9.
- [7] D. R. Pehlke, D. Pavlidis, *IEEE Transaction on Microwave theory and techniques*, 1992, vol. 40, No. 12, p2367.
- [8] J. M. M. Rios, Leda M. Lunardi, S. Chandrasekhar, Y. Miyamoto, *IEEE Transaction on Microwave theory and techniques*, 1997, vol. 45, No. 1, p39.

Saturation Charge Storage Measurements in GaInP/GaAs/GaAs and GaInP/GaAs/GaInP HBTs

P.F. CHEN, Y.M. Hsin, P.M. Asbeck

Department of ECE, University of California San Diego, La Jolla, CA 92093-0407

Abstract

Saturation charge storage effects can degrade bipolar transistor performance for both analog and digital applications in which the base-collector junction can become forward-biased. In this work, we have measured the saturation charge storage time of GaInP/GaAs HBTs with GaAs and GaInP collectors, and have shown that there is a significant reduction in the charge storage for the GaInP case (DHBTs). Krakauer's method was used to measure the charge storage time. This work illustrates that DHBTs are promising devices for circuits in which transistor saturation occurs. For these applications, the devices also benefit from low offset voltage and high breakdown voltage associated with the GaInP collector.

1. Introduction

Charge storage effects can degrade the performance of bipolar transistor for both analog and digital circuit applications when the transistor is used as a switching device. In the "on" condition, the voltage drop across the load impedance forces the collector voltage to fall below the base voltage, forward-biasing both the base-collector and the base-emitter junction, and injecting holes into both the neutral collector and the neutral emitter region. To turn the transistor "off," the minority carriers injected into the collector ("stored charge") must first be dissipated through external circuitry or through recombination. In this work, we have measured the recovery time of GaAs-based HBTs using Kraukauer's method. We show that the use of GaInP collectors dramatically reduces the charge storage effect.

2. Charge Storage Effects and Reduction Method

When the base-collector junction of an HBT becomes forward-biased, minority carrier concentrations increase from their equilibrium values. This corresponds to the build-up of excess electrons in the base of the device, and excess holes in the quasi-neutral collector. In general, the excess minority carrier charge in the base is much smaller than that stored in the collector, since the base is highly doped, and is thin. The build-up of minority carrier charge in the collector can subsequently prevent the junction voltage from changing rapidly after the sudden application of a reverse bias.

A common method to prevent charge storage is to connect a schottky diode across the base-collector junction. The schottky diode turns on before the base-collector diode, preventing charge storage in the base-collector junction. However, schottky barrier diode would increase capacitance, reduce breakdown voltage, and increase area.

One other way to reduce the charge storage is to block the hole injection into the lightly doped n region (collector). This can be achieved by the application of heterojunctions[1], by using a material for the collector having a bandgap larger than that of the base. The wide bandgap collector has the same function as the wide bandgap emitter of an HBT, that is, it creates a potential barrier for hole injection which is larger than the corresponding barrier in the conduction band that governs electron flow.

The hole concentration at the collector edge of the B-C depletion region can be expressed as

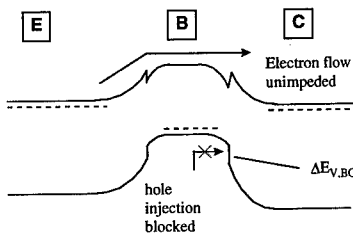


Fig 1. Band diagram of DHBT

$$p_n = p_{n0} \exp\left(\frac{qV}{kT}\right) \quad (1)$$

where V is the potential difference between the quasi-fermi level for the p type and the n-type regions (equal to the applied junction voltage), and p_{n0} is the equilibrium hole density in the collector. P_{n0} is related to the intrinsic carrier concentration n_i of the collector and its doping level n_c through $p_{n0} = n_i^2/n_c$. With the use of GaInP in the collector in place of GaAs, (with a bandgap greater by $\Delta Eg = 0.45\text{eV}$), the value of n_i is much lower, which in turn reduces the value of p_n by a factor of $\exp(-\Delta Eg/kT)$.

3. Device Structures

The HBTs and DHBTs were fabricated with MOCVD grown material from Kopin Corporation. The layer structures are shown in figure 2. The wide bandgap of the DHBT provides the desired blocking of the hole injection into neutral collector. The collector is designed such that the conduction band is pulled down by the undoped GaAs setback layer and the heavily doped GaInP layer, thereby minimizing the potential barrier

associated with the conduction band discontinuity between GaInP and GaAs [2][3].

The use of the GaInP collector also provides for higher breakdown voltage, because of its lower impact ionization coefficients at a given electric field [4].

Devices used for this study had emitter dimensions of $5 \times 12 \mu\text{m}^2$ and base-collector junction dimensions of $15 \times 22 \mu\text{m}^2$.

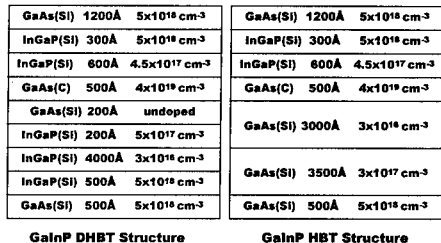


Fig.2. Device layer structures

4. Device DC and AC characteristics

The devices made exhibit DC common emitter curves as shown in fig.3. The IV curves illustrate low offset voltages for the DHBTs, which indicate that the technique used to reduce the B-C conduction band barrier was effective. The devices exhibit f_t and f_{max} values of 25 and 25 GHz, respectively. This means that these devices have small parasitic capacitances and inductances, making large signal analysis more accurate.

5. Measurement Technique

Krakauer's method was applied to HBTs in this work for the first time. This approach consists of a time-domain measurement of a diode's transient response to a large signal sinusoidal voltage input. By appropriate fitting of the observed transients, the charge storage time of the diode may be obtained. With subsequent modeling (for example, within SPICE) the behavior of the transistor can be obtained. The complete setup of the measurement is shown in figure 4.

The base collector diode is DC biased near the turn on voltage ($V_{d, \text{on}} = 1.3\text{V}$, $V_{dc} = 1.16\text{V}$). As the incoming sinusoidal excitation drives the base voltage in the positive direction, the diode turns on and conducts forward current. The forward current is a result of the injected electrons and holes which are stored in the

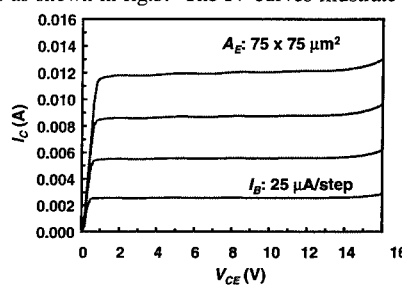


Fig.3. Measured DHBT Common-emitter I-V characteristics

neutral regions of the base and collector. As the input drops below the turn on voltage, the stored charges keep the diode turned on and the negative going input voltage causes a reverse current to extract the stored charges. In the absence charge storage effect, then the output signal is a half-wave rectified sine wave, as verified for the case of the Schottky diode.

Bias-tees were used to allow flexibility in establishing dc bias conditions. In our data, the effect of the output bias-tee has been de-embedded by numerical calculation from the measured oscilloscope waveform.

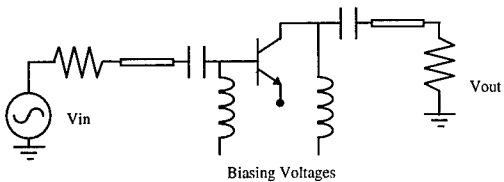


Fig. 4. Saturation charge storage measurement setup

observed transient waveforms and the charge storage time of the diode, in a manner similar to the well-known derivation of the minority carrier response to a step excitation [5]. The minority carrier distributions within the collector is calculated from drift-diffusion transport equations. An approximate solution to the distributions can be obtained assuming sinusoidal steady-state distributions during the period that the junction is forward-biased, and during the reverse-bias period, until the time at which the junction minority carrier density drops to zero. Subsequently, the device transients are controlled by depletion capacitance rather than minority charge storage. As a result of this analysis, it is found that

$$T_s = \frac{1}{2\omega} \tan^{-1}(\omega\tau) \quad (2)$$

where T_s is the duration of the negative recovery transient, τ is the recombination time of minority carriers within the collector, and ω is the angular frequency of the sinusoidal input signal. This simple result embodies some approximations, including the following:

- 1) the current waveform is taken to be strictly sinusoidal (while in the experiment, the device voltage is more accurately sinusoidal).
- 2) details of the circuit embedding of the device are ignored, and the effect of elements such as B-C depletion capacitance is omitted.
- 3) low level injection has been assumed; similarly, the finite extent of the collector region, and the possibility of built-in drift fields within are ignored.
- 4) the junction is taken to be effectively one-sided, and all the current (in both forward and reverse directions) flows due to hole diffusion.

The total minority charge storage in the collector for a one-sided junction is of the order of $J_{max}\tau$. For a more realistic situation in which the total current flow has contributions from hole diffusion, electron diffusion in the base, and recombination in the space-charge region, the hole storage is given by $\gamma J_{max}\tau$, where γ is a factor describing the fraction of the total forward current contributed by hole diffusion in the collector.

Measurement Results

The measured time domain responses are shown in figures 5a and 5b. There is significant reverse current (which manifested itself as a negative "dip") as observed in the rectified sinusoidal waveform for the SHBT base-collector junction (GaAs homojunction). The response for the DHBT base collector (GaInP/GaAs) heterojunction, the reverse current has significantly reduced amplitude. This is an indication of the reduction in stored charge. From the integral of the reverse current, the magnitude of the charge storage for the GaAs homojunction can be estimated to be at least 20 times the magnitude of the GaInP/GaAs heterojunction. Due to

Analysis:

The complete analysis of the current transient waveforms obtained in HBTs is complex, and will be treated in a separate publication. A simplified treatment, however, can provide a semiquantitative understanding of the relationship between the

the limited resolution of the oscilloscope and parasitic elements in the setup, it is difficult to accurately determine the charge storage time of the DHBTs. However, it can be readily seen that the reduction in charge storage effect is dramatic with a heterojunction. For the SHBT BC junction, the durations of the reverse current were measured and plotted against the magnitude of the input sinusoidal excitation as shown in figure 6. The charge

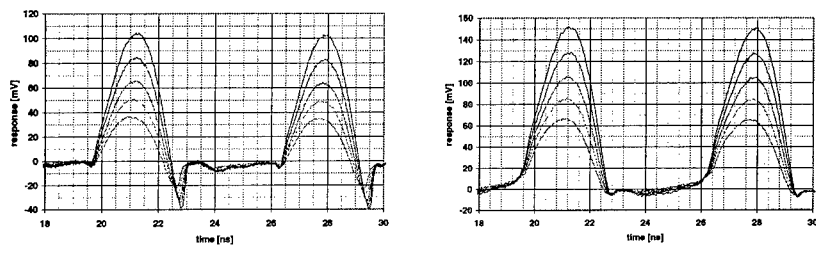


Figure 5. a) SHBT BC response b) DHBT BC response to sinusoidal input with peak to peak voltage of 250mV to 500mV

storage time is approximately a constant at 550ps. The life time of the minority carrier in GaAs then is approximately 1.1ns from equation (2).

Conclusion

The saturation charge storage has been measured for HBTs and DHBTs for the first time, using the Krakauer method. The results indicate recombination times of the order of 1 nsec, and show that the total stored charge is dramatically less in the case of HBTs with wide-bandgap collectors. These results suggest that DHBTs will be useful devices for operation under conditions of transistor saturation, for example, in switching mode power amplifiers.

Acknowledgments

The authors wish to acknowledge support from the U.S. Army Research Office through the MURI program, and are grateful to S. Park, S.L. Fu, M.F. Chang, W.J. Ho and T. Nakamura for many helpful conversations. Epitaxial material for this work was provided by N. Pang and D.P. Vu from Kopin Corporation, Taunton, MA.

References

1. H. Kroemer, Proc. IEEE 70, 1982, p. 13
2. Y.M. Hsin, Ph.D. Thesis, UCSD, 1997, p. 96
3. A.W. Hanson et al, "Comparison of $In_{0.5}Ga_{0.5}P/GaAs$ Single and Double-Heterojunction Bipolar Transistors with a Carbon-Doped Base," Electron Device Letter, vol.14, no. 1, 1993, pp.25-28
4. S.L. Fu, T.P. Chin, B. Zhu, C.W. Tu, and P.M. Asbeck, "Impact Ionization Coefficients in (100) GaInP," Applied Physics Letters, June 19, 1995, vol. 66, no.25, pp.3507-3509
5. R.H. Kingston, "Switching Time in Junction Diodes and Junction Transistors," Proc. IRE, Vol. 42, May 1954, pp. 829-834

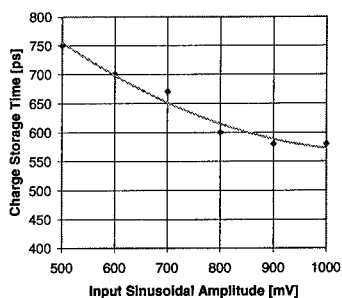


Figure 6. Measured duration of the reverse charge storage current (SHBT)

Low-Frequency Noise Characterization of High- and Low-Reliability AlGaAs/GaAs Single HBTs

Saeed Mohammadi, Dimitris Pavlidis and Burhan Bayraktaroglu*

Department of Electrical Engineering and Computer Science, The University of Michigan, Ann Arbor, MI 48109-2122, USA

* Northrop Grumman, Electronic Sensors and Systems Division, Baltimore, MS 21203, USA

Abstract: Self-aligned AlGaAs/GaAs Single HBTs were fabricated using different epilayers with identical layer structure and processing technology. These HBTs manifested different long-term reliability characteristics despite their identical device design and similar DC characteristics. The low-frequency noise characterization of these devices revealed generation-recombination centers with activation energies from 120 meV to 200 meV. The base-emitter region 1/f noise of these devices was found to be in correlation with the long-term reliability.

I. Introduction

AlGaAs/GaAs heterojunction bipolar transistors (HBTs) are being explored for a large number of microwave power applications [1][2]. Their reliability has been studied using bias and thermal stressing techniques [3][4]. The technique explored in this work is based on a possible relationship between low-frequency noise properties and HBT reliability[5]. Recently the long-term reliability of HBTs has been improved to values comparable to Silicon devices. Using different methods such as Indium co-doping in the base as well as GaInP emitter, has resulted in MTTF values over 10^7 hours[6].

II. Device Technology and Electrical Characteristics

Single heterojunction self-aligned AlGaAs/GaAs HBTs were fabricated on Metalorganic Chemical Vapor Deposition (MOCVD) grown layers. The same device design was used for all devices analyzed in this work, but MOCVD materials of different origin were employed for comparison. Identical technology was used for HBT processing to minimize the influence of technology on reliability characteristics. The DC analysis of 8 finger $2.5 \mu\text{m} \times 20 \mu\text{m}$ HBTs revealed a current gain (β) of 30 and very similar Gummel, β vs. I_c and I_c-V_{ce} characteristics independent of layer used. The microwave analysis of HBT characteristics revealed f_T and f_{max} values of 60 and 100 GHz, respectively.

The HBTs were subjected to bias and temperature stress to evaluate their long-term reliability. The stress test was performed under 25 kA/cm^2 and 125°C junction temperature using 20% degradation in current gain as criterion for reliability. A median time to failure (MTTF) of 100 hours (low-reliability devices) to 10^9 hours (high-reliability devices) was evaluated. The degree of device reliability appeared to depend on the choice of material used for fabrication.

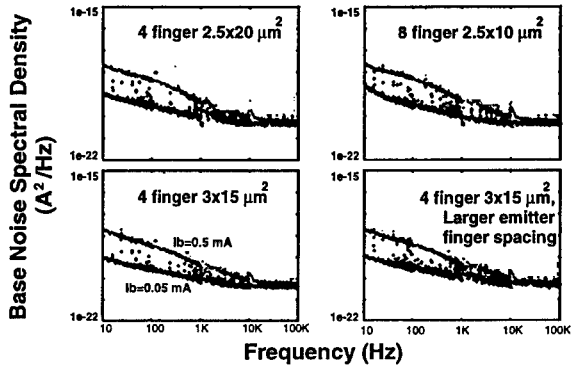


Fig. 1: Base noise of HBTs with different emitter geometry. Results permit investigation of P/A influence on noise.

III. Low-Frequency Noise Characterization

Low-frequency noise tests were performed using an HP3561A dynamic signal analyzer and a system with specially made bias networks to minimize the influence of external components on noise measurement [7]. Tests of low and high-reliability HBTs were performed on 38 devices under different bias conditions. The devices were also measured under variable temperature conditions in order to study the presence of generation-recombination noise and traps associated with it.

The origin of 1/f noise was first investigated by studying several devices with the same emitter area but different perimeter to area ratio (*P/A*). No geometry-dependence was observed for the base low-frequency noise as shown by Fig. 1. The same observation was also made for collector noise. Therefore, it was concluded that the origin of the low-frequency noise of these HBTs is not related to surface effects. These observations are in agreement with long-term reliability tests, which show no particular dependence on *P/A*.

Fig. 2 shows the collector noise spectral density of stressed and unstressed low and high-reliability HBTs. The collector voltage V_{ce} was 3 Volts and the collector current, I_c was set to 0.5 mA and 10 mA. The base was grounded with a large capacitor to eliminate the base noise current. The collector noise observed in these devices has a 1/f noise component with a relatively low corner frequency (f_{corner}) ($1 \text{ kHz} < f_{corner} < 10 \text{ kHz}$ for low-reliability HBTs and $200 \text{ Hz} < f_{corner} < 1 \text{ kHz}$ for high-reliability HBTs). The results of Fig. 2 show that the magnitude of the 1/f noise component increases upon stress for both low and high-reliability HBTs. However, stress does not affect the HBT collector noise at higher frequencies. These trends suggest that the 1/f noise component of collector noise spectral density can be indicative of the device quality. Statistically, however, it was found that the collector noise spectral density of low and high-reliability HBTs is comparable and cannot consequently be used as a good measure of device quality and reliability.

Fig. 3 shows the base noise spectral density of the low and high reliability HBTs measured before and after stress. The bias condition was $V_{ce} = 3 \text{ Volts}$ and $I_b = 50 \mu\text{A}$ and $250 \mu\text{A}$. For this measurement, collector was grounded with a large capacitor to eliminate any collector noise current being fed back to the base.

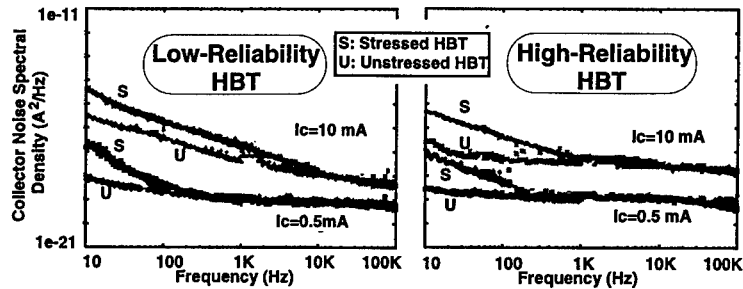


Fig. 2: Collector Noise Spectral Density of low and high-reliability HBTs before and after stressing.

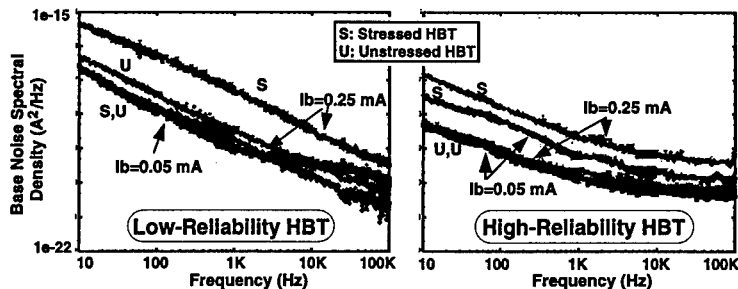


Fig. 3: Base Noise Spectral Density of low and high-reliability HBTs before and after stressing.

In both low and high-reliability HBTs, stress application increases the base noise spectral density. This increase is much more pronounced at higher base currents as shown by the results of Fig. 3. Another important observation is that the high-reliability HBTs show significantly lower base noise than low-reliability HBTs. In fact, the average base noise spectral density of high-reliability HBTs was found to be more than one order of magnitude lower than that of low-reliability HBTs at $f = 10 \text{ Hz}$. This establishes, for the first time, a significant selection criterion namely the correlation of the base noise of AlGaAs/GaAs single HBTs to their long-term reliability characteristics. On the other hand, as explained earlier on, the collector noise does not show any significant correlation with the HBT long-term reliability.

Low-temperature base and collector noise characterization was also performed on low and high-reliability HBTs. These tests were performed before and after stress application to permit a study of traps as a function of stress. Base and collector noise at different temperatures were plotted in Arrhenius plots to find activation energies of base-emitter and base-collector trap centers, respectively. For stressed and unstressed low-reliability HBTs, collector-base activation energies of 120 meV and

125 meV were found, respectively. Stressed and unstressed low-reliability HBTs had base-emitter activation energies of 140 and 149 meV, respectively. High-reliability HBTs did not show any significant generation-recombination noise in the base-emitter region while an activation energy of 207 meV was estimated for the collector-base region of unstressed high-reliability HBTs. The activation energy of the latter region for stressed high-reliability HBTs was estimated to be about the same (202 meV). Thus, stress *does not affect* the activation energy of generation-recombination centers in the base-collector region of high-reliability HBTs.

The average trapping time (τ) was evaluated from the Arrhenius plots. It was found that $\tau_{T=300K}$ in the base-collector region of low-reliability HBTs decreased by an 18% upon stress application. For high-reliability HBTs, the change in the average trapping time within the base-collector region was also insignificant. However, in the base-emitter region of low-reliability HBTs a decrease of more than two orders of magnitude occurred in the average trapping time at T=300 K due to stress application. This signifies a much higher density of traps in the base-emitter region of low-reliability HBTs upon stress application. Since the average trapping time of carriers can be related to the local defect density, the number of defects generated in the base-emitter appears to increase dramatically upon stress application. Thus, the defect density in the base-collector region does not vary significantly with stress application.

IV. Conclusion

In conclusion, the reliability of single heterojunction AlGaAs/GaAs HBTs appear to be correlated to their low-frequency noise characteristics. The low-frequency noise associated with the base-emitter region was found to be a more sensitive parameter than collector noise for predicting the reliability of these devices. The origin of the low-frequency noise was found to be independent of surface effects. The activation energies of generation-recombination centers estimated from low-temperature noise characterization were between 120 meV to 200 meV. Stress application did not change the activation energy of these traps but resulted in an increase of defect density in the base-emitter region.

Overall, the base noise and the corner frequency of the 1/f noise appear to be smaller for high-reliability HBTs. If used as a statistical method, this technique can provide a time-saving alternate to the bias and thermal stress reliability tests that are currently used in practice for HBT reliability screening.

Acknowledgement: This work was supported by DARPA MAFET Thrust 2 Program, Contract No: N00014-95-C-6026.

References

- [1] M.A. Khatibzadeh and B. Bayraktaroglu, *IEEE Microwave Symposium Technical Digest*, 1990, pp. 993-996.
- [2] B. Bayraktaroglu, *et al.*, *IEEE MTT-S Microwave and Millimeter-wave Monolithic Circuits Symposium Digest*, 1990, pp. 43-46.
- [3] M.E. Hafizi, *et al.*, *GaAs IC Symposium Technical Digest*, Oct. 1990, pp. 329-332
- [4] T. Henderson, *IEEE International Electron Device Meeting*, 1995, pp. 811-814.
- [5] L.K.J. Vandamme, *IEEE Trans. Electron Devices*, Vol. 41, No. 11, Nov. 1994.
- [6] J. Stich, *TWHM Workshop*, Sapporo, Japan, Aug. 1996.
- [7] M. Tutt, *et al.*, *Proceeding of the 18th International Symposium on GaAs and Rel. Comp.*, 1991

High Gain AlGaAs/GaAs HBTs Grown by MOCVD

R. E. Welser, N. Pan, D. P. Vu, M. A. Knowles, and I. Taulananda

Kopin Corporation, 695 Myles Standish Blvd., Taunton, MA 02780

J. G. Miller and G. E. Stillman

Center for Compound Semiconductor Microelectronics, University of Illinois at Urbana-Champaign
208 N. Wright St., Urbana, IL 61801

Abstract We report on a study of the DC characteristics of MOCVD-grown AlGaAs/GaAs HBT structures with C-doped ($3\text{-}5\text{E}19 \text{ cm}^{-3}$) base layers. Analysis of several series of AlGaAs/GaAs HBTs suggest the DC gain is dependent upon base current only, and that the base current is largely limited by bulk recombination in the neutral base. As part of this study, we have obtained DC gains of ~ 250 (@ 1kA/cm^2) at a base sheet resistance of 330 Ohms/square, which we believe is the highest DC gain ever observed for an AlGaAs/GaAs HBT at this base sheet resistance. Proportionally high DC gains have also been realized in HBTs with base sheet resistance values as low as 115 Ohms/square.

1. Introduction

The DC gain of large area heterostructure bipolar transistors (HBTs) is an important figure of merit reflecting the material quality of the requisite epitaxial layers [1]. To reduce series resistance, which can degrade RF performance, it is desirable to maintain or enhance DC gain while decreasing base sheet resistance (R_{sb}). Examination of the literature suggests that gain instead decreases with R_{sb} . Moreover, the DC gain of AlGaAs/GaAs HBTs, measured from large area devices, can vary substantially at any given R_{sb} value in the 100 to 350 Ohms/square range (Figure 1). While part of this variation may be due to differences in the collector current at which the gain is obtained, we demonstrate in this work that a significant part of this variation in gain at fixed R_{sb} can also be due to differences in the material quality of the base layer and its interfaces. By optimizing the growth parameters, we have improved the DC gain of several basic AlGaAs/GaAs HBT structures by over 30%, compared to control samples at a fixed base sheet resistance. The observed improvements in DC gain are shown to be a result of a reduction in base current. The base current, in turn, behaves as if it is limited by bulk recombination in the neutral base.

2. Experiment

The MOCVD-grown HBT structures described in this work consist of a Si-doped GaAs subcollector and collector, C-doped base, Si-doped $\text{Al}_{0.25}\text{Ga}_{0.75}\text{As}$ emitter, and a Si-doped GaAs emitter contact with an $\text{In}_{0.5}\text{Ga}_{0.5}\text{As}$ cap. In one growth matrix, a series of HBT structures, differing only in the thickness of the carbon-doped ($4\text{E}19 \text{ cm}^{-3}$) base, were grown under three different conditions (hereafter labeled Series A, B, and C). In this set, the growth time of the base layer was adjusted to target R_{sb} values of 115, 200, 250, 300, and 350 Ohms/square, corresponding to thicknesses of approximately 1550, 875, 700, 575, and 500 Å. In a second matrix, the base thickness was fixed at 700 Å and the doping level was varied between 2.9 and $4.6\text{E}19 \text{ cm}^{-3}$ under standard growth conditions (Series D).

After growth, a quarter of each as-grown 4" wafer was processed into large area devices ($75 \mu\text{m} \times 75 \mu\text{m}$). Gummel plots were obtained using an HP 4145B Semiconductor Analyzer, and the gain was

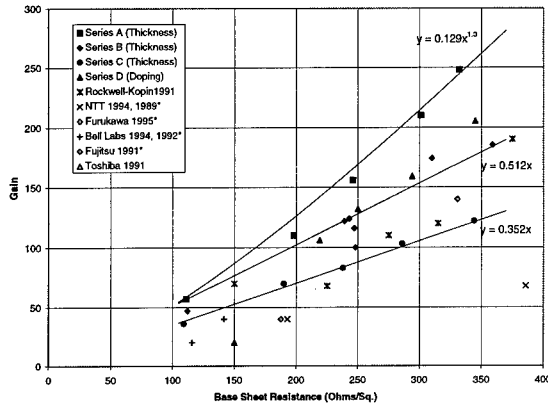


Figure 1. DC gain of large area devices versus base sheet resistance from this work (Series A-D) and the literature [3-10]. In cases where the base sheet resistance was not measured (*), R_{sb} was estimated from quoted base thickness and doping levels. The gain is reported at a variety of different collector currents, but presumably represents near maximum values. The lines represent fits to Series A, B plus D, and C.

extracted at a collector current corresponding to 1 kA/cm^2 . The base sheet resistance was determined both from TLM measurements and a cross pattern. We believe the cross pattern, in which current is driven between two adjacent contacts and the voltage measured across the other two, gives a more accurate measurement, and we report these values here. Typically the TLM measurements are 5% lower than the cross measurements. The base current at a forward bias of $V_{be} = 1.75 \text{ V}$ was also analyzed as a function of base thickness, doping level, and growth series.

In an attempt to probe the minority carrier properties of the base, the minority carrier mobility of the 1550 \AA base samples was obtained via a magnetotransport measurement [2]. Secondary ion mass spectroscopy (SIMS) and double crystal x-ray diffraction (DCXRD) spectra were also obtained to further elucidate the role of impurities and residual strain on the minority carrier lifetime in the base.

3. Results

Examination of the literature suggests that a publication by Wang *et al.* sets the standard for DC gain from large area AlGaAs/GaAs HBTs doped in the 1 to $4E19 \text{ cm}^{-3}$ range [3]. While similar results have since been achieved at other laboratories, to the best of our knowledge the gains reported by Wang *et al.* have not been surpassed. In addition to results reported by other laboratories [3-10], Figure 1 shows the variation in DC gain with base sheet resistance of identical HBT structures grown recently at Kopin under three different conditions. Series B, C, and D replicate many of the previously reported results; the DC gain of the control HBTs (Series B and D) matches or exceeds all previously published results on high gain AlGaAs/GaAs HBTs. Series A results in a substantial improvement in gain over the entire range of R_{sb} investigated (100 - 350 Ohms/square).

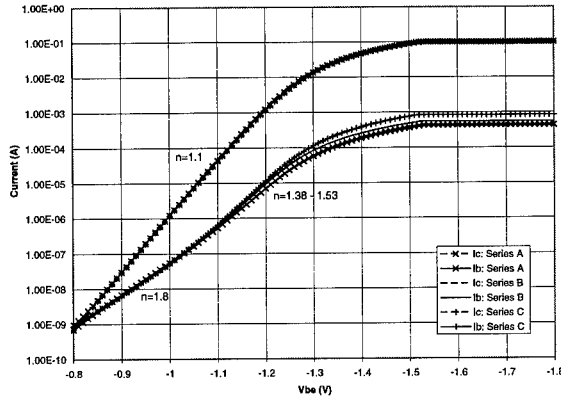


Figure 2. Gummel plots from three HBTs with R_{sb} of 350 Ohms/square from Series A, B, and C.

As seen in Figure 2, the increase in gain results from a reduction in the base current. The collector current is essentially unaffected by the growth conditions, having an ideality factor near 1.1 in all cases and a turn-on voltage of roughly 1.125 volts (@ $I_c = 100 \mu A$). However, the base current for the 350 Ohms/square HBT's decreases from $832 \mu A$ in Series C to $429 \mu A$ (@ $V_{be} = -1.75V$) in Series A. Note also that the base current moves from a low current density regime in which the current is limited by space-charge recombination ($n=1.8$) to a higher current density regime in which neutral base recombination can dominate ($n=1.38$ to 1.53) [11]. In the high current density regime, the base current of the lower gain series (Series A, B, and D) varies linearly with thickness and doping. A linear fit of base current as a function of thickness does not work as well for Series A.

4. Discussion

At the advent of the widespread use of MBE and MOCVD for the growth of high quality III-V epitaxial layers, Kroemer proposed that the gain of heavily doped III-V HBTs at high current densities would be limited by bulk recombination in the base [12]. This assumption suggests that the minority carrier diffusion length in the base is on the order of the base width (w_b) rather than much larger than w_b as typically assumed in Si BJTs, and leads to the following gain behavior:

$$\beta \sim 1/J_b \sim \tau/w_b$$

where J_b is the base current density and τ is the base minority carrier lifetime. If the minority carrier lifetime is limited by trap recombination (i.e. Sah, Noyce, and Shockley) rather than Auger recombination, then τ is expected to be inversely proportional to trap density, which is in turn proportional to the carrier concentration in the heavily doped base layers. Thus we expect the gain to be directly proportional to the base sheet resistance in the regime where gain is limited by bulk recombination via traps. Despite the improvements in MOCVD and MBE growth over the past 15

years, it appears the gain of heavily doped ($4E19 \text{ cm}^{-3}$) AlGaAs/GaAs HBTs is still limited by bulk recombination in the neutral base, as Kromer originally predicted. As shown in Figure 1, a linear fit of gain as a function of R_{sb} matches very nicely for Series C, and reasonably well for Series B and D. However, the high gains achieved with Series A definitely begin to exhibit a non-linear behavior. This non-linear behavior suggests that in Series A the trap-limited diffusion length has finally increased enough that other mechanisms, such as space-charge recombination, may also begin to play a role in limiting the gain.

Preliminary magnetotransport measurements are consistent with the suggestion that the observed improvements in DC gain result from improvements in the diffusion of minority carriers across the base. The room temperature minority carrier mobility (measured at the University of Illinois) increases linearly from $2246 \text{ cm}^2/\text{Vs}$ under Condition C to $2320 \text{ cm}^2/\text{Vs}$ under Condition A. The physical differences (e.g. impurity levels, strain state, native defect densities) leading to the improved minority carrier lifetime have yet to be determined. SIMS analysis of the C, Si, H, N, Te, O, In, and Al content reveals that the impurity levels are the same in HBTs grown under all three conditions. This SIMS analysis also confirms that the carbon concentration is $4E19 \text{ cm}^{-3}$, and that it is constant across the entire width of the base. DCXRD spectra of the as-grown HBTs exhibit a shoulder on the right side of the substrate reflection which is dependent on the thickness and doping level of the base. Spectra of identical samples grown under the three conditions reveal no significant difference, suggesting that the strain state in the samples is identical. No attempt has yet been made to measure native defect densities (e.g. vacancies, interstials, etc.).

5. Conclusions

We have observed that the DC gain of MOCVD-grown AlGaAs/GaAs HBT structures with C-doped ($3-5E19 \text{ cm}^{-3}$) base layers is controlled by the base current, and that the base current is largely limited by bulk recombination in the neutral base. Thus the gain can still be enhanced by improving the quality of the base. We have indeed obtained high DC gains for a range of R_{sb} values between 115 and 330 Ohms/square, which we believe are the highest ever reported.

6. References

- [1] Asbeck P, Chang M, Higgins J, Sheng, N, Sullivan G, and Wang K, 1989 *IEEE Trans. Electron Dev.* 36 2032-2041
- [2] Betser Y, Ritter D, Bahir G, Cohen S, and Sperling J, 1995 *Appl. Phys. Lett.* 67 1883-1884
- [3] Wang G, Pierson R, Asbeck P, Wang K, Wang N, Nubling R, Chang M, Shastry S, Hill D, and Salerno J, 1991 *IEEE Electron Dev. Let.* 12, 347-349
- [4] Ashizawa Y, Noda T, Morizuka K, Asaka M, and Obara M, 1991 *J. Crystal Growth* 107 903-908
- [5] Sandhu A, Fujii T, Ando H, Takahashi T, Ishikawa H, Okamoto N, and Yokoyama N, 1991 *Jap. J. Appl. Phys.* 30 464-465
- [6] Makimoto T, Kobayahi N, Ito H, and Ishibashi T, 1989 *Appl. Phys. Lett.* 54, 39-41
- [7] Nittono T, Watanbe N, Ito H, Sugahara H, Nagata K, and Nakajima O, 1994 *Jap. J. Appl. Phys.* 33, 6129-6135
- [8] Abernathy C, Ren F, Wisk P, Pearton S, and Esagui R, 1992 *Appl. Phys. Lett.* 61, 1092-1094
- [9] Abernathy C, Ren F, Pearton S, Wisk P, Bohling D, Muhr G, Jones A, Stavola M, and Kozuch D, 1994 *J. Cryst. Growth* 136 11-17
- [10] Tanaka S, Kato S, Hattori S, Kojima, Ikeda M, and Kitamura K, 1995 *Proc. International Microwave Symposium* 297
- [11] Day D, Jue S, Margittai A, and Houston P, 1989 *IEEE Trans. Electron Dev.* 36, 1015-1019
- [12] Kromer H, 1982 *Proc. IEEE* 70, 13-25

Pd/Ge-based ohmic contacts to n-InGaAs and n-GaAs for heterojunction bipolar transistors

I.-H. Kim, S.H. Park, T.-W. Lee, M.P. Park, B.R. Ryum, K.E. Pyun and H.-M. Park

Semiconductor Division, Electronics and Telecommunications Research Institute
161 Kajong-dong, Yusong-gu, Taejon, 305-350, Korea

Abstract. Pd/Ge-based ohmic contact behaviors on n-type InGaAs and GaAs were investigated. Good ohmic contacts were obtained by rapid thermal annealing up to 400°C, but in the contact to n-InGaAs, degradation was observed above 425°C. This was related to phase transformation and atomic redistribution. AlGaAs/GaAs heterojunction bipolar transistors using this ohmic contact system showed good DC and RF performances, which were strongly dependent on the specific contact resistance.

1. Introduction

Heterojunction bipolar transistors (HBTs) based on GaAs and its compounds have recently received great interest for their applications in microwave circuits [1]. It is critical that parasitic components should be reduced to fully take advantage of the device performance. One of the substantial parasitic elements is the ohmic contact resistance. Although various contact systems have been developed, further researches and improvements are still necessary to keep pace with the developments in the novel devices. Pd/Ge-based system has been investigated as an ohmic contact mainly on n-GaAs [2,3]. It has been understood that contact resistance is lowered due to an increase in doping level at the metal/n-GaAs interface by substitution of the Ga vacancies with the in-diffused Ge atoms. Moreover, it was reported that its penetration depth after annealing is as small as several hundreds Å, and it shows a planar contact interface and a smooth surface morphology. It is believed that a similar phenomenon would occur on n-InGaAs, but there is little information on the Pd/Ge-based ohmic contact to n-InGaAs and its annealing temperature dependence. In this study, Au/Ni/Au/Ge/Pd ohmic contact on n-InGaAs was investigated and compared with that on n-GaAs, and its effect on the performance of HBT was also analyzed.

2. Ohmic Contacts

Ohmic contact materials, Pd(400Å)/Ge(300Å)/Au(600Å)/Ni(500Å)/Au(900Å) were deposited sequentially on both n-InGaAs (800Å doped with $1 \times 10^{19} \text{ cm}^{-3}$ Si) and n-GaAs (1000Å doped with $3.7 \times 10^{18} \text{ cm}^{-3}$ Si) by an electron beam evaporator, and ohmic contact patterns were made by conventional lift-off technique. They were carried out by the rapid thermal annealing (RTA) process in N_2/H_2 forming gas atmosphere at various temperatures for 10 seconds. The standard transmission line method (TLM) was used to measure the specific contact resistance. Figure 1 shows

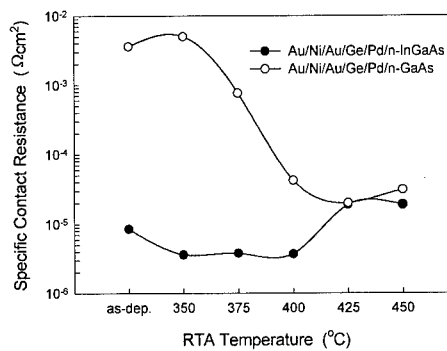


Fig. 1 Variation of the specific contact resistance with RTA temperature.

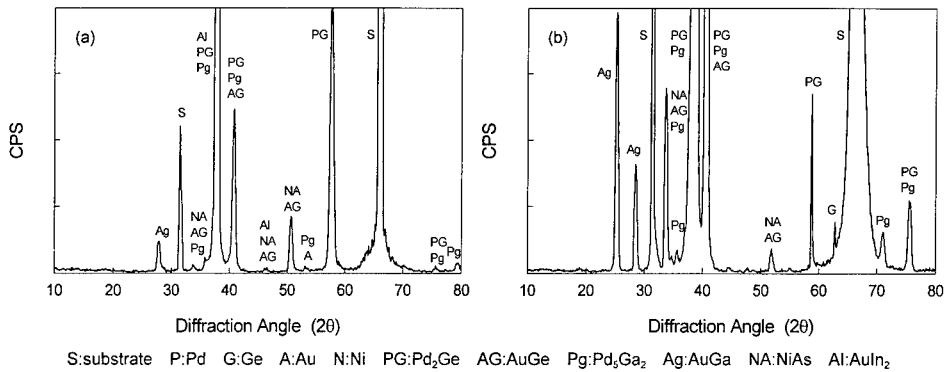


Fig. 2 XRD patterns of Au/Ni/Au/Ge/Pd contacts to (a) n-InGaAs and (b) n-GaAs annealed at 425 °C for 10 s.

the RTA temperature dependence of the specific contact resistance. In the case of contact to n-InGaAs, it showed the relatively low value (high- $10^6 \Omega\text{cm}^2$) even without annealing. This is responsible for the low barrier height of metal/n-InGaAs contact. As the temperature increased up to 400 °C, the specific contact resistance was lowered to low- $10^6 \Omega\text{cm}^2$. However, degradation of ohmic contact characteristics was observed above 425 °C. As for the contact to n-GaAs, nonohmic behavior was shown before annealing, but considerable reduction of contact resistance was made by RTA. It has been understood that contact resistance is decreased due to increase in doping level at the metal/n-GaAs interface by substitution of Ga vacancies with in-diffused Ge elements.

Phase transformations due to RTA were investigated by XRD. No remarkable phase change was observed below 350 °C, but the reaction of ohmic metals with InGaAs (or GaAs) or among ohmic metals was initiated at ~375 °C so that a little phase transitions were observed. Significant phase transformations were generated at 425 °C and various compounds were produced as seen in Fig. 2. It is believed that formation of Pd₅Ga₂ and AuGa phases helps Ge atoms to substitute Ga vacancies and thus increase in

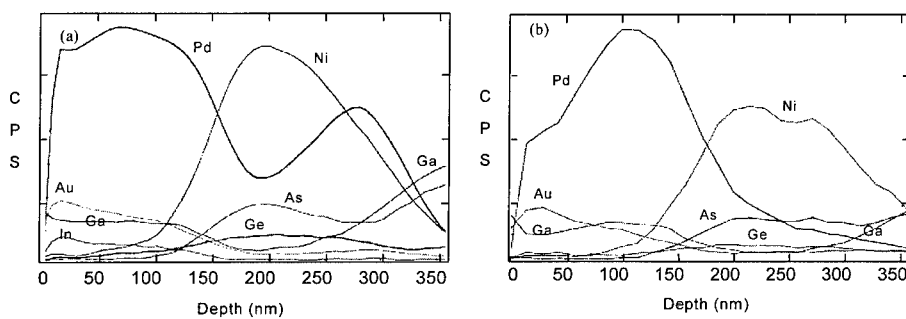


Fig. 3 AES depth profiles of Au/Ni/Au/Ge/Pd contacts to (a) n-InGaAs and (b) n-GaAs annealed at 425 °C for 10 s.

surface doping level reduces the contact resistance. However, in the case of contact to n-InGaAs, the specific contact resistance increased at the temperature higher than 425 °C. It is attributed to the considerable reaction between ohmic metals and InGaAs, especially the formation of AuIn₂ and Pd₅Ga₂ compounds. As a result, InGaAs is changed to be nonstoichiometric, and it causes higher barrier height of metal/n-InGaAs contact to degrade the ohmic contact behavior.

Figure 3 shows the AES depth profiles of Au/Ni/Au/Ge/Pd contacts to n-InGaAs and n-GaAs. In both cases, no significant diffusion was detected except a little interdiffusion of Au and Ge below 375 °C. However, considerable intermixing was observed at 425 °C, and especially for the contact to n-InGaAs. As shown in Fig. 3-a, out-diffusion of In would degrade the ohmic contact due to higher barrier height. Out-diffusion of As is also responsible for the degraded ohmic contact at 425 °C because it encourages the Ge from the contact layer to occupy the As sites where it behaves as an acceptor. It is well consistent with the results of specific contact resistance measurement and XRD analysis.

3. Application to HBT

Au/Ni/Au/Ge/Pd ohmic contact system on n-InGaAs was applied to AlGaAs/GaAs HBTs. Heterojunction epitaxial layers for the fabrication of HBT were grown by metal-organic chemical vapor deposition (MOCVD) on 3-inch semi-insulating GaAs wafer. They consisted of an n-AlGaAs emitter doped with Si at $2 \times 10^{17} \text{ cm}^{-3}$, a p-GaAs base doped with C at $3 \times 10^{19} \text{ cm}^{-3}$, and an n-GaAs collector doped with Si at $2 \times 10^{16} \text{ cm}^{-3}$. As an emitter capping layer, n-InGaAs doped with Si at $1 \times 10^{19} \text{ cm}^{-3}$ was also grown. The detailed layer structure and fabrication process of the HBT were described elsewhere [4]. In this study, aforementioned Au(900 Å)/Ni(500 Å)/Au(600 Å)/Ge(300 Å)/Pd(400 Å) system was used as emitter ohmic contact (actually contacted to emitter capping layer of n-InGaAs), and Au(800 Å)/Pt(300 Å)/Ti(300 Å)/Pt(50 Å) and Au(600 Å)/Ti(200 Å)/Au(600 Å)/Ge(300 Å)/Ni(100 Å) were deposited as base and collector ohmic contact, which are widely used as contact systems on p- and n-GaAs, respectively. After ohmic alloying by the RTA process, the effects of ohmic contact behavior on the DC and RF performance of the HBT were investigated.

In our previous work [5], the specific contact resistances of both base and collector were not significantly changed with RTA temperature up to 450 °C unlike the case of emitter ohmic contact. Thus, it is expected that the performance of HBT employing these ohmic contact schemes would be mainly dependent on the variation of emitter contact resistance with RTA temperature. Common emitter

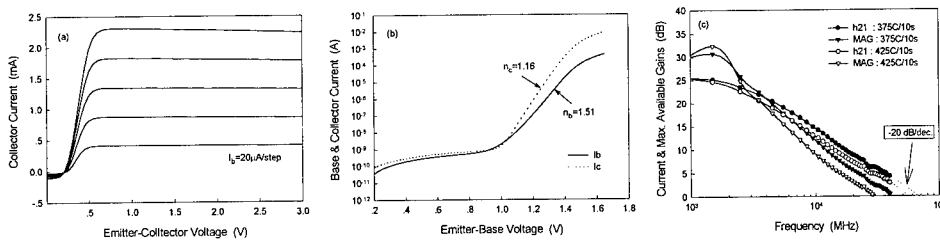


Fig. 4 Performance of $1.5 \times 10 \mu\text{m}^2$ AlGaAs/GaAs HBT. (a) Common emitter I-V characteristics (b) Gummel plot (c) Frequency response of current and maximum available gains ($V_{ce} = 1.5 \text{ V}$, $I_c = 12.9 \text{ mA}$).

current-voltage characteristics (Fig. 4-a) and Gummel plot (Fig. 4-b) of the HBT with emitter size of $1.5 \times 10 \mu\text{m}^2$ were examined, and a good DC performance was achieved. The ideality factors were changed with RTA temperature and the minimum values of n_b (1.51) and n_c (1.16) were observed in the HBT annealed at 375°C for 10 seconds. RF performance of HBT was also examined and the results are shown in Fig. 4-c. The maximum values of cutoff frequency and maximum oscillation frequency of the HBT annealed at 375°C were obtained to be 65 GHz and 42 GHz, respectively. However, both frequencies were reduced to be 55 GHz and 33 GHz, respectively, by higher temperature annealing. It is confirmed that RF performance of the HBT is strongly dependent on Pd/Ge-based ohmic contact behaviors with RTA temperature. Therefore, it is critical to make reliable and low-resistance Pd/Ge-based ohmic contacts to apply to high speed devices.

4. Conclusion

Au/Ni/Au/Ge/Pd ohmic contact system on n-InGaAs and n-GaAs was studied. In the case of n-InGaAs, it showed a relatively good ohmic behavior even without annealing due to lower barrier height, and a better ohmic contact was obtained by RTA up to 400°C . However, above 425°C it was deteriorated by intermixing and phase reaction of ohmic metals and InGaAs substrate. The out-diffusion of In and As degraded the ohmic contact due to increased in barrier height and charge compensation. As for the contact to n-GaAs, nonohmic behavior was shown before annealing, but significant reduction of specific contact resistance was made by RTA. Au/Ni/Au/Ge/Pd ohmic contact system on n-InGaAs was applied to AlGaAs/GaAs HBT. The HBT utilizing this ohmic scheme showed a acceptable performance and it depended strongly on the ohmic contact characteristics with RTA temperature.

References

- [1] Asbeck P M 1990 *High-Speed Semiconductor Devices* (Wiley, New York)
- [2] Hao P H, Wang L C, Deng F, Lau S S and Cheng J Y 1996 *J. Appl. Phys.* **79**, 4211-4215
- [3] Cole M W, Han W Y, Casas L M, Eckart D W and Jones K A 1994 *J. Vac. Sci. Technol.* **A12**, 1904-1909
- [4] Park S H, Park M P, Lee T-W, Song K M, Pyun K E and Park H M 1995 *Proc. 22nd Int. Symp. Comp. Semicon.* 295-300
- [5] Kim I-H, Park S H, Lee T-W and Park M P 1997 *Appl. Phys. Lett.* **71**, 1854-1856

An Au/Pt/Ti/WN_x Ohmic Contact to n-InGaAs and Its Application to AlGaAs/GaAs HBTs

SUNG HO PARK, Il-Ho Kim, Tae-Woo Lee, and Moon-Pyung Park

Semiconductor Division, Electronics and Telecommunications Research Institute
161 Kajong-dong, Yusong-gu, Taejon, 305-350, Korea

Abstract. We report the experiments that were performed to investigate the alloying temperature dependence of Au/Pt/Ti/WN_x ohmic contacts to n-InGaAs. Very low resistance contacts ($10^{-8} \sim 10^{-7} \Omega\text{cm}^2$) were obtained after RTA at the temperatures from 250 to 450°C. It was observed from XRD and AES analyses that there were no remarkable phase transformations for the contact system subjected to heat treatments. When Au/Pt/Ti/WN_x ohmic contacts were applied to AlGaAs/GaAs HBTs, moderate DC and RF performances were also achieved. It is believed that these ohmic schemes can be used as stable and low resistance contacts for high temperature HBT applications.

1. Introduction

Compound semiconductor heterojunction bipolar transistors (HBTs) have been acknowledged as potential devices for mm-wave and microwave applications [1]. It is very critical to obtain the thermally stable, low resistance ohmic contacts to realize high-speed and high-frequency devices. Due to its low barrier height, InGaAs has been often used as a capping layer for obtaining the low resistivity ohmic contact of high performance electronic devices. This low barrier height on heavily doped InGaAs makes various non-alloyed ohmic contacts possible [2,3]. It has been reported briefly by Shantharama *et al.*[4] that Pd/AuGe, Ti/Pt/Au, AuBe/Pt/Au, and Au/SnAu ohmic metals are suitable for n-type InGaAs. In addition, a moderately low specific contact resistance (ρ_c) of $1.3 \times 10^{-6} \Omega\text{cm}^2$ was obtained using a refractory W metal contact to n-type InGaAs[5]. There are few reports on WN_x ohmic contact to n-type InGaAs for HBT application, even though it has been widely used as a gate metal of MESFET or HEMT due to the high Schottky barrier height and low stress. In this paper we have investigated the alloying temperature dependence of Au/Pt/Ti/WN_x ohmic contact to heavily doped n-InGaAs and successfully applied it to fabricate an AlGaAs/GaAs HBT for high temperature operation.

2. Experiment

HBT epi-layer structures, prepared by MOCVD on a 3-inch semi-insulating GaAs substrate, include an InGaAs emitter cap layer (800Å), an AlGaAs emitter layer (2000Å), a carbon-doped GaAs base layer (700Å), and a GaAs collector layer (4000Å), as shown in Table 1. Ohmic contact materials, WN_x (1200Å) and Ti/Pt/Au (500Å/200Å/1300Å), were deposited sequentially on n-InGaAs by a sputter and an electron beam evaporator, respectively.

Table 1. AlGaAs/GaAs HBT epi-layer structures.

Layer		Thick. (Å)	Doping (cm ⁻³)	Al(In) Fraction
Cap	n ⁻ InGaAs	400	1x10 ¹⁹	0.5
	n ⁻ InGaAs	400	1x10 ¹⁹	0 → 0.5
	n ⁻ GaAs	1000	4x10 ¹⁸	
Emitter	n-AlGaAs	500	5x10 ¹⁷	0.3 → 0
	n-AlGaAs	1500	2x10 ¹⁷	0.3
Base	p ⁻ GaAs	700	3x10 ¹⁹	
Collector Subcollector	n-GaAs	4000	2x10 ¹⁶	
	n ⁻ GaAs	5000	4x10 ¹⁸	

Ti/Pt/Au overlayers were patterned by conventional lift-off technique. WN_x ohmic contact were formed by MERIE (magnetically-enhanced reactive ion etching) using SF_6/CHF_3 mixture gases. After emitter and base mesa etching, Au/Pt/Ti/Pt (800Å/300Å/300Å/50Å) and Au/Ti/Au/Ge/Ni (700Å/100Å/400Å/200Å/100Å) metal layers were deposited as base and collector ohmic contacts, respectively. These ohmic contacts were heat-treated by RTA in nitrogen atmosphere at temperatures ranging from 250°C to 450°C for 10 seconds. The standard transmission line method (TLM) was used to measure the specific contact resistance. The microstructural interactions at the $\text{WN}_x/\text{InGaAs}$ interface were analyzed by XRD and AES. Each HBT was isolated by wet mesa etching and PECVD-SiN film was deposited for passivation. Prior to the first metallization, via-holes were formed by MERIE using C_2F_6 plasma. And then metal interconnection was provided by Ti/Au (500Å/4500Å). Finally, the DC and RF performances of fabricated HBTs were studied.

3. Results and Discussions

Fig. 1 shows the RTA temperature dependence of the specific contact resistance of Au/Pt/Ti/ WN_x ohmic contact to n-InGaAs. The contact system exhibited the relatively low value ($2 \times 10^{-6} \Omega\text{cm}^2$) even without annealing to enhance the specific contact resistance. This is due to the low barrier height of metal/n-InGaAs contact. The lowest contact resistivity of $9.5 \times 10^{-8} \Omega\text{cm}^2$ was obtained when the annealing temperature was increased up to 400°C. After annealing above 450°C, its ohmic performance was a little bit degraded. It is believed that this degradation of contact resistivity is induced by the stress increase at $\text{WN}_x/\text{InGaAs}$ interface, as like the case of WSi/InGaAs ohmic contact in our previous work [3]. Nevertheless, it maintained the low specific contact resistances of $\sim 10^{-7} \Omega\text{cm}^2$ and smooth surface morphology at wide annealing temperature range.

XRD and AES were used for the microstructural analysis of Au/Pt/Ti/ WN_x contact to n-InGaAs. Phase transformations of the ohmic contact according to the RTA were studied by XRD. As shown in Fig. 2, no significant phase changes were detected before and after annealing heat treatment, because the refractory WN_x layer prevents any phase transitions from proceeding. Fig. 3 shows the RTA temperature dependence of AES depth profiles of Au/Pt/Ti/ WN_x contact to n-InGaAs. In spite of high temperature annealing up to 450°C, there was not any remarkable in-diffusion and/or out-diffusion of such active element as indium to degrade the metal/semiconductor interface. This AES result is well consistent with that of XRD measurement. In conclusion, it is proved that WN_x metal is a potential candidate as diffusion barrier for ohmic contact to InGaAs.

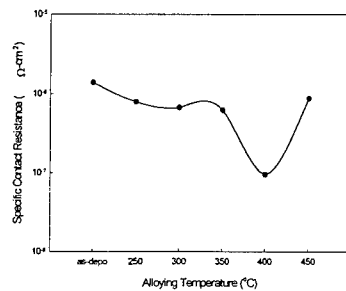


Fig. 1. Variation of the specific contact resistances with RTA temperature.

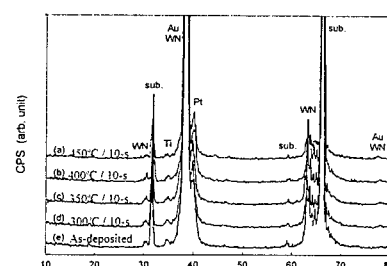


Fig. 2. XRD patterns of Au/Pt/Ti/ WN_x contact to n-InGaAs annealed at various RTA conditions.

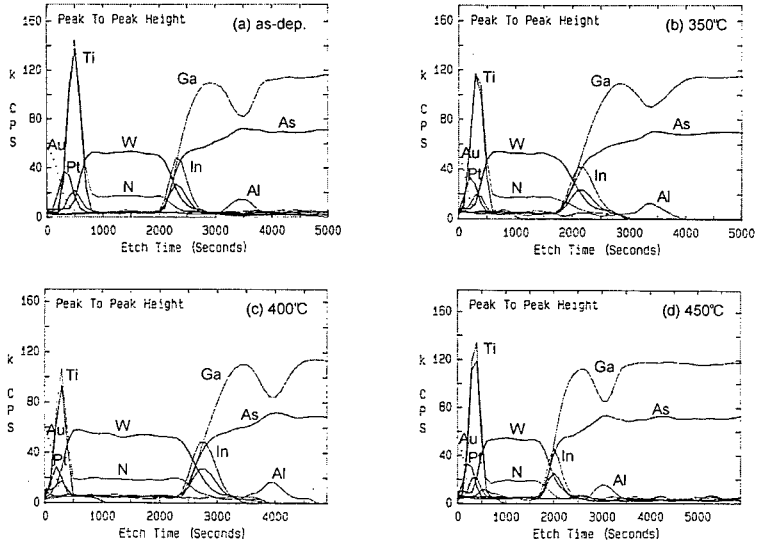


Fig. 3. AES depth profiles of Au/Pt/Ti/WN_x contact to n-InGaAs annealed at various RTA temperatures for 10 sec.

Fig. 4 and Fig. 5 show an optical microscope photograph and a common-emitter I-V characteristics of the AlGaAs/GaAs HBT with the emitter area of $2(2 \times 10 \mu\text{m}^2)$, which was fabricated using WN_x emitter ohmic contact annealed at 400°C for 10 sec and non-self-aligned process. Our HBT exhibited an offset voltage of 0.26 V, a current gain (β) of about 55. Also, the ideality factors of the collector and base currents were 1.15 and 1.50 from the Gummel plot, respectively.

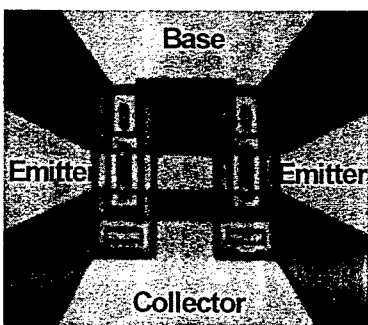


Fig. 4. SEM photograph of a fabricated AlGaAs/GaAs HBT (emitter area: $2(2 \times 10 \mu\text{m}^2)$).

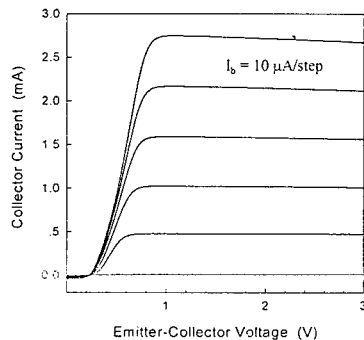


Fig. 5. Common emitter I-V characteristics of the HBT.

Microwave S-parameters were measured over the frequency range of 0.5 to 39.5 GHz using a HP8510B Network Analyzer and a CASCADE Microtech probe station, in which the current gain (H_{11}) and maximum available gain (MAG) were calculated from S-parameters. In Fig. 6(a), the

cutoff frequency (f_T) and maximum oscillation frequency (f_{max}) of HBTs were 57 GHz and 36 GHz at the bias condition of collector-emitter voltage (V_{ce}) of 1.5 V and collector current (I_c) of 18 mA, respectively. Fig. 6(b) shows the variation of f_T and f_{max} of the HBT with V_{ce} and I_c . It is believed that better performance will be obtained if HBTs are fabricated using the base-emitter self-aligned process by undercutting of WN_x emitter metal.

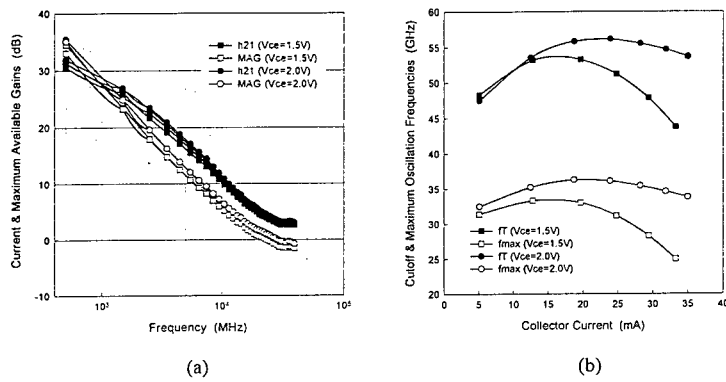


Fig. 6. RF performances of AlGaAs/GaAs HBT with the emitter area of $2(2 \times 10 \mu\text{m}^2)$. (a) frequency response of current and maximum available gains ($V_{ce}=1.5$ V, $I_c=18.0$ mA). (b) f_T and f_{max} as a function of V_{ce} and I_c .

4. Conclusion

The effects of RTA on the Au/Pt/Ti/ WN_x ohmic contact to n-InGaAs were investigated. Au/Pt/Ti/ WN_x contact system showed the relatively low specific contact resistances of $\sim 10^{-7} \Omega\text{cm}^2$ at the annealing temperature range of 250°C to 450°C. From XRD and AES analyses, it was observed that no significant phase changes and diffusions occurred before and after RTA. When Au/Pt/Ti/ WN_x ohmic contacts were applied to AlGaAs/GaAs HBTs, moderate DC and RF performances were also obtained. It is believed that these ohmic schemes to n-InGaAs can be used as stable and low resistance contacts for high temperature HBT applications.

References

- [1] Asbeck P M 1990 *High-Speed Semiconductor Devices* (Wiley, New York)
- [2] Shen T C, Gao G B and Morkoç H J. 1992 *Vac. Sci. Technol. B* 10 2113-2132
- [3] Park S H, Park M P, Lee T-W, Song K M, Pyun K E and Park H M 1995 *Proc. 22nd Int. Symp. Comp. Semicon.* 295-300
- [4] Shantharama L G, Schumacher H, Leblanc H P, Esagui R, Bhat R and Koza M 1990 *Electron. Lett.*, 26 1127-1129
- [5] Lahav A, Ren F and Kopf R F 1989 *Appl. Phys. Lett.* 54 1693

Real Space Transfer Noise of GaAs p-HEMTs

M. Feng, D. Caruth, S. K. Hsia and J. A. Fendrich,

Department of Electrical and Computer Engineering, Center for Compound Semiconductor Microelectronics,
University of Illinois, Urbana, IL 61801

Abstract From the measured noise data in a GaAs p-HEMT over a 2-18 GHz frequency range, we have identified the magnitudes of the gate and drain noise sources in the 2-DEG saturation velocity region of undoped InGaAs channel. Additional gate and drain noise sources in the parallel doped AlGaAs channel contribute to the overall noise in p-HEMT. We call this additional noise the real space transfer noise.

1. Introduction

Two dimensional electron gas (2-DEG) at the AlGaAs/GaAs interface was first discovered by Dingle et al. in 1978 [1]. Utilizing the 2-DEG concept, a new class of field effect transistor, called the high electron mobility transistor (HEMT), was first demonstrated by Mimura et al. in 1980 [2]. In GaAs HEMT or p-HEMT device operation, the drain current is mainly carried by 2-DEG in the GaAs or InGaAs channel under reverse gate bias. However, some of the drain current can transfer from 2-DEG channel to the doped channel of AlGaAs layer (called real space transfer effect) under forward gate bias. The real space transfer effect in HEMTs or p-HEMTs was first proposed and device simulated by Hess et. al. in 1982[3]. However, the noise contribution due to the real space transfer effect was not known and uncharacterized.

In this work, we have performed microwave noise measurements and noise modeling of a $0.25\mu\text{m}$ gate length GaAs p-HEMTs. From the measured data, we have characterized the gate and drain noise in the saturation velocity region of 2-DEG InGaAs channel. The additional drain noise in the AlGaAs channel due to the real space transfer effect in p-HEMTs under high frequency operation is then determined.

2. GaAs p-HEMT Fabrication

The AlGaAs/InGaAs/GaAs p-HEMT material is grown by molecular beam epitaxy (MBE) and was purchased from commercial vendors. The material structure is composed of a GaAs/AlGaAs superlattices buffer, GaAs buffer, InGaAs channel (15% of Indium composition), AlGaAs barrier with Silicon δ -doped profile and an n-GaAs cap layer. The peak transconductance is 135 mS (450 mS/mm) at $I_{ds} = 170 \text{ mA/mm}$ with $f_t = 61 \text{ GHz}$. The pinchoff voltage is $V_p = -0.4\text{V}$ for the p-HEMT. For the GaAs p-HEMT, For comparison, the $0.25 \mu\text{m}$ gate GaAs MESFET is fabricated by direct ion implant into LEC GaAs substrate. The peak transconductance is 105 mS (350 mS/mm) with $f_t = 56 \text{ GHz}$. The pinchoff voltage is $V_p = -0.8\text{V}$ for MESFET. Both devices are fully passivated by Si₃N₄.

3. Microwave Noise Measurement and Modeling Techniques

The measured noise parameters and S-parameters from 2 to 18 GHz of the p-HEMT are used to extract the equivalent noise model. Note that correlation between the intrinsic gate and drain noise sources is provided by the feedback capacitor C_{gd} . The extrinsic parasitic resistance (R_g , R_s and R_d) were treated as thermal noise sources. The intrinsic noise elements (v_g and v_d) are then determined by optimizing the model to fit the measured noise parameter data (F_{min} , R_n , and Γ_{opt}). The contribution of each of the noise sources to the minimum effective noise temperature referenced to the input of the device was then computed by turning on the sources one by one and then determining the effective noise temperature engendered by that source alone. Figure 1 illustrates the measured minimum noise figure, F_{min} and associated gain over a wide drain current range (15 to 60 mA) at 10 GHz for both GaAs MESFET and p-HEMT. Both devices exhibit a 0.9 dB noise figure with 11 to 11.5 dB associated gain at 10 GHz. Figure 2 illustrates the intrinsic noise model where extrinsic resistance such as R_g , R_d , and R_s are removed.

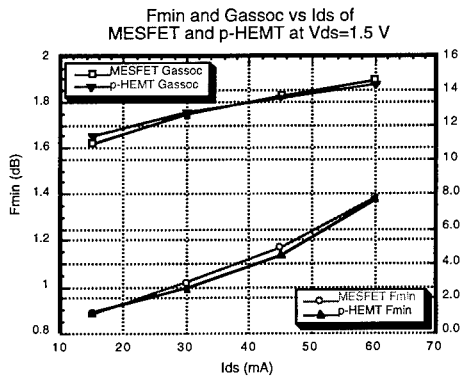


Figure 1. Noise figure and associated gain at 10 GHz for GaAs MESFET and p-HEMT.

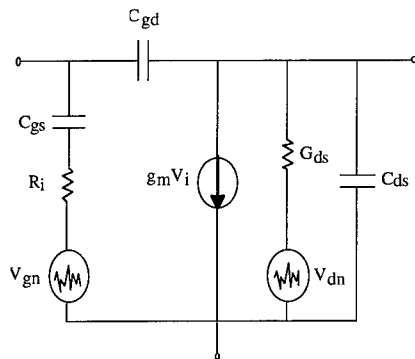


Figure 2. Intrinsic FET model

4. Extrinsic and Intrinsic Noise

We have plotted total noise temperature (referenced to the input of the device) of GaAs p-HEMT and GaAs MESFET as a function of drain current at fixed $V_{ds} = 1.5V$ as shown in Figure 3. In this case, the noise temperature for both devices is nearly identical for $I_{ds} < 30$ mA, but they begin to have strongly diverge when the p-HEMT is under forward gate bias for $I_{ds} > 30$ mA.

We can separate extrinsic noise (Johnson Noise) due to R_s , R_d and R_g from intrinsic noise as shown in Figure 4. The extrinsic noise of GaAs p-HEMT is slightly lower than the extrinsic noise of GaAs MESFET for all I_{ds} . The intrinsic noise of GaAs p-HEMT is slightly higher than the intrinsic noise of GaAs MESFET for $I_{ds} < 30$ mA where GaAs p-HEMT is under reverse gate biased. Under this condition, the intrinsic noise of GaAs p-HEMT is generated predominately in InGaAs channel. In contrast, for $I_{ds} > 30$ mA, the intrinsic noise of GaAs p-HEMT is much higher than the intrinsic noise of GaAs MESFET. For these high currents, the GaAs p-HEMT is forward biased. The forward bias creates a real space transfer of carriers from the undoped 2-DEG InGaAs layer to the doped AlGaAs layer. Hence, the noise is generated from both channel for p-HEMT and results in much higher noise than MESFET.

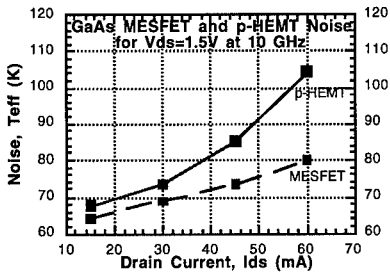


Figure 3. Total noise temperature (input equivalent) of p-HEMT and FET

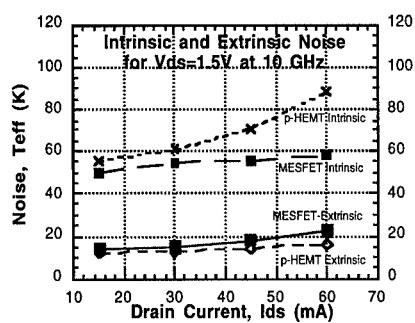


Figure 4. Extrinsic and Intrinsic Noise Temperature of p-HEMT and FET

5. Intrinsic Drain and Gate Noise

In Figure 5, we have plotted intrinsic drain noise and gate noise of p-HEMT and MESFET. The gate and drain noise sources on the p-HEMT can be subdivided into six noise components, namely, $\langle id1 \rangle$ and $\langle ig1 \rangle$ Johnson noise from ohmic region in the channel, $\langle id2 \rangle$ and $\langle ig2 \rangle$ dipole noise source in the undoped InGaAs channel and $\langle id3 \rangle$ and $\langle ig3 \rangle$ dipole noise in the doped AlGaAs channel. The gate and drain noise source in the MESFET are composed of 4 noise components, namely, $\langle id1M \rangle$ and $\langle ig1M \rangle$ Johnson noises from ohmic region in the channel, $\langle id2M \rangle$ and $\langle ig2M \rangle$ dipole noise source in the doped GaAs channel. For a $0.25\text{ }\mu\text{m}$ gate FET and p-HEMT with a $V_{ds}=1.5\text{ V}$, 97% of the channel is under high field saturation velocity region.[4] Hence, $\langle id1 \rangle$, $\langle id1M \rangle$, $\langle ig1 \rangle$ and $\langle ig1M \rangle$ can be neglected for both devices. The drain noise in GaAs MESFET is only due to the dipole diffusion noise in the doped GaAs channel.[4]

For the $15\text{ mA} < I_{ds} < 30\text{ mA}$ ($V_{gs} = 0\text{ V}$), the drain noise of p-HEMT is nearly the same as MESFET. Hence, the drain noise is primarily dominated by the noise source from the 2-DEG in InGaAs channel. The $\langle ig2 \rangle$ is slightly higher than $\langle ig2M \rangle$ because of the gate capacitance of GaAs p-HEMT is larger than GaAs MESFET. Hence, the capacitance coupling gate noise should be higher for GaAs p-HEMT.

For $I_{ds} > 30\text{ mA}$ where GaAs p-HEMT is under forward gate biased condition, the drain noise is composed of $\langle id2 \rangle$ from undoped InGaAs channel and $\langle id3 \rangle$ from doped AlGaAs channel. Obviously, the measured data in Figure 5 indicated that the noise sources in AlGaAs channel is much higher than the noise in the InGaAs channel. The dipole noise generated in InGaAs (15% In) channel is nearly the same as GaAs channel. From Figure 5, the drain noise temperature of GaAs MESFET, T_{NM} , can be determined using a linear fit to the low current data, where $T_{0M}=30\text{ K}$ with a noise slope of $(1/3)\text{ K/mA}$.

$$T_{NM} = T_{0M} + \frac{\Delta T}{\Delta I_{ds}} (\Delta I_{ds}) = 30\text{ K} + \frac{1\text{ K}}{3\text{ mA}} (60\text{ mA}) = 60\text{ K}$$

The same technique can be done for the GaAs p-HEMT, where $T_0=30\text{ K}$. The change in noise (T_{N-T_0}) is linearly dependent on the drain current difference in InGaAs layer and also in AlGaAs layer.

Hence, the amount of current flow in InGaAs channel is estimated from the intercept point of linear fit between 15 mA and 30 mA as well as linear fit between 40 mA and 60 mA. The current flow in InGaAs channel $\Delta I_{ds1} = 36mA$, with a lower noise slope of (1/3)K/mA. On the other hand, the current flow in AlGaAs channel $\Delta I_{ds2} = 24mA$, and has a higher noise slope of (5/6) K/mA.

$$T_n = T_o + \frac{\Delta T}{\Delta I_{ds1}} (\Delta I_{ds1}) + \frac{\Delta T}{\Delta I_{ds2}} (\Delta I_{ds2})$$

$$T_n = 30K + \frac{1}{3}(36mA) + \frac{5}{6}(24mA) = 62K$$

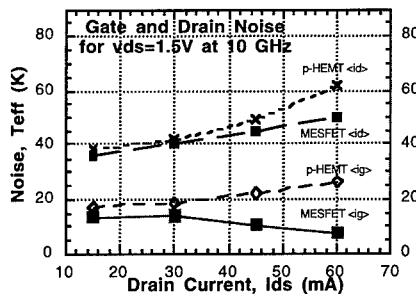


Figure 5. Intrinsic Gate and drain Noise Temp of GaAs MESFET and p-HEMT over drain current.

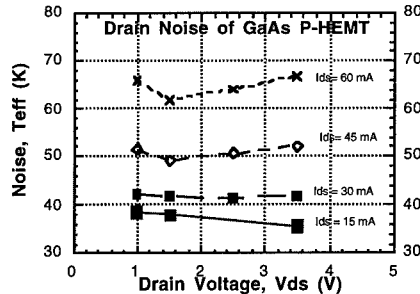


Figure 6. Intrinsic drain Noise Temp of GaAs MESFET and p-HEMT over drain voltage

We have plotted intrinsic drain noise temperature of p-HEMT as a function of drain voltage for a fixed current in Figure 6. For a given I_{ds} , the drain noise is nearly constant over $1V < V_{ds} < 3.5V$. This result indicates that drain noise is directly proportional to the magnitude of drain current, and is nearly independent of drain voltage.

6. Conclusion

We have measured the noise figure of a GaAs p-HEMT and a MESFET under forward and reverse gate bias. Through the accurate equivalent noise model of FET, we are able to separate extrinsic and intrinsic noise sources. Furthermore, we are able to separate intrinsic gate and drain noise. We can then determine noise contribution due to the InGaAs channel and the doped AlGaAs channel. The noise associated with AlGaAs channel is due to the real space transfer effect. This noise can be as large as 50% of total drain noise under forward gate biases.

Reference

- [1] Dingle R, Stomer H. L, Gossard A. G, and Wiegmann W, 1988 *Appl. Phys. Lett.*, vol. 33, p. 1088
- [2] Mimura T, Hiyamizu S, Fujii T, and Nanbu K, 1980 *Japan J. Appl. Phys.*, vol. 19, p. L255,
- [3] Hess K, in advances in Electron and Electron Physics, vol 59. AP, 1992
- [4] Statz H, Haus H A, and Pucel R A, 1974 *IEEE Trans. Electron Devices*, vol. ED-21, pp. 549-562

PdGe on GaAs: A Study of the Applicability in InGaP/GaAs HBT Fabrication

D.A. Ahmari, M.L. Hattendorf, D.F. Lemmerhirt, Q. Yang, Q.J. Hartmann, and G.E. Stillman

University of Illinois, Department of Electrical and Computer Engineering
Microelectronics Laboratory, 208 N. Wright St., Urbana, IL 61801

Abstract. Recently InGaP/GaAs HBTs have demonstrated performance comparable to AlGaAs/GaAs and have proven to be well suited for high-speed and low-noise applications [1-3]. Despite the excellent performance of InGaP/GaAs HBTs, continued efforts towards reducing the delay associated with the emitter resistance and capacitance are required. To help minimize the emitter resistance, PdGe contacts on n-type GaAs were studied. This experiment studies the behavior of the PdGe alloyed on a hot plate for times less than 30 minutes and compares results to RTA alloys. Also studied is the behavior of the PdGe contacts alloyed in various ambients. Finally, the issues associated with performing a self-aligned emitter etch with PdGe contacts are also discussed.

1. Introduction

In the past, GaAs based HBTs often employed AuGeNiAu on a GaAs emitter contacting layer. However, during HBT operation, such metalization schemes have been shown to be unreliable due to Au spiking and balling. Most modern HBTs employ a non-alloyed TiPtAu emitter contact on a strained InGaAs contacting layer to eliminate the possibility of spiking. However the strained InGaAs causes difficulty during crystal growth and during a self-aligned, wet chemical emitter etch.

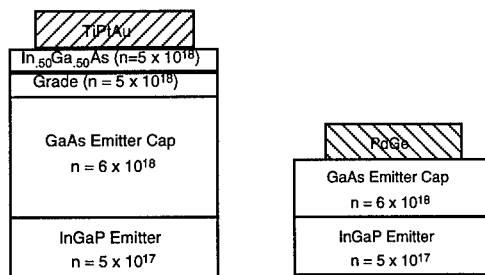


Figure 1. (a-left) Standard HBT structure with an $\text{In}_{0.50}\text{Ga}_{0.50}\text{As}$ contacting layer that is graded to GaAs. (b-right) New GaAs cap layer with PdGe contacts.

We propose using a non-spiking, alloyed PdGe metalization on a GaAs cap layer to prevent spiking problems, while eliminating the need for an InGaAs contacting layer. This study focuses on understanding the ohmic behavior and etching characteristics of electron-beam evaporated PdGe. Hot plate alloys will be discussed and compared to RTA results. The effects of alloy ambient upon contact resistance will be presented, and then the reactivity and etch undercutting of the PdGe in a wet chemical emitter etch will be discussed.

2. Experiment

The structures used in this study were grown on a GaAs substrate by LP-MOCVD. The standard structure, depicted in Figure 1 (a), consists of a 3000 Å GaAs buffer, a 700 Å InGaP emitter ($N = 5 \times 10^{17} \text{ cm}^{-3}$), a 1300 Å GaAs cap ($n = 6 \times 10^{18} \text{ cm}^{-3}$), and a 600 Å InGaAs contacting layer. The experimental cap structure shown in Figure 1 (b) has the same structure up to the emitter, but only a 600 Å GaAs cap layer ($n = 6 \times 10^{18} \text{ cm}^{-3}$).

For a control sample, mesas were etched into the standard structure and then transmission line model (TLM) patterned TiPtAu pads were deposited. The control sample was first alloyed for 3 minutes at 325 °C in N₂. Next, isolated TLM mesas were fabricated on the GaAs contacting layer, and then PdGe was deposited by e-beam evaporation. The PdGe TLMs were alloyed on a hot plate in 100% N₂, 100% H₂, and 15% H₂/85% N₂ ambients at various times and temperatures.

To study the etch characteristics of the PdGe on GaAs (under various alloy conditions), an HBT emitter metalization was deposited on the experimental GaAs cap structure. The resistance of the contact to a wet chemical etchant as well as the etch undercutting was observed.

3. Results

3.2 Time and temperature

Most of the PdGe work to date utilized an RTA to minimize alloy time [4]. To demonstrate that a short hot plate alloy can produce results comparable to an RTA alloy, this experiment studied PdGe contacts alloyed on a hot plate for less than 30 minutes. Figure 2 summarizes this data for a 15% H₂/ 85% N₂ ambient and also shows data for a 3 minute, 350 °C alloy with TiPtAu on a standard structure.

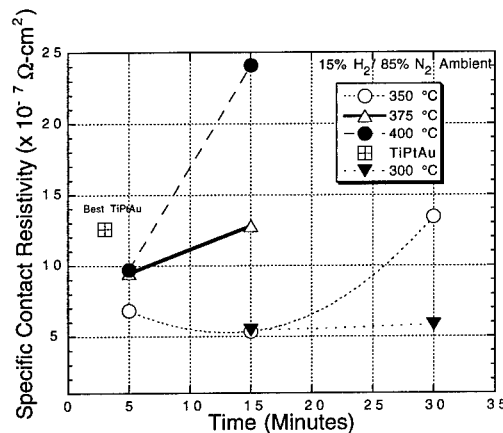


Figure 2. A plot of specific contact resistivity versus time at various temperatures for PdGe in a 15% H₂/ 85% N₂ alloy. Results for TiPtAu on a standard structure are included.

PdGe contacts were not ohmic after a five minute alloy at 300 °C, but after 15 minutes at 300 °C the PdGe alloy was ohmic. The specific contact resistivity did not change significantly after longer alloys at this relatively low alloy temperature. At 350 °C, the PdGe formed a low resistivity ohmic contact after both 5 and 15 minute alloys, and rose sharply after a 30 minute alloy. At both 375 °C and 400 °C the contact resistivity rose sharply with time immediately after a 5 minute alloy. These data suggest that there is a minimum combination of time and temperature necessary for ohmic contact formation. For times or temperatures beyond this threshold, the contact resistance begins to rise. Also, at alloy temperatures above 300°C, a short hot plate alloy can be used to achieve a specific contact resistivity, $p_c \approx 5 \times 10^{-7} \Omega\text{-cm}^2$, which is comparable to most results produced by an RTA alloy.

3.2 Alloy ambient

The effect of alloy ambient on contact resistance was studied, and Figure 3 shows the PdGe behavior for alloys in ambients of 100% H₂ and 100% N₂. The results show that for a given set of alloy conditions the hydrogen ambient always produces the lowest specific contact resistivity. However, the trend of contact resistivity versus time and temperature are similar for each alloy ambient.

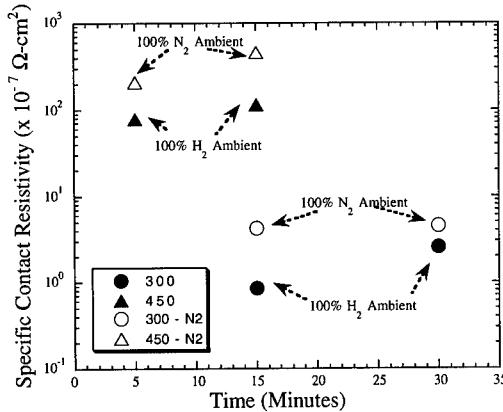


Figure 3. A plot of the specific contact resistivity versus time for PdGe at various temperatures in a 100% H₂ ambient. Also depicted is the dramatic increase in contact resistance for an alloy in a 100% N₂ ambient at various temperatures. For simplicity of presentation, the data for the 15% H₂/85% N₂ alloy shown in Figure 3 is not included in this plot.

A 5 minute alloy at 300 °C produced non-ohmic contacts in any ambient. After 10 minutes of alloying, the N₂ ambient produced an ohmic contact and the H₂ did not. The 10 minute N₂ alloy had the lowest contact resistance of any of the N₂ alloys, and a 15 minute H₂ alloy produced the lowest contact resistance for H₂. The 15 minute H₂ alloy at 300 °C produced the lowest reported specific contact resistivity ($\rho_c < 1 \times 10^{-7} \Omega\text{-cm}^2$) of any alloy methods employed for PdGe on GaAs. It is possible that using a N₂ ambient can also produce similar contact resistance to that of an H₂ ambient if the alloy time is slightly reduced.

3.3 Etching

Another important issue for using a PdGe HBT emitter contact is the reactivity of the contact during a wet chemical, self-aligned emitter etch. This study has shown that PdGe contacts are very reactive and etched easily in many of the oxidizing agents and acids used in GaAs wet chemical etches.

All of the HBT emitters that were alloyed in nitrogen were highly reactive and were removed by the emitter etch. However, PdGe emitter contacts alloyed in hydrogen remained after the emitter etch and are shown in Figure 4. As seen in Figure 4 (a), an unalloyed sample withstood the etch, but displayed a non-ideal self-aligned etch profile. After a 2 minute H_2 alloy, the emitters displayed excellent undercut characteristics, which are shown in Figure 4 (b). After 6 minutes, the contacts became more reactive and the etch profiles were observed to be inconsistent across the sample. One such emitter contact that showed an inconsistent etch profile on opposite sides of the same device is shown in Figure 4 (c). After a 10 minute alloy, the emitters were all removed as shown in Figure 5, where large PdGe alignment marks have almost been completely removed. When fabricating HBTs that employ a PdGe contact, one must either use dry etching or optimize the alloy conditions to decrease the reactivity of PdGe with various etchants.



Figure 4. PdGe HBT emitters after the GaAs cap and InGaP emitter were removed in a self-aligned etch. (a - left) un-alloyed. (b-middle) 2 minute alloy. (c-right) 6 minute alloy.



Figure 5. A PdGe (10 min. H_2) alignment mark that has been readily attacked during a self-aligned emitter etch.

4. Conclusion

This experiment has shown that PdGe contacts are potentially useful in HBT applications. A standard hot plate alloy can achieve comparable results to that of RTA in very short alloy times. In addition, the ambient alloy conditions were shown to significantly effect the alloy behavior, and the lowest reported PdGe contact resistance on GaAs was produced. Finally, the alloy conditions were shown to have significant effects on the reactivity of PdGe to wet chemical etchants as well as the etch undercutting.

5. Acknowledgments

The authors thank Bruce Flachsbart for helpful insight and discussions and DARPA for support under contract N6601-96-C-8615. D.A. Ahmari thanks Hughes Research Labs for support under a Hughes Fellowship.

References

- [1] Oka T, Ouchi K, Uchiyama H, Taniguchi T, Mochizuki K, Nakamura T 1997 *Elect. Dev. Lett.* 18 154-6
- [2] Chen W L, Chau H F, Tutt M, Ho M C, Kim T S, Henderson T 1997 *Elect. Dev. Lett.* 18 355-7
- [3] Ahmari D A, Fresina M T, Hartmann Q J, Barlage D W, Mares P J, Feng M, Stillman G E 1996 *Elect. Dev. Lett.* 17 226-8
- [4] Lai, J and Lee, Y 1994 *Appl. Phys. Lett.* 64 229-231

An Investigation of Breakdown in Power HEMTs and MESFETs Utilising An Advanced Temperature-Dependent Physical Model

Lutfi Albasha, Robert G. Johnson, Christopher M. Snowden and Roger D. Pollard

Institute of Microwaves and Photonics

School of Electronic and Electrical Engineering

University Of Leeds, Leeds, LS2 9JT, UK

Abstract: This paper presents a physical model and experimental validation for the breakdown process in HEMTs and MESFETs. The model is integrated into a fast quasi-two-dimensional physical simulation. The model takes account of the tunnelling effects in the region of the gate metallization. A new thermal model monitors the channel temperature and controls the tunnelling mechanism. The effects of the substrate conduction on breakdown in HEMTs is highlighted. Experimental results are presented which confirm the physical interpretations of the numerical model.

1. Introduction

The operation of many high frequency large-signal circuits is limited by the device's breakdown characteristics, restricting the power output. The accuracy of the large-signal design relies on the availability of suitable breakdown models. The popular breakdown theories have not been adequate to independently explain the full picture of the breakdown process in HEMTs and MESFETs. The relationship between the physical behaviour and thermal performance have also not been fully related. The effects of the gate leakage and substrate conduction on avalanche have not previously been fully presented. These issues are covered in this paper. It has been observed in [1] that the pattern of the MESFET measured DC $I_D - V_{DS}$ and V_{GS} characteristics has three distinctive regions with regard to avalanche breakdown. These were divided into pre-pinch-off, pinch-off and post-pinch-off. The width of the active channel with regard to depletion and the high fields at the gate edge played a role in the above divisions.

2. Model Description

The theory of the breakdown model is based on physical interpretations derived from measured and simulated observations. In contrast to MESFETs, spurious substrate current occurs in HEMT buffer layers due to the lateral E_x field component [2]. This current is drawn around the depleted channel and reduces the magnitude of the fields under the gate; this is expected to result in an increase in the breakdown voltage. Electrons leaking from the gate into the semiconductor using the different leaking mechanisms present the explanation for the soft breakdown observation. This is assumed in this model to always occur prior to avalanche breakdown.

The extent of its visible observation on the DC characteristics is influenced by the type and design parameters of the device under test. The level of current tunnelling from the gate, with respect to its

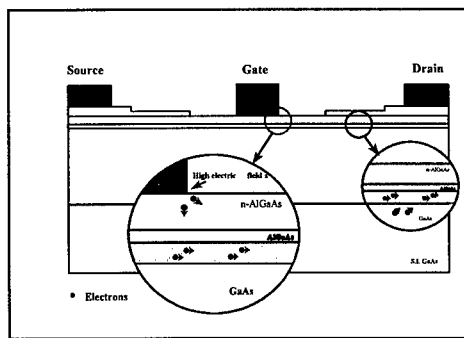


Figure 1 Schematic diagram of a HEMT device showing leaking electrons into the 2DEG channel

relation with design parameters and power dissipation, contributes towards the build up of impact ionization. Figure 1 shows a schematic diagram of a HEMT device illustrating the leakage mechanisms.

The breakdown model presented in this paper places important emphasis on the thermal conditions of the active channel in particular and the device in general. It is known [3] that gate tunnelling and leakage mechanisms are temperature and design parameters dependent. The accurate simulation of breakdown requires, consequently, an appropriate modelling of the thermal status inside the device.

3. Thermal Model

The new thermal model continuously computes the channel temperature and updates the gate leakage model. The temperature of the channel, consequently, stimulates the appropriate gate current process. The thermal model was initially based on a uniform channel temperature model [5]. The temperature in the channel is defined as:

$$T_{chan} = T_{amb} + I_{ds} V_{ds} R_{th} \quad (1)$$

where R_{th} is the thermal resistance of the device, T_{chan} is the channel temperature and T_{amb} is the ambient temperature. R_{th} quantifies the rate at which heat propagates through the device. One of the consequences of the uniform channel temperature model is that using the thermal breakdown model, the type of gate current is the same along the whole of the gate. In an actual device, however, the bulk of the heat is generated near the drain edge of the gate. This has been shown by two-dimensional simulations [6]. The mechanism of gate current leakage may be different here than under the rest of the gate. In order to take these effects into account, it was necessary to develop a non-uniform channel temperature model.

3.1 Non-uniform channel temperature model

The non-uniform channel temperature model is based on solving the one-dimensional heat flow equation to find the temperature profile along the channel. Instead of using equation (1). A simplified form of the heat equation has been solved across the device width:

$$\frac{d}{dx} \left[\frac{k dT}{dx} \right] + H_s = 0 \quad (2)$$

Temporal variations of temperature have been neglected as the thermal time constants are much greater than those of the microwave RF signals. Physically this corresponds to the temperature remaining constant over one cycle of the RF signal. This will be the case in the range 1-100GHz of the model. H_s is the heat generation term which is modelled by:

$$H_s = J \cdot E \quad (3)$$

where J is the current density and E is the electric field. The heat equation is solved using a Runge-Kutta scheme with a shooting method employed to ensure that the temperature reaches the appropriate gradient at both the source and drain edges of the device. This creates a temperature profile along the

channel and the mobility at a given position is this dependent on the temperature at that point. In addition, the type of gate current leakage mechanism is now also dependent on the exact temperature at each node under the gate region. Consequently, the model now reflects the fact that the gate leakage occurs primarily at the drain edge of the gate. Only at much higher field values does leakage occur under the whole of the gate region. Figure 2 shows the temperature profile across the active channel of a HEMT. The electric field pattern is also shown. Both patterns indicate a maximum value at the drain edge of the gate as expected.

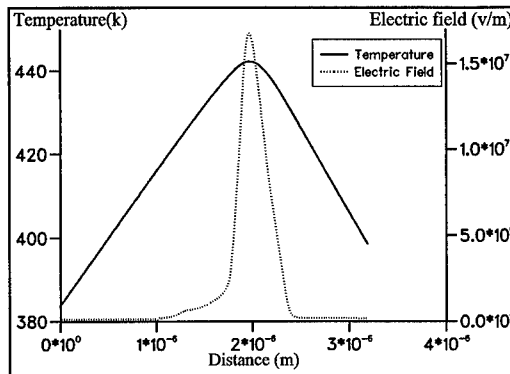


Figure 2 Temperature and electric field profiles across HEMT active channel

4. Temperature-Dependent Breakdown Model

The thermal breakdown model is integrated into the long standing and efficient quasi-two-dimensional physical model (Q2D) [4]. The Q2D model assumes that carrier transport takes place predominantly in a single spatial dimension (x -directed) from the source to drain.

4.1. Thermally dependent gate currents

The gate leakage and tunnelling currents are based on Padovani [3] equations. These equations involve complex functions of temperature, barrier height and semiconductor parameters. The Thermionic-Field (T-F) current is defined as [3]:

$$I_{TF} = AJ_s \exp(E/\epsilon') \quad (4)$$

where A is gate area, E applied voltage and ϵ' is an energy term defined in [3]. J_s is the saturation current defined in [3] as:

$$J_s = \frac{R(\pi E_{00})^{1/2}}{KT} \left(qV_r + \frac{q\phi_b}{\cosh^2\left(\frac{E_{00}}{KT}\right)} \right)^{1/2} \exp\left(-\frac{q\phi_b}{E_0}\right) \quad (5)$$

parameters are, again, as defined in [3]. E_{00} is a parameter which quantifies the diffusion potential from metal into semiconductor. It was observed that in equation (5), the term qV_r under the square root dominates the summation. Therefore, the equation simplifies to:

$$J_s = \frac{R(\pi E_{00} q V_r)^{1/2}}{KT} \exp\left(-\frac{q\phi_b}{E_0}\right) \quad (6)$$

which is a simpler term integrated into the model. An empirical difference limit between (5) and (6) was reached after some experimentation beyond which the solution obtained from equation (6) was observed to affect the numerical accuracy of the tunnelling current. The model then switches to the more stringent expression of equation (2). The term R in equations (5) and (6) is Richardson constant which is assumed temperature dependent. The field-emission tunnelling current and the Thermionic leakage current are as defined in [3]. Temperature and bias thresholds on the thermal model of the Q2D physical simulator were enforced and they control the tunnelling mechanism type for the thermionic, thermionic-field and field emission gate currents to be active.

5. Simulation Results and Experimental Validation

A 0.5um MESFET device was simulated using the Q2D model incorporating the thermal breakdown model. The result is shown in Figure 3. The result is compared with another simulation for the same device without the new model. Soft breakdown characteristics are clearly observed. This result also agrees with experimental results shown in Figure 4. The HP4145A Semiconductor Parameter Analyzer was used to perform the DC breakdown characterisation.

6. Conclusions

In this paper, a new thermal gate breakdown model has been presented. A non-uniform channel temperature model was presented and integrated with the breakdown model. The model is compatible with a fast quasi-two-dimensional physical device simulator used in CAD. Measured and simulated results of the DC characteristics of a MESFET have compared well.

References

- [1] J. Ashworth, *The physical mechanisms covering breakdown in GaAs MESFETs*, Ph.D thesis, Leeds University, UK, 1993
- [2] C.G. Morton, J.S. Atherton, C.M. Snowden, R.D. Pollard, M.J. Howes, "A large-signal physical HEMT model," *Int. Microwave Symp. MTT-S*, Vol. 3, pp.1759-1762, San Francisco, June 1996
- [3] F.A. Padovani, R. Stratton, "Field and thermionic-field emission in schottky barriers," *Solid-State Electronics*, Vol. 9, pp. 695-707, 1966
- [4] C.M. Snowden, R.R. Pantoja, "Quasi-two-dimensional MESFET simulation for CAD," *IEEE Trans.*, ED-36, No 9, pp. 1564-1574, 1989
- [5] R.G. Johnson, C.M. Snowden, R.D. Pollard, "A physics based electro-thermal model microwave and mm-wave HEMTs," *International Microwave Symposium, MTT-S*, Vol. 3, pp. 1485-1488, Denver, USA, June 1997.
- [6] J.C.A.D. Santos, *Modelling of short-gate length MESFETs for power amplifiers*, Ph.D thesis, Leeds University, UK, 1991

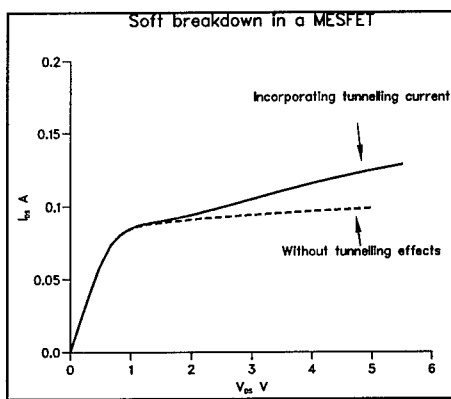


Figure 3 Simulated breakdown of MESFET, $V_{GS} = 0$ v

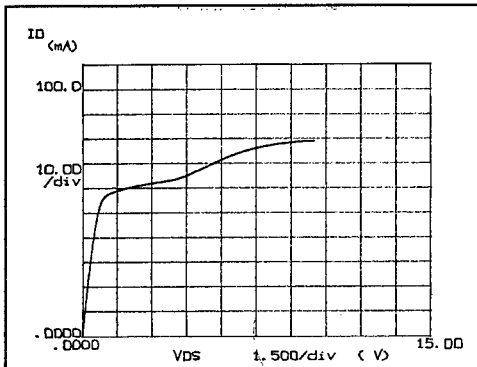


Figure 4 Drain current before breakdown for MESFET, $V_{GS} = 0.0$ v

Ultra - Linear Pseudomorphic HEMTs for Wireless Communications : A Simulation Study

Z. Borsosfoldi*, D. R. Webster[^], I.G. Thayne*, A. Asenov*,
D. G. Haigh[^], S. P. Beaumont*

** Nanoelectronics Research Centre, Dept of Electronics and Electrical Engineering,
University of Glasgow, Glasgow, G12 8QQ*

*[^] Dept of Electronic and Electrical Engineering, University College London,
Torrington Place, London, WC 1E 7JE*

In this paper, we apply numerical device simulation in the design of pseudomorphic HEMTs with improved linearity and reduced intermodulation products aimed at wireless communications applications. We show that in channel doped GaAs pHEMTs the introduction of a p-doped buffer layer significantly improves the device linearity leading to a 10dB suppression of 3rd order distortion over a wide bias range with similar gain when compared with a more standard δ -doped GaAs pHEMT device.

1. Introduction

In recent years, there has been rapid and sustained growth in the telecoms industry, especially in the field of mobile communications, as well as the emergence of large potential markets in the areas of wireless local area networks. The growth of digital services such as fax, video conferencing and internet access has led to an ever increasing pressure to maximise the utilisation of available bandwidth, which has led to the use of highly efficient modulation schemes together with tight channel spacings. Intermodulation distortion in key parts of the radio link can lead to serious degradation of channel quality resulting in data loss. A range of design techniques exist for minimising intermodulation distortion in components such as amplifiers and mixers, but performance is ultimately determined by the distortion introduced by the transistors around which such circuits are designed. In this paper, we use well calibrates numerical simulations in the design of pseudomorphic HEMTs with improved linearity and reduced intermodulation products aimed at wireless communications applications.

2. Calibration

The starting point for the simulation based design is a standard 0.12 μm gate length T-gate pHEMT fabricated at the Nanoelectronics Research Centre of Glasgow University [1]. The vertical layer structure of the device is shown in Fig. 1. The free carriers in the 2DEG are supplied by a δ -doping layer separated by a 2.5 nm spacer from the pseudomorphic InGaAs channel.

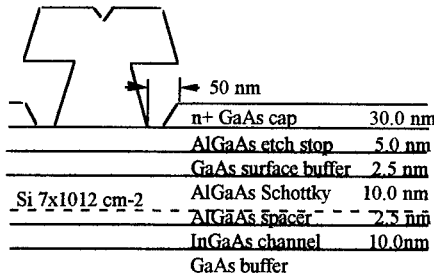


Fig. 1. Structure of the University of Glasgow existing $0.12\mu\text{m}$ gate length pseudomorphic HEMT.

For the purposes of this investigation, the drift-diffusion module of the commercial device simulator MEDICI [2] is utilised. When compared with Monte Carlo simulations, it has been established that a well calibrated drift-diffusion simulation, including enhanced saturation velocity in the mobility model, can represent accurately the channel velocity and the DC characteristics of deep sub-micron pHEMTs [3].

The drift-diffusion simulations in our study have been carefully calibrated against Monte Carlo simulations and the measured characteristics of $0.12\mu\text{m}$ gate length pHEMTs. Typical measured and simulated DC output characteristics of the standard pHEMTs are compared in Fig. 2. The average velocities in the pHEMT channel used in the drift-diffusion simulations are obtained from Monte Carlo simulation.

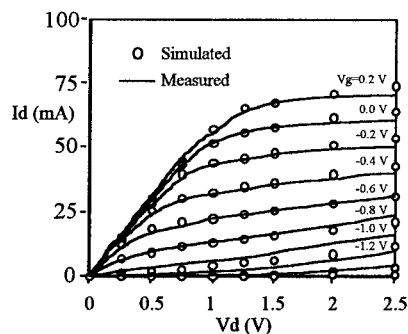


Fig. 2. Comparison of measured and simulated DC I-V curves for the University of Glasgow p-HEMT.

3. The Improved p HEMT

In the first set of simulation based design experiments, the δ -doping layer in the conventional pHEMT was replaced by a uniform channel doping with concentration which reproduces the threshold voltage of the original pHEMT. In order to improve further the linearity, the threshold voltage uniformity and to sharpen the pinch off, a p-doped buffer layer was introduced below the uniformly doped channel in the simulations.

The transconductance with respect to gate bias of the conventional, channel doped and p-buffered pHEMTs are compared in Fig. 3. The channel doped pHEMTs show flatter $gm(VGS)$ response compared to the conventional devices. The introduction of a p-doped buffer results in further improvements in linearity whilst also extending the useful gate voltage range.

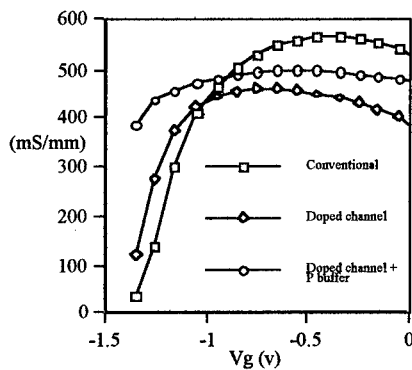


Fig. 3. Simulated transconductance of Conventional and Channel doped p-buffered pHEMTs.

4. Predicted Nonlinear Performance of the Improved HEMT

The transconductance (g_1) data sets generated by the physical model were imported into a numerical package and a tenth order polynomial was fitted to each of the data sets. By differentiating the polynomials, it was possible to obtain the derivatives g_2 and g_3 .

By making some simplifying assumptions, it is possible to use the derivatives to approximately calculate the 2-tone 3rd order RF intermodulation distortion performance of each device. It was assumed that

- (i) the extrinsic RF transconductance (g_{1rf}) of the device is 10% lower than that of the DC transconductance due to frequency dispersion arising from trapping effects.
- (ii) the RF output conductance (g_{dsrf}) of the device is 10% of the RF transconductance (as approximately seen in real sub-micron devices).
- (iii) the load impedance is sufficiently small that the nonlinear effects associated with output conductance and can be neglected.
- (iv) the amplitude of the applied signal is sufficiently small to allow the use of a Volterra Analysis approach.
- (v) the applied signal is clean from all distortion products

This leads to expressions for the 2nd and 3rd order nonlinear voltages at the output:

$$R_{L_{eff}} = \frac{R_L}{1 + g_{dcrf} R_L}$$

$$V_{out}(\omega_i) = g_{1rf} R_{L_{eff}} V_{in}(\omega_i)$$

$$V_{out}(\omega_2 \pm \omega_1) = g_{2rf} R_{L_{eff}} V_{in}(\omega_1) V_{in}(\omega_2)$$

$$V_{out}(2\omega_1 \pm \omega_2) = 0.75 g_{3rf} R_{L_{eff}} V_{in}(\omega_1)^2 V_{in}(\omega_2)$$

where R_L is the load resistance. $V_{in}(\omega_i)$ is the peak amplitude of the input signal at frequency ω_i . $V_{out}(\omega_i)$ is the peak amplitude of the output signal at frequency ω_i .

The simulated gain and 3rd order intermodulation distortion of the standard HEMT and the channel doped HEMT with p-doped buffer are shown in Fig. 4. The devices are defined to be 200μm wide working into a 50 Ω load with -16dBm/tone excitation. It can be seen that the improved device gives 10dB reduction of 3rd order distortion over a wide range bias whilst giving comparable gain.

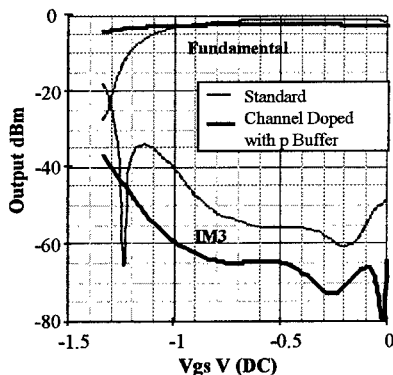


Fig. 4. Simulated bias dependent gain and 3 order intermodulation distortion of the University of Glasgow p-HEMT and the doped channel HEMT. The devices are 200μm wide working into 50 Ω with -16dBm/tone excitation.

Acknowledgements

The authors gratefully acknowledge the UK Engineering and Physical Sciences Research Council for funding this work.

References

- [1] N I Cameron, S Murad, H McLelland, A Asenov, M R S Taylor, M C Holland, S P Beaumont 1996 *Electronics Letters* p770
- [2] MEDICI 2.3 Technology Modeling Associates 1996
- [3] S Babiker, N I Cameron, A Asenov, S P Beaumont 1995 *Proc. ESSDERC '95*, (Editions Frontiers) p173

GaAs Homojunction Phototransistor with Minority Carrier Transport Assisted by Photo-generated Carrier Profile in the Base

Jun Ohsawa, Satoshi Yamaguchi, Kaoru Saigoh and Masatoshi Migitaka

Toyota Technological Institute
2-12 Hisakata, Tempaku, Nagoya 468 Japan

Abstract. Optical gain was observed in a structure that was unusual for transistors. Symmetric $\pi n^+ \pi$ layers on p⁺-substrate were formed using selective overcompensation by iron-diffusion. Devices of 100 μm diameter showed asymmetric photocurrent with bias polarity: the gain of 10 is nearly constant when the hole injection is along the carrier profile built up by photoabsorption, while for the reverse injection a smaller gain decreases with incident optical power. A double heterojunction device with π -AlGaAs layers also showed similar asymmetric photocurrent. Since the hole diffusion length is less than the base width, the photocarriers generated in the base region is believed to be responsible for the asymmetric gain.

1. Introduction

Bipolar transistors use the minority carriers injected from the emitter, whereas in phototransistors considerable amount of the carriers are generated by photoexcitation all over the base region. Especially when the carrier lifetimes are short, the generated carriers dominate and contribute to the diffusion current. We have examined this effect in an unusual doping combination of $\pi n^+ \pi$ GaAs homostructure where hole diffusion length is reduced to less than 0.2 μm by iron-diffusion, and found that gain can be obtained even for the heavily doped n-type base of 0.8 μm thick.

Our previous experiments have already shown that the iron energy level in GaAs makes an efficient recombination center but not a generation center. Carrier lifetime close to 10 ps was inferred from optical pulse responses[1], and also a low leakage diode was fabricated by iron diffusion into GaAs[2]. Since the n-type base is heavily doped and much thicker than the diffusion length, current gain is not expected for the usual transistor operation.

2. Device Fabrication

2.1 Selective overcompensation of n-type epitaxial layers

Table 1 specifies the layer structure of the phototransistor. The $\pi n^+ \pi$ layers were prepared using selective overcompensation by deep acceptors: iron-diffusion converted only lightly doped n-type material of nn⁺n VPE layers into p-type with low hole concentration. Compensation of donors in GaAs by iron acceptors is well established, and has been described elsewhere[2]. Choosing the diffusion temperature in the range of 650-900 °C, the deep acceptor concentration can be controlled from 5×10^{15} cm⁻³ to 2×10^{17} cm⁻³[3]. This time the diffusion was performed at 650 °C and the converted GaAs p-type layers is expected to have a hole concentration of 3×10^{11} cm⁻³ with the resistivity of 10^5 Ωcm.

Table 1 Layer structure of homojunction phototransistor

material	carrier conc. [cm ⁻³]	thickness [μm]
p-GaAs	3×10^{11}	0.7
n ⁺ -GaAs	1×10^{18}	0.8
p-GaAs	3×10^{11}	0.7
p ⁺ -GaAs sub.	2×10^{19}	150

2.2 Device processing

Two types of phototransistors were made: one uses GaAs homojunctions with a circular mesa structure, the other is composed of AlGaAs/GaAs double heterojunctions(DH) with a larger square mesa. The circular mesa of 100 μm diameter was passivated by a polyimide film, whereas no passivation was applied to the square DH type. AuZn/Au ohmic electrodes were formed both on the surface and on the p⁺-substrate. The AlGaAs/GaAs DH wafer was added for comparison. Here both n-GaAs epilayers were replaced by n-AlGaAs($X_{Al}=0.4$) with an additional p⁺ contact layer to assure its ohmic characteristics.

3. Characteristics

3.1 Current -Voltage Characteristics

The lowest curves in Fig. 1 and Fig. 2 show the dark current characteristics of the homojunction and DH devices. The low current level plus the symmetry in terms of bias polarity verify the successful formation of $\pi\pi^+\pi$ structures. The higher leakage current of the homojunction device in spite of the smaller junction area is suspected to be due to poor polyimide passivation. This is based on the facts that the current is nearly proportional to the voltage, and that much lower leakage current density in the order of 10^{-9} A/cm² at V_r = 1 V has been obtained with GaAs pn mesa diodes[2]. On the other hand, the DH device showed leakage current density as low as the value quoted above. These low dark currents are partly due to the nature of iron deep level at E_t - E_V = 0.42 eV in GaAs: deep levels located off the midgap energy in general do not make generation centers for thermal excitation, resulting in low generation current[4].

3.2 Photocurrent -Voltage Characteristics

Also shown in Fig. 1 are the dependence of photocurrent on the bias voltage with the incident optical power as a parameter. Photoexcitation was made at λ=827 nm by a diode laser. The photocurrent is asymmetric, and is higher when the surface-side junction is forward biased(plus bias). Zero-current points are shifted to minus bias side by a few tenth of a volt. The photocurrent at minus bias slightly increases with the voltage. Figure 3 shows the photocurrent as a function of incident optical power density at the bias of ±0.5 V. At plus bias linear dependence is observed, and the slope is equal to the responsivity of 4 A/W, which corresponds to the gain of about 10. In contrast, the relation is sublinear at the minus bias.

Similar characteristics for the DH device is shown in Fig. 2. Again, zero-current points are shifted to minus bias side, and the photocurrent is higher at plus bias. Since the emitter and the collector of this device does not absorb the incident light, and since the dark current itself is symmetric, the common

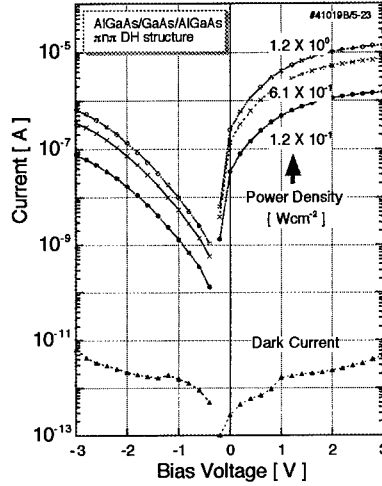
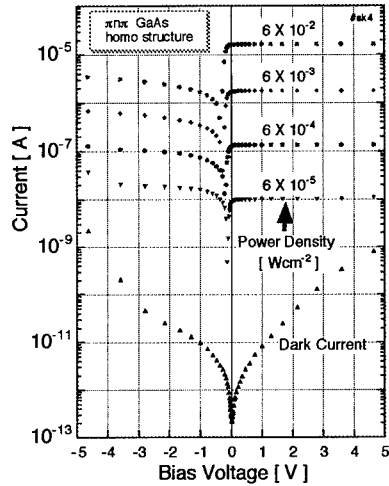


Fig. 1 Photocurrent vs. bias voltage for a homojunction device. Fig. 2 Photocurrent vs. bias voltage for a DH device.

asymmetric bias dependence observed in homo- and hetero-junction devices should derive from the asymmetric profile of the photo generated carriers in the base.

4. Simple Model Calculation and Discussion

To examine the minority carrier distribution in the base, the continuity equation for holes are solved in the base region of the homojunction device under illumination:

$$\frac{\partial p}{\partial t} = D_p \frac{\partial^2 p}{\partial x^2} + \alpha \Phi \exp[-\alpha x] - \frac{p - p_0}{\tau} = 0 \quad (1)$$

where α is the absorption coefficient, Φ the photon flux density, and τ the hole lifetime. Here we employ the usual Shockley's boundary condition of quasi-equilibrium. The self forward-biasing by accumulation of photo generated electrons are calculated by the balance of electron flow at the p-side depletion edges x_{pi} ($i=1,2$):

$$\left[-D_n \frac{\partial n}{\partial x} \right]_{x=x_{pi}} = - \int_{x_{ni}}^{x_{pi}} \alpha \Phi \exp[-\alpha x] dx \quad (2)$$

For simplicity all photo generated electrons in the depletion regions ($|x_{ni} - x_{pi}|$) are assumed to drift into the base region.

The results for the carrier lifetime of 10 ps are illustrated in Fig. 4, where hole profiles are compared with and without applied bias, V_{app} . The solid line stands for the profile when a forward bias of 0.5 V is applied to the surface-side junction, while the dotted line is for the open-circuit case. Because the absorption coefficient at 827nm corresponds to a decay length of 0.8 μm , the basic hole profile is determined by photo generation not by diffusion of injected holes. In this example the diffusion length is less than 0.1 μm , hence the injected holes would decay abruptly without photoexcitation in the base.

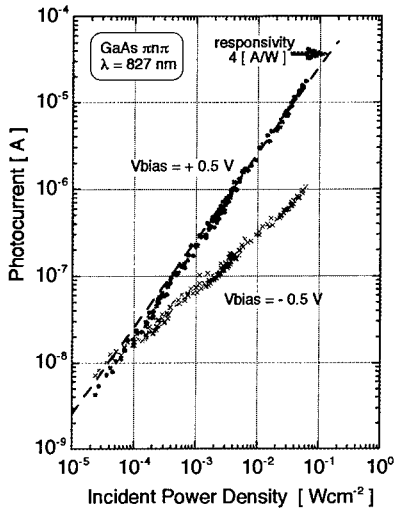


Fig. 3 Photocurrent vs. incident power relation for the homojunction device.

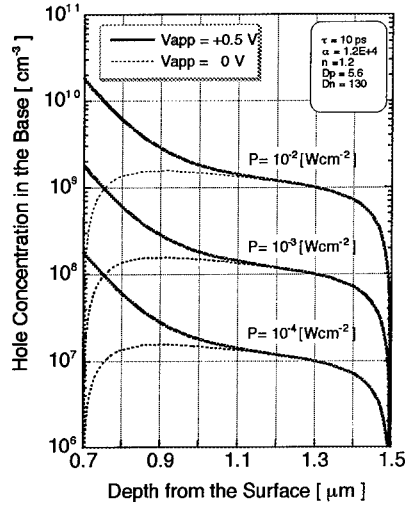


Fig. 4 Calculated hole concentration in the base for the homojunction device.

The photoexcitation, however, replenish the minority carriers lost by recombination, and creates the more slowly decaying hole distribution, which assists inward transport of the holes, but inhibits outward transport. That is, injection along the built-up hole distribution is favored.

Both in Fig. 1 and Fig. 2, zero-current points are shifted to minus bias side by 0.1-0.3V. This means the hole current balances when an additional bias is applied to the deeper junction. A tentative estimate gives a value of 0.35V for the forward bias needed to cancel the difference in photo generated hole densities at the two junctions. Closer examination including defect current is necessary to explain the details.

5. Conclusion

By use of an usual $\pi n^+ \pi$ structure, the importance of photo generated carriers in the base region for the optical gain has been pointed out. In preparing the device with short diffusion length of minority holes, iron diffusion into GaAs has been successfully utilized to selectively overcompensate n-type layers. With an appropriate design of carrier lifetime and device structure, both gain and response speed will be obtained even with a bipolar transistor scheme.

The Telecommunications Advancement Foundation assisted in attending the Symposium. The authors also wish to thank Dr. Y. Maeda, Mr. S. Nagira and Mr. H. Misawa of this Institute for the cooperation in this research.

References

- [1] Ohsawa J, Hashimoto N and Migitaka M 1993 *Jpn. J. Appl. Phys.* 32 L1066-69
Ohsawa J, Hashimoto N, Nakamura M and Migitaka M 1995 *Application of Photonic Technology* 479-82
- [2] Ohsawa J, Kakinoiki H, Ikeda H and Migitaka M 1990 *J. Electrochem. Soc.* 137 2608-11
- [3] Ohsawa J, Nakamura M, Nekado Y and Migitaka M 1995 *Jpn. J. Appl. Phys.* 34 L600-02
- [4] Schröder D K 1982 *IEEE Trans. Electron. Devices* ED-29 1336-38

Metamorphic HFETs with composite In_{0.8}Ga_{0.2}As/InAs/In_{0.8}Ga_{0.2}As channels on GaAs substrate

Christer Karlsson*, Niklas Rorsman*, Shumin Wang, and Magnus Persson

Department of Microwave Technology, Chalmers University of Technology, S-412 96 Göteborg, Sweden
*are now with Ericsson Microwave Systems, S-431 84 Mölndal, Sweden

Abstract. Metamorphic HFET materials with InAs/In_{0.8}Ga_{0.2}As channels have been grown on GaAs substrates. The influence of the insertion of an InAs layer has been investigated regarding the thickness and the position of the layer. The insertion of InAs results in 20 % increase in electron mobility at room temperature (34 % at 77 K). HFETs with 0.3 μm gate length have been fabricated and characterized. An extrinsic DC transconductance of 1100 mS/mm was achieved. Excellent high frequency performance has been achieved at low voltages. An f_{max} of 100 GHz and an f_T of 100 GHz were achieved at a drain voltage of 0.25 V and 0.75 V respectively. The f_T·I_d product of 30 GHz·μm corresponds to a carrier velocity of 1.9·10⁷ cm/s. The minimum noise figure was 0.8 dB with an associated gain of 9.2 dB at 25 GHz.

1. Introduction

Heterostructure Field-Effect Transistors (HFETs) using InAlAs/InGaAs lattice matched to InP have demonstrated excellent high frequency and low-noise performance [1]. It has been shown that the device performance can be further improved by increasing the indium concentration in the channel. This is partly due to the improvement of the electron mobility and velocity of In_xGa_{1-x}As with increasing x. Different approaches have been demonstrated, such as a pseudomorphic In_xGa_{1-x}As (x>0.53) channel [2], and insertion of a thin InAs layer in an otherwise lattice matched channel [3]. These approaches limit the channel thickness to be less than a critical value to prevent generation of dislocations. Furthermore, the material will be highly strained which reduces the electron mobility and velocity [4, 5].

Fully relaxed layers with optional indium content can be grown on either GaAs or InP substrates by growing a graded In_xAl_yGa_{1-x-y}As buffer. The use of GaAs is motivated by lower substrate price, less fragility, and more developed etching techniques. Different approaches for the graded buffer have been tried: linearly graded In_xGa_{1-x}As [6], step graded In_xAl_{1-x}As [7], linearly graded In_xAl_{1-x}As [8, 9], and linearly graded In_xAl_yGa_{1-x-y}As [10-12]. The structures in this study use a linearly graded In_xAl_{1-x}As (x=0-0.8) buffer on GaAs substrate.

Excellent results have been obtained from In_{0.52}Al_{0.48}As/In_{0.53}Ga_{0.47}As materials with inserted InAs layers, and investigations have been performed to optimize the position and thickness of the InAs layer [3, 13]. The position of the layer is normally chosen to confine as many electrons as possible inside the InAs quantum well. In this work we investigate the influence on device performance of the position and the thickness of an InAs layer in an In_{0.8}Ga_{0.2}As channel on GaAs substrate.

2. Material design and device fabrication

The materials were grown in a Varian GEN II MBE system. Details of the MBE growth have been published elsewhere [14]. The large lattice mismatch between substrate and active layers (5.7 %) are accommodated using a compositionally graded In_xAl_{1-x}As buffer. The large lattice mismatch causes a random surface roughness. The roughness was measured with atomic force microscope (AFM) and the rms value varied between 4.6 and 5.3 nm for the materials in this investigation.

Table I: Hall measurement results, t_{InAs} is the thickness of the inserted InAs layer and d_{InAs} is the distance between the channel-spacer interface and the InAs layer.

Material	t_{InAs} [nm]	d_{InAs} [nm]	μ @ RT [cm ² /Vs]	n_s @ RT [10 ¹² cm ⁻²]	μ @ 77K [cm ² /Vs]	n_s @ 77K [10 ¹² cm ⁻²]
#589	4	3	12900	1.79	31600	2.03
#590	6	3	11300	2.38	23000	2.60
#598	8	3	10600	2.28	19100	2.46
#599	6	0	13700	2.44	34500	2.61
#600	0	-	11400	2.05	25800	2.15

Five materials were grown with the basic structure as follows: 1 μm linearly graded $\text{In}_x\text{Al}_{1-x}\text{As}$ buffer ($x=0\rightarrow 0.8$), 100 nm $\text{In}_{0.8}\text{Al}_{0.2}\text{As}$ buffer, 35 nm channel, 5 nm $\text{In}_{0.7}\text{Al}_{0.3}\text{As}$ spacer, Si δ -doping $4 \cdot 10^{12} \text{ cm}^{-2}$, 25 nm $\text{In}_{0.7}\text{Al}_{0.3}\text{As}$ Schottky layer, and 5 nm $\text{In}_{0.8}\text{Ga}_{0.2}\text{As}$ cap layer. The channel layer was varied according to Table I. Three materials were grown with an InAs layer 3 nm (d_{InAs}) from the $\text{In}_{0.7}\text{Al}_{0.3}\text{As}$ spacer while the thickness of the InAs layer, t_{InAs} , was varied from 4 to 8 nm. A fourth material was grown with a 6 nm InAs layer positioned at the spacer interface. The last material was grown as a reference, without InAs layer. The total channel thickness was 35 nm for all materials.

3. Results and discussion

The influence of the thickness of the InAs layer was first investigated with materials #589, 590, 598, and 600. The InAs layers were positioned 3 nm from the $\text{In}_{0.7}\text{Al}_{0.3}\text{As}$ spacer in this part of the investigation. Our results show that the optimum thickness of the InAs layer is 6 nm (Figure 2). The initial increase in f_{max} for increasing InAs thickness is explained by the improvement in electron transport properties for InAs relative to $\text{In}_{0.8}\text{Ga}_{0.2}\text{As}$. When the layer thickness is increased above the critical thickness, the number of dislocations increase, degrading the performance. The theoretical critical layer thickness for thin InAs films on $\text{In}_{0.8}\text{Ga}_{0.2}\text{As}$ is approximately 8 nm (depending on growth conditions) [15].

The influence of the position was tested by a structure with a 6 nm InAs layer positioned at the spacer interface (Material #599). This material had the highest mobility, 13700 cm²/Vs at 300 K. This is 20 % higher than the reference material without InAs (#600) and 21 % higher than the material with the same thickness but different position of the InAs layer (#590) (Table I). This indicates that the best confinement of the electrons is achieved by positioning the InAs layer at the spacer interface. This is consistent with RF measurements where #599 had an f_{max} of 164 GHz at $V_{\text{ds}}=1 \text{ V}$ compared to 147 GHz for #590 at the same voltage.

The high mobility of the reference material (#600) compared to the materials with spacers can be explained by better crystal qualities in the channel since there is no lattice mismatched layer in the channel of this material.

The transconductance versus t_{InAs} follows the same trend as f_{max} . Accordingly, material #599 also gave the highest transconductance (1100 mS/mm) (Figure 1). Previous generations of this material family had problems with the pinch-off characteristics [11]. This has been solved (Figure 1) by decreasing the leakage currents in the graded buffer by using InAlAs instead of InGaAlAs.

At higher voltages, material #600 was superior. It does not contain any InAs layer, and its breakdown characteristics are better. The off-state breakdown voltage was measured using the drain current injection method [16]. BV_{ds} was 2.5 V and BV_{dg} was 3.4 V.

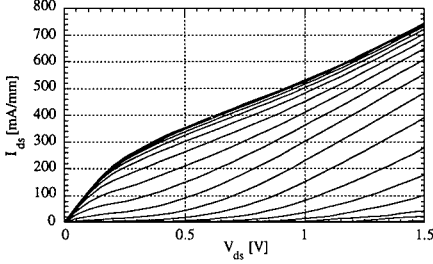


Figure 1a: Drain-source current, I_{ds} , versus drain-source voltage, V_{ds} , at gate voltage, V_g , from -1.5 to 0.4 V (0.1 V steps). (Material #599).

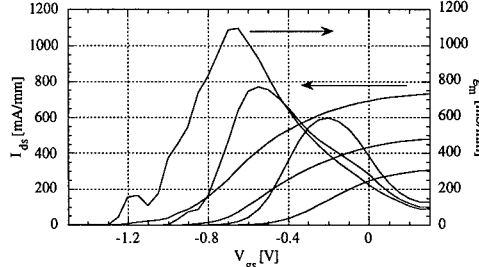


Figure 1b: Transconductance, g_m , and drain-source current, I_{ds} , versus gate voltage, V_g , at drain-source voltage, V_{ds} , 0.5, 1.0, and 1.5 V. (Material #599).

The devices were RF-measured up to 50 GHz using a HP8510C network analyzer. Small signal equivalent circuits were extracted using a direct extraction method [17]. These metamorphic devices with a composite channel exhibit excellent high frequency performance at low voltages. An f_{max} of 100 GHz was obtained at $V_{ds}=0.25$ V and $I_{ds}=26$ mA/mm for material #599 (Figure 3). All materials in this investigation have an f_{max} exceeding 100 GHz at 0.5 V. Below $V_{ds}=1$ V, these materials are superior to lattice matched InP-based devices fabricated with the same layout and processing techniques in our laboratory, in spite of the longer gate length (~ 0.30 μ m) compared to the lattice matched devices (0.15 μ m). Above 1 V the gate leakage current degrades the high frequency performance. Material #600 has the best high bias performance with an f_{max} of 230 GHz at 2.0 V. The excellent transport properties of these materials are also shown by the f_T of 100 GHz with a gate length of 0.3 μ m for material #599. The $f_T \cdot l_g$ product of 30 GHz· μ m corresponds to a carrier velocity of $1.9 \cdot 10^7$ cm/s. This is comparable to the best $f_T \cdot l_g$ results from InP-based devices [18, 19].

Noise measurements were performed at 3-25 GHz. The variation of the noise figure, NF_{min} , versus thickness of the inserted InAs layer follows the same trend as f_{max} with a minimum for 6 nm InAs. Material #599 exhibited the best noise characteristics with an NF_{min} of 0.8 dB and an associated gain of 9.2 dB at 25 GHz. This was achieved at $V_{ds}=0.4$ and $I_{ds}=85$ mA/mm.

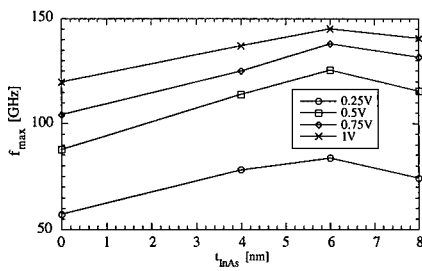


Figure 2: f_{max} versus thickness of the inserted InAs layer for different V_{ds} .

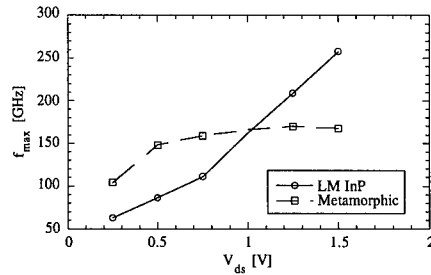


Figure 3: f_{max} versus V_{ds} for a lattice matched InP-based material (InP15) and a metamorphic structure with inserted InAs layer (#599).

4. Conclusions

Metamorphic HFET materials with InAs/In_{0.8}Ga_{0.2}As channels have been grown on GaAs substrates. The insertion of a 6 nm InAs layer at the In_{0.7}Al_{0.3}As spacer interface resulted in a 20 % increase in room temperature mobility (34 % at 77 K).

An extrinsic transconductance of 1100 mS/mm was achieved with a 0.3 μm gate length. Excellent high frequency performance has been achieved at low voltages. An f_{\max} of 100 GHz was achieved at $V_{ds}=0.25$ V and $I_{ds}=26$ mA/mm. Below 1.0 V, these devices are superior to lattice matched InP-based devices with 0.15 μm gate length fabricated with the same layout and fabrication processes. The $f_T \cdot L_g$ product of 30 GHz· μm corresponds to a carrier velocity of $1.9 \cdot 10^7$ cm/s. Compared to a reference structure without InAs layer, the insertion of a thin InAs layer caused an increase in f_{\max} with 12 %, f_T with 64 %, and the $f_T \cdot L_g$ product with 19 %. The minimum noise figure was 0.8 dB with an associated gain of 9.2 dB at 25 GHz for a material with a 6 nm InAs layer at the spacer interface. This was measured at a V_{ds} of 0.4 V and an I_{ds} of 85 mA/mm.

Our results show that the metamorphic InAs/InGaAs HFET is a promising device for low noise applications with a very high gain at low DC power consumption.

5. Acknowledgment

The authors wish to thank the following organizations and persons: the Swedish Research Council for Engineering Sciences (TFR), the Swedish Defence Material Administration (FMV), and the Swedish National Board for Industrial and Technical Development (NUTEK) for financial support, the Swedish Nanometer Laboratory for access to the e-beam system, and Prof. H. Zirath, Prof. E. Kollberg, and Dr. T. G. Andersson for their support of this work.

6. References

- [1] Nguyen L D, Larson L E, Mishra U K. Proceedings of the IEEE 1992;80(4):494-518.
- [2] Smith P M, Liu S-M J, Kao M-Y, et al. IEEE Microwave and Guided Wave Letters 1995;5(7):230-232.
- [3] Akazaki T, Arai K, Enoki T, Ishii Y. IEEE Electron Device Letters 1992;12(6):325-327.
- [4] Jaffe M D, Sekiguchi Y, Singh J, Chan Y J, Pavlidis D, Quillec M. Cornell Conference on High Speed Semiconductor Devices and Circuits, Ithaca, NY, 1987:70-79.
- [5] Liu C T, Lin S Y, Tsui D C. Applied Physics Letters 1988;53(25):2510-2512.
- [6] Win P, Druelle Y, Legry P, et al. Electronics Letters 1993;29(2):169-170.
- [7] Higuchi K, Kudo M, Mori M, Mishima T. International Electron Devices Meeting 1994:891-894.
- [8] Chertouk M, Heiss H, Xu D, et al. IEEE Electron Device Letters 1996;17(6):273-275.
- [9] Kawano M, Kuzuhara T, Kawasaki H, Sasaki F, Tokuda H. IEEE Microwave and Guided Wave Letters 1997;7(1):6-8.
- [10] Inoue K, Harmand J C, Matsuno T. Journal of Crystal Growth 1991;111:313-317.
- [11] Rorsman N, Karlsson C, Wang S M, Zirath H, Andersson T G. Electronics Letters 1995;31(15):1292-1294.
- [12] Karlsson C, Rorsman N, Wang S M, Olsson E, Andersson T G, Zirath H. European Solid State Device Research Conference 1996.
- [13] Enoki T, Arai K, Akazaki T, Ishii Y. IEICE Transactions on Electronics 1993;E76-C(9):1402-1411.
- [14] Wang S M, Karlsson C, Rorsman N, et al. Ninth International Conference on Molecular Beam Epitaxy, Malibu, California, 1996.
- [15] Matthews J W, Blakeslee A E. Journal of Crystal Growth 1974;27:118-125.
- [16] Bahl S R, del Alamo J A. IEEE Transactions on Electron Devices 1993;40(8):1558-1560.
- [17] Rorsman N, Garcia M, Karlsson C, Zirath H. IEEE Transactions on Microwave Theory and Techniques 1996;44(3):432-437.
- [18] Wojtowicz M, Lai R, Streit D C, et al. IEEE Electron Device Letters 1994;15(11):477-479.
- [19] Streit D C, Tan K L, Dia R M, et al. Electronics Letters 1991;27(13):1149-1150.

A Novel High-Performance WSi-gate Self-Aligned N-AlGaAs /InGaAs/N-AlGaAs Pseudomorphic Double Heterojunction MODFET by Ion Implantation

**K. Nishii, M. Nishitsuji, T. Uda, T. Yokoyama, S. Yamamoto,
T. Kunihiba and A. Tamura**

Electronics Research Laboratory, Matsushita Electronics Corporation,
3-1-1 Yagumo-Nakamachi, Moriguchi, Osaka 570, Japan

Abstract. A novel high performance WSi-gate self-aligned N-AlGaAs/InGaAs/N-AlGaAs pseudomorphic double heterojunction MODFET was fabricated by ion implantation into the epitaxial layers. To obtain high activation for the Si implanted epitaxial layers, we have optimized the layer structure, especially AlGaAs thickness, and annealing conditions using a graphite heater. The 0.8 μ m-gate DH-MODFET exhibited a K-value of 400 mS/Vmm, gm_{MAX} of 450 mS/mm and I_{MAX} of 300 mA/mm with V_{th} of -0.05 V. The standard deviation of V_{th} was 18.1 mV across a 3 inch wafer. Operated with drain bias of 3.0 V, the DH-MODFET demonstrated 28% power added efficiency (PAE) with -56.4 dBc adjacent channel leakage power ratio (ACPR) at $P_{out} = 21.5$ dBm and 600 kHz off center frequency from 1.9 GHz.

1. Introduction

In recent years, GaAs MMIC power amplifiers have attracted much attention in cellular phones because of their low voltage operation and low power consumption. These conventional GaAs MMIC power amplifiers[1] usually need dual (positive and negative) voltage supplies. However, negative voltage generation becomes one of the large obstacles to realize very compact and low cost handsets. Therefore, single voltage supply MMIC power amplifiers have been strongly demanded. A good example has been reported on the single low voltage supply GaAs MMIC power amplifier[2] by using the N-AlGaAs /InGaAs/N-AlGaAs pseudomorphic double heterojunction modulation doped FET(DH-MODFET) because of its advantageous high frequency characteristics and drain current capability. However, in the conventional fabrication process of DH-MODFET, the gate recess is performed by wet chemical etching, which cause poor uniformity of device characteristics such as threshold voltage (V_{th}).

In this work, we report successful fabrication of WSi-gate self-aligned pseudomorphic DH-MODFETs by ion implantation into the epitaxial layers with high-performance and very uniform device characteristics.

2. DH-MODFET Structure

Figure 1 shows the cross-sectional view of the DH-MODFET. The epitaxial structure was grown by MBE on a semi-insulated GaAs substrate. Following the undoped GaAs buffer layer and undoped AlGaAs layers, 5 nm bottom N-AlGaAs layer, 2 nm undoped AlGaAs bottom spacer layer, 15 nm InGaAs quantum well, 2 nm undoped AlGaAs top spacer layer, 10 nm top N-AlGaAs layer, and 5 nm

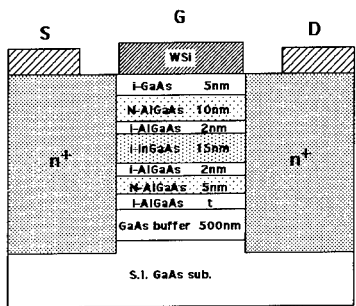
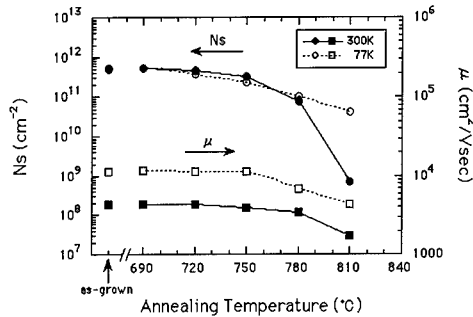


Fig. 1 Cross-sectional view of the DH-MODFET

Fig. 2 Dependence of Ns and μ on annealing temperature

undoped GaAs layer were grown. The AlAs mole fraction in the AlGaAs layers was 0.25 and the doping level of Si in the N-AlGaAs layers was $2.0 \times 10^{18} \text{ cm}^{-3}$. The In mole fraction in the InGaAs layer was 0.2. The sheet electron concentration and Hall mobility obtained for this DH structure were $5.2 \times 10^{11} \text{ cm}^{-2}$ and $4400 \text{ cm}^2/\text{V}\cdot\text{s}$ at room temperature and $5.0 \times 10^{11} \text{ cm}^{-2}$ and $11200 \text{ cm}^2/\text{V}\cdot\text{s}$ at 77K, respectively.

The n⁺ regions self-aligned to the refractory WSi gate were formed by Si ion implantation into the epitaxial layers. In order to obtain high activation for Si implanted N-AlGaAs/InGaAs/N-AlGaAs heterostructure layers without degrading the characteristics of the epitaxial layers, we have studied the annealing conditions and the epitaxial layer structure. We adopted hotplate annealing using a graphite heater for activating the implanted layers, because it allows rapid thermal processing with good temperature control. Figure 2 shows the dependence of sheet electron concentration (Ns) and Hall mobility (μ) for the DH structure on annealing temperature. Annealing time is 30 sec. A drastic degradation of Ns and μ were observed in the region of temperature above 780 °C. This phenomenon is considered to be caused by degradation of the DH structure.

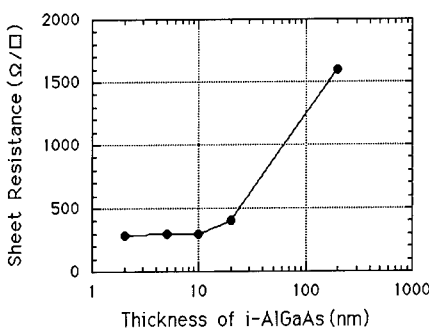


Fig. 3 Dependence of the sheet resistance of the Si implanted epitaxial layers on bottom undoped AlGaAs layer thickness (annealed at 750 °C for 30 sec)

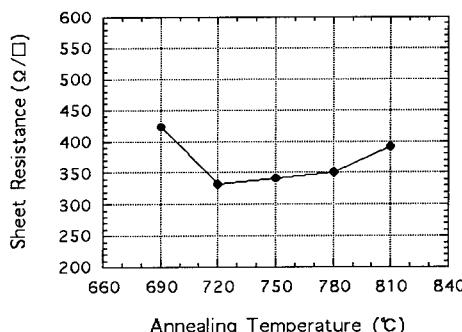


Fig. 4 Dependence of the sheet resistance of the Si implanted epitaxial layer on annealing temperature (annealing time is 30 sec)

It is known that AlGaAs has poor activation compared to GaAs in the case of Si implantation[3,4]. Therefore, we studied the relation between AlGaAs layer thickness and sheet resistance of the Si implanted epitaxial layers. Figure 3 shows the dependence of the sheet resistance of the Si implanted region at 50 keV with a dose of $5 \times 10^{13} \text{ cm}^{-2}$ on the thickness of the bottom undoped AlGaAs layer between the GaAs buffer layer and the bottom N-AlGaAs layer. From this figure, the thickness of the bottom undoped AlGaAs layer must be less than 20 nm to obtain high activation and we typically used 10 nm. Figure 4 shows the dependence of the sheet resistance of the Si implanted region at the above conditions on the hotplate annealing temperature for the sample with 10 nm undoped AlGaAs layer. The low sheet resistances were obtained in a range of annealing temperature from 720 °C to 750 °C. From the result, we adopted 750 °C on annealing temperature.

3. Fabrication and Device Characteristics

3.1 Fabrication Process

The device fabrication process begins with the mesa-etching for the definition of the channel region. Then a WSi refractory metal gate was formed by DC sputtering and reactive ion etching with mixed CF₄/SF₆ gas. Then 60 nm thick SiO₂ film was deposited. We carried out self-aligned Si ion implantation using WSi gate and 45 nm width SiO₂ sidewall as a mask at an energy of 50 keV with a dose of $5 \times 10^{13} \text{ cm}^{-2}$. After that, the implantation layer was annealed by hotplate annealing at 750 °C for 30 sec in a H₂ atmosphere with a SiO₂ capping film. Ohmic contacts were formed by evaporation of AuGe/Ni/Au. Finally, a Ti/Au layer was deposited as a gate over-layer and interconnect metal.

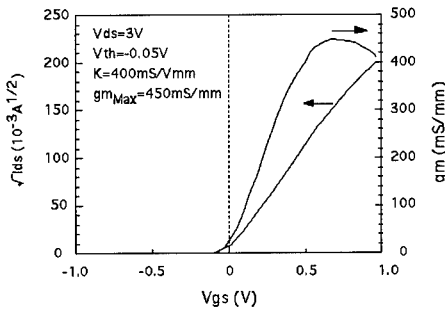


Fig. 5 Dependence of $\sqrt{I_{ds}}$ and g_m on V_{gs}
($L_g=0.8\mu\text{m}$, $W_g=100\mu\text{m}$)

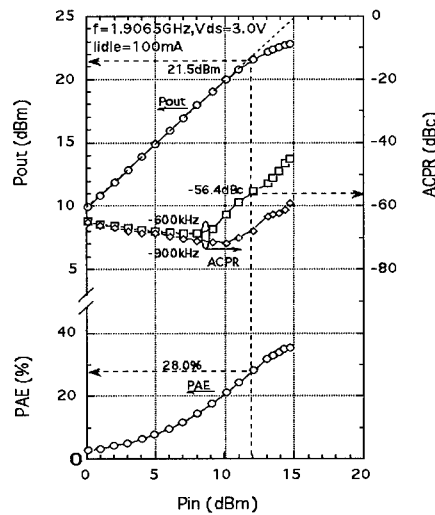


Fig. 6 Input-output characteristics with ACPR and PAE of the DH-MODFET ($W_g=4\text{mm}$)
Input Signal : $\pi/4$ shift QPSK (PHS mode)

3.2 DC and RF Characteristics

Figure 5 shows the typical $\sqrt{I_{ds,gm}}$ - V_{gs} characteristics of a $0.8\mu\text{m}$ -gate DH-MODFET formed by this process. The DH-MODFET with $100\mu\text{m}$ gate width exhibited a K-value of 400 mS/Vmm , a gm_{MAX} (maximum transconductance) of 450 mS/mm and I_{MAX} (maximum drain current) of 300 mA/mm with a V_{th} of -0.05 V at V_{ds} of 3 V . The measured contact resistance was $0.08 \Omega\text{mm}$ and the sheet resistance of n^+ layer was $300 \Omega/\square$. The typical gate-drain breakdown voltage was -9 V measured at a gate-drain current of $100 \mu\text{A/mm}$.

The V_{th} of 35 devices was measured across a 3 inch wafer. The V_{th} was determined by linear extrapolation of the square root of the drain current. The average V_{th} of 35 devices was -0.05 V . The standard deviation of V_{th} is 18.1 mV across a 3 inch wafer.

Figure 6 shows input-output power performance of the DH-MODFET ($W_g=4\text{mm}$) with adjacent channel leakage power ratio(ACPR) and power added efficiency(PAE). Operated with a single drain bias of 3.0V , we obtained PAE of 28.0% with low ACPR of -56.4 dBc at $P_{out} = 21.5 \text{ dBm}$ and $f=1.9 \text{ GHz}$. The characteristics of this DH-MODFET satisfies the requirements for low current operation in the single voltage supply condition.

4. Conclusion

We have developed a novel high performance WSi-gate self-aligned N-AlGaAs/InGaAs/N-AlGaAs pseudomorphic double heterojunction MODFET by ion implantation into the epitaxial layers. To obtain high activation for the Si implanted epitaxial layers, we have optimized the layer structure, especially bottom undoped AlGaAs layer thickness, and the annealing condition using a graphite heater. The $0.8 \mu\text{m}$ -gate DH-MODFET exhibited K-value of 400 mS/Vmm , gm_{MAX} of 450 mS/mm and I_{MAX} of 300 mA/mm with V_{th} of -0.05 V . The standard deviation of V_{th} was 18.1 mV across a 3 inch wafer. Operated with drain bias of 3.0 V , the DH-MODFET demonstrated PAE of 28% with ACPR of -56.4 dBc at $P_{out} = 21.5 \text{ dBm}$ at 600 kHz off center frequency from 1.9 GHz . These excellent results suggest that this process is very suitable for fabrication of GaAs power MMIC's operated with a single voltage supply, with very uniform device characteristics.

Acknowledgment

The authors wish to thank Dr. G. Kano and Dr. M. Inada for their encouragement throughout this work.

References

- [1] Yokoyama T, Kunihisa T, Fujimoto H, Takehara H, Ishida K, Ikeda H, and Ishikawa O
1994 *IEEE Trans. on Microwave Theory and Techniques* 42 2623-2628
- [2] Yokoyama T, Kunihisa T, Nishijima M, Yamamoto S, Nishitsuji M, Nishii K, Nakayama M, and Ishikawa O
1996 *Proc. Int. Conf. on IEEE GaAs IC Symp.* 107-110
- [3] Adachi S 1988 *J. Appl. Phys.* 63 64-67
- [4] Christine S L and Clifton G F 1988 *J. Appl. Phys.* 64 2103-2106

Novel applications of HEMTs for future 4.2K low-power and low-frequency cryoelectronics

Y. Jin

L2M, CNRS, 196, avenue Henri RAVERA, 92225 Bagneux Cedex, France

Abstract. Pseudomorphic $(Al,In)GaAs/GaAs$ HEMTs have been fabricated and investigated. These devices exhibit high DC and low-frequency noise performances at 4.2K. Neither collapse nor kink effect has been detected. Large current variation from sub-nano to milli-Ampere with a good saturation behaviour has been characterised with a gate bias variation of about half a volt. Even at an extremely low-power supply of 57pW, an intrinsic voltage gain of 160 has been reached. With a power supply smaller than 10 μ W, we obtained an equivalent input noise as small as 1.9nV/ \sqrt{Hz} at 1kHz, a white noise lower than 0.5nV/ \sqrt{Hz} , a shot noise of 0.76fA/ \sqrt{Hz} , and the corresponding Hooge parameter of 5.5×10^{-6} . Finally, a real application of this type of device in a 4.2K preamplifier has demonstrated an equivalent input noise level of 0.12nV/ \sqrt{Hz} with a bandwidth of 2MHz.

1. Introduction

Low-power, low-frequency and low-noise cryogenic transistors are widely demanded for preamplifiers in cryogenic systems working at 4.2K or below. Applications include superconducting particle detectors and bolometers in nuclear physics, very low signal measurements in mesoscopic physics, and photodetectors in spacecraft telescopes. So far, the lowest noise level transistors are *Si* JFETs, but with a minimum operating temperature of about 100K [1-2]. In order to decrease this limit, many efforts have been devoted. The well investigated devices are *GaAs* MESFETs which can work at 4.2K or below [3], and their performances have been considerably improved [4]. However, their $1/f$ noise level, *e.g.*, at 1kHz and at 4.2K, is still several times higher than that of *Si* JFETs. In this work, we have introduced and investigated pseudomorphic *GaAs* HEMTs for the goal of low-power, low $1/f$ noise and cryogenic working temperature.

Comparing HEMTs to MESFETs, the fundamental difference is that the former is based on a two-dimensional electron gas (2DEG) while the latter uses a three-dimensional electron gas. The 2DEG can be obtained by a heterostructure arrangement, *e.g.*, $AlGaAs/GaAs$, or pseudomorphic $(Al,In)GaAs/GaAs$. The electrons in the 2DEG reside in a very pure crystal material and they are isolated from the donors by a spacer layer. Thus, electron-donor collisions and electrons frozen at ionised donors at low temperature can be avoided. Electrons therefore present high qualities in mobility and in concentration, especially at low temperature. The 2DEG has been largely used in mesoscopic physics experiments, in particular we have investigated the quantum shot noise in a Quantum Point Contact (QPC) constructed by split gates on a $AlGaAs/GaAs$ 2DEG [5]. At milli-Kelvin temperature range and with very low bias and low frequency measurement conditions, the shot noise in the QPC decreases with the reduction of the current flowing through it and reaches the limit, *i.e.*, the thermal noise level which is determined by the cryostat. Furthermore, from a device point of view, *e.g.*, the transconductance and the cut-off frequency, HEMTs have also demonstrated an increase in performances with decreasing working temperature [6]. Indeed, from the above experiments, electrons in a 2DEG exhibit essential features for cryogenic devices.

Pseudomorphic *GaAs* HEMTs, compared to classical *GaAs* HEMTs, have the advantages of a better 2DEG confinement, higher electron density and lower *Al* mole fraction in the $AlGaAs$ material. High *Al* mole fraction in *GaAs* HEMTs is considered as the source of DX centers and DX centers can generate collapse [7] in current-voltage (I-V) characteristics for transistors at low temperature.

2. Experiment

The fabricated HEMTs are based on a commercially available pseudomorphic $(Al,In)GaAs/GaAs$ heterostructure from Picogiga [8], grown by Molecular Beam Epitaxy. Source and drain ohmic contacts are performed by using $Ni/Ge/Au$ process [9]. Device isolation and gate recess are achieved by wet chemical etching. The devices are finally packaged into TO-18 boxes.

Typical low temperature $I-V$ curves obtained for HEMT N°9-4 and measured with a HP4142B are shown on Fig.1. Collapse and kink effect [10] are totally absent in these devices. This indicates the high qualities of both the heterostructure material and the fabrication process. In the low drain-source current I_{ds} region, the saturating of I_{ds} can be observed at drain-source bias V_{ds} much lower than 1V. At $V_{ds}=0.1V$ and $I_{ds}=0.57nA$, the transconductance $g_m=\delta I_{ds}/\delta V_{gs}$, where V_{gs} , the gate-source bias, is $0.16\mu S$, and the drain conductance $g_d=\delta I_{ds}/\delta V_{ds}$, is $1.0nS$. Consequently, an intrinsic voltage gain $G_o=g_m/g_d$ of 160 with an operating power as small as $57pW$ can be deduced.

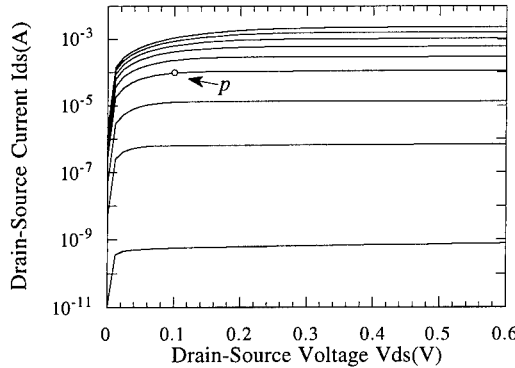


Fig.1 $I_{ds}-V_{ds}$ curves versus V_{gs} for HEMT N°9-4 at 4.2K. The logarithmic scale is used for full I_{ds} illustration. From bottom to top, V_{gs} varies from -0.70V to 0V with a step of 0.05V.

In Tab.1 we display the typical parameters obtained at working point "p", where I_{gs} is the gate leakage current, $R_{ds}=1/g_d$, the drain-source channel resistance, $G=g_mR_L/(g_dR_L+1)$, the effective voltage gain and $R_L=10k\Omega$ is the load resistance. The G calculated using DC parameters is verified with an alternative amplifier circuit setup using the same device. The shot noise i_n induced by I_{gs} can be written as $\sqrt{(2eI_{gs})}$, where e is the electron charge. In order to reduce this noise, a very careful recess is carried out. I_{gs} has thus been significantly reduced to the pico-Ampere range. With $I_{gs}=1.8pA$, the corresponding i_n is only $0.76fA/(\sqrt{Hz})$.

Tab.1

point	$V_{gs}(V)$	$V_{ds}(V)$	$I_{ds}(mA)$	$I_{gs}(pA)$	$i_n (fA/\sqrt{Hz})$	$g_m(MS)$	$R_{ds}(k\Omega)$	G_o	G	$e_n(nV/\sqrt{Hz})@1kHz$
p	-0.55	0.1	0.095	1.8	0.76	1.6	2.3	3.7	3.0	1.9

For the equivalent input $1/f$ noise voltage measurement, a 5004 EG&G BROOKDEAL preamplifier and a HP35665A dynamic signal analyser, have been applied. It is well known that the Hooge $1/f$ empiric current noise spectrum formula [11] can be written as follows for FETs :

$$S_{I_{ds}} = \alpha_H I_{ds}^2 / N f \quad (1)$$

where α_H is the Hooge parameter, N , the carriers number under the gate and f , the frequency. The equivalent input noise voltage e_n can be written as $e_n^2 = S_{e_n} = \alpha_H I_{ds}^2 / N f g_m^2$, where S_{e_n} is the input

voltage noise spectrum. As the effective load resistance of the DUT is $R_L' = R_L/(g_d R_L + 1)$, we have $S_{e_n} = \alpha_H I_{ds}^2 R_L'^2 / N_f g_m^2 R_L'^2 = S_{V_{ds}} / G^2$, where $S_{V_{ds}} = \alpha_H I_{ds}^2 R_L'^2 / N_f$ is the output voltage noise spectrum. e_n can thus be finally deduced from the ratio of the measured value $S_{V_{ds}}^{-1/2}$ over the corresponding G .

In Fig.2 we plot the typical e_n as a function of f at working point "p". e_n varies as $f^{-0.6}$ as illustrated by the dotted line. It must be mentioned that the evolution of S_{e_n} is $f^{-1.2}$. An e_n as small as 1.9nV/Hz at 1kHz is obtained with a power supply of only 9.5μW. In addition, the spectrum weight $e_n=0.5nV/\sqrt{Hz}$ at 10kHz implies that the white noise level should be even lower. These values, both in $1/f$ noise and in power supply, are smaller than those of any FET at 4.2K reported in the literature [3-4]. The $1/f$ noise at 4.2K is very close to that of the best Si JFET at 135K, and white noise is even lower[1].

Referring to the work of [12], at low drain bias conditions, the Hooge parameter in formula (1) can be deduced from the electron mobility and the voltage bias. Using the experimental electron mobility value of about $3 \times 10^4 \text{ cm}^2/\text{Vs}$ in $(Al,In)GaAs/GaAs$ heterostructures measured at 4.2K, we can evaluate $\alpha_H = 5.5 \times 10^{-6}$ at point "p". This value is about ten times smaller than that obtained in the GaAs HEMT at 300K [12]. To our knowledge, α_H at 4.2K has not yet been well investigated. Besides, according to the theory in [13], if one considers only the elastic collision process at low drain bias and low temperature in a FET, the calculated α_H for this pseudomorphic HEMT at 4.2K should be as small as 3.4×10^{-10} . The large difference between the experiment and the theory calls for more detailed investigations.

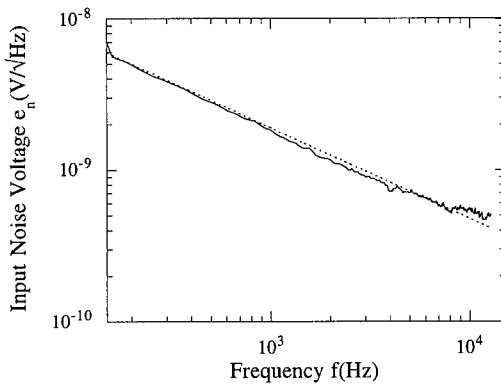


Fig.2 Spectrum of e_n versus f from 150Hz to 12.8kHz for HEMT N°9-4 at 4.2K, and the bias conditions listed in Tab.1.

One HEMT of this type has been used in a 4.2K preamplifier for a metastable superconducting particle detector. This detector is used in order to increase the efficiency and the energy resolution for the possibilities of solar neutrinos, cold dark matter, and double beta decay detection[14]. The detector consists of tin microspheres with a diameter of about 10μm, suspended in paraffin wax at 100mK, and superheated by a magnetic field. When these grains are irradiated by β beam or X ray, their magnetic state changes from superconductor diamagnetism to normal metal. This change can thus be picked up by a copper coil. The very weak signal is then amplified by connecting it to the HEMT input which is at 4.2K, away from the detector. The HEMT's bias and characteristics are $V_{ds}=1.6\text{V}$, $I_{ds}=2.8\text{mA}$, and $g_m=57\text{mS}$. An equivalent input noise level of 0.12nV/ $\sqrt{\text{Hz}}$ with a bandwidth of about 2MHz has been attained. Moreover, important distance reduction in the connection between detector and HEMT improves significantly the signal over noise ratio. In this way, the detector's electronic sensibility has been increased four times [15]. It must be mentioned that the preamplifier in this study was initially designed with Si JFETs. It is well known that operating bias values for Si devices are higher than for GaAs HEMTs. Hence, for HEMTs, these bias values can be reduced by a specific configuration of the

preamplifier. In addition, the working temperature and the distance from the detector can still be decreased, therefore more sensible cryoelectronics by HEMTs can be expected.

3. Conclusions

In conclusion, we provide a first investigation of 4.2K pseudomorphic HEMTs for the fabrication of low-power, low-frequency and low-noise cryoelectronics. The preliminary performance analysis from our experiments suggests that the HEMT can be a very promising device. This device has excellent cryogenic properties owing to the high intrinsic qualities of the 2DEG, free from collapse and kink effect, and very good saturation behaviour even at source-drain bias much lower than 1V. A high intrinsic voltage gain of 160 can be obtained with an extremely low operating power supply of 57pW. In addition to the DC performances, this device also shows a very low input noise. A $1/f$ noise of $1.9\text{nV}/\sqrt{\text{Hz}}$ at 1kHz, a white noise smaller than $0.5\text{nV}/\sqrt{\text{Hz}}$, and a very low shot noise of $0.76\text{fA}/\sqrt{\text{Hz}}$ can be reached with a power supply less than $10\mu\text{W}$. In addition, a real application in a 4.2K preamplifier has demonstrated an equivalent input noise level of $0.12\text{nV}/\sqrt{\text{Hz}}$ with a bandwidth of 2MHz. These transistors can thus be considered as good candidates for future applications in low-power and low-frequency cryoelectronics from 4.2K down to the milli-Kelvin range.

From quantum $1/f$ noise theory, the Hooge parameter in *GaAs* and related III-V compounds is penalised by the light electron effective mass and the Debye temperature. But the advantages of 2DEG at 4.2K overcome these unfavourable aspects by more important linear and exponential thermal factor reduction. Although our experimental Hooge parameter $\alpha_H=5.5\times 10^{-6}$ at 4.2K is about ten times less than α_H measured in a classical HEMT at 300K by another group [12], it is still much higher than α_H predicted by quantum theory [13]. Investigations both in theory and in experiment have to be performed, in order to understand the theoretical and practical limitations of the $1/f$ noise in cryogenic HEMTs.

Acknowledgements

We thank C.Mayeux and L.Couraud for technical assistance, and R.Bruère-Dawson for experimental results of the real 4.2K preamplifier. Helpful conversations with, and encouragements from, Dr. D.C.Glattli, Dr. D.Yvon, Dr. Z.Z.Wang, Dr. H.Launois, Prof. L.C.L.Yuan, Prof. C.Y.Huang, and Dr. G.Waysand were most appreciated. This work is supported in part by the project "R.O.C.-Europe collaboration on transition radiation detection with superheated superconducting detectors".

References

- [1] F.Ayela J.L.Bret and J.Chaussy 1991 *Rev. Sci. Instrum.* 62 (11) 2816-2821
- [2] G.V.Pallottino A.E.Zirizzotti 1994 *Rev.Sci. Instrum.* 65 (1) 212-220
- [3] A.T-J.Lee 1993 *Rev. Sci. Instrum.* 64 (8) 2373-2378
- [4] D.V.Camin G.Pessina and E.Prevali 1994 *IEEE Trans. on Nucle. Scien.* Vol.41 No.4 1260-1266
- [5] A.Kumar L.Saminadayar D.C.Glattli Y.Jin and B.Etienne 1996 *Phys. Rev. Lett.* Vol. 76 N°15 2778-2781
- [6] A.Sylvestre P.Crozet R.Adde A.de Lustrac Y.Jin J.C.Harmant M.Quillec 1993 *Electr. Lett.* Vol.29 N°24 2152-2154
- [7] J-M.Dieudonne M.Pouyssegur J.Grafeuil and J-L.Cazaux 1986 *IEEE Trans. Electron Devices* ED-33 No5 572-575
- [8] Picogiga, 5, rue de la Réunion Z.A. de Courtabœuf, 91952 Les Ulis Cedex, France, Fax. 33 1 6907 3208
- [9] Y.Jin 1991 *Solid-State Electronics* Vol.34 No.2 117-121
- [10] C.Claeys and E.Simoen 1994 *J.Electrochm.Soc.* Vol. 141 No. 9 2522-2532
- [11] F.N.Hooge 1969 *Phys.Lett.* vol.A-29 139-140
- [12] K.H.Duh and A.van der Ziel 1985 *IEEE Trans. Electron Devices* ED-32 No3 662-666
- [13] A.van der Ziel P.H.Handel X.C.Zhu and K.H.Duh 1985 *IEEE Trans. Electron Devices* ED-32 No3 667-671
- [14] T.A.Girard G.Waysand J.I.Collar O.Heres D.Limagne H.Dubos and V.Jeudy 1994 *Nuclear Physics B* 35 397-399
- [15] private communication with R.Bruère-Dawson

Influence of backside doping on the nonlinear capacitances of a PHEMT affecting the VCO frequency characteristics

H. Brech[†], T. Grave[†], A. Werthof[†], H.-J. Siweris[†], T. Simlinger[‡], and S. Selberherr[‡]

[†]Siemens AG, Corporate Technology, D-81730 Munich, Germany

[‡]Institute for Microelectronics, TU Vienna, Gußhausstraße 27-29, A-1040 Vienna, Austria

Abstract - A local maximum in the $C_{GS}(V_{GS})$ characteristics of an AlGaAs/InGaAs/AlGaAs PHEMT is both calculated by hydrodynamic simulations and extracted from S-parameter measurements. It is found by simulation that the doping on the backside of the channel is the origin of this behavior. VCO measurements demonstrated that this $C_{GS}(V_{GS})$ characteristic can result in a partially reversed tuning behavior.

1. Introduction

High Electron Mobility Transistors (HEMTs) on GaAs substrate are becoming widely used for Microwave Monolithic Integrated Circuits (MMICs) with operating frequencies up to 100 GHz. The most common pseudomorphic HEMT, the AlGaAs/InGaAs/GaAs HEMT without doping below the channel shows high cut-off frequency but low power capability. A second drawback is the high output conductance at short gate lengths. This is a major limiting factor for high frequency performance. However, both power capability and output conductance can be improved by the introduction of a second AlGaAs barrier below the channel which enhances the confinement of the electrons to the quantum well. To improve the power capability, the electron density in the channel is increased by a doping in the AlGaAs buffer. This doping also affects the capacitances of the device.

In the present paper we analyze the mechanisms determining the gate-source capacitance C_{GS} of HEMTs with doping on the backside of the channel. In contrast to HEMTs without backside doping these devices exhibit a local maximum in their $C_{GS}(V_{GS})$ characteristics. Measurements of VCOs employing this type of HEMT [1] show a partially reversed tuning behavior opposite to VCOs with HEMTs without backside doping [2].

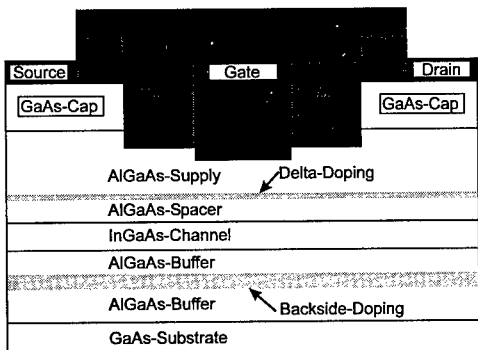


Fig. 1. Schematic cross section of the investigated HEMT.

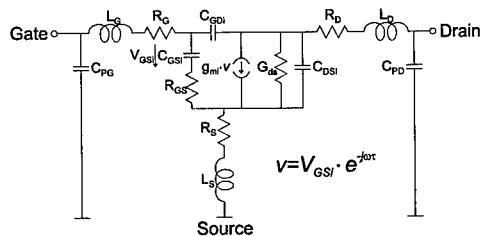


Fig. 2. Small signal equivalent circuit used for parameter extraction.

2. Device structure and simulation

The basic structure of the investigated HEMT is shown in Fig. 1. An InGaAs channel is sandwiched between two AlGaAs barriers. In the barrier below the channel a 5 nm thick layer with a doping concentration of $1.0 \times 10^{18} \text{ cm}^{-3}$ is used. The upper barrier layer contains a delta doping with a sheet concentration of $3.6 \times 10^{12} \text{ cm}^{-2}$. The T-shaped gate with a footprint length l_g of 120 nm was manufactured by optical stepper lithography and a side wall spacer process. Source and drain contacts are self-aligned to the T-gate [1].

The simulations were performed with the hydrodynamic simulator MINIMOS-NT [3]. A hydrodynamic transport model was used in the channel and drift diffusion in the remaining semiconductor layers. The simulation takes into account the complete epitaxial structure, a realistic device topology, i. e., an approximated gate shape, source and drain contacts only on top of the cap layers, and passivation [4].

3. Determination of C_{GS}

The device structure described above enables us to simulate an extrinsic HEMT but without contacting network and pads. The extrinsic gate capacitance $C_{GS}(V_{GS})$ was determined by means of the quasi static approximation

$$C_{GS}(V_{GS}, V_{DS}) = \frac{\partial Q_G}{\partial V_{GS}} \Big|_{V_{DS}} + \frac{\partial Q_G}{\partial V_{DS}} \Big|_{V_{GS}} \quad (1)$$

where Q_G is the total (negative) charge on the gate metal surface. Additionally, small signal parameters were extracted from S-parameter measurements according to [5] using the equivalent circuit shown in Fig. 2. The circuit includes parasitic elements such as pad capacitances and inductances. The quantities determined this way are intrinsic parameters in contrast to the C_{GS} determined by simulation. To compare the intrinsic gate source capacitance C_{GSi} with the simulated extrinsic C_{GS} the following approximation was used

$$C_{GS} \approx (1 + g_{mi} R_s) C_{GSi}, \quad (2)$$

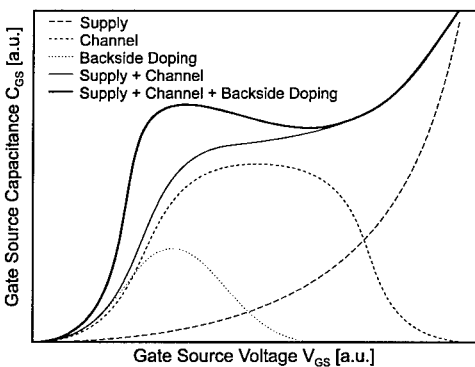


Fig. 3. Contributions to C_{GS} due to backside doping (dots), channel (short dashes) and upper barrier doping (long dashes).

where the intrinsic transconductance g_{mi} , the source resistance R_s and C_{GSi} are parameters of the small signal equivalent circuit shown in Fig. 2.

4. Contributions to C_{GS}

The different contributions to C_{GS} are sketched schematically in Fig. 3. In HEMTs with doping only above or in the channel, contributions of channel and upper barrier doping sum up to a well known monotonous increase of C_{GS} with V_{GS} . With an additional doping on the backside of the channel, a third contribution is added. Depending on the doping density and the energy level relative to the channel this can

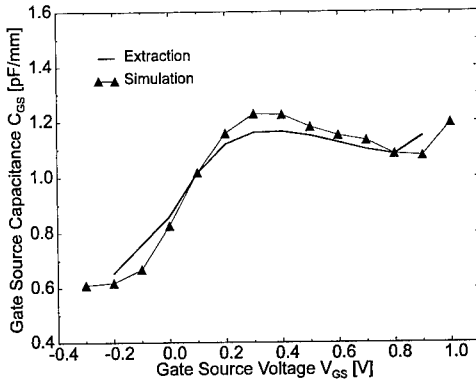


Fig. 4. Simulated and extracted C_{GS} of the investigated HEMT at $V_{DS}=3.0$ V.

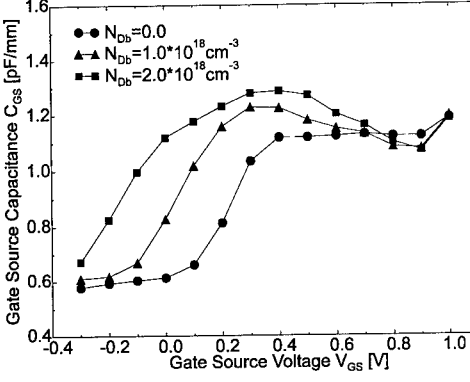


Fig. 5. Simulated C_{GS} of the same HEMT but with different backside doping at $V_{DS}=3.0$ V.

result in a curve with a local maximum shown by the bold line in Fig. 3.

In Fig. 4, both simulated and extracted $C_{GS}(V_{GS})$ are shown which compare very well. If V_{GS} is increased from pinchoff C_{GS} increases until it reaches a maximum. Both, simulated and extracted C_{GS} show a negative gradient over more than 400 mV of V_{GS} which is the largest part of the usable V_{GS} swing of the device.

Simulations of the same device were performed where only the backside doping N_{Db} was changed. Fig. 5 proves that N_{Db} is the reason for the local maximum of $C_{GS}(V_{GS})$. It demonstrates the dependence of the location and magnitude of the maximum on the concentration of N_{Db} . No local maximum can be observed in the case of $N_{Db}=0$. With increasing N_{Db} , the pinch off voltage decreases and the local maximum in $C_{GS}(V_{GS})$ appears. The higher the contribution of N_{Db} to the total doping, the more pronounced is the local maximum in the C_{GS} curve. This behavior has an impact on circuits with properties strongly dependent on the $C_{GS}(V_{GS})$ characteristics such as some types of VCOs.

5. VCO characteristics

If a voltage controlled oscillator (VCO) is tuned directly by V_{GS} variations, the change in C_{GS} is one of the most important parameters for its frequency characteristics. Fig. 6 shows a photograph of such

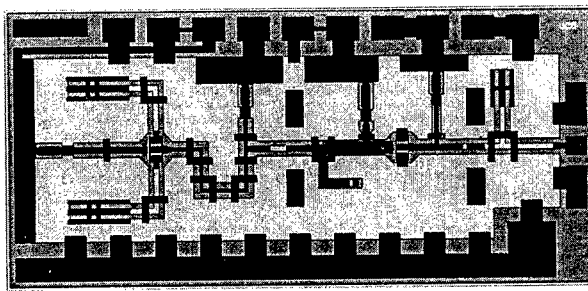


Fig. 6. Layout of the measured VCO.

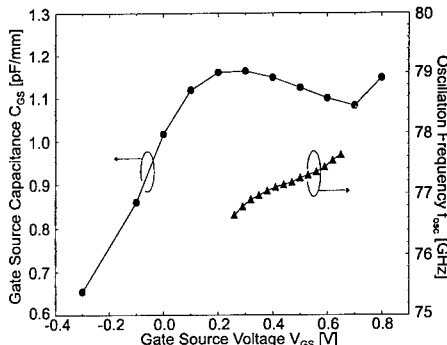


Fig. 7. Measured f_{osc} of the VCO versus the tuning voltage V_{GS} and the extracted C_{GS} of the HEMT used in the VCO.

no oscillation could be observed for V_{GS} below 0.2 V and above 0.65 V.

6. Conclusion

We have reported a local maximum in the C_{GS} versus V_{GS} characteristics of HEMTs. The same behavior was observed for C_{GS} extracted from S-parameters as well as for C_{GS} obtained from hydrodynamic simulations. We identified the doping on the backside of the channel to be the reason of the local maximum. In agreement with this result we have measured VCO tuning behavior opposite to the one usually observed.

Acknowledgment

The authors would like to thank Dr. H. Tischer for the RF measurements.

References

- [1] J.-E. Müller, A. Bangert, T. Grave, M. Kärner, H. Riechert, A. Schäfer, H. Siweris, L. Schleicher, H. Tischer, L. Verweyen, W. Kellner, T. Meier, "A GaAs Chip Set for Automotive Radar Systems Fabricated by Optical Stepper Lithography," *IEEE GaAs IC Symp. Techn. Digest 1996*, pp 189-192.
- [2] H. Wang, K. W. Chang, T. H. Chen, K. L. Tan, G. S. Dow, B. Allen, J. Berenz, "Monolithic W-band VCOs using Pseudomorphic AlGaAs/InGaAs/GaAs HEMTs," *IEEE GaAs IC Symp. Techn. Digest 1992*, pp 47-50.
- [3] T. Simlinger, H. Brech, T. Grave, and S. Selberherr, "Simulation of Submicron Double-Heterojunction High Electron Mobility Transistors with MINIMOS-NT," *IEEE Transactions on Electron Devices*, Vol. 44, No. 5, pp. 700-707, May 1997.
- [4] H. Brech, T. Simlinger, T. Grave, and S. Selberherr, "Current Transport in Double Heterojunction HEMTs," in *ESSDERC'96 - 26th European Solid State Device Research Conference* (G. Baccarani and M. Rudan, eds.), (Gif-sur-Yvette Cedex, France), pp.873-876, Editions Frontiers, 1996.
- [5] M. Berroth and R. Bosch, "High-Frequency Equivalent Circuit of GaAs FET's for Large-Signal Applications," *IEEE Trans. on Microwave Theory and Techniques*, VOL. 39, No. 2, pp 47-50, Feb. 1991.

a monolithic VCO with buffer amplifier [1]. In this type of VCO the output frequency usually decreases with increasing V_{GS} if HEMTs with doping only in or above the channel are employed [2]. This can be different in the same type of VCO if backside doped HEMTs are used [1]. The change in the C_{GS} dependence on V_{GS} due to the backside doping changes the tuning behavior. In particular, the frequency response can be reversed for a certain interval of V_{GS} . Fig. 7 shows the oscillation frequency f_{osc} and the corresponding C_{GS} of the HEMT employed in the VCO, both as a function of V_{GS} . In this case f_{osc} is increasing over the whole range in which the VCO is oscillating. This clearly coincides with the range in which C_{GS} is decreasing with rising V_{GS} . In the case of the measured VCOs

Photoinduced Instability in Microwave Excited GaAs MESFETs

E. Y. Lan, J. H. Huang, J. Blaugh, and E. Schirmann*

Phoenix Corporate Research Laboratory, Motorola Inc.

*Communication Products Laboratory, Semiconductor Product Sector, Motorola Inc.
2100 East Elliot Road, MD EL508, Tempe, AZ 85284, USA

Abstract. A photoinduced low frequency oscillation (LFO) is observed in GaAs MESFETs under microwave excitation at room temperature. The phenomenon is a self-sustained externally driven output power amplitude modulation and occurs within a range of light intensity, microwave power excitation level, and quiescent bias state. The oscillation frequency depends on the light intensity and microwave power, varying from 0.1 to 100 Hz. This oscillation phenomenon is found to be a strong function of device surface condition.

1. Introduction

Spontaneous oscillations have been observed at low temperatures under the combination of DC electric field and photoexcitation in undoped GaAs [1-3], or a combination of DC and magnetic field in p-type Ge [4]. These instabilities are commonly analyzed within the framework of the phenomenological impurity breakdown model that assumes impact ionization of two neutral donor levels by energetic free carriers that are heated by the applied electric field [5]. At room temperature, current oscillations in semi-insulating GaAs were also observed under an applied DC electric field and were attributed to deep levels such as EL2 at the onset of trap-filled-limited-voltage [6-8]. The similarity of the phenomenon and the condition the phenomenon occurs at low and room temperature hints that a similar physical mechanism might be operating in both cases.

In this paper, we report a photoinduced low frequency output power oscillation of GaAs MESFET devices at room temperature under microwave excitation.

2. Experimental Results and Discussions

Ion implanted GaAs MESFETs on LEC (Liquid-Encapsulated-Czochralski) substrates were used in this experiment. The typical gate length is 0.8 μm , gate-source spacing 0.3 μm , and gate-drain spacing 0.7 μm . The device was connected in a class C common source amplifier configuration with a sinusoidal microwave excitation of 850 MHz. Light from a tungsten-halogen projector lamp passing through a monochromator illuminated on the top surface of the device. The output signal was measured by a power meter and by a spectrum analyzer in the time sweep mode.

We observed the instability of output power as a function of photoexcitation intensity (I_L) and input microwave power level (P_{IN}). The output power of the device oscillates at a very low frequency, e.g. approximately 1 Hz. The oscillation frequency increases with light intensity and microwave power, whereas the magnitude decreases with light intensity and microwave power, as shown in Figs. 1 and 2. It was found that this low frequency oscillation occurs in a certain range of light intensity and microwave power level. Both lower and upper excitation thresholds exist. Below the lower excitation threshold, or above the upper excitation threshold, LFO behavior disappears.

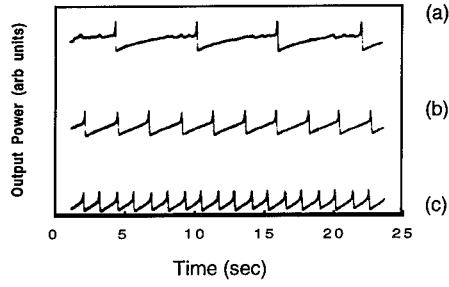


Fig. 1. The low frequency oscillation of output power at several photoexcitation intensities (a) $I_L=7$, (b) 17, (c) $208 \mu\text{W}/\text{cm}^2$, $P_{IN}=200 \text{ mW}$, $\lambda_{EXC}=800 \text{ nm}$.

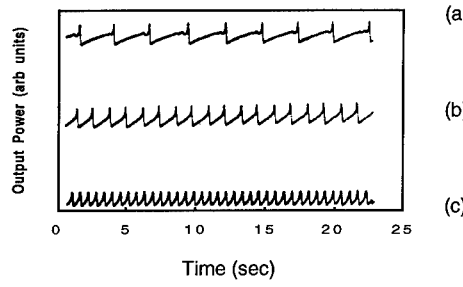


Fig. 2. The low frequency oscillation of output power at several microwave excitations (a) $P_{IN}=190$, (b) 200, (c) 208 mW , $I_L=30 \mu\text{W}/\text{cm}^2$, $\lambda_{EXC}=800 \text{ nm}$.

Fig. 3 shows a collection of such oscillation states on the light intensity versus microwave power plane. It can be seen that the oscillation occurs in a very narrow range of microwave power level from 182 mW to 225 mW, and light intensity from 4 to $34 \mu\text{W}/\text{cm}^2$. This feature is very similar to the phenomenon reported in Ref. [2] which was observed at a much lower temperature (2°K).

The LFO is also observed when the photoexcitation energy is lower than the band-gap energy. There is an abrupt increase in the oscillation frequency when the photoexcitation energy reaches the band-gap, as seen in Fig. 4. Fig. 4 is consistent with Fig. 1 and 2, in that the higher the excitation energy, either I_L , P_{IN} , or λ_{EXC} , the higher the oscillation frequency.

The LFO of output power observed in this experiment is the direct result of drain current oscillation as verified by monitoring both output power and drain current response as a function of time under the oscillation condition. This is not surprising since there have been reports [9-10] on the dc drain current low frequency oscillations of GaAs MESFETs.

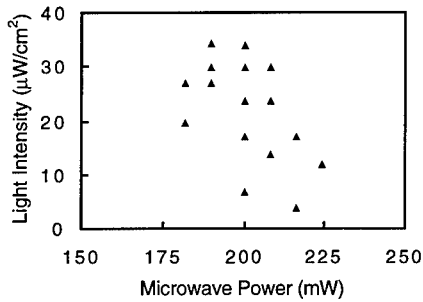


Fig. 3. The low frequency oscillation occurs in a range of light intensity and microwave power $\lambda_{EXC}=800 \text{ nm}$.

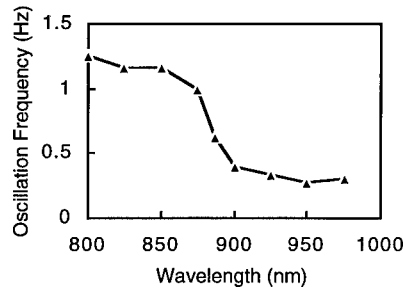


Fig. 4. The LFO frequency as a function of photoexcitation wavelength around band-gap energy, $P_{IN}=200 \text{ mW}$, $I_L=30 \mu\text{W}/\text{cm}^2$.

The LFO frequency depends on temperature. According to Ref. [7], the activation energy suggests that trapping and ionization of EL2 and EL0 produce the oscillation. In Fig. 5, we also calculated activation energy from the temperature dependence of oscillation frequency data, using the same technique as in Ref. [7]. However, an activation energy of 1.8 eV larger than that of EL2/EL0 was obtained, implying that band-to-band impact ionization takes part in the oscillation process in addition to ionization of deep levels.

A strong process dependence of LFO was observed. An experiment was conducted in which the surfaces of devices were subject to different degrees of surface damage introduced via plasma etch process. Fig.6 is a transmission electron micrograph of the dielectric/semiconductor interface of a FET showing damages induced by the plasma process. The device with the greatest damage was found to have LFO when biased near 50% of I_{dss} , while the device with the surface protected from plasma damage did not exhibit LFO in any of the bias conditions explored. The frequency of oscillation among these devices, under similar bias conditions, typically increases and the amplitude decreases as the device surface condition is improved.

This leads to our speculation that LFO in the test device is a result of the interaction between surface states and bulk traps. We postulate that injected carriers are trapped and build up a space charge field in the bulk adjacent to the channel. When the field reaches a threshold, impact ionization of trapped carriers sets in, resulting in an increase of the free carrier density. Electrons generated by impact ionization move toward the positive drain region, and holes move toward the negative gate and ungated surface area adjacent to the gate. There, holes combine with negative surface states and relax the field in the channel. Subsequently, the electric field drops below impact ionization threshold, and the carriers are to be trapped again. This carriers trapping and ionization process is believed to be the cause of drain current oscillation observed above.

When the microwave power or equivalently the electric field is below the lower threshold of LFO, impact ionization of the traps can not be initiated, therefore no oscillation occurs. On the other hand, when the microwave power is higher than the upper threshold, the population of trapped carriers is significantly reduced. The magnitude of ionization and trapping process becomes so small to be detected. Above upper threshold, the current noise floor can be dramatically higher than that below the lower threshold due to the amount of excited traps [11]. The action of light intensity on LFO can be explained by the similar argument.

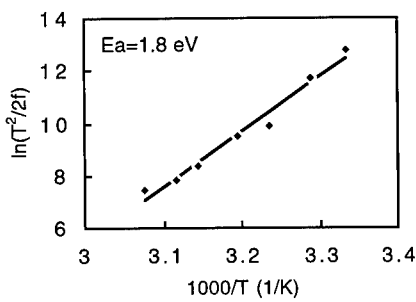


Fig. 5. Arrhenius plot of the LFO.

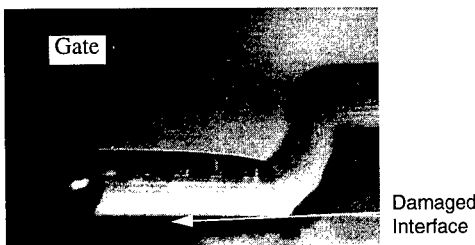


Fig. 6. Transmission electron micrograph of the damaged dielectric/GaAs interface.

3. Summary

Photoinduced low frequency oscillation of output power of GaAs MESFETs under microwave excitation was observed for the first time at room temperature within a range of light intensity and microwave input power level. The oscillation frequency falls into the range of 0.1-100 Hz. The phenomenon may be explained by the interaction between surface states and bulk traps under trap impact ionization condition which is generated by external applied electric field and photoexcitation.

Acknowledgments

We would like to express our gratitude toward Bill Knappenburg, Keith Barkley, Bob Baeten and Ron Legge and his team for the help in experimental setup, to Saeid Tehrani, Herb Goronkin and George Maracas for very insightful discussions, and to Bill Ooms for his encouragement and management support.

References

- [1] Ashkinadze B M, Cohen E, Ron Arza, and Pfeiffer L N 1994 *Semicond. Sci. Technol.* 9 570-2
- [2] Kozhevnikov M, Ashkinadze B M, Cohen E, and Ron Arza 1995 *Physical Review B* 52 4855-63
- [3] Karel F, Oswald J, Pastrnak J, and Petricek O 1992 *Semicond. Sci. Technol.* 7 203-9
- [4] Rau U, Clauss W, Kittel A, Lehr M, Bayerbach M, Parisi J, Peinke J, and Huebener R P 1991 *Physical Review B* 43 2255-62
- [5] Scholl E 1989 *Appl. Phys. A* 48 95-106
- [6] Goronkin H and Maracas G N 1984 *International Electron Device Meeting* 182-5
- [7] Maracas G N, Johnson D A, and Goronkin H 1985 *Appl. Phys. Lett.* 46 305-7
- [8] Kaminska M, Parsey J M, Lagowski J, and Gatos H C 1982 *Appl. Phys. Lett.* 41 989-91
- [9] Saito Y, Suga T, Inoue K, Mitani T, Tomizawa Y, Nishio J, Terashima K, Katsumata T, Fukuda K, Washizuka S, Yashiro S, Takami S, Nakajima M, and Watanabe M 1992 *Mat. Res. Soc. Symp. Proc.* 262 791-6
- [10] Saito Y 1990 *J. Appl. Phys.* 68 830-9
- [11] Canfield P and Forbes L 1985 *IEEE Electron Device Letters* 5 227-8

Optimization of the doping levels in doubly doped InAlAs/InGaAs HEMTs

S.Kraus, M. Sexl, G. Böhm, G. Tränkle¹, and G. Weimann²

Walter Schottky Institut, Techn. Univ. München, D-85478 Garching, Germany

¹ Ferdinand Braun Institut, D-12489 Berlin, Germany

² Fraunhofer Institut IAF, D-79108 Freiburg i. Br., Germany

Abstract. Delta-doped InAlAs/InGaAs-HEMTs were grown by MBE lattice matched on InP-substrates. The ratio of upper doping to lower doping was varied from 1:0, 4:1, 2:1, 1:1 to 0:1, while total doping concentration was kept constant. By increasing the bottom doping concentration, the drain current is increased and the kink effect reduced. Ultimately the inversely doped transistor shows absolutely no kink and a very low output conductance of 25mS/mm. These new results offer a better understanding of the kink effect, related to the band structure of the HEMTs and its dependence on doping.

1. Introduction

The typical DC output characteristics of InAlAs/InGaAs-HEMTs with sub- μm gate length show an anomalous increase in drain current depending on drain source voltage (kink effect). Several theories for the physical origin have been proposed, however no transistors with kink-free output characteristics have been reported. With a single side high doping concentration ($>7 \cdot 10^{12}\text{cm}^{-2}$) it is possible to eliminate the kink in the characteristics, at the price of a high output conductance, inferior diode characteristics and a very high drain current with a low drain source breakdown voltage. If the supply is split into an upper and lower modulation doping of the channel, a reduction of the output conductance can be achieved. For our investigations, we use a low total doping concentration of $4.5 \cdot 10^{12}\text{cm}^{-2}$ and a short gate length of $L_g=150\text{nm}$, making the HEMT structures very sensitive to the kink effect. The influence of doping ratio on electron transport properties and device performance was systematically investigated.

2. Device Structure and Device Fabrication

The layer sequence of the doubly doped HEMT structure is shown in Fig.1. For the optimization of the doping levels, we used the identical layer structure only varying the concentrations of the upper and lower δ -doping. Structures were grown by molecular beam epitaxy on 2-inch Fe-doped semi-insulating InP substrates. The epilayers consist of 250nm InAlAs buffer, followed by the 12nm wide channel, which is separated on each side by 5nm thick InAlAs-spacers from the doping. The ratio of upper doping to lower doping was varied from 1:0, 4:1, 2:1, 1:1 to 0:1, while total doping concentration was

kept constant ($4.5 \cdot 10^{12} \text{ cm}^{-2}$). An additional very high δ -doping underneath the 60nm thick InGaAs cap-layer reduces source and drain resistances [1] and compensates surface states. This doping does not effect the carrier density in the channel. T-shaped gates of 150nm length were defined by electron beam lithography in a two layer resist process. The gate region was recessed by a selective succinic acid etch and metallized with Ti/Pt/Au.

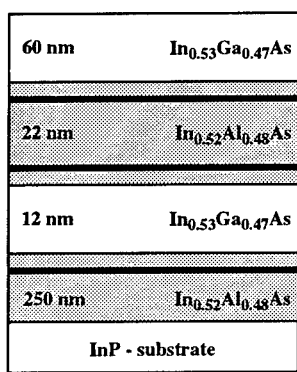


Fig. 1: HEMT layer structure

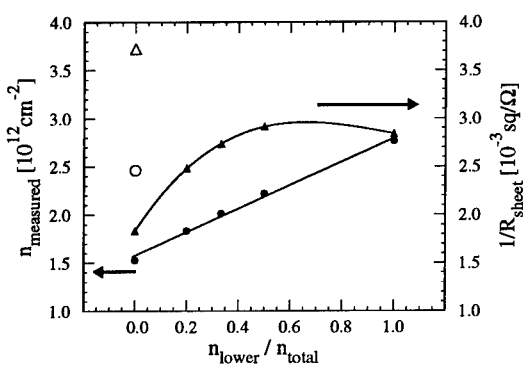


Fig. 2: Dependence of sheet carrier densities and sheet conductance on fraction of lower to total doping

3. Transport Properties

In Figure 2 the measured sheet densities and the sheet conductances are plotted versus the ratio of lower to total doping concentration. To avoid conductivity in the cap layer, the complete 60nm InGaAs was removed by a selective etch in the same way as the gate recess for the HEMTs was made. A linear increase can be observed for the carrier density in the channel, as we increase the lower doping. The effective carrier transfer goes from only 34% up to 63%. The electrons from the lower doping supply are not influenced by the surface depletion and have a higher affinity to the channel. The second curve in figure 2, the sheet conductance, shows the correlation between electron mobility and sheet density depending on the doping distribution. Here the curve shows a broad maximum. The reason for this is the decrease of electron mobility from $8500 \text{ cm}^2/\text{Vs}$ for a ratio of 1:0 to $6400 \text{ cm}^2/\text{Vs}$ for the inversely doped structure. This is due to silicon segregation at 470°C growth temperature from the lower δ -doping into the channel. The structure with the ratio 1:1, that is near the maximum of this curve seems to be a good compromise for high electron mobility and high carrier density, adequate to achieve good transistor performance.

4. DC Characteristics

We measured the IV characteristics of these HEMT structures and indeed a distinct kink behaviour is revealed (Fig. 3). The strongest kink can be observed in single side upper doped structure (a). By increasing the lower doping concentration, the drain current increases and the kink effect is reduced.

Ultimately the 1:1 doped (d) and the inversely doped (e) transistors show absolutely no kink and a very low output conductance of 50 mS/mm and 25 mS/mm. All transistors show for all doping ratios a good pinchoff characteristic even for the inversely doped sample. That is a strong indication, that the conduction band offset in the buffer is quite high. The values for the threshold voltages decrease from -0.45 V for structure (a) to -0.7 V for structure (c) and (d). Simultaneously the Schottky diode characteristics changed drastically, although the surface treatment with our selective gate recess is the same. The forward breakdown voltage (1mA/mm) increases monotonously from 0.40V for 1:0 to 0.48V for 1:1 doping ratio, but for the inversely doped transistor the breakdown voltage increases dramatically by a factor of two (0.83V). While the barrier height Φ_B shows only a light increase (0.47 to 0.53 eV), the ideality factor n increases from the 1:1 doped to the inversely doped transistor from 1.35 to 2.34. Obviously the diode characteristic is changed from a $1/kT$ -like to a $1/2kT$ - like dependence. This could be due to a recombination current via the InGaAs-channel.

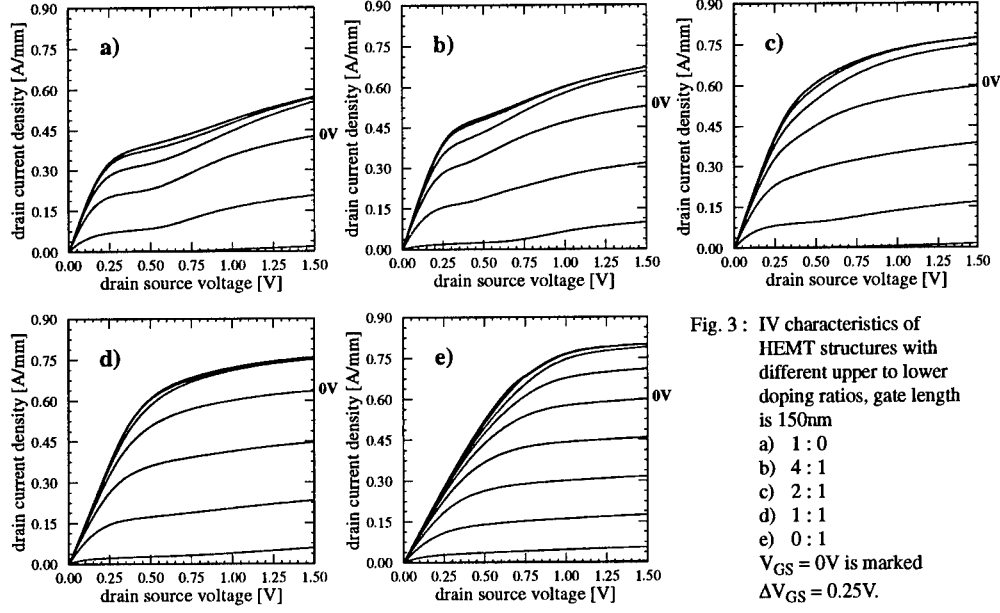


Fig. 3 : IV characteristics of HEMT structures with different upper to lower doping ratios, gate length is 150nm
 a) 1 : 0
 b) 4 : 1
 c) 2 : 1
 d) 1 : 1
 e) 0 : 1
 $V_{GS} = 0V$ is marked
 $\Delta V_{GS} = 0.25V$.

The IV-behaviour of the kink effect can be very well described by a simple equivalent circuit (Fig. 4). Here the function of the transistor is divided into two parts. The first branch, in which the transistor is marked with T_m , represents the main transistor, in which the major part of drain current flows. The second part (T_t) can be described as an additional current flow, like a transfer current, which is controlled by a diode and a resistance. If a drain voltage is applied, the main transistor is immediately open whereas in the second branch no current flows because the diode is closed. By a further increase of the voltage the diode is open and an additional current flow causes the kink in the IV characteristic. The transfer resistance R_t influences the magnitude of the kink. A low resistance leads to a distinct kink, on the contrary by a high resistance makes the second part ineffective. Although in this model the HEMT is divided in two transistors with the same gate voltage applied, this does not mean that there are two separated current paths or channels. We believe, that the low Schottky barrier to the surface and high

band offset between Fermi level and conduction band in the buffer tilts the band structure to the surface. The consequence of this is an incomplete carrier transfer from the upper doped region to the channel. Only an increasing drain voltage can effect a carrier transfer to the channel. This explains the high output conductance and the threshold voltage shift by increasing drain voltages.

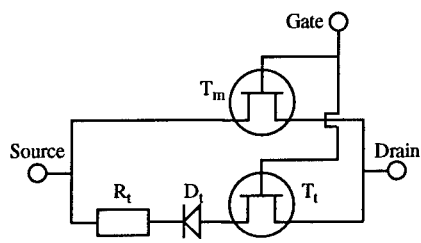


Fig. 4: Equivalent circuit for kink effect description

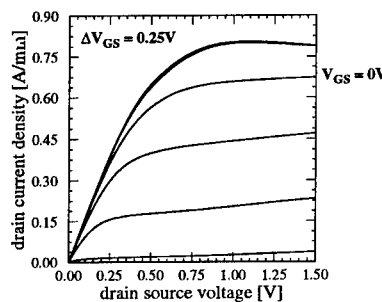


Fig. 5: IV characteristic of a single side upper doped metamorphic InGaAs/InAlAs HEMT

5. Discussion and Conclusion

In order to understand the observed improvements in the IV characteristics due to the lower δ -doping, we changed the buffer design with the aim to reduce the conduction band offset. For this purpose we used a single side doped metamorphic HEMT structure on GaAs with exactly the same active layers (Fig. 1) as the lattice matched structures on InP. The lattice mismatch was accommodated by a linearly graded InGaAlAs buffer with an additional overshoot in the In-content of 11% followed by 250nm low temperature InAlAs layer [2]. From buffer leakage measurements we conclude that the conduction band offset in the metamorphic sample is much lower than in the lattice matched structures with the different doping ratios. For this metamorphic structure the values for sheet density and sheet conductance in Fig. 2 (open circle and triangle) are evident better than of those of lattice matched structures. The IV characteristic of a single upper side doped metamorphic HEMT show excellent performance without any kink, low source and drain resistances and a transconductance of 1000mS/mm (Fig. 5).

From the above results it shows that the optimization of the doping levels can improve the device performance. We also learn that the position of the Fermi level in the buffer has a significant influence on sheet carrier density and on the DC performance of InGaAs/InAlAs HEMTs. A lower doped HEMT structure or a changed buffer design, with low conduction band offset, can achieve the same improvements. The good correlation with the kink effect confirms, that the anomalous increase in drain current is a consequence of incomplete carrier transport from the doped region to the channel.

References

- [1] Kraus S et al 1996 IEE Electronics Letters 32 1619-20
- [2] Sexl M et al on this symposium

500°C Operation of GaAs Based HFET Containing Low Temperature Grown GaAs and AlGaAs

K.M. Lipka, P. Schmid, N. Nguyen*, L.L. Pond†, C.E. Weitzel†,
U. Mishra*, E. Kohn

Dept. of Electron Devices and Circuits, University of Ulm, D-89069 Ulm, Germany

*Dept. of Electrical Eng., University of California at St. Barbara, Santa Barbara, CA 93106

†Motorola Inc., Phoenix Corporate Research Lab., 2100 E. Elliot Rd., Tempe, AZ 85284

Abstract. A novel FET concept has been developed to overcome the limitations of conventional GaAs based devices operating at high temperature. Due to the replacement of the Schottky gate control diode by a heterojunction, containing AlAs and LTG AlGaAs, and the use of low temperature grown GaAs as buffer layer material, high thermal stability in the electrical performance could be obtained. The device shows DC operation up to 500°C with essentially unchanged characteristics. On wafer microwave measurements were carried out up to 200°C. Whereas f_T remains essentially unchanged the f_{max}/f_T ratio decreases steadily. Though standard contact metallization was used, destructive degradation occurred not before 570°C.

1. Introduction

GaAs based devices are suitable for operation at elevated temperatures due to the higher band gap of GaAs as compared to silicon. However, device performance usually deteriorates at high temperatures due to the reduction of carrier mobility, peak velocity and the degradation of the contacts used, and result already at moderate heating in reduced power gain and output power and a higher noise [1,2]. In this study, a novel approach to avoid high temperature degradation was investigated. Since the reduction of the high field velocity in GaAs at high temperatures is comparatively small [3], this device is designed to operate in the high field velocity region to improve the temperature degradation of the cut-off frequencies.

We have realized an FET concept with a LTG AlGaAs/AlAs heterojunction as control diode to avoid problems encountered with conventional metal semiconductor Schottky gate diodes. Low temperature grown layers were also incorporated to avoid buffer leakage and AlAs to prevent contact diffusion.

2. Device Concept

Operation of GaAs based devices at high temperature normally leads to a strongly reduced output current density [1] due to a reduction of carrier mobility and peak velocity. Since the high field velocity remains largely unchanged up to high temperatures [3], a device concept has been designed to ensure operation in the high field velocity region and current confinement to a narrow channel. The gate length of the device is $1\mu m$, thus velocity overshoot should be negligible. Additionally, we have incorporated a low temperature grown (LTG) AlGaAs passivation layer and a LTG GaAs buffer for confinement of the carriers to the n-doped GaAs channel.

Low temperature grown GaAs and AlGaAs contain a high amount of surplus As found on interstitials and antisites. Upon annealing at elevated temperatures, the excess As precipitates into clusters in case the density of surplus As is sufficiently high. These metallic clusters act as buried Schottky barriers, depleting the entire material. Therefore, annealed LTG GaAs is highly resistive and

may be used as a buffer layer to reduce buffer leakage and therefore output conductance up to high temperatures.

Since the As concentration in LTG AlGaAs is lower as compared to LTG GaAs, As precipitation into clusters is not expected in the LTG AlGaAs surface layer, when annealed. Thus, this layer remains in its lossy dielectric state, leading to a reduced feedback capacitance due to a gate to drain lateral field redistribution resulting in an expansion of the drift region [4,5], as seen in the high f_{max} value. This is important for high frequency operation at high temperatures where additional feedback is expected from increased conductance of the buffer and passivation layers [6]. The expansion of the drift region should also lead to a high field velocity dominated carrier transport.

High temperature operation of conventional GaAs based devices is also limited by contact degradation, especially interdiffusion. Therefore, a diffusion barrier is highly desired within the contact system to stabilize the contact alloy region. Here, thin AlAs layers have been used to restrict the alloying depth of the contacts. At the gate, the AlAs barrier is placed between the LTG AlGaAs passivation and the channel layer and it is believed that the AlAs/GaAs junction acts as the contact, because no Schottky barrier is formed at the interface between the surface LT-AlGaAs layer and gate contact metallization due to the high defect concentration. Additionally, the Ti Schottky metallization will penetrate into the LTG AlGaAs layer upon temperature stressing, forming a stable Ti:Al:As alloy. Because the barrier modulating the channel current is formed at the AlAs/channel interface, no effect on the device properties has been observed. To implement this concept, the entire gate metallization consisted of Ti/Pt/Au.

The second AlAs diffusion barrier positioned below the channel is used to prevent uncontrolled diffusion of the ohmic contact materials into the buffer.

3. Device structure and technology

The device was fabricated using a standard MBE system. Figure 1 shows the cross section of the device structure.

A 600 nm thick GaAs buffer layer was grown at a temperature of approx. 300°C. On top of this buffer layer, a 20 nm thick AlAs layer was incorporated as a diffusion barrier for As outdiffusion into the channel, to restrict the alloying depth of the ohmic contacts and to prevent spiking. Next, the 65 nm thick, silicon doped GaAs channel was grown. Doping concentration was $8 \times 10^{17} \text{ cm}^{-3}$. The 10 nm thick AlAs diffusion barrier, grown on top of the channel, acts as a barrier for outdiffusion of As from the LT-AlGaAs cap layer and as a stop layer for gate contact interdiffusion, as described above. The $\text{Al}_{0.3}\text{Ga}_{0.7}\text{As}$ top layer was 40 nm thick. The channel layer and diffusion barriers were grown at approx. 600°C.

The technology for device fabrication was a conventional sequence of mesa isolation by wet etching and contact deposition by e-beam evaporation of Ni/Au/Ge/Ni and Ti/Pt/Au for ohmic and Schottky gate contacts, respectively. Ni/Au/Ge based contacts are known to have a limited high temperature stability [7] but still can be used in this concept. Nevertheless, for further improvements,

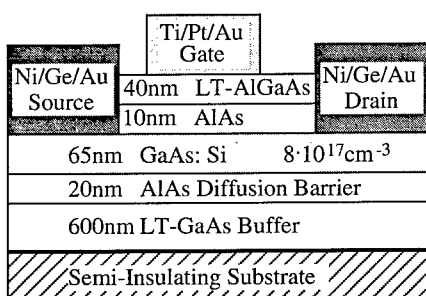


Figure 1: Cross section of the device structure

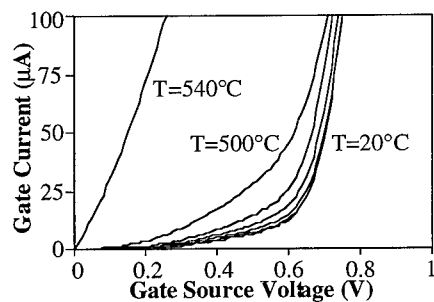


Figure 2: Characteristic of the input diode

refractory materials should be employed [7]. The ohmic contacts were deposited into contact windows etched through the AlGaAs and AlAs layer and then alloyed directly into the channel. The Ti gate was deposited on top of the AlGaAs layer, forming Ti:Al:As upon annealing.

The devices were not passivated, thus long time stability at high temperatures is not expected due to decomposition of GaAs and AlGaAs.

4. Results

4.1 Input diode characteristics

To modulate the channel the gate input diode must sustain rectification behaviour up to high temperatures. Therefore the IV-characteristics of the input diode was measured up to a temperature of 570°C in a vacuum chamber. The vacuum is necessary to prevent corrosion of the unpassivated AlGaAs surface. Figure 2 shows the characteristic of the gate source input diode in the temperature range between 20°C and 540°C. As can be seen, the characteristic remains essentially unchanged up to a temperature of approx. 500°C. Reverse currents can also be tolerated for FET operation up to 500°C. Only at 540°C, the gate diode becomes conductive. However the device does not degrade permanently at 540°C, the original characteristics can be restored upon cooling. The diode was found to degrade irreversibly at 570°C.

4.2 FET characteristics

4.2.1 DC characteristics. Figure 3 and 4 show the DC output characteristics of a FET at R.T. and 500°C, respectively. An open channel drain current of 380mA/mm is obtained at $V_G=+1V$ for R.T. operation. Increasing the temperature to 500°C leads to a reduction of the drain current by only 10% to 350mA/mm. This reduction is extremely low compared to data found in literature [1]. No noticeable leakage current is observed at pinch off up to 400°C. This is attributed to the use of the highly resistive low temperature grown buffer layer. Only at 500°C a leakage current of about 1.5% of the maximum current can be found, probably due to thermally activated carriers in the buffer layer. The threshold voltage remains unchanged, indicating a good carrier confinement to the channel even at 500°C. The negative slope in the R.T. output characteristic is believed to be a measurement artifact related to the high output resistance (see below) and not to self-heating.

4.2.1 High frequency characteristics. To determine the high frequency performance, the temperature dependent s-Parameters were measured at various bias points. Since an on-wafer measurement setup

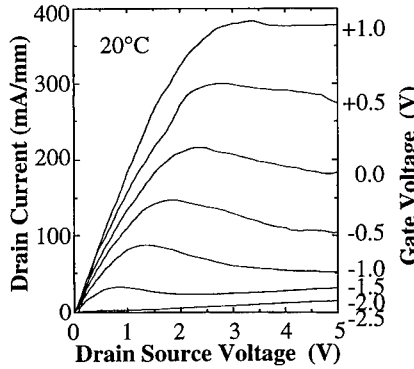


Figure 3: DC Characteristics at 20°C

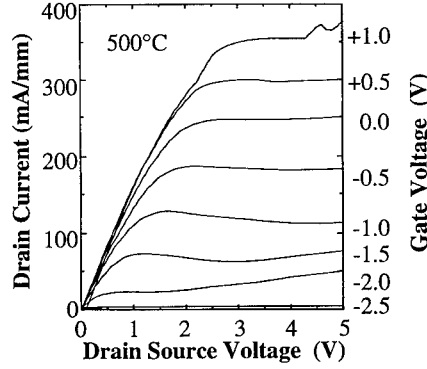


Figure 4: DC Characteristics at 500°C

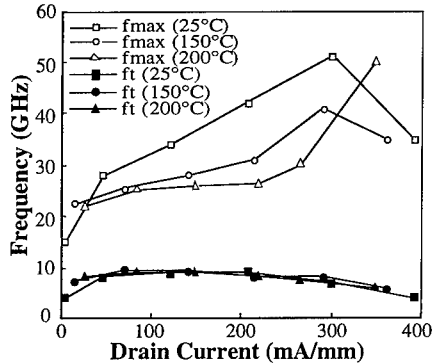


Figure 5: Drain current dependence of f_t and f_{\max} at different temperatures ($V_{DS}=4V$)

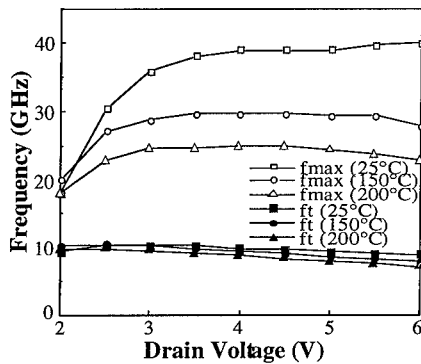


Figure 6: Drain voltage dependence of f_t and f_{\max} at different temperatures ($V_{GS}=-0.5V$)

with a temperature limit of 200°C was used, the temperature range was from 25°C to 200°C. The current gain cut-off frequency f_T and the maximum frequency of oscillation f_{\max} were extracted representative of the power gain and switching characteristics. Figures 5 and 6 show the drain current and drain voltage dependence of f_T and f_{\max} at different temperatures. In contrast to previous results reported in the literature [2], the current gain cut-off frequency is nearly temperature independent. However, the maximum frequency of oscillation decreases with increasing temperature. By extracting the small signal equivalent circuit elements this was found to be caused by an increase of the output conductance of 50%, probably due to a higher conductivity in the LT-AlGaAs and LT-GaAs passivation and buffer layer [6]. The slight reduction in f_T results from a slight reduction of g_m . Nevertheless, it should be noted, that at a temperature of 200°C the f_{\max}/f_T ratio is still more than 2 for all bias points in saturation.

5. Conclusion

A novel device structure has been shown, which is able to overcome the up to date limitations of other GaAs based high temperature device structures. 500°C operation of a GaAs based HFET has been demonstrated using conventional contact materials. High frequency on-wafer measurements up to 200°C are reported, showing an f_{\max}/f_T ratio of more than 2 even at 200°C and no essential change in f_T . The main parameter responsible for the change is an increase in output conductance. The DC characteristic remains essentially unchanged up to 500°C. At 570°C the device degrades irreversibly, probably due to a degradation of the ohmic contacts. This degradation may be avoided by using refractory contact materials.

References

- [1] Würfl J, Janke B, Nebauer E, Thierbach S and Wolter P, *IEDM*, 1996, 219-222
- [2] Goertzel Y and Salmer G, *IEEE Transaction on Electron Devices* Vol.41 No.3, 1994, 299-305
- [3] Shur M S, Kahn A, Gelmont B, Trew R J and Shin M W, *Inst. Phys. Conf. Ser.* No.141: Ch.4, 1994, 419-424
- [4] De Jaeger J C, *ISSSE*, 1995, 111-114
- [5] Kohn E, Lipka K M, Spingart B, Salmer G and Playez E, *18th European Workshop on Compound Semiconductor Devices and Integrated Circuits (WOCSDICE)*, Kinsale, Ireland : 'LT-GaAs MISFET Small Signal Characteristics', 1994, 24-25
- [6] Luo J K, Thomas H, Morgan D V, Westwood D, Williams R H and Theron D, *ISCS*, 1994
- [7] Shen T C, Gao G B and Morkoç H, *J. Vac. Sci. Technol. B* 10(5), 1992, 2113-2132

Ultra Low Power (<2mW) Noise Performance of InGaP/GaAs HBT

D. W. Barlage, M. S. Heins, J. H. Mu, M. T. Fresina, D. A. Ahmari,

Q. J. Hartman, G. E. Stillman and M. Feng

Department of Electrical and Computer Engineering,

University of Illinois, Urbana, IL 61801-2355

Abstract: The noise parameters of Npn InGaP/GaAs HBT devices are reported for an array of bias conditions from 2-18 GHz. A minimum noise figure of 0.8 dB with associated gain of 16 dB at 2 GHz was achieved at a collector bias of 0.83mA and a collector-emitter voltage of 2V. This was achieved by a device with emitter area of $3 \times 10 \mu\text{m}^2$. A model is also presented that is used to compare measured and theoretical results. The low power consumption, high associated gain, low equivalent noise resistance, and variable optimum noise match coupled with an excellent degree of linearity [1] makes the InGaP/GaAs HBT an ideal candidate for low noise amplifiers (2-6GHz) with minimal power consumption.

Introduction: Portable, battery operated circuit applications require devices that provide minimum noise figure and maximum linearity with minimal power consumption. In particular, CDMA and PCM CIA communication applications call for these components to be designed for 2.4 and 5.8 GHz. By carefully selecting the device emitter area and bias condition, the topology of the matching network and associated loss and added noise can be minimized [2]. InGaP/GaAs HBTs have lower number of recombination centers in the emitter-base junction and subsequently exhibit lower 1/f noise than comparable AlGaAs/GaAs HBTs. In fact the 1/f noise performance is comparable to that of silicon based BJTs [3,4]. The high frequency noise performance is improved with the InGaP/GaAs HBT compared to silicon through superior gain at microwave frequencies which is the direct result of a shorter emitter-collector transition time. We believe that the minimum noise figure presented in this work is among the lowest achieved for a bipolar technology in this frequency band.

Device Fabrication and Measurement: The devices were fabricated and measured as described in [5]. Lower recombination current in the base-emitter junction from enhancements in material growth and lower base resistance through improvements in processing have contributed to minor improvements in overall noise performance over previously reported results. All of the devices tested had a current gain of approximately fifty. Devices with $3 \times 10 \mu\text{m}^2$, $3 \times 5 \mu\text{m}^2$, $3 \times 20 \mu\text{m}^2$, $2 \times 3 \times 10 \mu\text{m}^2$, $3 \times 40 \mu\text{m}^2$, and $8 \times 3 \times 5 \mu\text{m}^2$ emitter areas were used for this study. Results are reported for the $3 \times 10 \mu\text{m}^2$ device which achieved the best noise performance of the devices tested.

Modeling: The simplest form of the equivalent circuit for the HBT is shown in Figure 1. The shot noise current is simply determined from an examination of each junction within the transistor [6]. The relation of the noise currents to the bias currents is given below:

$$\overline{i_c^2} = 2qI_c\Delta f \quad [1]$$

$$\overline{i_b^2} = 2q\Delta f(I_B + 2I_{BE} + 2I_{BC}) \quad [2]$$

Under forward bias operation the base-emitter and base-collector space charge recombination current, I_{BE} and I_{BC} , can be neglected. While no hole current flows across the base junction for the HBTs in this study, the base current still exhibits shot noise from the electrons with which they recombine. The correlation of the currents is also determined from the equivalent circuit model. This current is from the portion of current that the base and collector have in common. This correlation current spectral density is given as follows

$$\overline{i_b i_c} = -2qI_{BC}\Delta f \quad [3].$$

This correlation current is ordinarily very small. However, when operating the device at moderate microwave frequencies, the displacement current due to the base collector capacitance can become significant. The correlation factor will take a form as given below:

$$c = \frac{\overline{i_b i_c}}{\sqrt{\overline{i_b^2} \cdot \overline{i_c^2}}} = \frac{-j\omega C_{bc} \cdot \sqrt{P_{in} Z_0}}{\sqrt{I_B I_C}} \quad [4].$$

This correlation factor is shown to take a frequency dependent form but the input power and bias current dependence have not been verified.

Figure 1 The noise model of the HBT in the as-tested configuration. The emitter, collector and base terminal resistance contribute additional sources of noise.

In addition to the noise currents across junctions, the series resistance at each terminal can contribute a significant amount of noise power. This resistance will contribute noise according to the Johnson relation

$$\overline{e^2} = 4kTR \quad [5].$$

It is important that the noise temperature is determined from a self heating model and not the ambient temperature. The temperature of the device for calculation of the Johnson noise was determined from the measured thermal resistance and from the power dissipated across the device. The temperature of the device is related to the power through the following relation:

$$T = R_{th} P_{dis} + T_0 \quad [6].$$

This played a significant role in the determination of the equivalent noise resistance.

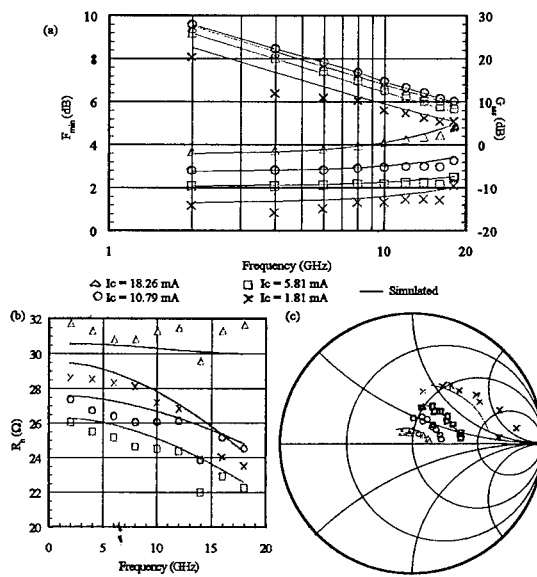
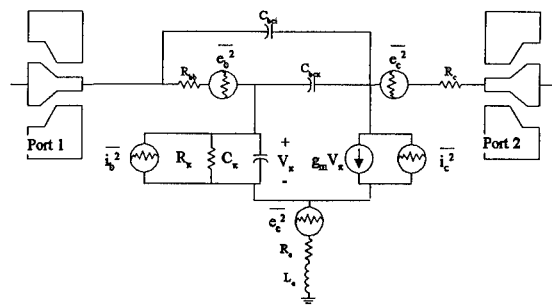


Figure 2 Plots of the measured and simulated values of minimum noise figure F_{min} and associated Gain G_{iss} (a), equivalent noise resistance R_e (b), and optimum noise match Γ_{opt} (c).

Measurement and Analysis: The noise parameters were measured using a Cascade



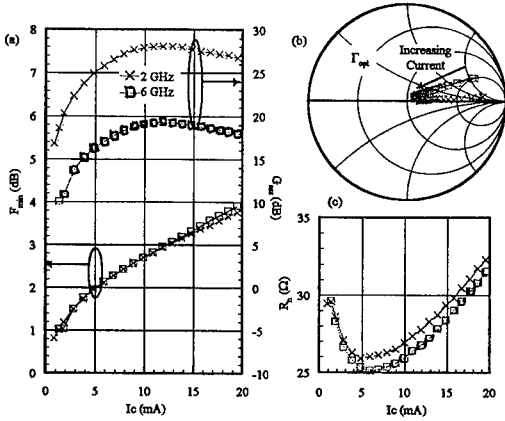


Figure 3 Measured minimum noise figure vs. collector current at 2 and 6 GHz for a $3 \times 10 \mu\text{m}^2$ device: (a) F_{\min} and G_{\min} vs. collector current, (b) Γ_{opt} vs. collector current and (c) R_n vs. collector current.

device noise for devices operating at large currents. This indicates that the optimum bias condition for the devices is at low current levels. However, there will be a current when this is no longer true [8-11]. In particular the noise resistance is minimized at a particular current while the minimum noise figure continues to decrease with lower bias currents. The gain of the device will also decrease significantly as the current is decreased. Plots of the minimum noise figures, associated gain, equivalent noise resistance vs. current are shown in Figure 3 for the $3 \times 10 \mu\text{m}^2$ device.

When the noise figure is plotted against the collector-emitter voltage, Figure 4, the noise figure shows a small but steady increase. This increase is accentuated for higher currents. The associated gain, also plotted in Figure 4, shows a slight decrease. The optimum matching condition changes little with respect to voltage. The equivalent noise resistance increases as the voltage is increased. This is because the equivalent noise resistance is directly dependent on the noise power at the input terminal. This is largely due to the Johnson noise of the emitter and base resistance. The measured temperature is plotted with the equivalent noise resistance of the device in Figure 5. The equivalent noise resistance and the temperature go up comparably with applied voltage. All of the temperature dependence of the noise parameters have been included in the small signal noise model.

As the size of the device changes so will the noise parameters. For a given frequency range there should be an optimum device size to produce minimum noise figure and optimum noise match [11]. The greatest difference between a larger device and a smaller device is that a large device exhibits very small parasitic resistance at the terminals. The large junction

Microtech 2-18 GHz noise parameter test set, an Hewlett Packard 8510B network analyzer and a Hewlett Packard 4145 for bias. The noise parameters are shown with modeled data in Figure 2 for different currents at a collector-emitter bias of 2V. The modeled data agrees well with the measured data. All model parameters came from analysis from the bias conditions and from the measured S-Parameters [7]. The only optimized parameter in the model was the correlation factor. The frequency dependent form of the correlation factor was assumed and subsequently verified.

As a function of current, both the shot noise increases and the thermal noise will increase due to self-heating. The correlation factor will also decrease with respect to current; this will tend to increase the overall

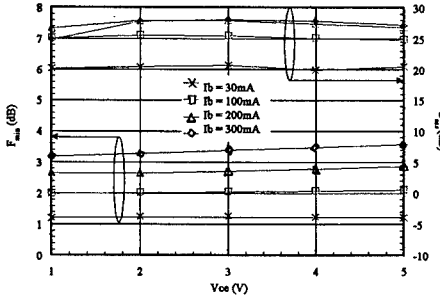


Figure 4 Measured F_{\min} minimum noise figure and associated gain G_{\min} vs. collector-emitter voltage at 2 GHz for a $3 \times 10 \mu\text{m}^2$ device for multiple base bias currents.

areas also bring about large parasitic capacitance values. This reduces associated gain and, subsequently, the noise figure rises under very low bias conditions. This only applies for the lowest bias conditions. For moderate values of associated gain, the noise figure is always lower for a large area device due to the lower terminal resistance. Of the devices tested, the device with emitter area of $3 \times 10 \mu\text{m}^2$ exhibited the best overall performance.

Results and Conclusions: Excellent noise performance has been reported. A minimum noise figure of 0.8 dB with associated gain of 16 dB at 2 GHz was achieved at a collector bias of 0.83 mA and a collector-emitter voltage of 2 V. A noise model was presented. The incorporation of self-heating effects is critical to the accurate simulation of noise for the full range of biases of the transistor. The correlation coefficient is apparently both bias and input power dependent. It is clearly linearly frequency dependent and imaginary. One theoretical explanation was given based on the total current flowing through the base collector junction by means of the depletion capacitance. The bias dependence of the correlation coefficient has not been clearly determined.

The noise measurements for a range of biases displayed the complex nature of the noise figure, equivalent noise resistance, and the optimum matching condition. The correlation factor between the collector and base current played a large role. The larger area devices displayed lower noise figures but smaller associated gains. There was a trade-off between lower resistance and larger depletion capacitance. The lower current noise figures did not scale exactly as the area. Shot noise placed an absolute dependence on the noise with respect to current, and thus limited the scaling of the noise figure as area increased at small currents.

References:

- [1] S. A. Maas, et al, 1992, *IEEE Trans. Microwave Theory Tech.*, pp. 442-448.
- [2] G. N. Henderson and D-W Wu, 1996, *IEEE MTT-S Digest*, pp. 1221-1224.
- [3] W. J. Ho, et al, 1993, *IEEE Electron Device Letters*, pp.572-574.
- [4] M. S. Heins, et al, 1997, *IEEE MTT-S Conference Proceedings*.
- [5] M. T. Fresina, et. al, 1995, *IEEE Electron Device Letters*, pp. 540-541.
- [6] A. van der Zeil, 1986, *Noise in Solid State Devices and Circuits* (NY: John Wiley & Sons) pp. 97-119.
- [7] D.W. Barlage, 1997, *Modeling of InGaP/GaAs Heterojunction Bipolar Transistors for ADC and MMIC Circuit Design*, Ph.D. dissertation, Univ. of Illinois, Urbana, IL, pp. 20-65.
- [8] R. J. Hawkins, 1977, *Solid State Electron.*, pp. 191-196.
- [9] R. A. Pucel and U. L. Rhode, 1993, *IEEE Microwave and Guided Letters*, pp. 35-37.
- [10] A. F. M. Anwar and M. M. Jahan, 1995, pp. 296-302.
- [11] J. J. Liou, et al, 1996, *IEEE Transactions on Electron Devices*, pp. 116-122.

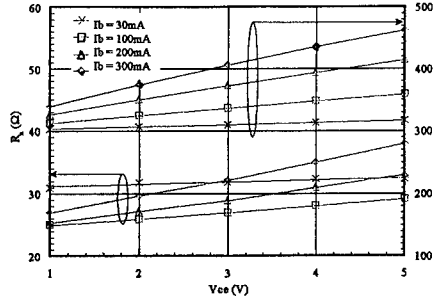


Figure 5 Measured equivalent noise resistance and operating temperature of the device vs. collector-emitter voltage at 2 GHz for a $3 \times 10 \mu\text{m}^2$ device for multiple base bias currents.

DHBT/RTD-Based Active Frequency Multiplier for Wireless Communications

Héctor J. De Los Santos, Kelvin Chui, David H. Chow*, and Howard L. Dunlap*

Hughes Space and Communications Company, Los Angeles, CA 90009

*Hughes Research Laboratories, Malibu, CA 90265

Abstract We present, for the first time, measured data pertaining the microwave performance and characterization of a X_6 (127-->762MHz) active frequency multiplier (FM), based on AlInAs/GaInAs/InP double heterostructure bipolar transistor (DHBT) and AlAs/InGaAs resonant tunneling diode (RTD) active devices. At +23°C and a nominal input power of -3 dBm, the X_6 DHBT/RTD multiplier exhibits a conversion gain of +1 dB, a power dissipation of 22 mW, a dc efficiency of 3%, and an overall 0 to 60°C output power variation of 0.7 dB. The rich output harmonic content makes the DHBT/RTD combination a prime candidate for high-order multiplication applications.

1. Introduction

As user demand for ever more powerful wireless products is expected to continue for the foreseeable future [1], research on device and systems technologies with the potential to reconcile conflicting expectations, such as, portability and low cost, together with unprecedented levels of functionality, flexibility and sophistication, must be vigorously pursued. In the current industrial R&D climate, however, it is imperative that the first fruits of such research be exploited soon after they become available. Because of their small size and radical operating principles, quantum devices (QDs) have demonstrated the potential for highest speed/lowest power-consumption operation [2], and these properties are expected to be exhibited by the conventional circuit/system functions employing them. Within the realm of QD's, the ability to successfully operate at both low and high temperature, together with their relative maturity, singles out resonant tunneling diodes (RTDs) as prime candidates for wireless products. In particular, the highly-nonlinear current-voltage characteristic of RTDs, is expected to enable power-efficient high-order frequency multiplication, a function that is ubiquitous in the frequency synthesis section of wireless systems. In this paper we present, for the first time, measured data pertaining the microwave performance and characterization of a X_6 (127-->762 MHz) active frequency multiplier (FM), based on AlInAs/GaInAs/InP double heterostructure bipolar transistor (DHBT) and AlAs/InGaAs resonant tunneling diode active devices, for utilization in power-efficient local oscillator (LO) chains in future wireless communications applications.

2. Approach

The potential of DHBTs as active RF and microwave frequency multipliers has been recently demonstrated [3]. While the conversion efficiency of these FMs is greatly enhanced by the high f_T

germane to these devices, the non-exponential nature of their I_C - V_{BE} characteristic, which results from incomplete grading of the base-collector conduction band discontinuity [4], limits the maximum obtainable conversion gain at high-order frequency multiplication. Given the high-frequency capability of RTDs coupled with their highly nonlinear characteristics, it is expected that their application in DHBT/RTD FMs will result in highly-efficient higher-order-multiplication circuits. A standard circuit topology, Fig. 1, *currently used in production* for Si-based multipliers was used as vehicle for this work.

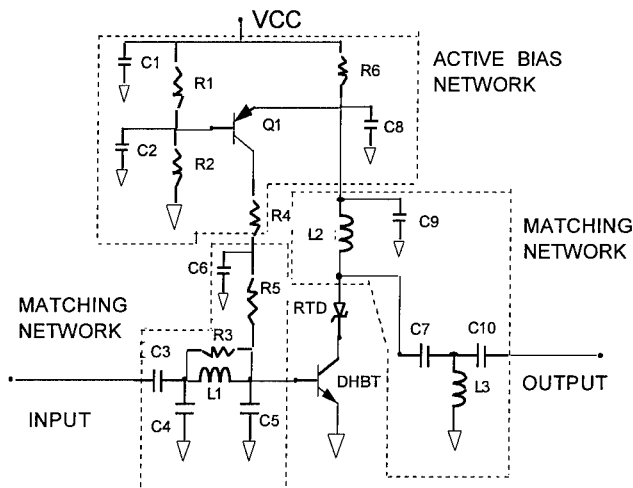


Figure 1. Frequency multiplier circuit topology.

The DHBT/RTD were die-attached using Silver epoxy to a 70 mil ceramic package. The device contacts were wire bonded to the package leads using an approximately 40 mil long/1 mil diameter Gold wire. The circuit was then submitted to our production line where it was iteratively tuned and tested for best conversion gain, input/output return loss, output power, DC power and temperature performance, as routinely done in production. The details of the DHBT device design and characteristics have been discussed elsewhere [3].

The procedure for deposition of the RTD structure by molecular beam epitaxy, Fig. 2, was as follows: Following oxide desorption, the substrate temperature was lowered to 480°C, as determined by absorption band edge spectroscopy of the InP substrate, for growth of the structure. A 5000 Å thick, heavily silicon doped InGaAs ($x = 0.53$) layer forms the bottom contact of the RTD. Asymmetrically doped ($n = 1 \times 10^{17} \text{ cm}^{-3}$ and $5 \times 10^{17} \text{ cm}^{-3}$), 250 Å thick, InGaAs ($x = 0.53$) spacer layers were employed to lower the voltage position of the peak in one bias direction. The AlAs barriers were 13 Å thick (slightly greater than 4 monolayers), and the well consisted of two 30 Å thick InGaAs ($x = 0.53$) layers sandwiching a 12 Å InAs layer. The growth is completed by a 2000 Å heavily

silicon doped InGaAs ($x = 0.53$) layer which forms the top contact to the device. A typical I-V characteristic is shown in Fig. 3.

GalnAs contact ($n+=5E18$)	2000Å
GalnAs spacer ($n=5E17$)	250Å
GalnAs spacer (und.)	15Å
AlAs barrier	13Å
GalnAs/InAs/GalnAs well	30Å/12Å/30Å
AlAs barrier	13Å
GalnAs spacer (und.)	15Å
GalnAs spacer ($n=1E17$)	250Å
GalnAs contact layer ($n+=5E18$)	5000Å
GalnAs buffer (und.)	100Å
InP substrate (semi-insulating)	

Figure 2. AlAs/InGaAs($x=0.53$) RTD layer structure.

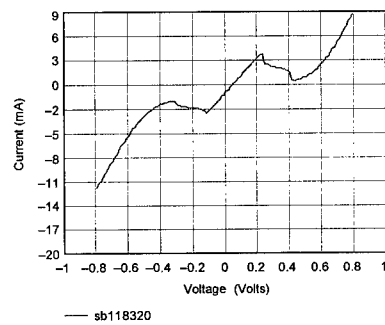


Figure 3. Typical AlAs/InGaAs($x=0.53$) RTD current-voltage characteristic.

3. Results and conclusion

The measured conversion gain versus input power performance of the X6 DHBT/RTD FM ($f_{in} = 127$ MHz and $f_{out} = 762$ MHz) is shown in Fig. 4. At the nominal temperature of $+23^\circ\text{C}$ the FM circuit utilized a power supply of 3.5 volts, consumed a current of 6.26 mA, and exhibited a maximum conversion gain of +1dB, for a power dissipation of 22 mW and a dc efficiency of 3%. The nominal input and output return loss were measured to be 23 dB and 4 dB, respectively, and the overall 0 to 60°C output power variation was 0.7 dB. Fig. 5 shows the measured output power spectrum of the FM. Comparing this data with that obtained for a X6 FM using a similar DHBT active device [3], indicates that the X6 DHBT/RTD FM exhibits more than 7dB higher amplitude improvement, from the seventh through the fifteenth harmonic. In particular, the improvement in the amplitude of the fifteenth harmonic is 20dB. It can be concluded, therefore, that the inclusion of the RTD produces a rich harmonic content, thus making the DHBT/RTD combination a prime candidate for high-order multiplication applications. Future work will concentrate on performing a detailed analysis of the individual role of the devices, on improving the output power by optimizing the relative DHBT and RTD device areas, and the RTD peak voltage, and on designing higher-order FMs for applications at 12 to 14 GHz.

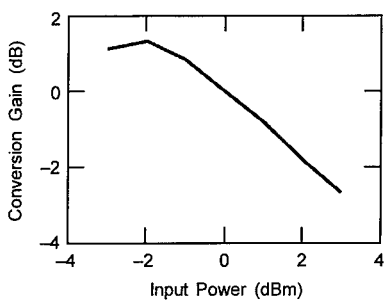


Figure 4. Conversion gain of DHBT/RTD X6 frequency multiplier. The input/reference output frequencies are 127 MHz/762 MHz.

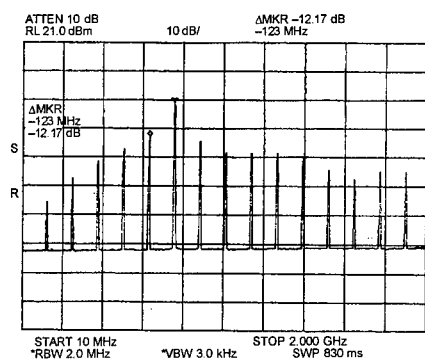


Figure 5. DHBT/RTD X6 multiplier output spectrum. The input/reference output frequencies are 127 MHz/762 MHz.

Acknowledgment

The authors thank M. Hafizi and W. Stanchina of Hughes Research Labs, for supplying the DHBTs. The support and encouragement of N. Anderson and B. Dobratz from Hughes Space and Communications Company is gratefully acknowledged.

References

- [1] Heilmeyer G H 1992 *IEEE Int. Solid-State Cir. Conf. Dig.* 24-26
- [2] Capasso F 1990 *Physics of Quantum Electron Devices* (Springer-Verlag: Berlin)
- [3] De Los Santos H J, Nardi D D, Hargrove K L, Hafizi M, and Stanchina W E, 1996 *IEEE Trans. Microwave Theory and Tech.* 44 1165-1167
- [4] De Los Santos H J, Hafizi M, Liu T, and Rensch D B, 1994 *Inter. Symp. on Compound Semiconductors* 645-650

Optical and Microscopic Properties of $\text{In}_{0.5}\text{Ga}_{0.5}\text{As}/\text{GaAs}$ highly strained heterostructures

A. Polimeni^{a)}, M. Henini^{a)}, L. Eaves^{a)}, S. T. Stoddart^{a)}, P. C. Main^{a)}, R. K. Hayden^{b)}, K. Uchida^{b)}, and N. Miura^{b)}

a) Department of Physics, University of Nottingham, Nottingham NG7 2RD, United Kingdom

b) Institute for Solid State Physics, University of Tokyo, Roppongi, Minato-ku, Tokyo 106, Japan

Abstract. The evolution of the optical and microscopic properties of highly strained $\text{In}_{0.5}\text{Ga}_{0.5}\text{As}/\text{GaAs}$ heterostructures is studied as a function of the $(\text{InGa})\text{As}$ layer thickness, L , for different GaAs substrate orientations, (100) and (311). Optical and microscopic properties have been investigated by means of low temperature photoluminescence (PL) and atomic force microscopy (AFM), respectively. Samples grown on (100) show a clear transition in their photoluminescence (PL) spectra at a critical value of L due to the self-assembling of quantum dots. On the other hand, the same structures grown on (311) show a quite smooth evolution of the PL with L . The microscopic measurements indicate that these differences are associated with the morphology of dots formed on the (311) substrates. A study of the (311) heterostructure photoluminescence as a function of applied magnetic field is also reported.

The study of strained heterostructures based on $(\text{InGa})\text{As}/\text{GaAs}$ has attracted much interest recently due to the possibility of obtaining defect-free quantum dots (QD) by spontaneous self-assembling [1,2]. Previous studies on highly strained $(\text{InGa})\text{As}/\text{GaAs}$ materials focused mostly on the determination of the critical thickness for the formation of dislocations [3]. More recently, this type of heterostructure has provided QDs having good optical quality [4] and size homogeneity [5]. It has been shown that the photoluminescence properties of $\text{In}_{0.5}\text{Ga}_{0.5}\text{As}$ QDs on GaAs can be improved by growing the dots on (n11) substrates [6,7,8]. Specifically in reference [6], a remarkable narrowing of the PL spectrum linewidth was reported for InAs and $\text{In}_{0.5}\text{Ga}_{0.5}\text{As}$ QDs grown on (311)B with respect to the same structures grown on (100).

In this paper we report a study of the optical and microscopic properties of $\text{In}_{0.5}\text{Ga}_{0.5}\text{As}/\text{GaAs}$ heterostructures having different alloy thickness and grown on (100) and (311) oriented substrates. The dependence of the PL on magnetic field up to 40T is also studied for the high index planes and interpreted in terms of the structural measurements.

Our heterostructures were grown by molecular beam epitaxy (MBE) on (100) and (311) GaAs substrates. For the high index plane orientation, the layers were deposited on both A and B type surfaces. The samples form a series having different $(\text{InGa})\text{As}$ thickness, $L=5, 7, 8, 10, 11, 14, 17$, and 20\AA , and the same nominal indium concentration, $x=0.5$. Before depositing the $\text{In}_{0.5}\text{Ga}_{0.5}\text{As}$ layer, the substrate temperature was reduced from 600 to 450 °C. We have found that this value of the growth temperature for the QDs gives optimum optical properties (i. e., smaller linewidth and higher efficiency of the PL), regardless of the substrate orientation. The $(\text{InGa})\text{As}$ layer was capped by 250\AA of GaAs. In this study samples having the same L but different substrate orientation were grown simultaneously. In order to determine the transition from a two-dimensional to a three-dimensional growth mode, the reflection high-energy electron-diffraction (RHEED) pattern was monitored for each substrate orientation in a

separate growth run. It was found that this transition occurs for $L \approx 11\text{\AA}$ for both (100) and (311) samples.

The PL measurements were performed in a gas-flow cryostat at temperature $T=5\text{K}$. Optical excitation was provided by the 514.5nm line of an Ar^+ laser. The luminescence was dispersed by a 3/4m monochromator and detected by a cooled Ge diode detector with lock-in amplification. The study of the dependence of the PL on the magnetic field, B , was performed up to 43T in pulsed fields. The laser beam ($\lambda_{\text{exc}}=488\text{nm}$) was chopped and the sample illuminated for 1ms at the top of the field pulse, with the PL emission detected by a CCD array.

Contact mode atomic force microscopy (AFM) was used for structural characterisation of the samples with $\text{In}_{0.5}\text{Ga}_{0.5}\text{As}$ thickness of $L=7$ and 11\AA on (100) and (311)B substrates. For AFM imaging, the samples were grown under the same conditions as above, but they were not capped with a GaAs layer.

Figure 1 shows the low temperature PL spectra for different values of L on (100) and (311)A substrates. No significant difference was found between the (311)A and B samples. For ease of comparison the spectra have been normalised to each other. In general, the PL from samples grown on the high index planes is about one order of magnitude brighter than for those grown on (100).

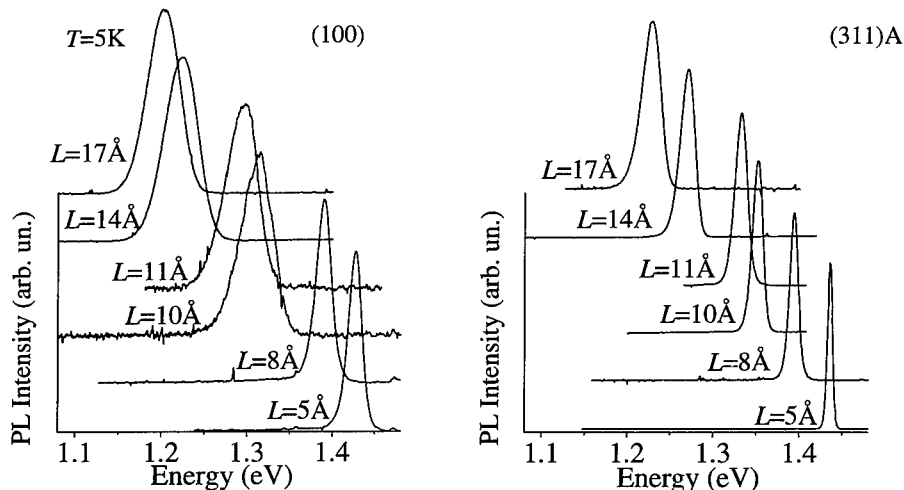


Figure 1: Low temperature PL for different layer thickness L on (100) and (311)A oriented substrates. The excitation wavelength is 514.5nm. The PL intensities have been normalised to each other for ease of comparison.

The dependence of the peak energy emission, $h\nu$, and of the full-width at half-maximum, FWHM, of the PL are shown in Figure 2a) and b), respectively. Both $h\nu$ and FWHM show a clear transition for the (100)-oriented samples at $L \approx 10\text{\AA}$. Note that for $L < 10\text{\AA}$ the quantum well (QW) structures grown on (311) have the same energy peak as the layers grown on (100) but a PL linewidth about three times smaller. This observation can be explained by noting that for the (311) oriented lattice the extent of a monolayer fluctuation along the growth direction

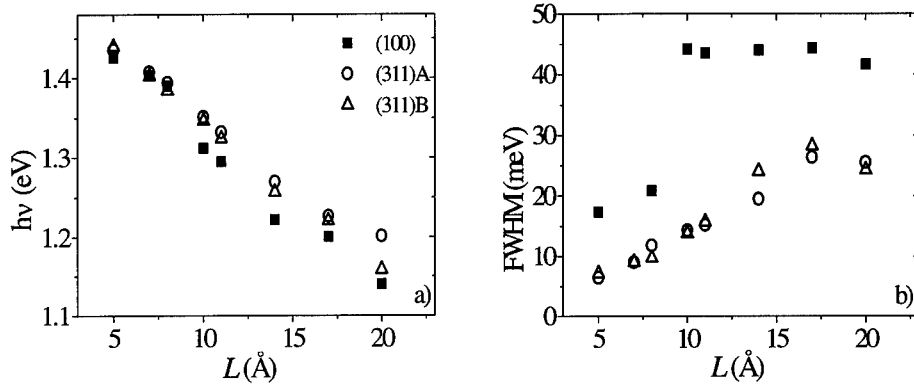


Figure 2: (a) Low temperature PL peak energy position $h\nu$, and (b) full-width at half-maximum FWHM as a function of the layer thickness L for different substrates. Note the abrupt change in $h\nu$ and FWHM at $L=10\text{\AA}$ for the samples grown on (100).

is a factor $\sqrt{3^2 + 1^2 + 1^2}$ smaller than for (100). For the (311) QWs, this results in a smaller contribution from the interface roughness to the excitonic energy distribution (namely the PL linewidth), as can be demonstrated by means of a statistical model [9,10]. Note in Figure 2b) the constant value of FWHM for the (100) samples for $L>10\text{\AA}$: This indicates that the dot size distribution is the same, independent of the mean dot size. The presence of a transition for $L=10\text{\AA}$ in the (100) samples is in agreement with the RHEED pattern observations, which signal the onset of a different growth mode around 11\AA , corresponding to the formation of quantum dots. Despite the fact that the same transition was detected in the RHEED for the (311) orientated heterostructures, the optical properties of these samples are characterised by a quite smooth evolution from the thinnest (5\AA) to the thickest layer (20\AA). Compared to an atomically flat (100) surface, a (311) plane has a corrugated surface due to the presence of edge steps [11]. This could give rise to the formation of dots having microscopic and electronic properties quite different from the "classical" ones formed on (100).

This observation is supported by the AFM pictures shown in Figure 3 for $L=11\text{\AA}$ on (100) and (311)B substrates. The dots grown on the (100) oriented substrate have average diameter $d=36\text{nm}$, height $h=2.2\text{nm}$ and a surface density $\rho=1.5\cdot10^{10}\text{cm}^{-2}$ and appear isolated from each other. These values compare well with those reported previously [5,6,12]. In contrast, for the (311)B sample the surface coverage due to the dots appears much more uniform with a corresponding density $\rho=1.5\cdot10^{11}\text{cm}^{-2}$. The mean dot diameter and height are respectively $d=26\text{nm}$ and $h=1.0\text{nm}$. The structures having a smaller $\text{In}_{0.5}\text{Ga}_{0.5}\text{As}$ layer thickness $L=7\text{\AA}$ show no clear evidence of three-dimensional nanostructures in RHEED and AFM.

Our study of the microscopic properties thus indicates that the (311) dots are flatter than those formed on the (100) substrate. Both the density and the size of the dots clearly affect the electronic properties of the samples as revealed by the optical measurements. In the (311) oriented samples, photogenerated electron-hole pairs localise in the potential minima of the quantum dots with a non-negligible fraction of the exciton wavefunction spreading out into the

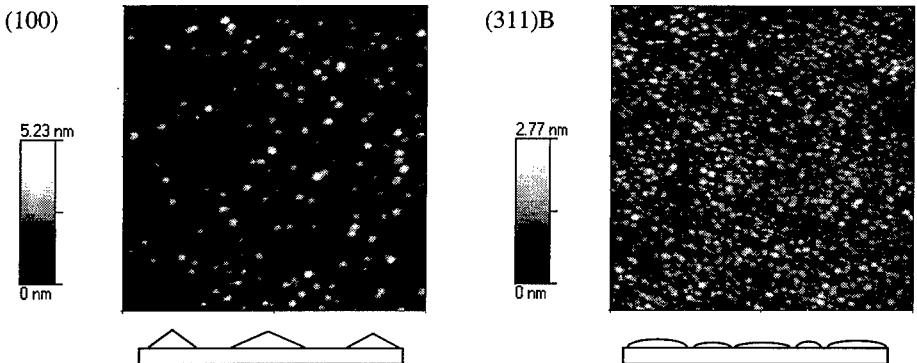


Figure 3: $1\mu\text{m} \times 1\mu\text{m}$ AFM images recorded on samples having $L=11\text{\AA}$ and different substrate orientation. The dots on the (311)B substrate are flatter (compare the height scale on the left of each picture) and have a larger density compared to those formed on the (100) oriented plane. Below each figure is a schematic diagram of the proposed transverse section of the sample.

wetting layer (QW beneath the self-assembled dots). In contrast, more complete confinement is achieved in the dots formed in the (100) sample. Both the value of $h\nu$ and FWHM can be understood from the AFM analysis as follows. The higher energy emission for the (311) samples is due to the weaker confinement of carriers in the dots; moreover the small distance between the dots allows the carriers to recombine in the lowest energy minimum available within their diffusion length. As a consequence, the PL arises from only a part of the dot size distribution, which results in a smaller PL linewidth at $B=0$ compared to the (100) dots.

In order to derive useful information about the exciton confinement in the dots, we studied the dependence of the PL lineshape on magnetic field, B , applied along the growth direction. The measurements were performed on (311)B oriented samples having $L=11$ and 7\AA .

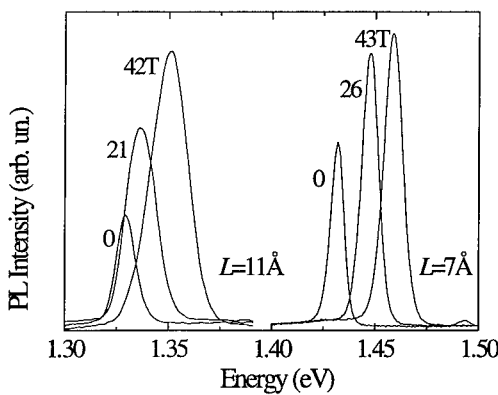


Figure 4: PL dependence on magnetic field for (311)B oriented samples having different layer thickness. For $L=11\text{\AA}$, the PL lineshape shows a gradual broadening of the spectrum as discussed in the text.

Figure 4 shows the PL spectra for different values of B . In comparison with the quantum well sample ($L=7\text{ \AA}$), the thicker one ($L=11\text{ \AA}$) shows a 15% lower diamagnetic shift corresponding to a smaller wavefunction extent due to confinement into the dot potential minima [13]. Another striking feature of the PL spectra of 11 \AA sample is the increasing PL linewidth with increasing B . However this broadening is much less for $L=7\text{ \AA}$. This can be explained by the fact that the magnetic field acts as a further confining potential for the carriers which can prevent them from reaching the lowest energy dots. In other words, with increasing B the electron and hole diffusion in the dot plane is quenched and the radiative recombination of the exciton takes place closer to the point where the carriers have been photogenerated. Therefore, for high magnetic fields, the PL lineshape reflects more closely the microscopic distribution of dot sizes.

In conclusion, we have studied the optical and microscopic properties of highly strained $\text{In}_{0.5}\text{Ga}_{0.5}\text{As}/\text{GaAs}$ heterostructures grown on (100) and (311) substrates. With increasing strained layer thickness, we observe a different evolution in the optical properties of the samples grown on different planes. The differences between the (100) and the (311) orientations arise from the geometrical configuration of the self-assembled dots. The AFM study reveals a flatter dot geometry and a dot density one order of magnitude larger for the (311) substrate than for (100). Magneto-PL experiments are consistent with this picture deduced from the AFM.

Acknowledgements:

This work is supported by EPSRC (UK). L.E., M. H. and R. K. H. acknowledge the support of EPSRC, the British Council and JSPS (Japan) respectively.

References:

- [1] Goldstein L, Glas F, Marzin J-Y, Charasse M N and Le Roux G 1985 *Appl. Phys. Lett.* **47** 1099-1102
- [2] Snyder C V, Orr B G, Kessler D and Sander L M 1991 *Phys. Rev. Lett.* **66**, 3032-3035
- [3] Andersson T G, Chen Z G, Kulakovskii V D, Uddin A and Vallin J T 1987 *Appl. Phys. Lett.* **51**, 752-754
- [4] Oshinowo J, Nishioka M, Ishida S and Arakawa Y, *Appl. Phys. Lett.* 1994 **65**, 1421-1423
- [5] Leonard D, Krishnamurthy M, Reaves C M, Denbaars S P and Petroff P M 1993 *Appl. Phys. Lett.* **63**, 3203-3205
- [6] Nishi K, Mirin R, Leonard D, Medeiros-Ribeiro G, Petroff P M and Gossard A 1996 *J. Appl. Phys.* **80**, 3466-3470
- [7] Lubyshev D I, Gonzalez-Borrero P P, Marega E, Petitprez E and Basmaji P 1996 *J. Vac. Sci. Technol. B* **14**, 2212-2215
- [8] Vaccaro P O, Hirai M, Fujita and Watanabe T 1996 *J. Phys. D: Appl. Phys.* **29** 2221-2228
- [9] Singh J and Bajaj K K, *J. Appl. Phys.* **57** 1985 5433-5437
- [10] Patané A, Polimeni A, Capizzi M and Martelli F 1995 *Phys. Rev. B* **52** 2784-2788
- [11] Brandt O, Kanamoto K, Tokuda Y, Tsukada N, Wada O and Tanimura J 1993, *Phys. Rev. B* **48** 17599-17602
- [12] Leon R, Kim Y, Jagadish C, Gal M, Zou J and Cockayne D J H 1996 *Appl. Phys. Lett.* **69** 1888-1890
- [13] Itskevich I E, Henini M, Carmona H, Eaves L, Main P C, Maude D K and Portal J C, *Appl. Phys. Lett.* **70** 1997 505-507

Strain Tensor, Electronic Spectra and Carrier Dynamics in In(Ga)As/GaAs Self-assembled Quantum Dots

**K.Kamath, H.Jiang, D.Klotzkin, J.Phillips, T.Sosnowski, T.Norris, J.Singh, and
P.Bhattacharya**

Department of Electrical Engineering and Computer Science, University of Michigan, Ann Arbor, MI 48109, USA

Abstract : The strain tensor in pyramidal Ga(In)As/GaAs self-assembled quantum dots is characterized in detail using a valence force field model and is applied to an eight-band $k.p$ formalism to find the electronic spectra in the highly strained dots. Results obtained for the conduction band spectra using the effective mass approach are shown to have serious errors. The energy difference between the ground and excited states obtained from both eight-band calculations and experimental results indicates phonon bottleneck in these dots which is confirmed by a relatively simple high frequency electrical impedance measurements on quantum dot lasers. The electron capture times of 30-40ps are obtained compared to 2-5ps in SCH quantum well lasers and 1ps in tunneling injection lasers, and the modulation band width is found to be limited by the capture times. The time resolved photoluminescence measurements gave decay time constants of ~700ps and ~200-250ps for the ground and excited state transitions, respectively.

1. Introduction

Self-organized growth of semiconductor quantum dots (QD) has gained widespread attention due to the reports on the improvement in performance of some electronic and optoelectronic devices. Semiconductor lasers with quantum dots as the gain media have shown performance characteristics better than the quantum well lasers. Extremely low threshold current densities[1,2] with excellent temperature stability[2-4] and more than an order of magnitude improvement in differential gain [5,6] reported in In(Ga)As/GaAs quantum dot lasers leads to the possibility of operating these lasers with no DC bias and no temperature stabilization. Charge storage and quantum tunneling, in these quasi-zero dimensional structures, have opened up new potential applications such as single electron transistor, memory and multi-level logic elements. However, the details of some of the fundamental issues such as the control of shape, size and position of the quantum dots, estimating the strain distribution and band structure of the dots, dynamics of carrier relaxation etc., are still not complete. In this paper we address the issues related to the strain tensor, electronic spectra, and the carrier dynamics in self-organized In(Ga)As/GaAs quantum dots.

It is well known that the self-assembled In(Ga)As quantum dots are of pyramidal shape with a complex strain tensor. The fact that although the bandgap of bulk InAs is ~0.4eV, the bandgap of the InAs/GaAs quantum dots are ~1.1eV, suggests that strain induced level shifts can approach values equal to the bandgap of the semiconductor. Therefore, the effective mass approach, which requires decoupling of remote bands, can cause serious errors in the calculation of the band structure and electronic spectra. We have calculated the electronic spectra with both effective mass approach and a full eight-band $k.p$ model, and compared the results of our calculations with some of the experimental results reported in literature and our own results. The energy separation between the ground and excited states, derived both from our theoretical and experimental results, indicate that the phonon processes are severely suppressed due to the singular density of states in the quantum dots. We report an estimate of the carrier capture times obtained from a

relatively simple measurement of high frequency electrical impedance of quantum dot lasers. The overlap of the electron and hole wave functions calculated by our model and the recombination time constants obtained from the time resolved photoluminescence (TRPL) measurements are also reported.

2. Strain model

In strained quantum wells the strain tensor is biaxial in nature, while it is expected to be quite complicated in buried strained quantum dots. Assuming that the growth process is slow enough to allow energy minimization, one can estimate the shape and strain in buried dots. We have developed a lattice gas model for the quantum dots using the valence force field (VFF) model [7,8]. The VFF model is a microscopic theory, which includes bond stretching and bond bending and avoids the potential failure of elastic continuum theory in the atomically thin limit. The total VFF energy is,

$$V = \frac{1}{4} \sum_{ij} \frac{3}{4} \alpha_{ij}^2 (d_{ij}^2 - d_{0,ij}^2)^2 / d_{0,ij}^2 + \frac{1}{2} \sum_i \sum_{j \neq k} \frac{4}{3} \beta_{ijk} (\mathbf{d}_{ij} \cdot \mathbf{d}_{ik} + d_{0,ij} d_{0,ik} / 3)^2 / d_{0,ij} d_{0,ik}$$

where i runs over all atomic sites, j,k run over the nearest neighbor (NN) sites of i , \mathbf{d}_{ij} is the vector joining the sites i and j and d_{ij} is the length of the bond, $d_{0,ij}$ is the corresponding equilibrium length in the binary constituents, α_{ij} and β_{ijk} are the bond stretching and bond bending constants respectively. Martin [7] calculated α and β for InAs and GaAs and obtained values that give satisfactory agreement with experiments. We have used these values in this work. For bond-bending parameter β of In-As-Ga, we take,

$$\beta_{ijk} = \sqrt{\beta[ij]\beta[ik]}$$

following Ref. [9].

In order to find the strain tensor in the InAs/GaAs quantum dots, with arbitrary choice of initial atomic positions, minimization of the total VFF energy has to be carried out. This requires one to solve coupled set of equations with $3N$ variables, where N is the total number of atoms. Since this is impractical in our case with more than one hundred thousand atoms, we have used a perturbation technique where the atoms are originally placed in a GaAs matrix and are allowed to deviate from this starting position. All the atoms are displaced in sequence minimizing the system energy each time, and the whole sequence is repeated until the maximum distance moved is so small that there is essentially no change in the system energy [8]. Typical strain distribution derived from this model is shown in Fig.1 for an InAs/GaAs quantum dot with (101) limiting planes. The following conclusions can be drawn from these results : (i) there is relaxation for ϵ_{xx} , ϵ_{yy} at the top of the dot as was experimentally observed [10], (ii) the biaxial strain changes sign from the bottom to the top of the pyramidal dot which means there is more confinement for heavy holes near the bottom and light holes near the top of the dot, (iii) there is a strong shear component, and (iv) C_{4v} symmetry is broken microscopically and there are only two reflection symmetries (110) and (11̄0).

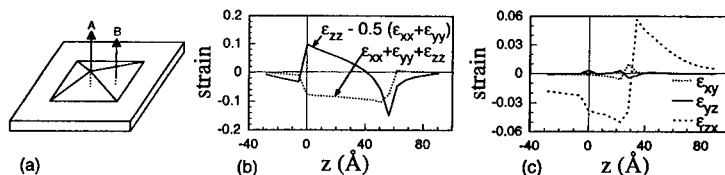


Figure 1 : (a) Schematic of pyramidal quantum dot (b) biaxial and hydrostatic strain along A and (c) shear strain along B of InAs/GaAs quantum dot

3. Electronic spectrum

In self-organized quantum dots the effect of strain is too strong to allow the decoupling of the remote bands. As mentioned earlier, the strain-induced shift of energies can approach the energy band gap of the semiconductor. Therefore the influence of remote bands becomes very critical in estimating the positions of the electronic states as well as the central cell character of the eigenstates (s and p mixing).

We have developed a full eight-band $k \cdot p$ model [8] and have calculated the electronic spectrum by both effective mass approach and the eight-band model. The size and shape of the quantum dots are chosen close to measured values. Figure 2(a) shows the electronic spectrum calculated for the InAs/GaAs dot with base width 124Å and height 62Å using the effective mass approach for conduction band and four-band $k \cdot p$ model for valence band. This shows two bound levels in the conduction band. The electronic spectrum calculated by eight-band model is shown in Fig.2(b), which gives multiple excited states in the conduction band. Such richness of the electronic spectrum has been observed experimentally [11]. Moreover, the energy values agree very well with the two transitions observed in Ref.[12].

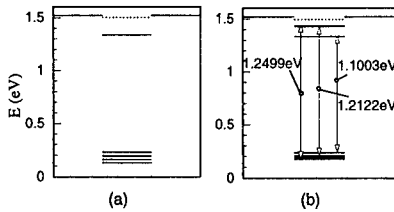


Figure 2 : Electronic spectra calculated for InAs/GaAs Quantum dot (124Å base width and 62Å height)
(a) by effective mass approach and (b) by eight-band model

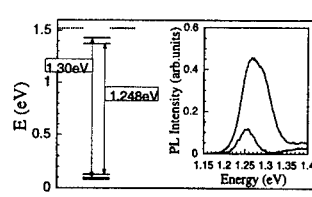


Figure 3 : Electronic spectrum calculated by eight-band model and the PL spectrum for $\text{In}_{0.4}\text{Ga}_{0.6}\text{As}/\text{GaAs}$ quantum dot

In order to calculate the electronic spectrum in InGaAs quantum dots we have used a biaxial strain model. This assumption is more appropriate in InGaAs quantum dots due to the smaller lattice mismatch, which results in lower strain and larger dot size. The cross sectional transmission electron microscope images showed a dot base width of 140Å and a height of 70Å for $\text{In}_{0.4}\text{Ga}_{0.6}\text{As}/\text{GaAs}$ quantum dots. The electronic spectrum calculated by eight-band model for this particular size is shown in Fig.3. The PL spectrum is also shown for comparison. The good agreement between the calculated and measured emission energies confirms that the biaxial strain model is adequate in this case.

4. Carrier dynamics

4.1 Carrier capture dynamics

Due to the large energy separation between the ground state and excited states (much greater than phonon energies of 30-40meV), and due to the singular density of states in quantum dots, single and 2LO-phonon scattering processes are not significant. Therefore, carrier-carrier scattering is the dominant scattering mechanism in quantum dots. We have calculated the electron relaxation times by e-h scattering as a function of hole life time in InAs quantum dots, which gives an electron relaxation time of 100 times that of the hole life time. This means for a typical hole lifetime of 0.6ps, the electron relaxation time is 60ps. This phonon bottleneck plays a major role in the performance characteristics of certain devices such as lasers.

We have derived the quantum capture times for electrons in quantum dot lasers from high frequency electrical impedance (HFEI) measurement [13,14]. The quantum dot lasers with single and multiple layers of self-organized $In_{0.4}Ga_{0.6}As/GaAs$ quantum dots were grown by MBE. The structure consists of the quantum dot active layers in the center of an SCH structure with GaAs waveguiding region and $Al_{0.3}Ga_{0.7}As$ clad. Cross sectional TEM showed the quantum dots with a base width of 140\AA and a height of 70\AA in a single dot layer. The density of the dots as measured by atomic force microscopy on a single layer of dots on the surface, is $\sim 5 \times 10^{10}\text{cm}^2$. The broad area lasers have room temperature threshold current densities of 650A/cm^2 and 320A/cm^2 for single and 4-layer quantum dot lasers, respectively. Ridge waveguide lasers were fabricated in the ground-signal-ground configuration to facilitate microwave probing. Typical modulation characteristics are shown in Fig.4(a). The differential gain of $1.7 \times 10^{-14}\text{cm}^2$ obtained both from modulation characteristics and Hakki-Pauli measurements is more than an order of magnitude higher than quantum well lasers. However, maximum modulation bandwidth obtained in these lasers is 5-7.5GHz. The K-factor is $\sim 1\text{ns}$ which gives gain compression limited bandwidth to be $\sim 9\text{GHz}$. In order to obtain the electron capture times, the magnitude of the HFEI data is analyzed using rate equation model appropriate for quantum well lasers. Figure 4(b) shows the measured and fit impedance data for a single-layer quantum dot laser. The capture time extracted from this fit is $\tau_o \sim 40\text{ps}$. The characteristics of the multiple layer quantum dot lasers are not

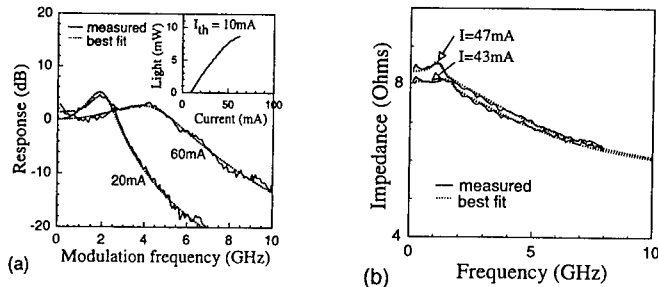


Figure 4 : (a) Modulation response of a single layer quantum dot laser, and (b) measured and fit high frequency electrical impedance data. The value of capture time constant τ_o obtained from this fit is $\sim 40\text{ps}$.

significantly different, with a best-fit $\tau_o \sim 30\text{ps}$ for 4 layers of quantum dots. Compared to the values of 2-5ps in SCH quantum well lasers, values of 30-40ps indicate the severity of phonon bottleneck in quantum dot lasers. We believe that the modulation bandwidth of $\sim 5\text{GHz}$ in these quantum dot lasers is limited by the long carrier capture times.

4.2 Carrier recombination dynamics

One of the main reasons for the improved performance of quantum dot based devices is the singular density of states in these quasi-zero dimensional structures. However, in interband transition devices such as lasers, the carrier recombination rate also plays a major role. Therefore it is important to characterize the carrier recombination dynamics in quantum dots. From our calculations a relatively high overlap of $\sim 90\%$ is obtained for ground state electron and ground state hole wave functions in pyramidal quantum dots. This indicates a fairly efficient radiative recombination of the carriers in these quantum dots, which is also reported widely in literature. We have measured the time resolved photoluminescence (TRPL) spectra in single and multiple layers of $InGaAs/GaAs$ quantum dots. Figure 5 shows the TRPL signal for both ground and excited state transitions. It is observed that decay time constants are 700ps and 200-250ps for the ground state and excited state transitions, respectively. The time constant of 700ps for the ground state is comparable to quantum wells. If the inter-level relaxation rate is fast compared to the radiative lifetimes, and all the radiative transitions have the same time constant, the excited state is expected to decay with a time constant of one thirds of that of the ground state[15], which is approximately valid in our case.

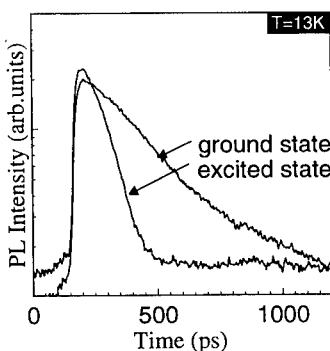


Figure 5 : Time resolved photoluminescence for ground and excited state transitions in 8-layer $\text{In}_{0.4}\text{Ga}_{0.6}\text{As}/\text{GaAs}$ quantum dots

radiative recombination. Time resolved PL spectra showed decay time constants of 700ps and 200ps for the ground and excited state transition, respectively.

5. Conclusions

In conclusion, we have developed a model for the strain tensor in self-assembled quantum dots based on the valence force field model. The strain tensor is found to be quite complicated leading us to believe that a simple effective mass approach to calculate the electronic states is not adequate. We have developed a full eight-band $k.p$ model to obtain the electronic spectra, which show good agreement with experimental results. Carrier relaxation times of 30-40ps obtained by the HFEI technique in InGaAs/GaAs quantum dot lasers show evidence of phonon bottleneck in these lasers. The calculated wave function overlap of 90% between ground state electrons and holes in these pyramidal quantum dots indicate efficient

References

- [1] N.N.Ledentsov, V.A.Shchukin, M.Grundmann, N.Kirstaedter, J.Bohrer, O.Schmidt, D.Bimberg, V.M.Ustinov, A.Yu.Egorov, A.E.Zhukov, P.S.Kop'ev, S.V.Zaitsev, N.Yu.Gordeev, and Zh.I.Alferov, *Phys.Rev.B* **54**, 1996
- [2] K.Kamath and P.Bhattacharya, to be published
- [3] Zh.I.Alferov, N.Yu.Gordeev, S.V.Zaitsev, P.S.Kop'ev, I.V.Kochnev, V.V.Komin, I.I.Krestnikov, N.N.Ledentsov, A.V.Luney, M.V.Maximov, S.S.Ruvimov, A.V.Sakharov, A.F.Tsapulnikov, and Yu.M.Shernyakov, *Semiconductors* **30**, 197 (1996)
- [4] H.Shoji, Y.Nakata, K.Mukai, Y.Sugiyama, M.Sugawara, N.Yokoyama, and H.Ishikawa, *Appl.Phys.Lett.* **71**, 193 (1997)
- [5] N.Kirstaedter, O.G.Schmidt, N.N.Ledentsov, D.Bimberg, V.M.Ustinov, A.Yu.Egorov, A.E.Zhukov, M.V.Maximov, P.S.Kop'ev, Zh.I.Alferov, *Appl.Phys.Lett.* **69**, 1226 (1996)
- [6] K.Kamath, J.Phillips, H.Jiang, J.Singh, and P.Bhattacharya, *Appl.Phys.Lett.* **70**, 2952 (1997)
- [7] P.N.Keating, *Phys.Rev.* **145**, 627 (1966); R.M.Martin, *Phys.Rev.B* **1**, 4005 (1969)
- [8] H.Jiang and J.Singh, *Phys.Rev.B* (to be published)
- [9] M.Podgorny, M.T.Czyzyk, A.Balzarotti, P.Letardi, N.Motta, A.Kisiel, and M.Zimnal-Starnawska, *Solid State Commun.* **55**, 413 (1985)
- [10] T.Benabbas, P.Francois, Y.Androussi, and A.Lefebvre, *J.Appl.Phys.* **80**, 2763 (1996)
- [11] K.H.Schmidt, G.Medeiros-Ribeiro, M.Oestreich, P.M.Petroff, and G.H.Dohler, *Phys.Rev.B* **54**, 11346 (1996)
- [12] F.Adler, M.Geiger, A.Bauknecht, F.Scholz, H.Schweizer, M.H.Pilkuhn, B.Ohnesorge, and A.Forchel, *J.Appl.Phys.* **80**, 4019 (1996)
- [13] S.Weisser, I.Esquivas, P.J.Tasker, J.D.Ralston, B.Romerov, and J.Rosenzweig, *IEEE Photon.Tech.Lett.* **6**, 1421(1994)
- [14] D.Klotzkin, K.Kamath, and P.Bhattacharya, *IEEE Photon.Tech.Lett.* (in press)
- [15] M.Grundmann, et.al. *Phys.Rev.B* (in press), private communication

Positioning of InAs Quantum Dots on Sub-250 nm Facets using Selective Area Epitaxy

Raymond Tsui*, Ruth Zhang, Kumar Shiraliagi, and Herbert Goronkin

Phoenix Corporate Research Laboratories, Motorola, Inc., 2100 East Elliot Road, M/S-EL308, Tempe, Arizona 85284, USA.

Abstract. Using oxide-patterned substrates, we have selectively grown GaAs mesas with (100) top facets ranging from several μm to less than 250 nm in width and InAs quantum dots (QDs) on top of these facets. For a given total InAs coverage, the dot density varies with the facet width. The QDs also tend to form at the facet edges. These observations suggest a strong surface diffusion effect of In-containing species adsorbed on the various GaAs facets of a mesa. By designing the oxide pattern in an appropriate manner, a two-dimensional array of QDs could be positioned in a pre-determined configuration at specific wafer locations.

1. Introduction

In recent years, there has been a considerable amount of research on semiconductor self-organized quantum dots (SOQDs) formed by the Stranski-Krastanow (SK) growth mode [1]. One limitation with conventional growth techniques is that positioning of the SOQDs on a wafer is difficult to control. To overcome this, various approaches have been studied, including growth on wafers patterned with ridges [2] and tetrahedral pits [3], and on buffer layers with multi-atomic steps formed by substrate misorientation [4]. The disadvantage in using a non-planar starting wafer is that etch damage can occur during the substrate patterning process, while the use of vicinal substrates has constraints on the location and spacing of the SOQDs imposed by the angle of misorientation.

In this paper we describe an approach that provides improved positioning control in the formation of SOQDs which makes uses of the results of our earlier studies on selective area epitaxy (SAE) and faceted epitaxial growth [5,6]. The idea is based on the selective formation of InAs SOQD arrays on specific regions on a wafer. These regions of GaAs are grown on an oxide-patterned substrate using SAE, and well-defined crystallographic facets are formed while no growth occurs on the oxide. Then SAE is used again to form the InAs SOQDs. The InAs growth rates are different on the various GaAs facets. We utilize this fact so that only on a specific facet (e.g., the (100) top surface) is the InAs sufficiently thick for strain-induced islanding (SK growth mode) to occur and SOQDs are formed. The width of these (100) facets can be reduced to the sub-250 nm range by crystal growth without using fine-line lithography. By patterning the oxide in an appropriate manner, arrays of SOQDs can then be formed. This points to a possible path to realize few- or single-electron devices using “natural” crystal growth processes.

*Electronic mail: ambk40@email.mot.com

2. Experimental Procedures

In our work, the GaAs was selectively grown at a substrate temperature of ~ 620 °C using chemical beam epitaxy (CBE). Triethylgallium and arsine were used as the source materials in a VG V90 CBE system. Utilizing the faceted growth behavior provided by SAE, the (100) top facet of a mesa grown in an unmasked region 1 μm wide can be reduced to less than 250 nm in width for a mesa height of ~ 0.4 μm . The substrate temperature was reduced to ~ 520 °C for the selective formation of the InAs SOQDs. Here, trimethylindium was used as the In source material. We have previously reported on the SAE of thick InAs layers by CBE [5]. The ability to avoid InAs growth on the oxide and the amount of InAs that nucleates on the various GaAs facets are strongly dependent on the growth conditions. In this work, the conditions were chosen such that no InAs SOQDs were formed on the side facets of the GaAs mesas.

3. Results and Discussions

For the SOQDs formed selectively on the top GaAs (100) facet, their uniformity and areal density are strongly dependent on the facet width and the amount of InAs deposited on the wafer. Figure 1 shows SEM images as viewed from the top of long GaAs mesas grown on oxide-patterned (100)-oriented substrates using SAE. InAs SOQDs can be seen to have formed only on the top facets (dark regions). In each case, the total amount of InAs deposited is indicated in the unit of monolayers (MLs). This amount is the equivalent thickness of a continuous InAs layer grown on a planar, non-patterned (100) GaAs surface.

The width of the top facet in both Figs. 1a and 1b is about 1 μm . For the deposition of less than 2 ML of InAs on a planar surface, it is known that the dot density increases with the total deposited amount of InAs [7]. Thus it is not surprising that, in our case, the deposition of 1.5 ML of InAs (Fig. 1a) resulted in an average dot density of $\sim 2 \times 10^{10}/\text{cm}^2$ which is higher than that of $\sim 0.6 \times 10^{10}/\text{cm}^2$ for the deposition of 1.3 ML (Fig. 1b). However, the dot densities are not uniform in both cases and tend to be higher at the edges of the top facet. It is also of interest to note that for the formation of InAs SOQDs on a planar (100) GaAs surface, the dot density does not reach $\sim 1 \times 10^{10}/\text{cm}^2$ until the InAs coverage exceeds ~ 1.7 ML, and is basically zero for a coverage of less than ~ 1.5 ML [7,8]. The SOQD densities on the top facets are significantly larger in our case, for the deposition of smaller amounts of InAs.

The result on reducing the top facet width to ~ 250 nm is quite striking (Fig. 1c). When compared with Fig. 1b, the dot density is much higher ($\sim 5.5 \times 10^{10}/\text{cm}^2$) and more uniform on the narrower facet, for the same 1.3 ML of InAs deposited. On the other hand, for a top facet width of $\sim 2 \mu\text{m}$ and 1.3 ML of InAs deposited (not shown), the dot density is basically zero except for the very edges of the facet. To make the comparisons valid, these three mesas with top facet widths of about 0.25, 1, and 2 μm , respectively, are on the same wafer which was rotated during growth to reduce flux non-uniformity as well as run-to-run variations.

With the deposition of larger amounts of InAs (1.7 ML and 2.0 ML of InAs, respectively), the average dot density on the $\sim 1 \mu\text{m}$ wide facets increased to $\sim 8 \times 10^{10}/\text{cm}^2$ (not shown). Such an observation with increasing amounts of deposited InAs is again expected. However, well-defined individual SOQDs were not formed on the narrower (~ 250 nm) facets in these cases. Instead, what appeared to be coalesced islands were observed, as shown in Fig. 2 for the case of a facet about 150 nm wide and for 1.7 ML of deposited InAs. In comparison, the formation of coalesced islands is only seen on planar,

Positioning of InAs Quantum Dots on Sub-250 nm Facets using Selective Area Epitaxy

Raymond Tsui*, Ruth Zhang, Kumar Shiraliagi, and Herbert Goronkin

Phoenix Corporate Research Laboratories, Motorola, Inc., 2100 East Elliot Road, M/S-EL308, Tempe, Arizona 85284, USA.

Abstract. Using oxide-patterned substrates, we have selectively grown GaAs mesas with (100) top facets ranging from several μm to less than 250 nm in width and InAs quantum dots (QDs) on top of these facets. For a given total InAs coverage, the dot density varies with the facet width. The QDs also tend to form at the facet edges. These observations suggest a strong surface diffusion effect of In-containing species adsorbed on the various GaAs facets of a mesa. By designing the oxide pattern in an appropriate manner, a two-dimensional array of QDs could be positioned in a pre-determined configuration at specific wafer locations.

1. Introduction

In recent years, there has been a considerable amount of research on semiconductor self-organized quantum dots (SOQDs) formed by the Stranski-Krastanow (SK) growth mode [1]. One limitation with conventional growth techniques is that positioning of the SOQDs on a wafer is difficult to control. To overcome this, various approaches have been studied, including growth on wafers patterned with ridges [2] and tetrahedral pits [3], and on buffer layers with multi-atomic steps formed by substrate misorientation [4]. The disadvantage in using a non-planar starting wafer is that etch damage can occur during the substrate patterning process, while the use of vicinal substrates has constraints on the location and spacing of the SOQDs imposed by the angle of misorientation.

In this paper we describe an approach that provides improved positioning control in the formation of SOQDs which makes uses of the results of our earlier studies on selective area epitaxy (SAE) and faceted epitaxial growth [5,6]. The idea is based on the selective formation of InAs SOQD arrays on specific regions on a wafer. These regions of GaAs are grown on an oxide-patterned substrate using SAE, and well-defined crystallographic facets are formed while no growth occurs on the oxide. Then SAE is used again to form the InAs SOQDs. The InAs growth rates are different on the various GaAs facets. We utilize this fact so that only on a specific facet (e.g., the (100) top surface) is the InAs sufficiently thick for strain-induced islanding (SK growth mode) to occur and SOQDs are formed. The width of these (100) facets can be reduced to the sub-250 nm range by crystal growth without using fine-line lithography. By patterning the oxide in an appropriate manner, arrays of SOQDs can then be formed. This points to a possible path to realize few- or single-electron devices using “natural” crystal growth processes.

*Electronic mail: ambk40@email.mot.com

4. Summary

In conclusion, we have demonstrated a new technique in the formation of SOQDs. This approach makes use of selective area epitaxy and faceted growth on oxide-patterned substrates, and allows InAs SOQDs to be positioned selectively on GaAs facets with sub-250 nm widths. Our initial results show that selective positioning of SOQDs can be achieved by controlling crystal facet growth, and the surface diffusion of In adatoms on these facets strongly influence the spatial uniformity and density of the SOQDs being formed by the Stranski-Krastanow growth mode. With an appropriate design of the oxide pattern, a two-dimensional array of SOQDs can be positioned in a pre-determined configuration at a specific location on a wafer. It is believed that, on further development, this approach can provide a path for the realization of few- or single-electron devices and other novel nanometer-scale structures without requiring the use of fine-line lithography.

Acknowledgments

We would like to thank J. Escher for the support of this work. Also acknowledged is the technical assistance of S. Allen, D. Convey, T. Hopson, J. Markham, K. Palmer, and J. Tresek, Jr. This work was performed in part under the management of FED within the MITI R&D Program on Quantum Functional Devices supported by NEDO, Japan.

References

- [1] Eberl K, Petroff P M and Demmester P (Eds.) 1995 *Low Dimensional Structures Prepared by Epitaxial Growth or Regrowth on Patterned Substrates* (Dordrecht: Kluwer)
Nötzel R 1996 *Semicond. Sci. Technol.* **11** 1365-1379 (and references therein)
- [2] Mui D S L, Leonard D, Coldren L A and Petroff P M 1995 *Appl. Phys. Lett.* **66** 1620-1622
- [3] Sugiyama Y, Sakuma Y, Muto S and Yokoyama N 1995 *Appl. Phys. Lett.* **67** 256-258
- [4] Kitamura M, Nishioka M, Oshinowo J and Arakawa Y 1995 *Appl. Phys. Lett.* **66** 3663-3665
- [5] Shiraliagi K, Walther M, Tsui R and Goronkin H 1996 *J. Cryst. Growth* **164** 334-338
- [6] Tsui R, Walther M, Shiraliagi K and Goronkin H 1996 *Proc. 22nd International Symposium on Compound Semiconductors* (Bristol: IOP) 1283-1288
- [7] Leonard D, Pond K and Petroff P M 1994 *Phys. Rev. B* **50** 11687-11692
- [8] Moison J M, Houzay F, Barthe F, Leprince L, André E and Vatet O 1994 *Appl. Phys. Lett.* **64** 196-198
- [9] Amano C, Rudra A, Grunberg P, Carlin J F and Illegems M 1996 *J. Cryst. Growth* **164** 321-326

Increased Surface Ordering of InAs Island Arrays Using a Multi-Dot Column Subsurface Structure

S. A. Komarov, G. S. Solomon *, J. S. Harris Jr.

Solid State Electronics Laboratory, Stanford University, Stanford, CA, 94305
 * Ginzton Laboratory, Stanford University, Stanford, CA, 94305-4075

Abstract. We report experimental evidence of improved in-plane self-organization resulting from vertically stacked self-assembled InAs islands in a GaAs matrix. Samples under investigation were grown by molecular beam epitaxy in Stranski-Krastanow growth mode and consisted of one, five, ten, and twenty layers of coherently strained islands of InAs with all but the last layers covered with GaAs. We have studied atomic force microscope images of the sample surface morphology and performed real space, as well as Fourier space image processing. Along with the evolution of island size and long range surface roughness, we clearly observe the onset of in-plane island ordering with stacking.

1. Introduction

Natural restrictions imposed on conventional lithography techniques have led to the development of alternative approaches for the fabrication of 0-D quantum size structures. Currently, one of the most attractive and interesting methods is the growth of self-assembled coherently strained semiconductor islands, where the dimensions and material choice of the islands create the 3-dimensional confinement. While extensive research had been devoted to the structural, optical and electronic properties of these structures, little improvement in the size uniformity and in-plane ordering has occurred. Thus, characterization on large sample areas is dominated by inhomogeneous broadening.

Theoretical models predicting island array self-organization were proposed by several authors [1,2] and some evidence of the island ordering has been detected in a number of experimental works [3,4]. Though complete characterization and analysis of this ordering has not been done. In the present communication we report experimental evidence of improved in-plane self-organization resulting from vertically stacked self-assembled InAs islands in a GaAs matrix and provide some instruments for the characterization of this ordering. These layered have previously been shown to be vertically aligned in columns and dislocation-free [5].

2. Experimental Samples

Samples under investigation were grown by molecular beam epitaxy using Varian Gen II system in Stranski-Krastanow growth mode and consisted of one, five, ten, and twenty layers of coherently strained islands of InAs with all but the last layers covered with GaAs. The InAs islands and the GaAs cap layer deposition was conducted at 500 °C with a growth rate of 0.1 μm/hr. As₂ from a valved cracker was used and a V/III ratio of nine was maintained during the growth. Three monolayers of InAs were deposited to obtain coherently strained islands and then a 5 nm cap layer of GaAs was grown on top for multilayered structures. The top layer of islands remained uncovered.

3. Results and Discussion

Our results are based on atomic force microscope (AFM) scans taken in contact mode in the height regime on a Digital Instruments Multimode AFM. All scans were performed along the (110) crystallographic direction of the GaAs substrates. Figure 1 shows two such scans obtained on the samples grown under conditions described above. Figure 1(a) shows the top view of a surface with a

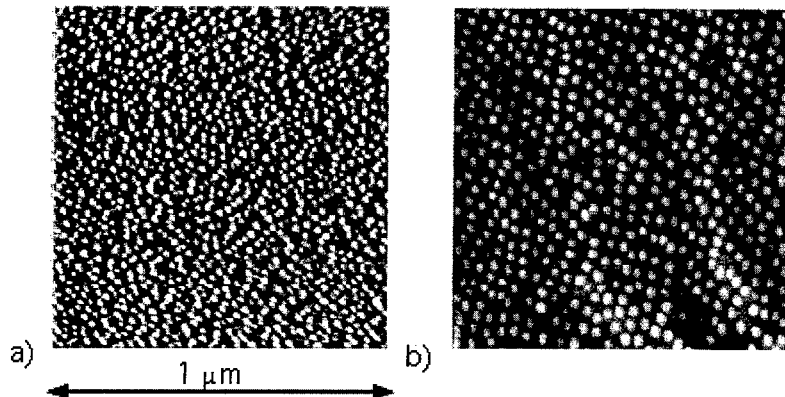


Fig.1. Visual comparison of the surface morphology of one (left) and twenty (right) layered samples of InAs self-assembled coherently strained islands on GaAs. Length scale applies to both plots.

single layer of coherently strained InAs islands on GaAs, while figure 1(b) shows the surface morphology of a sample containing twenty stacked layers of InAs islands, with all layers but the top covered with 5 nm of GaAs. As one can see from the direct visual comparison of the two images the island density in the top layer of the 20-layered sample is less than that of the single layer of islands and because of conservation results in an increase of the island dimensions in the top layer, since the InAs monolayer coverage remains unchanged. As well, spatial island distribution appears to be more uniform in the 20-layered sample with some evidence of island chain formation along the (100) directions. Therefore, besides the vertical alignment of these layered islands, some kind of lateral island ordering occurs.

While it can be seen from the surface images that some island self-organization is occurring, quantitative characterization of this process is important. In this connection, various image processing techniques become helpful. Figure 2 (a, b) shows 2-dimensional Fourier transforms of the AFM scans of the samples with one and twenty layers of InAs islands respectively. Here, the difference between the two samples is much more pronounced. The spectrum of the single-layered sample image is round in shape and does not have any particular features connected with directionality or with particular spatial frequencies. On the other hand, the Fourier spectrum of the AFM scan of the 20-layered sample surface contains rather strong low-frequency components originating from the increased long range (several hundred nanometers) surface roughness accumulated with InAs layer stacking. As well it exhibits four clear peaks in the (100) directions corresponding to the spatial frequency of about 40 nm. These peaks indicate the formation of a partially ordered 2-dimensional lattice of InAs islands in the top layer of the 20-layered structure.

In order to clarify the nature of these peaks, we have performed an inverse Fourier transformation of the spectrum on figure 2(b), with low and high frequencies cut off. This results in the image presented in figure 2(c). One can see a distorted but recognizable square lattice oriented along the (100) crystallographic directions, with a period of approximately 40 nm.

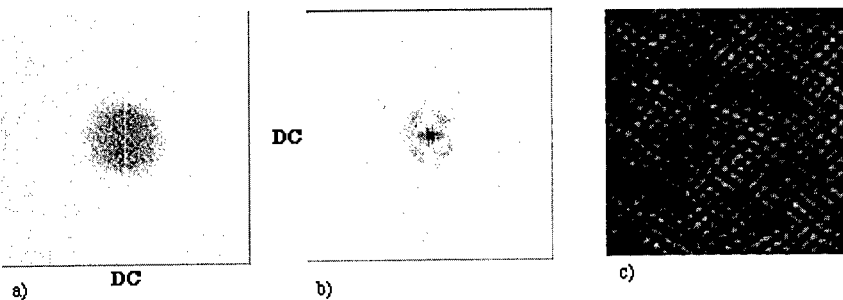


Fig.2 Fourier spectra of the AFM images for one (a) and twenty (b) layers of InAs islands and inverse Fourier transform of the “features of interest” in the 20-layered sample’s spectrum (c).

To further elaborate on the question of the evolution of the InAs island ordering occurring with layer stacking we have studied autocovariance of the AFM images, samples consisting of one, five, ten, and twenty layers of islands. The autocovariance of the function f of two variables is calculated according to the formula:

$$R_{ff}(\mu, v) = \lim_{T \rightarrow \infty} \frac{1}{2T} \int_{-T}^T \int_{-T}^T f(x, y)f(x + \mu, y + v) dx dy.$$

Figure 3 shows section of the autocovariance in the (100) direction for samples with one (a), five (b), ten (c), and twenty (d) layers of InAs islands. The choice of the (100) direction is stipulated by the previous observations of Fourier spectra with peaks along the (100) directions, as well as by the fact that autocovariance functions of the AFM scans from 10 and 20-layered samples have distinct peaks in these directions. Our interpretation of the autocovariance is that the ratio of the amplitude of the second peak in autocovariance function to the amplitude of the central peak is an appropriate parameter for characterization of short range ordering, while the peaks further from the central correspond to the long range order. This was verified by one-dimensional simulations performed using Gaussian-shaped islands with randomized positions. As one can see from figure 3, the island distribution is rather random for a single layer, where the second-to-central-peak-ratio $r = 0.023$. For the sample with five layers wing peaks start to appear in the autocovariance section with $r = 0.140$, indicating the onset of the short range order. For the 10-layered sample wing peaks in autocovariance section are quite pronounced ($r = 0.282$) and weak higher order peaks appear. Finally, for the sample with twenty layers of InAs islands short range order is further increased ($r = 0.366$), and the onset of the longer range ordering is apparent. The distance between the central and the wing peaks in the autocovariance sections on is about 40 nm, and is constant for all four samples. These facts can be interpreted as evidence of the lattice formation with a period of about 40 nm that does not depend on the number of layers stacked.

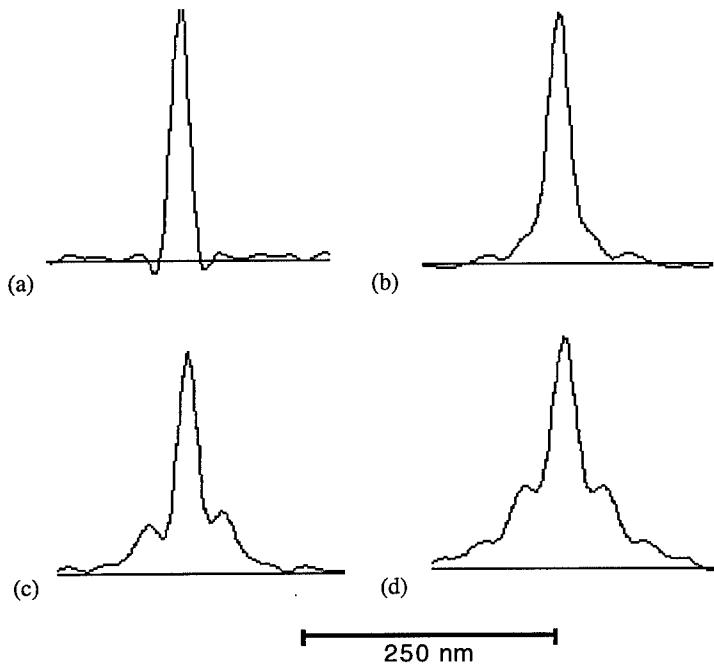


Fig. 3 AFM image autocovariance (100) sections for one (a), five (b), ten (c) and twenty (d) stacked layers of InAs self-assembled islands. Length scale applies to all plots

4. Conclusions

We observed an increased ordering of InAs coherently strained self-assembled islands in GaAs matrix induced by the multi-dot column subsurface structure. Fourier transform and autocovariance function were used as instruments for characterization of the island array ordering.

Although island layer stacking improves island array self-organization, perfect uniformity of the island distribution is most probably unreachable using this technique, because of the overall surface roughening accompanying this process.

5. References

- [1] T. T. Ngo ,P. M. Petroff, H. Sakaki, J. L. Merz, Phys. Rev. (B) 53 (1996) 9618
- [2] J. Tersoff, C. Teichert and M. G. Lagally. Phys. Rev. Lett. 76 (1996) 1675
- [3] G. S. Solomon, S. Komarov, J. S. Harris, Jr., Y. Yamamoto, J. Cryst. Growth (1997) 175/176 707
- [4] S. Ruvimov, Z. Liliental-Weber, N. N. Ledentsov, M. Grundmann, D. Bimberg, V. M Ustinov, A. Yu. Egorov, P. S. Kop'ev, Zh. I. Alferov, K. Scheerschmidt, U. Gosele, Compound Semiconductor Electronics and Photonics. Symposium Proc., (1996) 383
- [5] G.S. Solomon, J. A. Trezza, A. F. Marshall, J. S. Harris , Jr., Phys. Rev. Lett. 76 (1996) 952

Electron Transport Through Tetrahedral-Shaped Recess (TSR) Stacked Double Quantum Dot Structures

M. Shima, Y. Sakuma, C. Wirner**, T. Strutz**, E. Taguchi*, T. Futatsugi, Y. Awano, and N. Yokoyama

*Fujitsu Limited, *Fujitsu Laboratories Ltd. **NEDO (Industrial technology researcher)
10-1 Morinosato-Wakamiya, Atsugi, Kanagawa 243-01, Japan*

Abstract. We formed a stacked double TSR quantum dot structure and measured its I-V characteristics. The fine structure related to TSR quantum dots was observed in the low bias region, while negative differential resistances on the order of μA were observed in the higher bias region. The fine structure is well explained by the resonant tunneling through individual TSR quantum dot states.

1. Introduction

Quantum dot technology is one of the most advanced technologies to date for the fabrication of nanometer-sized semiconductors. However, there are problems related to controllability of size, position, and reproducibility of quantum dots for device applications. Recently, some groups have reported on electron transport through a single self-organized InAs quantum dot that are based on the S-K mode material growth method [1, 2]. The positioning of InAs quantum dots has also been studied by several groups, but none have yet succeeded in obtaining precise control. Some other groups have formed quantum dots by mesa-etching and depleting from the surface and succeeded in measuring electron transport through quantum dots[3, 4, 5, 6]. It is, however, considered to be difficult to achieve high reproducibility by this method because of the complexity of the fabrication process.

We previously proposed a new technology [7] that produced quantum dots grown in tetrahedral-shaped recesses (TSRs) with better control in positioning, sizing, and reproducibility using a self-organized formation mechanism. Especially, we can stack quantum dots easily using our technology. In this paper, we report on the formation of a stacked double TSR quantum dot structure and the electron transport through it.

2. Fabrication of TSR quantum dots

TSR is an inverted, tetrahedral-shaped recess, which consists of three equivalent $\{111\}\text{A}$ side faces, formed by the selective chemical etching of a $(111)\text{B}$ -oriented GaAs substrate with a SiO_2 mask. After etching, a GaAs/InGaAs/GaAs heterostructure is grown in the TSRs by LP-MOVPE. Indium-rich regions are formed spontaneously at the

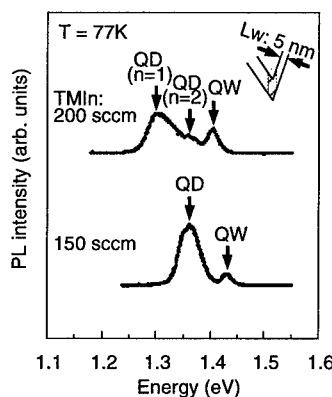


Fig 1. TMIn flow rate dependence of PL spectra

bottom of the TSRs. In other words, quantum dots are formed by self-organized growth. They confine electrons vertically by the InGaAs/GaAs heterostructure and laterally by the modulation of the indium composition. Figure 1 shows the 77K PL spectra measured for different flow rate of TMIn being used as an indium source. A peak due to quantum dot states is observed at a lower energy than that due to quantum well states in the spectrum for TMIn flow rate of 150 sccm. These peaks shift to a lower energy and a new peak due to excited quantum dot states is observed by increasing TMIn flow rates. These results show that both the lateral and vertical potential profiles of the quantum dots could be controlled by changing indium content.

3. Stacking of TSR quantum dots

Stacked quantum dot structures are very attractive from the device application point of view. TSR technology allow us to fabricate such kind of structures easily. Figure 2 shows a TEM image of a cross-sectional view of stacked double TSR quantum dots. We grew 20 nm-thick double InGaAs layers on both sides of a 30 nm thick GaAs intermediate layer. Dark regions at the bottom of a TSR in Figure 2 clearly show the formation of stacked double quantum dot structure. The upper TSR quantum dot is precisely stacked over the lower one of the same size, indicating that TSR technology is suitable for the formation of stacked structures.

4. I-V characteristics of stacked double TSR quantum dots

The stacked double TSR quantum dot structure for the I-V measurement is shown in Figure 3. We formed TSRs in an i-GaAs layer grown on n-GaAs substrates. After that, we grew n-GaAs/InGaAs buffer layers, an i-AlGaAs/InGaAs triple barrier resonant tunneling structure, and n-GaAs/InGaAs ohmic contact layers. Ohmic contacts were formed by evaporating AuGe/Au on the ohmic contact layer and on the backside of the n-GaAs substrates. The structure have two remarkable features. One is that the bottom of the TSR is close to the interface of i-GaAs and n-GaAs substrate. We can measure the transport properties through the quantum dots with suppressing the current through the TSR side faces. The other is that AlGaAs barriers are used instead of GaAs to increase the

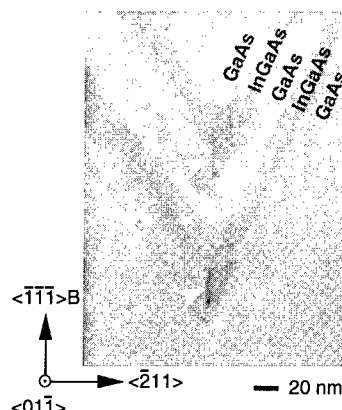


Fig 2. TEM Image of Stacked Double TSR

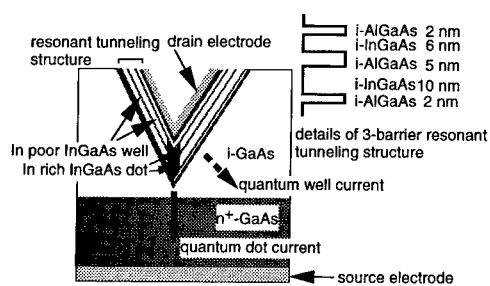


Fig 3. Stacked double TSR quantum dot structure

vertical confinement and thus increase the energy separation between quantum levels.

Figure 4 shows I-V characteristics of a single TSR structure having stacked double quantum dots measured at 500mK. Negative differential resistances (NDRs) on the order of μA were observed on both positive and negative biases. Fine structure on the order of nA was also observed at the lower bias as shown in the magnified inset figure. The NDRs at the higher bias and the fine structure in the low bias region are considered due to resonant tunneling through quantum well levels and quantum dot levels, respectively. It is because TSR quantum dot levels are formed at lower energy than TSR quantum well levels as described in PL measurements. Figure 5 shows details of the structure on the order of nA on positive bias. Characteristic features of the current turning on at some bias and decreasing gradually were observed. Bryant calculated resonant tunneling through coupled, double-quantum-dot nanostructures[8]. As his calculated result for strongly coupled double quantum dots agrees qualitatively with our observed fine structures, we attribute the fine structure to resonant tunneling through individual quantum dot states.

We estimated the energy levels of individual quantum dot states from the turn-on voltages in the I-V characteristics on positive bias. We assumed that gradually decreasing NDRs (b, e in Figure 5) are attributed to the states in the bottom-side quantum dot and the other sharp NDRs (a, c, d in Figure 5) to the top-side quantum dot, because the energy level shift in the top-side quantum dot is larger than that in the bottom-side quantum dot for electrons injected from the emitter when a positive bias is applied to the top contact. The estimated energy levels from the emitter Fermi level is shown in Figure 6. The energy level separations of the bottom-side and top-side quantum dots are 40 meV and 48 meV, respectively. Figure 7 shows the details of the I-V characteristics on negative bias. No NDRs but turn-on characteristics were observed. These turn-on biases are explained well by the resonant tunneling through the individual quantum dot states, using the estimated energy levels as shown in Figure 6. Therefore we conclude that the resonant tunneling through individual quantum dot states of a TSR stacked double quantum dot structure produces the fine structure in I-V characteristics.

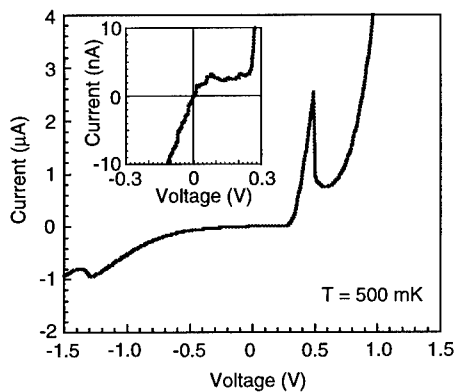


Fig 4. Overall I-V characteristics

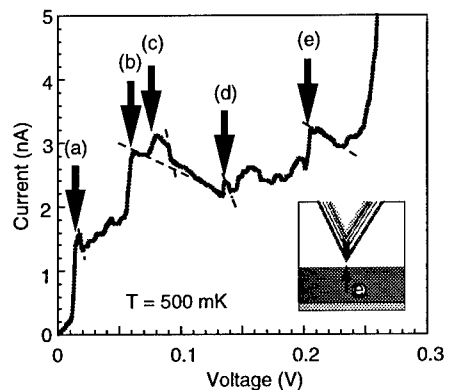


Fig 5. I-V characteristics on positive bias

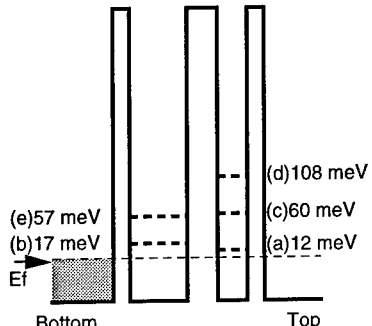


Fig. 6. Estimated energy levels

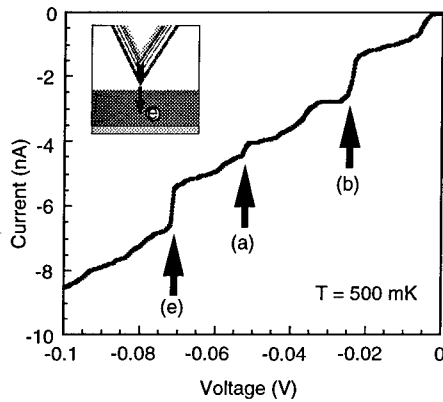


Fig. 7. I-V characteristics on negative bias

5. Conclusion

We formed a stacked double TSR quantum dot resonant tunneling structure, and succeeded in observing the electron transport through it for the first time. The fine structure related to TSR quantum dots was observed in the low bias region, while the NDRs on the order of μA were observed in the higher bias region. The fine structure is well explained by the resonant tunneling through individual TSR quantum dot states. The energy level separations of the TSR quantum dots are 40–50 meV.

Acknowledgements

This work was performed under the management of FED as a part of the MITI R&D program (Quantum Functional Devices project) supported by NEDO. The authors would like to thank Dr. Takatsu from Fujitsu Laboratories Ltd. for his discussions.

References

- [1] Narihiro M et al., 1997 *Appl. Phys. Lett.* **70**, 105.
- [2] Iskevich E I et al., 1996 *Phys. Rev. B* **54**, 16401.
- [3] Tewordt M et al., 1994 *Solid State Electron.* **37**, 793.
- [4] Austing G D et al., 1996 *Semicond. Sci. Technol.* **11**, 388.
- [5] Nomoto K et al., 1997 *Phys. Rev. B* **55**, 2523.
- [6] Schmidt T et al., 1997 *Phys. Rev. Lett.* **78**, 1544.
- [7] Sugiyama Y et al., 1995 *Jpn. J. Appl. Phys.* **34**, 4384.
- [8] Bryant W G, 1991 *Phys. Rev. B* **44**, 3064.

Electronic states in quantum dots: Effects of symmetry of the confining potential

T. Ezaki, Y. Sugimoto, N. Mori, and C. Hamaguchi

*Department of Electronic Engineering, Osaka University Japan
2-1 Yamada-oka, Suita, Osaka 565, Japan*

N -electron eigen states in circular, elliptic, and triangular shaped quantum dots (QDs) are calculated by numerically diagonalizing the N -particle Hamiltonian. In a circular QD, addition energy exhibits large values for $N = 2$ and 6 due to the complete shell filling, and shows slightly large values for $N = 4$ and 9 which corresponds to a spin-polarized half filling shell structure with the total spin of $S = \hbar$ (spin-triplet state) and $S = 3\hbar/2$ (spin-quadruplet state), respectively. In elliptic QDs, the degeneracy of the single-particle states is removed, resulting in transition of the ground state from the spin-polarized half filling configuration to the spin singlet state for a QD containing four electrons. The states with 3, 6, and 9 electrons in a triangular QD are found to be slightly more stable compared to a circular QD, which is interpreted in terms of a geometrical effect.

1 Introduction

In quantum dots (QDs) containing a few electrons, the Coulomb interaction plays an important role in determining the energy states, and thus many particle energy levels depend strongly on the number of electrons in the QDs [1]. Numerical calculations, therefore, require more sophisticated treatments such as an exact diagonalization method to obtain the electronic states in QDs. In this paper we calculate eigen states in QDs by numerically diagonalizing the N -particle Hamiltonian. We especially focus on the effects of the symmetry of confining potential on the electronic states.

2 Model and method

We consider a vertical QD formed in an $\text{In}_{0.05}\text{Ga}_{0.95}\text{As}/\text{AlGaAs}$ double-barrier heterostructure [2, 3] as shown in the inset in Fig 1, where the x - y plane and the z direction are taken to be parallel and perpendicular to the heterointerfaces, respectively. In our model, electrons are assumed to be confined by the infinite square potential well, $H(z)$, of width W along the z direction, for simplicity. We model the lateral confining potential $V(x, y)$ by the following equation

$$V(x, y) = \frac{1}{2}m^*(\omega_x^2x^2 + \omega_y^2y^2) \left\{ 1 + \alpha \frac{2}{7} \cos 3\phi \right\}, \quad (1)$$

where ω_ν is the confining frequencies along the ν direction ($\nu = x$ or y), α ($= 0$ or 1) is a parameter to specify the shape of the lateral confining potential, and ϕ is the angle with respect to the specific axis in the x - y plane. When $\alpha = 0$, the contour line of $V(x, y)$ becomes an ellipse (for $\omega_x \neq \omega_y$) or a circle (for $\omega_x = \omega_y$). A triangular shaped confining potential can be obtained by setting 1 for the parameter α and putting $\omega_x = \omega_y$.

For the QD modeled above, the N -electron Hamiltonian can be written as follows

$$\mathcal{H} = \sum_{i=1}^N \mathcal{H}_0(\mathbf{r}_i) + \sum_{i < j} \frac{e^2}{4\pi\epsilon|\mathbf{r}_i - \mathbf{r}_j|}, \quad (2)$$

where $\mathcal{H}_0(\mathbf{r}_i) = (\mathbf{p}_i + e\mathbf{A}_i)^2/2m^* + V(x_i, y_i) + H(z_i)$ is the single-electron Hamiltonian with \mathbf{A} being the vector potential. The material parameters for $\text{In}_{0.05}\text{Ga}_{0.95}\text{As}$ are computed by the linear interpolation of the parameters between bulk InAs and bulk GaAs, and we obtain the effective mass of an electron of $m^* = 0.065m_0$ and the static dielectric constant of $\epsilon = 12.9\epsilon_0$. In the

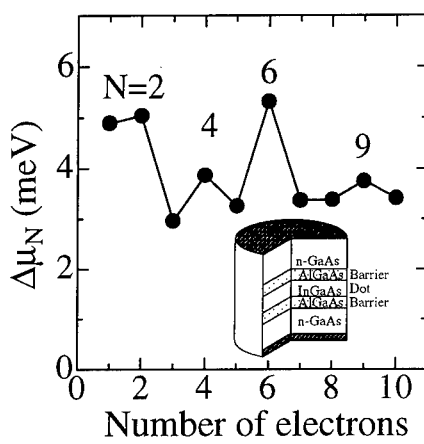


Figure 1: Chemical potential differences in circular quantum dots with confining energy of 3.0meV as a function of number of electrons. Schematic illustration of a vertical quantum dot formed in a double barrier heterostructure is shown in the inset.

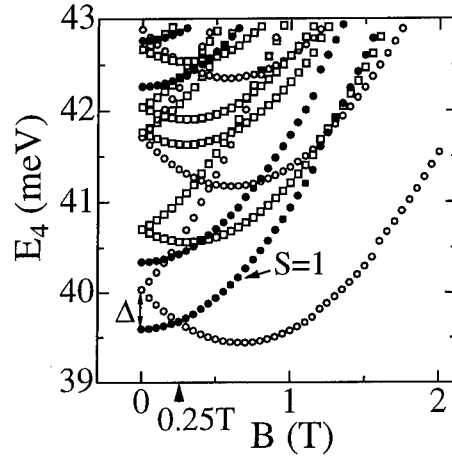


Figure 2: The ground state energy in a circular quantum dot containing four electrons as a function of the magnetic field. Solid circles, open squares and open circles are the eigen states with total angular momentum of 0 , $\pm\hbar$ and $\pm 2\hbar$, respectively. The transition of the ground state from spin-triplet to spin-singlet takes place at $B \approx 0.25$ T.

present study, N -particle Slater determinants composed from the single-particle eigen functions of the two dimensional isotropic and harmonic oscillator are taken as a basis set to diagonalize the total Hamiltonian of Eq. (2). Because the confinement along the z direction is strong in real QDs [2, 3] compared to the confinement in the x - y plane, many eigen-states fall in the lowest subband formed by the confining potential along the z direction, and the single-particle excited states along the z direction is ignored in the following. The QD is, therefore, regarded as a disc-like QD.

3 Results and discussion

Figure 1 shows the chemical potential difference, or addition energy, $\Delta\mu_N \equiv \mu_{N+1} - \mu_N$ for the circular QD with $\hbar\omega_x = \hbar\omega_y = 3$ meV as a function of N . The chemical potential, μ_N , is defined by $\mu_N \equiv E_N - E_{N-1}$ with E_N being the ground state energy for the QD with N electrons. $\Delta\mu_N$ has peaks at $N = 2$ and 6 because of the complete shell filling. In addition, a weak structure can be seen at $N = 4$ and 9 with the total spin of $S = \hbar$ (spin-triplet state) and $S = 3\hbar/2$ (spin-quadruplet state), respectively, which corresponds to the spin-polarized half filling shell structure [2, 4]. Figure 2 shows the ground state energy in a circular quantum dot containing four electrons as a function of the magnetic field applied along the z direction. Solid circles, open squares and open circles are the eigen states with total angular momentum of $M = 0$, $\pm\hbar$ and $\pm 2\hbar$, respectively. The energy shift Δ due to the exchange interaction is found to be 0.44meV. The transition of the ground state from the spin-triplet ($M = 0$) to the spin-singlet ($M = -2\hbar$) takes place at $B \approx 0.25$ T.

In Fig. 3, we plot $\Delta\mu_N$ for two different elliptic QDs with the same average confining energy of $(\hbar\omega_x + \hbar\omega_y)/2 = 3$ meV. Open squares and open triangles indicate $\Delta\mu_N$ for the QD with

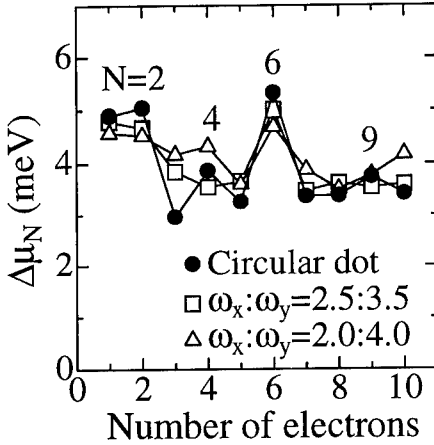


Figure 3: Addition energies in circular and elliptic quantum dots as a function of number of electrons. Solid circles are the addition energies for the circular quantum dot with confining energy of 3 meV. Open squares and triangles show the addition energies for elliptic quantum dots with $(\hbar\omega_x, \hbar\omega_y) = (2.5 \text{ meV}, 3.5 \text{ meV})$ and $(2 \text{ meV}, 4 \text{ meV})$, respectively.

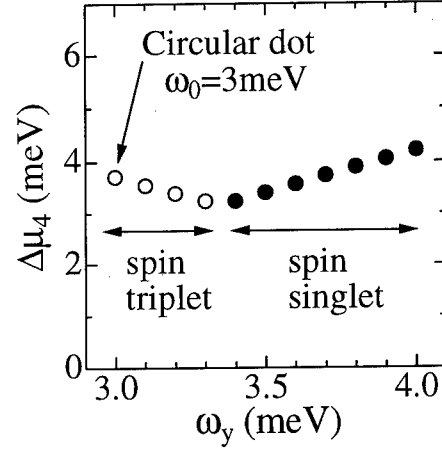


Figure 4: Addition energies for QDs with four electrons as a function of the confining energy $\hbar\omega_y$ keeping the average confining energy a constant value of 3 meV. Open and solid circles correspond to the spin triplet and spin singlet ground state, respectively.

$(\hbar\omega_x, \hbar\omega_y) = (2.5 \text{ meV}, 3.5 \text{ meV})$ and $(2 \text{ meV}, 4 \text{ meV})$, respectively. Solid circles show the addition energies for the circular QD. For the elliptic QDs, the addition energy has no large peaks except for the peak at $N = 6$. This may be interpreted in terms that the asymmetry of the confining potential results in removal of the degeneracy of the single-particle states and mixing of many eigen states with various angular momenta. Figure 4 shows the addition energy for the elliptic QDs with $N = 4$ as a function of the confining potential $\hbar\omega_y$ keeping the average confining energy a constant value of 3 meV. Open and solid circles correspond to the spin triplet and the spin singlet ground state for the QD containing four electrons, respectively. For elliptic QDs with weak asymmetry ($3 \text{ meV} < \hbar\omega_y \lesssim 3.3 \text{ meV}$), the spin triplet states remain the lowest eigen state, and the addition energy decreases with increasing the asymmetry due to the removal of the degeneracy of the single-particle states as mentioned above. For QDs with $\hbar\omega_y > 3.3 \text{ meV}$, the spin singlet state becomes the ground state, and the addition energy increases with increasing ω_y . This may be explained by considering the following fact. With increasing the asymmetry of the confining potential in the x - y plane, a disc-like QD approaches to a needle-like QD, and the complete shell filling may take place in a needle-like QD containing four electrons.

Figure 5 shows $\Delta\mu_N$ for the triangular QD of $\hbar\omega_x = \hbar\omega_y = 3 \text{ meV}$ in which $\Delta\mu_N$ for the circular QD are again plotted by solid circles for comparison. The addition energies for the circular and the triangular QDs are found to exhibit almost the same characteristics. The addition energy for the triangular QD with $N = 3, 6$, and 9 , however, is found to be slightly larger than that of the circular QD. This feature may be explained as follows. The density distribution of electrons in

QDs containing three electrons is plotted in Fig. 6(a) for the circular QD and Fig. 6(b) for the triangular QD. As seen in the figure, electrons in the circular QD form a rotationally symmetric distribution, and the electron density becomes small in the center of the QD due to the electron-electron repulsion. On the other hand, in the triangular QD, each electron moves toward each corner of the triangle and forms more stable state, giving rise to a slightly larger addition energy. For the same reason, electronic states for $N = 6$ and 9 in the triangular QD become slightly more stable compared to the case in the circular QD.

4 Conclusion

We calculated N -electron eigen states in QDs with vertical confinement of square quantum well and with lateral confinement of circular, elliptic and triangular shaped potentials. The eigen states are obtained by diagonalizing N -particle Hamiltonian utilizing the Slater determinants composed from the single particle eigen states for the isotropic and harmonic system. Due to the rotational symmetry in a circular QD, electrons form the complete shell filling structures for $N = 2$ and 6, and the spin polarized half filling structures for $N = 4$ and 9. In elliptic QDs, the addition energy exhibits no longer clear structure in the plot of addition energy *vs.* number of electrons N , except for $N = 6$, which is explained in terms of the asymmetry of these systems. In a triangular QD, slightly stable states due to the localization of the electrons at the corners are expected for $N = 3, 6$, and 9.

- [1] Ashoori R C *et al.* 1993 *Phys. Rev. Lett.* 71 613-16
- [2] Tarucha S *et al.* 1996 *Phys. Rev. Lett.* 77 3613-16
- [3] Austing D G, Honda T and Tarucha S 1996 *Semcond. Sci. Technol.* 11 388-91
- [4] Tanaka Y and Akera H 1997 *J. Phys. Soc. Jpn.* 66 15-8

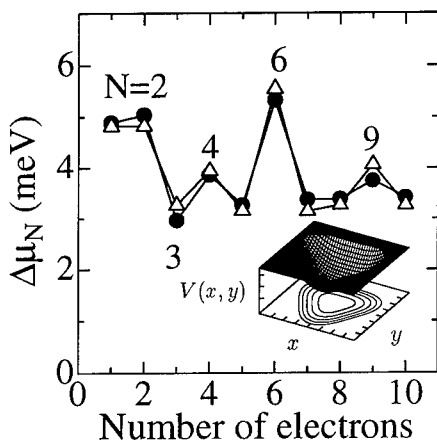


Figure 5: Chemical potential differences in a circular quantum dot (solid circles) and a triangular quantum dot (open triangles) as a function of number of electrons. $\hbar\omega_x = \hbar\omega_y = 3$ meV. Three dimensional view and contour lines of the triangular confining potential are plotted in the inset.

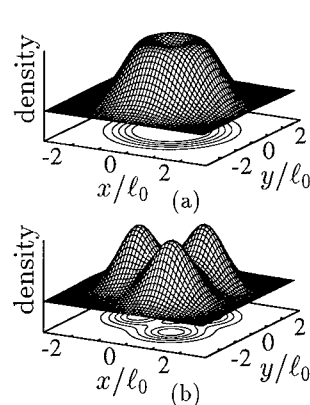


Figure 6: Density distribution of electrons in the quantum dots containing three electrons with a circular (a) and a triangular (b) shaped confining potential in the plane parallel to the heterointerface. ℓ_0 is 20 nm.

Fabry-Perot and Vertical Cavity Surface Emitting InAs Quantum Dot Lasers

D. Bimberg, N.N. Ledentsov, M. Grundmann, F. Heinrichsdorff

Institut für Festkörperphysik, Technische Universität Berlin, 10623 Berlin, Germany

V.M. Ustinov, P.S. Kop'ev and Zh.I. Alferov

A.F. Ioffe Physical Technical Institute, 194021, St. Petersburg, Russia

J.A. Lott

Air Force Institute of Technology, DECE 2950, Wright-Patterson AFB, Ohio USA 45433

Abstract

Quantum dot (QD) edge emitting and vertical cavity lasers are realized using a self-organized growth approach. Threshold current densities at room temperature (RT) of about 60 A/cm^2 for edge emitting and 170 A/cm^2 for vertical cavity lasers are measured. High internal (>96%) and differential (70%) efficiencies are obtained for InGaAs-AlGaAs lasers based on vertically coupled QDs and RT 1 W continuous wave operation is demonstrated. QD lasers exhibit much larger gain, differential gain and smaller linewidth enhancement factor as compared to conventional quantum well devices.

1. Introduction

Significant improvements in characteristics of injection lasers are achieved for QDs as gain medium [1]. Such structures provide an ultimate limit of size quantization in solids and an extremely large change of electronic properties as compared to quantum wells and wires is observed. δ -function like density of states and strong confinement of electron and hole wavefunctions in a QD result in reduction of threshold current density, improved temperature stability of threshold current, ultrahigh material and differential gain of QD lasers [2]. On the other hand, until recently, there was a lack of fruitful ideas to fabricate QDs which can be used for realistic devices and are compatible to modern device technology.

2. Growth

A layer of a material having a lattice constant different from that of the substrate, after some critical thickness is deposited, can spontaneously transform to an array of *three-dimensional* islands [3]. More recently it was shown, that there can exist a range of deposition parameters, where the islands are small ($\sim 10 \text{ nm}$), have a similar size and shape [4, 5] and form dense arrays. Due to the *strain-induced renormalization* of the surface energy of the facets, an array of *equisized and equishaped* 3D islands can represent a *stable state* of the system [6]. This is directly confirmed for the most extensively studied MBE growth in the InAs-GaAs material system by the reversibility of the islanding - surface planarization process. The reversible transition occurs when the surface stoichiometry is changed from As-rich (islanding) to In-rich (planarization), and vice versa [7]. High arsenic pressure results in reduction of the characteristic QD size and in formation of high concentrations of dislocated InAs clusters. Thus, a stable array of 3D InAs islands on GaAs (100) substrate exists only in some part of the "arsenic overpressure - substrate temperature" phase diagram as is demonstrated also for MOCVD growth [7]. When the surface density of the QDs is high, interaction of the islands via the substrate makes also their *lateral ordering* favorable [6]. If strained InAs islands are covered with a thin GaAs layer, the islands in the second sheet are formed over the dots in the first sheet, resulting in a *three-dimensional ordered array* of QDs either isolated [3, 9] or strongly *vertically-coupled* [3, 7, 10, 11]. The size and the shape of InAs islands can be changed by changing the deposition mode. Bright luminescence

(300 K) from InGaAlAs QDs in (Al,Ga)As matrices can be tuned in the range 0.7 - 1.36 μm . Modification of the QD PL energy is also possible via *post-growth annealing* [12].

2. Electronic spectrum

Experimentally observed energy levels for electrons and holes agree with theoretical calculations based on QD geometry derived by HRTEM images. A remarkable property of a QD is a narrow (FWHM<0.1 meV) *atomic-like luminescence line* [13, 14] which does not show broadening with temperature [14] and directly manifests formation of electronic QD.

The transparency condition in a QD is realized when it captures one exciton. Then, the probabilities to emit or to absorb light are equal since the ground state can be populated by two electrons and two holes [15]. This assumption is valid if the separation between exciton and biexciton recombination energy is smaller than the inhomogeneous broadening, otherwise after the exciton is created, the biexciton absorption line can be significantly shifted towards lower photon energies, and the absorption and gain spectra of a QD filled with one exciton become separated in energy. Thus, in this model finite gain appears also for *single* excitons. Increase in the excitation density results in saturation of QD excitonic gain followed by its decrease, due to the larger fraction of QDs filled with biexcitons. As Oppositely, biexciton absorption first increases and then drops to zero and converts to gain, when most of the QDs become populated with two electron-hole pairs. Charged excitons and biexcitons provide finite gain since the ground state absorption is no longer possible. If there is no transport between QDs (particularly at low temperatures) the population of QDs with electrons, holes and excitons is defined by the capture and recombination probabilities and is not a function of temperature [15]. The gain-current relation depends on the capture mechanism [15] whether electrons and holes are captured correlated or uncorrelated. We note that the recombination current is *not* simply given by the product of electron and hole density [16]. At high temperatures, thermal evaporation of carriers from dots may result in the predominant population of deeper QDs. Gain behavior is different in these cases: the gain maximum keeps its maximum energy with excitation density in the first case while it shifts to higher photon energies in the second [15].

4. Capture and Relaxation of Carriers in a Quantum Dot

Carrier capture efficiency is very high in properly designed structures with high concentration of QDs [17]. No degradation in PL efficiency at low temperatures and only moderate decrease at RT were found in deep etched mesa structures fabricated from samples with QDs when the mesa size was varied between 1 and 0.2 μm . As opposite, no luminescence at RT can be recorded from deep mesas of similar size fabricated from quantum well samples. The nonequilibrium carrier capture time to QD was estimated in [17] to be below 1 ps.

Carrier relaxation to the InAs-GaAsQD *ground state* was found to be about 40 ps for excitation in the GaAs matrix and 25-40 ps for direct excitation in the QD excited state. In the latter case the lifetime of the exciton in the QD excited state and the population time of the QD ground state coincide [18]. Lower values are measured when the energy separation between the QD ground and excited state fits to integer number of InAs LO phonons. These results are in agreement with the PLE data, also showing enhanced relaxation in this case [5, 19]. The measured values agree favorably with the ground state population time in high quality QWs which are about 100 ps [20], while they are much longer than the higher subband depopulation time (~1 ps) in the QW case making QDs potentially important for application in IR lasers based on electron interlevel transitions.

5. Realization of Quantum Dot Lasers

InGaAs-GaAs QD lasers operating under photopumped excitation both at low and at room temperature have been fabricated already in 1993 [21]. The first report on injection lasing already revealed most important fingerprints and problems of QD lasers [22]. At low observation temperatures very high characteristic temperatures (>400 K) are observed. At high temperatures, however, evaporation of excitons from dots results in a decrease of QD gain for the same drive current, and in order to keep lasing conditions fulfilled (gain equals total losses) one needs to increase the current. Electroluminescence from QDs in edge geometry is significantly depolarized [7] due to hole quantization in all three dimensions, as opposite to QW structures, where heavy hole emission is completely TE polarized. Lasing resonant to the ground state (GS) of QDs and low threshold current densities (J_{th}) have been demonstrated in this range as well. At higher temperatures, evaporation of carriers from InGaAs QDs into a GaAs matrix resulted in a decrease in the QD gain, increase in J_{th} , and at 300 K, the lasing energy comes closer to the wetting layer energy [23]. To overcome this problem vertically electronically coupled QDs have

been applied reducing the J_{th} both at low and at high temperatures down to 90 A/cm^2 (300K, $N=10$) resulting in GS QD lasing up to room temperature (RT). Using MOCVD ground state lasing for a single QD layer at RT was obtained for GaInP barriers [8] (see Fig. 1).

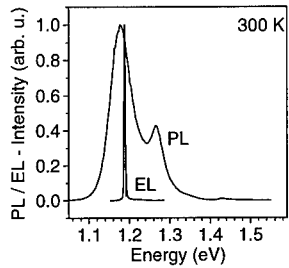


Figure 1. Photo- and electroluminescence of single-sheet InAs/InGaAs/GaAs QD laser with InGaP cladding layer showing near-to-groundstate emission. $j_{th}=110 \text{ A/cm}^2$ at 300 K.

Ultrahigh material gain [24] and suppression of gain saturation in coupled QDs [25] have been demonstrated. Further improvements were obtained by putting coupled QDs in an AlGaAs matrix, providing better localization of carriers in QDs. J_{th} was further reduced down to 60 A/cm^2 [9, 18] and a RT CW lasing with 1W has been realized for a structure with 10 stacks of InGaAs-AlGaAs QDs [26] (see Fig. 2). High internal ($>96\%$) and differential (70%) efficiencies at 300 K are also obtained for InGaAs-AlGaAs lasers based on vertically coupled QDs [27]. High quantum efficiency is realized also in [28].

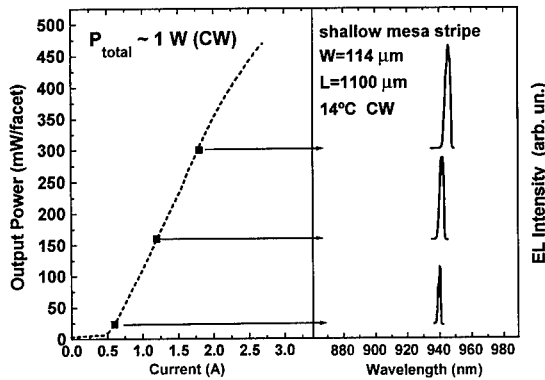


Figure 2: Room temperature output power versus current for ten stacks of InGaAs quantum dots in an AlGaAs matrix (left). Electroluminescence spectra at various output powers (right).

6. Basic Advantages of Quantum Dot Lasers

6.1 Edge-emitting lasers

Low transparency currents and complete temperature insensitivity of the laser parameters to temperature for appropriate QD and barrier parameters provide basic advantages of QD lasers. For the currently achieved 10% QD size dispersion, the

theoretical threshold current density equals to only 10 A/cm^2 [15,29] and much lower values might be obtained in structures with improved QD homogeneity. J_{th} values of $12\text{-}16 \text{ A/cm}^2$ are measured for QD lasers in the temperature range up to 180 K [8].

Saturation material gain as high as $150\,000 \text{ cm}^{-1}$ is reported in [24] as compared to QW values of about 3000 cm^{-1} . This observation agrees fairly well with calculated values [15,30].

Maximum differential gain reported for QD lasers approaches 10^{12} cm^2 and exceeds the QW laser values by about three orders of magnitude [24].

Chirp. Any absorption or gain peak causes modulation of the refractive index near the resonance energy in agreement with Kramers-Kronig transformation. The refractive index increases on the low energy side and decreases on the high energy side of the the absorption maximum. A gain peak results in the opposite behavior. Thus, the photon wavelength in the crystal can change during the excitation pulse, causing lasing intensity jumps between Fabry-Perot modes, described by the linewidth enhancement factor (α). Highly asymmetric absorption and gain profiles in QWs, which also change their shape with excitation density, cause the α factor to be about two. For sysmmetric QD gain (or absorption spectrum), the change in the refractive index near the gain maximum is zero and α is zero. In real QDs, due to the finite contribution of the QD excited states to the total gain α is less or about 0.5 [2].

Dynamics. From direct observations of relaxation oscillations cut-off frequencies close to 10 GHz have been determined [2,31, 32]

Exciton waveguiding. The QD exciton absorption peak can be used intentionally to induce resonant refractive index enhancement on the low energy side of the absorption peak and can lead to entirely exciton-induced waveguiding and lasing [33]. This approach is particularly attractive in materials, where no suitable lattice-matched heterocouple with significantly lower refractive index exists, such as diamond, silicon, etc.

6.2 Surface-emitting lasers

The first surface-emitting laser (VCSEL) operating via the QD GS has been reported for photopumped excitation at low temperatures [34]. Injection VCSELs based on stacked InGaAs-AlGaAs QDs were realized later [35]. The lasing at 300K occurred via excited states and J_{th} was about $\sim 5000 \text{ A/cm}^2$. Using oxide defined $7 \mu\text{m}$ mesa and a single sheet InGaAlAs-GaAs QD structure, injection lasing via the QD GS at $\sim 1000 \text{ A/cm}^2$ (300K) has been realized with $\sim 0.5 \text{ mA}$ total threshold current [36]. Using the novel concept of electronically-coupled InGaAs-GaAs QDs and oxide-defined $10 \mu\text{m}$ mesas, QD GS CW lasing with a total current of $180 \mu\text{A}$ has been recently manifested (180 A/cm^2 , 300K) [37]. Maximum efficiencies amount to 16%. Total currents of $68 \mu\text{A}$ are measured for $1 \mu\text{m}$ apertures (see Fig. 3).

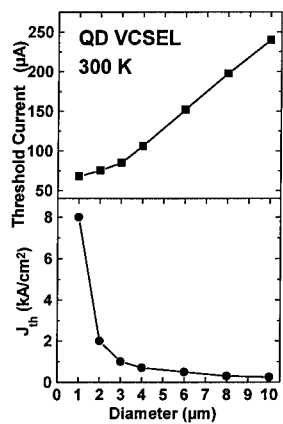


Figure 3: Threshold current (top) and threshold current density (bottom) versus diameter of an oxide aperture QD-VCSEL. The active layer consists of 3 vertically coupled QD planes.

7. Conclusion

It took about 7 years since the first realization of photopumped lasing in QWs until QW lasers with improved parameters with respect to double heterostructure lasers were created. The recent progress in the area of injection lasers based on self-organized QDs let us hope that QD lasers with dramatically improved properties as compared to recent QW lasers characteristics will be fabricated. To conclude we summarize basic characteristics of QD lasers in comparison with QW lasers. Further progress in the area of QD lasers is related to further optimization of the structure geometry and growth conditions.

Table 1: PHYSICAL ADVANTAGES OF QD LASERS

Laser Parameter	Quantum Well	Quantum Dot
Threshold current density J_{th}	40 A/cm ² (theoretical limit at RT)	~10 A/cm ² , 10% size dispersion, 150 K 60 A/cm ² , 300 K
Temperature stability (T_0) of J_{th}	285 K	infinity
Saturation Material Gain	~3000 cm ⁻¹	150 000 cm ⁻¹
Maximum Differential Gain	5×10^{-16} cm ²	$\sim 10^{-12}$ cm ²
Lasing Mechanism	e-h plasma or excitonic phonon-assisted (wide gap)	excitonic/biexcitonic (symmetric gain curve, low chirp, excitonic waveguide)
Ground state population time	20-100 ps	20-40 ps (single QD) <15 ps (coupled QDs)
Intersubband or interlevel relaxation time	1 ps	20-40 ps (single QD)

Table 2: TECHNOLOGICAL ADVANTAGES OF QD LASERS

Laser Parameter	Quantum Well	Quantum Dot
Nonequilibrium carrier spreading out of the stripe (or cavity) region	YES	NO
Facet overheating due to surface recombination	YES	NO
Nonradiative recombination enhanced dislocation growth (due to carrier diffusion to dislocations)	YES	SUPPRESSED
Free-standing microstripes or microcavities	NOT POSSIBLE	POSSIBLE
1.3 μm at RT on GaAs(100)	YES	POSSIBLE

References

- Y. Arakawa, H. Sakaki, *Appl. Phys. Lett.*, **40**, 939 (1982)
- D. Bimberg, N.N. Ledentsov, N.Kirstaedter, O. Schmidt, M. Grundmann, V.M. Ustinov, A.Yu. Egorov, A.E. Zhukov, M.V. Maximov, P.S. Kop'ev, Zh.I. Alferov, S.S. Ruvimov, U. Gösele, J. Heydenreich, *Jpn. J. Appl. Phys.* **35**, 1311 (1996), D. Bimberg, N. Kirstaedter, N.N. Ledentsov, Zh.I. Alferov, P.S. Kop'ev, V.M. Ustinov, *IEEE J. Selected Topics in Quantum Electronics* **3**, 1 (1997).
- L. Goldstein, F. Glas, J.Y. Marzin, M.N. Charasse, and G. Le Roux, *Appl. Phys. Lett.* **47**, 1099 (1985)
- J.M. Moison, F. Houzay, F. Barthe, L. Leprice, E. Andre, and O. Vatel, *Appl. Phys. Lett.* **64**, 196 (1994), D. Leonard, M. Krishnamurthy, C.M. Reaves, S.P. Denbaars, and P.M. Petroff, *Appl. Phys. Lett.* **63**, 3203 (1993).
- N.N. Ledentsov, M. Grundmann, N. Kirstaedter, J. Christen, R. Heitz, J. Böhner, F. Heinrichsdorff, D. Bimberg, S.S. Ruvimov, P. Werner, U. Richter, U. Gösele, J. Heydenreich, V.M. Ustinov, A.Yu. Egorov, M.V. Maximov, P.S. Kop'ev and Zh.I. Alferov, *Proc. ICPS-22*, Vancouver, 1994, (World Scientific, Singapore, 1995), vol. 3, 1855.
- V.A. Shchukin, N.N. Ledentsov, P.S. Kop'ev, and D. Bimberg, *Phys. Rev. Lett.* **75**, 2968 (1995) and *Surf. Sci.* **352**, 117 (1996)

7. N.N. Ledentsov, M. Grundmann, N. Kirstaedter, O. Schmidt, R. Heitz, J. Böhrer, D. Bimberg, V.M. Ustinov, V.A. Shchukin, P.S. Kop'ev, Zh.I. Alferov, S.S. Ruvimov, A.O. Kosogov, P. Werner, U. Richter, U. Gösele and J. Heydenreich, *Solid State Electronics* **40**, 785 (1996).
8. F. Heinrichsdorff, M.-H. Mao, N. Kirstaedter, A. Krost, D. Bimberg, A.O. Kosogov and P. Werner, *Appl. Phys. Lett.* **71**, 22 (1997).
9. Q. Xie, A. Madhukar, P. Chen, N.P. Kobayashi, *Phys. Rev. Lett.* **75**, 2542 (1995).
10. G.S. Solomon, J.A. Trezza, A.F. Marshall, J.S. Harris, *Phys. Rev. Lett.* **76**, 952 (1996).
11. N.N. Ledentsov, V.A. Shchukin, M. Grundmann, N. Kirstaedter, J. Böhrer, O. Schmidt, D. Bimberg, S.V. Zaitsev, V.M. Ustinov, A.E. Zhukov, P.S. Kop'ev, Zh.I. Alferov, A.O. Kosogov, S.S. Ruvimov, P. Werner, U. Gösele and J. Heydenreich, *Phys. Rev. B* **54**, 8743 (1996).
12. A.O. Kosogov, P. Werner, U. Gösele, N.N. Ledentsov, D. Bimberg, V.M. Ustinov, A.Yu. Egorov, A.E. Zhukov, P.S. Kop'ev, N.A. Bert, and Zh.I. Alferov, *Appl. Phys. Lett.* **69**, 3072 (1996), R. Leon, Yong Kim, C. Jagadish, M. Gal, J. Zou, and D.H. Cockayne, *Appl. Phys. Lett.* **69**, 1888 (1996).
13. J.-Y. Marzin, J.M. Gerard, A. Izraël, D. Barrier, G. Bastard, *Phys. Rev. Lett.* **73**, 716 (1994).
14. M. Grundmann, J. Christen, N.N. Ledentsov, J. Böhrer, D. Bimberg, S.S. Ruvimov, P. Werner, U. Richter, U. Gösele, J. Heydenreich, V.M. Ustinov, A.Yu. Egorov, A.E. Zhukov, P.S. Kop'ev and Zh.I. Alferov, *Phys. Rev. Lett.* **74**, 4043 (1995).
15. M. Grundmann, D. Bimberg, *Jpn. J. Appl. Phys.* **36**, 4181 (1997).
16. M. Grundmann, D. Bimberg, *Phys. Rev. B* **55**, 9740 (1997).
17. N.N. Ledentsov, M.V. Maximov, P.S. Kop'ev, V.M. Ustinov, M.V. Belousov, B.Ya. Meltsner, S.V. Ivanov, V.A. Shchukin, Zh.I. Alferov, M. Grundmann, D. Bimberg, S.S. Ruvimov, W. Richter, P. Werner, U. Gösele, U. Heydenreich, P.D. Wang and C.M. Sotomayor Torres, *Microelectronics Journal* **26**, 871 (1995).
18. N.N. Ledentsov, *Proc. ICPS23, Berlin 1996*, p. 19 (1996) and references therein.
19. R. Heitz, M. Grundmann, N.N. Ledentsov, L. Eckey, M. Veit, D. Bimberg, V.M. Ustinov, A. Yu. Egorov, A. E. Zhukov, P. S. Kop'ev and Zh. I. Alferov, *Appl. Phys. Lett.* **68**, 361 (1996).
20. B. Deveaud, F. Clérot, N. Roy, K. Satzke, B. Sermage, and D.S. Katzer, *Phys. Rev. Lett.* **67**, 2355 (1991).
21. N.N. Ledentsov, , V.M. Ustinov, A.Yu. Egorov, A.E. Zhukov, M.V. Maximov, I.G. Tabatadze, P.S. Kop'ev, *Semiconductors* **28**, 832 (1994).
22. N. Kirstaedter, N.N. Ledentsov, M. Grundmann, D. Bimberg, U. Richter, S.S. Ruvimov, P. Werner, J. Heydenreich, V.M. Ustinov, M.V. Maximov, P.S. Kop'ev, and Zh.I. Alferov, *Electronics Letters* **30**, 1416 (1994).
23. K. Kamath, P. Bhattacharya, T. Sosnowski, T. Norris, and J. Phillips, *Electronics Letters* **32**, 1374 (1996).
24. N. Kirstaedter, O.G. Schmidt, N.N. Ledentsov, D. Bimberg, V.M. Ustinov, A.Yu. Egorov, A.E. Zhukov, M.V. Maximov, P.S. Kop'ev and Zh.I. Alferov, *Appl. Phys. Lett.* **69**, 1226 (1996).
25. O.G. Schmidt, N. Kirstaedter, N.N. Ledentsov, M.-H. Mao, D.Bimberg, V.M.Ustinov, A.Y. Egorov, A.E. Zhukov, M.V. Maximov, P.S. Kop'ev and Zh.I. Alferov, *Electronics Lett.* **32**, 1302 (1996).
26. Yu.M. Shenyakov, A.Yu. Egorov, A.E. Zhukov, S.V. Zaitsev, A.R. Kovsh, I.L. Krestnikov, A.V. Lunev, N.N. Ledentsov, M.V. Maximov, A.V. Sakharov, V.M. Ustinov, Zhao Zhen, P.S. Kop'ev, Zh.I. Alferov and D. Bimberg, *Pis'ma v Zh. Tekhn. Fiz.* **23** (1), 51-54 (1997) (*Tech. Phys. Lett.* **23** (1997)).
27. M.V. Maximov et al., to be published.
28. R. Mirin, A. Gossard, J. Bowers, *Electron. Lett.* **32**, 1732 (1996).
29. L.V. Asryan, R.A. Suris, *Semicond. Sci. Technol.* **11**, 1 (1996).
30. Y. Arakawa, A. Yariv, IEEE J. Quantum Electron., **QE22**, 1887 (1986).
31. K. Kamath, J. Phillips, H. Jiang, J. Singh, and P. Bhattacharya, *Appl. Phys. Lett.* **70**, 2952 (1997).
32. M.-H. Mao, F. Heinrichsdorff, A. Krost, D. Bimberg, *Electron. Lett.*, in print.
33. N.N. Ledentsov, I.L. Krestnikov, M.V. Maximov, S.V. Ivanov, S.L. Sorokin, P.S. Kop'ev, Zh.I. Alferov, D. Bimberg, and C.M. Sotomayor Torres, *Appl. Phys. Lett.* **69**, 1343 (1996); *ibid. Appl. Phys. Lett.* **70**, 2766 (1997).
34. R. Schur, F. Sogawa, M. Nishioka, S. Ishida, Y. Arakawa, *Jpn. J. Appl. Phys.* **35**, L357 (1997).
35. H. Saito, K. Nishi, I. Ogura, S. Sugou, and Y. Sugimoto, *Appl. Phys. Lett.* **69** 3140 (1996).
36. D.L. Huffaker, O. Baklenov, L.A. Graham, B.G. Streetman, and D.G. Deppe, *Appl. Phys. Lett.* **70**, 2356 (1997)
37. J.A. Lott, N.N. Ledentsov, V.M. Ustinov, A.Yu. Egorov, A.E. Zhukov, P.S. Kop'ev, Zh.I. Alferov, D. Bimberg, *Electron. Lett.* **33**, 1150 (1997).

Microcavity Lasers: Emission from a Fully Confined Photon State

J. P. Reithmaier, M. Röhner, F. Schäfer, H. Zull, A. Forchel
 Technische Physik, Universität Würzburg, Am Hubland, 97074 Würzburg, Germany

Optically pumped three-dimensionally confined microcavity lasers were fabricated by electron beam exposure and dry chemical etching with lateral sizes between 1 - 5 μm . These photonic quantum dot lasers exhibit a well pronounced optical mode spectrum below threshold with a large mode splitting. Above threshold lasing takes place in the fundamental mode with fourier transform limited line widths. Due to the enhancement of the coupling of the spontaneous emission into the lasing mode a significant reduction of the threshold density was observed by reducing the lateral size in comparison to planar vertical cavity emitting structures.

1. Introduction

In conventional high performance edge emitting semiconductor lasers a significant part of the laser threshold can be attributed to the spontaneous emission loss which limits a further reduction of the threshold density [1]. A significant improvement of the spontaneous emission coupling factor into the lasing mode can be achieved by microcavity [2] or microdisk structures [3]. By using a vertical cavity surface emitting laser (VCSEL) geometry low threshold values and spontaneous emission coupling factors β up to 10^{-2} [4] were reported. From theoretical considerations a further significant improvement is predicted by a full three-dimensional optical confinement [5].

In this letter, we will report on the stimulated emission from single photon states of an optically pumped microcavity laser structure with fully three-dimensional optical confinement. In these microcavities the optical modes are discretized in all three space directions [6,7]. The spontaneous emission is therefore restricted to the allowed photon states in the microcavity. For large energy splitting of the photon states the spontaneous emission will couple into a single mode and will reduce the threshold for laser emission.

2. Experiment

The microcavity laser structures are based on a VCSEL layer structure grown by molecular beam epitaxy. The vertical cavity consists of two AlAs/GaAs Bragg mirrors separated by a one wavelength thick GaAs layer (λ -cavity). At the center of the cavity a single GaInAs quantum well is located which is spectrally adjusted slightly on the short wavelength side of the resonance of the vertical cavity for low temperature (2 K). Reflection measurements on unpatterned VCSEL structures with 19 and 21 mirror layer pairs of the top and bottom Bragg reflector, respectively, show a resonance width of the cold cavity of 0.4 meV.

The lateral confinement was realized by the large refractive index step between air and deep etched semiconductor. The square shaped posts were patterned by electron beam lithography and low damage electron cyclotron resonance reactive ion etching (Ar/Cl₂ mixture). The size of the posts were varied between 1 and 5 μm . The structure was etched down approximately 2.6 μm through the whole λ -cavity and a few mirror layers of the bottom Bragg reflector.

Single microcavity structures as well as arrays of structures were optically pumped by a Kr⁺ (647 nm) or Ti:sapphire laser (830 nm) in continuous wave operation at low temperature (2 K). The excitation energy is above the reflectivity stop band of the VCSEL structure and well below the AlAs band-gap. Because the light absorption in the GaAs layers of the top Bragg reflector can not be avoided, the internal excitation density is about two orders of magnitude lower than the external excitation density. Only the internal excitation density can create carriers for recombination in the GaInAs quantum well. The light output of these microcavity laser structures was analyzed by a 0.32 m (low resolution spectra) and 1 m double monochromator (high resolution spectra), respectively. As detector a liquid nitrogen cooled CCD camera was used.

3. Stimulated emission from single photon states

In Figure 1 emission spectra of microcavity laser arrays were plotted slightly above threshold for two different lateral sizes. The emission takes place mainly on the fundamental mode but also higher order modes are stimulated. The arrows mark the energetic positions of the calculated photonic states. By reducing the lateral size from 4.7 μm down to 3.7 μm the emission shifts to higher energies and the splitting between the fundamental mode and the next higher order mode increases while the energetic position of the spontaneous emission remains (c.f. dashed line in Figure 1). This behavior can be clearly seen already at structure sizes slightly below 5 μm due to the strong lateral confinement (> 75% of light intensity are laterally confined). The energetic positions of these emission peaks agree with model calculations (arrows in Figure 1) taken into account the real box like geometry in a fully three-dimensional approach (more details in [7]).

In Figure 2 a highly resolved emission spectrum of the fundamental mode of a single microcavity post is plotted at an excitation power of about 20% above the threshold power. The linewidth changes from 0.4 meV below threshold to 30 μeV above threshold. A further reduction at much higher excitation power could not be observed but the linewidth is already near the resolution limit of the measurement setup. Also the line shape changes significantly from Gaussian like below threshold to Lorentz like above threshold as it is indicated by the solid line data fit in Figure 2. This homogeneously broadened linewidth coincides well with the estimated photon cavity lifetime of about 20 ps deduced from time resolved measurements above threshold and can be interpreted as Fourier transformation limited linewidth of a single photon state.

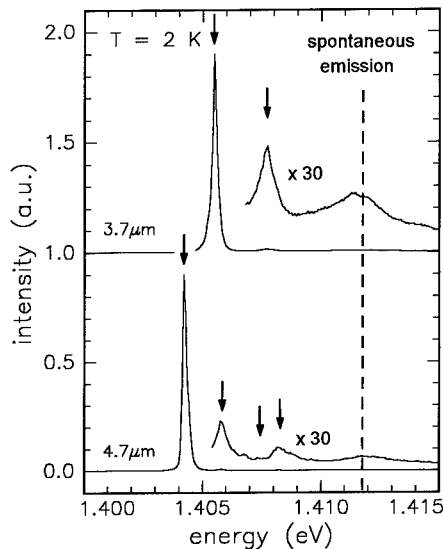


Figure 1: Emission spectra of microcavity laser arrays with different lateral sizes (labeled in μm). The arrows mark the lasing modes which coincides with the photonic eigenstates of the cavity. The dashed line marks the energetic position of the spontaneous emission from the GaInAs quantum well.

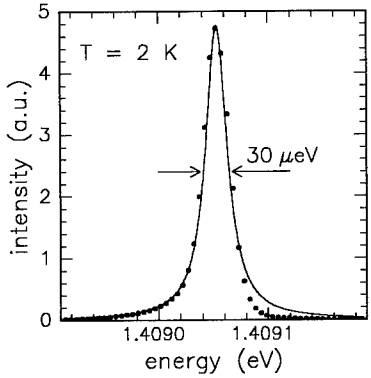


Figure 2: Emission spectrum of a single microcavity laser structure emitting in the fundamental mode. The solid line corresponds to a Lorentz fit of the data points.

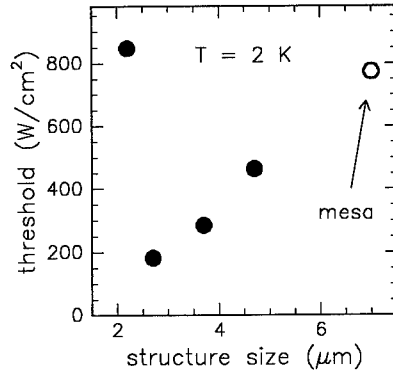


Figure 3: External threshold excitation densities of arrays of microcavity lasers with different lateral sizes (filled dots). For comparison the threshold value of a mesa structure with a lateral size of 100 μm is also included (open dot).

4. Size dependence of laser threshold and spontaneous emission coupling factor

In Figure 3 the external threshold excitation density is plotted against the geometrical lateral width of the microcavity posts. A significant reduction of the threshold excitation density down to 200 W/cm² for a lateral size of 2.7 μm can be observed which is about four times lower than the value for a mesa structure and corresponds to an internal threshold power of 0.15 μW per post. By further reduction of the lateral size the threshold density increases once again and below 2 μm no lasing operation could be observed.

By reducing the lateral size one expect first the optical losses will increase due to diffraction and side wall scattering as well as losses due to surface recombination of carriers [8, 9]. But there are additional gain effects in microcavity laser structures which has to be taken into account and can overcompensate these losses. One is the change of the spectral overlap of the resonance position with the gain function (c.f. Figure 1) and the second one is an improved spontaneous coupling factor into the lasing mode. Due to the well prepared photon states in these microcavity laser structures the splitting energy between fundamental mode and the next higher order mode exceeds the linewidth of the spontaneous emission for smaller lateral sizes than 3 μm . Therefore an increased coupling efficiency of the spontaneous emission can take place and will reduce the threshold excitation density as long as the losses are not too large.

In Figure 4 the light output intensity of a microcavity laser structure with a lateral size of 2.7 μm (dots) is plotted in comparison to a mesa structure (triangles) by varying the excitation power over about 5 orders of magnitude. The onset of lasing can be clearly seen as well as the significant shift to higher output intensity and lower threshold for the microcavity geometry. For estimating the spontaneous coupling factor theoretical calculations were made according to the theory of Björk et al. [10]. For the one dimensional confined mesa like structure we can evaluate a value for the β -factor of about 0.5-1% which is already more than one order of magnitude larger as for an edge emitting laser. A further significantly large increase of the β -factor can be achieved with a three-dimensionally confined photon state in a microcavity geometry. A value of about 10% can be roughly estimated although it can

not be distinguished between 5 and 20%. Due to the high β -factor in microcavity laser structures we believe that an important part of the threshold reduction effect is attributed to the enhancement of the spontaneous emission coupling into the laser mode.

5. Conclusions

Microcavity laser structures with lateral dimensions between 1 - 5 μm were fabricated which allows a three-dimensional photon confinement. Due to the discretization of the photon modes and the large splitting energies between the fundamental mode and the higher order modes a significant enhancement of the coupling of the spontaneous emission into the lasing mode was achieved. In this microcavity laser geometry the photon states are well defined and allows single mode lasing operation with Fourier transformation limited emission linewidths as well as ultralow laser thresholds in the sub- μW range.

7. Acknowledgment

We like to acknowledge A. Wolf and S. Kuhn for technical assistance, B. Ohnesorge and M. Bayer for time resolved measurements. The financial support of the Deutsche Forschungsgemeinschaft is gratefully acknowledged.

8. References

- [1] Vurgaftman I Singh J 1995 *IEEE J. Quantum Electron.* 31 852-63
- [2] Yokoyama H Ujihara K 1995 *Spontaneous Emission and Laser Oscillation in Microcavities* (Chemical Rubber, Boca Raton)
- [3] Slusher R E Levi A F J Mohideen U McCall S L Pearton S J Logan R A 1993 *Appl. Phys. Lett.* 63 1310-2
- [4] Björk G Heitmann H Yamamoto Y 1993 *Phys. Rev. A* 47 4451-63
- [5] Baba T Hamano T Koyama F Iga K 1991 *IEEE J. Quantum Electron.* 27 1347-58
- [6] Gérard J M Barrier D Marzin J Y Kuszelewicz R Manin L Costard E Thierry-Mieg V Rivera T 1996 *Appl. Phys. Lett.* 69 449-51
- [7] Reithmaier J P Röhner M Zull H Schäfer F Forchel A 1997 *Phys. Rev. Lett.* 78 378-81
- [8] Thibeault B J Strand T A Wipiejewski T Peters M G Young D B Corzine S W Coldren L A Scott J W 1995 *J. Appl. Phys.* 78 5871-5875
- [9] Tezuka T Nunoue S 1996 *J. Appl. Phys.* 79 2875
- [10] Björk G Yamamoto Y 1991 *IEEE J. Quantum Electron.* 27 2386-96

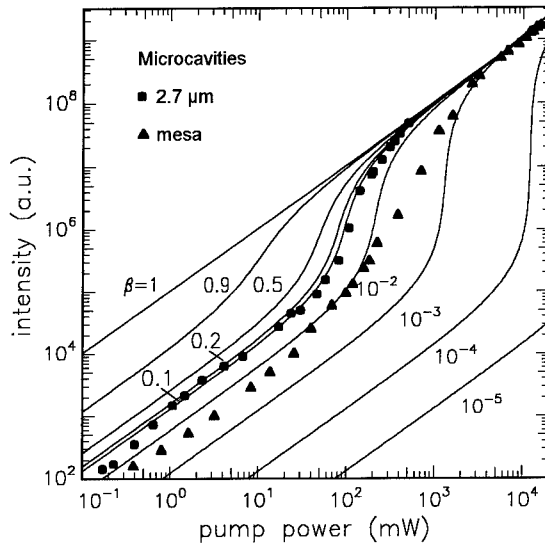


Figure 4: Comparison of the light output characteristic between mesa like (triangles) and microcavity structures with a diameter of 2.7 μm (dots). The solid lines mark the theoretical dependence according to the theory of Björk et al. [10] as a function of the spontaneous emission coupling factor β .

Subband structure of GaAs Coupled Quantum Wires on V-grooved Substrate

Kazuhiro KOMORI^{1,2}, Xue-Lun WANG¹, Mutsuo OGURA¹,
Hirofumi MATUHATA¹, and Ali HAMOUDI¹

¹Electrotechnical Laboratory, Agency of Industrial Science and Technology,
Ministry of International Trade and Industry, 1-1-4 Umezono, Tsukuba, Ibaraki, 305, JAPAN
²Japan Science and Technology Corporation (JST)

Abstract: The subbands structure of crescent shaped GaAs coupled quantum wires is clearly observed by photoluminescence excitation (PLE) measurements. In the PLE spectra of single quantum wires (wire thickness = 4.5nm), sharp exciton peaks of the first two heavy hole-like transitions are observed with large energy difference of 47meV. However, two adjacent peaks with small energy splitting of 24meV are observed in the coupled quantum wires (wire thickness = 5nm, barrier thickness = 3nm). From the measurements of the barrier thickness dependence, these peaks agree well with the symmetric and antisymmetric states of the coupled quantum wires calculated by the finite element method.

1. Introduction

Coupled nano structures[1], such as coupled quantum-wires and -dots, are expected to be the future nano structures for applications not only to new functional devices, but also to ultrafast devices with quantum oscillations[2]. The coupled electron waveguide structures, which are the weakly coupled quantum-wires, were proposed[1] for use in electronic devices and the fabrication has been reported using the split gate method[3]. However, the confinement extent of the electron-wave by depletion is not sufficient for application to opto-electronic devices with optical nonlinearities or intersubband-transitions. We have reported the fabrication of coupled quantum wires by flow rate modulation epitaxy (FME)[4] on V-grooved substrate in order to realize the small size structure with strong coupling[5]. Also we have reported the theoretical analysis of the electronic states in the coupled quantum wires[6]. In this paper, we experimentally investigate the subband structure of the coupled quantum wires by the photoluminescence excitation (PLE) measurements.

2. Structure and Electronic States

The coupled quantum wire array with period of $4.8 \mu\text{m}$ was grown by flow rate modulation epitaxy (FME) described in the previous publication[5]. After the growth of quantum wires, the mask was formed on the quantum-wires and the (100) quantum-films on the mesa top and the (111) quantum-films around the mesa top were removed using chemical etching.

Figure 1 shows the cross-sectional TEM view of the multi-period sample with different barrier thickness of (a) 3.3nm, and (b) 1.5nm. Very small crescent shaped GaAs quantum wires with a central thickness of 5nm and a lateral width of 30nm separated by a thin $\text{Al}_{0.38}\text{Ga}_{0.62}\text{As}$ barrier layer are clearly observed at the bottom of the V-grooves. The vertical quantum film[7] with Al contents of 0.28 can be seen along the (100) direction which is automatically formed during the growth. The top and the bottom quantum wires have almost the same crescent shape but the top quantum wire is slightly thinner and slightly wider than the bottom one. The energy difference between the two quantum wires is small (from 5meV to 10meV).

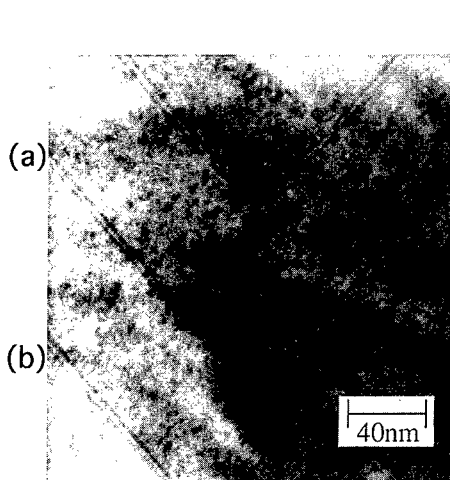


Fig.1 TEM picture of GaAs/AlGaAs coupled quantum wires with wire thickness of 5nm

- (a) Average barrier thickness of 3.3nm:
- (b) Average barrier thickness of 1.5nm

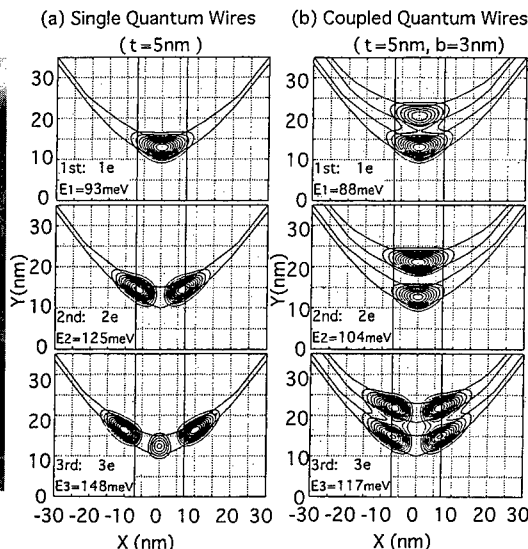


Fig.2 Charge density probability of electron states in
(a) single and (b) coupled quantum wires

The electron states associated with the first three confined states (conduction sub-bands) for (a) single quantum wire with wire thickness of 5nm and (b) coupled quantum wires with wire thickness of 5nm and barrier thickness of 3nm are calculated by the finite element method and the counter plot of charge density probability are shown in Fig.2. The structure is modeled from TEM picture with considering the vertical quantum film region and analyzed using the same procedure in ref.8 with same parameters in ref.6.

In single quantum wires, the higher order electron states quantized in y direction (100 direction) are cut off due to the small thickness, while transverse electron states of e₂, e₃ quantized in the transverse (x) direction are shown. In such small quantum wires, the energy separation between the 1st (1e) and 2nd (2e) electron states is as large as 32meV.

In the case of coupled quantum-wires (thickness of bottom quantum wire t₁=5.1nm, top quantum wire t₂=4.6nm, barrier layer b=3.2nm), the first, the second and the third states, correspond to symmetric state (1e), antisymmetric state (2e) and the transverse electron-wave state (3e). The doublet state, symmetric and anti-symmetric state, are clearly seen even for the crescent shaped asymmetric coupled quantum wires with small energy difference of several meV.

In the following, we call the electron and heavy hole like transition as i-e-jhh, and the light hole like transition as i-e-jlh, where i (= 1, 2, --- , n) and j (= 1, 2, ---, m) are the quantized numbers of the wave function for electron and holes, respectively.

3. PLE characteristics

PLE spectra of single period quantum wires are measured at 20K with the polarization of excitation laser parallel (PLE//) and perpendicular (PLE_⊥) to the quantum wires. The heavy hole like transition and light hole like transition can be distinguished by using the information of polarization[9].

Figure 3 shows those of single quantum wires with wire thickness of 4.5nm. In the Figure sharp exciton peaks of the first two heavy hole-like transitions of the energy of 1.652eV and 1.698eV are observed with large energy difference of 46.6meV. These peaks are due to the transition of fundamental states (1e-1hh), and the second states (2e-2hh) because the energy

separation of between 2e-2hh and 1e-1hh are in good agreement with theoretical FEM result of 44meV. In the spectra of PLE \perp , light hole-like transitions 1e-1lh and forbidden transition 1e-2lh with energy of 1.666eV and 1.6773eV are also observed.

Figure 4 shows PLE characteristics of weakly coupled quantum wires with wire thickness of 5nm and barrier thickness of 3nm. The adjacent two peaks at 1.6325eV and 1.6568eV appear near the fundamental transition energy in PLE//. These peaks are regarded as the symmetric states 1e-1hh, antisymmetric states 2e-2hh because the energy separation of 24.3meV between 1e-1hh and 2e-2hh is close to theoretical result of 19meV. The light hole-like transition is not well resolved because 1e-1lh peak lies behind the 2e-2hh peak. In the strongly coupled quantum wires with barrier thickness of 2nm, the separation energy between 1e-1hh and 2e-2hh is 33meV which becomes larger compared to the weakly coupled quantum wires and the light hole like transition 1e-1lh with energy of 1.6641eV are observed between 1e-1hh and 2e-2hh in PLE \perp .

The barrier thickness dependence on the PLE spectra of coupled quantum wires are measured not only from a) different samples with different barrier thickness, but also from b) different positions on the same wafer where the growth rate differs near the edge. Since the quantum wire array was fabricated on a large area (10mm x 10mm) in GaAs wafer, the thickness of quantum wire near the edge of the wafer differs from that in the center of the wafer. We have measured the PL from the different position on the same wafer, and the PL wavelength of the quantum wire and (111) quantum film was different near the edge while those of AlGaAs cladding layer and vertical quantum film (VQF) remain almost the same all over the wafer. From these results the difference of PL wavelength of quantum-wire is mainly due to the growth rate difference between the central and the edge region and is not due to the difference of Al composition.

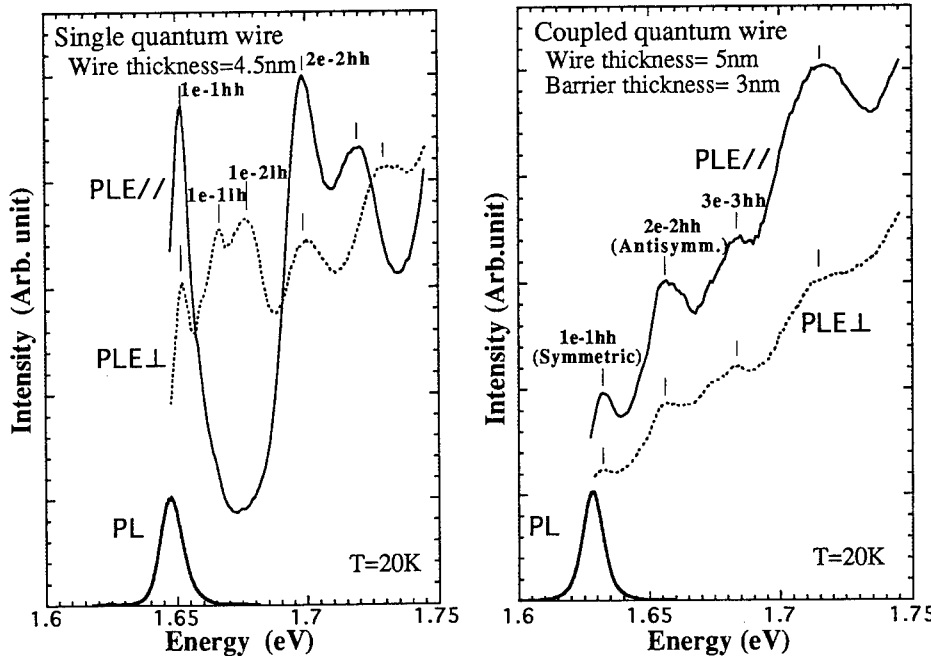


Fig.3 PLE spectra of single quantum-wires
(wire thickness of 4.5nm)

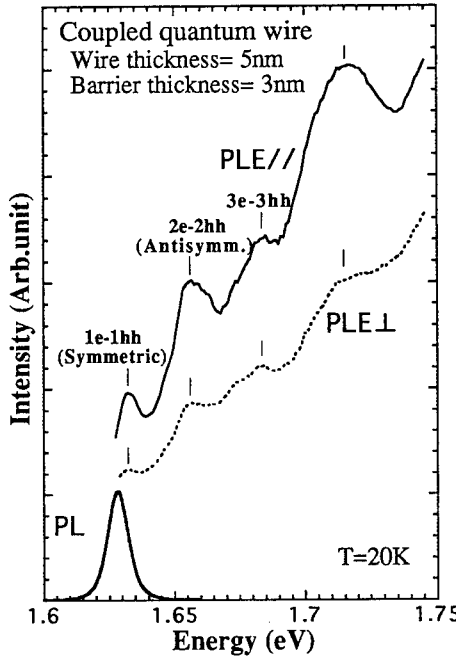


Fig.4 PLE spectra of coupled quantum-wires
(wire thickness of 5nm and barrier thickness of 3nm)

Figure 5 shows the PLE spectra from five positions in the same coupled quantum wire wafer ($t=5\text{nm}$, $b=3\text{nm}$) with different PL wavelength of (a) 761nm (1.6292eV) (b) 759nm (1.6335eV), (c) 757nm (1.6378eV), (d) 755nm (1.6421eV) and (e) 753nm (1.6465eV). The PL wavelength of the quantum wires decreases as the edge is approached due to decreasing thickness of each layer near the edge.

In the Figure, the transition energy of 1e-1hh, 2e-2hh, and 3e-3hh increases as the PL energy is increased. From the theoretical analysis, the decrease in thickness of quantum wire increases each transition energy. The decrease in the thickness of barrier layer increases the splitting energy between symmetric states 1e-1hh and antisymmetric state 2e-2hh, decreases the transition energy of symmetric states 1e-1hh, 3e-3hh, and increases the transition energy of antisymmetric states 2e-2hh[6]. Thus we can expect theoretically that the increase in the energy of 1e-1hh and 3e-3hh is smaller than the increase in the energy of 2e-2hh versus the increase of PL energy. In order to confirm this, we have plotted the transition energy of $E(1e-1hh)$, $E(2e-2hh)$, and $E(3e-3hh)$ as a function of the PL energy $E(\text{PL})$ of 1e-1hh and obtained the line with the slope of $\Delta E(1e-1hh)/\Delta E(\text{PL}) \sim 1.0$, $\Delta E(2e-2hh)/\Delta E(\text{PL}) = 1.546$, $\Delta E(3e-3hh)/\Delta E(\text{PL}) = 1.357$. These results are in good agreement with the theoretical results with the slope of 1.00, 1.67, 1.31 for 1e-1hh, 2e-2hh, and 3e-3hh, respectively.

4. Conclusions

We investigated the subband structure of GaAs coupled quantum wire by the photoluminescence excitation (PLE) measurement. In the weakly coupled quantum wire, adjacent two states are observed near the ground transition energy. The thickness dependence on the PLE spectra of coupled quantum wires are measured not only from different samples with different barrier thickness, but also from different positions on the same wafer. From these measurements, adjacent two peaks agree well with the symmetric and antisymmetric states of the coupled quantum wires in the theoretical analysis.

References

- [1] J.A.Alamo J A and Eugster C C 1990 Appl.Phys.Lett. 56 78
- [2] Roskos H G et.al. 1992 Phys. Rev. Lett. 68 2216
- [3] Eugster C C and Alamo J A 1991 Phys. Rev. Lett. 67 3586
- [4] Wang X L and Ogura M 1995 Appl.Phys.Lett. 66 1506
- [5] Komori K et.al. 1996 Appl. Phys. Lett. 68 3787
- [6] Komori K and Arakawa M 1997 Jpn. J. Appl. Phys. 36 1927
- [7] Walter M et.al. 1992 Appl. Phys. Lett. 60 521
- [8] Pryor C 1991 Phys. Rev. B 44 12912
- [9] Vouilloz F et.al. 1997 Phys. Rev. Lett. 58 1263

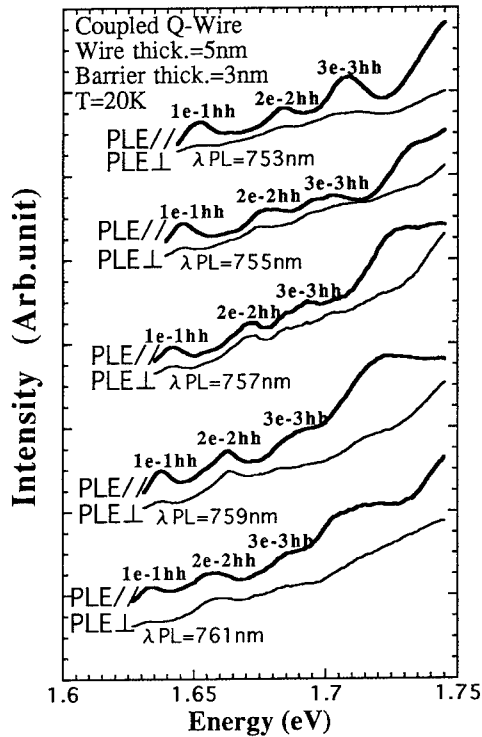


Fig.5. PLE spectra measured from five position in the same coupled quantum wire wafer ($t=5\text{nm}$, $b=3\text{nm}$) with different PL wavelength

Micromachined Tunable Vertical Cavity Lasers as Wavelength Selective Tunable Photodetectors

F. Sugihwo, C.-C. Lin, *J.-C. Bouteiller, ^{*}M. Larson, and J. S. Harris, Jr.

Solid State Electronics Laboratory, CIS-X 328, Stanford University, Stanford, CA, 94305, USA

*Currently with Ecole Polytechnique Institute, Palaiseau, France

^{*}Currently with Lawrence Livermore Laboratory, Livermore, CA, USA

Abstract. Micromachined tunable VCSELs are particularly useful for wavelength division multiplexing applications because of their large continuous wavelength tuning range without mode-hopping. We have achieved 26 nm single mode continuous wavelength tuning with threshold current density as low as 550 A/cm². By reverse biasing the laser, we can obtain a tunable resonant cavity photodetector with simulated linewidth less than 2 nm. Narrow linewidth tunable photodetectors are particularly useful in extending the wavelength separation between WDM channels beyond those offered by other techniques.

1. Introduction

The explosive growth of communications in recent years has put an enormous strain on the existing communication infrastructure. As we are rapidly approaching an era where 1 Gb/s communication ports are becoming a common place item, much will have to be done to upgrade the existing telecommunication and datacommunication infrastructures which are still largely based on coaxial cables. It is a widely accepted fact that the future of communications is in the area of optoelectronics, in particular, the use of optical interconnects with low cost optoelectronic components is perceived to be the key to the development of communication networks of the future [1]. Although optical fibers, in particular erbium doped fiber amplifiers, have shown great promises as optical interconnects, their data carrying capability has been limited by the electronic modulation speed of the optoelectronic component, namely the semiconductor lasers. In contrast to optical fiber's terahertz bandwidth, the best semiconductor lasers can only be modulated up to < 20 GHz. Therefore, in order to fully utilize the fiber bandwidth, Wavelength Division Multiplexing (WDM) scheme becomes a necessity.

Current WDM system uses fixed wavelength laser arrays. However, fixed wavelength laser array has temperature-control, system reliability, and manufacturability problems [2]. Because of these shortcomings, wavelength tunable lasers are indispensable elements of such an array since the lasing wavelength of each laser can be set, maintained, or changed to any wavelength within its tuning range. Micromachined Tunable VCSELs (Mi-TVCSELs) are of particular interest because of their large continuous wavelength tuning range without mode-hopping.

Besides lasers, the other important optoelectronic component for WDM is the photodetector. Since semiconductor laser's linewidth is much less than 1 Å, wavelength selective photodetectors become the limiting factor in the number of WDM channels possible. Resonant cavity photodetectors with wavelength selection capability have long been demonstrated and recently wavelength tunable photodetectors have been shown [3]. Due to resonant cavity effect, these devices have a large responsivity in addition to a narrow linewidth and are particularly useful in extending the wavelength separation between WDM channels beyond those offered by techniques such as Dragone multiplexers [4].

In this communication, we described a dual function tunable optoelectronic device which operates as a Mi-T-VCSELs in the forward bias mode and as a Micromachined Tunable Resonant Cavity Photodetectors (Mi-T-RCP) in the reversed bias mode. Due to its dual functionality, this device could conceivably play an important role in extending data transmission rate through optical fibers. In the following, we will first describe the structure of the device followed by its operation as a tunable laser. We will then present the simulation results of its tunable photodetection capability.

2. Device Structure

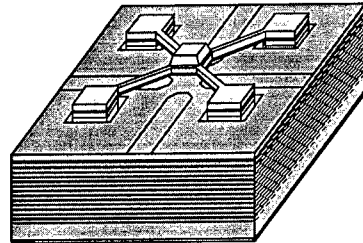


Fig. 1 Schematic diagram of micromachined tunable Vertical-Cavity Surface-Emitting Laser and Microelectromechanical Tunable Resonant Cavity Photodetector

The epitaxial structure is grown using molecular beam epitaxy (MBE). The device structure is shown in Fig. 1. The bottom mirror is consisted of a 22.5 pair AlAs/GaAs DBR centered at 970 nm. The semiconductor cavity region contains two 6 nm $In_{0.21}Ga_{0.79}As$ quantum wells inside a 1 λ $Al_{0.31}Ga_{0.69}As$ cavity. The cavity is then followed by 1/4 λ $Al_{0.31}Ga_{0.69}As$, 1/4 λ AlAs, and 1/2 λ GaAs layer with a 60 \AA heavily doped GaAs contacting layer on top. The 1/4 λ AlAs layer is later oxidized [5] to funnel current to the area underneath the membrane central reflector.

Immediately following the heavily doped GaAs layer is a 8600 \AA $Al_{0.85}Ga_{0.15}As$ sacrificial layer and a 1/4 λ GaAs layer. The $Al_{0.85}Ga_{0.15}As$ layer is later etched to release the deformable membrane. The hybrid top mirror is fabricated on top of the 1/4 λ GaAs layer and is made up of 1/2 λ Si_3N_4 mechanical layer, 2.5 pairs SiO_2/Si_3N_4 dielectric DBR, and 1500 \AA gold. We removed the 2.5 pairs SiO_2/Si_3N_4 dielectric DBR layer from the membrane legs to reduce tuning voltages.

The membranes have 16 to 40 μm diameter square or round central reflector region and the membrane legs are approximately 85 μm long and 5 μm wide. The mechanical support for the suspended membrane is primarily provided by the 1/2 λ Si_3N_4 mechanical layer. The calculated top mirror reflectance of the hybrid mirror is 99.934% (at 970 nm) and is largely aided by the two air-semiconductor interfaces as well as by the highly reflective gold layer. The calculated bottom mirror reflectance is 99.874% (at 970 nm). Both top and bottom mirror reflectance are larger than 99.7% within 20 nm off the center wavelength.

Diode current is injected through four intracavity Ti-Au contact and the backside of the substrate acts as ground. Tuning contact is made on top of the membrane posts. Electrostatic force applied between the tuning contact and the top p-layer of the cavity reduces the air gap spacing between the membrane and the semiconductor cavity. This changes the Fabry-Perot cavity length and results in a change of lasing wavelength. The complete fabrication process is given in Ref. 6.

3. Device Characteristics

3.1 As Tunable Lasers

Diode lasing characteristics are measured by forward biasing the device at room temperature without heat sinking. The lasing spectra is taken with an optical spectrum analyzer and the output power is measured with a calibrated power meter. The lowest measured threshold current and threshold current density at zero membrane bias are 0.323 mA and 258 A/cm² respectively. The largest measured output power is 0.39 mW for a 20 μm current aperture and the largest measured quantum efficiency is 0.088 W/A at zero membrane bias.

Shown in Fig. 2a is the logarithmic intensity versus lasing wavelength for a single mode device operated at different membrane bias and at 2.6 mA constant driving current. This device has a 16 μm central reflector with 6 μm current aperture.

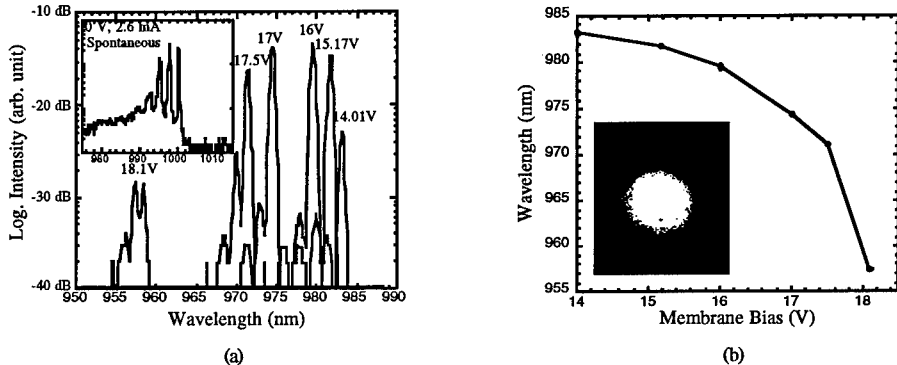


Fig. 2 (a) Logarithmic intensity versus lasing wavelength for a single mode device, inset is the spontaneous spectra of the device at 0 V membrane bias. (b) Plot of lasing wavelength versus membrane bias, inset is the lasing mode image.

We attribute the failure to lase at 0 V membrane bias to a combination of low material gain and reduced mirror reflectance near 1 μm . Shown in the inset of Fig. 2a is the spontaneous emission of the device at 0 V membrane bias. Lasing starts with 14 V membrane bias and the device is continuously tunable with a 26 nm wavelength tuning range. Lasing is single mode with 20 dB maximum side mode suppression ratio near 980 nm. Side mode suppression ratio reduces as the device detunes from 980 nm and multi transverse mode lasing appears near the end of the tuning range. Single mode operation is still visible up to 960 nm and this represents a 23 nm single mode continuous tuning range. Fig. 2b shows the wavelength vs. membrane bias with inset showing the lasing mode image.

3.2 As Tunable Detectors

Tunable photodetection simulation is separated into two parts. In the first part, we calculate the energy levels of the quantum wells under different applied field. This part of the program will then calculate the absorption strength of the quantum wells. Incorporating this information into the second part of the program, we then calculate the linewidth and the quantum efficiency of the tunable photodetector.

The quantum well analysis is done using “transfer matrix” formalism [7], similar to those used for optics simulations. First, the program divides the quantum well structure into layers of finite width. A matrix which relates the forward and backward amplitudes on one interface with the forward and backward amplitudes on the other interface is then generated. By multiplying these matrices, we obtain a single transfer matrix for the whole structure whose eigenstates are then found using a “tunneling resonance” method. We modelled the applied bias on the quantum wells using a series of step-wise approximation.

The optical absorption is calculated using Fermi’s Golden Rule. However, for simplicity of the treatment we neglect excitonic effects. The probability of a photon being absorbed in passing through the quantum wells is then given by [7]:

$$P_{\text{abs}} = \frac{e^2 \mu_{\text{eff}} (2\pi)^2}{m_0^2 n_r c \epsilon_0 \omega h^2} |P_{cv}|^2 \sum_{nc, nv} |\langle \psi_{nc} | \psi_{nv} \rangle|^2 \Theta\left(\frac{\hbar\omega}{2\pi} - E_{nc} - E_{nv} - E_g\right)$$

where e is the electron charge, μ_{eff} is the reduced effective mass, given as: $\frac{1}{\mu_{\text{eff}}} = \frac{1}{m_e} + \frac{1}{m_h}$

, m_0 is the mass of electron, n_r is the refractive index, c is the velocity of light, ϵ_0 is the permittivity of free space, and Θ is the heaviside function. We assume P_{cv} is approximately constant. The calculate

absorption at different wavelengths is then fed into an optical simulation program that calculates the linewidth and quantum efficiency of the detector.

Since there is no bandgap narrowing due to a high concentration of injected carriers (the case for lasers), absorption starts at 974 nm (for simulations without linewidth broadening) which corresponds to an airgap thickness of 700nm. Accounting for the electromechanical limitations of the membrane, this allows us to modulate about 125 nm of the airgap spacing hence wavelength tuning range is rather limited, approximately 27 nm. Using a more realistic approach which includes Lorentzian linewidth broadening, the weak absorption tail enables photodetector operation beyond 974 nm, hence tuning in excess of 50 nm should be realizable, limited only by the electromechanical limitations of the membrane. Shown in Fig. 3a is a plot of quantum efficiency versus wavelength for different airgap thickness at 10 kV/cm applied field without linewidth broadening and Fig. 3b is a similar plot with linewidth broadening. Without linewidth broadening, the simulated photodetector linewidth is < 2nm. Including linewidth broadening, linewidth varies from a minimum of 0.1 nm (for 780 nm air gap thickness) to a maximum of 1.8 nm (for 640 nm air gap thickness). The smaller linewidth at longer wavelengths is caused by the absorption tail. Due to the small absorption coefficient in the tails, the back mirror (the hybrid mirror in this case) reflectance is not degraded by much. This increases the finesse of the cavity, resulting in narrower linewidths.

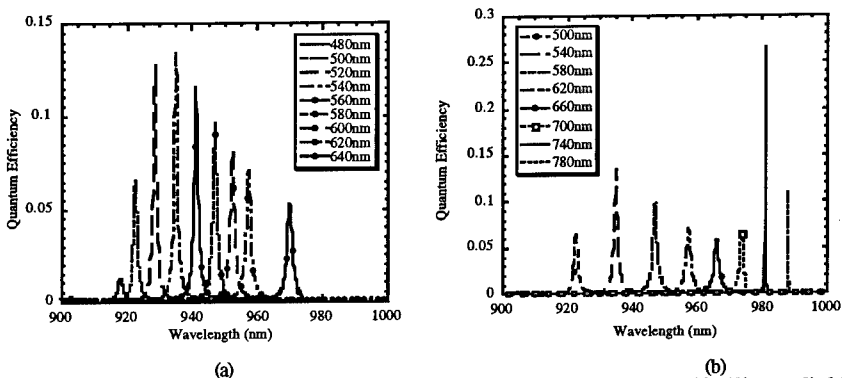


Fig. 3 Plot of quantum efficiency versus wavelength for different airgap thickness at 10 kV/cm applied field:
(a) without linewidth broadening, (b) with linewidth broadening .

This work is supported by ARPA through contract MDA972-94-1-0003.

4. References

- [1] Ishak W 1997 *Proceedings of Device Research Conference* 55 4
- [2] Larson M C 1996 *Ph.D. thesis* Stanford University
- [3] Wu M S, et al. 1996 *IEEE Photon. Technol. Lett.* 8 98-100
- [4] Dragone C, et al. 1991 *IEEE Photon. Technol. Lett.* 3 896-9
- [5] Dallesasse J M, et al. 1990 *Appl. Phys. Lett.* 57 2844-6
- [6] Sugihwo F, et al. 1997 submitted to *Journal of Microelectromechanical Systems*
- [7] Chuang S L 1995 *Physics of Optoelectronic Devices* (New York: John Wiley)

Number of the Technical Area listed above in the Scope Section: 3, 5, 6.

Characterization of GaAs/AlGaAs mid-infrared emitters

L. Hvozdara⁽¹⁾, J.N. Heyman⁽²⁾, G. Strasser⁽¹⁾, K. Unterrainer⁽¹⁾, P. Kruck⁽³⁾,
M. Helm⁽³⁾ and E. Gornik⁽¹⁾

⁽¹⁾ Institut für Festkörperelektronik, Technische Universität Wien, A-1040 Vienna, Austria

⁽²⁾ Department of Physics and Astronomy, Macalester College, St. Paul, MN, 55105, USA

⁽³⁾ Institut für Halbleiterphysik, Universität Linz, A-4040 Linz, Austria

Abstract. We report the design, growth, and characterization of mid-infrared emitters based on the GaAs/AlGaAs material system. The structures are unipolar intersubband emitters. Photocurrent, transmission and integral emission power measurements are performed. We also report the temperature dependence of the photocurrent and current voltage characteristics of two emitters.

1. Introduction

The advent of a unipolar semiconductor laser based on intersubband transitions in quantum wells in 1994 marked a breakthrough in the application of band structure engineering [1]. Since the first unipolar Quantum Cascade Laser (QCL) was demonstrated in 1994 [1], great progress in the performance and operating characteristics of these lasers has been achieved. In 1996 operation above room temperature and peak powers of 100 mW [2] as well as CW operation of these lasers up to 110K was reported [3]. In 1997 a QCL with distributed feedback was demonstrated [4], tunability of this unipolar semiconductor lasers was shown recently [5].

Until now all the results have only been reported using a single material system, InGaAs/InAlAs lattice matched to InP. Strain requirements limit the composition of the InGaAs and the InAlAs ternary compounds. The GaAs/AlGaAs system offers very good lattice match over the whole range of aluminum content in AlGaAs.

2. Samples

Two samples, A and B, are both MBE grown on semi-insulating GaAs substrates. Their active regions consist of 25 sequences of an active cell and an injector. The growth sequence of the active cell (3 wells) of sample A (B) is 10 (10) Å GaAs, 15 (15) Å AlGaAs, 45 (47) Å GaAs, 20 (22) Å AlGaAs and 45 (40) Å GaAs (see fig. 1). The aluminum content of the AlGaAs layers is 45%. The undoped active cells are separated by doped ($2 \times 10^{17}/\text{cm}^3$) miniband funnel injectors (gray areas in fig. 2). The injectors are designed as superlattices. Under bias they form minibands that “funnel” electrons from the lower states (first and second) of the previous active cell into the upper (third) state of the following active cell. The active region of sample B is embedded between two waveguide cladding layers, while sample A has only doped ($10^{18}/\text{cm}^3$) contact layers but no cladding. For the cladding layer of sample B a doped ($10^{17}/\text{cm}^3$) superlattice of AlAs/GaAs (30 Å/60 Å) is used.

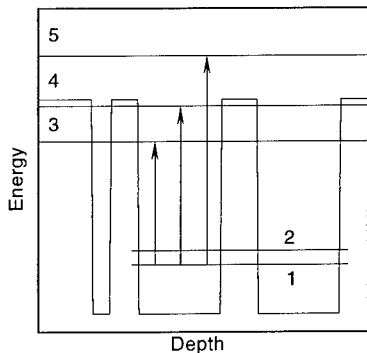


Figure 1: Scheme of the conduction band of active cell under zero external bias, and the possible intersubband transitions.

3. Experiment

The current-voltage characteristics (fig. 5) are measured using a standard quasi-static method. The samples are processed by wet chemical etching into $70 \times 100 \mu\text{m}^2$ mesa structures for this purpose. The sample is metallized by AuGeNi contacts. Measurements are performed at liquid helium temperature (4.2K).

For transmission measurements the sample is polished, metallized and wedged on opposite facets for coupling light into the sample in the waveguide geometry. The wedging angle is 38° . The sample is mounted on the cold finger of a LHe-flow cryostat equipped with ZnSe windows. The absorption spectra are obtained using a Fourier transform spectrometer (FTS).

For the near zero bias photocurrent measurements (fig. 3) the sample is processed into mesa structures, metallized and wedged on one facet. The measurements are done using FTS and a broadband light source. The photocurrent signal from the sample is amplified and fed into the spectrometer detector input.

Measurements of the total emission power are performed on the same mesas characterized by photocurrent spectroscopy. The sample is driven with electrical pulses with a repetition rate of about 20 kHz and a duty cycle between 2% and 30%. The measurements are performed at temperatures around 10 K. The emitted light is collected using parabolic mirrors and focused to a liquid nitrogen cooled MCT detector. The output signal is processed using lock-in techniques and is recorded as a function of the input power (fig. 4).

The positions of the allowed energetic states in the active cell are depicted in fig. 1. The spacing between the second and the first state is tailored in a way that the energy difference under bias is larger than the energy of the optical phonon in GaAs (36 meV). Therefore, $\tau_{(2-1)} \ll \tau_{(3-2)}$ and thus a population inversion is expected when electrons are injected in level three.

Under bias (see fig. 2) the miniband of the injector is aligned with the third state of the active cell. Electrons injected into this state can make an optical transition to the second state by emitting an infrared photon. The second state is emptied by LO phonon assisted transition to the first state of the active cell. Then the electrons tunnel into the injector of the next period of the cascade.

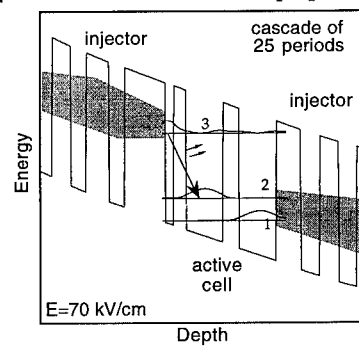


Figure 2: Schematic of the conduction band under bias. Current injection produces infrared emission between subbands 3-2.

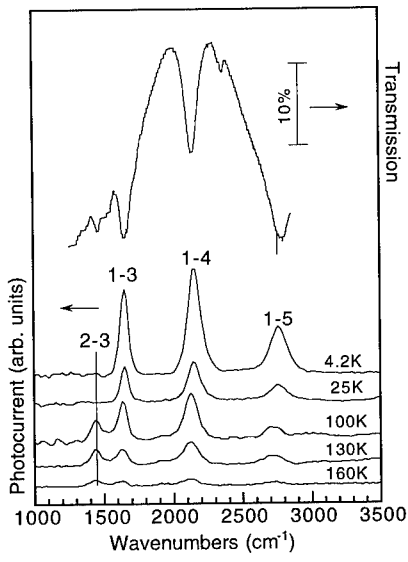


Figure 3a: Absorption and photocurrent spectra of sample A. At elevated temperatures we can observe the transition between subband states 2 and 3.

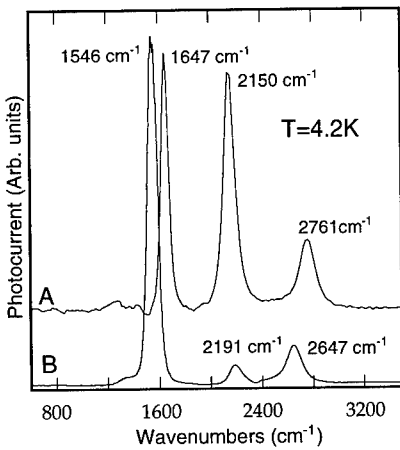


Figure 3b: Comparison of the photocurrent spectra of samples A and B. The positions of the peaks are in good agreement with the calculations (see Tab. 1).

4. Results and discussion

The absorption spectrum of sample A at 4.2 K is shown in fig. 3a. All minima in the spectrum correspond to the calculated subband spacings (see fig. 3a and table 1). Some deviations from the model can be caused by simplifications in the modeling and by inaccuracy in the growth.

Typical photocurrent spectra of sample A are shown in fig. 3a. The spectra are recorded for different temperatures. Above 100K we can observe an additional peak at 1420 cm^{-1} wavenumbers. This corresponds to the transition (2-3) (see tab. 1). It occurs only at elevated temperatures since an activation energy is required to create a population in the second state. The temperature dependence of the ratio between the (1-3) and (2-3) peak heights yields an activation energy of $E_A=20\pm4\text{ meV}$ which agrees with the measured spacing between the first and the second energy level of 23.4 meV ($=188\text{ cm}^{-1}$).

Transition	sample A [cm ⁻¹] calc.	sample A [cm ⁻¹] meas.	sample B [cm ⁻¹] calc.	sample B [cm ⁻¹] meas.
1-2	168	188	200	-
1-3	1588	1633	1546	1546
1-4	2196	2153	2214	2191
1-5	2660	2730	2694	2647
2-3	1420	1433	1346	-

Table 1
Calculated and measured energetic spacing of the states for samples A and B in wavenumbers.

Figure 3b depicts a comparison of the photocurrent spectra of samples A and B. A larger dominance of the peak corresponding to (1-3) transition can be observed in the spectrum of sample B.

The electroluminescent light was analyzed by a set of filters to isolate the mid-infrared emission. The polarization of the emission was analyzed by a grid polarizer. Both samples emit only with the electric field perpendicular to the quantum well layers indicating that the emission is due to intersubband transitions.

In fig. 4 the comparison of the total emission

output power vs. input power is shown for both samples in arbitrary units. The ratio of the total output powers P_B/P_A for an input power density of 20 kW/cm^2 is 15.7. Sample B is much more efficient compared to A.

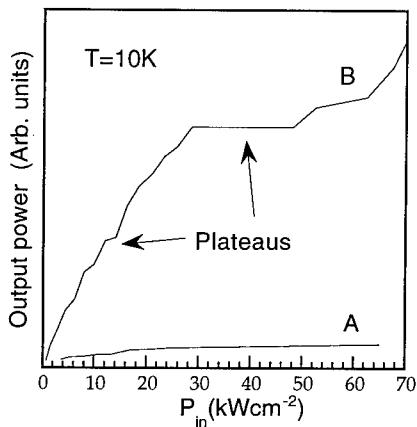


Figure 4: Total output power of the emitted radiation vs. input power density. Sample B is more efficient and we can observe the effect of the cladding layer on the curve of sample B.

We acknowledge the support of the Society of Microelectronics (GMe, Austria) and Austrian Science Foundation (START-Programm Y47-PHY). JH acknowledges support of Cottrell Science award from Research Corporation.

References

- [1] J.Faist *et al.* 1994 Science Vol.264 477
- [2] J.Faist *et al.* 1996 Appl. Phys. Lett. Vol. 68 3680
- [3] C.Sirtori *et al.* 1996 Appl. Phys. Lett. Vol.68 1745
- [4] J.Faist *et al.* 1997 Appl. Phys. Lett. Vol. 70 2670
- [5] J.Faist *et al.* 1997 Nature Vol. 387 777
- [6] H.T.Grahn World scientific 1995 Semiconductor Superlattices 212

The current-voltage characteristics (fig. 5) of sample A is diode like with an onset at about 6 volts. The current-voltage characteristics of sample B has two negative differential resistance (NDR) regions due to the presence of the waveguide cladding layers, which are grown as superlattices [6]. In these NDR regions the current, and consequently the integral emission power, doesn't rise. Therefore, plateaus are observed in the P_{out} vs. P_{in} characteristics (fig. 4).

5. Conclusion

We have designed and grown intersubband quantum cascade emitters using the GaAs/AlGaAs material system. We have performed electrical and optical measurements. The results of the measurements are in good agreement with our calculations. First attempts to fabricate a laser structure from these devices encountered difficulties with the electrical properties of the waveguide cladding layer.

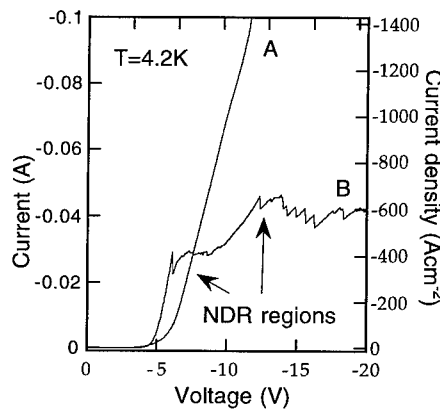


Figure 5
Current -voltage characteristics of samples A and B. In case of sample B we can observe the influence of the cladding layers.

Multi-Staged, InAsSb Mid-Infrared Lasers and Light-Emitting Diodes, Grown by MOCVD

S. R. Kurtz, A. A. Allerman, R. M. Biefeld, and K. C. Baucom

Sandia National Laboratories, Albuquerque, New Mexico 87185-0603

Abstract. We describe the first mid-infrared ($4 \mu\text{m}$) lasers and LEDs utilizing strained InAsSb, multi-stage (or “cascaded”) active regions. An (n)InAs / (p)GaAsSb semimetal layer is incorporated into each stage as an internal electron-hole source. To date, 2-stage LEDs and 2-stage lasers have been demonstrated. Our multi-stage devices were grown by MOCVD.

1. Introduction

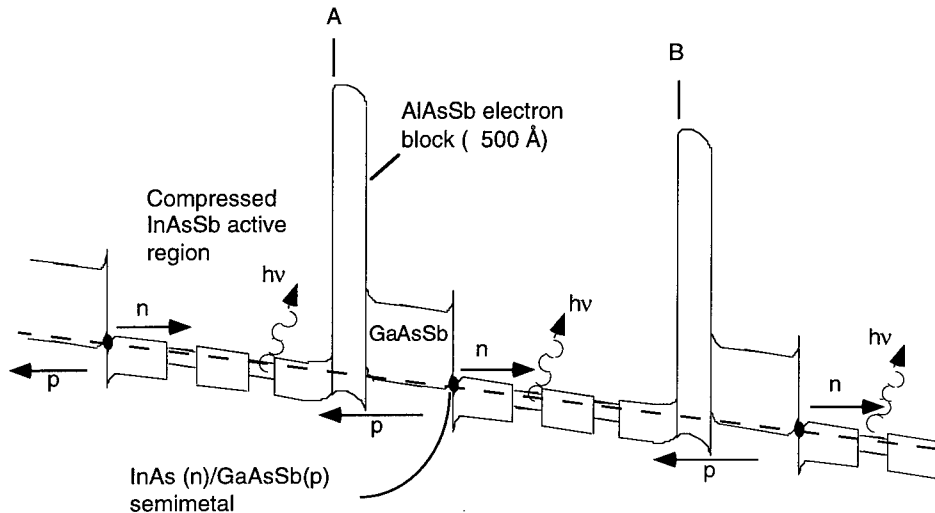
Chemical sensor and infrared countermeasure technologies would become viable with the availability of high power, mid-infrared ($3\text{-}6 \mu\text{m}$) lasers and LEDs operating near room temperature. However, the performance of mid-infrared emitters has been limited by nonradiative recombination processes (usually Auger recombination), which dominate radiative recombination in narrow bandgap semiconductors. Potentially, Auger recombination can be suppressed in “band-structure engineered”, strained Sb-based heterostructures. Along with material development efforts, we are exploring novel multi-stage (or “cascaded”) active regions to improve the performance of Sb-based, mid-infrared lasers and LEDs. In this paper, we present a “progress report” on novel InAsSb-based, mid-infrared devices grown by metal-organic chemical vapor deposition (MOCVD), and compare these results with molecular-beam epitaxy-grown, InAs/GaInSb type II superlattice devices.

The injection devices described in this work contain a GaAsSb (p) / InAs (n) heterojunction to form an internal, semi-metal layer.[1,2] In these devices, the semi-metal acts as an internal electron source which can eliminate problems associated with electron injection (specifically electron blocking by cladding conduction band offsets, n-type doping of claddings, and excess heating due to thermalization of hot carriers), and this design is compatible with MOCVD materials and background dopings. Furthermore, the use of an internal electron-hole source enables us to consider alternative laser and LED designs that would not be feasible with conventional, bipolar devices. Using the semi-metal, InAsSb-based multi-staged active regions can be constructed (see Figure 1a) where in the absence of non-radiative losses, several photons would be generated for every carrier injected at the device contacts. A two stage LED and a 2-stage laser are described in this work to demonstrate the feasibility of our idea. Similar to the multi-staged InAsSb devices, we have reported cascaded, type II InAs/GaInSb LEDs and lasers.[3,4] (see Figure 1b) Competing with the Sb-based mid-infrared devices, unipolar quantum cascade lasers have received much acclaim.[5] However, the nonradiative (optical phonon) lifetimes of the unipolar devices are orders of magnitude shorter than the Auger-limited lifetimes for interband devices, and with multi-staging, mid-infrared interband Sb-based lasers should have lower threshold currents than unipolar quantum cascade lasers.

2. Multi-Staged (Cascaded) Device Demonstrations

As an initial demonstration of a multi-staged bipolar device, we produced a 2-stage/ 2-color LED using InAsSb quantum wells with 11% Sb in one stage and 13% Sb in the other.[1] Each stage is the segment A-B in Figure 1a. In each stage, pseudomorphic InAsSb quantum wells are separated by 500 Å of InAs. (The InAsSb devices are grown on n-type, InAs substrates.) A 600Å thick AlAs_xSb_{1-x} electron barrier is placed between the 2 stages. Low temperature emission spectra from the 2-stage LED showed two peaks, corresponding to emission from each stage for the 2-stage device. Emission from a 1-stage

(a) Multi-stage, Strained InAsSb Active Region -



(b) Cascaded, Type II InAs/GaInSb Active Region -

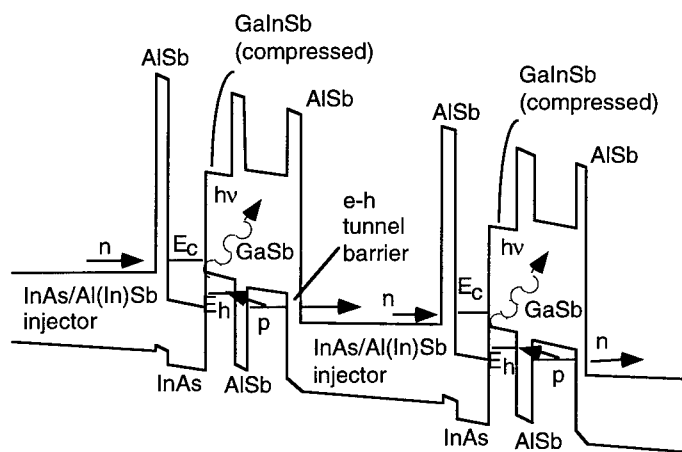


Figure 1 - (a) Diagram of a multi-stage laser active region with compressed, type I InAsSb quantum wells, semimetal electron injection, and AlAsSb electron block.[1] (b) Diagram of a cascaded laser active region with a type II, InAs/GaInSb lasing transition. Electron-hole (e-h) pairs are generated at the AlSb, e-h tunnel barrier in each stage.[2,3]

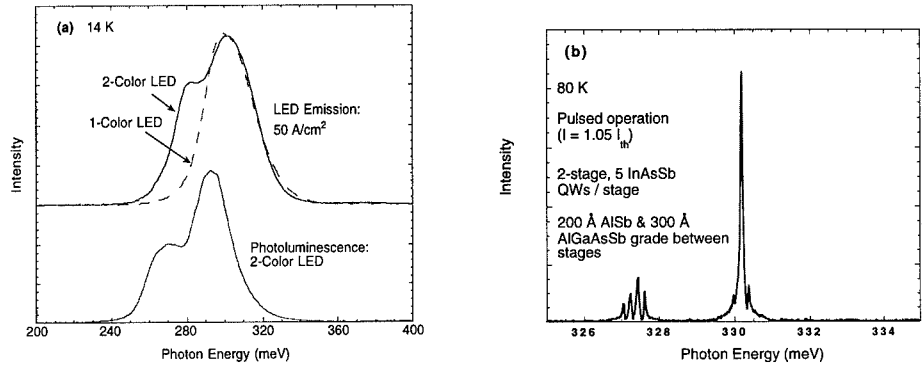


Figure 2 - (a) Emission and photoluminescence spectra of a 2-stage, 2-color LED with InAsSb MQW active regions with 11% and 13% Sb respectively. Emission from a 1-stage LED, with 11% Sb, is also shown. (b) Emission spectrum of a 2-stage semimetal injection laser with 5 InAsSb QWs in each stage.

LED (grown during the same run and removed from the growth chamber in the middle of the run) which clearly corresponds to 1 peak of the 2-stage emission is also shown. (see Figure 2a) The relative intensities of the peaks of the 2-stage device are comparable to those observed in PL, which indicates that electrons are independently generated in each stage.

Multi-stage injection laser emission at 3.8 μm is shown in Figure 2b. Similar to the previous LED, the laser active region consisted of 2 stages, each containing 5 pseudomorphic InAsSb quantum wells. Between stages, 200 \AA of $\text{AlAs}_{0.16}\text{Sb}_{0.84}$ and 300 \AA of compositionally graded AlGaAsSb are used to confine electrons in the active region and to prevent the build-up of holes in the GaAsSb layer. The top and bottom claddings were 2 μm of $\text{AlAs}_{0.16}\text{Sb}_{0.84}$. The overall material quality for this laser was poor. Compositional drift during growth caused lattice mismatch, and 2-color lasing may be occurring in Fig. 2b due to differing Sb composition of the InAsSb quantum wells of the 2 stages. Gain guided stripe lasers, 1 mm long were fabricated, and the lasers were tested under pulsed conditions. The threshold current density at 80K was 3.2 kA/cm^2 , and the maximum operating temperature was 140 K. With poor hole confinement in the multi-quantum well active region and only 2 stages, differential quantum efficiencies > 1 (photon/injected carrier) have not been observed for the multi-stage, pseudomorphic InAsSb devices.

In contrast, emission from a 20 stage, type II InAs/GaInSb laser (see Fig. 1b) has been demonstrated.[3] Similar to the InAsSb devices, electron-hole pairs are generated in each stage at an InAs(n)/AlSb/GaSb(p) semi-metal layer with a thin (20 \AA) AlSb tunnel barrier. Unlike the InAsSb devices, electrons and holes injected into the InAs/GaInSb lasing states cannot escape. The electrons and holes must recombine either radiatively or nonradiatively at the type II, lasing transition. With "perfect" carrier confinement and 20 stages, differential quantum efficiencies of 1.3 (photon/injected carrier) have recently been reported for these type II cascaded lasers.[4] Despite this advance, the type II cascaded lasers still exhibit large threshold currents and turn-on voltages, producing unmanageable heating. Subsequent, 3.8 μm type II devices display pulsed operation up to 165 K and have a threshold current density of 3 kA/cm^2 at 80 K.[4]

3. Discussion

The unipolar quantum cascade laser illustrates the value of using multiple, cascaded lasing transitions to increase gain and to overcome high non-radiative recombination rates. Optimizing the performance of the cascaded design, recent unipolar quantum cascade lasers approach "perfect" carrier confinement with the development of "Bragg reflectors" that prevent electrons injected into the lasing state from escaping to the continuum.[5] Also, electron transport in the unipolar quantum cascade laser is very efficient, with turn-on voltages approaching $N \cdot \hbar\omega$ (N is the number of stages, and $\hbar\omega$ is the laser emission energy).

In Sb-based active regions with poor hole confinement, like psuedomorphic InAsSb multiple quantum wells with InAs barriers, multi-staging is a convenient method for generating multi-color emission. (Adequate electron confinement is provided by the AlAsSb barrier as in Fig. 1a) However, multi-staging of psuedomorphic InAsSb lasers would be equivalent to growing a thick active region to increase gain, and differential quantum efficiencies >1 should not be expected. Instead, multi-staging should prove effective to increase gain from active regions with larger valence band offsets and improved hole confinement, such as InAsSb quantum wells with InAsP barriers, where injection laser studies indicate that holes diffuse over < 10 quantum wells.[6] Development of MOCVD-grown, multi-staged InAsSb/InAsP quantum well lasers are in progress.

To overcome non-radiative recombination, mid-infrared lasers will require higher threshold currents and produce larger heat loads than comparable, shorter wavelength devices. If the voltage drop per stage greatly exceeds $\hbar\omega$, too much heat will be produced in a multi-stage laser to realize any benefit from the increased gain. In each stage, barriers like that produced by the AlAsSb/GaAsSb valence band offset in InAsSb devices (Fig. 1a) or by heavy hole tunnelling through AlSb layers in type II devices (Fig. 1b) can produce unwanted charge build-up and voltage drops. More efficient carrier transport is required to demonstrate practical, Sb-based multi-stage lasers. Initial results indicate that turn-on voltages of multi-staged InAsSb devices may be controlled with heterobarrier doping and grading.

4. Summary

Using a semi-metal, GaAsSb(p) / InAs (n) heterojunction as an internal electron-hole source, interband multi-stage lasers and LEDs have been demonstrated which emit at $4 \mu\text{m}$. An MOCVD-grown, 2-stage LED and a 2-stage laser with psuedomorphic InAsSb quantum well active regions are described and compared with recently demonstrated type II InAs/GaInSb "cascaded" devices. Improved carrier confinement and efficient carrier transport in multi-stage active regions are critical to achieve differential quantum efficiencies >1 and to demonstrate "cascaded" mid-infrared lasers with manageable heating.

5. Acknowledgements

We thank J. A. Bur and J. H. Burkhardt for technical assistance. This work was supported by the United States Department of Energy under Contact DE-AC04-94AL85000.

6. References

- [1] Allerman A A, Kurtz S R, and Biefeld R M 1996 *Appl. Phys. Lett.* 69 465-7
- [2] Meyer J R, Vurgaftman I, Yang R Q, and Ram-Mohan L R 1996 *Electron. Lett.* 32 45-6
- [3] Lin C H, Yang R Q, Zhang D, Murry S J, Pei S S, Allerman A A, and Kurtz S R 1997 *Electron. Lett.* 33 598-9
- [4] Yang R Q, Yang B H , Zang D, Lin C H, Murry S J, Wu H, and Pei S S (submitted for pub.)
- [5] Faist J, Capasso F, Sirtori C, Sivco D L , Hutchinson A L , and Cho A Y 1995 *Appl. Phys. Lett.* 66 538-40
- Sirtori C, Faist J, Capasso F, Sivco D L , Hutchinson A L , and Cho A Y 1997 *IEEE Photon. Tech. Lett.* 9 294-6
- [6] Kurtz S R, Allerman A A, and Biefeld R M 1997 *Appl. Phys. Lett.* 70 3188-90
- Kurtz S R, Allerman A A, and Biefeld R M (unpublished)

GaP-Al_xGa_{1-x}P waveguide Raman lasers and amplifiers for optical communication

K. Suto^{1,3}, T. Kimura², T. Saito¹, A. Watanabe³, and J. Nishizawa^{2,3}

1 Tohoku University 2 Semiconductor Research Institute
3 Telecommunication Advancement Organization, SENDAI Research Center

Abstract. GaP-Al_xGa_{1-x}P tapered waveguide semiconductor Raman lasers have been cw-operated using a Ti-sapphire pump laser. The first Stokes output power is perfectly saturated and the intensity noise level reduces over 30dB. Also they are operated under pumping by a laser diode. Also, the semiconductor Raman amplifier characteristics are shown to be suitable for light frequency discrimination in future THz band as well as WDM optical communication systems.

1. Introduction

Semiconductor Raman lasers as well as Raman amplifiers are promising devices for future optical communication[1-3]. Very low pump power operation of semiconductor Raman lasers has been achieved by using a tapered waveguide structure with GaP core and Al_xGa_{1-x}P cladding layers. The lowest threshold pump power has been 55mW[4].

As for Raman scattering nature of GaP, there are several papers. It is also noted that there are other kinds of solid-state Raman lasers such as spin-flip semiconductor Raman lasers, LiNbO₃ Raman lasers, and glass-fiber Raman lasers.

In principle, a laser light with frequency ω_L introduced into a semiconductor waveguide causes stimulated Raman scattering by exciting a longitudinal optical phonon with frequency ω_{ph} , so that the optical gain is obtained at the Stokes light frequency $\omega_s = \omega_L - \omega_{ph}$, when a signal light with frequency ω_s is introduced into a semiconductor Raman amplifier waveguide. A laser diode will be the most suitable pump light source because its frequency can be quickly tuned by changing laser diode current.

In this paper, we report cw operation of semiconductor Raman lasers, as well as operation under pumping by cw laser diodes. It has been found that the cw-operated Raman lasers show extremely low noise characteristics, which is a result of cascade lasing of the second Stokes light[5]. We also report the frequency discriminating characteristics of the semiconductor Raman amplifiers, which can be utilized as demodulators in future terahertz-band optical communication as well as dense WDM optical communication.

2. Experimental and discussion

Figure 1 illustrates the structures of GaP-Al_xGa_{1-x}P waveguide semiconductor Raman lasers and Raman amplifiers. In the case of the Raman lasers, the input face of the waveguide is highly transparent to the pump light, while it is highly refractive for the Stokes light. In the case of the Raman amplifiers the input face is usually anti-reflection coated and the backside face is coated

with high reflection film. Growth of the heterostructures has been performed by TDM-CVP (temperature difference method under controlled vapor pressure) liquid phase epitaxy. The optical waveguides with GaP core and $\text{Al}_x\text{Ga}_{1-x}\text{P}$ cladding layers fabricated by TDM-CVP show very low loss characteristics (typical optical loss is 0.36dB/cm). Also, we have introduced the tapered waveguide structure in order to increase the pump field intensity inside the waveguide with keeping high efficiency coupling of the incident lights to the waveguide. As a result, the threshold pump power for lasing has been reduced lower than 55mW[4], and room temperature cw operation has been achieved. Moreover, it has been found that when the pump power is increased, very perfect output power saturation occurs[5].

The Raman laser is pumped by Ti-sapphire laser light. The first Stokes light starts to lase at a threshold pump light power $P_{th}=50$ to 100mW. Then, increasing the pump light power to about $1.3P_{th}$, the first Stokes light power is suddenly saturated at an output power level of about 3mW (output mirror reflectance is 99% in the present experiment). At this point, the second Stokes light starts to lase. We have measured the output intensity noise spectrum under cw operation condition in the frequency range from 10Hz to 100KHz using a FFT analyzer. As shown in Fig.2, the intensity noise level of the saturated first Stokes light reduces more than 30dB compared to the intensity noise level of the pump light.

We have shown that, in a scheme of cascade lasing, the lasing condition of the second Stokes light requires the constant internal power level of the first Stokes light which acts as a pump source for the second Stokes light. This is a kind of negative feedback mechanism, which is effective as long as nonlinear optical loss can be neglected. The detailed analysis will be discussed elsewhere. The above experiment has been performed by using a Ti-sapphire laser as a pump source. Then, we have demonstrated the pumping by a laser diode instead of the Ti-sapphire laser. We have used a MOPA laser diode which operates at a wavelength of 980nm with a single longitudinal mode. As shown in Figure 3, lasing with a threshold pump power less than 100mW has been observed.

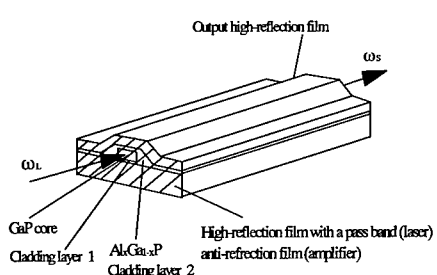


Fig. 1 Structure of the semiconductor Raman lasers and Raman amplifiers.

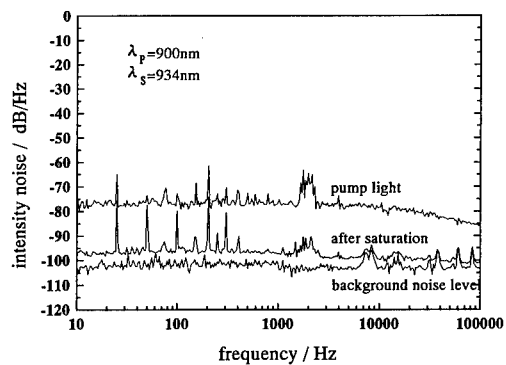


Fig. 2 The intensity noise spectrum of the cw-operated first Stokes light output power under saturation condition compared with the pump power noise spectrum.

The stokes light frequency tuning over 200 GHz can be made by changing the pump laser diode temperature.

In contrast to the Raman lasers, Raman amplifiers have a structure shown in Fig.1, in which the input face of the waveguide is anti-reflection coated so that both the pump light and the signal light are introduced without reflection. There is a backreflector at the other end face of the waveguide. As a result, the incident signal light is twice amplified in the waveguide and taken out from the input face through a Faraday rotator and a polarizer. The Ti-sapphire laser is used for the pump source, which can be frequency-tuned with resolution better than 100MHz. Typical amplifier characteristics is shown in Figure 4.

Typical waveguide dimensions are an average width $w=1.8 \mu m$, an average thickness $d=2 \mu m$, and a length $l=5mm$. Observed gain is 1.2dB at an internal pump power level of 100mW. This result means that we can expect 8.6 dB gain for a waveguide length 10mm, a width $1 \mu m$, and a thickness $1 \mu m$. It should be noted that the Raman gain in this structure with backreflector is a sum of the contributions of forward and backward Raman scatterings. From the Raman gain coefficient profile shown in Fig. 4, the amplifier band width is known to be about 24GHz. This fact means that we can discriminate optical frequencies with a resolution of about 24GHz. This band width is quite suitable for future high density WDM optical communication systems in which each channel is expected to have band width over 10GHz. Figure 5 illustrates a possible dense WDM optical communication system with total frequency bandwidth over 1THz. Semiconductor Raman amplifiers can be used to both post amplifiers after each transmitter/modulators and also as demodulators at each subscriber receivers. In the latter applications the semiconductor Raman amplifier acts as a frequency tunable filter which has an optical gain. If the signals are amplitude-modulated, the optical gain should be at least higher than 10dB in order to suppress the cross talks

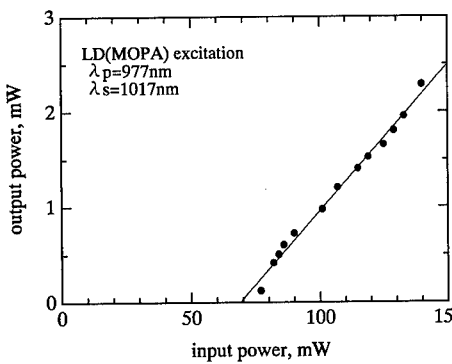


Fig.3 Lasing characteristics of a semiconductor Raman laser under laser diode pumping.

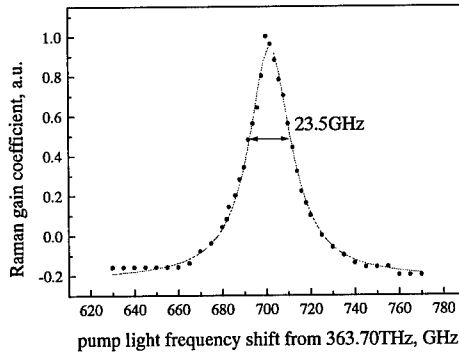


Fig.4 Semiconductor Raman amplifier characteristics measured by using frequency tunable Ti-sapphire laser pump source.

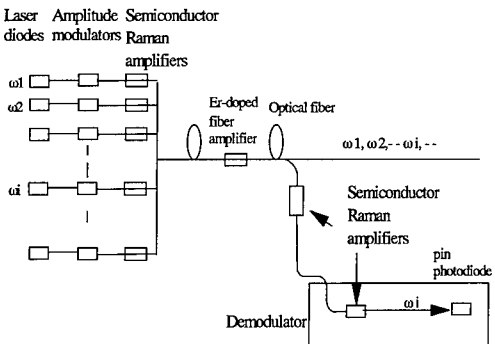


Fig. 5 WDM optical communication system with THz frequency band width applying semiconductor Raman amplifiers as demodulators as well as post amplifiers.

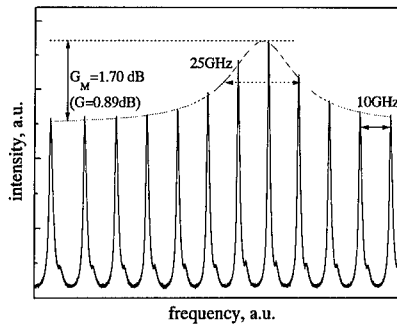


Fig.6 Demonstration of regenerative amplification by the semiconductor Raman amplifier

with other channels, if we do not use any kind of passive filters in combination with a Raman amplifier. The amplifier gain can be increased by regenerative amplification as is demonstrated in Fig.6. The input face of the waveguide is coated with a mirror which has a reflectance $R=50\%$ at the Stokes light wavelength and $R=0$ at the pump light wavelength, instead of anti-reflection coating .The regenerative amplifier gain has been increased about two times of that of the broad band amplifier gain.

3. Conclusion

Semiconductor Raman lasers has been cw-operated. The intensity noise of the semiconductor Raman laser has reduced over 30dB of that of the pump light. They will be applicable where low noise light sources are required such as in optical heterodyne detection. Origin of the power stabilization is a feedback mechanism through the lasing of the second Stokes light.

The semiconductor Raman amplifier has a frequency discriminating characteristics with bandwidth 24GHz, which will be able to be applied to terahertz bandwidth as well as dense WDM optical communication systems.

4. References

- [1] Nishizawa J. 1963 Denshi Kagaku 14 17-20 , Nishizawa J. 1965 Denshi Gijutsu 7 101-106
- [2] Nishizawa J. and Suto K. 1980 J. Appl. Phys. 51 2429-31
- [3] Suto K. and Nishizawa J. 1994 Semiconductor Raman Lasers (Boston-London: Artech House)
- [4] Suto K. Kimura T. and Nishizawa J. 1996 IEE Proc. J. 143 113-118
- [5] Suto K. Kimura T. and Nishizawa J. 1997 IEE Proc. J. 144 87-90

Atomic Force Microscope Nanoscale Lithography For Single-Electron Device Applications

Yoshitaka Okada, Shinji Amano and Mitsuo Kawabe

Institute of Materials Science, Tsukuba University, 1-1-1 Tennodai, Tsukuba, Ibaraki 305, Japan

Barden N. Shimbo and James S. Harris, Jr.

Solid State Electronics Laboratory, Stanford University, Stanford, CA 94305, U.S.A

Abstract. Fundamental results obtained in an atomic force microscope (AFM) chemically-induced direct nanolithography process are presented, which is regarded as a simple method for fabricating nm-scale devices such as single electron tunneling transistors (SETs) and quantum effect electronic devices. Using Au-coated Si cantilevers, we have succeeded in drawing nm-scale oxide patterns in GaAs-based semiconductor surfaces by AFM; n⁺-GaAs (100) and self-assembled InGaAs quantum dots grown by molecular beam epitaxy (MBE) on GaAs (100) and (311)B substrates. The effects of AFM drawing parameters such as bias voltage and writing speed on oxide line quality have been explored. GaAs oxide lines as narrow as ~ 40 nm have been patterned by this technique.

1. Introduction

There is a rapidly growing interest in quantum effect electronic devices and single electron tunneling transistors (SETs) operating near room temperature. The primary fabrication requirement for such devices is uniform dimensions on the order of 10 nm and even smaller. One approach is to use self-organized or self-assembled small structures such as poly-crystalline Si grains [1] and quantum dots [2,3], while the other is to artificially fabricate such nano-structures. Though crystal growth methods such as molecular beam epitaxy (MBE) can provide monolayer control in the vertical direction, techniques for controlling lateral dimensions remain limited. Although common techniques such as optical, x-ray and e-beam lithography may continue to approach these small dimensions, they will do so only at a greater cost. We seek for a simple and inexpensive alternative for fabricating nm-scale structures and devices using GaAs-based semiconductors [4].

Surface modification capabilities of scanning tunneling microscope (STM) have been realized shortly after its original development as a tool for atomic-scale microscopy. An STM operated in air was used to oxidize local regions of a hydrogen-passivated Si(111) surface for use as etch masks [5]. Recently, an STM in UHV was used to form Si oxide lines as narrow as 1 nm wide [6]. On the other hand, atomic force microscope (AFM) has become an attractive option for performing similar work, because, among other reasons, it allows for independent control over the oxidation mechanism that requires a voltage bias and AFM imaging mechanism that is done by a contact force. In STM, a bias is required for both the oxidation and feedback control of imaging so that the imaging of an oxidized

pattern must be done carefully not to oxidize the surface any further. Recently, AFM-induced oxide lines have been used as etch masks to fabricate Si MOSFETs [7] and Si side-gated FETs [8]. On a thin Ti film, Matsumoto *et al.* have successfully fabricated room temperature operable SETs with 15 nm features [9]. One important aspect that has made their work particularly unique was that AFM-generated oxides were used as integral parts of the SET device, and not just as one step in the fabrication process. In this work, we report on drawing nm-scale oxide patterns in GaAs-based semiconductor surfaces, which have not been studied in depth at present. For this, n⁺-GaAs (100) and self-assembled InGaAs quantum dots grown by molecular beam epitaxy (MBE) on GaAs (100) and (311)B substrates have been chosen for study. The effects of AFM drawing parameters such as tip bias voltage and writing speed on oxide line quality have been explored using Au-coated single-crystal Si cantilevers (tips).

2. Experimental

By applying a bias voltage to a conductive AFM tip, negative with respect to the sample, an intense and localized electric field is created at the substrate. There are two known mechanisms working in parallel that will lead to localized oxidation; anodization through a thin film of water adsorbed to the substrate surface, and field-enhanced oxidation that helps ionized water molecules diffuse through the existing oxide. Such process is commonly referred as AFM nano-lithography or nano-oxidation process. GaAs substrates used in this work were chemically prepared by a standard etching process after a thorough degrease in the organic solvents. Also a detailed account on MBE growth of GaAs and InGaAs self-assembled quantum dots can be found elsewhere [10].

First, we have conducted an investigation of the drawing parameters such as tip bias and writing speed on the oxide line quality in terms of linewidth and height. For this, a computer script directed the AFM to draw pairs of 1 μm-long lines; one left-to-right, and another right-to-left, at tip voltages ranging 4 to 12 V. Cross-sectional measurements of linewidth and height were taken at three or four different points on each oxide line. The full line-pattern was drawn for tip writing speeds ranging 0.01 to 3.0 μm/s. Second, a square-like script was used to draw oxide lines in self-assembled InGaAs quantum dots on GaAs in an attempt to selectively isolate or surround some of those quantum dots.

3. Results and Discussion

The effect of tip bias voltage and writing speed on width and height of GaAs oxide lines are plotted in Fig. 1(a) and (b), respectively. The ambient humidity at the time of experiment was < ~ 40%. As shown, faster writing speeds led to thinner and narrower lines as the tip spent less time over the oxidizing areas. Figure 2 displays an AFM image (rotated by 90° for better viewing) showing the effect of tip bias voltage on oxide line quality. Here pairs of 1 μm-long lines as described above were drawn with tip voltages ranging 8 to 12V at a fixed writing speed of 0.05 μm/s. Though higher voltages resulted in wider and thicker oxide lines due to both enhanced anodization and ion diffusion mechanisms, it did not result in any noticeable oxidation for bias voltages below 6V. Lower humidity

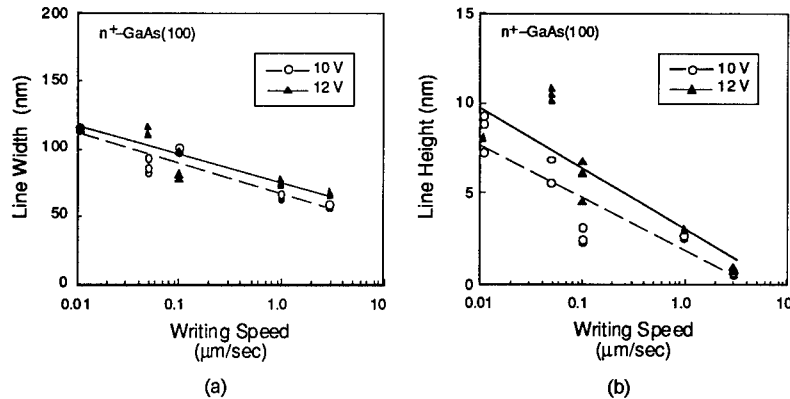


Fig. 1. Effects of AFM tip bias voltage and writing speed on (a) linewidth and (b) height of oxide lines, in n^+ -GaAs (100) surface, respectively. Both the linewidth and height increase with higher voltage and slower writing speeds.

generally resulted in narrower (and thinner) lines. Under ambient humidity of 15 ~ 20 %, oxide lines as narrow as ~ 40 nm were uniformly patterned at a tip bias of 8 V and writing speed of 0.05 $\mu\text{m/s}$. This humidity dependence therefore demonstrates that water vapor is necessary for nano-oxidation process using AFM, and by optimizing these drawing parameters and controlling local humidity [4], we believe it is possible to achieve smaller nm-scale dimensions with higher reliability.

Another application of AFM nano-oxidation process was demonstrated in self-assembled InGaAs quantum dots grown on GaAs by MBE. It can be seen from Fig. 3 that several of those $\text{In}_{0.8}\text{Ga}_{0.2}\text{As}$ quantum dots, which were formed after 3.5 ML deposition on GaAs (100) at a growth temperature of 500°C were geometrically separated by AFM-induced oxide lines. Here the average quantum dot diameter and height were 30nm and 6nm, and oxide lines were drawn at a tip bias = 12 V and writing

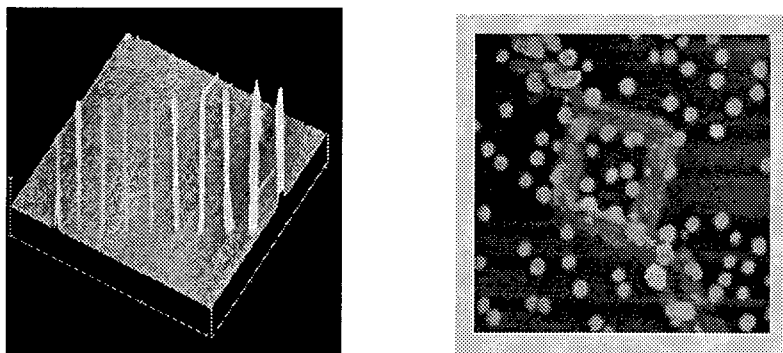


Fig. 2. AFM image showing the effect of tip bias (8–12 V) on oxide line quality. Scan area is 3 μm \times 3 μm .

Fig. 3. AFM-induced oxide lines used to isolate several InGaAs quantum dots (diameter ~ 30nm) which were self-assembled on GaAs(100).

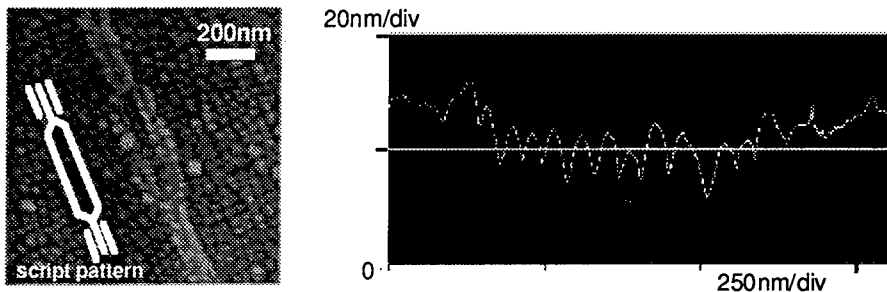


Fig. 4 AFM-induced oxide lines used to isolate one dimensional uniformly-spaced array of self-organized $\text{In}_{0.4}\text{Ga}_{0.6}\text{As}$ stacked quantum dots grown on GaAs (311)B surface by MBE; top view (left) and cross-section (right).

speed = $0.5\mu\text{m}/\text{s}$, respectively. The results were more intriguing for the stacked quantum dots grown on GaAs (311)B substrate [11], in which the dots were self-organized to form an ordered structure rather than being randomly distributed. Figure 4 shows AFM-induced oxide lines used to isolate one dimensional uniformly-spaced array of $\text{In}_{0.4}\text{Ga}_{0.6}\text{As}$ quantum dots grown in GaAs (311)B surface. The oxide lines were drawn at a tip bias = 10 V and writing speed = $0.05\mu\text{m}/\text{s}$ under 50 % humidity. These configurations shown in Figs. 3 and 4 may be used to form Coulomb islands in SETs and fundamental elements in quantum effect devices with the oxide lines directly acting as tunnel barriers.

4. Summary

We have demonstrated nm-scale direct lithography of GaAs-based semiconductor surfaces by AFM. Higher tip voltages resulted in wider and thicker oxide lines and faster writing speeds led to thinner lines, however there appeared to be minimum threshold conditions for nano-oxidation to take place. In the scale range studied, the resolution appeared not to be set by intrinsic sharpness of AFM tips, but probably related to local humidity though it remains to be a future work to clarify the mechanism.

References

- [1] Yano K, Ishii T, Sano T, Mine T, Murai F and Seki K 1996 *Proc. IEEE Int. Solid-State Circuits Conf.*, p. 266
- [2] Sakaki H 1992 *Surf. Sci.* 267 623
- [3] Drexler H, Leonard D, Hansen W, Kotthaus J P and Petroff P M 1994 *Phys. Rev. Lett.* 73 2252
- [4] Shimbo B N, Harris, Jr. J S, Okada Y, Komarov S and Vartanian B J 1996 *MRS Symp. Proc.*, 1996 *MRS Spring Meeting, San Francisco*, C5.8
- [5] Dagata J A, Schneir J, Harary H H, Bennett J and Tseng W 1991 *J. Vac. Sci. Technol.* B9 1384
- [6] Lyding J W, Shen T C, Hubacek J S, Tucker J R and Abeln G C 1994 *Appl. Phys. Lett.* 64 2010
- [7] Minne S C, Soh H T, Flueckinger P and Quate C F 1995 *Appl. Phys. Lett.* 66 703
- [8] Campbell P M, Snow E S and McMarr P J 1995 *Appl. Phys. Lett.* 66 1388
- [9] Matsumoto K, Ishii M, Segawa K, Oka Y, Vartanian B J and Harris, Jr. J S 1996 *Appl. Phys. Lett.* 68 34
- [10] Chun Y J, Nakajima S, Okada Y and Kawabe M 1996 *Physica B* 227 299
- [11] Chun Y J, Nakajima S and Kawabe M 1996 *Jpn. J. Appl. Phys.* 35 L1075

Comparison of the Effects of Different Lateral Boundary Conditions on Transport in Resonant Tunneling Diodes

A. T. Hunter and J. N. Schulman

Hughes Research Laboratories, 3011 Malibu Canyon Road, Malibu, CA 90265

Abstract. Small resonant tunneling diodes (RTDs) will be required to achieve high speed with low power dissipation. We have modeled transport in RTDs including lateral boundary conditions, and find that the peak-to-valley-current ratio of small RTDs can be significantly degraded. For an example in which p-type regions were used to restrict the electron current to the central 200 nm of the RTD, the peak-to-valley-current ratio was reduced to 2.8:1 from 26:1 calculated for a large area device. Similar, but smaller, effects were calculated when semi-insulating regions (as might be produced by a damage implant) were used to define the device area.

1. Introduction

The high switching speed and unique functionality of resonant tunneling diodes (RTDs) provides circuit designers with an important tool to increase speed or to reduce device count and power dissipation in high speed analog and digital circuits. RTDs with small lateral dimensions will be required in order to achieve simultaneously high speed and low power dissipation. For large lateral dimensions the problem is essentially one dimensional, and the physics of this situation are well understood. However, for lateral dimensions of the order of 100 nm, while we can safely ignore lateral quantum effects, we can not ignore effects of boundary conditions used to define the device area. We find that for many cases, the peak-to-valley-current ratio of the RTD is significantly degraded by these two dimensional effects. The degree to which the peak-to-valley-current ratio is degraded depends on the method used to limit the tunneling current in the lateral dimension. In this paper, we discuss the procedure used to model these two-dimensional effects, and compare results of the modeling for different approaches to limiting device size.

Our modeling procedure includes effects due to the electrostatic boundary conditions imposed by the method used to define the device dimension. We use a commercial device modeling package[1] essentially to solve the electrostatics problem. This in itself is useful because for many device designs we find that the current densities (even at 10^5 amp-cm $^{-2}$) are low enough that they do not alter the potentials calculated by the program. We calculate the tunneling current across the diode using a physics based parametric formula for the tunneling current[2], which is

$$J = \kappa \cdot \ln \left[\frac{1 + \exp((E_F - E_R + E \cdot w/2)/kT)}{1 + \exp((E_F - E_R - E \cdot w/2)/kT)} \right] \cdot \left[\pi/2 + \tan^{-1}((E_R - E \cdot w/2)/(\Gamma/2)) \right].$$

In this formula, E_F is the Fermi level position, E_R is the resonance position, E is the electric field, w is the barrier width, T is the temperature, Γ is the resonance width, k is Boltzmann's constant, and κ is $(em^* kT\Gamma)/(4\pi^2 \hbar^3)$, where e is the electron charge, m^* is the carrier effective mass, and \hbar is Planck's constant over 2π . The denominator in the log term involves the occupation of states on the collector side of the barrier, and can be set equal to 1 in what follows. While the formula is used to solve a one-dimensional example in the reference, it can be used for the two dimensional case by treating the Fermi-level position and the electric field perpendicular to the barrier at the

emitter edge of the barrier as functions of lateral position. κ and Γ are treated as adjustable parameters. We include tunneling through a second, higher lying, resonance using a similar expression as an approximation for the valley current and beyond. We numerically integrate this expression across the device, using the position dependent electric field and Fermi-level position calculated by the device simulator. This provides us with the total current through the device under the bias conditions used for the simulation. Repeating this procedure for a range of biases, we obtain the current-voltage characteristic of the device.

2. Results

We compared results for several different methods of limiting the lateral current flow. The first approach uses p-type regions[3] outside the collector contact (see Fig. 1). We performed the calculation for the GaAs/AlGaAs material system, but any material system that can be handled by the drift-diffusion simulator can be treated in a similar fashion. The outside part of barrier is then in the depletion region of a p-n junction, and passes no current. The current through the central part of the diode is controlled in the usual way by varying the emitter-collector bias. Figure 2 shows the current as a function of position across the emitter side of the tunneling barrier just below resonance (1.5 v) and well above resonance (2.0 v). Above resonance, the current in the center of the device is very low. However, there is a transition region between the center of the device which is above resonance, and the outside of the device which is below resonance in which a large tunneling current flows. The current in this edge region is responsible for the degradation in the peak-to-valley-current ratio. For this example, the peak-to-valley current ratio was reduced from 26 to 1 in a large area device to 2.8 to 1 for a device with 200 nm between the p-type regions and a 100 nm collector contact.

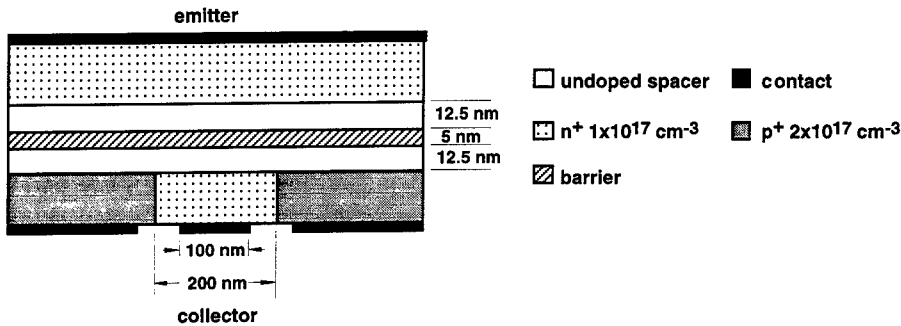


Figure 1: Schematic diagram of a structure in which p-type regions to either side of the collector are used to limit current flow to the central 200 nm of the RTD.

We repeated this calculation for a RTD with similar dimensions in which semi-insulating regions limit current flow at the outside of the device, as would be formed by a damage implant, for example. The device used for the modeling is schematically illustrated in Fig. 3. The p-type material used at the outer edge of the device in Fig. 1 is replaced by semi-insulating material. The semi-insulating regions was assumed to extend through the barrier layer in this case. "High conc." refers to a case with $2 \times 10^{18} \text{ cm}^{-3}$ deep donors compensated by $1 \times 10^{18} \text{ cm}^{-3}$ acceptors, while "low conc." refers to a case with $2 \times 10^{16} \text{ cm}^{-3}$ deep donors and $1 \times 10^{15} \text{ cm}^{-3}$ acceptors. The second case may be unrealistically low for a damage implant, but was investigated to determine the trends expected as the dose is varied, for example. The depth of the donor level below the conduction band was fixed at 0.67 eV, near the middle of the GaAs band gap.

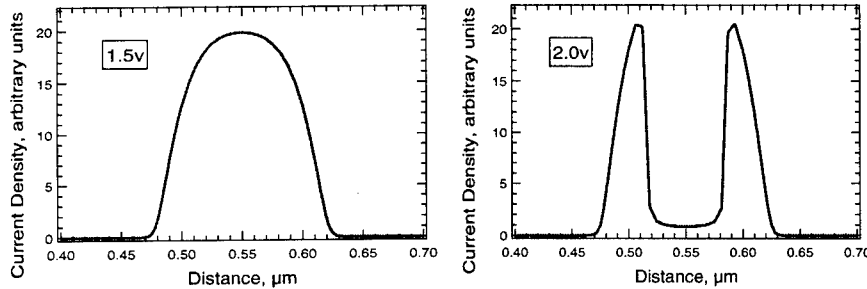


Figure 2: Current density versus lateral position on the emitter side of the tunneling barrier for a bias of 1.5v, just below resonance, and 2.0v, in which the center of the RTD is above resonance, for the structure shown in Fig. 1.

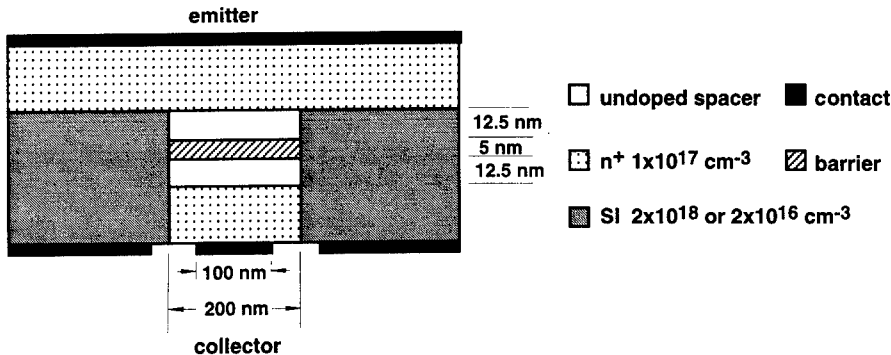


Figure 3: Schematic diagram of a structure in which semi-insulating regions to either side of the collector are used to limit current flow to the central 200 nm of the RTD. Deep level concentrations and compensation in the semi-insulating regions are as described in the text.

We find a qualitatively similar, but smaller effect than for the p-type case. Examination of electric field, carrier concentration, and tunneling current distributions at the emitter side of the barrier show differences between the p-type case and the semi-insulating cases. First, the transition regions are pushed farther out in the semi-insulating cases, so that the fraction of current in the transition region is smaller compared to the current flowing in the middle of the device than for the p-type case. Furthermore, particularly for the high concentration deep level case, the width of the transition regions is thinner. The narrower width of the transition region comes about because the carrier concentration falls off more rapidly in the transition region. These differences are reflected in the calculated peak-to-valley current ratios. Fig. 4 shows current voltage characteristics calculated for the two different semi-insulating cases described above, and compares these curves to one calculated for the p-type case by integrating current distributions like those shown in Fig. 2. In all three cases, the curves were normalized so that the maximum current is set equal to 1. The degradation in peak-to-valley current ratio depends significantly on the method used to limit the current to the center of the diode. We obtain a peak-to-valley current ratio of 6.7 to 1 assuming a high concentration of deep donors compared to 4.4 to 1 for a concentration two orders of magnitude lower. In both of these semi-insulating cases, we obtain a more favorable peak-to-valley current ratio than we did for the p-type case described above, where the ratio was degraded to 2.8 to 1. In all three cases, the peak-to-valley current ratio is substantially lower than

would be predicted for a diode with an area large enough to allow the neglect of transverse boundary conditions.

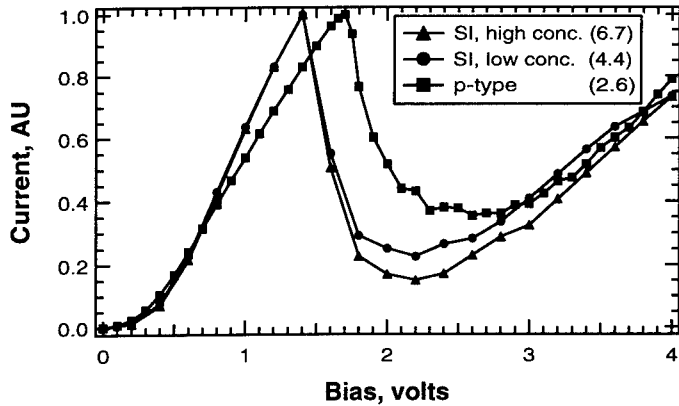


Figure 4: Current through the tunneling diode as a function of applied bias, comparing results for different methods of limiting current flow to the central part of the diode, as described in the text.. The number in the legend shows the peak-to-valley current ratio for each case.

For the high concentration deep level case, the width of the transition region is small enough that some caution must be used in interpreting the results. One concern is that for very small transition widths, we can no longer treat the diode as a parallel collection of short, independent tunneling regions in the lateral directions. At 2.0 volts bias for the high concentration semi-insulating case, the full width at half maximum of the current spike in the transition region is approximately 120 Å, compared to 300 Å for the p-type case. This effect may limit quantitative accuracy for the narrower case, but the calculation should still show qualitative trends. The other concern is more of a practical limitation of the fabrication technique. The modeling assumes an abrupt transition from the undoped spacer to the semi-insulating guard rings in the lateral direction. The transition is more likely to be somewhat smeared out due to lateral straggle of the ion used to create the damage leading to the semi-insulating guard ring. This effect will probably increase the electrical transition region width, which would tend to degrade the peak-to-valley current ratio from the value calculated. The investigation of this effect can be done within the context of our modeling approach.

3. References

- [1] Silvaco Atlas II device modeling framework with the Blaze heterostructure package. Atlas II and Blaze are copyrighted by Silvaco International.
- [2] Schulman J N, De Los Santos H J, and Chow D H 1996 *IEEE Electron Device Lett.* 17 220-222
- [3] Reddy M, Mondry R E, Rodwell M J W, Martin S C, Muller R E, Smith R P, Chow D H, and Schulman J N 1995 *J. Appl. Phys.* 77 4819-4821.

Model of Intra and Extracavity Photodetection for Planar Resonant Cavity Light Emitting Diodes

J. A. Lott and M. J. Noble

Air Force Institute of Technology, Department of Electrical and Computer Engineering
2950 P Street Building 640, Wright-Patterson AFB, Ohio, USA 45433-6583

Abstract. A classical model of spontaneous emission in resonant cavity light emitting diodes is developed. The model is based on a plane wave expansion of a randomly distributed ensemble of noninteracting optical dipole emitter pairs placed within a planar microcavity. The model accounts for losses due to leaky guided modes and intracavity absorption. Given an arbitrary device structure, the model predicts the total power emitted, the radiation pattern, and the relative magnitude of photocurrent generated in an intra or extracavity photodetector. Selected modeling results for an example device emitting at 650 nm are included.

1. Introduction

Conventional resonant cavity light-emitting diodes (RCLEDs) consist of a quantum well (QW) gain region within a planar optical microcavity that is surrounded by distributed Bragg reflector (DBR) mirrors [1]. Many of the performance characteristics of RCLEDs can be derived from intra or extracavity photodetection measurements of spontaneous emission. Intracavity measurements can be accomplished by embedding a resonant cavity *pin* photodetector (PD) within one of the DBRs as shown in Fig. 1. The intracavity PD contains a QW absorbing *i*-layer positioned at a standing wave antinode [2]. A small fraction of the QW emission from the active region is absorbed by the intracavity PD, thus generating a photocurrent. The PD's responsivity depends on several factors including the absorbing *i*-layer's position and the angle of incidence of incoming radiation. In this paper, a classical model of intra and extracavity photodetection of spontaneous emission in RCLEDs is developed. Selected modeling results for an example RCLED emitting at 650 nm are included.

2. Classical Spontaneous Emission Model

A schematic diagram of a planar RCLED is shown in Fig. 2. The spontaneous emission from the QW active layer is modeled by coupling a pair of crossed dipoles to the vacuum field plane wave modes modified by the Fabry-Perot cavity [3-4]. Since the electric field for QW emitters predominantly lies within the x-y horizontal plane, the z-axis dipole components are neglected. The irradiance (I_r) due to a single crossed pair of optical dipoles (with equal strength) oriented along the x- and y-axes is

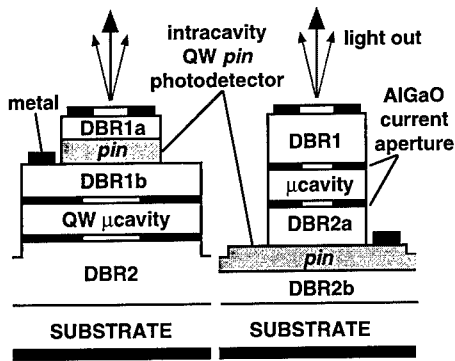


Fig. 1. Microcavity emitters with intracavity detectors.

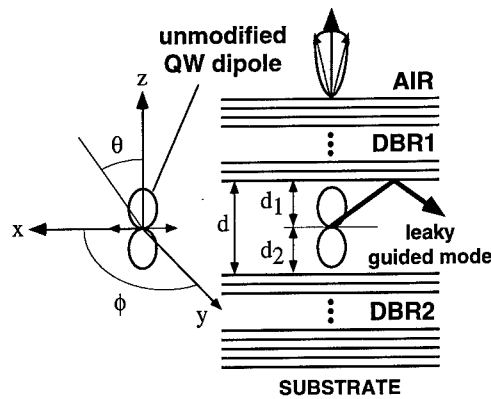


Fig. 2. Model of an optical dipole source in a microcavity.

$$I_{rx} + I_{ry} = I_r = \frac{CE_{xy}^2}{r^2} \begin{cases} \cos^2\theta & \hat{\theta} \text{ p-wave} \\ 1 & \hat{\phi} \text{ s-wave} \end{cases} \quad (Watt/m^2) \quad (1)$$

The term $CE_{xy}^2 = \eta_o P_o^2 \omega^4 n_{cav} / 32\pi^2 c^2$ (Watt); P_o (Coulomb-m) is the magnitude of the time varying dipole moment; $2\pi/\lambda_o = \omega/c$ is the wave number; and $\eta_o = 1/c\epsilon_o$ is the impedance of free space. The term E_{xy}^2 is the modified field intensity of the dipole moments for dipoles oriented along the x- and y-axes. The exact angular orientation of the dipole pair within the x-y plane is arbitrary due to rotational symmetry about the z-axis. For emission directed toward the top DBR1, the value of E_{xy}^2 within the microcavity is

$$E_{xy}^2 = E_o^2 \frac{T_1 \left[e^{2\zeta_1} + 2\sqrt{R_2} \cos\left(\delta_2 + \frac{4\pi n_{cav}}{\lambda} d_2 \cos\theta\right) e^{2\zeta} + R_2 e^{2(\zeta+\zeta_2)} \right]}{\left[1 - 2\sqrt{R_1 R_2} \cos\left(\delta_1 + \delta_2 + \frac{4\pi n_{cav}}{\lambda} d \cos\theta\right) e^{2\zeta} + R_1 R_2 e^{4\zeta} \right]} \quad (2)$$

where E_o^2 is the vacuum field intensity of the dipole moment at the origin ($r = 0$); T_1 is the power transmittance of DBR1; $R_1(R_2)$ is the power reflectance of DBR1(DBR2); $\delta_1(\delta_2)$ is the reflectivity phase of DBR1(DBR2); d is the thickness of the optical cavity ($d = d_1 + d_2$); $d_1(d_2)$ is the position of the QW dipole relative to DBR1(DBR2); n_{cav} is the real refractive index of the optical microcavity; and θ is the dipole emission angle referenced to the z-axis.

The values of T , R , and δ are determined by using the 2×2 characteristic matrix formalism for thin films and including absorption [5]. If the subscripts 1 and 2 are interchanged, then Eq. 2 gives the field intensity directed toward DBR2 for a given angle off normal and a given dipole emission wavelength. The exponential terms in Eq. 2 account for absorption in the cavity, where $\zeta_1 = -\alpha d_1$, $\zeta_2 = -\alpha d_2$, and $\zeta = -\alpha d$. The term α (cm^{-1}) is the cavity absorption constant.

The power radiated (P_{rad}) out of a DBR within an area dA defined by critical angles θ_{cp} and $\theta_{\text{cs}} \leq \pi/2$ radians, relative to the z-axis is

$$P_{\text{rad}} = \int_0^{2\pi} \int_0^{\theta_{\text{cp}}} I_r \cdot r^2 \sin\theta d\theta d\phi = C \left[\int_0^{2\pi} d\phi \int_0^{\theta_{\text{cp}}} E_{xy}^2 \cos^2\theta \sin\theta d\theta + \int_0^{2\pi} d\phi \int_0^{\theta_{\text{cs}}} E_{xy}^2 \sin\theta d\theta \right] \text{ (Watt)} \quad (3)$$

The radiation intensity $U(\theta)$ is

$$U(\theta) = \frac{dP_{\text{rad}}}{d\Omega} = I_r \cdot r^2 = C \begin{cases} E_{xy}^2 \cos^2\theta & \text{p-wave} \\ E_{xy}^2 & \text{s-wave} \end{cases} \text{ (Watt/steradian)} \quad (4)$$

where $d\Omega = dA/r^2 = \sin\theta d\theta d\phi$. The values of P_{rad} and $U(\theta)$ in Eqs 3 and 4 are for a single wavelength. The QW emitter is modeled as an ensemble of noninteracting dipole pairs. The dipole pairs have a wavelength distribution with a weighted emission intensity given by a normalized function $f(\lambda)$. The total P_{rad} and $U(\theta)$ are found by numerical integration over the full range of possible emission wavelengths. The intracavity photocurrent due to spontaneous emission follows as $I_{\text{det}} = (\eta q/\hbar\omega)\Delta P_{\text{rad}}$, where η is quantum efficiency and ΔP_{rad} is the amount of power absorbed in the PD's i-layer. This differential power is obtained numerically when solving Eq. 3 for a given RCLED structure.

3. Example Numerical Results

Consider an example RCLED designed for peak emission at 650 nm. The device contains a 20.5 period bottom and a 10 period top $\text{Al}_{0.5}\text{Ga}_{0.5}\text{As}/\text{Al}_{0.92}\text{Ga}_{0.08}\text{As}$ DBR surrounding a 1λ -thick $(\text{Al}_{0.5}\text{Ga}_{0.5})_{0.5}\text{In}_{0.5}\text{P}$ optical microcavity, all on a GaAs substrate. One InGaP QW is centered ($d_1 = d_2$) in the microcavity.

The calculated $U(\theta)$ for a single 650 nm dipole pair with $\alpha = 0$ (dark solid line) and 10^4 cm^{-1} (dotted line) is shown in Fig. 3. For reference, the thin solid line is the $U(\theta)$ for emission without the DBRs. The radiation intensity is enhanced or inhibited when above or below this reference line, respectively. The critical angle for emission toward DBR1 occurs near 17° . Above this angle, the radiation intensity forms a leaky guided mode propagating laterally away from the dipoles. A strongly guided mode occurs near $\theta = 88^\circ$ if $\alpha = 0$. Realistically the QW and optical cavity material absorb the lateral radiation ($\alpha > 0$), reducing the intensity of the guided mode.

A polar plot of $U(\theta)$ (within the RCLED's microcavity) due to an ensemble of dipole pairs with weighted intensity is shown in Fig. 4. The normalized weighting function is also shown. A single primary lobe directed toward DBR1 is centered on $\theta = 0^\circ$. A more complicated pattern of lower peak intensity is directed toward DBR2 due in part to contributions from the leaky guided mode.

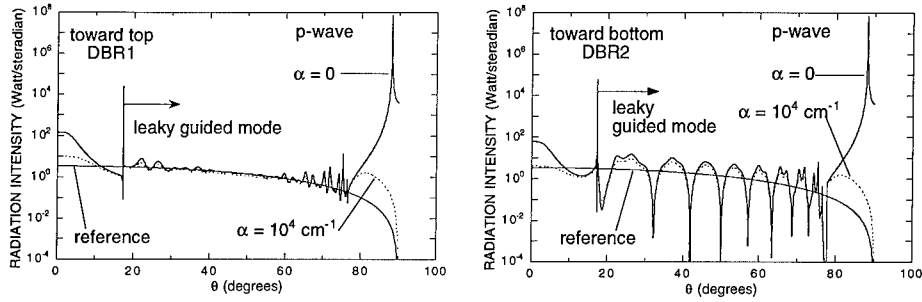


Fig. 3. Calculated $U(\theta)$ for the 650 nm RCLED for single dipole pair emission at 650 nm.

An intracavity PD with a 6 nm-thick GaAs absorbing i-layer is placed within DBR1 as in Fig. 1 [2]. The PD is 0.75λ -thick and replaces one of the high index $\text{Al}_{0.5}\text{Ga}_{0.5}\text{As}$ DBR layers. The total number of periods in DBR1 (DBR1a + DBR1b) is constant. Figure 5 shows the calculated intracavity photocurrent due to weighted 640, 645, and 650 nm dipole pairs, against the position of the PD within DBR1. The photocurrent due to the 645 nm dipole exceeds that due to the 650 nm dipole, even though the 645 nm dipole strength is about 0.58 times that of the 650 nm dipole. This is because P_{rad} goes through a maximum at an angle off normal where the resonant wavelength is shorter than 650 nm. Also, the i-layer absorption constant increases as the wavelength decreases. The magnitude of photocurrent decreases as the intracavity PD is placed further away from the QW because the standing wave field intensity decreases as it penetrates into a DBR.

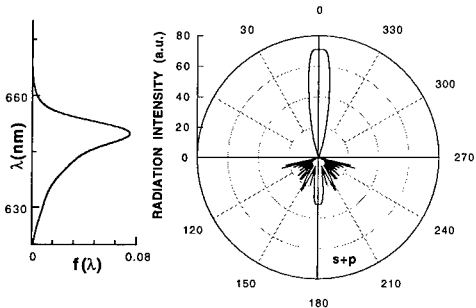


Fig.4. Calculated total $U(\theta)$ for an ensemble dipole source.
Side: normalized weighted dipole function $f(\lambda)$.

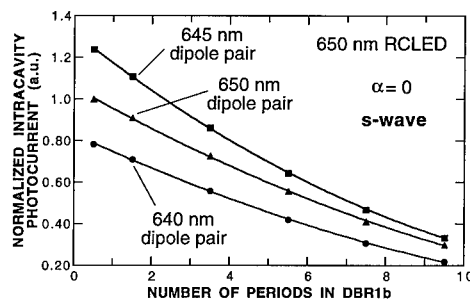


Fig.5. Calculated I_{det} for 640, 645, and 650 dipole pairs
against intracavity photodetector position.

References

- [1] De Neve H, Blondelle J, Van Daele P, Demeester P, and Baets R 1997 *Applied Physics Letters* 70(7) 799-801
- [2] Lott J A 1997 *Electronics Letters* 33(11) 955-957
- [3] Yamamoto Y, Machida S, and Björk G 1992 *Optical and Quantum Electronics* 24 S215-S243
- [4] Lei C, Huang Z, Deppe D G, Pinzone C J, and Dupuis R D 1993 *Journal of Applied Physics* 73(6) 2700-2704
- [5] MacLeod H A 1989 *Thin-Film Optical Filters*, 2nd ed. (New York: McGraw-Hill)

Photoluminescence study of the self-organized InAs/GaAs quantum dots grown by gas source molecular beam epitaxy

Ming-Chin Chen and Hao-Hsiung Lin

Room 419, Department of Electrical Engineering,
National Taiwan University, Taipei, Taiwan, R. O. C.

Abstract. Self-organized InAs quantum dots (QDs) grown on both (100) exact and (100) misoriented 7° toward (110) GaAs substrates using gas source molecular beam epitaxy (GSMBE) with V/III ratio ranging from 1.1 to 20 have been studied by photoluminescence (PL) measurements from 8.5 to 300 K. The QD structures grown on the misoriented substrates show a better uniformity than those grown on the exact substrates at the same growth conditions. Effects of AsH₃ flow rate on the PL intensity, peak energy and linewidth for QDs grown on both types of substrates are presented. Basically, higher AsH₃ flow rate gives higher PL intensity at 8.5 K. At room temperature(300K), on the contrary, lower AsH₃ flow rate results in higher PL intensity. The study of thermal quenching energy reveals that the larger the dot size the better the PL intensity at 300K.

1. Introduction

Recently, strain-induced In(Ga)As/GaAs QDs have been intensely studied because these QDs show an efficient carrier confinement which can be used for the realization of novel optoelectronic devices like quantum dot lasers. Such QD lasers with low threshold current density and high characteristics temperature (T_0) have been demonstrated [1]. For practical applications in optoelectronic devices, QD structures with high density and good uniformity are necessary to achieve the desired active volume. There are several groups [2,3,4] making great efforts on the conditions during the growth to improve the optical properties for QDs. The growth conditions include substrate temperature, V/III ratio, InAs growth rate and substrate orientation. Recent study on the effect of substrate orientation [3] shows that the QDs grown on (711)B substrate have better quantum efficiency than those on (511)B and (100) substrates. It implies that a slight misorientation for (100) substrate may improve the uniformity of the QDs. In this study, the QD structures are grown by using GSMBE at various V/III ratio

Table 1. Substrate orientation, AsH₃ flow rate, V/III ratio, thermal quenching energy and activation energy for all QDs samples.

Sample	Substrate orientation	AsH ₃ flow rate (SCCM)	V/III ratio	Thermal quenching energy (meV)	Activation energy (meV)
C490A	(100) exact	0.08	1.1	14	108
C491A	(100) exact	0.15	2	16	91
C492A	(100) exact	0.37	5	15	126
C493A	(100) exact	0.74	10	13	156
C494A	(100) exact	1.50	20	16	96
C490B	misoriented	0.08	1.1	14	71
C491B	misoriented	0.15	2	15	48
C492B	misoriented	0.37	5	13	108
C493B	misoriented	0.74	10	12	130
C494B	misoriented	1.50	20	13	103

during the growth of InAs layer. Exact and misoriented (100) GaAs substrates are also used to study the orientation effect.

2. Experiments

Ten QD samples were grown by using a VG V80H GSMBE system in this study. The growth procedure included a 200 nm thick buffer layer grown at 620°C, an InAs layer deposited with a nominal thickness of 3 monolayers at 490°C, a 10 nm GaAs layer grown at 490°C to avoid the In segregation, and a 40nm GaAs capping layer grown at 620°C. The growth rate was 0.09 ML/s and the V/III ratio during the growth of InAs layer was changed from 1.1 to 20 for various samples. For comparison, exact (100) (samples C490A-C494A) and (100) with 7° off-cut to (110) (samples C490B-C494B) semi-insulating GaAs substrates were used. In order to have the same growth conditions, they were mounted side by side on the same substrate holder. The AsH₃ flow rates and V/III ratio of these samples were listed in Table 1. After growth, PL measurements were performed from 8.5 to 300 K to probe the quality of the QD structures.

3. Results and Discussions

Fig.1(a), (b), and (c) show the 8.5 K PL peak energy, intensity and full width at half-maximum (FWHM) as a function of AsH₃ flow rate, respectively. From Fig.1(a), we can see that QDs grown on the vicinal plane have higher peak energy, which indicates they are with smaller size. Takayoshi et al. [5] reported a thicker critical thickness for InAs grown on (111) GaAs substrate. From their finding, InAs grown on misoriented (100) GaAs substrates is also expected to have thicker critical thickness as well. The smaller QD size for these misoriented samples resulted from their thicker wetting layer.

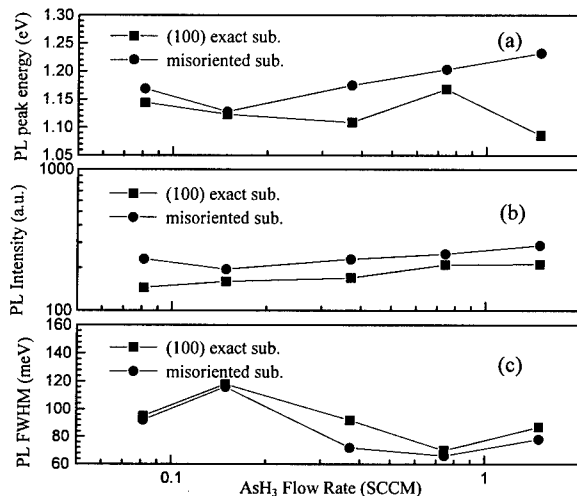


Fig.1. Spectra of the 8.5 K PL peak energy (a), intensity (b) and FWHM as a function of AsH₃ flow rate.

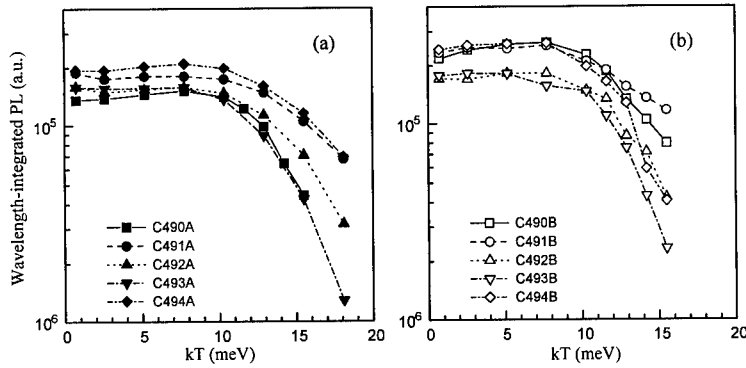


Fig. 2. Wavelength-integrated PL intensity as a function of thermal energy, kT , for QDs grown on the exact (a) and misoriented (b) substrates.

The PL peak energy of QDs grown on the vicinal surface increases with the increase of the V/III ratio. This phenomena is not found for the QDs grown on the exact substrates. A monotonously red-shift of PL peak, which implies the QD size increasing, with decreasing V/III ratio is shown in Fig. 1(a). It may be attributed to the increase of the In adatom migration length with decreasing As₂ pressure under As-stabilized circumstance. There is an abnormal increasing of the PL peak energy when V/III ratio reduced to 1.1. In this condition, the growth circumstance of InAs may change from As-stabilized to In-stabilized, and the critical thickness of InAs is thus greatly enhanced [6]. The increase of the wetting layer thickness will result in the small dot size and the high PL peak energy. As shown in Fig. 1(b), PL intensity is enhanced when AsH₃ flow rate increases. This trend is for QDs grown on both types of substrates. The increase of AsH₃ flow rate will limit the migration length of In adatom and enhance the dot density, which is believed to be the origin of the PL intensity enhancement. As can be seen in Fig.1(b) and (c), the QDs grown on the misoriented substrates have smaller PL linewidth and stronger PL intensity than those grown on the exact substrates. It indicates that the QDs grown on

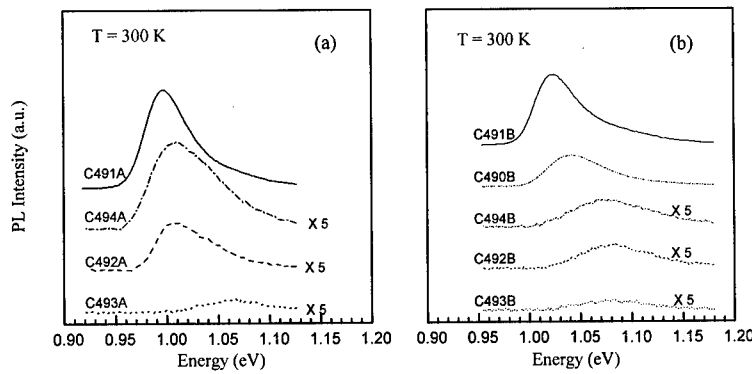


Fig. 3. The PL spectra at 300 K of the QDs grown on the exact (a) and vicinal (b) (100) GaAs substrates.

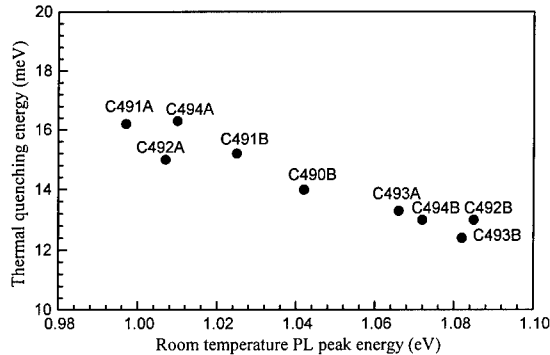


Fig. 4. Plots of the thermal quenching energy as a function of the room temperature (300 K) PL peak energy.

the misoriented substrates have better uniformity and higher dot density. Wavelength-integrated PL intensity as a function of thermal energy, kT , for QDs grown on the exact and misoriented substrates are shown in Fig. 2(a) and (b), respectively. As can be seen, QDs grown on the misoriented substrates have stronger PL intensities as temperature change from 8.5 to 120 K. However, when temperature is higher than 120 K, the PL intensities degrade faster than those of grown on the exact substrates. This phenomenon is especially noticeable for C492B, C493B and C494B. From these plots, the thermal quenching energy and the activation energy from exciton level to nonradiative level are determined and summarized in Table 1. The PL spectra at 300 K of the QDs grown on the exact and vicinal substrates are shown in Fig. 3(a) and (b), respectively. It is found the QDs grown at a V/III ratio of 2 showing the strongest PL intensity for both types of substrates, which is attributed to the largest dot size under this As-stabilized circumstance. The spectrum of C490A is not shown in the figure because its PL intensity is too weak to be available. Fig. 4 plots the thermal quenching energy as a function of the room temperature PL peak energy. It is found that the thermal quenching energy is increasing with the decreasing 300 K PL peak energy, which indicates that the larger the dot size the better the optical property at 300 K.

4. Conclusions

Self-organized InAs QDs grown on both (100) exact and misoriented 7° toward (110) GaAs substrates by using GSMBE with different V/III ratio are characterized by PL measurements. The QDs grown on the misoriented substrates show narrower PL linewidths and stronger intensities at the same growth conditions, which implies that they are with good uniformity. Low temperature PL intensities increase with AsH_3 flow rates for QDs grown on both two types of substrates at As-stabilized circumstance, which is attributed to the dot density increasing with the As_2 pressure. The samples grown at a V/III ratio of 2 show the best PL characteristics at 300 K. The study of thermal quenching energy reveals that the larger the dot size the better the PL intensity at 300 K.

References:

- [1] N. Kirstaedter et.al. 1994 *Electron. Lett.* 30 1416-7
- [2] D. Bimberg et.al. 1996 *Phys. Stat. Sol. (b)* 194 159-73.
- [3] D. I. Lubyshev et.al. 1996 *J. Vac. Sci. Technol. B* 14 2212-15
- [4] A. Madhukar et.al. 1994 *Appl. Phys. Lett.* 64 2727-9
- [5] Takayoshi Anan et.al. 1992 *Appl. Phys. Lett.* 60 3159-61
- [6] E. Tournie and K. H. Ploog 1994 *J. Cryst. Growth* 135 97-112

Resonant Interband Tunneling Through Multiple Subbands in an InAs/AlSb/GaSb Interband Tunneling Structure

J.L. Huber, M.A. Reed, Yale University; G. Kramer, H. Goronkin, Motorola, PCRL

Abstract— The magnetotunneling characteristics of a p-type well InAs/AlSb/GaSb resonant interband tunneling structure are investigated. Experimental results indicate that tunneling occurs through multiple subbands, including both light-hole and heavy-hole like subbands. The data can be used to plot out critical points on the GaSb subband structure.

I. INTRODUCTION

Most Resonant Tunneling Diodes (RTDs) involve carrier transport in either the conduction or valence band, but not both. Resonant Interband Tunneling (RIT) devices differ from conventional RTDs in that the confined states, accessible to electron (or hole) transport lie in the valence (or conduction) band rather than the conduction band [1], [2]. A single well resonant interband tunneling structure was first demonstrated by Soderstrom et al. [2].

Because of the opposite sense of the dispersions of the conduction and valence band, and the existence of both light- and heavy-hole subbands, the tunneling process is expected to be somewhat more complicated in an RIT structure than an RTD because of the multiple subbands involved. The dominant tunneling mechanism is coupling between the electron and light-hole states. However, detailed treatment by Ting et al. demonstrated that not only can there be significant contributions to the transmission coefficient from the heavy-hole band for $k_{\parallel} \neq 0$ [3], but that there can be significant contribution to the I(V) characteristics including additional transmission resonances [4]. Studies involving polytype interband tunneling structures have shown evidence supporting this idea [5], [6].

Measurements from a GaSb/AlSb/InAs/AlSb/GaSb tunneling structure with an applied magnetic field have shown to result in I(V) characteristics similar to that of intraband tunneling structures [7]. However, for this case, there is only a single quantized band (i.e. the conduction band). For a structure with a GaSb well, the valence band is accessible to interband tunneling so more than one quantized band will be involved, resulting in additional structure in the I(V) characteristics. Evidence for this has been reported for a polytype GaSb/AlSb/GaSb/AlSb/InAs structure [5] and for a homotype InAs/AlSb/GaSb/AlSb/InAs structure [8]. However, in these cases, the field was only applied parallel to the confining interfaces.

This paper describes experiments on a homotype (InAs/AlSb/GaSb/AlSb/InAs) structure which show evidence of interband through multiple subbands at $k_{\parallel} \neq 0$. A magnetic field applied to the tunneling structure will mod-

ify the subband structure in the well, and therefore, the transmission characteristics, with different effects occurring depending on the field orientation. These effects make it possible to experimentally determine critical points in the subband structure. The experimental data is superimposed on the approximate subband structure of the GaSb well showing good agreement with calculated results.

II. THEORY

Resonant tunneling can be modeled using a simple density of states argument first proposed by Luryi [9] and expanded on by Ohno [10]. A general expression for tunneling current density can be written as

$$J(E) = q \int N(\mathbf{k}) v(\mathbf{k}) T(E, \mathbf{k}) d\mathbf{k} \quad (1)$$

where $N(\mathbf{k})$ is the density of carriers available for tunneling, $v(\mathbf{k})$ is the carrier velocity, and $T(E, \mathbf{k})$ is the transmission coefficient through a plane in space perpendicular to the current direction. In (1), the term $T(E, \mathbf{k})$ contains, in effect, all the information about the quantum well.

For a 2DEG with no applied field, momentum states are uniformly distributed over k_x and k_y , as shown in Figure 1a, leading to a constant density of states and therefore, no specific dependence of T on \mathbf{k} .

With the application of a magnetic field perpendicular to the 2DEG, the allowed momentum states are constrained to concentric circles of constant radius as shown in Figure 1b, which results in a series of discrete Landau levels. The corresponding Energy vs k_{\parallel} curve is no longer continuous. Ideally, the 2DEG will now only take on discrete values of k_{\parallel} ; however, in a real system there will be both broadening associated with each level, and localized states so the density of states will be as shown in Figure 1c.

The magnetic field effects can be taken into account mathematically in (1) by adding a k_{\parallel} dependent term to the transmission coefficient. For simplicity, this was chosen to be

$$T(k_{\parallel}) = T_b + T_l(k_{\parallel}) \quad (2)$$

$$T_l(k_{\parallel}) = \begin{cases} T_{lo} & (k_{\parallel n}^2 - \Gamma_l)^{1/2} < k_{\parallel} < (k_{\parallel n}^2 + \Gamma_l)^{1/2} \\ 0 & \text{otherwise} \end{cases} \quad (3)$$

where T_b is the background transmission coefficient related to either localized states or Landau level broadening, T_{lo} is the transmission coefficient for a Landau level and Γ_l is the energy broadening associated with each Landau level.

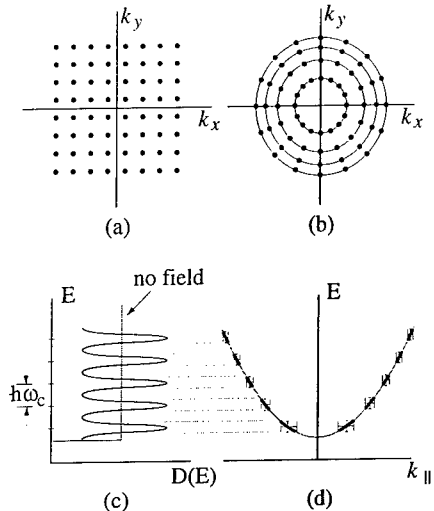


Fig. 1. Effects of a magnetic field applied perpendicular to a 2DEG system. (a) Allowed momentum states for a two dimensional electron gas with no applied magnetic field. The states are evenly spaced in both k_x and k_y . (b) With a magnetic field applied perpendicular to a 2DEG electron gas. Allowed states lie on concentric circles of constant radius $k^2 = (2qB/\hbar)(n + 1/2)$. An equal number of states lie on each circle. (c) Density of states for no applied field (gray line) and applied field (dark line). The effects of broadening are shown. (d) The gray curve corresponds to Energy vs k_{\parallel} for a 2DEG with no applied field. The dark segments correspond to energies where the density of states is greater than that of the no field case.

In Figure 1d, the gray curve is what is expected for the no-field case. The thick segments represent the spread of the energies where the density of states is greater than that for the no field case in Figure 1c. Because of this, fluctuations in the I(V) characteristics will occur as a function of applied magnetic field as the number of electrons able to conserve both energy and k_{\parallel} changes [11].

A 2DEG is only collapsed into Landau levels when the magnetic field is applied perpendicular to the confining interfaces. When the field is applied parallel to the interfaces, no such effect occurs. The only first order perturbation to the emitter electron population is an extra component of k_{\parallel} given by

$$\Delta k_{\parallel} = \frac{qB\Delta l}{\hbar} \quad (4)$$

while the electron energy distribution remains the same [12]. The result of this is a change in the threshold voltage for the turn-on of tunneling current for some particular band. Because of the opposite polarity of the emitter and well, the initial current flow involves carriers located away from $k_{\parallel} = 0$. By varying the strength of the field, E_{th} will map out that portion of the dispersion curve

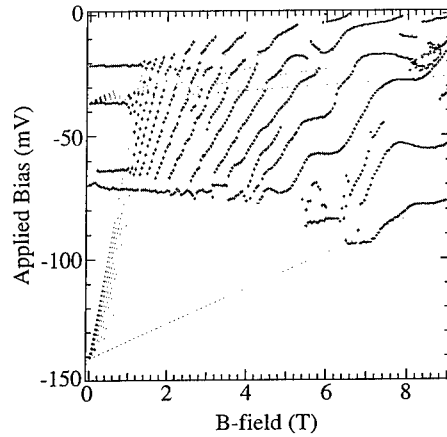


Fig. 2. Fan diagram from second derivative of the I(V) characteristics with $B \parallel I$. The two sets of dashed lines are fit to the structure. The fan converging to -36 mV corresponds to structure from HH1, while the fan converging to -141 mV corresponds to structure from LH1. The slopes are given by nm where n is an integer and $m = 0.01$ for HH1, and $m = 0.065$ for LH1

III. EXPERIMENTAL RESULTS

Measurements were done on a single p-type well InAs/AlSb/GaSb/AlSb/InAs interband tunneling structure with asymmetric barriers. The GaSb well thickness was 6.5 nm while the AlSb barriers were 2.5 nm and 1.5 nm thick. The device was a mesa structure with a diameter of 15 μm . Electrical measurements were carried out at 1.4 K. Maximum resolution for the field steps with the measurement setup used was 500 Gauss. I(V) sweeps were obtained from a 4-point measurement. All measurements described here are from reverse bias measurements defined as electrons initially tunneling through the 2.5 nm barrier which correspond to negative values of current.

Structure in the I(V) characteristics resulting from the magnetic field will appear as peaks, or shoulders in the data. Fan diagrams from peaks in the second derivative of the data are plotted versus the applied magnetic field. There is no physical significance to the second derivative in the sense that the first derivative represents the conductance, but this method allows for more accurate determination of shoulder positions.

A fan diagram generated from the I(V) data with $B \parallel I$ is shown in Figure 2. Each point in the diagram is a positive peak in the second derivative of each I(V) trace, which for negative values of current correspond to either a peak or a shoulder in the current magnitude. For biases larger than -70 mV, the device is in oscillation and no useful information occurs.

The fan diagram has B -field dependent structure that is immediately apparent. To first order, it is expected to move to lower bias with increasing magnetic field, converg-

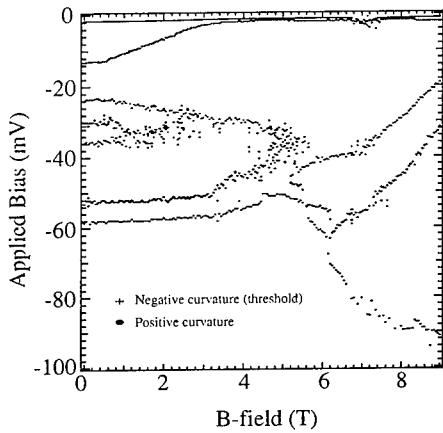


Fig. 3. Fan diagram from the second derivative of the $I(V)$ characteristics with $B \perp I$. Both positive and negative peaks in the second derivative are shown.

ing to a single point at zero field, with spacing between points to increase linearly with increasing field [7]. Using these assumptions, two distinct fans (before the oscillation region) can be drawn. The first converges to -141 mV with slopes given by $m \times 0.065 \text{ V/T}$ and the second converges to -36 mV with slopes given by $m \times 0.01 \text{ V/T}$ where m is an integer.

The fan diagram generated from $I(V)$ data with $B \perp I$ is shown in Figure 3. Points from both negative and positive curvatures are shown with the positive peaks corresponding to current magnitude maxima, while the negative peaks correspond to current magnitude minima.

The fan diagram shows two notable features. The first is a current minima at -13 mV which monotonically decreases to lower bias with increasing magnetic field. This initial minima indicates a current threshold occurring at the initial current increase. The positive peak at -2 mV is related to the experimental setup. The second is related to the positive peak which occurs at -58 mV at zero field. This is the main current peak occurring just before the main NDR. Starting about 5 T, there is a distinct change in the behavior of this peak. The single peak splits into two, with one, which is still the peak just before the main NDR, sharply increasing in bias with increasing field while a second shifts to lower bias, reaching -20 mV at 9 T. This behavior is similar to that seen by Marquardt et al. [8].

IV. DISCUSSION

The well subband structure was estimated by using extrapolated data from structures with similar well thickness, published by Marquardt et. al. [8]. The estimated subband structure, shown in Figure 4 for a 6.5 nm well is obtained by linearly extrapolating the calculated structure from a 7 nm and an 8 nm well. The obtained curves are the solid

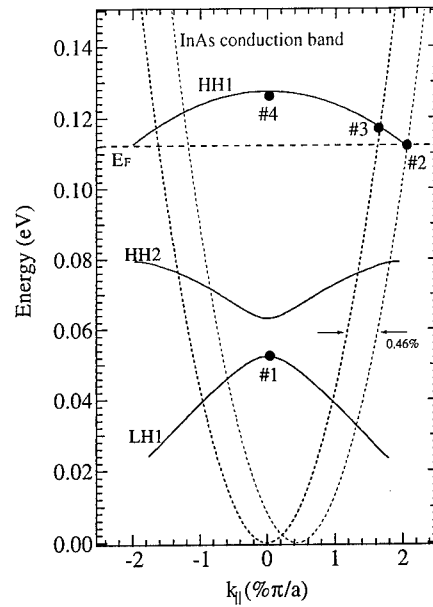


Fig. 4. Estimated parallel subband structure with experimentally determined critical points. The heavy dashed curve indicates the extent of occupied states in the emitter. The light dashed curve indicates the offset obtained by the application of a magnetic field parallel to the confining interfaces such that the current threshold moves to zero bias. For GaSb, the lattice constant $a = 0.6096 \text{ nm}$.

lines labeled HH1, HH2 and LH1. HH1 is the lowest index heavy-hole like subband, LH1 is the lowest indexed light-hole like subband. The dashed curve centered at 0 on the x -axis represents the boundary E vs k_{\parallel} dispersion for electrons in the emitter. The zero energy point is taken to be the bottom of the InAs conduction band. Electrons occupy those states from $k_{\parallel} = 0$ out to the dashed line for energies up to the Fermi energy. This discussion will make the initial assumption that the Fermi level lies below the intersection of HH1 and the boundary of the occupied k_{\parallel} states in the emitter. This assumption will later be shown to be consistent with the experimental data.

As the allowed values of k_{\parallel} (and therefore, the density of states), for the different subbands are quantized by the application of $B \parallel I$, a series of fluctuations in the $I(V)$ characteristics occur as the number of electrons able to conserve both energy and momentum changes. The fluctuation positions plotted vs B -field results in the demonstrated fan like structure, with the fan converging to a single point at zero-field.

Given the position of the Fermi level, the two fans in Figure 2 arise from two different mechanisms. The zero-field point at -36 mV occurs when the $k_{\parallel} = 0$ point of HH1

crosses the Fermi energy. The zero-field point at -141 mV occurs when the $k_{\parallel} = 0$ point for LH1 passes the bottom of the InAs conduction band. While theoretically there should also be a fan resulting from HH1 crossing the bottom of the InAs conduction band, it will be much weaker due to the relative transmission coefficient magnitudes between HH1 and LH1 [4] and is not resolvable or occurs in the oscillation region.

Using this simple picture, a number of critical points on the GaSb subband structure can be determined. The points are shown, superimposed on the subband structure in Figure 4. The size of the markers indicating these points are consistent with the experimental error of ± 2 mV.

The voltage of the LH1 zero-field point can be related to the subband energy by a conversion factor α with units of eV/V. This energy corresponds to Point #1 on Figure 4. The zero-field voltage of this point is -141 mV, and the estimated value of the zone center of LH1 is -53 meV, giving $\alpha = 0.38$.

Application of a magnetic field parallel to the confined well ($B \perp I$) results in a shift in k_{\parallel} for the emitter electrons according to (4). This shift is illustrated by the thin dotted curve offset from 0 on the x -axis in Figure 4. Given the position of the Fermi energy, at low biases, emitter electrons cannot tunnel into the unoccupied well states because of conservation of momentum [11]. This condition can occur by either shifting the emitter electron distribution in energy with an applied bias, or shifting the distribution with an applied magnetic field.

Once this occurs, by either method, or a combination of both, there will be a turn-on threshold in the I(V) characteristics as the new conduction channel is opened. This behavior can be seen in Figure 3 with the negative curvature peak that starts at -13 mV and moves to zero bias at 3.5 T. Given the emitter electron distribution and the curvature of HH1, this can be used to estimate the Fermi level by noting the value of magnetic field where the threshold goes to zero bias.

The quantity Δl in (4) is the average distance traveled by an electron while it is tunneling from the emitter to the well. The final position is assumed to be the center of the well, and the initial position is taken to be the position of the maximum of the electron accumulation layer in the emitter [12]. Using a self-consistent Poisson solver, this is estimated to be 5 nm, giving $\Delta l = 5 + 2.5 + 3.3 = 10.8$ nm. This gives the shift of $\Delta k_{\parallel} = 0.46\%(\pi/a)$ indicated in Figure 4 and allows the placement of the Fermi level at $E_F = 0.112$ eV, indicated by Point #2.

Given the determined Fermi energy the zero-field threshold should occur at an energy shift of 0.005 eV, indicated by Point #3. Using $\alpha = 0.38$ the zero-field threshold should occur at -13 mV, which is where it occurs in Figure 3. The zero-field point of the HH1 fan (Figure 2 corresponds to the top of HH1 crossing the Fermi level. This occurs at -36 mV. Again, using $\alpha = 0.38$, this gives the top of HH1 to be at 0.126 eV, indicated by Point #4.

V. CONCLUSIONS

A single GaSb well interband tunneling structure has been studied using magnetotransport to probe the subband structure of the well. Critical points in the results were extracted then compared to the approximate calculated electronic subband dispersion. By selecting the appropriate alpha (meV/mV) good agreement with the calculated results is achieved. This is a good validation of the fact that multiple subbands at $k_{\parallel} \neq 0$ are involved in the tunneling process.

REFERENCES

- [1] L.F. Luo, R. Beresford, and W.I. Wang. Interband tunneling in polytype GaSb/AlSb/InAs heterostructures. *Appl. Phys. Lett.*, 55:2023–2025, 1989.
- [2] J.R. Soderstrom, D.H. Chow, and T.C. McGill. A new negative differential resistance device based on resonant interband tunneling. *Appl. Phys. Lett.*, 55:1094–1096, 1989.
- [3] D.Z.-Y. Ting, E.T. Yu, and T.C. McGill. Role of heavy-hole states in interband tunneling structures. *Appl. Phys. Lett.*, 58:292–294, 1991.
- [4] D.Z.-Y. Ting, E.T. Yu, and T.C. McGill. Multiband treatment of quantum transport in interband tunnel devices. *Phys. Rev. B*, 45:3583–3592, 1992.
- [5] A. Nogaret, et al. Interband tunneling through a heavy hole state. *J. Appl. Phys.*, 74:6443–6445, 1993.
- [6] M.H. Liu, Y.H. Wang, M.P. Hwang, J.F. Chen, and A.Y. Cho. The low-temperature characteristics of GaSb/AlSb/InAs/GaSb/AlSb/InAs broken-gap interband tunneling structures. *Jpn. J. Appl. Phys., Part 1*, 35:1178–1183, 1996.
- [7] E.E. Mendez, H. Ohno, L. Esaki, and W.I. Wang. Resonant interband tunneling via Landau levels in polytype heterostructures. *Phys. Rev. B*, 43:5196–5199, 1991.
- [8] R.R. Marquardt, D.A. Collins, Y.X. Liu, D.Z.-Y. Ting, and T.C. McGill. Resonant magnetotunneling spectroscopy of p-type-well interband tunneling diodes. *Phys. Rev. B*, 53:13624–13630, 1996.
- [9] S. Luryi. Frequency limit of double-barrier resonant-tunneling oscillators. *Appl. Phys. Lett.*, 47:491–493, 1985.
- [10] H. Ohno, E.E. Mendez, and W.I. Wang. Effects of carrier mass differences on the current-voltage characteristics of resonant tunneling. *Appl. Phys. Lett.*, 56(18):1793–1795, 1990.
- [11] E.E. Mendez, J. Nocera, and W.I. Wang. Conservation of momentum, and its consequences, in interband resonant tunneling. *Phys. Rev. B*, 45:3910–3913, 1992.
- [12] R.K. Hayden, et al. Probing the hole dispersion curves of a quantum well using resonant magnetotunneling spectroscopy. *Phys. Rev. Lett.*, 66(13):1749–1752, 1991.

QUASI ONE-DIMENSIONAL CONFINEMENT IN DOUBLE-WELL SIDEWALL GATED RESONANT TUNNELING TRANSISTORS

V.R. Kolagunta^{a)}, D.B. Janes, M.R. Melloch,

School of Electrical and Computer Engineering,
Purdue University, West Lafayette IN 47907-1285.

^{a)}Electronic Mail: kolagunt@ecn.purdue.edu

C. Youtsey

Department of Electrical Engineering,
University of Illinois, Champaign, IL61801

Abstract In this paper we present gating effects in double well resonant tunneling heterostructures with sub-micron minimum feature widths. Resonant tunneling through one-dimensional states in the wells is observed as the device approaches pinch-off at temperatures as high as 77K. This is the first clear demonstration of resonant tunneling through such laterally confined one-dimensional sub-bands at 77K.

1. Introduction

Vertical gated heterostructures are interesting in their applications in multi valued, low-power, high-speed, logic systems. While a lot of work has been done on zero-dimensional (0D) confinement in single well resonant tunneling diodes (RTDs) very little work has been done on; i) low-dimensional double well RTDs and ii) demonstration of confinement effects at temperatures closer to room temperature. RT devices have been shown to oscillate at frequencies of a few hundred Gigahertz [1]. The inherent high speeds of these devices make them promising for high speed circuit applications. Other applications of such three terminal resonant tunneling transistors (RTTs) include oscillators and high frequency switching circuits. Almost no published work on vertical gated one-dimensional (1D) RTTs is available and most demonstrations, at $T \leq 4.2$ K, of resonant tunneling through one-dimensional states has been on fixed width single well RTDs [2]. In the case of RTTs, we have earlier demonstrated that the sidewall gating technique is ideally suited to observe confinement effects in multiple well RTDs, thus alleviating the problems associated with a previously used lateral gating scheme [5].

In this paper we shall demonstrate that, using the self-aligned sidewall gating technique, one is able to observe resonant tunneling through laterally confined states even for relatively high biases. The device presented herein is $0.5 \mu\text{m}$ wide which is one of the many devices fabricated in a single run with varying minimum widths (0.5 to $0.9 \mu\text{m}$) and lengths (10 to $40 \mu\text{m}$). In the wider 1D-RTT devices reported earlier (width 0.7 - $0.9 \mu\text{m}$), we have observed; i) room temperature pinchoff and ii) transformation of the tunneling characteristics from a 2D-RTD to a 1D-RTD at 77K with increasing negative gate bias [4,5].

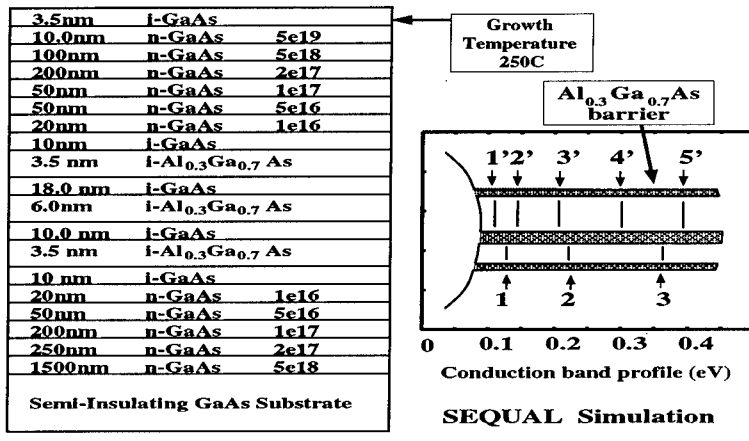


Fig. 1 The double well RTD structure grown in a Varian GEN II MBE. Shown also are the energy levels in the two wells (1, 2, 3 and 1', 2', 3', 4', and 5') at $V_{DS} = 0$ calculated using a self-consistent Poisson and Schrödinger equation solver (SEQUAL simulator).

2. Device Structure

The heterostructure grown on a semi-insulating substrate in a GEN II MBE system is shown in Fig 1. The asymmetric double wells are 180 Å and 100 Å wide with a 60 Å $Al_{0.3}Ga_{0.7}As$ barrier in between. The two i-GaAs wells are separated from the top and bottom contact n-GaAs regions using a 35 Å $Al_{0.3}Ga_{0.7}As$ barrier and a 100 Å undoped GaAs spacer layer. The access channels to the spacer layer from the n+ GaAs regions are graded to prevent breakdown of the gate Schottky barrier. The top-contact structure is a non-alloyed contact structure and uses the low-temperature grown GaAs (LTG:GaAs) capping technique. Fabrication details of such devices have already been published [5].

3. Device Characteristics

In this paper we shall demonstrate 1-D confinement effects in a device with physical mesa width of 0.5 μm and length of 10 μm. In addition, for this device, we shall concentrate on the tunneling from level 1 in the 100 Å well to level 3' in the 180 Å well. For the 0.5 μm wide devices the lower bias resonance peaks (i.e. tunneling between levels 1'-1 and 1-2') are nominally pinched off and the conduction at 300K for these low biases is dominated by off-resonance tunneling and conduction through the depletion region under the gate. Figures 2a and 2b show the measured DC characteristics at various gate biases for this RT peak at 77K of the 0.5 x 10 μm device. The I-V curves show clear indication of multiple sub-peaks with separation between the sub-peaks increasing with increasing negative gate bias. The separation between the first and second sub-peak (ΔV) is $\Delta V = 74\text{ mV}$ @ $V_{GS} = 0\text{ V}$ and increases to $\Delta V = 216\text{ mV}$ @ $V_{GS} = -0.5\text{ V}$. For $V_{GS} \leq -0.5\text{ V}$ further fine structure in each of the sub-peaks is observed. The separation between the fine structure within these sub-peaks is $\delta V \approx 36\text{ mV}$ and is illustrated in Fig. 2b.

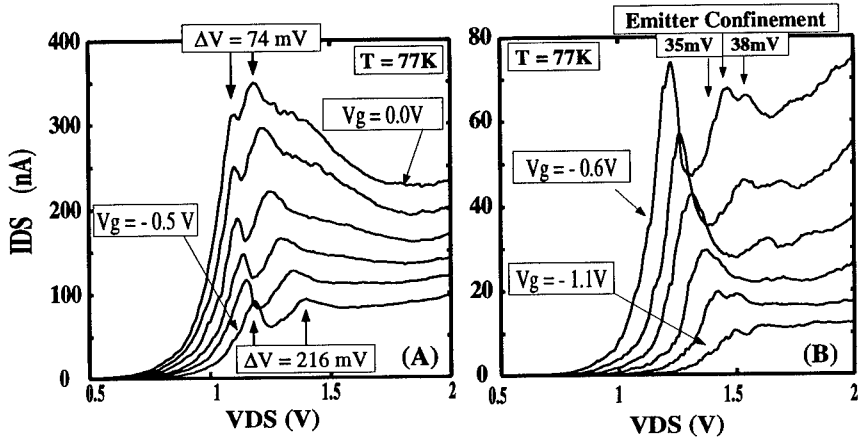


Fig. 2 Measured DC characteristics at 77K (a) for $0V \leq V_{GS} \leq -0.5V$ and (b) for $-0.6V \leq V_{GS} \leq -1.1V$ for a $0.5 \times 10 \mu\text{m}$ device. The arrows in (a) indicate the position of the first and second sub-peaks. The arrows in (b) indicate fine structure in the sub-peaks due to emitter confinement.

4. Discussion

As is well known, a RT peak in conductance (current) occurs when a resonant energy level in each well lines up with the conduction band edge in the emitter. For example in the present double well large area RTDs the main resonant levels (i.e. 1, 2, ... and 1', 2' ...) shown in Fig. 1 occurs due to the confinement of the carrier by the $Al_{0.3}Ga_{0.7}As$ barriers in the vertical direction (z-axis). As the width of this device is reduced the main resonant levels is split into sub-bands due to the lateral confinement (y-axis) with the energy separation between these sub-bands (ΔE_{sub}) being determined by the strength of the confinement. If the gating (i.e. ΔE_{sub}) in both quantum wells is identical, one would then observe resonant sub-peaks due to sub-band mixing wherein a conductance (current) peak occurs when a set of sub-bands of a main resonant level in one well align with the corresponding sub-bands of the main resonant level in the other well [2]. Additionally, confinement in the emitter that is usually weaker than in the well could manifest itself as fine structure within the sub-peaks. It is important to note that the ability to observe such sub-band mixing is determined by the linewidths of these sub-band levels and that any variation in the confinement either in; i) the wells or ii) along the length of the device would cause the broadening of sub-band levels and thus wash out the observation of sub-peaks.

Such sub-peaks have been observed at 4.2K in fixed width single well 1D-RTDs with maximum lengths of the order of $1 \mu\text{m}$ [6,7]. It should be noted that sub-peaks could occur due to inelastic processes like phonon assisted tunneling wherein ΔV corresponds to the energy of the phonon and is independent of the confinement. In the case of the fixed width 1D-RTDs, to distinguish the formation of sub-peaks due lateral confinement from that due to inelastic tunneling processes, a varying magnetic field parallel and perpendicular to the direction of current was used. Also, these sub-peaks are washed out at temperatures exceeding 20K [6]. In contrast, in the case

of the double well 1D-RTTs reported in this paper and earlier, sub-peaks in the RT current and fine structure within the sub-peaks corresponding to confinement in the emitter is clearly observed at temperatures of 77K [4,5]. Since the sub-peak separation (ΔV) is strongly dependent on the gate bias and increases with increasing negative gate bias, it demonstrates lateral confinement in these 1D-RTTs. The clear formation of sub-peaks even for relatively long devices (i.e. exceeding $10\mu\text{m}$) indicates very little variation in width and thus the confinement along the length of the device.

From, i) the energy difference (≈ 20 meV) between levels 1' and 1 from the SEQUAL simulation, ii) the corresponding extrinsic potential across the whole device at which the RT current peak occurs ($V_{DS} \approx 100$ mV) in large area RTDs and iii) assuming that the ratio of the inter-well potential to the applied device bias (V_{DS}) is the same for all biases, we can estimate the energy separation between sub-bands corresponding to the extrinsic difference (ΔV) in the position of the sub-peaks. The separation between sub-peaks $\Delta V = 74$ mV @ $V_{GS} = 0\text{V}$ corresponds to a lateral confinement energy $\Delta E_{sub} \approx 14.8$ meV. Similarly at $V_{GS} = -0.5\text{V}$, the measured $\Delta V = 216$ mV corresponds to $\Delta E_{sub} \approx 43.2$ meV. Using a simple parabolic potential wherein the fermi level at the mesa edges are pinned at midgap and the potential at the center of the mesa is determined by the emitter potential, the expected separation between similar sub-bands $\Delta E_{sub} \approx 10.1$ meV @ $V_{GS} = 0\text{V}$. The fine structure (δV) within the sub-peaks arising due to confinement in the emitter as shown in Fig. 2b is of the order of 35 - 38 mV and corresponds to a separation between sub-bands in the emitter of 7 - 7.6 meV. The ability to observe such structure in the I-V curves whose characteristic energy is close to that of the thermal broadening ($k_B T \approx 6.6$ meV @ $T=77\text{K}$), indicates that it is possible to exploit such confinement effects at room temperature in future novel high speed circuits.

6. Conclusions

We have demonstrated the ability to fabricate vertical quasi- one- dimensional resonant tunneling devices that show clear 1-D quantization at temperatures as high as 77K. Fine structure corresponding to resonant tunneling through sub-bands mixing formed in the well due to the lateral confining potential of the gate has been reported. In addition it has been demonstrated that such lateral confinement effects can be observed in relatively long devices and at biases far from zero drain biases. The strong gating and ability to pinch-off the RT current peak in these device s makes them promising in such applications as lower power, high speed logic circuits.

Acknowledgment We would like to thank Prof. S. Datta and Dr. G.L. Chen for motivating this work. We also acknowledge Prof. I. Adesida for providing the etching facilities. This work was supported in part by ARO, DARPA and NSF-MRSEC.

- [1] E.R. Brown et.al., Appl. Phys. Lett., **62**(23), **3016**(1993).
- [2] N. Mori et. al., Phys. Rev. B, **51**(3), **1735**(1995).
- [3] V.R. Kolagunta et. al., Appl. Phys. Lett., **69**(3), **374**(1996).
- [4] V.R. Kolagunta et. al., Proc. Electrochem. Soc. 191st Meeting, PV 97-11, to appear.
- [5] V.R. Kolagunta et. al., Appl. Phys. Lett., to appear.
- [6] J. Wang et. al., Appl. Phys. Lett., **65**(9), **1124**(1994).
- [7] S. Tarucha et. al., Surf. Sci., **305**, **547**(1994).

Ultralow Current Density RTDs for Tunneling-Based SRAM

**J. P. A. VAN DER WAGT, A. C. Seabaugh, G. Klimeck, E. A. Beam III,
T. B. Boykin*, R. C. Bowen, and R. Lake**

Raytheon TI Systems, P.O. Box 655936, MS 134, Dallas, TX 75265

Email: wagt@resbld.csc.ti.com Ph: (972) 995-6968

*Electrical and Comp. Eng. Dept., University of Alabama in Huntsville, Huntsville, AL 35899

Abstract. We report an improved tunneling-based SRAM (TSRAM) cell design using *symmetric* low current density InGaAs/InAlAs/AlAs/InAs resonant-tunneling diodes (RTDs). The new design eliminates an interconnect compared to the previous record low 50 nW TSRAM cell demonstrated with *asymmetric* low current density RTDs and heterostructure field-effect transistors (HFETs) in our InP-based integrated process. The simplified cell has 4x smaller area than III-V FET-only SRAM cells at the same design rule. We also investigate experimentally and theoretically the mechanism for reduced peak-to-valley current ratios for very low current density ($\sim 1 \text{ A/cm}^2$) RTDs which affects TSRAM cell standby power.

1. Introduction

High-speed static random access memory (SRAM) is required for fast processors. Although 1M transistor circuits can now be fabricated in III-V technology [1], one of the shortcomings remains the absence of reasonable density low-power on-chip memory. Access times as low as 0.5 ns have been realized for a 4 kbit HFET SRAM [2], but 64 kbit has been the integration limit with 5 W total power dissipation (1.2 ns access [3]). Using familiar circuit design, the n-channel GaAs 6-transistor (6T) cell cannot compete with the complementary Si 6T cell, which consumes less than 1 pW [4]. On the other hand, HFETs have intrinsic advantages for very high speed low power addressing because of the high cutoff frequency f_T at low drain current and good short channel behavior [5]. A low power compound semiconductor memory could enable on-chip data processing for ultrahigh speed chips.

We have recently demonstrated a III-V ultralow standby power (50 nW/bit, compared to about 20 $\mu\text{W}/\text{bit}$ in [3]) tunneling-based SRAM (TSRAM) gain cell using two transistors and two resonant-tunneling diodes (RTDs) [6]. The RTDs had asymmetric *I-V* characteristics (NDR in one bias direction only). For one-bit/cell storage, a static one-transistor (1-T) TSRAM cell design similar to a DRAM cell yields the highest bit density. In this paper, we outline the layout and fabrication of an ultra-compact single transistor low power TSRAM cell and also analyze the current-voltage (*I-V*) characteristics of low current density RTDs.

This cell concept also applies to silicon if a low current density Si-based NDR device is available. It would eliminate the power waste associated with the refresh operation [6]—a serious problem for the gigabit era [7]. Alternatively, TSRAM could allow relaxation of transistor leakage requirements and an increase in transistor current drive, i.e. higher read/write speed.

2. One-Transistor TSRAM Cell

To achieve the most compact one-transistor cell symmetric *I-V* RTDs are used. Asymmetric RTDs require a metal interconnect to tie one RTD emitter to the other RTD collector. The symmetric RTDs we have developed allow current to flow top-down in one RTD to the storage node and then bottom-up through the other RTD, see Figure 1. Both RTDs sit on an HFET source region, which is the storage node, to form a 1-T TSRAM cell with a shared bit line contact. Figure 2 shows a layout with only 2 $\frac{1}{2}$ via contacts versus 3 $\frac{1}{2}$ for a cell using asymmetric RTDs and achieving 4x smaller size than 6-transistor cells at the same design rule. The cell is read like a DRAM cell, the capacitance of the RTDs driving the bit line. Therefore, peak-minus-valley RTD currents need only be larger than HFET leakage currents.

Figure 3 shows a photo of a fabricated 4 bit x 4 word TSRAM die. Tests and SPICE simulation on such arrays show that the cell charge can be sensed dynamically with subnanosecond access times. This results from high storage node capacitance of 8 fF per μm^2 RTD area and a reduced bit line length because of the compact cell size.

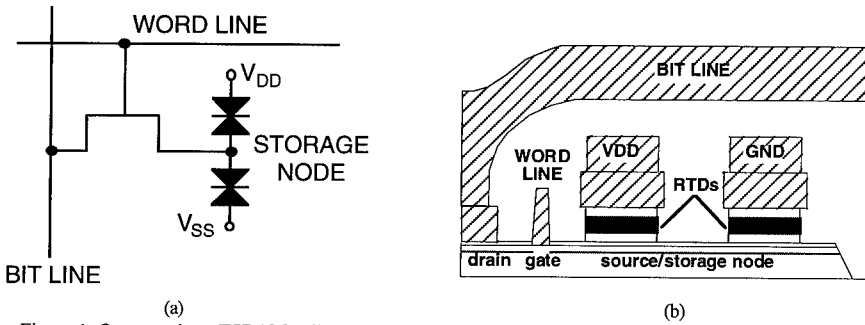


Figure 1. One-transistor TSRAM cell with symmetric RTDs storing a bit on the source of an HFET:
circuit (a) and schematic cross-section with self-aligned word line (b).

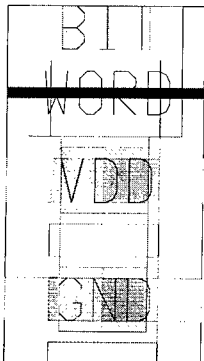


Figure 2. One-transistor TSRAM cell layout,
148.5 μm^2 , at a relaxed 5 μm metal pitch.

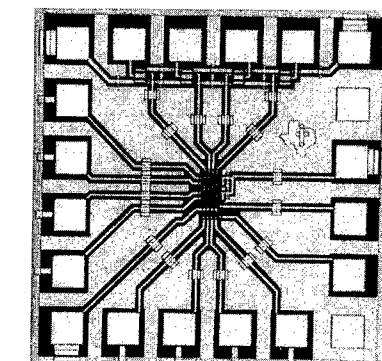


Figure 3. Fabricated 4x4 single-transistor cell TSRAM
array.

3. Low Current Density RTDs

Figure 4 shows experimental *I-V* characteristics of several low current density RTDs for peak current densities ranging from 10 to about 0.1 A/cm^2 . The low current density RTDs are modeled with our in-house developed nanoelectronic simulator, NEMO [8]. An asymmetric RTD energy band diagram is shown in Figure 5, with a prebarrier for current reduction. A 10 band sp^3s^* tightbinding model [8,9] including strained bandstructure parameters [10], full numerical integration of the current density over transverse momentum, full Hartree charge self-consistency [9,11], and strong electron-electron relaxation in the emitter region yield agreement with experiment. The coherent simulation uses incident electron energies up to 0.35 eV ($\sim 14 kT$) to capture current flow through wide resonances up to 0.25 eV above the emitter Fermi level. Reduced prebarrier attenuation for the high energy wavefunctions contributing to the valley current causes a PVCR decrease for thicker prebarriers. This trend [12] together with HFET leakage impacts the ultimate reduction of TSRAM cell standby power. Figure 6 shows measured low temperature *I-V* characteristics for the 17 ml prebarrier structure and simulated curves reproducing the thermionic emission near the top of the prebarrier. Bandstructure dependence on temperature and phonon or roughness scattering in the central device region were neglected.

An improved symmetric RTD has been designed and fabricated with measured *I-V* characteristic shown in Figure 7. Details of the material structure will be reported at a later date, but the structure is near-ideal in the forward direction: a very small peak voltage combined with a wide ($\sim 1 \text{ V}$) valley region. A latch (Fig. 1) constructed of such RTDs has stable points far apart and close to the supply voltages.

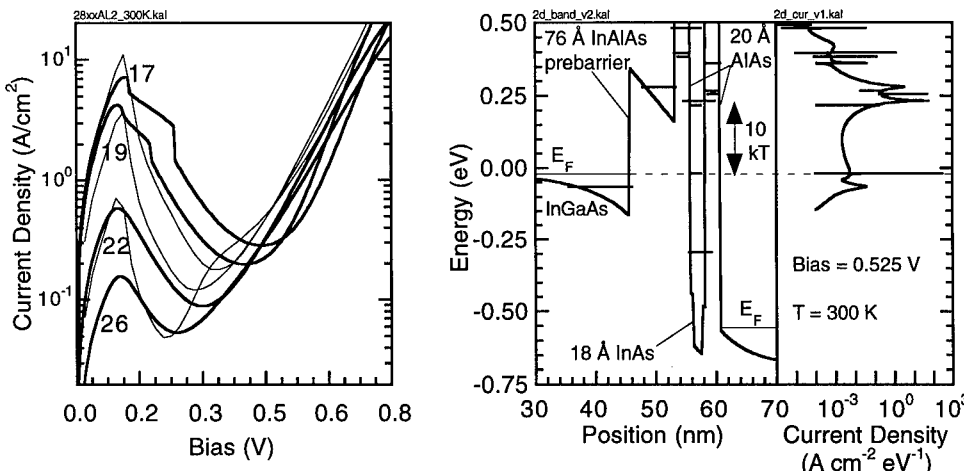


Figure 4. Room temperature experimental (thick) and theoretical (thin) *I-V* curves for asymmetric low current density RTDs of a design shown in Fig. 5. Numbers refer to prebarrier thickness in monolayers (1 ml = 2.93 Å).

Figure 5. Conduction band diagram and current density of 26 ml prebarrier RTD biased in the valley region. Significant current flows through high energy wide resonances. The narrow resonances are due to multiband Γ -X transitions and carry negligible current. The current density units apply to a parabolic transverse energy-momentum band.

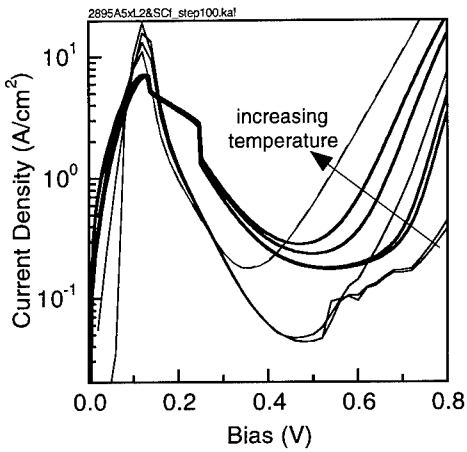


Figure 6. Experimental (thick) and theoretical (thin) I-V characteristics for an asymmetric 17 μm prebarrier RTD at 4, 100, 200, and 300 K.

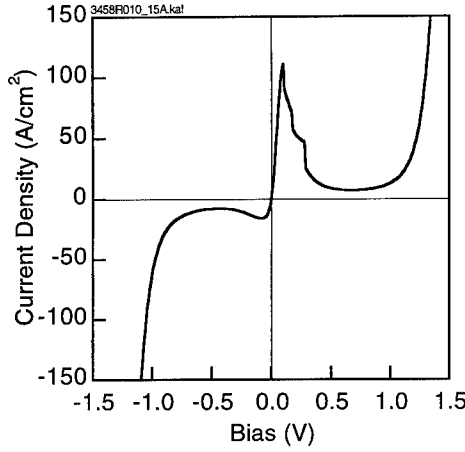


Figure 7. Room temperature experimental I-V curve for a symmetric low current density RTD. Asymmetry in growth causes the asymmetry in the I-V.

4. Conclusion

We have proposed and fabricated static memory cells using an ultracompact ($150 \mu\text{m}^2$) one-transistor tunneling-based SRAM cell. The cell uses two symmetric I-V low current density ($\sim 1 \text{ A/cm}^2$) RTDs and is capable of achieving nanowatt standby power per bit, which is orders of magnitude better than conventional 6-transistor cells. The valley current of the low current density RTDs was found to be caused in large part by thermionic electrons excited up to 0.25 eV ($\sim 10 kT$) above the emitter Fermi level, which may cause the decreasing peak-to-valley current ratios toward lower current densities.

Acknowledgment

The authors thank Thomas Smith, Pamela Stickney, and David Chasse for excellent technical assistance.

References

- [1] Tomasetta L R 1995 *Intl. Symp. Comp. Semicond.* 29-32
- [2] Notomi S et al 1987 *Proc. GaAs IC Symp.* 177-80
- [3] Suzuki M et al 1991 *ISSCC Tech. Dig.* 48-9
- [4] Goto H et al 1992 *IEEE J. Solid-St. Circ.* 27 1490-1496
- [5] Abe M and Mimura T 1990 *Proc. GaAs IC Symp.* 127-30
- [6] Van der Wagt J P A et al 1996 *IEDM Tech. Dig.* 425-8
- [7] Itoh K et al 1996 *Symp. VLSI Tech. Dig.* 2-7
- [8] Klimeck G et al 1995 *DRC Conf. Dig.* 52-53
- [9] Lake R et al 1997 *J. Appl. Phys.* 81 7845-69
- [10] Bowen R C et al 1997 *J. Appl. Phys.* 81 3207-13
- [11] Boykin T B et al 1997 *Phys. Rev. B* August 15 issue
- [12] Klimeck G et al 1995 *Appl. Phys. Lett.* 67 2539-41
- [13] Van der Wagt J P A et al 1996 *DRC Conf. Dig.* 168-9

Analysis of Heterojunction Interband Tunneling Diodes for MMICs

Nada El-Zein, George Maracas, Vijay Nair, Gary Kramer and Herb Goronkin

Phoenix Corporate Research Laboratories
2100 E. Elliot Road, Tempe, AZ 85284

Abstract

Heterostructure Interband Tunneling Diodes (HITDs) show great potential for power generation at high frequencies. Voltage Controlled Oscillators (VCOs) that utilize the negative differential resistance (NDR) region of the HITFET have been demonstrated and exhibit a wider tuning range than conventional FET-based VCOs. Additionally, the center frequency can be tuned by either drain or gate bias. MMIC VCOs that incorporate HITFETs require fewer passive components when compared to conventional VCO designs.

A Voltage Controlled Oscillator (VCO) consisting of an InAlAs/InGaAs interband tunneling diode connected onto the source of a heterojunction InGaAs channel FET has been demonstrated. Precise control of the center frequency (X-band) and the tuning range (~20 MHz) were achieved by varying the drain and gate voltages (~1 V) of the HITFET.

Since repeatability of the HITD equivalent circuit is crucial for accurate circuit design and circuit operation, a discussion of the growth optimization and material parameters of the diodes is presented. Secondary Ion Mass Spectrometry (SIMS), Transmission Electron Microscopy (TEM) and electrolytic capacitance voltage (ECV) profiling are used to study the effect of dopant compensation and dopant diffusion on the I-V characteristics and the peak-to-valley current ratios (PVCRs) of the HITDs. The data shows an exponential dependence of the PVCR on oxygen background concentration in the sample. It also shows that the presence of doping impurities in the well region (which is determined using SIMS analysis) produces a dramatic degradation of the PVCR and peak current density.

Introduction

Heterojunction interband tunneling diodes proposed by Sweeny and Xu [1] have demonstrated high peak-to-valley current ratios (PVCRs) [2]. Such devices have a potential to produce analog and digital circuits with reduced complexity and size and several memory and logic devices (SRAMs, XNORs, etc.) have been demonstrated [3,4,5]. The challenge has been to achieve high, reproducible PVCRs by judicious choice of heterojunction material structures and molecular beam epitaxy growth conditions [6]. The material system that is considered in this paper is InGaAs/InAlAs HITDs which have had the highest reported PVCR of 144 [2].

Toward achieving reproducible, high PVCR devices, the main material related factors addressed in this paper are: the presence of carrier compensation by oxygen in the structure, and Be dopant diffusion across the p-n heterojunction into the double quantum well (DQW) region. The experimental results are validated with simulations that model the effect of dopant compensation and diffusion on the PVCRs and the peak current densities (J_p).

Experimental Results

The NDR regions of the HITFET can be controlled by either the voltage applied to the gate or drain terminals of the HITFET. Because the center frequency depends on the equivalent circuit of the diode in the NDR region, the tuning range of the VCO is precisely controlled by the drain and/or gate voltage and the external tuning elements in the circuit. A hybrid VCO consisting of an HITD and HFET was built and the measured RF characteristics are discussed in the next section.

Measured RF characteristics of voltage controlled HITFET VCO

To demonstrate the HITFET VCO concept, a hybrid VCO consisting of a HITD and a GaAs HFET was designed (figure 1a). This circuit consists of a single HITFET (HITD integrated monolithically onto the source of the HFET) and an inductor. In Fig. 1b, the NDR region in the DC I-V curves of the HITFET can be seen clearly. The device functions as a conventional FET until the voltage across the diode reaches the threshold for negative resistance regime. In the particular case shown here, the circuit current is limited by the FET current. When the critical voltage is reached the current the HITD forces the HITFET current to switch to the diode valley current.



Fig. 1. a) Circuit diagram of the VCO which contains an HFET and a single inductor. b) I-V curves showing NDR of the HITFET. Scales are I_d at 5 mA/div. (vertical), V_d at 0.2 V/div. (horizontal), and V_g in -0.2 V/step ($V_g = 0$ for top curve).

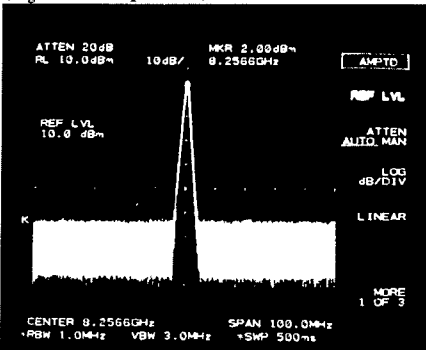


Fig. 2. Measured frequency spectrum of the HITFET-based VCO. The center frequency is 8.2566 GHz, the span is 100 MHz, and the amplitude is 2.0 dBm.

The measured frequency spectrum of this VCO circuit is shown in Fig. 2. The VCO was biased through an RF choke and the performance was measured as a function of drain and gate bias. An oscillation frequency of 8.2566 GHz was achieved with an output power of 2.0 dBm at $V_{ds} = 2.0$ and $V_{gs} = -0.77$ V

No other major peaks were observed around the oscillating frequency of the VCO indicating a clean spectral output. Fig. 3a plots the difference in frequency from the oscillation frequency (tuning) and power output as a function of drain bias. The NDR region of this device produces a tuning range of about 25 MHz. Oscillation was quenched by biasing the device outside of the NDR region either by changing the drain or gate voltage. Tuning was also achieved by varying the gate bias as shown in figure 3b.

Phase noise of -129 dB/Hz was exhibited at 3 MHz away from the carrier with the VCO operating in the free running oscillator mode. Corresponding phase noise at 2 MHz and 1 MHz away from the carrier were -124 dB/Hz, and -110 dB/Hz, respectively. A more accurate and improved phase noise is expected when measured with an optimized setup consisting of phase locked loop circuits in addition to integration and optimization of circuit parameters for low noise operation.

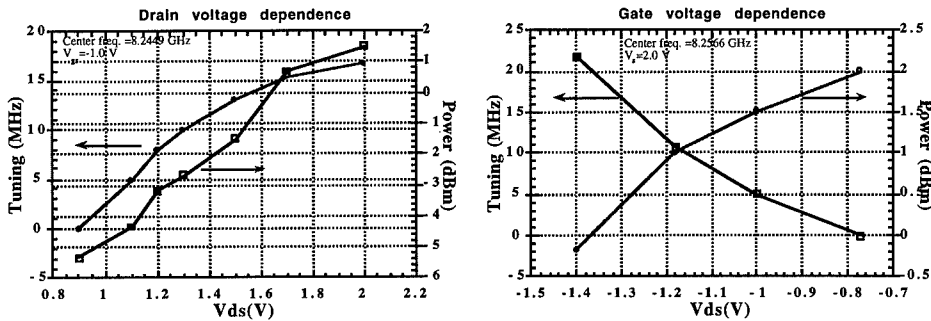


Fig. 3 Shift from the center frequency and power output of the HITFET-based VCO as a function of a) V_{ds} and b) V_{gs} .

Material Issues.

The HITDs are grown at 465 °C by MBE. Detailed growth conditions, band structure and cross section of these devices are published elsewhere [7,8].

The PVCR of these diodes varies from wafer to wafer because of variations in the doping profiles and background impurity levels. The presence of oxygen in the sample has a dramatic effect on the PVCR of the HITDs. Fig. 4a shows a SIMS analysis for two different samples grown at different times. One has a PVCR = 4 and a peak current $J_p = 8.41 \text{ A/cm}^2$, while the other has a PVCR = 47 and $J_p = 713 \text{ A/cm}^2$. The oxygen distribution in the two diodes is approximately uniform and differs by a factor of 2.5. This difference (of 2.5) is enough to decrease the PVCR by an order of magnitude and J_p by two orders of magnitude. Carrier compensation both in the wells and access regions thus affects the PVCR.

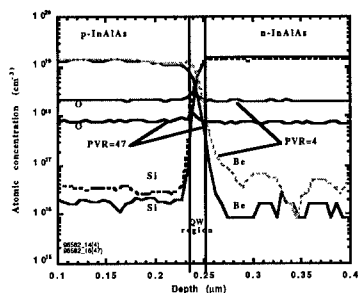


Figure 4a. SIMS analysis of two different samples grown within a few days of each other.

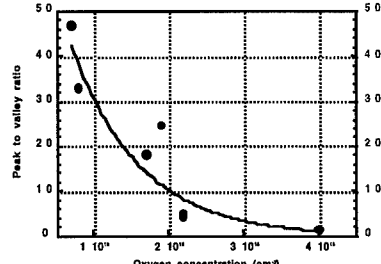


Figure 4b. Plot of PVCR versus O concentration. Curve fitting gives us a clear exponential dependence.

Also observed in figure 4a is a slight diffusion of Be into the DQW region in both samples. Both wells contain comparable levels of Be, yet a high PVCR (i.e. 47) is obtained for one diode. Therefore, in this case, the oxygen concentration has a greater effect because the Be diffusion is minimal. These HITDs exhibit "Esaki-like" behavior and therefore the cladding layers should be doped as high as possible to achieve high performance. The presence of oxygen compensates the high concentration of dopants and thus degrades the performance of the device. Collecting SIMS data from several samples

with different oxygen content, we obtain the plot of PVCR versus oxygen concentration shown in Fig. 4b. We find a clear exponential dependence of PVCR on oxygen concentration. The presence of oxygen is attributed to the well-known high reactivities of Al containing materials (InAlAs) and Be [9] which is the p-dopant used in these structures. Another source of oxygen was found to be the hot PBN crucible used for Be. While the PVCR changes dramatically the position of the voltage where J_p is reached does not vary much (0.25-0.45V).

A stack of two back-to-back (npn) diodes were characterized using SIMS, ECV and TEM analysis to show the effect of impurity diffusion on the PVCR and peak current density (J_p). Beryllium is known to have high diffusivity in III-V semiconductors and in this structure introduces impurities into the DQW region, as well as "smears" the interfaces between the InGaAs wells and InAlAs barriers.

The bottom diode (p on n) had a high PVCR = 30 and a J_p = 7.64 A/cm², while the corresponding values for the top diode (n on p) were PVCR = 6.8 and J_p = 0.56 A/cm². The Be signal showed diffusion of Be into the top Si doped layer making that junction less abrupt and possibly smearing the quantum wells. TEM cross sections confirmed this by showing the bottom diode DQW interfaces to be very sharp and the top diode DQW interfaces "hazy." The oxygen concentration, on the other hand, was constant throughout the structure. Therefore, in this case the Be diffusion degraded the PVCR (by carrier compensation and/or interface roughening). The presence of acceptors in the QW region reduces the number of carriers available for conduction and thus the hole tunneling current and thus J_p . In addition to the presence of impurities in the wells - and as mentioned in ref. 6 - interface abruptness greatly affects the PVCR because it results in high valley currents due to scattering mechanisms.

Self-consistent Schrödinger-Poisson simulations run on these structures, indicate that both compensation of dopants and impurities in the DQW region play an important role on the PVR. These simulation trends show that the impurities in the well have a larger effect on the PVCR degradation than does oxygen compensation. Deep trapping effects in the quantum wells related to oxygen are neglected in these calculations. Taking into consideration that both effects are detrimental, and that impurities in the wells play a more dramatic role than oxygen presence, we conclude that figure 4b probably shows the combined effect of both mechanisms.

Conclusions

In conclusion, we have performed microwave characterization of an InP based X-band voltage controlled oscillator (VCO) that uses a tunneling device as an active component. The power output, phase noise and tuning range of the VCO was measured for various drain and gate voltages. An improvement of the phase noise characteristics is expected when circuit is monolithically integrated. The use of HITDs and HITFETs allows for a reduction of the number of passive components required compared to a conventional approach, and can result in a three-fold reduction in circuit area.

In addition, experimental data (SIMS, TEM and ECV) shows that compensation of carriers due to the presence of oxygen and dopants in the DQW of the HITDs produce a strong degradation of the PVCR and J_p . Simulation trends confirm this data.

References

- [1] M. Sweeny and J.M. Xu, *Appl. Phys Lett.*, **54**, 546 (1989).
- [2] H. H. Tsai, Y. K. tsu, H. H. Lin, R. L. Wang, and T. L. Lee, *IEEE Electron Dev. Lett.* **15**, 357 (1994).
- [3] A. C. Seabaugh, A. H. Taddiken, E. A. Beam III, J. N. Randall, Y.-C. Kao, B. Newell, *IEDM* 93-149 (1993).
- [4] K. Maezawa, T. Mizutani, *Jpn. Appl. Phys. Lett.*, vol. 32, no. 1A-B, pp. L42-2, (1993).
- [5] J. Shen, S. Tehrani, H. Goronkin, and G. Kramer, *SPIE Photonics West Symposium 96*, San Jose, CA (1996).
- [6] T. S. Moise, Y.-C. Kao, and F. G. Celii, *SPIE Vol. 2694*, pp. 126-133, (1996).
- [7] N. El-Zein, G. Maracas, G. Harris, G. Kramer, and H. Goronkin, *Proceedings of the International conf. on InP and Related materials*, pp. 261-263 (1997).
- [8] R. Q. Yang, J. Lu, J. M. Xu and D. J. Day, *Proceedings of the 6th annual Can. Semi. Tech. Conf.* (Aug. 1992).
- [9] N. Chand, S. N. George Chu, N. K. Dutta, J. Lopata, M. Geva, A. Syrbu, A. Mereutza, and V. P. Yakovlev, *IEEE JQE*, Vol. 30, pp. 424-440 (1994).

Microwave Noise Properties for Resonant Tunneling Transistors (RTTs)

Yuji ANDO, Walter CONTRATA, Kenichi MARUHASHI, Hironobu MIYAMOTO

Kansai Electronics Research Laboratories., NEC Corporation, 2-9-1, Seiran, Otsu 520 JAPAN

Abstract. We propose and demonstrate a low noise amplifier utilizing the negative input conductance of resonant-tunneling transistors (RTTs). The fabricated RTTs, which integrate a resonant-tunneling diode (RTD) into the source of a heterojunction FET (HJFET), exhibited negative input conductance at low frequencies (≤ 10 GHz). When the gate bias is close to the resonance peak, not only F_{min} but also R_n increases at low frequencies. Also, F_{min} shows a sharp dip at the valley current. These behaviors are explained by shot noise generation at the RTD. Theoretical results suggest that reducing the valley current as well as reducing the series resistance would realize RTT noise performance superior to HJFETs.

1. Introduction

In 1983, van der Ziel presented the concept of low-noise amplification utilizing two-port devices with a negative input conductance [1]. In the early 1980's, however, such devices were not available. But, recently, negative differential conductance (NDC) is reported in various resonant-tunneling transistor (RTT) structures[2]-[5]. In this paper, we propose to use RTTs to realize van der Ziel's amplifier.

2. Concept of RTT Amplification

Figure 1 illustrates an equivalent circuit for an RTT amplifier. The input circuit can be represented by a negative input conductance $-g_R$ ($g_R > 0$) with a generator conductance g_S in parallel. As long as $g_S > g_R$, this circuit has an available power gain $G_{av} = g_S/(g_S g_R)$. As g_S approaches g_R from the upper side, G_{av} approaches infinity, and hence, the effect of the noise sources at the output is negligible. The principle of this amplifier is very similar to tunnel diode amplifiers, but separation of input and output terminals will suppress instability, which is a serious problem for tunnel diode amplifiers.

Noise properties for resonant-tunneling diodes (RTDs), and hence, for RTTs are characterized by the diode maximum oscillation frequency (f_{max}) and by the diode noise figure (NF). Frequency dependence of the diode NF is essentially flat, because it is dominated by shot noise, which has a white spectrum. The operation frequency is limited by the diode f_{max} , so that NF increases as f approaches f_{max} . As is well-known, decreasing the resistance $1/g_R$, the RTD capacitance (C_R), or the series resistance (R_s) would improve the diode f_{max} . From analogy to tunnel diode amplifiers, decreasing the current-to-conductance ratio I_R/g_R would improve the diode NF .

Figure 2 shows the DC bias dependence of a diode NF , which is calculated by applying the small-signal tunnel diode circuit to simulated AlAs (2 nm)/ GaAs (5 nm)/ AlAs (2nm) RTDs. When an RTD is biased at the NDC condition, the diode f_{max} sharply increases and the diode NF decreases. These features are more prominent for decreasing R_s . When R_s is reduced to $1 \times 10^{-7} \Omega \text{cm}^2$, a diode f_{max} of over 500 GHz and a diode NF of as low as 0.3 dB at 100 GHz are predicted [6].

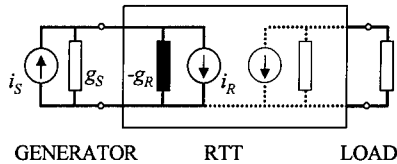


Fig. 1. Equivalent circuit for an RTT amplifier at tuning frequency, where reactance elements are canceled (i_S : signal current, i_R : noise current).

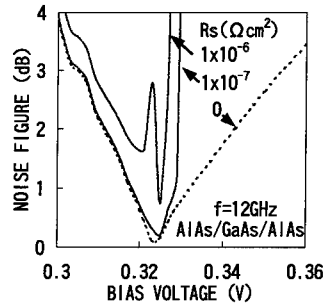


Fig. 2. Calculated diode NF vs. DC voltage ($R_s=0 - 1 \times 10^{-6} \Omega \text{ cm}^2$, $f=12 \text{ GHz}$, $T=290 \text{ K}$).

3. Fabrication of RTTs

We have fabricated RTTs, which integrate an RTD into the source of a heterojunction FET (HJFET) (see the inset in Fig. 3). RTT wafers were grown by MBE system on semi-insulating (100) GaAs. The epi-layer structure consists of an Al_{0.22}Ga_{0.78}As (40 nm)/ In_{0.2}Ga_{0.8}As (15 nm)/ GaAs HJFET structure followed by an n-type GaAs contact layer and an AlAs (2 nm)/ GaAs (5 nm)/ AlAs (2 nm) RTD structure. First, the RTD mesa was defined and this was followed by the HJFET fabrication process. Source and drain ohmic contacts were formed using AuGe/ Ni/ Au alloy. After gate recess etching, 0.6 μm -long gates were formed with Ti/ Al metallization.

4. DC and Small-Signal Performance for RTTs

The RTTs exhibited NDC characteristics at room temperature. The peak-to-valley current ratio was 1.4. Figure 3 shows measured drain current (I_d) - drain voltage (V_d) characteristics. When the gate voltage (V_{gs}) is high enough to turn on the RTD, NDC occurs in the I-V curves. As a result, transconductance (g_m) shows a sharp negative peak ($\sim -750 \text{ mS/mm}$) with respect to V_{gs} .

The S-parameters of 100 μm -gate-width devices (RTD area of 50 μm^2) were measured from 2 to 26 GHz. In Fig. 4, the magnitude of S_{11} at 8 GHz is shown as a function of V_{gs} . When V_{gs} is close to the resonance peak, a negative input conductance ($|S_{11}| > 1$), which is required for van der Ziel's amplifier, was observed. However, due to the high R_s , this NDC disappears at higher frequencies (>10 GHz), and hence, the predicted f_{max} upturn was not observed. At the resonance peak, 22 GHz f_T and 96 GHz f_{max} were obtained. An RTT equivalent circuit has been determined by fitting S-parameters, and it indicates that the comparatively wide bias range ($V_{gs} = -0.1$ to 0 V) for exhibiting NDC is due to the series feedback effect of the RTD capacitance.

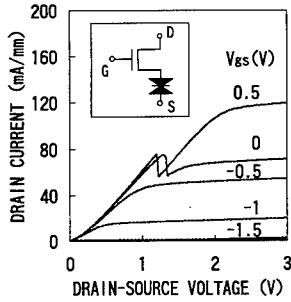


Fig. 3. Measured I-V characteristics.
Inset: circuit diagram for the fabricated RTT.

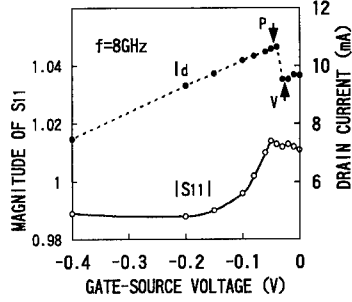


Fig. 4. Measured $|S_{11}|$ (8 GHz) and I_d vs. V_{gs} ($V_{ds}=2V$).
Arrows: peak (P) and valley (V) for the I-V curve.

5. Noise Performance for RTTs

Figure 5 shows the minimum noise figure (F_{min}) and the input noise resistance (R_n), measured at 2 GHz, with respect to V_{gs} . When V_{gs} is close to the resonance peak, not only F_{min} but also R_n increases (from 1 dB to more than 2 dB and from 200 to 600 Ω , respectively at 2 GHz) at low frequencies (≤ 10 GHz). Also, F_{min} shows a sharp dip at the valley current, as is theoretically predicted. On the other hand, variation of the noise optimum reflection coefficient (Γ_{opt}) is small.

Measured noise parameters have been fitted by the extracted equivalent circuit, where the shot noise current (i_R) is added in parallel to the RTD. Frequency dependence of measured and modeled noise parameters is shown in Fig. 6. Simulated noise parameters with and without shot noise compare well with the measured results on and off the resonance peak current, respectively. Hence, the increase in F_{min} and R_n at the resonance peak is attributed to the shot noise generated in the RTD. The frequency dependence of R_n with shot noise is due to a $1/\omega^2$ spectrum of the noise voltage $\bar{u} = \bar{i}_R^2/(g_R^2 + \omega^2 C_R^2)$. Comparatively high F_{min} values are due to the high R_s and consequently weakened NDC.

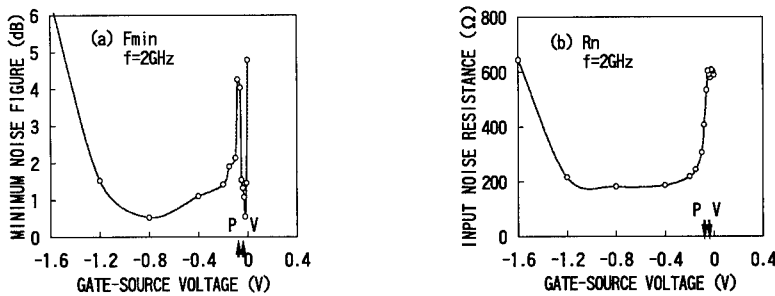


Fig. 5. Measured (a) F_{min} and (b) R_n vs. V_{gs} ($f=2$ GHz, $V_{ds}=2$ V, $T=290$ K).
Arrows: peak (P) and valley (V) for the I-V curve.

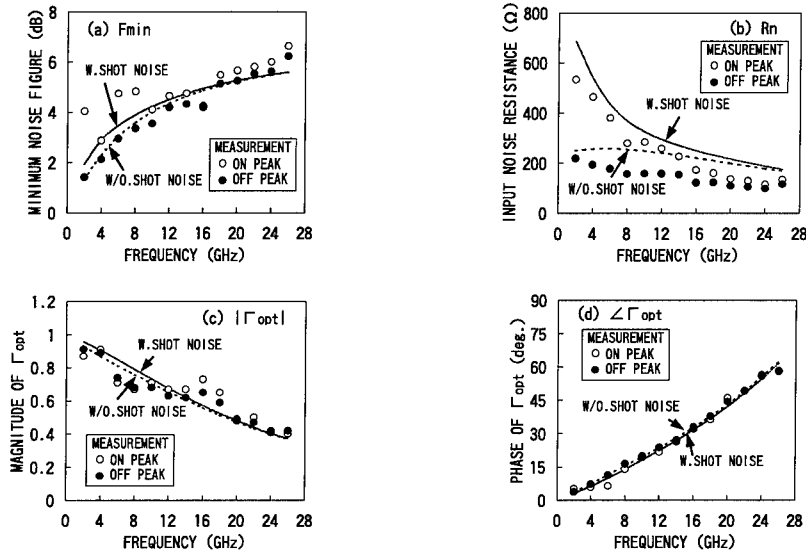


Fig. 6. Measured and modeled frequency dependence of (a) F_{min} , (b) R_n , (c) $|\Gamma_{opt}|$, and (d) $\angle\Gamma_{opt}$ ($V_{ds}=2$ V, $T=290$ K). Measurement: $V_{gs}=-0.06$ V (on peak), -0.2 V (off peak). Model: with and without shot noise.

6. Summary

We have proposed a low noise amplifier utilizing the negative input conductance of RTTs. In RTTs, a negative input conductance ($|S_{II}|>1$) was observed at low frequencies (≤ 10 GHz), but due to the high R_s , the NDC disappears at higher frequencies, and therefore, the predicted f_{max} upturn was not observed. When V_{gs} is close to the resonance peak, not only F_{min} but also R_n increases at low frequencies. Also, F_{min} shows a sharp dip at the valley current. These behaviors were explained by shot noise generation at the RTD. Since the power density of shot noise is proportional to DC current, reducing the valley current as well as reducing R_s would improve the noise performance of the RTTs. These results suggest the possibility for realizing low noise RTT amplifiers.

Acknowledgment

Discussions with Prof. A. Cappy with IEMN were very helpful. The technical assistance and support of E. Mizuki, A. Fujihara, K. Onda, M. Kuzuhara, T. Uji, and M. Ogawa are also appreciated.

References

- [1] van der Ziel A 1983 *Solid-State Electron.* 26 333-334
- [2] Yokoyama N *et al.* 1985 *Jpn. J. Appl. Phys.* 24 L853-L854
- [3] Capasso F *et al.* 1986 *IEEE Electron Device Lett.* EDL-7 573-576
- [4] Chen K J *et al.* 1995 *Appl. Phys. Lett.* 67 3608-3610
- [5] Tehrani S *et al.* 1995 *IEEE Electron Device Lett.* 16 557-559
- [6] Ando Y and Cappy A to be published in *IEEE Trans. Electron Devices*

Photoluminescence Study of Resonant-tunneling Transistor

Y. Ohno, S. Kishimoto, T. Mizutani, and T. Akeyoshi*

Nagoya University, Furo-cho, Chikusa-ku, Nagoya 464-01, Japan

*NTT System Electronics Laboratories, Morinosato Wakamiya, Atsugi-shi, 243-01, Japan

Abstract. The photoluminescence (PL) of a resonant-tunneling transistor was studied. An excitation energy close to the bandgap energy of the GaAs collector layer was chosen so as to excite neither the barrier layer nor the quantum well, resulting in simple luminescence spectra. The PL signal shows a strong correlation with resonant-tunneling current. The PL peak position shifts to lower energy with increasing collector voltage, V_{ce} , indicating the existence of the quantum-confined Stark effect. The V_{ce} dependencies of PL intensity and line width suggests charge buildup in the quantum well. The effect of gate voltage on PL spectra suggests a quantum confinement by the potential of the gate depletion layer.

1. Introduction

New functional devices based on resonant-tunneling phenomena have recently attracted much attention since they are expected to reduce circuit complexity through using negative-differential-resistance characteristics [1-3]. Maezawa et al. recently proposed a resonant-tunneling transistor (RTT) with a junction gate [4] and they demonstrated its usefulness in implementing functional logic circuits such as cellular automata and neural networks [5, 6]. Simulations have also been performed to predict the performance of the resonant-tunneling logic gate [7, 8].

Understanding the carrier transport phenomena in such an RTT is very important in improving its performance and in designing new resonant-tunneling devices. Photoluminescence (PL) study has been shown to be a useful method in understanding the carrier behavior in resonant-tunneling diodes [9, 10]. Charge buildup in the quantum well and sequential tunneling have also been pointed out.

In the present work, we study the PL of an RTT with a junction gate. A PL system which consists of a tunable Ti:Sapphire laser, a monochromator, and an objective lens allowed us to study carrier transport in the RTT. Correlation between luminescence and resonant-tunneling current was observed. The effects of gate voltage were also studied.

2. Device Structure

Figure 1 shows a schematic cross-sectional view of an RTT with a p⁺/n junction gate, which controls the emitter-to-channel area and hence the diode current. The epitaxial layer structure was grown by molecular beam epitaxy. It consists of n⁺-In_{0.6}Ga_{0.4}As/n⁺-In_xGa_{1-x}As/n⁺-GaAs emitter contact layers (30/50/20 nm, 2×10¹⁹ cm⁻³), an n⁻-GaAs emitter layer (200 nm, 5×10¹⁶ cm⁻³), an i-GaAs spacer layer (1.5 nm), an i-AlAs/i-GaAs/i-AlAs resonant-tunneling structure (2/6/2 nm), an i-GaAs spacer layer (5 nm), an n⁻-GaAs collector layer (600 nm, 5×10¹⁶ cm⁻³), and an n⁺-GaAs collector contact layer (300 nm, 4×10¹⁸ cm⁻³). Ni/Zn/Au/Ti/Au was deposited for the gate electrode and alloyed to form p⁺ region under the gate. The fabricated RTT had a 1×10 μm² emitter electrode.

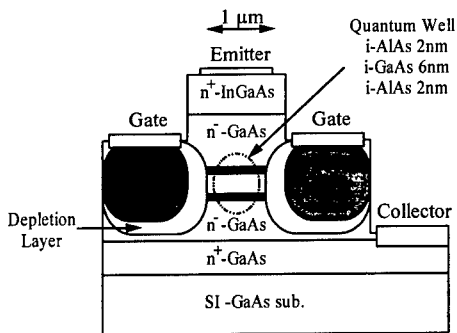


Fig. 1 Schematic device structure of resonant-tunneling transistor with junction gate.

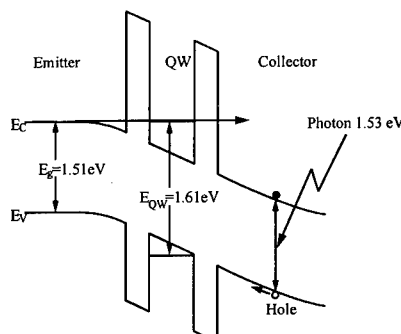


Fig. 2 Schematic band diagram of resonant-tunneling structure.

3. Measurement Condition of Photoluminescence

Figure 2 shows a schematic band diagram of the resonant-tunneling transistor. Holes excited in the collector layer drift to the collector barrier and tunnel into the quantum well. Electrons tunnel into the quantum well from the emitter layer on resonance. Some of the electrons and holes buildup in the quantum well recombine and radiate photons at an energy of about 1.61 eV which corresponds to $e_i - hh$ recombination.

An excitation energy of 1.53 eV was chosen, using the tunable Ti:Sapphire laser, which is slightly higher than the absorption edge of the GaAs collector layer, which is 1.51 eV. This was done so that electron-hole pairs would not be excited in the quantum well, excess heating of electrons by photo-excitation would not occur, and sufficient PL intensity to analyze PL spectra would be obtained. This method of excitation gave us simple luminescence spectra compared to conventional Ar laser (2.41 eV) excitation as shown in Fig. 3. When the device was excited by Ar laser, a luminescence tail of 1.5-1.6 eV energy overlapped the 1.61 eV peak of the quantum well as shown by the dotted line. With Ti:Sapphire laser excitation, on the other hand, a single luminescence peak from the quantum well can be observed as indicated by the solid line, which make it easy to analyze the spectra.

The excitation power was 4 W/cm², which was sufficiently low so that electrons would not be heated by irradiation [11]. The excitation laser was irradiated over the whole device area. The device was mounted in a cryostat and cooled down to 30 K. The laser was focused on the device by an objective lens. The PL signal was also collected by the objective lens, dispersed through a 1-m double monochromator, and detected with a cooled GaAs photomultiplier.

4. Analysis of PL spectra

Figure 4 shows the collector voltage dependence of PL spectrum observed at about 1.61 eV. The current-voltage characteristics of RTT at zero gate voltage are shown in the inset. No PL signal can be observed at zero bias voltage because there are no electrons in the quantum well. PL signal is obtained at a collector voltage above 0.1 V, at which resonant-tunneling current starts to flow. The peak position shifts to a lower energy as V_{ce} increases. The highest intensity was obtained at a resonant voltage of 0.3V.

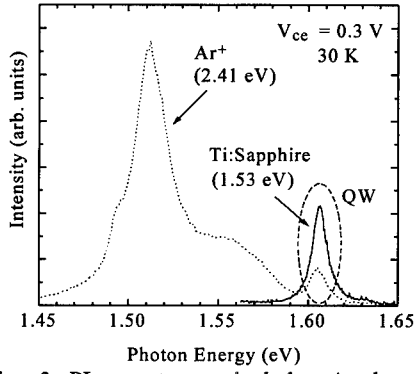


Fig. 3 PL spectra excited by Ar laser or Ti:Sapphire laser.

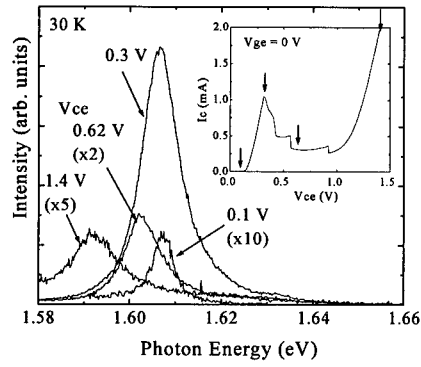


Fig. 4 Collector voltage dependence of PL spectrum.

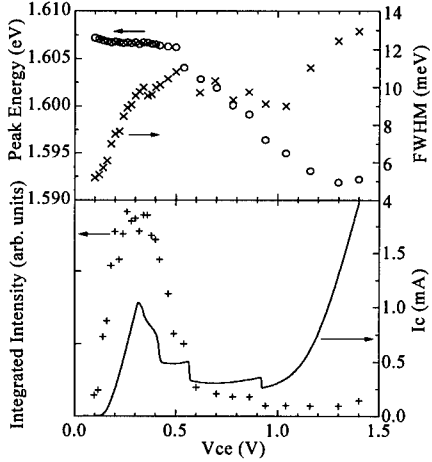


Fig. 5 Collector voltage dependencies of peak energy, FWHM, integrated luminescence intensity, and collector current.

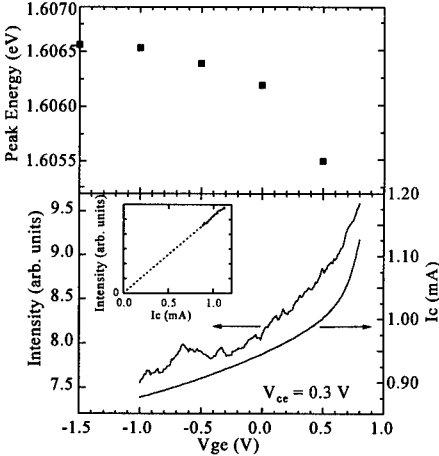


Fig. 6 Gate voltage dependencies of peak energy, luminescence intensity, and collector current.

Figure 5 shows V_{ce} dependencies of the peak energy, the FWHM of the peak, the integrated luminescence intensity, and the collector current, I_c . The integrated intensity shows strong correlation with resonant-tunneling current. The PL peak shifts to a lower energy with increasing V_{ce} , indicating the existence of the quantum-confined Stark effect. This means that the PL signal originates from electron-hole recombination in the quantum well. The possibility that luminescence is created by another mechanism is not plausible. If the PL signal originates from recombination between electrons in the quantum well and holes under the collector barrier, for instance, the peak position should shift to a higher energy. Electron-hole recombination in the collector region is also impossible due to the same reason. Electric field in the quantum well estimated from Stark shift is ≈ 50 kV/cm at peak voltage. The PL line

width increases from 5 meV at $V_{ce} = 0.1$ V to 10 meV at resonant voltage, $V_{ce} = 0.3$ V, as the resonant-tunneling current increases. This increase in line width suggests charge buildup in the quantum well. The electron density n_e in the quantum well estimated from line width increase is 2.4×10^{11} cm⁻² at 0.3 V.

Next, the effect of gate voltage, V_{ge} , on PL spectra is analyzed. The control of luminescence by gate voltage is characteristic of transistors. V_{ce} is fixed at a peak voltage of 0.3 V. Figure 6 shows the V_{ge} dependencies of the peak energy, the luminescence intensity, and the collector current, I_c . I_c and PL intensity increase with increasing V_{ge} . As shown in the inset, PL intensity is proportional to I_c , indicating that the area contributing to luminescence is modulated by gate voltage, similar to the modulation of the cross-section for current flow. The PL peak position shifts to a higher energy with increasing negative gate voltage, $|V_{ge}|$ ($V_{ge} < 0$). This can be explained as the quantum confinement of electrons by the potential of the gate depletion layer. Electrons are confined perpendicular to current flow. Assuming the parabolic potential of the gate depletion layer, calculated ground-state energy agrees semi-quantitatively with the energy shift of the PL spectrum.

5. Summary

The photoluminescence of a resonant-tunneling transistor was studied. An excitation energy close to the bandgap energy of the GaAs collector layer was chosen to simplify the luminescence spectra. The obtained photoluminescence signal had a strong correlation with the resonant-tunneling current. The photoluminescence peak position shifted to a lower energy with increasing collector voltage, indicating the existence of the quantum-confined Stark effect. The collector voltage dependencies of photoluminescence intensity and line width suggest charge buildup in the quantum well. The density of electrons in the quantum well was estimated to be 2.4×10^{11} cm⁻² at peak voltage. The gate voltage dependence of the photoluminescence spectrum indicated the quantum confinement of electrons by the potential of the gate depletion layer. The possibility of controlling luminescence intensity by gate voltage was also demonstrated.

Acknowledgments

The authors wish to thank Dr. K. Maezawa and Dr. M. Yamamoto for their valuable discussion. This work was supported in part by a Grant-in-Aid for Scientific Research from the Japanese Ministry of Education, Science and Culture.

References

- [1] Cappaso F, Sen S, Beltram F, Lunardi L M, Vengurlekar A S, Smith P R, Shar N J, Malik R J, and Cho A Y 1989 *IEEE Trans. Electron Devices* 36 2265
- [2] Takatsu M, Imamura K, Ohnishi H, Mori T, Adachihara T, Muto S and Yokoyama N 1992 *IEEE J. Solid-State Circuits* 27 1428
- [3] Seabaugh A C, Luscombe J H and Randall J 1993 *Future Electron Device J.* 3 9
- [4] Maezawa K and Mizutani T 1993 *Jpn. J. Appl. Phys.* 32 L42-4
- [5] Maezawa K, Akeyoshi T and Mizutani T 1993 *IEDM93 Tech. Dig.* 415-8
- [6] Maezawa K, Akeyoshi T and Mizutani T 1994 *IEEE Trans. Electron Devices* 41 148-54
- [7] Maezawa K 1995 *Jpn. J. Appl. Phys.* 34 1213-7
- [8] Ohno Y, Kishimoto S, Mizutani T and Maezawa K 1996 *IEICE Trans. Electron.* E79-C 1530-6
- [9] Young J F, Wood B M, Aers G C, Devine R L S, Liu H C, Landheer D, Buchanan M, SpringThorpe A J and Mandeville P 1988 *Phys. Rev. Lett.* 60 2085-8
- [10] Skolnick M S, Simmonds P E, Hayes D G, White C R H, Eaves L, Higgs A W, Henini M, Hughes O H, Smith G W and Whitehouse C R 1992 *Semicond. Sci. Technol.* 7 B401-8
- [11] Shah J 1978 *Solid-State Electron.* 21 43-50

Resonant Tunneling in Disordered Materials such as SiO₂/Si/SiO₂

R. Lake, B. Brar, *G. D. Wilk, A. Seabaugh, and G. Klimeck

Raytheon TI Systems, Box 655936, MS 134, Dallas, TX 75265
 *Texas Instruments, Box 655936, MS 147, Dallas, TX 75265

Abstract. We have analyzed the effect of disorder in both the well and barriers of a resonant tunneling diode (RTD). If the disorder is limited solely to the barriers, a good peak-to-valley ratio (PVR) is expected. We describe a general guideline relating the PVR to the bulk mobility and effective mass of the well material of an RTD. We compare the effects of correlated versus uncorrelated disorder on the valley current. We discuss why interband tunnel devices such as the Esaki diode are more robust than RTDs in the presence of disorder.

1. Well versus Barrier Disorder

There have been a number of studies of Si / SiO₂ multilayer structures to look for quantization and resonant effects [1,2]. While the interface can be made smooth, the entire multi-layer structure is amorphous. Core level x-ray spectroscopy gives unambiguous evidence that quantization does occur, and that it follows the standard inverse square relationship to the well width [1]. However, there have been no strong demonstrations of resonant tunneling and negative differential resistance (NDR) in such systems. The observation of state-quantization with core-level-spectroscopy requires only conservation of total energy. State quantization is a necessary but not sufficient condition to observe NDR. Observation of NDR in an RTD requires conservation of both total energy and transverse momentum. The random potential resulting from the noncrystalline nature of the Si/SiO₂ material breaks the translational periodicity and, thus, the transverse momentum conservation required for high peak-to-valley ratios in RTDs.

We simulate the effect of the disorder by creating a mathematical model which mimics the macroscopic effects of amorphous disorder. The model gives the same momentum independence to the scattering since the correlation length of amorphous disorder is approximately the lattice constant, and the model gives the same bulk mobility. We begin with a single-band, tight-binding Hamiltonian which parameterizes the Si-Si (or for III-Vs, the cation-anion) basis matrix elements into a single number, the site energy. Then we assign a random component, δV , to the site energy. The random component has a Gaussian distribution with a mean of 0 and a variance of σ . The random component is uncorrelated between any two sites. The only free parameter in the model is σ . To relate σ to a physical quantity, we use the fact that the mobility resulting from this disorder is

$$\mu = \frac{4e\pi^{1/2}\hbar^4}{3m_c m_d^{3/2} (k_B T)^{1/2} \Omega \sigma^2} \quad (1)$$

where e is the magnitude of the electron charge, Ω is the volume of the primitive cell, m_c is the conductivity effective mass and m_d is the density of states effective mass. The disorder is treated in the self-consistent Born approximation [3].

In Fig. (1), we choose the tight-binding parameters corresponding to an effective mass of 0.3 for the SiO₂ [4] and 0.5 for the a-Si [1]. In Fig. (1a) the disorder is restricted to the well region. We find that the NDR is destroyed when the mobility of the a-Si in the well is less than or equal to 250 cm²/Vs. If we take the same structure and restrict the same disorder to the barrier layers, there is almost no effect on the I-V and the PVR as is shown in Fig. (1b).

2. General Guideline Relating the PVR to the Bulk Mobility

When attempting to build an RTD in a new material system that is disordered or even amorphous, we would like to have some experimental measure which will predict whether the RTD will have a useful

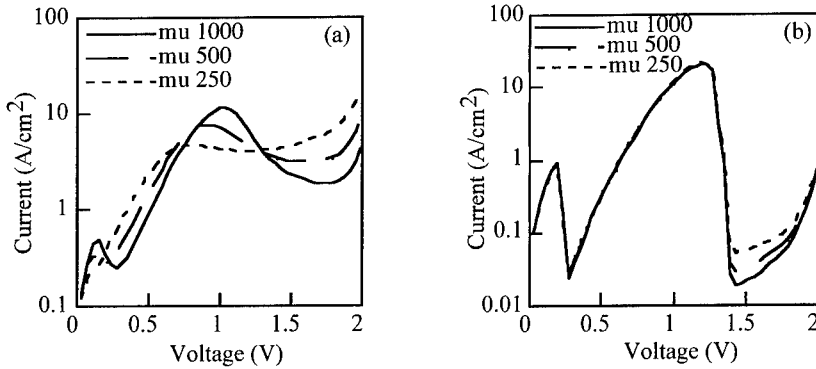


Figure 1. I-V of an amorphous $\text{SiO}_2/\text{Si}/\text{SiO}_2$ RTD with dimensions 1.35/2.97/1.35 nm and 10^{18} cm^{-3} doped leads. (a) The disorder is restricted to the well region. (b) The disorder is restricted to the barrier region.

peak-to-valley ratio. We consider the case in which (a) both the mobility of the bulk material and the valley current of the RTD are determined by the static disorder scattering resulting from substitutional disorder (alloys), geometric disorder (amorphous and poly-crystalline materials), impurities and dopants, and (b) the bulk material and the thin layer have the same microscopic structure. Under such circumstances, both analytical [5] and numerical calculations show that the PVR is related to the bulk, room-temperature mobility by

$$\text{PVR} \propto \tau = \mu m_c / e. \quad (2)$$

Doping provides an experimental knob on the disorder and mobility. In a set of experiments, we increased the doping throughout an AlAs/InGaAs/AlAs based RTD, measured the PVR, and measured the mobility of the well material by growth of bulk InGaAs epi-layers characterized by resistivity and Hall measurements. We also numerically calculated the PVR of the InGaAs RTD as a function of mobility. The experimental and numerical results are shown in Fig. (2). Except at low mobility, the numerical calculations tend to underestimate the PVR. Therefore, we use the experimental data combined with relation (2) to make predictions for other materials.

We propose a general guide relating PVR to the bulk mobility and conductivity effective mass illustrated in Fig. (3). The PVR vs. mobility curve for the InGaAs RTD is replotted. The other curves are obtained by scaling the InGaAs mobility by $m_{\text{InGaAs}}/m_{\text{new}}$. The scaling law suggests that to obtain a PVR of 5 in a-Si with $m_c = 0.5 m_0$ will require a mobility of $400 \text{ cm}^2/\text{Vs}$, well above values found for a-Si.

3. Correlated Versus Uncorrelated Disorder

In an ideal epitaxial structure, the periodic crystal potential is undisturbed in the transverse plane, therefore transverse crystal momentum is conserved, and the process illustrated in Fig. (4) is not

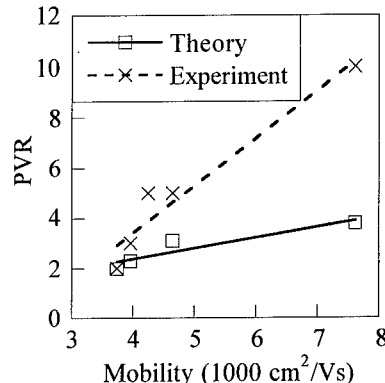


Fig. 2. Experimental and theoretical PVR vs. mobility for an InGaAs well.

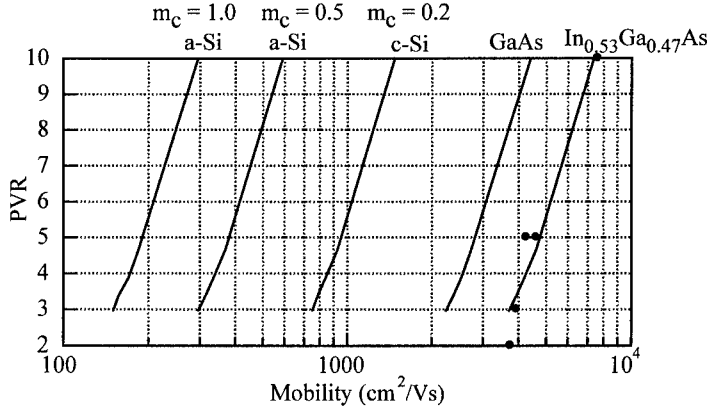


Figure 3. General guide relating PVR to the bulk mobility and conductivity effective mass of the well material.

allowed. In the presence of disorder, the incident electron can pick up a Fourier component of the disorder potential and scatter into a resonant transverse momentum state k_t^r . This is the process by which elastic scattering from disorder contributes to the valley current. The momentum coupling which determines the amount of momentum that an electron can obtain from the disorder is given by the Fourier transform of the random potential autocorrelation function.

When the disorder is uncorrelated $\langle V(\mathbf{R})V(\mathbf{R}') \rangle \propto U\delta(\mathbf{R} - \mathbf{R}')$, and the momentum coupling is a constant U . In this case, an incident electron can pick up any transverse momentum that it needs to get into the resonant state, and the scattering component of the valley current is nearly constant, independent of bias as illustrated schematically in Fig. (5a).

If the disorder is correlated, the inverse correlation length provides a cutoff to the momentum transfer. For example with Gaussian correlation,

$\langle V(\mathbf{R})V(\mathbf{R}') \rangle \propto e^{-|\mathbf{R}-\mathbf{R}'|^2/\Lambda^2}$ where Λ is the correlation length, and the momentum coupling falls off as $|U_q|^2 \propto \Lambda^3 \pi^{3/2} e^{-q^2 \Lambda^2/4}$. In the valley current region, as the bias is increased, an incident electron must pick up more transverse momentum to scatter into the resonant subband. The amount of momentum that the electron can obtain is governed by $|U_q|^2$. Therefore, for correlated disorder, the scattering component of the valley current falls off with bias as shown schematically in Fig. (5b).

We have numerically explored the effect of the correlation length for disorder limited to the interface layers of GaAs / AlAs RTDs for both exponentially and Gaussian correlated disorder [6]. Figs. (3) and (4) of reference [6] show that as the correlation length increases, the slope of the valley current region becomes more negative and the scattering assisted current decreases with bias. These results indicate that a polycrystalline well with large enough crystal sizes may be sufficient for observing NDR.

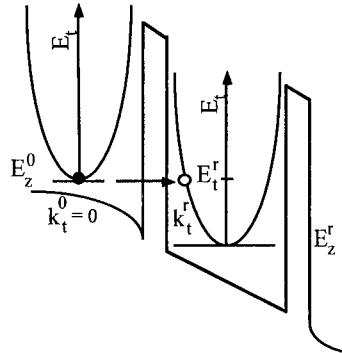


Figure 4. The parabolas represent the transverse kinetic energy. An off-resonant incident electron with longitudinal energy E_z^0 and zero transverse kinetic energy can elastically scatter into the resonant state by trading off longitudinal energy for transverse kinetic energy.

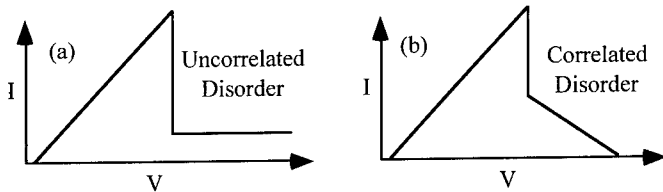


Figure 5. (a) The contribution to the valley current from uncorrelated disorder scattering is essentially flat, independent of bias. (b) The contribution to the valley current from correlated disorder scattering falls off with bias.

Interband Tunnel Diodes and Disorder

Very general reasons suggest that an interband tunnel diode (ITD) such as the Esaki diode [7], the quantum well Esaki diode [8], or the resonant interband tunnel diode [9] should be less affected by disorder than an RTD. A notable difference between an ITD and an RTD is that an ITD requires one less conservation law to exhibit NDR. RTDs require conservation of both total energy and transverse momentum whereas ITDs require only conservation of total energy. For an RTD, Fig. 4 shows that there is always a high transverse-energy state in the well into which an incident electron can scatter while conserving total energy. For an ITD biased in the valley current region, there are no valence states into which an electron can elastically scatter (see for example Figs. (4), (6), and (8) of reference [10]). Since disorder scattering is elastic, the ITD should be more resilient than the RTD to the presence of disorder. This is in fact evident for an Esaki diode since the active region is doped to concentrations of 10^{20} cm^{-3} . Such a high doping in the well of an RTD would destroy its NDR.

Summary

Although there is experimental evidence of coherent resonance effects in amorphous Si / SiO_2 materials, both numerical calculations and analytical theory do not show promise for good PVR from such materials. Amorphous barriers with a crystalline well, however, appear to be sufficient. The analysis of correlated disorder indicates that polycrystalline wells may be sufficient if the domain sizes are large enough. Interband devices are more robust in the presence of disorder since they require one less conservation law to work.

References

- [1] Lu Z, Lockwood D J, and Baribeau J M 1995 *Nature* 378 258-260
- [2] Hirose M, Morita M and Osake Y (1977) *Jpn. J. Appl. Phys.* 16 Suppl. 16-1 561-4
- [3] Lake R, Klimeck G, Bowen R C, and Jovanovic D 1997 *J. Appl. Phys.* 81 7845-7869
- [4] Brar B, Wilks G D, and Seabaugh A 1996 *Appl. Phys. Lett.* 69 2728-30
- [5] Lake R, Klimeck G., Anantram M P, and Datta S 1993 *Phys. Rev. B* 48 15132-7
- [6] Lake R, Klimeck G, Bowen R, Fernando C, Moise T, and Kao Y 1996 *Superlatt. Microstruct.* 20 279-285
- [7] Esaki L 1958 *Phys. Rev.* 109 603-4
- [8] Tsai H H., Su Y K, Lin H H, Wang R L, Lee . L 1994 *IEEE Electron Device Lett.* 15 357-359
- [9] Söderström J R, Chow D H, McGill M C (1989), *Appl. Phys. Lett.* 55 1094-1096
- [10] Seabaugh A and Lake R 1997 *Encyclopedia of Applied Physics* vol. 22 (New York:VCH Publishers) 1-24

Semi-insulating GaAs by Controlled Introduction of Metallic Nano-Schottkies

L.-E. Wernersson, A. Litwin, L. Samuelson, and W. Seifert
 Solid State Physics/Nanometer Structure Consortium
 Lund University, Box 118
 S-22100 Lund, Sweden

Abstract The formation of a semi-insulating GaAs-layer by overlapping depletion regions is investigated by controlled introduction of matrices of tungsten Nano-Schottkies. By varying the spacing between the buried metal discs, the effect of the Schottky-depletion on the current transport is demonstrated. A change in the conductivity by 7 orders of magnitude is measured with a disc separation of 200 nm. In this semi-insulating material, the presence and height of a potential barrier between the discs is deduced from the temperature dependence of the current transport. Finally, the Schottky-barrier height of the buried metal discs is obtained from photo-conductivity measurements.

1. Introduction

The creation of semi-insulating semiconductor materials has attracted much attention in the past, due to applications as insulating substrates, buffer-layers, and regrown layers in complicated structures such as lasers. A common way of realising the semi-insulating behaviour is to compensate the shallow dopants with deep-levels, for instance Cr in GaAs, which pins the Fermi-level in the middle of the band gap. However, it would be advantageous to create isolating layers in a controlled way without the compensation by defects, which may easily diffuse to active regions in the devices.

A special attention has been given the properties of GaAs, grown by Molecular Beam Epitaxy at low temperatures. In this material, arsenic precipitates can be formed, which have been proposed to act as buried Schottky contacts [1]. However, in the same material, a large amount of As-antisites has been detected by spin-resonance measurements [2]. Both mechanisms may lead to the formation of the observed semi-insulating behaviour. Numerous investigations have been made to clarify this issue, with results supporting either model. The purpose of this paper is to, in a controlled test experiment, investigate the effect and operation of buried nano-Schottkies in GaAs. Simultaneously, the used fabrication method offers a novel way for creating vertical isolation in complex circuits and for realisation of local injection with sub-micrometer openings [3].

2. Structure

A schematic of the structures used for this investigation is shown in fig. 1. 300 nm GaAs, Si-doped to $2 \times 10^{16} \text{ cm}^{-3}$, was grown on a (100) substrate by Metalorganic Vapour Phase Epitaxy (MOVPE).

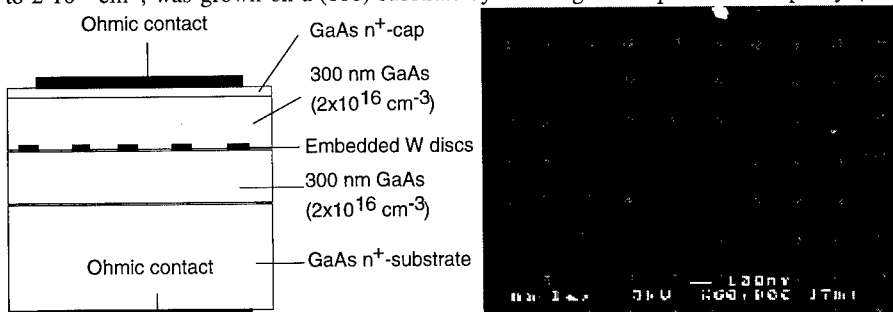


Fig. 1 A fabricated structure is shown to the left and a Scanning Electron Microscopy image of W discs before overgrowth to the right.

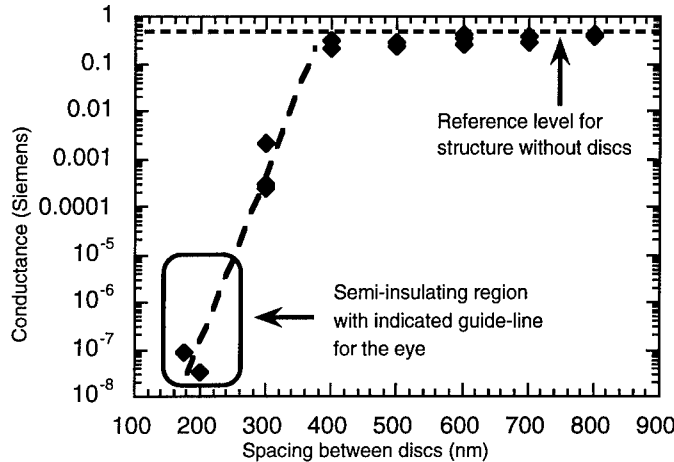


Fig. 2 Room-temperature conductance for structures with varying spacing between the discs.

Structures with tungsten (W) discs were defined by electron beam lithography and subsequent metal evaporation in a lift-off process. Tungsten was chosen as metal due to its outstanding thermal stability in GaAs, even during overgrowth [4], and in separate structures we measured a Schottky barrier height of 800 meV for buried gratings. The buried discs of 50 nm diameter were arranged in regular 2D square lattices. Structures with different periods in the pattern were included in order to study the change in conductance with respect to metal density. After cleaning, the sample was introduced into the growth chamber and all structures are covered by 300-nm-thick, single crystalline GaAs with the same doping. The details of the growth conditions were identical to our previously used conditions and they are described elsewhere [5]. Finally, mesas were formed and ohmic contacts were defined on the top of each mesa and to the substrate.

3. Characterisation

3.1 Conductance

The vertical current transport between the top and bottom ohmic contacts were measured for each structure at room-temperature to study the influence of the Schottky depletion around the buried metal discs on the conductance. In Fig. 2, the measured conductance are shown. The indicated reference level is the conductance of control structures without any buried discs. As metal discs are introduced into the GaAs, the conductance decreases due to the smaller, un-depleted area available for the current transport. However, as can be seen in the figure, only a minor change in conductance with increasing disc density is obtained for a spacing larger than 400 nm between the discs. In contrast, the conductance drops by 3 orders of magnitude for the structures with 300 nm between the discs, and for the structures with 200 nm separation, a change by 7 orders of magnitude is observed. Thus, a semi-insulating layer has been obtained by introducing W discs with a separation of 200 nm into the GaAs. The dramatic change in conductance indicates that overlapping depletion regions start to form at a disc spacing of around 400 nm for this chosen doping level as discussed below.

3.2 The potential barrier from overlapping depletion regions

In order to measure the potential barrier that is formed by the depletion regions, the temperature-dependence on the current transport was measured. Since the metal discs are arranged in square patterns, we believe that the current transport is going through the centre between the four discs in each unit cell of the buried disc lattice. Thus, the minimum in the metal-induced potential barrier can be deduced from temperature dependent measurements. Assuming that the current transport over the barrier can be described by thermionic emission

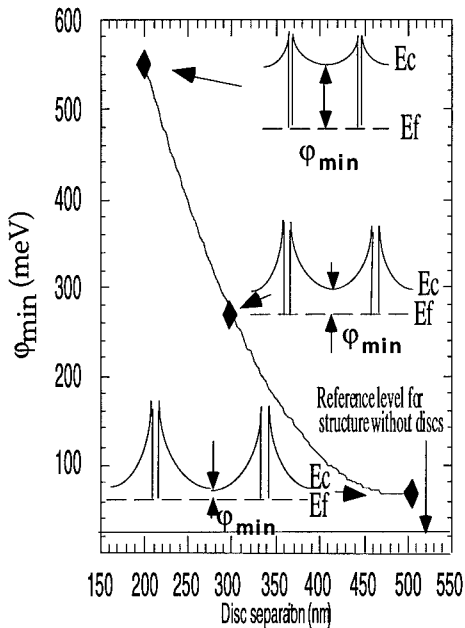


Fig. 3 Measured potential minima of the metal-induced barrier in the GaAs between the discs.

$$j = AT^2 e^{-q\varphi/kT}$$

the barrier, φ , can be deduced in Arrhenius plots. Now, the current level was measured at an applied bias of 0.01 V for varying temperatures and structures, and the obtained barriers from the Arrhenius plots are shown in fig. 3. This graph verifies the presence of overlapping depletion regions, as seen by an increase in the barrier, and it also explains the dramatic change in the conductivity as observed in fig. 1. We hence conclude that the semi-insulating behaviour in our material is created by overlapping depletion regions from the buried nano-Schottkies.

3.3 The Schottky barrier height

In this investigation, the height of the metal-semiconductor Schottky barrier of the buried nano-Schottkies have been deduced from photo-conductivity measurements. A bias of 0.5 V was applied to the top ohmic contact and the steady-state current level was measured between the two ohmic contacts during illumination at 77 K. Photons are absorbed in the buried layer and carriers are released from the metal, which results in an increased conductivity in the semiconductor between the discs. The maximum change in conductance we observed, was an increase by 3 orders of magnitude when the structure was illuminated. According to the Fowler theory, the photoresponse, R , is expected to vary with the photon energy as

$$R \propto (hv - hv_0)^2$$

where v_0 is the Schottky barrier height [6]. Indeed, plotting the square root of the measured photo-conductivity versus photon energy, a linear relationship is observed with a threshold of 840 meV as shown in fig. 4. In order to compare the barrier of the buried nano-Schottkies with macroscopic diodes, the sample also included W squares with 100 μm in side-length. Due to the selectivity between W and GaAs in the growth, the squares were not covered by GaAs and these diodes could be contacted directly after the overgrowth. The obtained values from the forward current-voltage

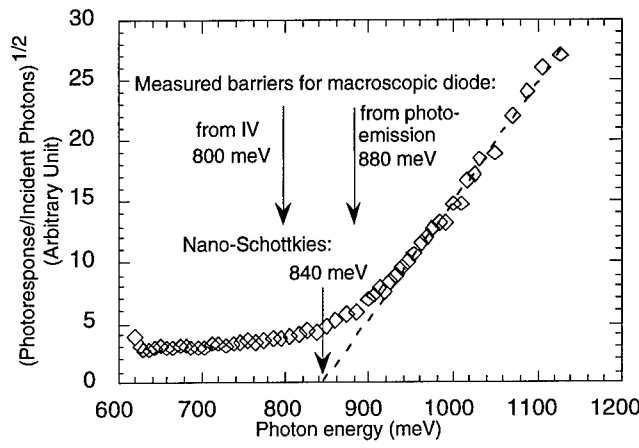


Fig. 4 Spectral distribution of photo-conductivity at 77 K

characteristics (800 meV) and from photo-conductivity measurements (880 meV) of these macroscopic diodes are included in fig. 4. The close agreement between the barrier heights is a strong indication that the W nano-discs do form a Schottky barrier to the GaAs and that the observed photo-conductivity is caused by carrier emission from the buried metal discs.

4. Conclusions and discussion

Patterns of tungsten discs with a diameter of 50 nm have been introduced in GaAs in a controlled way and the effect on the conductance in the GaAs has been measured. It is shown that the vertical conductance is reduced by 7 orders of magnitude as the disc separation is reduced from 400 nm down to 200 nm. The origin of this enormous drop in conductance is the formation of a potential barrier from overlapping depletion regions around the nano-Schottkies. A potential barrier of 550 meV has been measured for the structures with 200 nm separation between the discs. Furthermore, a Schottky barrier height of 840 meV for the buried metal discs have been measured by internal photo-emission. This Schottky barrier height is found to agree very well with the corresponding barrier which we measured for macroscopic W-GaAs diodes. The presented data show that semi-insulating GaAs can be created in a controlled way by overlapping depletion regions from metallic nano-Schottkies on a floating potential. This technique can be used for realisation of local injection in devices and circuits.

The authors would like to thank H. Pettersson, L. Montelius, and S. Anand for fruitful discussions during this work and the Swedish National Board for Technical and Industrial Development, the Swedish Foundation for Strategic Research, and the Swedish Natural Science Research Council for financial support.

References

- [1] Warren A C, Woodall J M, Freeouf J F, Grischkowsky D, McInturff D T, Melloch M R and Otsuka N 1990 *Appl. Phys. Lett.* **57** 1331-33
- [2] Liu X, Prasad A, Chen W M, Kurpiewski A, Stoscheck A, Liliental-Weber Z and Weber E 1994 *Appl. Phys. Lett.* **65** 3002-5
- [3] Wernersson L-E, Carlsson N, Gustafson B, Litwin A and Samuelson L to be published in *Appl. Phys. Lett.*
- [4] Bozler C O and Alley G D 1980 *IEEE Trans. Electron Devices* **27** 1128-41
- [5] Wernersson L-E, Georgsson K, Litwin A, Samuelson L and Seifert W 1996 *Jour. Appl. Phys.* **79** 500-3
- [6] Sze S M 1981 *Physics of Semiconductor Devices* (New York: Wiley)

Comprehensive Simulation of Quantum Well Lasers

M. S. Hybertsen, M. A. Alam, R.K. Smith, G.A. Baraff and M.R. Pinto

Bell Laboratories, Lucent Technologies, Murray Hill, NJ 07974, USA

Abstract. We demonstrate a simulation tool which treats a full two dimensional cross section of a semiconductor laser diode with multiple quantum wells in the active region. The free carrier transport, the bound quantum well populations, the capture of carriers into the quantum wells, the gain and spontaneous emission, the transverse optical mode and the photon mode population are all treated in a fully coupled and self consistent solution for each bias of the laser diode. The simulations are illustrated for an EMBH laser structure with seven quantum wells in the active region.

Optoelectronic devices pose a diverse range of problems for simulation. Many aspects of the device performance can be understood with phenomenological models. However, the demands for improved performance, especially in the telecommunications arena, drive a real need for predictive simulation tools based on a microscopic understanding of the physical device. This is a very challenging problem. The operation of a semiconductor laser diode depends on carrier transport on the scale of microns as well as quantum mechanical processes on the scale of 100 Å. These disparate scales must be treated simultaneously along with the optical field in the device. In recent years, several groups have worked on integrated models for the operation of quantum well lasers [1-4]. In this work, we integrate the necessary physical models with efficient numerical algorithms. This allows realistic simulation of the full two-dimensional cross section of the laser diode in a tractable amount of computer time.

As an overview, consider the flow of carriers from the external contacts through a typical semiconductor laser diode (Fig. 1). A laser is a fully three dimensional device which can be conceptually partitioned into an x-y cross section with a p-i-n diode structure and an extended optical cavity along z with mirrors on either end. The diode under forward bias results in simultaneous injection of electrons and holes into the n- and p-type cladding respectively. Flow of these carriers is governed by conventional semiconductor transport equations. The optically active region of the device is typically a lower band gap material. This double heterostructure both confines carriers and provides a higher refractive index region which confines the optical mode in the x-y plane. Accumulation of the electrons and holes in the active region under forward bias leads to optical inversion providing gain for the lasing mode. In a quantum well laser, the lowest bound electron and hole states in the wells provide the gain. This separate two dimensional population of carriers is coupled to the bulk-like three dimensional carriers by capture and emission processes. When the material gain due to the accumulated carriers approaches the other losses experienced by the photon mode in the optical cavity, stimulated emission of photons becomes significant. The stimulated emission time competes with other important time scales in the carrier transport: diffusion times, capture or emission times, and energy relaxation times. This has important consequences for the laser operation, particularly under high frequency modulation. So far, these issues arise for one-dimensional transport. In many applications, it is essential to have a single lasing mode. Therefore, the transverse waveguide formed by the active area will only have a few micron extent. At the same time, an efficient device requires that most of the current flow through this active area. Designs to restrict the current pose additional problems for simulation of the carrier trans-

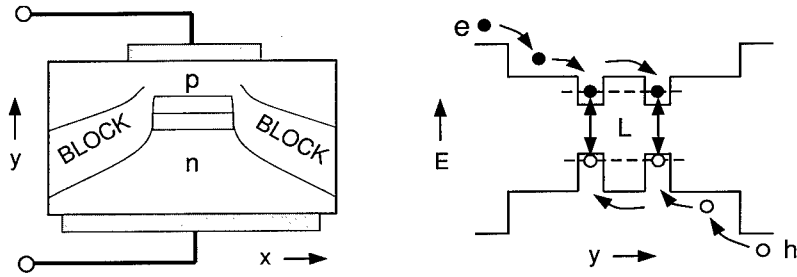


Figure 1. Schematic illustration of a semiconductor laser diode cross section (left) and energy band profile for the active region (right) indicating some of the microscopic processes.

port through the device and require that the full x-y cross section be treated.

These basic processes in the laser are embodied as follows. The electron and hole densities are decomposed into a classical three dimensional population (n , p) and confined populations in each quantum well (n_q , p_q). The carrier transport is described by classical drift-diffusion equations [5]:

$$\begin{aligned} -\nabla \bullet (\epsilon \nabla V_h) &= q(p + p_q - n - n_q + N_D - N_A), \\ \frac{1}{q} \nabla \bullet J_n &= R + C_n, \\ \frac{1}{q} \nabla \bullet J_p &= -(R + C_p), \end{aligned}$$

where V_h is the electrostatic potential, ϵ is the dielectric constant, N_D and N_A are the ionized donors and acceptors, J_n and J_p are the electron and hole current densities and R and C are the recombination and capture rates. The equations are written for the steady-state case.

The confined carriers in the quantum wells occupy bound subbands which must be computed quantum mechanically:

$$(H_0 + V_h)\psi = E\psi.$$

The Hamiltonian used here is an eight band effective mass model to which the electrostatic potential is added. The solutions provide the subbands and dispersions as well as the input for the calculation of the optical properties of the quantum wells including the gain [6]. The number of carriers in each well is determined by rate equations which balance the capture and emission, the stimulated emission and the other recombination mechanisms (written here for steady-state):

$$C_n - GS - R_q = 0,$$

$$C_p - GS - R_q = 0.$$

The recombination mechanisms for the bound carriers in R_q include the spontaneous emission, which is calculated directly along with the gain, as well as other mechanisms such as Auger which are included phenomenologically. The stimulated emission term consists of the modal gain G computed from the bound states using a density matrix formulation and the photon population in the lasing mode, S . These

equations are repeated for each quantum well and may be generalized to more than one photon mode.

The shape of the transverse optical mode is described by a scalar wave equation:

$$\nabla^2\phi + k^2 \epsilon \phi = \kappa^2 \phi,$$

where k is the vacuum wavevector and κ is the modal propagation constant. In general, the dielectric constant depends on the carrier density distribution in the device. The longitudinal optical cavity along the z -axis defines a set of cavity modes, each with an associated loss, or lifetime. The number of photons in each mode is determined by an integral rate equation:

$$\left(G - \frac{1}{\tau_p} \right) S + \beta R_{sp} = 0,$$

where G is the modal gain, τ_p is the photon lifetime and β describes the small coupling of the spontaneous emission into the cavity mode. For the present simulations of the laser cross section, information on the longitudinal modes must be supplied externally. In general, the photon lifetime (loss) depends on the carrier density distribution in the device due to free carrier absorption.

The equations describing the laser form a strongly coupled non-linear set which must be solved simultaneously for each bias of the laser. We discretize the transport and integral rate equations. The resulting set of order 20,000 algebraic equations are solved iteratively using a Newton update method. At each iteration, the eigenvalue problems associated with the optical mode and the subbands in the quantum wells are solved directly. A key feature of laser simulation is the threshold behavior of the photon population which rises by several orders of magnitude as the gain approaches the photon lifetime. A set of slack variables are introduced to insure stable and efficient convergence of the numerical solutions. The final set of equations are well conditioned and the algorithm is quadratically convergent. We have discussed these issues elsewhere [4,7].

To illustrate the simulations, we consider a multi-quantum well laser with an active layer which is roughly representative of 1.3 μm telecommunications lasers based on the InGaAsP materials system on an InP substrate. The 150 Å quaternary alloy barriers have a bandgap of 1.05 μm while the strained (1% compressive) 70 Å wells have a band gap chosen so that the lowest quantized transition occurs at 1.33 μm . The resulting gain and spontaneous emission computed from the eight band model are shown in Fig. 2. The splitting between the TE and TM spectra corresponds to the light hole to heavy hole sepa-

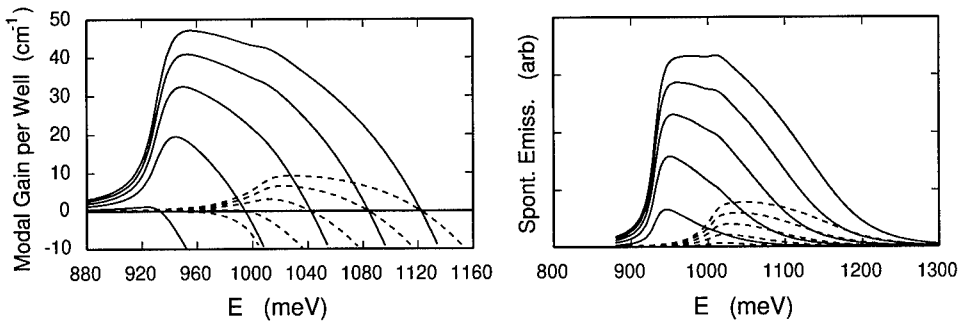


Figure 2. Calculated modal gain per quantum well (left) and spontaneous emission (right) spectra in the TE (solid) and TM (dashed) polarizations for $n = p = 1, 2, 3, 4$ and $5 \times 10^{12} \text{ cm}^{-2}$.

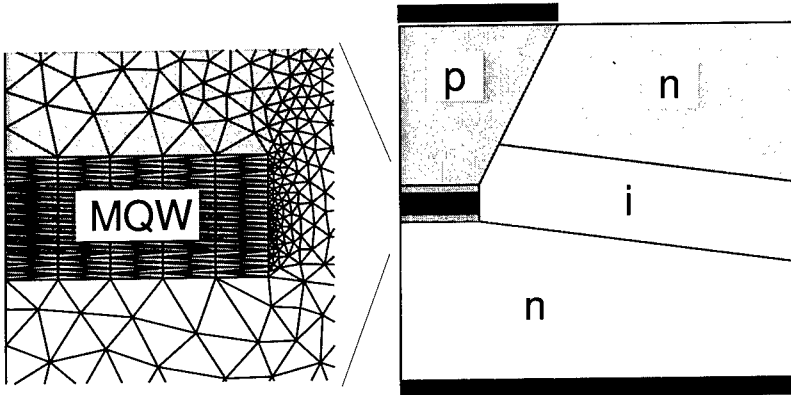


Figure 3. Schematic cross section of the EMBH laser simulated (right) and an expanded view of the region around the active layer (left). Half the device is shown. The quantum wells are still not easily resolved on this scale. The grid shown illustrates the topology of the mesh. The actual mesh is substantially refined.

ration resulting from the mass difference and the strain. Compressive strain suppresses the TM gain. The peak of the gain is quite close to $1.3 \mu\text{m}$. These spectra are calculated for a single quantum well under flat band conditions. The same full quantum calculation is done for the gain at the laser mode energy and for the integrated spontaneous emission rate at each iteration of the full device calculation.

The active region of the device studied here is composed of 7 wells. These are embedded in a diode with a so-called EMBH structure illustrated in Fig. 3. Contact is made to the top p-layer and the bottom n-layer. The floating n-layer and the i-layer serve to constrain the current to largely flow through the active layer at the center. The region labeled 'MQW' includes the 7 wells, 6 barriers and two further layers (700 Å) of $1.05 \mu\text{m}$ band gap to help confine the optical mode. A critical issue in the solution of the device equations is to achieve an adequate mesh for accurate discretization. Figure 3 gives an indication of the mesh topology that is necessary to accommodate both the small length scale quantum well regions as well as the wider areas of the device (width of $5 \mu\text{m}$ shown).

Many features of the device can be studied with a quasi-one-dimensional simulation. This is equivalent to simulating a wide area diode. We choose the mirror loss corresponding to a Fabry-Perot device

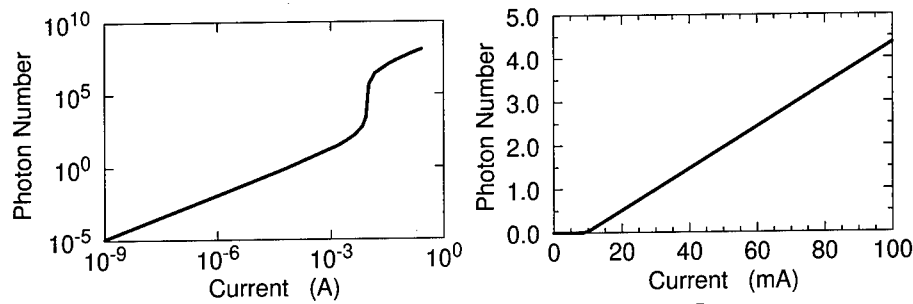


Figure 4. Photon number versus input current on a log (left) and a linear ($x10^7$) scale. This is related to output power by a conversion factor involving the length of the laser and the mirror reflectivity.

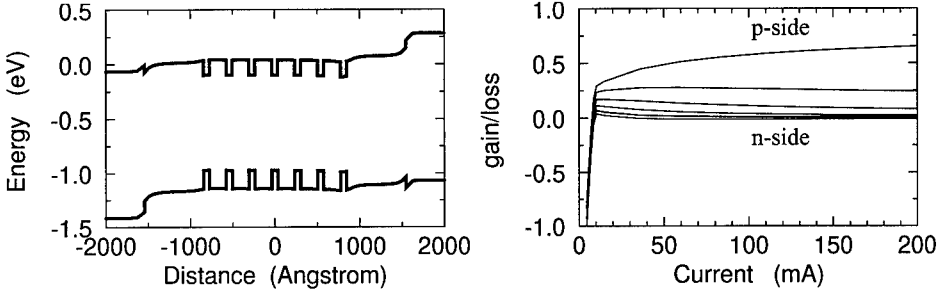


Figure 5. Band diagram for a voltage well above threshold (left) and the ratio of the gain in each well to the total loss as a function of current (right).

with cleaved facets and a cavity length of 1 mm. Waveguide loss and free carrier absorption are not included for simplicity, but can be at no additional cost in simulation time. The resulting light-current curves are shown in Fig. 4. The extended light-emitting diode region below threshold is followed by a roughly 6 order of magnitude rise in photon number at threshold. The threshold current is about 10 mA. Linear output is found above threshold since leakage current is minimal in the quasi-one dimensional case. The value of threshold is reasonable, but of course strongly dependent on the assumptions concerning loss as well as the Auger recombination coefficient (here chosen to be $2 \times 10^{-29} \text{ cm}^6/\text{sec}$).

Interesting features already appear in this one dimensional simulation. Firstly, the active region of the device is not in truly flat band conditions as seen in Fig. 5. This depends in part on the doping levels assumed, here 2×10^{17} for the separate confinement layers and 2×10^{15} for the well and barrier regions. The gain in each well is very sensitive to the local band profile and carrier density. The bound electron and hole populations vary substantially among the wells as shown by the difference in gain between the well nearest the p-contact and the ones closer to the n-contact. The gain is shown relative to the total loss, so the sum of contributions must approach unity above threshold. Especially at large laser output, most of the gain is supplied by a single well. This result depends in detail on such factors as the model for carrier capture into the wells, the device temperature and the other recombination mechanisms. It illustrates the competition between the rate for stimulated emission and the times associated with transport of carriers. Similar results have been seen in previous simulations [2, 3].

Full two dimensional simulations allow further microscopic details of the laser operation to be studied. Figure 6 illustrates this. Whereas the quasi-one dimensional simulation shows linear light versus current up to high bias, the full EMBH diode simulation gives a dramatically non-linear output. This is largely due to leakage paths which open up through the i-layer. This is illustrated by the relatively high carrier density in the i-region. This is shown in Fig. 6 for the three dimensional electron density. Other interesting details can also be found. The electron density in the active region is actually highest in the region near the p-contact. This is closely related to the strong variation in the gain among the various wells highlighted in Fig. 5. The holes tend to accumulate more in the wells nearest the p-contact because of the relative difficulty of moving them through the quantum well stack on a time scale which is in competition with stimulated recombination. The electrons tend to follow the holes to minimize the electrostatic energy and to support the relatively higher capture rate in those wells demanded by the stimulated emission.

This paper briefly describes an efficient and comprehensive laser diode simulation tool. Full bias scans can be done in minutes for the quasi one dimensional case and in one to two hours for the full two

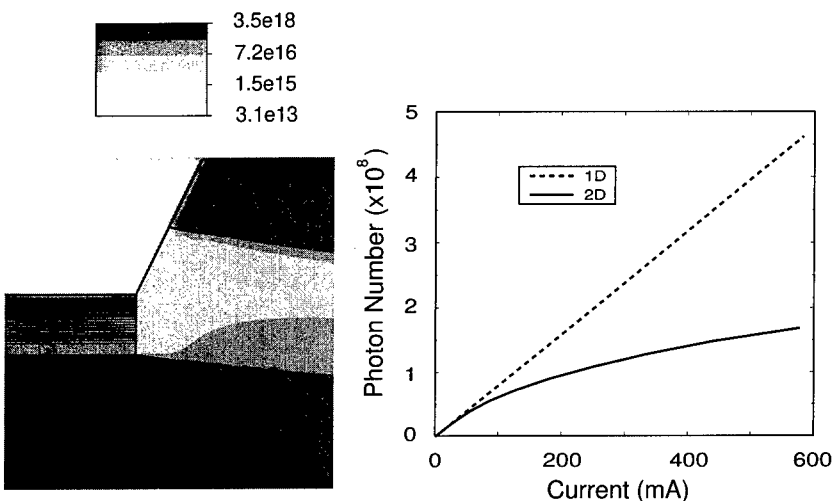


Figure 6. The light current curve for a full two dimensional simulation is compared to the one-dimensional case highlighting the carrier leakage around the active region at high bias (right). The three dimensional electron distribution near the active region is shown in gray scale (left) for a high bias

dimensional cases, both on workstations. This opens up the opportunity for detailed comparison to experiment. Possibilities include small and large signal modulation response, dynamic impedance and optical spectra.

References

- [1] Z-M. Li, K.I.M. Dzurko, A. Delage and S.P. McAlister, "A Self-Consistent Two Dimensional Model of Quantum Well Semiconductor Lasers: Optimization of a GRIN-SCH SQW Laser Structure," *IEEE J. Quantum Electron.*, vol. 28, pp. 792-803, 1992.
- [2] M. Grupen and K. Hess, "Hot Carrier Effects in COnventional Injection and Tunneling Injection Quantum Well Laser Diodes," SPIE Proc. Vol. 2994, *Physics and Simulation of Optoelectronic Devices V*, pp. 474-492, 1997; references therein.
- [3] N. Tessler and G. Eisenstein, "On Carrier Injection and Gain Dynamics in Quantum Well Lasers," *IEEE J. Quantum Electron.*, vol. 29, pp. 1586-1595, 1993.
- [4] M.A. Alam, M.S. Hybertsen, R.K. Smith, G.A. Baraff, and M.R. Pinto, "Simulation of Semiconductor Quantum Well Lasers," SPIE Proc. Vol. 2994, *Physics and Simulation of Optoelectronic Devices V*, pp. 709-722, 1997.
- [5] M.R. Pinto, W.M. Coughran, C.S. Rafferty, R.K. Smith, and E. Sangiorgi, "Device Simulation for Silicon ULSI," *Computational Electronics*, Eds. K. Hess, J.P. Leburton, and U. Ravaioli, Kluwer, 1991.
- [6] M.S. Hybertsen, R.F. Kazaninov, G.A. Baraff, D.A. Ackerman, G.E. Shtengel, P.A. Morton, T. Tanbun-Ek, and R.A. Logan, "Modeling of Gain for InGaAsP Based Lasers," SPIE Proc. Vol. 2399, *Physics and Simulation of Optoelectronic Devices III*, pp. 133-145, 1995.
- [7] R.K. Smith, M.A. Alam, G.A. Baraff, and M.S. Hybertsen, "Numerical Methods for Semiconductor Laser Simulations," Proc. of IWCE, to be published.

Monte Carlo Estimation of Excess Noise Factor in Thin p⁺-i-n⁺ Avalanche Photodiodes

D.S. ONG, K.F. Li, G.J. Rees, G.M. Dunn, J.P.R. David and P.N. Robson

Department of Electronic and Electrical Engineering,
University of Sheffield,
Mappin Street, S1 3JD, UK.

Abstract - A Monte Carlo model has been used to estimate the excess noise factor in thin p⁺-i-n⁺ GaAs avalanche photodiodes. The model predicts a decrease in excess noise factor as the multiplication length decreases from 1.0 to 0.05 μm, in good agreement with recent experimental measurements. Our simulations suggest that electron initiated multiplication in short devices has inherently reduced noise despite higher feedback from hole ionization, as compared to long devices. This low noise behaviour in short devices is explained from the ionization path length distribution.

1. Introduction

Recent experimental measurements on GaAs avalanche photodiodes(APDs) [1,2] have shown a significant reduction in excess noise factor, F as the length of the multiplication region decreases below one micron. This improvement in noise performance cannot be attributed to a large difference in the magnitude of the electron (α) and hole (β) ionization coefficients as argued from McIntyre's theory [3]. This is because, as the device shrinks in length, the operating electric field increases and α and β tend to approach one another [4]. Thus, the McIntyre noise theory cannot be a true representation when the length of the multiplication region is small. It has been noted earlier by Van Vliet *et al.*[5] that the continuous McIntyre noise theory is not applicable when the number of ionization per primary carrier transit is small. Although this theory has been used successfully by Hu *et al.*[1] to fit to their experimental data for GaAs APDs with multiplication lengths < 1.0 μm, it requires an unreasonable ratio of ionization probabilities. They conclude that the electron ionization probability is considerably enhanced in short devices, compared with the hole ionization probability. Marsland *et al.*[6] used a numerical method for determining F, based on the 'lucky drift' model of carrier transport. Their computer simulation of carrier transport is able to describe the random variations in multiplication. However, these authors point out that their idealized 'lucky drift' model of carrier transport gives only an approximate description of multiplication noise. In this paper, we apply a similar technique to estimate F, but use a Monte Carlo (MC) model for carrier transport to investigate the dependence of F on multiplication length in short GaAs APDs.

2. The Monte Carlo Estimation of Excess Noise Factor

The Monte Carlo model used in this work is similar to that reported by Dunn *et al.*[7]. This model has proven capable of calculating accurately electron and hole mean energies, drift velocities, ballistic overshoot and impact ionization coefficients, as well as the associated dead space and spatial dependence of ionization. The excess noise factor, F, is estimated following the approach introduced by Marsland *et al.* [6]. F is defined as $F = \langle M^2 \rangle / \langle M \rangle^2$, where $\langle M \rangle$ is the mean multiplication and

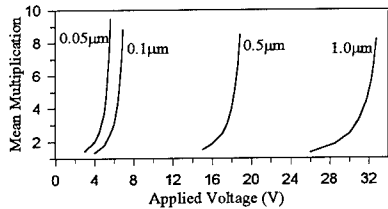


Fig.1: The electron multiplication curve versus applied voltage(V) for the range of GaAs PIN diodes with width as shown.

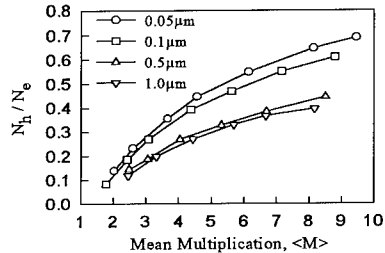


Fig.3: Ratio of N_h / N_e of the number of hole to electron ionization events, for electron injection as a function of mean multiplication.

$\langle M^2 \rangle$ is the mean square multiplication. For electron (hole) initiated multiplication, an electron (hole) is injected 'cool' from one edge of the multiplication region and both the motions of the primary carrier and of the carriers generated subsequently are considered simultaneously within the MC framework. The total number of ionization events, N_T is recorded when all the carriers have left the multiplication region; the multiplication for that trial is then given by, $M = N_T + 1$. By repeating the procedure for many trials, $\langle M \rangle$, $\langle M^2 \rangle$ and F can be calculated. The number of trials is extended until successive values of F differ by less than 10^{-4} .

3. Results and Discussion

In this study, the $p^+ - i - n^+$ structures were simulated using the depletion approximation with p^+ and n^+ doping density of $1 \times 10^{18} \text{ cm}^{-3}$ and undoped i-region lengths of 0.05, 0.1, 0.5, and 1.0 μm. Simulated multiplication characteristics, shown in figure 1 for electron multiplications are in good agreement with the experimental measurements of Plummer *et al.* [8]. Figure 2 shows the MC estimated excess noise factor for electron initiated multiplication for all devices as a function of mean multiplication value up to $\langle M \rangle = 10$. Also shown in the figure for comparison are the excess noise factors calculated from the McIntyre noise theory for different constant k values. The MC estimated values of F for all four devices increase monotonically with $\langle M \rangle$. Very importantly, over the whole range of $\langle M \rangle$, F decreases with decreasing length of the multiplication region. A similar multiplication noise characteristic was observed for hole injection in these devices. This is consistent with recent experimental measurements [2]. In shorter devices the electric field must increase to maintain the same value of $\langle M \rangle$. For GaAs the ratio β/α increases with electric field and so might be expected to

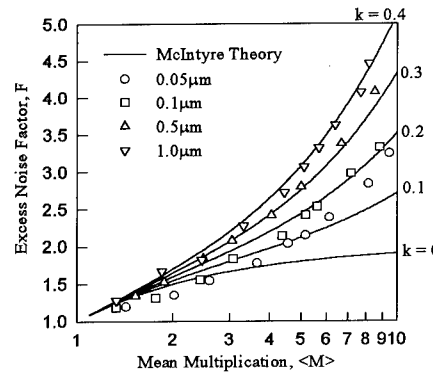


Fig.2: Excess noise factor versus mean multiplication for electron initiated multiplication in PIN GaAs diodes. Solid lines depict the results of McIntyre's theory ($k = \beta/\alpha$) and symbols denote values calculated from the Monte Carlo model.

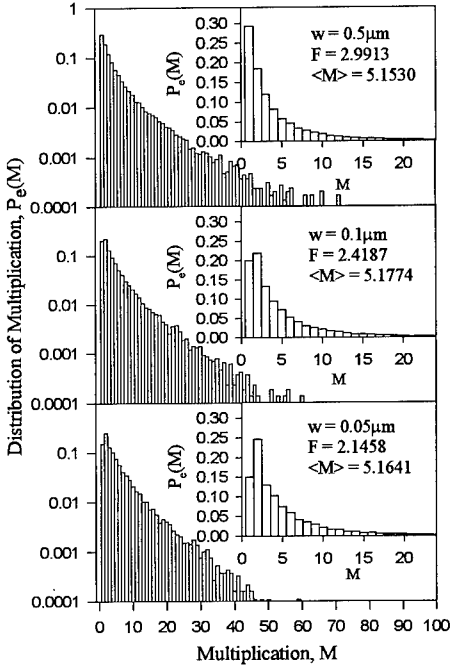


Fig.4: Distribution of multiplication $P_e(M)$ for single electron initiated multiplication in GaAs APDs with multiplication length, $w = 0.05, 0.1$ and $0.5\mu\text{m}$. The mean multiplication value and excess noise factor for each device are shown in the corresponding figure. Insert are results plotted to a linear scale.

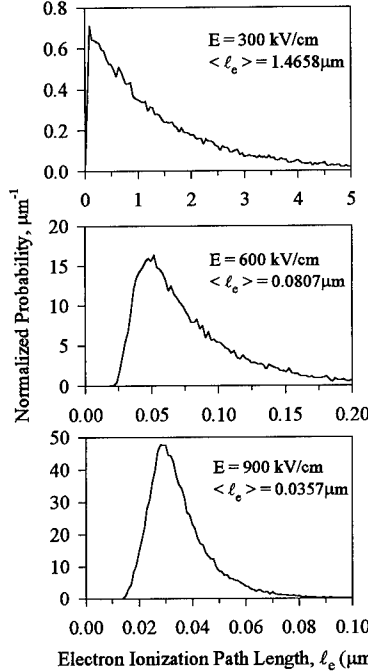


Fig.5: Probability distributions, $S(\ell)$ of electron ionization path lengths calculated from the MC model for the electric fields, $E = 300, 600$ and 900 kV/cm . $\langle \ell_e \rangle$ is the mean ionization path length.

increase the feedback ratio for electron injection, N_h/N_e , the ratio of the number of hole-initiated to electron-initiated ionization events, as seen in figure 3. This is accompanied again by a reduction in F (Fig.2), contrary to our expectations from the McIntyre model, in which multiplication noise is increased by feedback ionization from the opposite type of carrier from that injected.

The probability functions $P(M)$ for electron injected multiplication are presented in figure 4 for applied voltage, $V_{app} = 5.3, 6.55$ and 18.32V for increasing device length and corresponding to $\langle M \rangle$ of ~ 5.1 . These distribution histograms are seen to narrow as the i-length decreases from 0.5 to $0.05\mu\text{m}$, specially evident in the tail at high values of multiplication which is particularly important in determining $\langle M^2 \rangle$. In figure 4, we also present these results on a linear scale in the insets. From these it can clearly be seen that in long devices ($0.5\mu\text{m}$) the multiplication distribution is monotonically decaying. Moreover, the peak in probability is shifted closer to the mean value in shorter devices. The probability that an electron will traverse the device without initiating impact ionization $P(M = 1)$ reduces from 0.29 to 0.15 as the multiplication length decreases from 0.5 to $0.05\mu\text{m}$. This more deterministic behaviour is one of the main reasons for the low noise behaviour in short devices, where the high electric field enables more carriers to reach the impact ionization threshold energy for the same $\langle M \rangle$, compared to long devices.

The normalized ionization path length distribution functions, $S(\ell)$ for electron are shown in figure 5 for electric field, $E = 300, 600$ and 900kV/cm . These distribution functions were calculated by making a histogram of the distance travelled by a single electron between successive ionization events. For long devices (i -length $>0.5\mu\text{m}$) with operating electric field about 300kV/cm or less, $S(\ell)$ is approximately exponential with a very small displacement from the origin. As the devices become shorter and the electric field increases to maintain $\langle M \rangle$, the length scales of the distribution functions contract, corresponding to a larger ionization coefficient. Moreover, the displacement in the peak of $S(\ell)$ now becomes more prominent, indicating the increasing importance of the dead space for short devices. This result shows clearly that the implicit assumption in McIntyre's analysis, that the ionization path length distribution function is a simple exponentially decaying function, is not correct at high fields.

As can be seen in figure 5, the dead space represents a significant portion of the multiplication length in short devices. It serves to reduce the probability of higher order ionization events, as the subsequently generated carriers need to travel a larger fraction of the remaining device length (the dead space) in order to cause an impact ionization. As a result, the length of the multiplication chains in short devices is limited as the subsequently generated carriers are more likely to leave the multiplication region without inducing further impact ionization. This consequently narrows the probability distribution for multiplication as shown in figure 4. Hence, in short devices a lower excess noise factor is possible for electron initiated multiplication, despite the higher feedback from hole ionization, since the fluctuations introduced by higher order ionization process are reduced by the dead space effect.

4. Conclusions

The multiplication noise in GaAs p⁺-i-n⁺ APDs has been investigated using MC simulation. We have demonstrated clearly that the excess noise factor depends strongly on the deviation of ionization path length distribution function from the conventional assumed exponential distribution as the operating electric field increases in short devices. Simulation results suggest that electron initiated multiplication in short devices has inherently reduced noise despite higher feedback from hole ionization, as compared to long devices. Hence, a low noise and high speed APD structure is achievable even with materials having almost equal electron and hole ionization coefficient by using a submicron multiplication region.

Acknowledgement

This work was funded by the Engineering and Physical Science Research Council (UK) under grant GR/J49549.

References

- [1] Hu C, Anselm K A, Streetman B G, and Campbell J C, *Appl. Phys. Lett.*, 69, 3734-3736, 1996.
- [2] Li K F, Ong D S, David J P R, Robson P N, Tozer R C, Rees G J and Grey R, presented in 55th IEEE Device Research Conference, Colorado, USA, June 1997.
- [3] McIntyre R J, *IEEE Trans. Electron. Devices*, 13, 164-168, 1966.
- [4] Bulman G E, Robbins V M, and Stillman G E, *IEEE Trans. Electron. Devices*, 32, 2454-2466, 1985.
- [5] Van Vliet K M, Friedmann A, and Rucker L M, *IEEE Trans. Electron. Devices*, 26, 752-764, 1979.
- [6] Marsland J S, Woods R C, and Brownhill C A, *IEEE Trans. Electron. Devices*, 39, 1129-1135, 1992.
- [7] Dunn G M, Rees G J, David J P R, Plummer S A and Herbert D C, *Semicond. Sci. Technol.*, 12, 111-120, 1997.
- [8] Plummer S A, David J P R, Herbert D C, Lee T W, Rees G J, Houston P A, Grey R, Robson P N, Higgs A W, and Wight D R, *IEEE Trans. Electron. Devices*, 43, 1066-1072, 1996.

Numerical model of a 0.2 μm AlGaAs/GaAs HEMT including electromagnetic effects

A. Cidronali⁺, G. Leuzzi^{*}, G. Collodi⁺, and G. Manes⁺

[†]Dept. of Electronics Engineering, University of Florence, V.S Marta, 3 50139 Florence Italy

^{*}Dept. of Electronics Engineering, II University of Roma 'Tor Vergata' Italy

Abstract. The paper presents an efficient approach to evaluate the performance of electron devices under non stationary operation through an accurate mixed physics-electromagnetic based model. The analysis couples a three-dimensional (3-D) time domain solution of Maxwell's equation to the electron device model. The electron devices model is based on a simplified version of the first three moments of the Boltzmann transport equation (BTE). By means the proposed physics based model a conventional 0.2 μm HEMT has been simulated. The numerical results show the effect of the interaction between electron and fields on the behavior of high frequency FETs.

1. Introduction

Over the past few years an increasing interest in the development of integrated CAD environment for MMIC's (Monolithic Microwave Integrated Circuits) and MMMIC's (Monolithic Millimetre wave Integrated Circuits), which include *process simulation*, *device simulation*, *circuit analysis* and *optimization*, has led to the implementation of very powerful CAD tools. As the frequency of operation increases, the requirements of the CAD tools become more stringent, due to the growing interactions between different elements, both active and passive, on the circuit, and of the increased importance in parasitic effects. It is even more evident for monolithic circuits where the adjustment and trimming of the original design is too costly. Including active device modeling in the CAD analysis, arises from the need of adjusting their geometry, e.g. number and length of gate fingers, so as to achieve design optimization. In order to do this it required simultaneously perform both accurate electromagnetic analysis and the physical modeling of the active device. Some valuable works were performed in the area of investigating the electromagnetic (e.m.) wave effects within microwave transistors. The usual approach consists of simultaneously solving both the electromagnetic problem and charge transport problem [1]. This approach is useful to gain an detailed view of the transistor behavior and to improve in transistor design optimization. This requires an approach which is capable of implementing the model without requiring too much of computing time. Different strategies has been applied for circumvent that limitation [2].

A new approach combining a full-wave time-domain electromagnetic simulation with a quasi-2D physical simulation to analysis the basic transistor structure is presented in [3]. The method combines both high accuracy and speed, as required by practical circuit design. The proposed method was applied to a typical 0.2 μm AlGaAs/GaAs HEMT, where realistic geometry and material parameters were introduced. The numerical simulations are given in the results.

2. Model Description

The model consist of a link between a quasi two-dimensional model of a high electron mobility transistor and a finite difference time domain electromagnetic simulator. At first, the transistor active region is subdivided in elementary sections along the gate finger width. An elementary device was associated to each individual

section, whose non-stationary charge transport is treated as a quasi-two-dimensional problem [4]. This scheme is based on the assumption that the charge flow, normal to this direction in the active layer, can be neglected. In the model proposed, all sections are represented by an elementary transistor. The aim of this research is to implement a 3D non stationary analysis of the transistor. That is obtained by coupling the individual sections with a finite difference time domain electromagnetic analysis. The e.m. of the transistor structure, outside the active region, includes pads and metalisations. The electromagnetic problem was solved by introducing both an external generator and a local current source, which represents the electrical phenomena taking place in each elementary section of the active layer. Due to the non-linear nature of the active device, at all time-steps a number of iterations are required. The DC analysis was performed only for the active device, owing to its non-linear behavior, while AC analysis was performed for both of them. In the approach, the analysis of the bias condition is independently performed by that of transient and steady-state conditions. The transient and steady-state fields, which are computed by a conventional finite difference time domain code and the DC fields are related by the curl equations:

$$\nabla(H(x,t) + H(x)) = \epsilon \frac{d(E(x,t) + E(x,t))}{dt} + J_{ED}(x,t) ; \quad \nabla(E(x,t) + E(x)) = -\mu \frac{d(H(x,t) + H(x,t))}{dt}$$

Above, E and H represent the non DC components, while E and H are the DC components. J_{ED} represents the current density flow in the elementary device. The above equations clearly denotes the claimed possibility of separately analyzing DC and non DC fields.

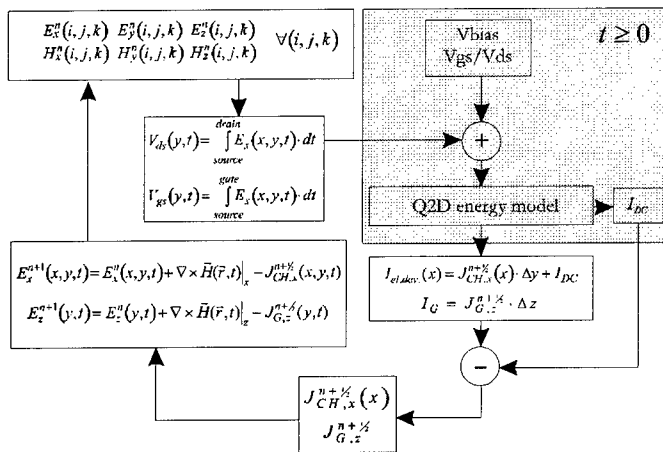


Fig. 1: flowchart of the proposed technique

The flowchart describing the sequence of the operation is shown in Fig.1. The elementary devices were modeled on the most important phenomena occurring in the active area of the electron device under analysis. Starting from the basic transport equation for electrons, derived from the Boltzmann transport equation which was simplified by a nil spatial variation of the electron energy; electron velocity; the electron temperature. The reduced model is:

$$\begin{aligned}\frac{\partial n(x,t)}{\partial t} + \nabla J_{ED}(x,t) &= 0 \\ \frac{\partial v(x,t)}{\partial t} &= \frac{e}{m^*(w)} E(x,t) - \frac{v(x,t)}{\tau_p(w)} \\ \frac{\partial w(x,t)}{\partial t} &= ev(x,t)E(x,t) - \frac{w(x,t) - w_0}{\tau_w(w)}\end{aligned}$$

the charge control law that has been solved along with the transport model is represented by the equation:

$$N_Y = \frac{\beta}{1 + \gamma \cdot N_Y^{-\frac{1}{3}}} (V_{ch} - V_{sur})$$

where: $\beta = \frac{\epsilon}{qa}$ and $\gamma = 0.385 \cdot 10^{-11} \beta$, V_{ch} is the potential into the 2DEG channel and V_{sur} the corresponding surface potential, [5]. The quantities τ_w , τ_p and m^* are functions of the energy w , while w_0 depends on the lattice temperature T_0 , which is evaluated using a Monte Carlo simulation. The main problem was represented by the difference occurring between the volumes subjected to e.m. and the transport phenomena. It is evident that there is a difficulty in modeling, using the same cell size. To circumvent this problem the effect related to the charge transport was included in a density current component flowing at the interface between the AlGaAs layer and the air (Fig.2). Thus only the surface field components interact with the charge flow in the channel, while the gate current was modeled with a current wire perpendicular to the gate metalization. These are the main differences between the proposed approach and the approach described in [1], where a full bidimensional interaction between fields and current is accounted in the active region.

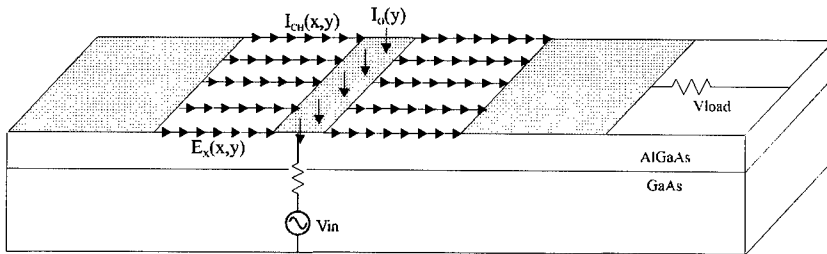


Fig. 2: Modelization of the interaction between field and charge transport.

However, in most FET structures for MMIC applications, two dimensional modelling based on the hydrodynamic approach show that the current density lines are all enclosed in a 100 nm region beneath the gate contact. Due to the dimension of the buffer layer, typically 100 μm , one can assume that there no dramatic change in the performance of the device. The scheme is shown in Fig.2.

3. Results

In order to evaluate the effect of the interaction between electrons and fields on the behavior of high frequency FETs, a simulation of a 0.2 μm AlGaAs/GaAs was carried out. The device considered has a two finger, 10 μm width and was constructed in the 'T' shape. The small amplitude test signal was a 80 GHz sinusoid modulated by a 160 GHz gaussian waveform. The transistor performance were evaluated in a broad

frequency spectrum. The drain metalization was terminated by a 50Ω load resistor and the source metalization was grounded. The effect of the interaction between the active region and the wave propagating through the metalization is shown in Fig. 3. In Fig. 3 there is a comparison between, the output signal of the transistor, i.e. ‘active’ trace, and the one obtained running the simulation without the effect of the elementary devices, i.e. ‘passive’ trace. The effect of the device-wave interaction results in a delay and in an increase in the amplitude between the two waveforms, Fig. 3a.

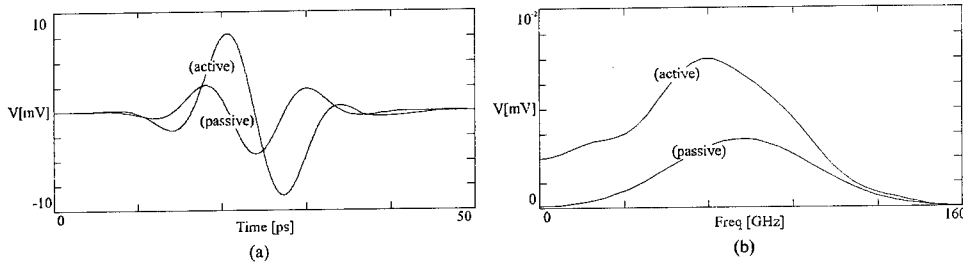


Fig. 3: Comparison between numerical simulation carried out with and without the effect of the active area, ‘active’ and ‘passive’. (a) time domain response, (b) frequency domain response. Simulation data: gate length=0.2 μ m; source and drain to gate distance=1.2 μ m; AlGaAs thickness 61 nm ; doping 10^{24} At./ m^3 ; substrate thickness 100 μ m

A secondary effect is an increase in the dispersivity of the active structure compared to the passive one. This is due to the electron transport which slows the propagation along the drain metalization. The FFT of the time domain signals show that the active area increases the output signal circa 60 GHz, were the particular device structure optimizes the signal amplification, Fig. 3b.

4. Conclusions

This paper presents a numerical model suitable for high frequency transistors given the interaction between the electromagnetic fields and the electron device. The proposed approach simplifies the model by the restriction of the channel charge transport at the interface between the air and the device. This method is sufficiently efficient from a numerical point of view, which is an important feature for the analysis of complex transistor structures. Finally the numerical simulation shows a frequency dependent device-wave interaction.

References:

- [1] M. A. Alsunaidi, S.M. Sohel Imtiaz, S. M. El-Ghazaly; “Electromagnetic wave effects on microwave transistors using a full-wave time domain model,” IEEE Trans. Microwave Theory Tech., Vol. 44 no.6, June 1996, pp. 799-807.
- [2] G. Avitabile, A. Cidronali, G. Vannini, G. Manes, “Multifinger effect in GaAs FET distributed large signal CAD model,” 1996 IEEE International Electron Devices Meeting, San Francisco, U.S.A, December 8-11, 1996.
- [3] P. A. Sandborn, A. Rao, P. A. Blakey; “An assessment of approximate non stationary charge transport models used for GaAs Device Modeling,” IEEE Trans. Electron Devices, Vol. 36, no.7, July 1989, pp. 1244-1253.
- [4] B. Carnez, A. Cappy, A. Kaszynski, E. Constant, G. Salmer; “Modeling of a submirometer gate field-effect transistors including effects of nonstationary electron dynamics,” J. Appl. Phys. Vol.51, January 1980, pp. 784-790.
- [5] A. Shey, W.H. Ku; “An analytical current-voltage characteristics model for high electron mobility transistor based on nonlinear charge control formulation,” IEEE Trans. Electron Devices, Vol. 36, no.10, October 1989, pp. 2299-2305.

NEMO: General Release of a New Comprehensive Quantum Device Simulator

Daniel K. Blanks, Gerhard Klimeck, Roger Lake, and Dejan Jovanovic

Raytheon TI Systems, Dallas, TX 75243

R. Chris Bowen and Chenjing Fernando

Corporate R&D, Texas Instruments Incorporated, Dallas, TX 75243

William R. Frensley and Manhua Leng

University of Texas at Dallas, Richardson TX 75083

Abstract. Device simulations are essential to explore new device designs, optimize performance, and analyze the underlying physics. Nanoelectronic devices pose a new challenge in this area since conventional drift-diffusion simulators are not applicable. **NEMO** (NanoElectronic MOdeling) is a new quantum device simulator based on a non-equilibrium Green's function formalism that simulates a wide variety of quantum devices, including RTDs, HEMTs, HBTs, superlattices, and Esaki diodes. Here we announce the general release of **NEMO** as a national resource freely available to the US scientific community. We will present **NEMO** calculations for InGaAs / AlAs and GaAs / AlAs RTD devices.

1. Introduction

Advances in epitaxial growth and device processing techniques have spurred development of heterostructure devices based on quantum confinement and resonant tunneling effects. As these devices transfer from the laboratory to commercial applications, accurate device simulations will be essential to optimize device performance, explore new device designs, and to understand the quantum effects that drive the transport process. Conventional simulators such as **PISCES** cannot analyze nanoelectronic devices without resorting to *ad hoc* models that do not include the underlying physics of the quantum transport.

To address this problem, we developed a general purpose 1-D quantum device simulator called **NEMO** (NanoElectronic MOdeling). Here we announce the general release of **NEMO** as a national resource available free of charge to the US scientific community and describe some of its features. We also give examples of **NEMO** calculations for InGaAs / AlAs and GaAs / AlAs RTD devices. Detailed discussion of the **NEMO** theory and its application to various devices are given in Refs. [1], [2], and references therein.

2. NEMO Features

NEMO uses a non-equilibrium Green's function algorithm that can incorporate any combination of potential, band structure, and scattering models. This approach has proven to be applicable to a wide range of device designs, numerically stable, and computationally efficient. Table 1 illustrates the some of the devices, material systems, and output options available in **NEMO**. Table 2 lists the potential, band structure, and scattering models.

NEMO Features	Devices	Material Systems	Output Options
Variety of device designs	RTD	AlGaAs	Current
Long devices (> 100 nm)	HBT	InGaAs	Energy Bands
Large biases	HEMT	InAlAs	Band Profile
Temperature range 0 - 300 K	MOS	Silicon (MOS only)	Transmission Coefficient
	Esaki diodes		Energy Resonances
	Superlattices		Charge Density
			Resonant Wavefunctions
			Density of States

Table 1. A summary of features, device types, material systems, and output options modeled with NEMO.

Potential	Band Structure	Scattering
Thomas-Fermi	Single-band effective mass	Single Band
Hartree	Multiple decoupled single bands	Acoustic phonon
Hartree w/ exchange correlation	Non-parabolic single-band $k \cdot p$ 2-band sp^3 s 10-band 1 st nearest neighbor 2 nd nearest neighbor spin-orbit coupling	Polar optical phonon Interface roughness Alloy disorder Multi-Band Relaxation-time approx. in contact layers

Table 2. Models provided by NEMO. The user can mix any combination of these models to optimize calculation accuracy, execution time, and memory usage.

A major thrust of the NEMO project was to provide a user-friendly tool designed for both scientific and engineering applications. To achieve this flexibility and ease-of-use, graphical user interface (GUI) development was a major part of the NEMO effort. The NEMO GUI gives user as much control as possible over every aspect of the simulation and plots the calculation results in real-time. Some of the key NEMO GUI features include:

- Display and entry of all device, material, and simulation parameters.
- Default values provided for material and simulation parameters.
- Display of calculation results in 2-D, 3-D, and contour plots.
- Real-time band profile calculation with mouse-adjustable Fermi level.
- Plot Slicers to display slices of 3-D data sets.
- Plot Slicers Linker connects all Plot Slicers to a cursor on the I-V data.
- Library of example NEMO simulations.
- Band Structure tool to display energy bands and electron density vs. Fermi energy.
- Material parameter tool that displays material parameter equations and allows exploration of material properties vs. composition and temperature.
- Operates on HP-UX, Sun, and SGI with possible extension to DEC/Alpha and IBM/AIX platforms.

The Plot Slicer is particularly useful as it allows the user to review all of the calculation results and link them to a master slide bar connected to the I-V calculation. Figures 1 and 2 illustrate some of these graphical tools.

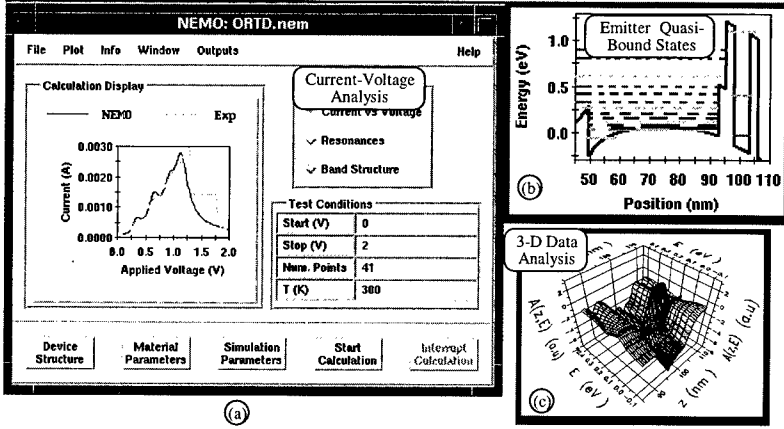


FIG. 1. Overview of several of **NEMO**'s interactive windows: (a) Main window compares a simulation of current vs. voltage for an optical resonant tunneling device (ORTD) to experimental data. The main window provides access to other tools used for the device design. (b) The energy band profile and resonance states calculated for the ORTD device. (c) 3-D display of the spectral function in the center of the ORTD.

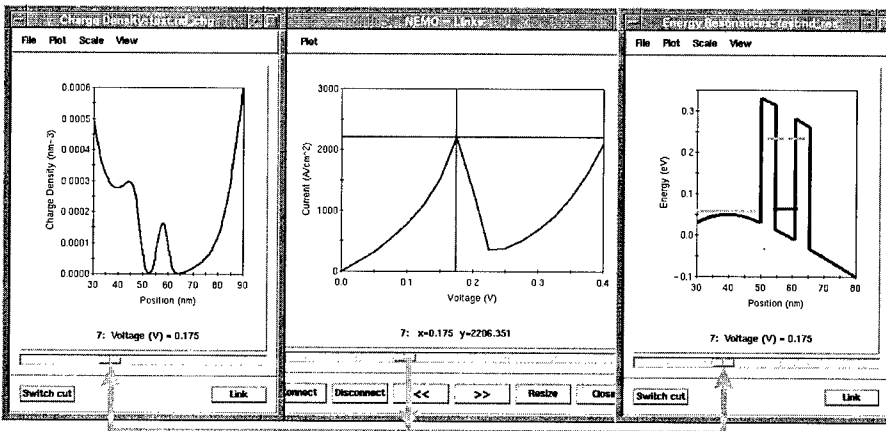


FIG. 2. Plot Slicers for the charge distribution (left) and band profile with energy resonances (right) linked to the current vs. voltage scan (center). The Link tool can couple all output graphs as a function of bias. Quick keys(" << " " >> ") switch the scroll bar between maximum and minimum extrema in the I-V data.

3. Simulation Examples

As an example, we illustrate RTDs built in two different material systems. The first device shown in the inset of Fig. 3 is an $\text{In}_{0.53}\text{Ga}_{0.47}\text{As} / \text{In}_{0.52}\text{Al}_{0.48}\text{As}$ RTD operating at room temperature. **NEMO** employs a 10-band sp^3s^* bandstructure model to determine the non-parabolic $E(\mathbf{k})$ dispersion for the InGaAs and InAlAs conduction bands. A numerical integration method calculates the transmission

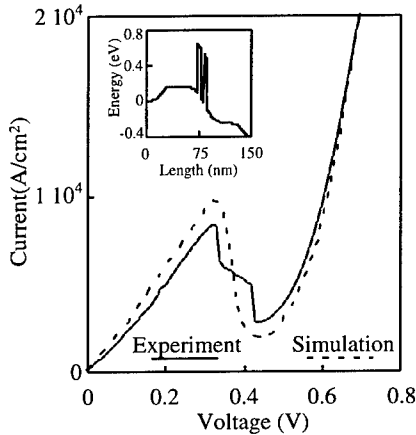


FIG. 3. Current vs. voltage characteristic of an $\text{In}_{0.53}\text{Ga}_{0.47}\text{As} / \text{In}_{0.52}\text{Al}_{0.48}\text{As}$ resonant tunneling diode (see the conduction band edge in the inset) at room temperature calculated in a 10-band model with full-band integration and no scattering in the central RTD region.

including the dependence on transverse momentum. The predicted valley current and peak-to-valley ratio show good agreement with the experiment even though the simulation neglects scattering effects in the central quantum region (a relaxation-time approximation accounts for scattering in the reservoirs outside the central region). This indicates that thermionic emission through the first excited quantum well state dominates the room temperature valley current.

The second device is a GaAs / AlAs RTD measured at $T=4.2\text{K}$. The **NEMO** simulation shows that a polar-optical-phonon assisted tunneling process dominates the valley current (Fig. 4). If we neglect polar optical phonon scattering, the calculated valley current is too low by 3 orders of magnitude.

4. Conclusion

In conclusion, **NEMO** is a comprehensive, versatile, and user-friendly quantum device modeling tool with predictive capability for a wide range of devices and operating conditions. The general release is slated for the December 15 of 1997 at which time it will be available to any interested domestic industrial and educational facilities. To obtain **NEMO**, contact Gerhard Klimeck at Raytheon TI Systems, phone 972-995-5510, email gekco@ti.com.

References

- [1] Klimeck G, Lake R, Bowen R C, Frensel W R, and Moise T S, "Quantum Device Simulation with a generalized tunneling formula", 1995 *Appl. Phys. Lett.* 67(17) 2539-41.
- [2] Lake R, Klimeck G, Bowen R C, Jovanovic D, "Single and Multi-Band Modeling of Quantum Electron Transport Through Layered Semiconductor Devices", 1997 *J. Appl. Phys.* 81(12): 7845-69.

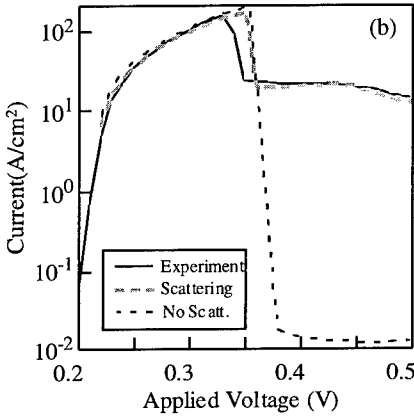


FIG. 4. Current vs. voltage characteristic of an GaAs / AlAs resonant tunneling diode at a temperature of 4.2 K. A phonon peak is visible in the valley current region.

Atomic scale calculations for strain distribution and electronic structure of InAs pyramidal quantum dots on (100) GaAs

T. Saito, J. N. Schulman,* and Y. Arakawa

Center for Collaborative Research, University of Tokyo
4-6-1 Komaba, Meguro-ku, Tokyo 153, Japan

Abstract. The theoretical investigations for the strain distribution and electronic structure of InAs pyramidal quantum dots (QDs) have been performed using the Keating potential and the sp^3s^* tight-binding method. The 161-, 1222-, and 4047-atom QDs on GaAs with no cap layers are studied. The strain energy is largest at the QD base layer and decreases rapidly with increasing distance from the base. We have calculated the energies, the wave function “inside” fractions, and the densities of states for the inside states and the surface states. The density of the inside states shows a large energy gap [2.71 eV (161-atom QD), 1.74 eV (1222-atom QD)] due to the strong confinement effect. We find the surface states from the {111}As facets, (100)In base, and {111}In facets of the QDs, which are distributed in the different energy regions in the gap.

1. Introduction

Growth of self-assembled InAs quantum dots (QDs) on GaAs substrates has recently become promising to fabricate three dimensional confined structures. Molecular beam epitaxy [1] and metalorganic chemical vapor deposition [2] have been used to grow InAs QDs using the Stransky-Krastanov growth mode, in which the driving force of the QD formation is the lowering of the strain energy due to island formation.

Theoretical calculations of the strain and electronic structure of the InAs QDs have been carried out using *macroscopic* methods; elastic continuum theory for the strain, and the effective-mass approximation for the electronic structure [3]. These methods are valuable especially when the QD has a large size and sharp interfaces. When the QD has a smaller size, or has surfaces, or has interfaces with atomic scale roughness or defects, *atomic scale* methods are then useful for calculating the strain and electronic structure.

Recently *atomic scale* calculations for electronic structures have been carried out for Si spherical QDs using a tight-binding method [4] and for InP cubic QDs using a pseudopotential method [5]. However calculations for InAs QDs with realistic shapes and strain are not available.

In this study, we calculate the strain distribution and electronic structure of InAs pyramidal QDs using *atomic scale* methods. For the strain calculation, we use the Keating potential [6] in which the strain energy is expressed in terms of changes in bond lengths and angles. For the electronic structure calculation, we use the tight-binding method with the sp^3s^* atomic orbital basis [7].

2. Strain distribution

2.1 Keating potential method

The calculation of the strain distribution in InAs pyramidal QDs is carried out by the following two steps: 1) generate the initial atomic positions in the QDs on GaAs, and 2) modify the initial atomic positions in order to minimize the strain energy. We calculate the strain distribution for the “energy-minimized” atomic positions.

We generate the initial atomic positions in the InAs pyramidal QDs on GaAs, in which the base plane of the pyramid is the (001) In-plane, the edges of the base are oriented along the [110] and [1 $\bar{1}$ 0] directions, and the pyramid facets are {111}In and {111}As planes (see the inset in Fig. 1). The initial atomic positions in the QDs are set identical to those in the InAs pseudomorphic epitaxial layer on (001) GaAs using the macroscopic elasticity theory. We generate 161-atom, 1222-atom, and 4047-atom pyramidal QDs whose base lengths are 20 Å, 44 Å, and 68 Å, respectively.

To minimize the strain energy, we use the Keating potential [6] in which the strain energy is expressed in terms of changes in bond lengths and bond angles. In the minimization process, the atomic positions on the base (001) In-plane are *fixed* to match the (001) As-plane of the GaAs substrate. The atomic positions above the base plane are moved in order to minimize the Keating potential; here each atom is moved in turn along the direction of the force on it determined by the Keating potential.

2.2 Results of calculation

Figure 1 shows the strain energy distribution in the 161-, 1222-, and 4047-atom QDs after the energy minimization. In the three QDs, the strain energy (per atom on a layer) is largest at the base layer and decreases rapidly with increasing distance from the base. The strain energy decreases less rapidly in a bigger QD, indicating a size effect in the strain energy distribution. The several layers near the pyramid top have essentially no strain energy. For example, in the 161-atom QD, the top five (of eleven) layers have essentially no strain. The total strain energy stored in the 161-atom QD after the energy minimization is only 36 % of that stored in the QD with the initial atomic positions which are set identical to the atomic positions in the pseudomorphic layer. This decrease in the strain energy is clearly a driving force for the QD formation in the Stransky-Krastanov growth mode.

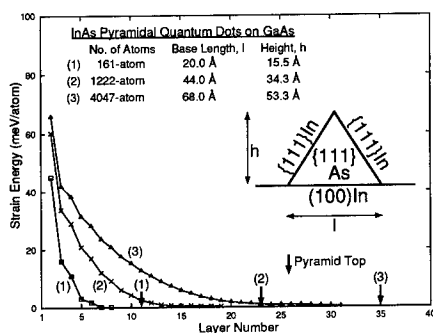


Figure 1: Strain distribution in the 161-, 1222-, and 4047-atom InAs pyramidal QDs. The strain energy per atom (excluding surface atoms) on each layer versus the layer number is shown. No plots are given for layers which consist of only surface atoms. The pyramid base is at the layer number = 1. The pyramid tops are indicated by the vertical arrows.

3. Electronic structure: inside states and surface states

3.1 Tight-binding method

The electronic structure calculations for the QDs are performed using the sp^3s^* semiempirical tight-binding method [7]. In this method, the five atomic orbitals per atom (s , p_x , p_y , p_z , and s^*) are used for the basis. The tight-binding Hamiltonian for an N_{total} -atom dot is a real symmetric ($5N_{total} \times 5N_{total}$) matrix, where N_{total} is the total number of atoms in the dot. The eigenvalues and eigenvectors (or wave functions Ψ) are obtained by diagonalizing the Hamiltonian matrix.

The tight-binding parameters for unstrained InAs are taken from the values of Vogl *et al.* [7]. The spin-orbit coupling is not included in the present study. The changes in the interatomic matrix elements due to strain are treated by the d^{-2} rule for bond length d and the Slater and Koster formulae [8] for bond angles.

To characterize a location, dot inside or surface, of the wave function Ψ , we define the “wave function inside fraction” F_{inside} as

$$F_{inside} = \int_{\Omega} |\Psi|^2 d\tau \quad (\Omega = \text{all inside atoms}).$$

Here “an inside atom” is defined as an atom with no dangling bonds. $F_{inside} \rightarrow 1$ when Ψ is strongly confined in the dot inside, and $F_{inside} \rightarrow 0$ when Ψ is strongly localized on the dot surface. We define the “critical inside fraction” F_{inside}^c which is F_{inside} when Ψ is distributed uniformly in the whole dot. Clearly $F_{inside}^c \equiv N_{inside}/N_{total}$, here N_{inside} is the number of inside atoms. We can classify all wave functions in the QD into “inside” states and surface states as follows.

Ψ is an inside state (a surface state) when $F_{inside} > F_{inside}^c$ ($F_{inside} < F_{inside}^c$).

3.2 Results of calculation

Figure 2 shows the wave function inside fraction F_{inside} [in (a)] and the corresponding densities of states for inside states and surface states [in (b)] in the 161-atom QD. Here $N_{inside} = 66$. In (a), we find two groups of inside states at the valence side and the conduction side, and several groups of surface states between the two groups of inside states. The above findings are reflected in the density of states in (b). The density of inside states shows a large gap (2.71 eV) due to the strong confinement effect of the QD.

At the same time, we find several peaks of surface states in the gap due to the large number of surface atoms in the QD. The surface states are localized mainly on the $\{111\}$ As facets for the

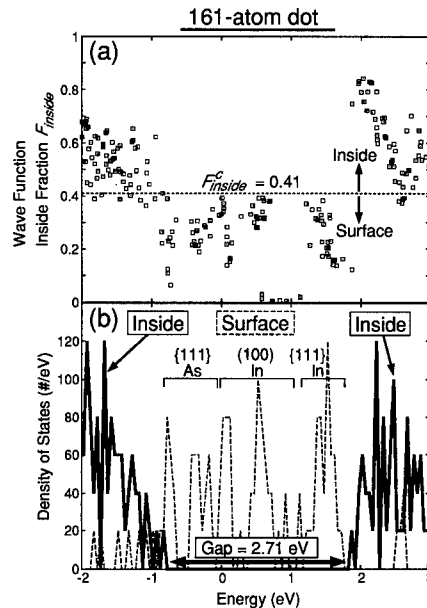


Figure 2: Wave function inside fraction F_{inside} (a) and the densities of inside states and surface states (b) in the 161-atom InAs pyramidal QD.

energy range $-1 \text{ eV} \sim 0 \text{ eV}$, on the $(100)\text{In}$ base for $0 \text{ eV} \sim 1 \text{ eV}$, and on the $\{111\}\text{In}$ facets for $1 \text{ eV} \sim 2 \text{ eV}$, as indicated in Fig.2(b). These surface states are similar to those known for polar semiconductor surfaces [9].

Figure 3 shows the maximum energy of inside states in the valence side (E_v) and the minimum energy of inside states in the conduction side (E_c) for the 161-, 372-, and 1222-atom pyramidal QDs. Here $N_{\text{inside}} = 197$ (372-atom QD), 815 (1222-atom QD). The gap values are also shown. For the 1222-atom QD, 1000 eigenvalues for the energy range $-1.4 \text{ eV} \sim 2.4 \text{ eV}$ are calculated to obtain the density of states and the gap. We find that the gap becomes smaller with increasing the QD size due to the reduction of the quantum confinement effect. On the other hand, the peak positions of the density of surface states [$\{111\}\text{As}$, $(100)\text{In}$, $\{111\}\text{In}$] do not depend on the QD size.

4. Conclusions

The theoretical investigations for the strain distribution and electronic structure of InAs pyramidal QDs have been performed using the Keating potential and the sp^3s^* tight-binding method. The strain energy is largest at the QD base layer and decreases rapidly with increasing distance from the base. The density of the inside states shows a large energy gap [2.71 eV (161-atom QD), 2.19 eV (372-atom QD), and 1.74 eV (1222-atom QD)] due to the strong confinement effect. We find the surface states from the $\{111\}\text{As}$ facets, $(100)\text{In}$ base, and $\{111\}\text{In}$ facets of the QDs, which are distributed in the different energy regions in the gap.

Acknowledgements

This work was supported in part by the Research for the Future Program of the Japan Society for the Promotion of Science (Project No. JSPS-RFTF96P00201), Grant in-aid of Priority Area by Ministry of Education, Science and Culture, and University-Industry Joint Project on Quantum Nanostructures.

References

- * Permanent address: Hughes Research Laboratories, RL-62, 3011 Malibu Canyon Road, Malibu, CA 90265-4799, USA.
- [1] D. Leonard, K. Pond, and P. M. Petroff, Phys. Rev. B **50**, 11687 (1994).
- [2] J. Oshinowo, M. Nishioka, S. Ishida, and Y. Arakawa, Jpn. J. Appl. Phys. **33**, L1634 (1994).
- [3] M. Grundmann, O. Stier, and D. Bimberg, Phys. Rev. B **52**, 11969 (1995).
- [4] S. Y. Ren, Phys. Rev. B **55**, 4665 (1997).
- [5] H. Fu and A. Zunger, Phys. Rev. B **56**, 1496 (1997).
- [6] P. N. Keating, Phys. Rev. **145**, 637 (1966).
- [7] P. Vogl, H. P. Hjalmarson, and J. D. Dow, J. Phys. Chem. Solids **44**, 365 (1983).
- [8] J. C. Slater and G. F. Koster, Phys. Rev. **94**, 1498 (1954).
- [9] J. Pollmann, Festkörperprobleme XX, 117 (1980).

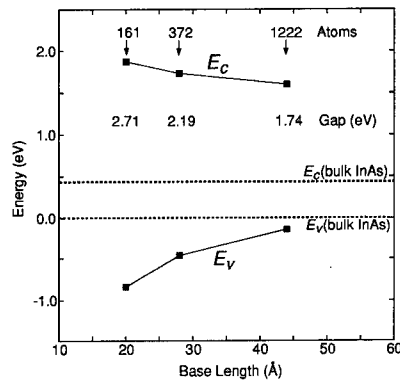


Figure 3: E_c and E_v for the 161-, 372-, and 1222-atom pyramidal QDs.

Two-dimensional Device Simulation for PHEMT Material and Process Control

Y.C. Pao

Litton Solid State Division, Santa Clara, CA 95054

J.S. Harris, Jr.

Department of Electrical Engineering, Stanford University Stanford, CA 94305

Abstract: Profound characteristic changes of quarter micron PHEMT as functions of material and process related parameters have been examined based on a novel two-dimensional PISCES heterojunction simulation. The construction of the PHEMT input structure is based on the physical values obtained from experimental measurements. It has been found that gate recess spacing, surface states and buffer are the most influential parameters, other than gate length, 2DEG sheet charge density and saturation velocity, which affect the PHEMT performance.

1. Introduction

A heterojunction PISCES device simulator [1] is a powerful tool to study, examine, and design complicated devices such as Pseudomorphic High Electron Mobility Transistors (PHEMTs). The two dimensional (2D) heterojunction PISCES simulation used in this work [2] is based on the following models and assumptions:

- Poisson's and carrier continuity equations
- Impact ionization and carrier generation/recombination
- Field dependent mobility with fixed saturation velocity
- Drift-diffusion and hydrodynamic (HDM) models
- Energy balance model for hot carrier transport
- 60/40 rule for band discontinuity

Calculations [3] for quantized energy states were not considered in this work due to a deficiency of the software, which causes the 2DEG population to increase with the donor concentration with no upper boundary. However, since the 2DEG density is initially matched by the actual experimental values, hence this deficiency does not limit the carrier transport and charge control computations.

This study focused on examining some important PHEMT process and material related effects on gate recess and surface states, and 2DEG buffer charge injection, which have been empirically shown to affect PHEMT characteristics profoundly. Even though some of these effects are known in principle, it is useful to quantitatively assess the scale of influences of these parameters on PHEMT performance.

The construction of the PHEMT input file is based on the physical values obtained from either device profile design or experimental measurements. The basic device used in this simulation is a pulse doped PHEMT structure, with a quarter micron gate length and a 3.5-micron drain-to-source spacing. It consists of an undoped $\text{In}_{0.2}\text{Ga}_{0.8}\text{As}$ channel of 120 angstroms, an undoped $\text{Al}_{0.24}\text{Ga}_{0.76}\text{As}$ spacer layer of 30 angstroms, a pulse doped sheet charge of $4 \times 10^{12} \text{ cm}^{-3}$, a $2 \times 10^{17} \text{ cm}^{-3}$ doped $\text{Al}_{0.24}\text{Ga}_{0.76}\text{As}$ Schottky layer of 220 angstroms, and a $4 \times 10^{18} \text{ cm}^{-3}$ doped GaAs ohmic contact layer of 450 angstroms. Figure 1 shows the measured and simulated I-V characteristics of the baseline PHEMT, where the simulated I-V curves match nicely with

actual PHEMT measurement data, and show good agreement in pinch-off and soft breakdown characteristics.

During the construction of the baseline file, we found that certain special arrangements were needed to simulate the device characteristics correctly. One major step is to ground the buffer through a highly resistive contact (e.g., $> 1 \times 10^6$ ohms) in order to pinch off the device completely. Otherwise the simulated I-V characteristic can not be pinched off due to buffer charge accumulation or a self biasing effect as shown in the simulated electron concentration plot.

2. Gate recess and surface states

One of the most common variables and uncertainties in PHEMT processing is the control of the gate recess depth and spacing, which is affected not only by the etch chemistry but also the photoresist adhesion and preparation. For a typical PHEMT device, a short recess spacing of 300-500 Å and a surface state density of 1.5 to 2.0×10^{12} cm⁻² are determined to match the experimental data. However, this recess spacing can be extended to as long as 1500 Å or more under certain circumstances. The simulation shows that when the gate recess spacing increases, both the Idss and g_m decrease due to reduced charge injection current and increased series resistance, and the impact ionization breakdown behavior diminishes due to lowering of the peak channel electric field near the edge of gate electrode [4]. At the same time, the surface state density of the ungated recess region plays an important role. It is useful to perform a systematic series of simulations by varying both gate recess spacing and surface state density. Figure 2a and 2b illustrate the Idss and g_m as functions of gate recess spacing with surface state densities of 1.0, 2.0, 2.5, and 3.0×10^{12} cm⁻² as parameters (A) through (D), respectively. It is obvious that in the high surface state condition, the device characteristics are more strongly influenced by the recess spacing. For a typical PHEMT fabrication process, a surface state density of 1.5 to 2.0×10^{12} cm⁻² is representative for a wet chemically etched, silicon nitride passivated recess surface. In Figure 2a, the initial Idss drop from 250 Å to 500 Å is significant and somewhat independent of the surface state densities, which indicates a uniform reduction of sidewall injection current at the recess edge. When the recess spacing further increases, the charge injection component diminishes and the g_m and Idss become more strongly dependent on surface states, which deplete the ungated recess area and increase the parasitic series resistance.

Figure 3 shows Idss and g_m as a function of gate recess depth with a work function of 5.1 eV. The recess depth is defined as the distance between the gate electrode and AlGaAs spacer layer, which is 30 Å above the 2DEG channel. One can see that the g_m peaks at around 200 Å while the Idss decreases when the gate electrode is moved toward the 2DEG channel. When using a stop layer etch process for gate recess, these simulations become very useful in designing the optimum stop layer position for best obtainable g_m and estimating the total sheet charge required for a desired Idss.

3. 2DEG deconfinement and buffer layer charge injection

In a PHEMT structure, GaAs or AlGaAs is typically used as the buffer layer. However, there is a significant parasitic current flow through the buffer directly below the InGaAs channel. This is mainly due to the charge injection from the 2DEG populated InGaAs channel into the buffer as a result of a high channel electric field (i.e., 2DEG deconfinement). This charge

injection behavior results in unwanted current flow through the buffer underneath the gate, which influences not only the saturation current but also the output conductance and transconductance.

One approach to improve the buffer charge injection situation is to replace the normal GaAs buffer by a low temperature grown, highly resistive (i.e., with extremely low carrier mobility) GaAs layer [5,6]. Figure 4 shows the comparison of simulated total current flow between normal and highly resistive GaAs buffers, and shows that the current flow through the buffer is clearly suppressed by the highly resistive buffer. However, the simulation has also demonstrated that the 2DEG charge injection remains the same through comparing the electron concentration contour plots. Thus the current flow reduction is mainly due to the low mobility nature of carrier transport in such a buffer, where the injected electrons are decelerated due to frequent imperfection scattering. Because of the extremely low carrier mobility and velocity associated with the low temperature buffer, the injection current flow through the buffer essentially goes to zero which reduces Id_{ss} and output conductance, as shown in Figure 5. It should be mentioned that since the injected charge is “trapped” in the low mobility state of the low temperature buffer, the accumulated charges will eventually self bias the buffer to retard further injection until equilibrium is reached. Which implies that the low temperature or highly resistive buffers may improve the device isolation and output conductance, but the accumulated buffer charges could degrade the device high frequency performance at the same time.

4. Conclusion

We have demonstrated the usefulness of using a two-dimensional heterojunction device simulator for solving practical problems with PHEMT fabrication. Through systematic simulation, one can generate quantitative assessment of how the material and process parameters affect the PHEMT performance and utilize them as process control and trouble shooting guide. It also aids in understanding the device physics of PHEMT operation, which is valuable for specific device design and new concept demonstration.

Acknowledgements

The authors would like to express their thanks to J. Guan and J. Franklin for their technical assistance.

References

- [1] Z. Yu, D. Chen, L. So, R.W. Dutton, Integrated Circuit Laboratory Technical Report, Stanford University (1994).
- [2] Atlas Device Simulation Manual, Silvaco International, October (1996).
- [3] F. Stern, S. Das Sarma, Physics Reviews B, Vol. 30, Number 2 (1984) 840.
- [4] Y.C. Pao, C. Nishimoto, R. Majidi-Ahy, J. Archer, N.G. Bechtel, J.S. Harris, Jr., IEEE Transaction on Electron Devices, Vol. 37, No. 10 (1990) 2165.
- [5] F. Smith, A.R. Calawa, C.L. Chen, M.J. Manfra, L.J. Mahoney, IEEE Electron Device Lett. 9 (1988) 77.
- [6] M.R. Melloch, N. Otsuka, J.M. Woodall, A.C. Warten, J.L. Freeouf, Appl. Phys. Lett. 57 (1990) 1531.

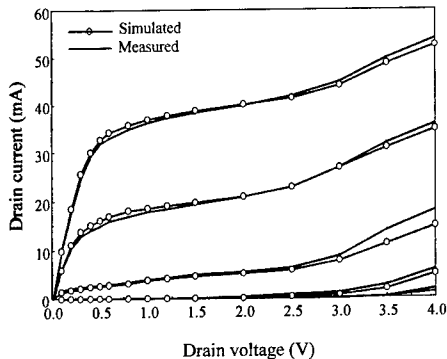


Figure 1 Comparison of simulated and measured 0.25 micron PHEMT I-V characteristics.

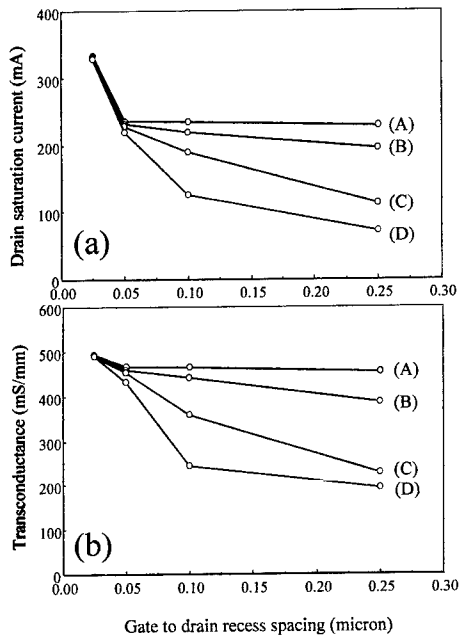


Figure 2 Comparison of (a) Id_{ss} and (b) gm as functions of gate recess spacing and surface state density of (A) 1×10^{12} , (B) 2×10^{12} , (C) 2.5×10^{12} and (D) $3 \times 10^{12} \text{ cm}^{-3}$, respectively.

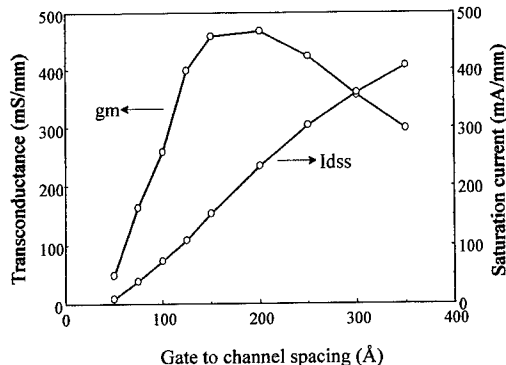


Figure 3 Id_{ss} and gm as a function of gate recess depth for a 0.25 micron PHEMT.

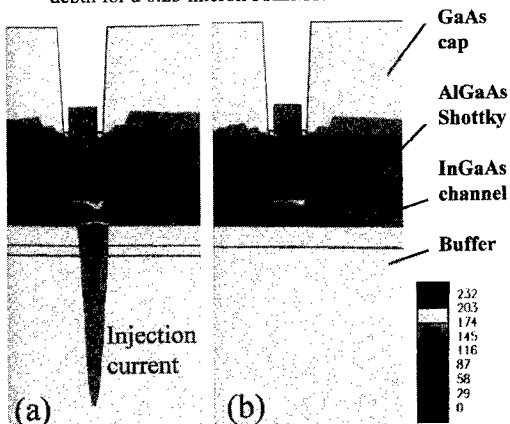


Figure 4 Comparison of current flow contour plots between (a) normal and (b) low mobility buffers, showing a strong normal buffer injection current.

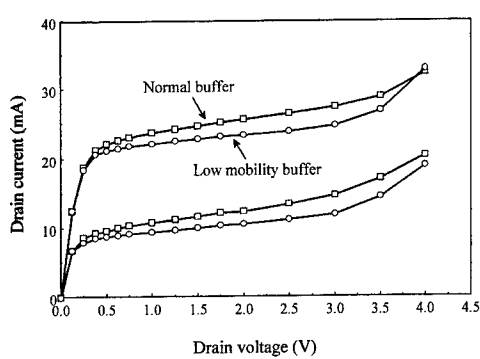


Figure 5 Comparison of 0.25 micron PHEMT I-V characteristics between normal and low mobility buffers.

Subject Index

Please note that the page numbers below refer to the title page of the paper containing the index entry.

- AlAs 329
- AlAs/GaAs 333
- AlGaAs 147
- AlGaAs/GaAs 45, 279, 291, 447, 455
- AlGaInN 227
- AlGaN 231, 431
- AlInN 227
- Alloys
 - II-VI 61
 - III-V 413
- AlSb 337
- Aluminium antimonide, see AlSb
- Aluminium arsenide, see AlAs and related entries
- Aluminium gallium arsenide, see AlGaAs
- Aluminium gallium indium nitride, see AlGaN
- Aluminium gallium nitride, see AlGaN
- Aluminium indium nitride, see AlInN
- Amorphous silicon 617
- Antimony 337
- As₂ flux 75
- Atomic force microscope 535, 577
- Auger analysis 353
- Avalanche multiplication 391
- Avalanche photodiodes 631
- Band edge discontinuity 391
- Band offsets 117, 167, 279
- Bandgap renormalization 187
- Beryllium diffusion 41
- Bias dependence 511
- Bragg reflector 121
- Breakdown 471
- Buffer 503
- Buffer layer thickness effect 11
- Bulk geometric structure 223
- Carbon 311
- Carbon content 53
- Carbon tetrabromide doping 395
- Carrier concentration saturation mechanism 87
- Carrier lifetime 479
- Carrier transport 391
- CBE, see Chemical beam epitaxy
- CBr₄ 151
- CCl₄ 151
- Characterization 61, 155, 163, 245, 287
- Charge buildup 613
- Charge storage 443
- Chemical beam epitaxy (CBE) 439
- Chemisorption 143
- Communications 515
- Compliant substrate 25
- Compliant universal (CU) 29
- Composite channel 483
- Composite emitter 439
- Compounds
 - III-V compounds 37
- Contact resistance 179, 353, 455
- Contact resistivity 175, 459
- Contacts 467
- Corner reflector 345
- Coupled electron waveguide 557
- Coupled nanostructure 557
- Critical points 593
- Cross incorporation 259
- Current 387
- Current density 307
- Cyclotron mass 275
- DBR, see Distributed Bragg reflector

- Deep levels 299, 307
 Defects 211, 283
 Delta doping 91, 245
 Detector 491
 Device characterization 341
 Diode 625
 Dislocation density 53
 Disorder 617
 Disordering 329
 Distributed Bragg reflector (DBR) 325
 Doping levels 503
 Double crystal X-ray rocking curve 255
 Dry etching 341
 DyAs 159
 DyP 159
 Electrical and optical anisotropy 183
 Electrical properties 53
 of layered structures 79
 Electroluminescence 413
 Electron device modelling 635
 Electron-electron interaction 543
 Electron transport 539
 Electronic interface properties 131
 Electronic structure 643
 Ellipsometry 239
 Emitters 379
 Energy gap 227
 Epitaxial films
 4" wafer 287
 Epitaxial growth
 overgrowth 621
 rate 143
 self-limited 71
 Epitaxy 155, 179
 selective area epitaxy 45, 83, 531
 Erbium 199
 Esaki diode 617
 Etching 337, 349
 selective 349
 Exact diagonalization 543
 Excess noise factor 631
 Excitons 195
 lifetimes 235
 Facets
 growth on 531
 FET, see Field effect transistors
 Field effect transistors (FETs) 427, 487, 597
 Flow rate modulation epitaxy 71
 Fluorescence-detected EXAFS 199
 f_{\max} 421
 Focused ion beam 353
 Frequency multiplier 515
 FTIR 311
 GaAs 131, 155, 179, 191, 499, 589, 621, 631
 and InGaAs/GaAs 577
 HEMT 383
 LEDs 417
 low-temperature 135
 low-temperature grown GaAs 507
 MOSFET 319
 patterned substrates 151
 semi-insulating 53, 621
 surface passivation 139
 GaAs/AlGaAs 287, 479
 (GaAsSb–GaInAs) superlattice 117
 Gain measurement 207
 GaInAs 383
 GaInAsP 99
 GaInN 231
 GaInP 439, 443
 GaInP/Ga(Al)As/GaInP DHBTs 435
 Gallium antimonide, see GaSb and related entries
 Gallium arsenide, see GaAs and related entries
 Gallium indium nitride, see GaInN
 Gallium nitride, see GaN and related entries
 GaN 11, 15, 211, 215, 219, 227, 235, 239, 349, 375, 427, 431
 (0001) 223
 cubic 5
 Er-implanted 203
 Mg-doped 215
 GaN/GaInN 371
 $\text{Ga}_2\text{O}_3(\text{Gd}_2\text{O}_3)$ 319

- GaP 199
 GaS 139
 GaSb 121, 337
 GaSb/InAs 259
 Gate source capacitance 495
 GdInP/GaAs 91
 Ge 467
 GeN
 isoelectronic impurities 271
 Germanium, see Ge
 Germanium nitride, see GeN
 Green's function 639
 GTO devices 363

 HBT, see Heterojunction bipolar transistors
 HEMT, see High electron mobility transistors
 Heterointerface 147
 Heterojunction bipolar transistors (HBTs) 435, 455, 459, 467, 439, 447
 AlGaAs/GaAs 451
 DHBT 443
 high-frequency performance 439
 Heterojunction field effect transistors (HFETs) 421, 483, 601, 609
 high-frequency 427
 high-power 427
 metamorphic 483
 Heterojunction interband tunneling 605
 Heterojunctions 167, 467, 647
 double heterojunction 487
 Heterostructure avalanche photodiode 391
 Heterostructure transistor 507
 Heterostructures 37
 pseudomorphic 91
 HFET, see Heterojunction field effect transistors
 HIFET, see High-frequency field effect transistors
 High electron mobility transistors (HEMTs) 91, 303, 341, 471, 435, 491, 635
 low-power 491
 low-temperature 491
 metamorphic 503
 pseudomorphic HEMT (PHEMT) 463, 475, 495, 647
 High-frequency field effect transistors (HIFETs) 463, 605
 High-frequency transistor 635
 High-temperature device 507
 High-index substrates 65
 Hydrazine 15
 Hydrogenation 307

 ICP 349
 Impact ionization measurements 435
 Impurity concentration 215
 (In, Ga)N
 cubic 5
 InAlAs/InGaAs
 HEMT 503
 InAs 483, 531, 589, 643
 InAs/AlSb/GaSb 593
 InAsSb 113, 569
 Indium arsenide, see InAs and related entries
 Indium gallium arsenide, see InGaAs and related entries
 Indium gallium nitride, see InGaN and related entries
 Infrared lasers 565
 InGaAs 57, 311, 395, 459
 In_{0.53}Ga_{0.47}As 171
 InGaAs/InAlAs/InGaAlAs/GaAs 49
 InGaAs/InGaAsP strained quantum well structures 103
 InGaAsP/AlGaAs 207
 InGaN 1, 375
 InGaP 307
 InGaP/GaAs 95
 HBT 511
 Injection 387
 InP 109, 117, 299, 303
 semi-insulating InP 295
 InSb 29
 In₂Se₃ 183
 Integrated twin-guide 345
 Inter-wire coupling 195

- Interband tunneling 593
 Interdiffusion 263
 Interface 57, 95, 263
 roughness 259
 state density 139, 319
 Intermediate-strain layers 103
 Intermixing 329
 Internal mechanical stresses 417
 Ion implantation 487
 Ionization path length 631
 Iron diffusion 479
 Kink effect 503
 Kirk effect 435
 Landau levels 187
 Laser-assisted growth 45
 Laser diodes (LDs) 1
 0.98 μm 103
 blue 1
 distributed feedback-laser diode 255
 Lasers 99, 113, 387, 553, 569, 625
 1.3 μm AlGaInAs/InP 399
 distributed feedback (DFB) laser
 109
 edge emitting lasers 547
 mid-infrared 569
 quantum well lasers 561
 surface emitting laser 345
 Lateral and vertical growth rates 151
 Lateral injection ridge quantum well
 387
 Lattice matching composition 283
 Lattice mismatched growth 25
 Layered structure 183
 LD, see Laser diodes
 LED, see Light emitting diodes
 Light emission 239
 Light emitting diodes (LEDs) 1, 113,
 569, 585
 influence of internal mechanical
 stresses 417
 Light excitation 499
 Liquid phase epitaxy 37
 Local oxidation
 anodization 577
 Low-frequency noise 341
 Low-frequency oscillation 499
 Low field transport and mobility 79
 Magnetoluminescence 187
 Magnetoresistance 275
 Magnetotunneling 593
 MBE, see Molecular beam epitaxy
 MESFET, see Metal semiconductor field
 effect transistors
 Metal semiconductor field effect
 transistors (MESFETs) 421, 471,
 499
 microwave 499
 Metal–semiconductor interface 179
 Metallization 175
 Metalorganic chemical vapor deposition
 (MOCVD) 45, 57, 113, 151, 215,
 231, 287, 311, 451,
 Metalorganic species
 chemistry of 143
 Metalorganic vapor phase epitaxy
 (MOVPE) 291, 219
 Metamorphic buffers 49
 Metastability 375
 Microcavity 553
 Microcavity devices 585
 Micromachined membrane 561
 Mid-infrared emitters 113
 MISFET 139
 MOCVD, see Metalorganic chemical
 vapor deposition
 Modeling 147, 581, 601
 MODFET 431
 Molar injection dependence 395
 Molecular beam epitaxial growth 409
 Molecular beam epitaxy (MBE) 5, 15,
 29, 33, 41, 49, 65, 75, 79, 99, 109,
 121, 125, 131, 147, 159, 163, 183,
 259, 307, 319, 371, 577, 589
 Monolithic integration 383
 Monte Carlo 147, 631
 Mosaic spread 29
 MOSFET 359
 MOVPE, see Metalorganic vapor phase
 epitaxy

- Multi-chamber UHV system 319
 Multidot columns 535
 Multiple-scattering cluster calculations 223
 Multiquantum barrier (MQB) 399
 N drag effect 5
 N-ion implantation 163
 Nanoelectronics 639
 Native oxide 403
 Neural networks 33
 Nitrides
 III-V Nitride 1
 Noise 447, 463, 609
 1/f noise 491
 low-frequency 447
 model 511
 parameters 511
 Non-destruction 287
 Nonlinear optics 573
 Nonstoichiometric GaAs 135
 n-type doping 211
 OEIC 383
 Ohmic contacts 171, 175, 427, 431, 455, 459
 Ohmic metallizations 353
 One-dimensional confinement 597
 One-step selective growth 151
 Optical communication 573
 Optical properties 65, 235
 Optoelectronic devices 41
 Optoelectronics 553
 Ordered dopant incorporation 245
 Ordering 87, 535
 Organic 379
 Oxidation 325, 329
 Palladium, see Pd
 Parameter extraction 495
 Patterned substrate 255
 Patterning 83
 Pd 171, 467
 Pd/Ge 455
 Peak-to-valley ratio 605
 Phonon bottleneck 525
 Phonon scattering 391
 Photo carrier profile 479
 Photocapacitance 299
 Photoconduction 303
 Photoconductivity characterization 565
 Photodetectors 585
 near-infrared photodetectors 395
 Photodiodes 409
 Photoexcited carriers 295
 Photoluminescence 131, 199, 215, 219, 231, 239, 279, 333, 371, 375, 613
 lifetime 283
 measurements 103
 of GaN impurities 271
 time-resolved photoluminescence 283
 Photon confinement 553
 Photoreflectance 57, 291
 Photoreflection 239
 Phototransistor 479
 Physical model 471
 PIN diode 163
 PIN photodiode 383
 PL
 site-selective PL 203
 PLD, See Pulsed laser deposition
 PLE
 site-selective PLE 203
 Positioning 531
 Power devices 363, 421
 Precipitation 135
 Pressure 279
 Principal component analysis 33
 Process modeling 33
 p-type doping
 Pulsed laser deposition (PLD) 11
 p-ZnSe 163
 Quantum confined Stark effect 613
 Quantum devices 515, 565, 639
 Quantum dots 65, 71, 525, 531, 539, 543, 547, 589, 643
 self-assembled and self-organized quantum dots 577
 Quantum transport 267

- Quantum wells 191, 403, 413, 537, 625
 double quantum well 275
 InGaAs/GaAs 333
 multiple quantum wells 231, 235, 291
 strained-layer multiple quantum well 255
 strained quantum well 207
 transport properties 275
 Quantum wires 65, 71, 195, 557
 atomically uniform 71
 coupled 557
 InGaAs 75
 Quasi-Fermi level 413
 Radiative recombination 413
 Raman scattering 211
 spectroscopy 337
 Raman spectroscopy 295
 Rare earth group V compound 159
 Reaction kinetics 143
 Reactive ion-beam etching 345
 Real space transfer 459
 Reciprocal space mapping 49
 Reflectance difference spectroscopy
 realtime in-situ control 87
 Reflection high-energy electron
 diffraction 33
 Reflectivity measurement 325
 Refractive index 121, 227
 Regrowth 431
 Reliability 447
 Resistless process 83
 Resonant cavity enhanced photodetector
 561
 Resonant interband tunneling 593
 Resonant interband tunneling diode
 (RITD) 83
 Resonant tunneling 597, 613, 617, 639
 Resonant tunneling diode 515, 581, 601, 609, 639
 transport 581
 Resonant tunneling transistor 609
 RHEED
 realtime in-situ control 87
- RITD, see Resonant interband tunneling diode
 Roughness 57
 RTD, see Resonant tunneling diode
 Sacrificial layer 29
 Sb-based solid solutions 37
 Scanning tunneling microscopy 245, 259
 Schottky barrier 167
 Schottky contact 621
 Secondary ion mass spectroscopy
 (SIMS) 311
 Selective oxidation 333
 Self-alignment process 487
 Self-assembled growth 525
 Self-assembled islands 535
 Self-assembly 135
 Self-heating 511
 Self-organization 535
 Semiconductors 61, 279, 387
 design and modelling 79
 device characterization 79
 III–V compound 79, 245
 III–VI compound 183
 laser diodes 207
 lasers 109, 403, 573
 narrow-gap 37
 power 359
 Raman laser 573
 Semi-metal 159
 Si 167
 doping 87, 219
 segregation 41
 SiC 359
 4H–SiC 363
 P–6H–SiC 353
 Silicon, see Si
 Silicon carbide, see SiC
 SIMS, see Secondary ion mass
 spectroscopy
 Simulation 475, 495, 625, 647
 Single crystalline 11
 Single electron tunneling 135
 SIT 421
 Solid source 99

- Space charge 379
 Spatially indirect type-II emission 117
 Spin-spin exchange 191
 Sputtering 61
 SRAM 601
 Stability 171
 Stimulated emission 371
 STM, see Scanning tunneling microscopy
 Stoichiometry 299
 Strain compensation 103
 Strain distribution 643
 Strain sensor 525
 Stresses 417
 Subband structure 557
 Sublevels 303
 Substrates
 (111)A 291
 Superlattice properties 267
 Surfaces
 coverage 143
 diffusion 75
 reconstruction 139
 termination 223
 Switching 95
 Thallium gallium arsenide 125
 Thallium indium arsenide 125
 Thermal effects 471
 Thin films 61
 Thyristor 363
 Ti 171
 Tight-binding method 643
 Titanium, see Ti
 Transistor 613
 Trap 379
 Trap-mediated excitation 203
 TSR 539
 Tunable vertical cavity lasers 561
 Tungsten 621
 Tungsten chemical vapor deposition 179
 Tunneling 605
 UMOS 359
 Undulation 255
 Unipolar devices 267
 VCO 605
 VCSEL, see Vertical cavity surface emitting lasers
 VCZ growth 53
 Vertical cavity surface emitting lasers 121, 325, 547
 V-grooved substrate 75
 Voltage controlled oscillator 495
 Water bonding 25
 Wavelength division multiplexing applications 561
 Wide bandgap semiconductors 235
 Wireless 515
 Wireless communications 475
 WN_x 459
 WSi gate 487
 X-ray CTR 263
 X-ray diffraction 219
 X-ray photoelectron diffraction 223
 Yellow luminescence 211
 Zeeman splitting 191
 Zinc oxide, see ZnO
 Zinc sulfide, see ZnS
 ZnO 11
 ZnS 167
 ZnS_xSe_{1-x} 283
 ZnSe/GaAs 263

Author Index

Please note that the page numbers below refer to the title page of the paper containing the index entry.

- Abare A C 367
- Abrokwah J 131
- Abstreiter G 49
- Agarwal A K 359, 363
- Agarwala S 409
- Ahmari D A 95, 467, 511
- Akasaki I 239
- Akeyoshi T 613
- Alam M A 625
- Albasha L 471
- Alferov Zh I 547
- Allerman A A 113, 569
- Alvis R 159
- Amano H 239
- Amano S 577
- Anderson W A 163
- Ando Y 609
- Andronescu S N 353
- Antipov V G 15
- Aoki S 263
- Arakawa Y 643
- Armour E 287
- Artús L 295
- Asbeck P M 443
- Asenov A 475
- Averbeck R 211
- Avrutsky I A 387
- Awano Y 539
- Bachem K-H 117
- Bächtold W 341
- Baillargeon J N 99, 109
- Balasubramaniam H 159
- Baltagi Y 57
- Baraff G A 625
- Barlage D W 511
- Barnes J 413
- Barnham K W J 413
- Baucom K C 569
- Bayraktaroglu B 447
- Beam III E A 601
- Beaumont S P 475
- Beck M 341
- Benz W 383
- Bhattacharya P 525
- Bicknell-Tassius R 33
- Biefeld R M 113, 569
- Bimberg D 547
- Bisaro R 155
- Bishop S G 203
- Blanks D K 639
- Blaugh J 499
- Blount M 187, 275
- Böhm G 49, 503
- Borsosfoldi Z 475
- Botchkarev A 427
- Bourgoin J C 155
- Bouteiller J-C 561
- Bowen R C 601, 639
- Bowers B 131
- Boykin T B 601
- Brandt C D 359, 363
- Brandt O 5, 211
- Brar B 167, 617
- Brech H 495
- Bremser M D 349
- Bronner W 41, 383
- Brown A 33
- Brown T 33
- Bru-Chavallier C 57, 219
- Bugge F 207
- Burkhart J H 113
- Burle N 155
- Burm J 427

- Button C C 435
 Cai W 25, 125, 395
 Cartwright A N 163
 Caruth D 463
 Casady J B 359, 363
 Catchen G L 125
 Chang G S 249
 Chang H C 163
 Chao B S 61
 Chen H 95
 Chen M-C 589
 Chen P F 443
 Chen Y J 409
 Chen Y K 319
 Cheng T S 413
 Cheskis D 303
 Chia C K 391
 Chik H 387
 Cho A Y 99, 109
 Cho H Y 307
 Cho S 291
 Choi I-H 151
 Choi Y 215
 Chong W K 171
 Choo H R 255
 Chor E F 171
 Chou W Y 249
 Chow D H 515
 Chow W 187
 Chu K K 427
 Chu S N G 99, 109, 159
 Chua S J 171
 Chui K 515
 Chumbes E M 91
 Chyi J-I 401
 Cidronali A 635
 Coldren L A 367
 Coleman J J 203
 Collodi G 635
 Contrata W 609
 Cook M J 45
 Cruscó R 295
 Cui D 311
 Curtis A P 95
 Dagnall G 33
 Dammann M 383
 David J P R 391, 435, 631
 Davis R F 349
 Däweritz L 65, 87
 De Anda F 37
 De Los Santos H J 515
 Deal M D 329
 DenBaars S P 367, 431
 Denecke R 223
 Dickey S A 291
 Dietrich R 121
 Dorsey D L 147
 Dorsey J 33
 Droopad R 131
 Dua C 439
 Dubois C 219
 Ducroquet F 311
 Dunlap H L 515
 Dunn G M 631
 Dunstan D J 279
 Dupuis R D 231, 375
 Duran H C 341
 Eastman L F 91, 427
 Eaves L 519
 Edinger K 353
 Eisenbach A 219
 Eiting C J 231, 375
 Ejekam F E 29
 Ekins-Daukes N 413
 El-Zein N 605
 Elyukhin V A 15
 Emerson D T 45
 Erbert G 207
 Eyink K G 29
 Ezaki T 543
 Fadley C S 223
 Faleev N N 15, 37
 Fay M 387
 Feld S A 325
 Fendrich J A 463
 Feng M 463, 511
 Feng Z C 287
 Fernando C 639

- Flitcroft R M 435
 Fobelets K 337
 Forchel A 121, 371, 553
 Foxon C T 413
 Frensley W R 639
 Fresina M T 511
 Friedland K-J 79
 Fuchs F 117
 Fujisaki S 103
 Fujita K 263
 Fujita Sg 263
 Fujita Sz 263
 Fujiwara Y 199
 Funato M 263
 Futatsugi T 539
 Ganser P 383
 Garcia J C 439
 Gaska R 387
 Gatzke C 337
 Gaymann A 41
 Goldman R S 303
 González-Díaz G 295
 Gorbachev A Yu 37
 Gornik E 267, 565
 Goronkin H 83, 593, 531, 605
 Gruber A 211
 Grattepain C 155
 Grave T 495
 Grey R 391
 Grotjahn F 41
 Grudowski P A 231, 375
 Grundmann M 547
 Grün N 383
 Guillot G 57
 Guriev A I 15
 Haigh D G 475
 Hamaguchi C 543
 Hamoudi A 557
 Hanser A D 349
 Hanson M 367
 Hara N 139
 Harff N E 275
 Harper J 259
 Harris Jr J S 11, 135, 329, 535, 561, 577, 647
 Hartmann Q J 95, 467, 511
 Hattendorf M L 467
 Hayden R K 519
 Heinrichsdorff F 547
 Heins M S 511
 Helm M 565
 Heng C H 171
 Henini M 519
 Herres N 117
 Hey R 79
 Heyman J N 565
 Hiramoto K 103
 Hobson W S 319
 Hong C-H 215
 Hong H 163
 Hong K 57, 311
 Hong M 249, 319
 Hong S-K 345
 Hopkinson M 279, 391
 Hornung J 41
 Hou H 187
 Houston P A 435
 Hryniwicz J V 409
 Hsia S K 463
 Hsin Y M 443
 Hsu S-H 409
 Huang J H 499
 Huang T F 11
 Huber J L 593
 Hung C-Y 135
 Hunter A T 581
 Hurm V 383
 Husain Z 387
 Hvozdara L 565
 Hwang J S 249
 Hwang W-Y 99, 109
 Hwu R J 159
 Hybertsen M S 625
 Ibáñez J 295
 Illegems M 341
 Iliadis A A 353
 Ito T 199

- Jadwisienczak W M 271
 Jakobus T 383
 Janes D B 597
 Jiang D S 211
 Jiang H 525
 Jiang H X 235
 Jiang S 167
 Jiménez-Sandoval S 61
 Jin Y 491
 Johnson F G 409
 Johnson M B 245
 Johnson R G 471
 Jones E D 187
 Jones K A 353
 Jovanovic D 639
 Kamath K 525
 Kamijoh T 333
 Kapolnek D 431
 Karlsson C 483
 Kaspi R 325
 Kawabe M 577
 Keller B P 431
 Keller S 367, 431
 Kempa K 267
 Khan M A 235
 Khirouni K 155
 Kiehl R A 135
 Kim B 215, 291
 Kim D 215, 283
 Kim D H 191, 195
 Kim D Y 307
 Kim E K 151
 Kim Hyung Mun 255
 Kim Hong Man 255
 Kim I-H 455, 459
 Kim J S 255
 Kim K 299
 Kim M D 307
 Kim M 379
 Kim S 203
 Kim S H 175
 Kim S-I 151
 Kim T I 175, 307
 Kim T-G 151
- Kim Y 151, 191, 195
 Kimura T 573
 Kirk W P 167
 Kishimoto S 613
 Klein P B 203
 Klimeck G 601, 617, 639
 Klotzkin D 525
 Kluftinger B 413
 Knowles M A 451
 Ko H S 191, 195
 Koenraad P M 245
 Koeth J 121
 Köhler K 41, 383
 Kohn E 507
 Kolagunta V R 597
 Kolbas R M 231, 375
 Komarov S A 535
 Komori K 557
 Konagai M 183
 Kop'ev P S 547
 Kostial H 79
 Kovalenkov O V 291
 Kozodoy P 367, 431
 Kramer G 593, 605
 Kraus S 503
 Kromann R 33
 Kruck P 565
 Kudriavtsev Yu A 15
 Kumar B R 159
 Kunihisa T 487
 Kuo H C 95
 Kuo J M 319
 Kurtz S R 113, 569
 Kwo J 249, 319
 Kwon Y H 307
 Kwon Y-S 345
 Lai T C 159
 Lake R 601, 617, 639
 Lambert D J H 375
 Lampert W V 29, 349
 Lan E Y 499
 Lareau R T 159
 Larson M 561
 Lay T S 319
 Lebedev A B 15
- www.wiley.com

- Ledentsov N N 547
 Lee D 283
 Lee E H 163
 Lee H-C 379
 Lee J I 215, 283
 Lee J Y 307
 Lee K 33
 Lee P P 159
 Lee T-W 455, 459
 Leem J-Y 283
 Leem Y A 191, 195
 Lemmerhirt D F 467
 Leng M 639
 Leuzzi G 635
 Li K F 631
 Li X 203
 Liaw J-W 401
 Liesegang J 223
 Lin C 95
 Lin C-C 561
 Lin C-H 259
 Lin H-H 589
 Lin J Y 235
 Lipinski M 371
 Lipka K M 507
 Litwin A 621
 Liu C T 319
 Lo Y-H 29
 Loehr J P 325
 López M 291
 López-López S 61
 Lothian J R 319
 Lott J A 547, 585
 Lozykowski H J 271
 Lubyshev D I 25, 125, 395
 Ludwig M 41, 383
 Luo H 163
 Lye B C 435
 Lyo S K 275
 Mack M P 367
 Mahalingam K 147
 Maier M 41, 49
 Main P C 519
 Majerfeld A 291
 Maksimov A 371
 Manes G 635
 Mani S 359, 363
 Mannaerts J P 249, 319
 Maracas G 605
 Marcus M A 319
 Marshall A F 135
 Maruhashi K 609
 Massengale A R 329
 Matsuhata H 71
 Matsumoto F 179
 Matuhata H 557
 May G 33
 Mayer T S 25, 125, 395
 Meléndez-Lira M 61
 Melliti R 291
 Melloch M R 597
 Micovic M 395
 Migitaka M 479
 Miller D L 25, 125, 395
 Miller J G 451
 Min S-K 151
 Mishra U 367, 431, 507
 Mishurnyi V A 37
 Miura N 519
 Miyamoto H 609
 Mizutani T 613
 Mohammadi S 439, 447
 Morais J 223
 Mori N 543
 Morkoç H 235, 427
 Mu J H 511
 Müller J 371
 Müller S 117
 Müllhäuser J R 5
 Murphy M J 427
 Muth J F 375
 Na M H 163
 Nagarathnam S 163
 Nagata K 315
 Nair V 605
 Nakagawa T 75
 Nakamura S 1
 Neal J 25, 395
 Nelson J 413
 Neubert M 53

- Nguyen N 507
 Nikishin S A 15
 Nishii K 487
 Nishitsuji M 487
 Nishizawa J 179, 299, 573
 Niu Z 65
 Noble M J 585
 Noh S K 283
 Norris T 525
 Nötzel R 65
 Ofuchi H 199
 Ogura M 71, 557
 Oh D K 255
 Ohno Y 613
 Ohsawa J 479
 Ohtsuka T 183
 Okada Y 577
 Okamoto N 139
 Okamoto T 183
 Olander E 383
 Olowolafe J O 227
 Ong D S 631
 Orloff J H 353
 Oshida Y 179
 Oster A 207
 Overgaard C 131
 Oyama Y 179, 299
 Pajot B 155
 Pan J-W 401
 Pan N 451
 Pao Y V 647
 Park H S 307
 Park H-M 455
 Park J 375
 Park J-W 439
 Park M-P 455, 459
 Park S H 455, 459
 Park Y K 151
 Passlack M 131
 Pavlidis D 57, 219, 311, 439, 447
 Pei S S 259
 Peng T 227
 Persson M 483
 Peter M 117
 Phillippe A 219
 Phillips J 525
 Pinto M R 625
 Piprek J 227
 Plimmer S A 391
 Ploog K H 5, 65, 79, 87, 211
 Plotka P 179
 Plummer J D 329
 Polimeni A 519
 Pollard R D 471
 Pond L L 507
 Popvici G 235
 Pratt A R 333
 Putero M 155
 Py M A 341
 Pyo H M 191, 195
 Pyun K E 255, 455
 Qui G 227
 Ramsteiner M 65, 211
 Rauch C 267
 Reed M A 593
 Rees G J 391, 631
 Reiche M 87
 Reithmaier J P 553
 Ren F 319
 Ren L 341
 Rhee S J 203
 Riechert H 211
 Roberts J S 413
 Robson P N 391, 631
 Röhner M 553
 Rorsman N 483
 Rosner S J 231
 Rowland L B 359, 363
 Rudolph P 53
 Ryum B R 455
 Sadwick L P 159
 Sagawa M 103
 Saigoh K 479
 Saito T 573, 643
 Sakuma Y 539
 Salemink H W M 245
 Salvador A 235

- Samic H 155
 Samuelson L 621
 Sanger P A 359, 363
 Sanz-Hervás A 291
 Schäfer F 553
 Schaff W J 427
 Schirmann E 499
 Schmid P 507
 Schmiedel T 191, 195
 Schuermeyer F 303
 Schulman J N 581, 643
 Schützendübe P 87
 Sciortino P F 109
 Scott D 95
 Seabaugh A 167, 601, 617
 Seaford M L 29
 Seifert M 53
 Seifert W 621
 Selberherr S 495
 Sergent A M 319
 Seshadri S 359, 363
 Sexl M 49, 503
 Shealy J R 45, 91
 Shelton B S 375
 Shen J 379
 Sheridan D C 359
 Sherriff R E 325
 Shi B Q 143
 Shima M 539
 Shimbo B N 577
 Shin E-J 215, 283
 Shiralagi K 83, 531
 Shmagin I C 231
 Shmagin I K 375
 Shubina T V 15
 Shur M 387
 Sibai A 311
 Sidorov D V 417
 Sidorov V G 417
 Siergiej R R 359, 363
 Simlinger T 495
 Simmons J A 187, 275
 Singh J 525
 Siweris H-J 495
 Smart J A 91
 Smirnov V M 37
- Smith M 235
 Smith R K 625
 Smith S A 349
 Snowden C M 471
 So F 379
 Sokolov V I 417
 Solomon G S 535
 Son C-S 151
 Son J-S 283
 Song N W 215
 Sosnowski T 525
 SpringThorpe A 387
 Spruytte S 11
 Stall R A 287
 Steinhoff R 167
 Stillman G E 95, 451, 467, 511
 Stoddart S T 519
 Stone D R 409
 Stradling R A 315, 337
 Strasser G 267, 565
 Strutz T 539
 Sugaya T 75
 Sugihwo F 561
 Sugimoto Y 543
 Sugiyama Y 75
 Sun D 405
 Suto K 179, 299, 573
- Tabatabaei S A 409
 Tabuchi M 199, 263
 Tager A A 387
 Taguchi E 539
 Tai C Y 329
 Takamori T 333
 Takeda Y 199, 263
 Talyansky V 353
 Tamura A 487
 Tanaka H 139
 Tang H 235, 427
 Tanigawa A 199
 Tanuma Y 75
 Taulanada I 451
 Temkin H 15
 Tews H 211
 Thayne I G 475
 Thibeault B 431

- Thompson A G 287
Tomich D H 29
Towner F J 409
Toyonaka T 103
Tränkle G 49, 503
Treat D W 405
Tronc P 291
Tsuchiya J 199
Tsui E S M 413
Tsui R 83, 531
Tu C W 143
Tu Y-K 401
Tyan S L 249

Uchida K 519
Uda T 487
Ueda T 11
Unterrainer K 565
Ustinov V M 547

Van der Wagt J P A 601
Vasil'ev V I 37
Venkat R 147
Villar C 291
Viswanath A K 215
Vu D P 451

Wagner J 117
Wang G 291
Wang S 483
Wang X-L 71, 557
Wankerl A 45
Watanabe A 573
Webb S J 315, 337
Webster D R 475
Weckwerth M V 275
Weimann G 49, 503
Weimer M 259
Weitzel C E 421, 507
Welser R E 451
Wenzel H 207
Wernersson L E 621
- Werthof A 495
Wetzel C 239
Whitaker M F 279
Wieder H H 303
Wiemer J 325
Wilk G D 617
Winkler K 117
Wirner C 539
Wolden C A 349
Wolter J H 245
Woo J C 191, 195
Wood M C 159
Woods M S 353
Wu Y-F 431

Xu J M 387
Xu J-H 379

Yamada A 183
Yamaguchi S 479
Yamamoto S 487
Yang B 5
Yang H 5
Yang Q 95, 467
Yokoyama M 139
Yokoyama N 539
Yokoyama T 487
Yonei K 75
Youtsey C 597
Yow H K 435
Yu J S 175
Yu Z 131
Yun C E 191, 195

Zeng K C 235
Zhang C 25
Zhang D 259
Zhang R 531
Zhou X 167
Zubrilov A S 15
Zull H 553